

Nanostructure Science and Technology

Masakazu Anpo
Prashant V. Kamat *Editors*

Environmentally Benign Photocatalysts

Applications of Titanium Oxide-based
Materials

 Springer

Environmentally Benign Photocatalysts

Nanostructure Science and Technology

Series Editor: David J. Lockwood, FRSC
National Research Council of Canada
Ottawa, Ontario, Canada

For further volumes:
<http://www.springer.com/series/6331>

Masakazu Anpo • Prashant V. Kamat
Editors

Environmentally Benign Photocatalysts

Applications of Titanium Oxide-based
Materials

 Springer

Editors

Masakazu Anpo
Department of Applied Chemistry
Osaka Prefecture University
Osaka, Japan
anpo@chem.osakafu-u.ac.jp

Prashant V. Kamat
Department of Chemistry
and Biochemistry
University of Notre Dame
Indiana, USA
pkamat@nd.edu

Series Editor

David J. Lockwood
National Research Council of Canada
Ottawa, Ontario
Canada

ISSN 1571-5744

ISBN 978-0-387-48441-9

e-ISBN 978-0-387-48444-0

DOI 10.1007/978-0-387-48444-0

Springer New York Dordrecht Heidelberg London

Library of Congress Control Number: 2010937642

© Springer Science+Business Media, LLC 2010

All rights reserved. This work may not be translated or copied in whole or in part without the written permission of the publisher (Springer Science+Business Media, LLC, 233 Spring Street, New York, NY 10013, USA), except for brief excerpts in connection with reviews or scholarly analysis. Use in connection with any form of information storage and retrieval, electronic adaptation, computer software, or by similar or dissimilar methodology now known or hereafter developed is forbidden.

The use in this publication of trade names, trademarks, service marks, and similar terms, even if they are not identified as such, is not to be taken as an expression of opinion as to whether or not they are subject to proprietary rights.

Printed on acid-free paper

Springer is part of Springer Science+Business Media (www.springer.com)

Preface

Over the past few decades, mankind has observed an unprecedented and remarkable growth in industry, resulting in a more prosperous lifestyle for peoples of many countries. In developing countries, however, explosive industrial growth is just now beginning to raise the living standards of the people. Most industries, especially in these developing countries, are still powered by the burning of fossil fuels; consequently, a lack of clean energy resources has caused environmental pollution on an unprecedented large and global scale. Toxic wastes have been relentlessly released into the air and water leading to serious and devastating environmental and health problems while endangering the planet and life itself with the effects of global warming.

To address these urgent environmental issues, new catalytic and photocatalytic processes as well as open-atmospheric systems are presently being developed that can operate at room temperature while being totally clean and efficient and thus environmentally harmonious. Essential to technologies harnessing the abundant solar energy that reaches the earth are the highly functional photocatalytic processes that can utilize not only UV light, but also visible light.

Titanium oxide-based catalysts are especially promising as some of the most stable, nontoxic, readily available photofunctional materials known today. The successful development of second-generation titanium oxide photocatalysts using an advanced metal ion-implantation technique, which was first reported at the TOCAT-3 international conference in 1998 in Tokyo, led to reactions that could be induced not only with UV light, but also visible light. Since then, efficiency has improved as new materials and synthesis methods have been developed.

Up until the early 1960s, scientists primarily investigated the effect of UV light irradiation of semiconducting catalysts on the rate and selectivity of catalytic surface reactions in connection with the semiconductor electric band theory. Since Honda and Fujishima's discovery in 1972 of the photosensitizing effect of TiO_2 electrodes on the electrolysis of water using Pt metal and TiO_2 semiconducting electrodes, investigations of the conversion of photon energy into useful chemical energy with photofunctional semiconducting catalysts have gained momentum.

The photocatalytic decomposition of water into H_2 and O_2 using semiconducting catalysts, such as TiO_2 particles, has also been investigated, and there have been many studies focusing on the mechanisms behind the primary processes of photocatalysis in order to prepare and design catalysts with high reactivity and efficiency. The small particle effect, size quantization effect, and high dispersion effect on photocatalysis were identified in the period 1980–1988, leading to the development of photofunctional zeolite catalysts that incorporated various transition metal cations, such as Ti^{4+} , Mo^{6+} , V^{5+} , et al., in their framework structures. Then, in the 1990s, the focus of the investigations shifted to the use of TiO_2 photocatalysts in the decomposition of toxic compounds dissolved in water and air since TiO_2 exhibited a high photocatalytic reactivity for the degradation of organic compounds into CO_2 and H_2O even under weak UV light irradiation from sunlight. In 1995, the photo-induced superhydrophilicity of TiO_2 thin film photocatalysts was observed by Fujishima et al., resulting in the use of TiO_2 thin films in photofunctional materials having self-cleaning and antifogging properties. Thus, not only powdered catalysts, but also thin film catalysts could be utilized in photofunctional materials in applications for creating and sustaining a cleaner and safer environment.

Through the years, we have seen a great evolution not only in catalytic and photocatalytic research, but also in various applications. TiO_2 catalysts are especially promising as some of the most stable, nontoxic, readily available and photofunctional materials known today. Since the development of visible light-sensitive second-generation TiO_2 photocatalysts using advanced ion-engineering techniques, such as metal ion-implantation and RF magnetron sputtering deposition, the challenge now is to engineer more highly efficient and effective TiO_2 photocatalysts that can operate under both UV and solar or visible, natural light.

This book covers the various approaches in the design of efficient titanium oxide-based photocatalysts by such methods as sol-gel, precipitation, dip-coating, metal implantation, and sputtering deposition. It will introduce the most recent advances in TiO_2 research and its potential applications as well as detailed and fundamental characterization studies on the active sites and mechanisms behind the reactions at the molecular level. This book should serve not only as a text for research into photochemistry and photocatalysis, but also to inspire additional applications into environmentally-harmonious technologies.

The editors would like to thank each contributor for his/her valuable efforts not only for their tireless research into the development of efficient photocatalysts, but also for their important role in making this world a better place for all.

Contents

Part I Introduction

- 1 Introduction**..... 3
M. Anpo and P. Kamat

Part II Synthesis and Characterization Studies of Highly Active Titanium Oxide-based Photocatalysts

- 2 Chemical Methods for the Preparation of Multifunctional Photocatalysts**..... 7
Jinlong Zhang, Ye Cong, and Masakazu Anpo
- 3 Second Generation Visible-Light-Active Photocatalysts: Preparation, Optical Properties, and Consequences of Dopants on the Band Gap Energy of TiO₂**..... 35
Nick Serpone, Alexei V. Emeline, Vyacheslav N. Kuznetsov, and Vladimir K. Ryabchuk
- 4 Preparation of Titanium Oxide-Based Powders and Thin Films of High Photocatalytic Activities Using Solvothermal Methods**..... 113
Hiroshi Kominami and Bunsho Ohtani
- 5 Preparation of Highly Transparent TiO₂-based Thin Film Photocatalysts by an Ion Engineering Method: Ionized Cluster Beam Deposition**..... 133
Masato Takeuchi and Masakazu Anpo

6 UV Raman Spectroscopic Studies on Titania: Phase Transformation and Significance of Surface Phase in Photocatalysis	153
Jing Zhang, Qian Xu, Zhaochi Feng, and Can Li	
7 Photoluminescence Spectroscopic Studies on TiO₂ Photocatalyst	185
Jianying Shi, Xiuli Wang, Zhaochi Feng, Tao Chen Jun Chen, and Can Li	
8 Surface Chemistry of TiO₂ Photocatalysis and LIF Detection of OH Radicals	205
Yoshio Nosaka	
9 Local Structures, Excited States, and Photocatalytic Reactivities of “Single-Site” Ti-Oxide Photocatalysts Constructed Within Zeolites or Mesoporous Materials	217
Masaya Matsuoka and Masakazu Anpo	
Part III Development of Visible Light-Responsive Titanium Oxide Photocatalysts	
10 Visible-Light-Responsive Titanium Dioxide Photocatalysts	235
Jinkai Zhou and X.S. Zhao	
11 Development and Sensitization of N- or S-Doped TiO₂ Photocatalysts	253
Teruhisa Ohno and Toshiki Tsubota	
12 Visible Light-Responsive Titanium Oxide Photocatalysts: Preparations Based on Chemical Methods	277
Marcos Fernández-García, Arturo Martínez-Arias, and José C. Conesa	
13 Development of Well-Defined Visible Light-Responsive TiO₂ Thin Film Photocatalysts by Applying a RF-Magnetron Sputtering Deposition Method	301
Masato Takeuchi and Masakazu Anpo	

Part IV Photocatalytic Reactions for Environmentally-Harmonious Applications

- 14 Photo-assisted Mineralization of the Agrochemical Pesticides Oxamyl and Methomyl and the Herbicides Diphenamid and Asulam.....** 321
Hisao Hidaka, Teruo Kurihara, and Nick Serpone
- 15 Purification of Toxic Compounds in Water and Treatment of Polymeric Materials** 345
Ho-In Lee, Jae-Hyun Kim, Han-Su Lee, and Weon-Doo Lee
- 16 Development of Highly Active Titanium Oxide Photocatalysts Anchored on Silica Sheets and their Applications for Air Purification Systems.....** 403
Takeshi Kudo, Yuko Kudo, Akira Hasegawa, and Masakazu Anpo
- 17 Photocatalytic Application of TiO₂ for Air Cleaning.....** 415
Yong-Gun Shul, Hak-Soo Kim, Hyun-Jong Kim, and Myung-Keun Han
- 18 Photocatalytic Removal of Gas-Phase Elemental Mercury Using TiO₂** 437
Tai Gyu “Teddy” Lee
- 19 Photocatalytic Purification of Benzene in Air.....** 451
Xinchen Wang and Xianzhi Fu
- 20 The Effect of Addition of Pt on the Gas Phase Photocatalysis over TiO₂.....** 479
Deniz Uner
- 21 Photoreactions of Organic Compounds with TiO₂ Single Crystal Surfaces** 503
Hicham Idriss

Part V Photo-Induced Superhydrophilicity for Materials with Self-Cleaning Properties	
22 Investigations of the Photoinduced Superhydrophilicity of the TiO₂ Photocatalyst Surface by Near-Infrared Spectroscopy	527
Masato Takeuchi, Gianmario Martra, Salvatore Coluccia, and Masakazu Anpo	
Part VI Photocatalytic Water-splitting for the Evolution of H₂ from H₂O	
23 Photocatalytic Hydrogen Production from Water on Visible Light-Responsive TiO₂ Thin Films Under Solar Light Irradiation	545
Masaaki Kitano, Masato Takeuchi, Masaya Matsuoka, Michio Ueshima, and Masakazu Anpo	
24 Construction of Solid-State Thin Film Solar Cell by Applying Visible Light-Responsive TiO₂ Thin Film Materials	561
Masaya Matsuoka, Masayuki Minakata, Afshin Ebrahimi, Masakazu Anpo, Hung-chang Chen, and Wen-ting Lin	
Part VII Photocatalytic Organic Syntheses	
25 Photocatalytic Transformations of Sulfur-Based Organic Compounds	579
Alexander V. Vorontsov and Panagiotis G. Smirniotis	
26 TiO₂-Based Photocatalysis for Organic Synthesis	623
Vincenzo Augugliaro, Tullio Caronna, Agatino Paola, Giuseppe Marci, Mario Pagliaro, Giovanni Palmisano, and Leonardo Palmisano	
27 Photocatalytic Organic Syntheses	647
Hisao Yoshida	

Part VIII Renewable Energy from the Photocatalytic Reduction

- 28 Renewable Energy from the Photocatalytic Reduction of CO₂ with H₂O..... 673**
Jeffrey C.S. Wu

Part IX Photofunctionalization

- 29 Photofunctionalization of TiO₂ for Optimal Bone-titanium Integration: A Novel Phenomenon of Super Osseointegration 699**
Takahiro Ogawa

Part X Conclusions and Emerging Applications

- 30 Emerging Applications of TiO₂ -Based Composites..... 717**
Prashant V. Kamat and Masakazu Anpo

- Index..... 741**

Part I
Introduction

Chapter 1

Introduction

M. Anpo and P. Kamat

These past decades, mankind has embarked on an unprecedented and remarkable growth in industry that has led to a more prosperous lifestyle for the people of many countries. And in many developing countries, such explosive industrial growth is just now beginning to raise the living standards of the people. However, most industries, especially in these developing countries, are still powered by the burning of fossil fuels so that the lack of clean energy resources has caused environmental pollution also on an unprecedented, huge global scale. Toxic wastes have been relentlessly released into the air and water, leading to serious and devastating environmental and health problems while endangering the planet itself with the effects of global warming.

To address these urgent issues, new catalytic and photocatalytic processes and open-atmospheric systems, which can operate at room temperature and are totally clean, safe and efficient, and thus environmentally harmonious, are presently being developed. In particular, highly functional photocatalytic processes that can utilize not only UV but also with visible light will be essential in technologies that can harness the abundant solar energy that reaches the earth.

Titanium oxide-based catalysts are especially promising as one of the most stable, nontoxic, easily available photofunctional materials known today. Previously, the successful development of second-generation titanium oxide photocatalysts using an advanced metal ion-implantation technique led to reactions that could be induced not only with UV but also visible light. Since then, not only has efficiency been improved but new materials and synthesis methods have also been developed. This book will cover the various approaches to the design of efficient titanium oxide-based photocatalysts by methods such as sol-gel, precipitation, dip-coating, metal implantation, and sputtering deposition. It will cover the most recent advances in TiO₂ research and their potential applications as well as detailed and fundamental characterization studies on the active sites and mechanisms behind the reactions at the molecular level. The book should serve not only as a text for research into photochemistry and photocatalysis but also to inspire more applications into environmentally-harmonious technologies.

Part II
Synthesis and Characterization Studies
of Highly Active Titanium Oxide-based
Photocatalysts

Chapter 2

Chemical Methods for the Preparation of Multifunctional Photocatalysts

Jinlong Zhang, Ye Cong, and Masakazu Anpo

Abstract Recent research trends of the preparation and characterization of highly efficient titanium oxide-based photocatalysts modified by different methods are reviewed on the basis of studies done in our laboratory. Special attention is focused on the preparation and characterization of TiO₂ photocatalysts such as control of the crystalline phase and morphology; the synthesis of mesoporous structured titania; and modification by nonmetal doping, transitional metal doping, noble metal depositing, as well as various combinations of these methods. A proposed mechanism concerning the synergistic effects is discussed to explain the improvement of the photocatalytic activities.

1 Introduction

Nanosized TiO₂, one of the most promising photocatalysts, has been the focus of various investigations in the photocatalytic degradation of organic pollutants, dissociation of water, solar energy conversion, and disinfection (Fujishima et al. 2001; Hu et al. 2003; Yu et al. 2005; Hoffmann et al. 1995; Kamat 1993; Takeuchi et al. 2001; Kitano et al. 2005; Matsuoka et al. 2005a, b; Kikuchi et al. 2006; Kitano et al. 2007c). However, due to its large band gap of 3.2 eV, TiO₂ can only be excited by a small UV fraction of solar light, making it impractical for use under natural sunlight. The high rate of electron–hole recombination also results in a low quantum yield and poor efficiency for photocatalytic reactions.

J. Zhang (✉)

Laboratory for Advanced Materials and Institute of Fine Chemicals, East China University of Science and Technology, Shanghai 200237, PR China
e-mail: jlzhang@ecust.edu.cn

In order to address these concerns, there have been various attempts to sensitize TiO_2 for much larger visible light regions. One of these investigations has been the chemical doping of TiO_2 with transition metals ions (Kato and Kudo 2002; Choi et al. 1994; Anpo 1997, 2000a, b, 2004; Anpo et al. 1998, 1999; Anpo and Takeuchi 2003). A large bathochromic shift of light absorption for TiO_2 was observed with the doping of such transitional metals (Choi et al. 1994; Yamashita et al. 2002); however, the effect of the dopant transitional metals on the photocatalytic activity has been inconclusive (Zhang et al. 1998; Araña et al. 2002). Transitional metals chemically doped in TiO_2 can introduce donor and/or acceptor impurity energy levels in the wide forbidden band of TiO_2 , allowing the photocatalyst to exhibit visible light response. Observations on the kinetics of the excited electrons and holes show the lifetime of these charge carriers to change upon the doping of transitional metals (Yang et al. 2004).

In line with the concept of metal doping, noble metal deposition has also been actively investigated (Liu and Juang 2004; Xu et al. 2002; Kitano et al. 2006). Metal deposition is assumed to act as traps for the photo-induced electrons, leading to a reduction in the electron-hole recombination. However, it has also been confirmed that the catalytic properties of noble metals depend greatly on the preparation methods, leading to differences in the size of the Au particles and their interaction with the supports (Haruta 1997). As has been established, only highly dispersed noble metal-loaded TiO_2 has been shown to be active for various reactions (Rodriguez et al. 2002). Thus, an important challenge is to find a way to prepare highly dispersed, microsize noble metal-deposited TiO_2 .

Recently, it has been found that doping or modification with nonmetals such as boron (Zhao et al. 2004), carbon (Li et al. 2005c; Sakthivel and Kisch 2003; Ohno et al. 2004), nitrogen (Asahi et al. 2001; Sathishi et al. 2005; Chen and Burda 2004; Li et al. 2006; Kitano et al. 2007a, b; Cong et al. 2007a, b), and sulfur (Ohno et al. 2003) can shift the absorption edge of TiO_2 to lower values of energy. Asahi et al. (2001) have reported that $\text{TiO}_{2-x}\text{N}_x$ films and powders reveal a dramatic improvement over pure titanium dioxide under visible light in their optical absorption and photocatalytic activity. According to their hypothesis, the substitution doping of N can contribute to the narrowing of the band gap by mixing its 2p state with O 2p states. Thus, success in nitrogen doping and increase in the photocatalytic activity of TiO_2 in visible light regions will lead to the use of these photocatalysts in various applications such as the oxidation of CO, ethanol, gaseous 2-propanol, acetaldehyde, NO_x , and the decomposition of dyes such as methylene blue.

Our group has carried out extensive research on several aspects in the preparation of high performance visible and UV light reactive TiO_2 such as control of the crystalline phase and morphology; the synthesis of mesoporous structured titania; and modification by nonmetal doping, transitional metal doping, noble metal depositing, as well as various combinations of these methods. The presented work is a summary of the studies that have been done in our laboratory and the work in the related area reported by other groups.

2 Preparation and Mechanism in the Control of the Crystalline Phase and Morphology of Titania

2.1 Preparation of Controlled Crystalline Phase Titania by a Microemulsion-Mediated Hydrothermal Method

Nanocrystalline TiO_2 catalysts with different anatase/rutile ratios and high surface area (113–169 m^2/g) were prepared at low temperature by a microemulsion-mediated hydrothermal method. The contents of the anatase and rutile phase in the TiO_2 powders were successfully controlled by changing the mole percentage of the SO_4^{2-} in the Cl^- and SO_4^{2-} $n_{\text{SO}_4^{2-}} / (n_{\text{Cl}^-} + n_{\text{SO}_4^{2-}}) \times 100$ in the aqueous phase of microemulsion.

The X-ray diffraction patterns (not shown) indicated that the S-100, S-1.60, and S-0.00 samples are pure anatase or rutile, while the other samples consist of both anatase and rutile. The content of the anatase phase increased with an increasing in the mole percentage of SO_4^{2-} in the range of 0–1.6. When the mole percentage of SO_4^{2-} was adjusted to more than 1.60% in the preparation procedure, only an anatase phase was observed in the TiO_2 powder. The content of the anatase phase, thus, increased with an increase in the concentration of SO_4^{2-} in the aqueous phase of microemulsion in some range and a large amount of SO_4^{2-} resulted in the presence of only an anatase phase.

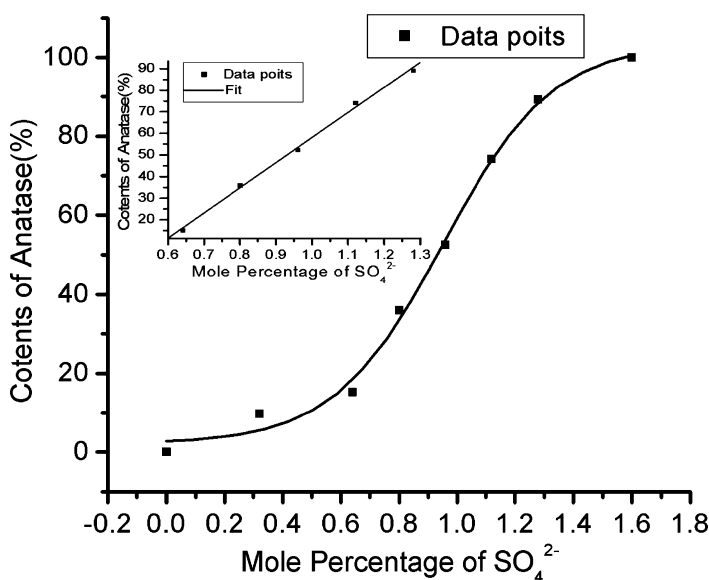


Fig. 1 Relationship between the content of anatase and the mole percentage of SO_4^{2-} . The inset shows the linear relationship of samples S-1.28, S-1.12, S-0.96, S-0.80, and S-0.64

In order to study the relationship between the concentration of the anion and content of the anatase phase of the prepared TiO_2 , it was found that the mole percentage of SO_4^{2-} in Cl^- and SO_4^{2-} and the content of the anatase phase in the TiO_2 powder showed an S-shape relationship (Fig. 1). It is interesting to note that the S-1.28, S-1.12, S-0.96, S-0.80, and S-0.64 samples can be reasonably described by a linear relationship (Fig. 1, inset). These results imply a good control of the

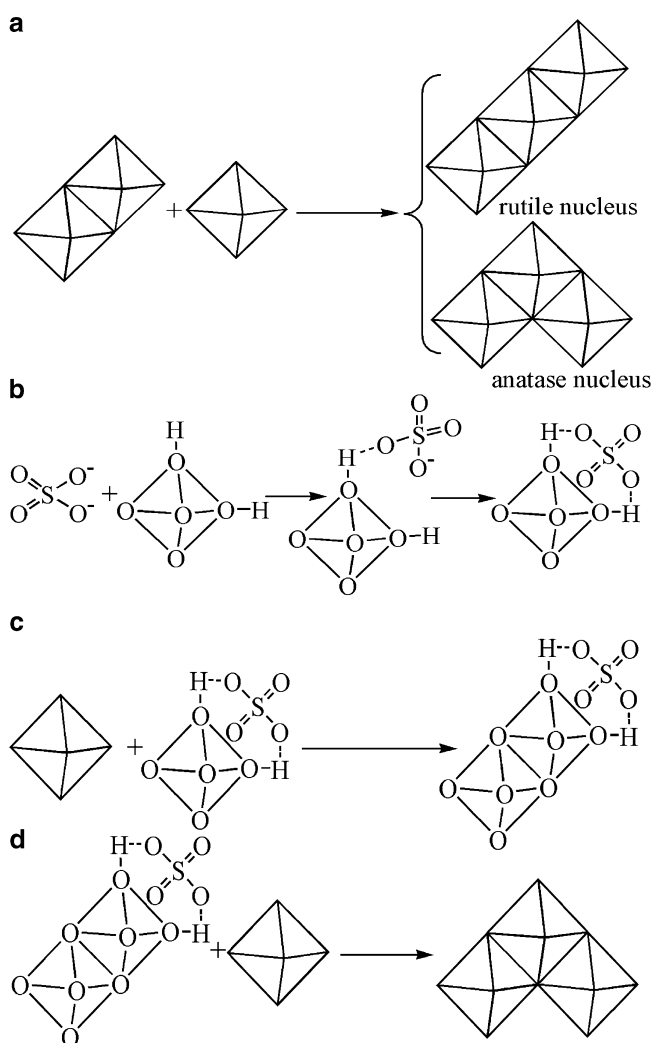


Fig. 2 Proposed mechanism: (a) orientation of the third octahedron determines whether a rutile or anatase nucleus is formed; (b) interaction between SO_4^{2-} and TiO_6^{2-} octahedral hydroxyls; (c) two TiO_6^{2-} octahedra share edges in the presence of SO_4^{2-} ; and (d) formation of anatase in the presence of SO_4^{2-}

content of the anatase and rutile phase around the anatase content of 15–90% by varying the proportion of Cl^- and SO_4^{2-} in the aqueous phase of microemulsion.

From metal alkoxide to the formation of metal oxide, there are two processes: hydrolysis and polycondensation (Wang and Ying 1999). When the titanate alkoxide reacts with water, the titanium ion first increases its coordination by using its vacant d -orbitals to accept oxygen electron pairs from the nucleophilic ligands (such as the $-\text{OH}$ group) (Livage et al. 1988). Consequently, the titanium ion forms an octahedral structure of $\text{Ti}(\text{O})_m(\text{OH})_n(\text{H}_2\text{O})_{6-m-n}^{(2m+n-4)-}$. Since the reaction is performed under an acidic medium, only the $-\text{OH}$ and $-\text{OH}_2$ groups will be present and the octahedral structure of the titanium ion becomes $\text{Ti}(\text{OH})_m(\text{H}_2\text{O})_{6-m}^{(m-4)-}$ (Gopal et al. 1997). The structure then dehydrates and is polycondensed into the final precipitate. All of the TiO_2 crystal structures consist of TiO_6^{2-} octahedra, which share edges and corners in different manners that result in the formation of different crystal phases. Octahedra in anatase share four edges and are arranged in zigzag chains, [221] while the rutile octahedra share only two edges and form linear parallel chains [001] (Gopal et al. 1997; Fahmi et al. 1995; Penn and Banfield 1999; Li et al. 2004b).

The mechanism of forming anatase in the presence of SO_4^{2-} is proposed in Fig. 2. In the formation of the anatase or rutile nucleus, the placement of the third octahedron is very important and determines whether a rutile or anatase nucleus is formed (Fig. 2a) (Gopal et al. 1997). However, the presence of SO_4^{2-} would influence the orientation of the third octahedron. When SO_4^{2-} ions exist in the acid reaction media, they interact with the octahedral hydroxyls by static electricity (Fig. 2b). The presence of a SO_4^{2-} bidentately bounding to the titania could be confirmed by the FT-IR spectra (not shown). Similar observations have been reported earlier in the case of SO_4^{2-} on ZrO_2 in studies by IR spectroscopy and theoretical calculations using an ab initio method (Babou et al. 1993, 1995). Because of the steric effect of SO_4^{2-} , the octahedron with SO_4^{2-} and another octahedron would polycondense along converse directions in order to decrease the repulsion (Fig. 2c), and the orientation of the third octahedron more easily forms an anatase nucleus (Fig. 2d). The more SO_4^{2-} there is, the more anatase nucleus can be formed. The TiO_2 clusters grow further on the nucleus and then form an anatase phase. It has been reported that the presence of SO_4^{2-} accelerated the growth of TiO_2 clusters to anatase (Zhang and Gao 2003). On the other hand, there is a weak steric effect for Cl^- due to its small radius. Meanwhile, the addition of Cl^- generally favors the formation of rutile crystallites (Zhang et al. 2000; Kittakal et al. 1997). As a result, different rutile/anatase mixtures can be prepared by changing the proportion of Cl^- and SO_4^{2-} in the aqueous phase of microemulsion.

2.2 Preparation of TiO_2 with Different Crystalline Phases and Morphologies Under Ultrasound Irradiation

Nanocrystalline TiO_2 powders were rapidly prepared by the hydrolysis of $\text{Ti}(\text{OC}_4\text{H}_9)_4$ under ultrasound irradiation. Moreover, the influences of acids (HCl,

HNO₃, and H₂SO₄) as well as their corresponding salts on the crystalline phase and morphology of the products were investigated.

Our experiments show that increasing the HCl concentration favors the formation of rutile and restrains the formation of anatase. When $[\text{HCl}] \leq 0.5 \text{ M}$, the products are mainly anatase and contained a little brookite. At $0.8 \text{ M} \leq [\text{HCl}] \leq 1.0 \text{ M}$, a mixture of anatase, rutile, and brookite is formed. At $[\text{HCl}] = 1.1 \text{ M}$, bicrystalline phases of anatase and rutile were obtained. When $[\text{HCl}] \geq 1.3 \text{ M}$, the anatase phase disappeared and only a pure rutile phase was formed. With an increase in HCl concentration from 1.3 to 4.0 M, the average particle size decreased from 8.3 to 6.5 nm. In addition, NaCl and KNO₃ had no evident influence on the crystalline phase of the products. Meanwhile, the influence of HNO₃ on the crystalline phase was similar to that of HCl. Prepared in either H₂SO₄ or Na₂SO₄

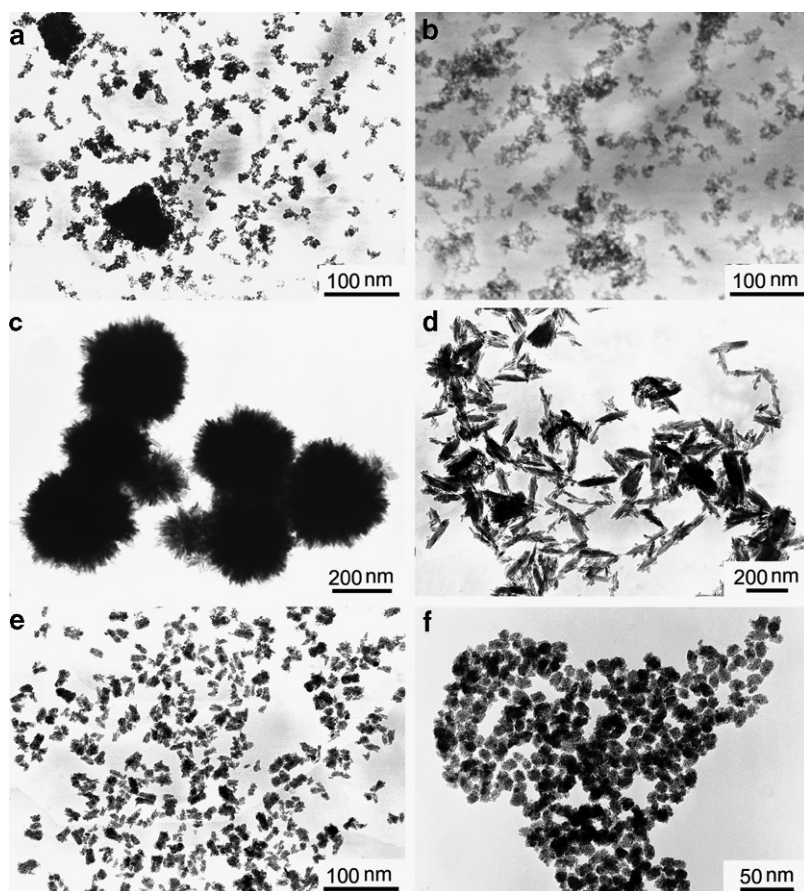


Fig. 3 TEM images of TiO₂ samples prepared in a solution of (a) H₂O (sample A), (b) 2 M NaCl (sample J), (c) 2 M HCl (sample G), (d) 2 M HCl containing CTAB ($1.5 \times 10^{-4} \text{ M}$), (e) 2 M HNO₃ (sample M), and (f) 1 M H₂SO₄ (sample Q)

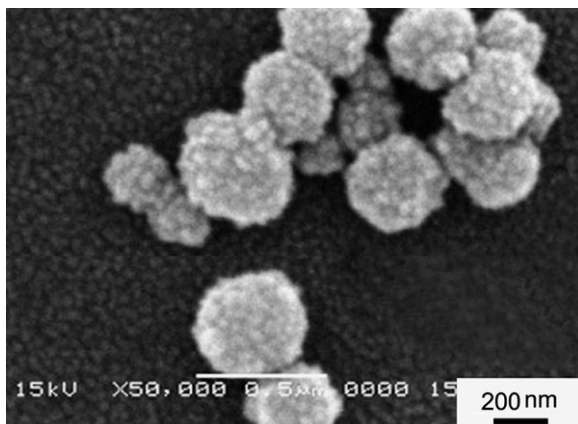


Fig. 4 SEM image of sample G (prepared in 2 M HCl)

solutions, all the samples were pure anatase phase. This indicates that the acidity plays a key role in determining the crystalline phase and SO_4^{2-} favors the formation of anatase.

TEM and SEM images were investigated to observe the morphology of the obtained TiO_2 particles. As shown in Fig. 3a and b, the TiO_2 particles prepared in water or 2 M NaCl have no regular shapes. Similar results were also found for KNO_3 and Na_2SO_4 (TEM images not shown). The influence of HCl, HNO_3 , and H_2SO_4 on the morphology are shown in Fig. 3c, e, and f, respectively. Prepared in 2 M HCl, the primary hair-like rutile TiO_2 particles were found to agglomerate, leading to ball-like aggregates with a size of several ten to several hundred nanometers in diameter (Fig. 3c). From SEM analysis of this sample (Fig. 4), it was clearly seen that the ball-like aggregate consists of oriented combinations of spherical particles. The sizes of the spherical particles varied from 10 to 50 nm in diameter. According to Yin et al. (2002), the acidity of the reaction solution plays a critical role in the formation of the particle aggregates. The surface properties of TiO_2 could be changed by protonation as follows (Bahnmann et al. 1984): $\text{TiO}_2 + n\text{H}^+ = \text{TiO}_2\text{H}_n^{n+}$, at $\text{pH} < 3.5$. The agglomeration of rutile TiO_2 under highly acidic conditions could be attributed to hydrogen bonding among the protonated rutile nanocrystallites. Prepared in 2 M HNO_3 solution, short rod-like crystallites were formed (Fig. 3e). Moreover, when prepared in 2 M H_2SO_4 solution, the obtained anatase crystallites were predominately composed of well-dispersed oblate habitus with an average diameter of about 12 nm (Fig. 3f), which were found to be close to the average crystallite sizes estimated by XRD. The high dispersion of the crystallites may be relative to the presence of SO_4^{2-} , which has been confirmed by the bidentately bonding on the surface of TiO_2 by static electricity measurements (Yan et al. 2005).

It is known that the presence of inorganic and organic anionic species in the starting solution influences the nucleation, crystal growth, and the morphology of

the particles (Wang et al. 2004; Stathatos et al. 1997). Here, the influence of the cationic surfactant cetyltrimethylammonium (CTAB) on the morphology of the TiO_2 particles was examined by a 2 M HCl solution containing CTAB as the starting solution. In Fig. 3d, it was found that the addition of a small amount of the surfactant (1.5×10^{-4} M in reaction solution) leads to changes in the morphology of the TiO_2 crystallites from spherical particles to rod-like, spindle-like, and broom-like particles. By careful observation, it was seen that the rod-like, spindle-like, and broom-like particles consist of many needle-shaped primary particles. It is confirmed that the morphology of the TiO_2 crystallites can be modified by the addition of surfactants, which may adsorb on the surface TiO_2 and modify the surface energies depending on the difference in crystallographic faces (Jun et al. 2003).

3 Synthesis of Mesoporous TiO_2 with High Photocatalytic Activity

Since the mesoporous silica was successfully synthesized by Mobile in 1992, many efforts have been devoted to the field of mesoporous transition metal oxides for their distinctive properties (Zhang and Banfield 1998). However, there are problems that need to be resolved in order to obtain mesoporous TiO_2 with high photocatalytic activity. On the one hand, mesoporous TiO_2 synthesized by conventional approaches using a surfactant as the template has poor photocatalytic activity since the surfactant is bound so tightly to the mesoporous TiO_2 that it cannot be removed entirely by either calcination at low temperatures or solvent extraction (Antonelli and Ying 1995; Do 1999; Stone and Davis 1998). On the other hand, mesoporous TiO_2 calcined at low temperatures or extracted by solvents to remove the template often has an amorphous or semicrystalline structure resulting in negligible photocatalytic activity. Calcination at high temperatures is, thus, necessary to obtain crystalline TiO_2 . However, crystallization for mesoporous TiO_2 takes place at high temperatures (723–823K) and is always accompanied by the total collapse of the mesoporous structure due to the extensive growth of the nanocrystals. It is known that anatase has higher photocatalytic activity than amorphous, so the challenge is to synthesize anatase mesoporous TiO_2 with high photocatalytic activity.

Thus, two aspects of our work is discussed, i.e., the synthesis of a mesoporous TiO_2 with high photocatalytic activity by assembling nanocrystalline particles with dodecylamine (DDA) as organic linkers and the synthesis of La^{3+} doped mesoporous TiO_2 by a similar self-assembly (EISA) method, leading to mesoporous structures with highly crystalline walls and high photocatalytic activity.

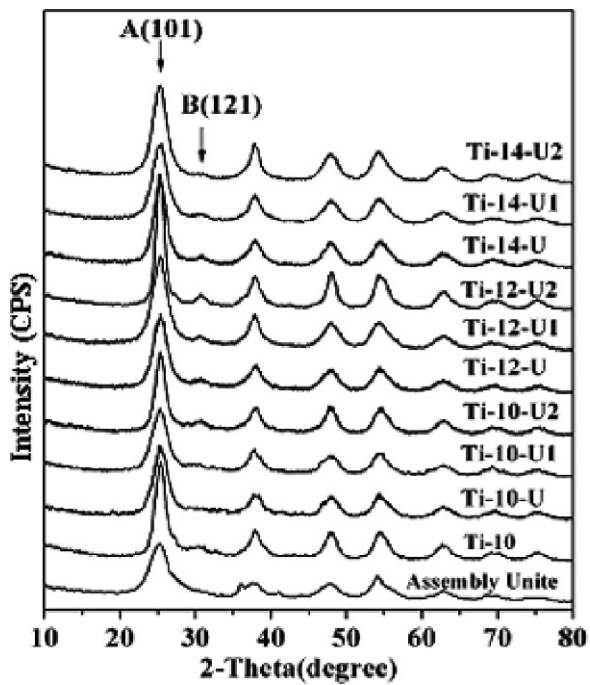


Fig. 5 Wide-angle XRD patterns of the assembly units and the samples prepared under different conditions

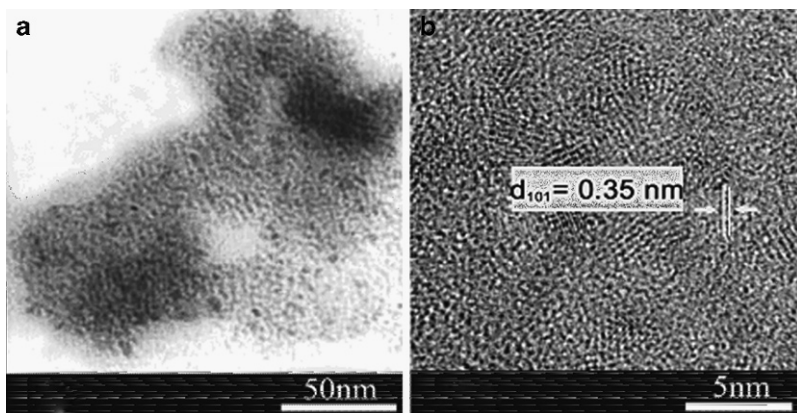


Fig. 6 (a) TEM image and (b) HRTEM image of the Ti-10-U sample

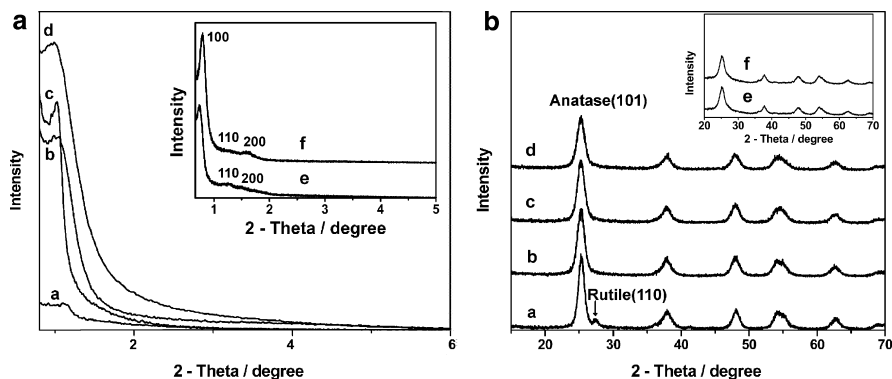


Fig. 7 Low-angle powder XRD patterns and wide-angle powder XRD patterns of as-synthesized and calcined samples: (a) undoped TiO_2 -673; (b) 0.25 at.%La- TiO_2 -673; (c) 0.5 at.%La- TiO_2 -673; and (d) 0.75 at.%La- TiO_2 -673; (e) 0.25 at.%La- TiO_2 -383

3.1 Synthesis of Mesoporous TiO_2 by Nanocrystalline Particle Assembly

Mesoporous TiO_2 with an anatase framework was synthesized by assembling nanocrystalline particles. The first step was the synthesis of nanocrystalline particles. The second step was assembling the as-prepared nanocrystalline particles using DDA as the organic linkers to form a mesoporous structure.

In this study, wide-angle X-ray diffraction was used to investigate the phase of the as-synthesized assembly units, as seen in Fig. 5. The characteristic anatase peaks appeared in the wide-angle XRD patterns which showed the as-synthesized assembly units to be anatase.

The mesoporous structure and nature of the channel walls of the as-synthesized mesoporous TiO_2 were characterized by TEM and HRTEM. Figure 6a shows the TEM image of Ti-10-U which exhibited a wormhole-like mesoporous structure. Moreover, the corresponding HRTEM image of Ti-10-U (Fig. 6b) indicated the presence of many nanocrystalline particles with lattice fringes of anatase (101). These nanocrystalline particles were connected to each other to form a crystalline framework.

Figure 7 presents the low angle powder XRD patterns and wide-angle powder XRD patterns for the different lanthana-doped titania samples. The low angle XRD patterns (Fig. 7a) shows that there is no peak for sample (a), the undoped TiO_2 -673, which indicates that the mesoporous structure was destroyed and the long-range order was lost after calcination at 683K. While the other samples doped with different amounts of La still have distinguishable peaks, the strength of the peaks increases remarkably compared with the samples before calcination. It can be concluded that the thermal stability was improved by La doping. The wide-angle XRD patterns (Fig. 7b) shows that all of the peaks correspond to the anatase phase, and there are no characteristic peaks belonging to brookite, rutile, or La_2O_3 .

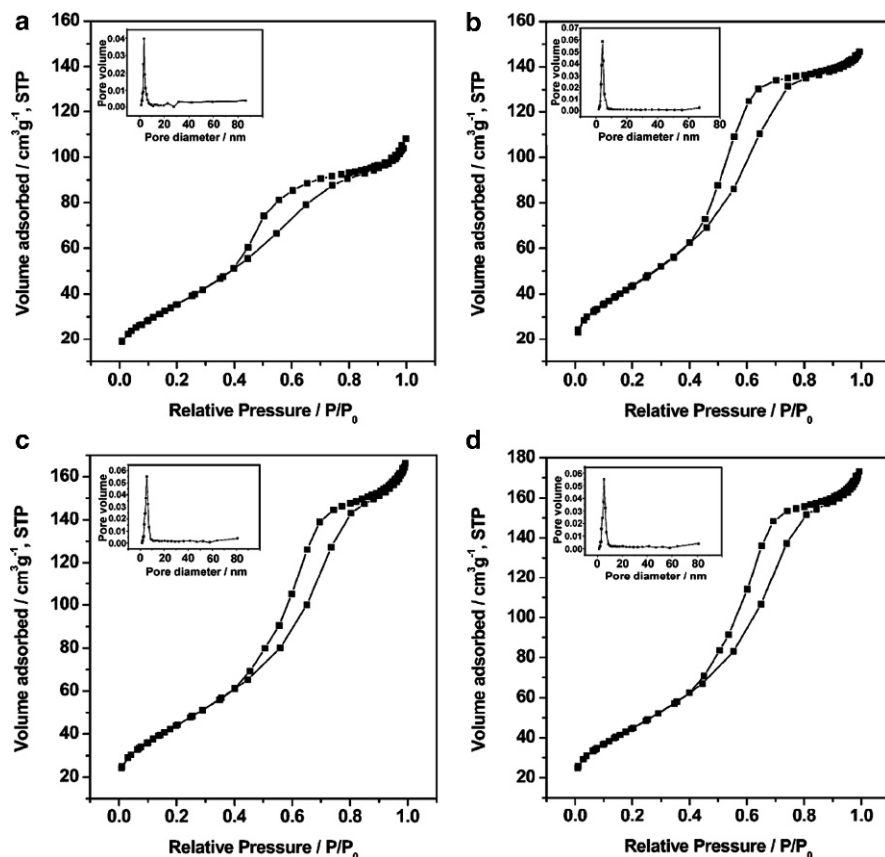


Fig. 8 The N_2 adsorption–desorption isotherms and the BJH pore size distribution (*inset*) of the samples: (a) undoped TiO_2 -673; (b) 0.25 at.%La- TiO_2 -673; (c) 0.5 at.%La- TiO_2 -673; and (d) 0.75 at.%La- TiO_2 -673

Sample (e), 0.25 at.%La- TiO_2 -383, also has an anatase crystalline structure which indicated that an anatase framework was formed before calcination. The crystalline particle sizes calculated by the Scherrer equation decreased after La doping. As expected, the introduction of La as a stabilizer was effective in restraining the growth of anatase nanoparticles. Even the presence of a very small amount of La could inhibit the increase of the nanoparticle size. However, an increase in the amount of La doping only had a slight effect on the decrease of the nano-anatase size.

Figure 8 shows that the prepared materials have a type IV gas adsorption isotherm, which is representative of materials containing large mesoporous channels. The hysteresis loops of the La^{3+} -doped samples seem to be intermediate between type H1 and H2. These results indicate that the La^{3+} -doped samples still reserve the uniform cylindrical mesopores. The hysteresis loop of the pure titania has more characteristics of type H2 than type H1, which indicates that the regularity

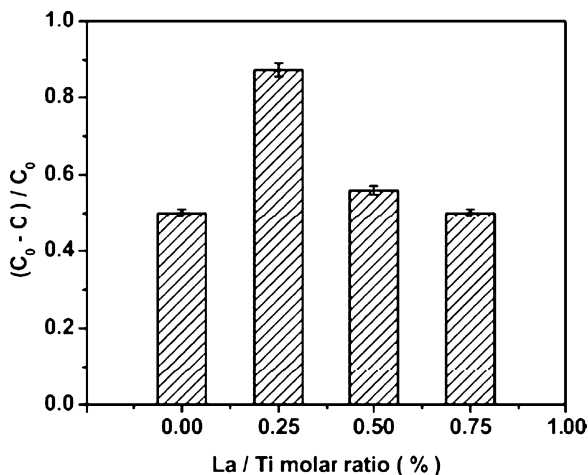


Fig. 9 Photocatalytic activities evaluated by the degradation of methyl orange solution illuminated by a UV light source for 60 min

of the mesoporous structure has been destroyed. The average pore diameter calculated by the BJH model corresponds well with the results of TEM analysis. For example, the average pore diameter of sample 0.25 at.%La-TiO₂-673 BJH is 4.2, which is comparable to the size obtained by the TEM image.

Compared with the La³⁺-doped mesoporous titania, undoped titania has the least surface area, pore size, and pore volume, which is due to the collapse of the mesoporous structure after calcination. La³⁺ doping, thus, increases the thermal stability of the mesoporous titania. It should be noted that the surface area, pore sizes and pore volumes increase very little. A small amount of La³⁺ is sufficiently beneficial to improve the stability of the mesoporous structure by restraining the growth of the nano anatase particles, in good agreement with the results of XRD analysis.

The photocatalytic activity of the samples were tested for the degradation of an aqueous solution of methyl orange in a certain time irrespective of the degradation of various reaction intermediates. Figure 9 shows that the photocatalytic activity of the series of samples first increased then decreased with an increase in the La doping ratio. The sample 0.25 at.%La-TiO₂ has the highest photocatalytic activity. First, a large BET specific surface area favors the contact between the reactant in the solution and the active site on the mesoporous titania surface. Its high photocatalytic ability can be attributed to an increase in the quantum yield more than an enhancement of absorption in the UV region. Though the samples containing more La show a stronger absorption in the UV region than sample 0.25 at.%La-TiO₂, their photocatalytic activity is lower than that of TiO₂ containing higher La. It can, thus, be concluded that La doping increases the quantum yield by promoting the increase of the Ti³⁺ species which act as hole traps (Li et al. 2004a). An optimal La

content is essential since more Ti^{3+} acts as the charge-carrier recombination center, advancing the recombination of the electron–hole pairs.

Based on these studies, we have used a simple and effective method to further prepare highly dispersed Pd nanoparticles in La-doped mesoporous titania with a crystalline framework by co-assembly and in situ photoreduction. The loading amount of Pd is easy to control since there is no loss of Pd in such a process. Compared with the thermal reduction by H_2 , photoreduction by H_2 is highly efficient and complete due to the high dispersion of the sites due to the polycrystalline framework of mesoporous titania. The Pd nanoparticles and La-doped mesoporous titania.

4 Preparation of Nonmetal-Doped Titanium Dioxide with Visible Light-Induced Photocatalytic Activity

Nitrogen-doped nanocrystalline titanium dioxides were successfully synthesized by a wet method, i.e., a microemulsion–hydrothermal process, which did not need high calcination temperatures and, consequently, could avoid the agglomeration and sintering of the TiO_2 particles. Some organic compounds were used as nitrogen sources such as thiethylamine, urea, thiourea, and hydrazine hydrate. Using the photodecomposition of rhodamine B under visible light irradiation as a model, a considerable improvement in the photocatalytic activity was observed for the nitrogen-doped TiO_2 powders when compared to Degussa P-25 and the undoped TiO_2 prepared under the same experimental conditions. By comparing the photocatalytic activity of the nitrogen-doped TiO_2 with different nitrogen sources, the optimum results were obtained with triethylamine so that characterizations of the structure, chemical states and doping concentration were investigated in detail. In order to further investigate the photocatalytic activity, dichlorophenol was also chosen as a probe organic pollutant molecule. Furthermore, the reasons attributed to the improvement of the photocatalytic activity have also been discussed.

In order to investigate the chemical states and concentration of the nitrogen atoms incorporated into the TiO_2 photocatalyst, the N 1s binding energy was measured by X-ray photoemission spectroscopy (XPS). Assignment of the XPS peak of N1s is still under debate and various hypotheses have been provided. In many cases, the peak at about 396 eV is attributed to substitutional nitrogen doping (Asahi et al. 2001; Irie et al. 2004). In recent literatures, such details are lacking but peaks at higher binding energies (399–404 eV) were detected (Chen et al. 2004; Sakthivel et al. 2004; Gole et al. 2004). Moreover, in some other cases, photocatalytic reactivity in visible regions was observed (Asahi et al. 2001; Li et al. 2005a, b).

Figure 10 shows the XPS spectra for the N 1s region of the N-doped TiO_2 with different N/Ti and its fitting curves. It can be seen that there is a broad peak from 397 to 403 eV which is in the range of 396–404 eV, as observed by several other

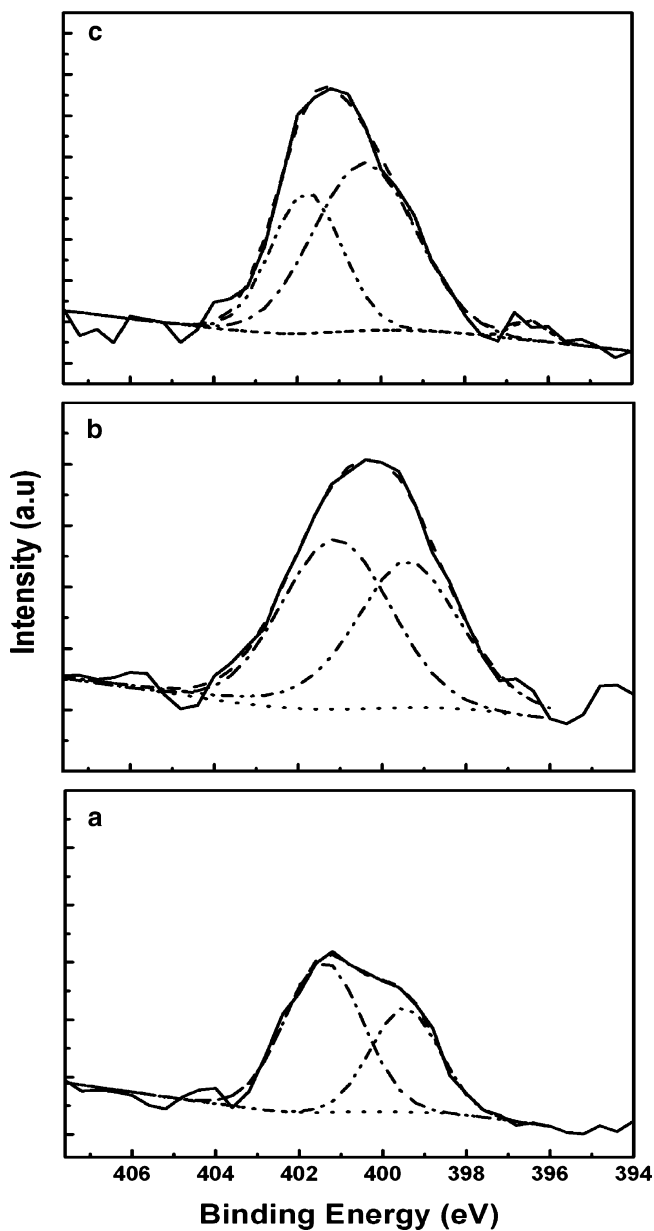


Fig. 10 The fitting XPS spectra for the N 1s region of the N-doped TiO₂ with different mole ratios of N/Ti: (a) 1; (b) 2; (c) 4

researchers and is typical of nitrogen-doped titanium dioxide (Asahi et al. 2001; Sakthivel et al. 2004; Gole et al. 2004; Nakamura et al. 2004). After curve fitting analysis, two peaks were obtained at 399.2 (peak 1) and 401.2 eV (peak 2).

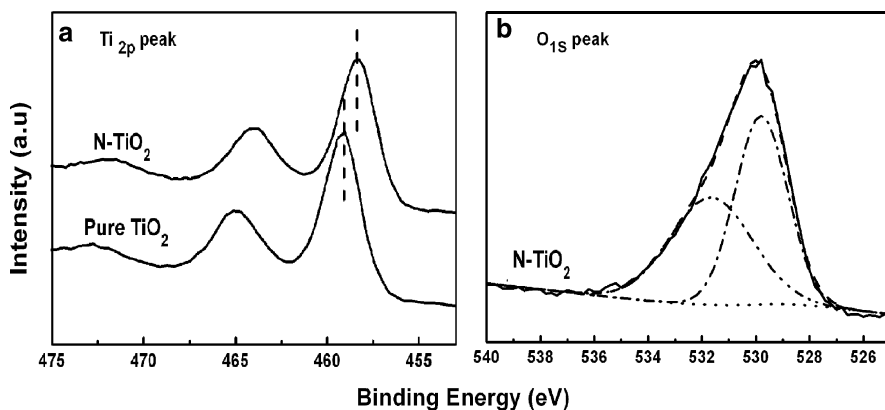


Fig. 11 XPS spectra of the pure TiO_2 and N-TiO_2 : (a) Ti 2p and (b) O 1s core levels

Peak 1 was attributed to the anionic N^- in the O–Ti–N linkages, which is consistent with the characteristics described in other literatures (Sathishi et al. 2005; Chen et al. 2004; Li et al. 2006). The binding energy of this peak is higher than that of TiN appeared at ≤ 397.5 eV, which may be because nitrogen doping into the TiO_2 lattice reduces the electron density on the nitrogen due to the high electronegativity of oxygen. These changes in the nitrogen environment can produce significant differences in the nitrogen 1s XPS spectra region. The results of XPS spectra for the Ti 2p region (Fig. 11a) also support these conclusions. The Ti 2p_{3/2} core levels of the pure TiO_2 and N-TiO_2 appear at 459.05 and 458.25 eV, respectively. The binding energy of Ti 2p_{3/2} after nitrogen doping decreases and suggests different electronic interactions of Ti with the anions, which is attributed to the partial electron transformation from N to Ti and an increase in the electron density on Ti due to the lower electronegativity of nitrogen compared to that of oxygen (Sathishi et al. 2005; Chen et al. 2004; Li et al. 2006). These results further confirm that nitrogen is incorporated into the lattice and substituted oxygen.

The other peak at a higher binding energy is also hard to identify its assignment from the N 1s XPS spectra alone. Therefore, we have combined the N 1s and O 1s core levels for analysis, as shown in Fig. 11b. It was found that an additional peak in N-TiO_2 appears at about 532 eV and is attributed to the presence of the Ti–O–N bonds (Battiston et al. 2001). It is a feature that was first observed by Saha and Tomkins (1992) and was most recently characterized by Gyorgy et al. (2003). They have assigned this feature to the formation of oxidized Ti–N, which leads to the Ti–O–N structure. These results also correspond with the fact that the presence of oxidized nitrogen such as Ti–O–N appears at higher binding energy of above 400 eV. From these observations, it can be concluded that the chemical states of the nitrogen doped into TiO_2 may be varied and coexist in the form of N–Ti–O and Ti–O–N.

After nitrogen doping, the optical absorption edges of the samples shift to lower energy regions as compared to the undoped sample, and the absorption after nitrogen doping is dramatic and stronger in the wavelength range of 400–600 nm.

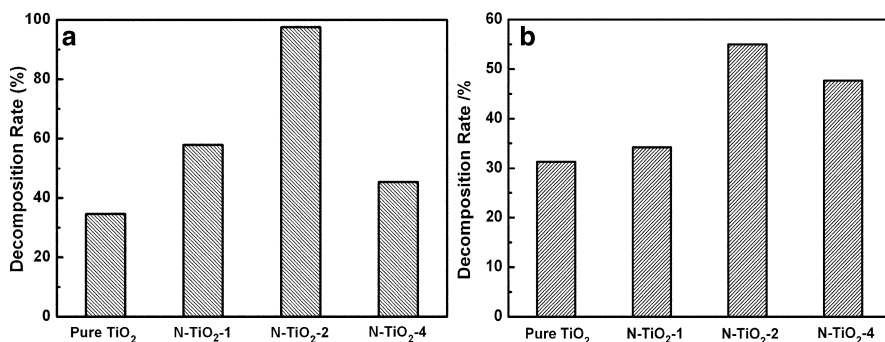


Fig. 12 Decomposition rate of (a) rhodamine B for 1 h and (b) 2,4-dichlorophenol for 5 h on undoped and doped TiO₂ with different N/Ti under visible light irradiation

Nitrogen doping was observed to contribute to the red-shift due to the narrowing of the band gap.

In order to specify the effect of the doping concentration on the photocatalytic activity, the decomposition of rhodamine B (20 mg/L) and 2,4-dichlorophenol (100 mg/L) in visible light irradiation of N-TiO₂ with different mole ratios of N/Ti were carried out and compared with that of undoped TiO₂ (Fig. 12). The results indicate that the photocatalytic activity is greatly improved by nitrogen doping. As can be seen from Fig. 12a, when the mole ratio of N/Ti is 2, the decomposition rate is the highest, probably due to the highest nitrogen doping percentage. When the N/Ti value of triethylamine is higher than 4, the actual doping percentage is decreased. Consequently, we consider that the nitrogen doping concentration had an optimal value. Considering the DRS, XPS, and PL results, the local structures of the titanium dioxide species are altered by nitrogen doping, which not only improves the absorption of titania in the visible light region but also decreases the recombination of the photo-induced electrons and holes. Therefore, it is reasonable that the photocatalytic activity of the nitrogen-doped titania are improved accordingly. In addition, when the N/Ti ratio is 2, the photocatalyst has the highest photocatalytic activity due to its higher absorption, the highest actual nitrogen doping percentage and the lowest photoluminescence efficiency.

Since rhodamine B can absorb visible light ($\lambda > 420$ nm), it can be degraded under visible light irradiation through two competitive processes: a photocatalytic process and a self-photosensitized process. The higher photocatalytic activity of the photocatalyst after nitrogen doping can be attributed to a self-photosensitized process and we have also carried out the degradation of a 2,4-dichlorophenol solution (100 mg/L), which does not absorb visible light and the results are shown in Fig. 12b. As can be seen, the photocatalytic activity of the TiO₂ after nitrogen doping is improved compared with the pure TiO₂. Furthermore, when the N/Ti ratio is 2, the photocatalyst has the highest activity, which is consistent with the results of the decomposition of rhodamine B. The decomposition rate of 2,4-dichlorophenol (100 mg/L) is lower than that of rhodamine B, which may be due to the difference in absorption properties of these reactant molecules on the surface of

the photocatalyst, leading to differences in the surface oxygen concentration and different concentration and structure of these reactant molecules, etc.

These results show that nitrogen doping can effectively improve the photocatalytic activity in visible light regions. However, the chemical state (N–Ti–O or/and Ti–O–N), as the decisive factor in improving the photocatalytic activity, requires further investigation.

5 Preparation of Metal-Doped, Noble Metal Deposition TiO₂

5.1 Transitional Metal-Doped TiO₂ with High Photocatalytic Activity Prepared by Hydrothermal Treatment

The photocatalytic activities of doped TiO₂ photocatalysts substantially depend on the nature and concentration of the dopant ions as well as the preparation methods, the thermal and reductive treatments. A hydrothermal method has been applied to synthesize nano-sized materials already, since products prepared by this method have a well-crystalline phase which benefits the thermal stability of the nanosized materials. Our group has successfully prepared iron ion-doped TiO₂ using this method and conducted a systematic study on the effects of Fe content and Fe ions precursors on the enhancement of the photocatalytic activity of TiO₂, especially under visible light irradiation (Zhu et al. 2004).

The UV–Vis diffuse spectra of TiO₂ doped with Fe³⁺ and Fe²⁺ indicate that the absorbance increased in the visible range with an increase in the doping content. The samples doped with FeCl₃ had more remarkable absorption in visible light regions than those doped with FeCl₂ under the same doping content conditions.

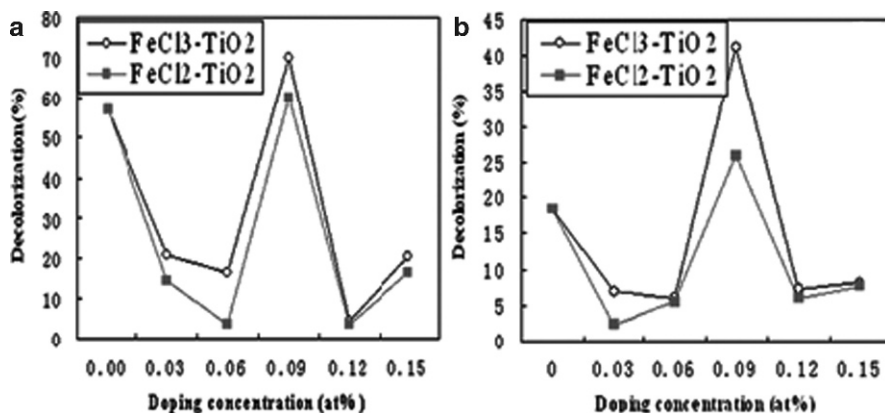


Fig. 13 Photodecolorized amounts of XRG by the Fe-doped TiO₂ as a function of the doping concentration (a) under UV irradiation time for 1 h and (b) under visible light irradiation time for 7 h, exclusive of the equilibrium adsorption

Figure 13 shows the photodecolorized amounts of XRG by the Fe-doped TiO_2 as a function of the doping concentration under UV light illumination for 1 h and visible light illumination for 7 h, respectively. It is obvious that only 0.09% $\text{FeCl}_3\text{-TiO}_2$ and 0.09% $\text{FeCl}_2\text{-TiO}_2$ are more photoactive than the undoped TiO_2 , while 0.09% $\text{FeCl}_3\text{-TiO}_2$ has the best photocatalytic activity. It is worth noting that the amount of doped iron is very critical to the photoactivity, i.e., a high or low level of the dopant decreases the photocatalytic activity markedly. Thus, the hydrothermal method can be applied to dope TiO_2 with metal ions deeply and uniformly, effectively enhancing the photoactivity of TiO_2 and use of visible light.

Although most reports of Cr^{3+} doping was not effective in enhancing TiO_2 photocatalytic activity, the Cr^{3+} ion was selected as the dopant in this work to examine whether the dopant transitional metal distribution in TiO_2 could yield better results. The preparation process consisted of two steps: first, the formation of dried amorphous TiO_2 gel and secondly, hydrothermal treatment for the mixture of the as-prepared TiO_2 gels, appropriate amount of $\text{Cr}(\text{NO}_3)_3 \cdot 9\text{H}_2\text{O}$, water and isopropanol. The UV-Vis DRS of TiO_2 doped with Cr^{3+} are presented in Fig. 14. The Cr^{3+} -doped TiO_2 greatly increases the absorption of the TiO_2 photocatalysts in visible regions, as compared with TiO_2 . The enhanced absorption of around 450 nm can be assigned to the charge transfer band $\text{Cr}^{3+} \rightarrow \text{Ti}^{4+}$ or ${}^4\text{A}_{2g} \rightarrow {}^4\text{T}_{1g}$ of Cr^{3+} in an octahedral environment, while the broad absorption band from 620 to 800 nm can be assigned to ${}^4\text{A}_{2g} \rightarrow {}^4\text{T}_{2g}$ d-d transitions of Cr^{3+} (Dvoranová et al. 2002; Serpone et al. 1994; Borgarello et al. 1982; Palmisano et al. 1988).

The doping of chromium ions were seen to improve the photocatalytic activity under both UV light irradiation (Fig. 15a) and visible light irradiation (Fig. 15b). The optimal doping levels of chromium ions for photocatalysis under UV and visible light were 0.15 and 0.2%, respectively. Although the photocatalytic activity of the

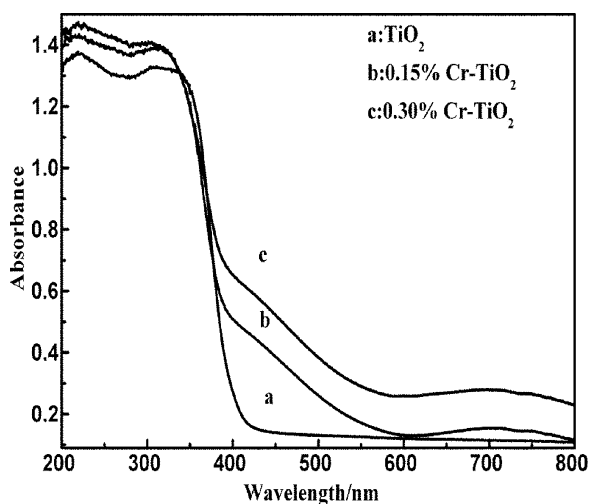


Fig. 14 UV-Vis DRS of TiO_2 , 0.15% Cr-TiO_2 and 0.3% Cr-TiO_2

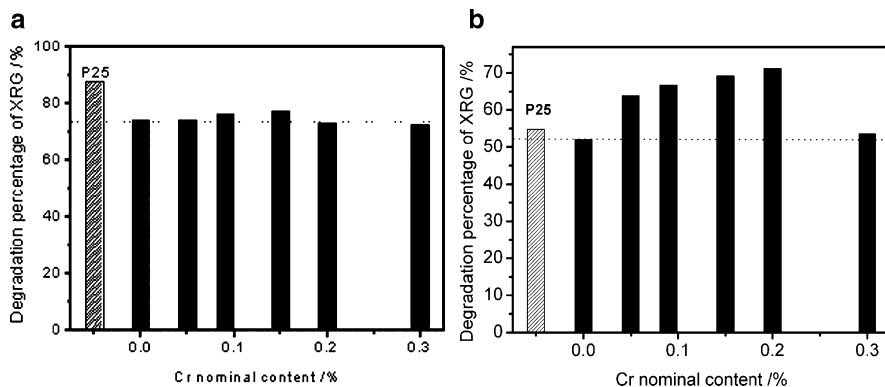


Fig. 15 Photodegradation of XRG by Cr-TiO₂ with various Cr³⁺ doping concentrations and P25 (a) under UV irradiation for 1 h (b) under visible light irradiation for 7 h

as-prepared Cr-TiO₂ is somewhat lower than that of P25 under UV irradiation, the photocatalytic activity of Cr-TiO₂ under visible irradiation was higher. The effect of Cr³⁺ on the improvement of the photocatalytic activity may be attributed to the enhanced light absorption in visible regions and the active role Cr³⁺ played in reducing electron-hole recombination. Furthermore, the location of Cr³⁺ at the exterior rather than the interior of TiO₂ may also be of great significance. The generation of active oxygen species, such as hydroxyl radical and superoxide anion radicals, occurs on the surface of the doped TiO₂ and arises from doping, i.e., in order to favor the interfacial charge transfer reactions instead of recombination reactions, the Cr³⁺ dopants may be located at the exterior rather than the interior of TiO₂.

5.2 Noble Metal (Ag, Au) Deposited TiO₂ with High UV Light Activity

The noble metals deposited on the surface of TiO₂, such as Au, Pt, and Ag, have excellent performance in promoting the organics degradation with TiO₂ under UV irradiation (Yang et al. 1997; Rao et al. 2003; Subramanian et al. 2003). The catalytic properties of noble metal-deposited TiO₂ markedly depend on the preparation methods. Our group has developed a novel deposition precipitation (DP) method for the deposition of metal Ag on TiO₂ (You et al. 2005). Since this novel DP method does not require calcination, the agglomeration of Ag particles on TiO₂ can be avoided in contrast to other methods. The preparation of Ag/TiO₂ was carried out by the reaction of Ag⁺ ions with hydrogen peroxide in a TiO₂ suspension. The reaction mechanism is as follows:



Figure 16 shows the high-resolution XPS of the Ag 3d region. The XPS curve of Ag/TiO₂ can be well fitted with a distribution of which there are two peaks centered at 368.5 eV and 374.5 eV corresponding to Ag 3d_{5/2} and Ag 3d_{3/2}, respectively, indicating the Ag species deposited on the TiO₂ powders are all metal Ag.

Figure 17 shows the percentage of methyl orange decomposed after irradiated with Ag/TiO₂ for 1.5 h. It can be seen that the decomposition of methyl orange increases

Fig. 16 Ag 3d high-resolution XPS spectrum of 1.5 wt% Ag/TiO₂ powders prepared by a novel deposition precipitation method. (a) original curve; (b) fitted curve

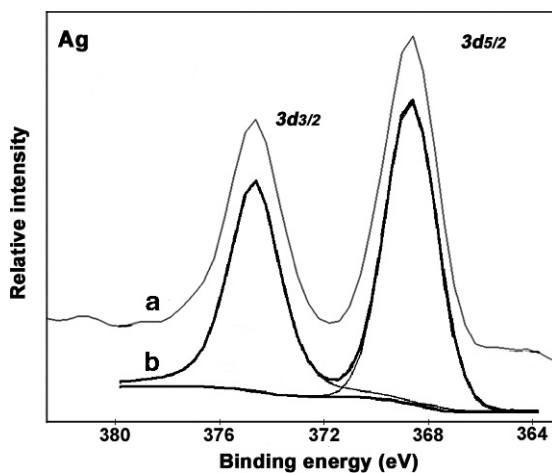
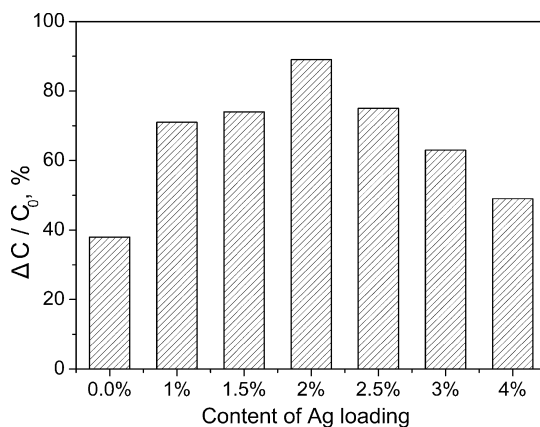


Fig. 17 Decomposed percentage of methyl orange on Ag/TiO₂ samples irradiated for 1.5 h



significantly with an increase in Ag loaded from 0.0 to 2.0 wt%, and reaches a maximum at 2.0 wt%, then decreases with a further increase of the loaded Ag. The photocatalytic activity of 2.0 wt% Ag/TiO₂ is about 2.3 times that of unmodified TiO₂. Thus, it can be concluded that the deposition of Ag on the surface of TiO₂ leads to an enhancement of the photocatalytic activity for TiO₂ under UV light illumination.

Gold-deposited TiO₂ has also attracted attention due to its high efficiency for many photocatalytic reactions. The size and distribution of Au particles are critical factors impacting the photoactivity of TiO₂. Recently, with gold–thiosulfate complex as a gold precursor, our group has successfully deposited microsized gold nanoparticles in a highly dispersed state on the surface of TiO₂. The obtained gold-loaded TiO₂ (Au/TiO₂) catalysts exhibited higher photocatalytic activity for the degradation of methyl orange as compared to the samples prepared by a deposition–precipitation (DP) or impregnation (IMP) method. The obtained samples were labeled S_{x-y}, in which the “x” refers to the nominal mass percentage content of Au in Au and TiO₂, and “y” refers to the heat-treating temperature in centigrade. For comparison, Au-loaded TiO₂ catalysts were also prepared by the DP (NaOH, pH = 8.0) and impregnation (IMP) methods, and denoted DP_{x-y} and IMP_{x-y}, respectively.

Figure 18(a–d) shows the TEM images of samples DP₄-300, S₄-300, DP₈-300, and S₈-300, respectively. Spherical Au particles were observed as dark spots

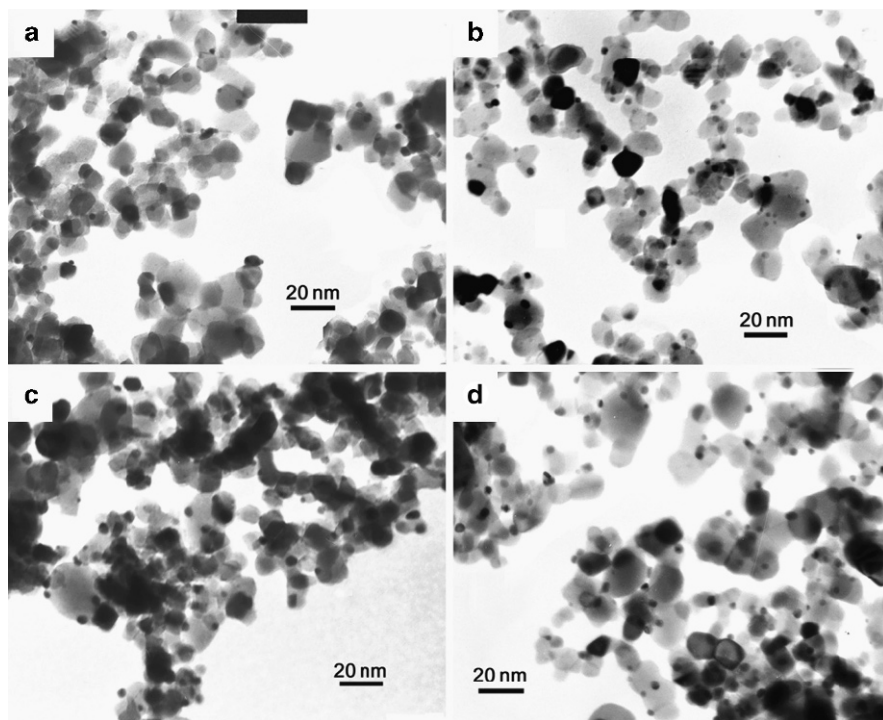


Fig. 18 TEM images of (a) DP₄-300, (b) S₄-300, (c) DP₈-300 and (d) S₈-300

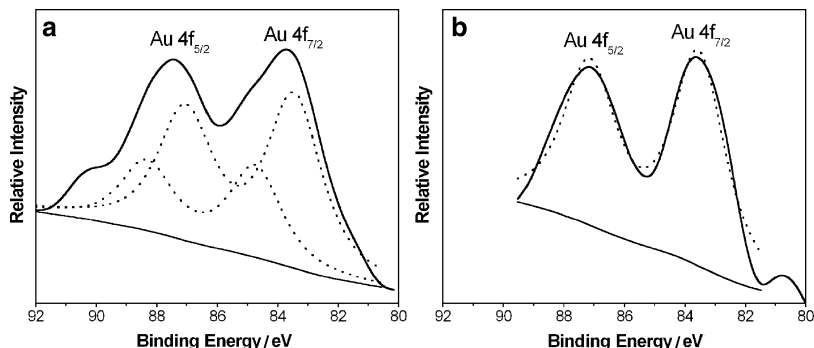


Fig. 19 XPS spectra of Au 4f region for (a) S₄-100 and (b) S₄-300

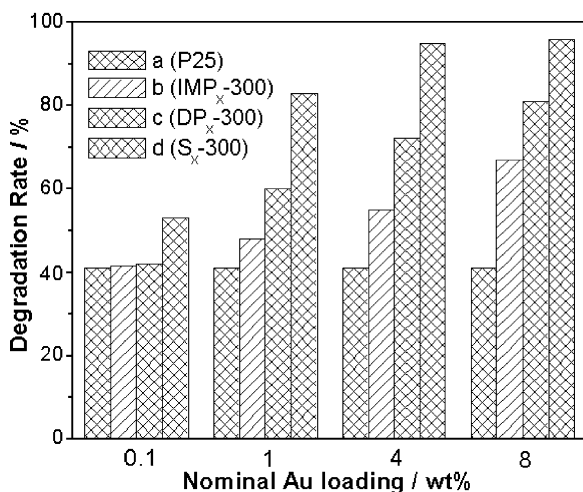


Fig. 20 Photodegradation rate of MO after UV light irradiation for 20 min over various Au/TiO₂ catalysts. (a) P25; (b) IMP_x series; (c) DP_x series; (d) S_x series

dispersed on the surface of the TiO₂ particles. The mean diameter of the Au particles for DP₈-300, S₄-300, and S₈-300 were estimated to be 3.4, 2.5, 3.0 nm, respectively. Results from AAS measurements show that the actual amount of Au for the three samples were similar; nevertheless, TEM observations showed that the number of Au nanoparticles on S₄-300 was more than for DP₄-300. These results suggest that not only the diameter of the Au particles but also their numbers is relative to the preparation method.

Figure 19a and b showed the X-ray photoelectron spectra of samples S₄-100 and S₄-300, respectively. In Fig. 19b, the doublet peaks located at 83.4 and 87.0 eV can be assigned to the characteristic doublets of Au⁰ according to a previous report

(Barr and Seal 1995), confirming the formation of elemental Au. For S₄-100 (Fig. 19a), the deconvoluted Au 4f peaks indicate that two components may coexist for the Au 4f_{7/2} and Au 4f_{5/2} signals, giving peaks at 83.4 and 84.8 eV for the Au 4f_{7/2} signal as well as 87.0 and 88.3 eV for the Au 4f_{5/2} signals. The two components can be attributed to the metallic Au⁰ and nonmetallic Au (Au⁺), respectively (Minicò et al. 2001).

Figure 20 illustrates the degradation rates of MO with various Au/TiO₂ catalysts under UV light irradiation for 20 min. For each of the Au loadings, 0.1, 1.0, 4.0, and 8.0 wt%, the photocatalytic activity varies in descending order: S_x-300 > DP_x-300 > IMP_x-300 > P25, confirming that the photocatalytic activity depends more on the preparation method. We believe that highly dispersed Au derived from a gold–thiosulfate complex enhances photocatalytic activity and that the appropriate diameter and number of Au particles are also essential.

5.3 Transitional Metal (Fe³⁺) Doped Together with Noble Metal (Au) Deposited TiO₂ (Au/Fe³⁺-TiO₂) with High Visible and UV Light Activity

Although our group has done extensive work to prepare transition metal ion-doped (Fe³⁺, Cr³⁺) TiO₂ that exhibit high activity under visible light illumination, the photocatalytic performance in the UV region has not been significantly improved. Meanwhile, noble metal-doped TiO₂ (Au/TiO₂, Ag/TiO₂) with high photoactivity under UV light has been successfully obtained in our work through some unconventional methods. At present, one of the most challenging tasks is how to engineer highly efficient TiO₂ photocatalysts which can operate under both UV and solar or visible,

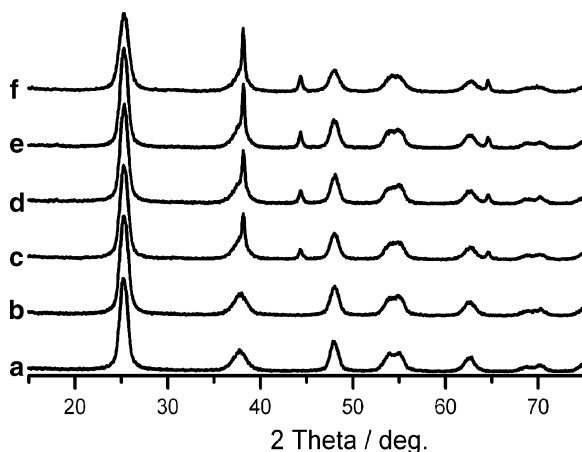


Fig. 21 XRD patterns of the different samples: (a) TiO₂, (b) 0.57Fe-TiO₂, (c) 2.0Au/0.57Fe-TiO₂, (d) 2.0Au/TiO₂, (e) 3.0Au/0.57Fe-TiO₂, and (f) 3.0Au/TiO₂

natural light. The promising advantages of doping and deposition have led us to attempt a combination of doping Fe^{3+} with the deposition of Au to improve the visible and UV light activity of the titania through the synergetic effects of Fe^{3+} and Au. The preparation procedure of Fe^{3+} -doped TiO_2 deposited with Au ($\text{Au}/\text{Fe}^{3+}\text{-TiO}_2$) consists of two steps. First, Fe^{3+} -doped TiO_2 was prepared using a hydrothermal treatment, and 0.57 at.% Fe^{3+} -doped TiO_2 , referred to as 0.57Fe– TiO_2 , showed the highest activity under visible light illumination. Next, Au was deposited onto 0.57Fe– TiO_2 by the deposition–precipitation method, described by Catherine Louis (Zanella et al. 2002). The content of Au deposited on 0.57Fe– TiO_2 was 0.0, 1.0, 1.5, 2.0, 3.0 and 4.0 wt%, designated as 0.57Fe– TiO_2 , 1.0Au/0.57Fe– TiO_2 , 1.5Au/0.57Fe– TiO_2 , 2.0Au/0.57Fe– TiO_2 , 3.0Au/0.57Fe– TiO_2 , 4.0Au/0.57Fe– TiO_2 , respectively. Pure TiO_2 deposited with 2.0, 3.0 wt% Au were designated as 3.0Au/ TiO_2 , 4.0Au/ TiO_2 , respectively.

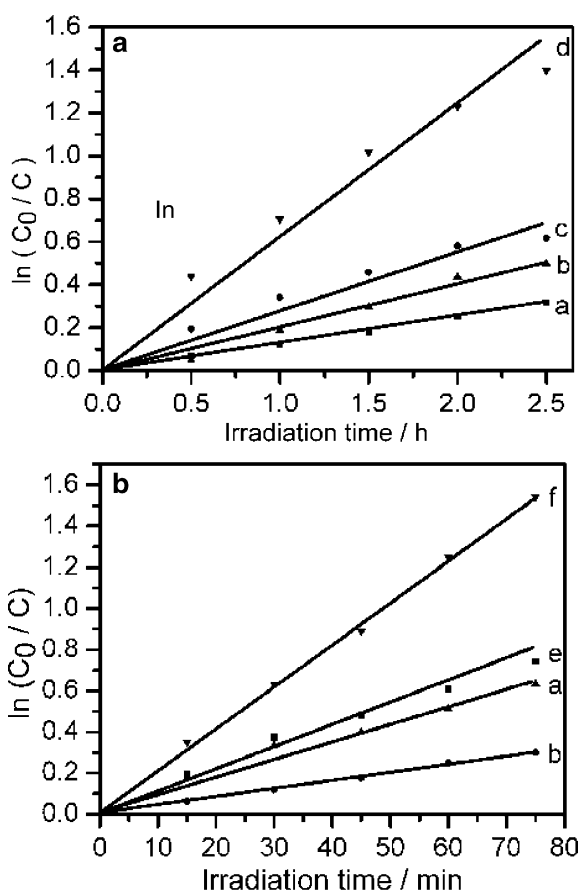


Fig. 22 Fit of (a) visible light ($\lambda > 420$ nm) and (b) UV light photodegradation data to a first-order kinetic model: (a) TiO_2 , (b) 0.57Fe– TiO_2 , (c) 2.0Au/ TiO_2 , (d) 2.0Au/0.57Fe– TiO_2 , (e) 3.0Au/ TiO_2 , (f) 3.0Au/0.57Fe– TiO_2

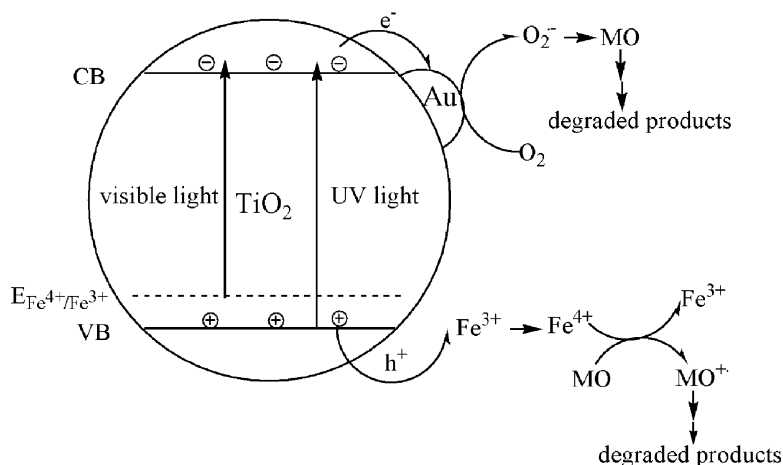


Fig. 23 Proposed mechanism for the synergistic effects of Fe³⁺ and Au

The XRD patterns of the samples are shown in Fig. 21. All the samples are seen to consist of anatase as the unique phase. Samples c, d, e, and f show reflections at 38.2, 44.4, and 64.6°2θ values which are characteristic of Au⁰, demonstrating the deposited Au mainly exists as Au⁰ on the surface of the samples (Debeila et al. 2004). The crystalline sizes corresponding to TiO₂ are estimated to be 10–11 nm, and the intensities of the peaks assigned to anatase are almost the same among all the samples. It could, thus, be concluded that the doped Fe³⁺ as well as deposited Au exerted no significant influence on the crystalline phase, crystalline size and crystallinity of TiO₂.

The photocatalytic activity of the samples were evaluated for the degradation of MO under visible and UV light illumination. The optimum weight content of Au was found to be 2.0 and 3.0 wt%. To test and verify the respective roles Fe³⁺ and Au play as well as their synergistic effects on the photocatalytic activity of TiO₂, several typical samples were chosen for further analysis. The photocatalytic degradation data of the selected samples were converted to a linear pattern using the first-order kinetics model and the results are shown in Fig. 22. The activity of 2.0Au/0.57Fe–TiO₂ is fairly higher than that of the remaining samples and this may be due to the synergistic effects of the doped Fe³⁺ and deposited Au on the enhancement of the photocatalytic activity. Furthermore, 3.0Au/0.57Fe–TiO₂ exhibits a clear increase in the photocatalytic activity, confirming the synergistic effects of doped Fe³⁺ and deposited Au on UV photocatalytic activity.

The mechanism for the synergistic effects of Fe³⁺ and Au on the photocatalytic activity of TiO₂ is proposed in Fig. 23. Under visible light, Fe³⁺ substituted for Ti⁴⁺ in the TiO₂ lattice plays a positive role in the extension of light absorption into visible regions while the deposited Au acts as traps for the photo-induced electrons, reducing electron–hole recombination in the photocatalytic process. Under UV light illumination, a large number of excited electrons can be rapidly trapped by Au while the remaining holes are shallowly trapped by Fe³⁺ and then transfer to the

surface to initiate the photocatalytic processes. During this procedure, electron–hole recombination is largely suppressed, leading to high photocatalytic activity. Thus, Au and Fe³⁺ can be seen to efficiently improve the visible and UV light activity of TiO₂ by their synergistically effects.

Acknowledgments This work has been supported by the National Nature Science Foundation of China (20577009), National Basic Research Program of China (973 Program 2007CB613306), and the Ministry of Science and Technology of China (2006AA06Z379, 2006DFA52710).

References

- Anpo M (1997) *Catal Survey Jpn* 1:169
Anpo M (2000a) *Pure Appl Chem* 72:1265
Anpo M (2000b) *Pure Appl Chem* 72:1787
Anpo M (2004) *Bull Chem Soc Jpn* 77:1427
Anpo M, Takeuchi M (2003) *J Catal* 216:505
Anpo M, Ichihashi Y, Takeuchi M, Yamashita H (1998) *Res Chem Intermed* 24:143
Anpo M, Takeuchi M, Kishiguchi S, Yamashita H (1999) *Surf Sci Jpn* 20:60
Antonelli DM, Ying JY (1995) *Angew Chem Int Ed Engl* 34:2014
Araña J, Díaz OG, Saracho MM, Rodríguez JMD, Melián JAH, Peña JP (2002) *Appl Catal B* 36:113
Asahi R, Morikawa T, Ohwaki T, Aoki K, Taga Y (2001) *Science* 293:269
Babou F, Bigot B, Sautet P (1993) *J Phys Chem* 97:11501
Babou F, Coudurier G, Viedrine JC (1995) *J Catal* 152:341
Bahnemann D, Henglein A, Spanhel L (1984) *Faraday Discuss Chem Soc* 78:151
Barr TL, Seal S (1995) *J Vac Sci Technol A* 13:1239
Battiston GA, Gerbasi R, Gregori A, Porchia M, Cattarin S, Rizzi GA (2001) *Thin Solid Films* 371:126
Borgarello E, Kiwi J, Grätzel M, Pelizzetti E, Visca M (1982) *J Am Chem Soc* 104:2996
Chen X, Burda C (2004) *J Phys Chem B* 108:15446
Choi W, Termin A, Hoffmann MR (1994) *J Phys Chem* 98:13669
Cong Y, Zhang JL, Chen F, Anpo M, He D (2007a) *J Phys Chem C* 111:10618
Cong Y, Chen F, Zhang JL, Anpo M (2007b) *J Phys Chem C* 111:6976
Debeila MA, Coville NJ, Scurrall MS, Hearne GR, Witcomb MJ (2004) *J Phys Chem B* 108:18254
Do TO (1999) *Langmuir* 15:8561
Dvoranová D, Brezová V, Mazúr M, Malati MA (2002) *Appl Catal B* 37:91
Fahmi A, Minot C, Fourre CP, Nortier P (1995) *Surf Sci* 343:261
Fujishima A, Rao TN, Tryk DA (2001) *J Photochem Photobiol C* 1:1
Gole JL, Stout JD, Burda C, Lou Y, Chen X (2004) *J Phys Chem B* 108:1230
Gopal M, Moberly Chan WJ, De Jonghe LC (1997) *J Mater Sci* 32:6001
Gyorgy E, Perez del Pino A, Serra P, Morenza JL (2003) *Surf Coat Technol* 173:265
Haruta M (1997) *Catal Surv Jpn* 1:61
Hoffmann MR, Martin ST, Choi W, Bahnemann DW (1995) *Chem Rev* 95:69
Hu C, Yu JC, Hao Z, Wong PK (2003) *Appl Catal B* 42:47
Irie H, Watanabe Y, Hashimoto K (2004) *J Phys Chem B* 107:5483
Jun YW, Casula MF, Sim JH, Kim SY, Cheon J, Alivisatos AP (2003) *J Am Chem Soc* 125:15981
Kamat PV (1993) *Chem Rev* 93:267
Kato H, Kudo A (2002) *J Phys Chem B* 106:5029
Kikuchi H, Kitano M, Takeuchi M, Matsuoka M, Anpo M, Kamat PV (2006) *J Phys Chem B* 110:5537

- Kitano M, Takeuchi M, Matsuoka M, Thomas JM, Anpo M (2005) *Chem Lett* 34:616
- Kitano M, Tsujimaru K, Anpo M (2006) *Appl Catal A Gen* 314:179
- Kitano M, Funatsu K, Matsuoka M, Ueshima M, Anpo M (2007a) *J Phys Chem B* 110:25266
- Kitano M, Kudo T, Matsuoka M, Ueshima M, Anpo M (2007b) *Mater Sci Forum* 544–545:107
- Kitano M, Takeuchi M, Matsuoka M, Thomas JM, Anpo M (2007) *Catal Today* 120:133
- Kittakal S, Matsuno K, Takahara S (1997) *J Solid State Chem* 132:447
- Li FB, Li XZ, Hou MF (2004a) *Appl Catal B Environ* 48:185
- Li Y, White TJ, Lim SH (2004b) *J Solid State Chem* 177:1372
- Li D, Haneda H, Hishita S, Ohashi N (2005a) *Chem Mater* 17:2588
- Li D, Haneda H, Hishita S, Ohashi N (2005b) *Chem Mater* 17:2596
- Li Y, Hwang D, Lee N, Kim S (2005c) *Chem Phys Lett* 404:25
- Li H, Li J, Huo Y (2006) *J Phys Chem B* 110:1559
- Liu YC, Juang LC (2004) *Langmuir* 20:6951
- Livage J, Henry M, Sanchez C (1988) *Prog Solid State Chem* 18:259
- Matsuoka M, Kitano M, Takeuchi M, Anpo M, Thomas JM (2005a) *Mater Sci Forum* 486–487:81
- Matsuoka M, Kitano M, Takeuchi M, Anpo M, Thomas JM (2005b) *Top Catal* 35:305
- Minicò S, Scirè S, Crisafulli C, Galvagno S (2001) *Appl Catal B* 34:277
- Nakamura R, Tanaka T, Nakato Y (2004) *J Phys Chem B* 108:10617
- Ohno T, Mitsui T, Matsumura M (2003) *Chem Lett* 32:364
- Ohno T, Tsubota T, Nishijima K, Miyamoto Z (2004) *Chem Lett* 33:750
- Palmisano L, Augugliaro V, Sclafani A, Schiavello M (1988) *J Phys Chem* 92:6710
- Penn RL, Banfield JF (1999) *Am Mineral* 84:871
- Rao KVS, Lavédrine B, Boule P (2003) *J Photochem Photobiol A Chem* 154:189
- Rodríguez JA, Liu G, Jirsak T, Hrbek J, Chang ZP, Dvorak J, Maiti A (2002) *J Am Chem Soc* 124:5242
- Saha NC, Tomkins HC (1992) *J Appl Phys* 72:3072
- Sakthivel S, Kisch H (2003) *Angew Chem Int Ed* 42:4908
- Sakthivel S, Janczarek M, Kisch H (2004) *J Phys Chem B* 108:19384
- Sathishi M, Viswanathan B, Viswanath RP, Gopinath CS (2005) *Chem Mater* 17:6349
- Serpone N, Lawless D, Disdier J, Herrmann JM (1994) *Langmuir* 10:643
- Stathatos E, Lianos P, Del Monte F, Levy D, Tsiourvas D (1997) *Langmuir* 13:4295
- Stone VF Jr, Davis RJ (1998) *Chem Mater* 10:1468
- Subramanian V, Wolf EE, Kamat PV (2003) *Langmuir* 19:469
- Takeuchi M, Anpo M, Hirao T, Itoh N, Iwamoto N (2001) *Surf Sci Jpn* 22:561
- Wang C, Ying JY (1999) *Chem Mater* 11:3113
- Wang W, Gu BH, Liang LY, Hamilton WA, Wesolowski DJ (2004) *J Phys Chem B* 108:14789
- Xu AW, Gao Y, Liu HQ (2002) *J Catal* 207:151
- Yamashita H, Harada M, Misaka J, Takeuchi M, Ikeue K, Anpo M (2002) *J Photochem Photobiol A Chem* 148:257
- Yan MC, Chen F, Zhang JL, Anpo M (2005) *J Phys Chem B* 109:8673
- Yang JC, Kim YC, Shul YC, Shin CH, Lee TK (1997) *Appl Surf Sci* 121/122:525
- Yang Y, Li X-J, Chen J-T, Wang L-Y (2004) *J Photochem Photobiol A Chem* 163:517
- Yin H, Wada Y, Kitamura T, Sumida T, Hasegawa TY, Yanagida S (2002) *J Mater Chem* 12:378
- You X, Chen F, Zhang J, Anpo M (2005) *Catal Lett* 102:247
- Yu JC, Ho W, Yu J, Yip H, Wong PK, Zhao J (2005) *Environ Sci Technol* 39:1175
- Zanella R, Giorgio S, Henry CR, Louis C (2002) *J Phys Chem B* 106:7634
- Zhang HZ, Banfield JF (1998) *J Mater Chem* 8:2073
- Zhang Q, Gao L (2003) *Langmuir* 19:967
- Zhang Z, Wang C, Zakaria R, Ying JY (1998) *J Phys Chem B* 102:10871
- Zhang Q, Gao L, Guo J (2000) *J Eur Ceram Soc* 20:2153
- Zhao W, Ma W, Chen C, Zhao J, Shuai Z (2004) *J Am Chem Soc* 126:4782
- Zhu J, Chen F, Zhang J, Chen H, Anpo M (2004) *J Mol Catal A Chem* 216:35

Chapter 3

Second Generation Visible-Light-Active Photocatalysts: Preparation, Optical Properties, and Consequences of Dopants on the Band Gap Energy of TiO₂

Nick Serpone, Alexei V. Emeline, Vyacheslav N. Kuznetsov,
and Vladimir K. Ryabchuk

Abstract First generation metal-oxide photocatalysts based mostly on nominally pure, pristine titanium dioxide have been the object of great debate in the past 30 years with regard (i) to the nature of the oxidative agent ($\bullet\text{OH}$ radicals vs. holes h^+); (ii) to the site at which the reaction takes place (surface vs. bulk solution); (iii) to whether TiO₂ is indeed a photocatalyst since turnover numbers are difficult to determine owing to the nature of the particle surface; and (iv) to how the process efficiency can be ascertained, among many other issues yet to be resolved satisfactorily. One issue that has taken some time to be resolved is the notion of how we can make better use of sunlight's visible radiation seeing that the absorption edge of TiO₂ is at 387 nm (ca. 3.2 eV – the band gap energy) for the anatase polymorph. A successful strategy that is gaining some momentum is to dope this metal oxide with suitable dopants (e.g., metal ions and/or non-metals) to shift the absorption edge to longer wavelengths. Doping has been achieved using various physical and chemical strategies, which have led to materials whose absorption edges have been red-shifted to wavelengths ~ 550 nm (and beyond in some cases). The debate that now occupies discussions of doped-TiO₂ materials regards the causes for this red shift. Several reports, based on density functional theory (DFT), have asserted that the band gap of doped-TiO₂ is narrowed because of interactions between the dopant states and the O 2p states of the valence band, thereby pushing the valence band edge upward. Others have proposed isolated dopant states located within the band gap to explain the red shift of the absorption edges of doped-TiO₂ systems through excitation of the electrons in these states to the conduction band of TiO₂. Absorption spectra, calculated from several diffuse reflectance spectra (DRS) reported in the literature for both metal ion-doped TiO₂s and systems doped with non-metals (e.g., carbon, sulfur, nitrogen, and fluorine), are remarkably similar if not identical in the visible spectral region. The broad spectral envelope observed at wavelengths

N. Serpone (✉)

Dipartimento di Chimica Organica, Università di Pavia, Pavia, Italy
e-mail: nick.serpone@unipv.it

greater than 400 nm can be deconvoluted into 2–3 single bands, which indicate different species give rise to these bands. This chapter is therefore concerned, albeit in a very restrictive way, with the various strategies used to dope TiO₂, with their modeling by DFT methods, and finally with their optical properties with which we shall argue that the absorption edge red-shift originates from a singular source involving mostly the formation of (additional to existing) oxygen vacancies in the metal-oxide lattice (both surface and bulk) that can act as electron traps to yield F-type color centers and/or Ti³⁺ color centers.

1 Introduction

Metal-oxide heterogeneous photocatalysis developed with the several studies of the late 1970s and the 1980s that explored means to photogenerate clean alternative fuels (e.g., H₂ from water splitting). Semiconductor particulate systems provided stability and the possibility of modifying the particle surface, itself having good catalytic properties, by addition of functional or bifunctional co-catalysts (e.g. Pt, RuO₂, and others) to improve catalytic functions and to accentuate process dynamics. The search for solar energy conversion methodologies provided the impetus that ultimately led to significant advances in the last two decades of the twentieth century. Active exploration of irradiated semiconductors was aimed at the production of hydrogen and at the photooxidation of organic substrates, as the latter had been recognized as *sacrificial electron donors* in energy conversion processes.

Of a more practical nature were the problems encountered in rendering and implementing metal-oxide photocatalysis as a viable technology in energy conversion and environmental remediation, which ultimately rested with the use of TiO₂ as the major focus of hundreds of studies. This exhaustive literature describes heterogeneous photocatalysis and TiO₂ as an excellent photocatalyst in a variety of details as applied to the photochemical remediation of air and water. An extensive review by Diebold (2003) has summarized the properties of TiO₂ from the physics and surface science perspectives.

One issue quickly recognized with TiO₂ was that it absorbs but a small fraction (ca. 3–5%) of the sunlight reaching the Earth's surface. The absorption onset of UV light by the anatase polymorph begins around 387 nm (band gap energy, $E_{bg} \sim 3.2$ eV; for rutile $E_{bg} \sim 3.0$ eV or ca. 413 nm) and increases to shorter wavelengths. This led to the use of sensitizers to harness much of the solar energy to convert it into useful work. As a viable technology in environmental remediation, an issue that hampered heterogeneous photocatalysis in practical applications with aqueous slurries was the need for an additional filtration step to devices/reactors. TiO₂ needed to be immobilized on some appropriate inert support (glass, metals and plastics, among others). Of a more fundamental nature, however, was the issue that, once photogenerated, electrons and holes tend to recombine rather efficiently and rapidly against an otherwise slow redox chemistry occurring on the photoactivated TiO₂ surface.

The science underlying heterogeneous photocatalysis shows that the energy level of the bottom of the conduction band (CB) in a semiconductor like TiO_2 is a measure of the reduction potential of photogenerated electrons, whereas the upper level of the valence band is a measure of the oxidation potential of photogenerated holes. The flatband potentials, V_{fb} , of the conduction and valence bands, fixed by the nature of the material and in the case of metal oxides by proton exchange equilibria at the interface (i.e., pH dependent), determine the energy of electrons and holes at the interface. Hence, reductive and oxidative processes of couples with redox potentials more positive and more negative than the V_{fb} of the conduction and valence bands, respectively, can be driven by surface trapped electrons and holes. That is, the charge carriers (e^- and h^+) are ultimately poised at the particle surface to engage in various processes, the most important of which are photoreductions and photooxidations. Most research efforts in understanding the fundamental nature of heterogeneous photocatalysis with metal oxides (TiO_2 , ZrO_2 , and others) have focused on assessing the factors that underlie the temporal evolution of surface redox reactions on such metal-oxide materials.

Clearly, photoactivated semiconductor particles function as pools of electrons and holes that can be exploited in a variety of multi-electron transfer processes. The presence of a redox catalyst (e.g. Pt, RuO_2) loaded onto the particle surface greatly improves the catalytic efficacy of the semiconductor material. Such deposits usually lead to more efficient charge separation since the particle becomes polarized subsequent to irradiation, with the deposits tending to be good electron sinks. However, such deposits (i.e., dopants) can also act as recombination centers of photoelectrons and photoholes so that the redox efficacy can become largely compromised.

As a first-generation material, pristine TiO_2 has served well in photoassisted degradation and mineralization reactions of a large number of organic substrates in the quest to dispose of environmental contaminants in aqueous and atmospheric ecosystems. Unfortunately, its absorption edge at $\lambda < 400$ nm and thus its overall efficiency and usefulness, based on the total solar radiation reaching the Earth's surface, are limited. Accordingly, efforts were expended in the late 1980s to develop second-generation titanium dioxides (Lawless 1993) that could bridge both the UV (290–400 nm) and the visible (400–700 nm) radiation, and thereby enhance overall efficiency. The requirement was to red-shift the absorption edge of TiO_2 to wavelengths longer than 400 nm. Attempts toward achieving this goal rested, in part, on photosensitizing this metal oxide with suitable dyes that act as visible-light-harvesters, but which eventually lead to their own destruction, and with suitable metal-ion dopants, which unfortunately act either as recombination centers of photogenerated charge carriers (in some cases) or are simply ineffective in aiding the surface redox reactions, especially when metal doping is achieved by wet impregnation methods (Lawless 1993). However, studies by Anpo and Takeuchi (2003) have shown that metal-ion implantation produces metal-doped TiO_2 that enhances photo-induced surface redox reactions even in the visible-light region, where the wet chemical methods failed.

First reports of anion-doped TiO_2 began to appear in the early 1990s, although an earlier article by Sato (1986) also reported hints of an N-doped TiO_2 . It was not until the 2001 study in *Science* by Asahi and coworkers (2001) on the doping of TiO_2 by various anions to produce visible-light-active (VLA) N-doped TiO_2 , that researchers took anion-doping seriously as a prelude to produce second-generation TiO_2 materials that would increase photoactivity over the UV and much of the visible-light region. Subsequent studies reported several other VLA N-doped TiO_2 materials, together with C-doped TiO_2 and S-doped TiO_2 . Since these reports appeared, a lively debate in the recent literature has centered on the causes that lead the absorption onset of TiO_2 to be shifted to the visible region. Asahi and coworkers (Asahi et al. 2001; Morikawa et al. 2001) proposed that N-doping of TiO_2 shifts the absorption edge of $\text{TiO}_{2-x}\text{N}_x$ to lower energies and increases the photoactivity in the visible light region through narrowing of the TiO_2 band gap. Carbon- and sulfur-doped TiO_2 displayed similar red-shifts of the absorption edges and increased photoactivity. Others, however, have proposed that electronic transitions in these doped TiO_2 systems subsequent to visible-light irradiation involve transitions from N $2p$ localized states to the CB of titanium oxide.

Just as first-generation TiO_2 specimens led to several lively debates on the fundamental science that underlies TiO_2 -assisted photoredox surface processes (oxidations and reductions) following photoactivation, so are the second-generation TiO_2 specimens generating enthusiastic discussions on the root cause that shifts the absorption onset to longer wavelengths, and thereby increase photoactivity into the visible spectral range. This chapter focuses, albeit not exhaustively, on (i) various preparative methods of VLA TiO_2 materials, (ii) their XRD and XPS spectroscopic features, followed by (iii) their optical properties in the visible spectral region, (iv) the causes that lead to the red shift of the absorption edges of doped TiO_2 s, and finally (v) a brief visit into the lively debate concerning band gap narrowing.

2 Visible-Light Photoactivity of Undoped TiO_2 Specimens

To the best of our knowledge, the first study that dealt with VLA nominally pristine (undoped) TiO_2 was reported in the early 1970s by Teichner and coworkers (Formenti et al. 1971) who prepared anatase TiO_2 by a flame reactor method, and when irradiated in an O_2 atmosphere (120 Torr, 1 h, 27°C) found it to be photoactive in a broad range of wavelengths from 290 to 575 nm (4.30–2.15 eV). This induced the formation of $\text{O}_2^- \bullet$ species as evidenced by its EPR spectral signature. Spectral dependencies of the quantum yields (Φ) of simple photostimulated reactions have been measured for various undoped specimens (Cherkashin et al. 1980; Emeline et al. 2000, 2002). The reported data are in reasonably good agreement (see Figs. 1 and 2); however, the interpretations of the spectral dependencies of Φ in the visible region have not been coherently uniform (Cherkashin et al. 1980; Emeline et al. 2000, 2002).

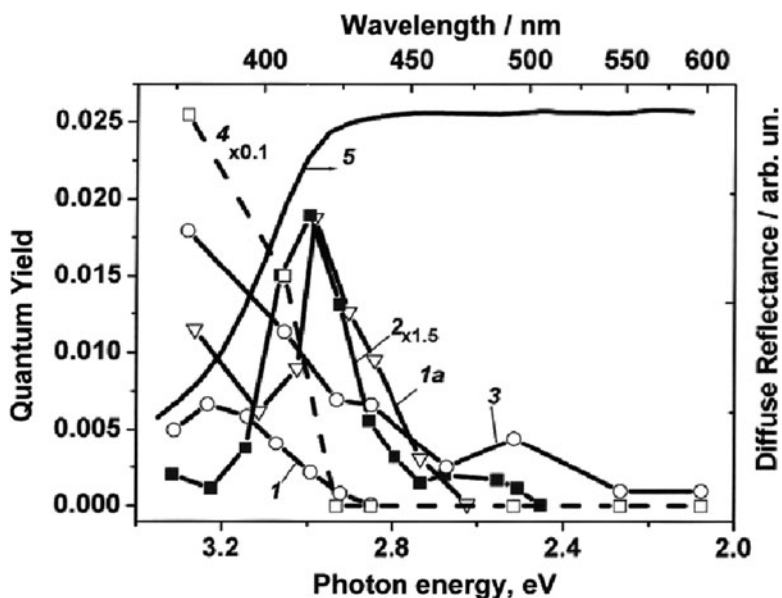


Fig. 1 Spectral dependencies of the quantum yields of photostimulated adsorption of O_2 on the surface of TiO_2 specimens: Degussa P25 pre-treated at $327^\circ C$ (curve 1) and at $577^\circ C$ (curve 1a), rutile (Aldrich) pretreated at $327^\circ C$ (curve 2), homemade rutile pretreated at $547^\circ C$ (curve 3). Spectral dependence of the quantum yield of photostimulated adsorption of CO on the surface of homemade rutile pre-treated at $547^\circ C$ (see text) (curve 4). Curve 5 represents the diffuse reflectance spectrum of Degussa P25 TiO_2

A large number of absorption spectra of various TiO_2 specimens that absorb in the visible region have been examined (Kuznetsov and Serpone 2006); they are discussed in greater detail later in the chapter (see Sect. [Optical Features of Doped \$TiO_2\$](#)). For the moment, suffices to note that in all cases the spectra could be interpreted as the sum of overlapping absorption bands (ABs) that originate from the reduction of TiO_2 under some pretreatment conditions, or otherwise when the specimen was prepared. It seems reasonable, therefore, to revisit the earlier data on nominally clean TiO_2 .

The spectral dependencies of Φ in the visible and near-band-gap regions, reported earlier by Cherkashin et al. (1980) and by Emeline and coworkers (2000, 2002), were digitized and are collected in Figs. 1 and 2. Three types of action spectra are clearly evident: (1) spectra 1 and 4 of Fig. 1 demonstrate excitation of the photo-reaction in the region of *intrinsic* (i.e., band-to-band) absorption; (2) spectra 1a, 2 and 3 of Fig. 1 and spectra 1, 1a, 2, 3, and 4 of Fig. 2 display maximal absorption at 2.9–3.0 eV, i.e., in the region of *extrinsic* absorption; and (3) spectra 2 and 3 of Fig. 1 and spectra 3 and 4 of Fig. 2 clearly show additional bands with maxima in the region 2.5–2.6 eV. Comparison of the positions of band maxima constituting the spectral dependencies (Figs. 1 and 2) and the main absorption bands in the spectra of various reduced TiO_2 samples (AB1 at 2.9 eV and AB2 at 2.55 eV) (Kuznetsov and Serpone

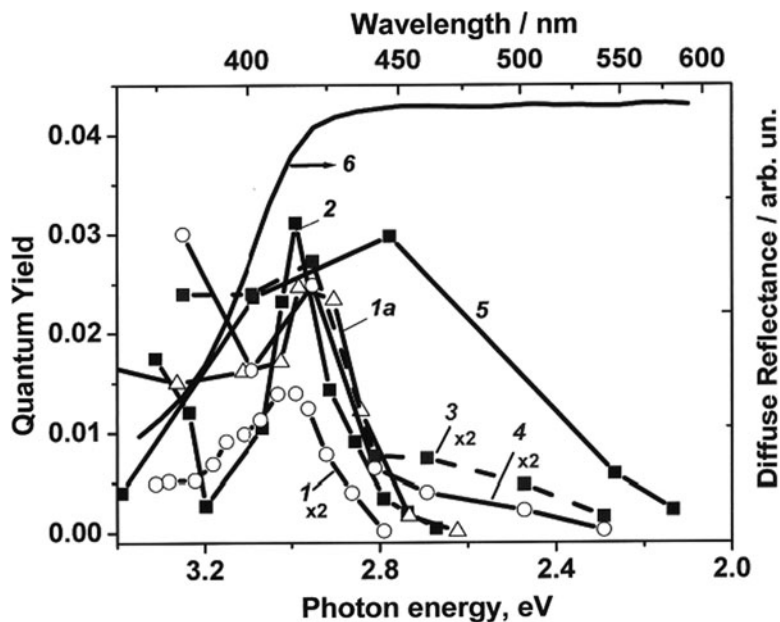


Fig. 2 Spectral dependencies of the quantum yields of photostimulated adsorption of H_2 (curves 1, 1a, 2, 3) and CH_4 (curve 4) on the surface of TiO_2 specimens: Degussa P25 pre-treated at 327°C (curve 1) and at 577°C (curve 1a), rutile (Aldrich) pre-treated at 327°C (curve 2), rutile (curves 3 and 4). Spectral dependence of the efficiency of photoformation of a hole species $[\text{O}^- \text{O}_2]$ at -186°C on the surface of anatase pre-treated at 527°C (curve 5). Curve 6 represents the diffuse reflectance spectrum of P25 TiO_2

2006) infers that photoactivity in the visible region of nominally pristine TiO_2 originates from TiO_2 reduction, which gives rise to defects/color centers. Note that Figs. 1 and 2 illustrate the action spectra of TiO_2 specimens of *different origins*: in particular, Degussa P25 and Aldrich rutile (Emeline et al. 2002), rutile (Emeline et al. 2000), superfine anatase (Russia) and rutile obtained from homemade superfine anatase by calcination in air at ca. 1000°C for 2 h (Cherkashin et al. 1980).

The spectral dependencies of Φ of photostimulated adsorption of H_2 and O_2 in the studies of Cherkashin et al. (1980) and of Emeline and coworkers (2000, 2002) were determined using a “black-body”-like cell with the rate of photoadsorption measured manometrically. Curve 5 in Fig. 2 depicts the spectral dependence of the efficiency of photoinduced formation of $[\text{O}^- \text{O}_2]$, i.e., $[\text{O}_3^-]$ species. In this case, the rate of evolution of the EPR signal ($g = 2.001$ and $g_{\parallel} = 2.008$), attributed to the O_2 molecule adsorbed on the photoinduced hole center, was normalized by the intensity of the incident light. Thus, spectrum 5 of Fig. 2 can be considered as being independent of the other spectra, but does demonstrate at least the same spectral region of photo-activity.

Samples of TiO_2 used in earlier studies (Cherkashin et al. 1980; Emeline et al. 2000, 2002) were heat-treated in air and then under oxygen/vacuum conditions at

temperatures around 327–577°C for several hours to purify the TiO₂ specimens of adventitious organic impurities. Prior to every photoadsorption measurement, the samples were typically preheated in an O₂ atmosphere ($p_{\text{O}_2} = 100$ Pa) at 427°C for 1 h (Cherkashin et al. 1980), or at 327°C for 15–20 min (Emeline et al. 2002) and subsequently cooled down in an O₂ atmosphere (Cherkashin et al. 1980) or under a dynamic vacuum (Emeline et al. 2002). The surface of the samples was thus fully oxidized under these conditions. It is appropriate then to query whether a contradiction exists with the above assignment of the spectral bands in the spectral dependencies of photoreactions. Note that these purified samples exhibited no remarkable absorption features in the diffuse reflectance spectra at energies below 3.0 eV (i.e., at $\lambda > \text{ca. } 400$ nm).

Color centers (defects) responsible for the 2.9-eV (AB1) and 2.55-eV (AB2) bands are only slightly active and weakly interact with O₂ so that formation of defects from the reduction of TiO₂ can also take place in air (Kuznetsov and Serpone 2006). Processes involving preparation of VLA TiO₂ specimens normally occur when the samples are heat-treated in air, or otherwise involve heating TiO₂ samples in air as a separate treatment stage.

Related to the above seeming contradiction, it is of import to consider some results that show the coexistence of a partly reduced bulk and an oxidized surface of titania specimens. If organometallic precursors or addition of any organic substrate are used in preparing TiO₂ systems, the organic residues can provide heat-activated reduction of TiO₂. Only a few studies demonstrated the existence of carbon-type species in VLA TiO₂ systems obtained when using organic precursors. Lettmann and coworkers (2001) report that pyrolysis (247°C, 3 h) of various alcohols used in the sol-gel process to obtain undoped TiO₂ leads to carbonaceous species embedded in the TiO₂ matrix. Commercial Hombikat UV-100 TiO₂ can also be made VLA-active when impregnated with various alcohols and then heat-treated at 247°C (Lettmann et al. 2001).

Three types of carbonaceous species have been detected in TiO₂ samples prepared by sol-gel methods using as the precursor titanium tetraisopropoxide, Ti (i-PrO)₄, dissolved in i-PrOH (Colon et al. 2006). The principal species were: (i) organic residues from the alkoxide precursor, (ii) slightly oxidized organics, and (iii) species further oxidized such as e.g., carboxylates. The organic-like carbon could be removed after calcination at 697°C for 2 h in air, although some graphitic carbon and some CO₃²⁻-like species *still remained* in TiO₂ at C levels ≥ 4.5 at. %.

Nominally clean, commercial TiO₂ powders can also include some adventitious metallic impurities. Diebold (2003) described the basic concepts of metal deposition on TiO₂ and details about different metals embedded in this metal oxide. Evidently, several metals can reduce TiO₂ with the metal becoming oxidized in the process. Thus, redox reactions and metal-doping TiO₂ specimens are some of the possible pathways that can lead to formation of defects/color centers in titania.

Formation of defects and color centers, connected with the reduction of TiO₂ in the case of nominally clean specimens, is an uncontrollable process. It can occur during the stage of industrial production and/or during the treatment preceding experimental studies. Removal of adventitiously adsorbed organic impurities from

the metal-oxide surface is typically achieved by heat-treatment at temperatures about 327–627°C in air, followed by treatment under oxygen/vacuum conditions at the same temperatures for several hours. This is necessary when photostimulated reactions of oxygen-containing molecules are to be examined. Accordingly, calcination of a metal-oxide *surface* can potentially stimulate the formation of defects/color centers in the *lattice bulk* through organic/inorganic impurity-assisted reduction of the sample. To date, however, there exists only indirect evidence for these inferences.

The influence of temperature of the pretreatment stage on the photoactivity of Degussa P25 TiO₂ has been examined by Emeline and coworkers (2002). The dramatic increase of the 3.0-eV band in the wavelength-dependent quantum yield spectrum of the photoadsorption of O₂ (Fig. 1, curves *l* and *la*) and the significant increase of nearly the same band in the quantum yield spectra of photoadsorption of H₂ (Fig. 2, curves *l* and *la*) can be taken as an increase in the number of defects responsible for the absorption band at 2.9–3.0 eV. This increase in the number of defects originates from an increase in the pretreatment temperature of 327–577°C. The photoactivity at 2.86 eV (433 nm) of N-doped TiO₂ systems, prepared by hydrolysis of either Ti(*i*-PrO)₄ or TiCl₄ with aqueous NH₃, shows a remarkable growth (from 0 to maximum value) in a very narrow temperature range 297–397°C and 347–447°C, respectively (Sato et al. 2005). The visible-light absorption and visible-light activity of metal-ion implanted TiO₂ systems reported by Anpo and Takeuchi (2003) was observed only after the samples had been calcined at temperatures ranging from 450 to 550°C.

It is important to emphasize that nominally clean TiO₂ display long-term (months) photoactivity in the visible-light region owing to the stability of color centers under certain experimental conditions. Prior to every photoadsorption measurement, TiO₂ samples were preheated in an oxygen environment at 327–427°C and then cooled in an O₂ atmosphere or under vacuum conditions (Cherkashin et al. 1980; Emeline et al. 2000, 2002). We can thus conclude that defects/color centers in the lattice bulk that absorb visible light remain stable under such treatments.

Related to the above inference, we now consider some results that show the co-existence of partially reduced bulk and oxidized surface of titania. VLA TiO₂ thin films that absorb in the range 3.10–1.55 eV have been fabricated by a radio-frequency-magnetron sputtering (RF-MS) deposition method under an Ar atmosphere ($p_{\text{Ar}} = 1\text{--}3$ Pa) and a substrate temperature of 600°C (Kitano et al. 2006a). SIMS measurements revealed that the O/Ti ratio of VLA TiO₂ decreased from the top surface (2.00 ± 0.01) to the inside bulk (1.93 ± 0.01). Moreover, VLA TiO₂ was stable even under calcination treatment at 450°C in air or in photocatalytic reactions, indicating that the films' surface was covered with a stoichiometric and stable TiO₂ phase that prevented the complete oxidation of bulk TiO₂. Note also that the absorption band at 3.0 eV, originating from an impurity-assisted reduction of the anatase crystal, was suppressed fully *only* after calcination at 800°C for 60 h under an oxygen pressure of 1 MPa (Sekiya et al. 2000).

Temperature-programmed desorption (TPD) spectra of CO₂ after adsorption of O₂, both in the dark (chemisorption on a vacuum-reduced surface) or under

irradiation, confirmed the presence of adventitious carbonaceous species in Degussa P25 TiO₂. The sample of TiO₂ was deposited on the wall of a quartz cell and then heated in air to 327°C and kept at this temperature for ca. 4 h. The sample cell was connected to a high-vacuum system and pretreated in alternating O₂ flow (130 Pa) and vacuum (10⁻⁶ Pa) at 577°C for 30 h. During all stages of the experiments, the gas composition above the sample was controlled by an MI-1201 mass spectrometer. TPD spectra were obtained under heating at a constant rate $\beta = 0.25^\circ\text{C s}^{-1}$ in the range 17–577°C. Oxygen was purified by diffusion through the walls of a silver capillary tube. Further details regarding the TPD spectra analysis are available elsewhere (Kuznetsov 2002).

Figure 3 illustrates typical TPD spectra of oxygen chemisorbed (curve 1) and photoadsorbed (curve 2) on the surface of a TiO₂ sample cleaned using the above procedure. Oxygen coverage corresponding to spectrum 1 in Fig. 3 is $\sim 1 \times 10^9$ molecules cm⁻²; the corresponding coverage for spectrum 2 is ca. 6×10^{10} molecules cm⁻². Absence of the dependence of the 410-K peak on oxygen coverage is direct evidence for first-order kinetics of desorption (i.e., monomolecular desorption) with respect to coverage (Redhead 1962), and consequently infers adsorption of molecular O₂ rather than atomic oxygen. The principal peak at 410 K of the oxygen TPD spectra is characteristic of the vacuum-annealed (reduced at 527–577°C) rutile surface of single crystals (Henderson et al. 1999) and powdered samples (Beck et al. 1986).

Figure 3 also reports the TPD spectra of CO₂ measured simultaneously with the TPD spectra of O₂. The coverage of CO₂ in the range $\sim 5 \times 10^8$ molecules cm⁻²

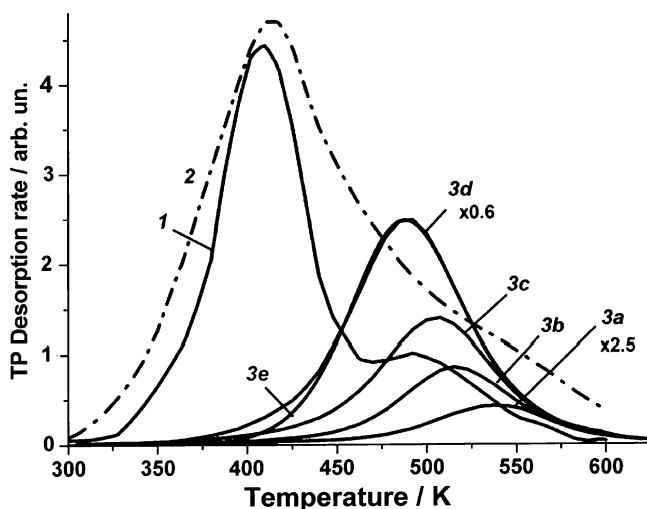


Fig. 3 Temperature-programmed desorption spectra of oxygen chemisorbed (curve 1) and photoadsorbed (curve 2) on the surface of Degussa P25 TiO₂ pre-treated in air and under O₂/vacuum conditions at 577°C for 30 h. Spectra 3a–3d represent the TPD spectra of CO₂ resulting from oxygen adsorption and thermal desorption. Curve 3e is a numerically calculated peak of recombinative desorption (see text)

(spectrum 3a) to ca. 10^{10} molecules cm^{-2} (spectrum 3d) always correlated with O_2 coverage and did not exceed 30% of O_2 coverage. Three main features of CO_2 desorption are worth noting: (i) desorption occurred only after O_2 was chemisorbed or photoadsorbed and was absent when the sample was kept in a vacuum, (ii) the TPD spectra of CO_2 consisted of a single peak of somewhat symmetrical shape, and (iii) the position of the peak's maximum (T_{max}) depended on coverage. A shift (decrease) of T_{max} of ~ 50 K when coverage increased by a factor of ~ 25 (Fig. 3) is direct evidence of second-order kinetics of desorption (i.e., recombinative desorption) with respect to coverage (Redhead 1962). Moreover, the near symmetrical TPD peak, characteristic only of recombinative desorption, could be calculated numerically using experimental values of the initial CO_2 coverage: ca. 10^{10} molecules cm^{-2} and $\beta = 0.25^\circ\text{C s}^{-1}$ along with the fitting values of the activation energy of desorption 0.88 eV and the pre-exponential factor 10^{-3} cm^2 molecules $^{-1}$ s^{-1} . The calculated (curve 3e) and experimental (curve 3d) peaks coincide quite well. However, near 410 K an additional CO_2 peak seems to appear. It is worth noting that TPD spectra of CO_2 , molecularly adsorbed on the surface of powdered rutile TiO_2 pre-heated at 727°C in vacuum, revealed a single peak at the lower temperature of ~ 415 K (Yanagisawa and Sumimoto 1994).

Because desorption of CO_2 and O_2 occurs simultaneously (Fig. 3), it is reasonable to suppose that once oxygen is liberated from adsorption sites (at $T > 400$ K atomic species can dominate) it can interact with any C-containing species leading to CO_2 formation. Thus, desorption of CO_2 having non-adsorptive origins is a very clear indicator of the presence of carbonaceous inclusions in TiO_2 specimens. After nearly 3 months of almost daily experiments, the effectiveness of O_2 -assisted CO_2 formation remained virtually unchanged. Hence, C-containing species are located in the volume/subsurface region of TiO_2 and rise to the surface by diffusion when TiO_2 is subjected to a heat treatment, including programmed heating. The overall quantity of CO_2 formed during the TPD experiments (after ca. 50 spectra) is $\sim 10^{16}$ molecules. Since the sample's weight $w = 0.1$ g, the sample contains $(N_A/M)w \approx 10^{21}$ entities (molecules) of TiO_2 ; N_A is Avogadro's number (6×10^{23} mol^{-1}) and M denotes the molecular weight of TiO_2 (80 g mol^{-1}). The invariant efficiency of formation of CO_2 indicated that a negligible fraction (a few %) of C-species took part in the reaction. Hence, the content C of the above species in the sample equaled to or exceeded 0.1% (i.e., $C \geq (10^{16}/10^{21})/10^{21}$).

Experimental data (Kuznetsov and Serpone, 2006) showed that nominally clean TiO_2 P25 included sufficient quantity of C-containing species, even after the long-term heat pretreatment in an O_2 atmosphere and after photo- and heat-treatment in O_2 and in vacuum during numerous experiments. With such evidence, we concluded that defects/color centers resulted from reactions of carbonaceous species with lattice bulk oxygen, thus leading to the display of photoactivity in the visible spectral region. Indeed, a specimen we investigated demonstrated permanent photoactivity under both UV- and visible-light ($\lambda \leq 546$ nm, $h\nu \geq 2.27$ eV) irradiation in the photodesorption of chemisorbed and photoadsorbed oxygen, as well as photoadsorption and photodisproportionation of nitric oxide (NO). Based on presently available published data, only the 2.9-eV AB1 and 2.55-eV AB2 bands

provide light absorption and consequently activation of TiO_2 in this spectral region (Kuznetsov and Serpone 2006).

Photostimulated adsorption of O_2 acceptor molecules occurs on electron surface centers formed by trapping of photogenerated free electrons by surface defects, whereas photoadsorption of H_2 donor molecules takes place at hole surface centers (trapped photogenerated holes). Thus, irradiation into the AB1 and AB2 bands (Figs. 1 and 2) should also generate free electrons and free holes. A similar manifestation of color centers responsible for the AB1 and AB2 absorption bands in compositions of TiO_2 with various polymers (Kuznetsov and Serpone 2007) suggests that formation of color centers is initiated by photoholes and assisted by organic molecules, whereas the destruction of the same centers is initiated by photoelectrons and assisted by oxygen (see Sect. [Optical Features of Doped \$\text{TiO}_2\$](#)).

The above analysis leads to the conclusion that preparative methods of nominally pristine TiO_2 and/or pretreatment of TiO_2 samples are reductive and ultimately provide an uncontrollable formation of intrinsic defect/color centers and thus long-term visible-light photoactivity. The number of these centers is unfortunately insufficient to be measured precisely by diffuse reflectance spectroscopy, but do become apparent in photoadsorption/photodesorption processes and in photoreactions of molecules. In practice, commercially available undoped TiO_2 photocatalyst specimens, including Degussa P25 TiO_2 (Lettmann et al. 2001; Li et al. 2004a; Ren et al. 2007) and Hombikat UV-100 TiO_2 (Lettmann et al. 2001) show appreciable activity in the photodegradation of various molecules even under visible-light irradiation. However, the origin of the visible-light activity of these specimens is not the subject of the present discussion.

3 Preparation and Characteristics of VLA TiO_2 samples

3.1 Undoped Titanium Dioxide Specimens

Hydrolysis of $\text{Ti}(\text{i-PrO})_4$ in aqueous isopropanol by dispersion in dilute H_2SO_4 followed by calcination at ca. 700°C yields a sulfated anatase TiO_2 , which displays weak absorption in the 400–600 nm region (Colon et al. 2006). XPS analysis shows that loss of surface acidic hydroxyl groups below 500°C , followed by decomposition of sulfate species, leads to formation of oxygen vacancies (V_{OS}) within the anatase lattice. Calcination above 600°C decomposes the surface sulfates, eliminates surface V_{OS} but leaves intact a significant number of stable subsurface oxygen vacancies, as indicated by XPS findings of low O/Ti ratios. Formation of stable V_{OS} during calcination at high temperatures leads to creation of intermediate states located within the band gap of TiO_2 , responsible for the small absorption band in the visible spectral range (Fig. 4) subsequent to electron trapping by the V_{OS} . Although the existence of Ti^{3+} in the bulk also leads to a red shift in absorption, the XPS results precluded these species, and no shift in absorption edge of the anatase TiO_2 occurred (see inset in Fig. 4).

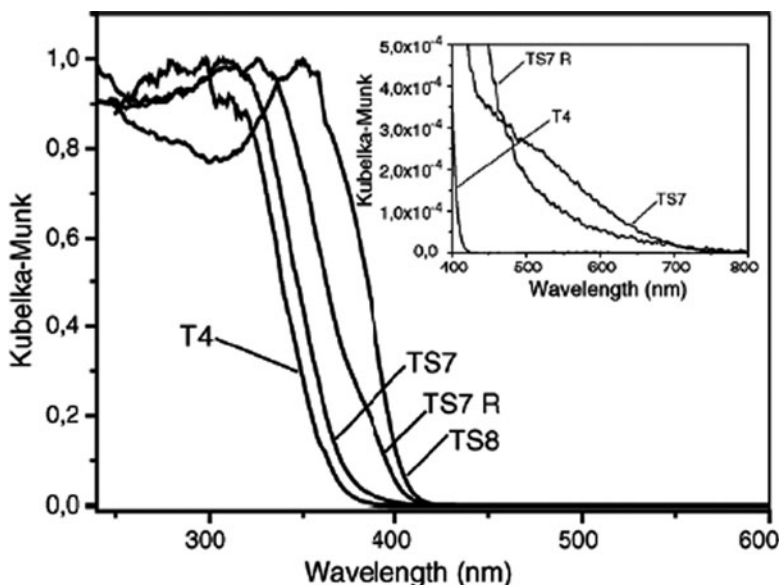


Fig. 4 UV-visible diffuse reflectance spectra for a series of sulfated TiO₂ specimens calcined at different temperatures (TS7 calcined at 700°C). Reproduced with permission from Colon et al. (2006). Copyright 2006 by Elsevier B.V.

Common methods used to create defect sites (e.g., V_O and/or Ti³⁺) on the TiO₂ surface are typically UV-light irradiation, annealing the sample in vacuum, ion sputtering, and plasma treatment. These methods follow a previous step, which typically involves preparing crystalline TiO₂ powders/films. Suriye and coworkers (2006) have reported a new method of creating surface defects on TiO₂, which occurs concomitantly with the preparation of TiO₂ by the sol-gel method through varying the quantities of oxygen during the calcination process. Hydrolysis of titanium ethoxide in water/ethanol yields white precipitates of hydrous oxides, following which separation of the amorphous oxides by centrifugation and redispersion in ethanol minimizes particle agglomeration. Drying the resulting materials and calcining at 450°C in a N₂ mixture containing various quantities of O₂ (0–100 %) produces specimens with the anatase architecture (XRD analysis). Low-temperature (–196°C) EPR analysis confirmed the presence of Ti³⁺ species ($g = 1.996$) on the TiO₂ surface formed not by reduction of Ti⁴⁺ (low calcination temperature and absence of H₂) but during calcinations. That is, during oxidation of inorganic and organic residues that releases enough energy (increases with increase in O₂) to facilitate loss of surface OH groups by a process depicted in Fig. 5 and best summarized by reaction (3.1), according to which removal of an OH group that occupies positively charged oxygen lattice sites (O[•]) releasing H₂O_{gas} in addition to forming an oxygen atom at a neutral lattice site (O_{Ox}) and a double positively charged oxygen

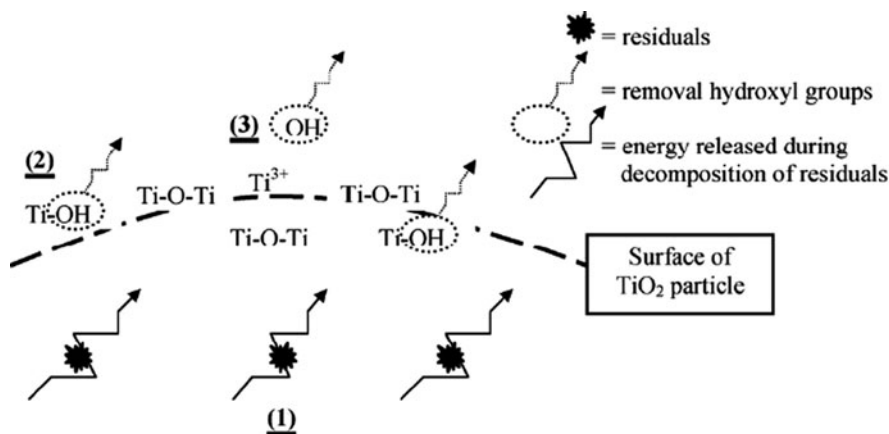
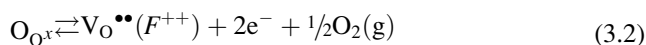


Fig. 5 Simplified scheme illustrating (1) the energy release during the degradation of residuals at high concentrations of O_2 , (2) the loss of OH groups and (3) the formation of the surface defects (Ti^{3+}). Reproduced with permission from Suriye et al. (2006). Copyright 2006 by Elsevier B.V.



notation; i.e., an F^{++} center, an anion vacancy V_A). Dehydroxylation of the metal-oxide surface can also lead to formation of F and F^+ centers other than F^{++} centers (Mori-Sanchez et al. 2002). Germane to this discussion, Nakamura et al. (2000) showed that plasma-treated TiO_2 exhibits visible-light activity up to ca. 600 nm compared to untreated TiO_2 in the removal of NO. This was later confirmed by Ihara and coworkers (Ihara et al. 2001) by irradiation at $\lambda > 406$ nm. The process requires trapped electrons to convert NO to NO_3^- ions. Combined optical and EPR studies placed the wavelength above which no trapped electrons are observed at 639 nm. These authors located the V_O energy levels at 0.75–1.18 eV below the CB of TiO_2 (Fig. 6). The V_O s trap the electrons on excitation of the TiO_2 valence band with 506–614 nm visible-light radiation. The trapped electrons in the oxygen vacancies (F centers) determine the VLA activity of TiO_2 , because the nanoparticles with F centers provide unique energy levels that correspond to visible-light excitation (see Fig. 6). Sun and coworkers (2004a, b) examined F centers quantitatively by EPR in high-surface-area TiO_2 anatase nanoparticles prepared by metal-organic chemical vapor deposition (MOCVD) techniques. Surface rather than bulk processes dominate the temperature- and time-dependent concentration of F centers. Oxygen evolution occurs by the thermodynamic mechanism illustrated by reactions (3.2, 3.3), the sum of which yields the overall reaction (3.4).



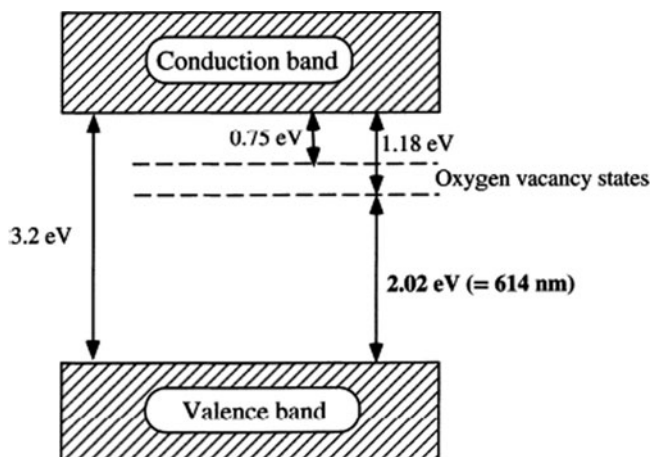
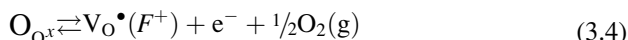
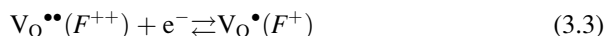


Fig. 6 A proposed band structure model for the anatase TiO_2 with oxygen vacancies. Reproduced with permission from Nakamura et al. (2000). Copyright 2000 by Elsevier Science B.V.



Germane to this, room-temperature photoluminescence (PL) spectra of TiO_2 nanowire arrays showed a broadband envelope in the visible spectral range that was resolved into three bands at ca. 425, 465, and 525 nm (Lei et al. 2001). In line with the work of Saraf et al. (1998), they were attributed to self-trapped excitons, F , and F^+ centers, respectively.

Hydrolysis of $\text{Ti}(n\text{-BuO})_4$ in ethanol/water acidified with HNO_3 to catalyze the hydrolytic process and the condensation reactions yields TiO_2 , which after drying at 120°C and calcining at $150\text{--}600^\circ\text{C}$ gives TiO_2 specimens that absorb visible light (Fig. 7) (Lin et al. 2006). Specimens calcined at $150\text{--}300^\circ\text{C}$ were particularly VLA in the degradation of NO_x pollutants. Anatase predominated at calcination temperatures below 500°C , while rutile was the dominant phase at 600°C . Some brookite also formed between 200 and 500°C (X-ray dispersion analysis, XRD).

Using a slightly modified but similar procedure from that of Lin et al. (2006), Dong and coworkers (Dong et al. 2006) placed $\text{Ti}(n\text{-BuO})_4$ in absolute alcohol acidified with HNO_3 , followed by dropwise addition of ethanol-water to hydrolyze completely the butoxide. Calcination at 300°C in air for 1 h gave a yellowish anatase (XRD) TiO_2 specimen whose absorption spectrum is reported in Fig. 8. Most intriguing, this procedure produced TiO_2 codoped with both C and N. X-ray photoelectron spectra (XPS) displayed two strong peaks in the C 1s spectrum at 284.6 and 281 eV due, respectively, either to graphitic or hydrogenated C–C bonds, or to Ti–C bonds with C in the latter case positioned either at interstitial or substitutional positions. The XPS N 1s spectrum showed peaks at 400 and

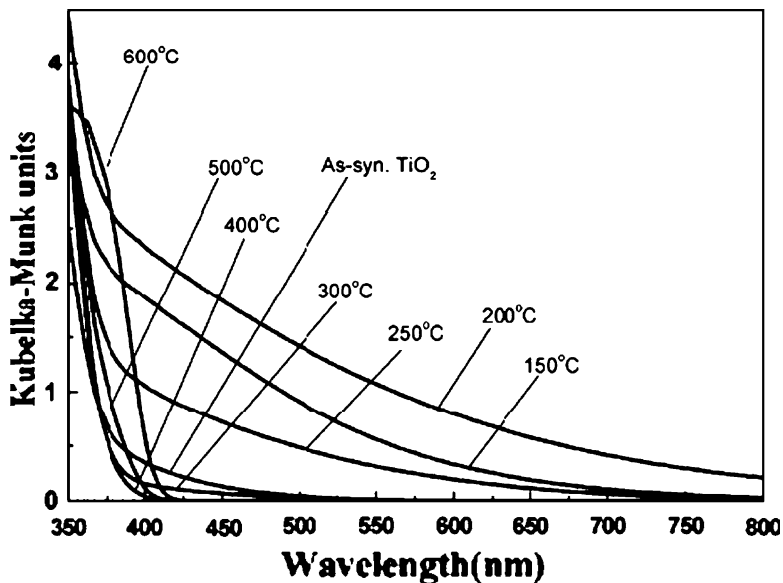


Fig. 7 UV-visible absorption spectra of sol-gel synthesized TiO₂ calcined at various temperatures. Reproduced with permission from Lin et al. (2006). Copyright 2006 by the American Chemical Society

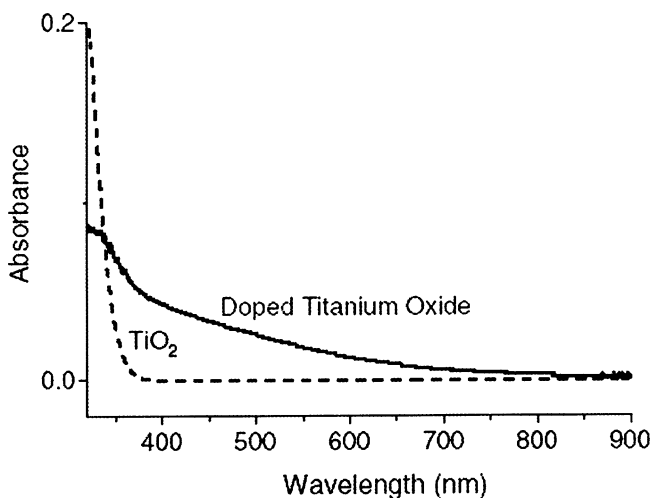


Fig. 8 UV-visible absorption spectra of TiO_{2-x-y}C_xN_y (1.1% C and 0.4% N) and a commercial sample of TiO₂. Reproduced from Dong et al. (2006). Copyright 2006 by Springer

396 eV resulting, respectively from N–O and Ti–N bonding with N atoms in the latter case (band at 396 eV) substituting the O atoms in the lattice.

An interesting innovative method of using visible-light radiation to photoactivate pristine TiO_2 (Wang et al. 2006) to photogenerate electrons and holes involves doping TiO_2 with the upconversion luminescence agent $40\text{CdF}_2 \cdot 60\text{BaF}_2 \cdot 1.0\text{Er}_2\text{O}_3$ which converts visible light at 488 nm into five UV wavelengths between 200 and 450 nm. The preparation involves adding a mixture of the upconversion agent and nano-rutile TiO_2 powder to distilled water and then adequately dispersing it by ultrasound for ca. 30 min; after filtration and separation of the resulting powder, calcination at 500°C for 3 h gives the doped nano TiO_2 material.

3.2 Transition Metal-Ion Doped Titanium Dioxides

Anpo and Takeuchi (2003) were one of the first groups (if not the first) to make extensive use of metal-ion-implantation and RF-MS deposition methods to develop second-generation VLA TiO_2 photocatalysts, together with VLA small TiO_2 species incorporated within cavities and frameworks of zeolites and mesoporous rous molecular sieves. These methods have opened up several innovative venues to utilize sunlight or artificial UV-visible light.

Metal-ion implantation of TiO_2 with various $3d$ transition metal ions (e.g., V, Cr, Mn, Fe, and Ni) has led to a non-insignificant shift of light absorption by TiO_2 materials into the visible spectral region. Figure 9 illustrates this spectral shift in the absorption onset in the case of Cr ion-implanted TiO_2 with the extent of the red-shift being a function of the quantity and nature of the metal-ion dopant. The order of the red-shift followed the trend: $\text{V} > \text{Cr} > \text{Mn} > \text{Fe} > \text{Ni}$. However, the red-shifts in the absorption features were observed *only* after calcination of the metal-ion implanted TiO_2 samples in an O_2 atmosphere at temperatures around $450\text{--}550^\circ\text{C}$. By contrast, absorption spectra of Cr ion-doped TiO_2 prepared by impregnation or by chemical methods showed no shift of the TiO_2 absorption edge (Fig. 10).

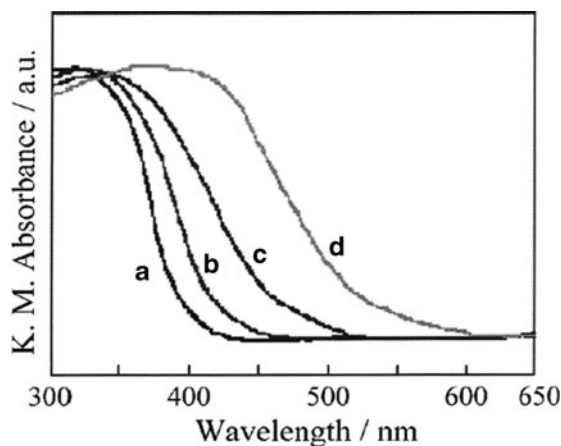


Fig. 9 UV-vis absorption spectra of (a) TiO_2 and (b-d) Cr ion-implanted TiO_2 . The quantity of implanted Cr ions ($\mu\text{mol/g}$) is, respectively: (a) 0, (b) 0.22, (c) 0.66, and (d) 1.3. Reproduced with permission from Anpo and Takeuchi (2003). Copyright 2003 by Elsevier Science (USA)

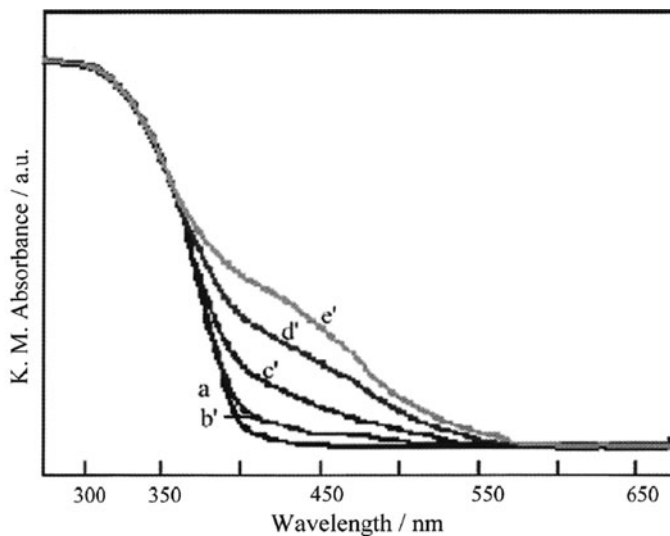


Fig. 10 UV-vis absorption spectra of (a) TiO₂ (a) and (b'–d') Cr ion-doped TiO₂ specimens prepared by an impregnation method. Amount (as $\mu\text{mol/g-TiO}_2$) of doped Cr ions was (a) 0, (b') 0.49, (c') 4.9, (d') 24.5, and (e') 49. Reproduced with permission from Anpo and Takeuchi (2003). Copyright 2003 by Elsevier Science (USA)

Clearly, the two completely different preparative methodologies altered the optical properties of TiO₂. UV-light ($\lambda < 400$ nm) photoactivity of the metal-ion-implanted TiO₂s remained unchanged relative to undoped TiO₂s. The major difference between the two sets of TiO₂s is that in metal-ion implanted TiO₂ the metal-ion dopants do not act as electron-hole recombination centers, contrary to impregnated systems. However, the quantity of metal ions that can be implanted into the TiO₂ lattice has an upper limit, below which the photoefficiency increases with metal-ion concentration but above which the photoefficiency decreases.

XAFS spectra showed that in TiO₂ systems, doped either by impregnation or by a sol-gel method, the Cr ions are present as aggregated chromium oxides reminiscent of Cr₂O₃ and CrO₃. In contrast, in metal-ion implanted TiO₂ systems the Cr ions are present in highly dispersed and isolated states, i.e., states in which the Cr ions substitute Ti ions in the metal-oxide lattice.

Electrochemical anodization of Ti yields layers of TiO₂ nanotubes which, subsequent to Cr doping by metal-ion implantation, produces a TiO₂ with the anatase structure (XRD) but with a certain degree of amorphization of the TiO₂ (Ghivov et al. 2007). The effect is, however, reversible by subsequent thermal treatment. Visible-light photoresponsive Cr- and V-doped TiO₂ thin films supported on Vycor glass can also be fabricated by metal-ion implantation (Takeuchi et al. 2000). The films are quite photoactive in degrading NO_x to N₂ and O₂ at $\lambda > 450$ nm.

Some unique VLA-active TiO₂ materials responsive to visible light at $\lambda > 450$ nm have also been developed by implantation of V ions into TiO₂ thin films supported on a quartz substrate (Zhou et al. 2006). The films are photoactive in degrading

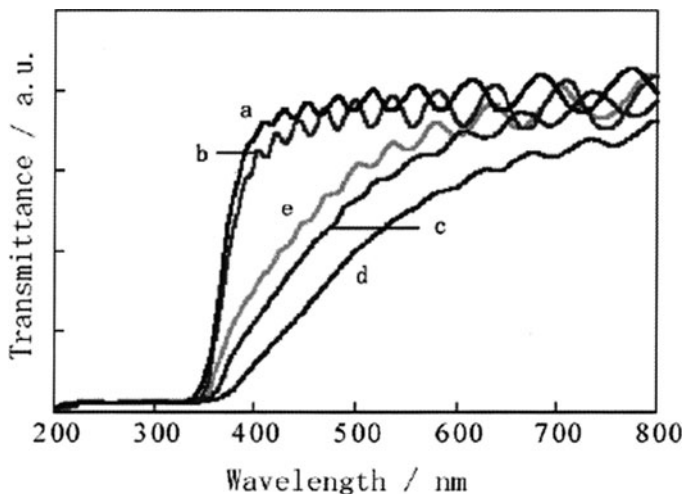


Fig. 11 UV-vis transmittance spectra of TiO₂ thin films prepared by the RF-MS deposition method at temperatures of (a) 100°C, (b) 200°C, (c) 400°C, (d) 600°C, and (e) 700°C. Reproduced with permission from Anpo and Takeuchi (2003). Copyright 2003 by Elsevier Science (USA)

HCOOH to CO₂ and H₂O under visible-light irradiation ($\lambda > 450$ nm). XPS spectra showed no peaks attributable to VO_x species, indicating that the implanted V ions were dispersed deep inside the TiO₂ bulk lattice.

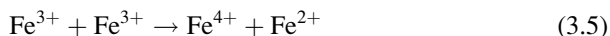
Anpo and Takeuchi (2003) also developed an alternative method to prepare VLA TiO₂ thin films by the RF-MS deposition method. Figure 11 displays the UV-visible diffuse reflectance spectra (DRS) of TiO₂ thin films prepared by RF-MS at different substrate temperatures. Films prepared at temperatures above 500°C exhibited efficient absorption in the visible region; the film prepared at 600°C showed the highest absorption.

VLA Cr-doped TiO₂s have also been obtained (Zhu et al. 2006a) by a combined sol-gel/hydrothermal treatment method in which the quantity of Cr decreased from the surface into the lattice (XPS, AAS). Preparation involves hydrolysis of Ti(i-PrO)₄ in acidified HNO₃ isopropanol/water. Aging the resulting mixture, followed by filtration and drying at 70°C yields a dried TiO₂ gel, which is then Cr-doped by mixing it with a hydrated Cr(NO₃)₃ salt in water/isopropanol solvent and autoclaving it at 200°C for 8 h. EPR analysis showed that Cr³⁺ occupy Ti⁴⁺ positions in the anatase lattice (XRD) along with Cr⁴⁺ ions to maintain electroneutrality. The photoactivity of Cr-doped TiO₂ greatly improved under UV- and visible-light irradiation for optimal concentrations of Cr of 0.15 and 0.2%, respectively. Doping Cr³⁺ greatly increases light absorption of the TiO₂ in the visible spectral region. The band at 450 nm originated from either a charge transfer band Cr³⁺ → Ti⁴⁺ or from a d-d transition ${}^4A_{2g} \rightarrow {}^4T_{1g}$ of Cr³⁺ in an octahedral environment of the anatase TiO₂ network. The broad band at 620–800 nm apparently originated from ${}^4A_{2g} \rightarrow {}^4T_{2g}$ transitions of Cr³⁺.

Except for metal-ion implantation, substitutional doping of TiO₂ with metal ions (e.g., Fe) by other preparative methods may also extend the photoresponse of TiO₂ to longer wavelengths. Regrettably, this does not guarantee photoactivity under visible-light irradiation.

VLA Fe-doped TiO₂ can be prepared (Teoh et al. 2007) by a one-step flame spray pyrolysis (FSP) technique. A mixture of Ti(i-PrO)₄, xylene and CH₃CN, together with a predetermined quantity of iron naphthenate (the Fe source), was atomized through a nozzle and combusted in a methane/oxygen flame. Increasing the Fe/Ti ratio from 0.005 to 0.30 gradually shifted the absorption threshold of the Fe-doped TiO₂ from 396 to 564 nm, corresponding to band gap energies of 3.13 and 2.20 eV, respectively. Donor levels of the Fe dopants were located within the TiO₂ band gap close to the valence band, allowing for *extrinsic* excitation of the doped TiO₂ under visible-light illumination. This implicates a transition of the higher energy level 3*d*-electrons from the Fe dopant to the TiO₂ CB. The absorption band at ~490 nm of Fe-doped TiO₂ at Fe/Ti ratios greater than 0.10, however, finds no accepted assignment as to whether it is due to a d–d transition or to a charge transfer transition. Both Navio et al. (1996) and Li et al. (2003) observed an absorption band centrally shifted to 530 nm in Fe-doped TiO₂ specimens synthesized by wet impregnation and sol-gel methods, respectively, followed by calcination at high temperatures. The 530-nm band was attributed to a segregated hematite phase subsequently confirmed by XRD methods.

Doping Fe³⁺ into TiO₂ during hydrothermal crystallization to optimize the distribution of iron in the TiO₂ anatase lattice (XRD) was achieved (Zhu et al. 2006b) by doping TiO₂ with different amounts of Fe³⁺ through a combined sol-gel/hydrothermal treatment methods in a manner otherwise similar to that used for Cr-doped TiO₂ (see above). EPR spectra confirmed incorporation of Fe³⁺ into the anatase lattice. UV–visible absorption spectra reported in Fig. 12 show both *intrinsic* band gap absorption at 380 nm for pure anatase TiO₂ ($E_{bg} \sim 3.2$ eV) and enhanced absorptions in the *extrinsic* region 400–650 nm with increasing Fe content. The band at ~415 nm is probably due to excitation of 3*d* electrons from Fe³⁺ levels to the TiO₂ CB (a charge transfer transition), whereas the broad band at ca. 500 nm likely originates from ²T_{2g} → ²A_{2g}, ²T_{1g} d–d transitions of Fe³⁺ or from charge transfer between two Fe³⁺ (reaction 3.5). However, the latter inference is highly unlikely, unless the two Fe³⁺ ions are in totally different environments in the TiO₂ lattice.



Doping with Fe³⁺ can introduce additional V_{OS} on the surface and in the bulk of TiO₂, thus favoring adsorption of H₂O, formation of surface OH[−] group, and promoting photoactivity. Efficient separation of photogenerated charge carriers (reaction 3.6) can also lead to increased activity as the Fe³⁺ can trap photogenerated holes (reaction 3.7) through Fe³⁺/Fe⁴⁺ energy levels apparently located above the valence band edge of anatase TiO₂. Trapped holes in Fe⁴⁺ migrate to the surface and oxidize the OH[−] groups to •OH radicals (reaction 3.8). Countering reactions

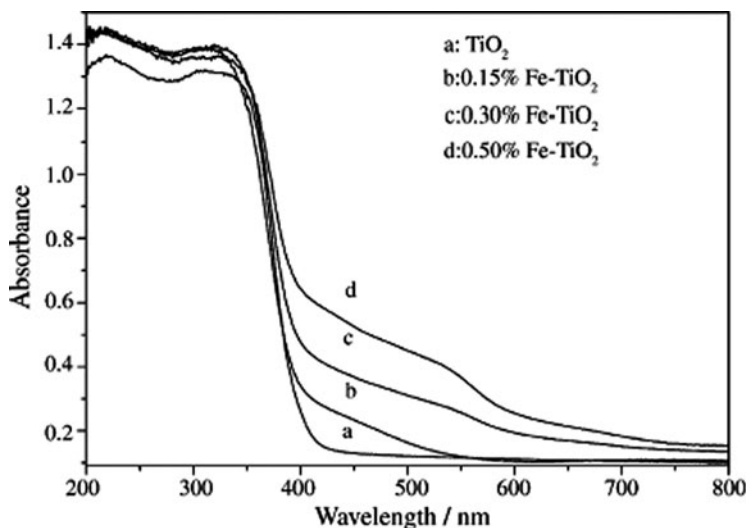
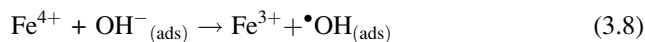
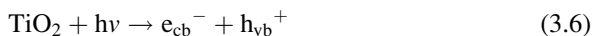


Fig. 12 UV-visible absorption spectra of: (a) TiO_2 ; (b) 0.15% Fe-TiO_2 ; (c) 0.3% Fe-TiO_2 ; and (d) 0.5% Fe-TiO_2 . Reproduced with permission from Zhu et al. (2006b). Copyright 2006 by Elsevier B.V.

(3.6–3.8) are reactions involving the scavenging of photogenerated electrons at the surface by O_2 yielding superoxide radical anions, $\text{O}_2^{\bullet-}$, and ultimately $\bullet\text{OOH}$ radicals on protonation. EPR spectral evidence showed that Fe^{3+} ions also act as traps of photogenerated electrons (Soria et al. 1991).



VLA zinc-ferrite doped titania, $\text{TiO}_2/\text{ZnFe}_2\text{O}_4$, prepared by a sol-gel method followed by calcination at different temperatures (400–600°C) displays DRS spectra that show the absorption edge to be red-shifted to longer wavelengths (Fig. 13) (Cheng et al. 2004). XRD results indicated a stable TiO_2 anatase phase under these conditions.

Thin films of Au-doped TiO_2 on various supports (glass slides, glass helix, silica rashig rings), prepared by sol-gel dip coating from a sol of colloidal gold and titanium peroxide (Sonawane and Dongare 2006), showed a red-shift of the absorption edge (band at 550 nm). This resulted from incorporation of Au particles into the TiO_2 nano-architecture subsequent to calcination at 200–800°C. XRD analyses indicated an anatase structure and no rutile until 600°C. However, at 800°C the XRD pattern showed little change in the anatase/rutile ratio. Apparently, the

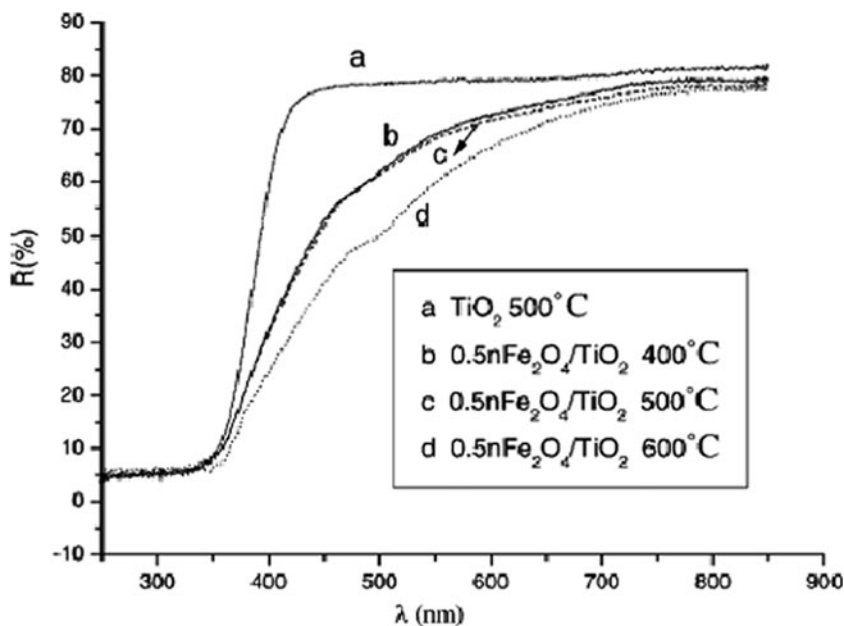


Fig. 13 Diffuse reflectance spectra of $\text{TiO}_2/\text{ZnFe}_2\text{O}_4$ calcined at the various indicated temperatures. Reproduced with permission from Cheng et al. (2004). Copyright 2004 by Elsevier B.V.

anatase-to-rutile phase change was inhibited, or at best slowed down, due to the presence of gold.

VLA platinum-loaded TiO_2 thin films decomposed H_2O in the presence of CH_3OH (H_2 evolved) and in the presence of AgNO_3 (O_2 evolved) under visible-light irradiation at $\lambda \geq 420$ nm. The latter process also occurred at $\lambda > 550$ nm on thin films fabricated at 600°C using the RF-MS method (Matsuoka et al. 2005; Kitano et al. 2006a, 2007). A calcined TiO_2 plate was the source material and Ar gas was the sputtering gas at pressures $p_{\text{Ar}} = 1.0\text{--}3.0$ Pa during deposition. The films, denoted Vis- TiO_2/X ($\text{X} = 1.0, 2.0$ or 3.0 for p_{Ar}), displayed absorption bands extending to the near-IR region with a broad band at $\sim 600\text{--}800$ nm, particularly for Vis- $\text{TiO}_2/1.0$ due to Ti^{3+} centers. The latter centers were later confirmed by EPR spectroscopy. XRD spectra showed a Pt-loaded TiO_2 and the presence of a small quantity of PtO. This particular specimen displayed only low visible-light-activity toward O_2 evolution, probably because the Ti^{3+} sites acted as charge carrier recombination centers. More successful was the Vis- $\text{TiO}_2/2.0$ specimen for the decomposition of water. A SIMS examination revealed that the latter sample exhibited an O/Ti ratio at the surface of 2.00 ± 0.01 ; the O/Ti ratio was 1.93 ± 0.01 deep in the bulk. Band gap energies of Vis- TiO_2/X were smaller than for the UV- TiO_2 . This particular point will be discussed later in the chapter when we take up the question of whether or not there is band gap narrowing in doped TiO_2 s.

Deposition and adsorption of Au on TiO₂ lead to the appearance of occupied metal-induced states above the TiO₂ valence band (~1.6 eV; oxygen vacancies), which enhance the reactivity by altering the rate of exchange of V_{OS} and thereby facilitating the migration of the V_{OS} from the bulk to the surface of the oxide, a highly exothermic process; $\Delta E = -41.6 \text{ kcal mol}^{-1}$ (Rodriguez et al. 2002). Gold adatoms also enhance the relative stability of surface V_{OS} through a complex situation in which the Au adatoms modify the rate of exchange of V_{OS}. The concomitant presence of V_{OS} on the TiO₂ surface electronically perturbs the Au adatoms and renders them chemically more active.

Cerium(III)-doped TiO₂ is preparable by a sol-gel process in which Ti(*n*-BuO)₄ is hydrolyzed in the presence of Ce(NO₃)₃, absolute ethanol and acetic acid (Li et al. 2005d). Aging and drying the gel at -20°C under vacuum followed by calcination at 500°C yields the Ce-doped TiO₂ containing Ti³⁺, Ce³⁺ and Ce⁴⁺ ions in the TiO₂ lattice (XPS analysis). Diffuse reflectance spectra showed significant absorption between 400 and 500 nm due to excitation of valence band electrons to the cerium 4*f* levels.

3.3 Anion-Doped Titanium Dioxide Specimens

So far we have seen that VLA TiO₂s, in which the absorption onset is red-shifted to longer visible wavelengths, can be produced by reductive methods (e.g., H₂ plasma, high-temperature treatments, UV-light irradiation) and by doping TiO₂ with suitable first-row transition metal ions by a metal-ion implantation technique. Since the latter requires sophisticated instrumentation, otherwise not available in many laboratories, the combined sol-gel/hydrothermal treatment methods has achieved equivalent aims in preparing VLA-active TiO₂s responsive to sunlight wavelengths with increased photoactivity and photoefficiency. TiO₂s doped with non-metal dopants such C, S, N, and F (and others) have received exceptional attention since they require less sophisticated methods. Accordingly, non-metal doped TiO₂s have attracted the imagination of many aficionados of heterogeneous photocatalysis for both environmental remediation and solar energy harvesting and storage. It is therefore relevant to describe various preparative procedures and the pertinent UV-visible spectral properties that have made non-metal doped TiO₂s such a fascinating topic of current research with recent reports describing TiO₂ materials codoped with two non-metals.

The facile preparation of TiO₂ specimens that respond to visible-light activation, in particular N-doped TiO₂, has attracted considerable interest ever since the study (although not the first) by Asahi and coworkers (2001). It is, therefore, instructive to examine some of the reasons that led this group to propose non-metals as being more suitable dopants to achieve photocatalysis in the visible spectral region.

Asahi et al. (2001) initially set three requirements to achieve visible-light-activity: (i) doping should produce states in the band gap of TiO₂ that absorb visible light; (ii) the CB minimum, including subsequent impurity states, should be as high as that of

TiO₂ or higher than the H₂/H₂O level to ensure photoreductive activity; and (iii) the states in the (band) gap should overlap sufficiently with the band states of TiO₂ to transfer photoexcited carriers to reactive sites at the TiO₂ surface within their lifetime. Metal dopants were not deemed desirable because they did not meet conditions (ii) and (iii) as they often produce localized d states deep in the band gap of TiO₂ and tend to act as recombination centers of e⁻ and h⁺. Calculations of density of states (DOS) of substitutional doping with several non-metals (C, N, F, P, or S) into O sites in anatase TiO₂ by the full-potential linearized augmented plane-wave (FLAPW) formalism in the framework of the local density approximation (LDA), led these workers to chose N as most effective because the N 2*p* states apparently contribute to band gap narrowing (more on this topic later) through mixing with O 2*p* states in the valence band. Though S doping also led to band gap narrowing, it was dismissed because of apparent difficulties in substituting an S²⁻ ion into O²⁻ sites (the size of S²⁻ is greater than O²⁻), Carbon and phosphorous doping were also dismissed as they may introduce states too deeply buried in the band gap and so would not satisfy condition (iii). However, both C- and S-doped TiO₂s have since been reported, and DFT calculations have since been also refined.

3.3.1 Carbon-Doped Titanium Dioxide

Soon after the study by Asahi et al. (2001), Khan and coworkers (Khan et al. 2002) reported efficient (apparently ~8.35%) photochemical water splitting by C-doped rutile TiO₂ produced by controlled combustion of a Ti metal sheet in the presence of CO₂ and water vapor in a natural gas flame (850°C) that led C atoms to substitute the lattice O atoms. The two rutile TiO₂ films (XRD) absorbed visible light to $\lambda < 535$ nm with two absorption thresholds: 535 nm and 440 nm that were attributed to two compositions of the TiO_{2-x}C_x system. The band gap of TiO₂ was said to be lowered from 3.0 eV of rutile to 2.32 eV.

Hoping to synthesize N-doped TiO₂ through hydrolysis of TiCl₄ in the presence of (Butyl)₄NOH, Sakthivel and Kisch (2003a) discovered that after calcination of the TiO₂ powder at 400°C, followed by a further heat treatment at 550°C produced C-doped rather than N-doped anatase TiO₂ (XRD; traces of rutile). XPS spectra displayed C 1*s* peaks at 285.6, 287.5, and 288.5 eV with the first peak attributed to adventitious elemental carbon and the latter two peaks to the presence of carbonate species later confirmed by IR spectroscopy. Diffuse reflectance spectra showed new absorption features in the range 400–700 nm with an absorption onset at 735 nm (1.70 eV) attributed to various surface states above the valence band of TiO₂. Benzoic acid was converted to salicylic acid on excitation of the C-doped TiO_{2-x}C_x specimen in the presence of oxygen at $\lambda \geq 320$ nm (3.88 eV), 455 nm (2.73 eV) and 495 nm (2.51 eV); 4-chlorophenol was photomineralized at $\lambda = 455$ nm.

Thermal treatment of TiO₂ photoelectrodes in a hexane-rich environment led (a) to incorporation of C into TiO₂ after annealing in an *n*-hexane/argon atmosphere at 500°C (Enache et al. 2006) and (b) to creation of oxygen vacancies in the blackish-colored TiO₂. The coloring originated with C deposits on the TiO₂ surface, which

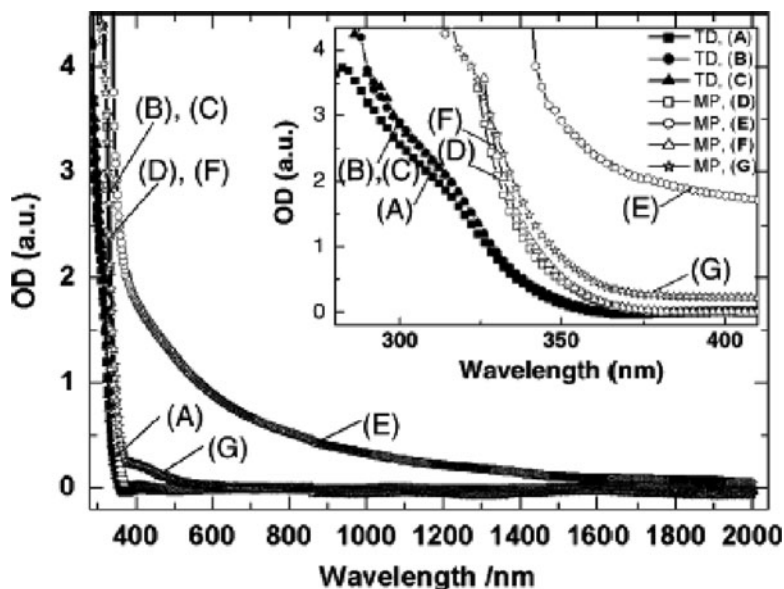


Fig. 14 Optical absorption spectra for thin dense and mesoporous TiO_2 films. (A, D) undoped TiO_2 ; (B, E) annealed in hexane/argon at 500°C ; (C, F) re-oxidized in air at 450°C ; (G) mesoporous TiO_2 film reduced in an argon/hydrogen atmosphere at 500°C . Reproduced with permission from Enache et al. (2006). Copyright 2006 by Elsevier B.V.

failed to enhance photoactivity in the visible spectral range. Some C (<0.1 at.%) did diffuse into the bulk of TiO_2 causing a very small shift (~ 0.05 – 0.1 eV) of the absorption edge to longer wavelengths (Fig. 14). The presence of C atoms prolonged the anatase-to-rutile phase conversion to temperatures greater than 800°C , and the films retained the anatase structure after the hexane treatment even after subsequent reoxidation (XRD measurements).

Using a different approach, Xu et al. (2006) prepared C-doped TiO_2 by hydrolyzing TiCl_4 in the presence of $(\text{C}_4\text{H}_9)_4\text{NOH}$ as the C source and in the presence of glucose/NaOH. Extended aging at ambient temperatures and calcination at 400 – 500°C gave $\text{TiO}_{2-x}\text{C}_x$ (anatase; XRD) that absorbed visible light to ca. 800 nm (Fig. 15). The $\text{TiO}_{2-x}\text{C}_x$ sample prepared from $(\text{C}_4\text{H}_9)_4\text{NOH}$ as the C source showed a single band gap energy (2.76 eV), whereas $\text{TiO}_{2-x}\text{C}_x$ made from glucose exhibited two band gap energies (2.78 and 1.45 eV), in apparent accord with the calculations of Nie and Sohlberg (2004). Although the carbonaceous $\text{TiO}_{2-x}\text{C}_x$ prepared from $(\text{C}_4\text{H}_9)_4\text{NOH}$ (16 C atoms) vs. glucose (6 carbons) showed enhanced visible light absorption, it nevertheless hindered visible-light activity. With glucose as the C source, more C atoms entered the TiO_2 lattice by replacing O atoms, lowering the band gap energy and contributing to the visible-light activity of $\text{TiO}_{2-x}\text{C}_x$. Soaking P-25 TiO_2 into a solution of $(\text{C}_4\text{H}_9)_4\text{NOH}$ for ~ 150 h followed by calcination also produced a TiO_2 material with significant absorption in the visible spectral range (Xu et al. 2006). An alternative to the latter procedure involved

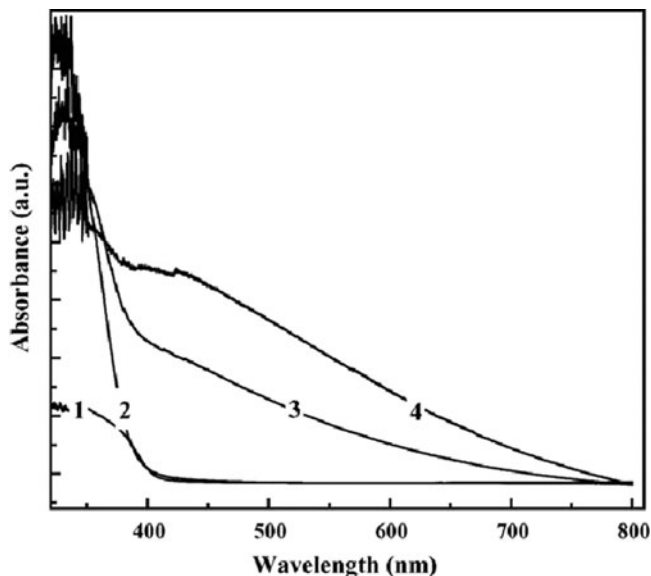


Fig. 15 Effect of aging time on UV-vis spectra of the samples: (1) reference or regular TiO_2 (hydrolysis of TiCl_4 with NaOH); (2), (3), and (4) C-doped TiO_2 samples aged for 12, 100, and 150 h, respectively, in the presence of tetrabutylammonium species; all samples were rinsed thoroughly before calcinations at $400\text{--}500^\circ\text{C}$. Reproduced with permission from Xu et al. (2006). Copyright 2006 by Elsevier B.V.

subjecting TiO_2 to ethanol vapors at $150\text{--}400^\circ\text{C}$, yielding a VLA C-doped TiO_2 that could photodegrade phenol (Janus et al. 2006).

The use of a hydrothermal method at temperatures as low as 160°C also produced VLA $\text{TiO}_{2-x}\text{C}_x$ in two stages (Ren et al. 2007). The first stage prepared amorphous TiO_2 by controlled hydrolysis of $\text{Ti}(\text{i-PrO})_4$. In the second stage, the aqueous TiO_2 /glucose (the C source) suspension was autoclaved at 160°C yielding anatase $\text{TiO}_{2-x}\text{C}_x$ (XRD). The XPS spectrum showed C 1s signals at 284.8 and 288.6 eV; the first signal due to elemental carbon and the 288.6 eV peak consistent with C–O bonds in the lattice in which C substituted Ti atoms to form a Ti–O–C structure. This is in fact different from the case (Khan et al. 2002) where C-doped TiO_2 was fabricated by flame oxidation in which the C dopant substituted lattice O atoms. Optical absorption of the as-prepared VLA $\text{TiO}_{2-x}\text{C}_x$ extended to 450 nm. Three reasons might explain the VLA photoactivity: (i) the C-doped TiO_2 had a high surface area and thus provided more active sites and adsorbed more reactive species, (ii) C substituted lattice Ti atoms close to or on the surface, and (iii) with the apparent narrowing of the band gap more light was absorbed than was otherwise the case for undoped TiO_2 .

Photoactivities of photogenerated h^+ during UV or visible laser flash photolyses of pure anatase TiO_2 and S- and C-doped TiO_2 powders have been examined by time-resolved diffuse reflectance (TDR) spectroscopy (Tachikawa et al. 2004).

Although one-electron oxidation of methanol and 4-(methylthio)phenyl methanol occurred under 355-nm laser irradiation, no oxidation of these substrates occurred during the 430-nm laser photolysis of S- and C-doped TiO₂ powders, even though sufficient charge carriers were generated. The C-doped anatase TiO₂ was prepared by mixing thiourea, urea and (ST-01) TiO₂ powder, followed by calcination at 400°C. The content of C atoms on the C-doped TiO₂ surface was ~0.4 at.%; carbonate (CO₃²⁻) species were incorporated into the bulk phase of the TiO₂. XPS spectra showed no peaks attributable to either N or S atoms in the C-doped specimen. Absorption of visible light by TiO_{2-x}C_x was stronger than for the S-doped TiO₂, even though the content of S atoms (1.6 at.%) on the surface of TiO₂ was greater than that of C (0.4 at.%).

3.3.2 Sulfur-Doped Titanium Dioxides

Despite the earlier reservations by Asahi et al. (2001), Umebayashi and coworkers (2002) synthesized S-doped anatase TiO₂ (XRD) by oxidative annealing of TiS₂ at 600°C, causing S atoms to occupy O-atom sites and to shift the absorption edge to longer wavelengths. *Ab initio* calculations inferred that mixing of the S 3*p* states with the valence band O 2*p* states presumably contributed to the narrowing of the TiO₂ band gap through an increase of the valence band width. In an alternate method, mixing Ti(i-PrO)₄ and thiourea in ethanol followed by evaporation of the solvent and calcination of the white residue at 400°C in air gave S-doped anatase TiO₂; S content was 1.6 at.% (Ohno et al. 2003, 2004). XPS analyses revealed no peak attributable to either C or N atoms or to S²⁻ ions after the calcination treatment. The absorption edge shift to lower energy in the spectrum of S-doped TiO₂, relative to pure anatase TiO₂, was again attributed to an increase of the valence band width and to a narrowing of the band gap (Tachikawa et al. 2004). Adsorption of Fe³⁺ ions (0.90 wt.%) on S-doped TiO₂ increased the photo-activity of TiO_{2-x}S_x further, but decreased it at loadings of 1.0 wt.% or greater (Ohno et al. 2006). In their XPS study of S 2*p* spectra, Ohno et al. (2004) detected no signals for S²⁻ ions but clearly detected signals for S⁴⁺. They speculated that the latter species substituted Ti⁴⁺ in cation sites. This led to some controversy about the nature of the S dopants in TiO_{2-x}S_x specimens, because of the likelihood that the quantity of S²⁻ anions in O²⁻ sites may have been too low to be detected and that a large quantity of SO₃²⁻ ions may have been produced by the partial oxidation of thiourea when mixed with TiO₂ particles (Matsushima et al. 2007).

Calcination of a mixture of TiCl₃ and NH₄SCN at 400°C yielded (yellowish) S-doped anatase TiO₂ whose XPS spectra showed a S 2*p* signal at 170 eV, consistent with an S⁶⁺ species doped on the TiO₂ surface. The 170-eV peak vanished following Ar⁺-ion etching of the specimen (Kato et al. 2006). The XPS results inferred the presence of SO₄²⁻ species on the TiO₂ surface. UV-visible absorption spectra (Fig. 16) show the absorption edge of S-doped TiO₂ to be shifted to longer wavelengths (lower band gap energy) relative to undoped TiO₂ prepared under otherwise identical conditions but in the absence of thiocyanate, and relative to ST-01 TiO₂.

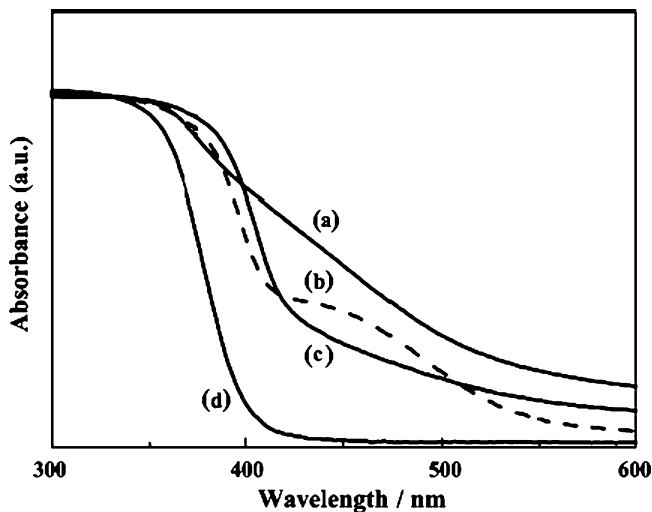


Fig. 16 Diffuse reflectance spectra of (a) S-doped TiO₂ (NH₄SCN = 13 M), (b) S-doped TiO₂ (NH₄SCN = 1 M), (c) TiO₂ prepared without ammonium thiocyanate, and (d) ST-01 TiO₂. Reproduced with permission from Katoh et al. (2006). Copyright 2006 by Elsevier Inc.

The degradation of methylene blue was significantly greater for the VLA S-doped specimen (1 M) than for ST-01 TiO₂ alone under otherwise identical irradiation conditions at $\lambda > 400$ nm.

Subjecting a mixture of TiO₂ and TiS₂ powdered samples of different ratios to mechanical grinding, using a planetary ball mill for different times, produced S-doped anatase TiO₂ whose S doping limit was around 1% (Wang et al. 2007b). For short milling times (e.g., 20 min) Raman spectra and XRD analyses indicated the S-doped TiO₂ to consist mostly of anatase. Milling for 60 min produced a specimen with a rutile TiO₂ structure.

3.3.3 Fluorine-Doped Titanium Dioxide

Spray pyrolysis (SP) of an aqueous solution of H₂TiF₆ at temperatures 800, 900, and 1,000°C produced F-doped TiO₂ powders with a single anatase architecture at T < 900°C (XRD analysis). The samples showed significant visible-light activity even though F-doping had no effect on the fundamental absorption edge (Fig. 17a) (Li et al. 2005a) in accord with the calculated results of F-doped TiO₂ reported by Yamaki et al. (2003). It appears that localized levels of the F 2p state lie below the valence band of TiO₂ and consequently cannot mix with states in the valence and conduction bands. Thus, they cannot contribute to the optical absorption by F-doped TiO₂. PL spectra revealed two kinds of (surface) oxygen vacancies (F and F⁺ centers) formed by F-doping (Fig. 17b) and responsible for the high visible-light activity in the decomposition of acetaldehyde (CH₃CHO) and trichloroethylene

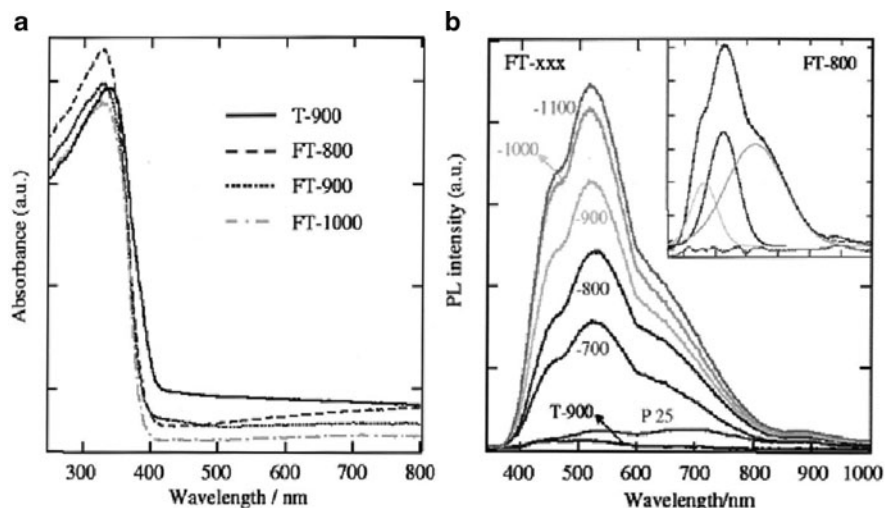


Fig. 17 (a) UV–Visible absorption spectra of the F-doped TiO_2 powders. The spectrum of TiO_2 prepared at 900 C under otherwise identical conditions but using a TiCl_4 precursor is also reported for comparison. (b) Photoluminescence spectra of the F-doped TiO_2 powders prepared by spray pyrolysis at various temperatures. The inset shows the spectral deconvolution of the spectra of the F-doped sample prepared at 800 C. Reproduced with permission from Li et al. (2005a). Copyright 2005 by Elsevier B.V.

($\text{CCl}_3\text{CH}=\text{CH}_2$). Evidently, the visible-light-driven photoactivity was achieved by excitation into the absorption bands of the V_{OS} , i.e., by excitation of the F and F^+ centers. XRD analyses demonstrated a significant inhibition of the anatase-to-rutile phase change by the addition of “complexing” F^- ions. The broad band at 465 nm (peak 1) was attributed to the oxygen vacancy with two trapped electrons (i.e., the F center), whereas peak 2 at 525 nm was due to the oxygen vacancy with one trapped electron, i.e. F^+ center (Li et al. 2005a). However, that one or all three bands originated from the existence of Ti^{3+} centers is not precluded.

3.3.4 Nitrogen-Doped Titanium Dioxides

This section will illustrate several methods used to synthesize N-doped TiO_2 specimens, which Yates and coworkers (2006) have divided into three classes: (i) modify existing TiO_2 by ion bombardment, (ii) modify existing TiO_2 in powdered form, film, and single crystal, or else modify TiN by gas phase chemical impregnation, and (iii) grow $\text{TiO}_{2-x}\text{N}_x$ (crystals) from liquid or gaseous precursors.

In one of the earliest (1986) studies of N-doping TiO_2 , Sato (1986) noted that calcination of $\text{Ti}(\text{OH})_4$ in the presence of NH_4Cl , or aqueous NH_3 leads to photosensitization of TiO_2 if exposed to visible-light radiation. The powdered samples were NO_x -doped TiO_2 and NO_x impurity was the sensitizer. The same year, Noda et al. (1986) prepared yellow-colored anatase TiO_2 powders from aqueous

hydrazine and TiCl_4 solutions, and inferred that the visible-light absorption was due to the presence of oxygen vacancies.

In their 2001 seminal report in *Science*, Asahi et al. (2001) prepared crystalline $\text{TiO}_{2-x}\text{N}_x$ films by sputtering a TiO_2 target in a N_2/Ar gas mixture followed by annealing at 550°C in a N_2 atmosphere. XRD features indicated mixed anatase and rutile phases; a clean anatase TiO_2 film formed under an O_2/Ar atmosphere under otherwise identical conditions. The yellowish $\text{TiO}_{2-x}\text{N}_x$ films absorbed light below 500 nm. XPS N 1s spectra of $\text{TiO}_{2-x}\text{N}_x$ showed signals at 402, 400 and 396 eV, in contrast to the undoped TiO_2 film, which showed no 396 eV peak. In line with the work of Saha and Tompkins (1992), the 396-eV signal was assigned to atomic $\beta\text{-N}$, whereas the other two peaks were attributed to molecularly chemisorbed dinitrogen $\gamma\text{-N}_2$. Powdered samples of $\text{TiO}_{2-x}\text{N}_x$ were prepared using NH_3/Ar as the source of N followed again by calcination at $550\text{--}600^\circ\text{C}$. Only $\text{TiO}_{2-x}\text{N}_x$ systems with XPS peaks at 396 eV were photoactive toward the decomposition of methylene blue; optimal loading of N was ~ 0.25 at.%. Combined with theoretical results, Asahi et al. (2001) deduced that the sites for photoactivity under visible-light irradiation were those that substitutionally replaced O, i.e., sites associated with atomic $\beta\text{-N}$ at 396 eV. In an earlier study, Lee et al. (1995) fabricated N-doped TiO_2 anatase films by MOCVD using $\text{Ti}(\text{i-PrO})_4$ and N_2O at 420°C . Raman spectra showed no signs of rutile nor of a TiN phase. The XPS Ti 2p spectrum indicated that N was incorporated into the TiO_2 lattice forming Ti–N bonds.

A VLA anatase TiO_2 ($\lambda < 550$ nm) has also been prepared (Ihara et al. 2003) by calcining the hydrolysis product from $\text{Ti}(\text{SO}_4)_2$ with NH_3 in dry air at 400°C . XPS spectra showed only trace amounts of N. Most of the visible-light response was due to the oxygen-deficient stoichiometry.

Pale yellow, yellow, and dark green $\text{TiO}_{2-x}\text{N}_x$ ($x = 0, 0.0050, 0.011, 0.019$) powdered samples can be prepared by annealing anatase TiO_2 powder (ST-01) in a flow of NH_3 at 550, 575, and 600°C , respectively. XRD patterns indicated the samples retained the anatase structure and no TiN phase was present. XPS patterns revealed a 396 eV signal that confirmed N doping substitutionally into O sites to form O–Ti–N bonds. Noticeable shifts of the absorption edge into the visible spectral region were evident for $\text{TiO}_{2-x}\text{N}_x$ with the feature at $\lambda > 550$ nm attributed to Ti^{3+} since NH_3 decomposes into N_2 and H_2 at ca. 550°C , and H_2 reduces Ti^{4+} under these conditions. However, according to Irie et al. (2003) the band gap energy remained at 3.2 eV. Degradation of isopropanol with UV-light and visible-light radiations resulted in different quantum yields for the evolution of CO_2 . This suggested that N-doping formed a narrow N 2p band above the valence band of TiO_2 as the existence of band gap narrowing in $\text{TiO}_{2-x}\text{N}_x$, espoused by Asahi et al. (2001), would have required identical spectral dependencies of quantum yields. Moreover, when irradiating with visible light the quantum yields decreased with increase in the quantity (x) of the dopant N because of the increase in V_{OS} with increase of x in $\text{TiO}_{2-x}\text{N}_x$. In this case, V_{OS} acted as recombination centers for the photogenerated charge carriers. Under UV irradiation, the quantum yields also decreased with increase in x , suggesting that the doping sites also acted as recombination centers.

Nanocrystalline porous N-doped TiO₂ thin films have been prepared by introducing N into TiO₂ by means of DC magnetron sputtering in N₂-containing plasma (Lindgren et al. 2003). At low N concentrations, the anatase product displayed new spectral features in the range 410 < λ < 535 nm due to excitation of electrons to unoccupied states from local states located close to the valence band edge within the band gap. Nitrogen-doping had no effect on the CB edge. Band gap narrowing was deemed somewhat questionable by these authors. Despite the intense recombination of charge carriers caused by N-doping, the new band gap states created by N-doping improved the visible-light photoresponse at the expense of some losses of the UV response.

An alternative method used by Sakthivel and Kisch (2003b) to prepare slightly yellow N-doped anatase TiO₂ with various N loadings involved hydrolysis of TiCl₄ with a N-containing base such as aqueous NH₃, (NH₄)₂CO₃, or NH₄HCO₃, followed by calcination at 400°C. XPS spectra showed only a broad signal at ~404 eV, but no 396-eV peak attributable to nitridic N atoms. The broad signal was attributed to hyponitrite (NO⁻) whose presence was confirmed by its IR spectrum. Contrary to assertions by Asahi et al. (2001), the valence band edge did not change on N-doping, despite the red shift of the TiO₂ absorption edge to ~520 nm. However, contrary to the inference by Lindgren et al. (2003), results from a photoelectrochemical study (Sakthivel and Kisch 2003b) noted a slight change in the electrochemical potentials of the CB of TiO₂ (Fig. 18) for three of the specimens. N-doping led only to a “modest band gap narrowing.” In a subsequent study, Sakthivel et al. (2004) attempted to prepare a S-doped TiO₂ specimen following the procedure of Ohno et al. (2003), only to find that the specimen contained no S but did contain 0.09 wt.% N and 0.03 wt.% C (specimen TiO₂-N/A). XPS analysis of the N 1s spectra of this sample before and after sputtering revealed signals at 400.1 eV, 405.3 eV, and 412.2 eV in the “before” case. The lower energy peak was attributed to hyponitrite,

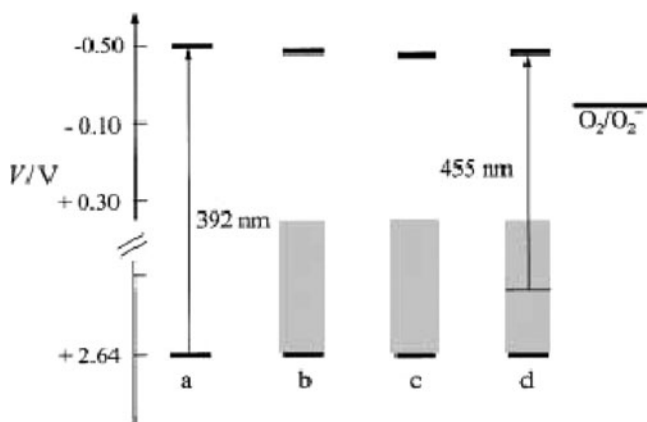


Fig. 18 Electrochemical potentials (vs. NHE) of band edges; shaded areas denote surface states; the oxygen redox potential at pH 7 is also shown. (a) TiO₂, (b) TiO₂-N/1, (c) TiO₂-N/2, (d) TiO₂-N/3. Reproduced from Sakthivel and Kisch (2003b). Copyright 2003 by Wiley-VCH

whereas the latter signals likely originated from NO_2^- ions. On removal of a 5-nm surface layer after sputtering, the 400.1-eV peak disappeared leaving the nitrite peaks that slightly shifted to 405.0 and 411.8 eV and two new peaks appeared at 406.8 and 409.2 eV that were assigned to NO_3^- and NO_2^- , respectively. They deduced that the hyponitrite species was located in the surface region, whereas NO_3^- and NO_2^- were present in the doped TiO_2 bulk lattice. Infrared evidence confirmed the presence of hyponitrite and nitrite ions in the TiO_2 -N/A sample and also revealed the presence of CO_3^{2-} species. However, any visible-light photore-sponse was due to the N dopants and not to the presence of C. Two additional anatase specimens, TiO_2 -N/B and TiO_2 -N/C, were prepared from the hydrolysis of Ti (i-PrO) $_4$ and TiCl_4 in the presence of thiourea in (absolute) ethanolic media, followed by calcining the resulting powders at 600 and 400°C, respectively. Diffuse reflectance spectra showed only a minor red shift of the TiO_2 absorption edge affording band gap energies 2.99, 2.95, 2.95, and 2.91 eV for non-doped TiO_2 and for the TiO_2 -N/A, TiO_2 -N/B, and TiO_2 -N/C samples, respectively.

Yellowish N-doped rutile TiO_2 samples can also be prepared mechanochemically by high-energy ball milling of P-25 TiO_2 with various quantities of hexamethylene-tetramine (HMT) under different milling conditions at near-ambient temperature (Yin et al. 2003). This method converted all the anatase phase (ca. 80%) in P-25 TiO_2 to rutile. Post-milling calcination in air at 400°C gave an N-doped product which displayed two absorption edges at ca. 400 and 550 nm and good visible-light photoresponse toward the oxidation of NO.

Yang and Gao (2004) obtained N-doped TiO_2 by hydrolysis of tetrabutyl titanate in the presence of thiourea in ethanolic media. On treating the white powder in an NH_3 flow at 450 and 500°C for 6 h and at 450°C for 3 h produced, respectively, brown (A), blackish brown (B), and wine-colored (C) specimens. The XPS N 1s spectrum of (A) displayed a relatively strong peak at 396 eV assigned to substitutional β -N states (O substituted by N in the TiO_2 lattice) considered the photoactive sites under visible-light irradiation. The peak at ~400 eV was attributed to molecularly chemisorbed nitrogen, γ - N_2 . No peak attributable to S was observed for the three samples (XPS analyses).

Crystallized anatase $\text{TiO}_{2-x}\text{N}_x$ films with considerable amount of substitutional N atoms (1.8 at.%) and chemisorbed molecular N_2 are produced by ion-assisted electron-beam evaporation using rutile titania powder as the TiO_2 source material and molecular nitrogen as the N source (Yang et al. 2004). XPS spectra showed two peaks with binding energies at 402 and 396 eV, also assigned to molecularly chemisorbed γ - N_2 and atomic β -N, respectively; Ti 2p XPS spectra revealed $\text{Ti}^{4+} 2p_{3/2}$ and $\text{Ti}^{4+} 2p_{1/2}$ in the anatase TiO_2 film indicating the majority of titanium in the $\text{TiO}_{2-x}\text{N}_x$ film to consist of Ti^{4+} confirming results from XRD patterns. Raman spectra revealed N-doping caused no changes to the anatase TiO_2 structure.

Using a simple nanoscale synthetic route, Gole et al. (2004) produced in a matter of seconds at room temperature $\text{TiO}_{2-x}\text{N}_x$ samples employing direct nitridation of anatase TiO_2 nanostructures with alkylammonium salts. The resulting doped specimens could be tuned to absorb light across the visible spectral region (to λ ~550 nm). The method required first formation of the metal-oxide colloids by controlled

hydrolysis of $\text{Ti}(\text{i-PrO})_4$ in an aqueous/isopropanol medium at pH 2 (HNO_3). Subsequent treatment of the initial nanoparticle colloidal sol or the partially agglomerated gel (solution) to excess triethylamine led to nitridation of the TiO_2 nanocolloids to $\text{TiO}_{2-x}\text{N}_x$. XRD and HRTEM results demonstrated the treated $\text{TiO}_{2-x}\text{N}_x$ nanoparticle structures to correspond predominantly to the anatase architecture. Diffuse reflectance spectra of the $\text{TiO}_{2-x}\text{N}_x$ crystallites, generated from the nanoparticle solutions, rose sharply at ~ 450 nm, whereas the corresponding spectrum for the nitrated $\text{TiO}_{2-x}\text{N}_x$ from the partially agglomerated nanoparticles rose at ~ 550 nm. XPS analysis with Ar^+ -ion sputtering revealed the presence of N dopants not only at the surface but also incorporated into the sublayers of the $\text{TiO}_{2-x}\text{N}_x$ agglomerates (N content, 3.6–5.1 at.%). Although interstitially dissolved nitrogen and perturbation of the TiO_2 lattice structure might be associated, at least in part, with $\gamma\text{-N}_2$ features that contribute to the XPS spectra, no evidence was found for conversion of the anatase structure into the rutile architecture on N-doping for the initial TiO_2 nanocolloids and for the agglomerated gel solutions. More surprisingly, little if any XPS evidence of atomic $\beta\text{-N}$ binding at 396 eV was found that might have been associated with any of the $\text{TiO}_{2-x}\text{N}_x$ or Pd-treated oxynitride samples. Rather, the XPS observations were consistent with nonstoichiometric surface-based Ti–O–N bonding.

That the visible-light responses of N-doped TiO_2 originates from an N-induced mid-gap level that forms slightly above the top of the O $2p$ valence band was inferred by Nakamura and coworkers (2004) from their mechanistic study into the photooxidation of water (evolution of O_2) through measurements of anodic photocurrents at N-doped TiO_2 film electrodes. These materials were prepared by two methods. In one (the dry method), anatase ST-01 TiO_2 was heated to 550°C in a reactor under a dry NH_3 flow. In the second (the wet method), the $\text{Ti}(\text{i-PrO})_4$ precursor was hydrolyzed in aqueous NH_3 at 0°C followed by calcining the resulting white precipitate at 400°C . Both methods produced $\text{TiO}_{2-x}\text{N}_x$ anatase. The study concluded that photooxidation of organic compounds under visible-light illumination proceeds mainly by reactions with surface intermediates of water oxidation ($\bullet\text{OH}$ radicals) or oxygen reduction (superoxide radical anion, $\text{O}_2^{\bullet-}$), and not by direct reactions with holes that may have been trapped at the N-induced mid-gap level.

In a single-crystal study, Yates group at the University of Pittsburgh reported (Diwald et al. 2004a) that ion implantation of atomically clean $\text{TiO}_2(110)$ surfaces with mixtures of N_2^+ and Ar^+ ions, followed by subsequent annealing under ultra-high-vacuum conditions, leads to incorporation of N into the TiO_2 lattice. XPS spectra revealed only the N $1s$ feature at 396.6 eV that they attributed to substitutionally bound nitride nitrogen (O^{2-} ions substituted by N^{2-} anions). However, contrary to expectations, the N-doped crystals containing only nitride ions exhibited a shift in the photothreshold energy of 0.2 eV to *higher* rather than *lower* energy compared to undoped $\text{TiO}_2(110)$. By contrast, N-doped $\text{TiO}_2(110)$ rutile single crystals that had been treated in the presence of an NH_3/Ar gas mixture at ca 600°C exhibited photoactivity at the *lower* photon energy of 2.4 eV, i.e., 0.6 eV below the band gap energy of rutile TiO_2 (3.0 eV) (Diwald et al. 2004b). The active dopant state of the interstitial N responsible for this effect showed a N $1s$ binding energy at 399.6 eV attributed to a form of nitrogen likely bound to H. This is different from the

substitutional nitride state which displays an N 1s binding energy at 396.7 eV. Thus, a codoping effect between N and H may have been responsible for the enhanced visible-light photoactivity. Doped and undoped TiO₂(110) samples also showed an impurity XPS feature centered at 399.6 eV, which upon UV treatment in air and/or removal of the first 5 Å of the surface by Ar⁺-ion sputtering led to extensive depletion of this signal. Evidently, traces of nitrogen had contaminated the metal-oxide surface. The inferences made by the Yates group *disagree totally* with the conclusions of Asahi et al. (2001) and those of others who claimed that nitridic nitrogens that substitute O²⁻ ions in the TiO₂ lattice are the necessary dopant species for TiO₂ photoactivity in the visible-light region.

In a subsequent report, Thompson and Yates (2005) again emphasized that the exclusive XPS N 1s signal at 396.7 eV, typically attributed to substitutional β-nitrogen seen in ion-implanted N-doped TiO₂, in and by itself alone cannot account for the *decrease* in the phototreshold of TiO₂(110) as observed for interstitially located N–H bound species. They proposed that the 0.2-eV *increase* in the phototreshold energy of N-doped TiO₂ systems was due to the deposition of charge in the low levels of the CB (the band-filling mechanism), thus the need for higher energy photons to excite valence band electrons into higher levels of the CB.

Although there is clear XPS evidence for the incorporation of β-substitutional N in N-doped TiO₂, there is no firm evidence of any appreciable photoactivity when these doped systems are irradiated with visible light (Yates et al. 2006), a point also raised by Frach et al. (2004) who noted no improvement in visible-light activity on N-doping TiO₂, and by Li and coworkers (2004b) who reported that the nature and level of visible-light activity depend on the nitriding compound employed. To confirm that N is indeed incorporated into TiO₂, Yates and coworkers (2006) used an atmospheric pressure thermal CVD coater to grow thin films of N-doped TiO₂ on glass substrates. The precursors were TiCl₄, ethylacetate and NH₃ with N₂ as the carrier gas. Of all the samples grown, only three displayed the XPS N 1s peak at 396 eV of atomic β-substituted N. These were films denoted N(1), N(2), and N(6) grown at 650°C under N₂ with flow rates of NH₃ in excess of 100 sccm. However, XPS N 1s spectra showed no evidence of the 397-eV signal typically due to the N³⁻ ion (TiN), but did reveal the presence of other fairly weak signals at 400 and 402 eV that may have arisen from molecularly chemisorbed N₂, from NH_x species located at interstitial sites (399.6 eV), from NO_x or NH_x (400 eV), or from an oxynitride (399.3 eV) of stoichiometry equivalent to TiN_{0.5}O_{0.5}. Some of the films displayed absorption features in the visible spectral region, but so did nominally undoped TiO₂ films indicating that N incorporation cannot be assumed on the basis of red-shifts of the absorption edge, a point that cannot be overemphasized enough. XPS evidence is required. And even though the presence of β-N incorporation and absorption spectral features in the visible region were seen in N-doped TiO₂ specimens, no visible light-induced photoactivity was observed, while the more conventional UV photoactivity was considerably reduced compared to films grown in the absence of NH₃. This led to the suggestion that the presence of β-nitrogen alone cannot be claimed to induce visible-light activity in N-doped TiO₂ films. This point has also been raised by Mrowetz and coworkers (2004) who prepared

two different yellow-colored N-doped TiO_2 samples: sample *A* obtained by the room temperature procedure described by Gole et al. (2004) using triethylamine as the N source, and sample *H* prepared by high-temperature nitridation of commercial anatase TiO_2 at 550°C under a NH_3/Ar gas flow. XPS spectra of sample *A* surface revealed intense peaks at 399.6 and 404.5 eV in the N 1s region. By contrast, the peak at 396 eV in the XPS spectra of *H* powders was weak and diffuse, even after Ar^+ -ion sputtering. Despite these observations, however, the N-doped TiO_2 materials *failed to catalyze* the oxidation of HCOO^- into $\text{CO}_2^- \cdot$, or $\text{NH}_3\text{-OH}^+$ into NO_3^- under visible-light illumination. The reaction between colloidal TiO_2 and triethylamine at 25°C most likely led to the formation of surficial organotitanium complexes that are readily degraded by UV light, rather than to substitutional N-doped TiO_2 .

Nitrogen-doped TiO_2 nanoparticles consisting (XRD patterns) of pure anatase (pH 9, methanol), rutile (pH 9, ethanol), and brookite (pH 1, methanol) phases have been prepared successfully by a solvothermal process using a $\text{TiCl}_3/\text{HMT}/\text{alcohol}$ (methanol or ethanol) mixed solution in an autoclave at 90°C , and then at 190°C yielding yellow and beige powders. These showed excellent visible-light absorption and visible-light activity at wavelengths greater than 510 nm (Fig. 19) (Aita et al. 2004). The two-step absorption seen in the DRS spectra of these samples became apparent only after calcination at 400°C . The first absorption edge related to the band structure of nondoped TiO_2 , whereas the second absorption edge around 520–535 nm was due to the formation of an N 2p band located above the O 2p valence band in $\text{TiO}_{2-x}\text{N}_y$. No XPS data was reported.

Nitrogen-doped nanocrystalline TiO_2 (yellow) powders have also been synthesized by a procedure developed by Ma and coworkers (2005). It involved commercial anatase ST-01 TiO_2 heated at 500°C under a dry N_2 gas flow in the presence of

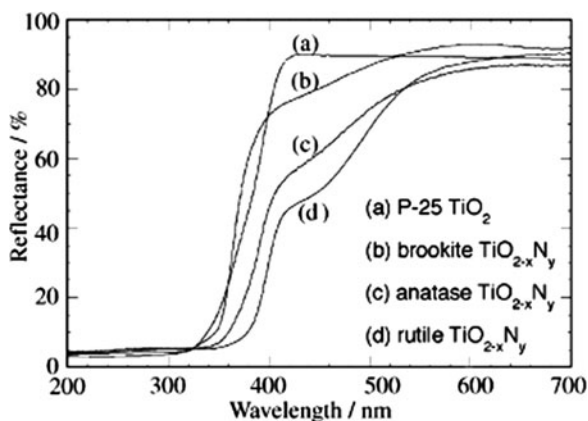


Fig. 19 Diffuse reflectance spectra of (a) P-25 titania powder, and N-doped TiO_2 powders prepared at 190°C and calcined at 400°C in (b) $\text{TiCl}_3\text{-HMT-methanol}$ solution at final pH 1, (c) $\text{TiCl}_3\text{-HMT-methanol}$ solution at final pH 9, and (d) $\text{TiCl}_3\text{-HMT-ethanol}$ solution at final pH 9. Reproduced with permission from Aita et al. (2004). Copyright 2004 by Elsevier Inc.

a small quantity of carbon. X-ray diffraction patterns were consistent only with the anatase crystal phase, even after annealing at 500°C. XPS spectra displayed three binding energy peaks at 396.2, 398.3, and 400.4 eV in the N 1s region. The first two signals were attributed to a chemically bound N-species and to O–Ti–N linkages within the crystalline TiO₂ lattice, respectively, whereas the signal at 400.4 eV was assigned to molecularly chemisorbed N₂ species.

The RF-MS deposition method using various N₂/Ar mixtures as the sputtering gas ($X = 2, 4, 10, 40$) and a calcined TiO₂ plate as the source material has been used to prepare N-substituted TiO₂ (denoted N-TiO₂(X)) photoactive thin films (Kitano et al. 2006b). The absorption edge of the samples shifted smoothly to the visible spectral region to 550 nm, with the extent of the shift depending on the concentration of N (X) substituted within the TiO₂ lattice (range 2.0–16.5%). The specimen with 6.0% N exhibited the highest visible-light activity in the photooxidation of isopropanol in aqueous media at $\lambda \geq 450$ nm, and the photo-oxidation of H₂O at wavelengths up to 550 nm. Specimens were thermodynamically stable even up to 400°C. XPS and XRD measurements showed significant substitution of lattice O atoms of TiO₂ by N atoms, which, according to these authors, played a crucial role in the *band gap narrowing* of the TiO₂ thin films (from 2.58 to 2.25 eV relative to 3.2 eV for anatase depending on X) enabling the visible-light photo-response. In samples with $X > 4$, Ti³⁺ species formed in the N-TiO₂(X) samples, which acted as recombination centers for electrons and holes causing a decrease of photoactivity.

Factors that govern the relationship between photoactivity and preparative conditions of VLA N-doped TiO₂ materials were reported in a study by Joung et al. (2006). The materials were prepared by hydrolysis of Ti(*i*-PrO)₄ in anhydrous ethanol containing HCl, followed by treatment of the resulting colloids in a stream of NH₃ at different temperatures (400, 500 and 600°C) and at various times (5–60 min). The highest photo-activities were seen for samples prepared at 400 and 600°C and calcination times of 5 and 10 min, whereas for samples prepared at 500°C the highest photoactivity was observed for a calcination time of 60 min. XRD patterns of the TiO₂ powders taken before and after N-doping as a function of calcination time showed only the anatase phase. The N 1s XPS spectra of the TiO_{2-x}N_x samples displayed a peak at 399.95 eV that was tentatively assigned to adsorbed NO or to N in Ti–O–N. No peak attributable to Ti–N bonding at 396 eV was observed. Band gap energies of N-doped TiO₂ inferred from absorption spectra ranged from 2.92 to 3.04 eV, for samples prepared at 400°C (5 min) and at 500°C (60 min), respectively. Active species for each calcination temperature were tentatively identified: for samples prepared at 400°C (5 and 10 min) the active species were NO, NO₂, NO₂⁻, NH₂, whereas for samples prepared at 500°C (60 min) the active species was doped atomic N and active species for samples prepared at 600°C (5 and 10 min) may be doped atomic N and the above nitrogenous species. EPR spectra indicated the presence of both Ti³⁺ and O^{-•} ions in the doped specimens.

At this time it is important to realize that visible-light photoactivity of N-doped TiO₂ materials are sensitive to the preparative routes, because even though such systems may absorb visible light, they are nonetheless frequently inactive in photo-oxidations. With the realization that photogenerated charge carriers in and by

themselves do not impart photoactivity and that charge carrier recombination must be muted to allow the carriers to reach the metal-oxide surface, In and coworkers (In et al. 2006) prepared a series of $\text{TiO}_{2-x}\text{N}_x$ systems with nominal N loadings from 0.2 to 1.0 wt.% involving the sequential reaction of H_2O with a small known excess of TiCl_4 in toluene (step 1) under dry O_2 -free argon. This was followed by the stoichiometric reaction of the remaining TiCl_4 with a standard solution of NH_3 in dioxane (step 2). The resulting species were heat-treated in air at 400, 500, and 600°C. Testing the $\text{TiO}_{2-x}\text{N}_x$ specimens for visible-light photoactivity they discovered (i) that calcination at 400°C yielded a solid with pronounced absorption in the visible spectral region but no visible-light photo-activity, (ii) that 500°C calcination produced an effective (yellow) VLA sample, and (iii) that the heat treatment at 600°C resulted in an inactive white material.

In addition to films and powdered specimens, self-organized N-doped TiO_2 nano-tubes can be fabricated (Vitiello et al. 2006) by electrochemical anodization of titanium in $\text{HF}/\text{H}_2\text{SO}_4$ electrolyte, followed by calcination at different temperatures (range 300–600°C) in pure NH_3 . This converted the initial amorphous nano-tubes into anatase with some rutile present depending on the heat-treatment temperature. Absorption spectra of the $\text{TiO}_{2-x}\text{N}_x$ nanotubes showed a sub-bandgap energy of ~ 2.2 eV and the regular band gap energy of anatase of ~ 3.2 eV. The $\text{N } 1s$ XPS spectrum revealed two clear peaks: one at 400 ± 0.2 eV ascribed to molecularly chemisorbed dinitrogen ($\gamma\text{-N}_2$ state), and the second at 396 ± 0.2 eV attributed to the atomic $\beta\text{-N}$ state.

In two extensive reports, Belver and coworkers (2006a, b) prepared and characterized a series of nanosized N-doped TiO_2 -based materials by a reverse micelle microemulsion method using a $\text{Ti}(\text{i-PrO})_4$ precursor and three N sources that were used as ligands (2-methoxyethylamine, $\text{N,N,N}',\text{N}'$ -tetramethylethylenediamine and 1,2-phenylenediamine) to produce titanium(IV) complexes in dry isopropanol under a N_2 atmosphere (in Schlench-type flasks). Dropwise addition of the solution to the inverse microemulsion, containing H_2O dispersed in n-heptane and Triton X-100 as the surfactant with hexanol as the co-surfactant, produced materials that were subsequently calcined at 200°C and then at 450°C. A XANES examination confirmed the anatase nature of $\text{TiO}_{2-x}\text{N}_x$, and also revealed a lack of correlation between the number of oxygen vacancies (V_{OS}) and the N content in the samples. Above a certain limit, the association of point defects, such as V_{OS} , and/or the presence of non-point extended defects, was detrimental to photoactivity. The distribution of defects and the nature of defects present in the N-doped samples were examined in a joint XANES/EXAFS investigation. It revealed that defect distribution was not simply related to V_{OS} since strong differences existed in the first cation–cation coordination shell, thus inferring the possible presence of non-point defects. The joint study confirmed the point defects to be the V_{OS} ; no interstitial defects were seen and the O/Ti atom ratio was less than 2. Evidently, there exists an optimal O/Ti ratio for maximum photoactivity achieved when oxygen vacancies are located in the bulk lattice that act as electron traps subsequent to visible-light photoactivation of the doped specimens. No apparent effect due to N-doping on the valence band edge was detected; some localized states were,

however, detected at the bottom of the CB with broad absorption around 500 nm. Results from diffuse reflectance Fourier transform spectra (DRIFTS) indicated the presence of several anion-related impurities of a substitutional (N^{n-}) and interstitial (NO^+) nature. Although they contributed to the absorption features, no clear correlation existed between any of these species and photoactivity. In fact, photoactivity best correlated with an optimal number of oxygen vacancies, above and below which a decrease of steady-state reaction rates occurred.

Nitrogen-doped or nitrogen-/sulfur-codoped titania $TiO_{2-x}A_y$ ($A = N, S$) systems that can be excited by visible light (400–550 nm) have been prepared (Yin et al. 2006) by mixing aqueous $TiCl_3$ solutions with various nitrogen sources, e.g., hydroxylamine (NH_2OH), HMT, urea $\{(NH_2)_2CO\}$ and thiourea $\{(NH_2)_2CS\}$ followed by hydrothermal treatment at $190^\circ C$ in an autoclave. The TiO_2 powders prepared with NH_2OH consisted of rutile crystals with non-homogeneous size distribution. The N-doped titania powders prepared using HMT consisted mainly of mono-size spherical brookite crystals, whereas those using urea and thiourea consisted of belt-like rutile particles (see Fig. 20). The $TiO_{2-x}A_y$ ($A = N, S$) powders showed excellent visible-light absorption with two absorption edges, one at 410 nm and the other at 530 nm, and displayed good visible-light photoactivity in the oxidative destruction of NO, except for the powder prepared in $TiCl_3/NH_2OH$ solution. Nearly 25 and 86% of NO was continuously destroyed under visible light ($\lambda > 500$) and UV-visible light irradiation ($\lambda > 290$) as shown in Fig. 21. In the XPS spectra, the N 1s peak around 400 eV was observed but not the peak at 396 eV for all the as-prepared $TiO_{2-x}A_y$ samples before Ar^+ -ion sputtering treatment. Apparently, the large amount of NH_3 and other nitrogen compounds adsorbed on the metal-oxide surface (400 eV) may have masked the existence of Ti–N binding (396 eV).

Yet an N-doped titania photocatalyst with high visible-light activity has been synthesized using a layered titania/isostearate nanocomposite prepared by a sol-gel technique (Matsumoto et al. 2007). Nitrogen-doping was achieved by treating the composite with aqueous NH_3 followed by calcination either in an O_2/N_2 mixture or in pure N_2 at various temperatures (300, 350, 400, 450, and $500^\circ C$). The vivid yellow samples absorbed visible light in the region 380–500 nm, and correlated with doped-N content in the samples. Not so for the visible-light photoactivity, which *failed to correlate* with the N content. Highest visible-light photoactivity was observed for the $400^\circ C$ calcined sample whose absorption spectrum is illustrated in Fig. 22. The quantity of N content in the sample decreased on increasing the calcination temperature, particularly significant between 300 and $350^\circ C$, with the decrease being more important for the sample calcined in O_2/N_2 than for the sample calcined in pure N_2 . The former was probably due to oxidation of doped N species by the O_2 during the heat treatment.

Thus far we have witnessed that VLA TiO_2 systems doped with either C, S, or N possess, in most cases, good attributes toward the photo-oxidation of organic and inorganic (e.g., NO_x) substrates. Of particular interest have been the materials doped with N whose preparative methods have been varied, but otherwise simple in a large number of cases. Most important, however, although all the C-, S-, and N-doped TiO_2 materials displayed absorption features and absorption edges

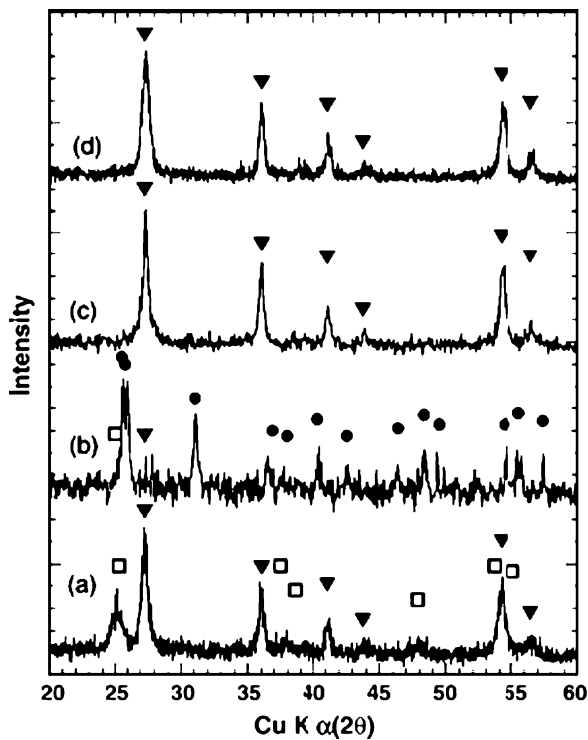


Fig. 20 XRD patterns of the titania powders prepared at 190°C for 2 h using (a) NH_2OH , (b) $\text{C}_6\text{H}_{12}\text{N}_4$, (c) $(\text{NH}_2)_2\text{CO}$, and (d) $(\text{NH}_2)_2\text{CS}$ as precipitation reagents. (*square*) Anatase; (*inverted triangle*) rutile; (*filled circle*) brookite. Reproduced with permission from Yin et al. (2006). Copyright 2006 by Elsevier B.V.

red-shifted to the visible spectral region (at least to 550 nm), photoactivity of these systems under visible-light irradiation has not always correlated with these absorption features. In a recent study, Tachikawa and coworkers (2007) addressed some of these issues and described mechanisms of the photoactivity of VLA TiO_2 specimens. Using solid-state NMR measurements combined with transient diffuse reflectance (TDR) spectroscopy, they provided direct evidence of the degradation of ethylene glycol with VLA-active $\text{TiO}_{2-x}\text{N}_x$ under visible-light irradiation. It appears that photoassisted oxidations of organic compounds on the surface of $\text{TiO}_{2-x}\text{N}_x$ proceed by surface intermediates generated from oxygen reduction (the superoxide radical anion, $\text{O}_2^{\cdot-}$) or otherwise water oxidation (the $\cdot\text{OH}$ radical) and *not* by direct reaction with h^+ that may be trapped at the N-induced midgap level (see Fig. 23). Based on their experimental results, it is rather evident that both an appropriate lower-energy photothereshold for visible-light absorption and high carrier mobilities are needed for advanced VLA TiO_2 -based photocatalysts.

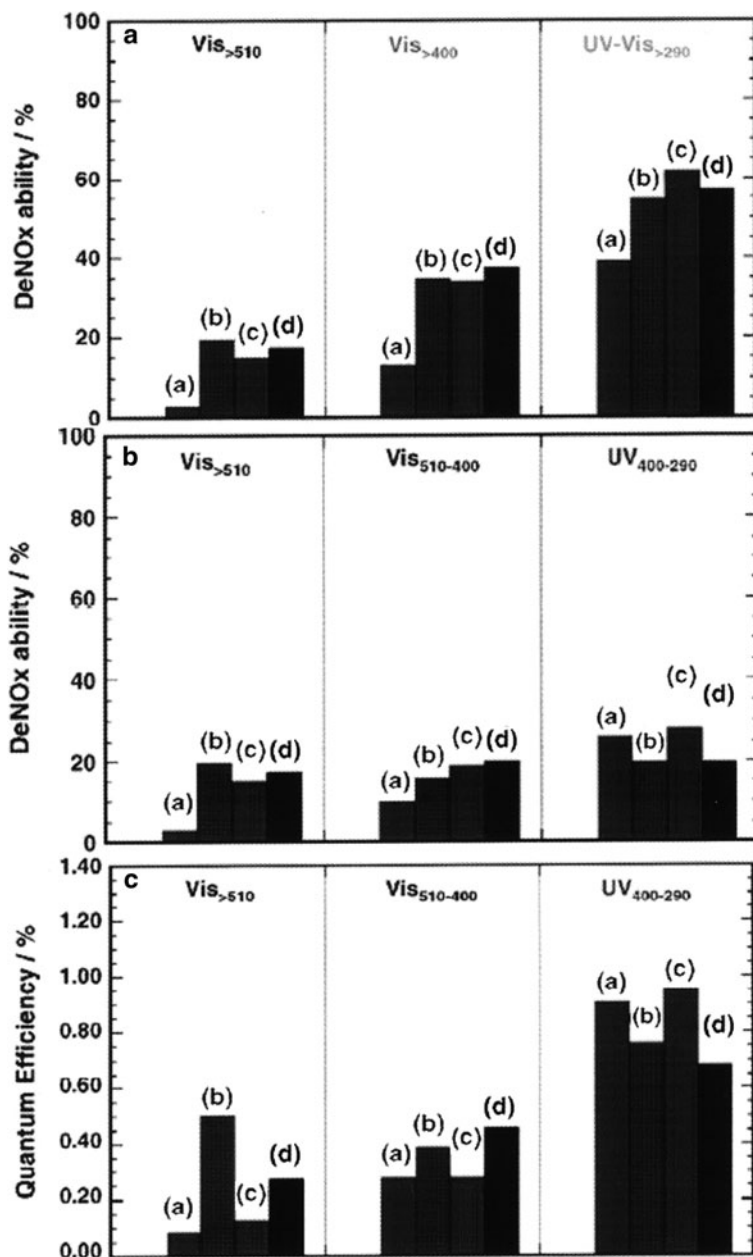


Fig. 21 Photocatalytic activity and quantum efficiencies in the degradation of NO_x by samples prepared at 190°C for 2 h using (a) NH₂OH, (b) HMT, (c) urea, and (d) thiourea as precipitation reagents. Data were treated against various wavelength ranges. Reproduced with permission from Yin et al. (2006). Copyright 2006 by Elsevier B.V.

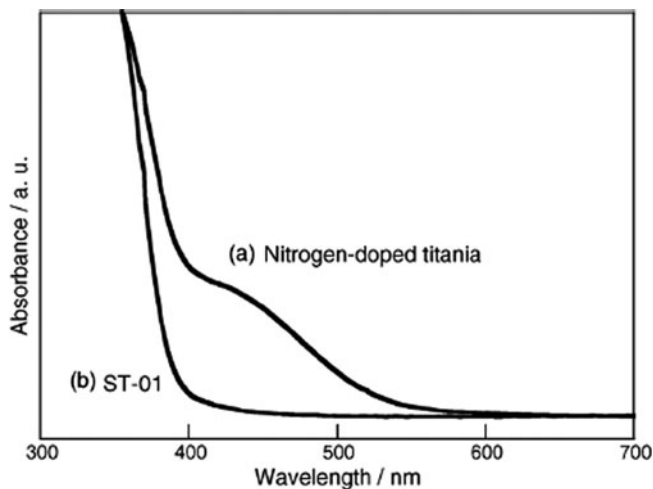


Fig. 22 UV-visible absorption spectra of (a) nitrogen-doped titania powder obtained by 400°C calcination and (b) commercial ST-01 anatase powder. Reproduced with permission from Matsumoto et al. (2007). Copyright 2007 by Elsevier B.V.

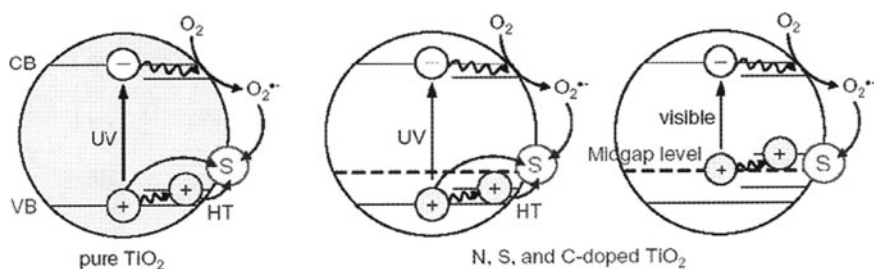


Fig. 23 Cartoons illustrating possible photoassisted processes of a substrate adsorbed on the surfaces of pure, N-, S-, and C-doped TiO₂ nanoparticles. Reproduced with permission from Tachikawa et al. (2007). Copyright 2007 by the American Chemical Society

3.3.5 N,F- and N,S-Codoped Titanium Dioxides

Vivid yellow N,F-codoped TiO₂ (NFT) powders have been prepared by SP at various temperatures from a mixed aqueous solution containing TiCl₄ and NH₄F with the aim of introducing new active sites by F-doping, while the visible-light absorption might be improved by N-doping (Li et al. 2005b, c). The powders showed new absorption features to $\lambda < 550$ nm (Fig. 24) and PL bands spanning the range 350–1,000 nm (Fig. 25) for a series of NFT systems (denoted NFT-xxx, where xxx is the temperature of the SP method) The new absorption features in the visible spectral region originated from the doped N atoms rather than F atoms, because doping only with F atoms TiO₂ caused no changes in the optical absorption of TiO₂.

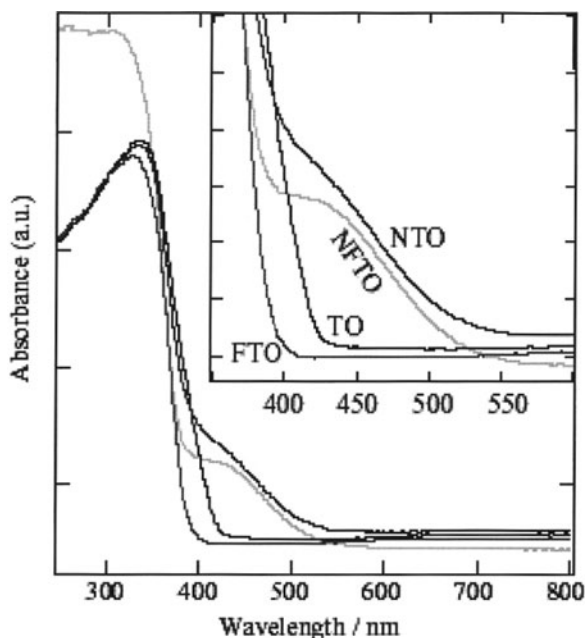


Fig. 24 UV-visible absorption spectra of pristine TiO_2 (TO), N-doped TiO_2 (NTO), F-doped TiO_2 (FTO) and N,F-codoped TiO_2 (NFTO) powders. The inset shows an expanded view of part of the adsorption spectra from 350 to 600 nm. Reproduced with permission from Li et al. (2005c). Copyright 2005 by Elsevier Inc.

The PL spectrum for the NFT-900 sample (Fig. 25a) was deconvoluted into no less than five bands. Band 1 at 465 nm arose from an oxygen vacancy with two trapped electrons, i.e., an F center, whereas band 2 at 525 nm was due to an oxygen vacancy with one trapped electron, i.e., an F^+ center. This assignment was based on the recognition that shallow traps exist at 0.51 and 0.82 eV below the CB of TiO_2 . A deep trap also exists at 2.0 eV below the CB, identified as an origin unidentified energy state (OUES). The band at 627 nm (3) was likely a consequence of the Franck-Condon principle and the polarizability of the lattice ions surrounding the vacancy, with the emitting center likely involving Ti^{3+} color centers. However, because the energy state induced by Ti^{3+} ions may be located just below the CB of TiO_2 , the authors attributed this band to OUES. Band 4 at 700 nm was said to originate from doped N atoms because no such band appeared for the T-800 and P25 TiO_2 samples: it was therefore assigned to the transfer of excited electrons between the F^+ center and the impurity energy state (IES), whereas band 5 at 905 nm was assigned to the transfer of excited electrons between the F center and the OUES. The presence of oxygen vacancies was significant because formation of the superoxide radical anion ($\text{O}_2^{\cdot-}$) and hydroxyl ($\cdot\text{OH}$) radicals, two important active species in initiating photoreaction, requires oxygen vacancy sites. These assignments are summarized in the scheme shown in Fig. 26.

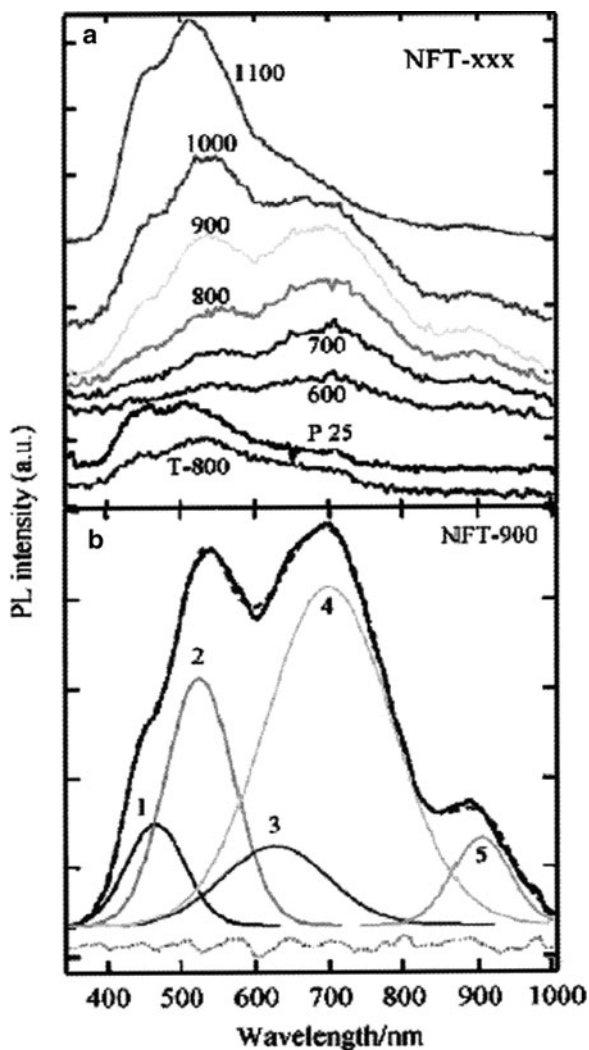


Fig. 25 (a) PL spectra of N-F co-doped TiO₂ (NFT-xxx) powders and reference samples; (b) deconvolution of the broad envelope for NFT-900. *Solid line* represents the original profile and deconvoluted peaks; *broken line* is the fitting curve, and the *dotted line* is the error of the fitting. Reproduced with permission from Li et al. (2005b). Copyright 2005 by the American Chemical Society

The photoactivity of the NFT powder prepared at 900°C proved superior to that of P25 TiO₂ under both UV- and visible-light irradiation in the decomposition of CH₃CHO. The reasons for such improved photoactivity may be closely related to the unique characteristics of the surface (porous, strongly acidic, and enhanced adsorptivity), to the doped N atoms, and to the doped F atoms. In this regard, the UV-visible spectra unequivocally indicated that N-doping caused no narrowing

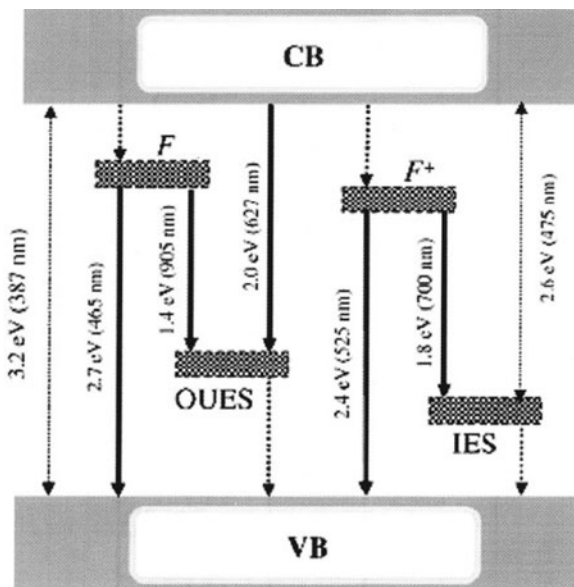


Fig. 26 Scheme of proposed energy states existing between the valence band and the conduction band of TiO₂. Dotted arrows represent additional possible existing PL emissions beyond 1,000 nm. Reproduced with permission from Li et al. (2005c). Copyright 2005 by Elsevier Inc.

of the band gap of the TiO₂ because no shift in the fundamental absorption edge of TiO₂ was observed. Rather, an isolated IES located near the VB of the TiO₂ improved light absorption in the visible region and increased the number of photons that can take part in surface photoreactions. Undoubtedly, this enhanced the photoactivity. However, in these N,F-codoped systems, the contribution of N-doping to the visible light photoactivity through oxygen vacancies may not be the sole factor, since the NFT powders displayed greater photoactivity than did N-doped TiO₂ alone. Thus, it appears that the contribution of N-doping to the visible-light photoactivity in the NFT systems is achieved mainly by improving the visible-light absorption. By contrast, F-doping produced several beneficial effects on photoactivity, namely (1) F-doping led to formation of new active sites such as oxygen vacancies (*F* and *F⁺* centers), (2) F-doping resulted in the formation of surface acid sites that led to increased adsorptive ability of the NFT powders for a substrate as well as acting as electron acceptors, and (3) F-doping increased the mobility of photogenerated electrons in TiO₂ so that they could easily diffuse from the inner lattice to the surface of the particles where reactions occurred. Consequently, the high visible-light photoactivity of NFT powders was likely the result of a synergetic effect of their unique surface characteristics, doped N atoms, and doped F atoms.

An overall comparative study carried out on N-doped, F-doped, and N, F-codoped TiO₂ powders (also denoted as NTO, FTO, NFTO) synthesized by SP confirmed the origins of the visible-light-driven photoactivity (Li et al. 2005c).

N-doping of TiO_2 resulted not only in improving visible-light absorption but also in creating surface oxygen vacancies, whereas F-doping produced several beneficial effects not least of which was the creation of surface oxygen vacancies, the enhancement of surface acidity and the increase in the number of Ti^{3+} color centers (EPR). Doped N atoms formed a localized energy state above the valence band of TiO_2 , whereas doped F atoms had no influence on the band structure. To complete this analysis of N,F-codoped titania, the N $1s$ XPS spectra of N-doped, F-doped and NFT powders after 60 min of Ar^+ -ion sputtering are illustrated in Fig. 27a. The figure clearly shows a peak (1) at 400 eV and a second peak (2) at 396.5 eV for the NTO and NFTO systems. By contrast, only one broad peak centered at ca. 400 eV is seen for FTO, likely the result of contamination from N_2 in air, since no N-source was used during the FTO preparation. In line with earlier assignments, peak 1 was attributed to the N atoms from molecularly adsorbed N-containing compounds (e.g., NH_3 and NO_x), which may have formed during the decomposition and oxidation of the N-precursors. Peak 2 was assigned to the presence of Ti–N bonds formed when N atoms replaced oxygen in the TiO_2 crystal lattice. The corresponding F $1s$ XPS spectra after 60 min of Ar^+ -ion sputtering are depicted in Fig. 27b. Peak 3 located at 687.8 eV originated from substitutional F atoms in the TiO_2 lattice; peak 4 located at 685.3 eV originated from the F atoms of TiOF_2 .

Anatase NFT powders can also be prepared by a sol-gel/solvothermal method using tetrabutyl titanate as a precursor, triethylamine as the N source and

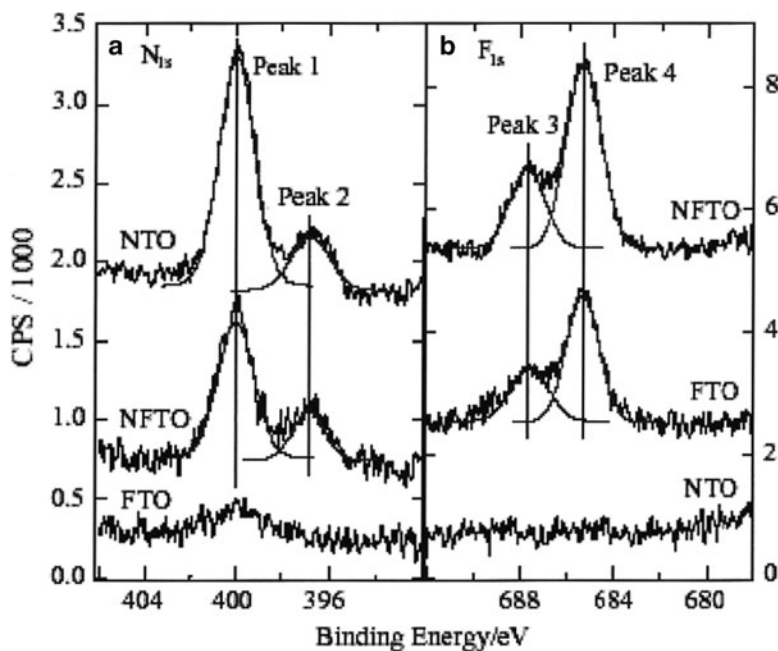


Fig. 27 XPS spectra of (a) N $1s$ and (b) F $1s$ for anion-doped TiO_2 powders after 60 min of Ar^+ ion sputtering. Reproduced with permission from Li et al. (2005c). Copyright 2005 by Elsevier Inc.

ammonium fluoride as the F source (Huang et al. 2006). Centrifugation of the powders followed by drying at 60°C in vacuum and calcining at 320°C for 6 h in air resulted in well-crystallized anatase NFT (XRD) specimens formed without contamination by any other phase, such as rutile or brookite, and by TiN, TiF₄, TiOF₂ for all samples prepared in different solvents. The UV–visible absorption spectra of TiO₂, N-doped TiO₂, F-doped TiO₂ and NFT samples showed that, apart from the fundamental absorption edge of TiO₂ at ca. 385 nm, a new absorption band appeared in the range 400–600 nm for the N-doped TiO₂ and NFT samples. The band caused by N- and F-codoping appeared slightly stronger than that caused by N-doping alone, contrary to the earlier observations reported in Fig. 23. However, it is again clear that F atoms caused no significant shift in the fundamental absorption edge of TiO₂. The NFT powder displayed good visible-light activity in the photo-assisted degradation of *p*-chlorophenol and rhodamine-B under visible-light irradiation (400–500 nm). This high activity originated from a synergetic effect between the doped N and F atoms. The doped N atoms improved visible-light absorption, whereas doped F atoms enhanced surface acidity, increased the adsorption of the reactant, and further enhanced the photoactivity. XPS spectra revealed that the NFT powder contained only Ti, O, F, N elements and a trace amount of C whose presence was due to residual carbon from the precursor solution and from adventitious hydrocarbons from the XPS instrument. The N 1s XPS spectra of the NFT and N-doped TiO₂ taken after calcination at 320°C displayed a peak at 400.0 eV ascribed to N atoms from adventitious N–N, N–H, O–N, or N-containing organic compounds adsorbed on the surface (Huang et al. 2006). The small peak 396.0 eV was taken as evidence for Ti–N bonds formed when N atoms replaced the oxygen in the TiO₂ lattice. The F 1s XPS spectra of NFT were composed of two contributions: a symmetrical peak at 685.5 eV originating from the F-containing compounds adsorbed on the surface, and a small peak at ca. 688.5 eV due to F atoms that occupy oxygen sites in the TiO₂ lattice. No evidence of TiF₄ and TiOF₂ bonds were evident in the XRD pattern.

A simple method for preparing highly photoactive nanocrystalline mesoporous N,S-codoped TiO₂ powders involved hydrolysis of Ti(SO₄)₂ in aqueous ammonia at room temperature yielding xerogels that were then calcined at 400, 500, 600, 700, and 800°C in air for 3 h, respectively (Yu et al. 2006). The as-prepared powders were amorphous, but at ca 400°C the XRD patterns (Fig. 28) indicated the appearance of the anatase phase which remained stable up to 700°C, after which the rutile phase began to appear.

An XPS survey spectrum of the N,S-codoped TiO₂ powders calcined at 500°C indicated that the powders contained Ti and O elements as well as a small amount of N, S, and C elements at binding energies: Ti 2*p*, 458 eV; O 1*s*, 531 eV; N 1*s*, 400 eV; S 2*p*, 169 eV; and C 1*s*, 285 eV (Yu et al. 2006). The latter peak for carbon was due to adventitious hydrocarbons from the XPS instrument. XPS spectra of other samples gave similar results. The high-resolution XPS spectra in Fig. 29a of the N 1*s* region taken on the surface of the TiO₂ powders show an asymmetric band that is resolved into two peaks: one at 400.4 eV attributed to Ti–N bonding formed by the nucleophilic substitution reaction between NH₃ and Ti(SO₄)₂ during the

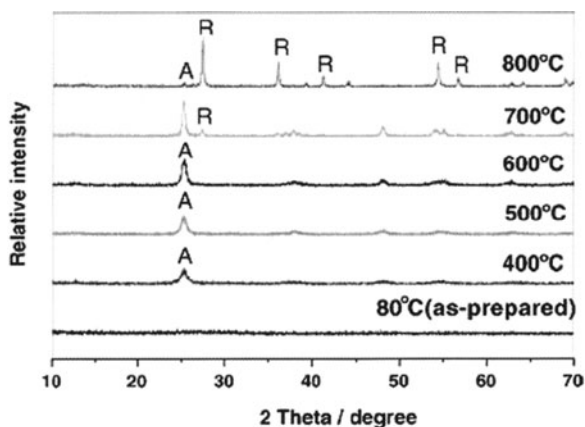


Fig. 28 XRD patterns of as-prepared TiO_2 powders calcined at different temperatures. Reproduced with permission from Yu et al. (2006). Copyright 2006 by Elsevier B.V.

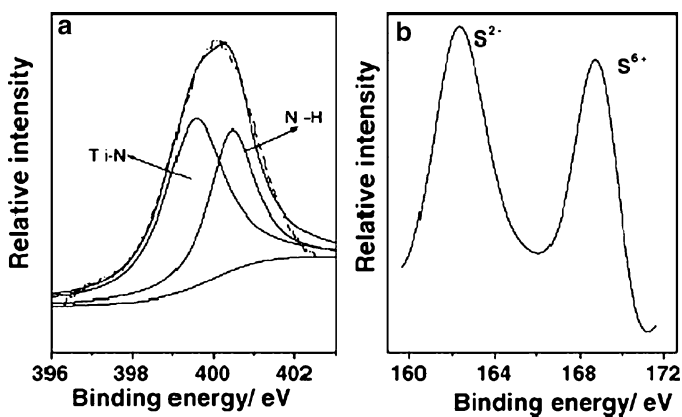


Fig. 29 High-resolution XPS spectra of (a) N 1s and (b) S 2p regions of the as-prepared N,S-codoped TiO_2 powders calcined at 500°C. Reproduced with permission from Yu et al. (2006). Copyright 2006 by Elsevier B.V.

hydrolysis, whereas the other was assigned to some NH_3 adsorbed on the surface of TiO_2 . In the case of the S $2p_{3/2}$ XPS spectra (Fig. 29b), two isolated peaks are seen at binding energies 168.7 and 162.3 eV that have been attributed to S^{6+} and S^{2-} species, respectively. The former was associated with some SO_4^{2-} ions on the surface of TiO_2 , whereas the peak at 162.3 eV corresponds to the Ti–S bond from substituting the O^{2-} in TiO_2 by S^{2-} species. Substitution of S^{2-} into O^{2-} sites should lead to some distortion of the TiO_2 lattice owing to the larger size of S^{2-} (1.7 Å) relative to O^{2-} (1.11 Å). XRD results confirmed this supposition. Absorption spectra of N,S-co-doped TiO_2 samples showed stronger absorption in the UV–visible spectral region than undoped TiO_2 , and a red shift in the band gap

transition, taken by Yu and coworkers (2006) as giving rise to band gap narrowing by the presence of dopants. The largest red shift was seen for the N,S-codoped TiO₂ powders calcined at 800°C because of the formation of rutile and growth of the TiO₂ crystallite.

The high visible-light photoactivities of as-prepared N,S-codoped TiO₂ powders heat-treated at 400–700°C toward the photooxidation of acetone and formaldehyde may be the result of synergetic effects of the strong absorption in the UV–visible light region, the red-shift of the absorption edge, good crystallization, large surface area, and the two-phase structures of undoped TiO₂ and N,S-codoped TiO₂ (Yu et al. 2006).

4 Theoretical Calculations of Band Gap Energies in Doped TiO₂

In Sect. [Nitrogen-Doped Titanium Dioxides](#), we described some of the principal preparative methods and strategies of doping TiO₂ (anatase or rutile) with nitrogen dopants. These have included (i) sol-gel syntheses, (ii) chemical treatment of the TiO₂, (iii) oxidation of TiN, (iv) ion implantation, and (v) RF-MS. There can be no doubt that these different methods lead to anion-doped metal-oxide materials with entirely different properties. The key question that keeps coming up in the literature is: what is the chemical nature and the location of the species that lead(s) to the red-shift of the absorption edge of TiO₂ and consequently to the visible-light activity of TiO₂? Species such as NO_x, NH_x, and N²⁻ have been proposed, not to mention the hyponitrite, nitrite and nitrate species that have in some cases been confirmed experimentally. Another key question regards the electronic structure(s) of the (anion)-doped materials and their fate when subjected to UV- and/or visible-light irradiation. Although these questions have been addressed in several interesting computational studies (see below), a consensual acceptance of the results has yet to be reached. As we shall witness below, significant advances can be made toward a clarification of these key questions by a combination of experimental and computational studies within the same laboratory or among collaborating laboratories.

Densities of states in anatase TiO₂ for substitutional doping of oxygen in the lattice by C, N, F, P, and S were first reported by Asahi and coworkers (2000, 2001) using the FLAPW formalism in the framework of the LDA. The calculations were carried out without geometry optimization for the five anion-dopings because the resulting atomic forces were apparently too large to obtain reasonable positions in the unit cell (eight TiO₂ units per cell). Sulfur has much larger formation energy for substitution (4.1 eV) than is required for N (1.6 eV). Thus, it was inferred that because of its large ionic radius it would be difficult to incorporate S²⁻ into the TiO₂ lattice. Carbon- and phosphorous-doping seemingly introduce states too deep in the band gap of TiO₂ to satisfy the condition that states within the band gap should overlap sufficiently with band states of TiO₂ to transfer photoexcited carriers to reactive sites at the catalyst surface within their lifetime. Three types of doping for N

were considered in the computations: (a) substitutional N doping (N_S), (b) interstitial N doping (N_I), and (c) both types of doping (N_{S+I}) in the anatase TiO_2 architecture. Optimization of the N positions in the cell inferred molecularly bonding states – NO and N_2 – for cases (b) and (c) with bond lengths (improved by the *generalized gradient approximation*, GGA) in fair agreement with accepted values: 1.20 vs. 1.15 Å (N–O) and 1.16 vs. 1.10 Å (N_2). Substitutional doping of N was the most effective because its $2p$ states (apparently) contributed to band gap narrowing by mixing with O $2p$ states of the valence band (Asahi et al. 2001). Calculated imaginary parts of the dielectric functions of $TiO_{2-x}N_x$ showed a shift of the absorption edge to lower energy by N doping, with dominant transitions from N $2p_\pi \rightarrow Ti d_{xy}$ rather than from O $2p_\pi$ as in TiO_2 . However, the calculated band gap energies were considerably underestimated relative to the experimental value ($E_{bg} = 2.0$ eV vs. $E_{bg} = 3.2$ eV for anatase). This was attributed, in part, to the well-known shortcomings of the LDA approach. Accordingly, to correct this underestimated band gap a scissors operator (a sort of *fudge factor*) was used that apparently displaces the empty and occupied bands relative to each other by a rigid shift of 1.14 eV, so that the minimum band gap would now be in line with experiment (corrected $E_{bg} = 3.14$ eV) for the band gap of anatase TiO_2 . The band gaps of the N-doped $TiO_{2-x}N_x$ systems were also adjusted by 1.14 eV on the assumption that the underestimated energy of the band gap in the LDA approach was not affected by N-doping, because long-range screening properties in $TiO_{2-x}N_x$ were likely similar to those in TiO_2 .

Contrary to the expectations of Asahi et al. (2000, 2001), Umabayashi and coworkers (2002) did incorporate S into anatase TiO_2 by oxidative annealing of TiS_2 at 600°C in which the S dopant caused a significant shift of the absorption edge (of TiO_2) to lower energy. However, in accord with Asahi et al. (2000, 2001), their ab initio band calculations also involved mixing S $3p$ states with O $2p$ states of the valence band, and thus taken to mean that the mixing contributes to the band gap narrowing of TiO_2 through an increase in the valence band width. A fuller study involving first-principles band calculations (WIEN97 code) by the FPLAPW method, again based on density functional theory (DFT) within the GGA approximation, led Umabayashi et al. (2003a) to conclude again that mixing of S $3p$ states with O $2p$ valence band states increases the width of the valence band and narrows the band gap.

In the work reported by Ohno and coworkers (2004), S-doped TiO_2 displayed significant visible-light activity attributed to the presence of S^{4+} species that substituted Ti^{4+} in the lattice. No S^{2-} species were seen from XPS spectral measurements. One possibility for the XPS presence of S^{4+} might have been due to SO_3^{2-} species formed by the partial oxidation of thiourea during the preparation of the S-doped TiO_2 sample. This peculiarity led Matsushima and coworkers (2007) to re-examine the electronic structure through first-principles DFT band calculations and to explore the plausible locations of the S atoms in the anatase TiO_2 structure. Four types of supercells were examined: type A (12 atoms) and B (48 atoms) in which a Ti atom was substituted by an S atom, and type C (12 atoms) and D (48 atoms) in which an O atom was substituted by an S atom. A tetragonal-to-orthorhombic phase transition occurred in type C and D supercells. In the small

supercell A, band-like S-related states appeared at energies in the range ~ 1.6 to 0 eV, whereas in the larger B supercell atomic-like S $3p$ states appeared at ca. 0.9 eV above the valence band. By contrast, in the large D supercell the S $3p$ states merged with the O $2p$ states of the valence band leading to a band gap shrinkage (narrowing) of ca. 0.7 eV. It would seem that, according to these calculations, the S atom could be located at either Ti or O sites in the anatase structure. The choice might depend on the preparative conditions. DFT calculations also predicted that S atoms located at Ti sites in S-doped TiO₂ lead to lower visible-light activity.

Contrary to this prediction, as-prepared sulfur-doped TiO₂ (Umebayashi et al. 2003b) was twofold more VLA than as-prepared N-doped specimens under visible-light irradiation (Sathish et al. 2005). Mixing of S $3p$ states with the O $2p$ states in the upper edge of the valence band of TiO₂ accounted for the visible-light activity from DFT considerations that used a two-unit-cell supercell as the basis of the calculations (Umebayashi et al. 2002). The effects of S-doping have been examined further theoretically by Tian and Liu (2006) using plane-wave-based pseudopotential DFT to characterize the electronic structure when O atoms are substituted by S in anatase TiO₂ to determine how its absorption behavior might be affected, and to probe how different doping levels through S concentration changes might impact the electronic structure and the optical absorption characteristics of S-doped TiO₂. Larger supercells were used: 72, 48, and 24 atom supercells to simulate S-doping levels of 0.0139, 0.0208, and 0.0417, respectively. The first observation was that the S-doped anatase TiO₂ is converted into a direct band gap semiconductor at the Γ position (in the Brillouin zone), in line with results for S-doped rutile TiO₂ (Yamamoto et al. 2004) caused by the presence of S $3p$ states localized above the upper edge of the valence band. However, band-to-band excitation was retained for anatase at different S-doping levels; that is, the *intrinsic band gap* of TiO₂ is retained on S doping. Another aspect resulting from the DFT analysis was the concentration-dependent behavior of band gap energies 3.20, 2.75, 2.67, and 2.55 eV (absorption edge at 387, 451, 465 and 488 nm) with doping levels of 0.0000, 0.0139, 0.0208 and 0.0417 (Table 1), respectively. Also, the width of the valence band increased as the doping level increased. In the data of Table 1, a scissors operator of +1.40 eV (note that others used a value of +1.14 eV; see above) was used to shift the CB states so that the estimated band gap energies corresponded to the experimental values. Effective mixing of S $3p$ with O $2p$ states occurred at about 4.2% doping level for S-doped anatase TiO₂, thus widening the valence band width, narrowing the band gap, and inducing visible-light activity for TiO₂. The table also shows that band gap lowering and red-shifts of the absorption edge increase as the S concentration increases.

The picture as to the exact cause of the red-shift of the absorption edge of TiO₂ seen experimentally for various N-doped TiO₂ (anatase) powders became somewhat confused with the report from Yates group (Diwald et al. 2004a) that the absorption edge of a N-doped TiO₂ rutile single crystal shifted to higher energy (see Sect. Nitrogen-Doped Titanium Dioxides). Using spin-polarized DFT calculations within the GGA approximation, Di Valentin and coworkers (2004) determined that whereas in anatase the localized N $2p$ states located just above the O $2p$ states of the

Table 1 DFT calculated properties of S-doped TiO₂ specimens. From Tian and Liu (2006)

Concentration (%)	Band gap energy (eV)	Corrected band gap energy (+1.4 eV)		Absorption edge (nm)	D ^b (eV)
		Band gap energy	Δ^a (eV)		
0.00	1.80	3.20	–	387	–
1.39	1.35	2.75	0.45	451	0.21
2.08	1.27	2.67	0.53	465	0.066
4.17	1.15	2.55	0.66	488	0.002

^aLowering of band gap relative to undoped TiO₂

^bEnergy difference between the lower energy levels of the S states and the upper edge states of the valence band

valence band red-shift the absorption edge to lower energy, in rutile the tendency to red-shift the absorption edge is offset by the concomitant contraction of the O 2*p* band resulting in an overall increase in the optical transition energy by ca. 0.08 eV (experimentally this blue-shift was 0.20 eV). Compared to anatase, rutile has a wider O 2*p* band due to both its higher density and its different structure (see Fig. 30).

Nitrogen-doping was modeled by replacing 1, 2, or 3 oxygen atoms in the 96-atom anatase supercell and 1 or 2 oxygen atoms in the 72-atom rutile supercell (Di Valentin et al. 2004), giving a stoichiometry comparable to that used in experiments for TiO_{2-x}N_x: 0.031 < *x* < 0.094 for anatase and 0.042 < *x* < 0.084 for rutile (note that a higher level of N-doping was used by Asahi et al. (2000, 2001) giving a stoichiometry of TiO_{1.875}N_{0.125}). Apparently, inclusion of more N atoms in the same supercell yields more accurate results than using smaller supercells. The calculated band gaps were 2.19 eV and 1.81 eV (at the Γ position) vs. the experimental 3.2 and 3.0 eV, respectively, for pure undoped anatase and rutile TiO₂, again because of the shortcomings of the DFT method. Nonetheless, analysis of the electronic energy levels showed that N-doping causes no shift of the position of both top and bottom of the O 2*p* valence band and of the CB relative to pure undoped TiO₂. This is in significant contrast with the conclusions of Asahi et al. (2000, 2001) with respect to the undoped material. Structural variations in the rutile TiO₂ structure subsequent to substitution of one O atom with N in the 72-atom supercell appear to be significant in rutile relative to anatase in which the variations were inconsequential. In any case, the N impurity states can act as deep electron traps in TiO_{2-x}N_x systems (Fig. 30). Di Valentin et al. (2004) also considered the contribution of oxygen vacancies (V_{OS}), experimentally estimated to be located 0.75–1.18 eV below the CB (their DFT calculations placed them at 0.3 eV below the CB *E_C*), to the overall visible-light photoactivity of N-doped systems when V_{OS} trap electrons to produce *F*-type color centers. The simultaneous presence of N dopants and V_{OS} may also lead to charge transfer states (reaction 3.9) that can also contribute to the photoactivity.



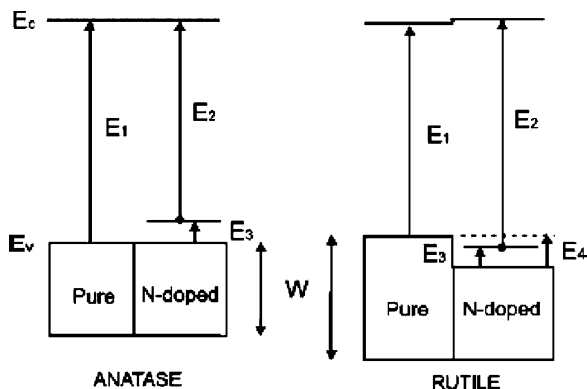


Fig. 30 Schematic representation of the energy band structure of pure and N-doped anatase and rutile (energies not to scale). Note the modest shift of 0.03 eV in E_C of the conduction band to higher energies and the contraction energy E_4 in the N-doped rutile TiO_2 . E_3 represents the energy of the N dopant levels above the valence band. Higher levels of doping, e.g., three N atoms per supercell, cause a small shift of ~ 0.05 eV to higher energies for E_C which is overcompensated by the presence of N-derived states just above VB, so that the excitation energy E_2 from these states to the conduction band is reduced by <0.1 eV compared to pure anatase. Reproduced from Di Valentin et al. (2004). Copyright 2004 by the American Physical Society

In a subsequent study, Di Valentin and coworkers (2005a) combined experiments (EPR, XPS) and DFT calculations, performed using the plane-wave-pseudopotential approach together with the Perdew–Burke–Ernzerhof (PBE) exchange correlation functional and ultrasoft pseudopotentials, to characterize the paramagnetic species present in N-doped anatase TiO_2 powders obtained by sol-gel synthesis, and to unravel some of the mechanistic details of the visible-light activity of N-doped TiO_2 s as to whether photoactivity is due to the presence of NO_x or NH_x species or simply to substitutional N-doping. The $\text{TiO}_{2-x}\text{N}_x$ sample was obtained by hydrolysis of $\text{Ti}(\text{i-PrO})_4$ in isopropanol media in the presence of an aqueous NH_4Cl solution as the N source, followed by calcination of the N-doped specimen at ca. 500°C for 2 h. XPS N 1s spectra indicated only a peak at ca. 400 eV, typically assigned to interstitial N (without precluding others), but no 396 eV peak usually originating from substitutional N-doping. EPR results indicated the presence of two different paramagnetic N-related species, whose hyperfine coupling constants were consistent with substitutional and interstitial N species. Accordingly, two structurally different locations were considered for the N dopant in the DFT calculations: substitutional N (N_S) and interstitial N (N_I) atoms in the TiO_2 anatase matrix. In the substitutional model, N that replaces O in the TiO_2 lattice was taken to be bonded to three Ti atoms in the 96-atom supercell so that the paramagnetic species is formally N^{2-} , whereas in the interstitial model N is added to the 96-atom supercell bonded to one or more O, and thus is in a positive oxidation state as in NO^- , NO_2^- and/or NO_3^- . Figure 31 illustrates the DFT band structure of the N-doped TiO_2 and reports the calculated albeit underestimated band gap energy of titania.

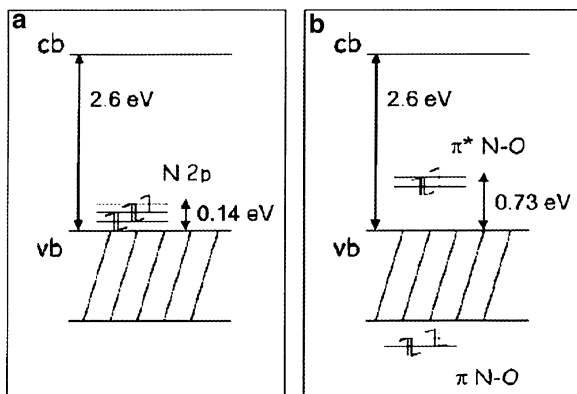
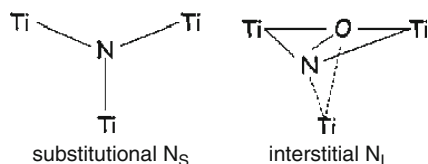


Fig. 31 Electronic band structure for (a) substitutional and (b) interstitial N-doped anatase TiO_2 as given by PBE calculations at a low-symmetry k -point. In the former, the site contains the paramagnetic N^{2-} species making the site electrically neutral (replaced O^{2-}), whereas in the latter the site is occupied by the radical NO. The estimated band gap energy is also indicated. Reproduced with permission from Di Valentin et al. (2005a). Copyright 2005 by the American Chemical Society



The two bonding π states in Fig. 31b for NO lie deep below the O 2p band but the two π^* still occupied states lie above (0.73 eV) the O 2p band and lie at higher energy than the 2p states of substitutional N (0.14 eV). A more interesting consequence of the portrait shown in Fig. 31 is that the two electrons left in the formation of an oxygen vacancy, that typically would form two Ti^{3+} color centers, might also be trapped by these two different N dopants yielding the azide species (N^{3-} denoted as N_S^-) and the hyponitrite species (NO^-). Another significant result deriving from the DFT calculations of Di Valentin and coworkers (2005a) is that N-doping led to a substantively reduced energy of formation of V_{O_S} (4.3–0.6 eV for anatase) with important consequences in the generation of F -type and Ti^{3+} color centers. Experimentally, which of the two types of N dopants predominates in the N-doped TiO_2 will depend on the experimental conditions, e.g., nitrogen and oxygen concentrations, and calcination temperatures. What Fig. 31 also implies is that moving from substitutional N to interstitial N is in fact an oxidative step, which according to DFT estimates is ca. 0.8 eV exothermic. Thus, there is a cost for the reverse, i.e., interstitial N-doping is preferred when $\text{TiO}_{2-x}\text{N}_x$ systems are prepared in excess nitrogen and oxygen, whereas high-temperature calcination of N-doped systems, commonly done in most

experiments, both substitutional N and formation of oxygen vacancies are likely the preferred occurrences.

The question on the blue-shift of the absorption edge of N-doped TiO₂ rutile single crystals contrasting the red-shifts in N-doped TiO₂ powders was also taken up in a DFT study by Yang and coworkers (Yang et al. 2007) using the plane-wave method. Results confirmed those of Di Valentin et al. (2004) that some N 2*p* states lie above the O 2*p* valence band when N substitutes O in the TiO₂ lattice and when N is located at interstitial positions. However, no band gap narrowing was predicted by these calculations. But when N substitutes Ti atoms in the rutile lattice, a bandgap narrowing in the rutile crystal is apparently possible because the N dopant introduces some energy states (the N 2*p* states) into the bottom of the CB. The authors rationalized this inference by the fact that removal of electrons from the supercell on replacing one Ti with a N atom leads to a reduction of the Coulomb repulsion and thus to a shift of the energy band edges, i.e., the band gap energy is reduced by ca. 0.25 eV relative to the undoped rutile supercell whose estimated band gap energy was calculated to be 1.88 eV. This is reminiscent of the assertion by Asahi et al. (2000, 2001) that N-doping TiO₂ causes band gap narrowing because the N 2*p* states mix with the O 2*p* states in the valence band, thereby widening the valence band and shrinking the band gap.

We have seen above that substitutional N-doping is stabilized by the presence of oxygen vacancies ($N_{S-O} + V_O$) under oxygen-poor experimental conditions, whereas under oxygen-rich conditions interstitial N species (N_i) become favored. According to DFT calculations of C-doping TiO₂ (Di Valentin et al. 2005b), otherwise performed in a manner identical to those for N-doping (96-atom supercell for anatase and 72-atom supercell for rutile; see above), at low C concentrations and under oxygen-poor conditions, substitutional (to oxygen) carbon and oxygen vacancies seem to be favored. By contrast, under oxygen-rich conditions, both interstitial and substitutional (to Ti) C dopings are preferred. However, in the latter case, no C states were found in the band gap except for a small band gap shrinking. Thus, C-doping of TiO₂ causes a modest variation of the band gap energy but induces several localized occupied states within the band gap. These features accounted for the experimentally observed red-shifts of the absorption edge toward the visible region (up to nearly 1.7 eV). The nature and density of localized mid-gap C-related states depended on the concentration of the doping C atoms, on the oxygen pressure, and on the calcination temperature during the preparation of C-doped TiO₂. DFT results also seem to indicate that C-doping favors formation of oxygen vacancies in bulk TiO₂. Once again, DFT calculations underestimated the band gaps: 2.19 eV (2.61 eV) and 1.81 eV (2.14 eV) at Γ (and at the low-symmetry κ -point) for anatase and rutile, respectively. In the case of carbon-doped anatase (as might also occur for N- and S-doped TiO₂s; see Sect. [Nitrogen-Doped Titanium Dioxides](#)), holes formed upon visible-light excitation are less reactive than those formed upon UV-light excitation in pure TiO₂, because holes are trapped at the midgap levels induced by carbon doping (Tachikawa et al. 2004). This means that holes are less mobile than the electrons excited to the CB, so that visible-light irradiated C-doped TiO₂ are less likely to be involved in direct oxidation of substrates by photogenerated holes. The

concomitant presence of C species and O vacancies in $\text{TiO}_{2-x}\text{C}_x$ (XPS and EPR) are responsible for the improved photoactivity in the visible region, as also predicted for N-doped TiO_2 . Evidently, the origin of increased photoactivity of C- and N-doped TiO_2 may be associated with more complex phenomena than the simple presence of dopant atoms, e.g., by concomitant changes in the stoichiometry of the sample (Di Valentin et al. 2005b).

The N-doped sample prepared by the sol-gel process of stoichiometry near $\text{TiO}_{1.907}\text{N}_{0.062}$ examined earlier by Di Valentin and coworkers (2005a) was re-examined more closely in a series of experiments and DFT calculations aimed at determining the fate of the doped specimen when irradiated at different wavelengths in the presence of adsorbates (Livraghi et al. 2006). The experiments asserted that N species were responsible for the absorption of visible-light radiation, and consequently for the visible-light activity, as well as for the photoinduced electron transfer from the solid to surface electron scavengers (adsorbates) such as molecular O_2 . The UV–visible diffuse reflectance spectrum of the sample (Fig. 32) is nearly identical to the many reported DRS spectra of N-doped TiO_2 specimens prepared in a variety of ways. However, as we shall see later, this spectral behavior is identical to the spectral behavior of so many other doped TiO_2 samples that have been doped with different types of dopants (e.g., transition metal ions, C, S, and others) and synthesized by different methods.

Previous EPR work (Di Valentin et al. 2005a) had identified two distinct nitrogenous paramagnetic species in N-doped TiO_2 , one of which was the molecular NO radical (Livraghi et al. 2005) located in closed pores within the crystals and thus had no influence on the electronic structure of the solid. No evidence of hydrogen EPR hyperfine lines were found, thus ruling out NH_x -type paramagnetic species as had been inferred by Yates' group (Diwald et al. 2004a, b). Whatever the nature of the paramagnetic species, it was stable to washing and to calcination in air up to ca. 500°C. This was taken to mean that the nitrogen radical species identified as N_b^\bullet interacted strongly with the TiO_2 lattice. DFT calculations carried out on a

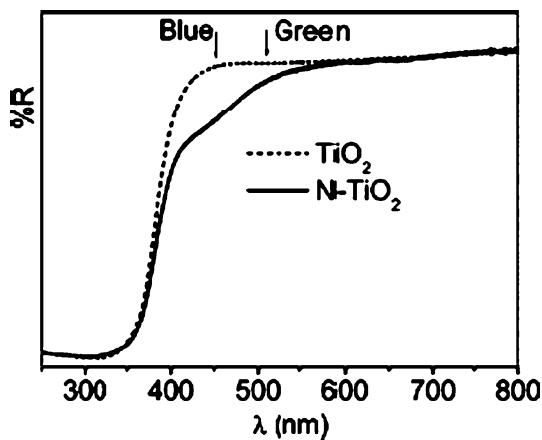


Fig. 32 UV–visible diffuse reflectance spectra of undoped and N-doped TiO_2 . Reproduced with permission from Livraghi et al. (2006). Copyright 2006 by the American Chemical Society

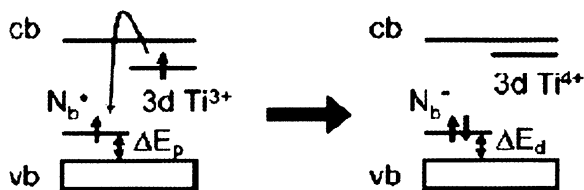


Fig. 33 Electronic band structure changes from interactions between N_b^\bullet (N_S^\bullet or N_I^\bullet) and Ti^{3+} color centers. Reproduced with permission from Livraghi et al. (2006). Copyright 2006 by the American Chemical Society

96-atom supercell involved two interstitial nitrogen (N_I^\bullet) or two substitutional nitrogen (N_S^\bullet) paramagnetic species plus an oxygen vacancy (V_O) located far away from these N-centers to avoid direct defect/impurity interactions. We need to recall that removal of an O atom from the TiO_2 lattice leaves behind two electrons to form the *neutral F center* (V_O in the Kroger–Vink notation), or they may be trapped by neighboring Ti^{4+} species to give two Ti^{3+} color centers, which Henderson et al. (2003) positioned 0.8 eV below the bottom of the CB. However, other studies have indicated otherwise, although there are electron traps around this energy; Ti^{3+} color centers certainly do exist as demonstrated by EPR measurements (Berger et al. 2005; Hurum et al. 2003). One of the consequences of the high number of V_O s under oxygen-poor conditions in N-doped TiO_2 is the partial quenching of N_b^\bullet paramagnetic species, which according to Di Valentin et al. (2005a) are transformed into N_b^- through reduction by Ti^{3+} color centers (Fig. 33). The energetically favored reduction of N_b^\bullet species may be the cause for the small energy cost in the formation of V_O s in N-doped TiO_2 (see above). The EPR peaks attributed to N_b^\bullet centers disappeared on reduction of the sample (reaction 3.10) whether by annealing in vacuo or by other means to then reappear on re-oxidation. Thus, the N-doped TiO_2 specimen (at least the one prepared by the sol-gel method) contained paramagnetic N-related species in the bulk lattice (N_b^\bullet) and a number of diamagnetic species (N_b^-) in the presence of



which depended on the oxygen content in the metal-oxide sample. The EPR signal due to N_b^\bullet increased on irradiation of the doped sample at 437 nm in O_2 ($p_{O_2} = 5$ kPa) and a new EPR line appeared, attributed to $O_2^{\bullet-}$ radical anions (reactions 11 and 12). These anions are apparently stabilized on two different surface



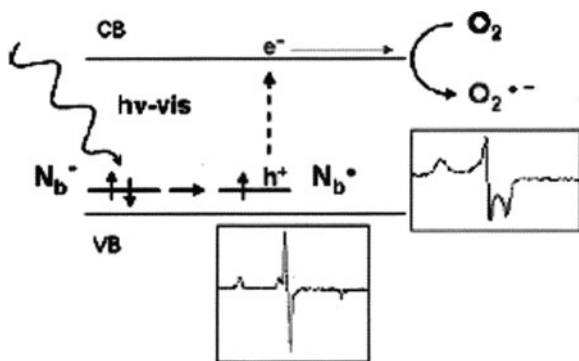


Fig. 34 Sketch of the proposed mechanism for the processes induced by vis-light irradiation of the N-doped sample in O_2 atmosphere. Reproduced with permission from Livraghi et al. (2006). Copyright by the American Chemical Society

Ti^{4+} species, which Livraghi et al. (2006) claimed could be typical of N-doped TiO_2 s. Figure 34 illustrates the process embodied in the formation of the superoxide radical anions.

So far all the DFT-based calculations *have failed* to calculate experimentally commensurate band gap energies for undoped anatase and rutile TiO_2 , and consequently for all anion-doped TiO_2 systems unless, as some have done, one resorts to the scissor operator.

In a comprehensive theoretical investigation of substitutional anion doping in TiO_2 , Wang and Lewis (2006) explored the electronic properties of C-, N-, and S-doped TiO_2 materials using an *ab initio* tight-binding method (FIREBALL) based on DFT and a nonlocal pseudopotential scheme. FIREBALL is a first-principles tight-binding molecular dynamics (TBMD) simulation technique based on a self-consistent version of the Harris–Foulkes functional. The method uses confined atomic-like orbitals as the basis set. To test the methodology, the electronic structures of bulk TiO_2 in the rutile and anatase architectures were examined first for comparison. The calculated direct band gap from Γ to Γ of 3.05 eV for rutile accords with the reported experimental gap of 3.06 eV (Pascual et al. 1978). We have seen that the LDA approach generally underestimates the experimental band gap for insulators and semiconductors, whereas the band gap obtained from *ab initio* plane-wave calculations for TiO_2 is around 2.0 eV (Glassford and Chelikowsky 1992). This underestimation by the LDA approach was compensated in the theoretical treatment of Wang and Lewis (2006) using a local-orbital basis set. For anatase, the direct band gap from Γ to Γ of 3.26 eV is in agreement with the experimentally observed gaps of 3.20 eV (Sanjines et al. 1994). The upper valence bands are composed mainly of O 2p states with band widths of 5.75 and 4.86 eV for rutile and anatase structures, respectively, in accord with experimental values of 5.50 and 4.75 eV. The lower CBs consist primarily of unoccupied Ti 3d states and have a full width of 5.8 eV (rutile) and 5.6 eV (anatase). The results are summarized in Table 2.

Table 2 Comparison of calculated values (Wang and Lewis 2006) for the electronic properties of undoped rutile and anatase TiO₂ with experimental and calculated values reported by others (E_{BG} is the direct band gap, and E_{VB} is the valence band width)

	E_{BG} (rutile), eV	E_{BG} (anatase), eV
Wang and Lewis	3.05	3.26
Experiments	3.06 (1)	3.20 (2), 3.42 (3)
Other calculations	2.00 (4); 1.78 (5)	2.22 (5), 2.00 (6)
	E_{VB} (rutile), eV	E_{VB} (anatase), eV
Wang and Lewis	5.75	4.86
Experiments	5.50 (7)	4.75 (2)
Other calculations	5.70 (4), 6.22 (5)	5.17 (5), 5.05 (6)

Pascual et al. (1978); Sanjines et al. (1994); Tang et al. (1995); Glassford and Chelikowsky (1992); Mo and Ching (1995); Asahi et al. (2000); Kowalczyk et al. (1977)

The congruence of the above results provides some confidence on calculations pertaining to anion-doped TiO₂ systems.

For C-doped anatase and rutile TiO₂, a 384-atom (64 primitive unit cells) supercell was employed (Wang and Lewis 2006) at two doping levels in carbon: one O atom was randomly substituted by C (doping level 0.26%), and 20 oxygen sites were randomly substituted by C (doping level 5.20%). Carbon-doping had no effect on the CB of TiO₂ but did introduce new states above the valence band edge of bulk TiO₂ in C-doped structures. Substituting C atoms for O atoms shifted the valence band edge to higher energy compared to bulk TiO₂ so that the band gap narrowed. For the 5.2% C-doping level, the new valence band states were fairly continuous leading to a significant red shift of the valence band edge such that the corresponding band gap was narrowed to 2.0 eV for *anatase* and 2.35 eV for *rutile*, in apparent reasonable accord with the experimental absorption edges reported by Khan and coworkers (2002) of 2.32 and 2.82 eV in ca. 5% C-doping. By contrast, at low C-doping (0.26%) the C states were isolated (localized) and only slightly affected the anatase TiO₂ O 2*p* valence band states. Accordingly, the mobility of the hole created under these conditions must be rather poor (hole is trapped in these localized states), which explains why the photoactivity was low at low C-dopings. However, at the high C concentration of 5.2% the states near the valence band edge of anatase TiO₂ were less localized; there was significant overlap with the O 2*p* states, and there were a greater number of occupied states near the valence band edge. These observations explained why the high C-doping level led to greater visible-light absorption and thus to higher visible-light photoactivity (Wang and Lewis 2006). In C-doped *rutile* TiO₂, both high and low doping concentrations shifted the valence band edge upward by 0.7 eV.

Because of the odd number of electrons in the N atom, two O atoms were replaced by one N yielding an effective N-doping level of 0.52% for the low concentration case (Wang and Lewis 2006). Here also, the CB minimum remained unchanged. New states were introduced by N-doping just above the valence band edge of bulk TiO₂, as well as states that penetrated into the upper valence band of the bulk states. Unlike C-doped *rutile* TiO₂, however, no significant energy shift (<0.05 eV) in the

valence band edge was seen in N-doped *rutile* TiO₂ at the high N concentration of 5.2%. A significant shift was observed only at the low N-doping level of 0.52% resulting in a narrowed band gap of 2.55 eV. DOS calculations inferred that low doping concentrations greatly improved the visible-light photoactivity. There was no significant overlap between the N 2*p* states and the O 2*p* states for the 0.52% N-doping level. Moreover, at the low N concentration the valence band edge was more localized compared to the high N-doping level in N-doped *rutile* TiO₂. Unlike N-doped *rutile* TiO₂, however, identical shifts of ca. 0.44 eV were obtained in N-doped *anatase* TiO₂ at both high and low doping levels resulting in a band gap of ca. 2.82 eV (440 nm). DOS calculations indicated a significant overlap between the N 2*p* states and O 2*p* states for the 5.2% N-doping. By contrast, at the low N-doping level, the states introduced by N were distinct and highly localized on the single dopant state, and there was no significant overlap for structures containing 0.52% N. Thus, the high N-doping level in N-doped *anatase* TiO₂ should lead to greater visible-light photoactivity.

Comparison of results of C-doped *rutile* with N-doped *rutile* TiO₂ shows that incorporation of C dopants produces a narrower band gap than does N-doping, regardless of the doping concentration (Wang and Lewis 2006). Hence, C-doped TiO₂ materials should absorb more energy in the visible-light region than N-doped materials, and should provide greater visible-light activity owing to less localized states at the high concentrations. Similar to the C-doped case, the greater number of occupied states near the valence band edge at the high N-doping concentration should lead to a greater participation of N-doped TiO₂ in photoreactions taking place under visible light.

For S-doped TiO_{2s}, DOS results showed that at low doping levels (0.26%) there was no significant shift of the valence band edge, which implies that at low S-doping levels the S-doped TiO₂ materials should show poor visible-light photoactivity because of the large band gap in such systems (>3 eV) (Wang and Lewis 2006). In contrast, a significant red-shift of the valence band edge was seen at the high S-doping levels in both *rutile* and *anatase* structures; the corresponding band gaps were narrowed down to 2.3 and 2.2 eV, respectively. In contrast to the C- and N-doped TiO₂, the valence band edge was much delocalized for the low S-doping level in S-doped TiO₂. And since the valence band edge remained virtually unchanged, there should be no great photoactivity when S-doped systems are subjected to visible-light irradiation. At the high S-doping concentration, photoactivity in the visible region should be more pronounced than at the low S concentration due to band gap narrowing and to delocalization of the valence band edge (Wang and Lewis 2006). According to this theoretical treatment, S-doped TiO₂ materials should afford the smallest visible-light photoresponse among the C, N, and S anion dopants. Indeed, among the anion dopants examined, C-doping should be the most promising candidate for second-generation photocatalytic TiO₂-based materials, because C dopants produce the largest red-shift of the valence band edge amongst the three anion-doped TiO₂ examined.

It is clear from the extensive discussion above that there is no consensus about whether or not there is *band gap narrowing* in doped TiO₂ materials based on DFT

calculations. Some of the theoretical studies have deduced from these calculations that there is a *rigid shift of the valence band edge* to higher energies, thus narrowing the *intrinsic* band gap of TiO_2 as a consequence of doping. The discrepancies cannot be a semantic problem. One thing is certain. Anion-doping (or for that matter any type of doping) of TiO_2 does shift the *absorption edge* of the doped metal oxide to longer wavelengths, thus affording visible-light potentially photoactive materials useful in several important applications of surface processes occurring on the TiO_2 surface. In the past, we have referred to the longest visible-light wavelength at which photoactivity was seen as the *red limit of photocatalysis*. What does change, however, is the lowest phototreshold (i.e., *extrinsic* absorption edge) of the actinic light that can activate TiO_2 by introducing dopants into the metal-oxide lattice. When C-, S- and N-doped TiO_2 systems are photoactivated by visible light absorption, they also generate electrons and holes, although the latter carrier will have a decreased oxidative power (lower redox potential) *vis-a-vis* holes photogenerated from pristine TiO_2 . The *intrinsic* absorption edge of the metal oxide itself is not changed by the doping. In other words, the valence and conduction bands are not affected by the doping, *at least* at low doping levels and weak interactions. But if they were to be affected through strong coupling interactions between the dopant states and the O $2p$ states of the valence band of TiO_2 , then we must face the inescapable conclusion that the material may no longer be TiO_2 , but more appropriately may be described as titanium oxynitride, titanium oxycarbide, or titanium oxysulfide materials possessing entirely different properties, not least of which are new electronic structures of their respective valence and conduction bands.

Next, we examine the optical properties of doped TiO_2 and TiO_2 /polymer compositions, and provide some evidence based on the photobleaching phenomenon that the absorption bands observed in the visible spectral region of the TiO_2 /polymer compositions can be bleached. That is, the species that give rise to or that are responsible for the absorption bands in the visible spectral region can be destroyed by irradiating the compositions with visible-light wavelengths corresponding to the absorption bands in the visible spectral region. In the TiO_2 /polymer compositions, the above-referred to species are located on the *particle surface*, or at best in the *near subsurface region*, and thus can be annihilated by oxygen-assisted photoreactions. Under these conditions, neither the *intrinsic* valence band nor the *intrinsic* CB can be destroyed.

5 Optical Features of Doped TiO_2

Optical properties of doped TiO_2 specimens are best analyzed by difference DRS methods. Calculation of difference spectra to obtain the more typical absorption spectra requires DRS spectra of various doped TiO_2 samples absorbing in the visible region [$\rho_{\text{ab}}(h\nu)$] and of undoped TiO_2 samples non-absorbing in the visible spectral region [$\rho_{\text{non-ab}}(h\nu)$]. The latter is typically the DRS spectrum of a nominally clean

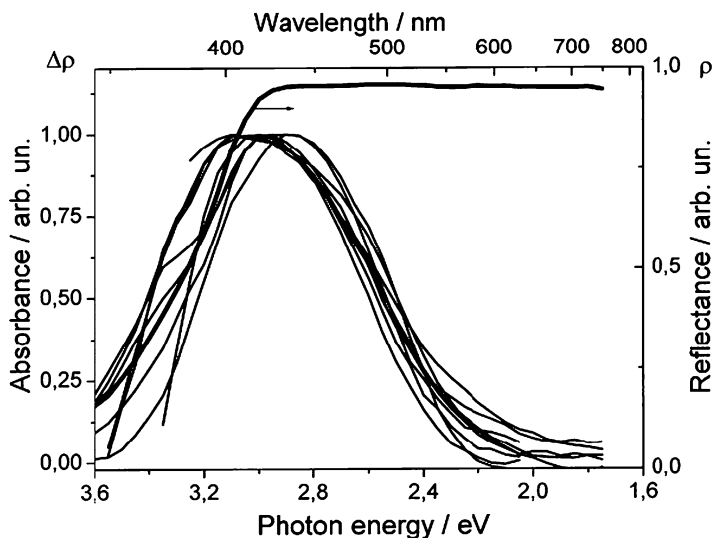


Fig. 35 Absorption spectra of various anion-doped TiO_2 specimens before averaging (see text) and the diffuse reflectance spectrum (DRS) of Degussa P25 TiO_2

TiO_2 sample or the DRS spectrum of the doped sample *prior* to any heat treatment that might induce visible-light absorption. For compositions consisting of TiO_2 and a number of polymeric substrates examined by Kuznetsov and Serpone (2006), the notation $[\rho_{\text{non-abs}}(h\nu)]$ and $[\rho_{\text{abs}}(h\nu)]$ referred, respectively, to the DRS spectra before and after the sample's treatment (heat or irradiation). If the DRS transmittance spectrum of a thick enough sample is 0, then the change in reflectance $\Delta\rho(h\nu)$, i.e., $[\rho_{\text{non-abs}}(h\nu) - \rho_{\text{abs}}(h\nu)]$, is identical to the change in absorbance $\Delta A(h\nu)$. Where optical properties of doped specimens have been characterized by absorption spectra $A(h\nu)$, the difference absorption spectra $\Delta A(h\nu)$ were calculated in a manner similar to difference DRS spectra, $\Delta\rho(h\nu)$. It should be emphasized that usage of difference diffuse reflectance and/or difference absorption spectra provide a means for numerical analysis of the optical characteristics of the samples. The numerical analysis typically involves (i) the characterization of each absorption spectrum by the position of the spectral maximum ($h\nu_{\text{max}}$), the intensity of this maximum ($\Delta\rho_{\text{max}}$, ΔA_{max}), and the spectral bandwidth at half-maximum amplitude; (ii) the comparison of the spectra of different samples after normalization by the $\Delta\rho_{\text{max}}/\Delta A_{\text{max}}$ factor; and (iii) the analysis of the shape of the absorption spectra, i.e., the ability of presenting the spectra as a sum of individual absorption bands.

The analysis illustrated below for anion-doped TiO_2 specimens involved (a) digitization (numbering) of the DRS spectra or the absorption spectra of the sample in non-VLA and VLA states, (b) calculation of the difference spectra, and (c) normalization of the spectra by the $\Delta\rho_{\text{max}}/\Delta A_{\text{max}}$ factor. The resulting absorption spectra display maximal absorption around 3.0 eV (Fig. 35); however, the shape of the spectra may differ (significantly for some). In some cases, the long-wavelength tail of the absorption may extend well into the near-infrared region ($h\nu < 1.5$ eV). Such

broad absorption spectra would be very complex for a numerical analysis. Only a few relatively narrow absorption spectra were selected for the numerical analysis to evaluate the inherent similarities among the spectral characteristics of anion-doped titania samples. Selected results are illustrated in Fig. 35, which reports the absorption spectra of several N-doped titania specimens: (i) mechanochemically activated N-doped TiO₂ (Yin et al. 2003), (ii) N-doped oxygen-deficient TiO₂ (Ihara et al. 2003), (iii) NFT sample prepared by a spray pyrolytic method (Li et al. 2005c), (iv) N-doped *anatase* TiO₂ specimen prepared by a solvothermal process (Aita et al. 2004), (v) N-doped *rutile* TiO₂ sample also prepared by a solvothermal process (Aita et al. 2004), (vi) *yellow* N-doped TiO₂ specimen synthesized in short time at ambient temperatures using a nanoscale exclusive direct nitridation of TiO₂ nanocolloids with alkyl ammonium compounds (Gole et al. 2004), (vii, viii) N-doped TiO₂ samples prepared by evaporation of the sol-gel with N-doping carried out under a stream of ammonia gas at different temperatures (Joung et al. 2006), and (ix) N-doped TiO₂ prepared via sol-gel by mixing a solution of titanium(IV) isopropoxide in isopropyl alcohol in the presence of an NH₄Cl solution (Livraghi et al. 2006).

Broad absorption spectra are often obtained for samples prepared by a procedure otherwise identical to that of samples exhibiting the narrow spectra. Temperature and time of calcination are frequently reported as factors that affect the shape of the spectra. For instance, an increase of temperature from 247 to 347°C for 2 h (Wang et al. 2007a) or prolonging the time of calcination from 5 min to 30 min at 400°C

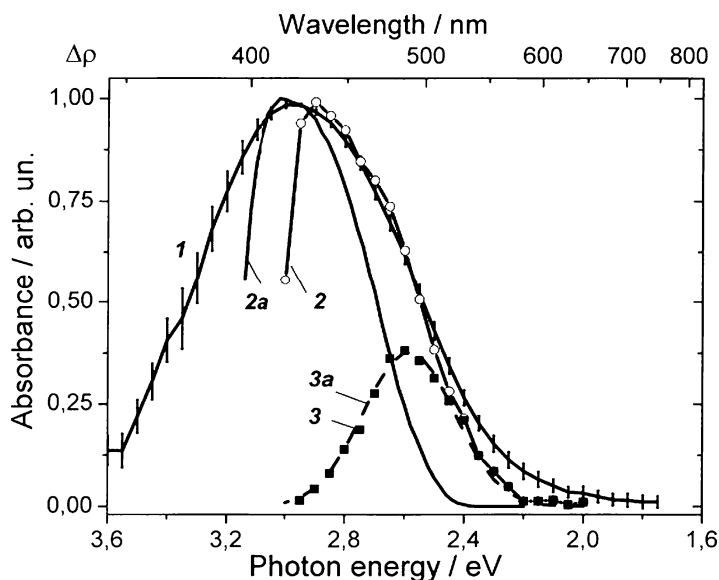


Fig. 36 Average absorption spectrum of visible-light-active N-doped TiO₂ specimens (curve 1); difference absorption spectra of N-doped rutile crystal (curve 2) and of the color centers in the yellow anatase TiO₂ crystal (curve 2a). Curve 3 (solid squares) depicts the difference between curves 2 and 2a; curve 3a (line) is the Gaussian fit of curve 3 (see text for more details)

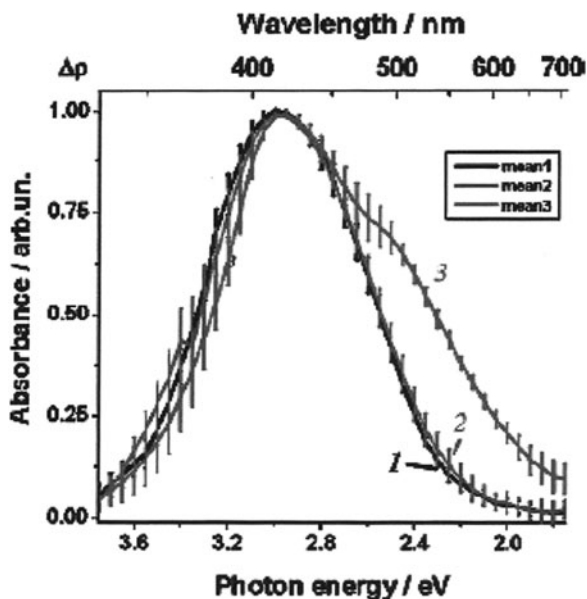


Fig. 37 Average absorption spectra ($\Delta\rho$) of various titania systems. See text for details of the origins of these spectra. Reproduced with permission from Kuznetsov and Serpone (2006). Copyright 2006 by the American Chemical Society

(Joung et al. 2006) decreased the absorption in the range $h\nu < 2.0$ eV, such that the absorption spectra then adopt a narrower shape. As an example, the broad absorption spectrum of the *orange* N-doped TiO_2 specimen, prepared in nearly the same manner as the *yellow* N-doped TiO_2 sample by Gole et al. (2004), shows a shoulder on the low-energy side at ca. 2.5 eV (see Fig. 37).

Figure 35 clearly demonstrates the strong similarity of selected spectra in the visible region at energies $h\nu < 3.0$ eV, and the noticeable differences in the range of *intrinsic* absorption at $h\nu > 3.0$ eV. The latter differences are not surprising because the samples differed in phase composition (see e.g., Aita et al. 2004) and sample thickness. Moreover, some workers often choose any available sample, e.g., Degussa P25 TiO_2 , as the non-absorbing specimen in the visible spectral region, rather than a specimen prepared in an otherwise identical fashion as the doped samples.

The spectral similarities in Fig. 35 allowed Kuznetsov and Serpone (2006) to calculate the average (mean) spectrum of the VLA N-doped TiO_2 samples that is illustrated in Fig. 36 (curve 1). Note that the standard error for the mean spectrum does not exceed 2.3% in the energy range $h\nu < 3.0$ eV.

Figure 36 also displays the absorption spectrum of the nitrogen-doped rutile crystal prepared by an NH_3 treatment at 597°C (curve 2) (Diwald et al. 2004b) and the absorption spectrum (curve 2a) of the anatase crystal reported by Sekiya and co-workers (2000, 2004). The difference in spectra 2 and 2a in the region $h\nu > 3.0$ eV originates from the difference in the phase composition of the TiO_2 ,

whereas the difference between curves 2a and 2 at $h\nu < 3.0$ eV exhibits a single absorption band with $h\nu_{\max} = 2.6$ eV, half-width of 0.35 eV and a near-Gaussian shape, i.e., the band is very similar to the 2.55-eV AB2 band reported earlier by Kuznetsov and Serpone (2006).

Sekiya and coworkers (2000, 2004) attributed the absorption band at 3.0 eV in the spectrum of anatase to oxygen vacancies that can trap electrons to yield *F*-type centers (Sekiya et al. 2004). It is important to emphasize that the absorption band AB1 can be obtained in a variety of ways: for instance, (i) by annealing the *as-grown* crystals under an oxygen atmosphere at $T > 374^\circ\text{C}$ (Sekiya et al. 2000, 2004) and (ii) by annealing *colorless* crystals by subjecting them first to a reductive H_2 atmosphere at 647°C and then to an O_2 atmosphere at 497°C (Sekiya et al. 2004). In both cases, only prolonged (ca. 60 h) annealing of the crystals at 797°C in an O_2 atmosphere, not in inert (a nitrogen) atmosphere, transformed the yellow crystals that display the absorption band at 3.0 eV to a colorless state (Sekiya et al. 2004). In the first case, the origin of the oxygen vacancies is associated with the uncontrolled reduction of TiO_2 assisted by impurities introduced into the crystal during its growth (Sekiya et al. 2000). The absorption of N-doped rutile crystals in the visible spectral region has only been partially associated with reduction of the TiO_2 bulk lattice (Diwald et al. 2004b). However, the main reason for the shift in the photochemical threshold from 3.0 eV to 2.4 eV was suggested by Yates and coworkers (Diwald et al. 2004a, b; Thompson and Yates 2005) to originate from the nitrogen dopant located in an interstitial site and probably bonded to hydrogen. This inference contrasts the interpretation given by Sekiya and coworkers (2000, 2004) for the spectral features in the visible region, by Di Valentin et al. (2005a) from their EPR study, and with our assignments of the absorption bands in the visible spectral region of titania/polymer compositions (Kuznetsov and Serpone 2006).

As a further attestation of the remarkable similarities in the absorption spectra of doped TiO_2 systems, Fig. 37 summarizes additional averaged spectra. Curve 1 depicts the average spectrum obtained from the absorption spectra reported in the literature (see Kuznetsov and Serpone 2006 for details) of (i) Cr-implanted TiO_2 , (ii) Ce-doped TiO_2 , (iii) mechanochemically activated N-doped TiO_2 , (iv) N-doped oxygen-deficient TiO_2 , and (v) from $\text{Sr}_{0.95}\text{La}_{0.05}\text{TiO}_{3+\delta}$ treated with HNO_3 acid. Curve 2 represents the average spectrum obtained from the difference DRS's (absorption spectra) of various anion-doped titania specimens: (i) NFT, (ii) N-doped anatase TiO_2 , (iii) N-doped rutile TiO_2 , and (iv) yellow nitrided $\text{TiO}_{2-x}\text{N}_x$ nanocolloids. Curve 3 illustrates the averaged spectra of cation-doped TiO_2 s, namely (i) Fe-doped TiO_2 nano-powders prepared by oxidative pyrolysis of organo-metallic precursors in an induction thermal plasma reactor, (ii) zinc-ferrite- doped titania ($\text{TiO}_2/\text{ZnFe}_2\text{O}_4$) synthesized by sol-gel methods followed by calcinations at various temperatures, and (iii) the orange N-doped TiO_2 sample prepared by a procedure otherwise identical to that of yellow N-doped TiO_2 but with the former consisting of partially agglomerated nanocolloids (i.e., larger $\text{TiO}_{2-x}\text{N}_x$ clusters). Hence, note the remarkable overlap of the relatively narrow average spectra 1 and 2 in Fig. 37, which illustrates convincingly the independence of the spectra on the method of photocatalyst preparation. This appears to be a general feature of the

electronic and spectral features of the color centers/defects in TiO₂. Comparison of the broader mean spectrum 3 in Fig. 37 with the narrower spectra 1 and 2 indicates that broadening of the absorption spectrum of TiO₂ photocatalysts originated from the long-wavelength absorption band, in this case the 2.55-eV AB2 band in the study of Kuznetsov and Serpone (2006).

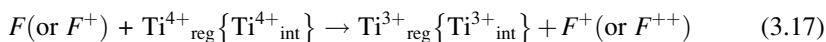
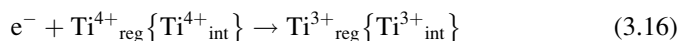
The coincidence of the absorption bands in the visible spectral region for reduced TiO₂ with those of VLA TiO₂ samples indicates that the processes involved in the preparation of VLA TiO₂ specimens (irrespective of the method) implicate a stage of TiO₂ reduction. As we saw earlier, many of the preparative methods included a heating stage at various temperatures. For instance, the absorption band appearing at 3.0 eV in anatase crystals and attributed to oxygen vacancies results from the removal of impurities at ca. 300°C introduced during the crystal growth (Sekiya et al. 2000). Related to this, the visible-light absorption of metal-ion-implanted TiO₂ systems reported by Anpo and Takeuchi (2003) was observed only after the samples had been calcined in the temperature range 450–550°C.

The absorption features displayed by TiO₂ specimens in the visible spectral region most likely originate from the formation of color centers through the reduction of TiO₂ after some form of heat treatment or after some photostimulated process.

Kuznetsov and Serpone (2006) concluded that the absorption spectra of anion-doped (or otherwise) TiO₂ in the visible spectral region originated from the existence of color centers, rather than from a narrowing of the original band gap of TiO₂ ($E_{\text{bg}} = 3.2$ eV; anatase), as originally espoused by Asahi et al. (2000, 2001), through mixing of oxygen and dopant states. True narrowing of the original band gap of the metal-oxide TiO₂ semiconductor would necessitate heavy anion or cation doping, which would require somewhat high concentrations of the dopants. In the latter case, however, one must ask whether the metal oxide retains its original integrity.

What is the nature of these color centers? Although we have seen these in various contexts earlier, it is nonetheless instructive to reiterate what they are and how they may be formed. On loss of an O atom in a metal oxide (reaction 3.13), the electron pair remaining behind is trapped in the V_O cavity (reaction 3.14) left behind giving rise to an *F* center, whereas a positively charged *F*⁺ center is equivalent to a single electron associated with the oxygen vacancy, V_O[•] (reaction 3.15; again in the Kroger–Vink notation). The electron-pair deficient oxygen vacancy, V_O^{••}, also known as an anion vacancy, V_A, can be viewed as a doubly charged *F*⁺⁺ center (reaction 3.13). Thus, the color centers associated with oxygen vacancies imply the existence of *F*-type centers in TiO₂ and other metal oxides. The electrons left behind can also interact with Ti⁴⁺ ions in regular lattice sites (Ti_{reg}⁴⁺) adjacent to the oxygen vacancy or located at interstitial lattice sites (Ti_{int}⁴⁺) to give Ti_{reg}³⁺ and Ti_{int}³⁺ color centers, respectively (reactions 3.16); *F*-type centers can also generate the latter color centers through charge transfer (reaction 3.17).





Spectrum 3 of Fig. 37 can be deconvoluted into 3 overlapping absorption bands depicted in Fig. 38 (Serpone 2006). Of these three bands, one is centered at 2.1 eV (590 nm; band 1), another at ca. 2.40 eV (517 nm; band 2), and band 3 occurs around 2.93 eV (413 nm) in good accord with the band positions reported by Kuznetsov and Serpone (2006) for the reduction of TiO_2 in polymeric media. The congruence of the bands in the absorption spectra of such disparate TiO_2 systems is remarkable when considering the large variations in the experimental conditions, which re-affirms the notion that the absorption bands all share the same origins. Bands 1–3 in Fig. 38 originate either from electron transitions involving F -type centers and/or from d - d transitions in Ti^{3+} color centers. Evidence for both has appeared in the literature (see references in Serpone 2006).

Using the embedded-cluster numerical discrete variational method, Chen et al. (2001) estimated the band gap energy of rutile TiO_2 as 3.05 eV in very good agreement with the experimental 3.0 eV for this polymorph. Calculations of the energy levels of the F -type centers gave energies for the F , F^+ and F^{2+} centers, respectively, of 0.87, 1.78, and 0.20 eV below the bottom level of the CB.

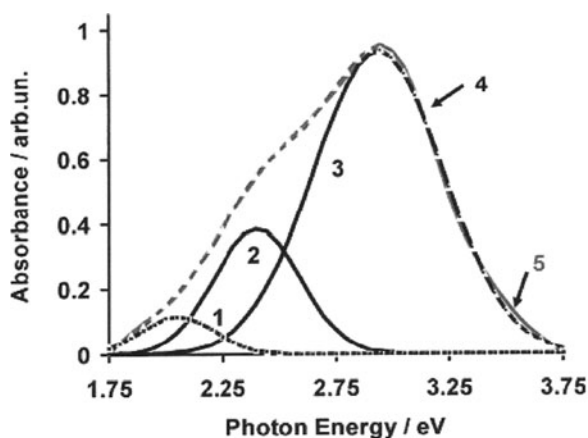
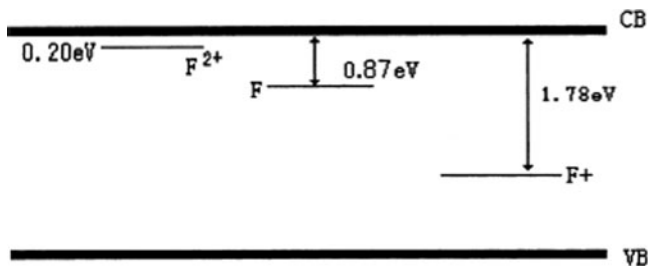


Fig. 38 Deconvolution of spectrum 3 of Fig. 37 (curve 5 herein). Band 4 represents the deconvolution sum of curves 1, 2, and 3. Reproduced with permission from Serpone (2006). Copyright 2006 by the American Chemical Society

The scheme below summarizes the positions of these F centers in rutile. A band seen at 760 nm (1.61 eV) was ascribed to the electron transition from the F^+ center to the CB of TiO_2 . The 0.87-eV level consisted of an admixture of the F center's $1s$ orbital and a $\text{Ti } 3d$ orbital; the respective charge population densities were -1.325 and -0.3014 , indicating that F color center electrons may be influenced by neighboring Ti^{4+} cations, and that (partial) charge transfer from the F center to adjacent Ti^{4+} ions may occur yielding formally Ti^{3+} color centers. Photoinduced detrapping of electrons from the F center to the CB followed by retrapping by the shallow F^{2+} centers can increase the number of F^+ centers



From past extensive experimental and theoretical studies, Serpone (2006) tentatively attributed the deconvoluted bands 3 and 2 in the three average spectra of Fig. 37 at 2.9–3.0 eV (428–413 nm) and 2.4–2.6 eV (ca. 517–477 nm), respectively, to Jahn–Teller split ${}^2T_2 \rightarrow {}^2E$ transitions of Ti^{3+} centers. The existence of these centers has been confirmed by EPR examination of N-doped TiO_2 specimens calcined at various temperatures (Joung et al. 2006; Suriye et al. 2006). Band 1 at 1.7–2.1 eV (729–590 nm) was tentatively assigned to a transition from the ground state of the F^+ center to its corresponding excited F^{+*} state, though transition to the CB of TiO_2 was not precluded. The transition from the singlet ground state S_0 of the F center to the first F^* excited singlet state ($S_0 \rightarrow S_1$) or to the CB likely occurs at much lower energies (in the infrared) as predicted from the energies in the above scheme. Nonetheless, ascertaining such assignments will require some rigorous systematic studies that will examine anion- and cation-doped TiO_2 specimens by diffuse reflectance spectroscopy, by EPR techniques and by photoconductivity methods. In this regard, in a recent feature article Kuznetsov and Serpone (2009) carried out a systematic analysis of the absorption spectral features of various titanium dioxide specimens, whether doped or undoped, in the visible spectral domain reported extensively in the literature. In addition they briefly examined the origins of such bands in visible-light-active TiO_2 photocatalysts, i.e. second-generation photocatalysts. They deduced that at energies of $h\nu$ less than 2.0 eV (i.e. $> \sim 600$ nm) the three spectral features occurring in the near-infrared and infrared regions originate from Ti^{n+} -related ($n = 3, 2$) color centers, whereas the three absorption bands seen in the visible spectral region AB1 (2.75–2.95 eV), AB2 (2.50–2.55 eV), and AB3 (2.00–2.30 eV) are associated with oxygen vacancies (i.e. with F -type color centers) on the basis of demonstrated experimental observations. Also discussed was the question as to why reduction of TiO_2 that accompanies the

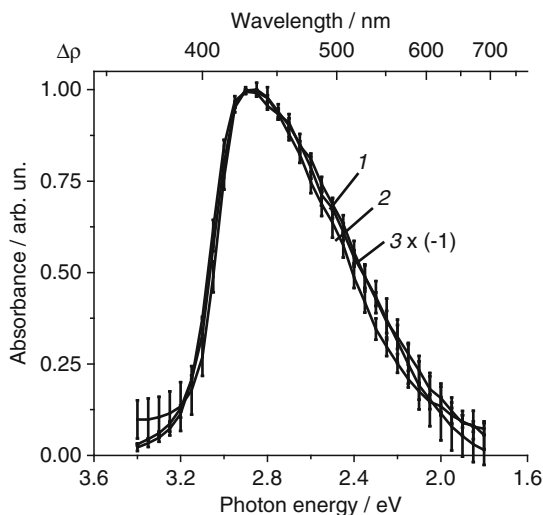
process of TiO₂ doping results only in the formation of the absorption bands AB1, AB2, and in some cases AB3; that is, the absorption features of Ti-related centers are totally suppressed. Recent studies that have demonstrated the reduction of TiO₂ during the doping process were also examined to argue on the dominant role of F-type color centers in the visible-light-activity of TiO₂ photocatalysts.

6 The Question of Band Gap Narrowing in Doped TiO₂

Taken literally, band gap narrowing in doped TiO₂ materials means that the band gap energy of TiO₂ has been decreased by the presence of dopants. To re-emphasize the point, however, what does change is the energy phototreshold for activating doped titania specimens to carry out surface photoinduced redox processes. Perhaps a better term in referring to the long-wavelength absorption edge might be (i) the *red-limit of TiO₂ photocatalysis* as used in the past to refer to photooxidations and photoreductions occurring in the visible spectral region or we might refer to the lowest-energy phototreshold or long-wavelength absorption edge as (ii) the *extrinsic band gap(s)* of doped TiO₂ vs. the term *intrinsic band gap* (for anatase, 3.2 eV; for rutile, 3.0 eV) that refers to pristine undoped titania. Nonetheless, band gap narrowing as used by some workers (e.g., by Asahi et al. 2000, 2001; and others) meant a rigid upward shift of the valence band edge toward the CB of TiO₂. If the absorption features seen in the visible spectral region were truly due to this rigid shift, then irradiation into these bands should cause no bleaching of the absorption bands. However, if the absorption features are due, as we have claimed, to the existence of color centers (F-type and/or Ti³⁺), then bleaching of the spectral features can be observed if photostimulated destruction of color centers occurs. Recent work has addressed this issue for both TiO₂/polymer compositions (Kuznetsov and Serpone 2007) and for an N-doped TiO₂ system (Emeline et al. 2007).

In the first instance, we examined the photocoloration of TiO₂ compositions with various polymers and the photobleaching of the color centers (Fig. 39) at various selected irradiation wavelengths (UV to the near infrared region) to probe the photoactivation of the color centers by irradiating into the absorption bands with maxima at 2.90 eV (427 nm; AB1), 2.55 eV (486 nm; AB2), and 2.05 eV (604 nm; AB3). This procedure aided in clarifying the mechanism of the photobleaching phenomenon as an oxygen-assisted photochemical reaction. A great advantage of degraded TiO₂/polymer compositions over VLA TiO₂s is that the color centers in the former are located at or near the surface. The color centers in the volume bulk lattice can be destroyed by a high-temperature treatment in the presence of oxygen, as for example in single crystals (Sekiya et al. 2000, 2004). Two principal types of photostimulated absorbance changes can occur: (i) increase in absorbance or (ii) decrease in absorbance. The decrease in absorbance would be a direct experimental manifestation of the photobleaching phenomenon of colored TiO₂/polymer compositions, which would clearly demonstrate the presence and the photoinduced

Fig. 39 Averaged absorption spectra (1, 2) of various TiO₂/polymer compositions normalized by $\Delta\rho_{\max}$ and averaged bleaching spectrum (3) of the TiO₂/[P(VDF-HFP)] composition irradiated at different wavelengths. From Kuznetsov and Serpone (2007)



disappearance/destruction of color centers in these titanium dioxide systems. In Fig. 39, the average spectrum of the bleaching of one colored TiO₂/ [P(VDF-HFP)] composition, where P(VDF-HFP) refers to the poly(vinylidene fluoride-co-hexafluoropropylene) polymer, irradiated at different wavelengths is depicted as curve 3 and is compared to the average heat-induced absorption spectrum (curve 1) and photoinduced absorption spectrum (curve 2) of several other TiO₂/polymer compositions (Kuznetsov and Serpone 2007). The unambiguous experimental data obtained confirmed an earlier proposal (Kuznetsov and Serpone 2006) that absorption of light by various TiO₂ systems in the visible region originates *only* from color centers and *not* from a narrowing of the band gap of pristine TiO₂. Also, results indicate that photobleaching of colored TiO₂/polymer compositions originates both from *intrinsic* absorption of light ($h\nu > 3.2$ eV, anatase) by TiO₂ and from (*extrinsic*) absorption of light by the color centers at wavelengths corresponding to their absorption spectral bands in the visible region. Note that these bands are also active in the photodestruction of the color centers. It is also relevant to point out that spectrum 3 in Fig. 39 corresponds to the nearly complete discoloration of the compositions under irradiation mostly in the visible region. The total overlap of the absorption and bleaching spectra illustrated in Fig. 39 *demonstrate unambiguously* that the *same* color centers are formed during the treatment that induced the absorption, and that they are subsequently destroyed on irradiation during the photobleaching process. This result obviously negates any inference of broadening of the valence band of TiO₂ to account for the red-shifts of the absorption edges in various doped VLA TiO₂ systems. The valence and conduction bands *can neither* be photodestroyed *nor* phototransformed, contrary to the color centers.

In another study, we examined the effect of molecular oxygen and hydrogen on the photostimulated formation of defects (color centers) on irradiation of TiO_{2-x}N_x with visible light at 546 nm; results are displayed in Fig. 40 as ΔR vs. λ (Emeline

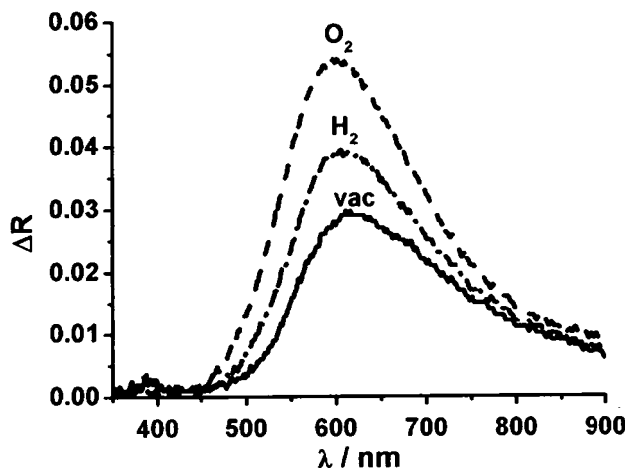


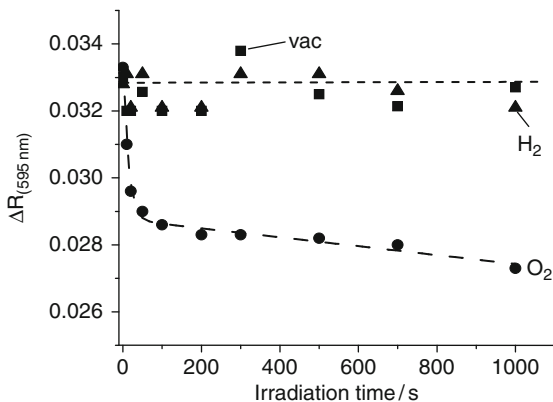
Fig. 40 Absorption spectra of photoinduced color centers in N-doped TiO_2 obtained after pre-irradiation at 546 nm in vacuum, in the presence of O_2 and H_2 . From Emeline et al. (2007)

et al. 2007); note that ΔR and $\Delta \rho$ have the same meaning. A similar behavior was observed on irradiating at 436 and 578 nm. The influence of hydrogen on photocoloration on irradiation at 546 nm was nearly the same as under UV irradiation, in that the number of photoinduced defects increased, in contrast to the presence of O_2 for which photostimulated adsorption of oxygen was the exact opposite at the visible wavelength to that seen under UV irradiation. That is, the ultimate level of photocoloration (increase in absorption) in the presence of oxygen was considerably greater under 546-nm irradiation relative to the level in vacuum and relative to what was observed under UV-light irradiation. This could only mean that the mechanism of photoexcitation and surface photoreaction that occur under visible-light excitation of $\text{TiO}_{2-x}\text{N}_x$ in the presence of O_2 must be different from the mechanism of processes that take place under UV irradiation. The effect of photobleaching of photoinduced color centers by red light at $\lambda > 610$ nm in vacuum and in the presence of oxygen and hydrogen is reported in Fig. 41. No significant changes in absorption of photoinduced color centers occurred during photoexcitation in vacuum and in the presence of hydrogen. However, the presence of oxygen caused significant changes on the absorption as seen by the effect of photobleaching (negative absorbance) of UV-induced defects, a typical behavior of electron-type color centers (i.e., F -type centers and Ti^{3+} centers).

7 Concluding Remarks

In this chapter, we have attempted to expose and explore some of the root causes that have had such an impact and so changed the field of heterogeneous

Fig. 41 Kinetics of photobleaching (recorded at $\lambda = 595$ nm) of photoinduced color centers on irradiation of $\text{TiO}_{2-x}\text{N}_x$ at $\lambda > 610$ nm in vacuum, in the presence of oxygen and in the presence of hydrogen. From Emeline et al. (2007)



photocatalysis involving second-generation materials. Various preparative methods have been described briefly and some characteristic features of the resulting cation- and anion-doped titanium dioxides presented. As in any healthy and novel scientific field of endeavor, controversies and debates are bound to occur. They are the expected norms. In this regard, note the variance in the experimental results and in the interpretations of X-ray photoelectron spectra with regard to assignments, particularly as they pertain to N-doped TiO_2 systems. Relative to pristine nominally clean TiO_2 , whose absorption edges are at 3.2 eV for anatase and at 3.0 eV for the rutile polymorph, cation- and anion-doped TiO_2 specimens of both architectures have displayed red-shifted absorption edges well into the visible spectral region. Several workers have taken this to mean that the *intrinsic band gap* of TiO_2 had been narrowed by the interactions of dopant energy states with valence band states. Calculations based mostly on DFT using various supercell sizes have supported such an inference, while other workers, also using DFT methods, have proposed that the red-shifted absorption edges, i.e., decreased photothresholds in activating TiO_2 , were due to the presence of dopant states within the band gap located above the upper level of the valence band. Irradiating into these dopant states with visible-light wavelengths would generate conduction band electrons and holes, the latter charge carrier remaining trapped at the dopant energy level(s). Analyses of the optical spectral features in the visible region, however, have inferred a common origin for the doped TiO_2 s as deduced from the strong similarities in the absorption envelopes of a large number of specimens, irrespective of the preparative methods and of the nature of the dopants, whether they be transition metal ions or non-metals such as nitrogen, carbon, sulfur, fluorine and others. Workers interested in photo-oxidative and/or photoreductive processes in degrading environmental polluting substances should find greater process engineering photoefficiencies in utilizing the second-generation photocatalytic materials (or perhaps not, as we saw in a few cases) as doped titanias absorb a greater quantity of sunlight. By contrast, workers interested in the fundamental science that underscores heterogeneous photocatalysis in general, and second-generation photocatalysts in particular will find a rich

playing field ripe for further research and exploration limited only by one's imagination.

Acknowledgments One of us (NS) wishes to thank Prof. Angelo Albini for his kind hospitality during the writing of this contribution in the winter semester 2007. It gave NS the opportunity to escape the rigors of the Canadian cold winters.

References

- Aita Y, Komatsu M, Yin S, Sato T (2004) Phase-compositional control and visible light photocatalytic activity of nitrogen-doped titania via solvothermal process. *J Solid State Chem* 177:3235–3238
- Anpo M, Takeuchi M (2003) The design and development of highly reactive titanium oxide photocatalysts operating under visible light irradiation. *J Catal* 216:505–516
- Asahi R, Taga Y, Mannstadt W, Freeman AJ (2000) Electronic and optical properties of anatase TiO₂. *Phys Rev B* 61:7459–7465
- Asahi R, Morikawa T, Ohwaki T, Aoki K, Taga Y (2001) Visible-light photo-catalysis in nitrogen-doped titanium oxides. *Science* 293:269–275
- Beck DD, White JM, Ratcliffe CT (1986) Catalytic reduction of carbon monoxide with hydrogen sulfide. 3. Study of adsorption of oxygen, carbon monoxide and carbon monoxide coadsorbed with hydrogen sulfide on anatase and rutile using Auger electron spectroscopy and temperature-programmed desorption. *J Phys Chem* 90:3132–3136
- Belver C, Bellod R, Fuerte A, Fernandez-Garcia M (2006a) Nitrogen-containing TiO₂ photocatalysts part 1. Synthesis and solid characterization. *Appl Catal B* 65:301–308
- Belver C, Bellod R, Stewart SJ, Requejo FG, Fernandez-Garcia M (2006b) Nitrogen-containing TiO₂ photocatalysts part 2. Photocatalytic behavior under sunlight excitation. *Appl Catal B Environ* 65:309–314
- Berger T, Sterrer M, Diwald O, Knozinger E, Panayotov D, Thompson TL, Yates JT Jr (2005) Light-induced charge separation in anatase TiO₂ particles. *J Phys Chem B* 109:6061–6068
- Chen J, Lin L-B, Jing F-Q (2001) Theoretical study of *F*-type color center in rutile TiO₂. *J Phys Chem Solids* 62:1257–1262
- Cheng P, Li W, Zhou T, Jin Y, Gu M (2004) Physical and photocatalytic properties of zinc ferrite doped titania under visible light irradiation. *J Photochem Photobiol A Chem* 168:97–101
- Cherkashin, A.E., Volodin, A.M., Koshcheev, S.V. and Zakharenko, V.S. (1980) Energy structure and photosorption and photocatalytic properties of titanium dioxide in carbon monoxide oxidation. *Uspekhi Fotoniki, Issue 7, Leningrad State University (LGU), Leningrad*, pp. 86–142
- Colon G, Hidalgo MC, Munuera G, Ferino I, Cutrufello MG, Navio JA (2006) Structural and surface approach to the enhanced photocatalytic activity of sulfated TiO₂ photocatalyst. *Appl Catal B* 63:45–59
- Di Valentin C, Pacchioni G-F, Selloni A (2004) Origin of the different photoactivity of N-doped anatase and rutile TiO₂. *Phys Rev B* 70:085116
- Di Valentin C, Pacchioni G-F, Selloni A, Livraghi S, Giamello E (2005a) Characterization of paramagnetic species in N-doped TiO₂ powders by EPR spectroscopy and DFT calculations. *J Phys Chem B* 109:11414–11419
- Di Valentin C, Pacchioni G-F, Selloni A (2005b) Theory of carbon doping of titanium dioxide. *Chem Mater* 17:6656–6665
- Diebold U (2003) The surface science of titanium dioxide. *Surf Sci Rep* 48:53–229
- Diwald O, Thompson TL, Goralski EG, Walck SD, Yates JT Jr (2004a) The effect of nitrogen ion implantation on the photoactivity of TiO₂ rutile single crystals. *J Phys Chem B* 108:52–57

- Diwald O, Thompson TL, Zubkov T, Goralski EG, Walck SD, Yates JT Jr (2004b) Photochemical activity of nitrogen-doped rutile $\text{TiO}_2(110)$ in visible light. *J Phys Chem B* 108:6004–6008
- Dong CX, Xian AP, Han EH, Shang JK (2006) Acid-mediated sol-gel synthesis of visible-light active photocatalysts. *J Mater Sci* 41:6168–6170
- Emeline AV, Kuzmin GN, Purevdorj D, Ryabchuk VK, Serpone N (2000) Spectral dependencies of the quantum yield of photochemical processes on the surface of wide band gap solids. 3. Gas/Solid Systems. *J Phys Chem B* 104:2989–2999
- Emeline AV, Smirnova LG, Kuzmin GN, Basov LL, Serpone N (2002) Spectral dependence of quantum yields in gas-solid heterogeneous photosystems. Influence of anatase/rutile content on the photostimulated adsorption of dioxygen and dihydrogen on titania. *J Photochem Photobiol A Chem* 148:97–102
- Emeline AV, Sheremetyeva NV, Khomchenko NV, Ryabchuk VK, Serpone N (2007) Photoinduced formation of defects and nitrogen-stabilization of color centers in N-doped titanium dioxide. *J Phys Chem* 111(30):11456–11462
- Enache CS, Schoonman J, van de Krol R (2006) Addition of carbon to anatase TiO_2 by n-hexane treatment – surface or bulk doping? *Appl Surf Sci* 252:6342–6347
- Formenti M, Juillet F, Meriaudeau P, Teichner SJ (1971) Heterogeneous photo-catalysis for partial oxidation of paraffins. *Chem Technol* 1:680–686
- Frach P, Gloess D, Vergohl M, Neumann F, Hund-Rinke K (2004) EJIPAC, Saarbrücken, Germany. Quoted by Yates et al (2006).
- Ghicov A, Schmidt B, Kunze J, Schmuki P (2007) Photoresponse in the visible range from Cr-doped TiO_2 nanotubes. *Chem Phys Lett* 433:323–326
- Glassford KM, Chelikowsky JR (1992) Structural and electronic properties of titanium dioxide. *Phys Rev B* 46:1284–1298
- Gole JL, Stout JD, Burda C, Lou Y, Chen X (2004) Highly efficient formation of visible light tunable $\text{TiO}_{2-x}\text{N}_x$ photocatalysts and their transformation at the nanoscale. *J Phys Chem B* 108:1230–1240. See also the web-site: <http://www.physics.gatech.edu/people/faculty/jgole.html#links>
- Henderson MA, Epling WS, Perkins CL, Peden CHF, Diebold U (1999) Interaction of Molecular oxygen with the vacuum-annealed $\text{TiO}_2(110)$ surface: molecular and dissociative channels. *J Phys Chem B* 103:5328–5337
- Henderson MA, Epling WS, Peden CHF, Perkins CL (2003) Insights into photo-excited electron scavenging processes on TiO_2 obtained from studies of the reaction of O_2 with OH groups adsorbed at electronic defects on $\text{TiO}_2(110)$. *J Phys Chem B* 107:534–545
- Huang D-G, Liao S-J, Liu J-M, Danga Z, Petrik L (2006) Preparation of visible-light responsive N-F-codoped TiO_2 photocatalyst by a sol-gel-solvothermal method. *J Photochem Photobiol A Chem* 184:282–288
- Hurum DC, Agrios AG, Gray KA, Rajh T, Thurnauer MC (2003) Explaining the enhanced photocatalytic activity of degussa P25 mixed-phase TiO_2 using EPR. *J Phys Chem B* 107:4545–4549
- Ihara T, Miyoshi M, Ando M, Sugihara S, Iriyama Y (2001) Preparation of a visible-light-active TiO_2 photocatalyst by RF plasma treatment. *J Mater Sci* 36:4201–4207
- Ihara T, Miyoshi M, Iriyama Y, Matsumoto O, Sugihara S (2003) Visible-light-active titanium oxide photocatalyst realized by an oxygen-deficient structure and by nitrogen doping. *Appl Catal B Environ* 42:403–409
- In S, Orlov A, Garcia F, Tikhov M, Wright DS, Lambert RM (2006) Efficient visible light-active N-doped TiO_2 photocatalysts by a reproducible and controllable synthetic route. *Chem Commun* 40:4236–4238
- Irie H, Watanabe Y, Hashimoto K (2003) Nitrogen-concentration dependence on photocatalytic activity of $\text{TiO}_{2-x}\text{N}_x$ powders. *J Phys Chem B* 107:5483–5486
- Janus M, Inagaki M, Tryba B, Toyoda M, Morawski AW (2006) Carbon-modified TiO_2 photocatalyst by ethanol carbonization. *Appl Catal B Environ* 63:272–276

- Joung S-K, Amemiya T, Murabayashi M, Itoh K (2006) Relation between photo-catalytic activity and preparation conditions for nitrogen-doped visible light-driven TiO₂ photocatalysts. *Appl Catal A Gen* 312:20–26
- Katoh M, Aihara H, Horikawa T, Tomida T (2006) Spectroscopic study for photo-catalytic decomposition of organic compounds on titanium dioxide containing sulfur under visible light irradiation. *J Colloid Interf Sci* 298:805–809
- Khan SUM, Al-Shahry M, Ingler WB Jr (2002) Efficient photochemical water splitting by a chemically modified n-TiO₂. *Science* 297:2243–2244
- Kitano M, Tsujimaru K, Anpo M (2006a) Decomposition of water in the separate evolution of hydrogen and oxygen using visible light-responsive TiO₂ thin film photo-catalysts: effect of the work function of the substrates on the yield of the reaction. *Appl Catal A Gen* 314:179–183
- Kitano M, Funatsu K, Matsuoka M, Ueshima M, Anpo M (2006b) Preparation of nitrogen-substituted TiO₂ thin film photocatalysts by the radio frequency magnetron sputtering deposition method and their photocatalytic reactivity under visible light irradiation. *J Phys Chem B* 110:25266–25272
- Kitano M, Takeuchi M, Matsuoka M, Thomas JM, Anpo M (2007) Photocatalytic water splitting using Pt-loaded visible light-responsive TiO₂ thin film photocatalysts. *Catal Today* 120:133–138
- Kowalczyk SP, McFeely FR, Ley L, Gritsyna VT, Shirley DA (1977) The electronic structure of strontium titanate(IV) and some simple related oxides (magnesium oxide, aluminum oxide, strontium oxide, titanium oxide). *Solid State Commun* 23:161–169
- Kuznetsov VN (2002) Study of oxygen adsorption and reoxidation of reduced titanium dioxide by thermal desorption mass spectrometry. *Kinet Catal* 43:868–873
- Kuznetsov VN, Serpone N (2006) Visible light absorption by various titanium dioxide specimens. *J Phys Chem B* 110:25203–25209
- Kuznetsov VN, Serpone N (2007) Photo-induced coloration and photobleaching of titanium dioxide in TiO₂/polymer compositions on UV- and visible-light excitation into the color centers' absorption bands. Direct experimental evidence negating band gap narrowing in anion-/cation-doped TiO₂. *Chem Phys* 111(42):15277–15288
- Kuznetsov VN, Serpone N (2009) On the Origin of the Spectral Bands in the Visible Absorption Spectra of Visible-Light-Active TiO₂ Specimens. *Analysis and Assignments, J Phys Chem C* 113:15110–15123
- Lawless D (1993) Photophysical studies on materials of interest to heterogeneous photocatalysis and to imaging science: CdS quantum dots, doped and undoped ultrasmall semiconductor TiO₂ particles, and silver halides. Ph.D. Thesis, Concordia University, Montreal, Canada (work carried out between 1988 and 2002)
- Lee DH, Cho YS, Yi WI, Kim TS, Lee JK, Jung HJ (1995) Metalorganic chemical vapor deposition of TiO₂:N anatase thin film on Si substrate. *Appl Phys Lett* 66:815–816
- Lei Y, Zhang LD, Meng GW, Li GH, Zhang XY, Liang CH, Chen W, Wang SX (2001) Preparation and photoluminescence of highly ordered TiO₂ nanowire arrays. *Appl Phys Lett* 78:1125–1127
- Lettmann C, Hildenbrand K, Kisch H, Macyk W, Maier WF (2001) Visible light photodegradation of 4-chlorophenol with a coke-containing titanium dioxide photo-catalyst. *Appl Catal B Environ* 32:215–227
- Li X, Yue P-L, Kotal C (2003) Synthesis and photocatalytic oxidation properties of iron doped titanium dioxide nanosemiconductor particles. *New J Chem* 27:1264–1269
- Li D, Haneda H, Ohashi N, Hishita S, Yoshikawa Y (2004a) Synthesis of nanosized nitrogen-containing MO_x-ZnO (M = W, V, Fe) composite powders by spray pyrolysis and their visible-light-driven photocatalysis in gas-phase acetaldehyde decomposition. *Catal Today* 93–95:895–901
- Li D, Haneda H, Hishita S, Ohashi N (2004b) Visible-light-driven nitrogen-doped TiO₂ photocatalysts: effect of nitrogen precursors on their photocatalysis for decomposition of gas-phase organic pollutants. *Mater Sci Eng B* 117:67–75

- Li D, Haneda H, Labhsetwar NK, Hishita S, Ohashi N (2005a) Visible-light-driven photocatalysis on fluorine-doped TiO₂ powders by the creation of surface oxygen vacancies. *Chem Phys Lett* 401:579–584
- Li D, Haneda H, Hishita S, Ohashi N (2005b) Visible-light-driven N-F-codoped TiO₂ photocatalysts. 2. Optical characterization, photocatalysis, and potential application to air purification. *Chem Mater* 17:2596–2602
- Li D, Ohashi N, Hishita S, Kolodiaznyi T, Haneda H (2005c) Origin of visible-light-driven photocatalysis: A comparative study on N/F-doped and N–F-codoped TiO₂ powders by means of experimental characterizations and theoretical calculations. *J Solid State Chem* 178:3293–3302
- Li FB, Li XZ, Hou MF, Cheah KW, Choy WCH (2005d) Enhanced photocatalytic activity of Ce³⁺-TiO₂ for 2-mercaptobenzothiazole degradation in aqueous suspension for odour control. *Appl Catal A Gen* 285:181–189
- Lin Y-M, Tseng Y-H, Huang J-H, Chao CC, Chen C-C, Wang A (2006) Photocatalytic activity for degradation of nitrogen oxides over visible light responsive titania-based photocatalysts. *Environ Sci Technol* 40:1616–1621
- Lindgren T, Mwabora JM, Avendan E, Jonsson J, Hoel A, Granqvist C-G, Lindquist S-E (2003) Photoelectrochemical and optical properties of nitrogen doped titanium dioxide films prepared by reactive DC magnetron sputtering. *J Phys Chem B* 107:5709–5716
- Livraghi S, Votta A, Paganini MC, Giamello E (2005) The nature of paramagnetic species in nitrogen doped TiO₂ active in visible light photocatalysis. *Chem Commun* 28(4):498–500
- Livraghi S, Paganini MC, Giamello E, Selloni A, Di Valentin C, Pacchioni G (2006) Origin of photoactivity of nitrogen-doped titanium dioxide under visible light. *J Am Chem Soc* 128:15666–15671
- Ma T, Akiyama M, Abe E, Imai I (2005) High-efficiency dye-sensitized solar cell based on a nitrogen-doped nanostructured titania electrode. *Nano Lett* 5:2543–2547
- Matsumoto T, Iyi N, Kaneko Y, Kitamura K, Ishihara S, Takasu Y, Murakami Y (2007) High visible-light photocatalytic activity of nitrogen-doped titania prepared from layered titania/isostearate nanocomposite. *Catal Today* 120:226–232
- Matsuoka M, Kitano M, Takeuchi M, Anpo M, Thomas JM (2005) Photocatalytic water splitting on visible light-responsive TiO₂ thin films prepared by a RF magnetron sputtering deposition method. *Top Catal* 35:305–310
- Matsushima S, Takehara K, Yamane H, Yamada K, Nakamura H, Arai M, Kobayashi K (2007) First-principles energy band calculation for undoped and S-doped TiO₂ with anatase structure. *J Phys Chem Solids* 68:206–210
- Mo SD, Ching WY (1995) Electronic and optical properties of three phases of titanium dioxide: rutile, anatase, and brookite. *Phys Rev B Condens Matter* 51:13023–13032
- Morikawa T, Asahi R, Ohwaki T, Aoki A, Taga Y (2001) Band-gap narrowing of titanium dioxide by nitrogen doping. *Jpn J Appl Phys* 2(40):L561–L563
- Mori-Sanchez P, Recio JM, Silvi B, Sousa C, Martin Pendas A, Luana V, Illas F (2002) Rigorous characterization of oxygen vacancies in ionic oxides. *Phys Rev B Condens Matter* 66:075103
- Mrowetz M, Balcerski W, Colussi AJ, Hoffmann MR (2004) Oxidative power of nitrogen-doped TiO₂ photocatalysts under visible illumination. *J Phys Chem B* 108:17269–17273
- Nakamura I, Negishi N, Kutsuna S, Ihara T, Sugihara S, Takeuchi K (2000) Role of oxygen vacancy in the plasma-treated TiO₂ photocatalyst with visible light activity for NO removal. *J Mol Catal A Chem* 161:205–212
- Nakamura R, Tanaka T, Nakato Y (2004) Mechanism for visible light responses in anodic photocurrents at N-doped TiO₂ film electrodes. *J Phys Chem B* 108:10617–10620
- Navio JA, Colon G, Litter MI, Bianco GN (1996) Synthesis, characterization and photocatalytic properties of iron-doped titania semiconductors prepared from TiO₂ and iron(III) acetylacetonate. *J Mol Catal A Chem* 106:267–276
- Nie X, Sohlberg K (2004) The influence of surface reconstruction and C-impurities on photocatalytic water dissociation by TiO₂. *Mater Res Soc Symp Proc* 801:205–210

- Noda H, Oikawa K, Ogata T, Matsuki K, Kamata H (1986) Preparation of titanium(IV) oxides and its characterization. *Chem Soc Jpn* 8:1084–1090
- Ohno T, Mitsui T, Matsumura M (2003) Photocatalytic activity of S-doped TiO₂ photocatalyst under visible light. *Chem Lett* 32:364–365
- Ohno T, Akiyoshi M, Umabayashi T, Asai K, Mitsui T, Matsumura M (2004) Preparation of S-doped TiO₂ photocatalysts and their photocatalytic activities under visible light. *Appl Catal A Gen* 265:115–121
- Ohno T, Miyamoto Z, Nishijima K, Kanemitsu H, Xueyuan F (2006) Sensitization of photocatalytic activity of S- or N-doped TiO₂ particles by adsorbing Fe³⁺ cations. *Appl Catal A Gen* 302:62–68
- Pascual J, Camassel J, Mathieu H (1978) Fine structure in the intrinsic absorption edge of titanium dioxide. *Phys Rev B Condens Matter* 18:5606–5614
- Redhead PA (1962) Thermal desorption of gases. *Vacuum* 12:203–211
- Ren W, Ai Z, Jia F, Zhang L, Fan X, Zou Z (2007) Low temperature preparation and visible light photocatalytic activity of mesoporous carbon-doped crystalline TiO₂. *Appl Catal B Environ* 69:138–144
- Rodriguez JA, Liu G, Jirsak T, Hrbek J, Chang Z, Dvorak J, Maiti A (2002) Activation of gold on titania: adsorption and reaction of SO₂ on Au/TiO₂(110). *J Am Chem Soc* 124:5242–5250
- Saha NC, Tompkins HG (1992) Titanium nitride oxidation chemistry: an X-ray photo-electron spectroscopy study. *J Appl Phys* 72:3072–3079
- Sakthivel S, Kisch H (2003a) Daylight photocatalysis by carbon-modified titanium dioxide. *Angew Chem Int Ed* 42:4908–4911
- Sakthivel S, Kisch H (2003b) Photocatalytic and photoelectrochemical properties of nitrogen-doped titanium dioxide. *Chemphyschem* 4:487–490
- Sakthivel S, Janczarek M, Kisch H (2004) Visible light activity and photoelectrochemical properties of nitrogen-doped TiO₂. *J Phys Chem B* 108:19384–19387
- Sanjines R, Tang H, Berger H, Gozzo F, Margaritondo G, Levy F (1994) Electronic structure of anatase TiO₂ oxide. *J Appl Phys* 75:2945–2951
- Saraf LV, Patil SI, Ogale SB, Sainkar SR, Kshirsager ST (1998) Synthesis of nanophase TiO₂ by ion beam sputtering and cold condensation technique. *Int J Mod Phys B* 12:2635–2647
- Sathish M, Viswanathan B, Viswanath RP, Gopinath ChS (2005) Synthesis, characterization, electronic structure, and photocatalytic activity of nitrogen-doped TiO₂ nanocatalyst. *Chem Mater* 17:6349–6353
- Sato S (1986) Photocatalytic activity of nitrogen oxide (NO_x)-doped titanium dioxide in the visible light region. *Chem Phys Lett* 123:126–128
- Sato S, Nakamura R, Abe S (2005) Visible-light sensitization of TiO₂ photocatalysts by wet-method N doping. *Appl Catal A Gen* 284:131–137
- Sekiya T, Ichimura K, Igarashi M, Kurita S (2000) Absorption spectra of anatase TiO₂ single crystals heat-treated under oxygen atmosphere. *J Phys Chem Solids* 61:1237–1242
- Sekiya T, Yagisawa T, Kamura N, Mulmi DD, Kurita S, Murakami Y, Kodaira T (2004) Defects in anatase TiO₂ single crystal controlled by heat treatments. *J Phys Soc Jpn* 73:703–710
- Serpone N (2006) Is the band gap of pristine TiO₂ narrowed by anion- and cation-doping of titanium dioxide in second-generation photocatalysts? *J Phys Chem B* 110:24287–24293
- Sonawane RS, Dongare MK (2006) Sol-gel synthesis of Au/TiO₂ thin films for photo-catalytic degradation of phenol in sunlight. *J Mol Catal A Chem* 243:68–76
- Soria J, Conesa JC, Augugliaro V, Palmisano L, Schiavello M, Sclafani A (1991) Dinitrogen photoreduction of ammonia over titanium dioxide powders doped with ferric ions. *J Phys Chem* 95:274–282
- Sun Y, Egawa T, Shao C, Zhang L, Yao X (2004a) EPR line broadening of F center in high-surface-area anatase titania nanoparticles prepared by MOCVD. *J Cryst Growth* 268:118–122
- Sun Y, Egawa T, Shao C, Zhang L, Yao X (2004b) Quantitative study of F center in high-surface-area anatase titania nanoparticles prepared by MOCVD. *J Phys Chem Solids* 75:1793–1797

- Suriye K, Praserthdam P, Jongsomjit B (2006) Control of Ti^{3+} surface defect on TiO_2 nanocrystal using various calcination atmospheres as the first step for surface defect creation and its application in photocatalysis. *Appl Surf Sci* 253:3849–3855
- Tachikawa T, Tojo S, Kawai K, Endo M, Fujitsuka M, Ohno T, Nishijima K, Miyamoto Z, Majima T (2004) Photocatalytic oxidation reactivity of holes in the sulfur- and carbon-doped TiO_2 powders studied by time-resolved diffuse reflectance spectroscopy. *J Phys Chem B* 108:19299–19306
- Tachikawa T, Fujitsuka M, Majima T (2007) Mechanistic insight into the TiO_2 photocatalytic reactions: design of new photocatalysts. *J Phys Chem B* 111(14):5259–5275
- Takeuchi M, Yamashita H, Matsuoka M, Anpo M, Hirao T, Itoh N, Iwamoto N (2000) Photocatalytic decomposition of NO under visible light irradiation on the Cr-ion-implanted TiO_2 thin film photocatalyst. *Catal Lett* 67:135–137
- Tang H, Levy F, Berger H, Schmid PE (1995) Urbach tail of anatase TiO_2 . *Phys Rev B* 52:7771–7774
- Teoh WY, Amal R, Madler L, Pratsinis SE (2007) Flame sprayed visible light-active Fe- TiO_2 for photomineralisation of oxalic acid. *Catal Today* 120:203–213
- Thompson TL, Yates JT Jr (2005) TiO_2 -based photocatalysis: surface defects, oxygen and charge transfer. *Top Catal* 35:197–210
- Tian F-H, Liu C-B (2006) DFT description on electronic structure and optical absorption properties of anionic S-doped anatase TiO_2 . *J Phys Chem B* 110:17866–17871
- Umabayashi T, Yamaki T, Itoh H, Asai K (2002) Band gap narrowing of titanium dioxide by sulfur doping. *Appl Phys Lett* 81:454–456
- Umabayashi T, Yamaki T, Yamamoto S, Miyashita A, Tanaka S, Sumita T, Asai K (2003a) Sulfur-doping of rutile-titanium dioxide by ion implantation: Photocurrent spectroscopy and first-principles band calculation studies. *J Appl Phys* 93:5156–5160
- Umabayashi T, Yamaki T, Tanaka S, Asai K (2003b) Visible light-induced degradation of methylene blue on S-doped TiO_2 . *Chem Lett* 32:330–331
- Vitiello RP, Macak JM, Ghicov A, Tsuchiya H, Dick LFP, Schmuki P (2006) N-doping of anodic TiO_2 nanotubes using heat treatment in ammonia. *Electrochem Commun* 8:544–548
- Wang H, Lewis JP (2005) Effects of dopant states on photoactivity in carbon-doped TiO_2 . *J Phys Condens Matter* 17:L209–L213
- Wang H, Lewis JP (2006) Second-generation photocatalytic materials: anion-doped TiO_2 . *J Phys Condens Matter* 18:421–434
- Wang J, Wen F-Y, Zhang Z-H, Zhang X-D, Pan Z-J, Zhang P, Kang P-L, Tong J, Wang L, Xu L (2006) Investigation on degradation of dyestuff wastewater using visible light in the presence of a novel nano TiO_2 catalyst doped with upconversion luminescence agent. *J Photochem Photobiol A:Chem* 180:189–195
- Wang J, Zhu W, Zhang Y, Liu S (2007a) An efficient two-step technique for nitrogen-doped titanium dioxide synthesizing: visible-light-induced photodecomposition of methyl-ene blue. *J Phys Chem C* 111:1010–1014
- Wang J, Zhang Q, Yin S, Sato T, Saito F (2007b) Raman spectroscopic analysis of sulfur-doped TiO_2 by co-grinding with TiS_2 . *J Phys Chem Solids* 68:189–192
- Xu C, Killmeyer R, McMahan L, Gray S, Khan UM (2006) Photocatalytic effect of carbon-modified n- TiO_2 nanoparticles under visible light illumination. *Appl Catal B Environ* 64:312–317
- Yamaki T, Umabayashi T, Sumita T, Yamamoto S, Maekawa M, Kawasuso A, Itoh H (2003) Fluorine-doping in titanium dioxide by ion implantation technique. *Nucl Instrum Methods Phys Res B* 306:254–258
- Yamamoto T, Yamashita F, Tanaka I, Matsubara E, Muramatsu A (2004) Electronic states of sulfur doped TiO_2 by first principles calculations. *Mater Trans* 45:1987–1990
- Yanagisawa Y, Sumimoto T (1994) Oxygen exchange between CO_2 adsorbate and TiO_2 surfaces. *Appl Phys Lett* 64:343–344

- Yang S, Gao L (2004) New method to prepare nitrogen-doped titanium dioxide and its photocatalytic activities irradiated by visible light. *J Am Ceram Soc* 87:1803–1805
- Yang M-C, Yang T-S, Wong M-S (2004) Nitrogen-doped titanium oxide films as visible light photocatalyst by vapor deposition. *Thin Solid Films* 469(470):1–5
- Yang K, Dai Y, Huang B, Han S (2007) Theoretical study of N-doped TiO₂ rutile crystals. *J Phys Chem B* 110:24011–24014
- Yates HM, Nolan MG, Sheel DW, Pemble ME (2006) The role of nitrogen doping on the development of visible light-induced photocatalytic activity in thin TiO₂ films grown on glass by chemical vapour deposition. *J Photochem Photobiol A:Chem* 179:213–223
- Yin S, Yamaki H, Komatsu M, Zhang Q, Wang J, Tang Q, Saito F, Sato T (2003) Preparation of nitrogen-doped titania with high visible light induced photocatalytic activity by mechano-chemical reaction of titania and hexamethylenetetramine". *J Mater Chem* 13:2996–3001
- Yin S, Ihara K, Aita Y, Komatsu M, Sato T (2006) Visible-light induced photo-catalytic activity of TiO_{2-x}A_y (A = N, S) prepared by precipitation route. *J Photochem Photobiol A Chem* 179:105–114
- Yu J, Zhou M, Cheng B, Zhao X (2006) Preparation, characterization and photo-catalytic activity of in situ N, S-codoped TiO₂ powders. *J Mol Catal A Chem* 246:176–184
- Zhou J, Takeuchi M, Zhao XS, Ray AK, Anpo M (2006) Photocatalytic decomposition of formic acid under visible light irradiation over V-ion-implanted TiO₂ thin film photocatalysts prepared on quartz substrate by ionized cluster beam (ICB) deposition method. *Catal Lett* 106:67–70
- Zhu J, Deng Z, Chen F, Zhang J, Chen H, Anpo M, Huang J, Zhang L (2006a) Hydrothermal doping method for preparation of Cr³⁺-TiO₂ photocatalysts with concentration gradient distribution of Cr³⁺. *Appl Catal B Environ* 62:329–335
- Zhu J, Chen F, Zhang J, Chen H, Anpo M (2006b) Fe³⁺-TiO₂ photocatalysts prepared by combining sol-gel method with hydrothermal treatment and their characterization. *J Photochem Photobiol A Chem* 180:196–204

Chapter 4

Preparation of Titanium Oxide-Based Powders and Thin Films of High Photocatalytic Activities Using Solvothermal Methods

Hiroshi Kominami and Bunsho Ohtani

Abstract Application of solvothermal methods to the synthesis of titanium-oxide based powders and thin films having high photocatalytic activities has been reviewed. Thermal treatment of titanium(IV) *n*-butoxide dissolved in alcohol under autogenous pressure (alcoholthermal treatment) yielded nanocrystalline anatase-type titanium(IV) oxide (TiO₂). Thermal treatment of oxobis(2,4-pentanedionato-O,O')titanium in ethylene glycol in the presence of sodium acetate and a small amount of water yielded nanocrystalline brookite-type TiO₂. Anatase TiO₂ products were calcined at various temperatures and then used for photocatalytic mineralization of acetic acid in aqueous solutions under aerated conditions and dehydrogenation of 2-propanol under deaerated conditions. Almost all the anatase-type TiO₂ samples showed the activities more than twice higher than those of representative active photocatalysts, Degussa P-25 and Ishihara ST01 in both reactions. A brookite TiO₂ sample with improved crystallinity and sufficient surface area exhibited the hydrogen evolution rate almost equal to P-25. Solvothermal decomposition of titanium(IV) *tert*-butoxide in toluene in the presence of silica gel (SiO₂) with continuous stirring yielded a TiO₂-SiO₂ composite. Solvothermally-synthesized TiO₂-SiO₂ composite exhibited higher photocatalytic performance in the oxidative removal of nitrogen oxides in air than that of the composite prepared by physical mixing or sol-gel method. Stable TiO₂ sol was prepared from TiO₂ powders synthesized by solvothermal method and transparent TiO₂ thin films were successfully produced by dip-coating from the sol. These films exhibited much higher rate of malachite green decomposition compared with those prepared from a commercially available TiO₂ sol.

H. Kominami (✉)

Department of Applied Chemistry, Faculty of Science and Engineering,
Kinki University, Kowakae, Higashiosaka, Osaka 577-8502, Japan
e-mail: hiro@apch.kiindai.ac.jp

1 Introduction

Semiconductor photocatalysis, chemical reactions occurring in photoirradiated semiconducting materials, have been explored extensively, and a number of the photocatalytic reactions have been applied to practical processes, such as detoxification or mineralization of waste and/or hazardous materials (Hoffmann et al. 1995; Fujishima et al. 1999), as reviewed in other chapters of this volume. In both fundamental and application studies, it is necessary to choose the most adequate semiconductor photocatalyst from a large number of candidates. Since the semiconductor photocatalysts are always solid materials, numerous variations, e.g., particle size and distribution, surface area, crystal and surface structure, etc., can be obtained even if the chemical composition is the same. In fact, one of the most significant and promising photocatalysts, titanium(IV) oxide (TiO_2), can be obtained from many manufacturers or prepared in laboratories in different forms, characteristics, and photocatalytic activities. A major goal of investigation on design and preparation (or selection from commercial products) of semiconductor photocatalysts is to make highly active ones that utilize light energy with high efficiency. However, no solid strategies to realize this goal have yet been established; we have very little empirical information, e.g., anatase TiO_2 tends to show higher activity compared with rutile. Consequently, theoretical considerations on the photocatalytic activity to clarify its correlation with characteristics, i.e., physical property and structure of photocatalysts, are important. In the previous review (Kominami et al. 2002), the design of metal oxide photocatalysts, especially TiO_2 , was discussed based on results of kinetic investigations and photocatalytic activities of TiO_2 powders prepared by one of solvothermal methods, HyCOM (*Hydrothermal Crystallization in Organic Media*) (Kominami et al. 1996b, 1999b). In this chapter, several solvothermal syntheses of TiO_2 -based powders and thin films having high photocatalytic activities will be reviewed.

2 What Is Solvothermal Method?

Solvothermal methods have been reviewed by Inoue (2005). The term “solvothermal” means reactions in liquid or supercritical media at temperatures higher than the boiling point of the medium. Hydrothermal reactions (Byrappa and Yoshimura 2001) are a type of solvothermal reaction in which water (H_2O) is used as the reaction medium. To carry out reactions at temperatures higher than the boiling point of the reaction medium, pressure vessels (autoclave) are usually required. Since autogenous pressure created by the vapor pressure of the solvent has only a minor effect on the reaction rate, there is no need to differentiate the reactions at the temperatures above and below the boiling point. Consequently, Inoue proposed, in his review, that “solvothermal” reaction should be defined more loosely as the reaction in a liquid (or supercritical) medium at high temperatures (Inoue 2005).

3 Design of Photocatalysts of High Activity

Many researchers have claimed that the structural characteristics, e.g., crystal structure (form), particle size, surface area, etc., of photocatalysts determine their photocatalytic activities. However, the relation between the physical properties and the photocatalytic activities is not so simple, and at least two parameters related to the surface reactions and recombination of electrons (e^-) and holes (h^+) must be optimized to obtain highly efficient semiconductor photocatalysts. As a working hypothesis for the preparation of highly active semiconductor photocatalysts, we have proposed that larger surface area and high crystallinity are minimum requisites of photocatalysts (Ohtani and Nishimoto 1993; Kominami et al. 2002). The larger surface area corresponds to higher rate of surface reaction of e^- and h^+ (Kominami et al. 1998), and the high crystallinity, i.e., little crystal defects to slower the rate of e^- - h^+ recombination (Murakami et al. 2007). Of course, other factors no doubt also have appreciable influence on the photocatalytic activity, but we believe that these two parameters are indispensable basic requirements.

In the ordinary processes of metal oxide preparation, metal hydroxide or hydrated metal oxide is precipitated in the first step and then calcined to dehydrate into metal oxide. The as-prepared precipitate is, generally, of large surface and low crystallinity, and the calcination reduces the surface area and improves the crystallinity. Thus, preparation of metal oxide powders having both large surface area and high crystallinity requires precise control of calcination conditions, because the calcination has negative and positive effects on the surface area and the crystallinity, respectively. Therefore, precise control by calcination of these factors of TiO_2 prepared from hydrated TiO_2 's is generally difficult.

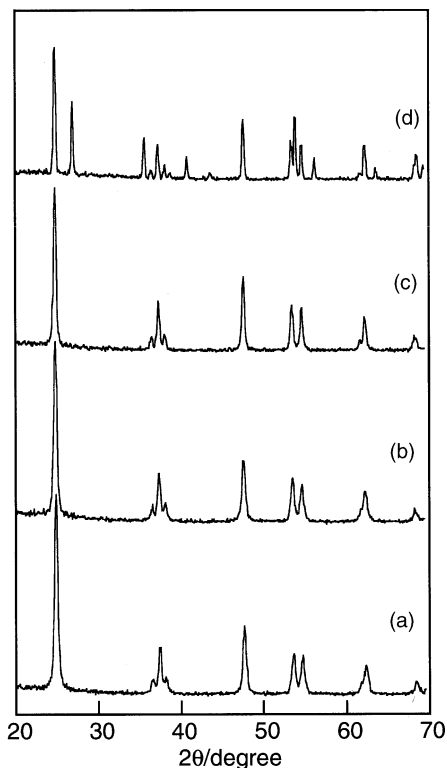
Nanocrystalline TiO_2 synthesized by solvothermal methods possess larger surface area and show higher thermal stability (Inoue et al. 1991; Kominami et al. 1996b, 1997, 1999a, b), i.e., the decrease in surface area on calcination is relatively smaller compared with TiO_2 's prepared by other methods. Since these nanocrystals have negligible amorphous and/or hydrated parts, appreciable dehydration and crystallization occurring in ordinary hydrated TiO_2 's do not take place in these nanocrystals. Therefore, the number of crystal defects of TiO_2 nanocrystal can be reduced by calcination without a large decrease in surface area.

4 Nanocrystalline Anatase-Type TiO_2 Powders

4.1 Characterization of Nanocrystalline Anatase-Type TiO_2 Powders

Typical synthesis procedure is as follows (Kominami et al. 1999a): Titanium(IV) *n*-butoxide (TNB), 10 g, was dissolved in a 70 cm³ portion of 2-butanol in a test tube which was then set in a 200-cm³ autoclave. The autoclave was thoroughly

Fig. 1 XRD patterns of (a) TiO_2 prepared by the alcohothermal treatment of titanium *n*-butoxide in 2-butanol at 573 K, and (b–d) the samples obtained by calcination of (a) at 823, 973 and 1,173 K, respectively



purged with nitrogen, heated to 573 K at a rate of 2.5 K min^{-1} , and kept at that temperature for 2 h. An XRD pattern of the product is depicted in Fig. 1a, which shows that anatase was formed without contamination of any other phases such as rutile or brookite. Addition of water to the supernatant after the autoclaving gave no precipitates, indicating that TNB was completely hydrolyzed during the thermal treatment. Judging from the fact that the treatment of TNB in toluene at the same temperature yielded no product, the source of water for the hydrolysis was that generated from 2-butanol. This sample possessed sufficient surface area of $63 \text{ m}^2 \text{ g}^{-1}$, and the crystallite size of this sample was calculated to be 19 nm from the line-broadening of the 101 diffraction peak of anatase. TEM observation (Fig. 2) revealed that the sample consisted of the agglomerates of primary particles of an average diameter of 20 nm, which was in good agreement with the crystallite size estimated from the XRD pattern. Therefore, each particle observed in TEM should be a single anatase crystal. TG analysis revealed that this sample showed gradual weight loss of 2.42% from 373 to 1,273 K and only a very weak exothermic peak at 560 K was observed in a DTA curve due to combustion of a small amount of remaining organic moieties. Absence of sharp exothermic peak due to crystallization of anatase at around 673–773 K suggests that the product contains a negligible amount of amorphous-like phase, which is well consistent with the results of XRD

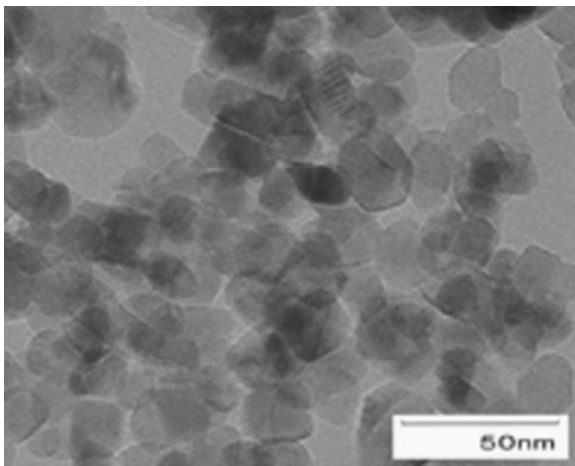


Fig. 2 A TEM photograph of TiO_2 prepared by the alcohothermal treatment of titanium *n*-butoxide in 2-butanol at 573 K

and TEM. When titanium isopropoxide (TIP) was dissolved in a mixed solvent of 7 vol% 2-propanol in toluene, TIP was completely hydrolyzed to give anatase as observed in 100% 2-propanol. The amount of water required for complete hydrolysis of TIP is calculated to be 0.14 mol. Assuming that 2-propanol in toluene is completely dehydrated, the amount of water formed from the mixed solvent is estimated to be 0.064 mol, which is smaller than that necessary for the complete hydrolysis of TIP. Two possibilities might account for this; 2-propanol formed by hydrolysis of TIP was dehydrated to yield water which was then used for the hydrolysis, and/or water generated by dehydration of hydrated TiO_2 was used again to hydrolyze TIP. In both processes water was recycled. The TiO_2 sample prepared by alcohothermal method is hereafter called THyCA (*Transfer Hydrolytic Crystallization in Alcohols*) TiO_2 .

Effect of calcination on physical properties of THyCA- TiO_2 prepared in the TNB-2-butanol system is shown in Fig. 3. Post-calcination at temperatures lower than 973 K reduced the BET surface area slightly. This is consistent with the result that the XRD pattern of the TiO_2 sample calcined at 823 K was almost identical to that before calcination, as shown in Fig. 1b. Even after calcination at 973 K, the THyCA- TiO_2 was composed of small anatase crystallite of 26 nm diameter (Fig. 1c) and still possessed sufficient surface area of $45 \text{ m}^2 \text{ g}^{-1}$. Calcination at 1,173 K induced partial transformation into the rutile, but the sample still predominantly consisted of the anatase crystallite (Fig. 1d). It is known that on a large-surface-area, amorphous TiO_2 samples can be prepared by precipitation and sol-gel method. It is often observed that the surface area of amorphous TiO_2 samples drastically decreased upon calcination at around 700 K due to formation of anatase crystallites and their sintering. The high thermal stability of THyCA- TiO_2 is interpreted by assuming that the as-prepared THyCA- TiO_2 consists of single

Fig. 3 Effect of calcination on surface area and crystallite size of THyCA-TiO₂

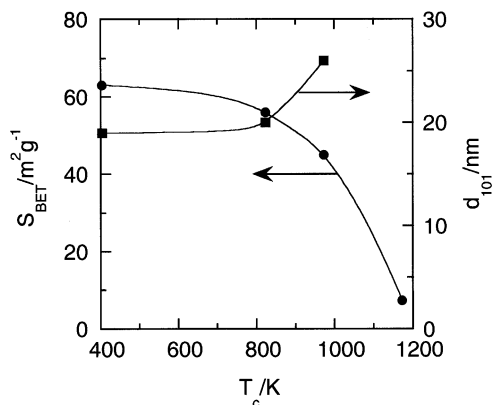
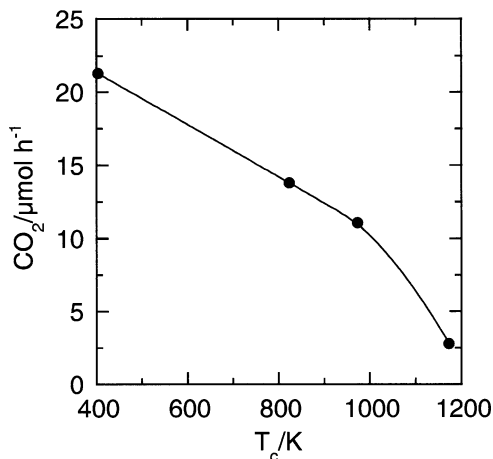


Fig. 4 Effect of calcinations on the CO₂ evolution rate of THyCA-TiO₂ in photocatalytic mineralization of acetic acid

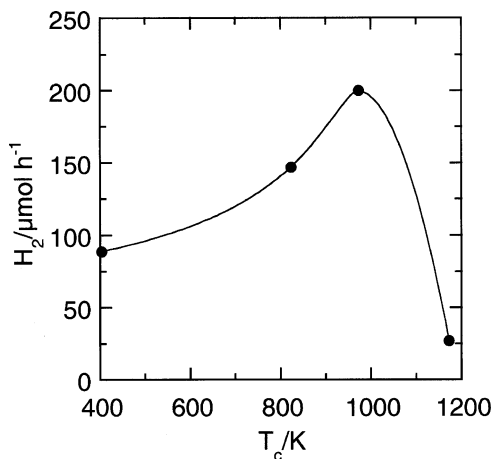


crystals and contains negligible amount of amorphous-like phase to be crystallized into anatase and to induce sintering of crystallites upon calcination.

4.2 Photocatalytic Activities of THyCA-TiO₂

(Figure 4) shows the effect of calcination on carbon dioxide evolution rate of THyCA-TiO₂ in photocatalytic mineralization of acetic acid. Uncalcined THyCA-TiO₂ exhibited the rate of 21.3 $\mu mol h^{-1}$ that was much larger than those of representative commercial TiO₂, Degussa P-25 and Ishihara ST01 (8.5 and 11.6 $\mu mol h^{-1}$, respectively), which have been known to show high photocatalytic activity. Since the THyCA-TiO₂ powders satisfied the basic requirements

Fig. 5 Effect of calcination on the H_2 evolution rate of platinumized THyCA-TiO₂ in photocatalytic dehydrogenation of 2-propanol in aqueous suspension



for active TiO₂ photocatalyst, i.e., both having large surface area and sufficient crystallinity, the present results can be reasonably accepted. An amorphous hydrated TiO₂ of quite a large surface area prepared by hydrolysis under atmospheric conditions showed negligible activity ($<1 \mu\text{mol h}^{-1}$), due to large recombination probability of $e^- - h^+$ at a large number of surface defects. Calcination of THyCA-TiO₂ powders decreased their photocatalytic activities, suggesting that surface area, i.e., adsorptivity toward acetic acid, is a decisive factor in this reaction system.

Effect of calcination on hydrogen (H_2) evolution rate of platinumized THyCA-TiO₂ in photocatalytic dehydrogenation of 2-propanol in aqueous suspension is shown in (Fig. 5). It should be noted that temperature dependency of the rate was different from that of mineralization of acetic acid. The rate increased with temperature until 973 K and sample obtained by calcination at that temperature exhibited a rate of $200 \mu\text{mol h}^{-1}$, which was much higher than that of P-25 ($100 \mu\text{mol h}^{-1}$) as well as the mineralization system. Calcination decreased the surface area of THyCA-TiO₂ samples but improved the crystallinity. This dependency suggests that surface area and crystallinity, which control adsorptivity and $e^- - h^+$ recombination probability, respectively, are both important in hydrogen evolution system.

5 Nanocrystalline Brookite-Type TiO₂ Powders

5.1 Characterization of Brookite-Type TiO₂ Powders

Typical synthesis procedure is as follows (Kominami et al. 2000): Oxobis (2,4-pentanedionato-O,O')titanium and sodium acetate were added to ethylene glycol in a test tube, which was then set in an autoclave. In the gap between the

test tube and the autoclave wall, a small amount of water was added. The autoclave was purged with nitrogen, heated at 573 K at a rate of 2.5 K min⁻¹, and held at that temperature for 2 h. XRD pattern of the product is shown in (Fig. 6a). All the XRD peaks of the product were assigned to brookite. The crystallite size of this brookite sample was calculated to be 16 nm from the 121 diffraction peak using Scherrer equation. Due to the nanocrystalline property, this brookite sample had a large surface area of 78 m² g⁻¹. Raman spectroscopy and TEM observation revealed that the product consisted of agglomerates of brookite nanocrystals without contamination of other phases, anatase and rutile. In the TG curve of the product, weight loss was observed at the range from 473 to 773 K and total weight loss up to 1,273 K was 6%. An exothermic peak was observed at 562 K in the DTA curve, which is attributed to combustion of organic moieties on the product. However, no DTA peak was observed in the high temperature region.

The brookite product was calcined at various temperatures and XRD patterns after calcination are shown in (Fig. 6b–f). A very weak peak due to the rutile phase was observed after calcination at 823 K. Peaks of brookite became sharper after calcination at 973 K and formation of rutile TiO₂ was remarkable on calcination at 1,173 K. The anatase form was not observed in XRD pattern of any calcined samples,

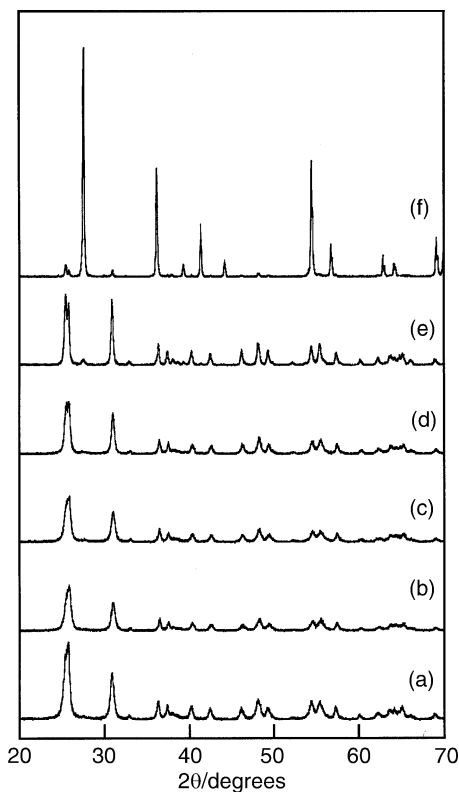


Fig. 6 XRD patterns of (a) TiO₂ prepared by the solvothermal treatment of TiO (acac)₂ in EG-H₂O in the presence of sodium acetate at 573 K, and (b–f) the samples obtained by calcination of (a) at 623, 823, 973, 1,073 and 1,173 K, respectively

indicating that brookite directly transformed to the rutile phase. These results of XRD were consistent with those of Raman spectroscopy. Calcination temperature-dependency of physical properties of the product is shown in (Fig. 7). Surface area of the sample gradually decreased with the elevation in calcination temperature while crystallite size increased, indicating that crystal growth of brookite occurred along with calcination and crystallinity of brookite sample was increased.

5.2 Photocatalytic Activities of Brookite-Type TiO_2

These brookite samples of various physical properties were platinumized and then used for photocatalytic dehydrogenation of 2-propanol in aqueous suspensions (Kominami et al. 2003). Effect of calcination on the H_2 evolution rate is shown in (Fig. 8). The rate increased with temperature until 873 K and the sample obtained

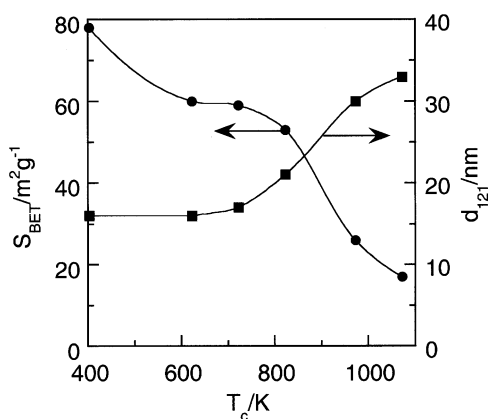


Fig. 7 Effect of calcination on surface area and crystallite size of brookite-type TiO_2

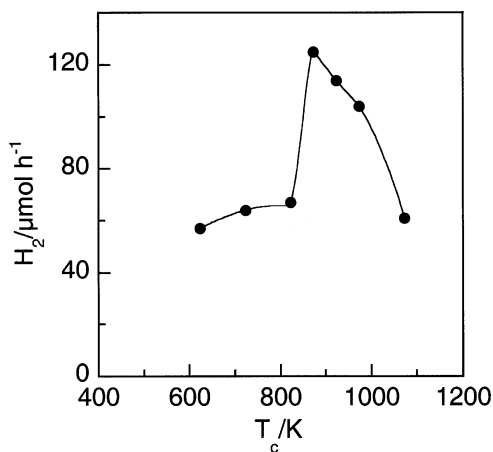


Fig. 8 Effect of calcination on the H_2 evolution rate of platinumized brookite- TiO_2 in photocatalytic dehydrogenation of 2-propanol in aqueous suspension

by calcination at that temperature exhibited a rate of $125 \mu\text{mol h}^{-1}$, which was larger than that of P-25 ($100 \mu\text{mol h}^{-1}$). It should be noted that brookite-type TiO_2 exhibited high photocatalytic activity if it possesses adequate physical properties. Severer calcination decreased the rate as was observed in THyCA- TiO_2 (Fig. 5). This same dependency suggests that balance of surface area and crystallinity, which control adsorptivity and e^- - h^+ recombination probability, respectively, is important in H_2 evolution system independent of the crystal structure of TiO_2 .

6 TiO_2 -Silica Gel (SiO_2) Composites

6.1 Synthesis of Nanocrystalline TiO_2 Powders by Thermal Decomposition (TD) Method

Since most readers are unfamiliar with the TD method (Kominami et al. 1997), the formation of nanocrystalline TiO_2 by this method is briefly described. Anatase-type TiO_2 was formed by the TD method at 573 K without contamination of any other phases such as rutile or brookite when titanium(IV) *tert*-butoxide (TTB) and toluene were used as the titanium source and synthesis medium, respectively. Formation of TiO_2 by the TD method involves two processes: decomposition of TTB in toluene yielding a TiO_2 precursor and crystallization of anatase-type TiO_2 from the precursor. Other inert organic solvents such as benzene, xylenes and cyclohexane can also be used. Some physical properties of the TiO_2 sample obtained in toluene at 573 K are summarized in Table 1. The crystallite size (d_{101}) of the sample was calculated to be 9 nm by the line-broadening technique. Corresponding to small particle size, this TiO_2 sample had a sufficient surface area of $149 \text{ m}^2 \text{ g}^{-1}$.

Table 1 Some physical properties of TiO_2 and TiO_2 - SiO_2 powders and their photocatalytic activities for oxidative removal of nitrogen oxides

Photo-catalyst	TiO_2 content/%		Method	Phase ^a	d_{101} ^{b/} nm	S_{BET} / $\text{m}^2 \text{ g}^{-1}$	NOx removal ^c /%	NO ₂ release ^c /%
	Charged	Observed						
TiO_2	100	100	TD	A	9	149	87	4.1
TiO_2 - SiO_2	75	74	TD	A	9	187	98	0.3
TiO_2 - SiO_2	50	52	TD	A	9	212	96	1.7
TiO_2 - SiO_2	25	13	TD	A	–	215	60	7.3
TiO_2 - SiO_2	74	ND	Sol-gel	A	–	88	57	2.9
TiO_2 - SiO_2	74	–	Mixture	A	9	ND	77	6.4
P-25 ^d	100	–	–	A,R	24	50 ^e	52	4.0

^aBy X-ray, A anatase; R rutile

^bCrystallite size calculated from the 101 diffraction of anatase

^cTotal removal and release for 3 h

^dP-25; Degussa

^eData reported by the supplier

6.2 Characterization of TiO_2 - SiO_2 Composites Prepared by TD Method

Solvothermal decomposition of TTB in toluene at 573 K, in the presence of SiO_2 (CARiACT Q-30, Fuji Silycia Chemical), with continuous stirring yielded a TiO_2 - SiO_2 composite (Kominami et al. 2008). Various TiO_2 - SiO_2 composites were prepared by changing the ratio of TTB and SiO_2 particles. Contents of TiO_2 in the composites determined by chemical analysis are summarized in Table 1. In all composites, the observed TiO_2 contents were almost the same as the charged contents except the 13 wt%-composite, indicating that TTB was almost completely decomposed in toluene at 573 K, yielding TiO_2 - SiO_2 composites. Figure 9 shows XRD patterns of TiO_2 - SiO_2 composites having various TiO_2 contents. Diffraction peaks attributed to the anatase phase are clearly observed for all composites, although the 13 wt%-composite exhibited weak peaks due to the small content of TiO_2 , and no peaks assignable to rutile or brookite were observed. Some physical properties of the TiO_2 - SiO_2 composites are summarized in Table 1. The TiO_2 - SiO_2 composites exhibited the same d_{101} (9 nm) as that of the 100 wt% TiO_2 sample. This result indicates that crystallization and crystal growth of anatase-phase TiO_2 in toluene were not affected by SiO_2 particles.

Figure 10 shows SEM photograph of 74 wt% TiO_2 - SiO_2 composite. For comparison, a photograph of bare SiO_2 is also shown. Agglomerates of fine

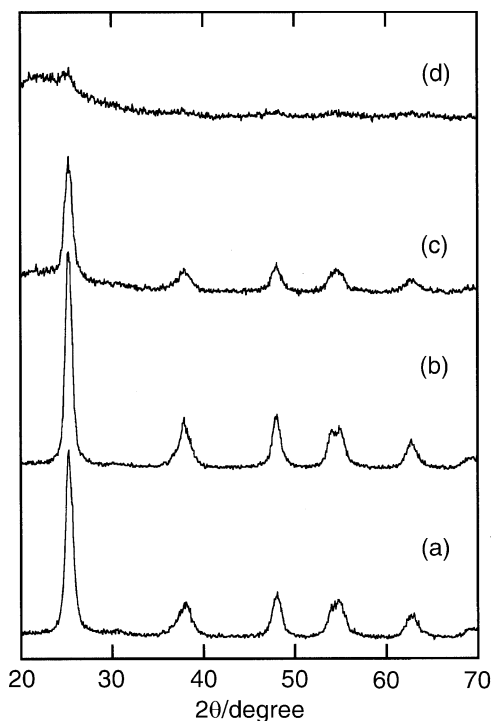


Fig. 9 XRD patterns of (a) TiO_2 and TiO_2 - SiO_2 composites with TiO_2 contents of (b) 74 wt%, (c) 52 wt% and (d) 13 wt%

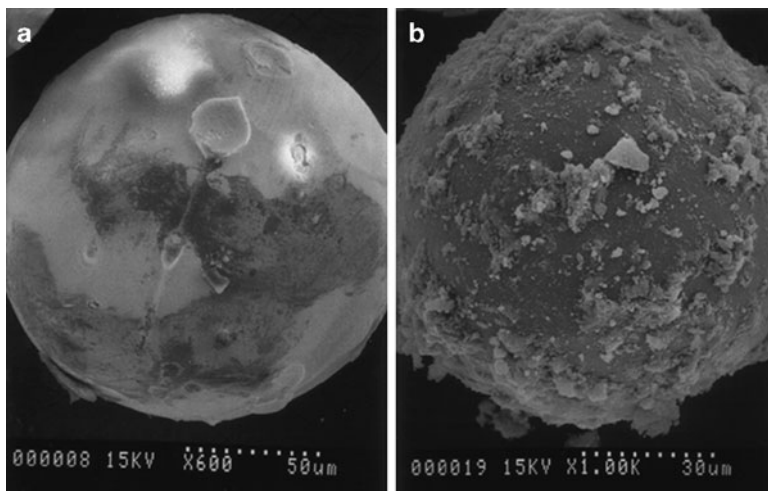


Fig. 10 SEM photographs of (a) SiO_2 and (b) 74 wt% TiO_2 - SiO_2 composites

particles were observed on the surfaces of SiO_2 particles in the composite. TEM observation of fine particles recovered from the composite revealed that the fine particles were nanocrystalline TiO_2 with an average size of 9 nm, which is in good agreement with the crystallite size of anatase-phase TiO_2 determined by XRD. These results indicate that the fine particles observed by TEM are single crystals of TiO_2 and that TiO_2 nano-crystals can be formed on SiO_2 particles by using the TD method. Figure 11 shows results of electron probe microanalysis (EPMA) of two different fields of vision of the 74 wt% TiO_2 - SiO_2 composite. Semi-quantitative analysis revealed that TiO_2 contents in fields A and B were 83 and 95%, respectively, indicating heterogeneous distribution and variation in thickness of nanocrystalline TiO_2 deposited on the SiO_2 surface.

Specific surface areas (S_{BET}) of TiO_2 - SiO_2 composites are also summarized in Table 1. An effect of combination with SiO_2 was clearly observed: the 74 wt% TiO_2 - SiO_2 composite had S_{BET} ($187 \text{ m}^2 \text{ g}^{-1}$) larger than that of 100% TiO_2 ($S_{\text{BET}} = 149 \text{ m}^2 \text{ g}^{-1}$), and S_{BET} increased with increase in SiO_2 content (decrease in TiO_2 content), indicating that pores of SiO_2 particles are open to the outside. Therefore, excellent adsorption ability of SiO_2 is expected for these TiO_2 - SiO_2 composites.

6.3 Photocatalytic Nitrogen Oxides (NO_x) Removal over TiO_2 - SiO_2 Composites

Photocatalytic activity of the TiO_2 - SiO_2 composite (100 mg) was evaluated using photocatalytic oxidative removal of NO_x (10 ppm) under UV light ($>300 \text{ nm}$) irradiation of a black light (10W) (Kominami et al. 2008). The reaction was carried

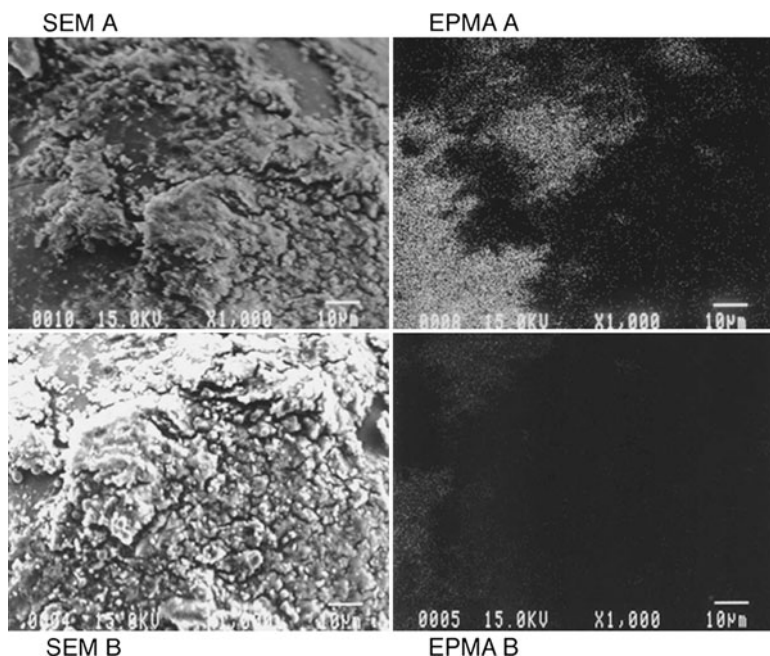
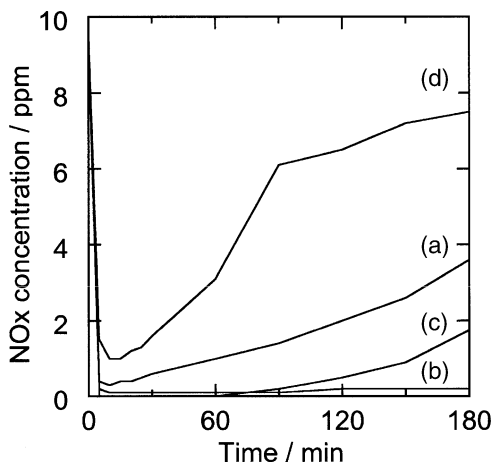


Fig. 11 SEM photographs (*left*) and electron probe microanalysis (EPMA, *right*) of two different fields of vision of the 74 wt% TiO₂-SiO₂ composite. *Dark*: TiO₂, *White*: SiO₂

out in a fixed-bed continuous flow ($110 \text{ cm}^3 \text{ min}^{-1}$) reactor at atmospheric pressure. Photocatalytic oxidative NO_x removal consists of two main processes: oxidation of nitrogen monoxide (NO) to nitrogen dioxide (NO₂) and subsequent oxidation of NO₂ to nitrate (NO₃⁻) (Ibusuki and Takeuchi 1994; Ao and Lee 2003; Komazaki et al. 1999; Nakamura et al. 2000). Totally, NO was fixed as NO₃⁻ on the surface of the photocatalyst. Since accumulation of NO₃⁻ gradually decreases subsequent adsorption of NO_x in the gas phase, higher holding capacity for NO₃⁻ and/or NO_x is required for photocatalytic material. The intermediate compound, NO₂, is more toxic than original NO. Therefore, NO₂ release to gas phase should be suppressed, i.e., low NO₂ release in addition to high NO_x removal is required for photocatalytic materials in a NO_x removal system. Figure 12 shows the time course of NO_x concentration in gas coming out of the reactor. Results for four kinds of photocatalytic materials with different TiO₂ contents prepared by the TD method are shown in the figure. Just after photoirradiation, NO_x concentration in the outlet gas decreased to almost 0 ppm for all samples, indicating that NO_x was photocatalytically removed. However, NO_x concentration in the outlet gas gradually increased with continuing introduction of NO_x gas, depending on the properties of samples. This decrease is caused by accumulation of NO₃⁻ in the composites and the resulting decrease in adsorption of NO and NO₂. TD-TiO₂ without SiO₂ (100 wt% TiO₂) exhibited total NO_x removal of 87%, which is much higher than the NO_x removal of representative Degussa P-25 TiO₂ (52%). This comparison

Fig. 12 Time course of NO_x concentration in the gas coming out of the reactor containing (a) TiO₂ and TiO₂-SiO₂ composites with TiO₂ contents of (b) 74 wt% TiO₂, (c) 52 wt% TiO₂ and (d) 13 wt% TiO₂



clearly shows the superior photocatalytic activity of the TD-TiO₂ sample. In this case, the higher removal of TD-TiO₂ is mainly attributed to its larger S_{BET} (149 m² g⁻¹) than that of P-25 (50 m² g⁻¹). However, relatively high NO₂ release (ca. 4%) was observed in both TiO₂ samples as shown in Table 1, suggesting that higher adsorption ability (and/or capacity) to NO₂ is indispensable in photocatalytic materials to suppress desorption of intermediate compound NO₂ to the gas phase. As expected, a high level of NO_x removal (98%) and very small NO₂ release (0.3%) were achieved in the 74 wt% TiO₂-SiO₂ composite, indicating that SiO₂ plays an important role in photocatalytic NO_x removal. Positive effects of adsorbents such as activated carbon (Ibusuki and Takeuchi 1994; Ao and Lee 2003) and hydroxyapatite (Komazaki et al. 1999) on photocatalytic NO_x removal has been reported. As an adsorbent of NO₂, SiO₂ suppressed NO₂ release to the gas phase and improved efficiency in photocatalytic oxidation of NO₂ to NO₃⁻. Since SiO₂ possesses excellent ability for adsorption of water (H₂O), another role of SiO₂ as a reservoir of H₂O may explain the synergy effect of SiO₂ in the TiO₂-SiO₂ composite. According to (1), two-thirds of NO₂ is converted to HNO₃ in the presence of H₂O.



Therefore, NO_x removal may be improved by this non-catalytic process in the presence of a large amount of H₂O adsorbed in SiO₂. In this process, HNO₃ should be formed in pores of SiO₂, which may delay saturation of the adsorption of NO_x and HNO₃ on the TiO₂ surface. The 52 wt% TiO₂-SiO₂ composite exhibited almost the same performance as that of the 74 wt% TiO₂-SiO₂ composite. A further decrease in the TiO₂ content to 13 wt% resulted in a decrease in NO_x removal as well as a large increase in NO₂ release, probably because of the small oxidation rate of NO₂ to NO₃⁻ due to a small amount of TiO₂. There are many parameters

controlling the NO_x removal in this reaction condition, i.e., photocatalytic activity of TiO₂ itself, amount of TiO₂, surface area of TiO₂, adsorption ability (and/or capacity) to NO, NO₂ and NO₃⁻ responding to Langmuirian adsorption parameters, and mixing level of TiO₂ and SiO₂. Therefore, these parameters were most highly balanced in the 74 wt% TiO₂-SiO₂ composite. The 74 wt% TiO₂-SiO₂ composite used for 3 h-reaction was washed with H₂O and then re-used for reaction under the same condition. Almost the same results (96 and 98% NO_x removal) were obtained after the second and third reactions, respectively, indicating that HNO₃ fixed on these TiO₂-SiO₂ composites is almost removed by H₂O washing and the composites can be repeatedly used for the photocatalytic reaction of NO_x removal.

6.4 Comparison with TiO₂-SiO₂ Composites Prepared by Different Methods

Two TiO₂-SiO₂ composites having the same TiO₂ content (74 wt%) were prepared by other methods and their photocatalytic performances were compared with that of the composite (TiO₂-SiO₂(TD)) prepared by the TD method. The first composite (TiO₂-SiO₂(SG)) was prepared by the sol-gel method (TiO₂ sol deposition on the surfaces of SiO₂ particles using TNB and Q-30 SiO₂) and subsequent activation of TiO₂. For preparation of TiO₂-SiO₂(SG), the procedure reported by Xu et al. (1999) was slightly modified for the present purpose. The second composite (TiO₂-SiO₂(PM)) was prepared by physical mixing of TD-TiO₂ and Q-30 SiO₂ in an aqueous suspension and subsequent fixation on a glass filter. Physical properties and results of NO_x removal of these two TiO₂-SiO₂ composites are summarized in Table 1. The first composite, TiO₂-SiO₂(SG), had a relatively small surface area of 88 m² g⁻¹, indicating that pore-mouth plugging by deposited TiO₂ species partially occurred in this composite. TiO₂-SiO₂(SG) exhibited lesser NO_x removal (57%) and relatively high NO₂ release (2.9%). The low performance of TiO₂-SiO₂(SG) is probably due to both low activity of TiO₂ deposited on SiO₂ and the small surface area. The second composite, TiO₂-SiO₂(PM), also exhibited low NO_x removal (77%) and high NO₂ release (6.4%), although the sample consisted of highly active TD-TiO₂ and porous SiO₂. Physical properties and photocatalytic activity of TiO₂ in TiO₂-SiO₂(PM) should be the same as those of TiO₂ in TiO₂-SiO₂(TD). The NO_x removal of TiO₂-SiO₂(PM) was inferior to that of 100% TD-TiO₂ (87%), although NO_x removal per weight of TiO₂ was slightly higher than that of 100% TD-TiO₂ roughly estimated from the TiO₂ content (77% vs. 64% = 87 × 0.74). It is clear that the mixing level of TiO₂ and SiO₂ in TiO₂-SiO₂(PM) is lower than that of TiO₂-SiO₂(TD) and that SiO₂ in TiO₂-SiO₂(PM) was not effectively utilized as an adsorbent. These results indicate that direct formation of highly active TiO₂ onto the surface of SiO₂ adsorbent is important to effectively utilize both the high photocatalytic activity of TiO₂ and the excellent adsorption ability of SiO₂.

7 TiO₂ Thin Films

7.1 Preparation of TiO₂ Thin Films by Immobilization of Highly Active TiO₂ Particles

As discussed in the previous section and the previous papers (Kominami et al. 1997; Kominami et al. 2002), the property of TiO₂ suitable for each reaction system depends on the type of reaction. Thus, design and control of the TiO₂ properties appropriate to the desired photocatalytic reaction system is required. A promising alternative strategy for producing highly active photocatalytic coatings is the attachment of stable TiO₂ particles of high photocatalytic activity onto a substrate without reduction of activity. If the size of the particles is small enough, transparent photocatalytic films are, in principle, available. HyCOM-TiO₂, which has been proved to exhibit ultra-high photocatalytic activity in several reaction systems (Kominami et al. 1995, 1996a; Ohtani et al. 1995), is one of the most suitable candidates for the starting material of TiO₂ thin films. HyCOM-TiO₂ powders were dispersed in aqueous solution of nitric acid to yield a TiO₂ sol stable for more than 90 days, and transparent TiO₂ thin films were successfully produced by dip-coating from the TiO₂ sol (Kominami et al. 2001).

Figure 13 shows absorption spectra of HyCOM-TiO₂ films with different thickness as well as the glass substrate. Clearly the TiO₂ coating absorbed light of the ultraviolet region and the absorption increased with the thickness (Table 2), while negligible absorption was seen in the visible region. Thus, the method enables us to immobilize the HyCOM-TiO₂ particles without losing transparency in the visible region.

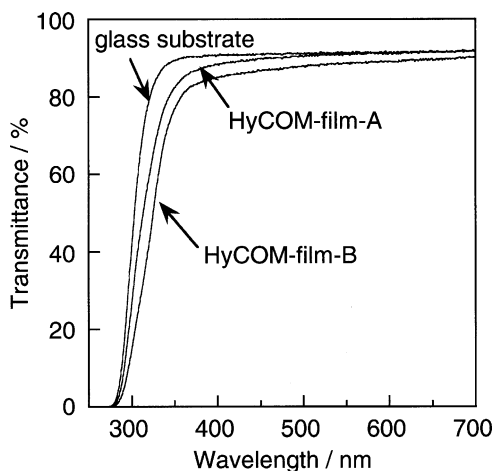


Fig. 13 Transmission spectra of TiO₂ thin films of different thickness (50 nm for HyCOM-film-A and 110 nm for HyCOM-film-B)

Table 2 Rate of photocatalytic decomposition of malachite green by TiO₂ thin films immersed in its aqueous solution (2.5×10^{-4} mol dm⁻³)

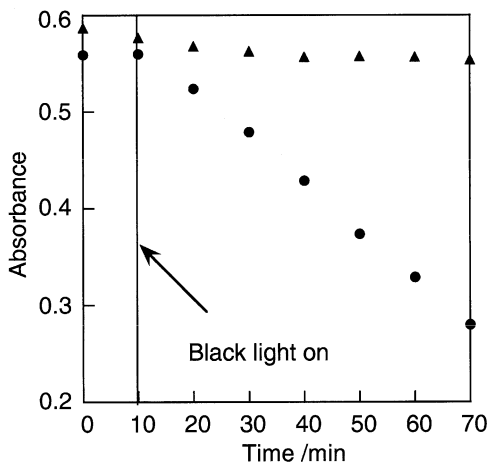
Film	Thickness/nm	% Absorption at 320 nm	Rate/% h ⁻¹
HyCOM-film-A	50	20	52
HyCOM-film-B	110	38	73
STS-film-A ^a	40	25	41
STS-film-B ^a	100	52	52

^aFilms prepared from Ishihara STS-01 TiO₂ sol

7.2 Photocatalytic Activity of TiO₂ Thin Films

Figure 14 shows the time course of the absorbance of a dye, malachite green (MG) solution, in the presence and absence of HyCOM-film-A. Practically no decrease in absorbance by immersing HyCOM-film-A or by keeping in the dark for 10 min indicates that adsorption of MG onto the film and thermal catalytic decomposition of MG can be neglected. In the absence of TiO₂ film, the UV irradiation reduced the absorbance negligibly, showing little direct photolysis of MG. On the other hand, the absorbance, i.e., the MG concentration, was reduced in the presence of HyCOM-film-A along with irradiation time. These results clearly show that MG was photocatalytically decomposed by TiO₂ under UV irradiation, though at present we have no mechanistic details at the molecular level. Photocatalytic oxidation of MG with participation of molecular oxygen (O₂) is most probable. The rate of MG decomposition by several TiO₂ films immersed in its aqueous solution is summarized in Table 2. For each TiO₂ film, HyCOM and STS, the rate increased with the film thickness, but not linearly; the rate of each thicker film (film-B) was less than that expected from the rate of each thinner film (film-A). This could not be attributed to nonlinear photoabsorption property, since the photoabsorption of the film, estimated by subtraction of the substrate part from the transmission spectrum shown in Fig. 13, was almost proportional to the thickness for each TiO₂ (Table 2). Therefore, one of the reasons for nonlinearity is that only the outer part of the TiO₂ was exposed to the MG solution, i.e., penetration depth of the solution into the film is limited. Along with the thickness of TiO₂ film, the total number of absorbed photons, which produce e⁻-h⁺, should increase, but the number of adsorbed MG molecules cannot be increased proportionally to result in nonlinearity of the photocatalytic reaction rate. Based on these considerations, we can compare the photocatalytic activity of HyCOM and STS TiO₂ films depending on the film thickness, i.e., photoabsorption. For each case, thinner (film-A) and thicker (film-B), the HyCOM films showed the higher rate but smaller photoabsorption while their thickness was even larger than the STS films. This clearly shows the higher efficiency of utilization of e⁻-h⁺ in HyCOM-TiO₂ compared with STS-TiO₂; the ratio of efficiency should be larger than that of apparent rate of MG

Fig. 14 Time course of absorbance of MG solution in the presence of slide glass (triangles) or HyCOM-film-A (circles)



decomposition (1.3 and 1.4 for films-A and films-B, respectively). In the present stage, we cannot determine which of the two significant factors of photocatalytic activity, larger amount of adsorbed substrate and smaller probability of e^-h^+ recombination, predominates in these results. It was clearly demonstrated that superior photocatalytic activity of source HyCOM-TiO₂ particles was preserved after immobilization on glass substrate.

8 Conclusions

Anatase and brookite-type TiO₂ powders were successfully synthesized by solvothermal methods. Physical properties of these TiO₂ samples can be controlled by changing solvothermal condition and post-calcination temperature. These solvothermal products exhibited higher or similar activities than representative active TiO₂ in some photocatalytic reaction systems. Hybridization of TiO₂ and SiO₂ by the solvothermal method was very effective for photocatalytic removal of NO_x in air. Transparent TiO₂ thin films with high photocatalytic activities were successfully produced by dip-coating from TiO₂ sol prepared using solvothermally-synthesized TiO₂ powders. Consequently various photocatalytic materials having excellent performance can be prepared by making the best use of solvothermal technique.

Acknowledgment Some works shown here were supported by a Grant-in-Aid for Scientific Research on Priority Areas (417) from the Ministry of Education, Culture, Science, and Technology (MEXT) of Japan. We thank Nippon Aerosil, Ishihara Sangyo and Fuji Silicia Chemical for supplying Degussa P-25 powders, STS-01 sol and CARiACT Q-30 powders, respectively.

References

- Ao CH, Lee SC (2003) Enhancement effect of TiO₂ immobilized on activated carbon filter for the photodegradation of pollutants at typical indoor air level. *Appl Catal B Environ* 44: 191–205
- Byrappa K, Yoshimura M (2001) Handbook of hydrothermal technology. Noyes, Park Ridge, NJ
- Fujishima A, Hashimoto K, Watanabe T (1999) TiO₂ photocatalysis – fundamentals and applications. BKC, Tokyo
- Hoffmann MR, Martin ST, Choi W, Bahnemann DW (1995) Environmental applications of semiconductor photocatalysis. *Chem Rev* 95:69–96
- Ibusuki T, Takeuchi K (1994) Removal of low concentration nitrogen oxides through photoassisted heterogeneous catalysts. *J Mol Catal* 88:93–102
- Inoue M (2005) Solvothermal synthesis. In: Lee B, Komarneri S (eds) Chemical processing of ceramics (materials engineering). CRC Press, Boca Raton, FL, pp 21–63
- Inoue M, Kominami H, Otsu H, Inui T (1991) Synthesis of microcrystalline titania in organic media. *Nippon Kagaku Kaishi* 1364–1366 [in Japanese]
- Komazaki Y, Shimizu H, Tanaka S (1999) A new measurement method for nitrogen oxides in the air using an annular diffusion scrubber coated with titanium dioxide. *Atmos Environ* 33:4363–4371
- Kominami H, Matsuura T, Iwai K, Ohtani B, Nishimoto S-I, Kera Y (1995) Ultra-highly active titanium(IV) oxide photocatalyst prepared by hydrothermal crystallization from titanium(IV) alkoxide in organic solvents. *Chem Lett* 693–694
- Kominami H, Kato J-I, Kohno M, Kera Y, Ohtani B (1996a) Photocatalytic mineralization of acetic acid in aerated aqueous suspension of ultra-highly active titanium(IV) oxide prepared by hydrothermal crystallization in toluene. *Chem Lett* 1051–1052
- Kominami H, Takada Y, Yamagiwa H, Kera Y, Inoue M, Inui T (1996b) Synthesis of thermally stable nanocrystalline anatase by high-temperature hydrolysis of titanium alkoxide with water dissolved in organic solvent from gas phase. *J Mater Sci Lett* 15:197–200
- Kominami H, Kato J-I, Takada Y, Doushi Y, Ohtani B, Nishimoto S-I, Inoue M, Inui T, Kera Y (1997) Novel synthesis of microcrystalline titanium(IV) oxide having high thermal stability and ultra-high photocatalytic activity: thermal decomposition of titanium(IV) alkoxide in organic solvents. *Catal Lett* 46:235–240
- Kominami H, Murakami S-Y, Kera Y, Ohtani B (1998) Titanium(IV) oxide photocatalyst of ultra-high activity: a new preparation process allowing compatibility of high adsorptivity and low electron-hole recombination probability. *Catal Lett* 56:125–129
- Kominami H, Kato J-I, Murakami S-Y, Kera Y, Inoue M, Inui T, Ohtani B (1999a) Synthesis of titanium(IV) oxide of ultra-high photocatalytic activity: high-temperature hydrolysis of titanium alkoxides with water liberated homogeneously from solvent alcohols. *J Mol Catal A Chem* 144:165–171
- Kominami H, Kohno M, Takada Y, Inoue M, Inui T, Kera Y (1999b) Hydrolysis of titanium alkoxide in organic solvent at high temperatures: a new synthetic method for nanosized, thermally stable titanium(IV) oxide. *Ind Eng Chem Res* 38:3925–3931
- Kominami H, Kohno M, Kera Y (2000) Synthesis of brookite-type titanium oxide nano-crystals in organic media. *J Mater Chem* 10:1151–1156
- Kominami H, Kumamoto H, Kera Y, Ohtani B (2001) Immobilization of highly active titanium (IV) oxide particles: a novel strategy of preparation of transparent photocatalytic coatings. *Appl Catal B Environ* 30:329–335
- Kominami H, Murakami S-Y, Kera Y, Ohtani B (2002) Design, preparation and characterization of highly active metal oxide photocatalysts. In: Kaneko M, Okura I (eds) Photocatalysis: science and technology. Kodansya, Tokyo, pp 29–49
- Kominami H, Kato J-I, Murakami S, Ishii Y, Kohno M, Yabutani K-I, Yamamoto T, Kera Y, Inoue M, Inui T, Ohtani B (2003) Solvothermal syntheses of semiconductor photocatalysts of ultra-high activities. *Catal Today* 84:181–189

- Kominami H, Yukishita K, Kimura T, Matsubara M, Hashimoto K, Kera Y, Ohtani B (2008) Direct solvothermal formation of nanocrystalline TiO₂ on porous SiO₂ adsorbent and photocatalytic removal of nitrogen oxides in air over TiO₂-SiO₂ composites. *Top Catal* 47:155–161
- Kominami H, Murakami S-Y, Kato J-I, Kera Y, Ohtani B (2002) Correlation between some physical properties of titanium dioxide particles and their photocatalytic activity for some probe reactions in aqueous systems. *J Phys Chem B* 106:10501–10507
- Murakami S-Y, Kominami H, Kera Y, Ikeda S, Noguchi H, Uosaki K, Ohtani B (2007) Evaluation of electron-hole recombination properties of titanium(IV) oxide particles with high photocatalytic activity. *Res Chem Intermed* 33:285–296
- Nakamura I, Sugiura S, Takeuchi K (2000) Mechanism for NO photooxidation over the oxygen-deficient TiO₂ powder under visible light irradiation. *Chem Lett* 1276–1277
- Ohtani B, Nishimoto S-I (1993) Effect of surface adsorptions of aliphatic alcohols and silver ion on the photocatalytic activity of titania. *J Phys Chem* 97:920–926
- Ohtani B, Iwai K, Kominami H, Matsuura T, Kera Y, Nishimoto S-I (1995) Titanium(IV) oxide photocatalyst of ultra-high activity for selective N-cyclization of an amino acid in aqueous suspensions. *Chem Phys Lett* 242:315–319
- Xu Y, Zheng W, Liu W (1999) Enhanced photocatalytic activity of supported TiO₂: dispersing effect of SiO₂. *J Photochem Photobiol A Chem* 122:57–60

Chapter 5

Preparation of Highly Transparent TiO₂-based Thin Film Photocatalysts by an Ion Engineering Method: Ionized Cluster Beam Deposition

Masato Takeuchi and Masakazu Anpo

Abstract Highly transparent TiO₂ and TiO₂-based binary oxide (TiO₂/SiO₂ and TiO₂/B₂O₃) thin films of different TiO₂ contents were successfully prepared by using an ion engineering technique as a dry process. These transparent thin films showed very high photocatalytic performance due to the low scattering of the incident light as compared to powdered TiO₂ samples. Also, TiO₂-based binary oxide thin films involving a highly dispersed tetrahedral Ti-oxide species showed unique photofunctionality for the direct decomposition of NO and surface wettability. In addition, the loading of small amounts of Pt increased the photocatalytic reactivity of the TiO₂ thin films without decreasing the high transparency.

1 Introduction

Much attention has been directed toward the various applications of photocatalysts for the recovery and sustenance of a clean environment. The development of TiO₂ photocatalysts, which can efficiently convert solar energy into useful chemical energy, is especially desired as a method of artificial photosynthesis (Fujishima and Honda 1972; Grätzel 1983; Pelizzetti and Schiavello 1991; Anpo and Yamashita 1996; Anpo and Takeuchi 2003; Anpo 2004). TiO₂ thin films coated on various substrates have been widely investigated not only for their high photocatalytic reactivity but also for their unique photoinduced superhydrophilic properties

M. Takeuchi (✉)

Department of Applied Chemistry, Osaka Prefecture University
1-1, Gakuen-cho, Naka-ku, Sakai, Osaka 599-8531, Japan
e-mail: masato-t@chem.osakafu-u.ac.jp

(Wang et al. 1997; Fujishima et al. 1999). And in fact, TiO_2 photocatalysts have recently been applied in commercially viable products. TiO_2 coatings are generally carried out by a wet process such as the dip, spin and spray coating methods, etc. The coatings are carried out by precursor solutions containing a TiO_2 source (Heller 1995; Negishi et al. 1998). These wet methods require a calcination process after coating the thin films onto substrates in order to obtain high crystallinity and strong adhesion. However, we have reported on a dry coating process such as the ionized cluster beam (ICB) (Yamashita et al. 1998a; Takeuchi et al. 2000; Yamashita and Anpo 2004) or RF-magnetron sputtering (RF-MS) (Anpo and Takeuchi 2003; Anpo 2004; Takeuchi et al. 2001a; Kitano et al. 2005, 2006, 2007) deposition methods as suitable techniques in preparing highly transparent TiO_2 film photocatalysts which do not require any calcination treatment at high temperatures after the deposition process. Moreover, since this dry coating process is carried out in a high vacuum chamber and does not necessitate any organic solvents, the contamination of the thin films with impurities can be prevented. This feature is quite important for the preparation of TiO_2 thin films with high photocatalytic reactivity.

In our previous research, we have reported that the photocatalytic reactivity of Ti/Si binary oxides prepared by coprecipitation or sol-gel methods are strongly affected by the Ti/Si ratios (Anpo et al. 1984, 1987, 1988; Yamashita et al. 1998b, 1998c). It has been revealed that Ti/Si binary oxides with low Ti content exhibit very unique photocatalytic properties which are caused by the existence of highly dispersed tetrahedral Ti-oxide species within the SiO_4 matrices. Such tetrahedrally coordinated TiO_4 units in zeolites or SiO_2 frameworks are also known to show high catalytic reactivity for the partial oxidation or selective epoxidation reaction of olefins. Moreover, in order to improve the photo-induced superhydrophilic property of the TiO_2 thin films, a combination or mixing system of TiO_2 moieties with other oxides as host materials, such as SiO_2 or B_2O_3 , have been widely investigated. In particular, the addition of SiO_2 fine particles (Machida et al. 1999) or the deposition of SiO_2 thin layers (Jpn. Kokai Tokkyo Koho JP) onto the surface of TiO_2 thin films have been shown to maintain the high wettability even under dark conditions for long periods after UV light irradiation was discontinued. However, to date, there have not been any detailed investigations clarifying the effect of the local structure of the Ti-oxide species on the photocatalytic reactivity and the surface wettability of binary oxide thin films containing the highly dispersed Ti-oxide species.

In this chapter, the preparation of highly transparent TiO_2 and binary oxide thin films such as $\text{TiO}_2/\text{SiO}_2$ and $\text{TiO}_2/\text{B}_2\text{O}_3$ by an ICB deposition method are presented. Characterizations of these TiO_2 -based thin films were carried out by various analytical methods such as XRD, XAFS and UV-vis absorption in order to elucidate the local structure of the Ti-oxide species. The photocatalytic reactivity of these thin films was evaluated by the decomposition of NO under UV light irradiation. The effect of UV light illumination on the surface wettability of these binary oxide thin films containing highly dispersed Ti-oxide species is also discussed.

2 Ion Engineering Techniques for the Preparation of Well-Defined TiO₂ Thin Film Photocatalysts

Ion engineering is considered to be one of the most advanced technologies and is widely applied in the development of semiconductor materials. In particular, ion implantation is effective in modifying the electronic properties of silicon semiconductors. The schematic interactions between accelerated ions of different energies and solid surfaces are shown in Fig. 1, as follows: (a) When ion beams with lower energies of several to a few hundred eV are irradiated onto solid surfaces, these ions accumulate on the surface to form thin films similar to a snow covering on the ground; (b) When ion beams with middle energies of a few hundred eV to several tens keV are bombarded onto the solid surfaces, these ions sputter the atoms of the

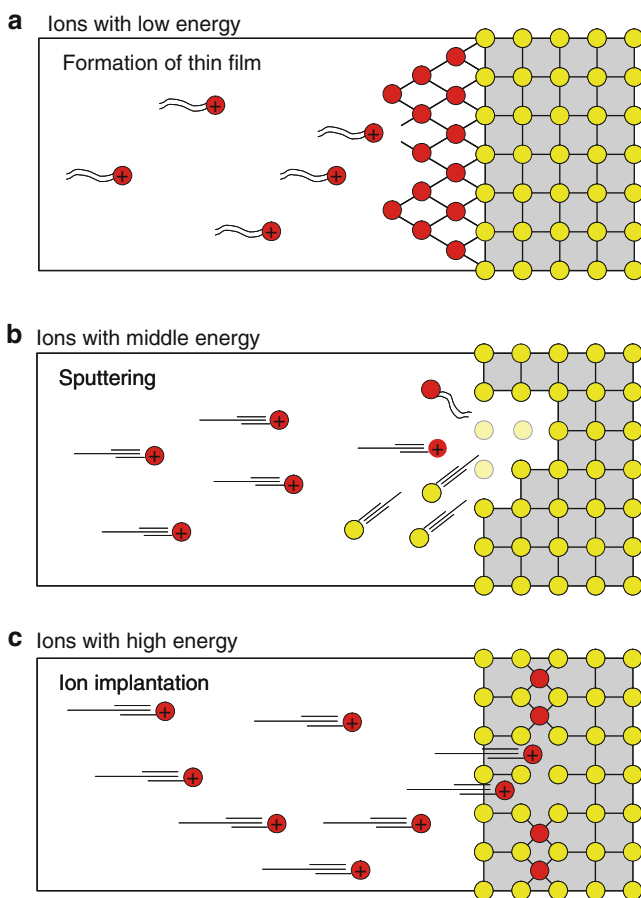


Fig. 1 Schematic diagrams of the interaction between accelerated ions of different energies and the solid surfaces

surfaces as secondary ions; (c) When ion beams with higher energies than several tens keV are exposed onto solid surfaces, these ions are implanted within the deep bulk of the solid without any significant damage to the surface. The solid surfaces implanted with metal ions using high energy bombardment sometimes change to their amorphous phases, however, it is known that the crystalline structures recover to their original phase by post calcination processes in air.

In many cases, TiO_2 thin films are prepared by wet processes. In contrast, we have applied ion engineering techniques as a dry process to prepare transparent TiO_2 -based thin film photocatalysts since the various preparation conditions can be controlled. The preparation of thin film materials in a high vacuum chamber have some potential advantages, as follows: (1) Contamination of the thin films with impurities can be prevented; (2) A dry preparation method does not require the use of any organic solvents so that it is an “environmentally-friendly process”; (3) Thin films with high crystallinity and strong adhesion can be easily prepared onto substrates without calcination at high temperatures; (4) The easy control of the various physical and chemical properties. We have successfully applied an ICB deposition method to prepare transparent TiO_2 -based thin films (Yamashita et al. 1998a; Takeuchi et al. 2000, 2001b, 2003a; Yamashita and Anpo 2004; Dohshi et al. 2001; Anpo et al. 2002). A schematic diagram of the ICB deposition method with multi ion-sources is shown in Fig. 2 (Fukushima et al. 1985). In the ICB deposition method, titanium vapor obtained by heating titanium metal as a source

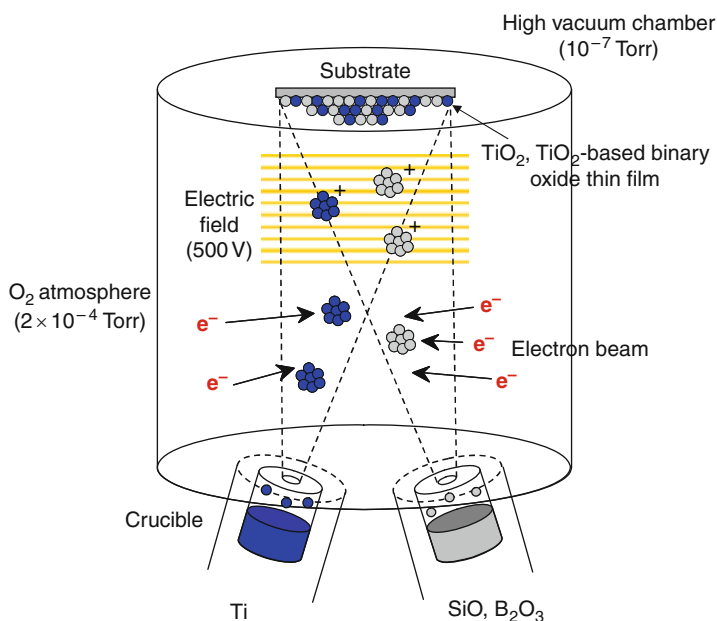


Fig. 2 Schematic diagram of the ionized cluster beam (ICB) deposition method using multi-ion sources

material at 2,200 K was introduced into a high vacuum chamber producing titanium clusters. The titanium clusters reacted with sufficient amounts of the O₂ molecules (O₂ pressure: 2×10^{-4} Torr) in the high vacuum chamber, forming stoichiometric TiO₂ clusters. These TiO₂ clusters ionized by electron beam irradiation were accelerated by an electric field (acceleration voltage: 500 V) and bombarded onto the substrates, resulting in the formation of transparent TiO₂ thin films. TiO₂-based binary oxide thin films, TiO₂/SiO₂ and TiO₂/B₂O₃, having different Ti-oxide compositions were prepared while SiO and B₂O₃ grains of high purity were used simultaneously as the ion source, respectively (Takeuchi et al. 2001b, 2003a; Dohshi et al. 2001; Anpo et al. 2002). The TiO₂/SiO₂ and TiO₂/B₂O₃ ratios, film thickness and deposition rate (ca. 0.1 nm/s) were strictly controlled by monitoring their parameters with a quartz film thickness meter during the deposition process. The temperature of the substrate was kept at 623 K in order to obtain good crystallinity and strong adhesion of the thin film onto the quartz substrates.

3 Preparation of Highly Transparent TiO₂ Thin Film Photocatalysts

Ion engineering techniques were seen to be an effective approach in the preparation of well-defined TiO₂ thin film photocatalysts. In this section, we deal with the preparation of highly transparent TiO₂ thin film photocatalysts on quartz substrates by applying an ICB deposition method (Yamashita et al. 1998a; Takeuchi et al. 2000; Yamashita and Anpo 2004). From XRD measurements, the TiO₂ films with thicknesses larger than 300 nm were confirmed to show typical diffraction patterns attributed to the anatase and rutile structures of the TiO₂ (not shown here). The ratio of anatase to rutile was estimated to be ca. 70%. On the other hand, TiO₂ thin films with film thicknesses smaller than 100 nm did not show any XRD patterns attributed to the crystalline structure of TiO₂ since their film thicknesses were less. However, as shown in Fig. 3, these TiO₂ thin films showed three typical pre-edge peaks in the XANES spectra attributed to the anatase structure. These results indicate that TiO₂ deposited onto quartz substrates exist not as highly dispersed TiO₂ clusters but as TiO₂ thin layers. Since the conventional TiO₂ powdered photocatalysts (Degussa, P-25) shows a mixed structure of anatase and rutile phases, it was expected that the TiO₂ thin films prepared by the ICB deposition method would also exhibit high photocatalytic reactivity. The optical properties of these TiO₂ thin films were investigated by UV-vis absorption measurements, as shown in Fig. 4. Clear interference fringes, which are a characteristic feature of transparent thin films, could be observed in visible light regions, indicating that uniform and highly transparent thin films were formed on the quartz substrates. The absorption edges of these films could be observed at around 350–380 nm, and shifted to shorter wavelength regions as the film thicknesses decreased. This phenomenon can be explained by the quantum size effect caused by the presence of nano-sized TiO₂ particles which make up the transparent thin films.

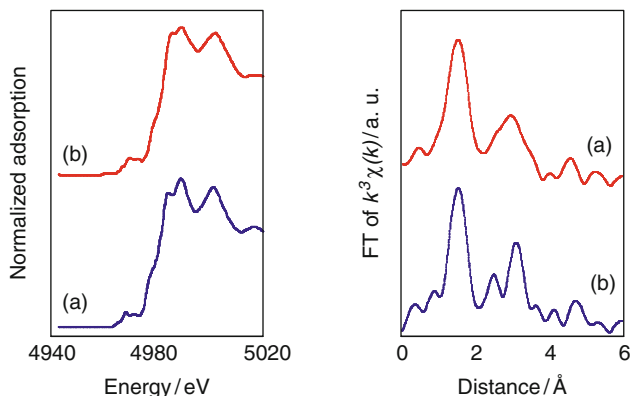


Fig. 3 Ti K-edge XANES spectra (*left*) and Fourier transforms of the EXAFS oscillation (*right*) of the TiO₂ thin films prepared by the ICB deposition method. Film thickness (nm): (a) 20, (b) 300

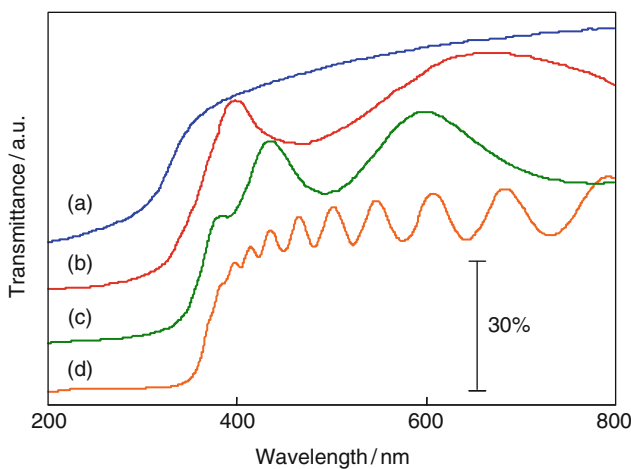


Fig. 4 UV-vis absorption (transmittance) spectra of the TiO₂ thin films prepared by the ICB deposition method. Film thickness (nm): (a) 20, (b) 100, (c) 300, (d) 1,000

UV light ($\lambda > 270$ nm) irradiation of these films in the presence of NO led to the photocatalytic decomposition of NO into N₂ and N₂O at 275 K. The formation of N₂ and N₂O was confirmed to increase linearly with the UV light irradiation time and no reaction products could be observed under dark conditions. It was, thus, clearly shown that TiO₂ thin films prepared by an ICB deposition method exhibit high photocatalytic reactivity for the decomposition of NO under UV light irradiation. The photocatalytic reactivity of the thin films prepared by this method was found to be comparable or even higher than the TiO₂ thin films prepared by sol-gel. It was also found that the photocatalytic reactivity of the films strongly depend on the film thickness.

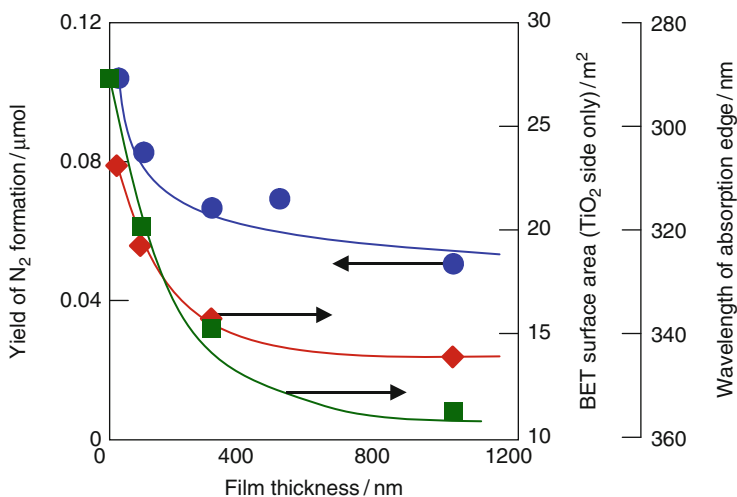


Fig. 5 Relationship between the photocatalytic reactivities for NO decomposition (*circle plots*), BET surface areas (*diamond plots*) and wavelengths of the absorption edges (*square plots*) of TiO₂ thin films prepared by the ICB deposition method

Figure 5 shows the effects of the film thickness on the photocatalytic reactivity, BET surface areas and wavelengths of the absorption edge for these thin films. The films having small film thicknesses showed much higher photocatalytic reactivity. As the film thicknesses increased, the photocatalytic reactivity was found to decrease slightly and then level off. Since these TiO₂ thin films prepared by ICB deposition are highly transparent, the incident UV light is hardly scattered by these thin films, resulting in an improvement of the utilization efficiency of UV light. Moreover, the BET surface areas and wavelengths of the absorption edge showed the same tendency toward photocatalytic reactivity.

4 Preparation of TiO₂/SiO₂ and TiO₂/B₂O₃ Binary Oxide Thin Film Photocatalysts Having Highly Dispersed Ti-Oxide Species

4.1 The Local Structures of the Ti-Oxide Species and the Optical Properties of TiO₂/SiO₂ and TiO₂/B₂O₃ Binary Oxide Thin Films

The optical properties of thin films such as the absorption edges and transparency in visible light regions are some of the most important factors that determine their photocatalytic reactivity (Takeuchi et al. 2001b, 2003a; Dohshi et al. 2001; Anpo et al. 2002). Figure 6 shows the UV-vis absorption (transmittance) spectra of the

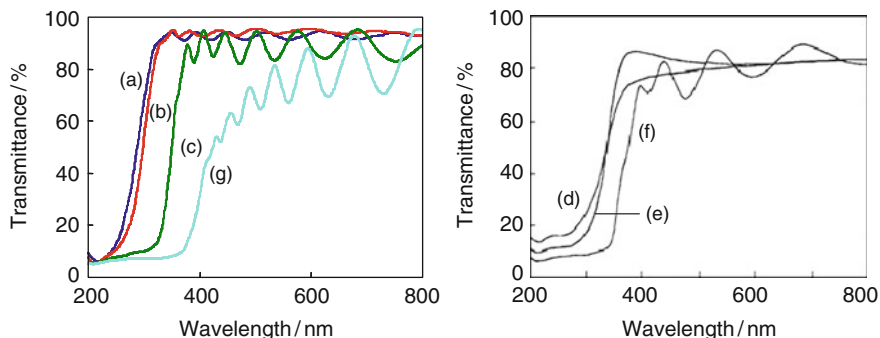


Fig. 6 UV-vis absorption (transmittance) spectra of: (a–c) $\text{TiO}_2/\text{SiO}_2$, (d–f) $\text{TiO}_2/\text{B}_2\text{O}_3$ thin films and (g) TiO_2 thin films prepared by ICB deposition method. TiO_2 content (%): (a) 6.6, (b) 9.5, (c) 50.1, (d) 5.0, (e) 10.0, (f) 50.0

$\text{TiO}_2/\text{SiO}_2$ (left) and $\text{TiO}_2/\text{B}_2\text{O}_3$ (right) thin films (film thickness: ca. 700 nm) with different Ti-oxide compositions. The SiO_2 and B_2O_3 thin films deposited on quartz substrates did not show any significant absorption in measurable ranges (200–800 nm). The absorption spectra of these binary oxide thin films could, thus, be attributed to the Ti-oxide species dispersed in the SiO_2 or B_2O_3 matrices. TiO_2 thin films showed typical interference fringes in visible light regions due to the highly transparent and uniform thin layers. On the other hand, as the Ti-oxide contents decreased, the intensity of the interference fringes was found to decrease as well. From these results, it could be expected that the Ti-oxide species does not have a long-range order and exists as small clusters or ultrafine particles highly dispersed within the SiO_2 or B_2O_3 matrices. Furthermore, a remarkable shift in the absorption edges toward shorter wavelength regions could be observed along with a decrease in the Ti-oxide compositions of both thin films. The degree of the blue shift was found to depend on the kind of host oxides such as SiO_2 and B_2O_3 . The absorption peak of the fourfold coordinated Ti-oxide species incorporated within the zeolite frameworks has been observed at around 220–230 nm (Anpo et al. 1989, 1998; Anpo 2000; Ikeue et al. 2001). The absorption peak of the $\text{TiO}_2/\text{SiO}_2$ thin film having a TiO_2 content of 6.6% was observed at around 220–250 nm. On the other hand, the $\text{TiO}_2/\text{B}_2\text{O}_3$ thin film having low Ti content exhibited an absorption edge at around 350–370 nm. These results clearly indicate that the Ti-oxide species in the SiO_2 matrices exist in a highly dispersed tetrahedral structure, while the Ti-oxide species in the B_2O_3 matrices exist as ultrafine octahedrally coordinated TiO_2 particles.

Since these binary oxide thin films with low Ti-oxide content did not show any significant XRD patterns due to the TiO_2 crystals, the Ti K-edge XAFS spectra were measured in order to clarify the local structures of the incorporated Ti-oxide species. Figure 7 shows the XANES spectra of the $\text{TiO}_2/\text{SiO}_2$ (A–C) and $\text{TiO}_2/\text{B}_2\text{O}_3$ (D) thin films with different Ti-oxide contents. The $\text{TiO}_2/\text{SiO}_2$ films with TiO_2 content lower than 10% were found to show only an intense single preedge peak at ca. 4.97 keV attributed to the highly dispersed tetrahedral TiO_4 units.

As the Ti-oxide content increased, the intensity of the sharp preedge peaks decreased, indicating that the highly dispersed Ti-oxide species aggregate to form small clusters containing TiO₆ octahedrons. On the other hand, three small preedge peaks attributed to an anatase structure were observed on the TiO₂/B₂O₃ films with a Ti-oxide content of 5 wt%. These results clearly indicate that the Ti-oxide species aggregate to form ultrafine TiO₂ particles with an anatase structure within the B₂O₃ matrices. The Fourier transforms of the EXAFS oscillation of the TiO₂/SiO₂ (a–c) and TiO₂/B₂O₃ (d) thin films are also shown in Fig. 7. The TiO₂/SiO₂ films showed a single peak attributed to the Ti–O bond at around 1.6–1.7 Å, indicating the preferential formation of fourfold coordinated TiO₄ structures within the SiO₂ matrices. On the other hand, the TiO₂/B₂O₃ films showed not only a peak due to the Ti–O bond but also a peak due to the Ti–O–Ti bond at around 2.6–2.9 Å, indicating the formation of aggregated TiO₂ particles within the B₂O₃ matrices. Information on the coordination numbers and the Ti–O bond distance obtained from curve fitting analysis in the Fourier transforms of the EXAFS oscillation are summarized in Table 1. The Ti–O bond distance in the TiO₂/SiO₂ films was estimated at ca. 1.81–1.82 Å, slightly longer than that of the isolated tetrahedral Ti-oxide species incorporated within zeolite frameworks (ca. 1.78 Å) (Anpo et al. 1989, 1998; Anpo 2000; Ikeue et al. 2001). On the other hand, the TiO₂/B₂O₃ films showed a Ti–O bond distance of ca. 1.90 Å which is very close to the anatase TiO₂ powder.

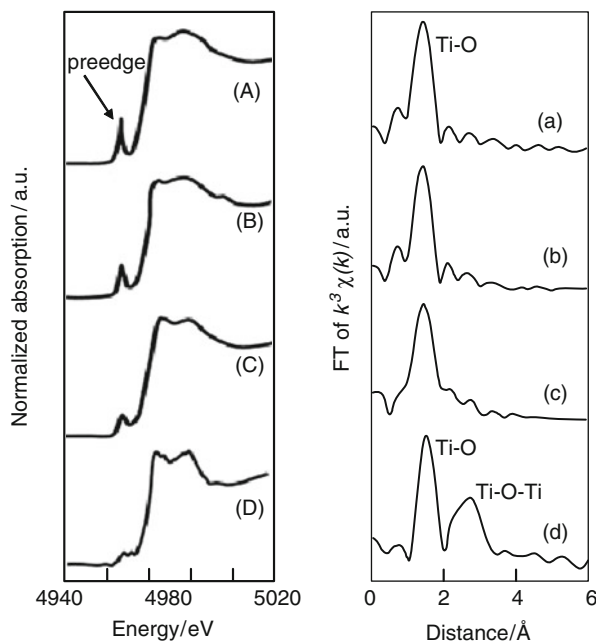


Fig. 7 Ti K-edge XANES spectra (*left*) and Fourier transforms of the EXAFS oscillation (*right*) of: (A–C, a–c) TiO₂/SiO₂ and (D, d) TiO₂/B₂O₃ thin films. TiO₂ content (%): (a) 6.6, (b) 9.5, (c) 50.1, (d) 5.0

Table 1 Coordination number and bond length of the Ti-oxide species in $\text{TiO}_2/\text{SiO}_2$ and $\text{TiO}_2/\text{B}_2\text{O}_3$ thin films as determined by the curve fitting for the Fourier transforms of the EXAFS oscillation

Catalyst	Shell	Bond distance (Å)	Coordination number
$\text{TiO}_2/\text{SiO}_2(6.6/93.4)$	Ti–O	1.81	4.3
$\text{TiO}_2/\text{SiO}_2(9.5/90.5)$	Ti–O	1.82	4.4
$\text{TiO}_2/\text{SiO}_2(50.1/49.9)$	Ti–O	1.85	4.9
$\text{TiO}_2/\text{B}_2\text{O}_3(5/95)$	Ti–O	1.91	5.98
$\text{TiO}_2/\text{B}_2\text{O}_3(10/90)$	Ti–O	1.90	5.97
$\text{TiO}_2/\text{B}_2\text{O}_3(50/50)$	Ti–O	1.90	5.97

These results also indicate that the Ti-oxide species in the $\text{TiO}_2/\text{SiO}_2$ thin films exist not as a completely isolated tetrahedral TiO_4 unit incorporated within the SiO_2 matrices at the atomic level but as highly dispersed Ti-oxide nano-clusters including the fourfold TiO_4 units, whereas, in the $\text{TiO}_2/\text{B}_2\text{O}_3$ thin films, octahedrally coordinated ultrafine TiO_2 particles are formed within the B_2O_3 matrices. These detailed investigations on binary oxide thin films of different Ti-oxide compositions showed their optical properties and local structures to be greatly dependent on the type and nature of the combined oxide materials. In turn, the differences in the local structures and optical properties of these binary oxide thin films are also expected to affect their photocatalytic reactivity.

4.2 Photocatalytic Reactivity of TiO_2 -Based Binary Oxide Thin Films

The photocatalytic reactivities of TiO_2 -based binary oxide thin films were evaluated for the decomposition of NO under UV light irradiation. Figure 8 shows the reaction time profiles of the photocatalytic decomposition of NO on the $\text{TiO}_2/\text{SiO}_2$ film (TiO_2 content; 6.6%) under UV light irradiation. Decomposition could be confirmed to proceed with a good linearity against the UV irradiation time. Figure 9 shows the effects of the local structure of the Ti-oxide species within the $\text{TiO}_2/\text{SiO}_2$ films on their photocatalytic reactivities. $\text{TiO}_2/\text{SiO}_2$ incorporated with tetrahedral TiO_4 species within its SiO_4 matrices showed high photocatalytic reactivity for the decomposition of NO and high selectivity for N_2 formation. As the TiO_2 content increased, the TiO_2 fine particles in the films were mainly found to decompose NO into N_2O under UV light. These results are in good agreement with our previous studies on photocatalysis involving the isolated tetrahedral TiO_4 species incorporated within SiO_2 or zeolite frameworks (Anpo et al. 1989, 1998; Anpo 2000; Ikeue et al. 2001). The $\text{TiO}_2/\text{B}_2\text{O}_3$ films were also confirmed to show efficient photocatalytic decomposition of NO under UV light irradiation (not shown). However, when the TiO_2 content was less than 10%, ultrafine TiO_2 particles of octahedral coordination were formed within the B_2O_3 matrices. In contrast to the $\text{TiO}_2/\text{SiO}_2$

Fig. 8 The reaction time profiles of the photocatalytic decomposition of NO on the TiO₂/SiO₂ thin film (TiO₂ content: 6.6%) under UV light irradiation at 275 K

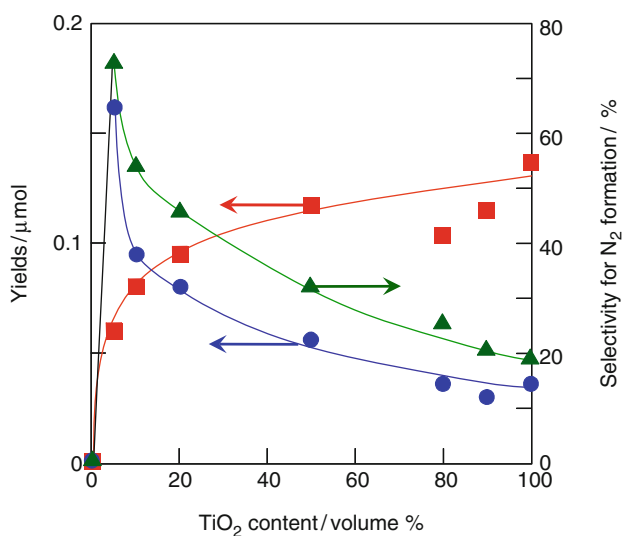
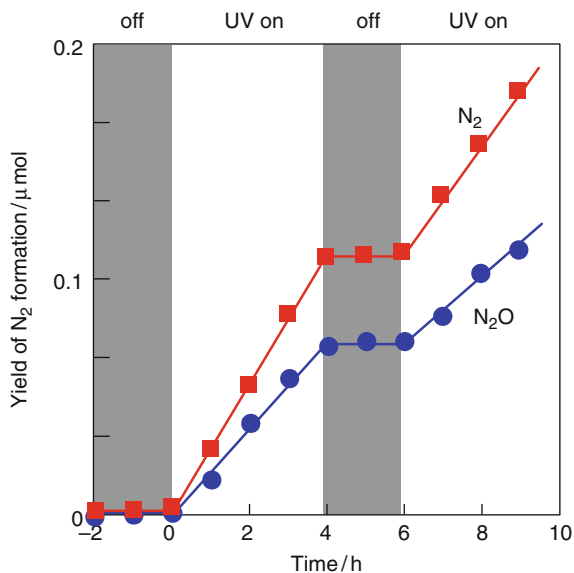


Fig. 9 Effect of the TiO₂ contents on the formation yields of N₂ (circle plots) and N₂O (square plots) and selectivity for N₂ formation (triangle plots) in the photocatalytic decomposition of NO on the TiO₂/SiO₂ thin films under UV light irradiation

thin films, UV light irradiation of $\text{TiO}_2/\text{B}_2\text{O}_3$ films with low TiO_2 content in the presence of NO led to the formation of N_2 with a high selectivity.

4.3 The Surface Wettability of TiO_2 -Based Binary Oxide Thin Films

TiO_2 surfaces are known to show photo-induced superhydrophilicity in which water droplets on the thin films are observed to spread out under UV light irradiation (Wang et al. 1997). Although the addition of SiO_2 fine particles (Machida et al. 1999) or a SiO_2 thin layer (Jpn. Kokai Tokkyo Koho JP) onto the surface of the TiO_2 thin films is known to improve superhydrophilic properties, the surface wettability of TiO_2 -based binary oxide thin films with highly dispersed tetrahedral TiO_4 species has yet to be investigated. Figure 10 shows the surface wettability of the $\text{TiO}_2/\text{SiO}_2$ thin films and the pure TiO_2 and SiO_2 thin films prepared by an ICB deposition method. The SiO_2 film did not show any changes in the surface wettability under UV light irradiation and after storage in dark conditions. These results indicate that changes in the surface wettability observed on $\text{TiO}_2/\text{SiO}_2$ are associated with the Ti-oxide species dispersed in the SiO_2 matrices. The contact angle of the H_2O droplets on a pure TiO_2 thin film was found to reach the superhydrophilic state with 2 h UV light irradiation. However, $\text{TiO}_2/\text{SiO}_2$ containing the tetrahedral TiO_4 species did not achieve a superhydrophilic state and the contact angle of the

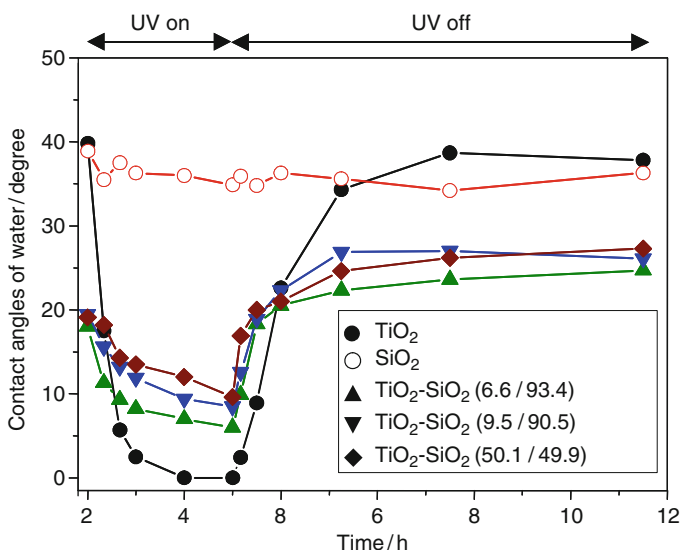


Fig. 10 Changes in the contact angle of H_2O droplets on $\text{TiO}_2/\text{SiO}_2$, TiO_2 and SiO_2 thin films prepared by the ICB deposition method under UV light irradiation for 3 h and under dark conditions

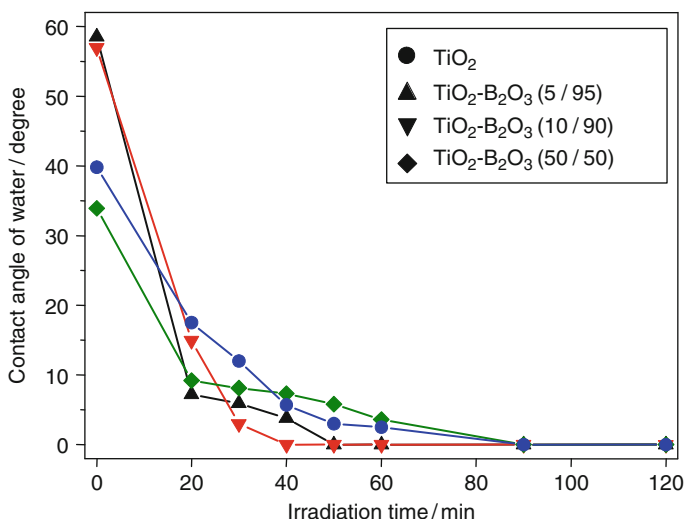


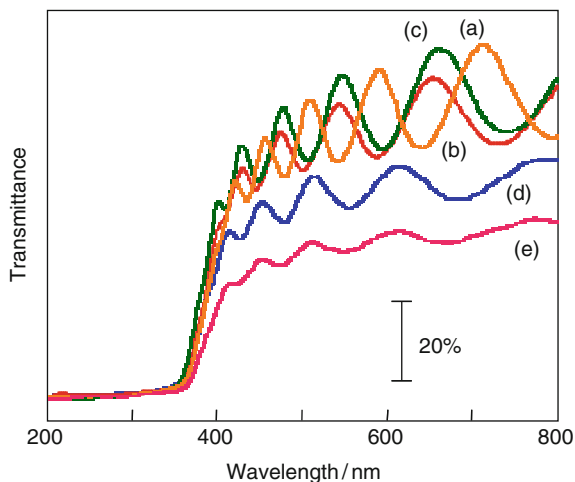
Fig. 11 Changes in the contact angle of H₂O droplets on the TiO₂/B₂O₃ thin films under UV light irradiation for 2 h

H₂O droplets on these films decreased to ca. 10°. It is, however, notable that the tetrahedral Ti-oxide species dispersed within the SiO₂ matrices showed photo-induced wettability conversion under UV light. These TiO₂/SiO₂ films also maintained a state of high wettability even under dark conditions as compared to pure TiO₂ thin films, attributed to the combination of TiO₂ with SiO₂ moieties by its dispersion into the SiO₂ matrices. On the other hand, as shown in Fig. 11, the TiO₂/B₂O₃ films showed higher efficiency in the photo-conversion of the surface wettability than the pure TiO₂ films, even when the TiO₂ composition was low. This can be explained by the effect of the highly hydrophilic B₂O₃ domain of the ultrafine TiO₂ particles. The photo-induced hydrophilicity has been shown to be improved by preparing TiO₂-based binary oxide thin films with different TiO₂ content as compared to pure TiO₂ thin films. Moreover, such TiO₂/SiO₂ and TiO₂/B₂O₃ thin films were found to sustain their high wettable surfaces even under dark conditions for prolonged periods.

5 Enhancement of the Reactivity of Transparent TiO₂ Thin Film Photocatalysts by the Loading of Small Amounts of Pt

The improvement of the photocatalytic reactivity of transparent TiO₂ thin films prepared by the ICB deposition method could be achieved by the loading of small amounts of Pt using a RF-magnetron sputtering (RF-MS) deposition method (Takeuchi et al. 2003b). The Pt loading amounts were described as the film thickness estimated by the deposition time and rate (ca. 1.0 nm/s). Figure 12

Fig. 12 UV-vis absorption (transmittance) spectra of: (a) unloaded TiO_2 and (b–e) TiO_2 thin films loaded with different amounts of Pt. Loading amounts of Pt (as the film thickness): (a) 0, (b) 5, (c) 10, (d) 30, (e) 60 nm



shows the UV–vis absorption (transmittance) spectra of the unloaded TiO_2 thin films and the TiO_2 films loaded with different amounts of Pt. The TiO_2 thin films without Pt loading showed high transparency in visible light regions. Pt loadings of less than 10 nm did not change the high transparency of the original TiO_2 thin films. Meanwhile, as the amount of Pt loaded onto the films was increased up to 30 nm, the transmittance of these films decreased to ca. 50–60% and clear interference fringes in the visible light region decreased. These results clearly indicate that the small amounts of Pt loaded exist as small clusters and do not interrupt the passage of the incident light into the TiO_2 thin film, while large amounts of Pt form a thin layer as a half mirror reflecting some parts of the incident light.

The chemical state of the Pt loaded onto the TiO_2 films was investigated by XPS measurements. As the amount of Pt increased, the peak intensity of the $\text{Ti}2p$ spectra lessened and the peak position shifted toward higher binding energies (Fig. 13a). The binding energy of the $\text{Ti}2p_{3/2}$ in the TiO_2 thin films prepared by this ICB method was found to be slightly higher (459.3 eV) as compared to the pure TiO_2 powder (458.5 eV) (Venezia et al. 1994) since the thin films were strained by the stress on the interface between the substrate and thin film. Moreover, as the amount of Pt was increased, the peak intensity of the $\text{Pt}4f$ spectra became larger and the peak position shifted toward higher binding energies (Fig. 13b). The binding energies of the $\text{Pt}4f_{7/2}$ peak for the Pt metal and PtO are known to be 70.9 and 73.6 eV, respectively (Ebitani et al. 1992; Sayari and Dicko 1994). The binding energy of the $\text{Pt}4f_{7/2}$ in the thin film loaded with Pt of 5 nm (spectrum b) was slightly higher, i.e., 72.0 eV, than for the Pt metal, but smaller than for PtO. These results indicate that a small part of the Pt loaded onto this thin film is slightly oxidized to PtO although most exist as Pt metal. Moreover, the binding energy of the $\text{Pt}4f_{7/2}$ in the thin film loaded with Pt of 60 nm (spectrum e) was 73.5 eV, indicating that the surface of the Pt loaded onto this film was completely oxidized to form PtO.

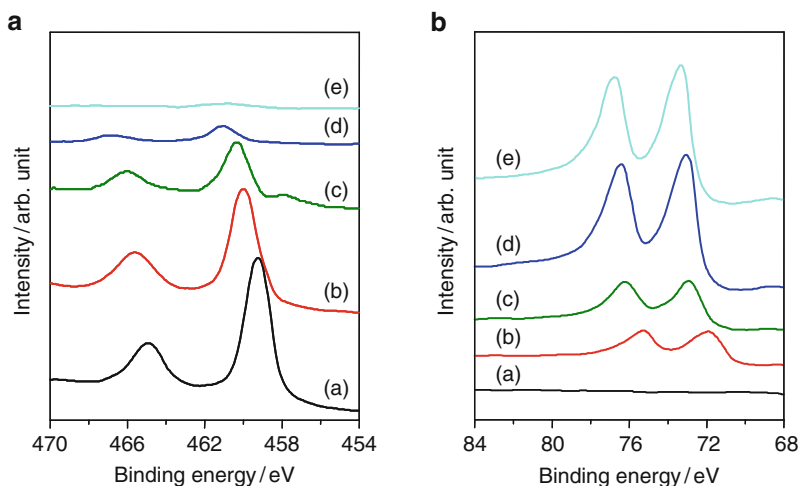


Fig. 13 Ti2p (left) and Pt4f (right) XPS spectra of: (a) unloaded TiO₂ and (b–e) TiO₂ thin films loaded with different amounts of Pt. Loading amounts of Pt (as the film thickness): (a) 0, (b) 5, (c) 10, (d) 30, (e) 60 nm

In order to obtain further detailed information on the chemical states of the Pt loaded onto the TiO₂ thin films, the Pt L_{III}-edge XANES spectra were measured in the fluorescence mode at the SPring-8 synchrotron radiation facilities in Harima. Figure 14 shows the Pt L_{III}-edge XANES spectra of the Pt loaded onto the TiO₂ thin films as well as the Pt foil and PtO₂ as reference. In these spectra, a sharp absorption peak, i.e., the so called “white line” at 11.56 keV could be observed. This peak is attributed to the electron transfer from 2p_{3/2} of the Pt L_{III}-edge to the vacant d-orbital of the absorbing atom (Tanaka et al. 1995). The intensity of the white line in the Pt metal is much smaller than that of PtO₂ and is in good correspondence with the chemical state of the Pt species. The intensities of the white line in the Pt species of 10 and 30 nm, loaded onto the TiO₂ thin films were larger than that of the Pt foil but smaller than that of PtO₂. In addition, the shape of the EXAFS oscillation in these samples was more similar to that of Pt foil than PtO₂, suggesting that the small amounts of Pt loaded onto the TiO₂ thin films exist as Pt metal rather than a Pt-oxide species. These results obtained from the XAFS measurements were in good correspondence with those of the XPS measurements.

The photocatalytic reactivity of the Pt-loaded TiO₂ thin films were evaluated for the oxidation of acetaldehyde with O₂ under UV light irradiation, as shown in Fig. 15. Since these photocatalytic reactions were carried out in the presence of small amounts of O₂, not only CO₂ as a fully oxidized product but also CO as a partially oxidized product were detected in the gas phase. However, when the same reactions were carried out in the presence of excess amounts of O₂, it was confirmed that acetaldehyde was completely oxidized into CO₂ and H₂O. It is notable that the TiO₂ thin films loaded with Pt of 10 nm showed three times higher photocatalytic reactivity than the TiO₂ thin film without Pt loading. The enhancement

Fig. 14 Pt L_{III} -edge XANES spectra of the TiO_2 thin films loaded with different amounts of: (a, b) Pt, (c) Pt foil and (d) PtO_2 as references. Amounts of Pt loaded (as the film thickness): (a) 10, (b) 30

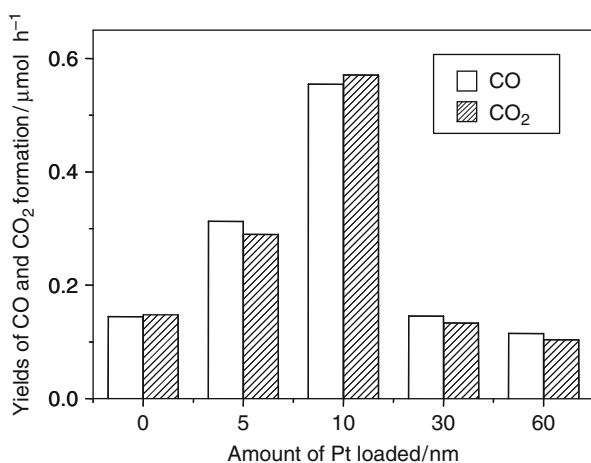
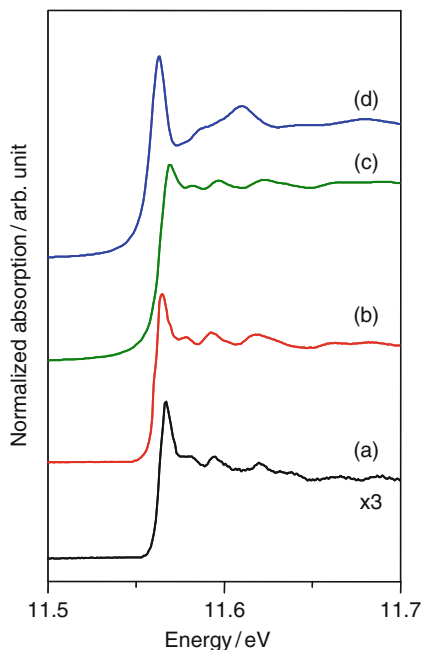


Fig. 15 Photocatalytic oxidation of CH_3CHO with O_2 on the TiO_2 thin films loaded with different amounts of Pt under UV light ($\lambda > 270 \text{ nm}$) irradiation

of the photocatalytic reactivity by Pt loading onto the TiO_2 photocatalyst, can be explained by the efficient charge separation of the photoformed electrons and holes in the TiO_2 semiconductor. Onishi et al. have reported that by using time-resolved

FT-IR measurements, the possibility for electron-hole recombination decreases when the TiO₂ powder loaded with Pt exists together with O₂ or methanol (Yamagata et al. 2001a, 2001b). The photo-generated electrons immediately transfer to Pt and the electrons trapped on the Pt sites catalyze the reduction of O₂ to form an O₂⁻ anion radical species while the photo-generated holes react with the organic compounds immediately at the TiO₂ surface, preventing charge recombination. Meanwhile, the further loading of Pt (more than 30 nm) decreased the photocatalytic reactivity. From XPS measurements, it was observed that when the loading amount of Pt was less than 10 nm, the coverage ratio of Pt on the TiO₂ surfaces could be estimated at less than 15%, indicating that the TiO₂ surface itself is exposed. In this case, the electrons trapped on the Pt sites can reduce O₂ and the holes trapped on the exposed TiO₂ surfaces can simultaneously oxidize the acetaldehyde. However, when the loading amount of Pt increased up to 30 nm, the surface of the TiO₂ thin films was mostly covered with Pt. In this case, the photoformed electrons in the TiO₂ semiconductors diffused onto the Pt surfaces but the photoformed electrons remained in the bulk of the TiO₂ thin films, resulting in a decrease of the photocatalytic performance.

References

- Anpo M (2000) Photofunctional zeolite. Nova, New York
- Anpo M (2004) Preparation, characterization, and reactivities of highly functional titanium oxide-based photocatalysts able to operate under UV-visible light irradiation: Approaches in realizing high efficiency in the use of visible light. *Bull Chem Soc Jpn* 77:1427
- Anpo M, Takeuchi M (2003) The design and development of highly reactive titanium oxide photocatalysts operating under visible light irradiation. *J Catal* 216:505
- Anpo M, Yamashita H (1996) Heterogeneous catalysis. Wiley, London
- Anpo M, Aikawa N, Kodama S, Kubokawa Y (1984) Photocatalytic hydrogenation of alkynes and alkenes with water over TiO₂ hydrogenation accompanied by bond fission. *J Phys Chem* 88:2569
- Anpo M, Shima T, Kodama S, Kubokawa Y (1987) Photocatalytic hydrogenation of CH₃CCH with H₂O on small-particle TiO₂ - Size quantization effects and reaction intermediates. *J Phys Chem* 91:4305
- Anpo M, Kawamura T, Kodama S, Maruya K, Onishi T (1988) Photocatalysis on titanium-aluminum binary metal oxides: enhancement of the photocatalytic activity of titania species. *J Phys Chem* 92:438
- Anpo M, Kondo M, Coluccia S, Louis C, Che M (1989) Application of dynamic photoluminescence spectroscopy to the study of the active surface sites on supported Mo/SiO₂ catalysts - Features of anchored and impregnated catalysts. *J Am Chem Soc* 111:8791
- Anpo M, Yamashita H, Ikeue K, Fujii Y, Zhang SG, Ichihashi Y, Park DR, Suzuki Y, Koyano K, Tatsumi T (1998) Photocatalytic reduction of CO₂ with H₂O on Ti-MCM-41 and Ti-MCM-48 mesoporous zeolite catalysts. *Catal Today* 44:327
- Anpo M, Dohshi S, Takeuchi M (2002) Preparation of Ti/B binary oxide thin films by the ionized cluster beam (ICB) method: their photocatalytic reactivity and photoinduced superhydrophilic properties. *J Ceramic Process Res* 3:258

- Dohshi S, Takeuchi M, Anpo M (2001) Photoinduced superhydrophilic properties of Ti-B binary oxide thin films and their photocatalytic reactivity for the decomposition of NO. *J Nanosci Nanotech* 1:337
- Ebitani K, Konno H, Tanaka T, Hattori H (1992) In-situ XPS study of zirconium-oxide promoted by platinum and sulfate ion. *J Catal* 135:60
- Fujishima A, Honda K (1972). Electrochemical photolysis of water at a semiconductor electrode. *Nature* 238:37
- Fujishima A, Hashimoto K, Watanabe T (1999) TiO_2 photocatalysis fundamentals and applications. BKC, Inc, Tokyo
- Fukushima K, Yamada I, Takagi T (1985). Characteristics of TiO_2 films deposited by a reactive ionized cluster beam. *J Appl Phys* 58:4146
- Grätzel M (1983) Energy resources through photochemistry and catalysis. Academic, New York
- Heller A (1995) Chemistry and applications of photocatalytic oxidation of thin organic films. *Acc Chem Res* 28:503
- Ikeue K, Yamashita H, Anpo M (2001) Photocatalytic reduction of CO_2 with H_2O on Ti- β zeolite photocatalysts: Effect of the hydrophobic and hydrophilic properties. *J Phys Chem B* 105:8350
- Jpn. Kokai Tokkyo (Jpn. Patent), No. 2002-161354 (2002)
- Kitano M, Takeuchi M, Matsuoka M, Thomas JM, Anpo M (2005) Preparation of Visible Light-responsive TiO_2 Thin Film Photocatalysts by an RF Magnetron Sputtering Deposition Method and Their Photocatalytic Reactivity. *Chem Lett* 34:616
- Kitano M, Tsujimaru K, Anpo M (2006) Decomposition of water in the separate evolution of hydrogen and oxygen using visible light-responsive TiO_2 thin film photocatalysts: Effect of the work function of the substrates on the yield of the reaction. *Appl Catal A-General* 314:179
- Kitano M, Matsuoka M, Ueshima M, Anpo M (2007). Recent developments in titanium oxide-based photocatalysts. *Appl Catal A: General* 325:1
- Machida M, Norimoto K, Watanabe T, Hashimoto K, Fujishima A (1999) The effect of SiO_2 addition in super-hydrophilic property of TiO_2 photocatalyst. *J Mater Sci* 34:2569
- Negishi N, Takeuchi K, Ibusuki T (1998) Surface structure of the TiO_2 thin film photocatalyst. *J Mater Sci* 33:5789
- Pelizzetti E, Schiavello M (1991) Photochemical conversion and storage of solar energy. Kluwer Academic, Amsterdam
- Sayari A, Dicko A (1994) The State of Platinum in Pt on Sulfated Zirconia Superacid Catalysts. *J Catal* 145:561
- Takeuchi M, Yamashita H, Matsuoka M, Anpo M, Hirao T, Itoh N, Iwamoto N (2000) Photocatalytic decomposition of NO on titanium oxide thin film photocatalysts prepared by an ionized cluster beam technique. *Catal Lett* 66:185
- Takeuchi M, Anpo M, Hirao T, Itoh N, Iwamoto N (2001a) Preparation of TiO_2 Thin Film Photocatalysts Working under Visible Light Irradiation by Applying a RF Magnetron Sputtering Deposition Method. *Surf Sci Jpn* 22:561
- Takeuchi M, Matsuoka M, Yamashita H, Anpo M (2001b) Preparation of Ti-Si binary oxide thin film photocatalysts by the application of an ionized cluster beam method. *J Synchrotron Rad* 8:643
- Takeuchi M, Dohshi S, Eura T, Anpo M (2003a) Preparation of titanium-silicon binary oxide thin film photocatalysts by an ionized cluster beam deposition method. Their photocatalytic activity and photoinduced super-hydrophilicity. *J Phys Chem B* 107:14278
- Takeuchi M, Tsujimaru K, Sakamoto K, Matsuoka M, Yamashita H, Anpo M (2003b) Effect of Pt loading on the photocatalytic reactivity of titanium oxide thin films prepared by ion engineering techniques. *Res Chem Intermed* 29:619
- Tanaka T, Shishido T, Hattori H, Ebitani K, Yoshida S (1995) The state of platinum in a Pt/ $\text{SO}_4^{2-}/\text{ZrO}_2$ super acid catalyst. *Physica B: Cond Matter* 208–209:649
- Venezia AM, Palmisano L, Schiavello M, Martin C, Martin I, Rives V (1994) Characterization of Chromium Ion-Doped Titania by FTIR and XPS. *J Catal* 147:115

- Wang R, Hashimoto K, Fujishima A, Chikuni M, Kojima E, Kitamura A, Shimohigoshi M, Watanabe T (1997) Light-induced amphiphilic surfaces. *Nature* 388:431
- Yamakata A, Ishibashi T, Onishi H (2001a) Time-resolved infrared absorption spectroscopy of photogenerated electrons in platinized TiO₂ particles. *Chem Phys Lett* 333:271
- Yamakata A, Ishibashi T, Onishi H (2001b) Water- and oxygen-induced decay kinetics of photogenerated electrons in TiO₂ and Pt/TiO₂: A time-resolved infrared absorption study. *J Phys Chem B* 105:7258
- Yamashita H, Anpo M (2004) Application of an ion beam technique for the design of visible light-sensitive, highly efficient and highly selective photocatalysts: ion-implantation and ionized cluster beam methods. *Catal Surv Asia* 8:35
- Yamashita H, Honda M, Harada M, Ichihashi Y, Anpo M, Hirao T, Itoh N, Iwamoto N (1998a) Preparation of titanium oxide photocatalysts anchored on porous silica glass by a metal ion-implantation method and their photocatalytic reactivities for the degradation of 2-propanol diluted in water. *J Phys Chem B* 102:10707
- Yamashita H, Kawasaki S, Ichihashi Y, Harada M, Takeuchi M, Anpo M (1998b) Characterization of titanium-silicon binary oxide catalysts prepared by the sol-gel method and their photocatalytic reactivity for the liquid-phase oxidation of 1-octanol. *J Phys Chem B* 102:5870
- Yamashita H, Kawasaki S, Takeuchi M, Fujii Y, Ichihashi Y, Suzuki Y, Park SE, Chang JS, Yoo JW, Anpo M (1998c) Photocatalytic reduction of CO₂ with H₂O on Ti/Si binary oxide catalysts prepared by the sol-gel method. *Stud Surf Sci Catal* 114:561

Chapter 6

UV Raman Spectroscopic Studies on Titania: Phase Transformation and Significance of Surface Phase in Photocatalysis

Jing Zhang, Qian Xu, Zhaochi Feng, and Can Li

Abstract Phase transformation of TiO_2 from anatase to rutile was studied by UV Raman spectroscopy with the excitation lines at 325 and 244 nm, visible Raman spectroscopy with the excitation line at 532 nm, X-ray diffraction (XRD) and transmission electron microscopy (TEM). It is found that UV Raman spectroscopy is more sensitive to the surface region of TiO_2 than visible Raman spectroscopy and XRD because TiO_2 strongly absorbs UV light. The anatase phase can be detected by UV Raman spectroscopy for the sample calcined at higher temperatures compared with that detected by visible Raman spectroscopy and XRD. It is suggested that the rutile phase nucleates at the interfaces of the contacting anatase particles; namely, for the agglomerated TiO_2 particles, the anatase phase in the inner region is easier to change into the rutile phase than that in the outer surface region. When the anatase particles are covered with highly dispersed La_2O_3 , the anatase phase can be stabilized both in the bulk and at the surface region even calcination at 900°C , owing to avoiding the direct contact of the anatase particles and occupying the surface defect sites of the anatase particles by La_2O_3 . Additionally, the La_2O_3 impregnation could effectively inhibit the growth of TiO_2 particles. The photocatalytic performance of TiO_2 samples with different surface phase structures was investigated. The surface-phase junction formed between the anatase nanoparticles and rutile particles can greatly enhance the photocatalytic activity for H_2 production.

C. Li (✉)

State Key Laboratory of Catalysis, Dalian Institute of Chemical Physics,
Chinese Academy of Sciences, Dalian, China
e-mail: canli@dicp.ac.cn

1 Instruction

Photocatalytic hydrogen production using semiconductor photocatalysts has attracted considerable interest because it has been considered an ideal method to deal with global energy problem. Among photocatalysts, TiO_2 appears to be one of the most promising and suitable materials because of its superior photocatalytic activity, chemical stability, low cost, and nontoxicity (Fujishima and Honda 1972; Grätzel 2001; Fox and Dulay 1993; Wang et al. 1997; Kamat 1993; O'Regan and Grätzel 1991). Heterogeneous photocatalysis utilizing TiO_2 materials has recently emerged as an efficient and feasible technology for the reduction of global atmospheric pollution and the purification of polluted water.

The structure of the two main polymorphs, rutile and anatase, can be discussed in terms of TiO_6 octahedrals. The two crystal structures differ by the distortion of each octahedron and by the assembly pattern of the octahedra chains (Linsebigler et al. 1995). These differences in lattice structures cause different mass densities and electronic band structures, and different physical and chemical properties. The anatase phase is suitable for catalysts and supports (Foger and Anderson 1986), while the rutile phase is used for optical and electronic purposes because of its high dielectric constant and high refractive index (Zhang et al. 1997). It has been well demonstrated that the crystalline phase of TiO_2 plays a significant role in catalytic reaction especially photocatalysis (Karakitsou and Verykios 1993; Zhu et al. 2004; Ding et al. 2000). Some studies have claimed that the anatase phase was more active than the rutile phase in photocatalysis (Karakitsou and Verykios 1993; Zhu et al. 2004).

Although at ambient pressure and temperature, the rutile phase is more thermodynamically stable than the anatase phase (Muscat et al. 2002); anatase is the common phase rather than rutile because anatase is kinetically stable in nanocrystalline TiO_2 at relatively low temperatures (Ovenston and Yanagisawa 1999). It is believed that the anatase phase transforms to the rutile phase over a wide range of temperatures (Shannon and Pask 1965). Therefore, understanding and controlling of the crystalline phase and the process of phase transformation of TiO_2 is important.

Catalytic performance of TiO_2 largely depends on the surface properties, where catalytic reaction takes place. For TiO_2 photocatalyst, the surface structure should be responsible for its photocatalytic activity because not only the photoinduced reactions take place on the surface (Linsebigler et al. 1995) but also the photoexcited electrons and holes might migrate through the surface region. Therefore, the surface phase of TiO_2 , which is exposed to the light source, should play a crucial role in photocatalysis. However, the surface phase of TiO_2 , particularly during the phase transformation has not been well investigated. The challenging question still remained: is the phase in the surface region the same as that in the bulk region, or how does the phase in the surface region of TiO_2 particle change during the bulk phase transformation? The difficulty in answering the above questions was mainly due to lacking suitable techniques that can sensitively detect the surface phase of TiO_2 .

UV Raman spectroscopy is found to be more sensitive to the surface phase of a solid sample when the sample absorbs UV light (Li et al. 2001, 2003; Li and Li 2002). This finding leads us to investigate the phase transformation in the surface region of TiO_2 by UV Raman spectroscopy as TiO_2 also strongly absorbs UV light. In this study, we compared the Raman spectra of TiO_2 calcined at different temperatures with excitation lines in the UV and visible regions. XRD and TEM were also recorded to understand the process of phase transformation of TiO_2 (Zhang et al. 2006).

2 UV Raman Spectroscopy

Raman spectroscopy is a light scattering process, which can be used to obtain information about the structure and properties of molecules from their vibrational transitions. Raman spectroscopy has been used in catalysis studies since the 1970s and it was expected that Raman spectroscopy would develop into one of the most useful techniques for the characterization of catalytic materials and catalytic reactions (Brown et al. 1977a, b; Brown and Maskovsky 1977). Although Raman spectroscopy has a number of potential applications in catalysis research, it is not as widely used in catalytic studies as expected. The main limitations are its relatively low sensitivity and

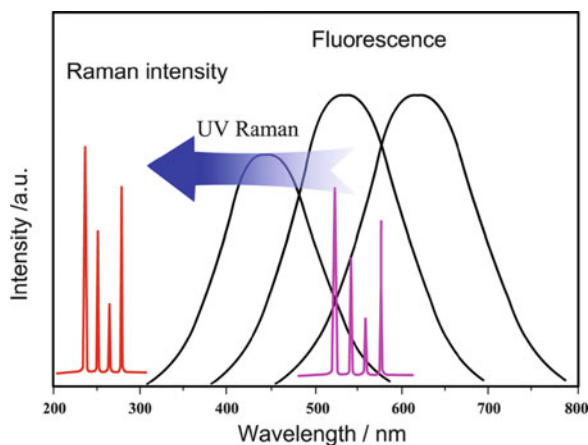


Fig. 1 The fluorescence bands appear mostly in the visible region from about 300 to 700 nm, and the Raman signal is usually obscured by the strong fluorescence interference. To avoid fluorescence interference in Raman spectrum, the Raman spectrum is shifted from the visible region to the UV region ($\lambda < 300$ nm), by shifting the excitation laser from the visible region to the UV region. Reprinted with permission from Journal of Catalysis, 216, Can Li, Identifying the isolated transition metal ions/oxides in molecular sieves and an oxide supports by UV resonance Raman spectroscopy, Copyright (2003), with permission from Elsevier

fluorescence interference (Knopps-Gerrits et al. 1997). Fluorescence interference could be avoided by shifting the excitation laser from the visible region usual for conventional Raman spectroscopy to the UV region (below 300 nm) without fluorescence interference (Fig. 1).

Since 1995, we have carried out the UV Raman spectroscopic studies of catalysts (Li and Stair 1996a) and studied sulfated zirconia (Li and Stair 1996b), coked catalysts (Li and Stair 1997; Li et al. 2000), zeolites and alumina-supported oxides (Xiong et al. 1999, 2000a, b; Li et al. 1999) and that all these have a strong fluorescence background in their visible Raman spectra, but are free of fluorescence interference in the UV Raman spectra. Hence, UV Raman spectroscopy opens up the possibility of characterizing those catalysts which are difficult to study by conventional visible Raman spectroscopy.

For UV Raman spectroscopy, not only is fluorescence avoided (Li 2003), but also the sensitivity can be improved (Stair and Li 1997). The Raman scattering intensity can be enhanced when the excitation laser is shifted from the visible (for conventional Raman) to the UV region because the Raman scattering is proportional to $1/\lambda^4$ (where λ is the wavelength of the scattering light, approximately that of the excitation laser). Furthermore, the Raman scattering can be greatly enhanced by the resonance Raman Effect, when the UV laser falls in the region of the electronic absorption of the samples.

More interestingly, UV Raman spectroscopy is found to be more sensitive to the surface phase of a solid sample when the sample absorbs UV light (Li et al. 2001, 2003; Li and Li 2002). We studied the phase transition of zirconia (ZrO_2) from tetragonal phase to monoclinic phase by UV Raman spectroscopy, visible Raman spectroscopy and XRD. Electronic absorption of ZrO_2 in the UV region makes UV Raman spectroscopy more surface sensitive than XRD or visible Raman spectroscopy. Zirconia transforms from the tetragonal phase to the monoclinic phase with calcination temperatures elevated and monoclinic phase is always detected first by UV Raman spectroscopy for the samples calcined at lower temperatures than that by XRD and visible Raman spectroscopy. UV Raman spectra clearly indicate that the surface phase of ZrO_2 is usually different from the bulk phase of ZrO_2 . Furthermore, the phase transition takes place initially at the surface regions and then gradually develops into its bulk when the ZrO_2 with tetragonal phase is calcined at elevated temperatures (Fig. 2).

For $\text{Y}_2\text{O}_3\text{-ZrO}_2$ and $\text{La}_2\text{O}_3\text{-ZrO}_2$, the transformation of the bulk phase from the tetragonal to the monoclinic is significantly retarded by the presence of yttrium oxide and lanthanum oxide (Li et al. 2003). However, the tetragonal phase in the surface region is difficult to stabilize, particularly when the content of stabilizer is low. The phase in the surface region can be more effectively stabilized by lanthanum oxide than yttrium oxide even though zirconia seemed to provide more enrichment in the surface region of the $\text{La}_2\text{O}_3\text{-ZrO}_2$ sample than the $\text{Y}_2\text{O}_3\text{-ZrO}_2$ sample, based on XPS analysis. Based on these findings, it is possible for us to further investigate the phase transformation, especially in the surface region of TiO_2 by UV Raman spectroscopy.

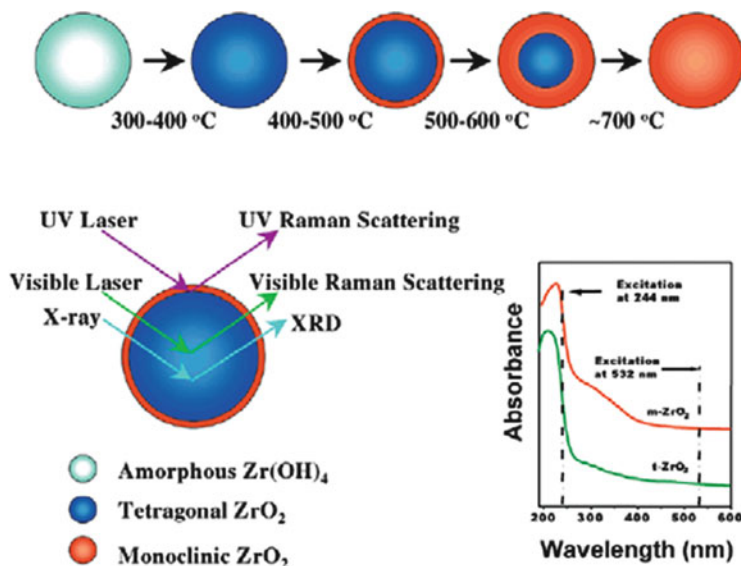


Fig. 2 Schematic description of the phase evolution of zirconia calcined at different temperatures and the information obtained from UV Raman spectroscopy, visible Raman spectroscopy, and XRD. The inset is the UV-visible absorbance of m- ZrO_2 and t- ZrO_2 . Reprinted with permission from Li et al. Copyright 2001 American Chemical Society

3 Spectral Characteristics of Anatase and Rutile TiO_2

Figure 3 shows UV-Vis diffuse reflectance spectra of the TiO_2 with anatase and rutile phase, respectively. For the anatase phase, the maximum absorption and the absorption band edge can be estimated to be around 324 and 400 nm, respectively. The maximum absorption and the absorption band edge shift to a little bit longer wavelength for the rutile phase (Bickley et al. 1991).

The anatase and rutile phase of TiO_2 can be sensitively identified by Raman spectroscopy. The anatase phase shows major Raman bands at 144, 197, 399, 515, 519 (superimposed with the 515 cm^{-1} band), and 639 cm^{-1} (Ohsaka et al. 1978). These bands can be attributed to the six Raman-active modes of anatase phase with the symmetries of E_g , E_g , B_{1g} , A_{1g} , B_{1g} , and E_g , respectively (Ohsaka et al. 1978). The typical Raman bands due to rutile phase appear at 143 (superimposed with the 144 cm^{-1} band due to anatase phase), 235, 447, and 612 cm^{-1} , which can be ascribed to the B_{1g} , two-phonon scattering, E_g , and A_{1g} modes of rutile phase, respectively (Chaves et al. 1974; West 1984). Additionally, the band at 144 cm^{-1} is the strongest one for the anatase phase and the band at 143 cm^{-1} is the weakest one for the rutile phase. Figure 4a, b display the Raman spectra of anatase and rutile TiO_2 with excitation lines at 532, 325, and 244 nm, respectively. Obviously, both visible Raman spectra and UV Raman spectra show that the TiO_2 sample is in the anatase and rutile phase.

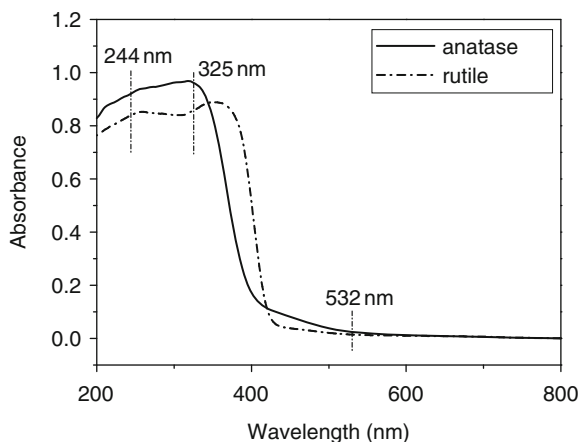


Fig. 3 UV-Vis diffuse reflectance spectra of TiO₂ calcined at 500 and 800°C. Reprinted with permission from Zhang et al. Copyright 2006. American Chemical Society

By comparing the Raman spectra of the anatase (Fig. 4a) or rutile phase (Fig. 4b) excited by 532, 325, and 244 nm lines, it is found that the relative intensities of characteristic bands due to anatase or rutile phase in the high frequency region are different. For the anatase phase (Fig. 4a), the band at 638 cm⁻¹ is the strongest one in the Raman spectrum with the excitation line at 325 or 532 nm while the band at 395 cm⁻¹ is the strongest one in the Raman spectrum with the excitation line at 244 nm.

For the rutile phase (Fig. 4b), the intensities of the bands at 445 and 612 cm⁻¹ are comparable in the visible Raman spectrum. The intensity of the band at 612 cm⁻¹ is stronger than that of the band at 445 cm⁻¹ in the Raman spectrum with the excitation line at 325 nm and the fact is reverse for the Raman spectrum with the excitation line at 244 nm. In addition, for the rutile phase, a band at approximately 826 cm⁻¹ appears in the UV Raman spectra. Some investigations show that the rutile phase of TiO₂ exhibits a weak band at 826 cm⁻¹ assigned to the B_{2g} mode (Chaves et al. 1974; West 1984).

The fact that the relative intensities of the Raman bands of anatase phase or rutile phase are different for UV Raman spectroscopy and the visible Raman spectroscopy are mainly due to the UV resonance Raman effect because the laser lines at 325 and 244 nm are in the electronic absorption region of TiO₂ (Fig. 3). There is no resonance Raman Effect observed for the TiO₂ sample excited by visible laser line because the line at 532 nm is outside of the absorption region of TiO₂ (Fig. 3). Therefore, for the anatase or rutile phase, the Raman spectroscopic characteristics in the visible Raman spectrum are different from those in the UV Raman spectrum. When different excitation lines of UV Raman spectroscopy are used, the resonance enhancement effect on the Raman bands of anatase or rutile phase is different. For example, for the rutile phase (Fig. 4b), the band at 612 cm⁻¹ is easily resonance enhanced when the excitation wavelength is 325 nm. Among all

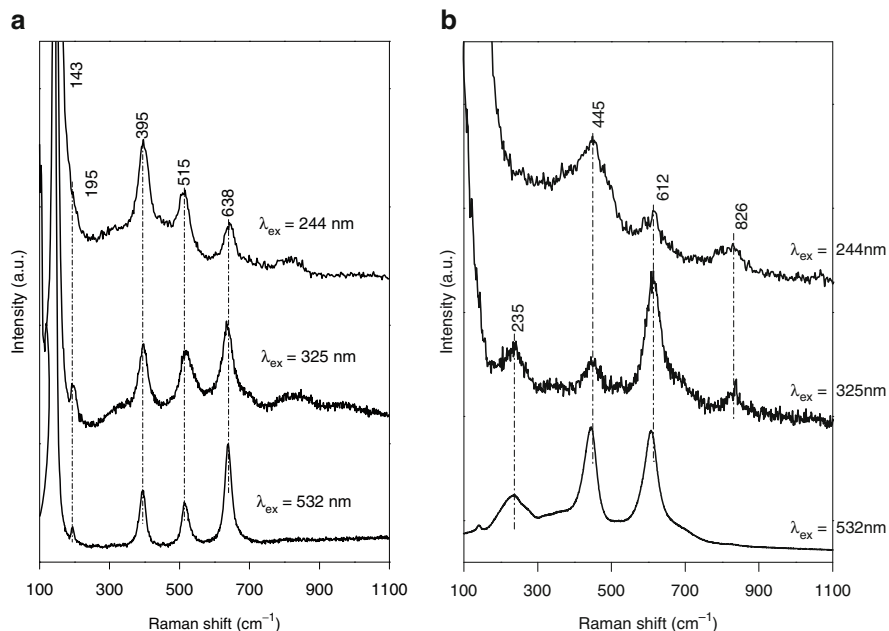


Fig. 4 (a) Raman spectra of TiO₂ calcined at 500°C with excitation lines at 532, 325, and 244 nm ($\lambda_{\text{ex}} = 532, 325, \text{ and } 244 \text{ nm}$). Reprinted with permission from Zhang et al. Copyright 2006 American Chemical Society. (b) Raman spectra of TiO₂ calcined at 800°C with excitation lines at 532, 325, and 244 nm ($\lambda_{\text{ex}} = 532, 325, \text{ and } 244 \text{ nm}$). Reprinted with permission from Zhang et al. Copyright 2006 American Chemical Society

the characteristic bands of the rutile phase, the extent of resonance enhancement of 445 cm⁻¹ is the strongest when the 244 nm laser is used as the excitation source (Fig. 4b).

4 Semiquantitative Analysis of the Phase Composition of TiO₂ by XRD and Raman Spectroscopy

The weight fraction of the rutile phase in the TiO₂ sample, W_R , can be estimated from the XRD peak intensities using the following formula (Gribb and Banfield 1997):

$$W_R = 1/[1 + 0.884(A_{\text{ana}}/A_{\text{rut}})]$$

Where A_{ana} and A_{rut} represent the X-ray integrated intensities of anatase (101) and rutile (110) diffraction peaks, respectively.

To estimate the weight fraction of the rutile phase in the TiO_2 sample by Raman spectroscopy, pure anatase phase and pure rutile phase of the TiO_2 sample, which have been prepared by calcination of TiO_2 powder at 500 and 800°C for 4 h, were mechanically mixed at given weight ratio and ground carefully to mix sufficiently.

Figure 5a displays the visible Raman spectra of the mechanical mixture with 1:1, 1:5, 1:10, 1:15, 5:1, and 10:1 ratios of anatase phase to rutile phase. The relationship between the area ratios of the visible Raman band at 395 cm^{-1} for anatase phase to the band at 445 cm^{-1} for rutile phase ($A_{395\text{cm}^{-1}}/A_{445\text{cm}^{-1}}$) and the weight ratios of anatase phase to rutile phase ($W_{\text{A}}/W_{\text{R}}$) is plotted in Fig. 5b. It can be seen that a linear relationship between the band area ratios and the weight ratios of anatase phase to rutile phase in the mixture is obtained. The rutile content in the Degussa P25, which usually consists of roughly about 80% anatase and 20% rutile phase (Yan et al. 2005) was estimated by this plot. Our Raman result indicates that the rutile content in the Degussa P25 is about 18.7%, which is close to the known result. Thus, above linear relationship based on visible Raman spectroscopy can be used to estimate the rutile content in TiO_2 .

Figure 6a presents the UV Raman spectra of mechanical mixture with 1:1, 1:2, 1:4, 1:6, 1:10, and 1:15 ratios of anatase phase to rutile phase with the excitation line at 325 nm. Figure 6b shows the plot of the area ratios of the UV Raman band at 612 cm^{-1} for rutile phase to the band at 638 cm^{-1} for anatase phase ($A_{612\text{cm}^{-1}}/A_{638\text{cm}^{-1}}$) versus the weight ratios of rutile phase to anatase phase ($W_{\text{R}}/W_{\text{A}}$). There is also a linear relationship between the band area ratios and the weight ratios of rutile phase to anatase phase.

5 Phase Transformation of TiO_2 at Elevated Calcination Temperatures

Many studies (Ovenstone and Yanagisawa 1999; Shannon and Pask 1965; Zhang and Banfield 2000a; Gouma and Mills 2001; Penn and Banfield 1999; Ma et al. 1998; Zhang et al. 1998; Busca et al. 1994; Hwu et al. 1997; Okada et al. 2001; Yoshinaka et al. 1997; Yang et al. 2000; Ozaki and Iida 1961; Navrotsky and Kleppa 1967; Ahonen et al. 1999; Lee and Zuo 2004; Ranade et al. 2002; Zhang and Banfield 2000b) have been carried out to understand the process of the phase transformation of TiO_2 . Shannon and Pask (1965) studied the phase transformation of anatase single crystals. They showed that the rutile phase nucleated at the surface and spread into the internal anatase phase during the phase transition, and the rutile phase has a slower surface energy compared to that of the anatase phase. Lee and Zuo (2004) studied the growth and phase transformation of nanometer-sized titanium oxide powders prepared by the precipitation method. In situ TEM observations showed

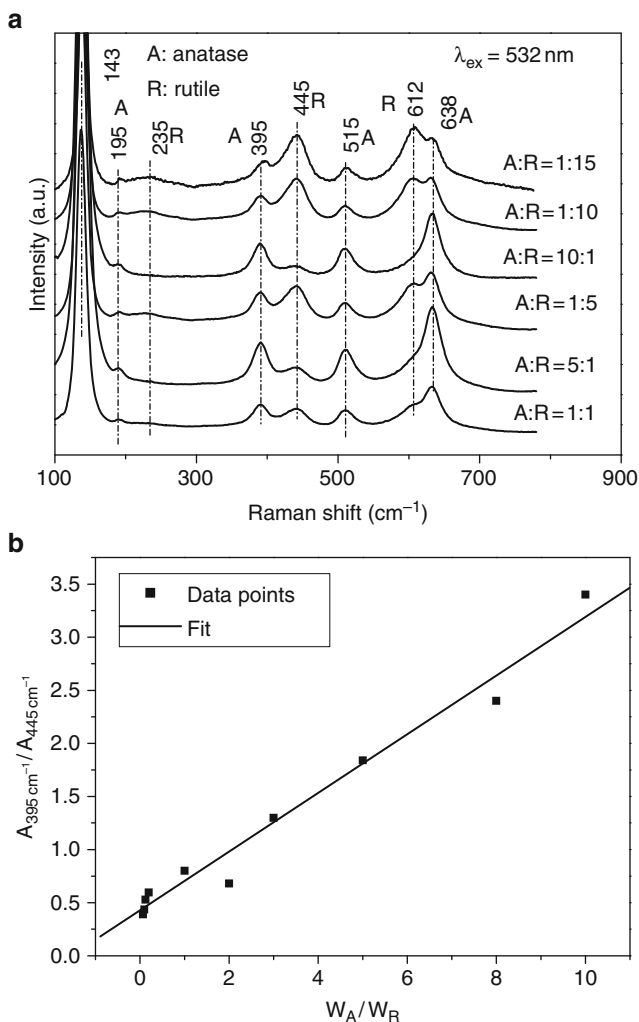


Fig. 5 (a) Visible Raman spectra of mechanical mixture with 1:1, 1:5, 1:10, 1:15, 5:1, and 10:1 ratios of anatase phase to rutile phase with the excitation line at 532 nm. (b) Plot of the area ratios of the visible Raman band at 395 cm^{-1} for anatase phase to the band at 445 cm^{-1} for rutile phase ($A_{395 \text{ cm}^{-1}}/A_{445 \text{ cm}^{-1}}$) versus the weight ratios of anatase phase to rutile phase (W_A/W_R). Reprinted with permission from Zhang et al. Copyright 2006 American Chemical Society

that the anatase particles were absorbed into rutile, and then rutile particles grew by coalescence (Fig. 7).

Zhang and Banfield (2000a) proposed that the mechanism of anatase-rutile phase transformation was temperature-dependent according to the kinetic data from XRD. The predominant nucleation mode may change from interface nucleation at low temperatures to surface nucleation at intermediate temperatures and to bulk

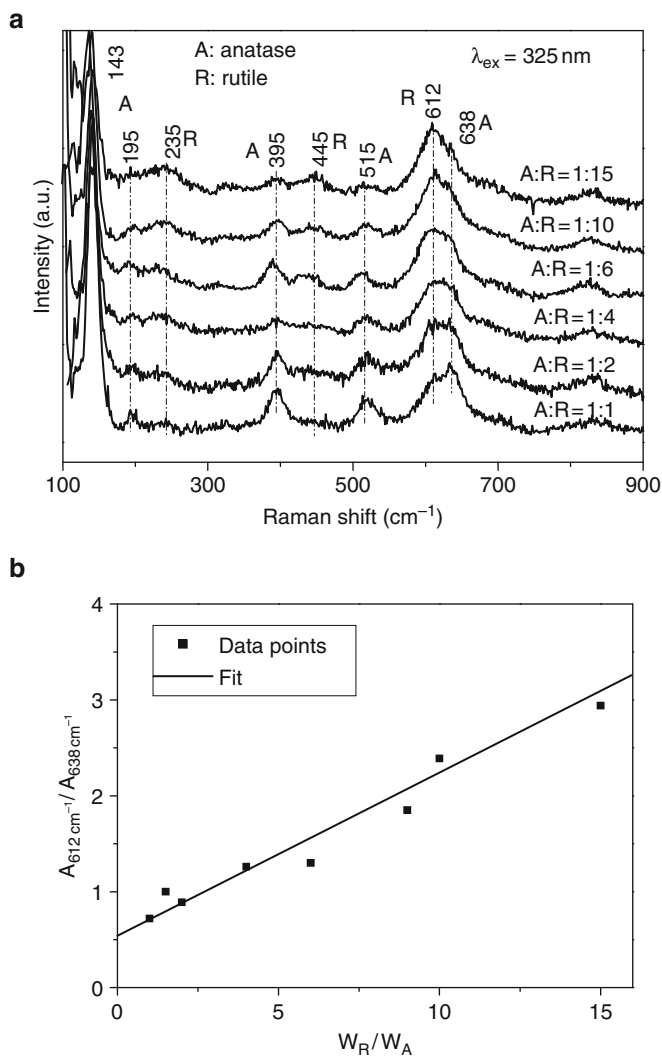


Fig. 6 (a) UV Raman spectra of mechanical mixture with 1:1, 1:2, 1:4, 1:6, 1:10, and 1:15 ratios of anatase phase to rutile phase with the excitation line at 325 nm. (b) Plot of the area ratios of the UV Raman band at 612 cm^{-1} for rutile phase to the band at 638 cm^{-1} for anatase phase ($A_{612 \text{ cm}^{-1}}/A_{638 \text{ cm}^{-1}}$) versus the weight ratios of rutile phase to anatase phase (W_R/W_A). Reprinted with permission from Zhang et al. Copyright 2006 American Chemical Society

nucleation at very high temperatures (Fig. 8). Based on transmission and scanning electron microscopy, Gouma and Mills (2001) suggested that rutile nuclei formed on the surface of coarser anatase particles and the newly transformed rutile particles grew at the expense of neighboring anatase particles. Penn and Banfield (1999)

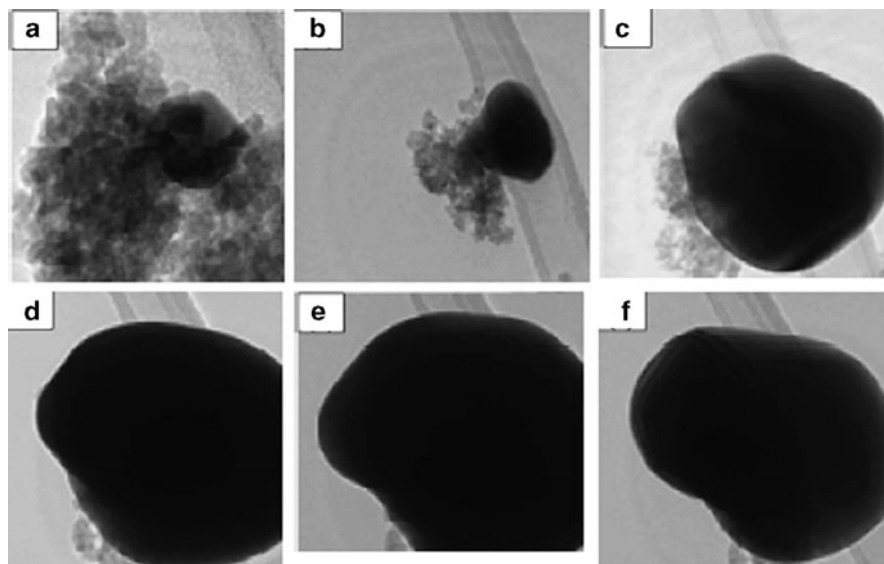


Fig. 7 In situ TEM observation of rutile particle growth. The TEM micrographs show the absorption of the anatase particles into a rutile particle heated at (a) 710° C, (b) 800° C (0 min), (c) 800° C (31 min), (d) 800° C (160 min), (e) 800° C (211 min), and (f) after cooling. Reprint with permission from Lee and Zuo. Copyright 2004 Wiley

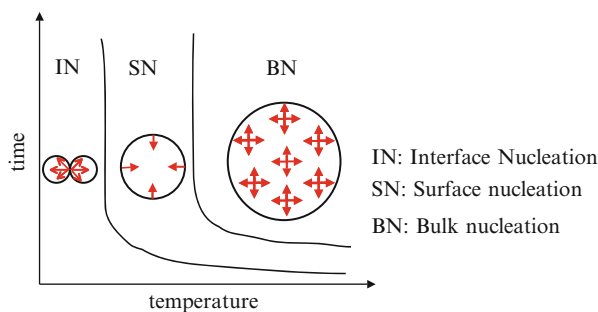


Fig. 8 The time and temperature dependence of the three dominant regions. Reprinted with permission from Zhang et al. Copyright 2000 Wiley

suggested that the formation of rutile nuclei at {112} twin interfaces of anatase particles heated hydrothermally (Fig. 9).

Figure 10 shows the XRD patterns of TiO₂ calcined at different temperatures. The “A” and “R” in the figure denote the anatase and rutile phases, respectively. For the sample before calcination, diffraction peaks due to the crystalline phase are not observed, suggesting that the sample is still in the amorphous phase. When the sample was calcined at 200°C, weak and broad peaks at $2\theta = 25.5, 37.9, 48.2, 53.8,$ and 55.0° are observed. These peaks represent the indices of (101), (004), (200), (105), and (211)

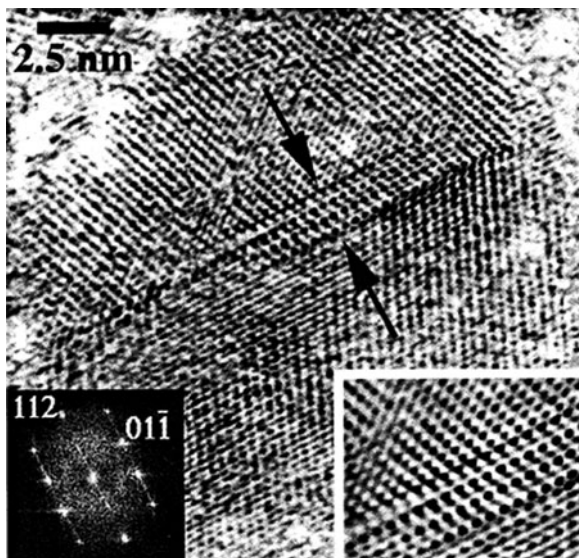


Fig. 9 Rutile nuclei (indicated *arrows*) on the {112} anatase twin surface (viewed down [131] anatase). Inset (lower right) shows rotationally filtered interface. Reproduced with permission from Penn et al. Copyright 1999 from the Mineralogical Society of America

planes of anatase phase, respectively (Sreethawong et al. 2005). These results suggest that some portions of the amorphous phase transform into the anatase phase. The diffraction peaks due to anatase phase develop with increasing the temperature of calcination. When the calcination temperature was increased to 500°C, the diffraction peaks due to anatase phase become narrow and intense in intensity. This indicates that the crystallinity of the anatase phase is further improved (Tsai and Cheng 1997).

When the sample was calcined at 550°C, weak peaks are observed at $2\theta = 27.6, 36.1, 41.2,$ and 54.3° , which correspond to the indices of (110), (101), (111), and (211) planes of rutile phase (Sreethawong et al. 2005). This indicates that the anatase phase starts to transform into the rutile phase at 550°C. The diffraction peaks of anatase phase gradually diminish in intensity and the diffraction patterns of rutile phase become predominant with the calcination temperatures from 580 to 700°C. These results clearly show that the phase transformation from anatase to rutile progressively proceeds at the elevated temperatures. The diffraction peaks assigned to anatase phase disappear at 750°C, indicating that the anatase phase completely changes into the rutile phase. The diffraction peaks of rutile phase become quite strong and sharp after the sample was calcined at 800°C, owing to the high crystallinity of the rutile phase.

Figure 11 displays the visible Raman spectra of TiO₂ calcined at different temperatures. For the sample before calcination, two broad bands at about 430 and 605 cm⁻¹ are observed, indicating that the sample is in the amorphous phase (Zhang et al. 1998). For the sample calcined at 200°C, a Raman band at 143 cm⁻¹ is observed and the high frequency region is interfered by fluorescence background,

which might come from organic species. After calcination at 300°C, other characteristic bands of anatase phase appear at 195, 395, 515, and 638 cm^{-1} , but some portions of the sample may exist in the amorphous phase because there is still broad background in Fig. 6.

It is found that, when the sample was calcined at 400°C, the fluorescence disappears possibly because the organic residues were removed by the oxidation. The bands of anatase phase increase in intensity and decrease in line width when the sample was calcined at 500°C. This result suggests that the crystallinity of the anatase phase is greatly improved (Ma et al. 1998), which is confirmed by XRD (Fig. 10). Besides the bands at 395, 515, and 638 cm^{-1} , two very weak bands at 320 and 796 cm^{-1} are observed. These two bands can be assigned to a two-phonon scattering band and a first overtone of B_{1g} at 396 cm^{-1} , respectively (Ohsaka et al. 1978). It is noteworthy that a very weak band appears at 445 cm^{-1} due to rutile phase for the sample calcined at 550°C. This indicates that the anatase phase starts to change into the rutile phase at 550°C. This result is in good agreement with that of XRD patterns (Fig. 10). The weight percentage of the rutile phase in the samples

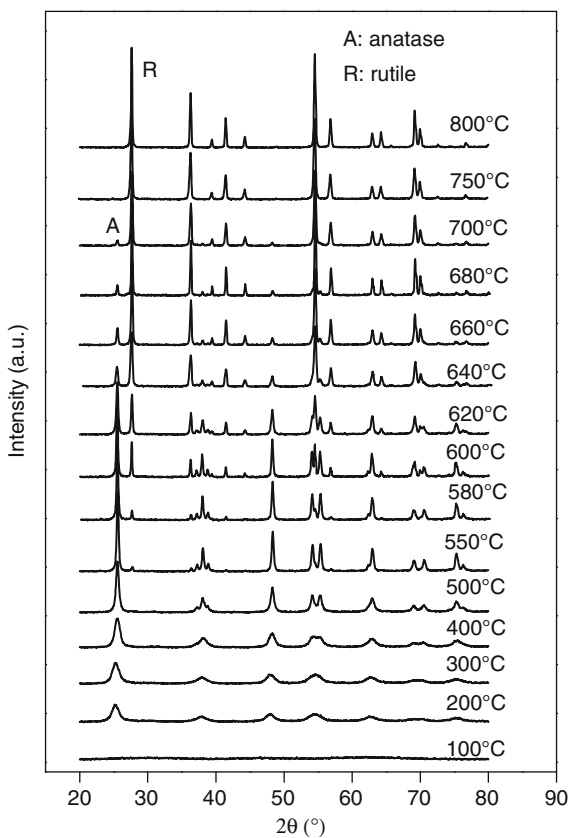
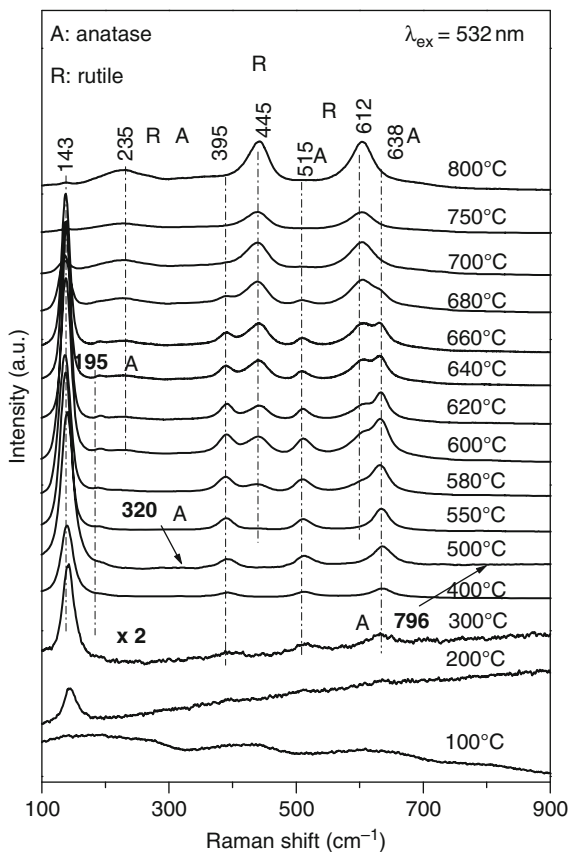


Fig. 10 XRD patterns of TiO₂ calcined at different temperatures. Reprinted with permission from Zhang et al. Copyright 2006 American Chemical Society

Fig. 11 Visible Raman spectra of TiO₂ calcined at different temperatures with the excitation line at 532 nm. Reprinted with permission from Zhang et al. Copyright 2006 American Chemical Society



calcined at different temperatures was estimated by visible Raman spectroscopy and XRD (shown in Fig. 12). As seen from Fig. 12, the rutile content estimated from visible Raman spectrum and XRD pattern of the sample calcined at 550°C is 4.2 and 5.7%, respectively. It can be seen that the rutile content estimated by visible Raman spectroscopy and XRD is also in accordance with each other.

When the sample was calcined at 580°C, the other two characteristic bands are observed at 235 and 612 cm⁻¹ due to Raman-active modes of rutile phase. Figure 12 shows that the rutile content is 13.6 and 10.9% based on the visible Raman spectrum and XRD pattern of the sample calcined at 580°C. The intensities of the bands of rutile phase (235, 445, and 612 cm⁻¹) increase steadily while those of the bands of anatase phase (195, 395, 515, and 638 cm⁻¹) decrease when the calcination temperatures were elevated from 600 to 680°C (Fig. 11). These results suggest that the TiO₂ sample undergoes the phase transformation from anatase to rutile gradually. The rutile content was estimated for the samples calcined from 600 to 680°C based on the visible Raman spectra. The result shows that the content of the rutile phase is increased from 33.1 to 91.2% respectively for the samples calcined at

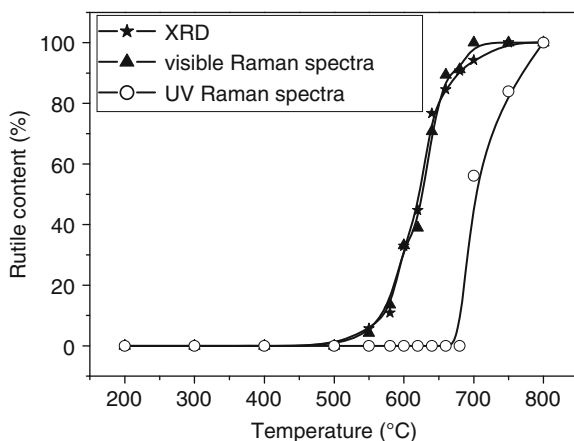


Fig. 12 The weight percentage of the rutile phase in the TiO_2 sample calcined at different temperatures estimated by visible Raman spectroscopy, XRD, and UV Raman spectroscopy

600 and 680°C (Fig. 12). The XRD results corresponding to the above two samples indicate that the rutile content is changed from 32.9 to 90.7% (Fig. 12). These results clearly show that the rutile content in the sample estimated by visible Raman spectroscopy is agreement with that estimated by XRD.

The Raman spectrum of the sample calcined at 700°C shows mainly the characteristic bands of rutile phase, but the very weak bands of anatase phase are still observed (Fig. 11). When the sample was calcined at 750°C, the bands of anatase phase disappear and only the bands due to rutile phase (143, 235, 445, and 612 cm^{-1}) are observed. These results indicate that the anatase phase completely transforms into the rutile phase, which are consistent with the results from XRD (Fig. 10). When the temperature was increased to 800°C, the intensity of characteristic bands due to rutile phase increase further.

Both the results of XRD and visible Raman spectra (Figs. 10 and 11) show that the anatase phase appears at around 200°C and perfect anatase phase is formed after calcination at temperature 400–500°C. The rutile phase starts to form at 550°C, and the anatase phase completely transforms into the rutile phase at 750°C. The signals of visible Raman spectra come mainly from the bulk region of TiO_2 because the TiO_2 sample is transparent in the visible region (Fig. 3) (Li et al. 2001, 2003; Li and Li 2002). XRD is known as a bulk sensitive technique. Therefore, it is essentially in agreement between the results of visible Raman spectra and XRD patterns.

UV-Vis diffuse reflectance spectra (Fig. 3) clearly show that TiO_2 has strong electronic absorption in the UV region. Thus, the UV Raman spectra excited by UV laser line contain more signal from the surface skin region than the bulk of the TiO_2 sample because the signal from the bulk is attenuated sharply due to the strong absorption (Li et al. 2001, 2003; Li and Li 2002). Therefore, if a UV laser line in the absorption region of TiO_2 is used as the excitation source of Raman spectroscopy, the information from UV Raman spectra is often different from that of visible Raman spectra.

The laser line at 325 nm was selected as the excitation source of the UV Raman spectra. The UV Raman spectra and the content of the rutile phase of the TiO₂ sample calcined at different temperatures are shown in Figs. 13a and 12, respectively. When the sample was calcined at 200 or 300°C, the Raman band at 143 cm⁻¹ with a shoulder band at 195 cm⁻¹ together with three broad bands at 395, 515, and 638 cm⁻¹ are observed, indicating that the anatase phase is formed in the sample. But the low intensity and the broad band indicate that the amorphous phase still remains in the sample. It can be seen that the fluorescence in the high frequency region can be avoided when the UV laser line is used as the excitation line. However, the corresponding visible Raman spectra (Fig. 11) are interfered by the fluorescence.

All bands assigned to anatase phase become sharp and strong after calcination at 500°C (Fig. 13a). These results are in agreement with those of XRD and visible Raman spectra (Figs. 10 and 11). The UV Raman spectra of the sample with the calcination temperatures from 550 to 680°C are essentially the same as those of the sample calcined at 500°C (Fig. 13a). But according to the XRD patterns and visible Raman spectra (Figs. 10 and 11), the anatase phase starts to transform into the rutile phase at only 550°C and the anatase phase gradually changes into the rutile phase in the temperature range of 550–680°C.

After calcination at 700°C, a new band at 612 cm⁻¹ and two weak bands at 235 and 445 cm⁻¹ due to rutile phase appear while the intensities of the bands of anatase phase begin to decrease (Fig. 13a). Based on the UV Raman spectrum and XRD pattern of the sample calcined at 700°C, the rutile content in the sample is 56.1 and 97.0%, respectively (Fig. 12). It is found that the rutile content estimated by UV Raman spectroscopy is far less than that estimated by XRD.

When the sample was calcined at 750°C, the intensities of the bands due to rutile phase increase, but the intensities of the bands due to anatase phase are still strong in the UV Raman spectra (Fig. 13a). UV Raman spectrum of the sample calcined at 750°C indicates that the rutile content is 84.3% (Fig. 12). However, the results of XRD and visible Raman spectrum (Figs. 10 and 11) suggest that the anatase phase totally transforms into the rutile phase after the sample was calcined at 750°C. The characteristic bands due to anatase phase disappear and the sample is in the rutile phase after calcination at 800°C (Fig. 13a). Obviously, there are distinct differences between the results from the UV Raman spectra, visible Raman spectra, and XRD patterns. It seems that the anatase phase remains at relatively higher temperatures when detected by UV Raman spectroscopy than by XRD and visible Raman spectroscopy.

Another UV laser line at 244 nm was also selected as the excitation source of UV Raman spectroscopy in order to get further insights into the phase transformation of TiO₂. The results of the UV Raman spectra of TiO₂ calcined at different temperatures with the excitation line at 244 nm are presented in Fig. 13b. When the sample was calcined at 200°C, four broad bands were observed at 143, 395, 515, and 638 cm⁻¹, which clearly indicate that the anatase phase exists in the sample. The intensities of the Raman bands due to anatase phase (143, 395, 515, and 638 cm⁻¹) become strong after calcination at 500°C. The UV Raman spectra hardly change for

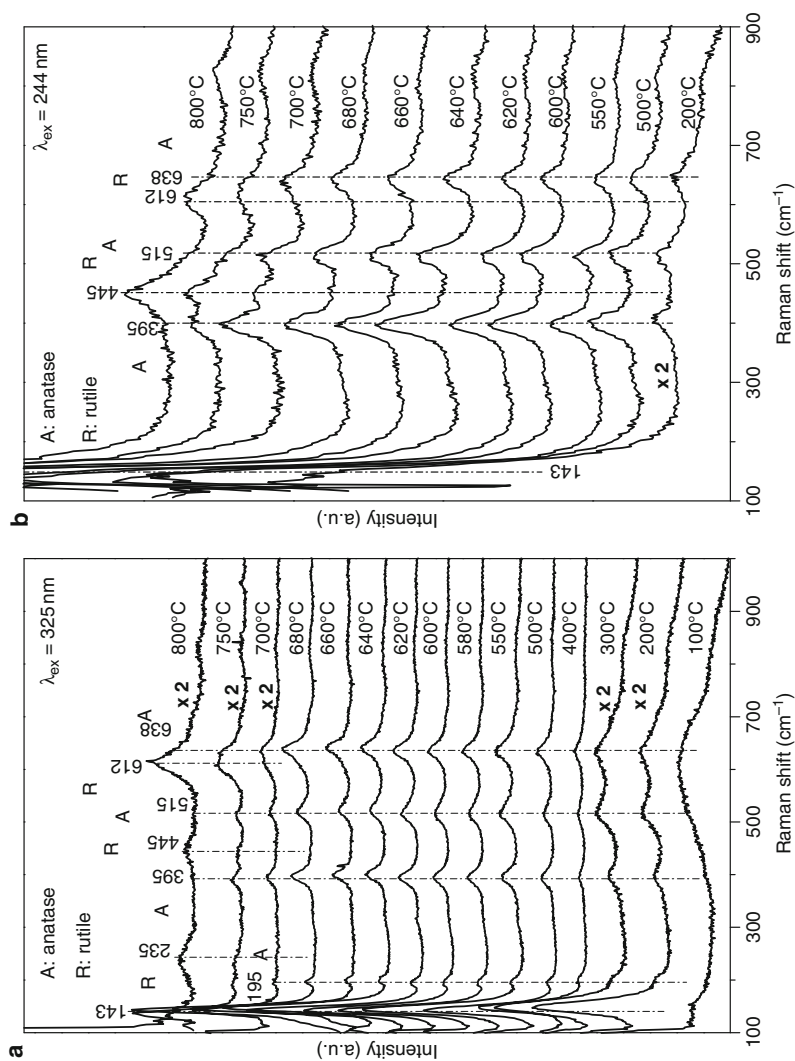


Fig. 13 (a) UV Raman spectra of TiO_2 calcined at different temperatures with the excitation line at 325 nm. Reprinted with permission from Zhang et al. Copyright 2006 American Chemical Society. (b) UV Raman spectra of TiO_2 calcined at different temperatures with the excitation line at 244 nm. Reprinted with permission from Zhang et al. Copyright 2006 American Chemical Society

the sample calcined at different temperatures even up to 680°C. The characteristic bands (445 and 612 cm^{-1}) of rutile phase appear only when the calcination temperature exceeds 700°C. This result is in good agreement with that from the UV Raman spectrum with 325 nm excitation of the sample calcined at 700°C (Fig. 13a). The intensities of the bands due to anatase phase (395, 515, and 638 cm^{-1}) decrease while those of bands assigned to rutile phase (445 and 612 cm^{-1}) increase after calcination at 750°C (Fig. 13b). When the sample was calcined at 800°C, the Raman bands due to anatase phase disappear, while the bands of rutile phase develop. This result indicates that the sample calcined at 800°C is in the rutile phase. It is interesting to note that the results of the UV Raman spectra with the excitation lines at 325 and 244 nm are consistent with each other but are different from those of XRD patterns and visible Raman spectra.

It has been clearly shown that the results of visible Raman spectra (Fig. 11) are in good agreement with the results from XRD patterns (Fig. 10) but different from those of UV Raman spectra (Fig. 13) for TiO_2 calcined at elevated temperatures. The inconsistency in the results from the three techniques can be explained by the fact that UV Raman spectroscopy provides the information mainly from surface region while visible Raman spectroscopy and XRD from bulk of TiO_2 . The discrepant results of UV Raman spectra, visible Raman spectra and XRD patterns are attributed to their different detective depth for TiO_2 particle (Li et al. 2001, 2003; Li and Li 2002).

The disagreements of UV Raman spectra, visible Raman spectra and XRD patterns suggest that the crystal phase in the surface region is different from that in the bulk during the phase transformation of TiO_2 . Busca et al. (1994) characterized the Degussa P25 using FT Raman spectroscopy and XRD technology. They estimated the rutile-to-anatase ratio by Raman spectroscopy and XRD, and found that the ratio estimated by Raman spectroscopy for the Degussa P25 was smaller than that evaluated by XRD. Therefore, they assumed that the rutile phase in the Degussa P25 was more concentrated in the bulk because Raman spectroscopy excited by near IR laser line should be more surface-sensitive than XRD. Different from their investigations, our experimental results give direct UV Raman evidences to show that the phases in the surface region are generally different from that in the bulk region of TiO_2 , particularly when TiO_2 is in the transition stage of the phase transformation.

As presented above, the anatase phase can remain at relatively higher temperatures as observed by UV Raman spectroscopy than by visible Raman spectroscopy and XRD. These facts lead us to the conclusion that the phase transformation of TiO_2 takes place from its bulk region and then extends to its surface region.

To further understand the process of the phase transformation of TiO_2 , we used TEM technique to observe the microstructure of the sample calcined at 500, 600, and 800°C (shown in Fig. 14). The most particles in the sample calcined at 500°C exhibit diameters in a range between 10 and 30 nm. On the other hand, remarkable agglomeration is observed for the TiO_2 sample calcined at 500°C. The particle size increases after calcination at 600°C. According to the results of XRD and visible Raman spectra (Figs. 10 and 11), the sample undergoes the phase transformation

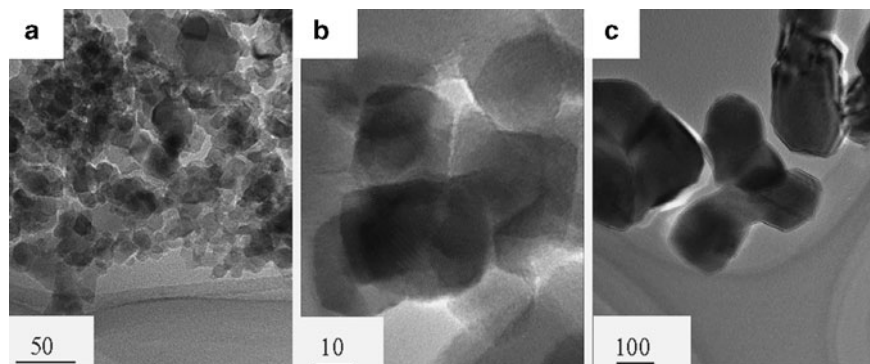


Fig. 14 TEM images of TiO_2 calcined at (a) 500°C, (b) 600°C, and (c) 800°C. Reprinted with permission from Zhang et al. Copyright 2006 American Chemical Society

from anatase to rutile gradually in the temperature range of 550–680°C. These results imply that the phase transformation and growth of the particle size are interrelated. Many researchers (Kumar 1995; Hague and Mayo 1993; Banfield et al. 1993; Mackenzie 1975; Kumar et al. 1992) reported similar phenomena. Kumar et al. (Kumar 1995) attributed this particle size growing to the higher atomic mobility because of bond breakage during the phase transformation. When the calcination temperature was increased to 800°C, TiO_2 particles further grow and the particle size can be as big as about 200 nm.

According to TEM measurements Penn and Banfield (1999) suggested that structural elements with rutilelike character can be produced at a subset of anatase interfaces, and these might serve as rutile nucleation sites. Lee and Zuo (2004) investigated the growth and transformation in nanometer-sized TiO_2 powders by in situ TEM. The nucleation of rutile was found to occur at the amorphous interface of anatase particles where there are strain and disorder. Based on the experimental observations and combined with the results from the literature, we suggest that the phase transformation of TiO_2 starts from the interfaces among the anatase particles of the agglomerated TiO_2 particles. Based on kinetic data from XRD, Zhang and Banfield (2000a) also proposed that interface nucleation dominated the transformation for nanocrystalline anatase samples with denser particle packing below 620°C, or in the temperature range of 620–680°C.

A proposed scheme for the phase transformation of TiO_2 with increasing calcination temperature is illustrated in Fig. 15. The TiO_2 particles with anatase phase intimately contact with each other. Thus, the surface and the bulk region of the TiO_2 sample actually refer to respectively the outer surface region and the inner region of agglomerated TiO_2 particles. The interfaces of contacting anatase particles, which only present in the inner region of agglomerated particles, provide the nucleation sites of the rutile phase. Therefore, the rutile phase is first detected by XRD and visible Raman spectroscopy for the sample calcined at 550–680°C. Once phase transformation takes place, the particle size increases rapidly. The agglomeration of the TiO_2 particles is along with the phase transformation from anatase to rutile.

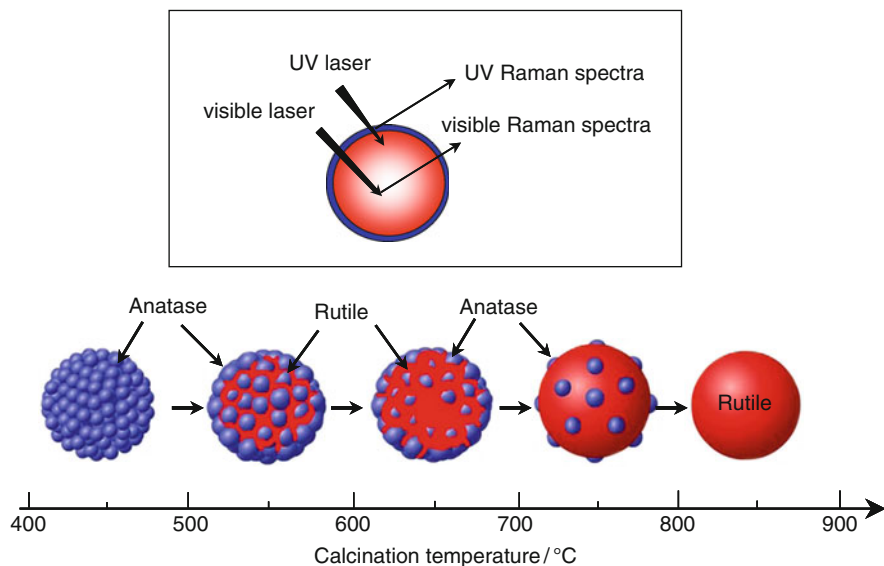


Fig. 15 A proposed scheme for the phase transformation of TiO_2 with increasing calcination temperature. Reprinted with permission from Zhang et al. Copyright 2006 American Chemical Society

The rutile phase needs fairly high temperature to progressively develop into the whole conglomeration composed of some neighboring particles coalescence as the phase transformation is a diffusing process. Thus, the outer surface region of the agglomerated particles without directly interacting with other particles maintains in the anatase phase when the calcination temperature is below 680°C . Accordingly, UV Raman spectroscopy detect only the anatase phase in the outer region of agglomerated particles in the temperature range of $550\text{--}680^\circ\text{C}$.

When the calcination temperature is higher than 700°C , the anatase phase of the outer surface region of agglomerated particles begins to change into the rutile phase. Therefore, the mixed phases of anatase and rutile are observed by UV Raman spectroscopy but the inner region of agglomerated particles is nearly in the rutile phase. Both XRD and visible Raman spectra show that the inner region of agglomerated particles is in the rutile phase when the sample is calcined at 750°C . However, the phase transformation is still not yet complete because the outer surface region is still in the mixed phases of anatase and rutile. After calcination at 800°C , the anatase phase in the outer surface region completely transforms to the rutile phase, the whole agglomerated particles are in the rutile phase.

Following the above reasoning, for the agglomerated particles of TiO_2 , the rutile phase nucleates at the interfaces of contacting anatase particles. However, from the point view of a single anatase crystal particle, the rutile phase starts to form at the surface of TiO_2 , where it is in contact with other particles. It is reasonably assumed that the phase transformation of single particle might start from the surface, where

there is no direct interaction with other particles, but it needs high temperature. Zhang et al. (Zhang and Banfield 2000a) indicated that thermal fluctuation of Ti and O atoms in anatase is not strong enough to generate rutile nuclei on the surfaces or in the bulk of the anatase particles at lower temperatures.

When the small anatase particles agglomerated into large particles, interface nucleation is easier, as compared to nucleation at the surface, where there is no contact with other particles. Zhang and Banfield (2000a) indicated that the activation energy for surfaces nucleation is expected to be higher than that for interfaces nucleation. Therefore, we observed the phenomenon that crystalline phase in the outer surface region of agglomerated TiO₂ particles is different from that in the inner region of agglomerated TiO₂ particles.

6 Phase Transformation of TiO₂ with La₂O₃ Loading

If the direct contact between anatase particles of TiO₂ is avoided, the phase transformation of TiO₂ from anatase to rutile could be retarded or prohibited. This assumption may be verified by covering the surface of anatase TiO₂ with an additive. It has been reported that La³⁺ did not enter into the crystal lattices of TiO₂ and was uniformly dispersed onto TiO₂ as the form of lanthana (La₂O₃) particles with small size (Jing et al. 2004; Xie and Tang 1990; Gopalan and Lin 1995). In order to verify the above assumption, this study also prepared the anatase phase of TiO₂ sample covered with La₂O₃ and characterized the above sample by XRD, visible Raman spectroscopy and UV Raman spectroscopy.

Figure 16a displays the visible Raman spectra of La₂O₃/TiO₂ with increasing La₂O₃ loading. TiO₂ support is in the anatase phase because only characteristic bands (143, 195, 395, 515, and 638 cm⁻¹) due to anatase phase are observed. When the TiO₂ support was calcined at 900°C (TiO₂-900), the Raman spectrum gives the characteristic bands of rutile phase, indicating that the TiO₂-900 sample is in the rutile phase. We firstly studied the crystalline phase of 6 wt% La₂O₃/TiO₂ calcined at 900°C. Only characteristic bands of anatase phase are observed, suggesting that the TiO₂ sample retains its anatase phase when La₂O₃ loading is 6 wt% while the TiO₂-900 sample is in the rutile phase. With decreasing the La₂O₃ loading to 3 or 1 wt%, it is observed that the TiO₂ sample can still be stabilized at its anatase phase.

It should be noted that TiO₂ sample maintain the anatase phase even when the La₂O₃ loading is only 0.5 wt%. The spectra of the sample with the La₂O₃ loadings from 1 to 6 wt% are almost the same as those for the sample with 0.5 wt% La₂O₃ loading, except for a small decrease in intensity. Figure 16b shows XRD patterns of La₂O₃/TiO₂ with increasing La₂O₃ loading. When the loading of La₂O₃ is varied from 0.5 to 6 wt%, it is obvious that the samples are stabilized at their anatase phase both in bulk and in the surface region even after the calcination at 900°C. The results from XRD patterns agree well with those of visible Raman spectra.

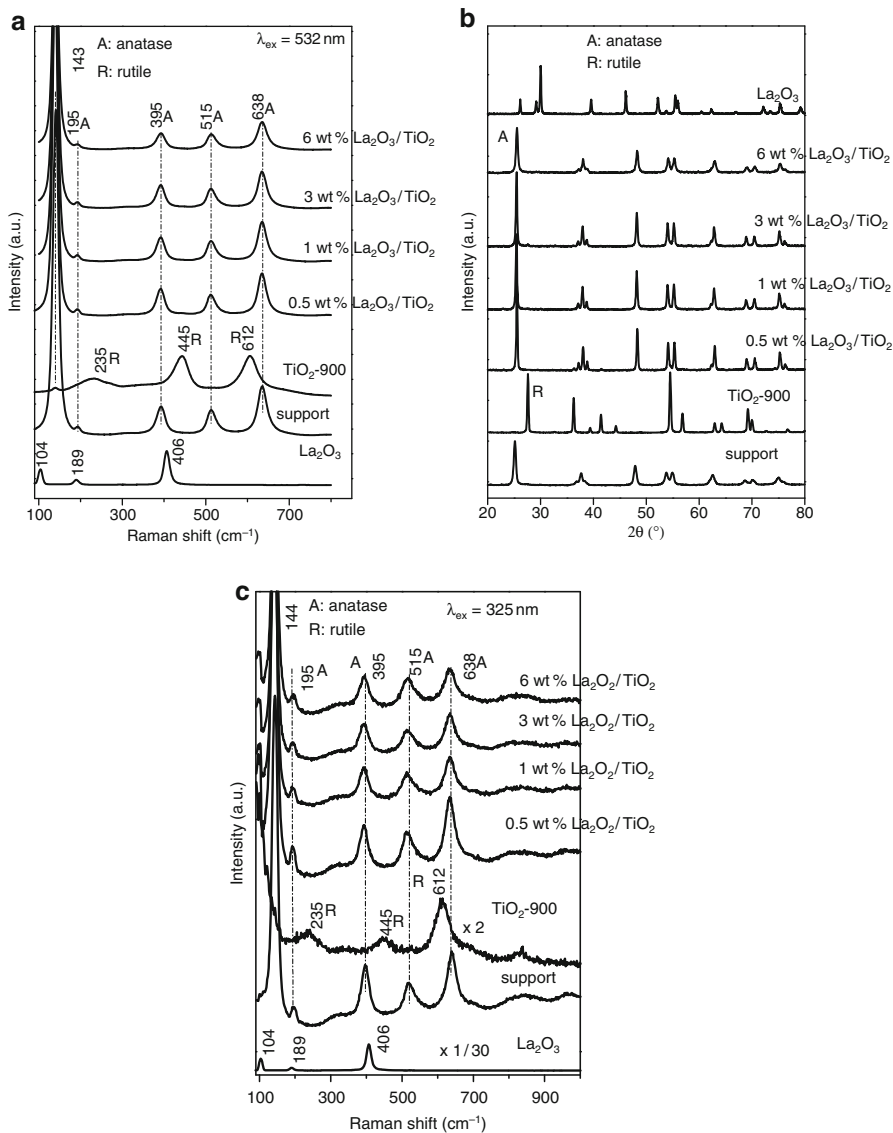


Fig. 16 (a) Visible Raman spectra, (b) XRD patterns, (c) UV Raman spectra of $\text{La}_2\text{O}_3/\text{TiO}_2$ with increasing La_2O_3 loading. Reprinted with permission from Zhang et al. Copyright 2006 American Chemical Society

Figure 16c shows the UV Raman spectra of $\text{La}_2\text{O}_3/\text{TiO}_2$ with increasing La_2O_3 loading. The Raman spectrum of the TiO_2 support and the TiO_2 -900 sample gives the characteristic bands of anatase phase and rutile phase, respectively. When La_2O_3 loading is varied from 0.5 to 6 wt%, the results of the UV Raman spectra

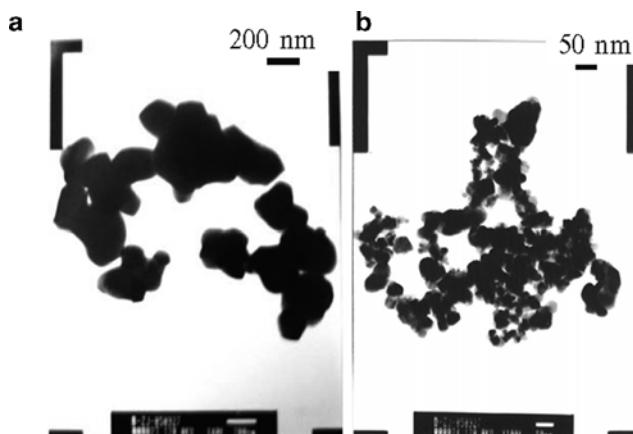


Fig. 17 TEM micrographs of (a) TiO₂-900 and (b) 1 wt% La₂O₃/TiO₂ sample calcined at 900°C

show that all the samples are in the anatase phase. These results are in accordance with those of visible Raman spectra and XRD (Fig. 16a, b). For both visible Raman spectra and UV Raman spectra, no bands due to crystalline phase of La₂O₃ are observed for all the La₂O₃/TiO₂ samples, showing that La₂O₃ is highly dispersed on the surface of anatase phase of TiO₂ particles (Xie and Tang 1990).

Figure 17 compares the TEM micrographs of TiO₂-900 and 1 wt% La₂O₃/TiO₂ sample calcined at 900°C. It could be found that the particle size is obviously decreased by addition of 1 wt% La₂O₃. It should be noted that both TiO₂ support and 1 wt% La₂O₃/TiO₂ sample appear similar average particle size, demonstrating that La³⁺ impregnation could effectively inhibit the increase of TiO₂ particle size.

Combined results of XRD, visible Raman spectra and UV Raman spectra of the La₂O₃/TiO₂ samples (Fig. 16), showed that 0.5 wt% La₂O₃ can stabilize the anatase phase both in bulk and in the surface region even after the calcination at 900°C. We further decreased the loading of La₂O₃ and recorded the corresponding XRD patterns and UV Raman spectra. Figure 18a displays XRD patterns of La₂O₃/TiO₂ with La₂O₃ loading from 0.1 to 0.4 wt%. Weak peaks due to anatase phase are observed for the 0.1 wt% La₂O₃/TiO₂ sample in addition to the characteristic peaks attributed to the rutile phase. The XRD result corresponding to the above sample indicates that the rutile content is 95%. With increasing the loading of La₂O₃, the diffraction peaks of rutile phase gradually diminish in intensity and the diffraction patterns of anatase phase become predominant. The result from XRD shows that the content of the rutile phase is decreased from 83 to 43% when La₂O₃ loading is increased from 0.2 to 0.4 wt%. This is strong evidence that the anatase phase of TiO₂ in the bulk can be stabilized by adding La₂O₃. Furthermore, the bulk region retain the anatase phase only when the loading of La₂O₃ is up to 0.5 wt%.

From UV Raman spectra (Fig. 18b), some weak peaks of the rutile phase are observed, while the main pattern is due to the anatase phase when the La₂O₃ loading

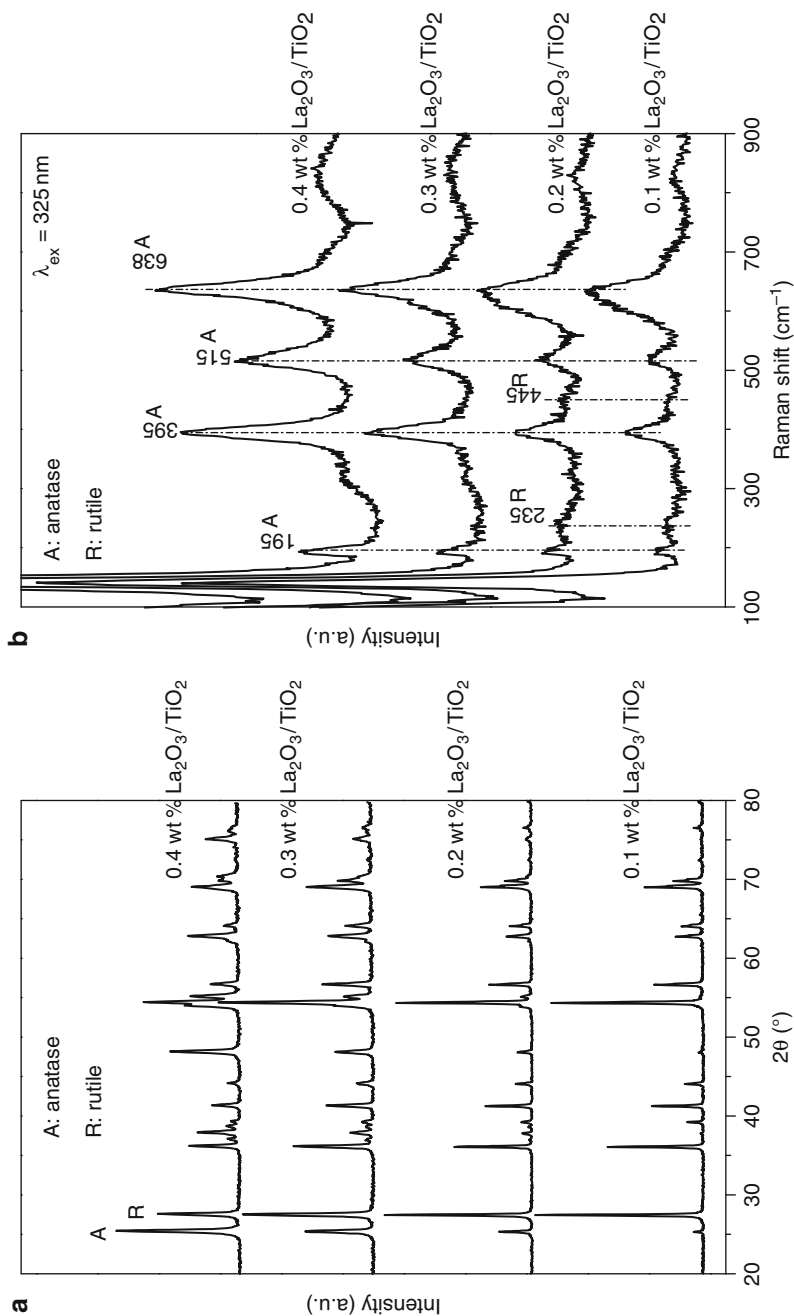


Fig. 18 (a) XRD patterns, (b) UV Raman spectra of $\text{La}_2\text{O}_3/\text{TiO}_2$ with La_2O_3 loading from 0.1 to 0.4 wt%

is 0.1 or 0.2 wt%. Further increasing the loading of La_2O_3 to 0.3 or 0.4 wt%, the surface region is stabilized at the anatase phase. Combined with the results from XRD, it can be seen that the impregnation of La_2O_3 not only stabilizes the anatase phase in the bulk region, but also retards the development of the rutile phase into the surface.

It is interesting to note that the impregnation of only 0.5 wt% La_2O_3 (3% the monolayer dispersion capacity La_2O_3 of the weight of TiO_2) can inhibit the phase transformation. The explanation of this interesting result could be as follows: the defect sites on the surface of the anatase particles are assumed to play an important role in the phase transformation of TiO_2 . When the defect sites of the anatase particle react with a neighboring anatase particle with or without defect sites, the rutile phase formation may start at these sites. La_2O_3 easily reacts with the defect sites of the anatase particles and the only 0.5 wt% La_2O_3 can occupy or deactivate all the defect sites of the anatase particles because usually the surface defect sites concentration is relatively low. The easy migration of surface atoms of anatase and the nucleation of rutile phase may most possibly take place at the surface defect sites. Therefore, only 0.5 wt% La_2O_3 can effectively inhibit the phase transformation of anatase and growing of the particle size.

In addition to occupying the defective sites, the highly dispersed La_2O_3 on the surface of the anatase particles effectively avoids the direct contact of the anatase particles for the sample with high La_2O_3 loadings. Therefore, the $\text{La}_2\text{O}_3/\text{TiO}_2$ sample can retain its anatase phase even when the calcination temperature is up to 900°C , owing to the above two roles played by La_2O_3 .

7 Photocatalytic Performance of TiO_2 with Different Surface Phase Structures

The surface phase of TiO_2 , which is directly exposed to light and the reactants, contribute to photocatalysis and solar energy conversion because the photocatalytic reaction or photoelectron conversion takes place only when photo-induced electrons and holes are available on the surface (Linsebigler et al. 1995; Sakthivel et al. 2006). The crystalline phase of TiO_2 particles in the surface region may be different from that in the bulk region (Busca et al. 1985, 1994; Zhang et al. 2006), particularly when TiO_2 is in its transition stage of the phase transformation from anatase to rutile (Zhang et al. 2006, 2008).

The rutile content in the bulk region and the anatase content in the surface region, estimated from visible and UV Raman spectra, are shown respectively by the solid curve and broken curve in Fig. 19a. The rate of H_2 evolution does not evidently change for the TiO_2 calcined from 500 to 680°C , although the amount of the rutile phase in the bulk region is greatly increased (Fig. 19b). It is obvious that the overall photocatalytic activity is more directly related to its surface phase because the anatase phase always exists in the surface region for

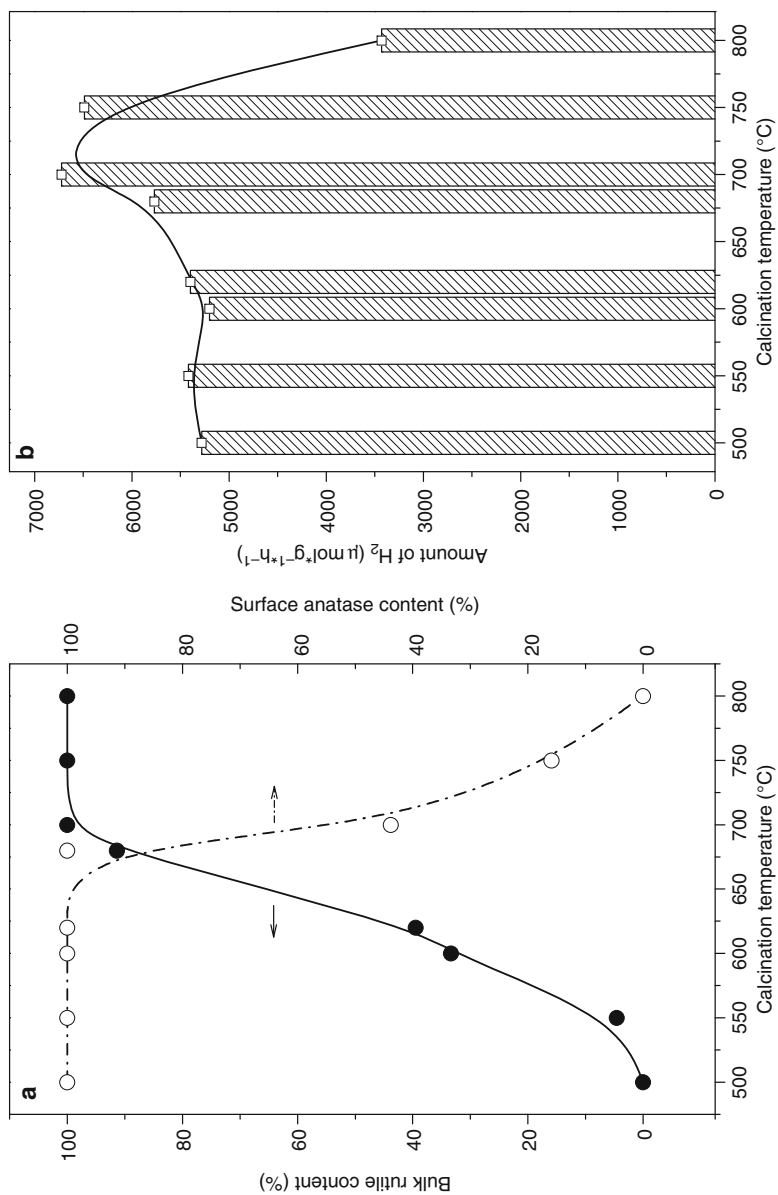


Fig. 19 (a) Dependence of bulk rutile content (filled circles, solid line) and surface anatase content (open circle, broken line), (b) TiO₂ samples calcined at different temperatures and their corresponding overall photocatalytic activity. Reprinted with permission from Zhang et al. Copyright 2008 Wiley

the samples calcined at 500–680°C. A maximum activity is observed for TiO₂ samples calcined at 700–750°C, where the bulk of TiO₂ is almost in pure rutile while the surface is in a mixed phase of anatase and rutile. The anatase phase in the surface region of TiO₂ sample is completely transformed into the rutile phase when the calcination temperature is increased to 800°C, and correspondingly the overall photocatalytic activity decreases dramatically. Thus, the pure rutile phase shows low overall activity for the H₂ production. This result suggests that the presence of the surface anatase on rutile TiO₂ can keep a relatively high overall photocatalytic activity. This effect should be attributed to the formation of surface-phase junction.

To further demonstrate if higher photocatalytic activity can be achieved for TiO₂ photocatalyst with surface junction formed between anatase and rutile TiO₂, anatase were deposited on rutile by a wet impregnation method (Loddo et al. 1999), and then the TiO₂ powder was calcined up to 400°C. To obtain the samples with different amounts of anatase on the surface of rutile, the impregnation procedure was repeated (the loading of anatase deposited on the surface of the rutile particles was roughly 5 wt% for each time). The as-prepared samples were denoted as TiO₂(A)/TiO₂(R)-n, in which TiO₂(A) indicates the surface anatase, TiO₂(R) indicates the rutile as the support, and the number n indicates the number of impregnation.

Figure 20a–c shows the SEM of TiO₂(A)/TiO₂(R)-0, 1, 4 samples, where it is clearly observed that fine anatase particles (particle size <30 nm) are highly deposited on the rutile particles (particle size ~500 nm) in the TiO₂(A)/TiO₂(R)-n samples.

The surface specific activity of TiO₂(A)/TiO₂(R) catalysts with increasing the amount of anatase on the surface of rutile are given in Fig. 20d. The anatase content estimated from XRD and UV Raman spectroscopy is also displayed in Fig. 20d. Compared with the pure rutile support, the photocatalytic activity is remarkably increased by supporting a small amount of anatase on the surface of rutile. For example, TiO₂(A)/TiO₂(R)-1,2 samples exhibit much higher photocatalytic activities despite their low surface anatase contents (<10 wt%), for TiO₂(A)/TiO₂(R)-3, the photocatalytic activity is greatly enhanced to about four times higher than that of pure rutile. This enormous increase in the photocatalytic activity can be attributed to the formation of the surface anatase/rutile phase junction. For TiO₂(A)/TiO₂(R)-4 sample, the photocatalytic activity is decreased somewhat because the surface of the rutile may be fully covered by the anatase, that decreases the amount of exposed anatase/rutile phase junction on the TiO₂ surface.

In order to visualize the surface phase junction, the TiO₂(A)/TiO₂(R)-n ($n = 1-4$) samples were investigated by HRTEM. Figure 21 shows the HRTEM result of a TiO₂(A)/TiO₂(R)-n sample. The result clearly shows that the junction structure between anatase and rutile phase is formed on the TiO₂(A)/TiO₂(R)-n sample. HRTEM gives the direct evidence for the surface anatase/rutile junction formed on rutile particles.

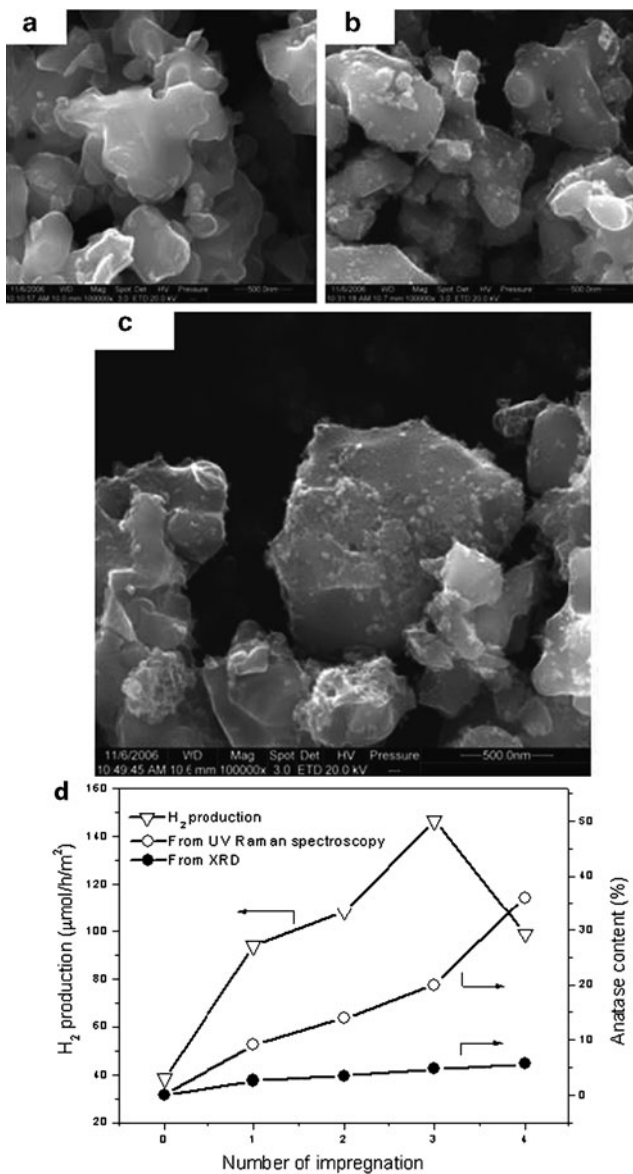


Fig. 20 Scanning electron micrographs of (a) TiO₂(R), (b) TiO₂(A)/TiO₂(R)-1, and (c) TiO₂(A)/TiO₂(R)-4 samples. (d) The photocatalytic activities for H₂ evolved per surface area of TiO₂(A)/TiO₂(R)-n samples with increasing the amount of anatase phase on the surface of rutile TiO₂. The rate of H₂ evolved per surface area of TiO₂(R) before depositing anatase TiO₂ is added for comparison. The anatase contents estimated from XRD and UV Raman spectroscopy for TiO₂(A)/TiO₂(R)-n samples are also displayed. Reprinted with permission from Zhang et al. Copyright 2008 Wiley

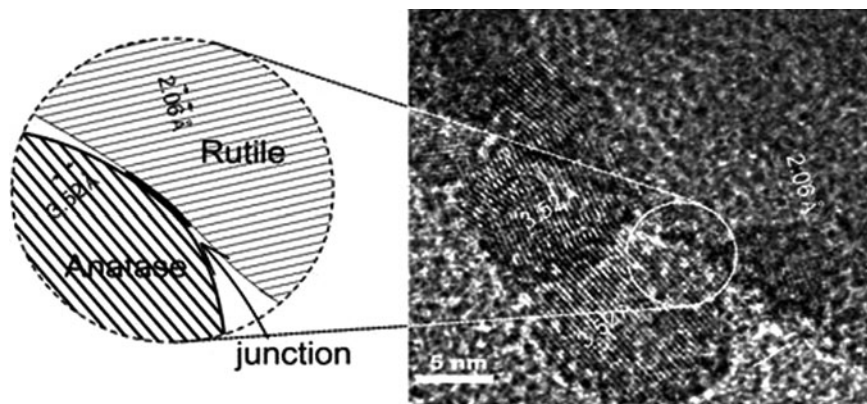


Fig. 21 HRTEM image of $\text{TiO}_2(\text{A})/\text{TiO}_2(\text{R})\text{-n}$ sample. Reprinted with permission from Zhang et al. Copyright 2008 Wiley

8 Conclusions

This chapter discussed the applications of UV Raman spectroscopy in the studies of TiO_2 , including phase transformation and significance of surface phase in photocatalysis. UV Raman spectroscopy combined visible Raman spectroscopy, XRD, and TEM indicated that the crystalline phases of TiO_2 particles in the surface region is different from that in the bulk region, particularly when TiO_2 is in its transition stage of the phase transformation from anatase to rutile.

A direct correlation between the surface phases of TiO_2 and its catalytic, especially photocatalytic performance is of great significance because catalytic reaction takes place on the surface. A great deal of research has been conducted to investigate the effect of the surface properties on the photoactivity of TiO_2 . However, the direct relationship between the photocatalytic performance and the surface phase of TiO_2 remained a challenging subject. This may be due to the difficulty to characterize the surface phase of TiO_2 , especially of TiO_2 nanoparticle, which has been practically used as a catalyst or a photocatalyst. Taking the advantage of UV Raman spectroscopy for understanding the surface phase of TiO_2 , if the photocatalytic activity of TiO_2 with different crystalline phase compositions was evaluated, it is possible to correlate the surface phase of TiO_2 and its photoactivity.

Acknowledgements This work was financially supported by the National Natural Science Foundation of China (NSFC, Grant No. 20673112), National Basic Research Program of China (Grant No. 2009CB220010), and Program for Strategic Scientific Alliances between China and the Netherlands (2008DFB50130).

References

- Ahonen PP, Kauppinen EI, Joubert JC, Deschanvres JL, Van Tendeloo G (1999) Preparation of nanocrystalline titania powder via aerosol pyrolysis of titanium tetrabutoxide. *J Mater Res* 14:3938–3948
- Banfield JF, Bischoff BL, Anderson MA (1993) TiO₂ accessory minerals: coarsening, and transformation kinetics in pure and doped synthetic nanocrystalline materials. *Chem Geol* 110:211–231
- Bickley RI, Gonzalez-Carreno T, Lees JS, Palmisano L, Tilley RJD (1991) A structural investigation of titanium dioxide photocatalysts. *J Solid State Chem* 92:178–190
- Brown FR, Maskovsky LE (1977) Raman spectra of a cobalt oxide-molybdenum oxide supported catalyst. *Appl Spectrosc* 31:44–46
- Brown FR, Maskovsky LE, Rhee KH (1977a) Raman spectra of supported molybdena catalysts. I. Oxide catalysts. *J Catal* 50:162–171
- Brown FR, Maskovsky LE, Rhee KH (1977b) Raman spectra of supported molybdena catalysts: II. sulfided, used, and regenerated catalysts. *J Catal* 50:385–389
- Busca G, Saussey H, Saur O, Lavalley JC, Lorenzelli V (1985) FT-IR characterization of the surface acidity of different titanium dioxide anatase preparations. *Appl Catal* 14:245–260
- Busca G, Ramis G, Amores JMG, Escribano VS, Piaggio P (1994) FT Raman and FT-IR studies of titanias and metatitanate powders. *J Chem Soc Faraday Trans* 90:3181–3190
- Chaves A, Katiyan KS, Porto SPS (1974) Coupled modes with asymmetry in tetragonal BaTiO₃. *Phys Rev B* 10:3522–3533
- Ding Z, Liu GQ, Greenfield PF (2000) Role of the crystallite phase of TiO₂ in heterogeneous photocatalysis for phenol oxidation in water. *J Phys Chem B* 104:4815–4820
- Foger K, Anderson JR (1986) Thermally stable SMSI supports: iridium supported on TiO₂-Al₂O₃ and on Ce-doped anatase. *Appl Catal* 23:139–155
- Fox MA, Dulay MT (1993) Heterogeneous photocatalysis. *Chem Rev* 93:341–357
- Fujishima A, Honda K (1972) Electrochemical photolysis of water at a semiconductor electrode. *Nature* 238:37–38
- Gopalan R, Lin YS (1995) Evolution of pore and phase structure of sol-gel derived lanthana doped titania at high temperatures. *Ind Eng Chem Res* 34:1189–1195
- Gouma PI, Mills MJ (2001) Anatase to rutile transformation in titania powders. *J Am Ceram Soc* 84:619–622
- Grätzel M (2001) Photoelectrochemical cells. *Nature* 414:338–344
- Gribb AA, Banfield JF (1997) Particle size effects on transformation kinetics and phase stability in nanocrystalline TiO₂. *Am Mineral* 82:717–728
- Hague DC, Mayo M (1993) Effect of crystallization and phase transformation in nanocrystalline TiO₂. *Nanostruct Mater* 3:61–67
- Hwu Y, Yao YD, Cheng NF, Tung CY, Lin HM (1997) X-ray absorption of nanocrystal TiO₂. *Nanostruct Mater* 9:355–358
- Jing LQ, Sun XJ, Xin BF, Wang BQ, Cai WM, Fu HG (2004) The preparation and characterization of La doped TiO₂ nanoparticles and their photocatalytic activity. *J Solid State Chem* 177:3375–3382
- Kamat PV (1993) Photochemistry on nonreactive and reactive (semiconductor) surfaces. *Chem Rev* 93:267–300
- Karakitsou KE, Verekios XE (1993) Effects of altrivalent cation doping of titania on its performance as a photocatalyst for water cleavage. *J Phys Chem* 97:1184–1189
- Knopps-Gerrits PP, De Vos DE, Feijen EJP, Jacobs PA (1997) Raman spectroscopy on zeolites. *Microporous Mater* 8:3–17
- Kumar KNP (1995) Growth of rutile crystallites during the initial stage of anatase-to-rutile transformation in pure titania and in titania-alumina nanocomposites. *Scripta Metall Mater* 32:873–877

- Kumar K-NP, Keizer K, Burggraaf AJ, Okubo T, Nagamoto H, Morooka S (1992) Densification of nanostructured titania assisted by a phase transformation. *Nature* 358:48–51
- Lee GH, Zuo HM (2004) Growth and phase transformation of nanometer-sized titanium oxide powders produced by the precipitation method. *J Am Chem Soc* 87:473–479
- Li C (2003) Identifying the Highly Isolated Transition Metal Ions/Oxides in Molecular Sieves and on Oxide Supports by UV Resonance Raman Spectroscopy. *J Catal* 216:203–212
- Li C, Li MJ (2002) UV Raman spectroscopic study on the phase transformation of ZrO_2 , Y_2O_3 - ZrO_2 and SO_4^{2-}/ZrO_2 . *J Raman spectrosc* 33:301–308
- Li C, Stair PC (1996a) An advance in Raman studies of catalysts: ultraviolet resonance Raman Spectroscopy. *Stud Surf Sci Catal* 101:881–890
- Li C, Stair PC (1996b) Ultraviolet Raman spectroscopy characterization of sulfated zirconia catalysts; fresh, deactivated and regenerated. *Catal Lett* 36:119–123
- Li C, Stair PC (1997) Coke formation in zeolites studied by a new technique: ultraviolet resonance Raman spectroscopy. *Stud Surf Sci Catal* 105:599–606
- Li C, Xiong G, Xin Q, Liu JK, Ying PL, Feng ZC, Li J, Yang WB, Wang YZ, Wang GR, Liu XY, Lin M, Wang XQ, Min EZ (1999) UV resonance Raman spectroscopic identification of titanium atoms in the framework of TS-1 zeolite. *Angew Chem Int Ed* 38:2220–2222
- Li J, Xiong G, Feng ZC, Liu ZM, Xin Q, Li C (2000) Coke formation during the methanol conversion to olefins in zeolites by UV Raman spectroscopy. *Micro Meso Mater* 39:275–280
- Li MJ, Feng ZC, Xiong G, Ying PL, Xin Q, Li C (2001) Phase transformation in the surface region of zirconia detected by UV Raman spectroscopy. *J Phys Chem B* 105:8107–8111
- Li MJ, Feng ZC, Ying PL, Xin Q, Li C (2003) Phase transformation in the surface region of zirconia and doped zirconia detected by UV Raman spectroscopy. *Phys Chem Chem Phys* 5:5326–5332
- Linsebigler AL, Lu GQ, Yates JT Jr (1995) Photocatalysis on TiO_2 surfaces: principles, mechanisms, and selected results. *Chem Rev* 95:735–758
- Loddo V, Marci G, Martí C, Palmisano L, Rives V, Sclafani A (1999) Preparation and characterisation of TiO_2 (anatase) supported on TiO_2 (rutile) catalysts employed for 4-nitrophenol photodegradation in aqueous medium and comparison with TiO_2 (anatase) supported on Al_2O_3 . *Appl Catal B* 20:29–45
- Ma W, Lu Z, Zhang M (1998) Investigation of structural transformation in nanophase titanium dioxide by Raman spectroscopy. *Appl Phys A* 66:621–627
- Mackenzie KJD (1975) The calcinations of titania: the effect of additive on the anatase-rutile transformation. *Trans J Br Ceram* 74:29–34
- Muscat J, Swamy V, Harrison NM (2002) First-principles calculations of the phase stability of TiO_2 . *Phys Rev B* 65:224112-1–224112-15
- Navrotsky A, Kleppa OJ (1967) Enthalpy of the anatase-rutile transformation. *J Am Ceram Soc* 50:626–630
- O'Regan B, Graetzel M (1991) A low-cost, high-efficiency solar cell based on dye-sensitized colloidal TiO_2 films. *Nature* 353:737–740
- Ohsaka T, Izumi F, Fujiki Y (1978) Raman Spectrum of Anatase, TiO_2 . *J Raman Spectrosc* 7:321–324
- Okada K, Yamamoto N, Kameshima Y, Yasumori A (2001) Effect of silica additive on the anatase-to-rutile phase transition. *J Am Ceram Soc* 84:1591–1596
- Ovenstone J, Yanagisawa K (1999) Effect of hydrothermal treatment of amorphous titania on the phase change from anatase to rutile during calcinations. *Chem Mater* 11:2770–2774
- Ozaki S, Iida Y (1961) Grain growth and phase transformation of titanium oxide during calcination. *J Am Ceram Soc* 44:120–127
- Penn RL, Banfield JF (1999) Formation of rutile nuclei at anatase 112 twin interfaces and the phase transformation mechanism in nanocrystalline titania. *Am Mineral* 84:871–876
- Ranade MR, Navrotsky A, Zhang HZ, Banfield JF, Elder SH, Zaban A, Borse PH, Kulkarni SK, Doran GS, Whitfield HJ (2002) Energetics of nanocrystalline TiO_2 . *Proc Natl Acad Sci USA* 99(suppl 2):6476–6481

- Sakthivel S, Hidalgo MC, Bahnemann DW, Geissen S-U, Murugesan V, Vogelpohl A (2006) A fine route to tune the photocatalytic activity of TiO₂. *Appl Catal B* 63:31–40
- Shannon RD, Pask JA (1965) Kinetics of anatase-rutile transformation. *J Am Ceram Soc* 48:391–398
- Sreethawong T, Suzuki Y, Yoshikawa S (2005) Synthesis, characterization, and photocatalytic activity for hydrogen evolution of nanocrystalline mesoporous titania prepared by surfactant-assisted templating sol–gel process. *J Solid State Chem* 178:329–338
- Stair PC, Li C (1997) Ultraviolet Raman spectroscopy of catalysts and other solids. *J Vac Sci Technol A* 15:1679–1684
- Tsai S-J, Cheng S (1997) Effect of TiO₂ crystalline structure in photocatalytic degradation of phenolic contaminants. *Catal Today* 33:227–237
- Wang R, Hashimoto K, Fujishima A, Chikuni M, Kojima E, Kitamura A, Shimohigoshi M, Watanabe T (1997) Light-induced amphiphilic surfaces. *Nature* 388:431–432
- West AR (1984) Solid state chemistry and its applications. Wiley, New York, p 174
- Xie YC, Tang YQ (1990) Spontaneous Monolayer Dispersion of Oxides and Salts onto surfaces of Supports: Application to Heterogeneous Catalysis. *Adv Catal* 37:1–43
- Xiong G, Li C, Feng ZC, Ying PL, Xin Q, Liu J (1999) Surface coordination structure of molybdate with extremely low loading on gamma-alumina characterized by UV resonance Raman spectroscopy. *J Catal* 186:234–237
- Xiong G, Li C, Li HY, Xin Q, Feng ZC (2000a) Direct spectroscopic evidence for vanadium species in V-MCM-41 molecular sieve characterized by UV resonance Raman spectroscopy. *J Chem Soc Chem Commun* 677–678.
- Xiong G, Feng ZC, Li J, Yang H, Ying PL, Xin Q, Li C (2000b) UV resonance Raman spectroscopic studies on the genesis of highly dispersed surface molybdate species on γ -alumina. *J Phys Chem B* 104:3581–3588
- Yan MC, Chen F, Zhang JL, Anpo M (2005) Preparation of controllable crystalline titania and study on the photocatalytic properties. *J Phys Chem B* 109:8673–8678
- Yang J, Mei S, Ferreira JMF (2000) Hydrothermal synthesis of nanosized titania powders: Influence of peptization and peptizing agents on the crystalline phases and phase transitions. *J Am Ceram Soc* 83:1361–1368
- Yoshinaka M, Hirota K, Yamaguchi O (1997) Formation and sintering of TiO₂ (anatase) solid solution in the system TiO₂-SiO₂. *J Am Ceram Soc* 80:2749–2753
- Zhang HZ, Banfield JF (2000a) Phase transformation of nanocrystalline anatase-to-rutile via combined interface and surface nucleation. *J Mater Res* 15:437–448
- Zhang HZ, Banfield JF (2000b) Understanding polymorphic phase transformation behavior during growth of nanocrystalline aggregates: insights from TiO₂. *J Phys Chem B* 104:3481–3487
- Zhang F, Zheng Z, Ding X, Mao Y, Chen Z, Yang S, Liu X (1997) Highly oriented rutile-type TiO₂ films synthesized by ion beam enhanced deposition. *J Vac Sci Technol A* 15:1824–1827
- Zhang YH, Chan CK, Porter JF, Guo W (1998) Micro-Raman spectroscopic characterization of nanosized TiO₂ powders prepared by vapor hydrolysis. *J Mater Res* 13:2602–2609
- Zhang J, Li MJ, Feng ZC, Chen J, Li C (2006) UV Raman Spectroscopic Study on TiO₂. I. Phase Transformation at the Surface and in the Bulk. *J Phys Chem B* 110:927–935
- Zhang J, Xu Q, Feng ZC, Li MJ, Li C (2008) Importance of the relationship between surface phases and photocatalytic activity of TiO₂. *Angew Chem Int Ed* 47:1766–1769
- Zhu J, Zheng W, He B, Zhang J, Anpo M (2004) Characterization of Fe-TiO₂ photocatalysts synthesized by hydrothermal method and their photocatalytic reactivity for photodegradation of XRG dye diluted in water. *J Mol Catal A* 216:35–43

Chapter 7

Photoluminescence Spectroscopic Studies on TiO₂ Photocatalyst

Jiaying Shi, Xiuli Wang, Zhaochi Feng, Tao Chen,
Jun Chen, and Can Li

Abstract Photoluminescence is a powerful technique in the study of semiconductor photocatalysts. This chapter deals with the application of photoluminescence techniques to the study of TiO₂ in relation to its photocatalytic performance. The assignment of the visible and the near-infrared luminescence characteristics of TiO₂ are discussed. The influence of the adsorbed molecules, such as H₂O, O₂, H₂, unsaturated hydrocarbons and Pt loaded on TiO₂, on the photoluminescence characteristics of TiO₂ is also discussed. The relationship between the photoluminescence features of TiO₂ and the photo-assisted reaction of water and methanol mixture is also summarized.

1 Introduction

Photoluminescence spectroscopy is a contactless, nondestructive method of probing the electronic structure of materials. Nowadays, the highly sensitive photoluminescence technique is widely used in the investigation of the photophysical and photochemical properties of solid semiconductors (Anpo et al. 1985a, b, 1989; Nakajima et al. 2001, 2004; Nakajima and Mori 2004; Jung et al. 2005; Murakami et al. 2006, 2007). Particularly, it is a powerful technique in the study of photocatalysis, since it can supply meaningful information about the relationship between the nature of the defect sites, such as surface oxygen or metal vacancies, and the efficiencies of charge carrier trapping, immigration and transfer (Jeon et al. 2009; Naito et al. 2009). Application of the photoluminescence to the study of the relationship between the solid surface properties and the efficiency of the photocatalysis has already been reviewed by others (Anpo and Che 2000;

C. Li (✉)

State Key Laboratory of Catalysis, Dalian Institute of Chemical Physics,
Chinese Academy of Sciences, Beijing, China
e-mail: canli@dicp.ac.cn

Jing et al. 2006). And this chapter mainly deals with the application of the photoluminescence techniques to a particular TiO_2 semiconductor photocatalyst.

Because of the high chemical stability and favorable energy band structure for the development of robust and efficient photocatalysts, TiO_2 has been drawing enormous attention over the past decades. Anatase and rutile, the two major crystal structures of TiO_2 , are commonly used in photocatalysis. It is well known that the photocatalytic activity of TiO_2 largely depends on its crystal structure (Tsai and Cheng 1997; Tanaka et al. 1991; Nishimoto et al. 1985; Ding et al. 2000; Ohno et al. 2001; Fujihara et al. 1998) and surface properties (Anpo et al. 1989; Yu et al. 2000; Wu et al. 2004), etc. The crystal structures (Tang et al. 1994a; Poznyak et al. 1992; Montoncello et al. 2003; Nakajima et al. 2005) and the surface properties (Anpo et al. 1989; Nakajima et al. 2002, 2004; Nakajima and Mori 2004) of TiO_2 also have essential correlation with the luminescence features of TiO_2 . Therefore, photoluminescence spectroscopy study can depict the surface photoactive sites of TiO_2 (Anpo et al. 1985a; Nakajima et al. 2001, 2002; Jung et al. 2005).

This chapter focuses on the review of the application of photoluminescence spectroscopy in the study of TiO_2 photocatalysts. The whole chapter is organized as follows: Sect. 2 will give a brief introduction of the fluorescence spectroscopy, followed by the photoluminescence characteristics of TiO_2 in Sect. 3; the influence of adsorbed molecules and loaded metal Pt on the photoluminescence properties of TiO_2 will be discussed in Sect. 4; the relationship between the photoluminescence features of TiO_2 and its photocatalytic activity will be discussed in Sects. 5 and 6; based on the above extensive discussion, the final conclusion will be made in Sect. 7.

2 Laser-Induced Fluorescence Spectroscopy

Fluorescence spectroscopy is an important spectroscopic technique for the exploration of the electronic structures of materials in a molecular level. It has been extensively applied in biology, pharmacology, and analysis sciences since it is not only sensitively gives the information about the electronic and vibrational states of the luminescent molecule, but also sensitively probes the influence of surrounding environment on the electronic structures of the fluorescent molecules. Fluorescence spectroscopy can help us better understand the mechanism of the chemical reaction and guide us to design efficient photocatalysts. Various kinds of commercially available autocompensating spectrophotofluorometers (photoluminescence instrumentation) have been employed in the study of catalysts. In these spectrophotometers, Mercury or Xenon arc lamps are commonly used as the excitation source. However, laser-induced fluorescence (LIF) spectroscopy, in which laser is used as the excitation source, has been developed in recent years. Compared with the traditional fluorescence spectroscopic technique, in which lamp is used as the excitation source, LIF spectroscopy has some distinguished advantages in terms of higher sensitivity, more facile control of

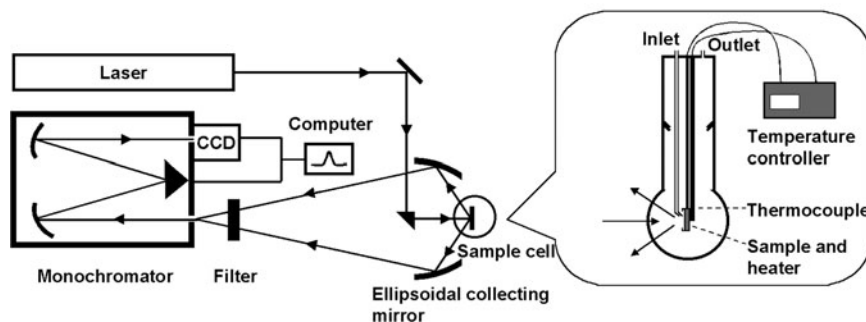


Fig. 1 The schematic diagram of the in situ laser-induced luminescence spectroscopy setup

the light system of the apparatus, and less sample area for luminescence. In literature, there are numerous reports on the application of LIF spectroscopy in biological science. Detection of single molecules using LIF spectroscopy has also been reported. However, this technique has not been well applied in the field of catalysis area.

In order to study heterogeneous catalysis using LIF, we designed and built up an in situ laser-induced fluorescence spectroscopy setup, as shown in Fig. 1. In this setup, continuous wave UV lasers and visible lasers are used as the excitation sources. It is equipped with the home-made ellipsoidal mirror collecting system, which can provide a large space to accommodate the sample treatment system. The CCD is mounted at the focal plane in the exit of the monochromator for efficient detection of the fluorescence signal and collection of the full spectrum simultaneously. A home-made in situ sample cell connected with the gas system is fixed at the focal point of the ellipsoidal mirror. This setup is very convenient to carry out in situ fluorescence studies under various experimental conditions. Using this setup, we have successfully investigated many photoluminescence properties of heterogeneous catalysts in our laboratory (Chen et al. 2004a, b, 2005). By using this technique, we detected the defects in catalyst, which is the crucial subject concerning active sites (Chen et al. 2004a, b). Furthermore, using aniline as the fluorescence probing molecule, this setup also enabled us to study the surface properties of the superacid sulfated zirconia catalysts (Chen et al. 2005).

The photoluminescence has been drawing a great deal of attention in the field of photocatalysis in recent years, because it is proved to be a powerful technique to explore the electron and hole related photocatalytic processes which take place on the surface of solid semiconductors. Indeed, combining the LIF spectroscopy with other spectroscopic techniques, we have successfully obtained some essential information regarding the surface properties of semiconductor photocatalysts as well as the relaxation processes of the photo-induced charge carriers (Shi et al. 2006, 2007a, b).

3 The Photoluminescence Characteristics of TiO₂

As an indirect wide band-gap semiconductor, the band edge luminescence of TiO₂ is difficult to be observed (Emeline et al., 2005). The photoluminescence wavelength of TiO₂ depends on its crystal structure and its particle size, while the photoluminescence intensity depends on the dopants, annealing temperatures and atmospheric conditions during the crystallization of TiO₂, and the ambient temperature and atmospheric environments during the photoluminescence measurements. The main features of TiO₂ are the broad and structureless visible or near-infrared luminescence bands (Anpo et al. 1985a, b, 1989, 1991; Serpone et al. 1995; Tang et al. 1993, 1994b; Zhang et al. 2000a, b; Montoncello et al. 2003; Mochizuki et al. 2003; Poznyak et al. 1992; Hachiya and Kondoh 2003; Nakato et al. 1983, 1986, 1997; Grabner et al. 1970; Ghosh et al. 1969; Fernández et al. 2005; Plugaru et al. 2004; de Haart and Blasse 1986; Forss and Schubnell 1993; Lei et al. 2001; Qian et al. 2005; Knorr et al. 2008).

In photoluminescence spectrum, the anatase TiO₂ has a visible emission with a broad spectral width. In general, the origin of the photoluminescence of anatase TiO₂ can be attributed to different kinds of species: self-trapped excitons, oxygen vacancies and defect sites, impurities or reduced metal ions, etc. The broad visible luminescence band of anatase TiO₂ was interpreted as the emission from the self-trapped excitons localized on TiO₆ octahedra by Tang (Tang et al. 1993, 1994b). Zhang et al. (2000a, b) observed the visible luminescence band at 2.15–2.29 eV and interpreted it as the recombination of the electron/hole pairs via the localized levels within the forbidden gap, which are related to some defect centers resided in the surface region of anatase nanocrystallites. In the study of pristine anatase, Mochizuki and co-workers reported that the broad visible luminescence band was originated from the surface oxygen defects (Mochizuki et al. 2003). Fernández et al. (2005) also observed a complex visible band in different surface orientations of TiO₂ single crystals by the cathodoluminescence spectra and ascribed it to oxygen vacancies accompanied with the formation Ti³⁺. For rutile TiO₂, a near-infrared luminescence band peaked at about 830 nm has been reported. The luminescence centers of this near-infrared band were identified as the Cr³⁺ impurities (Grabner et al. 1970; Haart et al. 1986), though many other researchers attributed it to the interstitial Ti³⁺ ions (Fernández et al. 2005; Plugaru et al. 2004; Ghosh et al. 1969). In the photoluminescence spectra of rutile electrode in aqueous electrolyte solutions, the near-infrared luminescence band was attributed to the intermediate species generated during the photooxidation reaction of water (Nakato et al. 1983, 1986, 1997). On the contrary, Poznyak et al. (1992) proposed that the near-infrared band was associated with the luminescence centers of the intrinsic defects in TiO₂, which shows more characteristic features of the rutile lattice other than anatase lattice.

In our work, the phase transformation of TiO₂ calcined at different temperatures was systematically studied by the UV-Raman spectroscopy (Zhang et al. 2006). We further studied the photoluminescence properties of TiO₂ in the progress of

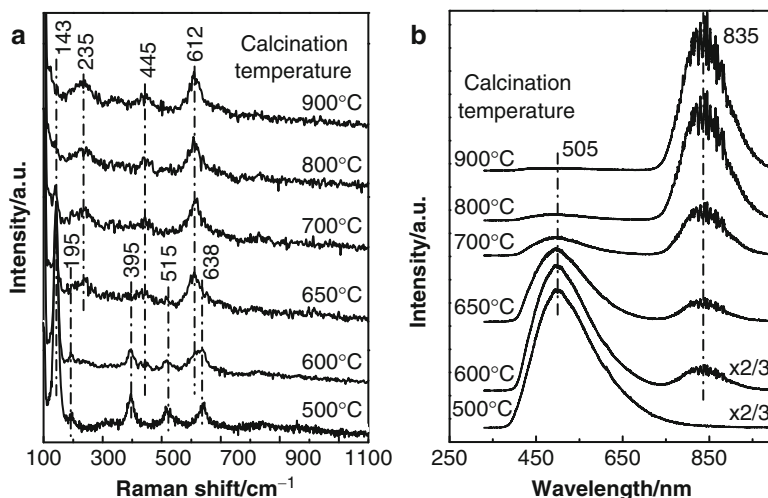


Fig. 2 (a) UV-Raman and (b) photoluminescence spectra of TiO₂ calcined at different temperatures (Shi et al. 2007a, b)

phase transformation. Interestingly, it was found that the visible luminescence band is related to the anatase structure and the near-infrared luminescence band is associated with the rutile structure (Shi et al. 2007a, b). The photoluminescence spectra and UV-Raman spectra of TiO₂ calcined at different temperatures are shown in Fig. 2. Comparison of the photoluminescence spectra with the UV-Raman spectra of TiO₂ clearly shows that the position of the luminescence bands is related to the crystalline structure of TiO₂. The sample calcined at 500°C is pure anatase phase and displays only the visible luminescence band centered at 505 nm. Elevating the calcination temperature to 600°C, the rutile phase begins to be detected by Raman spectroscopy; accordingly, the near-infrared luminescence band appears in the photoluminescence spectra. With the increase of the calcination temperature, the anatase phase is gradually transformed into the rutile phase, while the visible luminescence band is quenched and the near-infrared luminescence band is prevailed. When anatase phase completely transforms into the rutile phase, the visible luminescence band nearly disappears and the near-infrared luminescence band predominates in the photoluminescence spectra. The results obtained from commercial TiO₂ further indicates that the visible luminescence band located at about 505 nm and the near-infrared luminescence band centered at about 835 nm are respectively relative to anatase structure and rutile structure.

The photoluminescence properties of semiconductors are closely related to the surface stoichiometry and the kinds of surface states, which usually could be changed by annealing processes (Zacharias and Fauchet 1997). Sekiya et al. (2004) reported that the defects states of TiO₂ can be controlled by heat treatments under oxidation or reduction atmospheres. As shown in Fig. 3, the visible and the near-infrared luminescence bands exhibit obviously different characteristics in the in situ

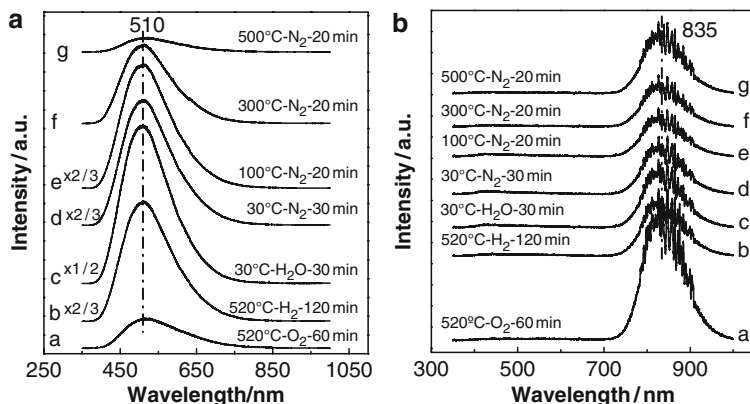


Fig. 3 In situ photoluminescence spectra of TiO₂ calcined at (a) 500°C and (b) 900°C. The in situ treatment process: (a) after calcined at 520°C for 1 h in O₂ and purged by N₂; (b) after calcined at 520°C for 2 h in H₂ and purged by N₂; (c) after exposure to water vapor for 30 min; (d) after purged water vapor by N₂; and followed by thermal desorption of water in N₂ for 20 min (e) at 100°C; (f) at 300°C; (g) at 500°C (Shi et al. 2007a, b)

photoluminescence experiment of TiO₂. The visible luminescence band is quenched after annealing TiO₂ in O₂ and enhanced in the following reduction treatment in H₂. On the contrary, the near-infrared luminescence band is increased in the oxidation treatment in O₂ and quenched in the reduction treatment in H₂. It has been reported that reducing TiO₂ in hydrogen atmosphere could generate oxygen vacancies (Cronmeyer 1959; Göpel et al. 1983; Salvador and García González 1992), accompanied by the formation of Ti³⁺ ions (Sekiya et al. 2004; Qian et al. 2005; Henderson et al. 1999), while oxidizing TiO₂ in oxygen atmosphere could remove oxygen vacancies and produce the stoichiometry surface (Sekiya et al. 2004; Sanjinés et al. 1994). Numerous spectroscopic studies (Henrich and Cox 1994) have observed isolated oxygen vacancy sites associated with the reduced Ti cations. For example, UPS shows a state located ca. 0.7–0.8 eV below the E_F in the band gap of reduced anatase TiO₂ (Kurtz et al. 1989), which was characterized by the XPS as the defect sites associated with Ti³⁺ ions (Sanjinés et al. 1994). Therefore, it is concluded that the visible luminescence band is originated from the oxygen vacancies associated with Ti³⁺ in anatase TiO₂. For the near-infrared luminescence band, we temporarily ascribe it to the intrinsic defects in rutile TiO₂ and more experiments are needed to confirm the nature of these intrinsic defects.

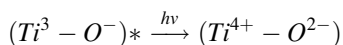
It is well known that anatase and rutile are the two major crystal structures of TiO₂, which are commonly used as TiO₂ based photocatalysts. The structures of these two crystals can be described as the chains of TiO₆ octahedra differed by the distortion of each octahedra and assembly pattern of the octahedra chains (Linsebigler et al. 1995). The structural differences of these two crystals in the form of anatase and rutile lead to the differences in their electronic and optical

properties (Chaves et al. 1974; Plugaru et al. 2004; Diebold 2003). So, it is reasonable to conclude that the different crystalline structures of TiO₂ result in the different luminescence centers in anatase and rutile. This conclusion is obviously supported by our experimental observations, i.e., the oxygen vacancies related to visible emission are prevailed in anatase while the defect states related to near-infrared emission are predominant in rutile. In the mean time, during the phase transformation processes of TiO₂ from anatase to rutile, it was found that the luminescence centers change from the oxygen vacancies in anatase to the intrinsic defects in rutile, evidenced by the visible emission band replaced by the near-infrared band.

4 The Influence of the Adsorbed Molecule on the Photoluminescence Properties of TiO₂

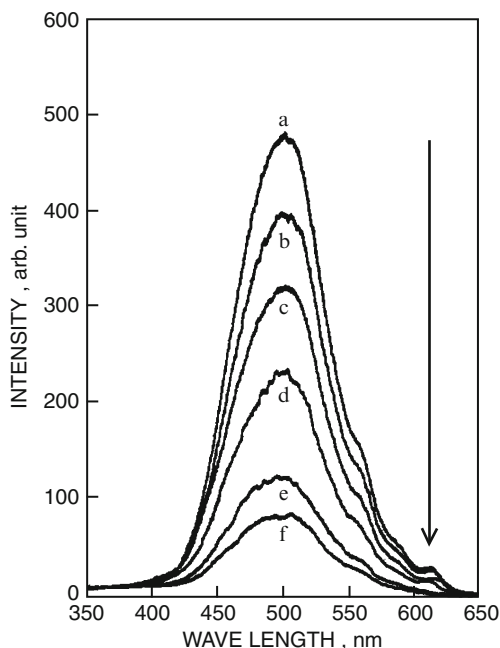
Photoluminescence is basically a kind of surface phenomena of the solid materials, hence the changes of the surface environment will have significant impact on the photoluminescence processes. Study the photoluminescence in the presence of reactant molecules is expected to be a useful approach toward better understanding the relationship between the surface structure and the excited states of the catalysts. Meanwhile, the reactant molecules can also act as molecular probes to explore the detailed photo-induced surface processes generating the electron and hole pairs. The photoluminescence intensity of TiO₂ largely depends on its surrounding chemical and physical environments, such as the nature of the adsorbed molecules. The photoluminescence intensity of TiO₂ depends heavily on its atmosphere. Anpo et al. (1991) had qualitatively depicted the dependence of the photoluminescence intensity of TiO₂ on its surrounding environments by correlating the photoluminescence with the change of the surface band bending.

For the highly dispersed titanium oxide with individual Ti–O sites anchored onto the porous Vycor glass (Anpo et al. 1985a), its photoluminescence peak located at about 485 nm with much higher intensity than that of bulk TiO₂, which is attributed to the radiative deactivation of the charge-transfer excited state of the titanium oxide species:



The addition of O₂ led to an efficient quenching of the photoluminescence at –196 or 27°C. The addition of N₂O also led to the quenching of the photoluminescence but with lower quenching efficiency than that of O₂. The efficient quenching of the photoluminescence was attributed to the efficient interaction of the emitting sites with the quencher molecules (O₂ or N₂O here), since the emitting sites were highly dispersed individual sites on the surface of porous Vycor glass. Here, the quenching of the photoluminescence is mainly due to the electron transfer from the excited states of the catalyst to the added O₂ or N₂O molecules.

Fig. 4 Photoluminescence of TiO_2 at -196°C in the absence (spectrum a) and presence of added O_2 (spectra b–f). Excitation wavelength = 300 nm; temperature = -196°C ; amounts of added O_2 (in 10^{-6} mol/g of catalyst): (a) 0; (b) 1.1; (c) 4.7; (d) 11.8; (e) 38.2; and (f) 72–150 (Anpo et al. 1989)

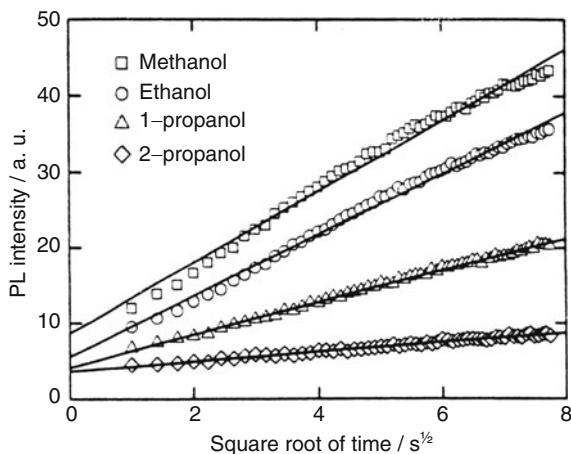


Anpo et al. (1989) also systematically studied the influence of the different adsorption molecules on the photoluminescence properties of TiO_2 powder. The TiO_2 powder exhibits a photoluminescence band at 450–550 nm when excited with the light of photon energy larger than the band gap of TiO_2 . As shown in Fig. 4, the intensity of the photoluminescence obviously decreases with the increase of the amount of O_2 adsorbed onto TiO_2 . However, addition of excessive amount of O_2 cannot quench the photoluminescence completely. In a typical experiment for a sample under 1 bar of O_2 atmosphere, it was found that about 15% of the photoluminescence remains unquenched. And the quenched photoluminescence could not be fully recovered upon evacuation of the sample at 25°C . ESR measurements indicated that addition of O_2 onto TiO_2 at 25°C leads to the formation of O_2^- anion radicals adsorbed onto the Ti^{4+} sites. This confirms that the irreversible quenching of the photoluminescence is due to the formation of thermally stable superoxide anion species which retains tightly on the surface of TiO_2 even after exhaustive evacuation at 25°C . It was also found that addition of N_2O also leads to the photoluminescence quenching but with relatively lower quenching efficiency compared to O_2 . The photoluminescence quenching by N_2O was interpreted as the consequence of electron transfer from TiO_2 to N_2O molecules which further decompose into N_2 and O^- . On the contrary, addition of various unsaturated hydrocarbons, such as 1- C_4H_8 , C_3H_6 , $\text{C}_2\text{H}_5\text{C}\equiv\text{CH}$, $\text{CH}_3\text{C}\equiv\text{CH}$, C_2H_4 , and $\text{CH}\equiv\text{CH}$, and small molecules such as H_2O and H_2 , can considerably enhance the photoluminescence of TiO_2 powder. Furthermore, the extent of the photoluminescence enhancement strongly depends on the ionization potentials of the added

compounds: the lower the ionization potential of the added compound, the higher the photoluminescence intensity. Addition of inert gas, such as N₂, has negligible influence on the photoluminescence. The quenching and enhancement of the photoluminescence intensity of TiO₂ powder can be understood by the changes of the surface band bending in the dead-layer model: the width of the TiO₂ depletion layer becomes larger if the negatively charged adduct species are formed through the electron capture; or it becomes smaller if positive adduct species are formed through the hole trapping. Consequently, the photoluminescence intensity of TiO₂ powder is quenched or enhanced.

Nakajima investigated the influence of C₁–C₃ alcohols on the photoluminescence properties of TiO₂ and discussed the relationship between the properties of the photoluminescence and the adsorbates on the TiO₂ surface (Nakajima et al. 2001, 2002, 2004). The photoluminescence of rutile and anatase TiO₂ powders was measured at room temperature in vacuum, in air, and in air with one of C₁–C₃ alcohols (methanol, ethanol, 1-propanol, and 2-propanol). For rutile TiO₂ powder (Fig. 5), the photoluminescence intensities in air with the C₁–C₃ alcohols and in vacuum increase linearly with $t^{0.5}$, and the time dependence of the photoluminescence intensities agrees with that of the integrated amount of photo-desorbed O₂ from rutile TiO₂ powder. For anatase TiO₂ powder, the photoluminescence intensities in air with methanol and in vacuum also increased linearly with $t^{0.5}$. But this is only the case for methanol, adsorption of other alcohols in air do not increase the photoluminescence intensities. This kind of time dependence of the photoluminescence intensities of TiO₂ in air caused by the interaction with alcohols is elucidated by considering the photo-desorption of O₂ and its effect on the surface band bending of the TiO₂ powder. It is known that the adsorbed O₂ on the rutile TiO₂ powder can be photo-desorbed by the irradiation of the excitation light during the photoluminescence measurement. Adsorption of alcohols inhibits the desorbed O₂ from re-adsorption onto the powder by taking the adsorption vacancies left by the desorbed O₂. Replacement of the adsorbed O₂ by alcohols reduces the surface

Fig. 5 The relationships between the photoluminescence intensities of rutile TiO₂ powder Kanto-R in air with C₁–C₃ alcohols (methanol, ethanol, 1-propanol, and 2-propanol) and the square root of the UV irradiation time from 1 to 60 s. The squares of the regression coefficients are more than 0.98 (Nakajima et al. 2002)



charge density of the powder and hence the thickness of the space-charge layer linearly with the increase of the $t^{0.5}$. Decrease of the space-charge layer surely facilitates the electron-hole recombination on the surface of the powder, resulting in the increase of the photoluminescence intensity. The inconsistency of the photoluminescence behavior of the anatase TiO_2 upon interaction with different alcohols might be originated from the different photocatalytic activities of anatase TiO_2 toward different alcohols.

The influence of H_2O molecules on the photoluminescence properties of TiO_2 has been studied in our group (Shi et al. 2007a, b). As shown in Fig. 3A, the intensity of the visible luminescence band increases in the presence of water vapor, decreases gradually upon the heat-treatment, and finally declines to the initial level after annealed in the oxygen atmosphere. The interaction between water and the surface of TiO_2 has been studied by a variety of spectroscopic techniques, such as temperature-programmed desorption (TPD), scanning tunneling microscopy (STM), X-ray and ultraviolet photoemission spectroscopy (XPS and UPS). Kurtz et al. (1989) reported that the dissociative adsorption of H_2O onto the TiO_2 surface results in the increase of the amount of the Ti^{3+} defect sites, which also serve as an indication of the increase of the amount of oxygen vacancy sites, since formation of these two sites are the parallel results of the Ti–O bond dissociative cleavages. These fundamental processes can aid us to understand the photoluminescence effect of water upon adsorption onto the TiO_2 . It was observed that the visible emission intensity was increased after exposing the surface of TiO_2 to water vapor. The interaction between the water molecules and the TiO_2 surface defect sites actually involves not only the adsorption and dissociation of water on the surface, but also the surface redox reaction such as re-oxidation of the reduced Ti^{3+} to Ti^{4+} by the adsorbed water molecules (Wang et al. 1999; Lu et al. 1994). The oxygen atoms of the water molecules are preferentially extracted by the substrate to fill the surface oxygen vacancies. Therefore, the gradual quenching of the visible luminescence band was observed in the following processes of the thermal treatment. Above the treatment temperature of 500°C , the surface of TiO_2 is fully oxidized by water and accordingly the nearly-perfect surface is formed, as a result, the visible-luminescence intensity decreases to the level of TiO_2 annealed in O_2 .

5 The Influence of Platinum Loading on Photoluminescence of TiO_2 Powder

It is well known that the deposited Pt on the surface of TiO_2 plays a vital role in the enhancement of the photocatalytic activity of TiO_2 . Excited electrons migrate from the semiconductor of TiO_2 to the metal Pt once the two Fermi levels are aligned (Linsebigler et al. 1995). The Schottky barrier formed at the Pt and TiO_2 interface can serve as an efficient electron trap preventing electron-hole recombination in photocatalysis (Linsebigler et al. 1995).

Nakajima and Mori 2004 compared the photoluminescence characteristic of TiO₂ before and after Pt loading by mixing the TiO₂ powder with platinum black. The photoluminescence intensity of the pure TiO₂ powder was greater than that of the Pt-loaded TiO₂ powder. The result was elucidated as follows: during the photoluminescence measurement, excitation of TiO₂ semiconductor with excitation light generates electron and hole pairs in conduction band and valence band, respectively. The photoinduced electrons in the conduction band will further migrates to the Pt deposited on the surface of TiO₂ by crossing the aligned Fermi energy levels. Because of the interfacial Schottky barrier between TiO₂ and Pt nanoparticles which inhibits back electron transfer from Pt to TiO₂, electron transfer from TiO₂ to Pt generates efficient electron/hole charge separation by the confinement of the excited electrons in the Pt nanoparticles and the holes in the valence band of TiO₂. This will result in the decrease of the photoluminescence intensity of TiO₂. The photoluminescence of two rutile TiO₂ powders with different specific surface areas upon Pt loading (5 wt%) was also investigated (Nakajima and Mori 2006). It was also found that the intensities of the photoluminescence bands observed at around 410 and 800 nm decreased upon Pt loading. The decrease of the photoluminescence intensity was also ascribed to the result of the electron transfer from TiO₂ to Pt nanoparticles.

Our group also investigated the influence of the deposited Pt on the photoluminescence properties of TiO₂ and the photocatalytic activities of TiO₂ for H₂ evolution in a solution of water and methanol mixture (Shi et al. 2007a, b), and the results are shown in Figs. 6 and 7. It can be seen that, upon Pt loading, the visible luminescence band of TiO₂ was obviously quenched while the near-infrared luminescence band was only slightly declined. In the photocatalytic reaction for hydrogen production from water and methanol mixtures, the amount of H₂ production is negligible on the pure TiO₂ samples calcined at various temperatures (500, 650 and 900°C); while hydrogen production were detected in the samples with Pt loaded. The photocatalytic activities of the Pt loaded TiO₂ samples calcined at different

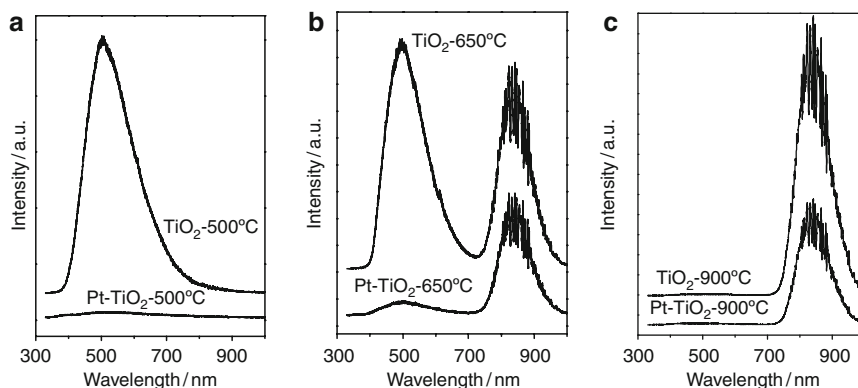
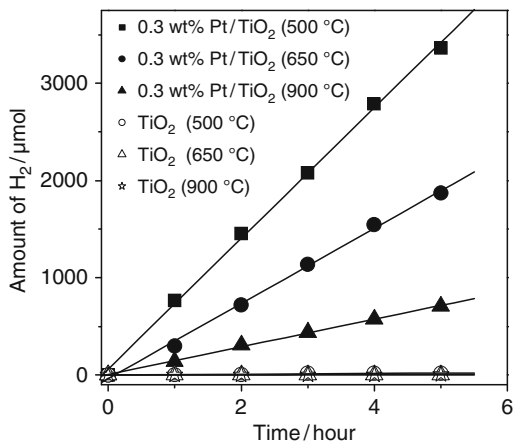


Fig. 6 Photoluminescence spectra of pure TiO₂ and Pt/TiO₂ powders: (a) TiO₂ calcined at 500°C; (b) TiO₂ calcined at 650°C; (c) TiO₂ calcined at 900°C (Shi et al. 2007a, b)

Fig. 7 Photocatalytic H₂ evolutions from methanol-water solution under UV light illumination on pure TiO₂ and Pt/TiO₂ catalysts, and the calcination temperature of TiO₂ are marked in the bracket. Light source, 300 W Xe lamp (Shi et al. 2007a, b)



temperatures follow the order of 500°C > 650°C > 900°C. Since high temperature calcination tends to result in the formation of rutile structure, high photocatalytic activity at relatively low calcination temperature is an indication that anatase TiO₂ has better photocatalytic activity than rutile TiO₂. For TiO₂ alone, the photoinduced charge carriers are mainly deexcited as the luminescence at the recombination centers of the different defects and its photocatalytic activity is negligible. After the deposition of Pt on TiO₂, a large number of photoinduced electrons are further transferred to Pt, which are readily consumed by the photo-assisted reaction. As a consequence, the effective enhancement of H₂ evolution rate is observed for Pt/TiO₂. The obvious quenching of the visible luminescence band and the negligible change of the near-infrared luminescence band indicate that the loading of Pt on the surface of TiO₂ inhibits the recombination of the photoinduced-carriers at the oxygen vacancies in anatase, while it has little influence on the recombination of the photoinduced-carriers at the intrinsic defects in rutile. This may be the reason why photocatalytic activity of anatase TiO₂ is usually higher than that of rutile TiO₂.

6 The Relationship Between the Photocatalytic Performance on TiO₂ and Its Photoluminescence Properties

The photoluminescence spectrum can directly give not only the information about the separation and recombination of the photoinduced charge carriers, but also the information about the surface defects, oxygen vacancies, and surface states, etc. Photoluminescence properties of TiO₂ is useful for monitoring the surface property changes associated with the photocatalytic reactions, for evaluating the photocatalytic activity of TiO₂, and for more thoroughly understanding the mechanism of TiO₂ photocatalysis. The inherent relationships between the photoluminescence

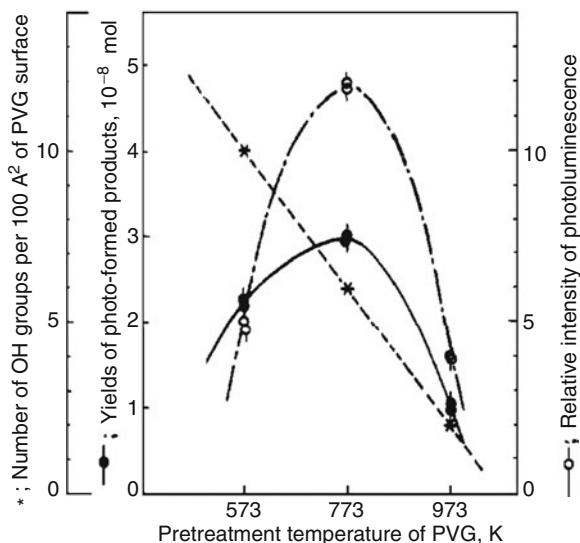


Fig. 8 Effect of the pretreatment temperature of PVG upon the yields of photohydrogenation reaction of CH₃-C≡CH with H₂O and of photoluminescence of the anchored titanium oxide catalyst at 27°C (UV excitation wavelength >290 nm; reaction temperature, 27°C; initial pressure of CH₃-C≡CH, 3.0 torr; initial pressure of H₂O 5.0 torr; excitation wavelength for photoluminescence, 280 ± 10 nm; emission slit width, 7.0 nm), (Anpo et al. 1985a)

intensity and photocatalytic activity have already been investigated and reviewed in detail (Jung et al. 2005; Jing et al. 2006; Jung and Kim 2009).

UV irradiation of the porous Vycor glass anchored with TiO₂ in the presence of H₂O and CH₃-C≡CH at 27°C leads to the photocatalytic hydrogenation of CH₃-C≡CH (Anpo et al. 1985a). As shown in Fig. 8, the yield of the photocatalytic hydrogenation products changes accordingly with the change of the photoluminescence intensity of the anchored titanium oxide. It was proposed that the photoluminescence originates from the charge-transfer excited state of the (Ti³⁺-O⁻)*, which plays a vital role in the photocatalytic hydrogenation reaction of water with CH₃-C≡CH on the anchored titanium oxide catalyst. UV irradiation of the TiO₂ in the presence of sufficient amount of H₂O and unsaturated hydrocarbon, such as C₃H₆ and C₄H₆, leads to the formation of photocatalytic hydrogenated products and oxygenated products (Anpo 1997; Anpo et al. 1984, 1987). As shown in Fig. 9, the rates of these photocatalytic reactions increase with the decrease of the ionization potential of the reactants (Anpo et al. 1989). There exists a parallel relationship between the enhancement of TiO₂ photoluminescence resulted from the addition of unsaturated hydrocarbons and the photocatalytic reaction rate of these unsaturated hydrocarbons with H₂O on TiO₂, since both of these two processes are closely associated with the electron transfer and the charge separated state. In other words, the initial electron transfer from the reactant molecules to TiO₂ to form cationic derivatives of the hydrocarbons is one of the crucial rate determining steps toward

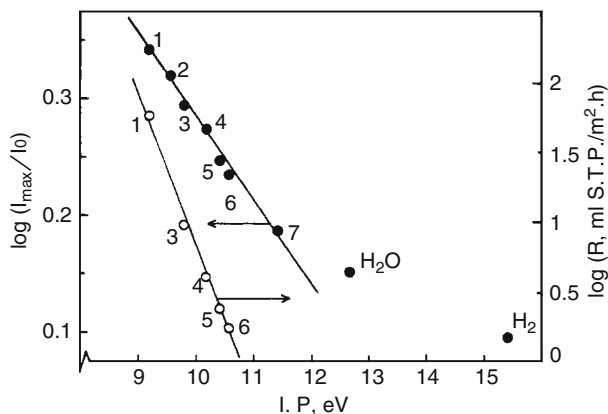


Fig. 9 Effect of additive ionization potentials on the photoluminescence intensity (*filled circle*) and the rate of the photocatalytic hydrogenation of the added unsaturated hydrocarbons with H_2O on TiO_2 (*open circle*). I_0 and I_{max} are maximum photoluminescence intensities, respectively, under vacuum (or in N_2) and in the presence of added compounds: (1) 1,3-butadiene; (2) 1-butene; (3) propene; (4) 1-butyne; (5) 1-propyne; (6) ethylene; and (7) acetylene. Photoluminescence spectra were recorded at -196°C . Photocatalytic reactions were carried out at 25°C (Anpo et al. 1989)

the efficient charge separation of the photoinduced electron/hole pairs, which in turn plays a vital role in determining the yields of the photocatalytic reaction and the intensity of the photoluminescence of the TiO_2 catalyst.

Jung et al. (2005) investigated the photoluminescence characteristics of anatase titania particles prepared by sol-gel method and found good correlations between the photocatalytic behavior and the sample's calcination temperature. They monitored the quenching behavior of the photoluminescence at -196°C by in situ oxygen supply. And Fig. 10 shows the dependence of the quenching intensity (the intensity difference at the peak position of the two photoluminescence spectra measured with and without oxygen) of prepared titania particles on the sample's calcination temperature. The photocatalytic activity of titania toward the decomposition of trichloroethylene (TCE) was measured and plotted as the function of the calcination temperature in Fig. 10. It can be seen that the photocatalytic activity changes in line with the quenching intensity with the variation of the calcination temperatures. The photoluminescence quenching is due to the upward bending of the band edge, which produces thicker space-charge layer for efficient separation of the photoinduced electron/hole pairs. The quenching level largely depends on the quantity of the surface-active sites on which oxygen can be adsorbed. The higher the photoluminescence quenching intensity implies the existence of larger amounts of surface-active sites which readily react with oxygen. Photocatalysis is a surface reaction and the reaction rate is proportional to the quantity of the surface-active sites taken by the electron acceptors or donors. And since titania shows efficient photoluminescence quenching, it is supposed that it should have high photocatalytic activity. The parallel relationship between the quenching intensity of the

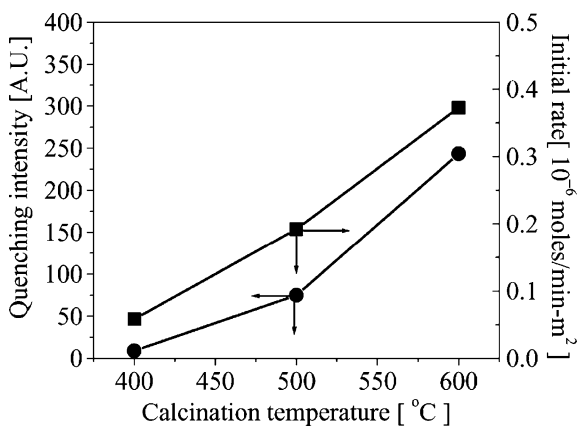


Fig. 10 The effect of the calcination temperature on the quenching intensity of photoluminescence measured at -196°C and the photoactivity of as-prepared titania particles (Jung et al. 2005)

photoluminescence and the photocatalytic activity of TCE decomposition suggests that the increase of the photocatalytic activity of titania particles with the increase of the calcination temperature is due to the formation of surface-active sites.

7 Conclusions

In this chapter, we discussed the application of photoluminescence spectroscopy in the study of TiO₂ photocatalysts. The origin of the TiO₂ photoluminescence, the influence of the adsorbates and loaded Pt on the photoluminescence properties of TiO₂, and the relationship between photoluminescence properties and the photocatalytic activities are summarized. Photoluminescence spectroscopy is an effective way to study the electronic structures, optical and photochemical properties of semiconductor materials. The photoluminescence spectrum applied in photocatalysis fields can provide useful information about the surface oxygen vacancies and defects, the efficiency of charge carrier trapping, immigration and transfer, which are useful for designing and synthesizing new semiconductor photocatalysts with high activity. Better understanding of these processes is crucial for the design and synthesis of new semiconductor photocatalysts with high photocatalytic activity.

It should mention that we haven't included the time-resolved photoluminescence spectroscopic technique in this chapter, though it can provide more direct information about the transfer and separation processes of the photo-induced charge carriers at or near semiconductor surfaces and their effects on photocatalytic activity. Several good studies on TiO₂ have been reported using time-resolved photoluminescence spectroscopy (Fujihara et al. 2000; Harada et al. 2007). Application of the steady-state and time-resolved photoluminescence spectroscopy

combined with other related techniques is a powerful tool to nail the nature of the complex photocatalytic processes, which is the main message we would like to deliver in this chapter.

Acknowledgements This work was financially supported by the National Natural Science Foundation of China (NSFC, grant 20673112 and 20373069), the National Basic Research Program of China (grant 2009CB220010), and Program for Strategic Scientific Alliances between China and the Netherlands (2008DFB50130).

References

- Anpo M (1997) *Catal Surv Jpn* 1:169
- Anpo M, Che M (2000) Applications of photoluminescence techniques to the characterization of solid surfaces in relation to adsorption, catalysis, and photocatalysis. *Adv Catal* 44:119–257
- Anpo M, Aikawa N, Kodama S, Kubokawa Y (1984) Photocatalytic hydrogenation of alkynes and alkenes with water over TiO₂. Hydrogenation accompanied by bond fission. *J Phys Chem* 88:2569–2572
- Anpo M, Aikawa N, Kubokawa Y, Che M, Louis C, Giamellot E (1985a) Photoluminescence and photocatalytic activity of highly dispersed titanium oxide anchored onto porous Vycor glass. *J Phys Chem* 89:5017–5021
- Anpo M, Shima T, Kubokawa Y (1985b) ESR and photoluminescence evidence for the photocatalytic formation of hydroxyl radicals on small TiO₂ particles. *Chem Lett* 168:1799–1802
- Anpo M, Shima T, Kodama S, Kubokawa Y (1987) Photocatalytic hydrogenation of CH₃CCH with H₂O on small-particle TiO₂: size quantization effects and reaction intermediates. *J Phys Chem* 91:4305–4310
- Anpo M, Tomonari M, Fox MA (1989) In situ photoluminescence of TiO₂ as a probe of photocatalytic reactions. *J Phys Chem* 93:7300–7302
- Anpo M, Chiba K, Tomonari M, Coluccia S, Che M, Fox MA (1991) Photocatalysis on native and platinum-loaded TiO₂ and ZnO catalysts – origin of different reactivities on wet and dry metal oxides. *Bull Chem Soc Jpn* 64:543–551
- Chaves A, Katiyan KS, Porto SPS (1974) Coupled modes with A₁ symmetry in tetragonal BaTiO₃. *Phys Rev* 10:3522–3533
- Chen J, Feng ZC, Ying PL, Li MJ, Han B, Li C (2004a) The visible luminescent characteristics of ZnO supported on SiO₂ powder. *Phys Chem Chem Phys* 6:4473–4479
- Chen J, Feng ZC, Ying PL, Li C (2004b) ZnO clusters encapsulated inside micropores of zeolites studied by UV Raman and laser-induced luminescence spectroscopies. *J Phys Chem B* 108:12669–12676
- Chen J, Feng ZC, Shi JY, Ying PL, Zhang HD, Li C (2005) The surface sites of sulfated zirconia studied in situ by laser-induced fluorescence spectroscopy. *Chem Phys Lett* 401:104–108
- Cronemeyer DC (1959) Infrared absorption of reduced rutile TiO₂ single crystals. *Phys Rev* 113:1222–1226
- de Haart LGJ, Blasse G (1986) The observation of exciton emission from rutile single crystals. *J Solid State Chem* 61:135–136
- Diebold U (2003) The surface science of titanium dioxide. *Surf Sci Rep* 48:53–229
- Ding Z, Lu GQ, Greenfield PF (2000) Role of the crystallite phase of TiO₂ in heterogeneous photocatalysis for phenol oxidation in water. *J Phys Chem B* 104:4815–4820
- Emeline AV, Ryabchuk VK, Serpone N (2005) Dogmas and misconceptions in heterogeneous photocatalysis. Some enlightened reflections. *J Phys Chem B* 109:18515–18521
- Fernández I, Cremades A, Piqueras J (2005) Cathodoluminescence study of defects in deformed (110) and (100) surfaces of TiO₂ single crystals. *Semicond Sci Technol* 20:239–243

- Forss L, Schubnell M (1993) Temperature dependence of the luminescence of TiO₂ powder. *Appl Phys B* 56:363–366
- Fujihara K, Ohno T, Matsumura M (1998) Splitting of water by electrochemical combination of two photocatalytic reactions on TiO₂ particles. *J Chem Soc Faraday Trans* 94:3705–3709
- Fujihara K, Izumi S, Ohno TA, Matsumura M (2000) Time-resolved photoluminescence of particulate TiO₂ photocatalysts suspended in aqueous solutions. *J Photochem Photobiol A* 132:99–104
- Ghosh AK, Wakim FG, Jr Addiss RR (1969) Photoelectronic processes in rutile. *Phys Rev* 184:979–988
- Göpel W, Rocker G, Feirabend R (1983) Intrinsic defects of TiO₂(110): interaction with chemisorbed O₂, H₂, CO, and CO₂. *Phys Rev B* 28:3427–3438
- Grabner L, Stokowski SE, Jr Brower WS (1970) No-phonon ⁴T_{2g}–⁴A_{2g} transitions of Cr³⁺ in TiO₂. *Phys Rev B* 2:590–597
- Hachiya K, Kondoh J (2003) Photoluminescence from localized states in rutile by Ar⁺-ion laser excitation. *Physica B* 334:130–134
- Harada N, Goto M, Iijima K, Sakama H, Ichikawa N, Kunugita H, Ema K (2007) Time-resolved luminescence of TiO₂ powders with different crystal structures. *Jpn J Appl Phys* 46:4170–4171
- Henderson MA, Epling WS, Perkins CL, Peden CHF (1999) Interaction of molecular oxygen with the vacuum-annealed TiO₂ (110) surface: molecular and dissociative channels. *J Phys Chem B* 103:5328–5337
- Henrich VE, Cox PA (1994) *The surface science of metal oxides*. Cambridge University Press, Cambridge
- Jeon K, Oh S, Suh YD, Yoshikawa H, Masuhara H, Yoon M (2009) Blinking photoluminescence properties of single TiO₂ nanodiscs: interfacial electron transfer dynamics. *Phys Chem Chem Phys* 11:534–542
- Jing LQ, Qu YC, Wang BQ, Li SD, Jiang BJ, Yang LB, Fu W, Fu HG, Sun JZ (2006) Review of photoluminescence performance of nano-sized semiconductor materials and its relationships with photocatalytic activity. *Sol Energ Mat Sol C* 90:1773–1787
- Jung HS, Kim H (2009) Origin of low photocatalytic activity of rutile TiO₂. *Electron Mater Lett* 5:73–76
- Jung KY, Park SB, Anpo M (2005) Photoluminescence and photoactivity of titania particles prepared by the sol–gel technique: effect of calcination temperature. *J Photochem Photobiol A Chem* 170:247–252
- Knorr FJ, Mercado CC, McHale JL (2008) Trap-state distributions and carrier transport in pure and mixed-phase TiO₂: influence of contacting solvent and interphasial electron transfer. *J Phys Chem C* 112:12786–12794
- Kurtz RL, Stockbauer R, Madey TE, Roman E, de Segovia JL (1989) Synchrotron radiation studies of H₂O adsorption on TiO₂ (110). *Surf Sci* 218:178–200
- Lei Y, Zhang LD, Meng GW, Li GH, Zhang XY, Liang CH, Chen W, Wang SX (2001) Preparation and photoluminescence of highly ordered TiO₂ nanowire arrays. *Appl Phys Lett* 78:1125–1127
- Linsebigler AL, Lu G, Yates JT Jr (1995) Photocatalysis on TiO₂ surfaces: principles, mechanisms, and selected results. *Chem Rev* 95:735–758
- Lu G, Linsebigler A, Yates JT Jr (1994) Ti³⁺ Defect sites on TiO₂(110): production and chemical detection of active sites. *J Phys Chem* 98:11733–11738
- Mochizuki S, Shimizu T, Fujishiro F (2003) Photoluminescence study on defects in pristine anatase and anatase-based composites. *Physica B* 340–342:956–959
- Montoncello F, Carotta MC, Cavicchi B, Ferroni M, Giberti A (2003) Near-infrared photoluminescence in titania: evidence for phonon-replica effect. *J Appl Phys* 94:1501–1505
- Murakami Y, Kenji E, Nosaka AY, Nosaka Y (2006) Direct detection of OH radicals diffused to the gas phase from the UV-irradiated photocatalytic TiO₂ surfaces by means of laser-induced fluorescence spectroscopy. *J Phys Chem B* 110:16808–16811

- Murakami Y, Endo K, Ohta I, Nosaka AY, Nosaka Y (2007) Can OH radicals diffuse from the UV-irradiated photocatalytic TiO₂ surfaces? Laser-induced-fluorescence study. *J Phys Chem C* 111:11339–11346
- Naito K, Tachikawa T, Fujitsuka M, Majima T (2009) Single-molecule observation of photocatalytic reaction in TiO₂ nanotube: importance of molecular transport through porous structures. *J Am Chem Soc* 131:934–936
- Nakajima H, Mori T (2004) Influence of platinum loading on photoluminescence of TiO₂ powder. *J Appl Phys* 96:925–927
- Nakajima H, Mori T (2006) Photoluminescence of Pt-loaded TiO₂ powder. *Physica B* 376–377:820–822
- Nakajima H, Itoh K, Murabayashi M (2001) Influence of the adsorbate and the crystal structure on the photoluminescence property of TiO₂ powder in air with ethanol vapor at room temperature. *Chem Lett* 4:304–305
- Nakajima H, Itoh K, Murabayashi M (2002) Influences of C₁–C₃ alcohols and purities of TiO₂ powders on their photoluminescence properties at room temperature. *Bull Chem Soc Jpn* 75:601–606
- Nakajima H, Mori T, Watanabe M (2004) Relationship between photoluminescence intensity of TiO₂ suspension containing ethanol and its surface coverage on TiO₂ surface. *Jpn J Appl Phys* 43:3609–3610
- Nakajima H, Mori T, Shen Q, Toyoda T (2005) Photoluminescence study of mixtures of anatase and rutile TiO₂ nanoparticles: influence of charge transfer between the nanoparticles on their photoluminescence excitation bands. *Chem Phys Lett* 409:81–84
- Nakato Y, Tsumura A, Tsubomura H (1983) Photo- and electroluminescence spectra from an *n*-TiO₂ semiconductor electrode as related to the intermediates of the photooxidation reaction of water. *J Phys Chem* 87:2402–2405
- Nakato Y, Ogawa H, Morita K, Tsubomura H (1986) Luminescence spectra from *n*-TiO₂ and *n*-SrTiO₃ semiconductor electrodes and those doped with transition-metal oxides as related with intermediates of the photooxidation reaction of water. *J Phys Chem* 90:6210–6216
- Nakato Y, Akanuma H, Magari Y, Yae S, Shimizu J-I, Mori H (1997) Photoluminescence from a bulk defect near the surface of an *n*-TiO₂ (rutile) electrode in relation to an intermediate of photooxidation reaction of water. *J Phys Chem B* 101:4934–4939
- Nishimoto S, Ohtani B, Kajiwarra H, Kagiya T (1985) Correlation of the crystal structure of titanium dioxide prepared from titanium tetra-2-propoxide with the photocatalytic activity for redox reactions in aqueous propan-2-ol and silver salt solutions. *J Chem Soc Faraday Trans* 81:61–68
- Ohno T, Sarukawa K, Matsumura M (2001) *J Phys Chem B* 105:2417–2420
- Plugaru R, Cremades A, Piqueras J (2004) The effect of annealing in different atmospheres on the luminescence of polycrystalline TiO₂. *J Phys Condens Matter* 16:S261–S268
- Poznyak SK, Sviridov VV, Kulak AI, Samtsov MP (1992) Photoluminescence and electroluminescence at the TiO₂-electrolyte interface. *J Electroanal Chem* 340:73–97
- Qian L, Jin ZS, Zhang JW, Huang YB, Zhang ZJ, Du ZL (2005) Study of the visible-excitation luminescence of NTA-TiO₂ (AB) with single-electron-trapped oxygen vacancies. *Appl Phys A* 80:1801–1805
- Salvador P, García González ML (1992) Catalytic role of lattice defects in the photoassisted oxidation of water at (001) *n*-TiO₂ rutile. *J Phys Chem* 96:10349–10353
- Sanjinés R, Tang H, Berger H, Gozzo F, Margaritondo G, Lévy F (1994) Electronic structure of anatase TiO₂ oxide. *J Appl Phys* 75:2945–2951
- Sekiya T, Yagisawa T, Kamiya N, Mulmi DD, Kurita S, Murakami Y, Kodaira T (2004) Defects in anatase TiO₂ single crystal controlled by heat treatments. *J Phys Soc Jpn* 73:703–710
- Serpone N, Lawless D, Khairutdinov R (1995) Size effects on the photophysical properties of colloidal anatase TiO₂ particles: size quantization or direct transitions in this indirect semiconductor? *J Phys Chem* 99:16646–16654

- Shi JY, Chen J, Feng ZC, Chen T, Wang XL, Ying PL, Li C (2006) Time-resolved photoluminescence characteristics of subnanometer ZnO clusters confined in the micropores of zeolites. *J Phys Chem B* 110:25612–25618
- Shi JY, Chen J, Feng ZC, Chen T, Lian YX, Wang XL, Li C (2007a) Photoluminescence characteristics of TiO₂ and their relationship to the photoassisted reaction of water/methanol mixture. *J Phys Chem C* 111:693–699
- Shi JY, Chen J, Zhou GH, Feng ZC, Ying PL, Li C (2007b) Photoluminescence spectroscopy of NaTaO₃ and NaTaO₃:Bi³⁺ photocatalysts. *Chem J Chin Univ* 28:692–695
- Tanaka K, Capule MFV, Hisanaga T (1991) Effect of crystallinity of TiO₂ on its photocatalytic action. *Chem Phys Lett* 187:73–76
- Tang H, Berger H, Schmid PE, Lévy F, Burri G (1993) Photoluminescence in TiO₂ anatase single crystals. *Solid State Commun* 87:847–850
- Tang H, Berger H, Schmid PE, Lévy F (1994a) Optical properties of anatase (TiO₂). *Solid State Commun* 92:267–271
- Tang H, Prasad K, Sanjinès R, Schmid PE, Lévy F (1994b) Electrical and optical properties of TiO₂ anatase thin films. *J Appl Phys* 75:2042–2047
- Tsai S, Cheng S (1997) Effect of TiO₂ crystalline structure in photocatalytic degradation of phenolic contaminants. *Catal Today* 33:227–237
- Wang LQ, Ferris KF, Skiba PX, Shultz AN, Baer DR, Engelhard MH (1999) Interactions of liquid and vapor water with stoichiometric and defective TiO₂(100) surfaces. *Surf Sci* 440:60–68
- Wu NL, Lee MS, Pon ZJ, Hsu JZ (2004) Effect of calcination atmosphere on TiO₂ photocatalysis in hydrogen production from methanol/water solution. *J Photochem Photobiol A Chem* 163:277–280
- Yu JC, Lin J, Lo D, Lam SK (2000) Influence of thermal treatment on the adsorption of oxygen and photocatalytic activity of TiO₂. *Langmuir* 16:7304–7308
- Zacharias M, Fauchet PM (1997) Blue luminescence in films containing Ge and GeO₂ nanocrystals: the role of defects. *Appl Phys Lett* 71:380–382
- Zhang WF, Zhang MS, Yin Z, Chen Q (2000a) Photoluminescence in anatase titanium dioxide nanocrystals. *Appl Phys B* 70:261–265
- Zhang WF, Zhang MS, Yin Z (2000b) Microstructures and visible photoluminescence of TiO₂ nanocrystals. *Phys Stat Sol (a)* 179:319–327
- Zhang J, Li MJ, Feng ZC, Chen J, Li C (2006) UV Raman spectroscopic study on TiO₂. I. Phase transformation at the surface and in the bulk. *J Phys Chem B* 110:927–935

Chapter 8

Surface Chemistry of TiO₂ Photocatalysis and LIF Detection of OH Radicals

Yoshio Nosaka

Abstract By means of laser induced fluorescence (LIF) method, OH radicals formed and released from the surface of TiO₂ photocatalysts were detected. The effect of heat treatments of TiO₂ on the OH radical formation shows that the amount of OH radicals is affected by the states of surface hydroxyl groups but not the crystalline phase. The effects of the surface hydroxyl groups were discussed based on the measurements of the trapped holes with low temperature ESR spectroscopy and adsorbed water with proton NMR spectroscopy. Then, the reaction mechanism of OH radical formation on the TiO₂ surface was suggested to be the reduction of adsorbed H₂O₂ which is accumulated on the surface by photo irradiation. Finally, the previously reported reaction mechanism of the acetic-acid decomposition was reconsidered based on the mechanism of OH radical formation.

1 Introduction

Surface chemistry of TiO₂ photocatalysts could be elucidated by monitoring the primary species produced on photoirradiation. The author has been studying the mechanism of TiO₂ photocatalysis by monitoring the primary species generated in the photocatalytic reaction process (Nosaka 2002, Nosaka et al. 2006b). The features of generated trapped holes and trapped electrons were elucidated by means of electron spin resonance (ESR) measurements under low temperature (Nakaoka and Nosaka 1997). Superoxide radicals were detected by means of luminol chemiluminescence probe method (Nosaka et al. 1997; Hirakawa and Nosaka 2002). Singlet oxygen was detected in TiO₂ photocatalysis by monitoring phosphorescence emission in near-infrared region (Nosaka et al. 2004; Daimon and Nosaka 2007). In

Y. Nosaka (✉)

Department of Chemistry, Nagaoka University of Technology, Nagaoka, Niigata, Japan
e-mail: nosaka@nagaokaut.ac.jp

this report, by employing a laser induced fluorescence (LIF) method, we attempted to clarify the contribution of OH radical in TiO_2 photocatalysis. The modification of the surface structure of TiO_2 by heat treatment affected significantly on the formation of OH radicals and the reaction mechanism, which will be discussed based on an overview of the surface structure of TiO_2 deduced from the experimental evidences in our previous reports.

2 Detection of OH Radicals by Laser Induced Fluorescence Method

Fluorescence has been utilized to detect various species as one of the most sensitive analytical methods. Among them the resonant emission of the fluorescence provides the information on the energy levels characteristic of the specific molecules. When the wavelength of excitation light is fine and can be swept, the excitation spectrum of the fluorescence corresponds to the absorption spectrum of the molecule. This could be realized by using a laser beam as the excitation light, which is acknowledged as a LIF method. The LIF method has the advantage of detecting OH radicals in the atmosphere because of the high sensitivity up to 10^6 molecules/ cm^3 . Then, we applied the LIF method to detect OH radicals in TiO_2 photocatalysis.

Figure 1 shows the outline of the experimental set-up to detect OH radicals. The apparatus for the LIF detection for TiO_2 photocatalytic systems consists of four parts; a gas flow reaction chamber, a pulse laser for TiO_2 excitation, a tunable dye laser for OH radical excitation, and a fluorescence detection system. A gas flow reaction chamber consists of a crossed Pyrex glass tube with quartz windows at each end. TiO_2 powder was placed on a holder at the center of the cross tube. For excitation of TiO_2 powder, a Nd:YAG laser of 355 nm (3 mJ/pulse at 10 Hz) or 266 nm was used. For OH radical excitation used was a dye (Rhodamine 590) laser with an SHG crystal which produced the light beam of the variable wavelength ranging from 282 to 284 nm. The dye laser was activated by a second harmonics of

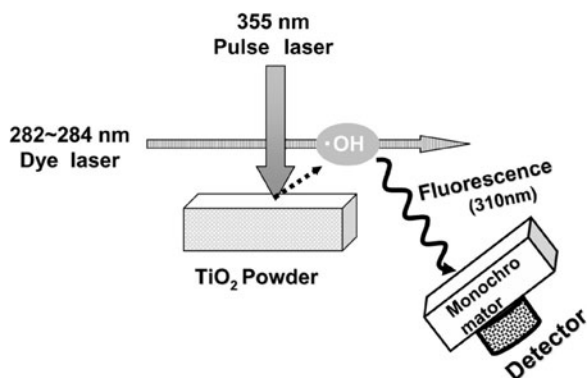


Fig. 1 Experimental outline to detect OH radicals released from TiO_2 photocatalyst

a Nd:YAG laser at 532 nm (80 mJ/pulse at 10 Hz). As shown in Fig. 1, TiO₂ powder was excited from the top, while the dye laser for the excitation of OH radical was irradiated from the side parallel to the TiO₂ surface. The distance of the dye laser beam and the powder surface was about 5 mm. The pulse of the dye laser was delayed from the 355 nm laser pulse by up to 800 μs. A fluorescence detection system was constituted by a monochromator to select 310 ± 10 nm, a photomultiplier, a boxcar integrator, and a computer (Murakami et al. 2006).

Figure 2 shows a typical excitation spectra monitored at 310 nm, which corresponds to the OH(A-X, 1'-1'') transition band. The position of the peaks in Fig. 2 corresponds to the absorption band of OH(A-X, 1'-0'') with different rotation quantum numbers. The peak at 282.93 nm, which is assigned to Q₁(6) transition was used as a measure of the intensity of OH-LIF.

Figure 3 shows the delay time dependence on the LIF intensity. The peak observed at 100 μs indicates that OH radicals diffused 5 mm away from the surface of TiO₂ by this time. The change in the distance between the dye laser beam and TiO₂ surface caused the shift of the peak position in Fig. 3, which correspond to the traveling time for OH radical. Thus, it was confirmed by the peak shift that the observed LIF signal corresponded to the OH radicals diffused from the surface of TiO₂ and that the radical was formed at the surface of TiO₂. In the mechanism for such a remote oxidation with TiO₂ photocatalysts, the formation of radicals by UV excitation of H₂O₂ released from the surface has been suggested (Kubo and Tatsuma 2006). However, the present observation suggests that the OH radicals should be released from the surface of excited TiO₂. In addition, when the UV laser wavelength was changed from 355 to 266 nm, the observed OH LIF intensity was comparable, although the absorption coefficient of H₂O₂ differs by three orders of magnitude. This experimental result also supports that OH radicals detected in the present study is released from the TiO₂ surface but not via excitation of H₂O₂.

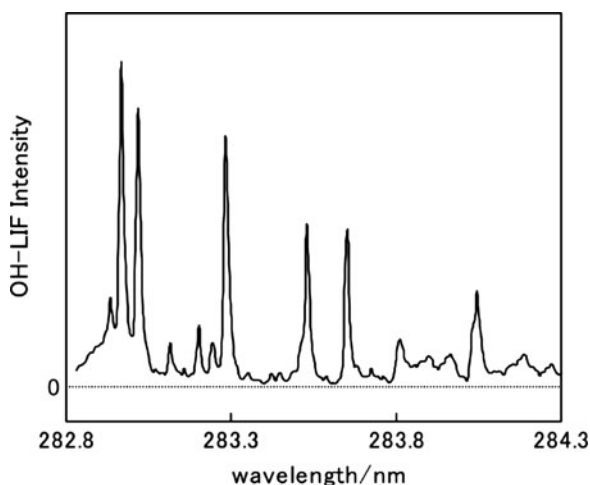


Fig. 2 OH LIF spectrum detected at 310 nm for TiO₂ on 355 nm excitation

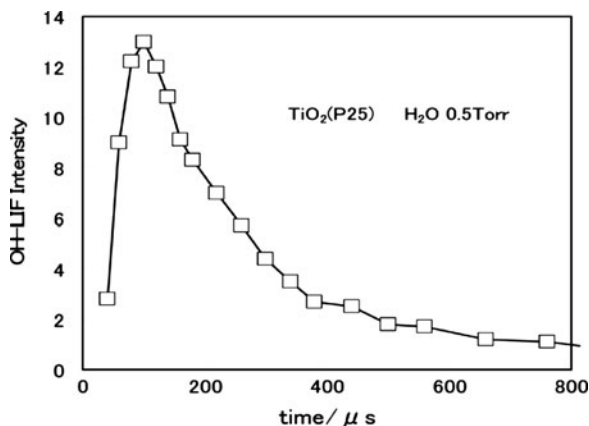


Fig. 3 OH LIF intensity as a function of delay time from the excitation of TiO_2

3 Effects of Calcination of TiO_2 on the OH LIF Intensity

To obtain more detailed information on the mechanism of the $\cdot\text{OH}$ formation, we prepared TiO_2 powders with different surface structures on calcinations, and investigated the effect on the $\cdot\text{OH}$ formation. Figure 4 shows the effect of the calcinations of ST-01 and P25 TiO_2 powders. ST-01 (Ishihara Sangyo Co. Ltd.) is anatase powder that is made from titanium sulfonate, while P25 (Degussa, Japan Aerosil) is made from titanium chloride at relatively high temperature. The anatase contents of the crystalline phase of TiO_2 on calcinations taken from the previous report (Nosaka et al. 2002) are shown in Fig. 4a. On calcinations, the amount of formed OH radical decreased for P25, while it increased for ST-01 calcined at up to 600°C . The formation of OH radical decreased for ST-01 calcined at 700°C , where the anatase content was still 96%. Thus, the OH LIF intensity does not always correlate with the crystalline phase on calcinations. This fact indicates that the crystallite phase does not affect the amount of OH radical formation (Nosaka et al. 2003), but that the chemical structure of TiO_2 surface should play important roles taking into account the fact that the calcination changes the chemical structure of TiO_2 surface.

4 Effect of Calcination on Trapped Holes in ESR Spectroscopy

In our previous work, we observed the change in the chemical structure of photoproduced holes, when anatase TiO_2 powder (UV100, Sachtleben Chemie) was heat-treated (Nosaka et al. 1997). We showed that this change was caused by the desorption of surface OH groups which resulted in the change of the surface chemical bonds, because the crystal structure was preserved after the heat treatments. For the unheated samples possessing a large quantity of surface hydroxyl

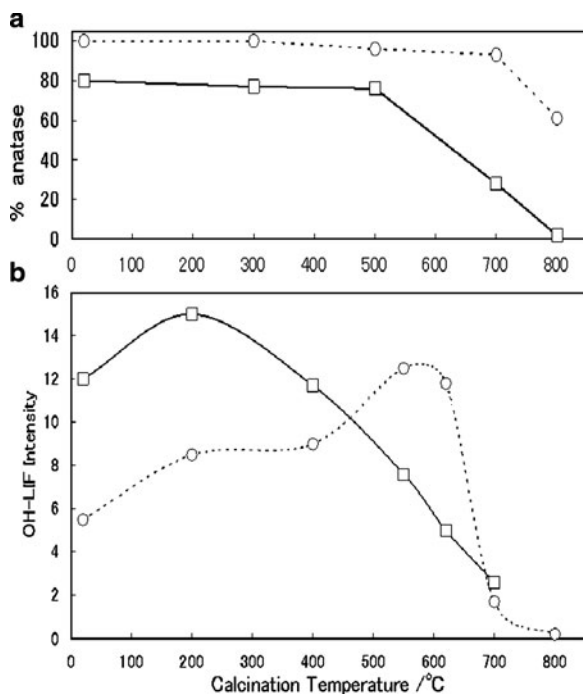


Fig. 4 Effect of calcination on the crystalline phase (a) and the amount of OH radical released (b) for P25 (square) and ST-01 (circle) TiO₂ powders

groups, the photogenerated holes produced a paramagnetic species having a set of g values of 2.004, 2.014, and 2.018, which was assigned to the bridge oxygen radical located under the surface Ti atoms, i.e., $\text{Ti}^{4+}\text{O}^{\bullet-}\text{Ti}^{4+}\text{OH}^-$. On the other hand, when the hydroxyl groups were desorbed by heat treatments, the photogenerated holes produced another paramagnetic species having a set of g values of 2.004, 2.018, and 2.030. This radical was assigned to the terminal oxygen radical located at the surface, $\text{Ti}^{4+}\text{O}^{2-}\text{Ti}^{4+}\text{O}^{\bullet}$, and showed a different reactivity from that of the $\text{Ti}^{4+}\text{O}^{\bullet-}\text{Ti}^{4+}\text{OH}^-$ radical, though both radicals can be involved in the photocatalytic reaction with the surrounding molecules. The two kinds of trapped holes were formed for several TiO₂ powders which are produced by the different manufacturing processes (Hirakawa et al. 1999).

Figure 5 shows the photoinduced ESR spectra measured at 77 K for four kinds of TiO₂ powders under vacuum. The signals observed at g values higher than 2.00 were assigned to the trapped holes, while those at lower than 2.00 were assigned to the trapped electrons. Though the significant change in the signal of trapped electrons was observed, trapped holes definitely showed two patterns. The signals for the trapped holes observed for ST-01 and UV100, which were prepared from sulfate at relatively low temperature were almost identical while the signal for UV100 treated at 800°C was almost the same as that of P25, which was prepared from titanium chloride at relatively high temperature. Similar change in the

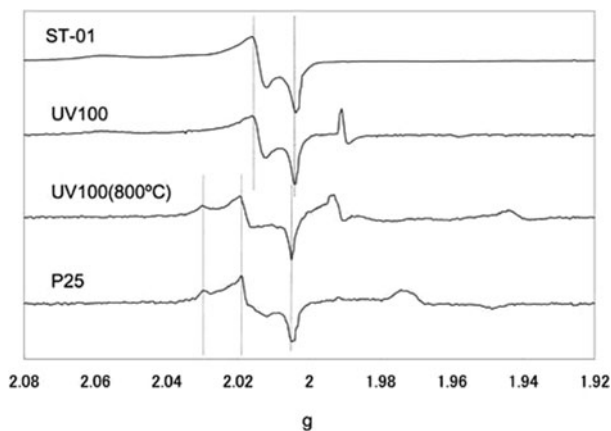


Fig. 5 ESR spectra for trapped holes and trapped electrons observed for different TiO₂ photocatalyst powders under UV irradiation at 77 K

structure of trapped holes has also been reported recently (Kumar et al. 2006). By comparing the calcination effects on OH LIF intensity, the surface structure which forms the trapped holes of $\text{Ti}^{4+}\text{O}^{2-}\text{Ti}^{4+}\text{O}^{\bullet}$ is supposed to take a role to produce OH radicals as observed in (Fig. 4).

5 Effect of Calcination on Surface OH Groups as Studied by NMR Spectroscopy

We measured ¹H NMR spectrum for water adsorbed on TiO₂, though ¹³C NMR spectroscopy has been often used to analyze the organic reactant molecules adsorbed on catalysts (Nakaoka and Nosaka 2005). The adsorbed water consists of at least three kinds of layers (outermost, intermediate, and innermost) which can be recognized by NMR signals as sharp, broader, and the broadest signals (Nosaka and Nosaka 2005). The time profiles of chemical shifts measured at 85°C for six TiO₂ photocatalysts are shown in Fig. 6, along with the schematic illustration of the corresponding signals (Nosaka et al. 2004).

The values at time 0 indicate the chemical shifts measured at 22°C that are mainly corresponding to those of the outermost layer water. On heating at 85°C, the water molecules in the outermost layer which exchange rapidly with the water molecules in air disappear rapidly. Then, the water molecules in the intermediate layer were successively removed in a few hours. For UV100, AMT-100, and ST-01, the water signal shifted to the lower field with time, whereas for F4 (Showa Titanium), AMT-600, and P25, it shifted to the higher field. The TiO₂ powders AMT-100 and AMT-600 were manufactured by TAYCA, the numbers of which indicate the temperature treated (at 100 and 600°C, respectively). The chemical shift observed 2 h after the temperature increase corresponds to that of the water molecules stabilized near the solid surface in the innermost layer. The adsorbed water is considered to be stabilized by strong hydrogen bonds to lead a lower-field shift of

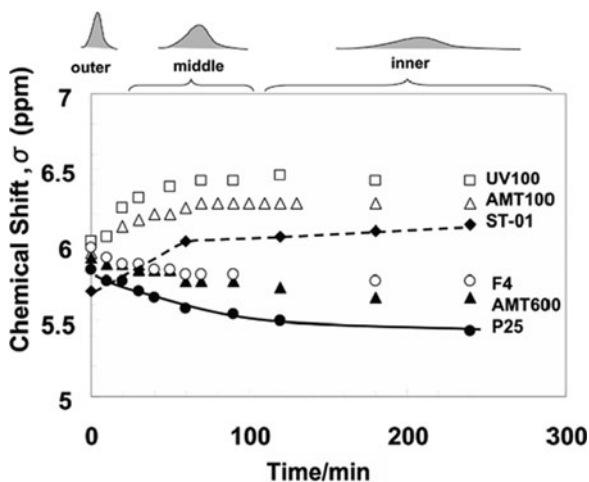


Fig. 6 Time profiles of chemical shifts of ¹H NMR signals of TiO₂ powders measured at 85°C. The signal features are illustrated in the *upper part*

the resonance lines. As expected, the signals of adsorbed water molecules for ST-01, UV100, and AMT-100 appear in the range from 6.5 to 5.4 ppm, which is lower than that of liquid water (4.8 ppm). Because the structure of the water molecules in the innermost layer would be stabilized by the hydrogen bonds that are stronger than those in the outermost layer, the water signals in the innermost layer are expected to appear at lower field than those in the outermost layer. On the other hand, for the three photocatalysts (P25, F4, and AMT-600) the water signals shifted to the upper field. This means water molecules in the innermost layer make weaker hydrogen bonds than those in the outermost layer. These TiO₂ contains less OH groups at the surface since P25 and F4 were prepared from titanium chloride at a higher temperature and AMT-600 (100% anatase) is heat treated for TiO₂ powders prepared from sulfate. The proton chemical shift of the water molecules significantly depends on the binding sites, which are represented as surface OH groups (Nosaka et al 2006a). The surface OH groups are roughly classified in two types; basic terminal OH and acidic bridged OH. In the heat treatment above 150°C, the concentration of terminal OH is reduced (Nosaka et al. 2006a). The observed proton signal in the innermost layer in the present study may contain the signals of the adsorbed water molecules hydrogen bonded to the terminally bound hydroxyl species. The high field chemical shift of water signals in the innermost layer observed for P25, F4, and AMT-600 might indicate the existence of the more basic bridged oxygen on the solid surface of these photocatalysts.

6 The Mechanism of OH Radical Formation

As stated above, OH radicals are produced on the photo irradiated TiO₂ surface and released from the surface to vacuum. The amount of OH radicals is larger for TiO₂ powders with a less hydrated surface which contains less terminal OH groups.

We confirmed, however, that OH radical is produced from water vapor (Murakami et al. 2006). As for the mechanism of water oxidation, a primary intermediate has been detected by means of IR spectroscopy (Nakamura and Nakato 2004). They suggested that a “surface-trapped hole,” which acts as a precursor of the oxygen photoevolution reaction, is produced by a nucleophilic attack of a H_2O molecule on a hole at a surface lattice O site accompanied by bond breaking (Fig. 7). Then, disproportionation or further oxidation of this “trapped hole” gives a bridged peroxy species, $[\text{Ti}-\text{O}-\text{O}-\text{Ti}]_s$, which is the intermediate for oxygen evolution. The oxygen photoevolution is not initiated by the dissociation of the terminal OH group.

Calcined TiO_2 powder and TiO_2 powder prepared at a higher temperature produce peroxy species easily at the surface. The peroxy species are also detected when H_2O_2 is adsorbed on the TiO_2 surface (Nakamura and Nakato 2004). Then, when no organic reactant is adsorbed on the surface, the peroxy species are accumulated on photoirradiation. Since the bonding energy of Ti–O is much larger than that of O–H, the trapped holes would not be released as OH radicals. Instead, the OH

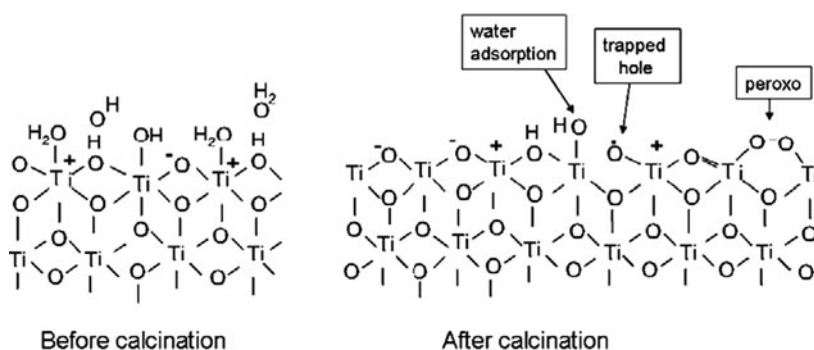


Fig. 7 Plausible surface structure on irradiation for TiO_2 hydrated before calcination and dehydrated after calcination. Adapted from Nakamura and Nakato (2004)

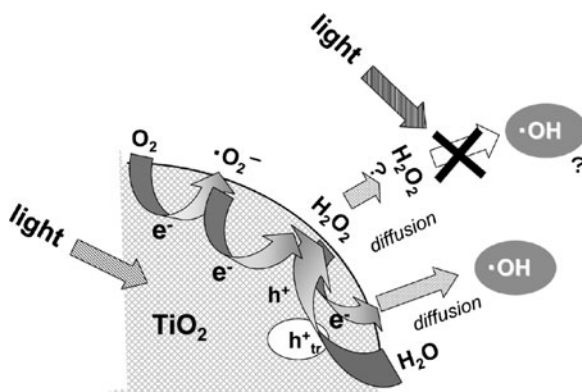


Fig. 8 Plausible reaction scheme for the OH radical formation on the irradiated TiO_2 surface

radicals would be generated from the surface peroxo species or the adsorbed H₂O₂ through the reduction by photoinduced conduction band electrons. Since the formation of H₂O₂ in TiO₂ photocatalysis has been confirmed (Kubo and Tatsuma 2006), OH radicals would be formed as illustrated in Fig. 8. The dissociation of H₂O₂ by UV light to OH radicals, which has been suggested by Kubo and Tatsuma., would not be the process for OH radical formation in the present reaction detected by LIF method as stated above.

7 Effect of Calcination on the Acetic Acid Decomposition

In our previous study, we could detect the primary oxidation procedure of acetic acid with several kinds of TiO₂ loaded with Pt (Nosaka et al. 1998). In this case, both $\bullet\text{CH}_3$ and $\bullet\text{CH}_2\text{COOH}$ radicals were detected as the primary radicals. Figure 9 shows the amount of these radicals observed for different TiO₂ powders. For heat treated UV100 (from 150 to 500°C) or P25 TiO₂, the amount of $\bullet\text{CH}_3$ was larger than that for non calcined UV100 or ST-01. This indicates that the dehydrated surface or the surface that contains less terminal OH groups produce $\bullet\text{CH}_3$ radicals more preferably.

In this chapter we suggested that only $\bullet\text{CH}_3$ radical could be formed through the direct oxidation by conduction band holes while both radicals would be produced via free OH radicals. The previous conclusion seems contradictory with the present study in terms that the dehydrated surface preferably produces OH radicals. The previous conclusion was based on the assumption that the surface holes could not abstract a proton from the methyl group to produce $\bullet\text{CH}_2\text{COOH}$. However, if the adsorption mode of acetic acid is different for the distinctive surface OH group, a proton could be abstracted from the methyl groups as illustrated in Fig. 10. If acetic acid is adsorbed on TiO₂ surface by one oxygen atom in the carboxyl group, a flexible single bond allows contacting methyl protons with TiO₂ surface and then $\bullet\text{CH}_2\text{COOH}$ could be produced.

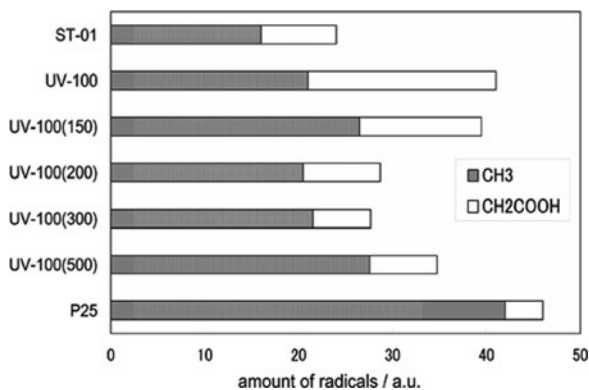


Fig. 9 The relative amount of the primary radicals observed for the acetic acid decomposition with different photocatalysts. Adapted from Nosaka et al. (1998)

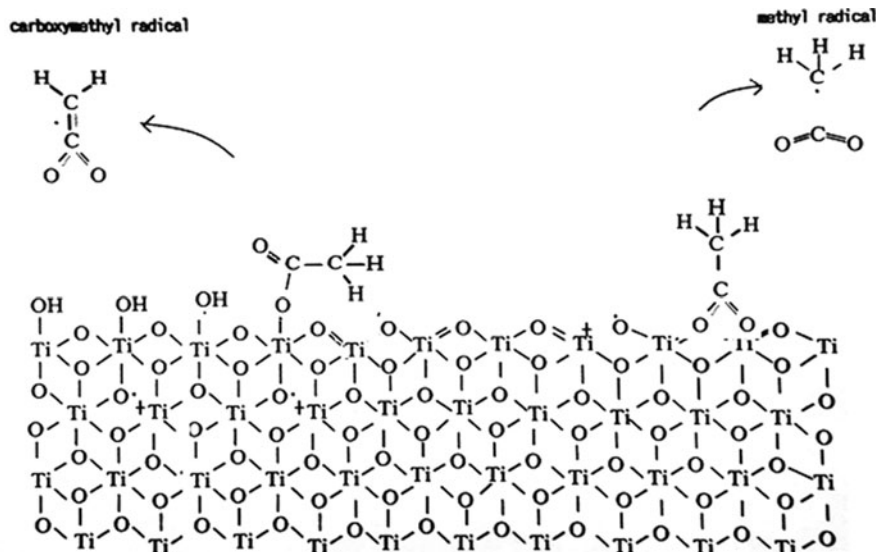


Fig. 10 Plausible reaction mechanism for the initial step in the photocatalytic decomposition of acetic acid

References

- Daimon H, Nosaka Y (2007) Formation and behavior of singlet molecular oxygen in TiO₂ photocatalysis studied by detecting near-infrared phosphorescence. *J Phys Chem C* 111:4420–4424
- Hirakawa T, Nosaka Y (2002) Properties of O₂^{-•} and OH[•] formed in TiO₂ aqueous suspensions by photocatalytic reaction and the influence of H₂O₂ and some ions. *Langmuir* 18:3247–3254
- Hirakawa T, Nakaoka Y, Nishino J, Nosaka Y (1999) Primary passages for various TiO₂ photocatalysts studied by means of luminol chemiluminescent probe. *J Phys Chem B* 103:4399–4403
- Kubo W, Tatsuma T (2006) Mechanisms of photocatalytic remote oxidation. *J Am Chem Soc* 128:16034–16035
- Kumar CP, Gopal NO, Wang TC, Wong MS, Ke SC (2006) EPR investigation of TiO₂ nanoparticles with temperature-dependent properties. *J Phys Chem B* 110:5223–5229
- Murakami Y, Kenji E, Nosaka AY, Nosaka Y (2006) Direct detection of OH radicals diffused to the gas phase from the UV-irradiated photocatalytic TiO₂ surfaces by means of laser induced fluorescence spectroscopy. *J Phys Chem B* 110:16808–16811
- Nakamura R, Nakato Y (2004) Primary intermediates of oxygen photoevolution reaction on TiO₂ (Rutile) particles, revealed by in situ FTIR absorption and photoluminescence measurements. *J Am Chem Soc* 126:1290–1298
- Nakaoka Y, Nosaka Y (1997) ESR investigation into the effects of heat treatment and crystal structure on radicals produced over irradiated TiO₂ powder. *J Photochem Photobiol A Chem* 110:299–307
- Nosaka Y (2002) Photoelectrochemical reactions at the semiconductor microparticles. In: Kaneko M, Ohkura I (eds) *Photocatalysis*. Kodansha Springer, Tokyo, pp 69–86

- Nosaka AY, Nosaka Y (2005) Characteristics of water adsorbed on TiO₂ photocatalytic surfaces as studied by ¹H-NMR spectroscopy. *Bull Chem Soc Jpn* 78:1595–1607
- Nosaka Y, Yamashita Y, Fukuyama H (1997) Application of chemiluminescent probe to monitoring superoxide radicals and hydrogen peroxide in TiO₂ photocatalysis. *J Phys Chem B* 101:5822–5827
- Nosaka Y, Kishimoto M, Nishino J (1998) Factors governing the initial process of TiO₂ photocatalysis studied by means of in-situ electron spin resonance measurements. *J Phys Chem B* 102:10279–10283
- Nosaka Y, Nakamura M, Hirakawa T (2002) Behavior of superoxide radicals formed on TiO₂ powder photocatalysts studied by a chemiluminescent probe method. *Phys Chem Chem Phys* 4:1088–1092
- Nosaka Y, Komori S, Yawata K, Hirakawa T, Nosaka AY (2003) Photocatalytic OH radical formation in TiO₂ aqueous suspension studied by several detection methods. *Phys Chem Chem Phys* 5:4731–4735
- Nosaka AY, Fujiwara T, Yagi H, Akutsu H, Nosaka Y (2004) Characteristics of water adsorbed on TiO₂ photocatalytic systems on temperature increase as studied by solid-state ¹H-NMR spectroscopy. *J Phys Chem B* 108:9121–9125
- Nosaka AY, Nishino J, Fujiwara T, Ikegami T, Yagi H, Akutsu H, Nosaka Y (2006a) Effects of thermal treatments on the recovery of adsorbed water and photocatalytic activities of TiO₂ photocatalytic systems. *J Phys Chem B* 110:8380–8385
- Nosaka Y, Natsui H, Sasagawa M, Nosaka AY (2006b) ESR studies on the oxidation mechanism of sterically hindered cyclic amines in TiO₂ photocatalytic systems. *J Phys Chem B* 110:12993–12999

Chapter 9

Local Structures, Excited States, and Photocatalytic Reactivities of “Single-Site” Ti-Oxide Photocatalysts Constructed Within Zeolites or Mesoporous Materials

Masaya Matsuoka and Masakazu Anpo

Abstract “Single-site” Ti-oxide species incorporated within the framework or cavities of zeolites as well as mesoporous materials in an isolated state exhibit high and unique photocatalytic activity for various reactions such as the direct decomposition of NO into N₂ and O₂ and the reduction of CO₂ with H₂O to produce CH₄ and CH₃OH. Various in situ spectroscopic investigations using photoluminescence, XAFS (XANES and FT-EXAFS), and ESR techniques revealed that the photo-excited triplet states of the single-site Ti-oxide species play a vital role in these photocatalytic reactions. The photocatalytic activity as well as the selectivity of the Ti-oxide species strongly depends on their local structures. Furthermore, it has been demonstrated that ion-implantation is an effective technique in modifying the electronic properties of single-site Ti-oxide photocatalysts, enabling them to absorb and operate as highly efficient photocatalysts under visible light irradiation ($\lambda > 420$ nm).

1 Introduction

TiO₂ photocatalysts have attracted much attention as unique photo-functional materials enabling effective environmental purification as well as the means for new energy production under UV or solar light irradiation. In fact, semiconducting powdered TiO₂ catalysts have been applied for the decomposition of NO_x in air (Anpo et al. 2005; Anpo and Thomas 2006), the degradation of toxic organic impurities diluted in water (Yamashita et al. 2003), and the decomposition of

M. Anpo (✉)
Department of Applied Chemistry, Graduate School of Engineering,
Osaka Prefecture University, 1-1 Gakuen-cho, Naka-ku, Sakai,
Osaka 599-8531, Japan
e-mail: anpo@chem.osakafu-u.ac.jp

water into H_2 and O_2 (Matsuoka et al. 2007; Kitano et al. 2007). At present, various attempts are being made to enhance the photocatalytic activity of such semiconducting TiO_2 catalysts. One approach is to reduce the particle size of the powdered TiO_2 catalysts. As the size of a TiO_2 particle is reduced below a certain dimension, especially below 100 Å, the energy gap between its highest occupied molecular orbital (HOMO) and lowest unoccupied molecular orbital (LUMO) starts to increase (Fig. 1), leading to an enhancement of the reduction ability of the photo-formed electrons in the LUMO as well as the oxidation ability of the photo-formed holes in the HOMO. This “size quantization effect” is significant when TiO_2 units (Ti -oxide species) are highly dispersed at the molecular level on various metal oxide supports such as zeolites or mesoporous materials with high surface areas (Anpo and Che 2000). In fact, UV irradiation of highly dispersed tetrahedral Ti -oxide species leads to the formation of a charge-transfer excited triplet state involving an electron transfer from $\text{O}^{2-}(\text{l})$ to $\text{Ti}^{4+}(\text{l})$, which is quite different from the bandgap excitation process which occurs on bulk TiO_2 powders.

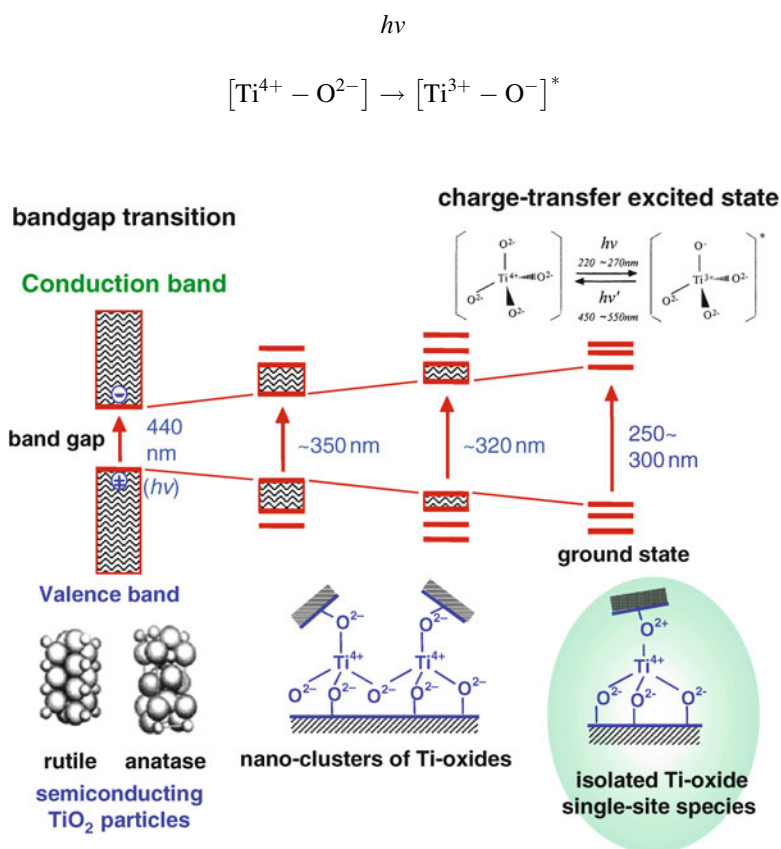


Fig. 1 Excitation and charge separation of Ti -oxide photocatalysts in molecules, clusters and extended semiconductors

This unique charge-transfer excited triplet state ($[\text{Ti}^{3+}\text{-O}^-]^*$) enables high and selective photocatalytic reactions quite different from photoelectrochemical reactions occurring on bulk TiO_2 powders (Anpo, 2000), due to the close existence of photo-formed electron and hole pairs and their balanced contribution to the reactions. The high reactivity of these charge-transfer excited triplet states can induce various significant photocatalytic reactions such as the decomposition of NO into N_2 and O_2 (Yamashita et al. 1996), the degradation of organic impurities in water (Yamashita et al. 1998), and the reduction of CO_2 with H_2O to produce CH_4 and CH_3OH (Ikeue et al. 2001). These photocatalytic reactions proceed with a high efficiency and selectivity, displaying quite different mechanisms from those observed on semiconducting TiO_2 photocatalysts in which the photoelectrochemical reaction mechanism or charge separation plays an important role. Furthermore, the photocatalytic activity as well as the selectivity of the highly dispersed tetrahedral Ti-oxide species was found to be greatly affected by the various physicochemical properties of the supports, i.e., the hydrophilicity, hydrophobicity, or condensation effect of the gasses for zeolite or mesoporous materials.

In this chapter, we have summarized the photocatalytic activity of single-site Ti-oxide species incorporated into the framework structures or cavities of various zeolites or mesoporous materials at ambient temperatures. The local structures of the Ti-oxide species are discussed based on results obtained by various in situ spectroscopic techniques. Special attention has been focused on the relationship between the local structure of the active sites and their activity for various photocatalytic reactions.

2 Preparation of Ti-Oxide Photocatalysts and Their Local Structures

When the TiO_2 units (Ti-oxide species) are very highly dispersed at the molecular level on various metal oxides supports such as zeolites or mesoporous materials, isolated Ti-oxide species can be formed within the frameworks or cavities of these supports. These Ti-oxide species are regarded as the “single-site” Ti-oxide species since they all exist in a tetrahedral coordination sphere in an isolated state. The introduction of single-site Ti-oxide species within zeolites can be achieved by an ion-exchange method or hydrothermal synthesis. In the case of ion-exchange, zeolites are treated with aqueous solution containing Ti^{4+} ions which are exchanged at the ion-exchange sites on the zeolite framework, i.e., at the Brönsted acid site near the framework aluminum. Ti-oxide-exchanged Y-zeolite (ex-Ti-oxide/Y-zeolite) can be prepared by the ion-exchange of the Y-zeolite ($\text{SiO}_2/\text{Al}_2\text{O}_3 = 5.5$) with an aqueous titanium ammonium oxalate solution (Yamashita and Anpo 2003). On the other hand, hydrothermal synthesis using the precursors silica and titanium oxide and structure directing agents (SDA) enables the direct incorporation of the single-site Ti-oxide species at T-sites within the framework of zeolites in tetrahedral coordination. For example, two types of Ti-oxide containing β -zeolites (Ti- β) with

different affinities to the water molecules can be hydrothermally synthesized by using different SDA having OH^- and F^- as the counter anions. These Ti- β are denoted according to the kind of SDA used, i.e., Ti- $\beta(\text{OH})$ and Ti- $\beta(\text{F})$, the former showing more hydrophilic properties than the latter (Yamashita 2002). Another type of single-site Ti-oxide catalyst is mesoporous silica materials containing Ti-oxide species within their amorphous silica wall structure (Ti-MCM-41, Ti-HMS), which can be hydrothermally synthesized or synthesized under ambient conditions using the precursors silica and titanium oxide and template agents.

Figure 2a–e shows the XANES and Fourier transform of EXAFS (FT-EXAFS) for the single-site Ti-oxide catalysts. The XANES for these catalysts showed an intense single preedge peak, indicating that the Ti-oxide species exist in tetrahedral coordination.

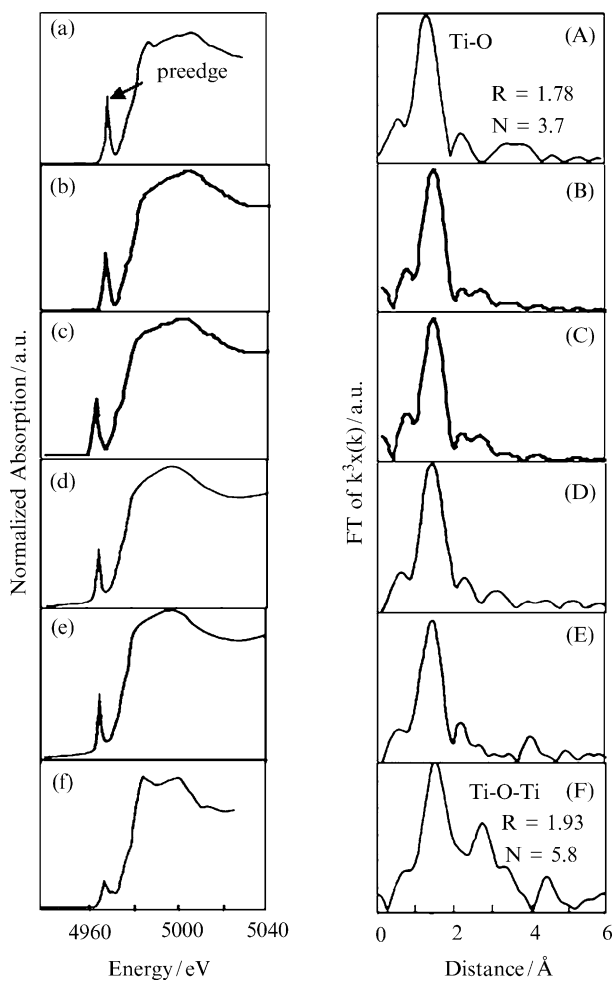


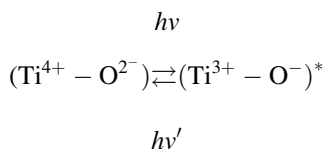
Fig. 2 XANES (left) and FT-EXAFS (right) spectra of the ex-Ti-oxide/Y-zeolite (a, A); Ti- $\beta(\text{OH})$ (b, B); Ti- $\beta(\text{F})$ (c, C); Ti-MCM-41 (d, D); Ti-HMS (e, E); and imp-Ti-oxide/Y-zeolite (f, F)

FT-EXAFS studies showed only a peak assigned to the neighboring oxygen atoms (Ti–O), indicating that the Ti-oxide species exist in an isolated state as “single-site” Ti-oxide species. From curve-fitting analysis of the EXAFS spectra, it was found that the Ti^{4+} ions are surrounded by four oxygen atoms with an atomic distance of around 1.78 Å, showing good agreement with the XANES results (Anpo and Takeuchi 2003). It should also be noted that TiO_2 clusters with small particle sizes can be easily prepared on zeolites or mesoporous silica materials by an impregnation method. As shown in Fig. 2f, the XANES of the Ti-oxide impregnated Y-zeolite (imp-Ti-oxide/Y-zeolite) exhibited a preedge peak which branches off into several distinct weak peaks, showing that the Ti-oxide species exist in octahedral coordination. Furthermore, the FT-EXAFS spectra showed the existence of peaks attributed to the neighboring Ti atoms (Ti–O–Ti) in addition to the neighboring O atoms (Ti–O). These results indicate that the Ti-oxide species loaded onto a Y-zeolite by an impregnation method exist in small aggregated TiO_2 clusters. The formation of small aggregated TiO_2 clusters were also observed by XAFS measurements for HMS prepared by an impregnation method (imp-Ti-HMS).

3 Excited States of Ti-oxide Photocatalysts and Their Photocatalytic Reactivities

3.1 Excited States of “Single-Site” Ti-Oxide Species and Their Reactivity

The Ti-oxide species, incorporated within zeolites (ex-Ti-oxide/Y-zeolite, Ti-β(OH), Ti-β(F)), and mesoporous silica (Ti-MCM-41, Ti-HMS) as single-site catalysts, exhibit a UV absorption band at around 230 nm which is attributed to the ligand-to-metal charge transfer transition (LMCT) of the isolated tetrahedral Ti-oxide species involving an electron transfer from the oxygen ligand to the central Ti^{4+} cation (Hu et al. 2006). As shown in Fig. 3, UV irradiation of the absorption band of the single-site Ti-oxide catalysts led to the appearance of a photoluminescence at around 490 nm at 77 K due to the radiative decay process from the charge-transfer excited triplet state to the ground state of the isolated tetrahedral Ti-oxide species, as shown below:



In contrast, the imp-Ti-oxide/Y-zeolite and imp-Ti-HMS catalysts did not exhibit any photoluminescence. Thus, these results clearly indicate that Ti-oxide catalysts prepared by an impregnation method involving the aggregated octahedral Ti-oxide

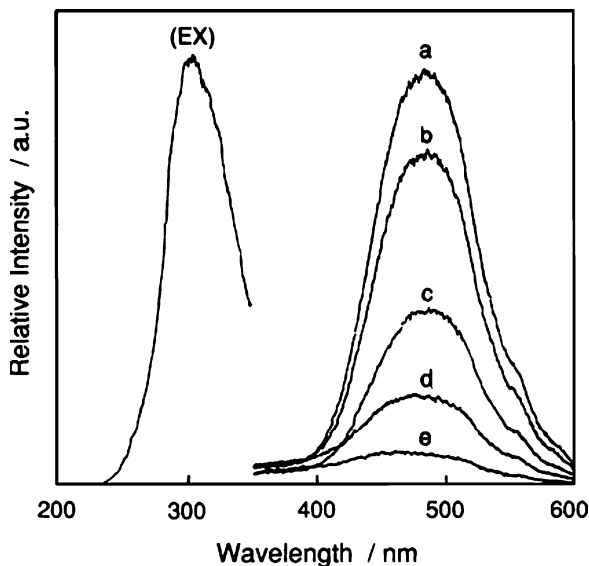


Fig. 3 Photoluminescence spectrum of the ex-Ti-oxide/Y-zeolite catalyst (a); its excitation spectrum (EX); and the effect of the addition of NO on the photoluminescence spectrum (b–e). Measured at 77 K; excitation beam: 290 nm; emission monitored at 490 nm; amounts of added NO: (a) 0.0, (b) 0.2, (c) 0.8, (d) 7.6, (e) 21.3 $\mu\text{mol/g}$

species do not exhibit any photoluminescence spectrum. The reactivity of the single-site Ti-oxide species in its photo-excited state has also been investigated by photoluminescence quenching measurements. The addition of various gasses such as NO, CO₂, and H₂O on single-site Ti-oxide catalysts (ex-Ti-oxide/Y-zeolite) led to an efficient quenching of the photoluminescence (Fig. 3). The lifetime of the charge transfer excited triplet state of the single-site Ti-oxide species was also shortened by the addition of these gasses, its extent depending on the amount of gasses added. Such an efficient quenching of the photoluminescence suggests not only that the tetrahedrally coordinated Ti-oxide species is located at positions accessible to the added gasses but also that the gasses interact and/or react with the single-site Ti-oxide species in their excited triplet states.

3.2 Photocatalytic Decomposition of NO on Single-Site Ti-Oxide Photocatalysts

Nitric oxide (NO) is an especially harmful atmospheric pollutant and the main cause of acid rain and photochemical smog, which is emitted largely from the reaction of N₂ with O₂ in high-temperature combustion processes. It has been reported that Ti-oxide photocatalysts can be applied for the clean, safe, and low-temperature removal of NO. UV irradiation of single-site Ti-oxide photocatalysts in the presence of NO efficiently led to the formation of N₂ and O₂ as major products with a good linearity against the UV irradiation time, as shown in Fig. 4. The formation of N₂O

was observed only as a minor product. On the other hand, when the powdered TiO_2 or imp-Ti-oxide/Y-zeolite loaded with small Ti-oxide clusters was applied as a photocatalyst for the decomposition of NO, the major products formed were N_2O and NO_2 (Zhang et al. 2001). Thus, the efficiency and selectivity for the formation of N_2 strongly depend on the type of catalysts. Figure 4 shows the relationship between the coordination number of the Ti-oxide species and the selectivity for N_2 formation in the photocatalytic decomposition of NO on various Ti-oxide photocatalysts. A clear dependence of the N_2 selectivity on the coordination number of the Ti-oxide species can be observed, i.e., the lower the coordination number of the Ti-oxide species, the higher the N_2 selectivity. From these results, a highly efficient and selective photocatalytic reduction of NO into N_2 and O_2 was found to be achieved using single-site Ti-oxide catalysts involving highly dispersed, isolated tetrahedral Ti-oxides as the active species. The formation of N_2O as the major product was observed for bulk TiO_2 catalysts and on imp-Ti-oxide/Y-zeolite catalysts involving aggregated octahedrally-coordinated Ti-oxide species.

From the investigations of these photocatalytic reactions as well as the quenching of the photoluminescence, the reaction mechanism for the photocatalytic decomposition of NO on the isolated tetrahedral titanium oxide species can be proposed, as shown in Scheme 1. The NO species are able to adsorb onto single-site Ti-oxide species as weak ligands to form the reaction precursors. Under UV

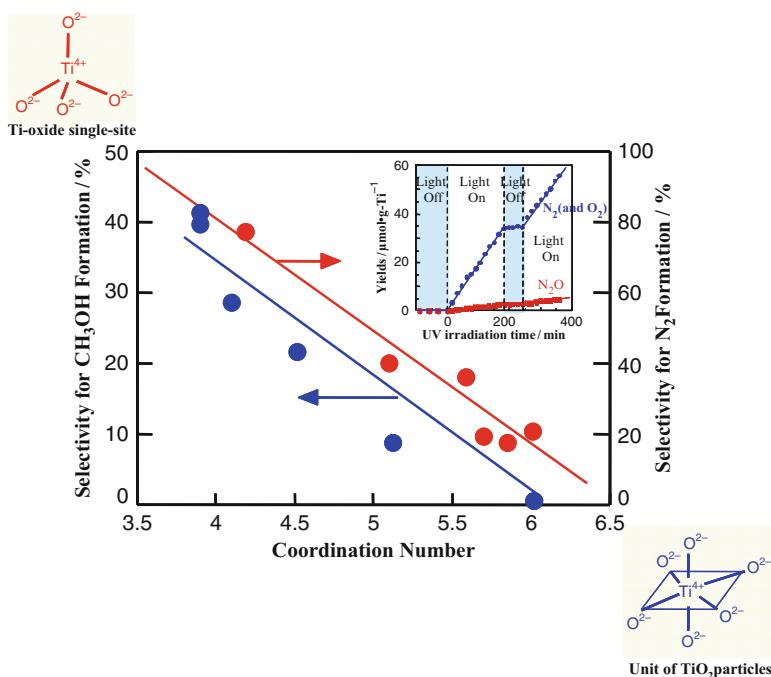
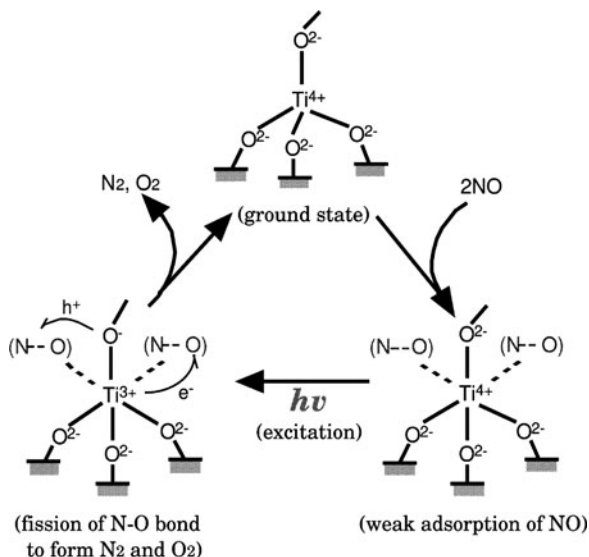


Fig. 4 Relationship between the coordination numbers and the photocatalytic reactivity of the titanium oxides. *Figure inset:* Time profiles of the photocatalytic decomposition of NO into N_2 and N_2O on the Ti-oxide/Y-zeolite catalyst

irradiation, the charge-transfer excited complexes of Ti-oxide species ($\text{Ti}^{3+}\text{-O}^-$)* are formed. Within their lifetimes, the electron transfer from the trapped electron center, Ti^{3+} , into the π -antibonding orbital of NO takes place. Simultaneously, the electron transfer from the π -bonding orbital of another NO into the trapped hole center, O^- , occurs. These electron transfers led to the direct decomposition of two sets of NO on ($\text{Ti}^{3+}\text{-O}^-$)* into N_2 and O_2 under UV irradiation in the presence of NO even at 275 K. On the other hand, with the aggregated or bulk TiO_2 catalysts, the photo-formed holes and electrons rapidly separate from each other with large space distances between the holes and electrons, thus preventing the simultaneous activation of two NO molecules on the same active sites and resulting in the formation of N_2O and NO_2 in place of N_2 and O_2 . The decomposed N and O species react with NO on different sites to form N_2O and NO_2 , respectively.

3.3 Photocatalytic Reduction of CO_2 with H_2O on Single-Site Ti-Oxide Photocatalysts

Photocatalysis for the reduction of CO_2 with H_2O is of interest not only as a reaction system utilizing artificial photosynthesis but as a way to use carbon sources for the synthesis of hydrocarbons and oxygenate such as CH_4 and CH_3OH . In this reaction, photon energy is converted into chemical energy and stored in the bonds of CH_4 and



Scheme 1 The reaction mechanism of the photocatalytic decomposition of NO into N_2 and O_2 on the tetrahedrally-coordinated Ti-oxide species under UV light irradiation

CH₃OH, accompanied by a large positive change in the Gibbs free energy ($\Delta G > 0$). It has previously been reported that the photocatalytic reduction of CO₂ with H₂O proceeds efficiently on single-site Ti-oxide photocatalysts (Shioya et al. 2003). UV irradiation of powdered TiO₂ and Ti-oxide/Y-zeolite catalysts prepared by ion-exchange or impregnation methods in the presence of a mixture of CO₂ and H₂O led to the evolution of CH₄ and CH₃OH in the gas phase at 328 K, as well as trace amounts of CO, C₂H₄, and C₂H₆. The evolution of small amounts of O₂ was also observed. It can be seen that the specific photocatalytic reactivity of the Ti-oxide/Y-zeolite catalysts, which have been normalized by unit gram of Ti in the catalysts, is much higher than bulk TiO₂. The ex-Ti-oxide/Y-zeolite exhibits a high reactivity and selectivity for the formation of CH₃OH, while the formation of CH₄ was found to be the major reaction on bulk TiO₂ as well as on the imp-Ti-oxide/Y-zeolite. A clear relationship between the coordination number of the Ti-oxide species and the selectivity for CH₃OH formation can be observed (Fig. 4), showing that the highly efficient, highly selective photocatalytic reduction of CO₂ with H₂O into CH₃OH can be achieved using the single-site Ti-oxide catalysts such as ex-Ti-oxide/Y-zeolite, which includes the highly dispersed isolated tetrahedral Ti-oxide as the active species. Furthermore, the reaction selectivity was shown to be greatly dependent on the hydrophilicity of single-site Ti-oxide catalysts. As shown in Fig. 5, two kinds of Ti- β catalysts, [Ti- β (OH), Ti- β (F)], i.e., single-site Ti-oxide photocatalysts, exhibited different adsorption isotherms, Ti- β (OH) showing much higher affinity to the H₂O molecules than Ti- β (F). Figure 6 shows the effect of the addition of H₂O on the preedge peak of the XANES spectrum of the Ti- β catalysts [Ti- β (OH), Ti- β (F)] (Yamashita et al. 2002). It has been established that when the coordination number of the Ti-oxide species increases, the intensity of the preedge peak decreases accompanied by a shift in the preedge peak to higher energy regions. The changes in the peak intensity and position upon H₂O addition are more remarkable for Ti- β (OH) than for Ti- β (F), indicating that the isolated tetrahedral Ti-oxide species within Ti- β (OH) can interact more efficiently with the H₂O molecules. As shown in Fig. 7, the photocatalytic reduction of CO₂ with H₂O proceeds with different reactivities and selectivities on hydrophilic Ti- β (OH) and hydrophobic Ti- β (F). The higher reactivity for the formation of CH₄ observed for Ti- β (OH) and the higher selectivity for the formation of CH₃OH observed for Ti- β (F) may be attributed to the different affinities of the zeolite pores on the H₂O molecules. These results suggest that the hydrophilic–hydrophobic property of zeolite cavities is one of the most important factor to determine the selectivity in the photocatalytic reduction of CO₂ with H₂O.

The reaction mechanism of photocatalytic reduction of CO₂ with H₂O was investigated by photoluminescence and ESR investigations. The addition of H₂O or CO₂ molecules to the ex-Ti-oxide/Y-zeolite led to an efficient quenching of the photoluminescence as well as a shortening of the photoluminescence lifetime, indicating that the added CO₂ or H₂O interacts and/or reacts with the single-site Ti-oxide species in both its ground and excited states.

It was also found that UV irradiation of the single-site Ti-oxide species in the presence of CO₂ and H₂O at 77 K led to the appearance of ESR signals due to the Ti³⁺ ions, H atoms, and carbon radicals (Anpo and Chiba 1992). From these

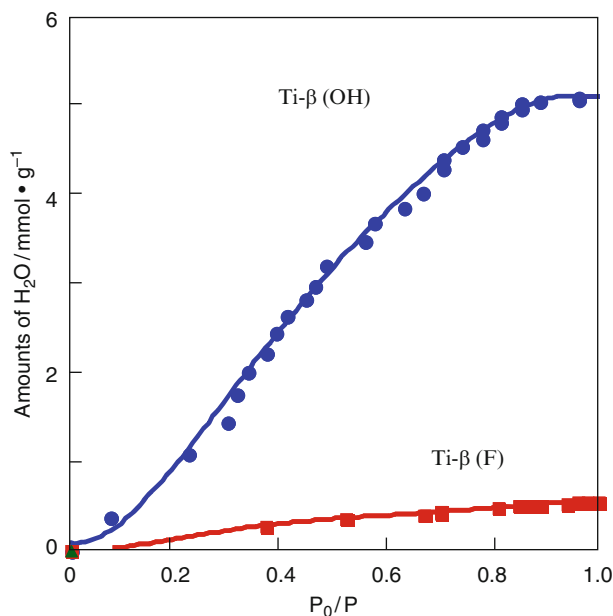


Fig. 5 H_2O adsorption isotherms at 298 K for (a) Ti- β (OH) and (b) Ti- β (F)

results, the following reaction could be proposed: CO_2 and H_2O molecules interact with the photo-excited Ti-oxide species ($Ti^{3+}-O^-$)* and the reduction of CO_2 and the decomposition of H_2O proceed competitively. Furthermore, H atoms and OH radicals are formed from the H_2O and react with the carbon species formed from CO_2 to produce CH_4 and CH_3OH . These results clearly demonstrate that single-site Ti-oxide photocatalysts within zeolite cavities are applicable as effective photocatalysts enabling artificial photosynthetic reactions such as CO_2 fixation with H_2O to produce CH_3OH with a high selectivity.

3.4 Photocatalytic Size-Screening Oxidation of Organic Compounds on Single-Site Ti-Oxide Catalysts Incorporated Within the Framework of Titanosilicate Molecular Sieves

Recently, Shiraishi et al. (2005) have reported that titanosilicate molecular sieves, when activated by UV irradiation in water in the presence of molecular oxygen, can catalyze oxidative conversions of molecules with a similar size as the pore size of the catalysts but are inactive for much larger or smaller sizes. In other words, titanosilicate molecular sieves act as unique “size-screening” photocatalysts. Photocatalytic oxidative conversions of 25 kinds of phenol derivatives have been investigated on titanosilicate molecular sieves (TS-1 and TS-2), TiO_2 , and $Ti-SiO_2$

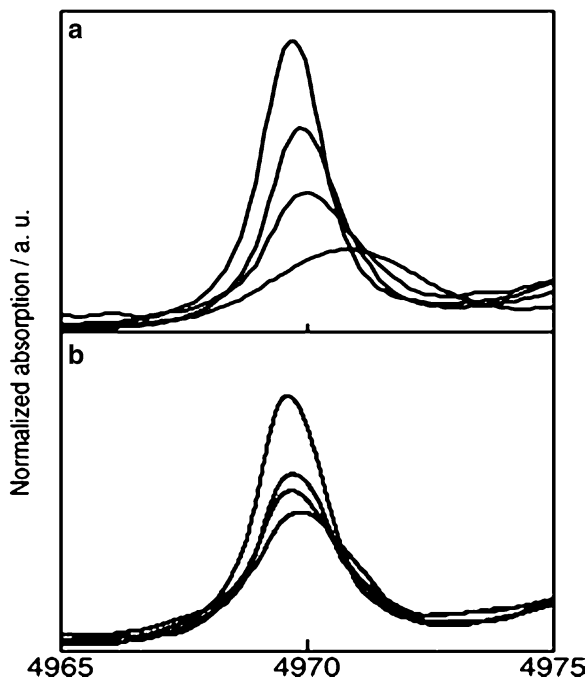


Fig. 6 The effect of the addition of H₂O molecules on the intensity and position of the pre-edge peak observed in the Ti K-edge XANES spectra of: (a) Ti-β(OH) and (b) Ti-β(F). Amount of added H₂O molecules: 0, 1.4, 3.0, and 4.6 mmol/g cat (*from top to bottom*)

catalysts under photo-irradiation ($\lambda > 280$ nm; 0.5 h) in the presence of water and O₂. Here, TS-1 and TS-2, both containing 0.4 mol % Ti (= Ti/(Ti + Si) ratio), were prepared by hydrothermal synthesis. Ti-SiO₂ having an amorphous structure and containing 0.4 mol % Ti was prepared by a sol-gel method. UV-Vis investigations suggested that highly dispersed “single-site” tetrahedral Ti-oxide species exist within the titanasilicate molecular sieves (TS-1 and TS-2) and Ti-SiO₂ catalysts as active species. Furthermore, XRD studies showed that TS-1 has a MFI structure with pore dimensions of 0.54×0.56 nm (sinusoid channel) and 0.52×0.58 nm (straight channel), while TS-2 has a MEL structure with pore dimensions of 0.53×0.54 nm. Photocatalytic oxidative conversions of phenol derivatives on TS-2 were also examined. The close relationship between the effective molecular width (EMW) of the phenol derivatives and their oxidative conversions was observed. The conversion of phenol derivatives with EMW of less than 0.55 nm was nearly zero, however, obviously higher for derivatives with EMW of 0.6–0.65 nm, which is 12–21% larger than the average pore diameter of TS-2 (0.535 nm). Moreover, conversions of the phenol derivatives with EMW of larger than 0.68 nm were found to be almost zero. Similar results have been obtained for reactions on TS-1. In contrast, no EMW-dependent profile was observed for bulk TiO₂ or Ti-SiO₂ having no micropore structures, while conversions of phenol

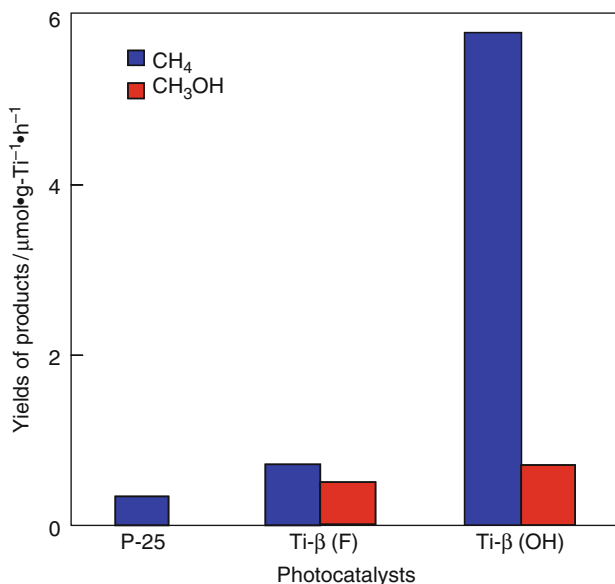


Fig. 7 Yields of CH₄ and CH₃OH in the photocatalytic reduction of CO₂ with H₂O at 323 K on the Ti-β(OH), Ti-β(F), and TiO₂ (P-25) catalysts

derivatives on Ti-SiO₂ was found to be negligible, independent of the EMW of phenol derivatives. From these results, the following mechanism could be proposed for the size-screening oxidation activity of TS-1 and TS-2: The lifetime of the photo-excited state of the single-site tetrahedral Ti-oxide species [Ti³⁺-O⁻]* is shortened significantly in the presence of H₂O, a strong quencher. A slim molecule having rather small EMW than the pore diameter of the catalyst diffuses smoothly inside the pore and can barely be trapped by the short-lived [Ti³⁺-O⁻]*. In contrast, the diffusion of a molecule with a size close to that of the pore is restricted by the pore wall, and such an “interlocked” molecule is trapped easily by [Ti³⁺-O⁻]*, resulting in high conversion. Considering that the zeolite framework is distorted in solution and the pore structure changes elastically, molecules of ca. 10–20% larger EMW than that of the pore may be interlocked more easily, allowing for, especially, high conversion. Zero conversion of phenol derivatives on Ti-SiO₂ is, therefore, attributed to the lack of pores that regulate the motion of the phenol derivatives. Such catalytic properties demonstrate the potential use of the catalyst for the selective transformation of molecules associated with size reduction, i.e., the “molecular shave” transformation.

The molecular shave transformation, induced by titanosilicate molecular sieves, was examined by the selective transformation of 2-chlorohydroquinone. The EMW of 2-chlorohydroquinone (0.6149 nm) was 12 and 15% larger than the TS-1 and TS-2 pores, respectively, thus allowing the effective photoconversion of 2-chlorohydroquinone into 1,2,4-trihydroxybenzene on both catalysts with high conversion (>67%) and high selectivity (>85%). This high selectivity can be

ascribed to the relatively smooth diffusion of 1,2,4-trihydroxybenzene (EMW: 0.5762 nm) inside the pores of the catalysts as compared to 2-chlorohydroquinone, which prevents the further oxidation of 1,2,4-trihydroxybenzene. In fact, photoirradiation of bulk TiO_2 in the presence of 2-chlorohydroquinone led to the formation of 1,2,4-trihydroxybenzene as the initial product, while its yield was quite low (1%) since the sequential oxidative decomposition of 1,2,4-trihydroxybenzene proceeds efficiently on TiO_2 . These results demonstrate that the molecular shave catalytic system enables the detoxification of chlorophenols and the synthesis of valuable phenol derivatives all at once, proving that this “green” photocatalyst may contribute to the development of economically and environmentally friendly chemical processes.

3.5 Design and Development of Visible-Light-Responsive Single-Site Ti-Oxide Photocatalysts

It has been shown that single-site Ti-oxide photocatalysts anchored within various zeolites or mesoporous silica support exhibit unique and high photocatalytic activity for various reactions such as the direct decomposition of NO into N_2 and O_2 or the reduction of CO_2 with H_2O . In fact, the isolated tetrahedral Ti-oxide species, the active site of the single-site Ti-oxide photocatalyst, can absorb UV light of wavelengths below 300 nm, since the HOMO–LUMO energy gap of the isolated tetrahedral Ti-oxide species becomes significantly larger than that of bulk TiO_2 due to the size quantization effect. However, single-site Ti-oxide photocatalysts which can operate efficiently under both UV and visible light irradiation would be ideal for practical and widespread use. Recently, Anpo et al. (2002) have applied a metal-ion-implantation method to modify the electronic properties of single-site Ti-oxide photocatalysts by bombarding them with high-energy metal ions, showing that metal ion-implantation with various transition metal ions such as V or Cr accelerated by high electric fields produces a large shift in the absorption band of the photocatalyst toward visible light regions. As shown in Fig. 8, the absorption spectra of Ti-HMS at around 200–260 nm, due to the tetrahedral single-site Ti-oxide species, shift smoothly toward visible light regions after V ion implantation, the extent of the shift strongly depending on the amount of V ions implanted. In order to investigate the interactions between the tetrahedral single-site Ti-oxide species and the implanted V ions, EXAFS measurements were carried out. The V K-edge FT-EXAFS spectra of the Ti-HMS catalyst implanted with V ions exhibited a peak due to the V–O–Ti bond, suggesting the direct interaction between the tetrahedral Ti-oxide species and implanted V ions. These findings show that the formation of V–O–Ti bridge structures between the isolated tetrahedral TiO_4 unit and implanted V ions affect the electronic structure of the single-site Ti-oxide species, leading to a red shift in the absorption spectra of these catalysts.

The photocatalytic activity of the V ion-implanted Ti-HMS (V-Ti-HMS) has been investigated for the decomposition of NO into N_2 and O_2 under visible light

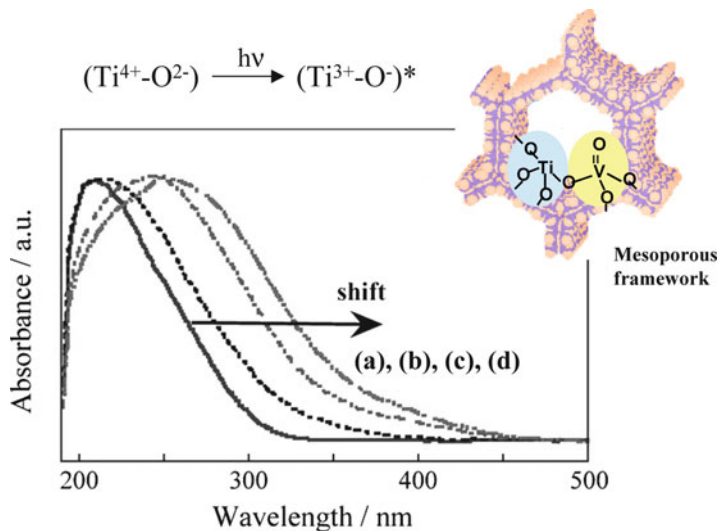


Fig. 8 The diffuse reflectance UV-Vis absorption spectra of V-Ti-HMS. The amount of implanted V ions ($\mu\text{mol/g}\text{-cat}$): (a) 0, (b) 0.66, (c) 1.3, and (d) 2.0

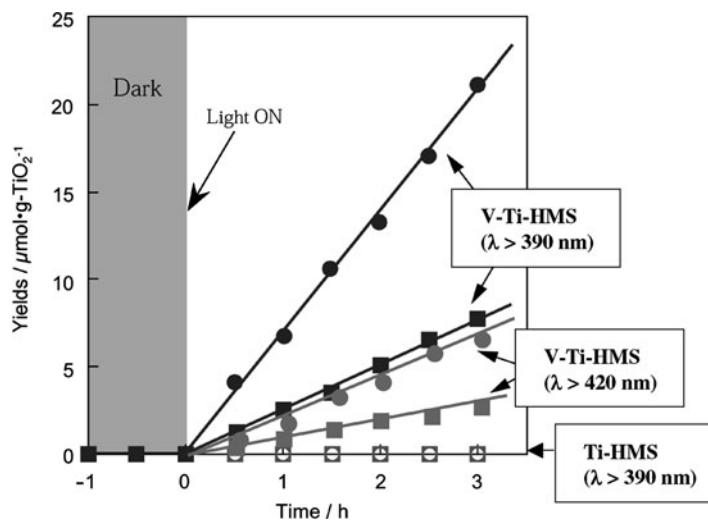


Fig. 9 Time profiles of the photocatalytic decomposition of NO into $\text{N}_2(\cdot)$ and $\text{N}_2\text{O}(\cdot)$ on the V-Ti-HMS and Ti-HMS catalysts

irradiation ($\lambda > 420$ nm). As shown in Fig. 9, visible light irradiation of V-Ti-HMS led to the efficient decomposition of NO into N_2 and O_2 , while the unimplanted original Ti-HMS exhibited no activity for the reaction under the same reaction conditions. It was also confirmed that NO decomposition did not proceed at all under UV ($\lambda < 300$ nm) or visible light irradiation ($\lambda > 420$ nm) on the

V ion-implanted HMS without Ti. These results clearly show that ion-implantation is an effective technique in modifying the electronic properties of single-site Ti-oxide photocatalysts, enabling them to absorb and operate as highly efficient photocatalysts under visible light irradiation ($\lambda > 420$ nm).

4 Summary

In this chapter, the local structures of the single-site Ti-oxide species incorporated into the zeolite framework or cavities as well as into the wall structure of mesoporous silica were discussed based on results of such in situ spectroscopic techniques as ESR, UV-Vis, photoluminescence, and XAFS (XANES and FT-EXAFS). The interactions of these active species with gaseous NO and CO₂ were investigated along with the photocatalytic reactivity of the catalysts for the decomposition of NO as well as the reduction of CO₂ with H₂O.

The Ti-oxide species, which are incorporated into the frameworks or cavities of various zeolites or mesoporous silica by ion-exchange or hydrothermal synthesis, were found to exist in highly dispersed tetrahedral coordination states and to act as efficient photocatalysts for the decomposition of NO into N₂ and O₂ as well as the reduction of CO₂ with H₂O to produce CH₄ and CH₃OH. Photoluminescence investigations revealed that the efficient interactions of the charge-transfer excited complexes of the single-site Ti-oxides (Ti³⁺-O⁻)* i.e., the electron-hole pair state with such reactant molecules as NO, CO₂, and H₂O, play a significant role in these photocatalytic reactions. The localized excitation of the single-site Ti-oxide species led to unique photocatalytic properties quite different from those of semiconducting powdered TiO₂ photocatalysts. It was also demonstrated that single-site Ti-oxide catalysts such as TS-1 can induce the size-screening oxidation of phenols, enabling the detoxification of chlorophenols and the synthesis of valuable phenol derivatives. Thus, by utilizing zeolites or mesoporous silica as a support, it was possible to control the local structure of the highly dispersed Ti-oxide species at an atomic level, leading to the precise control of the photocatalytic activity as well as selectivity of a reaction. Furthermore, the ion-implantation method described here has been shown to be effective in preparing visible light-responsive Ti-oxide photocatalysts involving zeolitic or mesoporous silica frameworks for the development of efficient systems to reduce or eliminate global air and water pollution even under visible or solar light irradiation.

References

- Anpo M (ed) (2000) Photofunctional zeolites, NOVA Publishers Inc., and references therein
Anpo M, Che M (2000) Applications of photoluminescence techniques to the characterization of solid surfaces in relation to adsorption, catalysis, and photocatalysis. *Adv Catal* 44:119–257
Anpo M, Chiba K (1992) Photocatalytic reduction of CO₂ on anchored titanium-oxide catalysts. *J Mol Catal* 74:207–212

- Anpo M, Takeuchi M (2003) The design and development of highly reactive titanium oxide photocatalysts operating under visible light irradiation. *J Catal* 216:505–516
- Anpo M, Thomas JM (2006) Single-site photocatalytic solids for the decomposition of undesirable molecules. *Chem Commun*, 3273–3278
- Anpo M, Takeuchi M, Ikeue K, Doshi S (2002) Design and development of titanium oxide photocatalysts operating under visible and UV light irradiation. The applications of metal ion-implantation techniques to semiconducting TiO₂ and Ti/zeolite catalysts. *Curr Opin Solid State Mater Sci* 6:381–388
- Anpo M, Dohshi S, Kitano M, Hu Y, Takeuchi M, Matsuoka M (2005) The preparation and characterization of highly efficient titanium oxide-based photofunctional materials. *Ann Rev Mater Res* 35:1–27
- Hu Y, Martra G, Zhang JL, Higashimoto S, Coluccia S, Anpo M (2006) Characterization of the local structures of Ti-MCM-41 and their photocatalytic reactivity for the decomposition of NO into N₂ and O₂. *J Phys Chem B* 110:1680–1685
- Ikeue K, Yamashita H, Anpo M, Takewaki T (2001) Photocatalytic reduction of CO₂ with H₂O on Ti-beta zeolite Photocatalysts: effect of the hydrophobic and hydrophilic properties. *J Phys Chem B* 105:8350–8355
- Kitano M, Takeuchi M, Matsuoka M, Thomas JM, Anpo M (2007) Photocatalytic water splitting using Pt-loaded visible light-responsive TiO₂ thin film photocatalysts. *Catal Today* 120:133–138
- Matsuoka M, Kitano M, Takeuchi M, Tsujimaru K, Anpo M, Thomas JM (2007) Photocatalysis for new energy production – recent advances in photocatalytic water splitting reactions for hydrogen production. *Catal Today* 122:51–61
- Shioya Y, Ikeue K, Ogawa M, Anpo M (2003) Synthesis of transparent Ti-containing mesoporous silica thin film materials and their unique photocatalytic activity for the reduction of CO₂ with H₂O. *Appl Catal A – General* 254:251–259
- Shiraishi Y, Saito N, Hirai T (2005) Titanosilicate molecular sieve for size-screening photocatalytic conversion. *J Am Chem Soc* 127:8304–8306
- Yamashita H, Anpo M (2003) Local structures and photocatalytic reactivities of the titanium oxide and chromium oxide species incorporated within micro- and mesoporous zeolite materials: XAFS and photoluminescence studies. *Curr Opin Solid State Mater Sci* 7:471–481
- Yamashita H, Ichihashi Y, Anpo M, Hashimoto M, Louis C, Che M (1996) Photocatalytic decomposition of NO at 275 K on titanium oxides included within Y-zeolite cavities: the structure and role of the active sites. *J Phys Chem B* 100:16041–16044
- Yamashita H, Kawasaki S, Ichihashi Y, Harada M, Takeuchi M, Anpo M, Stewart G, Fox MA, Louis C, Che M (1998) Characterization of titanium-silicon binary oxide catalysts prepared by the sol-gel method and their photocatalytic reactivity for the liquid-phase oxidation of 1-octanol. *J Phys Chem B* 102:5870–5875
- Yamashita H, Ikeue K, Takewaki T, Anpo M (2002) In situ XAFS studies on the effects of the hydrophobic-hydrophilic properties of Ti-beta zeolites in the photocatalytic reduction of CO₂ with H₂O. *Topic Catal* 18:95–100
- Yamashita H, Harada M, Misaka J, Takeuchi M, Neppolian B, Anpo M (2003) Photocatalytic degradation of organic compounds diluted in water using visible light-responsive metal ion-implanted TiO₂ catalysts: Fe ion-implanted TiO₂. *Catal Today* 84:191–196
- Zhang JL, Hu Y, Matsuoka M, Yamashita H, Minagawa M, Hidaka H, Anpo M (2001) Relationship between the local structures of titanium oxide photocatalysts and their reactivities in the decomposition of NO. *J Phys Chem B* 105:8395–8398

Part III
Development of Visible Light-Responsive
Titanium Oxide Photocatalysts

Chapter 10

Visible-Light-Responsive Titanium Dioxide Photocatalysts

Jinkai Zhou and X.S. Zhao

1 Chemical Methods

Semiconductor photocatalysis has received increasing interest in water splitting and degradation of organic pollutants in water and air since the discovery of the photosensitization of TiO_2 electrode (Fujishima and Honda 1972). Among all photocatalysts, TiO_2 is the most studied one because of its chemical stability, nontoxicity, and high photocatalytic reactivity. However, TiO_2 mainly absorbs ultraviolet light, giving rise to a very low energy efficiency in utilizing solar light. Therefore, new photocatalysts that can be activated under visible light irradiation have been recently extensively exploited.

Methods for preparing visible-light-responsive TiO_2 -based semiconductor photocatalysts include dye sensitization, doping of transition metals and nonmetal species, and surface modification. The absorption of TiO_2 sensitized by a proper dye molecule can be extended to visible region because the dye can absorb the visible light to reach an excited state (O'Regan and Grätzel 1991). The dye in the excited state has, in general, a lower redox potential than the corresponding ground state. If the redox potential is lower than the conduction band (CB) of TiO_2 , an electron may be injected from the excited state into the CB, and consequently the cationic radicals and CB electron are formed (Fig. 1). While the dye-sensitized TiO_2 is efficient in the utilization of visible light, all of the known sensitizers are toxic and unstable in aqueous solution, thus making them unsuitable for applications in photocatalysis (Zhao et al. 2005).

To design and develop TiO_2 -based photocatalysts that can operate under visible-light irradiation, modification of the electronic structure of the photocatalyst is indispensable. Two approaches are considered to control the electronic structure

X.S. Zhao (✉)

Department of Chemical and Biomolecular Engineering,
National University of Singapore, Kent Ridge, Singapore
e-mail: chezxs@nus.edu.sg

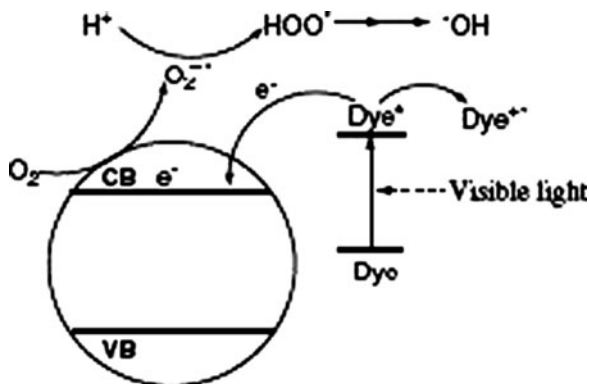


Fig. 1 The photocatalytic mechanism of dye-sensitized TiO₂ under visible-light illumination. With kind permission from Springer Science+Business Media: Zhao et al. (2005)

of TiO₂, namely (1) modification of the electronic structure of TiO₂ by metal doping and (2) formation of a new valence band instead of O 2p by the addition of proper atoms into the lattice of TiO₂ by nonmetal doping or formation of new binary oxides.

1.1 The Metal-Doping Method

Doping of transition metal ions has been used to modify the electronic structure of TiO₂ to utilize visible light. The doping of a foreign element into an active photocatalyst with a wide bandgap to make a donor or an acceptor level in the forbidden band is one of the ways to develop a new visible-light-responsive photocatalyst.

Many studies have been conducted to prepare transition-metal-ion-doped TiO₂. To date, these methods mainly include sol-gel method, impregnation method, microemulsion method, and solution combustion method. The first systematic study on the role of a metal ion dopant in quantum-sized TiO₂ has been performed by measuring their photoreactivities and the transient charge carrier recombination dynamics (Choi et al. 1994). The presence of metal ion dopants in the TiO₂ crystalline matrix significantly influences photoreactivity, charge carrier recombination rates, and interfacial electron-transfer rates. The photoreactivities of 21 metal ion-doped TiO₂ are quantified in terms of both the CB electron reduction of an electron acceptor (CCl₄ dechlorination) and the valence band hole oxidation of an electron donor (CHCl₃ degradation). Doping with Fe³⁺, Mo⁵⁺, Ru³⁺, Os³⁺, Re⁵⁺, V⁴⁺, and Rh³⁺ at 0.1–0.5 at.% significantly increases the photoreactivity for both oxidation and reduction, while Co³⁺ and Al³⁺ doping decrease the photoreactivity. Photoreactivities are shown to increase with the concentration of trapped charge carriers that remain after an initial fast recombination between free charge carriers. The relative efficiency of a metal ion dopant depends on whether it serves as a mediator of interfacial charge transfer or as a recombination center. The ability of a dopant to function as an effective trap is related to the dopant concentration, the energy level of dopants with the TiO₂

lattice, their d electronic configuration, the distribution of dopants within the particles, the electron donor concentration, and the incident light intensity. Enhanced interfacial charge transfer in the presence of effective dopants appears to be the most important factor in the enhancement of photoreactivity of doped TiO_2 . Although this study is a pioneering work in the research of metal ion-doped TiO_2 , the photoreactivity experiments were conducted under UV light irradiation, which indicates that the prepared metal ion-doped TiO_2 was not visible-light-responsive.

Many endeavors were made to extend the absorption of metal ion-doped TiO_2 to visible region after the pioneering work by Choi et al. (1994) by using sol-gel method, which is successful in the preparation of thin films, monoliths, and metal ion-doped TiO_2 through the formation of homogeneous sol. It is reported that the amorphous microporous titania modified with platinum chloride prepared by sol-gel method can photooxidize 4-chlorophenol under visible-light irradiation (Zang et al. 1998). In a typical experiment, the hybrid titania (Pt(IV)/AMM-Ti) was prepared by the slow hydrolysis of titanium isopropoxide in the presence of PtCl_6^{2-} ions in a strong acidic aqueous media. After the gel was kept in a hood for several days, it was heated to 250°C and cooled down to room temperature. As shown in Fig. 2, Pt(IV)/AMM-Ti exhibited significant absorption in the visible region in the diffuse reflectance spectra. The authors assigned this absorption to the ligand field transition of the PtCl_4 modifier by analogy with solution spectra of corresponding chloro-complexes. In the inset of Fig. 2, solid PtCl_4 itself has a similar reflectance spectrum. At short wavelengths below 400 nm, the absorption of Pt(IV)/AMM-Ti increased sharply, indicating the bandgap absorption of amorphous titania, AMM-Ti, as inferred from the absorption feature of P25 TiO_2 .

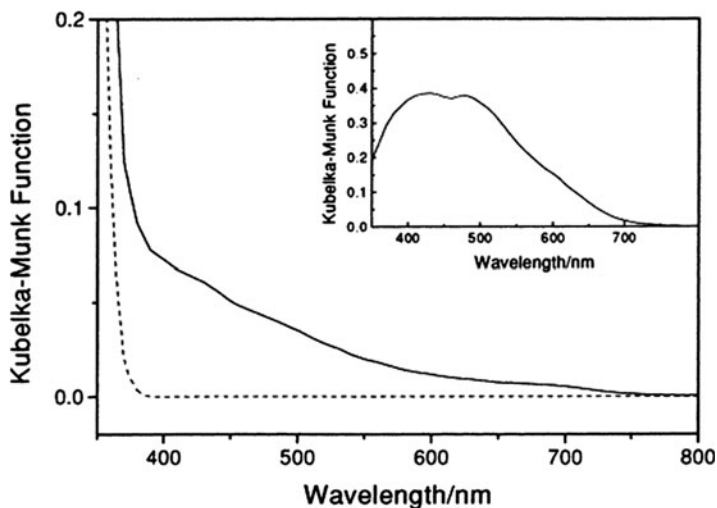
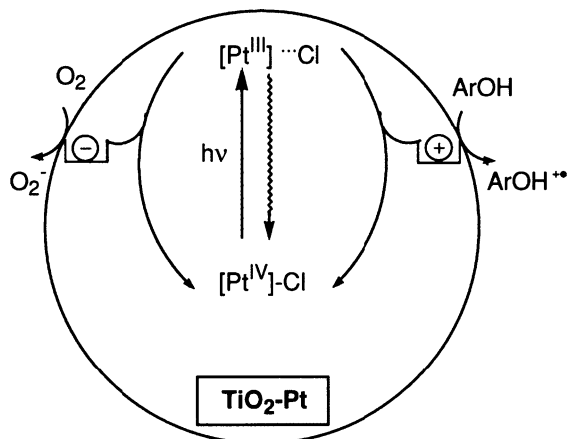


Fig. 2 Diffuse reflectance spectra of P-25 TiO_2 (dotted curve), Pt(IV)/AMM-Ti (solid curve), and PtCl_4 (inset). Reprinted with permission from Zang et al. (1998). Copyright American Chemical Society

Fig. 3 Pictorial view of the postulated primary processes occurring after light absorption by Pt(IV)/AMM-Ti. Reprinted with permission from Zang et al. (1998). Copyright American Chemical Society



The photoactivity of Pt(IV)/AMM-Ti for the photodegradation of 4-chlorophenol under visible-light irradiation was originated from the light absorption by the PtCl_4 component. A completely different mechanism of charge generation was applied to this new amorphous photocatalyst (Fig. 3). Local excitation of the platinum halide in the UV or visible light affords charge-transfer-ligand-to-metal or ligand field states, respectively, which both undergo homolytic Pt–X bond cleavage to yield Pt(III) and a halogen atom, as observed also for homogeneous aqueous solutions. The labile platinum(III) intermediate will rapidly transfer an electron to a Ti(IV) site of the amorphous TiO_2 matrix, while the chlorine atom abstracts an electron from the oxygen lattice. Both processes should be facilitated by the homogeneous distribution of platinum chloride within the metal oxide phase. At the resulting oxidizing and reducing surface centers, oxidation of the phenol and reduction of oxygen can occur, followed by complete mineralization, as known from the reaction photocatalyzed by crystalline TiO_2 . This mechanism of photoinduced charge generation significantly differs from that of metal ion-doped crystalline TiO_2 . In the latter case, light absorption occurs between states localized on both the doping metal ion and the semiconductor, whereas in the former, only the “doping” metal salt is involved.

A microemulsion method was used to prepare visible-light-activated metal-doped TiO_2 as this method facilitates the homogeneity of chemical composition at a nanoscale as well as the production of particles with a narrow size distribution (Fuerte et al. 2001). In this work, different transition metal ion-doped TiO_2 were prepared, and toluene mineralization in the gas phase under sunlight irradiation was chosen to investigate the photoactivity of these metal ion-doped TiO_2 nanoparticles. UV–visible spectra suggest that V- and Cr-containing samples do not present a simple bandgap as occurs with titania (shown in Fig. 4). In the visible region of the spectrum, V displays d–d charge localized transitions (for $\text{V}^{5+}/\text{V}^{4+}$ in the 400–600/600–800 nm region), while Cr has several O to Cr charge transfer bands. The electronic modifications induced in the anatase-like oxides with respect to titania evidence the main reason for the failure of the Ti–V and Ti–Cr catalysts.

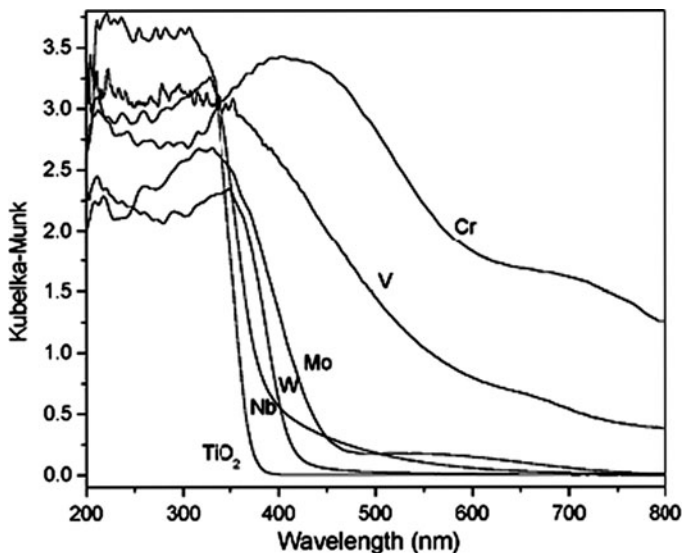


Fig. 4 UV-vis reflectance spectra of Ti-metal samples with the highest dopant-atom content. From Fuerte et al. (2001). Reproduced by permission from The Royal Society of Chemistry

The photocatalysts containing W appear to have the highest activity for the photo-oxidation of toluene under sunlight irradiation, although its absorption in visible region is not highest. This work indicates that the heavier elements of group VI are the best dopants for yielding efficient photocatalytic degradation of toluene using highly doped titania when illuminated under solar light.

Different from the above-mentioned work, another metal ion-substituted TiO₂ by W, V, Ce, Zr, Fe, and Cu was prepared by solution combustion method and it is found that the photodegradation rate of 4-nitrophenol over the prepared transition metal ion-substituted TiO₂ under visible-light irradiation was lower than that of undoped TiO₂ (Nagaveni et al. 2004). The presence of metal ions in titania does not modify the position of the valence band edge of anatase. Instead, it introduces new energy levels of the transition metal ions into the bandgap of TiO₂, which serve as electron-hole trapping centers (Fig. 5). When the energy levels of the metal ion impurities lie below the CB edge, it traps the excited electrons. When the energy level is above the valence band edge, electrons in the d orbitals can quench the photogenerated holes by indirect recombination before they can diffuse to the surface. The presence of metal ion dopants provides more trap sites for electrons and holes in addition to the surface trap sites. Trapping either an electron or a hole alone is ineffective for photodegradation because immobilized charge species quickly recombines with its mobile counterpart. Therefore, substituted metal ions act as recombination centers instead of suppressing electron-hole recombination, which influence the photoactivity detrimentally.

Additionally, ion beam technology using accelerated metal ions was applied to modify the electronic properties of TiO₂ to extend its absorption to visible region.

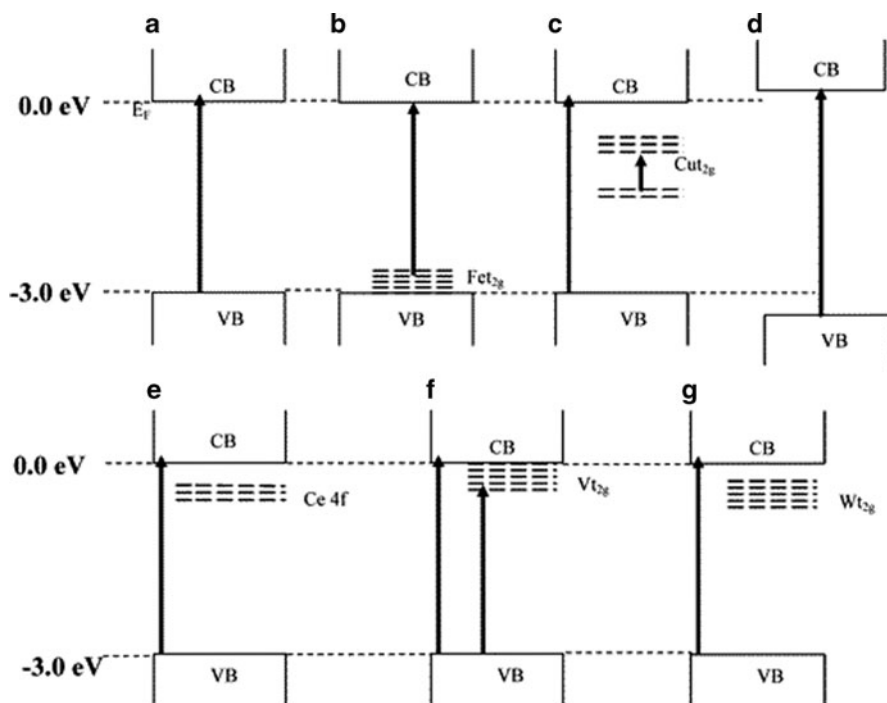


Fig. 5 Schematic representation of energy levels of dopant ions in TiO_2 : (a) TiO_2 , (b) Fe/TiO_2 , (c) Cu/TiO_2 , (d) Zr/TiO_2 , (e) Ce/TiO_2 , (f) V/TiO_2 , and (g) W/TiO_2 . Reprinted with permission from Nagaveni et al. (2004). Copyright Chemical Society

The ion beam technologies, such as the ion implantation method and the ionized cluster beam (ICB) method, use the accelerated metal ion beam generated by applying the unique properties of metal ions. Metal ions are electronic charged atoms whose kinetic energies can be controlled by the acceleration of metal ions under a controlled electric field. By these methods, the metal ions are accelerated in the electric field and injected into the sample target as an ion beam. In the case of the ion implantation method, metal ions are accelerated enough to have a high kinetic energy (50–200 keV) and can be implanted into the bulk of samples. However, the metal ions (ionized cluster) are accelerated to have a low kinetic energy (0.2–2 keV) in the ICB method and these ions are deposited to form a thin film on the top surface of the sample. With these unique properties of the ion beam techniques, well-defined semiconductor materials and thin films have been developed (Takeuchi et al. 2000a, 2000b; Zhou et al. 2006, 2007a).

In conclusion, the role of transition metal ions in the metal ion-doped TiO_2 is contradictory. Different behavior of various metal-doped TiO_2 can be related to the solubility of the transition metal ion in TiO_2 and the position of metal d levels within the bandgap energy of TiO_2 .

1.2 The Nonmetal Doping Method

If a doping method is efficient and effective for the modification of TiO_2 to extend its photoactivity to visible region, the following requirements should be met (Asahi et al. 2001): (1) doping should produce states in the bandgap of TiO_2 that absorb visible light; (2) the CB minimum of TiO_2 , including subsequent impurity states, should be as high as that of TiO_2 or higher than the $\text{H}_2/\text{H}_2\text{O}$ level to ensure its photoreduction activity; and (3) the states in the gap should overlap sufficiently with the band states of TiO_2 to transfer photoexcited carriers to reactive sites at the catalyst surface within their lifetime. Conditions (2) and (3) require that the anionic species should be used for doping rather than cationic metals, which often give quite localized d states deep in the bandgap of TiO_2 and result in recombination centers of carriers. Compared with metal ion-doping method, anionic species doping method is more efficient and effective in narrowing the bandgap of TiO_2 so that visible light can be fully utilized.

Since the first report on the visible-light photocatalysis of nitrogen-doped titanium dioxides prepared by sputtering the TiO_2 target in an $\text{N}_2(40\%)/\text{Ar}$ gas mixture followed by annealing at 550°C in N_2 gas for 4 h, a great deal of research efforts have been made at the study on anionic species-doped TiO_2 (Asahi et al. 2001). To date, the substitutional doping of nitrogen is the most effective means because its p states contribute to the bandgap narrowing by mixing with O 2p states. Theoretical calculation of density of states (DOSs) of the substitutional doping of C, N, F, P, and S for O in anatase TiO_2 using the full-potential linearized augmented plane wave (FLAPW) formalism in the framework of the local density approximation (LDA) has been made (Fig. 6) and only nitrogen doping can form intra-bandgap states, which overlap sufficiently with the edge of energy band (shallow surface states), inducing electronic coupling and prevent charge recombination. Doping with C and P leads to states located too deep in the gap to overlap with the energy band. Although doping with S shows a similar bandgap narrowing, it would be difficult to incorporate it into the TiO_2 crystal because of its large ionic radius, as evidenced by a much larger formation energy required for the substitution of S than that required for the substitution of N (Asahi et al. 2001). They further stated that the interstitial nitrogen-doping is unlikely to have efficient visible activity because the formed states are well screened and hardly interact with the band states of TiO_2 . Therefore, they concluded that the substitutional nitrogen doping plays an important role in the photocatalysis. The prediction has been proved perfectly by their experiments on the bleaching of aqueous methylene blue and the decomposition of gaseous acetaldehyde over N-doping TiO_2 ($\text{TiO}_{2-x}\text{N}_x$) under visible-light irradiation.

Besides the sputtering method, other wet chemical methods were adopted to synthesize N-doped TiO_2 by using triethylamine (Burda et al. 2003) or NH_3 in dioxane (In et al. 2006) as the nitrogen precursor and the controlled hydrolysis of titanium precursor. The change in color of the nanocrystals upon nitrogen incorporation demonstrates a profound effect on their optical response in the visible wavelength range. These methods were effective in largely shifting the absorption

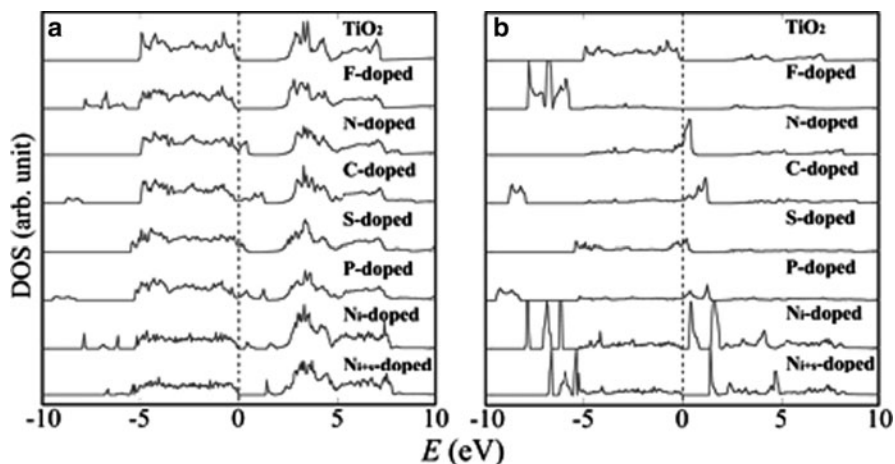


Fig. 6 (a) Total DOSs of doped TiO_2 and (b) the projected DOSs into the doped anion sites, calculated by FLAPW. The dopants F, N, C, S, and P were located at a substitutional site for an O atom in the anatase TiO_2 crystal (the eight TiO_2 units per cell). The results for N doping at an interstitial site (N_i -doped) and that at both substitutional and interstitial sites (N_{i+s} -doped) are also shown. The energy is measured from the top of the valence bands of TiO_2 , and the DOSs for doped TiO_2 are shifted so that the peaks of the O 2s states (at the farthest site from the dopant) are aligned with each other. From Asahi et al. 2001. Reprinted with permission from AAAS

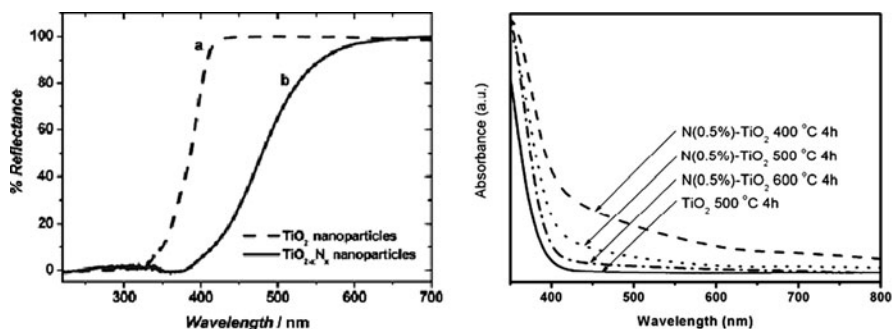


Fig. 7 UV-vis spectra of N-doped TiO_2 prepared by using different nitrogen precursors: (left) triethylamine; (right) NH_3 in dioxane (In et al. 2006). Reprinted with permission from Burda et al. (2003). Copyright American Chemical Society

edge of TiO_2 towards the visible region as shown in Fig. 7. Furthermore, these wet methods were low-cost, controllable, and reproducible, which enable them a promising application in the preparation of N-doped TiO_2 .

While the work of N-doped TiO_2 by Asahi and coworkers has provided a great opportunity to realize the visible-light activity of TiO_2 , and opened a new avenue to the modification of TiO_2 , some recent studies disagree to the theoretical calculations. For example, one study predicted that carbon-doped TiO_2 is impossible to exhibit

effective visible-light response due to the deep location of the formed states in the bandgap. However, it is reported that carbon-doped can efficiently split water into hydrogen and oxygen under visible-light irradiation (Khan et al. 2002). The bandgap of a chemically modified *n*-TiO₂ by controlled combustion of Ti metal in a natural gas flame can be decreased to 2.32 eV and the maximum photoconversion efficiency of 8.35% was obtained. It has been proposed that the substitution of carbon for some of the lattice oxygen atoms in TiO₂ can lower its bandgap to absorb visible light. Furthermore, it has been found that carbon-containing TiO₂ prepared using a sol-gel process with different alkoxide precursors is capable of photodegrading *p*-chlorophenol under visible-light irradiation (Lettmann et al. 2001). Subsequently, another carbon-modified TiO₂ was prepared by sol-gel method, whose bandgap energy was narrowed to 3.17 eV compared with undoped TiO₂ (Sakthivel and Kisch 2003). A solution of tetrabutylammonium hydroxide was added dropwise to a TiCl₄ solution at 0°C, during which the pH was mediated to 5.5. The precipitate was collected by filtration and dried under air at 70°C after aging the suspension for 24 h. The dried precipitate was calcined in a muffle furnace at 400°C for 1 h and at 550°C for 4 h. The superior photocatalytic activity of the carbon-doped TiO₂ is demonstrated by illumination experiments in diffuse indoor daylight. In solution 4-chlorophenol and the azo dye remazol red are efficiently mineralized by the carbon-doped TiO₂ and the filter paper supported carbon-doped TiO₂ can photocatalyze the oxidation of gaseous acetaldehyde, benzene, and carbon monoxide.

Another extensively studied example of visible-light-responsive TiO₂ was fluorine-doped TiO₂. The mechanism of F-doped TiO₂ which is responsive to visible light is essentially different from the N or C-doped TiO₂. The F-doped TiO₂ can show response to visible light by the creation of oxygen vacancies which induced extrinsic absorption, rather than the substitutional nitrogen doping. Generally, a surface photoreaction can be caused by the photoexcitation of both intrinsic and extrinsic absorption bands of a photocatalyst (Emeline et al. 1999; Volodin 2000). The former concerns electron transition from the valence band to CB of a semiconductor and thus requires the energy of the actinic light larger than the bandgap energy. The latter includes the light absorption of impurity, the photoionization of original or newly formed defects, and the excitation of surface states. However, the latter excitation requires the actinic light with less energy compared with that of former, it can be sometimes realized with visible light. Also, the photoexcitation by extrinsic absorption bands can generate free charge carriers which can participate in surface chemical reactions. UV-vis adsorption spectra showed that F-doped TiO₂ did not cause shift in the fundamental absorption edge of TiO₂ (Fig. 8). The localized levels with a high density appear below the valence band of TiO₂, and these levels are composed of F_{2p} state without any mixing with the valence band or CB of TiO₂, consequently they cannot contribute to the optical absorption of TiO₂ (Li et al. 2005a, b, c).

However, F-doped TiO₂ is very effective in the photocatalytic degradation of 4-chlorophenol and gaseous acetaldehyde or trichloroethylene under visible-light irradiation (Li et al. 2005a, b, c). Moreover, ESR signals of the DMPO-OH adduct with pulsed laser illumination in a F-doped TiO₂-DMPO dispersion showed that after visible-light irradiation, the characteristic 1:2:2:1 quadruple peaks of the

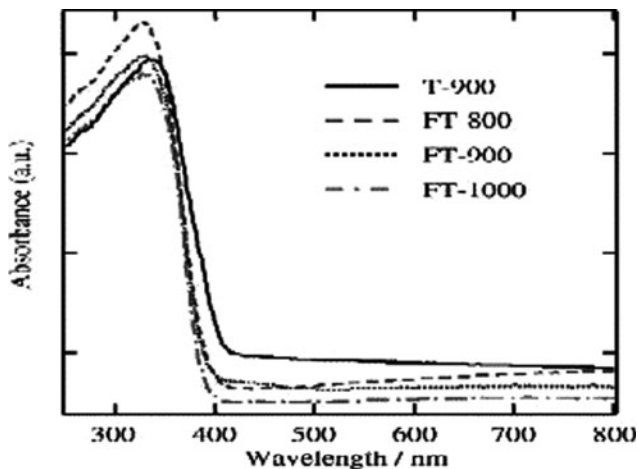


Fig. 8 UV-vis adsorption spectra of F-doped TiO₂ (Li et al. 2005a, b, c) Copyright with permission from Elsevier

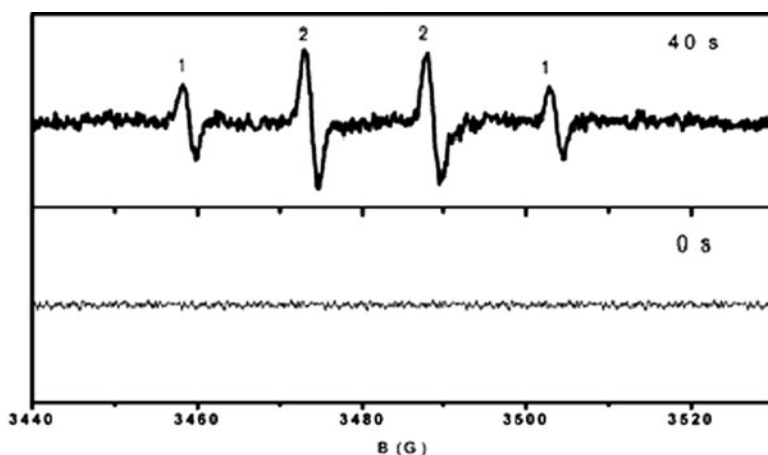


Fig. 9 ESR signals of the DMPO-OH[•] adduct in a porous F-doped TiO₂ microspheres-DMPO dispersion. The signals were recorded before and after illumination for 40 s with a Quanta-Ray Nd:YAG pulsed laser operated in the continuous mode at 10 Hz frequency Ho et al. (2006). Reproduced by permission from The Royal Society of Chemistry

DMPO-OH[•] adduct are observed, whereas no signals can be detected in the dark as shown in Fig. 9 (Ho et al. 2006). This indicates that the F-doped TiO₂ is activated when exposed to visible light and generate reactive oxygen species such as hydroxyl radicals, further confirming the existence of oxygen vacancies, which can generate hydroxyl radicals. The high photocatalytic activity of F-doped TiO₂ is

probably due to the excitation of the extrinsic absorption bands by these oxygen vacancies rather than the excitation of the intrinsic absorption band of bulk TiO_2 . This is not difficult to understand because general UV-vis absorption spectra only reflect the intrinsic optical property for the bulk of a solid, however, the actual absorption spectrum of a photocatalyst is an overlapping result of intrinsic and extrinsic absorption bands.

Over the past few years, the pursuit of the control of morphology and particle size of the synthesized TiO_2 has never been ceased because it is another crucial element determining the photocatalytic activity of TiO_2 (Zhang et al. 2006). Inorganic hollow structures, which can be achieved by nozzle-reactor systems, sacrificial cores, or emulsion/water extraction techniques, have attracted great attention because of their wide variety of potential applications as catalysts and catalyst supports, adsorbents, sensors, drug-delivery carriers, artificial cells, photonic crystals, acoustic insulators, lightweight fillers, and microreactors (Bruinsma et al. 1997; Kim et al. 2002; Sun et al. 2003; Lu et al. 2005; Yang et al. 2005; Titirici et al. 2006). In particular, many efforts have been devoted to the controlled fabrication of hollow TiO_2 particles due to its vital application in photocatalysis. The wet-chemical methods were successful in controlling the morphology of TiO_2 , at the same time, on the realization of doping nonmetal elements such as F into TiO_2 . The flower-like F-doped hollow microspheres were prepared by one-pot hydrothermal synthetic method by controlling the hydrolysis of TiF_4 in a Teflon-autoclave at 180°C .

XPS investigation confirms the existence of F as two forms, F^- ions physically adsorbed on the surface of TiO_2 and F in the solid solution $\text{TiO}_{2-x}\text{F}_x$ formed by the substitution of the oxygen in TiO_2 lattice for F^- ions generated by the hydrolysis of the precursor, TiF_4 (Fig. 10) (Zhou et al. 2008b). The self-generated HF by the hydrolysis reaction may act as the source of F-dopant. This process is easily occurred because the ionic radius of F is almost the same as that of O in the lattice of TiO_2 .

The FESEM image and TEM image confirm the hollow interior of F-doped TiO_2 presented as the morphology of flower (Fig. 11). The hydrolysis reaction product, HF, plays a very important role on the formation of flower morphology and the hollow structure. HF as a corrosive chemical etchant was released when the hydrolysis reaction was going on. It promotes the formation of the flower morphology by concurrently etching the surface of TiO_2 and the interiors of TiO_2 . Furthermore, the formation of the flower-like F-doped TiO_2 crystallites could also be attributed to the homogeneous nucleation, which indicates that the new TiO_2 particles were formed on the existing TiO_2 particles, taking place on some defect sites of the elongated crystallites formed earlier. Besides, the hydrogen bond formed on the surface of F-doped TiO_2 may also exert some influences on the formation of the flower morphology by self-assembly and organization. With regard to the hollow effect, the Ostwald ripening process, which must involve the mass transfer between the solid core and external chemical solution through inter-crystallite interstitials of the microspheres, must be involved. The prepared flower-like F-doped hollow microspheres exhibited high photocatalytic activity for the degradation of methylene blue under visible-light irradiation. After 8 h visible-light illumination, almost 90% of methylene blue was photodegraded.

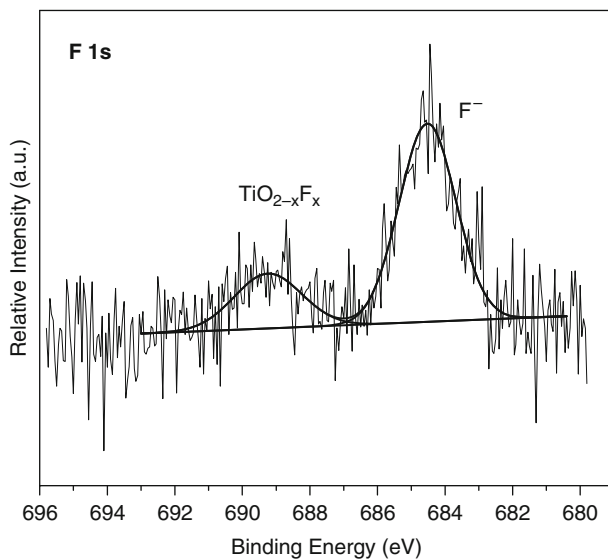


Fig. 10 XPS spectra of F 1s of F-doped TiO₂. Reprinted with permission from Zhou et al. (2008). Copyright American Chemical Society

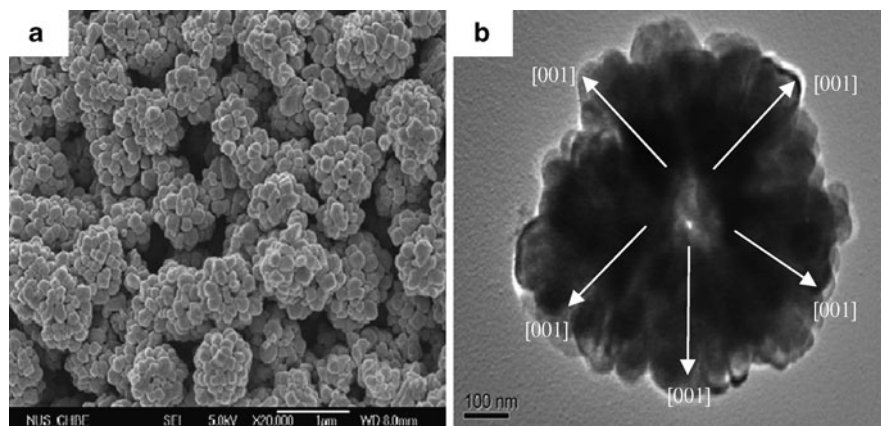


Fig. 11 FESEM (a) and TEM (b) image of F-doped TiO₂. Reprinted with permission from Zhou et al. (2008). Copyright American Chemical Society

Another strategy to extend the visible response of TiO₂ is modification of TiO₂ with two dopants, including metal/nonmetal dopants and nonmetal/nonmetal dopants. Recently, a novel TiO₂-based photocatalyst, prepared by doping with both a nonmetal element, boron, and a metal oxide, Ni₂O₃, can efficiently photodegrade the organic pollutants, such as trichlorophenol, 2,4-dichlorophenol and sodium benzoate under visible-light irradiation (Zhao et al. 2004). During the degradation of trichlorophenol, the reduction in COD_{Cr} of about 80% and in total organic carbon

(TOC) of 70% were achieved, with about 80% of the total chloride converted into Cl^- ions. The bandgap energies for undoped TiO_2 , B-doped TiO_2 , and

B,Ni-co-doped TiO_2 were estimated to be 3.18, 2.93, and 2.85 eV, respectively. In this system, incorporation of B into TiO_2 can extend the spectral response to the visible region and function as an antenna, and the further loading of Ni_2O_3 into the matrix can suppress the charge recombination and enhance greatly the photocatalytic activity. Subsequently, another co-doped TiO_2 by two nonmetal elements was reported (Li et al. 2005a, b). The yellow-colored N,F-co-doped TiO_2 was synthesized from a mixed aqueous solution containing TiCl_4 and NH_4F by spray pyrolysis at 900°C . The nitrogen doping was originated from NH_3 decomposed by NH_4Cl from the reaction of two precursors. The F doping underwent two pathways: the first one is that part of the Ti–F bonds did not break during the $(\text{NH}_4)_2\text{TiF}_6$ hydrolysis and directly remained in the TiO_2 crystal lattice. The second one is associated with the decomposition of the high-dispersed TiOF_2 . The uncompleted decomposition of the TiOF_2 led to some of the Ti–F bonds left in the TiO_2 crystal lattice. UV–vis adsorption spectra showed that a new absorption band was observed in the visible range of 400–550 nm in addition to the fundamental absorption edge of TiO_2 , which can be attributed to the doped N atoms. The high photocatalytic activity of N,F-co-doped TiO_2 for the degradation of acetaldehyde, trichloroethylene, and toluene under visible-light illumination was resulted from the oxygen vacancies, which can induce the formation of hydroxyl radicals, having strong capability to oxidize the organic pollutants, and the increase of the photogenerated electron mobility by the F doping.

1.3 Formation of New Binary Oxides

The modification of TiO_2 to extend its absorption to visible region can be realized by the formation of new binary oxides between TiO_2 and other metal oxides. The formation of binary oxides as solid solution was generally prepared by solid state reaction. Essentially, a visible-light-driven photocatalyst should have a small bandgap capable of absorb visible light. One of the ways to narrow the bandgap of a semiconductor is to control the position of valence band (Kato et al. 2002; Kim et al. 2004; Tang and Ye 2005). In many reported oxide photocatalysts, the valence band is commonly composed of O 2p. The valence band level is about 3 eV, which is deep enough to oxidize H_2O to O_2 . Because it causes oxide semiconductor photocatalysts to have wide bandgaps, it is necessary to make a valence band consisting of an orbital other than O 2p to develop a visible–light-responsive photocatalyst.

In view of the fundamental process for decomposition of organic contaminants, it involves: (1) photogenerated electrons in the CB are trapped by a recipient (such as oxygen) and (2) photogenerated holes in the valence band are consumed by a donor (such as organics). The deeper the valence band of a semiconductor, the stronger its oxidative activity, the higher the photocatalytic properties of the material for the decomposition of the organics (Sato et al. 2004). Therefore, the position of

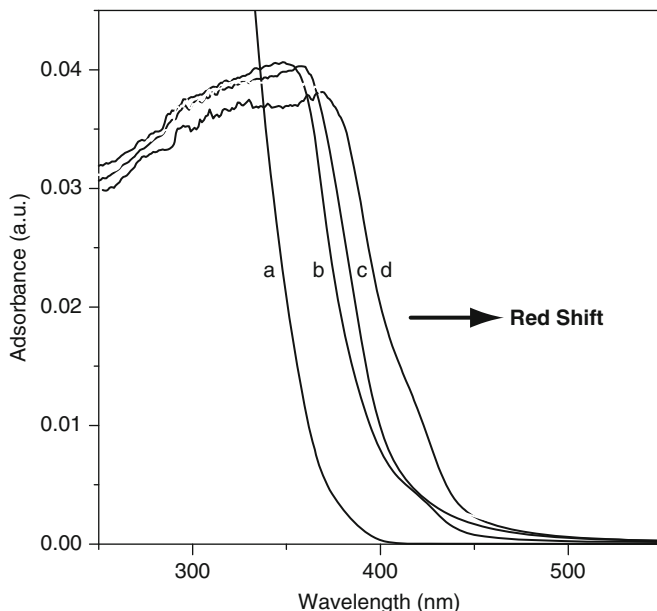


Fig. 12 UV-vis/diffuse reflectance spectra of $\text{Bi}_{12}\text{TiO}_{20}$ prepared by different molar ratio of Bi_2O_3 to TiO_2 and calcined at 600°C : (a) P25 TiO_2 , (b) 0.5, (c) 1, and (d) 2. Reprinted with permission from Zhou et al. (2007b). Copyright American Chemical Society

the valence band of a semiconductor is a key factor for the effective photocatalytic decomposition of organic contaminants. The position of the valence band of a semiconductor can be changed by the formation of a hybridized orbital between O 2p orbital and s, p, and d orbital of other metals. It has been reported that many semiconductors containing hybridized valence band often reveal the suitable band structure responsive to visible-light irradiation. It was found that Bi is a good candidate for valence-band-control (Kudo et al. 1999). A previous study has reported that the valence band control by the Bi 6s or hybridized Bi 6s–O 2p orbital can be realized by the reaction of TiO_2 and Bi_2O_3 to form $\text{Bi}_{12}\text{TiO}_{20}$, which exhibited high photocatalytic activity for the decomposition of methanol under visible-light irradiation (Zhou et al. 2007b). The bandgap of $\text{Bi}_{12}\text{TiO}_{20}$ photocatalyst prepared with a molar ratio of Bi_2O_3 to TiO_2 at 2 and calcined at 600°C was estimated to be 2.78 eV. UV-vis diffuse reflectance spectra showed that the onset of the absorption edge of the $\text{Bi}_{12}\text{TiO}_{20}$ samples was shifted to the visible-light region as the molar ratio of Bi_2O_3 to TiO_2 was increased (Fig. 12).

To clarify the band structure of $\text{Bi}_{12}\text{TiO}_{20}$, band calculation was carried out with the plane wave density function theory by CASTEP program package. Figure 13 shows the band structure and DOS of $\text{Bi}_{12}\text{TiO}_{20}$. It can be seen that $\text{Bi}_{12}\text{TiO}_{20}$ has a clear bandgap. Three occupied bands and one unoccupied band are seen from the density of the state diagram, in which the bands consist of O 2s, Bi 6s, O 2p, and Ti 3d orbitals in turn from the lowest to the highest band. Among them, the highest

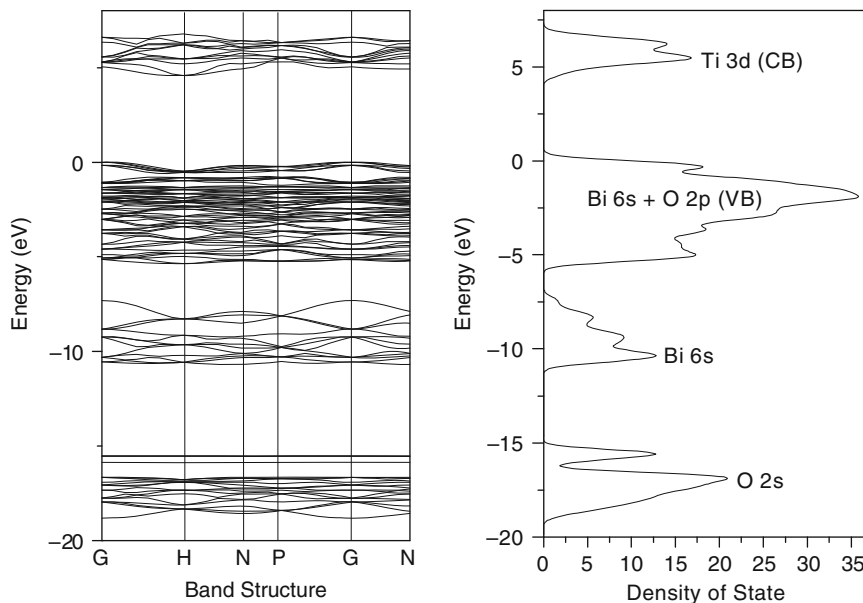


Fig. 13 Band structure and density of state for $\text{Bi}_{12}\text{TiO}_{20}$ calculated by the plane-wave-density function theory method using a CASTEP program package. Reprinted with permission from Zhou et al. (2007b). Copyright American Chemical Society

occupied band is composed of Bi 6s and O 2p, corresponding to the valence band (VB). The lowest unoccupied band consists of Ti 3d, corresponding to the CB. It is obvious that the Bi 6s and O 2p bands are hybridized to form the VB of $\text{Bi}_{12}\text{TiO}_{20}$. Therefore, the band structure of $\text{Bi}_{12}\text{TiO}_{20}$ is determined by Ti 3d and the hybridized band of Bi 6s and O 2p. This hybridization shifted the VB upward so that the bandgap of $\text{Bi}_{12}\text{TiO}_{20}$ was narrowed.

In addition to the valence band position, the mobility of photogenerated carriers also influences the activity of a photocatalyst. The higher the mobility of the photogenerated carriers (including holes and electrons), the better the performance of the photocatalyst (Tang et al. 2004). Also, the dispersion of the valence band can influence the mobility of photogenerated holes. The high photocatalytic activity of $\text{Bi}_{12}\text{TiO}_{20}$ prepared at a molar ratio of Bi_2O_3 to TiO_2 at 2 and calcined at 600°C can be ascribed to its band structure, in which the valence band was composed of Bi 6s orbital and O 2p orbital, namely a hybrid orbital of Bi 6s and O 2p. The Bi 6s orbital is largely dispersed in this hybrid orbital probably promoting the increase in the mobility of photogenerated carriers (Kudo et al. 1999; Kim et al. 2004). In the hybridized valence band of $\text{Bi}_{12}\text{TiO}_{20}$, the photogenerated holes possessed a high mobility, which contributed to the high activity of the photocatalyst. Meanwhile, if considering the crystal structure of $\text{Bi}_{12}\text{TiO}_{20}$, the Bi–O polyhedra in $\text{Bi}_{12}\text{TiO}_{20}$ may serve as the active electron donor sites, enhancing the electron transfer to O_2 and eliminating the recombination of the photogenerated electron–hole pairs.

References

- Asahi R, Morikawa T, Ohwaki T, Aoki K, Taga Y (2001) Visible-light photocatalysis in nitrogen-doped titanium oxides. *Science* 293:269–271
- Bruinsma PJ, Kim AY, Liu J, Baskaran S (1997) Mesoporous silica synthesized by solvent evaporation: Spun fibers and spray-dried hollow spheres. *Chem Mater* 9:2507–2512
- Burda C, Lou Y, Chen X, Samia ACS, Stout J, Gole JL (2003) Enhanced nitrogen doping in TiO₂ nanoparticles. *Nano Lett* 3:1049–1051
- Choi W, Termin A, Hoffmann MR (1994) The role of metal ion dopants in quantum-sized TiO₂: correlation between photoreactivity and charge carrier recombination dynamics. *J Phys Chem* 98:13669–13679
- Emeline AV, Ryabchuk VK, Serpone N (1999) Spectral dependencies of the quantum yield of photochemical processes on the surface of nano-/microparticulates of wide-band-gap metal oxides. 1. Theoretical approach. *J Phys Chem B* 103:1316–1324
- Fuente A, Hernández-Alonso MD, Maira AJ, Martínez-Arias A, Fernández-García M, Conesa JC, Soria J (2001) Visible light-activated nanosized doped-TiO₂ photocatalysts. *Chem Commun* 24:2718–2719
- Fujishima A, Honda K (1972) Electrochemical photolysis of water at a semiconductor electrode. *Nature* 238:37–38
- Ho W, Yu JC, Lee S (2006) Synthesis of hierarchical nanoporous F-doped TiO₂ spheres with visible light photocatalytic activity. *Chem Commun* (10):1115–1117
- In S, Orlov A, Garcia F, Tikov M, Wright DS, Lambert RM (2006) Efficient visible light-active N-doped TiO₂ photocatalysts by a reproducible and controllable synthetic route. *Chem Commun* (40):4236–4238
- Kato H, Kobayashi H, Kudo A (2002) Role of Ag⁺ in the band structures and photocatalytic properties of AgMO₃ (M: Ta and Nb) with the perovskite structure. *J Phys Chem B* 106:12441–12447
- Khan SUM, Al-shahry M Jr, Ingler WB (2002) Efficient photochemical water splitting by a chemically modified n-TiO₂. *Science* 297:2243–2245
- Kim SW, Kim M, Lee WY, Hyeon T (2002) Fabrication of hollow palladium spheres and their successful application to the recyclable heterogeneous catalyst for Suzuki coupling reactions. *J Am Chem Soc* 124:7642–7643
- Kim HG, Hwang DW, Lee JS (2004) An undoped, single-phase oxide photocatalyst working under visible light. *J Am Chem Soc* 126:8912–8913
- Kudo A, Omori K, Kato H (1999) A novel aqueous process for preparation of crystal form-controlled and highly crystalline BiVO₄ powder from layered vanadates at room temperature and its photocatalytic and photophysical properties. *J Am Chem Soc* 121:11459–11467
- Lettmann C, Hildenbrand K, Kisch H, Macyk W, Maier WF (2001) Visible light photodegradation of 4-chlorophenol with a coke-containing titanium dioxide photocatalyst. *Appl Catal B Environ* 32:215–227
- Li D, Haneda H, Labhsetwar NK, Hishita S, Ohashi N (2005a) Visible-light-driven photocatalysis on fluorine-doped TiO₂ powders by the creation of surface oxygen vacancies. *Chem Phys Lett* 401:579–584
- Li D, Haneda H, Hishita S, Ohashi N (2005b) Visible-light-driven N-F-codoped TiO₂ photocatalysts. 1. Synthesis by spray pyrolysis and surface characterization. *Chem Mater* 17:2588–2595
- Li D, Haneda H, Hishita S, Ohashi N (2005c) Visible-light-driven N-F-codoped TiO₂ photocatalysts. 2. Optical characterization, photocatalysis, and potential application to air purification. *Chem Mater* 17:2596–2602
- Lu C, Qi L, Yang J, Wang X, Zhang D, Xie J, Ma J (2005) One-pot synthesis of octahedral Cu₂O nanocages via a catalytic solution route. *Adv Mater* 17:2562–2567
- Nagaveni K, Hegde MS, Madras G (2004) Structure and photocatalytic activity of Ti_{1-x}M_xO_{2±δ} (M=W, V, Ce, Zr, Fe, and Cu) synthesized by solution combustion method. *J Phys Chem B* 108:20204–20212

- O'Regan B, Grätzel M (1991) A low-cost, high-efficiency solar cell based on dye-sensitized colloidal TiO₂ films. *Nature* 353:737–740
- Sakthivel S, Kisch H (2003) Daylight photocatalysis by carbon-modified titanium dioxide. *Angew Chem Int Ed* 42:4908–4911
- Sato J, Kobayashi H, Ikarashi K, Saito N, Nishiyama H, Inoue Y (2004) Photocatalytic activity for water decomposition of RuO₂-dispersed Zn₂GeO₄ with d¹⁰ configuration. *J Phys Chem B* 108:4369–4375
- Sun Y, Mayers B, Xia Y (2003) Metal nanostructures with hollow interiors. *Adv Mater* 15:641–646
- Takeuchi M, Yamashita H, Matsuoka M, Anpo M, Hirao T, Itoh N, Iwamoto N (2000a) Photocatalytic decomposition of NO on titanium oxide thin film photocatalysts prepared by an ionized cluster beam technique. *Catal Lett* 66:185–187
- Takeuchi M, Yamashita H, Matsuoka M, Anpo M, Hirao T, Itoh N, Iwamoto N (2000b) Photocatalytic decomposition of NO under visible light irradiation on the Cr-ion-implanted TiO₂ thin film photocatalyst. *Catal Lett* 67:135–137
- Tang J, Ye J (2005) Photocatalytic and photophysical properties of visible-light-driven photocatalyst ZnBi₁₂O₂₀. *Chem Phys Lett* 410:104–107
- Tang J, Zou Z, Ye J (2004) Efficient photocatalytic decomposition of organic contaminants over CaBi₂O₄ under visible-light irradiation. *Angew Chem Int Ed* 43:4463–4466
- Titirici M-M, Antonietti M, Thomas A (2006) A generalized synthesis of metal oxide hollow spheres using a hydrothermal approach. *Chem Mater* 18:3808–3812
- Volodin AM (2000) Photoinduced phenomena on the surface of wide-band-gap oxide catalyst. *Catal Today* 58:103–114
- Yang J, Qi L, Lu C, Ma J, Cheng H (2005) Morphosynthesis of rhombododecahedral silver cages by self-assembly coupled with precursor crystal templating. *Angew Chem Int Ed* 44:598–603
- Zang L, Lange C, Abraham I, Storck S, Maier WF, Kisch H (1998) Amorphous microporous titania modified with platinum (IV) chloride – a new type of hybrid photocatalyst for visible light detoxification. *J Phys Chem B* 102:10765–10771
- Zhang D, Yang D, Zhang H, Lu C, Qi L (2006) Synthesis and photocatalytic properties of hollow microparticles of titania and titania/carbon composites templated by Sephadex G-100. *Chem Mater* 18:3477–3485
- Zhao W, Ma W, Chen C, Zhao J, Shuai Z (2004) Efficient degradation of toxic organic pollutants with Ni₂O₃/TiO_{2-x}B_x under visible irradiation. *J Am Chem Soc* 126:4782–4783
- Zhao J, Chen C, Ma W (2005) Photocatalytic degradation of organic pollutants under visible light irradiation. *Top Catal* 35:269–278
- Zhou J, Takeuchi M, Zhao XS, Ray AK, Anpo M (2006) Photocatalytic decomposition of formic acid under visible light irradiation over V-ion-implanted TiO₂ thin film photocatalysts prepared on quartz substrate by ionized cluster beam (ICB) deposition method. *Catal Lett* 106:67–70
- Zhou J, Takeuchi M, Ray AK, Anpo M, Zhao XS (2007a) Enhancement of photocatalytic activity of P25 TiO₂ by vanadium-ion-implantation under visible light irradiation. *J Colloid Interface Sci* 311:497–501
- Zhou J, Ray AK, Zhao XS (2008) Self-organized flowerlike F-doped TiO₂ hollow microspheres and their photocatalytic activity under visible light irradiation (to be submitted)
- Zhou J, Zou Z, Ray AK, Zhao XS (2007b) Preparation and characterization of polycrystalline bismuth titanate Bi₁₂TiO₂₀ and its photocatalytic properties under visible light irradiation. *Ind Eng Chem Res* 46:745–749

Chapter 11

Development and Sensitization of N- or S-Doped TiO₂ Photocatalysts

Teruhisa Ohno and Toshiki Tsubota

Abstract Titanium dioxide photocatalysts are promising substrates for photodegradation of pollutants in water and air, but show photocatalytic activities only under UV light. To utilize a wider range of incident wavelengths such as solar light, development of photocatalysts active under visible light is very important. Chemically modified titanium dioxide photocatalysts containing anatase phase with S (S⁴⁺) substituted for some lattice Ti atoms or N substituted for some lattice O atoms were prepared. In addition, S, C-co-doped TiO₂ having rutile phase were also prepared. These catalysts showed strong absorption of visible light and high activities for degradation of 2-propanol in aqueous solution, partial oxidation of adamantane, and 2-methylpyridine under irradiation at wavelengths longer than 440 nm. The oxidation states of the S, C, and N atoms incorporated into the TiO₂ particles were determined to be mainly S⁴⁺, C⁴⁺, and N³⁻ from XPS spectra, respectively. The photocatalytic activities of S- or N-doped TiO₂ photocatalysts with adsorbed Fe³⁺ ions were markedly improved for oxidation of 2-propanol compared to those of S- or N-doped TiO₂ without Fe³⁺ ions under a wide range of incident wavelengths, including UV light and visible light. The photocatalytic activity reached maximum with 0.90 wt% Fe³⁺ ions adsorbed on S-doped TiO₂, and 0.36 wt% Fe³⁺ ions on N-doped TiO₂. Furthermore, redox treatment of S- or N-doped TiO₂ photocatalysts with adsorbed Fe³⁺ ions by reduction with NaBH₄ followed by air oxidation resulted in further improvements in photocatalytic activities. In this case, the optimum amounts of Fe³⁺ were 2.81 and 0.88 wt% on the surfaces of S- and N-doped TiO₂ photocatalysts, respectively.

T. Ohno (✉)

Department of Applied Chemistry, Kyushu Institute of Technology,
1-1 Sensui-cho, Tobata, Kitakyushu 804-8550, Japan
e-mail: tohno@che.kyutech.ac.jp

1 Introduction

The discovery of photoelectrochemical splitting of water on titanium dioxide (TiO_2) electrodes (Fujishima and Honda 1972) has led to many investigations of semiconductor-based photocatalysis (Hoffman et al. 1995; Cao et al. 1999; Wolfrum et al. 2002; Theurich et al. 1997; Yanagida et al. 1989; Ohtani et al. 1995; Ohno et al. 1998a, b, 1999; Soana et al. 2000; Matthews 1984; Fujihira et al. 1981; Dusi et al. 1999; Anpo 1997). TiO_2 is one of the most promising photocatalysts, and is now used in various practical applications (Hoffman et al. 1995; Soana et al. 2000), but converts only a small UV band of solar light, about 2–3%, because of its large band gap of 3.2 eV. Therefore, the development of a more efficient TiO_2 photocatalyst with a higher photoelectric conversion of visible light is needed. Doping of TiO_2 with transition metals (Ohno et al. 1999; Anpo 1997; Ghosh and Maruska 1994; Choi et al. 1997), reduced forms of TiO_x photocatalysts (Breckenridge and Hosler 1953; Cronmeyer 1957), and treatment of TiO_2 powder with hydrogen peroxide (Ohno et al. 2001) or chelating agents (Ikeda et al. 2002) have all been investigated, but most of these catalysts do not have long-term stability or sufficiently high activities for a wide range of applications.

N, S, or C anion-doped TiO_2 photocatalysts with an anatase structure show a relatively high level of activity when irradiated by visible light (Asahi et al. 2001; Sakatani et al. 2001; Ihara et al. 2001; Umebayashi et al. 2002a; Irie et al. 2003; Sakthivel and Kisch 2003). Recently, we prepared S or C cation-doped TiO_2 with an anatase phase and S and C cation-co-doped TiO_2 with a rutile phase (Ohno et al. 2003, 2004a, b). However, the photocatalytic activities under visible light irradiation were not sufficient for practical applications. Therefore, we modified these S- and N-doped TiO_2 photocatalysts to improve the photocatalytic activities, and developed S-cation-doped TiO_2 (Ohno et al. 2003, 2004a, b, c).

Here, we report the development of S- and N-doped TiO_2 powders having anatase or rutile crystal phase and S- and N-doped TiO_2 photocatalysts with adsorbed Fe^{3+} ions.

2 Experimental

2.1 Materials and Instruments

Various titanium dioxide (TiO_2) powders with anatase and rutile crystal structures were obtained from Ishihara Sangyo (ST-01, ST-41), Japan Aerosil (P-25) and TAYCA (MT-150A). The anatase contents and the surface areas of these powders were as follows: ST-01: 100%, $320.5 \text{ m}^2 \text{ g}^{-1}$; ST-41: 100%, $8.2 \text{ m}^2 \text{ g}^{-1}$; P-25: 70.0%, $42.5 \text{ m}^2 \text{ g}^{-1}$; and MT-150A: 0%, $88.0 \text{ m}^2 \text{ g}^{-1}$. Thiourea was obtained from Tokyo Chemical Industry Co. Ltd. 2-Propanol, and acetone were purchased from Wako Pure Chemical Industry. Other chemicals were obtained from commercial

sources as guaranteed reagents and were used without further purification. The crystal structures of TiO₂ powders were determined from XRD patterns measured by using an X-ray diffractometer (Philips, X'Pert-MRD) with a Cu target K α -ray ($\lambda = 1.5405\text{\AA}$). The relative surface areas of the powders were determined by using a surface area analyzer (Micromeritics, FlowSorb II 2300). The absorption and diffuse reflection spectra were measured using a Shimadzu UV-2500PC spectrophotometer. X-ray photoelectron spectra (XPS) of the TiO₂ powders were measured using a Shimadzu ESCA1000 photoelectron spectrometer with an Al K source (1,486.6 eV). The shift of binding energy due to relative surface charging was corrected using the C 1s level at 285 eV as an internal standard. The XPS peaks were assumed to have Gaussian line shapes and were resolved into components by a non-linear least squares procedure after proper subtraction of the baseline.

2.2 Preparation of Doped TiO₂ Powder

Doped TiO₂ powders having an anatase or rutile phase were prepared as follows. Thiourea (15.2 g) was mixed with 4.0 g of anatase or rutile TiO₂ powder in an agate mortar. The mixed powder was packed in a lidded double alumina crucible for rutile TiO₂ or in alumina crucible without lid for anatase TiO₂ and calcined at 400 and 500°C under aerated conditions for 3–5 h. After calcination, the powder was washed with distilled water. The resulting samples were dark yellow in color and were found to have a homogenous rutile phase. For TiO₂ powder calcined at a temperature higher than 600°C, no absorbance in the visible region was observed. The relative surface area decreased with increase in the calcination temperature.

2.3 Preparation of S- or N-Doped TiO₂ Powders with Adsorbed Fe³⁺ Ions

S- or N-doped TiO₂ powders were synthesized by previously reported methods (Ohno et al. 2003, 2004a, b, c; Nosaka et al. 2005). To synthesize the S-doped TiO₂ powder, titanium dioxide fine powder with anatase phase was mixed with thiourea at a molar ratio of 1:1. This mixed powder was calcined at various temperatures under aerated conditions. After calcination, the powder was washed with distilled water and NH₃ aqueous solution several times until the pH of the filtrate had become neutral. Urea was used as a doping compound instead of thiourea for preparation of N-doped TiO₂. The other experimental conditions were exactly the same as for S-doped TiO₂. An appropriate amount of FeCl₃ was dissolved in deionized water. The doped TiO₂ powder was suspended in an FeCl₃ aqueous solution, and the solution was stirred for 2 h. After filtration of the solution, the residue was washed with deionized water several times until the pH of the filtrate became neutral. The powders were dried under reduced pressure at 60°C for 12 h.

2.4 Reduction and Air Oxidation of S- or N-Doped TiO₂ Powders with Adsorbed Fe³⁺ Ions

S- or N-doped TiO₂ powder with adsorbed Fe³⁺ ions was suspended in deionized water. NaBH₄ was added to the solution. The solution was stirred for 2 h under aerated conditions. After filtration, the residue was washed with deionized water several times until the pH of the filtrate became neutral. The powders were dried under reduced pressure at 60°C for 12 h.

2.5 Oxidation States of Fe Ions During Photoirradiation Under Anaerobic or Aerobic Conditions

ESR spectra of the Fe³⁺ ions adsorbed on the surfaces of the doped TiO₂ particles were obtained under reduced pressure at 77 K. A 350-W high-pressure mercury lamp was used as the irradiation light source. The changes in the oxidation condition of Fe ions on doped TiO₂ were followed during photoirradiation under reduced pressure.

2.6 Photocatalytic Oxidation of 2-Propanol on TiO₂ Powder

Photocatalytic reactions were carried out in a Pyrex tube containing doped TiO₂ particles and acetonitrile solution of 2-propanol under aerated condition. S- or N-doped TiO₂ photocatalysts with or without adsorbed Fe³⁺ ions or pure TiO₂ powder (ST-01) were used as photocatalysts. The suspension was photoirradiated using a 500-W Xe lamp, which emits both UV and VIS light over a wide wavelength with an integrated photon flux of $1.1 \times 10^{-2} \text{ E s}^{-1} \text{ cm}^{-2}$ between 350 and 540 nm. To limit the irradiation wavelengths, the light beam was passed through a UV-34, L-42, Y-44 Y-50, or Y-54 filter (Kenko Co.) to cut off wavelengths shorter than 340, 420, 440, 500, or 540 nm, respectively. The amounts of acetone produced by the photocatalytic reactions were determined with a capillary gas chromatograph.

2.7 Photocatalytic Oxidation of Adamantane on TiO₂ Powder

A mixture of butyronitrile and acetonitrile was used as the solvent for the reaction because of the low solubility of adamantane in acetonitrile. Photocatalytic reactions were typically carried out in Pyrex glass tubes, to which a mixture of acetonitrile, butyronitrile, adamantane, and TiO₂ powder was added under aerated condition. During the reaction, the solution was magnetically stirred and externally photoirradiated. The light source and the method of choosing the incident light

wavelength were the same as those used for the photocatalytic degradation of 2-propanol. After photoirradiation for certain time periods, the solution was analyzed with a capillary gas chromatograph.

2.8 Photocatalytic Oxidation of 2-Methylpyridine upon Photoirradiation of TiO₂ Powder

Components of the experimental system, such as light source and filters, used for oxidation of 2-methylpyridine were the same as those used for photocatalytic degradation of methylene blue. Photocatalytic oxidation of 2-methylpyridine (1.0 mol dm⁻³) in an aqueous solution (5 mL) containing 100 mg of the TiO₂ photocatalyst proceeded under photoirradiation at wavelengths of a wide range. After photoirradiation for certain time periods, solutions were analyzed with high-performance liquid chromatographs (HPLC, Shimadzu LC-6A System) equipped with an TSK-GEL ODS-80Ts column. A mixture of aqueous solution (K₂HPO₄: 2.5 mmol dm⁻³; KH₂PO₄: 2.5 mmol dm⁻³; and NaClO₄: 0.1 mmol dm⁻³) and methanol (9:1) was used as an eluent.

2.9 Band Calculation

The electronic structures of the S-doped TiO₂ were examined using first-principle band calculations to clarify the S-doping effect. The band calculations were carried out by the F-LAPW method (Blaha et al. 1990) based on the density functional theory (Perdew et al. 1996) within the generalized gradient approximation (Kohn and Sham 1965). The calculation methods have been described in detail in previous reports (Umebayashi et al. 2003, 2002b).

3 Results and Discussion

3.1 Physical Properties of S- and N-Doped TiO₂ Powders

Figure 1 shows diffuse reflectance spectra of S-doped TiO₂ photocatalysts, with different calcination temperature, together with those of pure rutile and anatase powders. The photoabsorption in the visible region decreased in increase calcination temperature (Ohno et al. 1999). The relative surface areas of S-doped TiO₂ photocatalysts having anatase phase calcined at 400 and 500°C were 105.1 and 88.8 m² g⁻¹, respectively. The surface areas of the resulting powders having rutile phase calcined at 400 and 500°C were 70.7 and 56.3 m² g⁻¹, respectively.

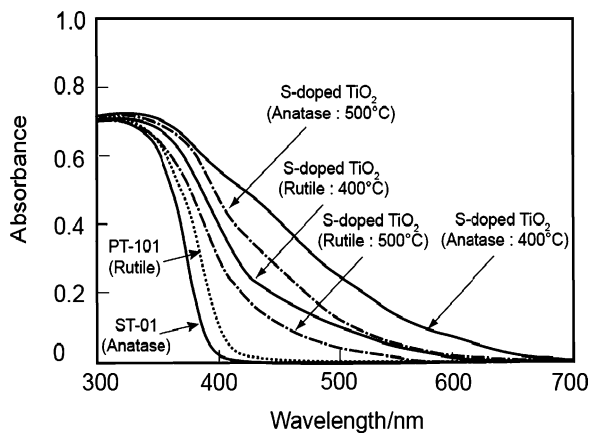


Fig. 1 Diffuse reflectance spectra of S-doped and pure TiO_2 powders (PT-101: rutile)

3.2 Identification of Chemical States of Doped Atoms in TiO_2 Particles

In order to investigate the chemical states of C, N, and S atoms incorporated into TiO_2 , C 1s, N 1s, and S 2p binding energies were measured by X-ray photoemission spectroscopy (XPS).

After the freshly-prepared S-doped TiO_2 powder having anatase phase was washed with deionized water and HCl aqueous solution several times, a rather strong peak attributable to S^{4+} ion together with two weak peaks assigned to S^{2+} ion and S^{6+} ion (Umebayashi et al. 2002a, b, 2003) was observed. The peak assigned to S^{4+} was also observed after Ar^+ ion etching of the sample as shown in Fig. 2. The atomic content of S atoms on the surfaces of the S-doped particles calcined at 400°C was about 1.9% after the washing treatment. The concentration of S^{4+} decreased gradually with depth from the surface of TiO_2 to about 0.7% in the bulk during Ar^+ etching (Nosaka et al. 2005).

In the case of doped TiO_2 having rutile phase, C and S atoms were incorporated into the lattice of TiO_2 . The results are shown in Fig. 3. Peaks at 288 eV were observed by XPS measurements of the C 1s binding energy of the resulting powders calcined at 400 and 500°C . This peak suggests the presence of carbonate species (Papirer et al. 1995). A peak around 168 eV, which is assigned to S^{4+} states (Sayago et al. 2001), also appears after calcination under aerated conditions as shown in Fig. 3. These peaks remained after Ar^+ ion etching of the sample. These results strongly indicate that C^{4+} and S^{4+} ions are incorporated into the bulk phase of TiO_2 . The atomic content of S^{4+} in the TiO_2 powder calcined at 400°C is about 0.1%. The amount of C^{4+} in the TiO_2 particles is about 0.2%. These assignments are supported by the IR spectrum

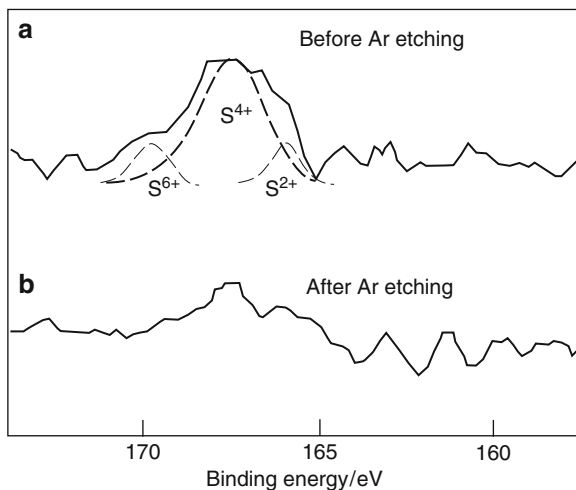


Fig. 2 XPS spectra of S-doped TiO₂ powder having anatase phase. (a) After calcination at 500°C and washing with distilled water for 1 h and (b) after Ar⁺ etching

of C⁴⁺ and S⁴⁺-co-doped TiO₂ powder exhibiting low-intensity peaks at 1,738, 1,096, and 798 cm⁻¹ that are indicative for the carbonate ion (Gablenz et al. 2000). On the other hand, we did not observe IR peaks assigned to SO₂ because the amount of S⁴⁺ atoms is very small and its IR peaks are considered to be very weak.

3.3 Electronic Structures of S-Doped TiO₂

To determine the effects of doping on the electronic and optical properties of TiO₂, the band structures of S-doped TiO₂ were analyzed by first-principle band calculations using the super-cell approach. Based on the experimental results, the super cell model, in which one S atom is replaced by one Ti atom, contains eight formula units. The density of states (DOS) of undoped TiO₂ and S-doped TiO₂ are shown in Fig. 4. In the undoped TiO₂ crystal, the valence band (VB) and conduction band (CB) consist of both Ti 3*d* and O 2*p* orbitals. Since the Ti 3*d* orbital is split into the t_{2g} and e_g states, the CB is divided into lower and upper parts. When TiO₂ is doped with S, an electron-occupied level appears above (I) and below (II) the VB. The S 3*p* states also contribute to the formation of a CB with O 2*p* and Ti 3*d* states. The electron-occupied level (I) above the VB, which consists of S 3*s* states, should be important in the photoresponse of TiO₂. Electron transition between this level and the VB should be induced by visible light irradiation. This process can explain the findings of visible-light absorption in S-doped TiO₂.

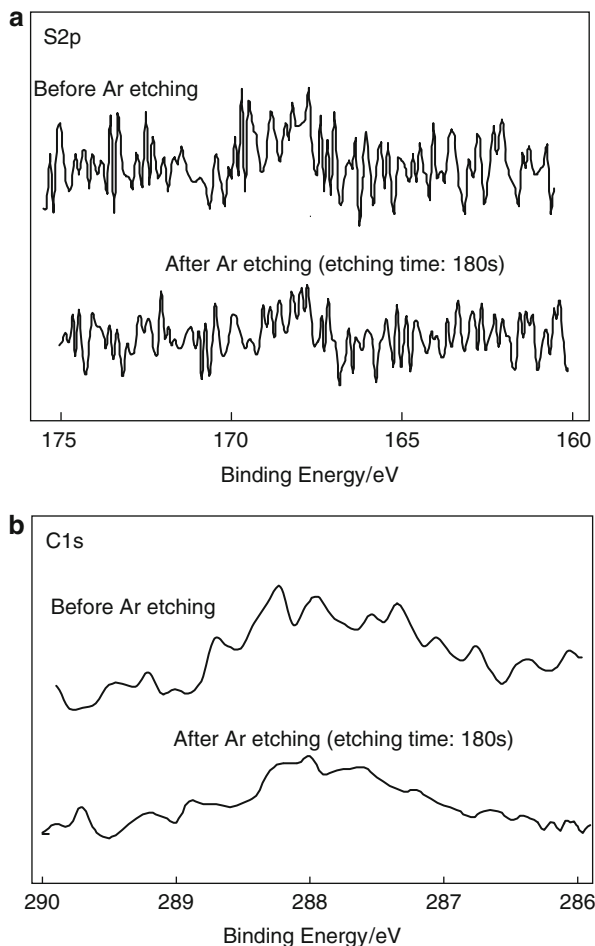


Fig. 3 XPS spectra (S2p and C1s) of S, C-co-doped TiO₂ powder having rutile phase. (a) After calcination at 500°C and washing with distilled water for 1 h and (b) after Ar⁺ etching

3.4 Absorption Spectra of S- or N-Doped TiO₂ with Adsorbed Fe³⁺ ions Before and After NaBH₄ Treatment Under Aerated Condition

Figure 5a shows absorption spectra of N-doped TiO₂ with adsorbed Fe³⁺ ions. The absorption spectra did not change if the amount of Fe³⁺ ions adsorbed on the doped TiO₂ was lower than 0.36 wt%. The absorbance of N-doped TiO₂ with an amount of Fe³⁺ ions greater than 0.88 wt% increased in the visible light region because Fe compounds are thought to show absorbance in the visible light region.

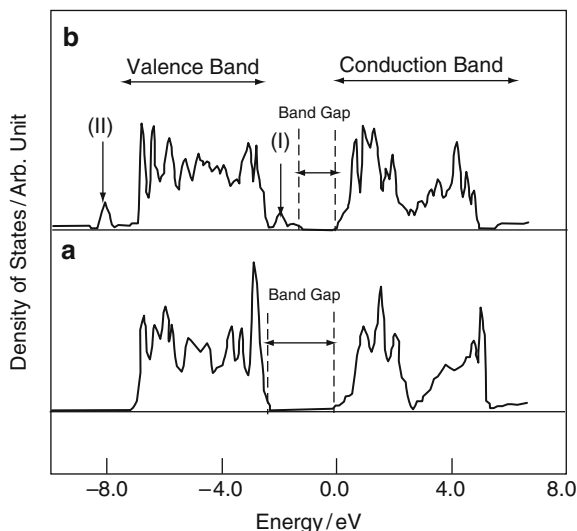


Fig. 4 Total density of states (DOS) of (a) undoped and (b) S-doped TiO₂

Figure 5b shows absorption spectra of S-doped TiO₂ with Fe³⁺ ions. The spectra of S-doped TiO₂ with adsorbed Fe³⁺ ions in the visible light region depended on the amount of Fe³⁺ ions. No change was observed if the amount of Fe³⁺ ions was less than 0.37 wt%. The absorbance of S-doped TiO₂ increased in the visible light region when the amount of Fe³⁺ ions was greater than 0.90 wt%.

When S- and N-doped TiO₂ powders with Fe³⁺ ions were treated with NaBH₄, the absorbance of Fe compound loaded S- and N-doped TiO₂ in the visible light region increased slightly as shown in Fig. 6a, b. The main factors accounting for these changes are under investigation.

3.5 ESR Spectra of S- or N-Doped TiO₂ with Adsorbed Fe³⁺ Ions Under Photoirradiation

Figure 7 shows ESR spectra of N-doped TiO₂ with adsorbed Fe³⁺ ions (0.36 wt%) under irradiation at reduced pressure. A broad peak at 4.4 assigned to the Fe³⁺ species was observed. Under photoirradiation using a high-pressure mercury lamp (350W; 18.5 mW cm⁻²) for 5 min, the intensity of the peak assigned to Fe³⁺ decreased by half as shown in Fig. 7. The peak disappeared completely under photoirradiation for more than 20 min. These results suggest that Fe³⁺ ions were efficiently reduced to Fe²⁺ ions that are not detected by ESR measurement, by trapping electrons generated during photoirradiation under reduced pressure. Furthermore, peak intensity was recovered by introducing air into the sample indicating that Fe²⁺ ions were efficiently re-oxidized under aerated condition. In addition,

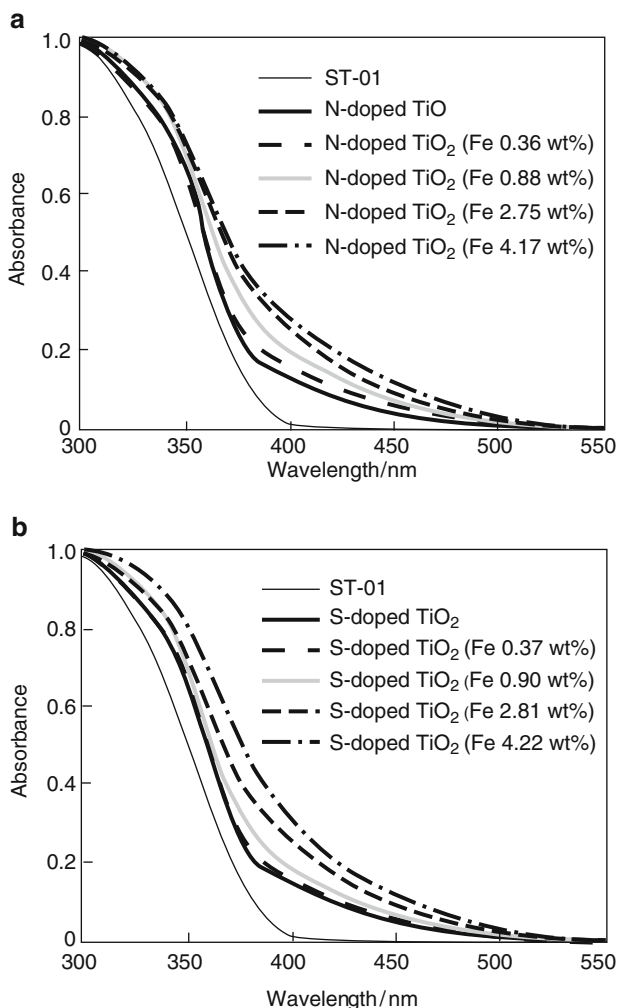


Fig. 5 Absorption spectra of N-doped TiO₂ with adsorbed Fe³⁺ ions (a) and S-doped TiO₂ with adsorbed Fe³⁺ ions (b)

the peak assigned to Fe³⁺ ions was not changed during photoirradiation under aerated conditions (data not shown here). These results suggest that the rate of generation of Fe²⁺ ions during photoirradiation is much slower than that of the oxidation of Fe²⁺ ions by oxygen.

ESR measurements for S-doped TiO₂ with adsorbed Fe³⁺ ions were similar to those for N-doped TiO₂ with Fe³⁺ ions. Under reduced pressure, the peak attributed to Fe³⁺ ions decreased because photogenerated electrons were trapped by Fe³⁺ ions on the surface of S-doped TiO₂. On the other hand, no change was observed during photoirradiation under aerated conditions.

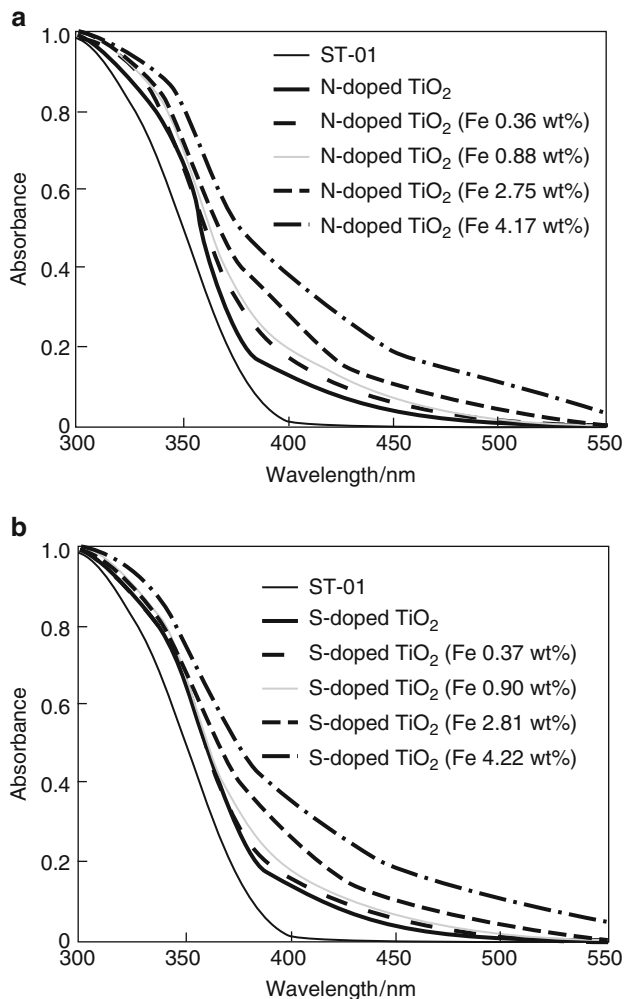


Fig. 6 Absorption spectra of N-doped TiO₂ with adsorbed Fe³⁺ ions after reduction with NaBH₄ followed by air oxidation (a) and S-doped TiO₂ with adsorbed Fe³⁺ ions after reduction with NaBH₄ followed by air oxidation (b)

These results suggest that charge separation between electrons and holes generated photocatalytically was improved because the photoexcited electrons were efficiently trapped by oxygen through Fe³⁺ ions adsorbed on the surface of the doped TiO₂ photocatalysts.

Changes in the ESR spectra of S- or N-doped TiO₂ with adsorbed Fe³⁺ ions treated with NaBH₄ and air oxidation were similar to those of S- or N-doped TiO₂ with adsorbed Fe³⁺ ions without treatment.

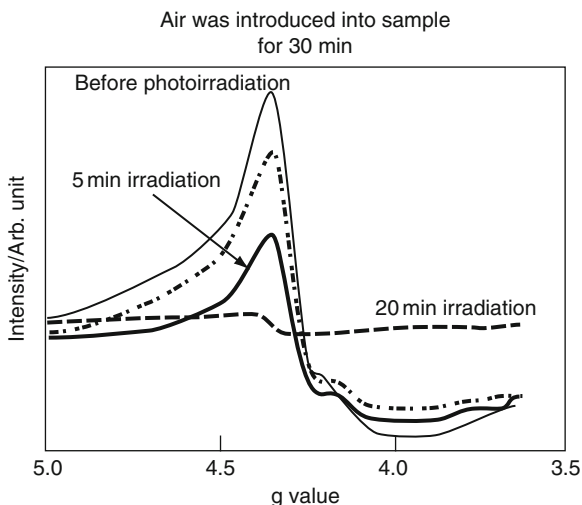


Fig. 7 ESR spectra of N-doped TiO_2 with adsorbed Fe^{3+} ions (0.36 wt%) before and after photoirradiation under reduced pressure

3.6 XRD Spectra of S-Doped TiO_2 with Adsorbed Fe^{3+} Ions Under Photoirradiation

Figure 8 shows XRD spectra of S-doped TiO_2 with adsorbed Fe^{3+} (4.33 wt%) ions before and after the treatment with NaBH_4 under aerated conditions. A small peak was observed at 35.8° assigned to $\gamma\text{-Fe}_2\text{O}_3$ before treatment with NaBH_4 . After treatment with NaBH_4 , a new peak appeared at 18.3° assigned to $\gamma\text{-FeO(OH)}$, while phase of $\gamma\text{-Fe}_2\text{O}_3$ completely disappeared as shown in Fig. 8 (Khaleel 2004; Stanjek 2002; Nakanishi et al. 2003). As discussed later, the photocatalytic activities of the S- or N-doped TiO_2 with adsorbed Fe^{3+} ions are related to the crystal structure of the Fe compounds on the doped TiO_2 .

3.7 Dispersibility of Fe Compounds on S-Doped TiO_2 Before and After NaBH_4 Treatment Under Aerated Condition

The dispersibility of nanoparticles of Fe compounds on S-doped TiO_2 was analyzed using EDX technique with TEM observations. Figure 9b, d show the dispersibility of Fe compounds before and after NaBH_4 treatment, respectively. Before the treatment, average diameter of the nanoparticles was about 3–5 nm (Fig. 9b). On the other hand, the diameter of Fe compounds decreased to 1–2 nm as shown in Fig. 9d. Consequently, the dispersibility and diameter of nanoparticles of Fe compounds on TiO_2 improved after the NaBH_4 treatment. The change in

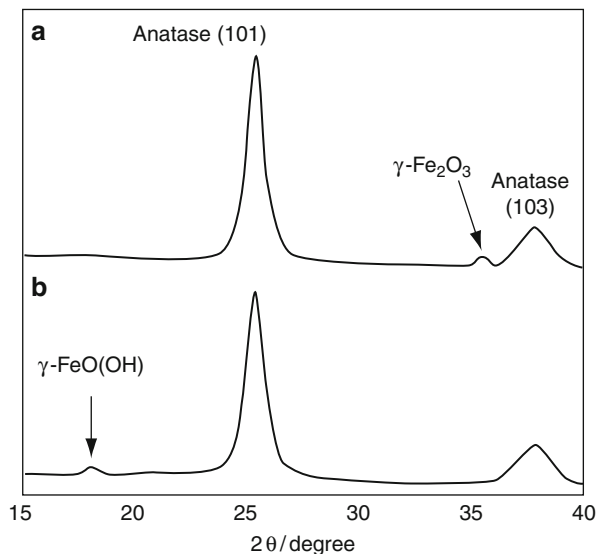


Fig. 8 XRD spectra of S-doped TiO₂ with adsorbed Fe³⁺ ions (4.33 wt%) (a) and that of Fe compounds loaded S-doped TiO₂ after the treatment with NaBH₄ under aerated condition (b)

dispersibility and diameter of Fe compounds on N-doped TiO₂ after the NaBH₄ treatment was similar to that on S-doped TiO₂.

3.8 Photocatalytic Activity of S-Doped TiO₂ Powder Having Anatase Phase for the Decomposition of 2-Propanol

The photodecomposition of 2-propanol was evaluated over pure TiO₂ (Degussa, P-25) and S-doped TiO₂ (calcined at 500°C for 3 h) powders. Figure 10 shows the decomposition rate of 2-propanol as a function of the cutoff wavelengths of the glass filters under Xe light. The pure TiO₂ powder had similar photocatalytic activity for the photodecomposition of 2-propanol to S-doped TiO₂ powders under UV light, but S-doped TiO₂ powder showed a much higher level of activity than pure TiO₂ powder under photoirradiation at wavelengths longer than 420 nm.

3.9 Photocatalytic Synthesis of Hydroxylated Adamantane Compounds on TiO₂ Photocatalysts Having Anatase Phase

Photocatalytic activities of various TiO₂ powders under UV light irradiation were investigated, as shown in Fig. 11 1-Adamantanol was the main product using all TiO₂ powders. In addition, 2-adamantanol and 2-adamantanone were observed as

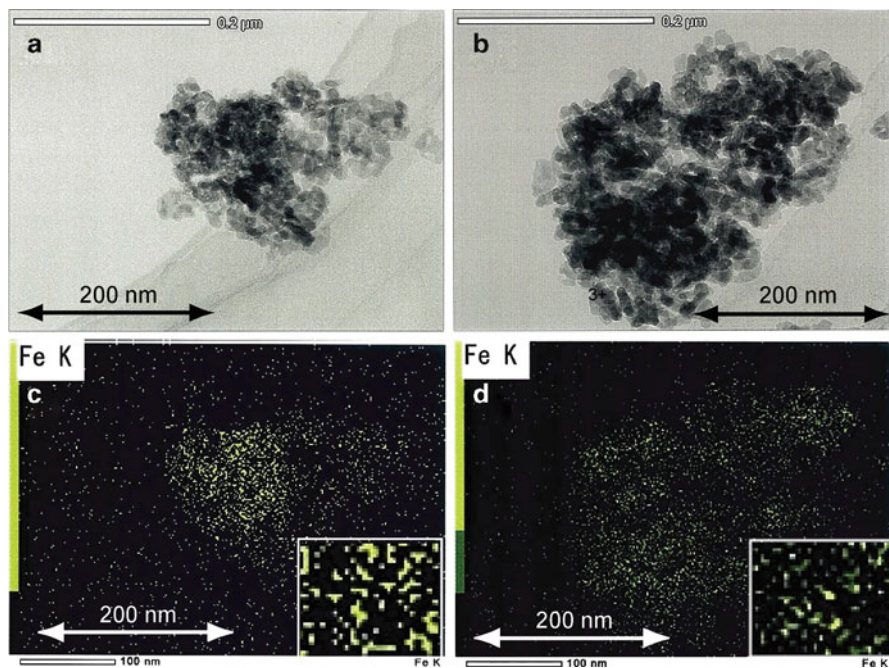


Fig. 9 Dispersibility of nanoparticles of Fe compounds on S-doped TiO₂. (a) TEM photograph of S-doped TiO₂ loaded with Fe compounds before NaBH₄ treatment; (b) EDX analyses of S-doped TiO₂ loaded with Fe compounds before NaBH₄ treatment; (c) TEM photograph of S-doped TiO₂ loaded with Fe compounds after NaBH₄ treatment; and (d) EDX analyses of S-doped TiO₂ loaded with Fe compounds after NaBH₄ treatment

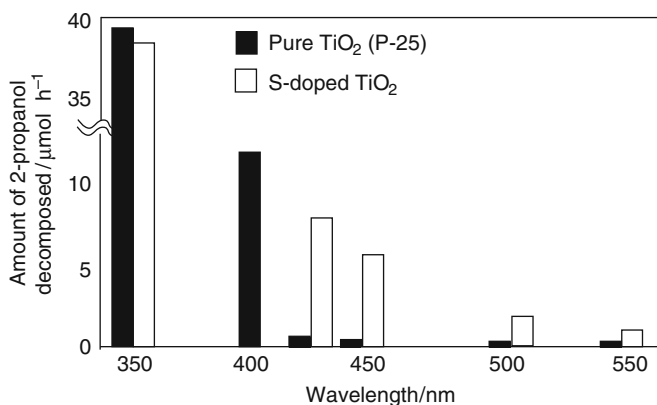


Fig. 10 Photocatalytic decomposition of 2-propanol using S-doped TiO₂ or pure TiO₂ (P-25) as a function of the cutoff wavelength for irradiation from a 1,000W Xe lamp

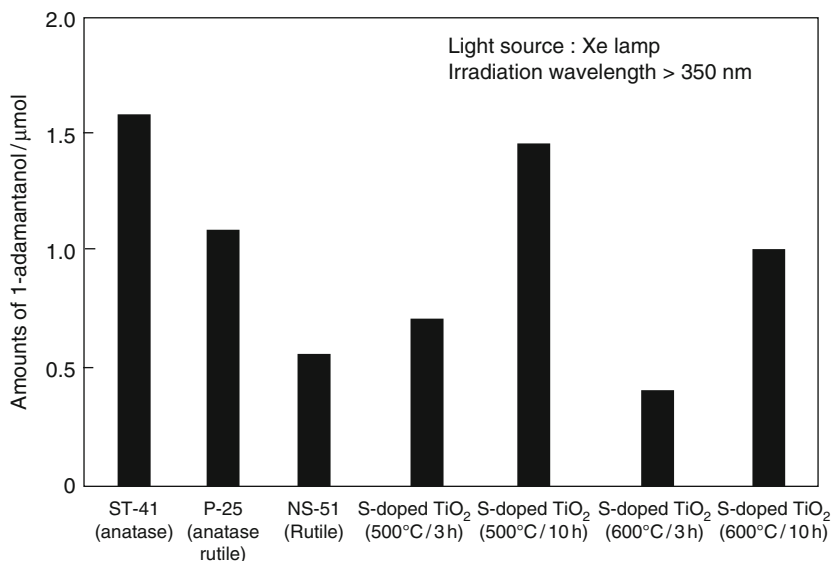


Fig. 11 Amounts of 1-adamantanol produced from adamantane after photoirradiation for 1 h using several TiO₂ and S-doped TiO₂ catalysts under photoirradiation at wavelengths longer than 350 nm

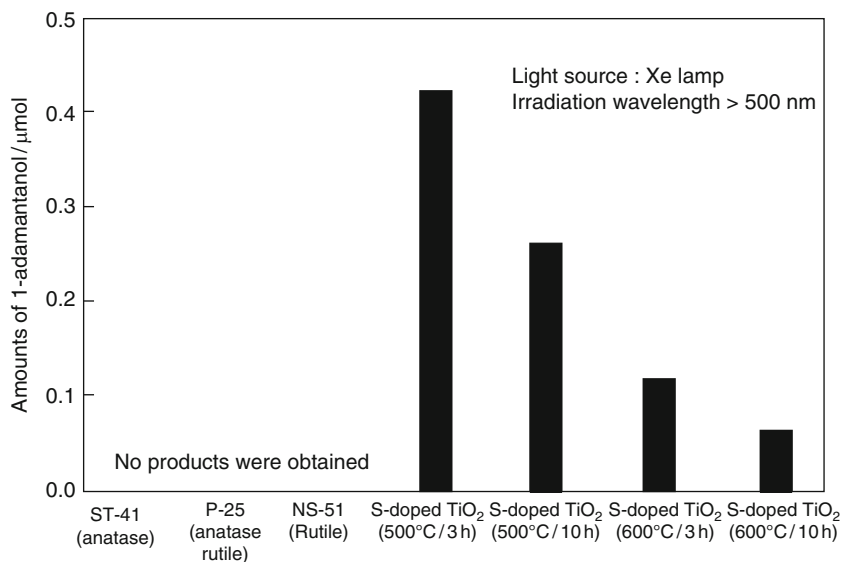


Fig. 12 Amounts of 1-adamantanol produced from adamantane after photoirradiation for 1 h using several TiO₂ and S-doped TiO₂ catalysts under photoirradiation at wavelengths longer than 500 nm

miner products. Among the pure TiO₂ powders, ST-41 powder showed the highest activity. S-doped TiO₂ powder calcined at 500°C for 10 h showed activity similar to that of ST-41. The total quantum efficiencies for the production of 1-adamantanol, 2-adamantanol, and 2-adamantanone using ST-41 and S-doped TiO₂ powder were about 10 and 8.7%, respectively. The activity of S-doped TiO₂ under UV light was relatively high compared to that of pure TiO₂ photocatalysts.

The photocatalytic activities of S-doped TiO₂ powders and pure TiO₂ powders were evaluated under visible light at wavelengths longer than 500 nm as shown in Fig. 12. S-doped TiO₂ calcined at 400°C for 3 h showed the highest activity among the S-doped TiO₂ powders examined. On the other hand, no photocatalytic activity was observed with any of the pure TiO₂ powders.

3.10 Photocatalytic Oxidation of 2-Methylpyridine on TiO₂ Photocatalysts Having Rutile Phase

In the case of oxidation of 2-methylpyridine, 2-pyridinecarboxyaldehyde and 2-pyridinecarboxylic acid were obtained as main products. It should be noted that C⁴⁺ and S⁴⁺-co-doped TiO₂ showed about 10–12 times greater activity than that of ST-01, which is one of most active photocatalyst among commercially available TiO₂ photocatalysts for oxidation a pollutant in air or water, even under photoirradiation at a wavelength longer than 350 nm. Figure 13 shows the photocatalytic activity of these photocatalysts for oxidation of 2-methylpyridine as a function of incident light wavelength. Furthermore, under visible light irradiation at

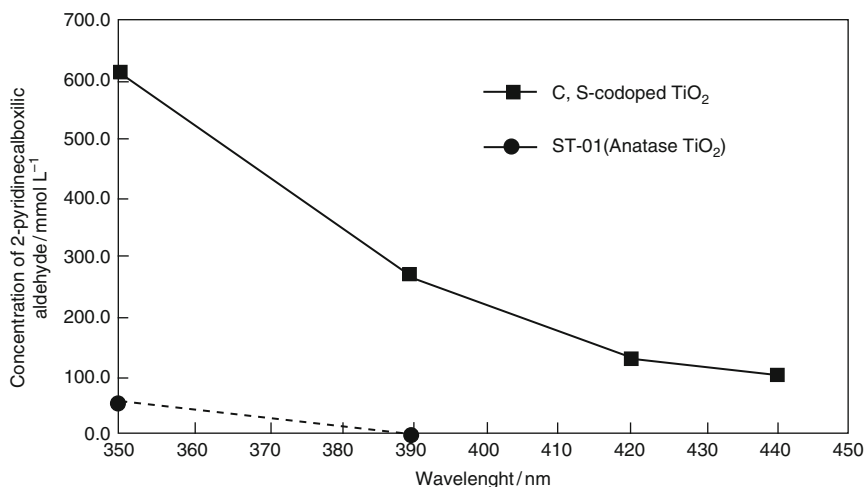


Fig. 13 Oxidation of 2-methylpyridine using C⁴⁺ and S⁴⁺-co-doped TiO₂ powder having a rutile phase calcined at 400 and 500°C and pure TiO₂ (ST-01, anatase)

wavelengths longer than 440 nm, only C⁴⁺ and S⁴⁺-co-doped TiO₂ powder showed a high level of activity. No oxidation of 2-methylpyridine was observed in the absence of TiO₂ powder or without irradiation.

3.11 Photocatalytic Oxidation of 2-Propanol

3.11.1 Photocatalytic Activities of N-Doped TiO₂ with Adsorbed Fe³⁺ Ions Before and After NaBH₄ Treatment Under Aerated Condition

Figure 14a shows the photocatalytic oxidation of 2-propanol using N-doped TiO₂ with various amounts of adsorbed Fe³⁺ ions. ST-01 with anatase fine particles was used as a reference. The main product of the reaction is 2-propanol. The photocatalytic activity of N-doped TiO₂ increased with higher amount of Fe ions. N-doped TiO₂ powders with 0.36 wt% adsorbed Fe³⁺ ions showed the highest activity for oxidation of 2-propanol. As described above, Fe³⁺ ions adsorbed on N-doped TiO₂ efficiently trapped the photoexcited electrons, which resulted in improvement of the charge separation between electrons and holes. Above 0.36 wt%, the activity of N-doped TiO₂ with Fe³⁺ ions gradually decreased with increased amount of Fe³⁺ ions because a large excess amount of Fe compounds was thought to occupy the active sites on the surface of N-doped TiO₂ and functioned as recombination centers between electrons and holes (Khaleel 2004).

The photocatalytic activities of N-doped TiO₂ with Fe³⁺ ions for oxidation of 2-propanol were also investigated after treatment with NaBH₄ followed by air oxidation. When 0.88 wt% Fe³⁺ ions were adsorbed on the surface of N-doped TiO₂ after the treatment with NaBH₄, the highest photocatalytic activity was observed as shown in Fig. 14b. The optimum amount of Fe³⁺ on N-doped TiO₂ for oxidation of 2-propanol after treatment with NaBH₄ and air oxidation was slightly higher than that without NaBH₄ treatment.

3.11.2 Photocatalytic Activities of S-Doped TiO₂ with Adsorbed Fe³⁺ Ions Before and After NaBH₄ Treatment Under Aerated Condition

Figure 15a shows the photocatalytic activity of S-doped TiO₂ photocatalysts with Fe³⁺ ions. The change in activity of S-doped TiO₂ powders with the amount of Fe³⁺ ions was similar to that of N-doped TiO₂ with Fe³⁺ ions except optimum amount of Fe³⁺ ions. S-doped TiO₂ with 0.90 wt% Fe³⁺ ions showed the highest photocatalytic activity for oxidation of 2-propanol. The optimum amount of Fe³⁺ cations was slightly different. These results indicated that the doping atoms and the density of defects located on the surface of the doped TiO₂ particles are important factors to determine the optimum amount of Fe³⁺ ions. S-doped TiO₂ with Fe³⁺ ions treated with NaBH₄ and air oxidation showed similar tendencies as shown in Fig. 13b.

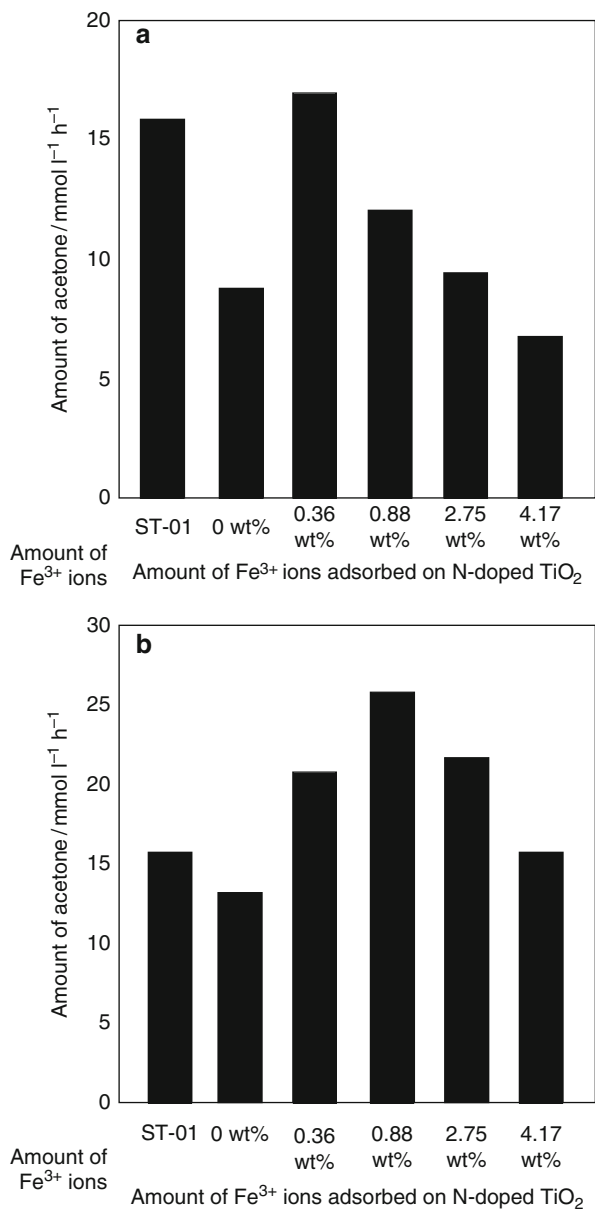


Fig. 14 Photocatalytic activities of N-doped TiO₂ with adsorbed Fe³⁺ ions before and after treatment with NaBH₄ under aerated condition as well as ST-01 for oxidation of 2-propanol under photoirradiation at wavelengths longer than 350 nm. (a) Before NaBH₄ treatment and (b) after NaBH₄ treatment

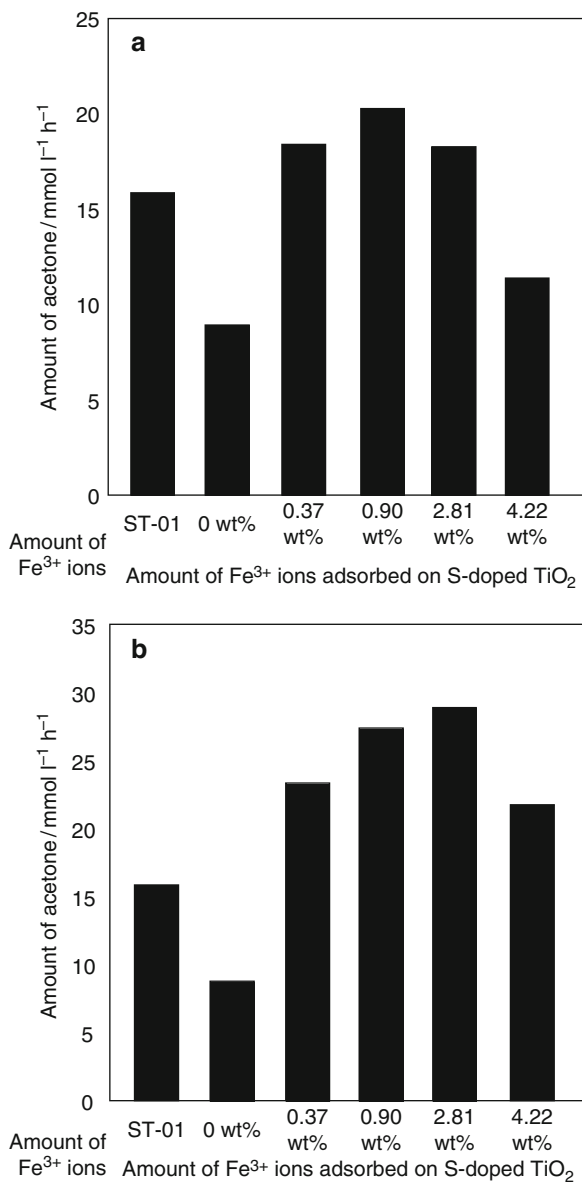


Fig. 15 Photocatalytic activities of S-doped TiO₂ with adsorbed Fe³⁺ ions before and after treatment with NaBH₄ under aerated condition as well as ST-01 for oxidation of 2-propanol under photoirradiation at wavelengths longer than 350 nm. (a) Before NaBH₄ treatment and (b) After NaBH₄ treatment

As described above, the crystal structure of Fe compounds on S- or N-doped TiO₂ changed from γ -Fe₂O₃ to γ -FeO(OH) after treatment with NaBH₄ and air oxidation. Although the main factor responsible for improving the photocatalytic activity of S- or N-doped TiO₂ with Fe³⁺ ions after treatment with NaBH₄ and air oxidation is not clear yet, the change in crystal structure of the Fe compounds is thought to be an important factor.

3.12 Dependence on Incident Light Wavelength for Degradation of 2-Propanol

Figure 16 shows the rate of decomposition of 2-propanol on S-doped TiO₂ with and without Fe³⁺ ions as a function of the cutoff wavelengths of the glass filters irradiated with a Xe lamp. Although the absorption spectra of S-doped TiO₂ with and without Fe³⁺ ions were very similar, the photocatalytic activity of S-doped TiO₂ with Fe³⁺ cations was about 2.5 times higher under a wide range of irradiation wavelengths. Similar improvement in the photocatalytic activity of N-doped TiO₂ with Fe³⁺ cations was also observed (data not shown). These results suggest that the improvement in photocatalytic activities of S- or N-doped TiO₂ with adsorbed Fe³⁺ ions under a wide range of irradiation wavelengths including UV and visible light originates from electron trapping by Fe³⁺ compounds on S- or N-doped TiO₂ particles.

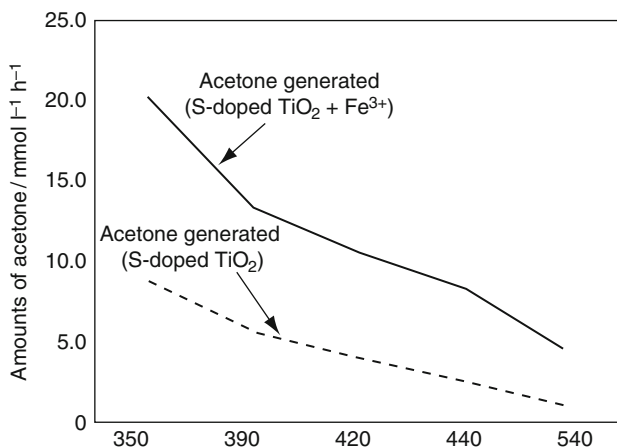


Fig. 16 Photocatalytic activities of S-doped TiO₂ powders with and without adsorbed Fe³⁺ ions for oxidation of 2-propanol as a function of cutoff wavelength of incident light. The amount of Fe³⁺ ion is 0.90 wt%

4 Conclusions

S-doped TiO₂ photocatalysts were prepared. The S atoms were mainly tetravalent. The S-doped TiO₂ powder, which has relatively high photocatalytic activity under visible light at wavelengths longer than 500 nm, may have a wide range of applications. In particular, hydroxylation of adamantane is interesting from the viewpoint of organic syntheses in connection with green chemistry, because adamantane can be converted to hydroxylated derivatives using molecular oxygen under a wide range of incident wavelengths including UV and visible light. In addition, we also succeeded in preparing S, C-co-doped TiO₂ having rutile phase. This visible photocatalyst shows much higher activity for oxidation of 2-methylpyridine than ST-01 having anatase phase, which is one of the most active commercially available photocatalyst.

In addition, S- or N-doped TiO₂ with adsorbed Fe³⁺ cations were also prepared. The photocatalytic activity for oxidation of 2-propanol was two to four times higher than for S- or N-doped TiO₂ without Fe³⁺ ions. Improvement in the photocatalytic activity by Fe³⁺ treatment was observed under a wide range of irradiation wavelengths, including UV light and visible light. Fe³⁺ ions adsorbed on the surface of S- or N-doped TiO₂ particles efficiently trapped the photoexcited electrons generated in the photocatalysts, resulting in improvement in charge separation between electrons and holes. In addition, the photocatalytic activities of S- or N-doped TiO₂ with adsorbed Fe³⁺ ions increased markedly after treatment with NaBH₄ and air oxidation. The change in the crystal structure of Fe compounds on the doped TiO₂ photocatalysts is probably important in the improvement of photocatalytic activity.

S- or N-doped TiO₂ powder with adsorbed Fe³⁺ ions, which have high photocatalytic activities under a wide range of irradiation wavelengths, may have a wide variety of practical applications. We expect that the catalytic activity will be further improved by optimizing the conditions for preparing the S- or N-doped TiO₂ powders with adsorbed Fe³⁺ ions.

Acknowledgment This work was supported by a Grant-in-Aid for Scientific Research on Priority Areas (417) from the Ministry of Education, Culture, Science, and Technology (MEXT), Japan and Nissan Science Foundation.

References

- Anpo M (1997) *Catal Surv Jpn* 1:169
- Asahi R, Morikawa T, Ohwaki T, Aoki A, Taga Y (2001) Visible-light photocatalysis in nitrogen-doped titanium oxides *Science* 293:269
- Blaha P, Schwarz K, Sorantin P, Trickey SB (1990) Full-potential, linearized augmented plane-wave programs for crystalline systems *Comput Phys Commun* 59:399
- Breckenridge RG, Hosler WR (1953) *Phys Rev* 91:793
- Cao L, Spiess F, Huang A, Suib SL, Obee TN, Hay SO, Freihaut JDJ (1999) Heterogeneous photocatalytic oxidation of 1-butene on SnO₂ and TiO₂ films *Phys Chem* 103:2912

- Choi W, Hoffmann MR (1996) Kinetics and mechanism of CCl_4 photoreductive degradation on TiO_2 : The role of trichloromethyl radical and dichlorocarbene *J Phys Chem* 100:2161
- Cronmeyer DC (1957) *Phys Rev* 113:1222
- Dusi M, Muller CA, Mallat T, Baiker A (1999) Novel amine-modified TiO_2 - SiO_2 aerogel for the demanding epoxidation of substituted cyclohexenols *Chem Commun* 197
- Fujihira M, Satoh Y, Osa T (1981) Heterogeneous photocatalytic oxidation of aromatic-compounds on TiO_2 *Nature* 293:206
- Fujishima A, Honda K (1972) *Nature* 238:5551
- Gablenz S, Abicht H-P, Pippel E, Lichtenberger O, Woltersdorf J (2000) New evidence for an oxycarbonate phase as an intermediate step in BaTiO_3 preparation *J Eur Ceram Soc* 20:1053
- Ghsh AK, Maruska HP (1994) *J Electrochem Soc* 98:13669
- Hoffman MR, Martin ST, Choi W, Bahnemann DW (1995) Environmental applications of semiconductor photocatalysis *Chem Rev* 95:69
- Ihara T, Miyoshi M, Ando M, Sugihara S, Iriyama Y (2001) Preparation of a visible-light-active TiO_2 photocatalyst by RF plasma treatment *J Mat Sci* 36:4201
- Ikeda S, Abe C, Torimoto T, Ohtani B (2002) Visible light-induced hydrogen evolution from aqueous suspensions of titanium(IV) oxide modified with binaphthol *Electrochemistry* 70:442
- Irie H, Watanabe Y, Hashimoto K (2003) Carbon-doped anatase TiO_2 powders as a visible-light sensitive photocatalyst *Chem Lett* 32:772
- Khaleel AA (2004) Nanostructured pure $\gamma\text{-Fe}_2\text{O}_3$ via forced precipitation in an organic solvent *Chem Eur J* 10:925
- Kohn W, Sham LJ (1965) *Phys Rev* 140:1133
- Matthews RW (1984) Hydroxylation reactions induced by near-ultraviolet photolysis of aqueous titanium-dioxide suspensions *J Chem Soc Faraday Trans* 80:457
- Nakanishi T, Iida H, Osaka T (2003) Preparation of iron oxide nanoparticles via successive reduction-oxidation in reverse micelles *Chem Lett* 32:1166
- Nosaka Y, Matsushita M, Nishino J, Nosaka AY (2005) Nitrogen-doped titanium dioxide photocatalysts for visible response prepared by using organic compounds *Sci Technol Adv Mater* 6:1468
- Ohno T, Kigoshi T, Nakabeta K, Matsumura M (1998a) Stereospecific epoxidation of 2-hexene with molecular oxygen on photoirradiated titanium dioxide powder *Chem Lett* 877
- Ohno T, Nakabeya K, Matsumura M (1998b) Epoxidation of olefins on photoirradiated titanium dioxide powder using molecular oxygen as an oxidant *J Catal* 176:76
- Ohno T, Tanigawa F, Fujihara K, Izumi S, Matsumura M (1999) Photocatalytic oxidation of water by visible light using ruthenium-doped titanium dioxide powder *J Photochem Photobiol A* 127:107
- Ohno T, Masaki Y, Hirayama S, Matsumura M (2001) TiO_2 -photocatalyzed epoxidation of 1-decene by H_2O_2 under visible light *J Catal* 204:163
- Ohno T, Mitsui T, Matsumura M (2003) Photocatalytic activity of S-doped TiO_2 photocatalyst under visible light *Chem Lett* 32:364
- Ohno T, Akiyoshi M, Umabayashi T, Asai K, Mitsui T, Matsumura M (2004a) Preparation of S-doped TiO_2 photocatalysts and their photocatalytic activities under visible light *Appl Catal A Gen* 265:115
- Ohno T, Tsubota T, Nishijima K, Miyamoto Z (2004b) Degradation of methylene blue on carbonate species-doped TiO_2 photocatalysts under visible light *Chem Lett* 33:750
- Ohno T, Tsubota T, Toyofuku M, Inaba R (2004c) Photocatalytic activity of a TiO_2 photocatalyst doped with C^{4+} and S^{4+} ions having a rutile phase under visible light *Catal Lett* 98:255
- Ohtani B, Kawaguchi J, Kozawa M, Nishimoto S, Inui T (1995) Photocatalytic racemization of amino-acids in aqueous polycrystalline cadmium(ii) sulfide dispersions *J Chem Soc Faraday Trans* 91:1103
- Paprer E, Lacroix R, Donnet J-B, Nanse G, Fioux P (1995) Xps study of the halogenation of carbon-black .2. Chlorination *Carbon* 33:63

- Perdew JP, Burke K, Ernzerhof M (1996) Generalized gradient approximation made simple *Phys Rev Lett* 77:3865
- Sakatani Y, Ando H, Okusato K, Koike H, Nunoshige J, Takata T, Kondo JN, Hara M, Domen (2004) Metal ion and N co-doped TiO₂ as a visible-light photocatalyst *J Mat Res* 19:2100
- Sakthivel S, Kisch H (2003) Daylight photocatalysis by carbon-modified titanium dioxide *Angew Chem Int Ed* 42:4908
- Sayago DI, Serrano P, Bonme O, Goldoni A, Paolucci G, Roman E, Martin-Gago JA (2001) Adsorption and desorption of SO₂ on the TiO₂(110)-(1X1) surface: A photoemission study *Phys Rev B* 64:205402
- Soana F, Sturini M, Cermenati L, Albini A (2000) Titanium dioxide photocatalyzed oxygenation of naphthalene and some of its derivatives *J Chem Soc Perkin Trans* 2:699
- Stanjek H (2002) XRD peak migration and apparent shift of cell-edge lengths of nano-sized hematite, goethite and lepidocrocite *Clay Miner* 37:629
- Theurich J, Bahnemann DW, Vogel R, Dhamed FE, Alhakimi G, Rajab I (1997) Photocatalytic degradation of naphthalene and anthracene: GC-MS analysis of the degradation pathway *Res Chem Intermed* 23:247
- Umebayashi T, Yamaki T, Ito H, Asai K (2002a) Band gap narrowing of titanium dioxide by sulfur doping *Appl Phys Lett* 81:454
- Umebayashi T, Yamaki T, Itoh H, Asai K (2002b) Analysis of electronic structures of 3d transition metal-doped TiO₂ based on band calculations *J Phys Chem Solids* 63:1909
- Umebayashi T, Yamaki T, Yamamoto S, Miyashita A, Tanaka S, Sumita T, Asai K (2003) Sulfur-doping of rutile-titanium dioxide by ion implantation: Photocurrent spectroscopy and first-principles band calculation studies *J Appl Phys* 93:5156
- Wolfrum EJ, Huang J, Blake DM, Maness PC, Huang Z, Fiest J, Jacoby WA (2002) Photocatalytic oxidation of bacteria, bacterial and fungal spores, and model biofilm components to carbon dioxide on titanium dioxide-coated surfaces *Environ Sci Technol* 36:3412
- Yanagida S, Ishimaru Y, Miyake Y, Shiragami T, Pac C, Hashimoto K, Sakata T (1989) Semiconductor photocatalysis .7. ZnS-catalyzed photoreduction of aldehydes and related derivatives - 2-electron-transfer reduction and relationship with spectroscopic properties *J Phys Chem* 93:2576

Chapter 12

Visible Light-Responsive Titanium Oxide Photocatalysts: Preparations Based on Chemical Methods

Marcos Fernández-García, Arturo Martínez-Arias,
and José C. Conesa

Abstract A review is presented on the present status of titania-based visible light-active photocatalysts prepared by chemical methods, with particular focus on developments made by the authors' group in doping TiO₂ with either transition metals (tungsten, iron or vanadium) or light electronegative elements such as nitrogen, and highlighting the importance of dopant concentration and of separating the effects of improved absorption spectrum range from those of recombination or surface modification.

1 Introduction

1.1 Background and Scope of the Review

The term photocatalysis is commonly applied to any catalyzed chemical process including an external energy input of electromagnetic radiation which has wavelength in the UV–visible range (Hoffmann et al. 1995; Linsebigler et al. 1995; Bahnemann 2004; Serpone 2006; Colón et al. 2007; Carp et al. 2004). Customarily, photocatalysts are solid semiconductors (1) able to absorb visible and/or UV light, (2) chemically and biologically inert and photostable, (3) inexpensive and (4) nontoxic. TiO₂, ZnO, SrTiO₃, CeO₂, WO₃, Fe₂O₃, CdS and ZnS can act as photoactive material for redox processes due to their electronic structure which is characterized by a filled valence band and an empty conduction band. Among these possible semiconductors, TiO₂ is the most used photocatalytic material that fulfills all of these requirements and exhibits adequate conversion values (Fox and Dulay 1993). However, in spite of the

J.C. Conesa (✉)

Instituto de Catálisis y Petroleoquímica, CSIC, Marie Curie 2, Cantoblanco 28049, Madrid, Spain
e-mail: jconesa@icp.csic.es

high conversion values obtained for TiO_2 the calculated quantum yields for the studied reactions are low, certainly well below 10% for most degradation processes (Blanco and Malato 1996); furthermore, TiO_2 only absorbs UV light, a drawback for any application where the use of solar radiation would be desired, as the latter has only ca. 4% of its energy in that range. Therefore extending to the visible region the wavelength range utilizable for photocatalysis would be very convenient for its practical use, and much effort and attention have been devoted worldwide to achieve it.

TiO_2 occurs in nature in three crystallographic phases: rutile, anatase, and brookite. Other known forms, such as $\text{TiO}_2\text{-B}$ (Marchand et al. 1980), hollandite-type $\text{TiO}_2\text{-H}$ (Latroche et al. 1989) and ramsdellite-type $\text{TiO}_2\text{-R}$ (Akimoto et al. 1994), as well as some high-pressure varieties, have been synthesized by elaborate methods but are not of practical interest. Of those forms, anatase is the most commonly employed in photocatalytic applications due to its inherent superior photocatalytic properties (Carp et al. 2004; Fox et al. 1993; Fujishima et al. 2000) and ease of synthesis in catalytically useful form. It is thermodynamically less stable than rutile as a bulk phase, though according to energy calculations it could be the favored phase when the grain size is below ca. 15 nm (Dietbold et al. 2003). High surface TiO_2 materials would thus present as a general rule the anatase polymorph, and indeed the latter appears in most TiO_2 photocatalyst preparations. Anatase consequently constitutes the base for most attempts of modifying TiO_2 to make it photoactive with visible light.

Anatase and rutile also differ in electronic properties: in the former the bandgap width is around 3.2 eV, while in the second it is ca. 3.0 eV; this has obviously a structural basis. The crystalline structure of all these TiO_2 oxides can be described in terms of TiO_6 octahedral chains differing in the distortion of each octahedron and the connection pattern of such octahedra chains. The Ti–Ti distances in the anatase structure are greater than in rutile, whereas Ti–O distances are shorter (Burdett et al. 1987). These structural differences cause different mass densities and lead to different electronic structure of the bands. Anatase phase is 9% less dense than rutile, presenting more pronounced localization of the Ti 3*d* states and, therefore, a narrower 3*d* band. Also the O 2*p*–Ti 3*d* hybridization is different in the two structures (more covalent mixing in rutile), anatase exhibiting valence and conduction bands with, respectively, more pronounced O 2*p* and Ti 3*d* character (Asahi et al. 2002). These different features are presumably responsible of the difference in bandgap width, mobility and ease of recombination of charge carriers, luminescence and other properties, and may affect the ways of obtaining visible light response by modifying TiO_2 .

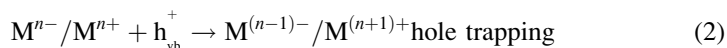
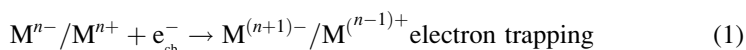
To achieve this much desired goal of extending the photocatalyst response into the visible light range, several alternatives have been tested where the light absorber is not made of anatase phase (or rutile); they are mainly based on the use of sensitizers (inorganic solids, polymer materials or molecules) located outside TiO_2 , of hypothetical cubic-type titania polymorphs or of other inorganic solids (sulfides, nitrides or non-Ti-based oxides) (Hoffmann et al. 1995; Linsebigler et al. 1995; Bahnemann 2004; Serpone 2006; Colón et al. 2007; Carp et al. 2004; Fox et al. 1993; Blanco et al. 1996; Mattesini et al. 2004). Still, most of the attempts to achieve visible light photocatalytic activity have been focused on the modification of anatase by doping with cations and/or anions. Depending on the dopant nature,

on its location (e.g., substitutional or interstitial), concentration and other subtle properties of the doping process, a moderate to important modification of anatase–TiO₂ bandgap and/or the creation of adequate, new electronic states localized in the gap are possible, leading to an increase in its visible light absorption power (Hoffmann et al. 1995; Serpone 2006; Colón et al. 2007; Carp et al. 2004; Anpo 1997). In a number of these cases, increase in photocatalytic activity with visible light has been reported. When interpreting these results it must be however recalled that, in addition to photo-physical properties, the doping process can influence anatase–TiO₂ morphological characteristics (e.g., primary and/or secondary particle size and porosity), thermal stability or surface properties such as acidity, and that the dopant itself could have a specific catalytic activity when exposed at the surface; all these additional factors, which must be taken into account, may influence the chemical steps of the reaction and therefore the potential of these systems as photoactive catalysts (Hoffmann et al. 1995; Linsebigler et al. 1995; Colón et al. 2007).

The rest of this review will be focused on attempts made to achieve, with chemical preparations, such doping-mediated spectral response improvement. We will discuss separately the influence of electropositive (Sect. 2) and electronegative (Sect. 3) doping agents on anatase–TiO₂ materials, which have been studied with the aim of exploring a new, powerful generation of visible light-active catalysts. The review is focused on, and emphasizes, the contribution of the authors' group to the field, but mention to other studies related to the systems concerned will also be made when significant.

1.2 Physical and Electronic Characteristics of Doping

When doping with foreign atoms, additionally to the absorption spectrum modification one must take into account that dopant atoms can act in certain cases as electron/hole trappers. In an idealized local view, this occurs through the following processes:



If the energy level of the pair $M^{n+}/M^{(n-1)+}$ (or $M^{n-}/M^{(n+1)-}$) is located below/near the conduction band edge (E_{cb}), and/or that of the pair $M^{n+}/M^{(n+1)+}$ (or $M^{n-}/M^{(n-1)-}$) is located above/near the valence edge (E_{vb}), such trapping of electron and holes may take place. Certain ions (like Fe) may act both as electron/hole trapping centers, but usually a given doping atom produces centers of only one of these two types. If only one type of trapping occurs it would lead to an increase of the charge carrier lifetimes, and therefore to a decrease in the recombination processes (Carlson and Griffin 1986; Sclafani et al. 1991; Choi et al. 1994a; Ikeda et al. 2001);

the not trapped carrier would be then able to diffuse to the surface, and (recombination there being decreased) its transfer to an external molecule could be made easier, increasing photocatalytic efficiency. Of course this mechanism requires that the trapped charge carrier be ultimately released and diffuse to the surface to complete the reaction cycle, i.e., the trapping must be transient.

On the other hand, if both types of trapping can occur on the same dopant atom this leads to recombination, which decreases efficiency. Note in this respect that trapping of the photogenerated charge carrier at a localized position will change the electrostatic interaction of the trapping atom with their neighbors, which will lead to movements of the latter. This interplay of photogenerated charge trapping and atomic displacements implies a strong coupling between the trapped charge and the lattice vibrations, i.e., phonons; and as is well known such electron–phonon coupling is crucial for determining a high recombination ratio. But this depends on the dopant concentration. Indeed, if the latter is high enough the wavefunctions of the dopant centers providing the new electronic levels can overlap with one another to a sufficient extent that these levels rather than behaving as localized entities constitute a delocalized band. In that case, with the charge being delocalized the electrostatic effects of the trapped carrier, and the correspondingly induced atomic displacements, will be much lower, decreasing the electron–phonon coupling and consequently the recombination. Recent theoretical modeling of this effect in covalent semiconductors (Luque et al. 2006) has indicated that pushing the dopant concentration above ca. 6×10^{19} at/cm³ (which in anatase would correspond to a cation substitution level of 0.2%) may suffice to change from localized to band-like behavior (a change akin to the Mott insulator-to-metal transition). In less covalent compounds (as is the case of TiO₂), and especially when the dopants are transition or lanthanide elements (the d and f orbitals of which overlap those of neighbors less efficiently), the concentration needed to achieve this delocalization may well be higher, but studies to determine the doping level required in these cases for such change of regime have not been carried out yet.

Finally one may recall that the introduction or substitution of a new element may affect the TiO₂ electronic structure not because that element provides new levels within the bandgap, but because it modifies the environment of titanium and/or oxygen so that the orbitals which contribute the valence or conduction bands are shifted. If the new element concentration is low, the shifted levels will tend to be localized, while if it is high these levels may develop a band character. The arguments in the previous paragraph can be applied also here. Of course, in some limiting cases a mixed oxide may form, having even different crystal structure (e.g., as with perovskite-type alkaline earth titanates), and still the electronic characteristics may be discussed in same way as for cation-modified titania.

In any case, it is clear that the photoactivity of doped semiconductors widely varies depending on the specific dopant considered, its concentration and the lattice position occupied by it. The extent of the photoactive spectral range increase will be related both to the efficiencies of the doping centers in allowing electron excitation with visible-light and to their ability to trap charge carriers and participate in the interfacial transfer steps.

2 Titania Doped with Metal Cations

Inclusion of cations, especially of transition elements, was attempted from the very beginning of the studies in photocatalysis as a (supposedly) straightforward means of obtaining visible light response in TiO_2 , as such inclusion was known to lead to colored specimens, implying absorption of visible radiation. The positions of cation dopant-induced new levels in the titania bandgap have been discussed since long ago in the literature (see e.g., Mizushima et al. 1979; Serpone et al. 1994). However, very frequently visible light absorption did not lead to better photocatalytic activity in that spectral range, and even could lead to a decrease in the photoactivity under UV light irradiation. It was soon recognized that the photogenerated electron or hole, if located on the added cation dopant, could have a too small mobility, leading to scarce transfer of that charge carrier to the surface and thus hinder the completion of the photoinduced chemical process. Furthermore, the added center could behave as a recombination center for the photogenerated electron and holes, as said above, leading to a decrease in photocatalytic activity. Both effects will be influenced by the localized or delocalized character of the new states (or of the modifications in the TiO_2 band states). Thus when considering the effect of adding or substituting a cation different of Ti in anatase it is pertinent to distinguish the situations of low and high concentration levels (at least in the limiting cases). In the former, one may find an increase or a decrease in photoactivity, but in any case one is not dealing with new or modified bands (so that speaking of reduction of the bandgap is not appropriate). In the latter, if new levels in the bandgap appear but they are well delocalized (only case in which it is appropriate to speak of a narrowed bandgap), and if they are not partially filled (which would lead to metallic rather than to semiconducting behavior; but here the possibilities of intermediate band-based two-photon processes, proposed by Luque and Martí (1997) for photovoltaic efficiency enhancement, should not be neglected), one may hope to achieve an improvement in visible light response without decreasing the basic quantum efficiency. Whether one can achieve high concentrations of dopant or not will depend on the solubility of the latter in anatase, or ultimately on the capability of forming a specific compound with titania. With these issues in mind, in what follows we will address separately these two types of situations, establishing between them the borderline (somewhat arbitrarily) at the 5% level.

2.1 High Concentration Doping

Only a limited number of cations have been proven to be able to enter the titania lattice in significant concentration levels and at the same time lead to increased photocatalytic activity specifically in the visible range. One such case is that of tungsten, as evidenced by our group in a paper comparing the effect of inserting different cations (Fuerte et al. 2001). Here the use of a microemulsion-based preparation method allowed to obtain final calcined materials with no XRD-detectable

phases other than titania-type and having high amount of dopant (>10% of cations) for elements of groups 5 and 6 of the periodic table, while somewhat lower but still significant amounts (6–7%) could be introduced in the cases of Fe and Ce; Mn and Ni could be inserted only at $\approx 3\%$ levels. When tested in a photocatalytic reaction (gas phase photo-oxidation of toluene) under sunlight-type light, W-containing samples showed activity levels several times higher (in terms of both per weight and per surface area reaction rate) than those of undoped TiO_2 (either the Degussa P25 standard or home-prepared by the same method), while if the same reaction was tested with mainly UV light irradiation the W-containing specimens showed no significant activity enhancement with respect to pure titania. This evidenced the visible light-specific photoactivity of these doped materials. A photoactivity enhancement was also found when doping with Mo (that could be introduced as well, with the same method, in amounts >10%), but here the effect was much lower.

It is noteworthy that in these works the maximum photocatalytic activity (Table 1) was found for W contents as high as 19% cationic, all samples up to this concentration constituting true solid solutions of TiO_2 and WO_3 with anatase structure where the environment around W was very similar in all of them as evidenced by XANES data (Fig. 1a); only for W contents above 20% cationic was some segregation of WO_3 phase evidenced, and then photoactivity decreased (Fuerte et al. 2002; Fernández-García et al. 2005). Evaluation of the bandgap from the UV–vis spectra (Fig. 1b) indicated a gradual dependence on W concentration that started to deviate from linearity only for the highest W contents (Fernández-García 2005). Such single-phase character was not proved in previous works claiming visible light photoactivity upon doping TiO_2 with large amounts of W or other ions (see e.g., Dai et al. 2005), while in other reported cases the visible light photoactivity decreased for W contents above 2–3%, possibly because the sol–gel procedure used in preparation led to phase segregation for W amounts approaching 5% (Li et al. 2001; Song et al. 2006). The structure was less clear in a poorly

Table 1 Photocatalytic activity data (incl. conversion rates per surface area and mass) for toluene gas phase oxidation on $\text{WO}_3\text{-TiO}_2$ (Fuerte 2002)

Catalyst ^a	Rate _s × 10 ¹⁰ (mol s ⁻¹ m ⁻²)	Rate _m × 10 ⁸ (mol s ⁻¹ g ⁻¹)	Selectivity (%) to benzaldehyde
TiO ₂ (P25)	0.65	0.35	14
TiO ₂ (m)	1.0	1.0	5
W 0.9 (m)	1.2	0.9	7
W 14 (m)	1.8	1.9	16
W 19 (m)	3.3	4.0	13
W 27 (m)	2.9	2.2	13
W 100 (m)	4.6	0.1	100
WO ₃ /TiO ₂ ^b	1.4	0.8	15

^a (m) Means prepared by microemulsion method followed by calcination

^b Prepared by impregnation on microemulsion-prepared TiO₂

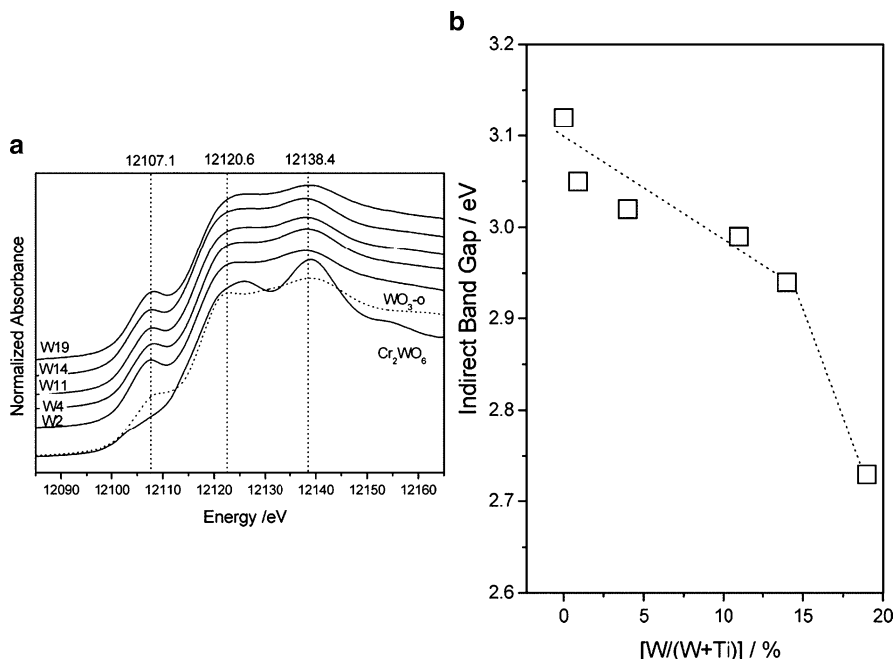


Fig. 1 (a) W L_1 -edge XANES spectra of W-containing anatase-TiO₂ photocatalysts with different W contents, compared to reference compounds. (b) Bandgap of the same specimens

crystalline W-doped (up to 5%) mesoporous titania material which showed as well significant visible light photocatalytic activity (Miyake and Tada 2004).

In the mentioned photocatalysts prepared in this laboratory via microemulsions, tungsten was clearly in the W(VI) redox state, as evidenced spectroscopically by EPR (Fuerte et al. 2002) and XANES (Fernández-García 2005) (Fig. 1a), while EXAFS data in the latter work indicated for W a nearest cation environment made mainly of Ti ions, i.e., no clustering or segregation of W occurred; indeed XPS showed that the surface W/Ti ratio was similar to the chemical analysis value (Fuerte et al. 2002). The reason for the extension of the photoactivity to the visible range was connected to the displacement observed in the light absorption edge to longer wavelengths, in a way that seemed a decrease in the bandgap rather than the insertion in the latter of a new, discrete level. Quantum mechanical calculations (Fernández-García et al. 2005) indicated that the effect of tungsten could consist in the development of electronic states at the bottom of the conduction band which, even if formed to a large extent by W-centered orbitals, were significantly mixed with the Ti 3d orbitals and had therefore real band character; bandgap narrowing could thus be rightly claimed. The exact nature and structure of the atomic arrangements compensating for the different charge of the W and Ti ions could not however be ascertained; while it was supposed that cation vacancies were involved, the quantum calculations made on simple models of this were unable to justify the W–O distance $d \approx 2.6 \text{ \AA}$ observed in the EXAFS spectra. A complex rearrangement of the atomic

environment, leading to a rather asymmetric coordination around W as already indicated by the XANES spectra (Fig. 1a), had thus to be assumed. This might well be connected with the tungsten concentration-dependent modifications observed in the Raman spectra of these samples (Fernández-García et al. 2005).

In any case, the photocatalytic activity data obtained in these works indicated that the highest activity was obtained with samples where the final crystallization was made by hydrothermal methods rather than by calcination in air (Fuerte et al. 2003). The lack of a clear correlation of these activity data with the amount of photogenerated radicals (detected with EPR) or with the type of surface W=O bonds detected in the Raman spectra led to the assumption that the increase in activity was a combined result of spectral range enlargement, surface chemistry modification (e.g., higher acidity) induced by the presence of surface W ions and a higher efficiency in electron transfer at the surface. The complexity of the processes involved is made clear by work in recent years (Tatsuma et al. 2003) showing that peroxide species photogenerated at the surface of this mixed oxide can continue their oxidizing action after ceasing illumination.

The number of works reporting visible light photoactivity for single phase titania materials prepared by chemical methods and homogeneously doped in high amounts ($\geq 5\%$ of cations) with cations other than W or Mo is relatively scarce. Thus, while TiO₂-CeO₂ mixed phase nanoporous materials (Pavasupree et al. 2005) were shown to have much higher visible light photoactivity for I⁻ oxidation than either of the two pure phases, anatase-type single phase materials were obtained by these authors only for lower Ce amounts (5%), for which however photoactivity data were not reported. In contrast, our work cited above (Fuerte et al. 2001) found no sunlight photoactivity for anatase doped with Ce at 9% levels. In this respect it is worth noting that a CeTiO₄ crystalline phase of unsolved structure, prepared by oxidation of a pyrochlore-type Ce₂Ti₂O₇ compound, was found to have photocatalytic activity under visible light for the photobleaching of methylene blue, while other Ti-Ce mixed oxides did not show it (Otsuka-Yao-Matsuo et al. 2004). Also the presence of a "Ce:TiO₂" phase of unsolved structure, coexisting with anatase in samples prepared with low Ce content (3%), was reported to produce enhanced visible light photoactivity for dye degradation (Xie and Yuan 2003). Further work is certainly required to clarify whether indeed some specific Ce-Ti mixed oxide has relevant photocatalytic activity with visible light. In connection with this, it is interesting to note that another simple titanate of a heavy metal, PbTiO₃, has also shown photocatalytic activity under visible light (Kim et al. 2006a), in this case for H₂ and O₂ evolution from water using sacrificial agents; other more complex Pb-containing titanates displayed similar activity. Within the area of lanthanide-doped TiO₂, insertion of Nd at levels up to ca. 5% has been claimed to produce visible light photoactivity for the degradation of chlorophenol (Li et al. 2003a), but in other works (Xie and Yuan 2004, reporting phenol photooxidation activity under visible light for lower amounts of Nd) it is suggested that clustering of Nd occurs in this type of materials.

In general, it seems to be difficult to introduce chemically first row transition metals in titania in homogeneous way at concentrations $\geq 5\%$, therefore those

dopants are described mainly in the next section. Reports have been made on the possibility of inserting such cations in amounts $\geq 10\%$ within the anatase lattice (Serpone et al. 1994; Shi et al. 2006a), but the characterization in these cases is not very complete, and one cannot discard the possibility that some XRD-undetectable phase segregation or clustering takes place in them at the temperatures used in the preparation. Also, rutile samples containing Ni up to 8%, prepared by ball milling of TiO₂ with Ni metal followed by oxidation, were claimed to be homogeneous and have visible light photoactivity for chlorophenol oxidation (Kim et al. 2005, 2006b), but the structural data reported were again not very precise. Indeed subsequent work by the same team (Kim et al. 2006c) showed formation of a separated NiTiO₃ phase, characterized by a strong luminescence of photons with energy 1.9 eV, upon thermal treatment at 1,000°C; the latter material increased its photoactivity, in comparison with the nontreated sample, with both visible and UV light irradiation, which might indicate some photoactivity of the stoichiometric titanate itself. A similar situation arises with a recent work on Co-doped TiO₂ (Shi et al. 2006b), where visible light photoactivity for oxidation of aniline was found with samples having up to 10% homogeneous doping but which segregated a separate CoTiO₃ phase after calcinations above 400°C. A situation at the borderline of what can be considered homogeneous doping of TiO₂ is found in the intercalation of laminar hydrated titania with chromium(III) oxide clusters (Kim et al. 2007). This material, prepared through exfoliation of a laminar hydrous titania in water followed by calcination and having a Cr:Ti ratio ≈ 0.9 , displayed diffraction lines typical of a regularly pillared laminar compound and showed clear activity for photooxidation of phenol under visible light.

2.2 Low Concentration Doping

Doping of titania with a small amount of transition metal cations has been for over two decades a typical method to improve the efficiency of the photocatalytic process, even with UV irradiation. This improvement is usually interpreted to be a consequence of the increase of the charge carrier lifetimes related to the role of the dopants as electron/hole trappers (1 and 2 above) (Carlson et al. 1986; Scalfani et al. 1991; Choi et al. 1994a; Ikeda et al. 2001). Additionally, the light absorption can be extended to the visible region upon doping with transition metal cations, which is normally interpreted as a consequence of the introduction of new energy levels in the titania bandgap (Zhao et al. 2005; Anpo 1997). These energy levels induce the red shift in the onset of light absorption, which occurs in the visible light range due to charge transfer transitions between the dopant and the semiconductor bands and/or to d-d transitions controlled by the crystal field. Nevertheless, there are still many unsolved items with respect to the photophysics and photochemistry of the processes involved in the catalytic reactions that take place at the surface of the photocatalysts. Among them, knowledge of details concerning the surface structure of the catalysts and the contribution of the charge carrier dynamics are generally lacking while it

must be considered that the ability of a dopant to function as an effective charge trap is the result of a compendium of factors like the dopant concentration, the energy level of dopants within the TiO_2 lattice, their d-level electronic configuration, the distribution of dopants within the catalyst particles, the electron donor concentration and the incident light intensity. The significant spread of these factors in the scientific literature is certainly one of the main causes for the controversy found concerning the doping effect.

The transition metal ions more studied to date for titania doping are, apart from those in the previous section, V (Klosek and Raftery 2001; Kubacka et al. 2007), Fe (Chen et al. 2002), Cr (Karvinen and Lamminmäki 2003; Takeuchi et al. 2000; Zhu et al. 2006a; Yu et al. 2006) and Au (Li and Li 2001), some studies existing also where the dopants are not transition elements but alkaline earth metals (Zielinska and Morawski 2005) or even Bi (Xu et al. 2002). As mentioned above, their contribution to the photocatalytic activity under visible light has mainly been related to the modification of the e^-/h^+ recombination rate (Ikeda et al. 2001), which can result in a positive effect, although in some instances, even if the metal induces an extension of the light absorption into the visible region, negative effects on the reaction rates have been also reported (Litter and Navío 1996). Some particular cases in which the authors' group has been more deeply involved are described in the next lines.

A notable example is that of iron-doped titania systems. The Fe(III)-doped catalyst has been reported to enhance significantly the quantum yields under visible light excitation of both oxidative and reductive reactions carried out on nanostructured configurations of the system (Choi et al. 1994a). The ability of Fe^{3+} centers for working in both types of reactions has been related to the fact that it can formally act both as electron ($\text{Fe}^{3+}/\text{Fe}^{2+}$ couple) and hole ($\text{Fe}^{3+}-\text{Fe}^{4+}$ couple) trapping center, in accordance with an electronic configuration in which both redox pairs energies lie within the bandgap, being, respectively, close to the conduction and valence bands of titania (Colón et al. 2007; Choi et al. 1994a; Nagaveni et al. 2004); as a consequence, the lifetimes of the charge carriers can be significantly increased (Moser et al. 1987). A mechanism in which shallow trapping of the photoelectron by Fe^{3+} followed by a rapid, iron-facilitated transfer of the electron to externally incorporated molecular oxygen has also been suggested as a tentative explanation for the enhancement of photocatalytic activity by this doped system (Wang et al. 2003). However, it has also been reported that the presence of iron can be detrimental to the photoactivity as a consequence of the Fe^{3+} centers acting as electron/hole recombination centers (Bickley et al. 1994; Navío et al. 1999; Beydoun et al. 2000). Certainly, the structural details in each case, which basically depend on the preparation parameters employed, and the iron concentration of the systems are most relevant to explain such discrepancies (Litter et al. 1996). In this respect, Fe^{3+} can be incorporated substitutionally on the TiO_2 matrix in accordance also with the similarity of its ionic radius and that of Ti^{4+} (Hoffmann et al. 1995; Litter et al. 1996). However, such substitutional incorporation can be maximized only at relatively low dopant content (ca. 1 wt. %), which also typically coincides with achievement of maximum photoactivity in organics photooxidation

reactions (Litter et al. 1996; Adán et al. 2007); higher iron amounts typically lead to the formation of segregated phases in which recombination processes can be the dominant route (Beydoun et al. 2000).

Nevertheless, the situation is typically more complex since isolated and aggregated iron species appear together even for very low iron-doping levels, as demonstrated by EPR (Adán et al. 2007). Fig. 2a shows that for a low doping level of anatase-TiO₂, in which substitutional iron predominates, an electronic transition appears excited by light in the visible region near 400 nm which is attributable to the excitation of 3d electrons of Fe³⁺ to the TiO₂ conduction band (charge transfer transition) (Adán et al. 2007; Umebayashi et al. 2002; Zhu et al. 2006b). For highly loaded iron-doped anatase, an additional absorption appears at ca. 500 nm, which is ascribed to the d-d transition of Fe³⁺ (${}^2T_{2g} \rightarrow {}^2A_{2g}, {}^2T_{1g}$) or to a charge transfer transition between interacting iron ions ($Fe^{3+} + Fe^{3+} \rightarrow Fe^{4+} + Fe^{2+}$), and which seems to be a characteristic of segregated iron-containing phases (Adán et al. 2007; Zhu et al. 2006b; Li et al. 2003b).

As displayed in Fig. 2b, EPR reveals the presence of such segregated phases already for relatively low iron contents (even as low as 0.4 wt. %) (Adán et al. 2007), in agreement with the relatively low solubility observed for Fe³⁺ in the titania lattice (Cordischi et al. 1985). The EPR spectra of the iron-doped anatase samples are essentially constituted by the overlapping of four Lorentzian lines (Adán et al. 2007; Zhang et al. 2003). Two of the lines appear at the same *g* value (*g* ≈ 2.00) although they differ in their respective linewidth (ca. 60 G versus 300 G); both of them can result from powder averaging of the moderately anisotropic spectrum expected for substitutional Fe³⁺ cations in the anatase structure (Zhang et al. 2003; Grätzel and Howe 1990). Another signal shows an anisotropic feature at *g* ≈ 4.30 and can be generically assigned to Fe³⁺ cations in a rhombic environment (Aasa 1970), attributable to the presence of oxygen vacancies in the anatase-like close environment of the cations (Adán et al. 2007; Grätzel et al. 1990). The fourth signal presents a relatively large linewidth (between ca. 900 and 1,300 G) and *g* value somewhat higher than 2.00. In contrast to the other signals,

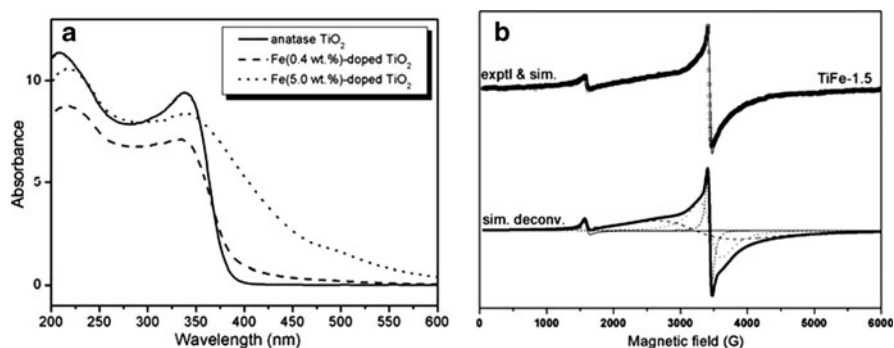


Fig. 2 (a) UV-vis spectra of anatase-TiO₂ photocatalyst samples doped with Fe at various levels. (b) EPR spectrum of sample doped with 1.5% Fe, and decomposition in various signals

this latter does not follow the Curie law on the basis of comparison of spectra recorded at different temperatures (Adán et al. 2007). The characteristics of this latter signal indicate that it corresponds to Fe^{3+} cations relatively close to each other and is affected by magnetic coupling interactions.

A further significant structural effect of iron incorporation into the TiO_2 lattice concerns the promotion of the anatase to rutile transformation (Litter et al. 1996; Zhu et al. 2006b; Iida and Ozaki 1961) with a consequent decrease of specific surface and surface hydroxyl concentration and which generally leads to a decreased photooxidation activity (Litter et al. 1996). Modifications of the surface acid/base properties upon Fe incorporation to the anatase– TiO_2 structure have also been claimed as relevant to the photoactivity (Adán et al. 2007). Further contributions to the photoactivity have been reported in cases where iron becomes lixiviated to the liquid reaction medium and forms complexes which can homogeneously assist the various photoreactions (Araña et al. 2001; Araña et al. 2003).

Another interesting dopant of titania is vanadium, taking into account that its introduction into the anatase structure allows to extend the light absorption into the 400–600 nm (visible) range (Kubacka et al. 2007; Fuerte et al. 2001; Anpo 2000; Yamasita et al. 2002). Indeed, photocatalysts based on Ti–V mixed oxides frequently overperform undoped TiO_2 when using a visible light excitation (Kubacka et al. 2007; Yamasita et al. 2002; Wu and Chen 2004; Kemp and Intyre 2006). There are, however, several physico-chemical issues of the Ti–V binary systems which affect photoactivity and which, in turn, are influenced by the preparation procedures; these latter display significant variability among the literature reports, which precludes an easy rationalization of the photo-chemical behavior of this mixed oxide system. First of all, as observed for other transition metal dopants, the presence of vanadium in the TiO_2 structure can decrease the anatase stability, favoring the generation of anatase/rutile mixtures even after calcinations at moderate temperature (723–873 K) (Kemp et al. 2006; Zhao et al. 1999). The joint presence of both phases is known to affect the photoactivity (Hoffmann et al. 1995; Litter et al. 1996; Herrmann 2004), shadowing the net catalytic influence of the vanadium heterocation on the anatase properties. Besides that, the binary Ti–V mixed oxides display a significant structural and electronic complexity depending on the preparation procedure. From a structural point of view, vanadium may have a certain tendency to segregate at the catalyst surface; besides, two electronic states (V^{4+} and V^{5+}) may appear commonly in V-doped TiO_2 -based materials (Yamasita et al. 2002; Wu et al. 2004). In fact, a recent theoretical study indicates that V^{4+} could be stabilized into the TiO_2 structure, while V^{5+} is probably the major chemical state at the surface of the materials (Vittadini et al. 2005). As a side but interesting point, it is worth mentioning that well-defined Ti–V mixed oxides display significant structural/electronic differences with respect to VO_x/TiO_2 systems, particularly concerning the absence of isolated or polymeric VO_x -type surface entities (Chatterjee and Dasgupte 2005; Luca et al. 1997). Additionally, it is obvious that the two states of vanadium (V^{4+} and V^{5+}) can have significant differences in electronic properties as the former can act as an acceptor of both electrons (e^-) and holes (h^+), which can positively influence e^- – h^+ recombination,

while the latter is only a potential electron acceptor, favoring charge unbalance and potentially enhancing e^-h^+ charge recombination (Hoffmann et al. 1995; Chatterjee et al. 2005; Choi et al. 1994b).

In the case of V-doped anatase samples prepared by a sol-gel/microemulsion method two well-defined structural situations are encountered with a turning point at a vanadium content of ca. 2.5 at. %. For V content ≤ 2.5 at. % the presence of truly Ti-V substitutional mixed oxides with dominance of V^{4+} states is demonstrated mainly by EPR (Kubacka et al. 2007; Luca et al. 1997). In contrast, for V contents > 2.5 at. % the heterogeneity of the material grows significantly, with the appearance of additional V^{4+} and V^{5+} species (forming metavanadate with rossite-like structures) mainly at bulk-interstitial and surface positions, respectively (Kubacka et al. 2007). Additional effects of vanadium incorporation are related to decreases of the specific surface associated with increases of the primary nanoparticle size (Kubacka et al. 2007). From an electronic point of view, samples with V content ≤ 2.5 at. % display a relatively small red shift of the bandgap, while new localized unoccupied states near the valence band or the middle of the gap are detected for higher dopant content (Kubacka et al. 2007). The photocatalytic activity of this type of samples for toluene degradation under sunlight excitation displays a maximum (Fig. 3) when the substitutional vanadium species becomes maximized. However, a strong decrease of activity with a concomitant increase of the selectivity to benzaldehyde is observed for high V content when the presence of surface V^{5+} species becomes apparent. Therefore, the optimization of the photoactivity seems to be achieved (along with structural and electronic effects correlated with it) upon maximization of the V^{4+} presence at substitutional positions of the

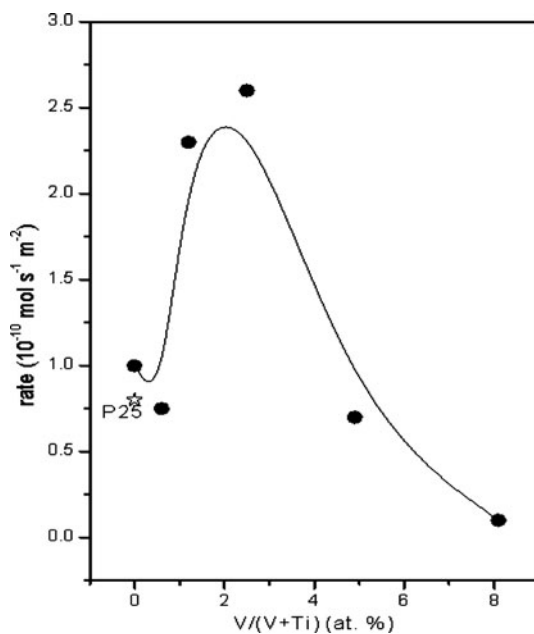


Fig. 3 Photocatalytic activity of TiO_2 doped with different amounts of vanadium for toluene mineralization with sunlight-type excitation

anatase structure, while the presence of other V^{4+} (interstitial) and, particularly, V^{5+} species appears detrimental to the photoactivity (Kubacka et al. 2007). Achievement of a maximum photoactivity at intermediate vanadium content has also been observed in samples prepared by ion implantation or sol–gel methods (Yamasita et al. 2002; Wu et al. 2004; Kemp et al. 2006; Hou et al. 2006).

One intriguing case of visible light activity upon transition metal doping is that reported recently about doped titania–silica aerogels (Wang et al. 2004). Here, with 5% transition metal oxide and 20% TiO_2 +75% SiO_2 in the amorphous material composition, activity for acetaldehyde photooxidation with visible light was observed while no such activity was found when doping TiO_2 alone. The effect was observed for several metals: V, Ni, Fe, Cr and Co, the latter two being outstanding since the activity observed was higher than that measured for pure P25-type TiO_2 under UV light.

3 Titania Doped with Electronegative Elements

There is currently a large interest in doping anatase– TiO_2 materials with main group light elements and understanding their effects and features. Numerous recent publications have reported on doping with C (Sakhivel and Kisch 2003; Irie et al. 2003a; Kamisaka et al. 2005; Zhao et al. 2005), N (Zhao et al. 2005; Sato 1986; Asahi et al. 2001; Irie et al. 2003b; Sakatani et al. 2003; Gole et al. 2004; Stewart et al. 2006; Livraghi et al. 2006; Nambru et al. 2006), F (Zhao et al. 2005; Hattori et al. 1998; Yu et al. 2002; Li et al. 2005a), S, and to a lesser extent with B (Zhao et al. 2004; Chu et al. 2005), Cl and Br (Luo et al. 2004), P (Lin et al. 2005), and I (Hong et al. 2005). Also codoping processes have been frequently analyzed; as examples we can mention the combined use of N/F (Li et al. 2005b, c), N/I (Long et al. 2006) or N/C (Noguchi et al. 2005). As we have centered our investigation on N-doping of materials (Belver et al. 2006a; Stewart et al. 2006; Belver et al. 2006b), we will detail our main findings on these, in relation with the literature reported data for them. As discussed elsewhere, many of the main physico-chemical effects and derived catalytic properties are presumed to have a common origin for all these anatase– TiO_2 systems doped with electronegative agents (Serpone 2006; Colón et al. 2007; Zhao et al. 2005).

Having this in mind, here we will discuss main results concerning the two fundamental questions that the N-doping of anatase– TiO_2 systems raises and that, in a more or less general way, still escape a definitive answer. The first concerns the exact nature of the N-containing species and their corresponding role in light absorption and photoactivity. It is obvious that different species may arise as a direct consequence of using different preparation methods; as we will see, most of the reported procedures in fact lead to the presence of a significant number of coexistent N-containing chemical species which, on the other hand, are frequently common to very different preparation methods. Such simultaneous presence of several N-containing species complicates the interpretation of the photoactivity

shown by different materials. The second important question arises from the way in which N-doping is structurally allowed to exist in the anatase structure, and concerns also whether point and/or extended defects associated to N doping but not containing N by themselves have or have not a preponderant effect in driving the enhanced visible-light absorption and the corresponding improvement of photocatalytic properties. This last point closely connects with the work reported on self-doped TiO₂ systems and their claimed activity under visible light excitation (Justicia et al. 2002; Martyanov et al. 2004).

We will therefore start by briefly describing the synthesis and main characterization results obtained for our N-doped TiO₂-based materials, prepared by sol-gel method inside microemulsions from Ti-isopropoxide precursors modified by reaction with three different amine ligands (2-methoxyethylamine CH₃OCH₂CH₂NH₂, *N, N, N', N'*-tetramethylethylenediamine (CH₃)₂NCH₂CH=CHCH₂N(CH₃)₂ and 1,2-phenylenediamine C₆H₄(NH₂)₂; in what follows, the samples so derived will be called M, N, and Ph, respectively) (Belver et al. 2006b). The dried gels were subjected to three different treatments under gas flow, consisting always of a ramp at 1 K min⁻¹ with 2-h plateaus at 200 and 450°C, the latter being the final temperature of treatment. Treatments differ in the specific point/temperature where O₂ (20 vol.%) is added to the flowing Ar: either incorporated from the beginning (treatment called “1”) or at the onset of the first (“2”) or second plateau (“3”). Reference samples (called T hereafter) were produced by using the unmodified Ti isopropoxide as precursor. An additional reference material (Taq) was obtained by a posttreatment of TiO₂ nanoparticles with the N ligand in order to facilitate a comparison with samples already studied in the literature. Table 2 summarizes the names of the samples and references and the main structural and photo-chemical (methylcyclohexene oxidative degradation) characterization results. All samples showed the exclusive presence of anatase by XRD and Raman techniques (Belver et al. 2006a, b).

Considering first the morphological properties, we note a decrease in BET area with small influence in primary particle size for treatment 3 with respect to the other

Table 2 Main characterization results of N-doped titania samples and titania references

Sample	S_{BET} (m ² g ⁻¹)	% N	Size (nm)	Rate × 10 ⁹ (mol s ⁻¹ m ⁻²)
M1	107.8	0.0	13.5	0.24
M2	104.2	0.0	10.1	0.49
M3	61.2	0.1	10.0	0.59
2M1	106.5	0.5	13.1	0.31
2M2	100.2	0.1	13.7	0.43
2M3	68.2	0.0	8.3	1.47
N3	46.5	0.1	30.3	0.7
Ph3	63.1	0.0	12.8	0.43
T1	107.3	–	13.3	0.33
T3	74.9	–	10.9	0.14
Taq3	69.7	0.0	19.8	0.22

treatments, 1 and 2. The comparison of Ti–N samples and T references, however, indicates that such common feature is accompanied by rather different catalytic effects on these two series of materials; therefore it is not a key factor on explaining photoactivity differences. Besides that, the Taq3 reference result would indicate that the presence of N-containing groups at the surface may not contribute to the detected activity enhancement.

Morphological/surface variables would thus have little impact on the significant photoactivity enhancement detected in Table 2 for Ti–N samples with respect to T reference systems. Additionally, no correlation is noted between the photoactivity and the N content of the materials, which is rather low in all samples except for 2M1. Although first reports suggested a possible relationship (Belver et al. 2006a), the lack of correlation seems now to be of rather general validity (Serpone 2006; Colón et al. 2007; Irie et al. 2003a). Thus, it can be concluded that most of the preparation methods tried in the literature do not appear to provide a direct link between N content and pollutant mineralization activity under visible light excitation. Nonetheless, since different N-containing species may be present in a single Ti–N sample, it might be that only one specific species among these, the amount of which could be scarcely correlated to the total N content, was responsible for the photoactivity of N-doped TiO₂ catalysts under visible light. The task to identify such a potential active N-species is not easy, as N–Ti–O, Ti–N–O (oxynitride), NO⁺, N[−], N^{3−}, NH, and/or NH_x have been detected in Ti–N samples, depending on the preparation method (Serpone 2006; Colón et al. 2007; Zhao et al. 2005; Belver et al. 2006a; Livraghi et al. 2006; Nambru et al. 2006). For our samples, a DRIFTS/EPR/XPS study of Ti–N species was performed to test this hypothesis, by first identifying the present N-species and then measuring their relative abundance (Belver et al. 2006a).

In Fig. 4 we display DRIFTS spectra which provide evidence for the presence of (CN)^{n−} and NO⁺ species. Additionally, N^{n−} species were detected by the other two techniques. So, for samples mentioned in Table 2 at least three types of species are present, two of them possibly occupying substitutionally anion positions and having negative charge, and the positive one being in interstitial positions. The majority of such N-containing species were at bulk positions of the material.

The presence of these N-containing species would have important electronic consequences. As sketched in Fig. 5, upon N introduction localized electronic states appear above the upper part of the valence band. According to theoretical calculations (Livraghi et al. 2006; Nambru et al. 2006) both substitutional and interstitial N-containing species may contribute to such electronic levels, although these would seem to appear in the former case at slightly lower energies. The degree of filling (partial or full) of these levels would depend on the concomitant presence of oxygen vacancies (or, similarly speaking, of excess electrons that normally appear as Ti³⁺ species), but in any case they would promote absorption of photons with energies around 2.5–3.0 eV by exciting electrons from those levels to the conduction band. Such an electronic transition appears between the anatase–TiO₂ bandgap edge energy, ca. 380 nm, and up to around 500 nm (Serpone 2006; Colón et al. 2007; Zhao et al. 2005; Belver et al. 2006a).

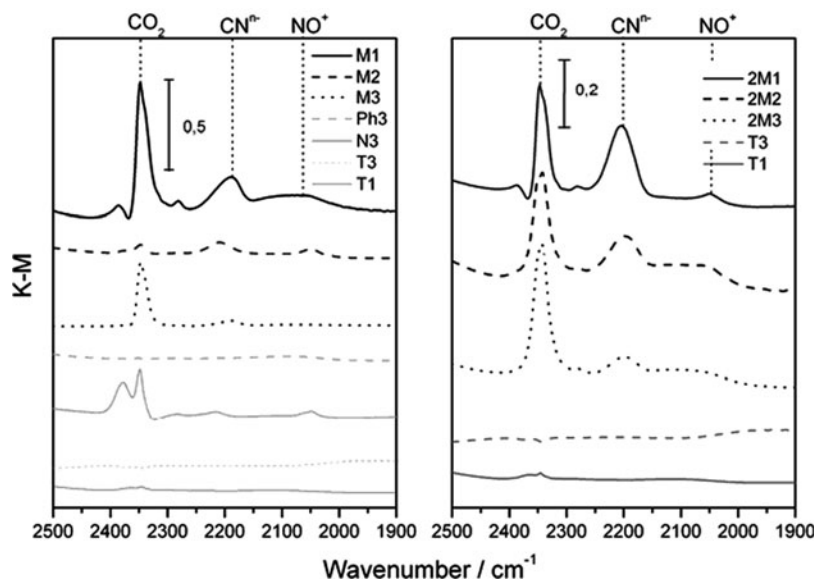


Fig. 4 DRIFT spectra of N-doped TiO₂ samples and reference materials

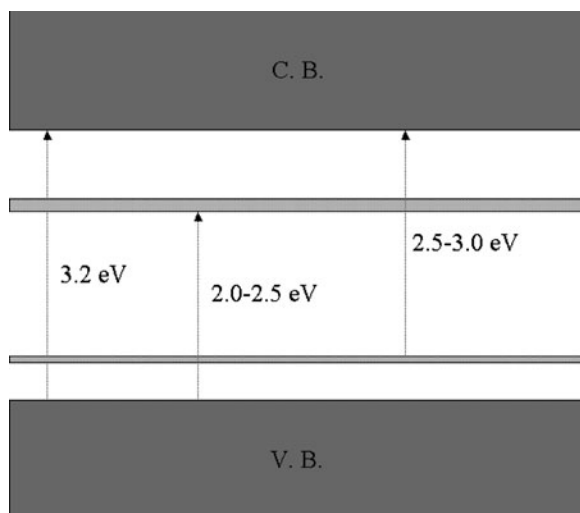


Fig. 5 Scheme of bands in N-doped TiO₂

This new absorption can be observed in the UV–visible spectra. Thus we detected for all samples an ill-defined bump in the absorption spectrum through this region, but could not assign specific electronic features to any of the three N-containing chemical species present. However, the key point was that none of these latter showed throughout the studied series of samples a trend in concentration (as measured by DRIFTS/

XPS/EPR) similar to that presented by the photoactivity. In consequence, although some electronic features corresponding to 3.0–2.5 eV visible-light can be directly ascribed to N-containing species, it seems that they may not be directly linked to the photoactivity of the samples. This may be related to the strong localization of the photogenerated hole at the N-containing species, considering the low concentration of these and the arguments given above. If the dopant sites are mostly at bulk positions and the so trapped holes have low mobility, these latter would not be involved in surface chemical reactions and could essentially act as recombination centers. As both charge carriers are necessary for mineralization reactions, the failure of the visible light to chemical energy conversion process may be envisaged. A certain degree of doubt concerns the case of mutually interacting N-containing species, which may allow some charge delocalization and mobility; however, the solubility limit of the N-containing species seems rather low and this possibility could have a low likelihood (Colón et al. 2007; Livraghi et al. 2006; Namburu et al. 2006). In fact, N concentration in photocatalytic N-doped titania samples is typically lower than 0.1% (as in Table 2), further stressing the low probability of an electronic interaction between N-containing species.

Figure 5 also depicts another type of gap states, appearing below the conduction band and corresponding to a defect-derived density of states (Serpone 2006; Colón et al. 2007; Zhao et al. 2005; Belver et al. 2006a; Livraghi et al. 2006; Hattori et al. 1998). They are typically ascribed to anion vacancy-derived sites, showing states at 0.7–1.2 eV below the anatase-TiO₂ conduction band (Cronemeyer 1959). Electronic transitions from the valence band would thus have energy in the 2.0–2.5 eV range and be detected in UV–visible spectra in the visible light wavelength interval from ca. 500 to 620 nm. In order to estimate the chemical potential of such absorption features we first need a structural interpretation of these electronic features. Very few studies have tried to interpret on a structural basis the N-derived defect electronic features.

We attempted to get structural information at a local level using XANES and EXAFS spectroscopies (Belver et al. 2006a; Stewart et al. 2006). In Fig. 6 we show the Ti K-edge XANES spectra (Fig. 6a) of some samples included in Table 2 and a graphical view of the numerical analysis of the Ti K-edge 1s → 3d pre-edge feature which was made in order to measure the distribution of different local coordinations of the Ti ions in these materials (Fig. 6b). Table 3 displays the corresponding numerical results for selected samples. In all the cases, Ti appears as Ti(IV), Ti(III) being practically absent. In anatase, Ti ions are octahedrally coordinated at bulk positions, but have a decreased coordination number at the surface; this may be a globally significant effect in nanomaterials (Fernández-García et al. 2004). From energetic considerations, it appears that only penta-coordinated Ti ions (besides hexa-coordinated ones) may be present at surfaces, while tetra-coordinated ones would be rarely detected. In fact, experimentally we only detected six- (Ti⁶(IV)) and fivefold (Ti⁵(IV)) coordinated Ti ions (Belver et al. 2006a; Stewart et al. 2006). For samples with a primary particle size above 10 nm about 5–10% of the Ti atoms can be at the surface, and only a reasonably small part of them could be penta-coordinated. Comparison of results corresponding to Ti–N samples

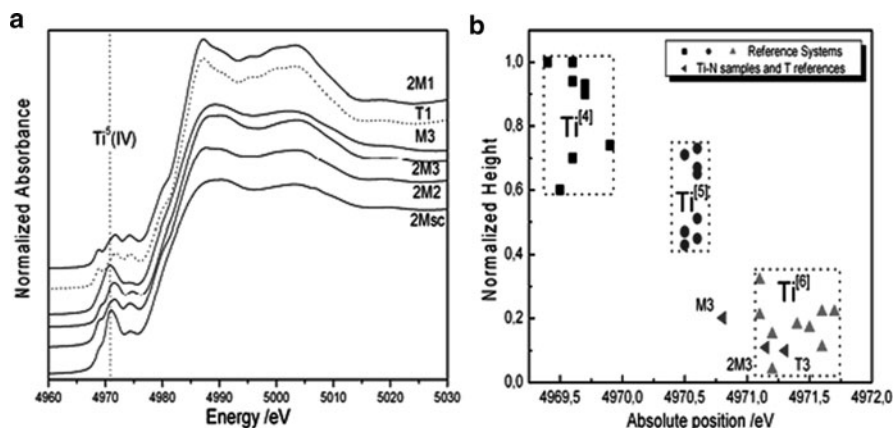


Fig. 6 (a) Ti K edge XANES spectra of N-doped TiO₂ photocatalysts. (b) Scheme of pre-edge position analysis in relation to Ti coordination type

Table 3 Results from the numerical analysis of the 1s → 3d Ti K-edge XANES spectra, N content and reaction rate for selected samples

Sample	% N	% Ti ⁵ (IV)	% O vacancy	Rate × 10 ⁹ (mol s ⁻¹ m ⁻²)
M3	0.1	33	5	0.59
2M3	0.0	5	1	1.47
T3	–	–	–	0.14

and T references reported in Fig. 6 and Table 3 gives evidence of a number of defects significantly higher (several orders of magnitude in certain cases) than that expected from surface positions.

Table 3 shows the number of Ti⁵(IV) species calculated from XANES results for the M3 and 2M3 samples and the hypothetical number of oxygen vacancies associated to them computed by assuming that the decrease in coordination number (from 6 to 5) is due to the presence of such anion vacancy point defects. The large number of these defects obviously indicates that these do not correspond to the oxygen vacancies appearing as charge compensation for N atoms located in substitutional anion sites (a maximum of one oxygen vacancy would be expected for each two of these N atoms). The data in Table 3 suggest rather the presence of some type of extended defect which would be able to accommodate undercoordinated Ti atoms in a +4 chemical state. A probable interpretation is related to the existence of dislocations at bulk positions of nanoparticles and/or of particle intergrowth leading to twinning planes (Fernández-García et al. 2004; Penn and Banfield 1998; Djerdj and Tonejc 2006). In this respect it is worth noting that our EXAFS results also indicate a significant decrease in the number of Ti neighbors in the first Ti–Ti cationic shell concomitantly with the observation of the Ti⁵(IV) species (Belver et al. 2006a).

These observations connect, as above mentioned, with reports on self-doped TiO_2 systems presenting both a significant substoichiometry (O/Ti atomic ratio well below 2) and localized electronic states near/below the conduction band. Thus, although such phenomena can appear already in pure anatase nanoparticles, they could be strongly promoted in the presence of anion dopants, acting as seed of the extended defects; in fact, this argument has been already applied to rationalize the photoactivity of anion-doped TiO_2 (Li et al. 2005a). In our case, the high number of defects evidenced by the XANES/EXAFS results (much higher than that of N-containing species) could make possible a significant overlap between the electronic wavefunctions associated to them, facilitating the formation of delocalized bands (which may help to decrease recombination as discussed above) and the mobility of the corresponding charge carriers. An increased mobility and surface accessibility of both holes (valence band) and electrons (in the new gap states) would be therefore possible, facilitating the transformation of visible light into chemical energy. However, Fig. 6 and Table 3 also show that there is an optimum number of defects above and below which photoactivity decreases. Maybe the Ti-related density of electronic states (i.e., the conduction band and/or any localized levels near it) suffers important changes affecting the charge mobility if the concentration of defects exceeds a certain level. The physico-chemical basis of the behavior of this complicated system is certainly not well understood, and additional pieces of information are needed to rationalize it. This point deserves further analysis and awaits for future research to be clarified.

To conclude this section we summarize the main findings obtained for our studies concerning N-doped Anatase- TiO_2 samples. A first point concerns the heterogeneity of the N-containing species present in these samples; here, at least three different chemical species were identified. Secondly, while the orbitals of such anion dopants can provide a (partially or fully occupied) density of new states near/above the valence band which may allow the absorption of visible light, they may lead to no significant conversion of the latter into chemical energy due to their small concentration and localized character. Thus light-to-chemistry conversion is linked with both the nature and (especially) the number of N-containing species present in the material, suggesting that a significantly improvement in it could be a key point in the enhanced photoactivity showed by certain anion-doped TiO_2 catalysts. This does not seem to be, however, the general case. A third point is that, concomitantly with N-doping, a very high number (in comparison with the number of N-containing species) of defects seems to be generated, yielding a significant density of unoccupied states which may be crucial to ensure the conversion of visible light into chemical energy. An optimum in the photoactivity is detected for a certain concentration of defects; this may be related to the medium-to long-range order associated to this doping, and, specifically, to the cationic order displayed by the material. This fact appears as capital in our system, but it is not clear whether it can be generalized to all studied systems.

Acknowledgment Financial support from Plan Nacional de Investigación (Projects Nrs. CTQ2004-03409/BQU and CTQ2006-15600/BQU) is acknowledged.

References

- Aasa R (1970) *J Chem Phys* 52:3919
- Adán C, Bahamonde A, Fernández-García M, Martínez-Arias A (2007) *Appl Catal B* 72:11
- Akimoto J, Gotoh Y, Oosawa Y, Nonose N, Kumagai T, Aoki K, Takei H (1994) *J Solid St Chem* 113:27
- Anpo M (1997) *Catal Surv Jpn* 1:169
- Anpo M (2000) *Stud Surf Sci Catal* 130:157
- Araña J, Díaz OG, Miranda M, Rodríguez JMD, Melián JH, Peña JP (2001) *Appl Catal B* 32:49
- Araña J, Díaz OG, Rodríguez JMD, Melián JH, Cabo CGI, Peña JP, Hidalgo MC, Navío JA (2003) *J Mol Catal A* 197:157
- Asahi R, Morikawa T, Ohwaki T, Aoki K, Ega Y (2001) *Science* 293:269
- Asahi R, Taga Y, Mannstadt W, Freeman AJ (2002) *Phys Rev B* 65:224112
- Bahnemann DW (2004) *Solar Energy* 77:445
- Belver C, Bellod R, Stewart S, Requejo FG, Fernández-García M (2006a) *Appl Catal B* 65:309
- Belver C, Bellod R, Fuente A, Fernández-García M (2006b) *Appl Catal B* 65:301
- Beydoun D, Amal R, Low GKC, McEvoy S (2000) *J Phys Chem B* 104:4387
- Bickley RI, González-Carreño T, González-Elipe AR, Munuera G, Palmisano L (1994) *J Chem Soc Faraday Trans* 90:2257
- Blanco J, Malato S (1996) *Tecnología de Fotocatálisis Solar* (Cuadernos Monográficos, CIEMAT Ed.)
- Burdett JK, Hughbands T, Gordon JM, Richardson JW, Smith J (1987) *J Am Chem Soc* 109:3639
- Carlson T, Griffin GL (1986) *J Phys Chem* 90:5896
- Carp O, Huisman CL, Rellr A (2004) *Prog. Solid State Chem* 32:33
- Chatterjee D, Dasgupte S (2005) *J Photochem Photobiol C: Rev* 6:185
- Chen C, Li X, Ma W, Zhao J, Hidaka H, Serpone N (2002) *J Phys Chem B* 106:318
- Choi W, Termin A, Hoffmann MR (1994a) *J Phys Chem B* 98:13669
- Choi W, Termin A, Hoffmann MR (1994b) *Angew Chem Int Ed Eng* 33:1091
- Chu SZ, Inoue S, Wada K, Li D, Suzuki J (2005) *Langmuir* 21:8035
- Colón G, Belver C, Fernández-García M (2007) Nanostructured oxides in photocatalysis. In: Rodríguez JA, Fernández-García M (eds) *Synthesis, properties and applications of solid oxides*. Wiley, New York
- Cordischi D, Burriesci N, D'Alba F, Petrerá M, Polizzoti G, Schiavello M (1985) *J Sol Stat Chem* 56:182
- Cronmeyer DC (1959) *Phys. Rev* 113:1222
- Dai QX, Xiao HY, Li WS, Na YQ, Zhou XP (2005) *Appl Catal A* 290:25
- Dietbold U, Ruzycski N, Herman GS, Selloni A (2003) *Catal. Today* 85:93
- Djerdj I, Tonejc AM (2006) *J Alloys Comp* 413:159
- Fernández-García M, Martínez-Arias A, Hanson JC, Rodríguez JA (2004) *Chem Rev* 104:4063
- Fernández-García M, Martínez-Arias A, Fuente A, Conesa JC (2005) *J Phys Chem B* 109:6075
- Fox MA, Dulay MT (1993) *Chem Rev* 93:341
- Fuente A, Hernández-Alonso MD, Maira AJ, Martínez-Arias A, Fernández-García M, Conesa JC, Soria J (2001) *Chem Commun*:2718–2719
- Fuente A, Hernández-Alonso MD, Maira AJ, Martínez-Arias A, Fernández-García M, Conesa JC, Soria J, Munuera G (2002) *J Catal* 212:1
- Fuente A, Hernández-Alonso MD, Iglesias-Juez A, Martínez-Arias A, Conesa JC, Soria J, Fernández-García M (2003) *Phys Chem Chem Phys* 5:2913
- Fujishima A, Rao TN, Tryk DA (2000) *J Photochem Photobiol C* 1:1
- Gole JL, Scout JD, Burda C, Lou Y, Chen X (2004) *J Phys Chem B* 108:1230
- Grätzel M, Howe RF (1990) *J Phys Chem* 94:2566
- Hattori A, Yamamoto M, Tada H, Ito S (1998) *Chem Lett* 27:707
- Herrmann J-M (2004) *Topics Catal* 34:49

- Hoffmann MR, Martin BT, Choi W, Bahnemann DW (1995) *Chem Rev* 95:69
- Hong X, Wang Z, Cai W, Lu F, Zhang J, Yang M, Ma N, Liu Y (2005) *Chem Mater* 17:1548
- Hou X-G, Hao F-X, Fan B, Gu X-N, Wu X-Y, Liu A-D (2006) *Nucl Instrum Methods Phys Res B* 243:99
- Iida Y, Ozaki S (1961) *J Am Ceram Soc* 44:120
- Ikeda S, Sugiyama N, Pal B, Marci G, Palmisano L, Noguchi H, Uosaki K, Ohtani B (2001) *Phys Chem Chem Phys* 3:267
- Irie H, Watanabe Y, Hashimoto K (2003a) *Chem Lett* 32:772
- Irie H, Watanabe Y, Hashimoto K (2003b) *J Phys Chem B* 107:5483
- Justicia I, Ordejón P, Canto G, Mozos JL, Fraxedas J, Battistoni GA, Gerbasí R, Figueras A (2002) *Adv Mater* 14:1399
- Kamisaka H, Adachi T, Yamashita K (2005) *J Chem Phys* 123:084704
- Karvinen S, Lamminmäki RJ (2003) *Solid State Sci* 5:1159
- Kemp TJ, Intyre RA (2006) *Polymer Degr Stabil* 91:165
- Kim DH, Park HS, Kim S-J, Lee KS (2005) *Catal Lett* 100:49
- Kim HG, Becker OS, Jang JS, Ji SM, Borse PH, Lee JS (2006a) *J Solid St Chem* 179:1214
- Kim DH, Lee KS, Kim Y-S, Chung YC, Kim S-J (2006b) *J Am Ceram Soc* 89:515
- Kim DH, Park HS, Kim S-J, Lee KS (2006c) *Catal Lett* 106:29
- Kim TW, Hur SG, Hwang S-J, Park H, Choi W, Choy JH (2007) *Adv Funct Mater* 17:307
- Klosek S, Raftery D (2001) *J Phys Chem B* 105:2815
- Kubacka A, Fuerte A, Martínez-Arias A, Fernández-García M (2007) *Appl Catal B* 74:26
- Latroche M, Brohan L, Marchand R, Tournoux M (1989) *J Solid St Chem* 81:78
- Li XZ, Li FB (2001) *Environ Sci Tech* 35:2381
- Li XZ, Li FB, Yang CL, Ge WK (2001) *J Photochem Photobiol A* 141:209
- Li W, Wang Y, Lin H, Shah SI, Doren DJ, Rykov SA, Barteau MA (2003a) *Appl Phys Lett* 83:4143
- Li X, Yue P-L, Kotal C (2003b) *New J Chem* 27:1264
- Li D, Haneda H, Hishita S, Ohashi N (2005a) *Chem Mater* 17:2588
- Li D, Haneda H, Hishita S, Ohashi N (2005b) *Mater Sci Eng B* 117:67
- Li D, Haneda H, Labhsetwar NK, Hishita S, Ohashi N (2005c) *Chem Phys Lett* 401:579
- Lin L, Lin W, Zhu Y, Zhao B, Xie Y (2005) *Chem Lett* 34:284
- Linsebigler AL, Lu G, Yates JT (1995) *Chem Rev* 95:735
- Litter MI, Navío JA (1996) *J Photochem Photobiol A* 98:171
- Livraghi S, Paganini MC, Giamello E, Selloni A, Di Valentin C, Pacchioni G (2006) *J Am Chem Soc* 128:15666
- Long M, Cai W, Wang Z, Liu G (2006) *Chem Phys Lett* 420:71
- Luca V, Thomson S, Howe RF (1997) *J Chem Soc Faraday Trans* 93:2195
- Luo H, Takata T, Lee Y, Zhao J, Domen K, Yan Y (2004) *Chem Mater* 16:846
- Luque A, Martí A (1997) *Phys Rev Lett* 78:5014
- Luque A, Martí A, Antolín E, Tablero C (2006) *Physica B* 382:320
- Marchand R, Brohan L, Tournoux M (1980) *Mater Res Bull* 15:1129
- Martyanov N, Uma S, Rodríguez S, Klabunde KJ (2004) *Chem Comm* 21:2476
- Mattesini M, Almeida JS, Dubrovinsky L, Dubrovinskaia N, Johansson B, Ahuja R (2004) *Phys Rev B* 70:115101
- Miyake Y, Tada H (2004) *J Chem Eng Jpn* 37:630
- Mizushima K, Tanaka M, Asai A, Iida S, Goodenough JB (1979) *J Phys Chem Solids* 40:1129
- Moser J, Grätzel M, Gallay R (1987) *Helv Chem Acta* 70:1596
- Nagaveni K, Hegde MS, Madras G (2004) *J Phys Chem B* 108:20204
- Namburu A, Graciani J, Rodríguez JA, Wu Q, Fujita E, Fernández-Sanz J (2006) *J Chem Phys* 125:094706
- Navío JA, Testa J, Djedjeian P, Padrón J, Rodríguez D, Litter MI (1999) *Appl Catal A* 178:191
- Noguchi D, Kawamata Y, Nagatomo T (2005) *J Electrochem Soc* 152:D124
- Ohno T, Mitsui T, Matsumura M (2003) *Chem Lett* 32:364

- Otsuka-Yao-Matsuo S, Omata T, Yoshimura M (2004) *J Alloys Comp* 376:262
- Pavasupree S, Suzuki Y, Pivsa-Art S, Yoshikawa S (2005) *J Solid St Chem* 178:128
- Penn LR, Banfield JF (1998) *Am Miner* 83:1077
- Sakatani Y, Nunoshige J, Ando H, Okusako K, Koike H, Takata T, Kondo JN, Hara M, Domen K (2003) *Chem Lett* 32:1156
- Sakthivel S, Kisch H (2003) *Angew Chem Int Ed* 42:4908
- Sato S (1986) *Chem Phys Lett* 123:126
- Sclafani A, Mozzanega MN, Pichat PJ (1991) *J Photochem Photobiol A* 59:181
- Serpone N (2006) *J Phys Chem B* 110:24287
- Serpone N, Lawless D, Disdier J, Herrmann JM (1994) *Langmuir* 10:643
- Shi JY, Leng WH, Zhu WC, Zhang JQ, Cao CN (2006a) *Chem. Eng Technol* 29:146
- Shi J, Leng W, Cao J, Zhang J, Cao C (2006b) *Chin J Chem Phys* 19:463
- Song H, Jiang H, Liu X, Meng G (2006) *J Photochem Photobiol A* 181:421
- Stewart S, Belver C, Fernández-García M, Mun BS, Requejo FG (2006) *J Phys Chem B* 110:16482
- Takeshita K, Yamakata A, Ishibashi T, Onishi H, Nishijima K, Ohno T (2006) *J Photochem Photobiol A* 177:269
- Takeuchi M, Yamashita H, Matsuoka M, Anpo M, Hirao T, Itoh N, Iwamoto N (2000) *Chem Lett* 67:135
- Tatsuma T, Takeda S, Saito S, Ohko Y, Fujishima A (2003) *Electrochem Comm* 5:793
- Tian FH, Liu CB (2000) *J Phys Chem B* 110:17866
- Umebayashi T, Yamaki T, Itoh H, Asai K (2002) *J Phys Chem Sol* 63:1909
- Umebayashi T, Yamaki T, Tanaka S, Asai K (2003) *Chem Lett* 32:330
- Vittadini A, Casarin M, Sambri M, Selloni A (2005) *J Phys Chem B* 109:21766
- Wang CY, Böttcher C, Bahnemann DW, Dohrmann JK (2003) *J Mater Chem* 13:2322
- Wang J, Uma S, Klabunde KJ (2004) *Appl Catal B* 48:151
- Wu JCS, Chen CH (2004) *J Photochem Photobiol A* 163:509
- Xie Y, Yuan C (2003) *Appl Catal B* 46:251
- Xie Y, Yuan C (2004) *Appl Surf Sci* 221:17
- Xu XH, Wang M, Hou Y, Yao WF, Wang D, Wang H (2002) *J Mater Sci Lett* 21:1655
- Yamasita H, Harada H, Misaka J, Takeuchi M, Ikue K, Anpo M (2002) *J Photochem Photobiol A* 148:257
- Yu JC, Yu JG, Ho WK, Jiang ZT, Zhang LZ (2002) *Chem Mater* 14:3808
- Yu JC, Li G, Wang X, Hu X, Leung CW, Zhang Z (2006) *Chem Commun*:2717
- Zhang Y, Ebbinghaus SG, Weidenkaff A, Kurz T, von Nidda H.-A Krug, Klar PJ, Güngerich M, Reller A (2003) *Chem Mater* 15:4028
- Zhao G, Kozola H, Lin H, Yoko T (1999) *Thin Sol Films* B39:123
- Zhao W, Ma W, Chen C, Zhao J, Shuai Z (2004) *J Am Chem Soc* 126:4782
- Zhao J, Chen C, Ma W (2005) *Topics Catal* 35:267
- Zhu J, Deng Z, Chen F, Zhang J, Chen H, Anpo M, Huang J, Zhang L (2006a) *Appl Catal B* 62:329
- Zhu J, Chen F, Zhang J, Chen H, Anpo M (2006b) *J Photochem Photobiol A* 180:196
- Zielinska B, Morawski AW (2005) *Appl Catal B* 55:221

Chapter 13

Development of Well-Defined Visible Light-Responsive TiO₂ Thin Film Photocatalysts by Applying a RF-Magnetron Sputtering Deposition Method

Masato Takeuchi and Masakazu Anpo

Abstract TiO₂ thin film photocatalysts which can work under visible light irradiation were successfully developed in a single process by applying a RF magnetron sputtering (RF-MS) deposition method. The TiO₂ thin films prepared at higher than 773 K showed efficient absorption of visible light, while the TiO₂ films prepared at around 473 K were highly transparent. This clearly means that the optical properties of these films, which absorb not only UV but also visible light, can be controlled by the preparation conditions using the RF-MS deposition method. These visible light-responsive films were found to exhibit effective photocatalytic reactivity at room temperature for the decomposition of NO and oxidation of acetaldehyde with O₂. Various characterization studies showed that orderly aligned columnar TiO₂ crystals of ca. 100 nm could be observed only for the visible light-responsive TiO₂ thin films. Such unique structural factors are considered to be essential in modifying the electronic properties of the TiO₂ semiconductors, enabling the efficient absorption of visible light. Moreover, crystalline TiO₂ thin films could be prepared on thermally unstable polycarbonate substrates at 353 K by using this RF-MS deposition method.

1 Introduction

Rapid economic growth in the twentieth century has been achieved, in large part, by the consumption of the earth's limited energy resources such as fossil fuels for petroleum oil. However, we are paying for the use of these resources with serious

M. Takeuchi (✉)

Department of Applied Chemistry, Osaka Prefecture University 1-1, Gakuen-cho, Naka-ku, Sakai, Osaka 599-8531, Japan
e-mail: masato-t@chem.osakafu-u.ac.jp

environmental problems such as the greenhouse effect caused by uncontrolled CO₂ emissions and acid rain caused by air pollutants from automobiles, power plants, and industrial factories as well as polluted waterways. We will also be confronted with serious energy issues as fossil fuel reserves become depleted and their prices rise dramatically in the near future. Taking these multiple and intertwined issues into consideration, the need to develop environmentally-friendly chemical processes to solve these problems is an urgent concern not only to mankind but also for all living creatures. With these issues in mind, scientists have increasingly turned to photochemistry and photocatalysis as promising “environmentally harmonious systems.” Especially, titanium dioxide photocatalysts possess the potential to reduce CO₂ into useful CH₄ and CH₃OH, to decompose NO_x into harmless compounds, and to oxidize various organic compounds into non-toxic CO₂ and H₂O. In fact, photocatalytic systems can even be expressed as “artificial photosynthesis” (Fujishima and Honda 1972; Serpone and Pelizzetti 1989; Ollis and Al-Ekabi 1993; Anpo 1996, 2004 and references therein; Schiavello 1997; Ertl et al. 1997; Fujishima et al. 1999; Anpo and Takeuchi 2003). In recent years, transparent and uniform TiO₂ thin films coated on various substrates have been shown to be promising photocatalytic and photofunctional materials for various applications. Although products using TiO₂ have been commercialized, since it is a semiconductor with a wide bandgap larger than 3.2 eV and corresponding to 388 nm in wavelength, irradiation with a UV light source is necessary for it to act as a workable photocatalyst. In order to realize clean and safe chemical processes as well as the efficient use of abundant solar energy, many different approaches to develop TiO₂ photocatalysts sensitive to visible light have been investigated but few breakthroughs have actually been reported. In 1991, Grätzel et al. reported on a dye-sensitized solar cell using a TiO₂ film electrode and photofunctional dye to absorb visible light (O’Regan and Grätzel 1991). This finding opened the way for the conversion of solar energy into usable electric energy in the field of solar cells. However, there are still several issues that need to be resolved, such as the development of more stable organic dyes and more efficient sealing techniques to prevent leakage of the liquid electrolyte. The development of visible light-responsive photocatalysts will, thus, play an important role in the purification of such polluted environments as air, water, and soil. Another important consideration for the widespread and practical applications of visible light-responsive TiO₂ thin films is the cost and various preparation methods such as sol–gel (Heller 1995; Negishi et al. 1995, 1998), chemical vapor deposition (CVD) (Sieferting and Griffin 1990; Maruyama and Arai 1992), and plasma-enhanced CVD (French et al. 1991; Kamishiro et al. 1993) are being intensively investigated.

In this chapter, we deal with an innovative application of the RF-MS deposition method for the preparation of well-defined TiO₂ photocatalysts, especially thin films that are visible light-responsive in a single preparation process as well as for the preparation of crystalline TiO₂ thin films onto thermally unstable plastic substrates at low temperature.

2 A RF-Magnetron Sputtering Deposition Method to Prepare Visible Light-Responsive TiO₂ Thin Film Photocatalysts

TiO₂ semiconductors absorb only UV light of wavelengths shorter than 388 nm. Thus, TiO₂ itself can make use of only 3–4% of the solar radiation that reaches the earth. From this viewpoint, TiO₂ photocatalysts which can operate efficiently under both UV and visible light are urgently required for practical applications. In a 1997 report, we have successfully shown that an advanced metal ion implantation method is the most effective in preparing such visible light-responsive TiO₂ powdered photocatalysts (Anpo and Takeuchi 2003; Anpo 1997, 2000a, b, 2004; Anpo et al. 1998). Various spectroscopic investigations on the chemical states and local structures of the implanted metal ions have revealed that the low-valent transition metal ions highly isolated within the TiO₂ lattice play an important role in the modification of the electronic states of the TiO₂ semiconductor to realize absorption in visible light regions. Moreover, this method was also effective in modifying transparent TiO₂ thin film photocatalysts to also absorb visible light. Studies in this novel metal ion-implantation method have provided valuable information on modifying the electronic properties of both TiO₂ powder and thin film photocatalysts (Anpo 1997, 2000a, b; Anpo et al. 1998; Takeuchi et al. 2000a; Yamashita et al. 1998; Kikuchi et al. 2006). However, since the complexity in the preparation processes impedes their mass production at low cost, less cumbersome preparation methods are strongly desired for widespread, global applications.

Various physical vapor deposition (PVD) methods of preparing functional thin film materials as a dry process are summarized in Table 1. Among these methods, we have successfully applied a RF-magnetron deposition method to develop transparent and visible light-responsive TiO₂ thin films in a single preparation process (Takeuchi et al. 2001; Kitano et al. 2005, 2006a, 2007a). A schematic diagram of the RF-MS deposition method is shown in Fig. 1. In a reactive sputtering method, the TiO₂ thin films are generally prepared using a metallic Ti target in the presence

Table 1 Various physical vapor deposition (PVD) methods

PVD
Vacuum deposition
Heat-resistance
Electron beam (EB)
Molecular beam epitaxy (MBE) deposition
Laser ablation deposition
Sputtering deposition
RF sputtering
RF magnetron sputtering (RF-MS)
Ion beam sputtering
ECR sputtering
Ion plating
Ionized cluster beam (ICB) deposition

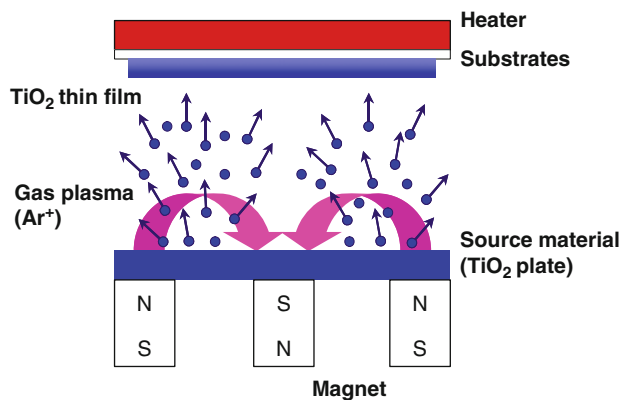


Fig. 1 Schematic diagram of the RF magnetron sputtering (RF-MS) deposition method

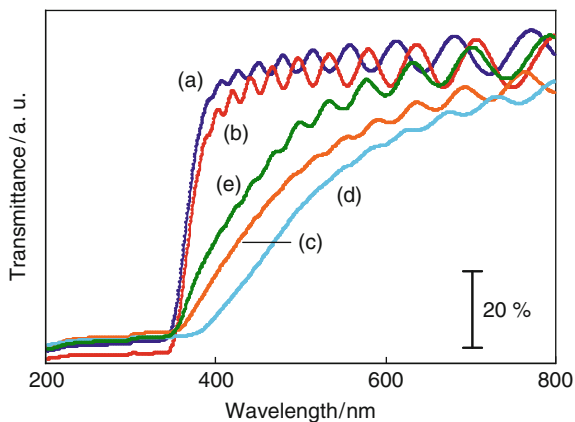
of O_2 as the reactive gas. However, since a stoichiometric TiO_2 plate was used as the sputtering target, only Ar gas was used for the sputtering gas without the coexisting O_2 as a reactive gas. When an orthogonal magnetic field to the electric field is applied in the presence of the sputtering gas (in this case, Ar), ring-state Ar plasma was induced on the target material. The Ar^+ ions in the Ar gas plasma sputtered the target surfaces to produce sputtered ions such as Ti^{4+} and O^{2-} using a TiO_2 plate with a rutile structure as the target material. The ions produced by the Ar gas plasma were accumulated onto the substrate surfaces to form highly transparent TiO_2 thin films. The interaction between the accelerated ion beams and solid surfaces are detailed in Chap. 5. The physicochemical, mechanical, and photocatalytic properties of the obtained TiO_2 thin films were found to be strongly affected by the preparation conditions such as the induced RF power, substrate temperature, distance between the target and substrates (D_{TS}), sputtering gas flow rate, etc. The induced RF power was adjusted to 300W, the substrate temperatures were changed from 373 to 973 K, and D_{TS} was fixed at 80 mm. Since TiO_2 thin films were deposited under high vacuum conditions, contamination of the films with impurities could be avoided. Post calcination treatments were not carried out. The film thicknesses were controlled at ca. 1 μm by changing the deposition time.

3 Physical and Optical Properties of TiO_2 Thin Films Prepared by a RF-MS Deposition Method

The optical property is one of the most important factors determining the photocatalytic performance. Figure 2 shows the UV-vis absorption (transmittance) spectra of the TiO_2 thin films prepared at different temperatures. The films prepared at low temperatures ($T < 473$ K) showed absorption edges at around 360 nm and clear interference fringes in visible light regions, similar to the TiO_2 thin films

Fig. 2 UV–vis absorption spectra (transmittance) of the TiO₂ thin films prepared at different temperatures.

Preparation temperatures: (a) 373, (b) 473, (c) 673, (d) 873, and (e) 973 K



prepared by sol–gel (Heller 1995; Negishi et al. 1995, 1998) or ionized cluster beam (ICB) deposition (Takeuchi et al. 2000a, b; Yamashita et al. 1998; Kikuchi et al. 2006) (Chap. 2.1). These results clearly indicate that, with this deposition process, stoichiometric and transparent TiO₂ thin films can be prepared using a TiO₂ plate as the sputtering target and Ar as the sputtering gas without the coexistence of O₂ as the reactive gas. As the preparation temperatures increase, the films were found to show effective absorption in visible light regions reaching a maximum for the film deposited at 873 K. Since the amount of impurities included in the TiO₂ target material is very low (less than 0.1%), hardly any impurities were included in the deposited thin films. Moreover, the TiO₂ thin films prepared by sputtering the TiO₂ target material in the presence of O₂ at 873 K did not exhibit any significant absorption in visible light regions (data not shown). These results indicate that visible light-responsive TiO₂ thin films could be successfully prepared only when the TiO₂ target as an ion source was sputtered with Ar gas, without a mixture of O₂ gas, at relatively high temperatures ($T > 773$ K).

The XRD patterns of TiO₂ thin films prepared at different substrate temperatures are shown in Fig. 3. The films prepared at temperatures lower than 673 K showed typical diffraction patterns attributed to the anatase phase of TiO₂. Conventional TiO₂ powders (Degussa, P-25) show a typical peak at 25.4° for (101) phase but do not show an intense peak at 37.9° due to (004) phase of the anatase structure, while TiO₂ thin films prepared at temperatures lower than 673 K showed a characteristic diffraction peak attributed to (004) phase. For the TiO₂ thin films prepared at 873 K, a diffraction peak at 25.4° due to the anatase (101) phase was found to dramatically decrease, however, the (004) phase was relatively stable. The TiO₂ thin films prepared at higher temperatures than 873 K and readily able to absorb visible light were mainly composed of a rutile phase for the TiO₂. The primary particle sizes of these films as estimated by Scherrer's equation are summarized in Table 2. The particle sizes of the TiO₂ in the thin films were not largely affected by the preparation temperatures in the deposition process and remained constant at

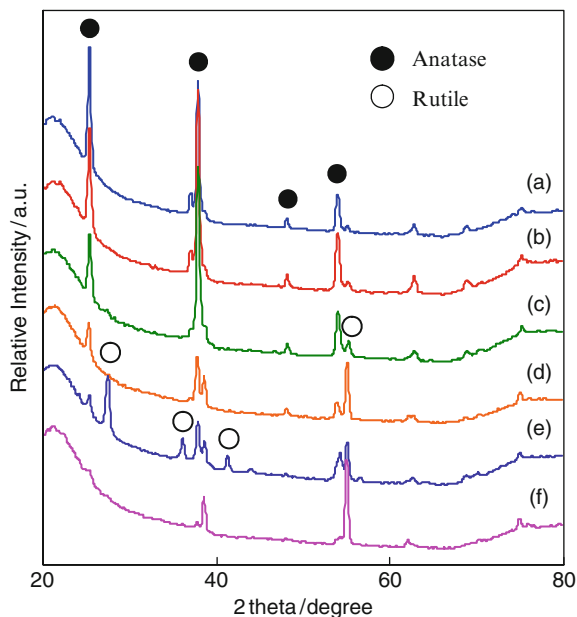


Fig. 3 XRD patterns of the TiO₂ thin films prepared at different temperatures. Preparation temperatures: (a) 473, (b) 573, (c) 673, (d) 773, (e) 873, and (f) 973 K

Table 2 The particle sizes as determined by XRD measurement analysis.

Preparation temperature (K)	Particle size (nm)	Crystal phase
473	18.4	Anatase
573	16.5	Anatase
673	18.9	Anatase
773	21.4	Anatase
873	20.8	Rutile
		(mainly)
973	–	Rutile

Scherrer's equation: $D = K\lambda/\beta \cos \theta$,

where

D = particle size (nm)

λ = wavelength of CuK α (0.15405 nm)

β = half width (rad)

θ = Bragg angle (degree)

K = constant (in this case: 0.9)

about 20 nm. When the anatase phase of the TiO₂ particles changes to rutile by calcination, a dramatic growth in the particle sizes as well as decrease in the BET surface areas can generally be observed. However, since the TiO₂ particles which compose the thin films are strained by interfacial stress on the substrates, crystallization along their depth direction may be restricted.

4 Photocatalytic Reactivity of TiO₂ Thin Films Prepared by a RF-MS Deposition Method Under UV and Visible Light Irradiation for the Decomposition of NO and Oxidation of Acetaldehyde with O₂

The photocatalytic reactivity of TiO₂ thin films prepared by a RF-MS deposition method was evaluated for the decomposition of NO under UV light ($\lambda > 270$ nm) irradiation. Figure 4 shows the reaction time profiles for the photocatalytic decomposition of NO over the TiO₂ thin film prepared at 473 K and TiO₂ powder (Degussa, P-25), as a reference, under UV light irradiation. As in the case of transparent TiO₂ thin films prepared by other methods such as sol-gel or ICB deposition, the decomposition of NO proceeded only under UV light irradiation and no reaction products could be observed under dark conditions. Although the physical surface areas of the thin films are essentially much smaller as compared to powdered catalysts, the reactivity per surface area for the TiO₂ films prepared by this deposition method was almost equal to that of the commercial TiO₂ powder (Degussa, P-25), known as a highly reactive photocatalyst. Figure 5 shows the effect of the preparation temperatures on the photocatalytic reactivity of the TiO₂ thin films for the decomposition of NO under UV light irradiation. The film prepared at 473 K showed the highest photocatalytic performance under UV light

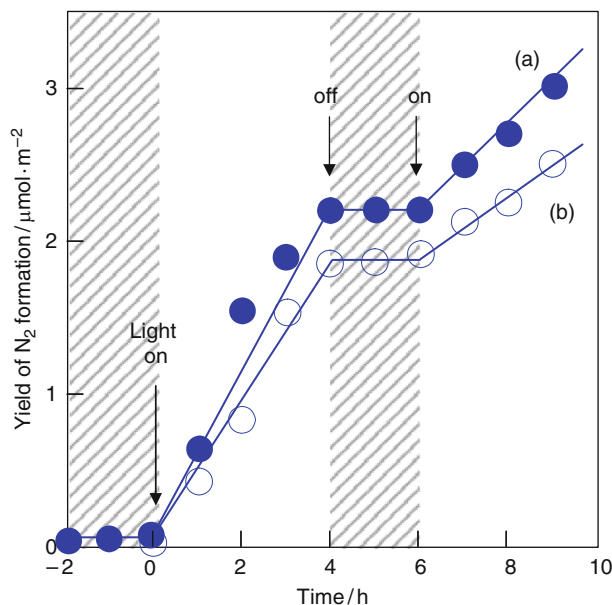


Fig. 4 Reaction time profiles of the photocatalytic decomposition of NO on: (a) the TiO₂ thin films prepared at 473 K and (b) P-25, as reference, under UV light ($\lambda > 270$ nm) irradiation at 275 K

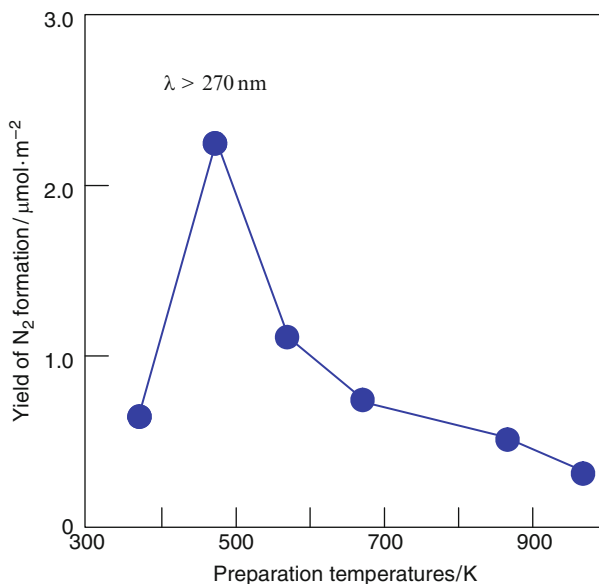


Fig. 5 Effect of the preparation temperatures of the TiO₂ thin films on the photocatalytic reactivity for the decomposition of NO under UV light irradiation

among these samples, however, as the preparation temperatures increased, the photocatalytic reactivity of the thin films decreased. These results indicate the reason why TiO₂ thin films prepared at relatively low temperatures are highly transparent. The incident UV light can pass through the deep bulk of the thin films, resulting in an effective photo-generation of the electron-hole pairs. XRD measurements also revealed that the thin films prepared at temperatures lower than 473 K mainly consist of an anatase phase, while those prepared at temperatures relatively higher than 773 K crystallize well to a rutile structure. These differences in crystal structures for the thin films showed a good correspondence with their photocatalytic reactivities under UV light irradiation. Furthermore, it is notable that thin films with high photocatalytic reactivity can be prepared at relatively low temperatures of ca. 473–573 K by using this RF-MS deposition method.

The photocatalytic reactivity of these TiO₂ thin films for the decomposition of NO under visible light ($\lambda > 450$ nm) was also investigated. As shown in Fig. 6, the commercial TiO₂ photocatalyst (Degussa, P-25) did not show any reactivity under visible light irradiation, however, the TiO₂ thin film prepared at 873 K exhibited efficient photocatalytic reactivity for the decomposition of NO in accordance with the visible light irradiation time. Figure 7 shows the effects of the preparation temperatures on the photocatalytic reactivity for the decomposition of NO under visible light irradiation as well as on the relative intensity at wavelengths of 450 nm in the UV-vis absorption spectra, as shown in Fig. 2. The transparent TiO₂ thin films prepared at lower temperatures did not show any reactivity under visible light, while, as the preparation temperatures became higher, the photocatalytic reactivity

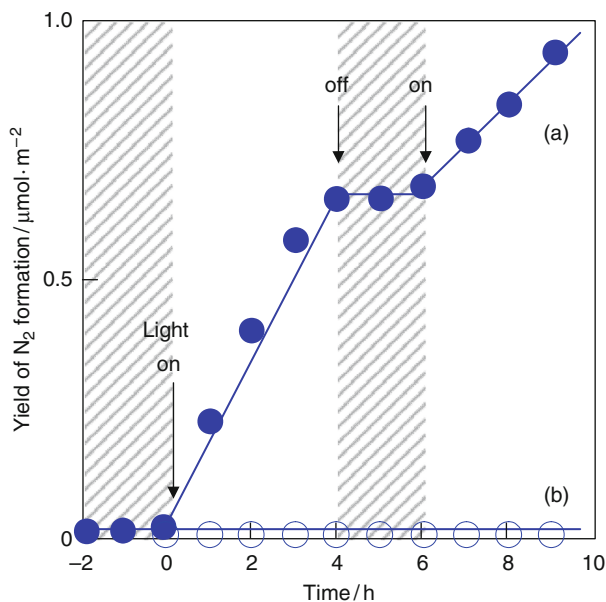


Fig. 6 Reaction time profiles of the photocatalytic decomposition of NO on: (a) the TiO₂ thin film prepared at 873 K and (b) P-25, as reference, under visible light ($\lambda > 450$ nm) irradiation at 275 K

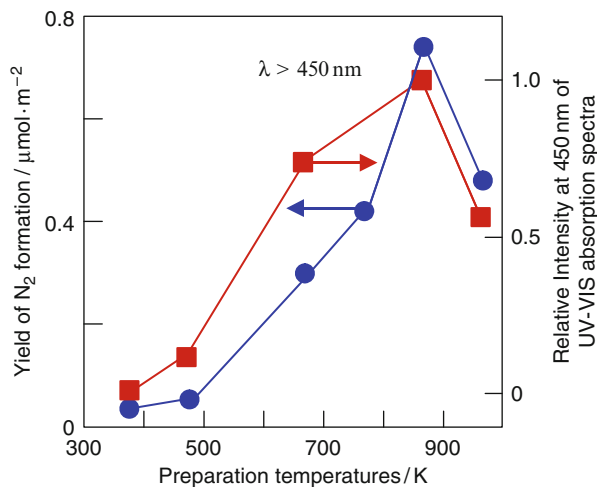


Fig. 7 Effect of the preparation temperatures on the photocatalytic reactivity for the decomposition of NO under visible light irradiation and the relative efficiency of light absorption at 450 nm in the UV-vis absorption spectra

under visible light was found to increase as well, reaching a maximum with the photocatalyst prepared at a substrate temperature of 873 K. Moreover, the order of the photocatalytic reactivities under visible light irradiation corresponded well with

the relative intensities at wavelength of 450 nm in the absorption spectra. These results clearly indicate that TiO₂ thin films prepared by the RF-MS deposition method work effectively as photocatalysts even under visible light of wavelength longer than 450 nm. The TiO₂ semiconducting photocatalysts are known to possess the potential to completely oxidize various organic compounds into such harmless compounds as CO₂ and H₂O under UV light irradiation. These visible light-responsive TiO₂ thin films prepared by RF-MS deposition could also be confirmed to show effective photocatalytic reactivity not only for the decomposition of NO but also for the oxidation of acetaldehyde with O₂ into CO₂ and H₂O in gas phase reactions. Recently, we have successfully applied these newly developed visible light-responsive TiO₂ thin films for the photocatalytic decomposition of H₂O into H₂ and O₂ under visible light irradiation at wavelength longer than 420 nm (Kitano et al. 2005, 2006a, b, 2007a, b, c; Matsuoka et al. 2005; Iino et al. 2006), the details of which are presented in Chap. 6.

5 Proposed Mechanism for Absorption Under Visible Light for TiO₂ Thin Films Prepared by a RF-MS Deposition Method

The mechanisms behind efficient absorption in visible light regions have been discussed from the viewpoint of the surface morphology of the TiO₂ thin films prepared at different substrate temperatures. Figure 8 shows the AFM images of the thin films prepared at 473 and 873 K. The surface morphology and roughness of the visible light-responsive film prepared at 873 K was found to be about three times higher as compared to the film prepared at 473 K. The cross-sectional SEM images of the thin films prepared at 473 and 873 K are shown in Fig. 9. The top views of the SEM images were almost similar to the above AFM images. The most obvious

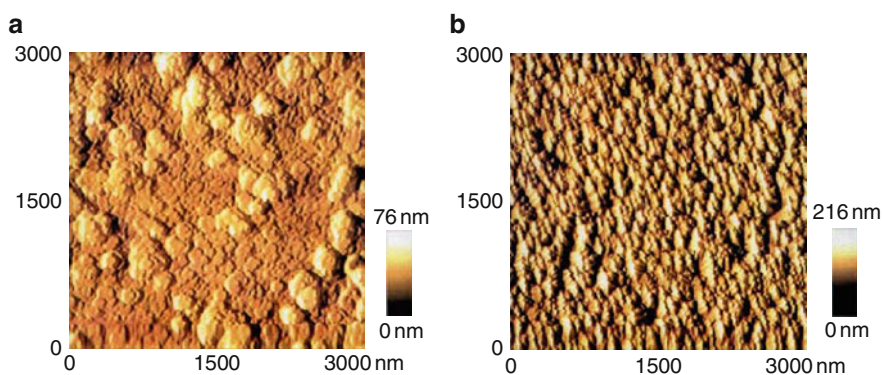


Fig. 8 AFM images of the TiO₂ thin films prepared at: (a) 473 and (b) 873 K

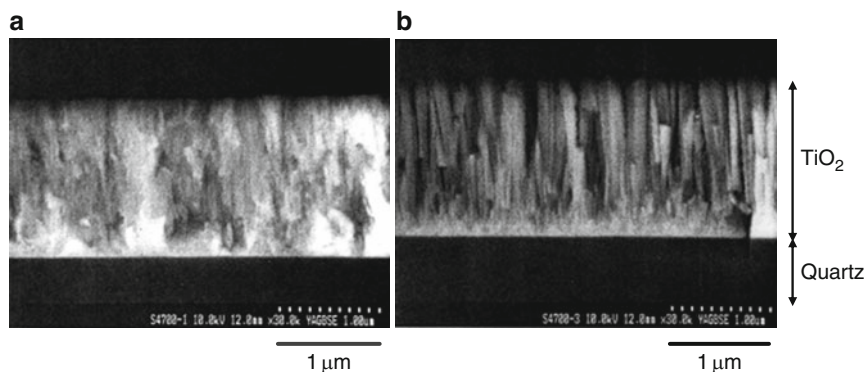


Fig. 9 Cross-sectional SEM images of the TiO₂ thin films prepared at: (a) 473 and (b) 873 K

difference between the UV and visible light-responsive TiO₂ thin films was seen in their cross-sectional views. The TiO₂ thin film prepared at 473 K has a structure in which the nano-sized TiO₂ particles randomly sintered with each other. On the other hand, the thin films prepared at 873 K were found to possess a unique and characteristic structure in which TiO₂ single crystals having a columnar structure (diameter: ca. 100 nm) are aligned in an orderly manner. This unique structure could be observed only when the TiO₂ thin films were prepared at relatively high temperatures by RF-MS deposition. From these observations, the high transparency of TiO₂ thin films was obtained for the denser thin films with less surface roughness. On the other hand, the efficient absorption of visible light was associated with such characteristic structures as the orderly aligned columnar TiO₂ crystals obtained only by RF-MS deposition.

The mechanism behind the efficient absorption of visible light could also be analyzed by the depth profiles of the O/Ti atomic ratio obtained from AES measurements. As shown in Fig. 10, the O/Ti atomic ratio of the thin films prepared at 473 K was constant at 2.0 from surface to deep bulk, showing a stoichiometric TiO₂ composition. On the other hand, the O/Ti atomic ratio of the films prepared at 873 K, which show an efficient absorption in visible light regions, was found to decrease gradually from surface to deep bulk until reaching about 1.933. The declined structure of the O/Ti ratio for the visible light-responsive TiO₂ thin films was confirmed to be stable even after calcination in air at 773 K since the stoichiometric TiO₂ layer at the surface (thickness: ca. 100 nm) can work as a passive layer to protect the bulk parts. Moreover, the declined structure may be closely associated with the modification of the electronic states of the TiO₂ semiconductor, enabling the efficient absorption of visible light. It has been reported that small amounts of oxygen vacancies in the TiO₂ lattice give rise to the distortion of the TiO₂ octahedral units and weaken the Ti–O bonds, resulting in a reduction of the splitting between the bonding and nonbonding levels (Bilmes et al. 2000). Taking these results into consideration, such a characteristic declined composition of the TiO₂ thin films may be the determining factor in modifications

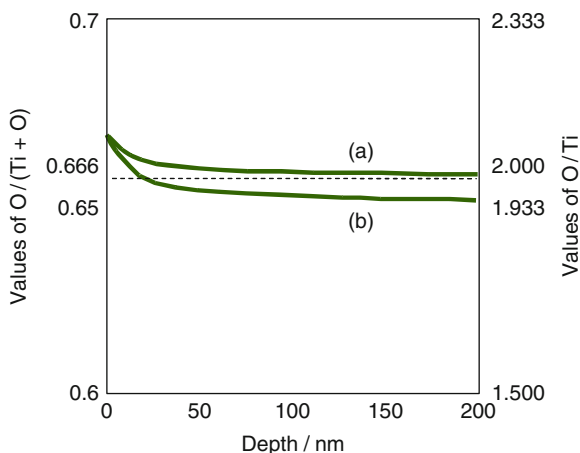


Fig. 10 Depth profiles of the Ti/O ratios determined by AES measurements from the surface to the bulk of the TiO₂ thin films prepared at: (a) 473 and (b) 873 K

of the electronic properties of the TiO₂ semiconductor so that they are able to operate as efficient photocatalysts even under visible light irradiation.

6 Preparation of Crystalline TiO₂ Thin Films on Polycarbonate Substrates at Low Temperatures by a RF-MS Deposition Method

Since the photo-induced superhydrophilicity of TiO₂ surfaces was reported in 1997 (Wang et al. 1997), TiO₂ thin films have attracted interest as effective photofunctional materials. However, for its widespread application, efficient coating methods for the crystalline TiO₂ films on such thermally unstable substrates as plastics, polymers, or textiles are greatly desired (Yamagishi et al. 2003). In this section, the direct coating of transparent TiO₂ thin films of high crystallinity on thermally unstable polycarbonate substrates without any binder layers by a RF-MS deposition method will be presented (Takeuchi et al. 2006).

Some of the TiO₂ thin films deposited at temperatures higher than 373 K easily peeled off due to mechanical scratching. However, the films prepared at temperatures lower than 373 K showed high mechanical stability. Figure 11 shows the XRD patterns of the films prepared on polycarbonate substrates at 353 K with different sputtering gas pressures. The diffraction peaks observed at around 25, 48, and 55° can be attributed to the (101), (200), and (211) phases of the anatase structure, respectively (Takeuchi et al. 2000a, 2001, 2006; Yamashita et al. 1998; Kitano et al. 2005, 2006a). Crystalline TiO₂ thin films could, thus, be successfully prepared on polycarbonate substrates at low temperatures by RF-MS deposition. The UV-vis absorption

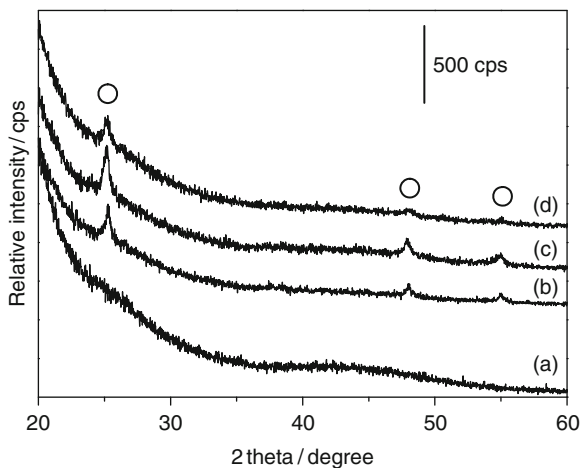


Fig. 11 XRD patterns of: (a) the polycarbonate substrate and (b–d) TiO₂ thin films prepared on the polycarbonate substrates. Sputtering gas pressures: (b) 1.0, (c) 2.0, and (d) 3.0 Pa

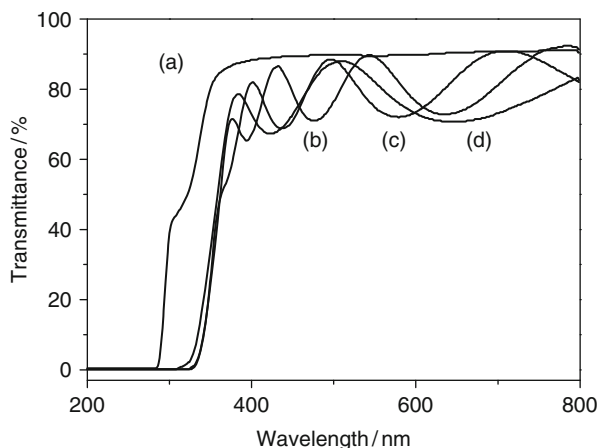


Fig. 12 UV–vis absorption spectra of: (a) the polycarbonate substrate and (b–d) TiO₂ thin films prepared on the polycarbonate substrates. Sputtering gas pressures: (b) 1.0, (c) 2.0, and (d) 3.0 Pa

spectra of these thin films are shown in Fig. 12. The polycarbonate substrates were seen to absorb UV light of wavelength shorter than 300 nm, however, the transmittance in visible light regions was ca. 90%. The films showed an absorption edge at around 370 nm attributed to the bandgap excitation of the TiO₂ semiconductor. A transmittance of ca. 80% and interference fringes in visible light regions indicated that highly uniform TiO₂ thin films could be obtained without any loss in the transparency of the polycarbonate substrates.

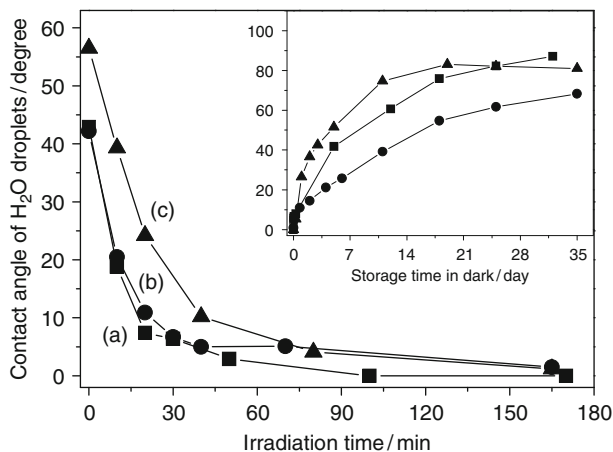


Fig. 13 Time courses for the changes in contact angles of the water droplets on TiO₂ thin films prepared on polycarbonate substrates under both UV light and under dark conditions (*inset*)

Figure 13 shows the surface wettability under UV light (intensity at 360 nm: ca. 1 mW/cm²) over the TiO₂ thin films on polycarbonate substrates. The polycarbonate substrate itself did not show any photo-response for wettability by UV light (data not shown). The films were prepared in a high vacuum chamber and hardly any contamination with impurities occurred so that the initial values for the contact angle of the water droplets before UV light irradiation were small. When the thin films were stored in a clean room under dark conditions for at least 2 weeks, the contact angles increased up to 40–60°. UV light was then irradiated on the films and the water contact angles gradually decreased by continuous UV light irradiation and reached less than 5° (superhydrophilic state) after 2–3 h. The superhydrophilic state of the TiO₂ surfaces slowly disappeared after UV light irradiation was ceased. The inset figure shows the changes in the contact angles under dark conditions. When the films were stored in the dark for 1 month, the contact angles increased up to 70–90° and finally leveled off at around 90–100°. The effect of the UV light intensity on the photo-induced superhydrophilic properties of the films prepared on a polycarbonate substrate is shown in Fig. 14. A decrease in the UV light intensities from 1.0 to 0.05 mW/cm² caused the light irradiation times to be prolonged from 100 to 1,400 min in order to achieve a superhydrophilic state. Although prolonged light irradiation of at least 1 day is necessary, it was notable that the TiO₂ thin films prepared on polycarbonate substrates still showed superhydrophilicity even under a weak UV light intensity of 0.05 mW/cm². Moreover, the films under UV light irradiation for 100–150 h were confirmed to be stable. From these results, the RF-MS deposition method was seen to be one of the most effective ways to prepare crystalline TiO₂ thin film photocatalysts on thermally unstable plastic substrates at low temperatures.

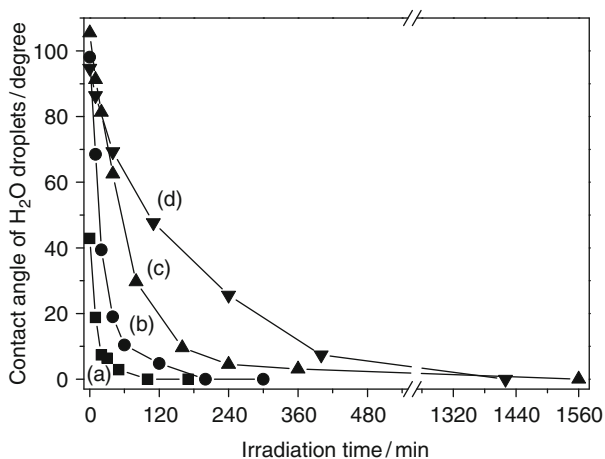


Fig. 14 Effect of UV light intensity on the photo-induced superhydrophilicity of the TiO₂ thin films prepared on polycarbonate substrates. UV light intensities: (a) 1.0, (b) 0.5 (c) 0.2, and (d) 0.05 mW/cm²

References

- Anpo M (ed) (1996) Surface photochemistry. Wiley, London
- Anpo M (1997) Photocatalysis on titanium oxide catalysts—Approaches in achieving highly efficient reactions and realizing the use of visible light. *Catal Surv Jpn* 1:169
- Anpo M (2000a) Utilization of TiO₂ photocatalyst in green chemistry. *Pure Appl Chem* 72:1265
- Anpo M (2000b) Applications of titanium oxide photocatalysts and unique second-generation TiO₂ photocatalysts able to operate under visible light irradiation for the reduction of environmental toxins on a global scale *Stad Surf Sci Catal: Corma et al. (eds.) 12th Inter Congr Catal* 130:157
- Anpo M (2004) Preparation, characterization, and reactivities of highly functional titanium oxide-based photocatalysts able to operate under UV-visible light irradiation: Approaches in realizing high efficiency in the use of visible light. *Bull Chem Soc Jpn* 77:1427
- Anpo M, Takeuchi M (2003) The design and development of highly reactive titanium oxide photocatalysts operating under visible light irradiation. *J Catal* 216:505
- Anpo M, Ichihashi Y, Takeuchi M, Yamashita H (1998). Design of unique titanium oxide photocatalysts by an advanced metal ion-implantation method and photocatalytic reactions under visible light irradiation. *Res Chem Intermed* 24:143
- Bilmes SA, Mandelbaum P, Alvarez F, Victoria NM (2000) Surface and Electronic Structure of Titanium Dioxide Photocatalysts. *J Phys Chem B* 104:9851
- Ertl G, Knözinger H, Weitkamp J (eds.) (1997) Handbook of heterogeneous catalysis. Wiley-VCH, Weinheim
- French HJ, Kulisch W, Kuhr M, Kassing R (1991) Deposition of TiO₂ thin films by plasma-enhanced decomposition of tetraisopropyltitanate. *Thin Solid Films* 201:327
- Fujishima A, Honda K (1972) Electrochemical photolysis of water at a semiconductor electrode. *Nature* 238:37
- Fujishima A, Hashimoto K, Watanabe T (eds.) (1999) TiO₂ photocatalysis fundamentals and applications. BKC, Tokyo
- Heller A (1995) Chemistry and applications of photocatalytic oxidation of thin organic films. *Acc Chem Res* 28:503

- Iino K, Kitano M, Takeuchi M, Matsuoka M, Anpo M (2006) Design and development of second-generation titanium oxide photocatalyst materials operating under visible light irradiation by applying advanced ion-engineering techniques. *Curr Appl Phys* 6:982
- Kamishiro Y, Kinoshita Y, Takaoka Y, Murasawa S (1993) Low temperature preparation of TiO₂ thin films by plasma-enhanced chemical vapor deposition. *J Ceram Soc Jpn* 101(5):514
- Kikuchi H, Kitano M, Takeuchi M, Matsuoka M, Anpo M, Kamat PV (2006) Extending the photoresponse of TiO₂ to the visible light region: Photoelectrochemical behavior of TiO₂ thin films prepared by the radio frequency magnetron sputtering deposition method. *J Phys Chem B* 110:5537
- Kitano M, Takeuchi M, Matsuoka M, Thomas JM, Anpo M (2005) Preparation of Visible Light-responsive TiO₂ Thin Film Photocatalysts by an RF Magnetron Sputtering Deposition Method and Their Photocatalytic Reactivity. *Chem Lett* 34:616
- Kitano M, Tsujimaru K, Anpo M (2006a) Decomposition of water in the separate evolution of hydrogen and oxygen using visible light-responsive TiO₂ thin film photocatalysts: Effect of the work function of the substrates on the yield of the reaction. *Appl Catal A Gen* 314:179
- Kitano M, Funatsu K, Matsuoka M, Ueshima M, Anpo M (2006b) Preparation of nitrogen-substituted TiO₂ thin film photocatalysts by the radio frequency magnetron sputtering deposition method and their photocatalytic reactivity under visible light irradiation. *J Phys Chem B* 110:25266
- Kitano M, Matsuoka M, Ueshima M, Anpo M (2007a) Recent developments in titanium oxide-based photocatalysts. *Appl Catal A Gen* 325:1
- Kitano M, Takeuchi M, Matsuoka M, Thomas JM, Anpo M (2007b) Photocatalytic water splitting using Pt-loaded visible light-responsive TiO₂ thin film photocatalysts. *Catal Today* 120:133
- Kitano M, Kudo T, Matsuoka M, Ueshima M, Anpo M (2007c) Photocatalytic and Photoelectrochemical Properties of Nitrogen-Substituted TiO₂ Thin Films Prepared by an RF Magnetron Sputtering Deposition Method. *Mater Sci Forum* 544:107
- Maruyama T, Arai S (1992) Titanium dioxide thin films prepared by chemical vapor deposition. *Solar Energy Mater Solar Cells* 26:323
- Matsuoka M, Kitano M, Takeuchi M, Anpo M, Thomas JM (2005) Photocatalytic water splitting on visible light-responsive TiO₂ thin films prepared by a RF magnetron sputtering deposition method. *Top Catal* 35:305
- Negishi N, Iyoda T, Hashimoto K, Fujishima A (1995) Preparation of Transparent TiO₂ Thin Film Photocatalyst and Its Photocatalytic Activity. *Chem Lett* 24:841
- Negishi N, Takeuchi K, Ibusuki T (1998) Surface structure of the TiO₂ thin film photocatalyst. *J Mater Sci* 33:5789
- O'Regan B, Grätzel M (1991) A low-cost, high-efficiency solar cell based on dye-sensitized colloidal TiO₂ films. *Nature* 353:737
- Ollis DF, Al-Ekabi H (eds.) (1993) Photocatalytic purification and treatment of water and air. Elsevier, Amsterdam
- Schiavello M (ed.) (1997) Heterogeneous catalysis. Wiley, London
- Serpone N, Pelizzetti E (eds.) (1989) Photocatalysis fundamentals and applications. Wiley, New York
- Siefering KL, Griffin GL (1990) Kinetics of Low-Pressure Chemical Vapor Deposition of TiO₂ from Titanium Tetraisopropoxide. *J Electrochem Soc* 137(3):814
- Takeuchi M, Yamashita H, Matsuoka M, Hirao T, Itoh N, Iwamoto N, Anpo M (2000a) Photocatalytic decomposition of NO under visible light irradiation on the Cr-ion-implanted TiO₂ thin film photocatalyst. *Catal Lett* 67:135
- Takeuchi M, Yamashita H, Matsuoka M, Hirao T, Itoh N, Iwamoto N, Anpo M (2000b) Photocatalytic decomposition of NO on titanium oxide thin film photocatalysts prepared by an ionized cluster beam technique. *Catal Lett* 66:185
- Takeuchi M, Anpo M, Hirao T, Itoh N, Iwamoto N (2001) Preparation of TiO₂ Thin Film Photocatalysts Working under Visible Light Irradiation by Applying a RF Magnetron Sputtering Deposition Method. *Surf Sci Jpn* 22:561

- Takeuchi M, Yamasaki T, Tsujimaru K, Anpo M (2006) Preparation of Crystalline TiO₂ Thin Film Photocatalysts on Polycarbonate Substrates by a RF-magnetron Sputtering Deposition Method. *Chem Lett* 35:904
- Wang R, Hashimoto K, Fujishima A, Chikuni M, Kojima E, Kitamura A, Shimohigoshi M, Watanabe T (1997) Light-induced amphiphilic surfaces. *Nature* 388:431
- Yamagishi M, Kuriki S, Song PK, Shigesato Y (2003) Thin film TiO₂ photocatalyst deposited by reactive magnetron sputtering. *Thin Solid Films* 442:227
- Yamashita H, Honda M, Harada M, Ichihashi Y, Anpo M, Hirao T, Itoh N, Iwamoto N (1998) Preparation of titanium oxide photocatalysts anchored on porous silica glass by a metal ion-implantation method and their photocatalytic reactivities for the degradation of 2-propanol diluted in water. *J Phys Chem B* 102:10707

Part IV
Photocatalytic Reactions
for Environmentally-Harmonious
Applications

Chapter 14

Photo-assisted Mineralization of the Agrochemical Pesticides Oxamyl and Methomyl and the Herbicides Diphenamid and Asulam

Hisao Hidaka, Teruo Kurihara, and Nick Serpone

Abstract Pesticides of the oximecarbamate type, such as Oxamyl and Methomyl, and the aromatic-bearing herbicides, Diphenamid and Asulam, undergo photo-assisted mineralization nearly quantitatively (ca. 90–100% within ~4 h) in aerated UV-illuminated aqueous TiO₂ dispersions. The complex structure of the agrochemicals that bear carbon, nitrogen, and sulfur functions are easily mineralized to CO₂, NH₄⁺ and NO₃⁻ ions, and SO₄²⁻ ions, respectively. Evolution of carbon dioxide has been monitored by gas chromatography and by loss of total organic carbon (TOC). The site and mode of adsorption of these agrochemicals onto the TiO₂ particle surface has been inferred from point charge calculations, whereas the position of attack by reactive oxygen species such as ·OH radicals has been estimated by frontier electron density calculations.

1 Introduction

Advanced oxidation technologies for wastewater treatment have been developed during the last two decades and are now being exploited in various industrial applications (Parsons 2004). Aquatic environments contaminated with difficult-to-biodegrade substances have become the subject of serious global concern. Some of the more promising technologies are the photo-assisted degradation methodologies that involve titanium dioxides photo-activated by Solar UV radiation despite the low content (ca. 3–5%) of the total solar flux. This lower UV irradiance impinges on the overall photon efficiencies. The highly oxidative ·OH

H. Hidaka (✉)

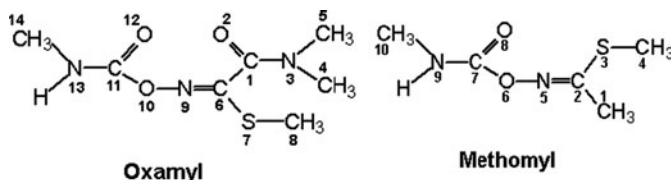
Frontier Research Center for the Global Environment Science, Meisei University,
2-1-1 Hodokubo, Hino, Tokyo 191-8506, Japan
e-mail: hidaka@epfc.meisei-u.ac.jp

and $\cdot\text{OOH}$ radicals photogenerated on the TiO_2 surface by oxidation of water and reduction of oxygen, respectively, through charge separation under UV-irradiation attack the organic substances converting the carbon function into CO_2 gas, the sulfur into SO_4^{2-} ions, and the nitrogen function to NH_4^+ and NO_3^- ions.

Photo-assisted rates of mineralization depend principally on the chemical structure of the agrochemicals examined. Rate-determining factors in the detoxification of most aquatic wastewater contaminants are their solubility in water and their mode of adsorption on the TiO_2 photo-mediator. In comparison to a hydrophilic pollutant, a hydrophobic contaminant exhibits poor adhesive properties toward the hydrophilic TiO_2 mediator, and to the extent that some agrochemical organics bearing complex functions are not commonly water-soluble, their decomposition in aqueous environments in high yields is difficult to achieve within a brief time period. As well, agrochemicals spread in fields tend to persist for relatively long periods of time without any visible decomposition. Many types of highly toxic pesticides and herbicides are typically used to exterminate vermin and other harmful insects. Within this context, the TiO_2 photo-assisted degradations of several agrochemicals such as permethrin (Hidaka et al. 1992a, b), atrazine (Pelizzetti et al. 1990; Pelizzetti et al. 2003), 2,4-dichlorophenoxyacetic acid (Watanabe et al. 2003, 2005), Diphenamid (Rahman et al. 2003), Asulam (Catastini et al. 2002a, b), paraquat (Cantavenera et al. 2006), and imazethapyr commonly used in Brazil (Ishiki et al. 2005) have been examined previously by us (Hidaka et al. 1992a, b; Watanabe et al. 2003, 2005) and by others (Pelizzetti et al. 1990, 2003; Rahman et al. 2003; Catastini et al. 2002a, b; Cantavenera et al. 2006; Ishiki et al. 2005).

Contamination of subsurface waters has recently shown increasing trends. Intake of agrochemicals by human and animals via the food chain and through drinking water, and sea and river waters has become a worrisome issue (FAO and WHO 1985; Cohen et al. 1986; Muszkat et al. 1994). Accordingly, many countries have introduced restrictive legislative regulations (EPA 2002; Dowd et al. 1988) to control and regulate the usage of these agrochemicals toward food safety since such chemicals are too often not easily biodegraded and tend to persist in nature for some time. Indeed, microbial detoxification of waters contaminated at ppm (mg L^{-1}) levels of pollutants tends to be rather difficult owing to the inefficiency of the biodegradation at such low substrate loadings (Muszkat et al. 1995) not to mention that some pollutants may also be toxic to the bacterial microorganisms.

The nitrogen- and sulfur-bearing pesticide Oxamyl is commonly used as an agrochemical in the protection of farm crops, vegetables, tobacco, and chrysanthemum among others, and is also effective in the extermination of eelworms and plant parasites (USDA 2005; Garthwaite et al. 2005). By comparison, the broad spectrum pesticide Methomyl is used (1) as an acaricide to control ticks and spiders, (2) in the foliar treatment of vegetables, fruit and field crops, cotton, and commercial ornamentals, and (3) in and around poultry houses and dairies (USDA 2005; Garthwaite et al. 2005). Note that in the structure for Oxamyl and Methomyl (and others – see below) the numbers identify the atoms for the point charge and electron density calculations.



These two pesticides belong to the class of oximecarbamates widely used to control insect and nematode pests and of which nearly 1,360 metric tons are used by the agricultural sector in the United States alone (Gianessi and Marcelli 2000). Another no less important source of pesticides in the aqueous environment is the disposal of used pesticide bottles and the rinsing of pesticide-spray containers (Malato et al. 2000). Both these carbamates inhibit the activity of the acetylcholinesterase enzyme resulting in the buildup of the neurotransmitter acetylcholine to toxic levels (Hassall 1990). Their acute toxicity ranks amongst the highest of several pesticides, thus generating some environmental concerns since both Oxamyl and Methomyl are highly water-soluble (280 g L^{-1} and 58 g L^{-1} , respectively; Hornsby et al. 1996) and both show low affinity for adsorption onto soils (Gerstl 1984; Cox et al. 1993). This latter property renders these two carbamates highly mobile throughout the soils and aqueous ecosystems, so much so that they have been detected in groundwaters that serve as drinking waters (Kolpin et al. 2000) at concentrations that often surpass recommended thresholds (Kolpin et al. 2000; Zaki et al. 1982; Moye and Miles 1988).

Carbamate pesticides can degrade under anoxic and abiotic conditions via a base-catalyzed elimination process to yield an oxime byproduct, methylamine and carbon dioxide. However, at pHs below 7 the process is extremely slow with half-lives of months to years (Bank and Tyrrell 1984; Chapman and Cole 1982; Harvey and Han 1978; Hegarty and Frost 1973). By contrast, a more rapid degradation occurs in an aqueous anoxic environment (e.g. a soil suspension) containing iron(II) through a two-electron reduction process generating, in addition to the oxime byproduct and methylamine, a nitrile, methanethiol, and carbon dioxide (see Fig. 1) (Strathmann and Stone 2001, 2002a, b; Bromilow et al. 1986; Smelt et al. 1983).

Others have reported the TiO_2 photo-assisted degradation of Oxamyl under direct sunlight using a compound parabolic collector system, with the pesticide being slowly mineralized to CO_2 via various non-identified intermediates subsequent to a postulated cyclization of the carbamate chain and/or ultimate cleavage of the carbamate function (Malato et al. 2000).

Diphenamid is a widely used herbicide for the control of annual broadleaf weeds such as carpetweed, chickweed, knotweed, lambs quarters, pigweed, purslane, and smartweed, as well as annual grasses. In short, it is used for the control of some broad-leaved weeds in cotton, potatoes, sweet potatoes, tomatoes, vegetables, capsicums, okra, soya beans, groundnuts, tobacco, stone fruit, citrus fruit, bush fruit, strawberries, forestry nurseries, and ornamental plants, shrubs, and trees (Elmore et al. 1968). It is also a plant growth regulator and moderately persists in the environment for about 1–3 months (Defelice 1999). Moreover, Diphenamid is

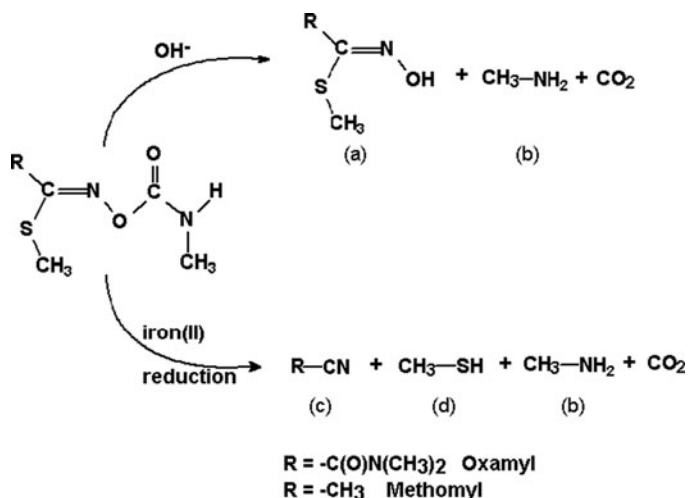
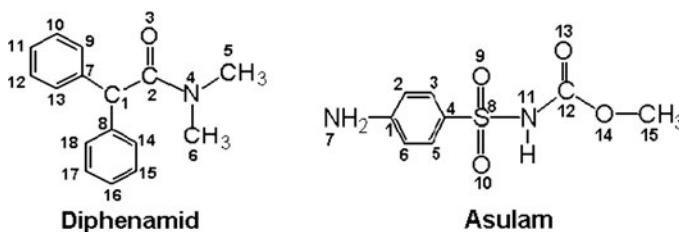


Fig. 1 Scheme illustrating the two pathways (base-catalyzed elimination and 2-electron reduction) in the degradation of the two oxime-carbamate pesticides: (a) oxime by product, (b) methylamine, (c) substituted nitrile, and (d) methanethiol. Adapted from Strathmann and Stone (2001) and from Bromilow et al. (1986)

stable to hydrolysis at pHs 5–9 for about 7–10 days at a temperature relatively higher than ambient (49°C) (Rahman et al. 2003).



The carbamate-type herbicide, Asulam, is toxic to insects and animals, and is largely used as a principal and selective herbicide in the control of bracken (Marrs et al. 1992; Bruff et al. 1995); additional details on the properties and toxicity of Asulam are available elsewhere (The International Programme on Chemical Safety (IPCS) 1996). Suffices to note that, in general, carbamate pesticides attack the nervous conveyance cell and cause abnormal excitement (IPCS 1996). This herbicide degrades photolytically faster in moist soils than in dry soils; the respective half-lives are 98 h and 350 h, respectively (Graebing et al. 2003). The photodegradation of Asulam in aqueous media in the presence of aqua complexes as the photoinducer under sunlight irradiation necessitated from 13 to 14 h for complete degradation to CO_2 ; the principal products formed in the initial stages were parasulfanilic acid, benzoquinone, and traces of hydroquinone (Catastini et al. 2002a, b).

This article addresses the photo-assisted disposal of the pesticides Oxamyl and Methomyl and the herbicides Diphenamid and Asulam in aerated aqueous TiO₂ dispersions under bench-top UV irradiation. We show that the mineralization of these agrochemicals to carbon dioxide is nearly quantitative (ca. 90–100%) within a relatively short time of ca. 4 h subsequent to the UV/TiO₂ treatment.

2 Experimental Section

2.1 Materials

All chemicals were used as received. The pesticide methyl-2-(dimethylamino)-*N*-{[(methyl- amino)carbonyl]oxy}-2-oxoethanimidothioate, referred to as Oxamyl, was supplied by Dr. Ehrenstorfer GmbH, Germany, in highly pure reagent grade form. The oral acute toxicity of Oxamyl LD₅₀(rat) is 2.5 mg kg⁻¹ and LD₅₀(mouse) is 2.3 mg kg⁻¹; additional information on the toxicity of Oxamyl is available elsewhere (Tomar 1997; European Food Safety Authority (EFSA) 2005). This pesticide is highly water-soluble (*pK* = 6.2), available for leaching and is relatively non-persistent in soil with its loss due mainly to decomposition via first-order kinetics degrading to <5% of the parent compound within 1 month of field application. Its reaction rate decreases with increase in concentration (Wagenet et al. 1984).

The pesticide methyl-*N*-{[(methylamino)carbonyl]oxy} ethanimidothioate, known commercially as Methomyl, was supplied by Wako Pure Chem. Co. Ltd. It has an oral acute toxicity of LD₅₀(rat) of 17 mg kg⁻¹ and the LD₅₀(mouse) is 10 mg kg⁻¹ (IPCS 1996). Methomyl is transformed in some greenhouse soils with half-lives of about 3–14 days. Microbial degradation appears to be the major transformation process in soil with CO₂ as the principal end product. However, a lag period of 1–2 weeks may be needed in unacclimatized soils before biodegradation begins. In aquatic ecosystems, hydrolysis half-lives of Methomyl in ethanol/water at pHs 6.0, 7.0, and 8.0 are 54, 38, and 20 weeks, respectively, at 25°C, whereas the hydrolysis half-life in pure water at 25°C is 37.5 weeks (MacCorquodale 2003).

The herbicide *N,N*-dimethyl- α -phenylbenzeneacetamide, also known as Diphenamid, was supplied by Kanto Chem. Co. Inc. It has an oral acute toxicity of LD₅₀ = 685 mg kg⁻¹ for the rat and 600 mg kg⁻¹ for the mouse; for additional details, see also Ref. Cantavenera et al. 2006. The herbicide methyl-[(4-aminophenyl)sulfonyl]-carbamate, commercially named Asulam, was supplied by Wako Pure Chem. Co. Ltd. The latter has an oral acute toxicity LD₅₀(rat) that exceeds 5 g kg⁻¹ and an acute inhalation LD₅₀(rat) that is greater than 5.0 mg kg⁻¹ (Morales et al. 2002).

Titanium dioxide was Degussa P-25 with particle size 20–30 nm assessed by transmission electron microscopy; surface area 53 m² g⁻¹ by BET methods; crystalline form 83% anatase and 17% rutile as determined by X-ray diffraction analysis.

2.2 Photomineralization Procedures

Aqueous solutions of each of the above substrates (0.10 mM; 50 mL; pH 4.5 unless noted otherwise) were placed in a 127-mL Pyrex vessel containing TiO₂ particles (100 mg; loading, 2.0 g L⁻¹) followed by supersonication to obtain uniform dispersions. The latter were subsequently purged with oxygen gas prior to UV irradiation. The TiO₂-containing aqueous dispersions were then illuminated with a 75-W mercury lamp (Toshiba SHL-100UVQ2) that emitted an irradiance of ca. 2.0 mW cm⁻² in the wavelength range 310–400 nm (maximal emission, 360 nm).

2.3 Analytical Procedures

The temporal evolution of CO₂ was assayed with a Shimadzu GC-8AIT gas chromatograph equipped with a TCD detector and a Porapak Q column; helium was the carrier gas. The loss of total organic carbon (TOC) in the dispersion was measured with a Shimadzu TOC-5000A TOC analyzer.

Additional measurements of the temporal degradation of Diphenamid (0.1 mM, 50 mL) were carried out in the presence of 100 mg of TiO₂ at pH 4.5. Opening of the rings during the photodecomposition of the Diphenamid and Asulam was monitored at 206 nm and 262 nm, respectively, with a JASCO V-570 UV–Visible spectrophotometer. The pH indicated in each of the Figures is the initial pH before UV illumination. When the pH of the degraded solution after a fixed time of illumination shifted gradually acidic, the surface charge of TiO₂ changes positively. The number of ·OH radicals which attack an organic substrate is the same as the number of protons formed theoretically.

Figure 2 illustrates the temporal spectral changes in the photodegradation of Diphenamid and Asulam. Formation of NH₄⁺ and NO₃⁻ ions was assayed on a

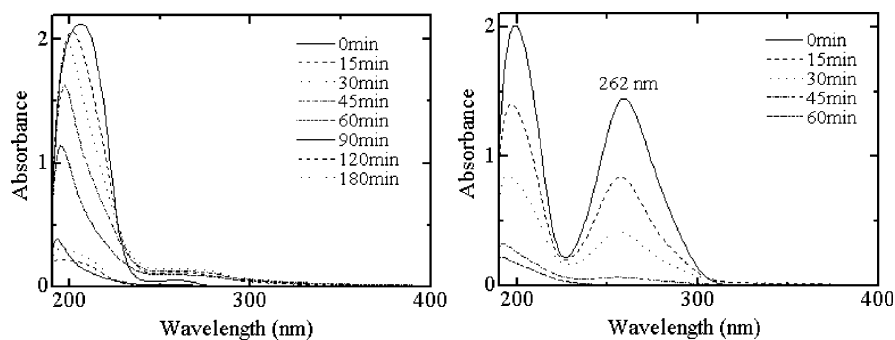


Fig. 2 Temporal spectral changes occurring during the photo-assisted degradation of (a) Diphenamid and (b) Asulam in aqueous TiO₂ dispersions

JASCO high-pressure liquid chromatographic system equipped with a CD-5 conductivity detector and either a Y-521 cationic column or an I-524 anionic column. Changes in the concentration of NH_4^+ ions were monitored with the JASCO ion chromatograph and the Y-521 cationic column; the eluent was nitric acid (4 mM). Nitrate ions were also monitored by ion chromatography with the I-524 anionic column using a mixed solution of phthalic acid (2.5 mM) and tris(hydroxymethyl) aminomethane (2.3 mM) as the eluent.

Fourier transform infrared spectroscopy (FT-IR; KBr method; JASCO spectrophotometer; Model FT/IR-620) was used in attempts to identify some of the intermediate products. Spectra were recorded after a freeze-dry procedure subsequent to removal of the TiO_2 particles from the photodegraded dispersions through filtration and/or centrifugation. Appropriate assignments of the observed IR bands were done according to standard infrared databases (Pouchert 1970; Schrader 1989; Socrates 2001).

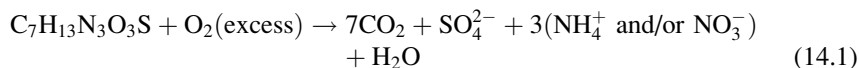
2.4 Point Charge and Electron Density Calculations (Dewar *et al.* 1985; Stewart 1989; Dewar and Yuan 1990; Horikoshi *et al.* 2003)

Molecular orbital calculations were performed by the parametric method 3 (PM3) with application of the Window MOPAC program. All the geometrical parameters for the above substances were calculated using the Broyden–Fletcher–Goldfarb–Shannon algorithm incorporated in the program for optimization, with the minimum energy obtained at the AM1 level. The geometries of the examined agrochemicals in aqueous solution were compared to those obtained in the gas phase by the conductor-like screening model orbital (COSMO) and electrostatic potential (point charge) calculations. The COSMO procedure generated a conducting polygonal surface around the system at van der Waal's distances. Standard values used herein were the number of geometrical segments per atom (NSPA) = 60; the dielectric constant was 78.4 at 25°C (in water). Initial positions of the OH radical attack are deduced from electron densities, whereas possible modes of closest approach of the agrochemical molecules onto the TiO_2 particle surface are inferred from the calculated point charges.

3 Results and Discussion

3.1 Photomineralization

The complete mineralization of Oxamyl, for example, as expressed by (14.1) should produce 35 μmol s of carbon dioxide for an initial concentration of 5 μmol s in the 50-mL dispersion (0.1 mM)



The temporal evolution of CO_2 gas (in % yield) produced in the photo-assisted degradation of the two pesticides and herbicides and monitored by gas chromatography is shown in Fig. 3. In all the cases, formation of carbon dioxide increased with increasing irradiation time attaining approximately 90% mineralization after ca. 4 h of UV illumination.

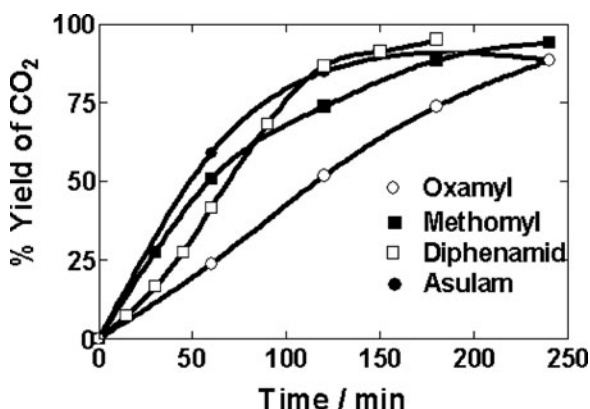


Fig. 3 Temporal CO_2 evolution yield (%) in the photo-assisted mineralization of Oxamyl, Methomyl, Diphenamid, and Asulam; initial concentrations of each, 0.10 mM in 50-mL dispersions (pH 4.5)

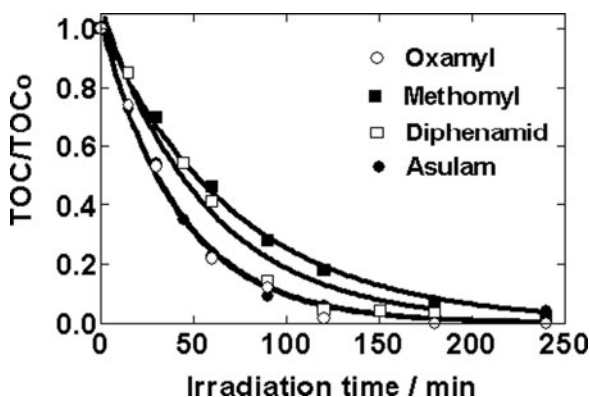


Fig. 4 Normalized temporal decrease of TOC in the photo-assisted degradation of Oxamyl, Methomyl, Diphenamid, and Asulam (pH 4.5). Initial concentrations in carbon content were, respectively, 6.6 ppm, 4.1 ppm, 19.1 ppm, and 9.2 ppm

The comparatively temporal decrease of TOC in the degradation of the two pesticides and the two herbicides is depicted in Fig. 14.4. TOC loss for Oxamyl organic carbon is 100% complete within 4 h into the mineralization process. In all the other cases, TOC loss is also quantitative and followed first-order kinetics with the rates being Diphenamid (19.5 ppm h^{-1}) > Asulam (12.7 ppm h^{-1}) > Oxamyl (9.1 ppm h^{-1}) > Methomyl (3.4 ppm h^{-1}), in reasonable accord with the trend in CO_2 evolution. Note that the slight discrepancies between the extent of CO_2 evolution (Fig. 3) and loss of TOC (Fig. 4) are due to the forms of CO_2 present at the prevailing pH of 4.5 ($\text{CO}_2 \cdot \text{H}_2\text{O} \approx \text{H}_2\text{CO}_3 \approx \text{H}^+ + \text{HCO}_3^-$; $\text{p}K_{\text{a}1} = 6.4$) in the form of small quantities of bicarbonate species during the chromatographic determinations of CO_2 .

3.2 Conversion of N and S Functions

The temporal formation of NH_4^+ , NO_3^- , and SO_4^{2-} ions against UV irradiation time in the photo-assisted mineralization of Oxamyl is shown in Fig. 5. Under acidic conditions (pHs 3.0 and 4.5), the generated amount of NH_4^+ ions was significantly greater than that of NO_3^- ions, which typically showed a lag time before its formation. By contrast, the amount of generated SO_4^{2-} ions was far smaller than expected, particularly at pH 3.0. We suppose that since the surface of TiO_2 catalyst is positively charged, the doubly charged SO_4^{2-} anions may remain adsorbed on the TiO_2 surface, thereby mitigating somewhat the quantity of SO_4^{2-} ion detected in the aqueous bulk solution. By comparison, at pH 4.5 the observed quantity of SO_4^{2-} ions increased while the amount of NH_4^+ ions formed decreased, whereas the amount of NO_3^- ions produced remained nearly constant at both acidic pHs. On the other hand, the quantity of NO_3^- anions formed at the alkaline pH of 11.0 was more significant than the quantity of NH_4^+ ions produced. As well, the amount of sulfate anions produced was more significant the more alkaline the solution bulk becomes, since adsorption is no longer a restrictive factor owing to electrostatic repulsion between the negatively charged TiO_2 surface and the sulfate anions. However, we also cannot preclude that the smaller quantity of ammonium ions observed in alkaline media may be due to a certain quantity of NH_4^+ that is oxidized to NO_3^- ions (Pollema et al. 1992). The stoichiometric sum of both NH_4^+ and NO_3^- ions produced in the photomineralization of Oxamyl (initial concentration, 0.1 mM) bearing three nitrogen atoms should theoretically be 0.30 mM. Experimentally we find the combined total amount of NH_4^+ and NO_3^- ions at pH 3.0 to be 0.297 mM after 4 h of UV illumination of the aqueous TiO_2 dispersion indicating maximal conversion of the N functions within experimental error. At pH 4.5, the $[\text{NH}_4^+ + \text{NO}_3^-]$ sum was 0.28 mM after the 4-h illumination period, whereas in alkaline media (pH 11.0), the sum was ~ 0.24 mM corresponding to about 80% of the expected amount.

The temporal formation of SO_4^{2-} , NH_4^+ , and NO_3^- ions during the photodegradation of Methomyl at pHs 3.0, 7.0, and 11.0 is illustrated in Fig. 6. The same

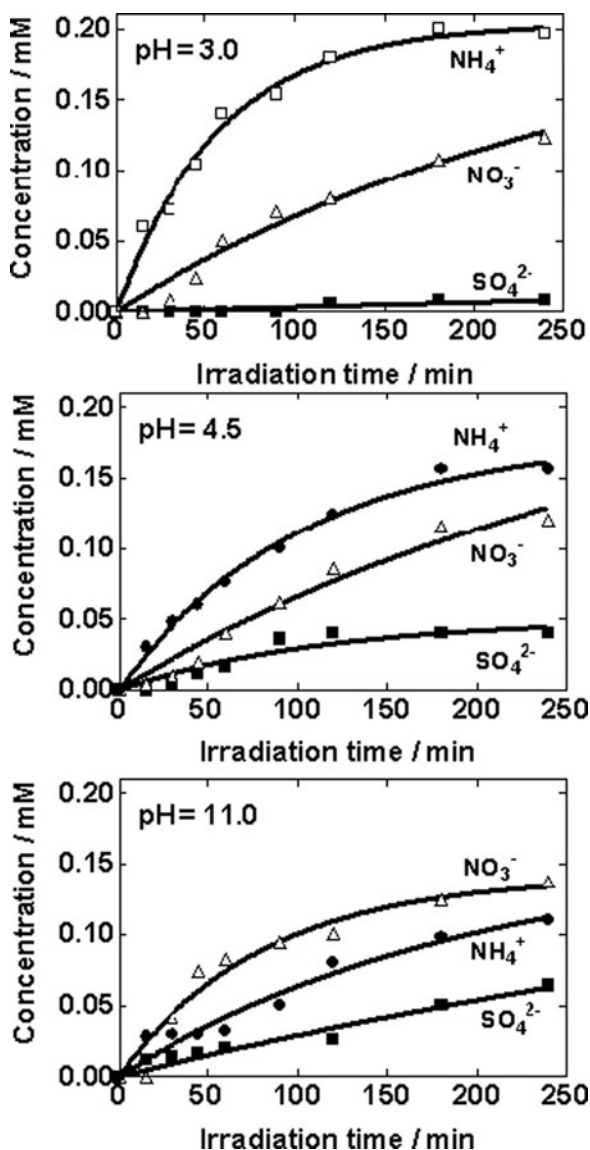


Fig. 5 Formation of SO_4^{2-} , NH_4^+ , and NO_3^- ions in the photodegradation of Oxamyl (initial concentration, 0.1 mM in 50 mL) at pHs 3.0, 4.5, and 11.0

tendency is evident with respect to Methomyl as observed in the case of Oxamyl. That is, the amount of SO_4^{2-} anions produced at pH 3.0 was relatively small owing to electrostatic attraction on the positive TiO_2 surface. By contrast, at pH 11.0 the amount of sulfate anions produced was greater attributable to repulsion between the negatively charged TiO_2 surface and SO_4^{2-} anions. Contrary to Oxamyl, however,

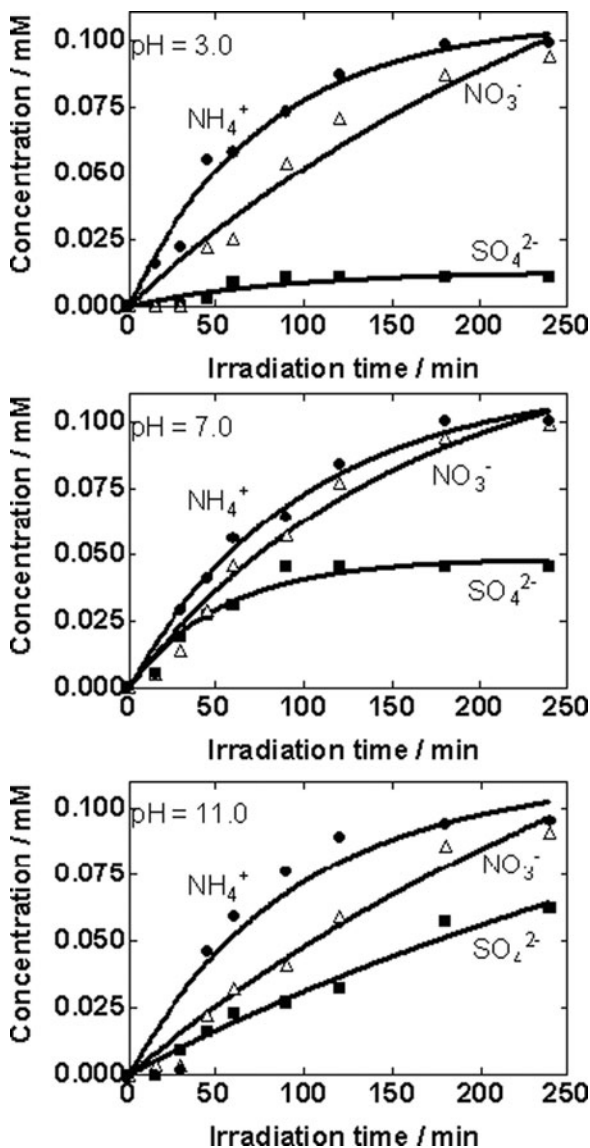


Fig. 6 Formation of SO_4^{2-} , NH_4^+ , and NO_3^- ions in the photodegradation of Methomyl (0.1 mM, 50 mL) at pHs 3.0, 7.0, and 11.0

the quantity of NH_4^+ cations formed during the degradation of Methomyl was always greater than the quantity of NO_3^- ions produced even under alkaline conditions of pH 11.0. The total amount of NH_4^+ and NO_3^- ions formed and expected to be theoretically 0.20 mM for the mineralization of Methomyl (0.1 mM) after 240 min of UV illumination reached 0.19 mM at pH 3.0, 0.20 mM at pH 7.0, and 0.19 mM at pH 11.0.

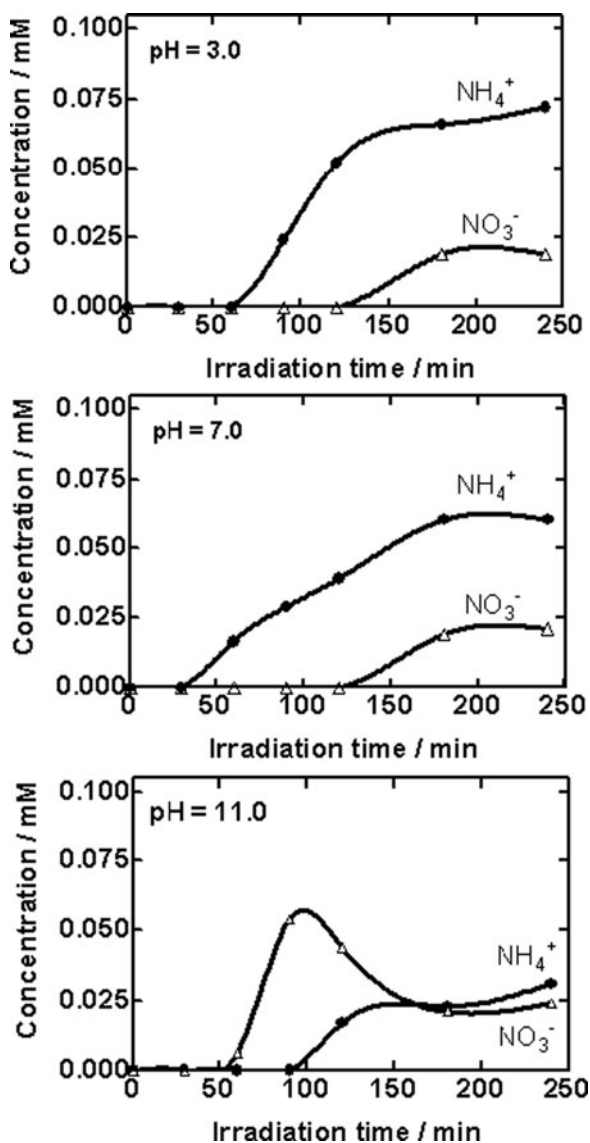


Fig. 7 Formation of NH_4^+ and NO_3^- anions during the photo-assisted degradation of Diphenamid (0.1 mM, 50 mL) at pHs 3.0, 7.0, and 11.0

The temporal evolution of ammonium and nitrate ions produced during the photo-assisted transformation of the nitrogen functions at pHs 3.0 and 7.0 in the Diphenamid structure is depicted in Fig. 7. After ca. 4 h into the process, approximately 19% of the nitrogen was converted into NO_3^- ions and ca. 72% into NH_4^+

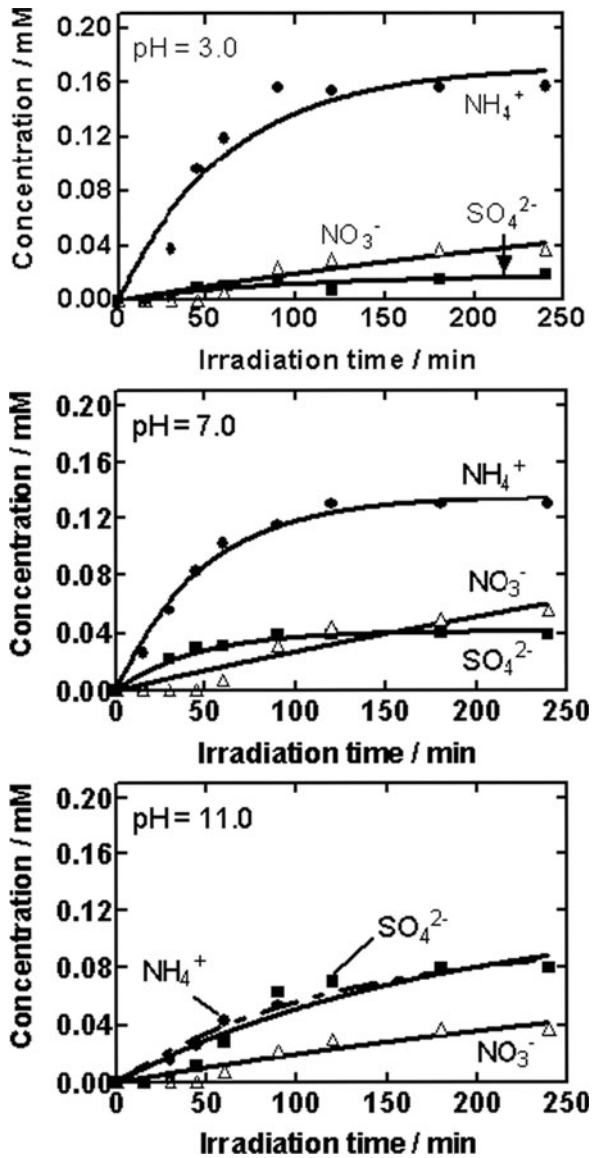


Fig. 8 Formation of SO_4^{2-} , NH_4^+ , and NO_3^- ions in the photo-assisted degradation of Asulam (0.1 mM, 50 mL) at pHs 3.0, 7.0, and 11.0

ions, giving a total of 91% at pH 3.0 or about 0.091 mM against a theoretical estimate of 0.10 mM. At pH 7.0, approximately 21% of the N function was transformed into NO_3^- ions and ca. 60% into NH_4^+ ions for a total of 81% or

0.081 mM. The remaining nitrogen was probably converted to primary and/or secondary amines, although they were not identified. At pH 11.0, both NH_4^+ and NO_3^- ions were also produced under such alkaline aqueous conditions.

Formation of SO_4^{2-} , NH_4^+ , and NO_3^- ions in the photodegradation of Asulam at pHs 3.0, 7.0, and 11.0 is depicted in Fig. 8.

Examining the pH dependence of the degradation of Asulam after 4 h into the process, the amount of NH_4^+ ions formed decreased in the order: pH 3.0 (0.16 mM) > pH 7.0 (0.13 mM) > pH 11.0 (0.080 mM). By contrast, the quantity of NO_3^- ions produced varied in the order: pH 3.0 (0.037 mM) > pH 7.0 (0.054 mM) < pH 11.0 (0.037 mM). The total sum of both NH_4^+ and NO_3^- ions produced was: pH 3.0 (0.19 mM) \geq pH 7.0 (0.18 mM) > pH 11.0 (0.12 mM), against the expected 0.20 mM. With respect to the quantity of SO_4^{2-} anions generated, a larger amount was produced in alkaline media (pH 11.0; 0.080 mM) than in neutral (pH 7.0; 0.039 mM) or acidic media (pH 3.0; 0.019 mM). Again it is tempting to attribute the greater quantity in alkaline media to electrostatic desorption (or repulsion) of SO_4^{2-} anions from the negatively charged TiO_2 surface at pH 11.0 than is the case in acidic media where the particle surface is positively charged.

Table 1 summarizes the dynamics of the photomineralization of the four substrates in terms of rates of evolution of carbon dioxide and conversion of the N and S functions into NH_4^+ and NO_3^- , and SO_4^{2-} anions, respectively, at three different pHs. The rates of formation of CO_2 varied in the order: Diphenamid > Asulam > Methomyl \geq Oxamyl, indicating that mineralization of the herbicides possessing an aromatic-ring is faster than for the non-aromatic pesticides. Formation of nitrate ions often necessitated a lag time before its formation could be detected, and was particularly significant in the degradation of Diphenamid and Asulam. Regardless, conversion of the N and S functions followed the first-order kinetics. A glance at the first-order rates shows that reduction of the N function predominates in acidic media, at least for Oxamyl, Diphenamid, and Asulam contrary to Methomyl for which NH_4^+ ion formation appears to be faster in alkaline media. By contrast, oxidation of N to give nitrate ions tends to predominate in alkaline media. Transformation of the S function appears best carried out at near neutral conditions according to the dynamics displayed in Table 1.

3.3 Identification of Some Intermediates by FTIR

The temporal changes observed in the infrared (FTIR) spectral patterns in the 400–1,800 cm^{-1} wavenumber region for the degraded products of Oxamyl are illustrated in Fig. 9.

The IR spectrum of Oxamyl has two strong characteristic bands at 1,736 cm^{-1} , one of which is attributable to the ketone $\text{C}=\text{O}$ stretching vibration and the other at 1,716 cm^{-1} is assigned to the ester $-\text{O}-\text{C}=\text{O}$ carbonyl stretching mode. This initial absorption peak of the ester at 1,716 cm^{-1} disappeared after 1 h of UV illumination,

Table 1 Summary of the dynamics of CO₂ evolution and formation of NH₄⁺, NO₃⁻, and SO₄²⁻ ions during the photo-assisted degradation of the substrates examined

Kinetics	Oxamyl			Methomyl			Diphenamid			Asulam		
	Lag (min)	R or k	pH	Lag (min)	k	pH	Lag (min)	k	pH	Lag (min)	k	pH
R _{CO₂} (μmol h ⁻¹)	-	14.3	4.5	-	17.3	4.5	-	54.7	4.5	-	35.0	4.5
k _{NH₄⁺} (h ⁻¹)	0	1.03	3.0	0	0.78	3.0	60	0.96	3.0	15	0.96	3.0
	0	0.58	4.5	0	0.60	7.0	30	0.51	7.0	0	1.20	7.0
	0	0.30	11.0	15	1.14	11.0	90	-	11.0	15	0.50	11.0
k _{NO₃⁻} (h ⁻¹)	15	0.22	3.0	30	0.20	3.0	120	1.26	3.0	45	0.12	3.0
	0	0.19	4.5	0	0.38	7.0	120	1.26	7.0	45	0.060	7.0
	15	0.74	11.0	0	0.41	11.0	30	-	11.0	45	0.11	11.0
k _{SO₄²⁻} (h ⁻¹)	90	0.0078	3.0	30	0.67	3.0	-	-	-	15	0.66	3.0
	15	0.51	4.5	0	1.09	7.0	-	-	-	15	1.32	7.0
	0	0.092	11.0	15	0.37	11.0	-	-	-	15	0.33	11.0

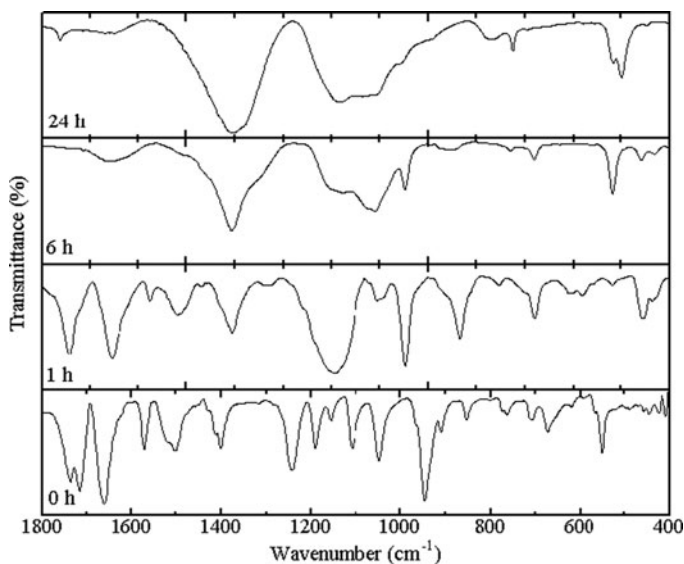


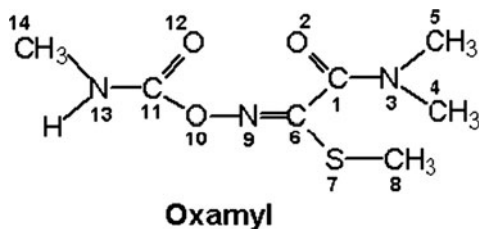
Fig. 9 Temporal variations in the FT-IR spectral patterns during the photodegradative process for Oxamyl spanning a 24-h period. Initial concentration was 1.0 mM and thus required longer irradiation times for the degradation

whereas the ketone carbonyl signal still remained strong. It would appear therefore that the ester group in Oxamyl can be cleaved more easily than the ketone carbonyl. The secondary $-\text{NH}-\text{CH}_3$ and tertiary $-\text{N}=(\text{CH}_3)_2$ amines in Oxamyl have a strong intensity band in the neighborhood of $3,300\text{ cm}^{-1}$ (not shown) that is attributable to $\text{N}-\text{H}$ stretching vibrations. After UV illumination for more than 1 h, this broad band broadened even more and spanned the range $3,000\text{--}3,500\text{ cm}^{-1}$, which suggests an increase in the extent of $\text{O}-\text{H}$ group stretching vibrations in the photooxidation of Oxamyl. Although the $\text{S}-\text{CH}_3$ group in Oxamyl can be mineralized to SO_4^{2-} ions, the intermediate product $\text{CH}_3\text{SO}_3\text{H}$ was also identified by IR spectroscopy. A strong absorption band at $1,662\text{ cm}^{-1}$ was observed after 1 h of irradiation and is attributed to the tertiary amide group in Oxamyl. The peak intensity of the $1,667\text{ cm}^{-1}$ band showed a remarkable decrease.

The strong broad band at $1,405\text{ cm}^{-1}$ still present even after the 24-h irradiation period is assigned to the $-\text{N}<(\text{CH}_3)_2$ group, indicating the presence of some dimethylamine derivative.

3.4 Point Charges and Electron Densities

The calculated point charges and electron densities for all non-hydrogen atoms in both the gas phase and in the presence of water molecules for Oxamyl, Methomyl, Diphenamid, and Asulam are reported in Tables 2–5, respectively.

Table 2 Molecular orbital calculation of electron densities and point charges for Oxamyl

Atom no	Type	Point charge		Electron density	
		Gas	Water	Gas	Water
1	C	0.3455	0.3754	3.6545	3.6246
2	O	-0.3449	-0.5227	6.3449	6.5227
3	N	-0.3178	-0.2616	5.3178	5.2616
4	C	-0.0829	-0.1051	4.0829	4.1051
5	C	-0.0799	-0.1123	4.0799	4.1123
6	C	-0.2476	-0.2281	4.2476	4.2281
7	S	0.2931	0.2366	5.7069	5.7634
8	C	-0.3877	-0.3856	4.3877	4.3855
9	N	-0.0472	-0.0582	5.0473	5.0582
10	O	-0.1882	-0.2237	6.1882	6.223
11	C	0.4089	0.4780	3.5911	3.522
12	O	-0.3325	-0.5454	6.3325	6.5454
13	N	-0.3647	-0.3107	5.3647	5.3106
14	C	-0.0728	-0.0961	4.0727	4.0961

As noted earlier, the atoms that approach most closely the positively charged TiO_2 particle surface will be those with the greatest negative point charge, which in the case of Oxamyl are the O^2 and O^{12} carbonyl oxygens; for Methomyl the largest negative point charge rests on the O^8 carbonyl oxygen, whereas for Diphenamid it lies on the O^3 carbonyl oxygen. By contrast, in the Asumal structure the largest negative point charge lies on the two sulfonyl oxygens O^9 and O^{10} followed by the phenyl C^4 carbon. What is also notable in these calculated point charges is that the negative charge on the atoms noted above is remarkably made more negative in water than they are in the gas phase. Accordingly, these will be the atoms that approach the particle surface in acidic media when the surface is positively charged. In alkaline media where the particle surface is negatively charged, the atoms that will approach most closely the surface are expected to be the corresponding carbonyl carbons in Oxamyl, Methomyl and Diphenamid, and the sulfonyl sulfur in the case of Asumal all of which bear the largest positive point charge.

More important, however, in TiO_2 photo-assisted oxidations will be the positions with the greatest electron density that will be most significant, as these sites are the ones most likely to be the points of attack by the photogenerated OH radicals. Evidently from Tables 2–5, these sites would appear to be the same

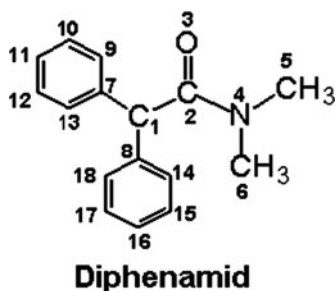
Table 3 Molecular orbital calculation of electron densities and point charges for Methomyl

Methomyl

Atom no	Type	Point charge		Electron density	
		Gas	Water	Gas	Water
1	C	-0.1723	-0.2169	4.1723	4.2169
2	C	-0.1935	-0.1277	4.1935	4.1277
3	S	0.2172	0.2237	5.7828	5.7763
4	C	-0.3645	-0.3954	4.3645	4.3954
5	N	-0.0899	-0.1685	5.0899	5.1684
6	O	-0.2099	-0.2446	6.2099	6.2446
7	C	0.4130	0.4284	3.5870	3.5716
8	O	-0.3493	-0.5374	6.3493	6.5374
9	N	-0.3655	-0.3021	5.3655	5.3020
10	C	-0.0711	-0.1053	4.0711	4.1053

oxygen atoms that bore the largest negative point charges. However, it is more likely that the sites for $\cdot\text{OH}$ radical attack be the atoms adjacent to these oxygens, namely the N^3 , N^9 , and N^{13} nitrogens, and the sulfur atom S^7 in Oxamyl, in the latter case yielding methylsulfonic acid as an intermediate and ultimately SO_4^{2-} ions. In Methomyl they are the nitrogens N^5 and N^9 as well as the S^3 sulfur atom again producing $\text{CH}_3\text{SO}_3\text{H}$ and ultimately sulfate anions. Attack on the nitrogens begins the path toward formation of nitrate and ammonium ions through what would be, no doubt, a complex mechanism.

In the herbicide Diphenamid, the most probable position of $\cdot\text{OH}$ radical attack should be the N^4 atom to yield a dimethylhydroxyl amine and diphenylacetic acid as the first two possible intermediates toward mineralization. Note that we made no attempt in this study to identify the intermediates photogenerated during the mineralization process as this was not the present goal. The work of Rahman and coworkers (2003) on the photodegradation of Diphenamid identified no less than five intermediates (I–V) under conditions that were not very dissimilar from the ones used herein. Formation of these byproducts was suggested to take place by attachment of an $\cdot\text{OH}$ radical at the carbonyl C^2 with loss of methylamine yielding species **I**, followed by further attack by the reactive oxygen species $\cdot\text{OH}$ and/or $\cdot\text{OOH}$ radicals producing intermediate **II**, and subsequent loss of benzene giving species **III**. By contrast, intermediate **IV** was derived from an oxidative process involving electron transfer to either the $\cdot\text{OH}$ and/or $\cdot\text{OOH}$ radicals or to the valence band holes (that is, direct hole oxidation), whereas species **V** was formed by $\cdot\text{OH}$ radical abstraction of the α -hydrogen at the C^1 position in the Diphenamid structure (see Table 4).

Table 4 Molecular orbital calculation of electron densities and point charges for Diphenamid

Atom no	Type	Point charge		Electron density	
		Gas	Water	Gas	Water
1	C	-0.9641	-0.08260	4.0015	4.0055
2	C	0.6436	0.6793	3.7365	3.6681
3	O	-0.3582	-0.5573	6.3562	6.5593
4	N	-0.2842	-0.2237	5.0692	5.0246
5	C	-0.2233	-0.2604	4.0750	4.0930
6	C	-0.0688	-0.0775	4.0872	4.1094
7	C	0.4962	0.3229	4.0823	4.0956
8	C	0.3222	0.2517	4.0765	4.1024
9	C	-0.3265	-0.2756	4.1019	4.1166
10	C	-0.1285	-0.2009	4.1028	4.1277
11	C	-0.1851	-0.1695	4.0974	4.1222
12	C	-0.0888	-0.1896	4.0977	4.1277
13	C	-0.3912	-0.3078	4.0890	4.1294
14	C	-0.2673	-0.3256	4.0856	4.1251
15	C	-0.1446	-0.1318	4.0995	4.1234
16	C	-0.1401	-0.2034	4.0972	4.1196
17	C	-0.1737	-0.1817	4.1043	4.1265
18	C	-0.2229	-0.1985	4.0959	4.1103

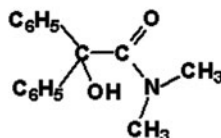
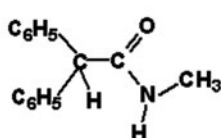
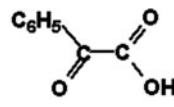
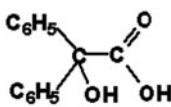
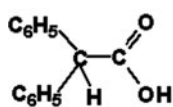
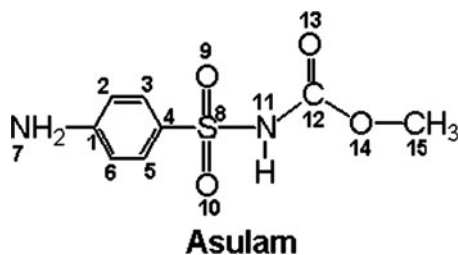


Table 5 Molecular orbital calculations of electron densities and point charges for Asulam

Atom no	Type	Point charge		Electron density	
		Gas	Water	Gas	Water
1	C	0.1771	0.2204	3.8229	3.7796
2	C	-0.2449	-0.2984	4.2450	4.2984
3	C	0.0406	0.0186	3.9594	3.9814
4	C	-0.9341	-1.0274	4.9341	5.0274
5	C	0.0406	0.0664	3.9594	3.9336
6	C	-0.2449	-0.3276	4.2450	4.3276
7	N	-0.3666	-0.3130	5.3666	5.3130
8	S	2.887	3.0271	3.1128	2.9729
9	O	-0.9193	-1.0875	6.9193	7.0875
10	O	-0.9194	-1.0842	6.9194	7.0842
11	N	-0.8245	-0.7958	5.8245	5.7958
12	C	0.4141	0.5122	3.5859	3.4878
13	O	-0.3635	-0.5279	6.3635	6.5279
14	O	-0.2796	-0.2905	6.2796	6.2905
15	C	-0.0534	-0.0699	4.0534	4.0699

Asulam possesses two pK_{as} of 1.3 and 4.1 (Catastini et al. 2002b) so that at pH 3.0 it exists in its neutral form, whereas at pH 7.0 it exists in its deprotonated form at the N¹¹ position, thereby increasing the electronic density at this N atom. In the same reasoning as above then, in the case of Asulam, \cdot OH radical attack should occur at N¹¹ and at the phenyl C⁴ positions to give a sulfonic acid and an aminophenol. The intermediates identified by Catastini and coworkers (1992b) were the parasulfanic acid and benzoquinone with traces of hydroquinone. The latter two were likely the result of photooxidation of the aminophenol known to degrade fairly rapidly under conditions somewhat similar to those used here (Serpone et al. 1998).

4 Concluding Remarks

This study examined the quantitative TiO₂ photo-assisted mineralization of two widely used pesticides and herbicides as evidenced by the evolution of carbon dioxide and by the loss of total organic carbon in aqueous dispersions under acidic

(pH 3.0), neutral (pH 7.0), and alkaline (pH 11.0) conditions. Conversion of the N functions into ammonium ions (or ammonia) appears to predominate at $\text{pH} \leq 7$, whereas formation of nitrate ions seems dominant in alkaline media. Nonetheless, the conversion is also nearly quantitative. The S function is transformed into SO_4^{2-} ions, the quantity of which increased toward more alkaline conditions.

Acknowledgments Our work in Tokyo is sponsored by the Ministry of Education, Culture, Sports, Science and Technology of Japan (Grand-in-Aid for Scientific Research (c) No. 17550145 to H.H.), whereas the research in Pavia has been supported by a grant from the Ministero dell'Istruzione, dell'Università e della Ricerca (MIUR-Roma; to N.S.). We are grateful to Ms. T. Ohno (Josai University) for the molecular orbital simulation as well as to Miss M. Itou, Miss R. Terayama, and Dr. T. Koike (Meisei University) for technical assistance.

References

- Bank S, Tyrell RJ (1984) Kinetics and mechanism of alkaline and acidic hydrolysis of aldicarb. *J Agric Food Chem* 32:1223–1232
- Bromilow RH, Briggs GG, Williams MR, Smelt JH, Tuinstra LGMT, Traag WA (1986) The role of ferrous ions in the rapid degradation of oxamyl, methomyl and aldicarb in anaerobic soils. *Pestic Sci* 17:535–547
- Bruff SA, Griffin JL, Richard EP (1995) Influence of rainfree period after asulam application on johnsongrass (*Sorghum halepense*) control. *Weed Technol* 9:316–320
- Cantavenera MJ, Catanzaro I, Loddo V, Palmisano L, Sciandrello G (2007) Photocatalytic degradation of paraquat and genotoxicity of its intermediate products. *J Photochem Photobiol A: Chem*, 185: 277–282
- Catastini C, Sarakha M, Mailhot G (2002a) Asulam in aqueous solutions: fate and removal under solar irradiation. *Int J Environ Anal Chem* 82:591–600
- Catastini C, Mailhot G, Malato S, Sarakha M (2002b) Iron (III) aqua-complexes as catalysts for pesticides mineralisation by sunlight irradiation. Proceedings workshop 2002, Plataforma Solar de Almeria, Spain
- Chapman RA, Cole CM (1982) Observations on the influence of water and soil pH on the persistence of insecticides. *J Environ Sci Health B* 17:487–504
- Cohen ZZ, Eiden C, Lober MN (1986) Evaluation of pesticide in ground water. In: Gerner WY (ed) American Chemical Society, Washington, D.C., ACS Symp. Ser. 315, 170–196
- Cox L, Hermosyn MC, Cornejo J (1993) Adsorption of methomyl by soils of Southern Spain and soil components. *Chemosphere* 27:837–849
- Defelice M (1999) Introduction and history of cell division inhibitor herbicides. *Crops insights. Pioneer Hi-Bred International Inc.* 9, No. 15
- Dewar MJS, Zoebisch EG, Healy EF, Stewart JJP (1985) Development and use of quantum mechanical molecular models. 76. AM1: a new general purpose quantum mechanical molecular model. *J Am Chem Soc* 107:3902–3909
- Dewar MJS, Yuan Y-C (1990) AM1 parameters for sulfur. *Inorg Chem* 29:3881–3890
- Dowd RM, Anderson MP, Johnson MI (1988) Ground water monitoring geophysical methods. In: Proceedings of the 2nd National Outdoor Action Conference on aquifer restoration. National Water Well Association, Dublin, OH, pp 1365–1379
- Elmore CL, Humphrey WA, Kretschum T (1968) Preemergence weed control in ground cover plantings. *California Turfgrass Cult* 18:9–10

- European Food Safety Authority (EFSA) (2005) Conclusion regarding the peer review of the pesticide risk assessment of the active substance oxamyl. EFSA Sci Rep 26:1–78
- Food and Agriculture Organization of the United Nations (FAO) and the World Health Organization (WHO) (1985) Pesticide residues in food – 1983. Data and recommendations of the joint meeting of the FAO Panel of Experts on Pesticide Residues in Food and the Environment and the WHO Expert Group on Pesticide Residues, Geneva, 5–14 December 1983; <http://www.inchem.org/documents/jmpr/jmpmono/v83pr33.htm>
- Garthwaite DG, Thomas MR, Anderson H, Stoddart H (2005) Pesticide usage survey report 202 Arable Crops in Great Britain 2004. Department for Environment, Food and Rural Affairs and the Scottish Executive Environment and Rural Affairs Dept. Central Science Laboratory, York, UK; see also, <http://www.csl.gov.uk/science/organ/pvm/puskm/arable2004.pdf>
- Gerstl Z (1984) Adsorption, decomposition and movement of oxamyl in soil. Pestic Sci 15:9–17
- Gianessi LP, Marcelli MB (2000) Pesticide use in U.S. Crop production: 1997. National summary report. National Center for Food and Agricultural Policy, Washington, DC
- Graebing P, Frank MP, Chib JS (2003) Soil photolysis of herbicides in a moisture- and temperature-controlled environment. J Agric Food Chem 51:4331–4337
- Harvey J, Han JCY (1978) Decomposition of oxamyl in soil and water. J Agric Food Chem 26:536–541
- Hassall KA (1990) The biochemistry and uses of pesticides, 2nd edn. VCH, New York
- Hegarty AF, Frost LN (1973) Elimination-addition mechanism for the hydrolysis of carbamates. Trapping of an isocyanate intermediate by an o-amino-group. J Chem Soc Perkin Trans 2:1719–1728
- Hidaka H, Nohara K, Zhao J, Serpone N, Pelizzetti E (1992a) Photo-oxidative degradation of the pesticide permethrin catalysed by irradiated TiO₂ semiconductor slurries in aqueous media. J Photochem Photobiol A: Chem 64:247–257
- Hidaka H, Jou H, Nohara K, Zhao J (1992b) Photocatalytic degradation of the hydrophobic pesticide permethrin in fluoro surfactant/TiO₂ aqueous dispersions. Chemosphere 25:1589–1598
- Horikoshi S, Hidaka H, Serpone N (2003) Environmental remediation by an integrated microwave/UV-illumination technique: IV. Non-thermal effects in the microwave-assisted degradation of 2, 4-dichlorophenoxyacetic acid in UV-irradiated TiO₂/H₂O dispersions. J Photochem Photobiol A: Chem 159:289–300
- Hornsby AG, Wauchope RD, Herner AE (1996) Pesticide properties in the environment. Springer, New York
- Ishiki RR, Ishiki HM, Takashima K (2005) Photocatalytic degradation of Imazetha-pyr herbicide at TiO₂/H₂O interface. Chemosphere 58:1461–1469
- Kolpin DW, Barbash JE, Gilliom RJ (2000) Pesticides in ground water of the United States, 1992–1996. Ground Water 38:858–863
- MacCorquodale DS (2003) Chemical fact sheet: methomyl. Spectrum Laboratories Inc. Georgia; <http://www.speclab.com/compound/c1675277.htm>
- Malato S, Blanco J, Richter C, Fernandez P, Maldonado MI (2000) Solar photocatalytic mineralization of commercial pesticides: oxamyl. Sol Energy Mater Sol Cells 64:1–14
- Marrs RH, Frost AJ, Plant RA, Lunnis P (1992) Aerial applications of asulam: a bioassay technique for assessing buffer zones to protect sensitive sites in upland Britain. Biol Conserv 59:19–23
- Morales JJ, Liccione J, O’Keef B (2002) Asulam. HED human health assessment for the Tolerance Reassessment Eligibility Decision (TRED). Chemical No. 106901/02. No MRID#. DP Barcode No. D276505. Office of Prevention, Pesticides and Toxic Substances, United States Environmental Protection Agency (EPA); http://www.epa.gov/oppsrrd1/REDS/asulam_tred.pdf
- Moye HA, Miles CJ (1988) Aldicarb contamination of groundwater. Rev Environ Contam Toxicol 105:99–146

- Muszkat I, Raucher D, Magaritz M, Romen D (1994) Groundwater contamination by organic pollutants. In: Zoller U (ed) Ground water contamination and control. Marcel Dekker, New York, pp 257–271
- Muszkat L, Bir L, Feigelson L (1995) Solar photocatalytic mineralization of pesticides in polluted waters. *J Photochem Photobiol A: Chem* 87:85–88
- Parsons S (2004) Advanced oxidation processes for water and wastewater treatment. IWA Publishing Ltd, London
- Pelizzetti E, Mauriono V, Minero C, Carlin V, Pramauro E, Zerbinati O, Tosato ML (1990) Photocatalytic degradation of atrazine and other s-triazine herbicides. *Environ Sci Technol* 24:1559–1565
- Pelizzetti E, Minero C, Piccinini P, Vincenti M (2003) Phototransformations of nitrogen containing organic compounds over irradiated semiconductor metal oxides: nitrobenzene and atrazine over TiO₂ and ZnO. *Coord Chem Rev* 125:183–193
- Pollema CH, Milosavljević EB, Hendrix JL, Solujić L, Nelson JH (1992) Photocatalytic oxidation of aqueous ammonia (ammonium ion) to nitrite or nitrate at titanium dioxide particles. *Monatsh Chem* 123:333–339
- Pouchert CJ (1970) The aldrich library of infrared spectra. The Aldrich Chemical Co. Inc
- Rahman MA, Muneer M, Bahnemann D (2003) Photocatalyzed degradation of a herbicide derivative, diphenamid in aqueous suspension of titanium dioxide. *J Adv Oxid Technol* 6:100–108
- Schrader B (1989) Raman/infrared atlas of organic compounds, 2nd edn. VCH Publishers, New York
- Serpone N, Calza P, Salinaro A, Cai L, Emeline A, Hidaka H, Horikoshi S, Pelizzetti E (1998) What becomes of nitrogen in the photoelectrochemical and photocatalyzed mineralization of N-containing substances at titania/water interfaces? Proceedings of the conference of the electrochemical society. 97-20, pp 301–320
- Smelt JH, Dekker A, Leistra M, Houx NWH (1983) Conversion of four carbamoyloximes in soil samples from above and below the soil water table. *Pestic Sci* 14:173–181
- Socrates G (2001) Infrared and Raman characteristic group frequencies, 3rd edn. Wiley, New York
- Stewart JJP (1989) Optimization of parameters for semiempirical methods. I. Method *J Comp Chem* 10:209–220
- Strathmann TJ, Stone AT (2001) Reduction of the carbamate pesticides oxamyl and methomyl by dissolved Fe^{II} and Cu^I. *Environ Sci Technol* 35:2461–2469
- Strathmann TJ, Stone AT (2002a) Reduction of the pesticides oxamyl and methomyl by Fe^{II}: effect of pH and inorganic ligands. *Environ Sci Technol* 36:653–661
- Strathmann TJ, Stone AT (2002b) Reduction of oxamyl and related pesticides by Fe^{II}: influence of organic ligands and natural organic matter. *Environ Sci Technol* 36:5172–5183
- The International Programme on Chemical Safety (IPCS) (1996) Environmental health criteria 178 methomyl. World Health Organization, Geneva; see <http://www.inchem.org/documents/ehc/ehc/ehc178.htm>
- Tomar R (1997) Public health goal for OXAMYL in drinking water. Pesticide and environmental toxicology section, Office of Environmental Health Hazard Assessment (OEHHA), California Environmental Protection Agency (Cal/EPA); See also http://www.oehha.ca.gov/water/phg/pdf/oxam2_c.pdf#search='Oxamyl'
- United States Department of Agriculture (USDA) (2005) Agricultural chemical usage – 2004 restricted use summary. see also <http://usda.mannlib.cornell.edu/usda/nass/AgriChemUsRestricted/2000s/2005/AgriChemUsRestricted-10-05-2005.pdf>
- U. S. Environmental Protection Agency (EPA) (2002) Atrazine, Bensulide, Diphenamid, Imazalil, 6-Methyl-1,3-dithiolo[4,5-b]quinoxalin-2-one, Phosphamidon S-Propyl dipropylthiocarbamate, and Trimethacarb; Tolerance Revocations. Federal Register Environmental Documents 67, 46888–46893; see also: <http://www.epa.gov/fedrgstr/EPA-PEST/2002/July/Day-17/p17870.htm>
- Wagenet LP, Lemley AT, Wagenet RJ (1984) A review of physical-chemical parameters related to the soil and groundwater fate of selected pesticides used in New York state: oxamyl.

- The Pesticide Management Education Program (PMEP), Cornell University; see <http://pmep.cce.cornell.edu/facts-slides-self/facts/pchemparams/gen-pubre-Oxamyl.html>
- Watanabe N, Horikoshi S, Suzuki K, Hidaka H, Serpone N (2003) Mechanistic inferences of the photocatalyzed oxidation of chlorinated phenoxyacetic acids by electro-spray mass spectral techniques and from calculated point charges and electron densities on all atoms. *New J Chem* 5:836–843
- Watanabe N, Horikoshi S, Kawasaki A, Hidaka H, Serpone N (2005) Formation of refractory ring-expanded triazine intermediates during the photocatalyzed mineralization of the endocrine disruptor amitrole and related triazole derivatives at UV-irradiated TiO₂/H₂O interfaces. *Environ Sci Technol* 39:2320–2326
- Zaki MH, Moran D, Harris D (1982) Pesticides in groundwater: the aldicarb story in Suffolk County, NY. *Am J Public Health* 72:1391–1395

Chapter 15

Purification of Toxic Compounds in Water and Treatment of Polymeric Materials

Ho-In Lee, Jae-Hyun Kim, Han-Su Lee, and Weon-Doo Lee

Abstract Among a variety of semiconductors as the medium for photocatalytic treatment of pollutants in the form of suspended powders or immobilized phases, titanium dioxide is the most widely used due to its high stability, good performance, and low cost. In this chapter, photocatalysis of aqueous pollutants covers both organic pollutants, including pyrimidines, phenols, pesticides, synthetic dyes, etc., and inorganic pollutants, mainly focusing on nitrogen-containing ones. In the latter section, application to polymer science encircles applications to pigmentation, photocatalyst–polymer composites, and functional coating.

1 Introduction

Since Fujishima and Honda (1972) discovered the photocatalytic splitting of water on TiO₂ electrodes under UV illumination, photocatalysis has been widely applied in solar energy conversion, air and wastewater treatment, sterilization, induction of super-hydrophilicity, cancer treatment, etc.

Excitation of semiconductor materials such as TiO₂ with light of wavelength shorter than the bandgap cutoff wavelength results in the formation of electron–hole pairs. The photogenerated electron–hole pairs experience a series of events as below (Serpone and Khairutdinov 1997).

Charge-carrier migration to surface:

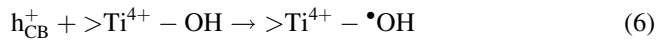


H.-I. Lee (✉)

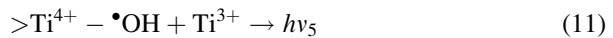
School of Chemical and Biological Engineering, Seoul National University,
Seoul 151-744, Korea
e-mail: hilee@snu.ac.kr



Charge-carrier trapping into shallow traps (ST):



Charge-carrier recombination:



Hole or electron trapping by shallow traps such as bulk defects triggers charge-carrier recombination and reduces the efficiency of photocatalysis. The holes that reach the surface and are trapped by surface defects or surface hydroxyl groups can cause photocatalytic oxidation. Simultaneously, surface electrons are able to cause photocatalytic reduction. When photocatalysis is applied to oxidation, a sacrificial electron acceptor must be used. On the contrary, an application to photocatalytic reduction requires a hole scavenger (Lee et al. 2001a).

Although the majority of photocatalytic organic pollutant treatments progress via oxidation mechanism, photocatalytic reduction also enables many useful reactions to occur. For example, hydrogen evolution, metal ion recovery, nitrogen fixation, CO₂ fixation, etc., take place via photocatalytic reduction (Lee and Lee 1998; Lee et al. 2001b).

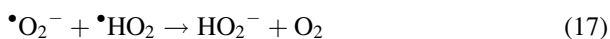
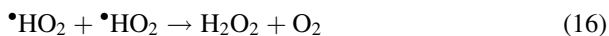
2 Mechanistic Approach

Photocatalytic processes make use of semiconductor metal oxide as a catalyst and oxygen as an oxidizing agent. Many catalysts have been tested so far, although only TiO₂ in the anatase form seems to have functional attributes such as high stability,

good performance, low cost, and easy separation/regeneration after processes (Lee et al. 2001c). It is no surprise that different samples of TiO₂ exhibit different photocatalytic activities toward same organic substrates under otherwise identical reaction conditions. Such differences can be qualitatively attributed to differences in morphology, crystal phase, specific surface area, particle aggregate size, and surface density of OH groups in the TiO₂ samples.

Bhatkhande et al. (2001) summarized the types of organic and inorganic substances that can be degraded using photocatalysis. Almost all kinds of substances can be treated and lists of these substances are also found in other review papers (Agustina et al. 2005; Carp et al. 2004; Gogate and Pandit 2004; Diebold 2003; Pirkanniemi and Sillanpää 2002; Blake 2001; Herrmann 1999; Mills and Le Hunte 1997; Jung and Lee 1997; Hoffmann et al. 1995; Lee and Lee 1992).

The photocatalytic oxidation of organic pollutants can progress via two mechanisms: “indirect oxidation” and “direct oxidation” (Serpone et al. 1995). In the first “indirect oxidation” mechanism, photogenerated valence holes react primarily with physisorbed H₂O and surface-bound hydroxyl groups (–OH) on TiO₂ particles to give OH radicals that may then react with organic molecules. Typically, the mechanism of OH radical formation has been presumed as follows (Wang et al. 1999; Hirakawa and Nokada 2002).



Turchi and Ollis (1990) proposed that the average diffusion distance of OH radicals could be extended to 10^{−6} m in slurry reactors. Therefore, the interaction of organic molecules with OH radicals is possible at solution bulk. In the second “direct oxidation” mechanism, the valence band holes directly react with organic substrates.

Following the formation of active species such as photogenerated holes and OH radicals explained above, the overall processes can be divided into five independent steps (Herrmann 1999):

1. Transfer of reactants in the fluid phase to the surface
2. Adsorption of at least one of the reactants
3. Reaction in the adsorbed phase
4. Desorption of products
5. Removal of the products from the interface region

Based on the above processes, Langmuir–Hinshelwood kinetic model could be applied to the reaction occurring at the solid–liquid interface (Fox and Duray 1993)

$$r_{\text{LH}} = -\frac{dC}{dt} = k\theta = \frac{kKC}{1 + KC}, \quad (21)$$

where C , k , and K , respectively, represent the concentration of the organic compound to be decomposed, the reaction rate constant, and the equilibrium adsorption coefficient.

For diluted solutions ($C < 10^{-3}$ M), KC becomes $\ll 1$ and the reaction is of the apparent first order, whereas for $C > 5 \times 10^{-3}$ M, ($KC \gg 1$), the reaction rate is maximum and of the zero order. This Langmuir–Hinshelwood kinetics has been widely used for the understanding of photocatalytic oxidation mechanism.

The oxidative ability of photocatalyst has been largely applied to the decomposition of various volatile organic compounds or aqueous organic pollutants (Herrmann 1999; Mills and Le Hunte 1997; Fox and Duray 1993). Nearly all of the organic pollutants can be totally mineralized to CO_2 by photocatalysis with the exception of *s*-triazine herbicides of which the final products are cyanuric acids. Photocatalysis and biodegradation must be combined for total mineralization of cyanuric acids and *s*-triazine ring compounds. Chlorinated organic compounds, organic nitrogen compounds, organic sulfur compounds, and organic phosphorous compounds are mineralized to release chlorine ions, ammonium and/or nitrate ions, sulfate ions, and phosphate ions, respectively (Halmann 1996). Recently, various commercial processes are adapted to wastewater treatment (see Fig. 1 from <http://purifics.com/products/photo-cat.html>).

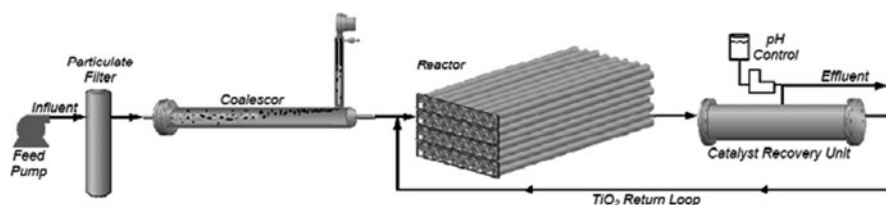
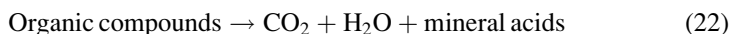


Fig. 1 Commercial photocatalytic wastewater process

2.1 Mechanistic Models

The main pathway of photomineralization (i.e., the breakdown of organic compounds) carried out in aerated solution may easily be summarized by the following reaction:



A schematic representation of this process is displayed in Fig. 2 (Carp et al. 2004).

The radical ions formed after the interfacial charge transfer reactions can participate in several pathways of the degradation process:

1. They may react chemically with themselves or with surface-adsorbed compounds.
2. They may recombine via back electron-transfer reactions, especially when they are trapped near the surface, due to either the slowed-down outward diffusion or hydrophobicity.
3. They may diffuse from the semiconductor surface and participate in chemical reactions in the bulk solution.

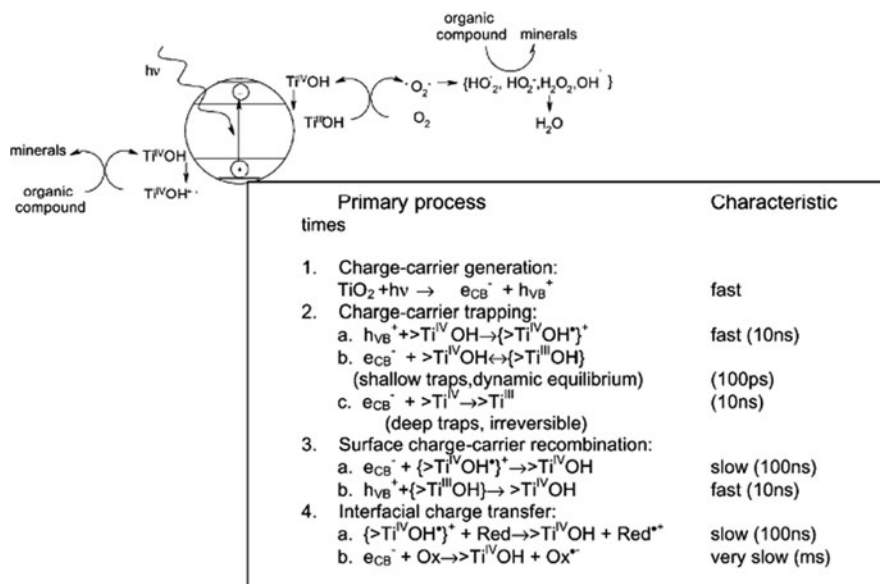


Fig. 2 Major processes and their characteristic times for TiO_2 -sensitized photo-oxidative mineralization of organic compounds by dissolved oxygen in aqueous solutions. Reprinted from Carp et al. (2004), Copyright with permission from Elsevier

Detailed mechanism of the photocatalytic process on TiO_2 surface is still not completely clear, particularly that of the initial steps involved in the reaction of reactive oxygen species and organic molecules.

A reasonable assumption is that both photocatalytic oxidative and reductive reactions occur simultaneously on the TiO_2 particle, since charge would build up otherwise. In most experiments, the electron transfer to oxygen, which acts as a primary electron acceptor, is rate-determining in photocatalysis. Hydroxyl radicals are formed on the surface of TiO_2 by reaction of holes in the valence band (h_{vb}^+) with adsorbed H_2O , hydroxide, or surface titanol groups ($>\text{TiOH}$). The photogenerated electrons are reduced enough to produce superoxide (O_2^-). This superoxide is an effective oxygenation agent that attacks neutral substrates as well as surface-adsorbed radicals and/or radical ions. Theoretically, the redox potential of the electron-hole pair permits H_2O_2 formation either by water oxidation (by holes) or by two conduction band electron reduction of the adsorbed oxygen. The latter represents the main pathway of H_2O_2 formation. H_2O_2 contributes to the degradation pathway by acting as an electron acceptor or as a direct source of hydroxyl radicals subsequent to homolytic scission. Depending on the reaction conditions, the holes, $\bullet\text{OH}$ radicals, O_2^- , H_2O_2 , and O_2 can play important roles in the photocatalytic reaction mechanism. These processes are presented in Fig. 3 (Hoffmann et al. 1995). If non-oxygenated products, derived from ion radicals, are desired, oxygen has to be replaced with other electron acceptors.

According to the above-mentioned mechanism and time characteristics, two critical processes determine the overall quantum efficiency of interfacial charge transfer:

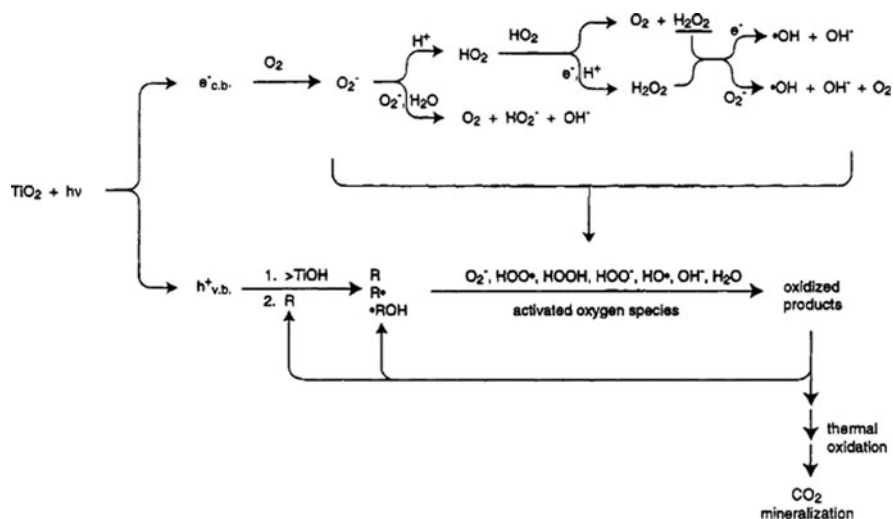


Fig. 3 Secondary reactions with activated oxygen species in the photoelectron-chemical mechanism. Reprinted with permission from Hoffmann et al. (1995), Copyright, American Chemical Society

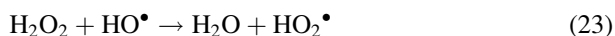
1. Competition between charge-carrier recombination and trapping (picoseconds to nanoseconds)
2. Competition between trapped carrier recombination and interfacial charge transfer (microseconds to milliseconds)

An increase in either charge-carrier lifetime or the interfacial electron-transfer rate is expected to lead to higher quantum efficiency for steady state photolysis.

2.2 Operational Parameters

It has been demonstrated that catalyst dosage, character and initial concentration of the target compound, coexisting compounds, UV light intensity, oxygen concentration, presence of supplementary oxidizable substances, temperature, circulating flow rate, pH for aqueous treatments, and water concentration for gaseous phase photoreactions are the main parameters affecting the degradation rate. Each of these parameters will be discussed in the following section (Carp et al. 2004; Gogate and Pandit 2004; Herrmann 1995).

Generally, decomposition rate increases with catalyst loading due to higher surface area of the catalyst that is available for adsorption and degradation. An optimum value is present, while above a certain concentration, the solution opacity increases (due to increased light scattering of the catalyst particles), causing a reduction in light penetration through the solution and a consequent rate decrease. Additionally, at high-TiO₂ concentrations, terminal reaction (23) could also contribute to the diminution of photodegradation rate. The formed hydroperoxyl radical is less reactive than the HO• one:



The optimal catalyst dosage or effective optical penetration length, under given conditions, is very important in designing a slurry reactor that makes effective use of the reactor space and the catalyst. If the solution layer thickness exceeds the optical penetration length at any given illumination intensity and catalyst concentration, the photoreactor will be under-utilized.

For TiO₂ immobilized systems, there is also an optimal thickness of the catalyst film. The interfacial area is proportional to the thickness of catalyst, as the film is porous. Thus, thick films favor catalytic oxidation. On the other hand, the internal mass transfer resistance for both organic species and photogenerated electrons/holes increases with increasing thickness. This increases the recombination possibility of the electron/hole pair and as a consequence, the degradation performance is reduced.

Usually reactor designs should be such that uniform irradiation of the entire catalyst surface is achieved at the incident light intensity. This is a major problem associated with the large-scale designs. Moreover, nearly complete elimination of mass transfer resistances is another point that needs to be considered while

designing large-scale reactors. The efficient reactor design must expose highest amount of the activated immobilized catalyst to the illuminated surface and must have a high density of active catalyst in contact with the liquid to be treated inside the reactor.

The degradation rate of organic substrates usually exhibits saturation behavior: the observed rate constant decreases with an increase in the initial organic pollutant concentration. Three factors may be responsible for this behavior:

1. The main steps in the photocatalytic process occur on the surface of the solid photocatalyst. Therefore, a high adsorption capacity is reaction favoring. Because most of the reactions follow an LH equation, this means that at a high initial concentration all catalytic sites are occupied. A further increase in the concentration does not affect the actual catalyst surface concentration and, therefore, may result in a decrease of the observed first-order rate constant.
2. The generation and migration of photogenerated electron-hole pairs and their reaction with organic compounds occur in series. Therefore, each step may become rate-determining for the overall process. At low concentrations, the latter dominates the process and, therefore, the degradation rate increases linearly with concentration. However, at high concentrations, the former will become the governing step and the degradation rate increases slowly with concentration. For a given illumination intensity, even a constant degradation rate may be observed as a function of concentration.
3. Intermediates generated during the photocatalytic process also affect the rate constant of their parent compounds. A higher initial concentration will yield a higher concentration of adsorbed intermediates, which will affect the overall rate.

It is well known that the photocatalytic oxidation rate is not affected much by minor changes in temperature. This weak dependence is reflected by the low activation energy of photocatalytic oxidation reactions (a few kJ/mol) compared to ordinary thermal reactions. This is due to the low thermal energy ($kT = 0.026$ eV at room temperature) that has almost no contribution to the activation energy of (the wide bandgap) TiO_2 . On the other hand, these activation energies are quite close to that of hydroxyl radical formation, suggesting that the photodegradation of these organics is governed by hydroxyl radical reactions (Matthews 1987). The effect of temperature on the rate of oxidation may be dominated by the rate of interfacial electron transfer to oxygen (Anpo et al. 1987). Alternatively, the more rapid desorption of both substrates and intermediates from the catalyst at higher temperatures is probably an additional factor, leading to a larger effective surface area for the reaction. At lower temperatures, desorption becomes the rate-limiting step of the process (Herrmann 1999).

Even though changes in relative positions of the Fermi level of TiO_2 powders at temperatures between 21 and 75°C have been reported as relatively small (0.04 eV), improved interfacial electron-transfer kinetics are observed when the temperature is increased (Kiwi 1985). In the range of 20–80°C, weak dependence of degradation rates on temperature has usually been observed. As a consequence, the optimum temperature is generally comprised between 20 and 80°C.

There are two regimes of the photocatalytic reaction with respect to the UV-photon flux. They comprise a first-order regime for fluxes up to about 25 mW/cm^2 in laboratory experiments and a half-order regime for higher intensities. In the former regime, the electron-hole pairs are consumed more rapidly by chemical reactions than by recombination reactions, whereas in the half-order regime, the recombination rate is dominant (Herrmann 1995). The variation of reaction rate as a function of the wavelength used follows the adsorption spectrum of the catalyst with a threshold corresponding to its band energy.

Oxygen was found to be essential for semiconductor photocatalytic degradation of organic compounds. Dissolved molecular oxygen is strongly electrophilic and thus an increase of its content probably reduces unfavorable electron-hole recombination routes. But higher concentrations lead to a downturn in the reaction rate, which could be attributed to the fact that the TiO_2 surface becomes excessively hydroxylated to the extent of inhibiting the adsorption of pollutant at active sites.

The influence of oxygen pressure on the liquid phase is difficult to study because the reaction is polyphasic. Generally, it is assumed that O_2 adsorbs on TiO_2 from the liquid phase, where its concentration is proportional to the gas phase oxygen pressure according to Henry's law. Apart from its conventional electron scavenging function, the dissolved O_2 may play a key role in the degradation of organic compounds.

Medium pH has a complex effect on the rate of photocatalytic oxidation, and the observed effect is generally dependent on the type of the pollutant as well as the point of zero charge (pzc) of the semiconductor used in the oxidation process, i.e., more specifically on the electrostatic interaction between the catalyst surface and the pollutant. The adsorption of the pollutant and hence the degradation rate will be maximum near the pzc of the catalyst. For some of the pollutants that are weakly acidic, rate of photocatalytic oxidation increases at lower pH due to an increase in the extent of adsorption under acidic conditions. Some of the pollutants that undergo hydrolysis under alkaline conditions or undergo decomposition over a certain pH range may show an increase in the rate of photocatalytic oxidation with an increase in the pH. Since the effect of pH cannot be generalized, it is recommended that laboratory scale studies are required to establish the optimum conditions for the operating pH unless data are available in the literatures with identical operating conditions, i.e., the type of equipments as well as the range of operating parameters, including the composition of the effluent stream (Gogate and Pandit 2004).

Presence of ions may affect the degradation process via adsorption of contaminants; reaction with hydroxyl radical ions and/or absorption of UV light. This is a very important point that needs to be considered as real life industrial effluents will have different types of salts at different levels of concentration and generally these are in ionized forms. In general, it can be said that CO_3^{2-} , HCO_3^- (they act as radical scavengers and also affect the adsorption process), and Cl^- (affects the adsorption step strongly and also partly absorbs UV light) ions have strong detrimental effect on the degradation process whereas other anions such as sulfate, phosphate, and nitrate affect the degradation efficiency marginally.



These radicals may initiate oxidation reactions with organic species. Yawalkar et al. (2001) have studied the effect of SO_4^{2-} , CO_3^{2-} , Cl^- , and HCO_3^- ions on the overall degradation rates of phenol and reported that the detrimental effects are observed in the order of $\text{SO}_4^{2-} < \text{CO}_3^{2-} < \text{Cl}^- < \text{HCO}_3^-$.

For cations, both beneficial and detrimental effects have been evidenced. The effect is strongly dependent on the metallic ion nature and their concentrations. The rate of photocatalytic degradation can be enhanced up to an optimum value. Metal ions may increase the photocatalytic rate due to:

1. The ability of metallic ions to trap either electrons or holes via oxidizing and reducing reactions
2. Alternative homogeneous Fenton-type reactions on the TiO_2 surface that lead to additional $\text{HO}\cdot$ production
3. Short-circuiting reactions that create a cyclic process without generation of active $\text{HO}\cdot$
4. Filter effect due to UV absorption of the species
5. Precipitation and deposition of the dissolved metallic ions as hydroxides on the TiO_2 surface

Although photocatalysis has shown to be adequate for the destruction of a wide variety of compounds, in some cases the complete mineralization is slowly attained, and the efficiency of the processes, in terms of energy consumption, is only advantageous for very dilute effluents. To overcome this difficulty, some additives such as H_2O_2 , Fe^{2+} , Fe^{3+} , $\text{S}_2\text{O}_8^{2-}$, Ag^+ , etc., with different chemical roles can be added to the photocatalytic systems (Agustina et al. 2005).

Another drawback in photocatalytic degradation of wastewaters is the need for transparency of treated wastewater at the spectral region where semiconductor absorbs. Some ideas have been published to enable the use of photocatalysis even when the wastewater is not transparent enough. In multiple tube reactor with TiO_2 -coated hollow glass tubes, UV-light travels through the inside of hollow tubes while wastewater flows over the outside of the tubes (Ray and Beenackers 1998). Somewhat similar idea is to embed TiO_2 onto glass fibers to increase the penetration of UV-light into the wastewater solution (Hofstadler et al. 1994).

3 Pyrimidine and Its Derivatives

Organic compounds containing nitrogen atoms are extremely common in nature. The prevalent category includes amino acids, proteins, and several classes of man-made substances of environmental concern that have nitrogen atoms in their structures, such

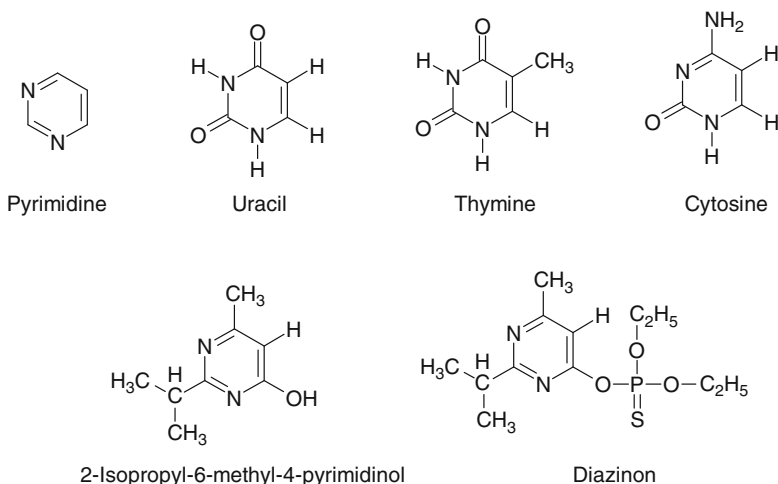


Fig. 4 Some examples of pyrimidine and its derivatives

as herbicides, pesticides, drugs, explosives, and dyes. Among organic nitrogen compounds, pyrimidine derivatives are mainly found in biomolecules and agrochemicals. Some examples of pyrimidine and its derivatives are shown in Fig. 4. There have been a few works about photocatalytic degradation of pyrimidine compounds. Major studies focused on the degradation mechanism of DNA bases (uracil, thymine, and cytosine) and the effect of coexistent ions on the activity of the photocatalyst (Dhananjeyan et al. 1996, 1997, 2000a, b; Horikoshi et al. 1999; Jaussaud et al. 2000; Horikoshi and Hidaka 2001; Calza et al. 2004). Several reports dealt with the photocatalytic degradation of pyrimidine derivative pesticides such as diazinon and 2-isopropyl-6-methyl-4-pyrimidinol (IMP) (Koulombos et al. 2003; Lee et al. 2003, 2004, 2005; Oh et al. 2006, 2007). These studies are reviewed in this chapter.

3.1 Oxidation Mechanism

It has been reported that pyrimidine glycols are found as reaction products, suggesting that photocatalytic oxidation of pyrimidine derivatives is progressed via indirect oxidation by hydroxyl radical (Dhananjeyan et al. 1996, 1997; Jaussaud et al. 2000). Hydroxylation of pyrimidine ring results in ring opening. The kinds and positions of functional groups, that cause differences in frontier electron density, determine the attack position of hydroxyl radical and chain cleavages leading to different degradation mechanisms and final products. In a decomposition case of pyrimidine molecules, C–N cleavage caused by hydroxyl radical gives birth to more NH_4^+ than NO_3^- (see Fig. 5) (Horikoshi and Hidaka 2001). The pyrimidine derivatives substituted by amino group, such as cytosine and 4-aminopyrimidine, also show similar results. However, the photocatalytic degradation of uracil and

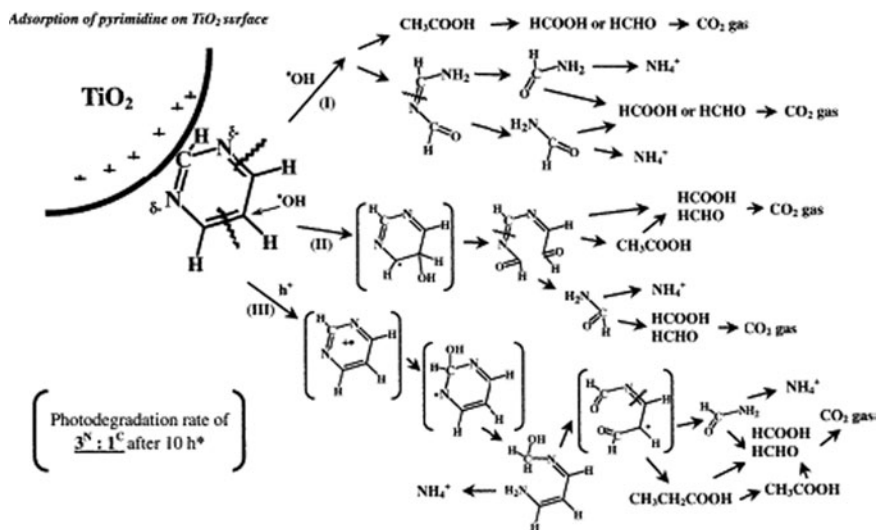


Fig. 5 Photodegradation mechanism of pyrimidine. Reprinted from Horikoshi and Hidaka (2001), Copyright with permission from Elsevier

thymine containing carboxyl groups produces more NO_3^- than NH_4^+ , following primary amine formation (Horikoshi et al. 1999; Calza et al. 2004). When the amino group is positioned on carbon 2 in aminopyrimidine, guanidine is formed as a very stable intermediate, as opposed to the case of 4-aminopyrimidine (Calza et al. 2004).

Diazinon, an organophosphorous insecticide with widespread agricultural and non-agricultural uses, is also decomposed by hydroxyl radical and as IMP is produced (see Fig. 6) (Kouloumbos et al. 2003).

IMP is totally mineralized via ring-opening by photocatalytic oxidation. UV absorption spectrum changes of IMP during photocatalytic reaction are shown in Fig. 7. Two peaks that result from pyrimidine ring disappeared as the reaction progressed, suggesting that pyrimidine ring opening took place by photocatalytic reaction. Acetamide, a possible fragment of the IMP ring, was also detected in the GC-Mass analysis of reaction intermediates. The theoretical amount of CO_2 that could be evolved through the complete oxidation of IMP was estimated to be about 1,250 μmol . Also, the total evolved amount of CO_2 was 1,200 μmol , similar to the theoretical amount (Lee et al. 2003).

Photocatalytic oxidation steps of pyrimidine derivatives are summarized as below (Horikoshi et al. 1999):

1. Diffusion and (or) adsorption of the derivatives to the catalyst surface
2. Hydroxyl radical attack at ring atoms with greater electron densities
3. Conversion of C to CO_2 , and N to NH_4^+ , NO_3^- , and N_2 , respectively.

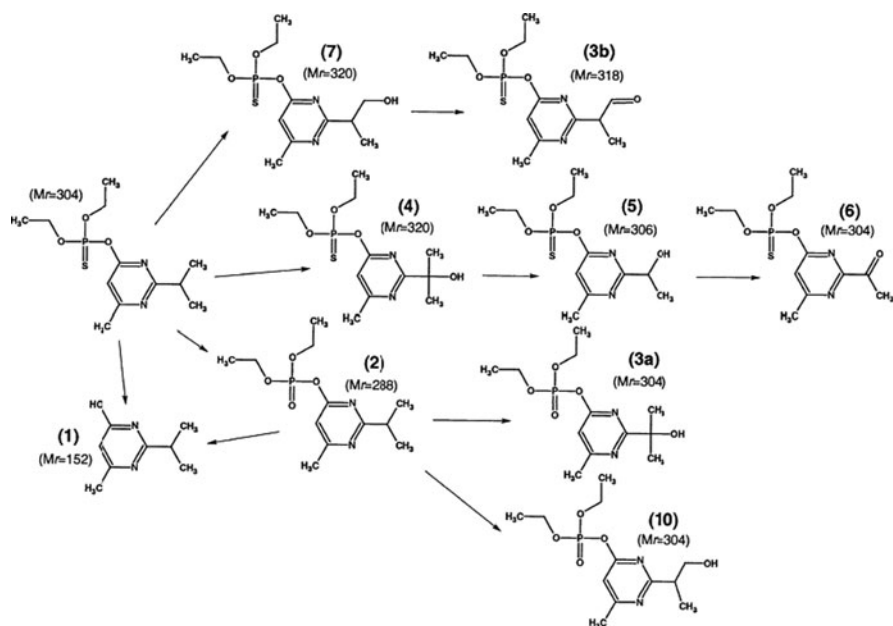


Fig. 6 Proposed degradation pathways for diazinon TiO₂ induced photocatalysis: IMP (1), diazoxon (2), hydroxydiazoxon (3a), diazinon aldehyde (3b), hydroxydiazinon (4), hydroxyethyl derivative of diazinon (5), diazinon methyl ketone (6), 2-hydroxydiazinon (7), and 2-hydroxydiazoxon (10). Reprinted from Kouloumbos et al. (2003), Copyright with permission from Elsevier

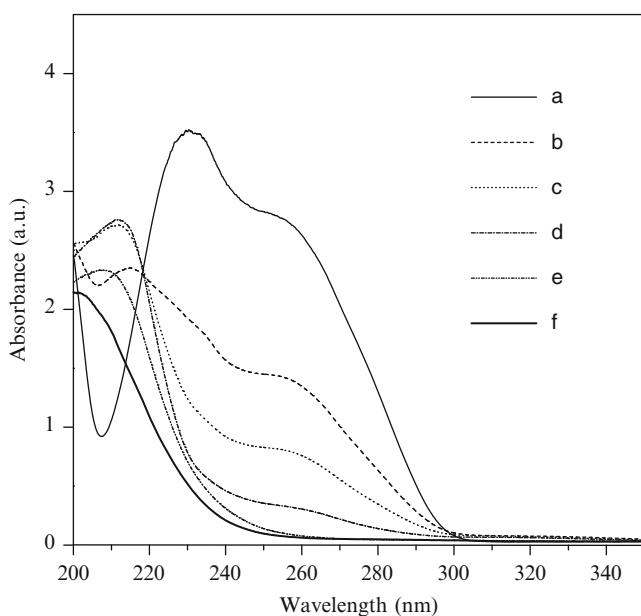


Fig. 7 Changes in the UV absorption spectrum of IMP after irradiation time of (a) 0 min, (b) 30 min, (c) 60 min, (d) 90 min, (e) 4 h, and (f) 8 h. Reprinted from Lee et al. (2003), Copyright with permission from Elsevier

3.2 pH Effect

The pH condition has been reported to affect the photocatalytic reaction rate. In the photocatalytic oxidation of pyrimidine base, the reaction rate is also influenced by the condition of pH. Pyrimidine bases such as thymine, 6-methyl uracil, and cytosine show lower reaction rates at higher pH values (Dhananjeyan et al. 1996, 1997, 2000b). The band edge positions of TiO₂ shift to more negative values with increasing pH, resulting in a decrease of oxidation potentials. Conduction and valence band edges increase at the rate of -60 mV per unit increase in pH under strongly basic conditions (Takeda et al. 1998). The dissociation of TiOH to TiO⁻ and H⁺ in basic solution can cause low concentration of surface hydroxyl groups that produce active hydroxyl radicals. Also, the pyrimidine bases become negatively charged under basic conditions, and there is a decrease in the extent of adsorbability that leads to a decrease in the reaction rate. The pK_a value of the reaction represented as in (15) ($\bullet\text{O}_2^- + \text{H}^+ \rightarrow \bullet\text{HO}_2$) is reported to be about 4.88 (Wang et al. 1999). In the pH region above the pK_a value of HO₂ radicals (=4.88), the reverse reaction of (15) dominates and (16)–(20) do not proceed. As a result, the electron scavenging by oxygen decreases under strongly basic conditions.

IMP also shows reaction rate-dependency on the pH condition (Lee et al. 2003). Under strongly acidic conditions, non-bonding electrons can accept protons easily, and IMP exists as positively charged protonated species. On the other hand, dissociation of a proton from the IMP hydroxyl group happens readily under strongly basic conditions. The deprotonated IMP molecules exist as negatively charged species. Similar trend is also observed in other pyrimidine compounds. Some kinds of pyrimidinol compounds have two kinds of pK_a values. Acidic pK_a is about 6.78–9.17 and basic pK_a is about 1.87–2.24 (Brown and Mason 1962). The surface charge state of TiO₂ also depends on the pH condition. The isoelectric point of TiO₂ is located at about 6.5 of pH and the surface hydroxyl of TiO₂ exists as TiOH₂⁺ and TiO⁻ forms, causing electrostatic repulsion between IMP and TiO₂ under strongly acidic and basic conditions, respectively. Therefore, the overall degradation rate constants under acidic, mildly acidic, and mildly basic conditions were higher than those under strongly acidic and basic conditions (see Table 1). In the case of pyridine derivatives, similar pH effect was observed (Nedoloujko and Kiwi 2000).

Table 1 Overall degradation rate constants of IMP by TiO₂ and SiO_x-loaded TiO₂ at different initial pH conditions (Lee et al. 2003)

Catalyst	Initial pH					
	2		6.3		10	
	<i>k</i> (min ⁻¹)	<i>R</i> ²	<i>k</i> (min ⁻¹)	<i>R</i> ²	<i>k</i> (min ⁻¹)	<i>R</i> ²
TiO ₂ (P-25)	0.0127	0.9885	0.0223	0.9979	0.0073	0.9915
0.5 mol% SiO _x -loaded TiO ₂ ^a	0.0180	0.9898	0.0206	0.9906	0.0079	0.9901
0.5 mol% SiO _x -loaded TiO ₂ ^b	0.0196	0.9976	0.0185	0.9980	0.0079	0.9956

^aPrepared by sol-gel method

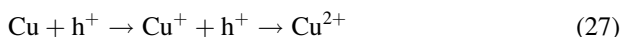
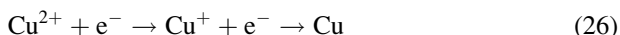
^bPrepared by impregnation method

The pH-dependent behavior of photocatalytic oxidation is explained as follows:

1. Nernstian shift of band edge position
2. Change in surface hydroxyl group concentration
3. Change in electron scavenging rate by O₂
4. Changes in surface charge state of TiO₂ and ionic state of reactant

3.3 Effect of Metal Ion

The existence of metal ions in solution affects the photocatalytic degradation rate of pyrimidine derivatives. For uracil and 6-methyluracil, an increase in the Ag⁺ concentration enhances the photocatalytic degradation rate, reducing the extent of hole–electron recombination (Dhananjeyan et al. 1997). However, Cu²⁺ retards the photocatalytic decomposition rate. The retardation is attributed to the short-circuiting reaction (26) and (27) and metal deposition, causing hole–electron recombination and impediment of light absorption, respectively (Dhananjeyan et al. 2000a).



Fe³⁺ can also be used as an electron scavenger instead of oxygen. In photocatalytic degradation of IMP, rutile TiO₂ shows poor activity. In the presence of Fe³⁺, however, photocatalytic decomposition of IMP over rutile TiO₂ occurs faster than anatase TiO₂ as shown in Table 2 (Lee et al. 2004). This result implies that conduction band position is responsible for the difference in activity between anatase and rutile. The standard redox potential of the O₂/•O₂⁻ is -0.33 V versus NHE and that of the Fe³⁺/Fe²⁺ is +0.77 V versus NHE (Bamwenda et al. 2001). The conduction band of anatase ($E \approx -0.5$ V versus NHE) is more negative than both of the standard redox potentials above. However, the conduction band of rutile ($E \approx -0.3$ V versus NHE) (Lin et al. 1999) is more positive than the standard potential of O₂/•O₂⁻ and more negative than that of Fe³⁺/Fe²⁺. This suggests that photogenerated electron from rutile cannot react with oxygen thermodynamically, but can react with Fe³⁺. As a result, rutile shows a poor activity in photocatalytic degradation of IMP when using oxygen as an electron scavenger, whereas it shows a good activity

Table 2 The activity comparison of photocatalytic degradation of IMP according to the kind of electron scavenger (Lee et al. 2004)

Electron scavenger	Oxygen	Ferric ion
CO ₂ formation over anatase (μmol)	599	556
CO ₂ formation over rutile (μmol)	56	614

with ferric ion. Lin et al. (1999) and Ohno et al. (2001) made similar conclusions in photocatalytic oxidations of acetone and 2-propanol, respectively.

Also, Fe^{3+} can be doped on TiO_2 to increase the photo-oxidation rate of pyrimidine bases. The maximum rate was observed with 0.75 at% of Fe^{3+} loading amount. Doped Fe^{3+} acts as an e^- -trap and a transfer site to Ti^{4+} , preventing the recombination of h^+ and e^- (Dhananjeyan et al. 2000a).

3.4 Effect of TiO_2 Property

The photocatalytic activity of TiO_2 is generally influenced by physicochemical properties, including crystal structure, crystallinity, surface state, particle size, surface area, etc. (Porter et al. 1999).

Anatase TiO_2 generally shows higher activity than rutile TiO_2 in photocatalytic oxidations of organic compounds (Porter et al. 1999; Ding et al. 2000; Devi and Krishnaiah 1999; Jung and Park 1999; Hong et al. 2001). For IMP, a similar result was reported with oxygen as an electron scavenger (Lee et al. 2004).

The effect of crystallinity is related to the bulk defect. Higher crystallinity results in lower bulk defects, enhancing hole–electron separation by surface traps (Jung and Park 1999).

As mentioned in the earlier chapter, pH condition affects the photo-oxidation rate of pyrimidine derivatives due to the isoelectric point of TiO_2 . The isoelectric point of TiO_2 can be controlled by surface modification. As shown in Fig. 8, The SiO_x loading on TiO_2 lowers the isoelectric point of TiO_2 (Lee et al. 2003; Lee 2004).

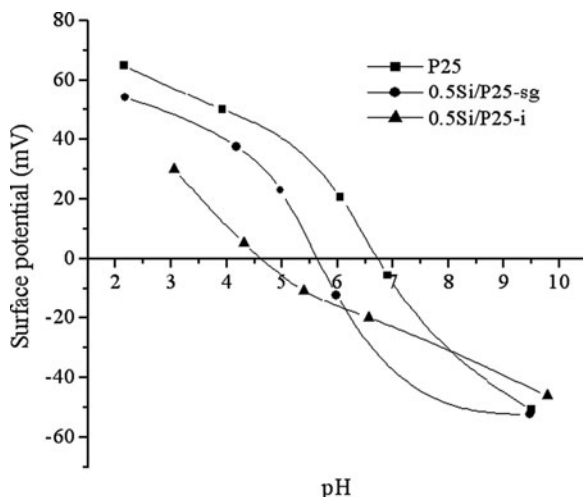


Fig. 8 Comparison of isoelectric point between pure TiO_2 and SiO_x -loaded TiO_2 . Reprinted with permission from Ding et al. (2000), Copyright, American Chemical Society

Under strongly acidic conditions, SiO_x -loaded TiO_2 showed higher activity and less positive surface charge than pure TiO_2 (see Table 1). As a result, less electrostatic repulsion exists between the catalyst and the IMP molecule under strongly acidic conditions, resulting in a faster photocatalytic oxidation of IMP.

The channel-structured TiO_2 with pore size of about 18 nm is obtained by in situ esterification method using PEG as alcohol source without H_2O addition. The channel structure is originated from the organic–inorganic interaction between Ti species and PEG template, which enhances the photocatalytic activity for IMP decomposition (Oh et al. 2006).

Particle size is an important factor in determining the efficiency of the photocatalyst. This is related with surface area to affect adsorption ability and quantum size effect that change electronic structure. Especially when the particle size of semiconductor material such as TiO_2 is less than the De Broglie wavelength, quantum size effects take place depending on the specific electronic properties of the semiconductor, such as the effective masses of electrons and holes. Quantum size effects are as follows (1) blue shift of the fundamental absorption edge of the quantum size particle that can be controlled by tuning the particle size, and (2) enhanced photoredox potential for photogeneration of electrons and holes. These effects occur because of the physical confinements of electrons and holes in potential wells defined with the crystallite boundaries, typically ranging from 5 to 25 nm (Ollis and Al-Ekabi 1993). The quantum size effects of nano-sized TiO_2 have been widely studied (Anpo et al. 1987; Kormann et al. 1988; Choi et al. 1994; Serpone et al. 1995). When nano-sized TiO_2 particles are obtained using various mesoporous materials determining particle size, the bandgap increments due to quantum size effect are observed in both anatase TiO_2 and rutile TiO_2 . The bandgap increment in rutile TiO_2 enhances the photocatalytic oxidation rate of IMP by virtue of the increase in redox potential of TiO_2 . However, the bandgap increment in anatase TiO_2 does not affect the efficiency of IMP photocatalytic oxidation (Lee et al. 2005).

3.5 Application Field

Because pyrimidine derivatives are mainly found in DNA bases or pesticides, their photocatalytic oxidations are useful for the treatment of microorganisms, wastewater, ground water, etc. Some examples are listed below:

1. Analysis of DNA sequence (Dhananjeyan et al. 1996)
2. Waste/Ground water treatment from pesticide synthetic process (Kouloumbos et al. 2003; Lee et al. 2003)
3. Sterilization of microorganisms such as bacteria, fungi, mold, and virus (Fujishima et al. 2000)
4. Cancer treatment (Fujishima et al. 2000)

4 Phenol Compounds

It is well known that phenol compounds constitute an important family of priority pollutants in wastewater. Their presence has been confirmed in many different industrial wastewaters from chemical, petrochemical or even from food-processing industries. Due to their toxicity and hazardous property, phenols need to be removed from wastewater before its release into the aquatic environment. Biological oxidation is usually the cheapest and the best way to deal with concentrated wastewaters. However, phenols might present some inhibitory problems and early removal of these compounds is highly recommended. Chemical oxidation is one possible way to accomplish this task. Ozone processes or advanced oxidation processes have been proved to be appropriate technologies.

Beltrán et al. (2005) showed that photocatalytic ozonation ($O_3 + UV + TiO_2$) is more efficient method in removing phenols (phenol, 4-chlorophenol, and 4-nitrophenol) than ozonation (O_3), catalytic ozonation ($O_3 + TiO_2$), ozone photolysis ($O_3 + UV$), photocatalysis ($TiO_2 + UV$), and photolysis (UV). Table 3 lists the intermediates identified in different oxidation processes. As can be seen, with some exceptions, the nature of intermediates is similar regardless of the process applied. With the exception of benzoquinone, the organic intermediates can be grouped into three different categories: polyphenols such as resorcinol, catechol, and hydroquinone, unsaturated carboxylic acids such as fumaric and maleic acids, and saturated carboxylic acids such as glyoxylic, oxalic, and formic acids. Also, nitrogen as nitrate from 4-nitrophenol and chloride from 4-chlorophenol were detected in solution.

From kinetic data available in the literature (see Table 4) the following considerations can be postulated. On the one hand, given the initial concentration of phenols, it is believed that these compounds and some polyphenols are mainly removed during the first minutes of reaction through direct ozone attack: electrophilic substitution and 1,3-cycloaddition reactions. On the other hand, unsaturated and saturated carboxylic acids, especially the latter ones that are more refractory to the ozone attack, are likely to be removed through hydroxyl radical oxidation.

Table 3 Intermediates identified in the photocatalytic ozonation of phenols (Beltrán et al. 2005)

In phenol oxidation	In <i>p</i> -nitrophenol oxidation	In <i>p</i> -chlorophenol oxidation
Hydroquinone	Hydroquinone	Hydroquinone
Resorcinol	Resorcinol	Resorcinol
Benzoquinone	Benzoquinone	Benzoquinone
Catechol	–	–
–	Phenol	–
Oxalic acid	Oxalic acid	Oxalic acid
Maleic acid	Maleic acid	Maleic acid
Fumaric acid	Fumaric acid	Fumaric acid
Glyoxylic acid	Glyoxylic acid	Glyoxylic acid
–	Formic acid	Formic acid

Table 4 Rate constants of the direct reactions of ozone and hydroxyl radicals with phenols, and intermediates detected (Beltrán et al. 2005)

Organic compound	pH	k_D ($M^{-1} s^{-1}$) ^a	Ha	k_{HO} ($M^{-1} s^{-1}$) ^b
Phenol	6.1 ^c	3.9×10^5	5.2	6.6×10^9
<i>p</i> -Chlorophenol	5 ^c	4.2×10^4	1.4	7.6×10^9
<i>p</i> -Nitrophenol	4.7 ^c	5.0×10^4	1.5	3.8×10^9
Hydroquinone	3.9 ^d	1.5×10^6	2.9	10^{10}
	3 ^e		3.7	
	3.1 ^f		0.8	
Resorcinol	5 ^d	9.8×10^4	0.1	1.2×10^{10}
	3 ^f		0.3	
Catechol	3.9 ^d	3.1×10^5	1.5	1.1×10^{10}
Fumaric acid	3.5 ^d	6,000	0.05	1.1×10^9
	2.9 ^e		0.1	
Maleic acid	3.9 ^d	1,000	0.01	6×10^9
	2.9 ^e		0.03	
	3 ^f		0.03	
Glyoxylic acid	3.5 ^d	1.34	0.005	NA
	3 ^{e,f}	0.82	0.01	
Formic acid	3 ^e	19.3	0.015	1.3×10^8
Oxalic acid	3.4 ^d	0.04	0.0005	5×10^7
	2.9 ^{e,f}		0.003	

^aRate constants of the direct reactions of ozone^bRate constants of the direct reactions of hydroxyl radicals^cFor the start of reaction^dIn phenol oxidation^eIn *p*-chlorophenol oxidation^fIn *p*-nitrophenol oxidation**Table 5** Apparent pseudo-first-order rate constants of the oxidation of phenols referred to COD (Beltrán et al. 2005)

Oxidation system	Phenol ($k \times 10^2 \text{ min}^{-1}$)	<i>p</i> -Chlorophenol ($k \times 10^2 \text{ min}^{-1}$)	<i>p</i> -Nitrophenol ($k \times 10^2 \text{ min}^{-1}$)
O ₃	0.47	0.57	0.43
O ₃ /UV	2.97	3.58	1.89
UV/TiO ₂	0.11	0.55	0.24
O ₃ /TiO ₂	0.54	0.59	0.35
O ₃ /UV/TiO ₂	5.56	5.25	3.21

Apparent pseudo-first-order rate constants of the oxidation of phenols are tabulated in Table 5. Regardless of the phenols treated, rate constant values referred to COD for the O₃/UV/TiO₂ system are the highest among the oxidation systems studied. In general, the oxidation order of reactivity was 4-nitrophenol < phenol < 4-chlorophenol. It should be highlighted that the order of reactivity of the phenols

studied with ozone is highly dependent on the presence of activating–deactivating groups in the aromatic ring for electrophilic aromatic substitution reactions. Thus, theoretical order of increasing reactivity is 4-nitrophenol < 4-chlorophenol < phenol since the nitro and chlorine groups strongly and slightly, respectively, deactivate the ozone electrophilic reactions. Thus, from the results obtained, regarding ozone electrophilic reactions, negative effect of the nitro group seems clear while that of the chlorine is not so clear since a better reactivity is observed compared to phenol. On the basis of these results, the addition of TiO₂ to improve the removal of phenols is appropriate in cases where the phenol contributes some strong deactivating groups to the electrophilic substitution reactions.

4.1 Chlorophenols

Chlorophenols occur in all components of the natural environment. They result from a variety of sources: the natural chlorination of organic material, biodegradation of phyto-defensive chemicals, or the large-scale disinfection of drinking water. Chlorophenols are weakly acidic, therefore in the aquatic environment they occur in both dissociated and undissociated forms. The main photochemical processes involving chlorophenols are photodissociation, photoisomerization, photosubstitution, photorearrangement, photo-oxidation, and photoreduction. In general, the photodegradation of any substance in the natural environment is a superposition of reactions of several or all of these types, and its rate and quantum yield depend on a variety of factors. The maximum absorption level of the compound, wavelength of radiation, duration of radiation exposure, and physical state of the compound undergoing the transformation process play central roles in determining the photochemical processes. Because of the ubiquitous presence of chlorophenols in the natural environment and their toxic properties, understanding the kinetics and mechanisms of the process of photodegradation of these compounds is critically important. Czaplicka summarized direct photolysis and photodegradation of chlorophenols in the presence of hydroxyl radicals and singlet oxygen (Czaplicka 2006).

The rate of direct photolysis of chlorophenols is proportional to the irradiation intensity. Chlorophenols strongly absorb radiation at wavelengths between 230 and 300 nm. Various studies show that the rate of photolysis of chlorophenols depends on the pH of the reaction environment and on the structure of the molecule – particularly the position of the chlorine atom relative to the hydroxyl group. It is generally accepted that an observed reaction rate is a sum of the reaction rates of the undissociated and dissociated forms of the compound. It is also known that the reactivity of these forms differs considerably. Observational analysis has regularly found that dissociated forms are more reactive than undissociated ones (Benitez et al. 2000). An increase in the reaction rate constant with increasing pH was observed (Benitez et al. 2000; Shen et al. 1995). Photolysis rate constants for chlorophenols determined under some conditions are presented in Table 6 (Czaplicka 2006). Boule et al. (1982) found that during direct photolysis, the dechlorination rates of 4-chlorophenol (also

Table 6 Rate constants for direct photolysis of chlorophenols (Czaplicka 2006)

Compound	Rate constant (min^{-1})	pH
2-Chlorophenol	7.1×10^{-3}	3
	7.7×10^{-3}	5
	20×10^{-3}	7
	101×10^{-3}	11
2,4-Dichlorophenol	3.6×10^{-3}	3
	4.5×10^{-3}	5
	28.6×10^{-3}	7
	126×10^{-3}	11
2,4,6-Trichlorophenol	2.3×10^{-3}	3
	6.3×10^{-3}	5
	29.4×10^{-3}	7
	36.3×10^{-3}	11
Pentachlorophenol	0.16	3
	0.19	5
	0.21	7
	0.26	9

Reprinted from Czaplicka (2006), Copyright with permission from Elsevier

known as *p*-chlorophenol) and 2-chlorophenol are faster than 3-chlorophenol. Kuo (1999) observed that the reaction rate for direct photolysis upon irradiation at $\lambda < 300$ nm decreases in the order: 2,4-dichlorophenol > 4-chlorophenol > 2-chlorophenol. Shen et al. (1995), on the basis of results obtained under similar conditions, found that rate constants during direct photolysis decrease in the order: 2,4-dichlorophenol > 2-chlorophenol > 2,4,6-trichlorophenol. These results indicated that *para* and *ortho* positions are more active in direct photolysis. The increased occurrence of *para* position in comparison to *ortho* position in this reaction is explained by the intermolecular hydrogen bonding between the *ortho*-positioned Cl atom and the hydrogen from the hydroxyl group. In the case of *ortho*-substituted chlorophenols, hydrogen bonds may be formed internally between Cl and OH as well as externally between molecules of chlorophenol and water.

Besides photocatalysis, hydroxyl radicals can be formed through various chemical reaction pathways such as (1) irradiation of H_2O_2 ; (2) photolysis of ozone, through the generation of singlet oxygen atoms which then react with water to generate $\bullet\text{OH}$; (3) photolysis of Fe^{3+} or polyoxometallates; (4) Fenton-type reaction of Fe^{+2} , Cu^{+1} , or Ti^{+3} ; and (5) radiolysis of water. In the case of natural water, present protonic forms of nitrate and nitrous ions are sources of hydroxyl radicals. The organic matter dissolved in aquatic environment, especially humic acids, absorb a large portion of photons, which can also instigate the formation of hydroxyl radicals.

The reaction of chlorophenols and hydroxyl radicals is described by a second-order reaction model or as a pseudo-first-order reaction (Czaplicka 2006). Antonaraki et al. (2002), investigating the effect of the position of chlorine atom substitution on the reaction rate, found that the rate of photo-oxidation of

monochlorophenols (for $\lambda > 320$ nm) by the $\bullet\text{OH}$ radicals decreases according to the order: 3-chlorophenol $>$ 4-chlorophenol $>$ 2-chlorophenol. It was also observed that the presence of two chlorine atoms in *meta* positions of a molecule (3,5-dichlorophenol) – when compared to a chlorophenol with chlorine atoms in two *ortho* positions (2,6-dichlorophenol) – increases the rate of the reaction (Antonarakis et al. 2002; Moza et al. 1988). A similar phenomenon was reported for trichlorophenols. Trichlorophenols with two chlorine atoms in *meta* positions reacted faster than trichlorophenols with only one chlorine atom in the *meta* position. This means that for mono-, di-, and trichlorophenols, the initial rate of the reaction is affected more by positions of the substituted chlorine atoms than by the number of these atoms in a molecule. In the case of observed reactions of $\bullet\text{OH}$ radicals with pentachlorophenol, Mills and Hoffmann (1993) confirmed that the additions of $\bullet\text{OH}$ radicals to *ortho* positions were more favorable than additions to *para* positions. It may be concluded that the increase in the number of substituted chlorine atoms on the ring blocks the favorable positions susceptible to hydroxyl attack, which results in a decrease in the degradation rate with increased number of chlorine atoms in the molecule.

Singlet oxygen is the first excited state of molecular oxygen. As a moderately reactive electrophile, it oxidizes numerous electron-rich organic substances. The method most frequently used for producing singlet oxygen in the laboratory is photosensitization. Both continuous irradiation and pulsed excitation studies have made much use of this method for singlet oxygen generation. Singlet oxygen in natural waters can also be produced in aqueous solutions of an appropriate sensitizer that absorbs light and transfers the energy to the dissolved triplet oxygen. The dissolved organic matter is a primary sensitizer responsible for the singlet oxygen formation.

Tratnyek and Holgné (1991), investigating reactions of chlorophenols with singlet oxygen using rose bengal as a sensitizer, observed that *ortho* and *meta* positions in monochlorophenol molecules were more active in reactions with singlet oxygen, independent of the presence of dissociated or undissociated forms. They also showed that increasing the number of chlorine atoms caused a decrease in the rate of the reaction.

Ozoemena et al. (2001), studying photosensitization transformations of polychlorophenols by radiation above 600 nm, suggested that negative inductive effects (when halogen substitution occurs on an aromatic ring) result in an electron-withdrawing effect from the benzene nucleus, deactivating it for an electrophilic attack by singlet oxygen. This electron withdrawal decreases the contribution of the type II pathway as the number of halogen substitutes increases. However, in the case of polychlorophenols, the electron-withdrawing effects of chlorine substituents cause a reduction in the electron donating ability of the substrate while the electron acceptor's ability is increased substantially.

Sakthivel and Kisch (2003) indicated that nitrogen-doped TiO_2 showed much better activity for the photocatalytic oxidation of 4-chlorophenol with visible light ($\lambda \geq 455$ nm). Three N-doped TiO_2 were prepared by hydrolysis of titanium tetrachloride with a nitrogen-containing base, such as ammonia, ammonium carbonate, or ammonium bicarbonate, respectively, followed by calcination in air

at 400°C. The slightly yellow resultants contained 0.08–0.13 wt% of nitrogen. In addition, the doped materials exhibited bandgap energies of 3.12 ± 0.01 eV, which suggested that a slight reduction in the bandgap, about 0.02 eV, was achieved compared to the undoped TiO₂. The nitrogen-doped materials all photocatalyzed the mineralization of 4-chlorophenol with artificial visible light ($\lambda \geq 455$ nm). About 50% conversion was observed after 6 h, whereas less than 1% of mineralization occurred in the case of unmodified titanium dioxide. The initial degradation rates were about 10–20 times larger.

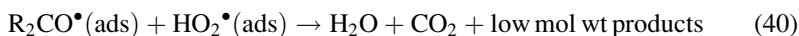
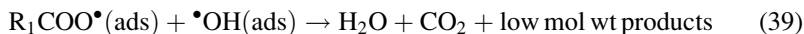
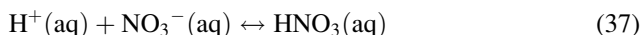
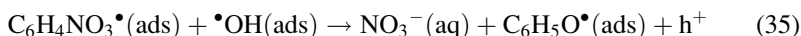
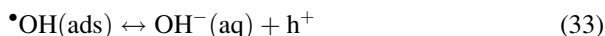
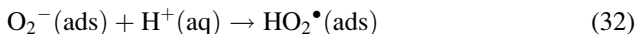
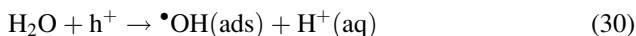
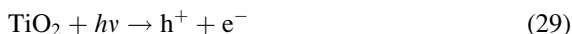
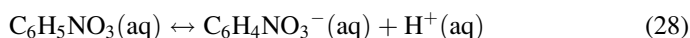
Visible light-assisted photomineralization of 4-chlorophenol was also performed by TiO₂ modified with platinum(IV) chloride (Burgeth and Kisch 2002). 4 wt% Pt/anatase TiO₂ was the best photocatalyst in comparison with anatase–rutile mixed TiO₂ (commercial name P-25), unmodified anatase TiO₂, and 1.1 wt% Pt/P-25, showing a six fold higher activity than that of P-25 ($\lambda \geq 455$ nm). Upon UV irradiation ($\lambda \geq 320$ nm), 4 wt% Pt/anatase TiO₂ was even more active than P-25. It was postulated that chemisorption of $[\text{PtCl}_6]^{2-}$ onto high surface area anatase TiO₂ powder led to the formation of a covalently bound surface complex. This novel hybrid semiconductor was an efficient photocatalyst for the mineralization of 4-chlorophenol both with visible and UV light. Activity was retained even in diffuse indoor light.

In general, the number and positions of chlorine atoms strongly influence the kinetics and mechanism of the chlorophenol photodegradation. Position of substituent chlorine atoms in the molecule is a key determinant in the reaction kinetics. In the case of direct photolysis, favorable positions are *para*- and *ortho*- due to the inductive and mesomeric effects of OH and Cl groups. When hydroxyl radicals are generated upon irradiation, the presence of a chlorine atom in *meta* position of monochlorophenols increases the reaction rate between chlorophenol and •OH. In the case of polychlorophenols, additions of hydroxyl radicals to *ortho* positions are more favorable than *para* positions. In addition, steric effects are very important for polychlorophenols.

4.2 Nitrophenols

Nitrophenols are common refractory pollutants that can be present in industrial wastewaters. In particular, effluent wastewater from the synthetic dye, petrochemical, pesticide, herbicide, and insecticide industries contain 4-nitrophenol (also known as *p*-nitrophenol) as a major pollutant (>10 ppm). The pollutant is also listed among the top 114 organic pollutants by the United States Environmental Protection Agency (USEPA). The feasibility of 4-nitrophenol-containing wastewaters being subjected to an ozonation process was investigated, whereas catalytic oxidation in a temperature range of 150–190°C was studied. Investigations on the photocatalytic abatement of 4-nitrophenol in TiO₂ aqueous slurries have also appeared in the literature (Lea and Adesina 2001; Andreozzi et al. 2000).

Lea and Adesina (2001) used an internally irradiated annular photoreactor to investigate the oxidative degradation of aqueous 4-nitrophenol with TiO_2 as the photocatalyst. The kinetics was determined as a function of nitrophenol concentration, oxygen partial pressure, catalyst loading, pH, temperature and light intensity. The photocatalytic oxidation of 4-nitrophenol was characterized by a relatively low activation energy of 7.83 kJ/mol, although transport intrusions were negligible. Rate decreased almost exponentially with pH while a quadratic behavior with respect to both oxygen pressure and nitrophenol concentration was symptomatic of self-inhibition. Possible explanation for this behavior is the formation of intermediates that competitively adsorb on similar sites to the reactants. Increased catalyst dosage also improved the reaction rate, although the possible effects of light scattering and solution opacity caused a drop at higher loadings. Rate, however, had a linear dependency on light intensity, suggesting that electron-hole recombination processes were negligible at the conditions studied. It was suggested that the photodegradation of 4-nitrophenol proceeded via aqueous dissociation to produce nitrophenoxide anions that subsequently adsorb on photogenerated holes and are attacked by hydroxide ions on the surface to yield oxygenated products as follows:



where h^+ and e^- are photogenerated holes and electrons, respectively, while R_1 and R_2 are alkyl groups.

5 Pesticides

Pesticide pollution of environmental waters is a pervasive problem with widespread ecological consequences. The major sources of pollution by pesticides are wastewater from agricultural industries and pesticide plants. Wastewater from those sources may contain pesticides at levels as high as several hundred mg/L. Whatever the concentration level detected, pesticides have to be removed either to protect our water resources or to achieve drinking water quality. The main characteristics of this wastewater are its extreme toxicity, low volume and well-defined location. Suitable treatment is therefore required to decontaminate it, which is much easier than cleaning up subsequent environmental hazards. Possible treatment methods include physical entrainment (e.g., activated carbon filtration, membrane technologies), biodegradation, and chemical reactions. Entrainment is losing acceptance as a final solution for waste disposal because of its low efficiency when dealing with high concentration of pollutants. Moreover, entrained pollutants must be further treated for complete destruction. Some form of biological processing is usually the preferred method for the treatment of effluents containing organic substances, since biological treatment techniques are well established and relatively cheap. However, these biological methods are susceptible to toxic compounds that inactivate the waste-degrading microorganisms. In such cases, a potentially useful approach is to partially pretreat the toxic waste by oxidation technologies to produce intermediates that are more readily biodegradable. Many oxidation processes are currently employed for this purpose, including photocatalytic processes (TiO_2/UV), photochemical degradation processes (UV/O_3 , UV/H_2O_2), and chemical oxidation processes (O_3 , O_3/H_2O_2 , H_2O_2/Fe^{2+}).

Pesticides, including herbicides, are classified and listed in terms of the characteristic structural groups in the review paper on photocatalytic transformation of pesticides in aqueous TiO_2 suspensions by Konstantinou and Albanis (2003). Among them, some chemical structures of pesticides are shown in Fig. 9 (Malato et al. 2000).

In order to assess the degree of mineralization reached during advanced oxidation processes (AOPs), the decrease of the total organic carbon (TOC) is generally estimated. Monitoring for chloride, nitrate, phosphate or ammonium ions using ion chromatography methods also provides useful data to follow the pesticide degradation. On the basis of the efficiency of AOPs, Chiron et al. (2000) concluded as follows:

1. Whatever the degradation system used, parameters linked to experimental conditions and reactor design are decisive in assessing the pesticide degradation rates. Among these parameters, light sources or ozone generator characteristics, treated water volumes, initial pesticide concentrations, details of analytical procedures, and types of equipments are especially relevant.

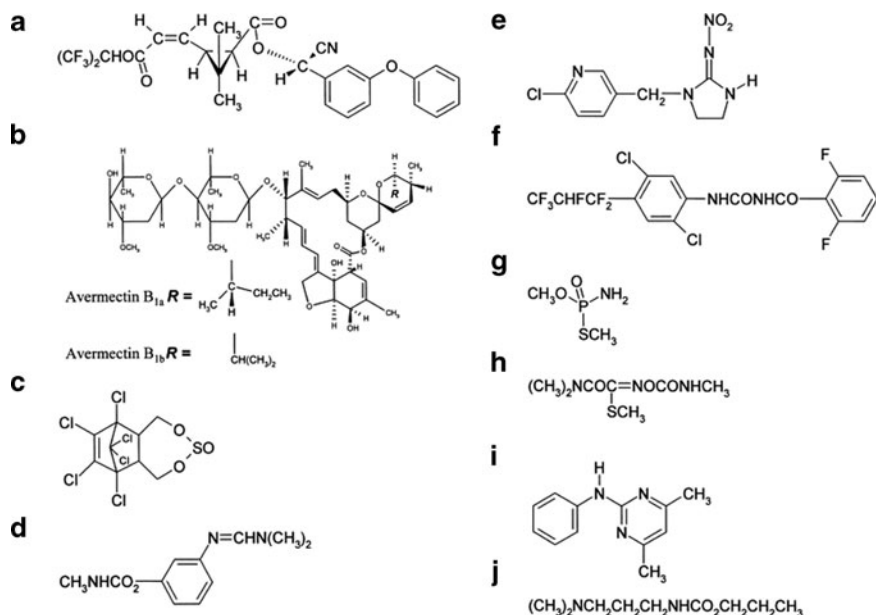


Fig. 9 Structures of the active ingredients in selected pesticides: (a) acrinathrin, (b) avermectin B1, (c) endosulfan, (d) formetanate, (e) imidacloprid, (f) lufenuron, (g) methamidophos, (h) oxamyl, (i) pyrimethanil, and (j) propamocarb (Malato et al. 2000). Reprinted from Malato et al. (2000), Copyright with permission from Elsevier

- Higher degradation times can be logically expected when formulated compounds are used instead of pure active ingredients because the chemical composition of water can influence the efficiency of the process. For example, carbonate ions and dissolved organic matter are well-known scavengers of hydroxyl radicals, hence reducing the degradation rates.
- Efficiency is usually not the bottleneck in the application of chemical oxidation processes for the elimination of contaminants from wastewaters. Nevertheless, the mineralization rate is usually much slower than the rate of pesticide disappearance, and total mineralization is not always achieved, indicating the importance of intermediate decomposition products. Toxic intermediates can be generated and incorporated into the effluent. Formation and decomposition kinetics of the intermediates, and identification of these by-products need to be established in order to (a) determine which specific compounds will appear in the effluent, (b) increase our understanding of the degradation pathways, and (c) establish which step is limiting the overall reaction rate.
- Different oxidants generally lead to different intermediates and different final products. It is important to distinguish reactions that occur by a common pathway (e.g., the hydroxyl radical mechanism) or from other steps such as ozone oxidation, direct hole attack, or even direct photolysis.

Selected representative compounds of the pesticide family are introduced below.

5.1 *s*-Triazines

s-Triazine herbicides such as atrazine, simazine, trietazine, prometon, and prometryn were rapidly degraded within several minutes but full mineralization was not observed during the photocatalytic oxidation process. Figure 10 shows the proposed degradation pathways of atrazine, (2-chloro-4-(ethylamino)-6-(isopropylamino)-*s*-triazine), which is widely used for weed control in the cultivation of corn and other crops (Ziegmann et al. 2006). Pathways for *s*-triazine transformation include displacement of the substituent at position 2, side alkyl chain oxidation, and further dealkylation and deamination. Different intermediates have been identified, mainly hydroxylated and dealkylated derivatives, ammeline, and cyanuric acid being the common final photo-products of all herbicides. The first reaction that takes place is the oxidation of the lateral chains, which yields acetamido and dealkylated derivatives as the main degradation products. Subsequent reactions are substituent hydrolysis reactions at position two and the final displacement of amino groups with hydroxyl groups, yielding cyanuric acid. The dealkylation mechanism follows the photo-Kolbe decarboxylation pattern through the formation of corresponding alcohol, aldehyde, and acid derivatives. Although the disappearance of initial compounds is very fast, the formation of the final product may require a relatively long irradiation time. In particular, substitution of the triazine ring-linked amino groups with hydroxy groups is a very slow process (Konstantinou and Albanis 2003). Moreover, reductive degradation paths that lead to dehalogenated *s*-triazines have been reported (Ollis and Al-Ekabi 1993; Minero et al. 1996).

Lackhoff et al. reported the induced degradation of atrazine on TiO₂- and ZnO-modified cement samples. The photocatalytic activity of the particles was determined by measuring the degradation rates of atrazine in comparison to unmodified cement samples (Lackhoff et al. 2003). Three kinds of TiO₂ were used to prepare 10 wt% TiO₂-modified cement samples: Degussa P-25, Hombikat UV 100, and anatase Jenapharm. For the atrazine degradation by irradiation of pure semiconductors and semiconductor-modified cement samples, the first-order rate coefficients were as shown in Fig. 11. Atrazine degradation rate was significantly enhanced due to the addition of 10 wt% Degussa P-25 and Hombikat UV 100 to Portland cement. The rate of Atrazine degradation by cement samples modified with 10 wt% anatase Jenapharm was increased only slightly in comparison to unmodified cement samples. The order of photocatalytic efficiency observed for different pure TiO₂ samples (Degussa P-25 > Hombikat UV 100 > anatase Jenapharm) compares well with the results obtained from modified cement samples. Drastic increase in pH caused by the presence of cement is speculated to be the potential reason for comparatively high reductions in photocatalytic efficiencies of modified cement samples. The pH values of pure metal oxide suspensions were in the range of pH 4.5–8.0 (4.9 for Degussa P-25, 5.5 for Hombikat UV 100, 4.5 for anatase Jenapharm, and 8.0 for ZnO), whereas all (modified) cement samples exhibited pH values of 12.5. At pH values greater than the pHPzc (point of zero charge, pH 6.3–6.6) TiO[−] dominated the surface, whereas slightly alkaline atrazine (pK_a = 1.6) was less

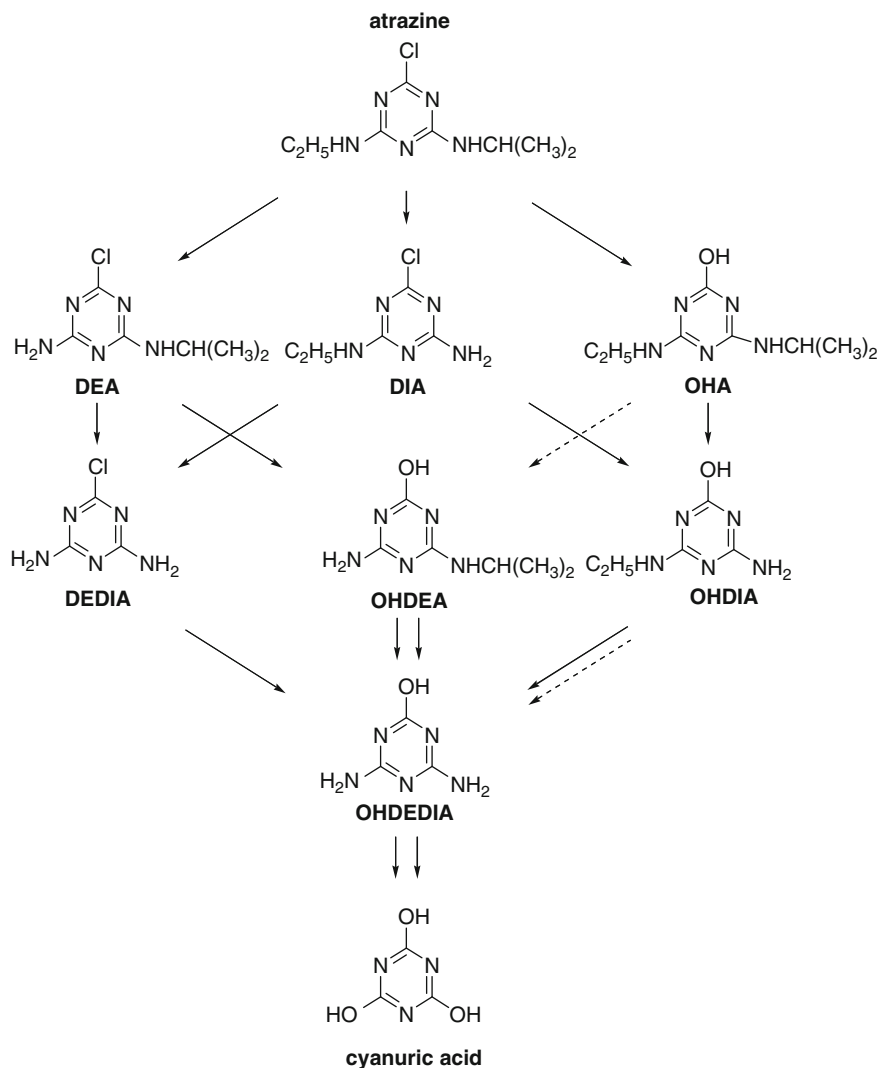


Fig. 10 Degradation pathways of atrazine (Ziegmann et al. 2006)

adsorbed due to electrostatic repulsion. The influence of the pH value is confirmed by the fact that photocatalytic activity of metal oxides with higher pH (Hombikat UV 100) is less retarded due to cement mixing (remaining activity of 7.8%) than metal oxides with lower pH (Degussa P-25 and anatase Jenapharm).

Upon photocatalytic treatment, sulfonylureas show similar behavior as *s*-triazines since they possess the characteristic *s*-triazine moiety in their molecules together with an aryl group and a sulfonylurea bridge. Three categories of photoproducts can be distinguished (see Fig. 12): The first one arises from the aromatic ring attack by $\cdot\text{OH}$, leading to the hydroxylation of the benzene ring. Hydroxylated aromatics are more

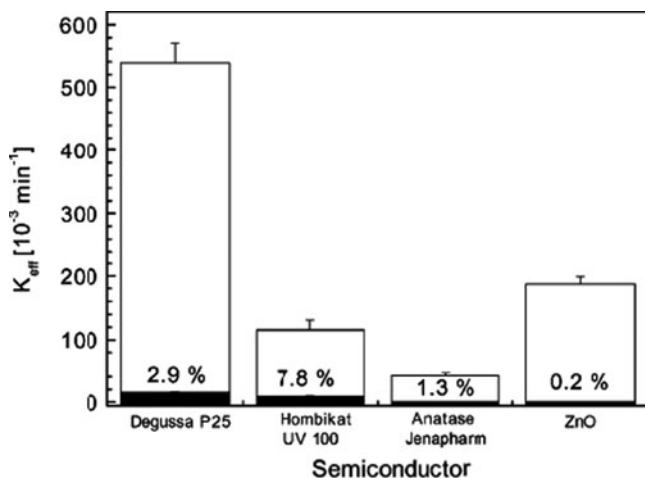


Fig. 11 First-order rate coefficients of atrazine degradation by irradiation of pure semiconductors (*white column*) and cement samples modified with these semiconductors (*black column*). The percentage values represent remaining photocatalytic efficiencies of modified cement samples in comparison to the belonging pure metal oxides. Reprinted from Lackhoff et al. (2003), Copyright with permission from Elsevier

easily oxidized than their parent compounds, and the reaction proceeds rapidly with further hydroxylation and ring opening. The second product family results from different cleavages of the sulfonylurea functional group to give various compounds containing a triazine ring. Finally, the third product class emerges from the photocatalytic degradation of *s*-triazine byproducts, as in the case of *s*-triazine herbicides, with ammelide and cyanuric acid being the final products. The degradation of both aliphatic and aromatic groups in sulfonylurea degradation lead to the formation of smaller and more oxidized metabolite molecules, such as short carboxylic acids (formic, acetic and oxalic) identified by LC-MS (Vulliet et al. 2002).

5.2 Phenylureas

Phenylurea and its derivatives have been used in weed control since the early 1950s because it was believed to inhibit photosynthesis of plants upon absorption by the roots. Their general structure and selected examples are shown in Fig. 13 (Amorisco et al. 2006; López et al. 2005). Phenylureas are highly persistent systemic herbicides, with half-lives of several months in soil, and are metabolized *in vivo* by soil microbes, plants, and animals via demethylation and hydroxylation. In recent years, the relatively high photochemical stability and water solubility of phenylurea herbicides have raised urgent questions about their role as persistent pollutants in soil and water, with consequent risks in the preservation of water supplies. Human health risks arising from water contamination by phenylurea herbicides is increased

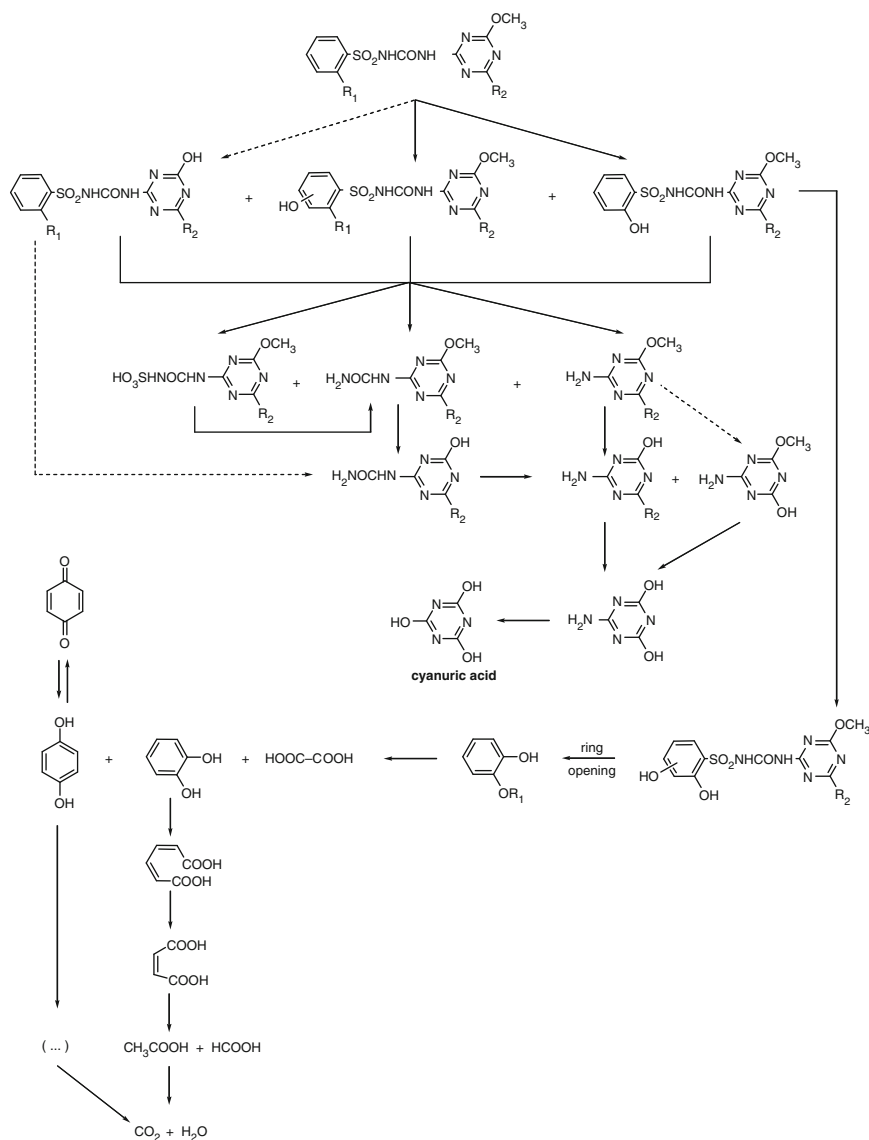


Fig. 12 Proposed pathway of photocatalytic degradation of sulfonylurea herbicides. Reprinted from Vulliet et al. (2002), Copyright with permission from Elsevier

upon considering the intensified toxicity of their by-products that are generated during water disinfection processes based on oxidants such as chlorine (hypochlorite) or ozone.

The photocatalytic transformation of phenylurea herbicides leads to the formation of several products. That results from (a) attack of the hydroxyl radicals on the aromatic ring and (b) abstraction of hydrogen atoms of the methyl group followed

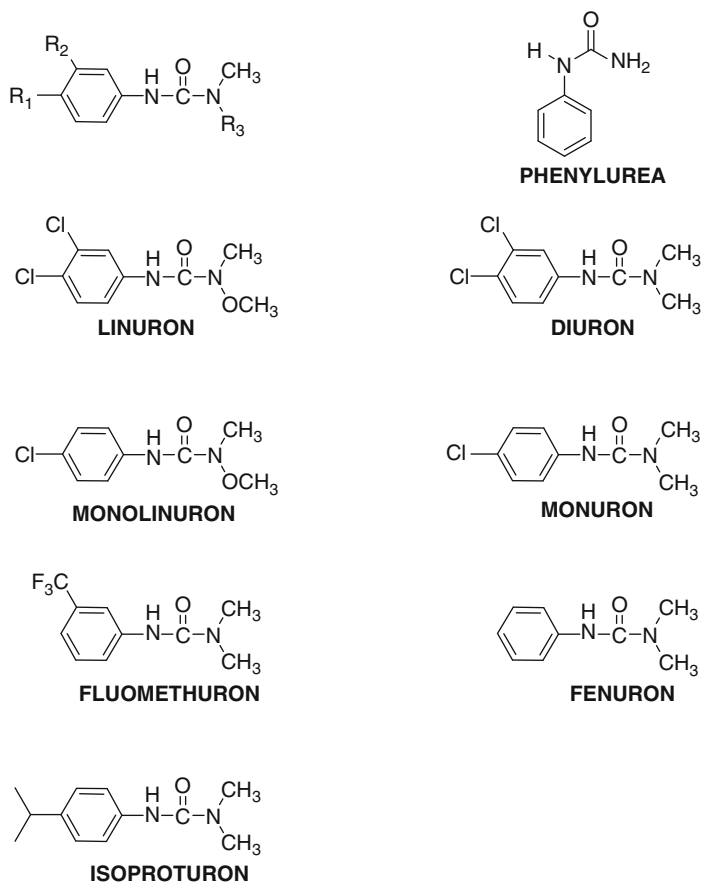


Fig. 13 General structure of phenylureas and selected examples (Amorisco et al. 2006; López et al. 2005)

by the addition of oxygen and decarboxylation, leading to the formation of dealkylated products. The distribution of products greatly depends on the pH of the medium. In neutral medium, the attack of the hydroxyl radicals is located both on the aromatic ring and on the methyl groups. In acidic medium, it is mainly located on the methyl groups, hydroxylation of the aromatic ring being clearly disfavored upon a decrease in pH.

López et al. (2005) compared the mechanism of TiO_2 photocatalytic degradation of Diuron (3-(3,4-dichlorophenyl)-1,1-dimethylurea) in aqueous solution compared with that of direct UV photodegradation. The radical anions, phenylurea \cdot^- , generated by one-electron reduction have $pK_a \approx 5$. From the rate constants of one-electron reduction, it can be deduced that the generation of phenylurea \cdot^- and $O_2\cdot^-$ on the surface of photocatalysts may be competitive. $HO\cdot$ reacts with phenylureas via addition to the aromatic ring and/or hydrogen abstraction from a saturated carbon atom (98%), rather than one-electron oxidation (2%). Adsorption studies on TiO_2

show that photocatalysis is independent of the specific area of the catalyst. A variety of compounds have been observed upon photocatalytic degradation of Diuron, while only two hydroxychloro derivatives (refer to Fig. 14b) were generated after direct 365 nm irradiation (main emission wavelength of a medium-pressure mercury lamp). The photocatalytic degradation proceeds by three main pathways (1) oxidation of the side chain methyl group, (2) hydroxylation of the aromatic ring, and (3) dechlorination (see Fig. 14). Different photoproducts of photocatalytic degradation are found depending on the polymorphic form of TiO_2 used, the reason for this being unclear.

Amorisco et al. studied the photocatalytic degradation of chlortoluron (3-(3-chloro-4-methylphenyl)-1,1-dimethylurea) and chloroxuron (3-[4-(4-chlorophenoxy)phenyl]-1,1-dimethylurea) under solar irradiation, using TiO_2 embedded into polyvinylidene fluoride transparent matrix as a heterogeneous photocatalyst (Amorisco et al. 2006). The structures of several by-products were obtained using ion trap tandem mass spectrometry coupled to high-performance liquid chromatography through an electrospray ionization interface. The most important and typical by-products were hydroxylated compounds arising from the interaction between hydrogen atoms either on aromatic or aliphatic carbons of the two chlorinated herbicides and OH radicals generated on the TiO_2 surface under irradiation. Other by-products were generated by slightly different processes, namely demethylation, dearylation, and dechlorination, eventually followed by the interaction with OH radicals. They could be more effective precursors than the herbicides themselves towards an extensive degradation of these two chlorinated.

Amorisco et al. also hypothesized a possible scheme of photocatalytic degradation of isoproturon (3-(4-isopropylphenyl)-1,1-dimethylurea) (Amorisco et al. 2005). Like other phenylureas exemplified above, most byproducts resulted from single or multiple hydroxylation (by photogenerated OH radicals) of the isoproturon molecule at different positions. Meanwhile, substitution of some functional groups of the herbicide (isopropyl or methyl) by OH radicals was also observed.

It has been reported that the extent of adsorption on TiO_2 is not decisive in the degradation process, and photocatalytic reactions may take place independently of the degree of adsorption of phenylureas. Correlation analysis showed that the reactivity of different phenylureas upon TiO_2 heterogeneous photocatalysis is associated with polar effects of the substituents in the aromatic ring. However, the aqueous photocatalytic degradation of Monuron (3-(4-chlorophenyl)-1,1-dimethylurea) has been found to follow Langmuir–Hinshelwood kinetics, thus leading to complete mineralization of the pollutant for $3 < \text{pH} < 9$, but only partial mineralization at acidic and alkaline pH, even with longer irradiation times.

Unlike phenylureas, alkylureas undergo different transformation schemes. Urea and alkylureas are building blocks of several anthropogenic compounds, such as pesticides and fertilizers, natural compounds like caffeine, constituents of drugs, antiepileptic and HIV drugs, and transformation products of DNA. In addition, they have been identified as final products of natural degradation. Calza et al. (2006) summarized the photocatalytic transformation pathways followed by methyl- and ethylurea derivatives (see Fig. 15). Both the methyl- and ethylurea derivatives have been shown to easily degrade in the presence of titanium dioxide with similar

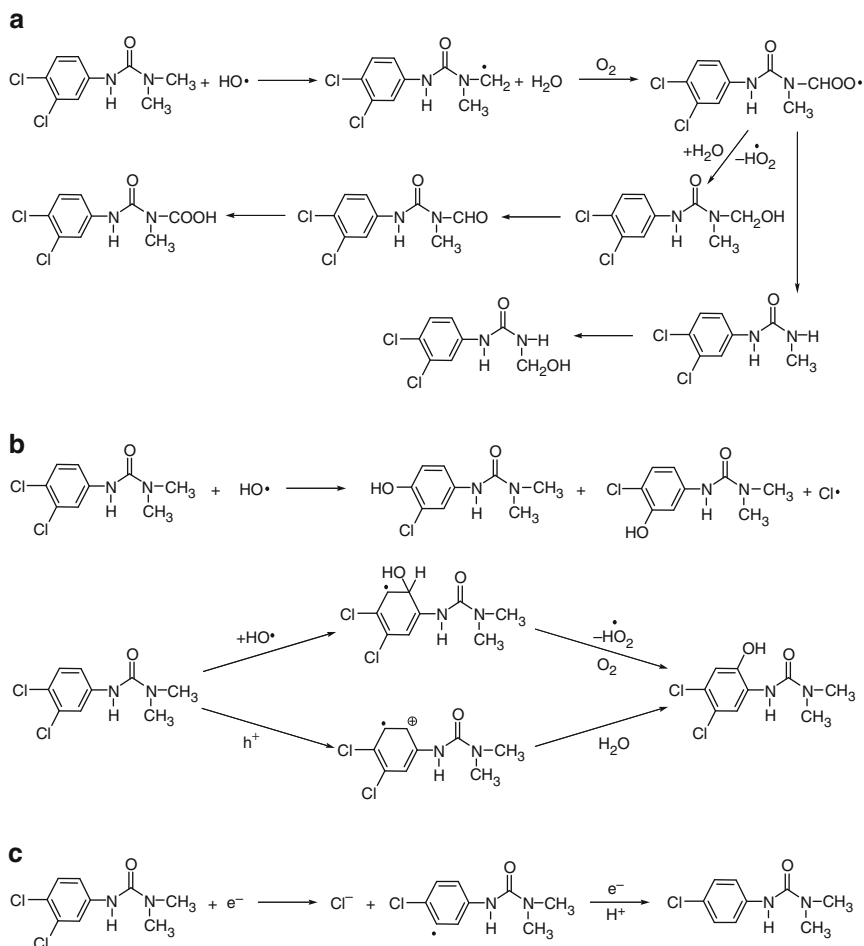


Fig. 14 Proposed pathway of photocatalytic degradation of phenylurea Diuron: (a) oxidation of the alkyl side chain, (b) chlorine substitution and hydroxylation of the aromatic ring, and (c) dechlorination (López et al. 2005)

kinetics, independent of the entity and the nature of the substitution. In contrast, the types of the formed intermediates and the rate and extension of the final mineralization are strongly dependent on the number of methyl or ethyl groups. These observations have been rationalized within the framework of a transformation mechanism in which all the investigated molecules (and the recognized intermediate compounds) are involved. In all cases, N-demethylation represents only a secondary pathway, while the main transformation proceeds by means of the unexpected cyclization of methylurea (MU), 1,1'-dimethylurea, 1,3'-dimethylurea (1,1'- and 1,3'-DMU), ethylurea (EU), and 1,3'-diethylurea (1,3'-DEU) with the formation of (methyl)-amino-2,3-dihydro-1,2,4-oxadiazol-3-one as the major intermediate. Furthermore, the presence of an electron-donor group, such as a methyl or

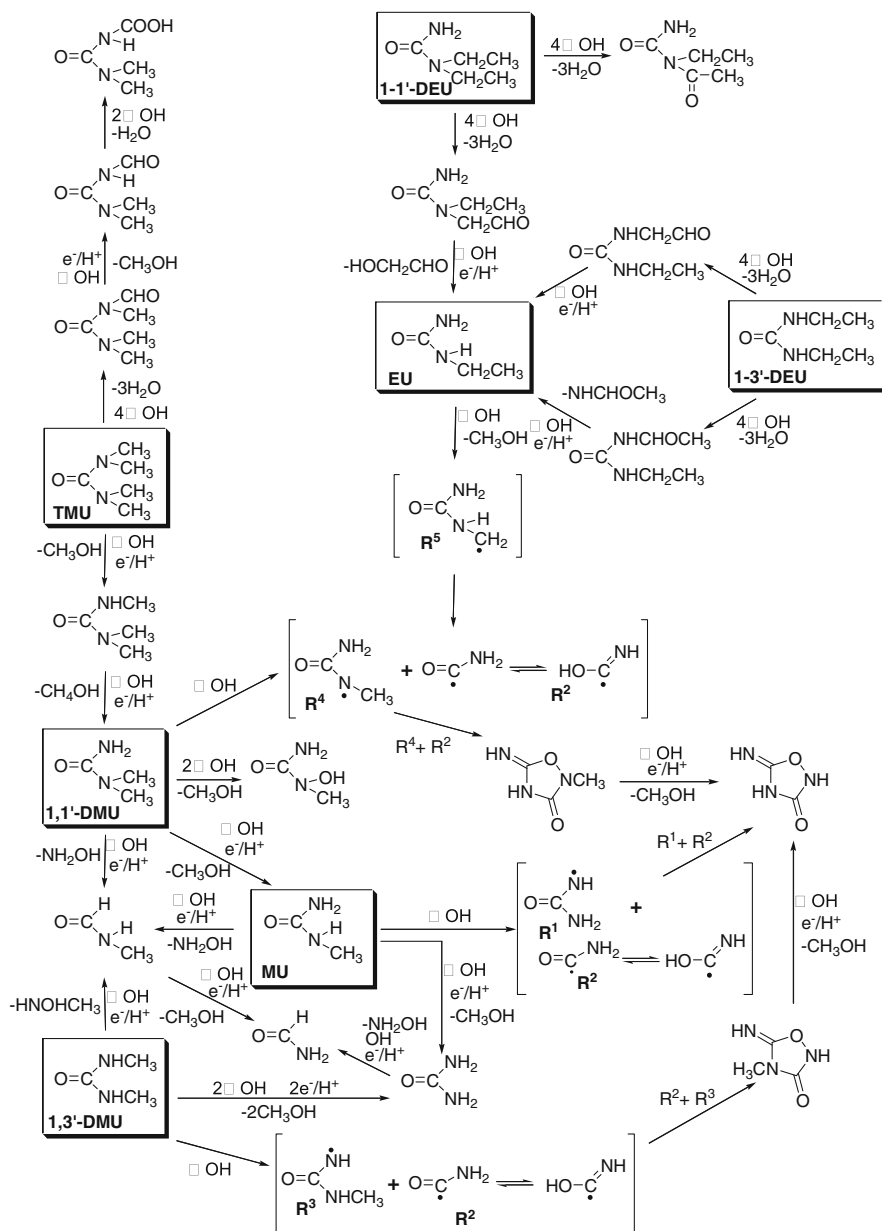


Fig. 15 Photocatalytic transformation pathways followed by methyl- and ethylurea derivatives (*1,1'*-DEU 1,1'-diethylurea, TMU tetramethylurea, EU ethylurea, *1,3'*-DEU 1,3'-diethylurea, *1,1'*-DMU 1,1'-dimethylurea, MU methylurea, *1,3'*-DMU 1,3'-dimethylurea) (Calza et al. 2006)

an ethyl group, favors both the release of the nitrogen atom (oxidation state -3) in the form of nitrate (oxidation state $+4$) and the mineralization of carbon, with respect to the unsubstituted urea.

6 Other Nitrogen-Containing Organic Compounds

6.1 Synthetic Dyes

Synthetic dyes are extensively used in many fields of up-to-date technology, e.g., in various branches of the textile industry, of the leather tanning industry in paper production, in food technology, in agricultural research, in light-harvesting arrays, in photoelectrochemical cells, and in hair colorings. Moreover, synthetic dyes have been employed for the control of the efficacy of sewage and wastewater treatment, for the determination of specific surface area of activated sludge for ground water tracing, etc. Synthetic dyes exhibit considerable structural diversity. Figure 16 shows synthetic dyes frequently studied in degradation researches (Forgacs et al. 2004).

Unfortunately, the exact amount of dyes produced in the world is unknown. It is estimated to be over 10,000 tons per year. Exact data on the quantity of dyes discharged in the environment are also unavailable. It is assumed that a loss of 1–2% in production and 1–10% loss in use are a fair estimate. For reactive dyes, this figure can be about 4%. Due to large-scale production and extensive application, synthetic dyes can cause considerable environmental pollution and are serious health-risk factors. Therefore, the growing impact of environmental protection on industrial development promotes the development of eco-friendly technologies, reduced consumption of freshwater, and lower output of wastewater. The release of significant amounts of synthetic dyes to the environment causes public concern and legislative problems, being a serious challenge to environmental scientists.

Decolorization of dye effluents has therefore received increasing attention. For the removal of dye pollutants, traditional physical techniques (adsorption on activated carbon, ultrafiltration, reverse osmosis, coagulation by chemical agents, ion exchange on synthetic adsorbent resins, etc.) can generally be used efficiently.

Nevertheless, these non-destructive techniques only transfer organic compounds from water to another phase, thus causing secondary pollution. Consequently, expensive operations such as regeneration of the adsorbent materials and post-treatment of solid-wastes are needed. Due to the large amount of aromatics present in dye molecules and the stability of modern dyes, conventional biological treatment methods are ineffective in decolorization and degradation. Furthermore, the majority of dyes are only adsorbed on the sludge and are not degraded. Chlorination and ozonation are also being used for the removal of certain dyes but at slower rates, as they often have high operating costs and limited effect on carbon content. Therefore, advanced oxidation processes that are able to degrade dye molecules in aqueous systems have been developed extensively during the last decade. Among these processes, heterogeneous photocatalysis using TiO_2 as photocatalyst appears

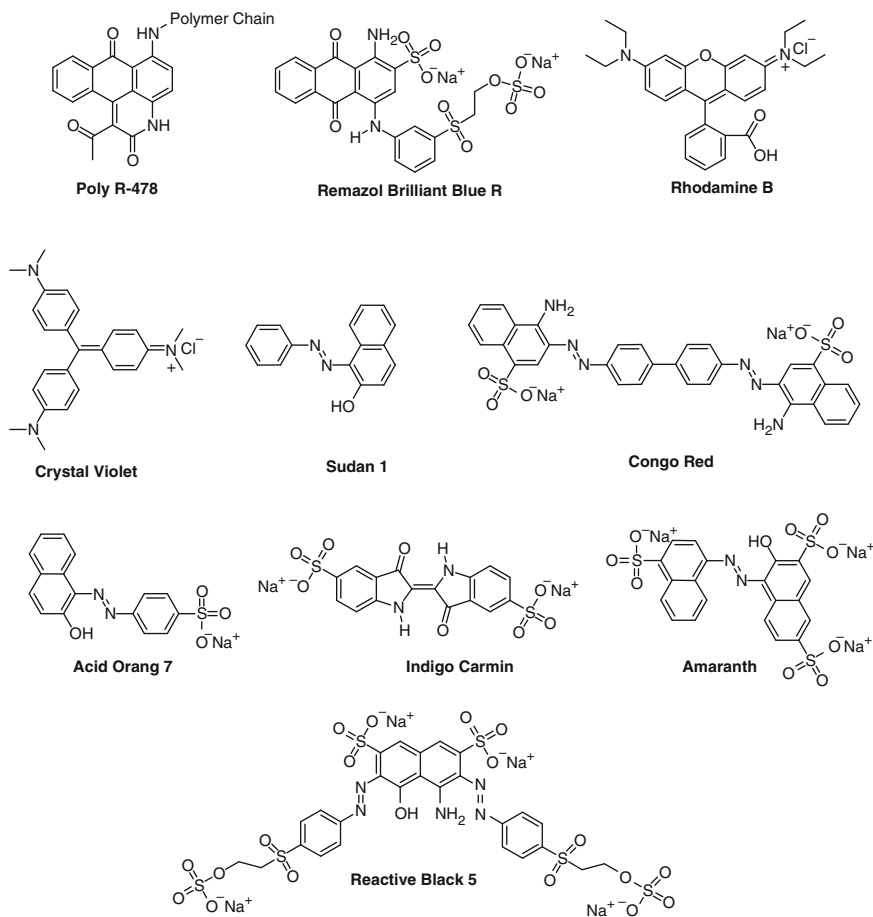


Fig. 16 Chemical structures of synthetic dyes frequently studied in degradation experiments. Reprinted from Forgacs et al. (2004), Copyright with permission from Elsevier

to be the most promising destructive technology. Various dyes, erythrosin B, eosin, Rose Bengal, rhodamine B, cresyl violet, thionine, chlorophyllin, anthracene-9-carboxylic acid, porphyrins, phthalocyanines, and carbocyanines have been reportedly employed as sensitizers. In these examples, the redox couples are often employed to regenerate the sensitizer (Cho et al. 2001). If one restricts such a regeneration process, the sensitizer undergoes oxidative degradation. This approach is useful for degrading colored contaminants, e.g., textile dyes. This process of self-sensitized oxidation is particularly effective in degradation of colored pollutants with visible light. The key advantage is its inherent destructive nature: it does not involve mass transfer; it can be carried out under ambient conditions (atmospheric oxygen is used as oxidant) and may lead to complete mineralization of organic carbon into CO_2 . Moreover, TiO_2 photocatalyst is largely available, inexpensive, non-toxic, and shows relatively high chemical stability.

Finally, TiO₂ photocatalytic process is receiving increasing attention due to its low cost when sunlight is employed as the irradiation source. The utilization of combined photocatalysis and solar technologies may develop a useful process for the reduction of water pollution by dyeing compounds, because of the mild conditions required and their efficiency in the mineralization.

The chemical classes of dyes that are employed more frequently on industrial scale are the azo, anthraquinone, sulfur, indigoid, triphenylmethyl (trityl), and phthalocyanine derivatives. However, it has to be emphasized that the overwhelming majority of synthetic dyes currently used in the industry are azo derivatives. Of the dyes available on the market today, approximately 50–70% are azo compounds, followed by the anthraquinone group. Azo dyes can be divided into monoazo, diazo, and triazo classes according to the presence of one or more azo bonds (–N=N–) and are found in various categories, i.e., acidic, basic, direct, disperse, and azoic pigments. Konstantinou and Albanis (2004) summarized azo dyes that were photocatalytically degraded with TiO₂. Some azo dyes and their dye precursors have been shown to be or are suspected to be human carcinogens as they form toxic aromatic amines. Therefore azo dyes are pollutants of high environmental impact, and were selected as the most relevant group of dyes concerning their degradation using TiO₂-assisted photocatalysis. It should be noted that azoketo hydrazone equilibria can be a vital factor in the easy breakdown of many of the azo dye system.

Acid orange 7, a representative of the class azo dyes, is the most studied compound among the azo dyes as far as its photocatalytic degradation under several experimental conditions is concerned. The dye acid orange 7 shows azo–hydrazone tautomerism. The hydrazone form of the dye shows a bathochromic shift in the absorption spectra ($\lambda_{\text{max}} = 485 \text{ nm}$) whereas a shoulder at 430 nm is attributed to the azo form of the dye. The azo peak at 430 nm was observed only in the aqueous phase, in which the TiO₂ particles were suspended in a homogeneous solution of the azo dye (see Fig. 17) (Chatterjee and Dasgupta 2005). The hydrazone form of the dye was reportedly found to be more stable when adsorbed on the surface of the TiO₂ semiconductor. When the spectra of the dye adsorbed on the TiO₂ surface were observed in a dry phase, the absorption peak corresponding to the hydrazone form of the dye was seen at 485 nm but the peak at $\lambda = 430 \text{ nm}$ (corresponding to the azo) disappeared. However, a tail in the red region of the visible spectrum up to $\lambda = 600 \text{ nm}$ was reportedly observed. Also, a peak at $\lambda = 520 \text{ nm}$ was seen, which indicated the formation of a donor–acceptor complex between the dye and the semiconductor on the surface of the TiO₂ semiconductor. The dye was subjected to FT-IR spectroscopy to probe the chemical reactions occurring on the semiconductor surface at intervals of $t = 0, 40,$ and 350 min. Results revealed the formation of many degradation products as the irradiation time proceeded from $t = 0$ to 350 min, due to the formation of new peaks and subjugation of old peaks with time. However, the absorption spectrum (recorded in solid state) of the dye taken after a 3-h irradiation of the TiO₂ suspension revealed no peaks corresponding to the two forms of the dye, indicating that the dye was effectively degraded (Bauer et al. 2001). The degradation pathways and the formation of by-products are also fully described (see Fig. 18) (Konstantinou and Albanis 2004). After the photoinjection of an electron in the conduction band of TiO₂, the cation

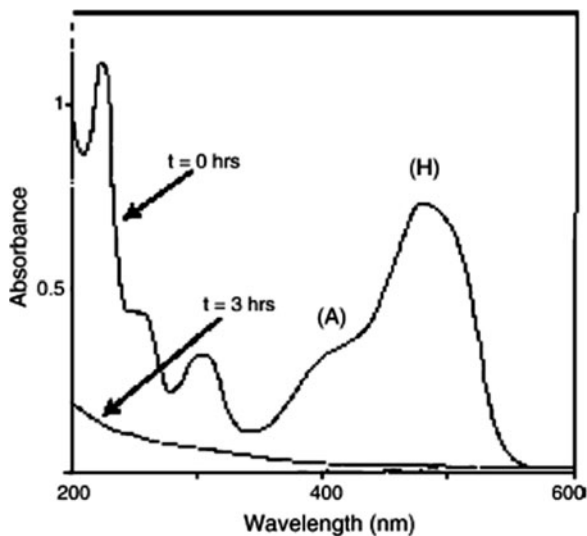


Fig. 17 Electronic absorption spectra of the aqueous solution of AO7 at $t = 0$ h and after 3 h of irradiation with visible light beam ($\lambda = 442$ nm). H and A show the electronic absorption bands linked to the hydrazone and the azo tautomer, respectively. Reprinted from Chatterjee and Dasgupta (2005), Copyright with permission from Elsevier

radical formed from the hydrazone form of the dye can undergo rapid deprotonation to create the deprotonated radical, which can react with the molecular oxygen. This oxidative attack could lead to the formation of benzene sulfonate and naphthaquinone but since naphthaquinone is very unstable, it would further degenerate to form phthalic acid. Twenty-two transformation products were identified in total, including 2-naphthol, 2-hydroxy-1,4-naphthoquinone, smaller aromatic intermediates such as phthalic acid and phthalimide, and aliphatic acids such as fumaric, succinic, maleic, and malonic acids. The lowest molecular weight compounds detected were oxalic, acetic, and formic acids. Evidences in favor of the formation of several aliphatic carboxylic acids and oxygenated sulfur derivatives have been provided in the destruction of phthalic acid as well as benzene sulfonate. Though the photocatalytic formation of several active oxygen species via hydrogen peroxide, perhydroxyl, and hydroxyl radicals has been proposed for the degradation of the azo dyes, the role of these radicals has not yet been fully elucidated. It is possible that just neutral molecular oxygen or superoxide anions are sufficient for the degradation of the acid orange 7 dye (Bauer et al. 2001).

Acid orange 52, also known as methyl orange, is frequently selected from the aminoazobenzene sub-category of monoazo dyes. Up to 18 intermediates were identified including aniline, *N,N*-dimethyl aniline, hydroxy anilines, hydroxy analogues of acid orange 52, phenols, quinone, benzene sulphonic acid, demethylated analogues of acid orange 52, and various aliphatic and carboxylic acids. Spadaro et al. (1994) proposed that oxidation of aminoazobenzene dyes proceeds by the addition of a hydroxyl radical to the carbon atom bearing the azo bond, followed by

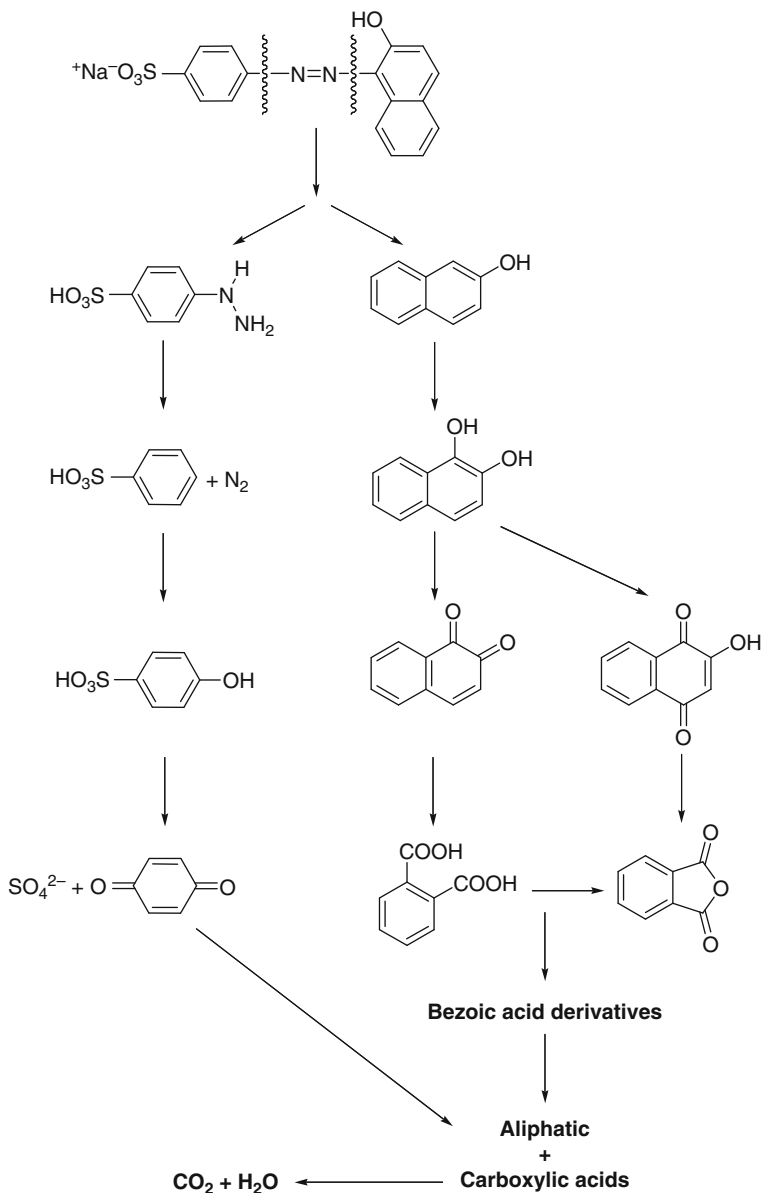


Fig. 18 Major photocatalytic pathways of acid orange 7. Reprinted from Konstantinou and Albanis (2004), Copyright with permission from Elsevier

the breaking of the resulting adduct. The products such as benzenesulfonic acid, *N,N*-dimethylaniline, and 4-hydroxy-*N,N*-dimethylaniline could arise from such reactions. The electron-withdrawing sulphonate group inhibits reactivity towards $\bullet OH$ of the ring that carried it, thus the ring with the amino group becomes the first target

for the hydroxy radicals. The addition of $\bullet\text{OH}$ on the carbon atom bearing the sulphonate group and the subsequent elimination of SO_3 is an improbable pathway due to the electron-withdrawing effect of sulphonate group and steric hindrance. On the contrary, hydroxyl-analogue derivatives of acid orange 52 are identified. The major degradation pathways for aminoazobenzene dyes are shown in Fig. 19 (Konstantinou and Albanis 2004).

Zhao et al. (2003) examined the effect of a TiO_2 surface-chemisorbed platinum (IV) chloride species (PtCl_6^{2-}) on the photodegradation of ethyl orange under visible light irradiation. Ethyl orange is an important representative of the azo dyes and is famous for its relatively stable features as a dye laser material. Addition of small quantities of hexachloroplatinic acid ($\text{H}_2\text{PtCl}_6 \cdot 6\text{H}_2\text{O}$) to the aqueous ethyl orange/ TiO_2 dispersions significantly enhanced the degradation of the ethyl orange dye. Results also showed that PtCl_6^{2-} was strongly adsorbed on the TiO_2 surface. In contrast, photodegradation appeared to be rather less efficient when carried out in the presence of TiO_2 alone. The primary step in the rapid degradation of the azo dye ethyl orange in the presence of PtCl_6^{2-} is essentially the photoexcitation of the dye, not the excitation of adsorbed PtCl_6^{2-} , although the catalyst specimen does exhibit a definite light absorption throughout a portion of the visible wavelengths. As evidenced from the TOC and COD results, no intrinsic differences were observed between Pt(IV)/ TiO_2 and TiO_2 dispersions in the mineralization of ethyl orange. It was emphasized that the existence of PtCl_6^{2-} had a negligible effect on the mineralization of the substrate when the dispersion had been discolored. The discolored dispersions contain small molecular intermediates that have no absorption features in the visible region and thus cannot be excited by visible light. Accordingly, if localized excitation of PtCl_6^{2-} were the primary step in the overall pathway, it should have led to the complete degradation (i.e., mineralization) of the azo dye. Proposed mechanism for the photodegradation of ethyl orange on Pt(IV)/ TiO_2 surfaces is shown in Fig. 20 (Zhao et al. 2003).

6.2 Nitroaromatic Compounds

Environmental contamination by nitro compounds is associated principally with the explosives industry. Modern explosives are nitrogen-containing organic compounds with the potential of self-oxidizing into small gaseous molecules (N_2 , H_2O , and CO_2). Many are polynitroaromatic compounds, including 2,4,6-trinitrotoluene (TNT), (which for many years dominated the explosive industry), 1,3,5-trinitrobenzene, dinitrotoluene (2,4-DNT, 2,6-DNT), dinitrobenzene, methyl-*N*,2,4,6-tetranitroaniline, and 2,4,6-trinitrophenol (picric acid). Some have additional industrial uses, e.g., the dinitrotoluenes are intermediates in the manufacture of polyurethanes.

Environmental contamination by nitro compounds is a problem because of the scale on which explosives have been manufactured, used, and tested. The United States ceased TNT production in the mid-1980s, but environmental contamination still exists due to activities before then and as a result of demilitarization.

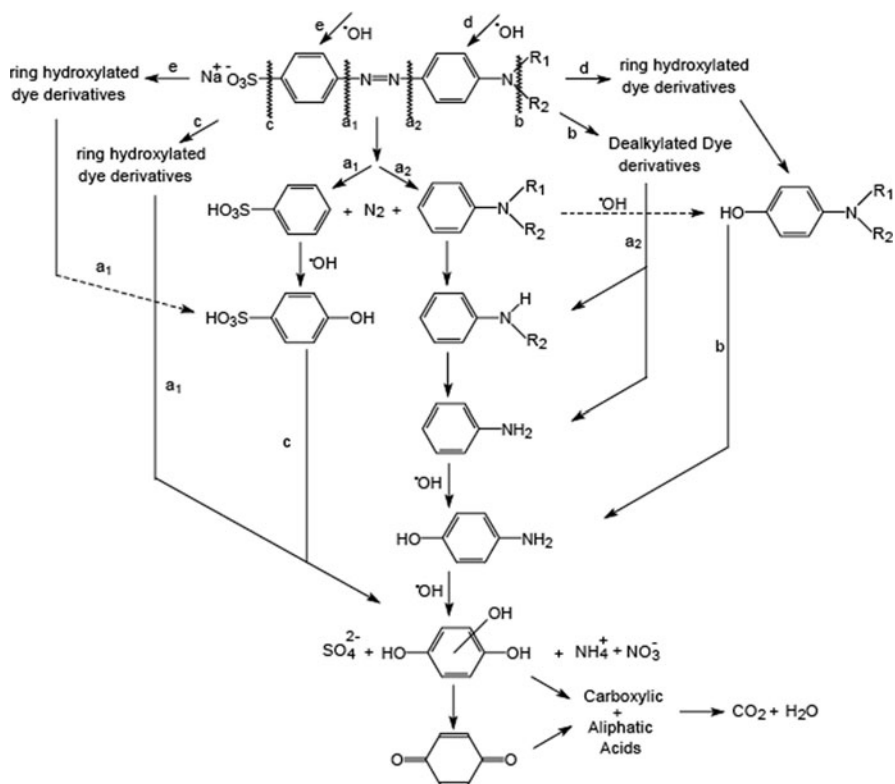


Fig. 19 Major photocatalytic degradation pathways for aminoazobenzene dyes based on the identification of by-products from degradation studies of acid orange 52. Reprinted from Konstantinou and Albanis (2004), Copyright with permission from Elsevier

Contamination occurs during the manufacture of TNT, which requires large amounts of water for purification. The aqueous wastes known as red water contains up to 30 nitroaromatics besides TNT. In addition, pink water, which is generated during loading, packing or assembling munitions, often contains high concentrations of other nitroaromatic explosives.

Nitroaromatic explosives are toxic, and their environmental transformation products, including arylamines, arylhydroxylamines, and condensed products such as azoxy and azo compounds, are equally or more toxic when compared to their parent nitroaromatics. Aromatic amines and hydroxylamines are implicated as carcinogenic intermediates as a result of nitrenium ions formed by enzymatic oxidation. TNT is on the list of US EPA priority pollutants: it is a known mutagen and can cause pancytopenia as a result of bone marrow failure. Aromatic nitro compounds are resistant to chemical or biological oxidation and to hydrolysis because of the electron-withdrawing nitro groups.

Rodgers and Bunce reviewed a variety of treatment technologies that are available or under research to remediate the contaminants, which include TiO_2 photocatalysis,

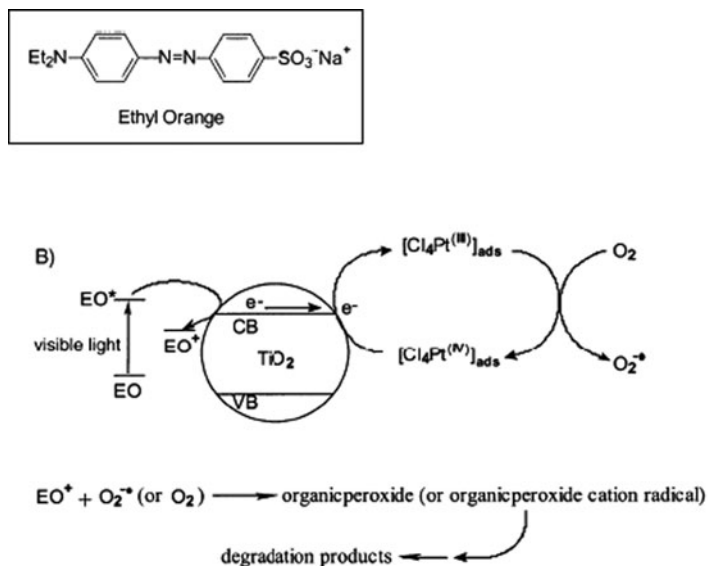


Fig. 20 Proposed mechanism for the photodegradation of ethyl orange on Pt(IV)/ TiO_2 surfaces under irradiation with visible light where EO denotes ethyl orange the chemical structure of which is shown in a *square box* (Zhao et al. 2003)

UV oxidation with hydrogen peroxide, UV oxidation with ozone, $\text{Fe}^{2+}/\text{H}_2\text{O}_2$, $\text{Fe}^{2+}/\text{H}_2\text{O}_2/\text{UV}$, adsorption, surfactant complexing, liquid–liquid extraction, ultrafiltration, reverse osmosis, chemical reduction (hydrogenation), microorganism remediation, and phyto-remediation (Rodgers and Bunce 2001).

Heterogeneous photocatalysis is inefficient due to electron–hole recombination, which competes with water oxidation. However, the process has attracted much attention because it employs UVA radiation, wavelength of which ranges from 320 to 400 nm, that allows the use of low-cost near-UV lamps or even natural sunlight (although the latter has never been commercialized) and hinders the competing light absorption by other substances. In the aqueous slurry of TNT with TiO_2 , the nitrogen atoms of TNT were converted to NH_4^+ and NO_3^- (Rodgers and Bunce 2001).

Kamble et al. (2006) studied the photocatalytic degradation of *m*-dinitrobenzene (*m*-DNB) by illuminated TiO_2 in a slurry reactor. *m*-DNB is one of the several compounds that are released to the environment during the manufacture of explosives and in loading, assembly and packing activities at military ammunition plants and other military installations. *m*-DNB is manufactured as a byproduct of the explosive TNT, with the potential for release to the environment in discharged wastewater. Additionally, any 2,4-dinitrotoluene present in the waste stream may be degraded to *m*-DNB by photolysis under certain pH conditions and organic matter content. Its widespread distribution as an environmental contaminant is a potential threat to wildlife and other ecological receptors. Therefore, removal of *m*-DNB from aqueous solution is very important. 2,4-Dinitrophenol and

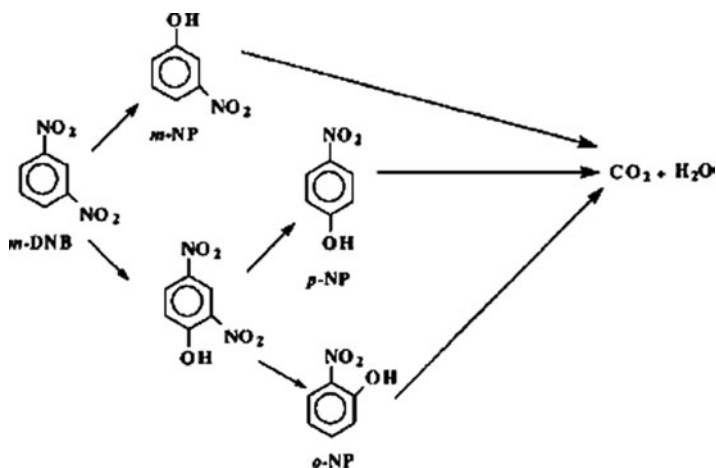


Fig. 21 Postulated reaction pathway for photocatalytic degradation of *m*-DNB where *o*-NP, *m*-NP, and *p*-NP denote *o*-nitrophenol, *m*-nitrophenol, and *p*-nitrophenol, respectively (Kamble et al. 2006)

m-, *o*-, and *p*-nitrophenol were detected as intermediates in very low concentrations during the degradation of *m*-DNB, using concentrated solar radiation and O₂ from air as the electron acceptor. It was observed that the rate of photocatalytic degradation of *m*-DNB is relatively low compared to that of nitrobenzene as a result of the poor adsorption of *m*-DNB compared to nitrobenzene. Figure 21 shows the postulated pathway for the photocatalytic decomposition of *m*-DNB.

7 Nitrogen-Containing Inorganic Compounds

In addition to organic compounds, a wide variety of inorganic compounds are photocatalytically sensitive on the surfaces of semiconductor particles. Toxic heavy metal ions can be reduced and deposited for easy disposal, since metal deposits can subsequently be extracted from the slurry by mechanical and/or chemical methods. The development of industries significantly increases the demand for metals. Waste metal recovery can potentially resolve two issues: metal pollution prevention and resource conservation. Metal ions are generally non-degradable, build up concentrations in food chains to toxic levels, and have infinite lifetimes. Hg²⁺, Pb²⁺, Cd²⁺, Ag⁺, Ni²⁺, and Cr⁶⁺ ions that are well known for high toxicity are extracted by semiconductor-assisted photoreduction or deposited on the semiconductor as insoluble oxides, depending on relative positions of their redox potentials. Concentrations lower than 0.005 ppm are allowed for Cr⁶⁺ and Ni²⁺, 0.004 ppm for Pb²⁺, and 0.001 ppm for Hg²⁺. The recommended level of Cd²⁺ is less than 5 ppm, also being included in the priority list of US EPA. The toxic effect of Ag⁺ is not completely understood but it is known as an effective bactericide that can damage

biological systems. Precious metals such as platinum, palladium, rhodium, gold, and copper can also be extracted by heterogeneous photodeposition.

In heterogeneous photocatalysis of organic substances, non-metal inorganic compounds are generated through subsequent total mineralization. The absence of total mineralization has been observed only in the case of *s*-triazine herbicides as mentioned earlier in this chapter. In this case, the final product obtained was essentially 2,4,6-trihydroxy-1,3,5-triazine (cyanuric acid), which is, fortunately, non-toxic. This is due to the high stability of the triazine nucleus, which resists most oxidation methods. For chlorinated molecules, Cl^- ions are easily released to the solution, which could be of interest in a process where photocatalysis is associated with a biological depuration system that is generally ineffective in treating chlorinated compounds. Sulfur-containing pollutants are mineralized into sulfate ions, whereas organophosphorous pesticides produce phosphate ions. However, phosphate ions remained adsorbed on TiO_2 within the pH range used. This strong adsorption partially lowers the reaction rate, which, however, remains acceptable. The analysis of aliphatic fragments resulting from the degradation of the aromatic ring has only revealed formate and acetate ions. Other aliphatics (presumably acids, diacids, and hydroxylated compounds) are very difficult to separate from water and to analyze. Formate and acetate ions are rather stable as observed in other advanced oxidation processes, which in part explain why the total mineralization takes much longer than dearomatization (Herrmann 1999).

Above all, ammonium (including ammonia), nitrate, and nitrite are the most frequently encountered and important inorganic species because nitrogen-containing organic molecules are mineralized into NH_4^+ and mostly NO_3^- . Ammonium ion is relatively stable and its proportion depends mainly on the initial oxidation degree of nitrogen and on the irradiation time. Presence of cyanide must not be overlooked because it is a significant source of the nitrogen-containing inorganic compounds.

The existence of free or complexed cyanides in industrial effluents is a problem of major concern because of infamous toxicity of these species to ecosystems. Cyanide has been used as an unparalleled leaching agent in the extraction of gold from ore. Harmful industrial aqueous wastes containing free or complexed cyanides are generated in large amounts from refining, electroplating, and heat-treating of gold as well as coal gasification process. There have been conventional treatment processes including physical, chemical, and biological methods to remove free or complexed cyanides dissolved in water. Physical treatments include ion exchange, adsorption by activated carbon, flotation-foam separation, reverse osmosis, and electro dialysis. Biological methods are based on biodegradation. Chemical processes involve the INCO process using SO_2 -air, the Degussa process using hydrogen peroxide, electrolytic decomposition, cyanide oxidation by oxidants such as ferrate (VI), ozone, and permanganate, and alkaline chlorination, which is currently the most reliable technique. These methods, however, are not free from some drawbacks. For instance, in the physical treatments, cyanides are not decomposed or treated but only shifted from water to another phase. For biological methods, the reaction rate is so low that the method is limited to low concentrations of cyanides. For chemical processes, oxidants are generally expensive and some metal cyanide

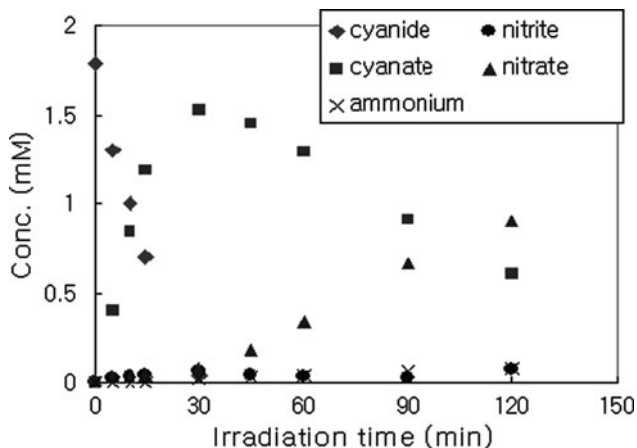


Fig. 22 Concentration of cyanide and products using TiO_2 when the suspension was bubbled with oxygen. Reprinted from Kim and Lee (2003), Copyright with permission from Elsevier

complexes are not decomposable by oxidation. Especially, for alkaline chlorination, highly toxic cyanogen chloride (CNCl) is produced (Kim and Lee 2004). Since the pioneer work by Frank and Bard, the photocatalytic decomposition of aqueous cyanide has been studied (Frank and Bard 1977; Kim et al. 2001; Chiang et al. 2002; Yeo et al. 2002; Sohn et al. 2003; Hernández-Alonso et al. 2002; Kim and Lee 2003). Cyanate reportedly appears as the first intermediate and undergoes further mineralization to ammonium, nitrite, nitrate, and gaseous products according to experimental conditions. Figure 22 shows the changes in the concentration of cyanide and the distribution of products using TiO_2 when the suspension was bubbled with oxygen (Kim 2003). It is still ambiguous whether the photocatalytic oxidation of cyanide proceeds via hydroxyl radicals or by photogenerated holes.

8 Application in Polymer Science

The active radical species such as hole or hydroxyl radicals originated from photocatalysis can be utilized to initiate polymerization or polymer decomposition according to reaction conditions. In the absence of water and oxygen, radicals can initiate polymerization. Styrene, 1,3,5,7-tetramethylcyclotetrasiloxane, methyl methacrylate, and pyrrole can be polymerized with photocatalysis (Fox and Duray 1993). When photocatalysts are incorporated into polymer matrices or coated on substrates, photocatalysis decomposes polymer matrices or polymeric substrates/binders, causing so-called weathering or chalking. Recently, many studies have been related with these phenomena to endow polymer-base materials with the positive effects of photocatalysis, such as self-cleaning property, anti-bacterial property, and self-degradation property for eco-friendly material (Gesenhues 2000, 2001; Allen

et al. 2004; Penot et al. 2003; Lacoste et al. 2003; Cho and Choi 2001; Zan et al. 2004; Xu et al. 2005; Kim et al. 2006; Sun et al. 2002; Iketania et al. 2003; Sanchez et al. 2006; Moustaghfir et al. 2006; Yang et al. 2006; Schmidt et al. 2006; Wakamura et al. 2003; Yoshida et al. 2006).

8.1 Photocatalyst as a Pigment

TiO₂, a representative photocatalyst, has been widely used as a white pigment for thermoplastic materials. However, its high photocatalytic activity can cause photo-degradation of thermoplastic materials. Therefore, commercial TiO₂ pigments must have a variety of properties: different crystal structures and surface modifications. Inorganic surface modification is needed to lower the activity of photocatalysts and additional organic surface modification is required to enhance the dispersibility of photocatalysts in polymer matrix. When PVC is pigmented with TiO₂, the weathering is affected by the type of TiO₂ pigment. Rutile TiO₂ pigment shows lower weathering rates than anatase TiO₂ due to its lower photocatalytic activity and Al-doping on rutile TiO₂ lowers photocatalytic activity to the level of commercially available white pigments (Gesenhues 2000). Therefore, Al₂O₃-doped rutile TiO₂ has been used as commercial whiter pigments. The weathering or chalking phenomenon of alkyd paint film containing TiO₂ pigments is also suppressed by Al-doping on TiO₂ pigments. It was reported that Al₂O₃ existing in bulk phase TiO₂ is functionally more important than surface Al₂O₃ because bulk Al₂O₃ provides recombination sites for hole and electrons (Gesenhues 2001). Besides Al₂O₃, SiO₂ can be coated on TiO₂ particles to inhibit the destructive oxidation of alkyd-based binders that leads to chalking phenomena. When hydrous aluminum oxide is used with other oxide materials, it decreases van der Waals force, which in turn improves the dispersibility. Particle size is also an important factor in determining the photo-oxidation rate of polyethylene. Nano-sized TiO₂ pigment showed higher photocatalytic activity in polyethylene degradation (Allen et al. 2004). For self-cleaning paint, it was suggested that a mixture of micron-sized rutile TiO₂ pigment with Al-doping and nano-sized anatase TiO₂ can be applied to limit the oxidation and chalking phenomena within the near surface layers (Allen et al. 2004). This application is dealt with as below.

ZnO also initiates the photocatalytic oxidations of isotactic propylene and ethylene-propylene copolymers in the absence of anti-oxidants or surface-coated layers (Penot et al. 2003; Lacoste et al. 2003).

8.2 Photocatalyst-Polymer Composite

In pigment/polymer system, photocatalytic oxidation has been an undesirable phenomenon to prevent. However, this reaction can be used in eco-friendly disposal of polymer wastes. Recently, photocatalyst-polymer composites have been

studied as self-degradable materials, decomposing under solar light via solid-phase photocatalysis.

When TiO_2 is embedded in polyvinylchloride (PVC), it is observed that PVC is photocatalytically degraded to a third of its molar weight after a 300-h irradiation. This phenomenon also takes place in the presence of oxygen, and cavity formation near TiO_2 aggregates is shown in Fig. 23. It seems that this degradation progressed via typical photocatalytic oxidation mechanism. However, the dispersion of TiO_2 was inefficient in PVC matrix, and it is suggested that only 0.02 wt% of TiO_2 is sufficient in decomposing PVC composite film when 5 nm TiO_2 particles are highly dispersed (Cho et al. 2001).

The dispersion of TiO_2 in polymer matrix can be enhanced by surface treatment. It was reported that polystyrene-grafted TiO_2 was prepared by the radical polymerization of polystyrene, following the pre-reaction of silicone coupling agent (γ -methacryloyloxypropyl triethoxysilane) and surface hydroxyl group of TiO_2 . The grafted TiO_2 could be composited with polystyrene (PS) via radical polymerization, and showed higher dispersion and photocatalytic degradation efficiency in TiO_2 -PS composite form than in unmodified TiO_2 form (see Fig. 24). The decomposition of TiO_2 -PS composite was observed as in Fig. 25. After irradiating for 300-h, the average molecule weight of PS-grafted TiO_2 composite decreased to about a quarter of its original value (Zan et al. 2004). This composite can be applied for the accelerated natural degradation of PS and EPS (expanded polystyrene) packaging wastes.

Similarly, optically transparent poly(methyl methacrylate-*co*-maleic anhydride)/ SiO_2 - TiO_2 composite film can be prepared by using 3-aminopropyl triethoxysilane as a coupling agent to form imide groups. The composite film shows high thermal stability and photocatalytic degradation property (Xu et al. 2005).

TiO_2 can be surface-modified by hyperbranched poly(ϵ -caprolactone) (HPCL) with $-\text{COOH}$ functional end groups. It was reported that HPCL-surface modification also enhanced the dispersibility of photocatalytic-degrading TiO_2 in PVC matrix (Kim et al. 2006).

HF surface-treatment of TiO_2 can increase the adsorption ability of TiO_2 . HF-treated TiO_2 was mixed with PVC to make TiO_2 -PVC composite film, and the enhanced adsorption property imparted by this incorporation reduced the emission of harmful chemicals such as dioxin. Harmful chemicals can be decomposed completely by subsequent photocatalysis (Sun et al. 2002).

8.3 Functional Coating on Polymeric Substrate

In recent years, photocatalysis has been applied to the coating technology. Surface coating with photocatalysts endows special properties to substrates as listed:

1. Hydrophilicity-hydrophobicity control
2. Self-cleaning property
3. Anti-bacterial property

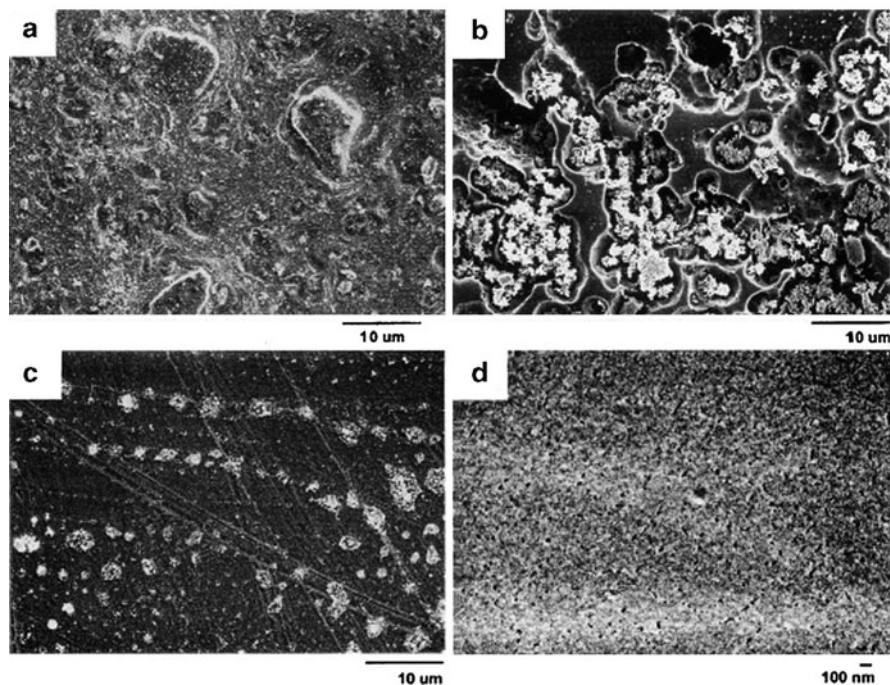


Fig. 23 SEM images of the pure PVC or PVC-TiO₂ (1.5 wt%) composite films: (a) PVC-TiO₂ film before irradiation; (b) PVC-TiO₂ film, 100-h irradiated; (c) PVC-TiO₂ film, 100-h irradiated under N₂; and (d) pure PVC film, 100-h irradiated (Cho et al. 2001). Reprinted from Cho and Choi (2001), Copyright with permission from Elsevier

4. UV-screening function

TiO₂ photocatalyst coating has been generally adapted on inorganic substrates. However, the coating on polymeric substrates is more attractive for practical applications. A well-known problem of photocatalyst coating on polymeric substrates is the degradation of substrates or binders by photocatalysis. To solve this problem, a special intermediate layer can be located between the photocatalyst coating layer and the substrate layer (Iketania et al. 2003). Additionally, an intermediate layer relaxes the stress exerted by the thermal expansion difference between the photocatalyst layer and the substrate layer. As an intermediate layer, inorganic/organic/hybrid (multi)layers can be used.

SiO₂ and Al₂O₃ are good candidates for inorganic intermediates. But, it is possible for inorganic intermediate layers to adhere poorly on polymeric substrates. When PET monolith was used as a TiO₂ photocatalyst support, SiO₂ intermediate layer was employed. To improve adherence, the surface of SiO₂ was coated with fluorinated surfactant to lower surface tension, or the surface of PET was modified

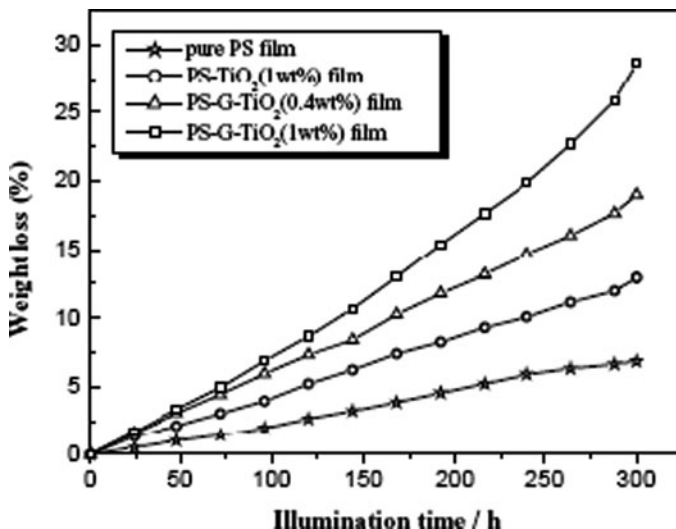


Fig. 24 Weight loss curve of pure PS, PS-TiO₂, and PS-grafted TiO₂ composite films under UV illumination in air. Reprinted from Zan et al. (2004), Copyright with permission from Elsevier

with a layer of poly(diallyldimethylammonium) chloride (PDDA) to form a positively charged surface (Sanchez et al. 2006).

The UV stability of polycarbonate (PC) film can be enhanced by ZnO coating. However, ZnO also results in photocatalytic oxidation of PC film and the effect of UV screening deteriorates. When Al₂O₃ interlayer was introduced between ZnO and PC layers by sputtering, UV stability of ZnO/PC film was enhanced due to the barrier effect of Al₂O₃ to O₂ (Moustaghfir et al. 2006).

Organic intermediate layer shows good adhesion property but poor affinity with the photocatalyst layer, and demonstrates long-term sustainability due to slow self-degradation. Therefore, organic-inorganic hybrid-multilayers are preferred as intermediate layers to prevent substrate degradation in practice. However, the coating procedure is so complicated that simple techniques excluding intermediate layers have been introduced.

When TiO₂/poly(dimethylsiloxane) (PDMS) hybrid sol was prepared through the sol-gel synthesis of TiO₂ in the presence of PDMS and spin-coated directly on poly(methylmethacrylate) (PMMA), the photocatalytic activity and stability of PMMA substrate were affected according to PDMS content as shown in Fig. 26 (Iketania et al. 2003). It seems that PDMS, at optimum amounts, enhances the affinity with PMMA substrate and suppresses the photocatalytic degradation of the substrate, sustaining the photocatalytic activity on organic compounds.

Also, the interfacial adherence between TiO₂ photocatalyst and acrylonitrile-butadiene-styrene polymer (ABS) could be enhanced without any interfacial layers, as TiO₂ was prepared in the presence of acetylacetone (Yang et al. 2006).

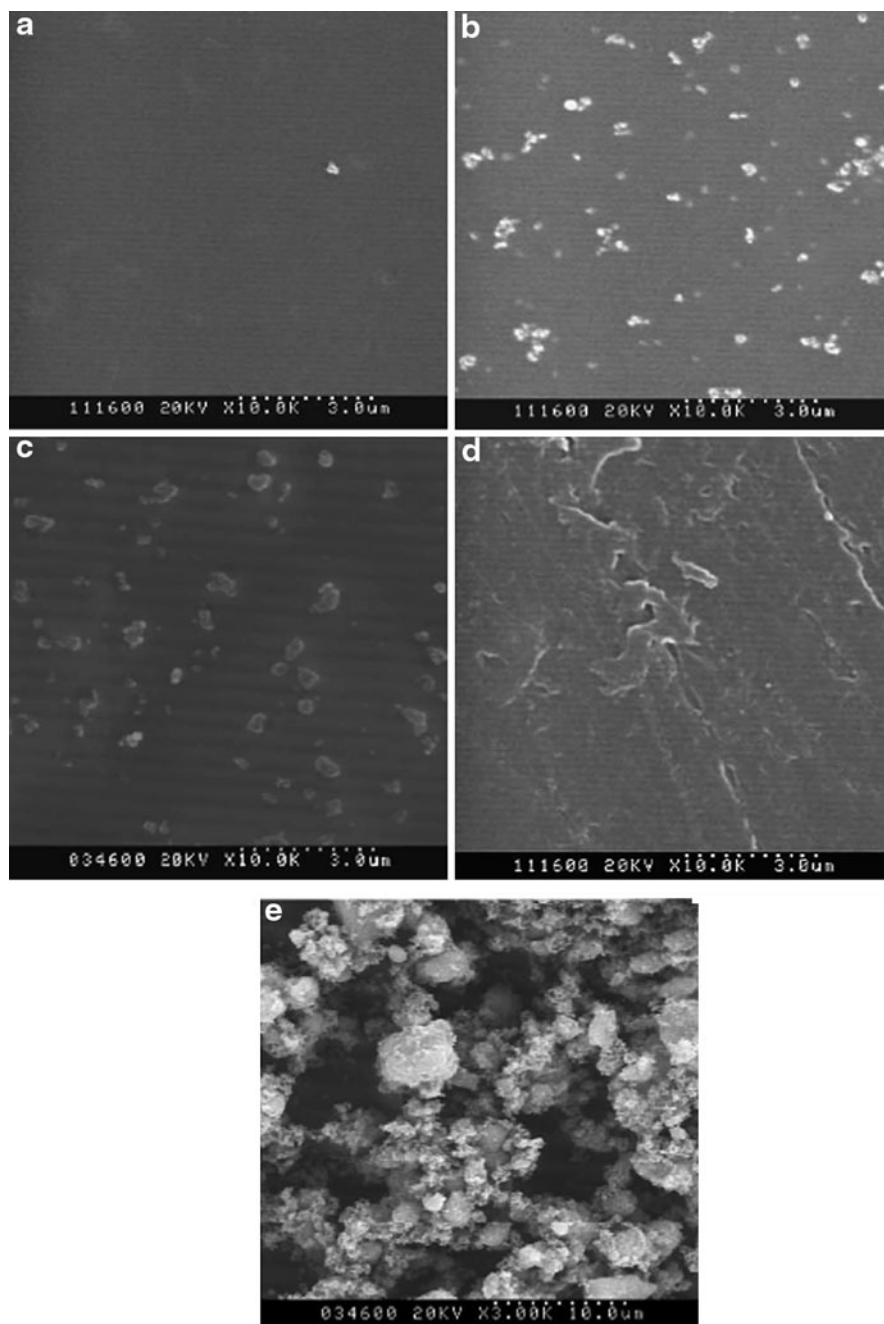


Fig. 25 SEM images of composite films: (a) pure PS film before irradiation, (b) PS-G-TiO₂ (1.0 wt%) film before irradiation, (c) PS-TiO₂ (1.0 wt%) composite film before irradiation, (d) pure PS film illuminated for 300-h, and (e) PS-G-TiO₂ (1.0 wt%) composite film illuminated for 300-h, Reprinted from Zan et al. (2004), Copyright with permission from Elsevier

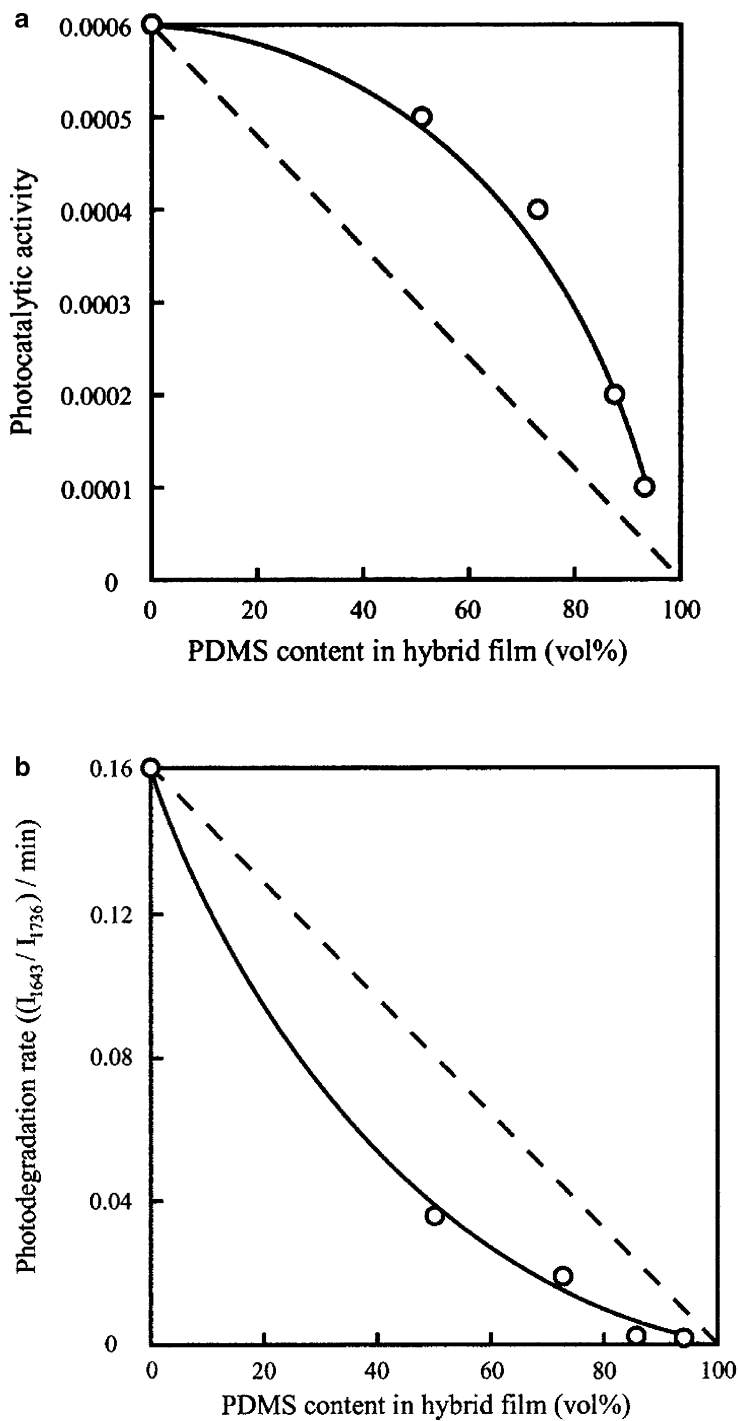


Fig. 26 Photodegradation rate for methylene blue (a) and of PMMA substrate (b) as a function of PDMS (vol%) in hybrid films. Reprinted from Iketania et al. (2003), Copyright with permission from Elsevier

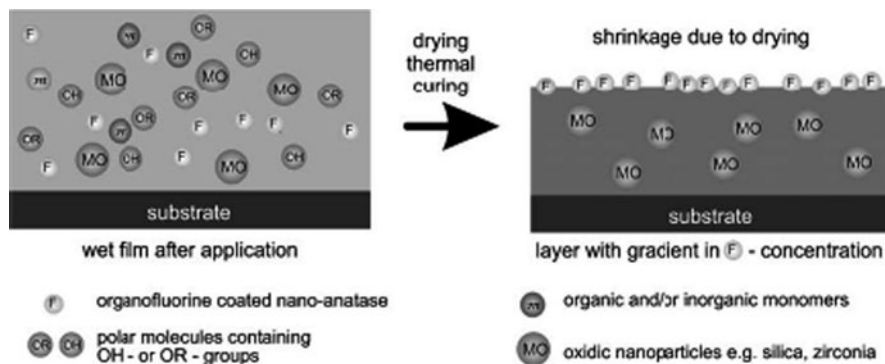


Fig. 27 Proposed mechanism of the gradient formation (Schmidt et al. 2006). Reprinted from Schmidt et al. (2006), Copyright with permission from Elsevier

Recently, photocatalyst gradient coating technology has been introduced (Schmidt et al. 2006). The surface of nano-size TiO_2 is modified with 3,3,4,4,5,5,6,6,7,7,8,8,8-tridecafluorooctyl-1,1,1-triethoxysilane (FTS) and mixed with methyltriethoxysilane (MTEOS), tetraethoxysilane (TEOS) sol, and binders such as NANOMER. The resulting mixture is coated on pre-treated PVC using primers. As the solvent is dried, a self-organizing gradient layer formation takes place with an up-concentration of photocatalyst at the interface layer between the coating and the air (see Fig. 27). After the activation by UV irradiation, the film shows good photocatalytic activities in pollutant-degrading, self-cleaning, and anti-fogging behaviors.

Calcium hydroxyapatite ($\text{Ca}_{10}(\text{PO}_4)_6(\text{OH})_2$) doped with Ti^{4+} (TiHAP) shows photocatalytic activity in acetaldehyde and albumin decompositions (Wakamura et al. 2003). This material was applied with PMMA polymer binder to a special coating for photocatalytic self-cleaning effect and retained its photocatalytic activity due to highly stabilizing polymer binders. FAS treatment on TiHAP enhanced the stability of PMMA binder (Yoshida et al. 2006).

Although several approaches have been successfully tested to suppress the chalking or weathering behavior of polymer binders or substrates, many interests and studies are still needed for practical industrial applications of the photocatalyst.

References

- Agustina TE, Ang HM, Vareek VK (2005) A review of synergistic effect of photocatalysis and ozonation on wastewater treatment. *J Photochem Photobiol C Photochem Rev* 6:264–273
- Allen NS, Edge M, Ortega A, Sandoval G, Liauw CM, Verran J, Stratton J, McIntyre RB (2004) Degradation and stabilisation of polymers and coatings: nano versus pigmentary titania particles. *Polym Degrad Stabil* 85:927–946

- Amorisco A, Losito I, Palmisano F, Zambonin PG (2005) Photocatalytic degradation of the herbicide isoproturon: characterization of by-products by liquid chromatography with electro-spray ionization tandem mass spectrometry. *Rapid Commun Mass Spectrom* 19:1507–1516
- Amorisco A, Losito I, Carbonara T, Palmisano F, Zambonin PG (2006) Photocatalytic degradation of phenyl-urea herbicides chlortoluron and chloroxuron: characterization of the by-products by liquid chromatography coupled to electrospray ionization tandem mass spectrometry. *Rapid Commun Mass Spectrom* 20:1569–1576
- Andreozzi R, Caprio V, Insola A, Longo G, Tufano V (2000) Photocatalytic oxidation of 4-nitrophenol in aqueous TiO₂ slurries: an experimental validation of literature kinetic models. *J Chem Technol Biotechnol* 75:131–136
- Anpo M, Shima T, Kodama S, Kubokawa Y (1987) Photocatalytic hydrogenation of CH₃CCH with H₂O on small-particle TiO₂: size quantization effects and reaction intermediates. *J Phys Chem* 91:4305–4310
- Antonarakis S, Androulaki E, Dimotikali D, Hiskia A, Papaconstantinou E (2002) Photolytic degradation of all chlorophenols with polyoxometallates and H₂O₂. *J Photochem Photobiol A Chem* 148:191–197
- Bamwenda GR, Uesigi T, Abe Y, Sayama K, Arakawa H (2001) The photocatalytic oxidation of water to O₂ over pure CeO₂, WO₃, and TiO₂ using Fe³⁺ and Ce⁴⁺ as electron acceptors. *Appl Catal A Gen* 205:117–128
- Bauer C, Jacques P, Kalt A (2001) Photooxidation of an azo dye induced by visible light incident on the surface of TiO₂. *J Photochem Photobiol A Chem* 140:87–92
- Beltrán FJ, Rivas FJ, Gimeno O (2005) Comparison between photocatalytic ozonation and other oxidation processes for the removal of phenols from water. *J Chem Technol Biotechnol* 80:973–984
- Benítez FJ, Beltrán-Heredia J, Acero JL, Rubio FJ (2000) Rate constants for the reactions of ozone with chlorophenols in aqueous solutions. *J Hazard Mater B* 79:271–285
- Bhatkhande DS, Pangarkar VG, Beenackers AACM (2001) Photocatalytic degradation for environmental applications: a review. *J Chem Technol Biotechnol* 77:102–116
- Blake DM (2001) Bibliography of work on the heterogeneous photocatalytic removal of hazardous compounds from water and air. National Renewable Energy Laboratory, Golden, CO
- Boule P, Guyon C, Lemaire J (1982) Photochemistry and environment IV: photochemical behaviour of monochlorophenols in dilute aqueous solution. *Chemosphere* 11:1179–1188
- Brown DJ, Mason SF (1962) *The pyrimidine*. Wiley, New York
- Burgeth G, Kisch H (2002) Photocatalytic and photoelectrochemical properties of titania-chloroplatinate(IV). *Coord Chem Rev* 230:41–47
- Calza P, Medana C, Baiocchi C, Pelizzetti E (2004) Photocatalytic transformations of aminopyrimidines on TiO₂ in aqueous solution. *Appl Catal B Environ* 52:267–274
- Calza P, Medana C, Baiocchi C, Hidaka H, Pelizzetti E (2006) Light-induced transformation of alkylurea derivatives in aqueous TiO₂ dispersion. *Chem Eur J* 12:727–736
- Carp O, Huisman CL, Reller A (2004) Photoinduced reactivity of titanium dioxide. *Prog Solid State Chem* 32:33–177
- Chatterjee D, Dasgupta S (2005) Visible light induced photocatalytic degradation of organic pollutants. *J Photochem Photobiol C Photochem Rev* 6:186–205
- Chiang K, Amal R, Tran T (2002) Photocatalytic degradation of cyanide using titanium dioxide modified with copper oxide. *Adv Environ Res* 6:471–485
- Chiron S, Fernandes-Alba A, Rodriguez A, Garcia-Clavo E (2000) Pesticide chemical oxidation: state-of-the-art. *Water Res* 34:366–377
- Cho S, Choi W (2001) Solid-phase photocatalytic degradation of PVC–TiO₂ polymer composites. *J Photochem Photobiol A Chem* 143:221–228
- Cho Y, Choi W, Lee C-H, Hyeon T, Lee H-I (2001) Visible light-induced degradation of carbon tetrachloride on dye-sensitized TiO₂. *Environ Sci Technol* 35:966–970

- Choi W, Termin A, Hoffmann MR (1994) The role of metal ion dopants in quantum-sized TiO₂: correlation between photoreactivity and charge carrier recombination dynamics. *J Phys Chem* 98:13669–13679
- Czaplicka M (2006) Photo-degradation of chlorophenols in the aqueous solution. *J Hazard Mater B* 134:45–59
- Devi LG, Krishnaiah GM (1999) Photocatalytic degradation of *p*-amino-azo-benzene and *p*-hydroxy-azo-benzene using various heat treated TiO₂ as the photocatalyst. *J Photochem Photobiol A Chem* 121:141–145
- Dhananjeyan MR, Annapoorani R, Lakshmi S, Renganathan R (1996) An investigation on TiO₂-assisted photo-oxidation of thymine. *J Photochem Photobiol A Chem* 96:187–191
- Dhananjeyan MR, Annapoorani R, Renganathan R (1997) A comparative study on the TiO₂ mediated photo-oxidation of uracil, thymine and 6-methyluracil. *J Photochem Photobiol A Chem* 109:147–153
- Dhananjeyan MR, Kandavelu V, Renganathan R (2000a) An investigation of the effects of Cu²⁺ and heat treatment on TiO₂ photooxidation of certain pyrimidines. *J Mol Catal A Chem* 158:577–582
- Dhananjeyan MR, Kandavelu V, Renganathan R (2000b) A study on the photocatalytic reactions of TiO₂ with certain pyrimidine bases: effects of dopants (Fe³⁺) and calcination. *J Mol Catal A Chem* 151:217–223
- Diebold U (2003) The surface science of titanium dioxide. *Surf Sci Rep* 48:53–229
- Ding Z, Lu Q, Greenfield PF (2000) Role of the crystallite phase of TiO₂ in heterogeneous photocatalysis for phenol oxidation in water. *J Phys Chem B* 104:4815–4820
- Forgacs E, Cserhati T, Oros G (2004) Removal of synthetic dyes from wastewaters. *Environ Int* 30:953–971
- Fox MA, Duray MT (1993) Heterogeneous photocatalysis. *Chem Rev* 93:341–357
- Frank SN, Bard AJ (1977) Heterogeneous photocatalytic oxidation of cyanide ion in aqueous solutions at TiO₂ powder. *J Am Chem Soc* 99:303–304
- Fujishima A, Honda K (1972) Electrochemical photolysis of water at a semiconductor electrode. *Nature* 238:37–38
- Fujishima A, Rao TN, Tryk D (2000) Titanium dioxide photocatalysis. *J Photochem Photobiol C Photochem Rev* 1:1–21
- Gesenhues U (2000) Influence of titanium dioxide pigments on the photodegradation of poly(vinyl chloride). *Polym Degrad Stab* 68:185–196
- Gesenhues U (2001) Al-doped TiO₂ pigments: influence of doping on the photocatalytic degradation of alkyd resins. *J Photochem Photobiol A Chem* 139:243–251
- Gogate PR, Pandit AB (2004) A review of imperative technologies for wastewater treatment I: oxidation technologies at ambient conditions. *Adv Environ Res* 8:501–551
- Halmann MM (1996) Photodegradation of water pollutants. CRC, Boca Raton, FL
- Hernandez-Alonso MD, Coronado JM, Maira AJ, Soria J, Loddo V, Augugliaro V (2002) Ozone enhanced activity of aqueous titanium dioxide suspensions for photocatalytic oxidation of free cyanide ions. *Appl Catal B Environ* 39:257–267
- Herrmann J-M (1995) Heterogeneous photocatalysis: an emerging discipline involving multiphase systems. *Catal Today* 24:157–164
- Herrmann J-M (1999) Heterogeneous photocatalysis: fundamentals and applications to the removal of various types of aqueous pollutants. *Catal Today* 53:115–129
- Hirakawa T, Nokada Y (2002) Properties of O₂^{•-} and OH[•] formed in TiO₂ aqueous suspensions by photocatalytic reaction and the influence of H₂O₂ and some ions. *Langmuir* 18:3247–3254
- Hoffmann MR, Martin ST, Choi W, Bahnemann DW (1995) Environmental applications of semiconductor photocatalysis. *Chem Rev* 95:69–96
- Hofstadler K, Bauer R, Novalic S, Heisler G (1994) New reactor design for photocatalytic wastewater treatment with TiO₂ immobilized on fused-silica glass fibers: photomineralization of 4-chlorophenol. *Environ Sci Technol* 28:670–674

- Hong S-S, Ju C-S, Lim C-G, Ahn B-H, Lim K-T, Lee G-D (2001) A photocatalytic degradation of phenol over TiO₂ prepared by sol-gel method. *J Ind Eng Chem* 7:99-104
- Horikoshi S, Hidaka H (2001) Photodegradation mechanism of heterocyclic two-nitrogen containing compounds in aqueous TiO₂ dispersions by computer simulation. *J Photochem Photobiol A Chem* 141:201-208
- Horikoshi S, Serpone N, Yoshizawa S, Knowland J, Hidaka H (1999) Photocatalyzed degradation of polymers in aqueous semiconductor suspensions. IV. Theoretical and experimental examination of the photooxidative mineralization of constituent bases in nucleic acids at titania/water interfaces. *J Photochem Photobiol A Chem* 120:63-74
- Iketania K, Sun R-D, Toki M, Hirota K, Yamaguchi O (2003) Sol-gel-derived TiO₂/poly(dimethylsiloxane) hybrid films and their photocatalytic activities. *J Phys Chem Solids* 64:507-513
- Jaussaud C, Pässe O, Faure R (2000) Photocatalysed degradation of uracil in aqueous titanium dioxide suspensions: mechanisms, pH and cadmium chloride effects. *J Photochem Photobiol A Chem* 130:157-162
- Jung KS, Lee H-I (1997) Photocatalysis and its applications. *J Korean Chem Soc* 41:682-710
- Jung KY, Park SB (1999) Anatase-phase titania: preparation by embedding silica and photocatalytic activity for the decomposition of trichloroethylene. *J Photochem Photobiol A Chem* 127:117-122
- Kamble SP, Sawant SB, Pangarkar VG (2006) Photocatalytic degradation of *m*-dinitrobenzene by illuminated TiO₂ in a slurry photoreactor. *J Chem Technol Biotechnol* 81:365-373
- Kim J-H (2003) Photocatalytic oxidation of aqueous cyanide using TiO₂ and heteropolytungstate-modified TiO₂. Ph.D. Thesis, Seoul National University, Seoul
- Kim J-H, Lee H-I (2003) Activity of TiO₂ and heteropolytungstate-modified TiO₂ in the photocatalytic degradation of aqueous cyanide. *Stud Surf Sci Catal* 145:161-164
- Kim J-H, Lee H-I (2004) Effect of surface hydroxyl groups of pure TiO₂ and modified TiO₂ on the photocatalytic oxidation of aqueous cyanide. *Korean J Chem Eng* 21:116-122
- Kim H-J, Lu L, Kim J-H, Lee C-H, Hyeon T, Choi W, Lee H-I (2001) UV light induced photocatalytic degradation of cyanides in aqueous solution over modified TiO₂. *Bull Korean Chem Soc* 22:1371-1374
- Kim SH, Kwak S-Y, Suzuki T (2006) Photocatalytic degradation of flexible PVC/TiO₂ nanohybrid as an eco-friendly alternative to the current waste landfill and dioxin-emitting incineration of post-use PVC. *Polymer* 47:3005-3016
- Kiwi J (1985) Direct observation of the variation of energy levels in powdered TiO₂ as a function of temperature. Beneficial effects for energy conversion through semiconductor devices. *J Phys Chem* 89:2437-2439
- Konstantinou IK, Albanis TA (2003) Photocatalytic transformation of pesticides in aqueous titanium dioxide suspensions using artificial and solar light: intermediates and degradation pathways. *Appl Catal B Environ* 42:319-335
- Konstantinou IK, Albanis TA (2004) TiO₂-assisted photocatalytic degradation of azo dyes in aqueous solution: kinetic and mechanistic investigations. *Appl Catal B Environ* 49:1-14
- Kormann C, Bahnemann DW, Hoffmann R (1988) Preparation and characterization of quantum-size titanium dioxide. *J Phys Chem* 92:5196-5201
- Kouloumbos VN, Tsipi DF, Hiskia AE, Nikolic D, van Breemen RB (2003) Identification of photocatalytic degradation products of diazinon in TiO₂ aqueous suspensions using GC/MS/MS and LC/MS with quadrupole time-of-flight mass spectrometry. *J Am Soc Mass Spectrom* 14:803-817
- Kuo WS (1999) Synergistic effects of combination of photolysis and ozonation on destruction of chlorophenols in water. *Chemosphere* 39:1853-1860
- Lackhoff M, Prieto X, Nestle N, Dehn F, Niessner R (2003) Photocatalytic activity of semiconductor-modified cement: influence of semiconductor type and cement ageing. *Appl Catal B Environ* 43:205-216

- Lacoste J, Singh RP, Boussand J, Arnaud R (2003) TiO₂-, ZnO-, and CdS-photocatalyzed oxidation of ethylene-propylene thermoplastic elastomers. *J Polym Sci A Polym Chem* 25:2799–2812
- Lea J, Adesina AA (2001) Oxidative degradation of 4-nitrophenol in UV-illuminated titania suspension. *J Chem Technol Biotechnol* 76:803–810
- Lee H-S (2004) Development of TiO₂ catalyst for the photocatalytic oxidation of 2-isopropyl-6-methyl-4-pyrimidinol. Ph.D. Thesis, Seoul National University, Seoul
- Lee GD, Lee H-I (1992) Application of photocatalysis. *J Korean Ind Eng Chem* 3:35–45
- Lee SG, Lee H-I (1998) A new sulfur-sensitive bismuth oxide on titania for photocatalyst. *Korean J Chem Eng* 15:463–468
- Lee S-A, Choo K-H, Lee C-H, Lee H-I, Hyeon T, Choi W, Kwon H-H (2001a) Use of ultrafiltration membranes for the separation of TiO₂ photocatalysts in drinking water treatment. *Ind Eng Chem Res* 40:1712–1719
- Lee SG, Kim J-H, Lee S, Lee H-I (2001b) Photochemical production of hydrogen from alkaline solution containing polysulfide dyes. *Korean J Chem Eng* 18:894–897
- Lee SG, Lee S, Lee H-I (2001c) Photocatalytic production of hydrogen from aqueous solution containing CN⁻ as a hole scavenger. *Appl Catal A Gen* 207:173–181
- Lee H-S, Hur T, Kim S, Kim J-H, Lee H-I (2003) Effects of pH and surface modification of TiO₂ with SiO_x on the photocatalytic degradation of a pyrimidine derivative. *Catal Today* 84:173–180
- Lee H-S, Hur T, Kim S, Kim J-H, Lee H-I (2004) Influences of electron scavenger and conduction band position of photocatalyst on the degradation of a pyrimidine derivative. *J Chem Eng Jpn* 37:174–180
- Lee H-S, Woo C-S, Youn B-K, Kim S-Y, Oh S-T, Sung Y-E, Lee H-I (2005) Bandgap modulation of TiO₂ and its effect on the activity in photocatalytic oxidation of 2-isopropyl-6-methyl-4-pyrimidinol. *Top Catal* 35:255–260
- Lin J, Yu JC, Lo D, Lam SK (1999) Photocatalytic activity of rutile Ti_{1-x}Sn_xO₂ solid solutions. *J Catal* 183:368–372
- López MC, Fernández MI, Rdgríguez S, Santaballa JA, Steenken S, Vulliet E (2005) Mechanisms of direct and TiO₂-photocatalysed UV degradation of phenylurea herbicides. *ChemPhysChem* 6:2064–2074
- Malato S, Blanco J, Richter C, Maldonado MI (2000) Optimization of pre-industrial solar photocatalytic mineralization of commercial pesticides: application to pesticide container recycling. *Appl Catal B Environ* 25:31–38
- Matthews RW (1987) Photooxidation of organic impurities in water using thin films of titanium dioxide. *J Phys Chem* 91:3328–3333
- Mills G, Hoffmann R (1993) Photocatalytic degradation of pentachlorophenols on TiO₂ particles: identification of intermediates and mechanism of reaction. *Environ Sci Technol* 27:1681–1689
- Mills A, Le Hunte S (1997) An overview of semiconductor photocatalysis. *J Photochem Photobiol A Chem* 108:1–35
- Minero C, Pelizzetti E, Malato S, Blanco J (1996) Large solar plant photocatalytic water decontamination: degradation of atrazine. *Sol Energy* 56:411–419
- Moustaghfir A, Tomasella E, Jacquet M, Rivaton A, Mailhot B, Gardette JL, Bêche E (2006) ZnO/Al₂O₃ coatings for the photoprotection of polycarbonate. *Thin Solid Films* 515:662–665
- Moza PN, Fytianos K, Samanidou V, Korte F (1988) Photodecomposition of chlorophenols in aqueous medium in presence of hydrogen peroxide. *Bull Environ Contam Toxicol* 41:678–682
- Nedoloujko A, Kiwi J (2000) TiO₂ speciation precluding mineralization of 4-tert-butylpyridine. Accelerated mineralization via Fenton photo-assisted reaction. *Water Res* 34:3277–3284
- Oh S-T, Lu L, Lee H-I (2006) Intrinsic effect of H₂O on the structural characteristic of TiO₂ synthesized by using polyethylene glycol as template. *Mater Lett* 60:2795–2798
- Oh S-T, Choi J-S, Lee H-S, Lu L, Kwon H-H, Song IK, Kim JJ, Lee H-I (2007) H₂O-controlled synthesis of TiO₂ with nanosized channel structure through in situ esterification and its application to photocatalytic oxidation. *J Mol Catal A Chem* 267:112–119

- Ohno T, Sarukawa K, Matsumura M (2001) Photocatalytic activities of pure rutile particles isolated from TiO₂ powder by dissolving the anatase component in HF solution. *J Phys Chem B* 105:2417–2420
- Ollis DF, Al-Ekabi H (1993) Photocatalytic purification and treatment of water and air. Elsevier, New York
- Ozoemena K, Kuznetsova N, Nyokong T (2001) Comparative photosensitized transformation of polychlorophenols with different sulphonated metallophthalocyanine complexes in aqueous medium. *J Mol Catal A Chem* 176:29–40
- Penot G, Arnaud R, Lemaire J (2003) ZnO-photocatalyzed oxidation of isotactic polypropylene. *Angew Makromol Chem* 117:71–84
- Pirkanniemi K, Sillanpää M (2002) Heterogeneous water phase catalysis as an environmental application: a review. *Chemosphere* 48:1047–1060
- Porter JF, Li Y-G, Chan CK (1999) The effect of calcination on the microstructural characteristics and photoreactivity of Degussa P-25 TiO₂. *J Mater Sci* 34:1523–1531
- Ray AK, Beenackers AACM (1998) Development of a new photocatalytic reactor for water purification. *Catal Today* 40:73–83
- Rodgers JD, Bunce NJ (2001) Treatment methods for the remediation of nitroaromatic explosives. *Water Res* 35:2101–2111
- Sakthivel S, Kisch H (2003) Photocatalytic and photoelectrochemical properties of nitrogen-doped titanium dioxide. *ChemPhysChem* 4:487–490
- Sanchez B, Coronado JM, Candal R, Portela R, Tejedor I, Anderson MA, Tompkins D, Lee T (2006) Preparation of TiO₂ coatings on PET monoliths for the photocatalytic elimination of trichloroethylene in the gas phase. *Appl Catal B Environ* 66:295–301
- Schmidt H, Naumann M, Muller TS, Akarsu M (2006) Application of spray techniques for new photocatalytic gradient coatings on plastics. *Thin Solid Films* 502:132–137
- Serpone N, Khairutdinov RF (1997) Application of nanoparticles in the photocatalytic degradation of water pollutants. *Stud Surf Sci Catal* 103:417–444
- Serpone N, Lawless D, Khairutdinov R (1995) Size effects on the photophysical properties of colloidal anatase TiO₂ particles: size quantization versus direct transitions in this indirect semiconductor? *J Phys Chem* 99:16646–16654
- Shen Y-S, Ku Y, Lee K-C (1995) The effect of light absorbance on the decomposition of chlorophenols by ultraviolet radiation and U.V./H₂O₂ processes. *Water Res* 29:907–914
- Sohn D-R, Kim J-H, Lee S, Lee H-I (2003) The effect of H₂O₂ on the photodegradation of cyanide over TiO₂ catalyst. *J Korean Ind Eng Chem* 14:391–396
- Spadaro JT, Isabelle L, Renganathan V (1994) Hydroxyl radical mediated degradation of azo dyes: evidence for benzene generation. *Environ Sci Technol* 28:1389–1393
- Sun R-D, Nishikawa T, Nakajima A, Watanabe T, Hashimoto K (2002) TiO₂/polymer composite materials with reduced generation of toxic chemicals during and after combustion-effect of HF-treated TiO₂. *Polym Degrad Stabil* 78:479–484
- Takeda N, Iwata N, Torimoto T, Yoneyama H (1998) Influence of carbon black as an adsorbent used in TiO₂ photocatalyst films on photodegradation behaviors of propylamide. *J Catal* 177:240–246
- Tratnyek PG, Holgné J (1991) Oxidation of substituted phenols in the environment: a QSAR analysis of rate constants for reaction with singlet oxygen. *Environ Sci Technol* 25:1596–1604
- Turchi CS, Ollis DF (1990) Photocatalytic degradation of organic water contaminants: mechanisms involving hydroxyl radical attack. *J Catal* 122:178–192
- Vulliet E, Emmelin C, Chovelon J-M, Guillard C, Herrmann J-M (2002) Photocatalytic degradation of sulfonyleurea herbicides in aqueous TiO₂. *Appl Catal B Environ* 38:127–137
- Wakamura M, Hashimoto K, Watanabe T (2003) Photocatalysis by calcium hydroxyapatite modified with Ti(IV): albumin decomposition and bactericidal effect. *Langmuir* 19:3428–3431
- Wang K-H, Hsieh Y-H, Chou M-Y, Chang C-Y (1999) Photocatalytic degradation of 2-chloro and 2-nitrophenol by titanium dioxide suspensions in aqueous solution. *Appl Catal B Environ* 21:1–8

- Xu J, Shi W, Gong M, Yu F, Yan L (2005) Preparation of poly(methyl methacrylate-*co*-maleic anhydride)/SiO₂-TiO₂ hybrid materials and their thermo- and photodegradation behaviors. *J Polym Sci A Polym Chem* 97:1714–1724
- Yang J-H, Han Y-S, Choy J-H (2006) TiO₂ thin-films on polymer substrates and their photocatalytic activity. *Thin Solid Films* 495:266–271
- Yawalkar AA, Bhatkhande DS, Pangarkar VG, Beenackers AACM (2001) Solar-assisted photochemical and photocatalytic degradation of phenol. *J Chem Technol Biotechnol* 76:363–370
- Yeo S-W, Kim J-H, Lee H-I (2002) Photocatalytic treatment of cyanide in water. *J Korean Chem Soc* 46:64–68
- Yoshida N, Takeuchi M, Okura T, Monma H, Wakamura M, Ohsaki H, Watanabe T (2006) Superhydrophobic photocatalytic coatings utilizing apatite-based photocatalyst. *Thin Solid Films* 502:108–111
- Zan L, Tian L, Liu Z, Peng Z (2004) A new polystyrene-TiO₂ nanocomposite film and its photocatalytic degradation. *Appl Catal A Gen* 264:237–242
- Zhao W, Chen C, Ma W, Zhao J, Wang D, Hidaka H, Serpone N (2003) Efficient photoinduced conversion of an azo dye on hexachloroplatinate(IV)-modified TiO₂ surfaces under visible light irradiation: a photosensitization pathway. *Chem Eur J* 9:3292–3299
- Ziegmann M, Doll T, Frimmel FH (2006) Matrix effects on the photocatalytical degradation of dichloroacetic acid and atrazine in water. *Acta Hydrochim Hydrobiol* 34:146–154

Chapter 16

Development of Highly Active Titanium Oxide Photocatalysts Anchored on Silica Sheets and their Applications for Air Purification Systems

Takeshi Kudo, Yuko Kudo, Akira Hasegawa, and Masakazu Anpoanpo

Abstract The purpose of this study is to develop highly active titanium oxide photocatalysts that can be anchored onto a substrate. We have, thus, prepared a titanium oxide photocatalyst using a wet or dry process and the results of this study have led to the successful development of highly active rectangular column-structured titanium oxide photocatalysts, which can be anchored onto silica sheets. These highly active photocatalysts were then applied to develop an effective air purification system.

1 Introduction

Economic advances in manufacturing and living standards have, unfortunately, led to serious environmental pollution and health hazards caused by chemical substances, bacteria, viruses, and toxic compounds from carbon fuel energy and waste materials. Even in the indoor environment, the volatile organic compounds used in building materials that cause the so-called “sick-house syndrome” have caused serious health problems. Also, contagious diseases such as SARS and bird influenza viruses as well as toxic molds can be easily spread through air. To address these concerns, various air cleaners have been developed and even commercialized. However, most air cleaners use activated carbon and adsorption materials in which the initial adsorptive performance is superior but slowly decreases and finally disappears. Also, unpleasant odors are inevitably caused by the desorption of these adsorptive materials. The used adsorption materials then become industrial waste, leading to greater environmental problems. For this reason, it is necessary to develop air purification systems that do not use such waste-producing adsorption

T. Kudo (✉)

Development Division, Andes Electric Co., Ltd, Hachinohe, Aomori, Japan
e-mail: t_kudou@andes.co.jp

methods as well as find new energy resources that are clean and safe. Photocatalytic reactions using ultraviolet light irradiation that can render toxic or odorous organic compounds harmless are considered a promising field of research in the development of new purification methods to replace conventional adsorption systems.

The development of TiO_2 photocatalysts for environmental purification systems is presently being carried out at Andes Electric Co., Ltd., on a commercial scale. Powdered TiO_2 photocatalysts such as the commercially available P-25 was first considered for use in these systems. However, powdered TiO_2 was not easy to use and various binder materials have to be combined to fix or immobilize a powdered photocatalyst onto substrate materials. The binder materials, however, decrease the photocatalytic reactivity of the TiO_2 itself since they act as a physical covering while the mechanical strength of the photocatalyst is also weakened.

We have investigated the development of highly active titanium oxide photocatalysts that can be anchored onto a substrate by using a wet or dry preparation process. These studies have led to the successful development of highly active rectangular column-structured TiO_2 photocatalysts anchored onto silica sheets for applications in effective air purification systems. In this work, the preparation method is described along with a characterization of these rectangular column-structured TiO_2 photocatalysts. Also, their photocatalytic reactivity and actual performance in air purification systems are introduced.

2 Experimental

2.1 *Preparation of Rectangular Column-Structured TiO_2 Photocatalysts*

Rectangular column-structured TiO_2 photocatalysts were prepared by a wet or dry process, as shown in Fig. 1. The photocatalysts were anchored onto silica sheets in the following ways: First, TiO_2 crystal nuclei were formed on the silica sheet by a sputtering or spray method. Second, synthetic materials consisting of titanium tetraisopropoxide, alcohol, and nitric acid were applied on the TiO_2 crystal nuclei formed on the silica sheets and crystallized with heat treatment by drying at 150°C for about 2 h and annealing at 550°C for about 2 h.

2.2 *Characterizations*

The surface morphology of the samples was observed by scanning electron microscopy (SEM, Model S-4100, S-5000, Hitachi, Ltd) and transmission electron microscopy (TEM, Model H-800). The X-ray diffraction (XRD) patterns

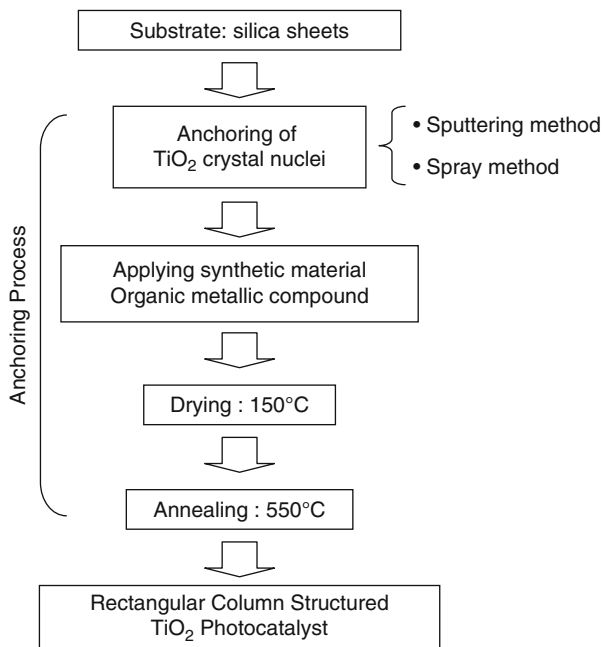


Fig. 1 Synthesis method of the rectangular column titanium oxide photocatalysts anchored onto a silica sheet

of the synthesized samples were recorded with a JEOL JDX-3530 XRD system using CuK α radiation (40 kV and 30 mA) at a scan speed of 1°min^{-1} in 2θ .

2.3 Evaluation of the Photocatalytic Reactivity

To evaluate the photocatalytic reactivity of the synthesized rectangular column-structured TiO₂ photocatalysts, the complete oxidation of organic compounds into CO₂ in a gas phase reaction system was investigated. The complete oxidation of gaseous acetaldehyde (CH₃CHO) was examined by monitoring the gas concentrations of CH₃CHO as well as CO₂ as a function of the irradiation time under a UV black light (λ : 365 nm; irradiation intensity: 4.0 mW/cm²; irradiation area: 60 × 60 mm).

The reaction was carried out at $25 \pm 3^\circ\text{C}$ under humidity of $60 \pm 5\%$ in a Pyrex glass reactor with a capacity of 20 L. First, gaseous acetaldehyde (Wako Pure Chemical Industries, Ltd.) was introduced into the reactor at a specified concentration and after reaching an adsorption equilibrium, UV light irradiation was carried out. The decrease in acetaldehyde concentration and its complete oxidation into CO₂ were monitored by a photo-acoustic multi-gas monitor (Model 1312-5, INNOVA).

3 Results and Discussions

3.1 Microstructure

Highly efficient photocatalysts that can be anchored onto a substrate, i.e., “Rectangular column-structured TiO_2 photocatalysts” were successfully developed. Figure 2a, b shows the SEM images of the synthesized TiO_2 photocatalysts. These rectangular column-structured crystals, with a width of 100–500 nm, and length of 1,000–5,000 nm,

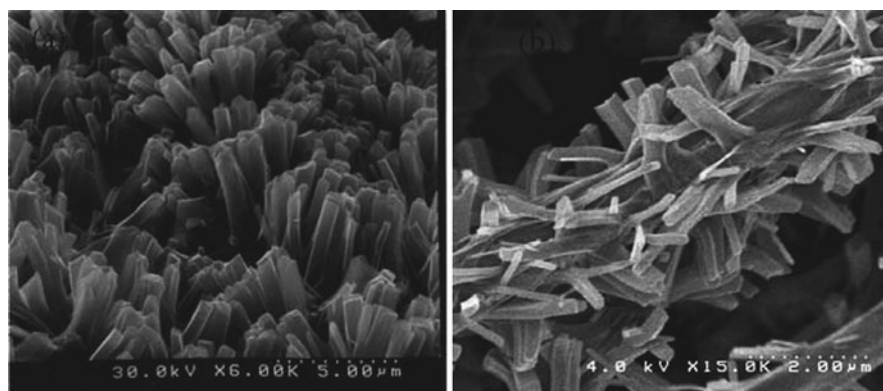


Fig. 2 The SEM images of the rectangular column-structured titanium oxide photocatalysts anchored onto a silica sheet. (a) $\times 6,000$, (b) $\times 15,000$

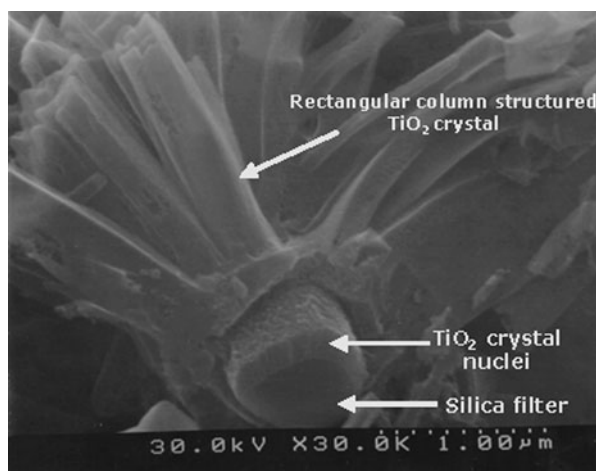


Fig. 3 A cross-sectional SEM image of the rectangular column-structured titanium oxide photocatalysts anchored onto a silica fiber

were observed to be anchored perpendicularly to the substrate in a very dense state and stable mechanical strength.

A cross-sectional SEM image of these rectangular column-structured TiO_2 photocatalysts shows that crystal nuclei of around 20–60 nm are formed on silica fibers of about 0.5–0.8 μm in diameter, as can be seen in Fig. 3. These TiO_2 crystal nuclei were prepared by a sputtering method; however, it was also possible to prepare them in a similar way with the spray method. On the contrary, rectangular column-structured TiO_2 crystals could only be formed on seeds of titanium oxide, which allowed the crystallization of the TiO_2 on the seeds.

However, without the titanium oxide seeds, even by applying the sputtering or spray methods, such rectangular column-structured TiO_2 crystals could not be formed. The preparation method for the TiO_2 crystal nuclei was, thus, seen to be the most important factor for the silica fibers, TiO_2 crystal nuclei, and rectangular column-structured TiO_2 crystals to be chemically combined in order to synthesize a stable photofunctional material.

TEM micrographs revealed that the TiO_2 crystal has a hollow structure which consists of an outer TiO_2 shell with high density and an inner region with low density, as shown in Fig. 4. The thickness of the shell was observed to be around 50 nm. Figure 5 shows the cross-sectional SEM image of the TiO_2 crystal. The inner region of the agglomerated 20–30-nm TiO_2 particles is covered by a dense TiO_2 wall, indicating that rectangular column-structured TiO_2 crystals have a high



Fig. 4 TEM image of the rectangular column-structured titanium oxide crystals

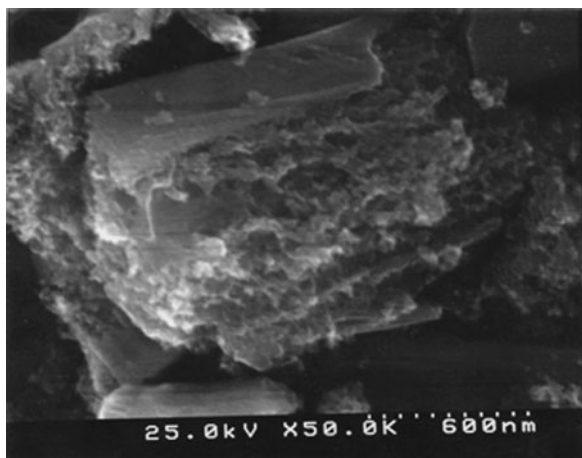


Fig. 5 Internal structure of the rectangular column-structured titanium oxide crystals

surface area of about $70 \text{ m}^2/\text{g}$. Moreover, XRD analysis revealed that the TiO_2 crystals have an anatase polycrystalline structure.

3.2 Photocatalytic Reactivity

The photocatalytic reactivity of the photocatalysts was examined for the decomposition of gaseous acetaldehyde by measuring the changes in the gas concentration as a function of the irradiation time under UV light. The reaction time profiles of the complete oxidation of acetaldehyde (CH_3CHO) compared with those of the most efficient marketed powdered photocatalyst (P-25) are shown in Fig. 6, and it can be seen that the acetaldehyde concentration decreased rapidly under UV light irradiation. The rectangular column-structured TiO_2 sample showed the fastest decrease in acetaldehyde concentration compared with P-25 and commercial slurry-type samples of powdered TiO_2 photocatalysts with binder materials. Thus, the rectangular column-structured TiO_2 showed a higher photocatalytic reactivity for the complete oxidation reaction of acetaldehyde as compared to a commercial powdered photocatalyst (Degussa, P25).

The reaction time profiles of the repeated and continuous oxidation of acetaldehyde in concentrated amounts are shown in Fig. 7. The complete oxidative decomposition of CH_3CHO into CO_2 was carried out six consecutive times in high concentration atmosphere to study the stability and efficiency of the photocatalysts. Figure 8 shows these rectangular column-structured TiO_2 to exhibit a constant and high reactivity for the complete oxidation of concentrated amounts of acetaldehyde into CO_2 , indicating that this type of structure is stable during the reaction since the TiO_2 crystals are anchored onto the silica fiber in a very dense state with stable chemical bonds.

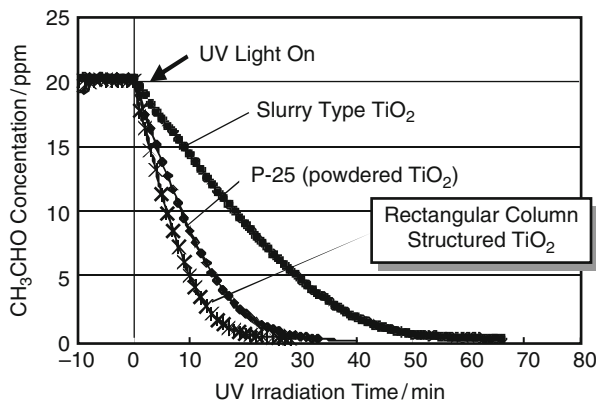


Fig. 6 Comparison of the reaction time profiles of the photocatalytic decomposition of CH_3CHO using various TiO_2 photocatalysts

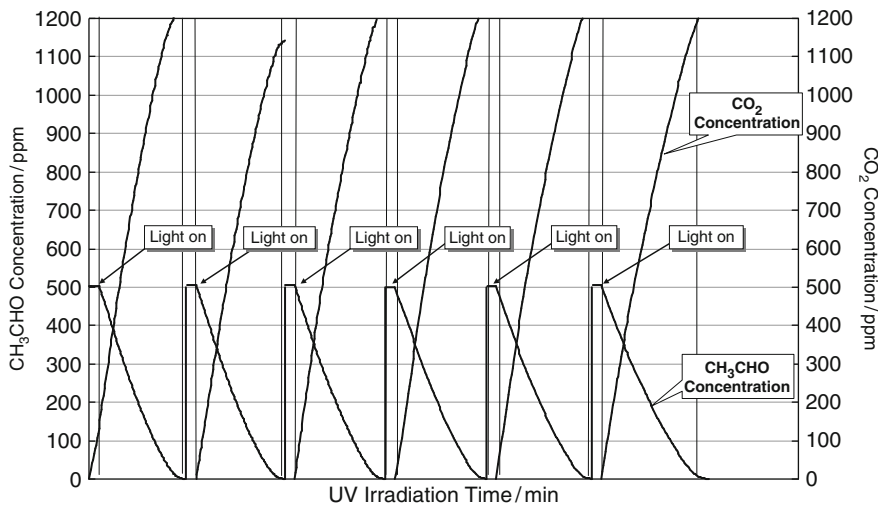


Fig. 7 The reaction time profiles of the photocatalytic decomposition of CH_3CHO into CO_2 and H_2O on the rectangular column structured titanium oxide photocatalysts anchored onto a silica sheet at 295 K

3.3 Applications for Rectangular Column-Structured TiO_2 Photocatalysts

The air purifying systems incorporating the rectangular column-structured titanium oxide photocatalysts are shown in Fig. 8. Figure 8a shows the air purifier which addresses the noxious fumes which cause “Sick House Syndrome” (Model

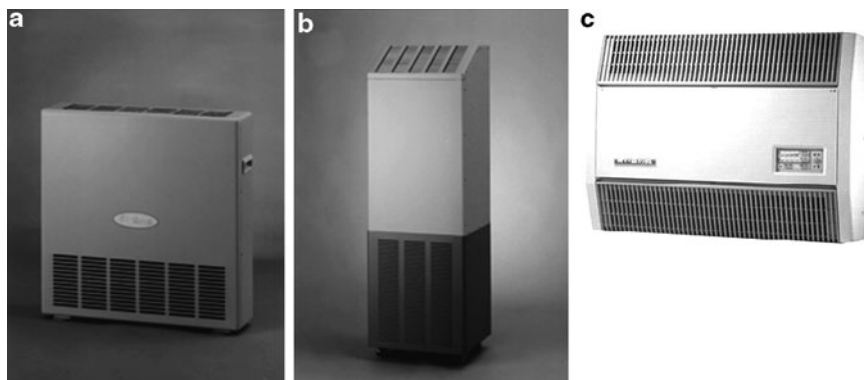


Fig. 8 Air purification systems applying the rectangular column-structured TiO_2 photocatalysts, Air purifier for Sick House Syndrome, Model (BF-H102A), Air purifier for Industrial Use, Model (BF-S103A), Air purifier for Walls, Model (BF-H201A)

BF-H102A) and Fig. 8b shows the air purifier for “Industrial Use” (Model BF-S103A). The inner structures of these purifiers are rather simple, consisting of anchored rectangular column-structured TiO_2 photocatalyst sheets, a UV light source, and a fan for air circulation.

The photocatalytic performance of these air purifiers for the complete oxidation reaction of contaminants such as formaldehyde into CO_2 compared with that of other TiO_2 photocatalytic systems is shown in Fig. 9. Evaluations of the photocatalytic reactivity for decomposition reactions were carried out in a 1 m^3 box. The efficiency of air purifiers using activated carbon or absorbents, Systems A and B, respectively, were seen to decrease gradually and reach zero as the absorbents and activated carbons became saturated with various contaminants such as formaldehyde. In contrast, the air purifier (BF-H102) applying the rectangular column-structured TiO_2 showed high and constant efficiency in decomposing formaldehyde, with the concentration decreasing rapidly to below the guideline limits issued by the Ministry of Health, Labor and Welfare of Japan.

Trial operations were carried out in a home specifically made with materials that can cause sick house syndrome, as shown in Fig. 10. The test conditions were as follows: Two air purifiers (BF-H102A) were operated for 90 min in a room of about 31.3 m^3 size. After air purification, the air in the room was collected and analyzed by gas chromatography and mass spectrometry (GC/MS). Analysis was carried out by solid phase adsorption/thermal desorption-GC/MS methods. Before air purification, a number of organic compounds were detected in the room, i.e., acetaldehyde, methanol, toluene, styrene, α -pinene, etc. However, after operating our air purifier systems, the peaks attributed to these compounds were seen to decrease dramatically, indicating the complete oxidation of these compounds into CO_2 and H_2O . Such field experiments could establish the actual efficiency and stability of air purifiers incorporating rectangular column-structured TiO_2 sheets for the decomposition of organic compounds outside the laboratory in the living environment.

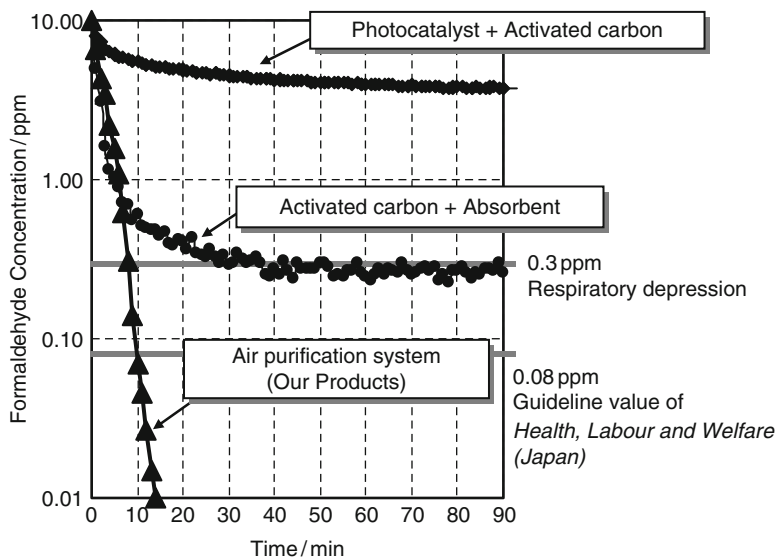


Fig. 9 Comparison of the capacity for formaldehyde decomposition with different purification systems

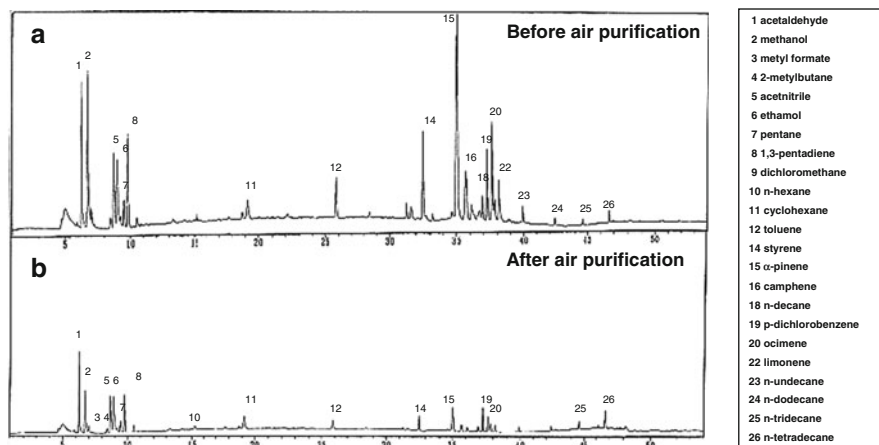


Fig. 10 GC/MS peaks before and after air purification (BF-H102A)

- Study institution: Research Center for Medical Environment, The Kitasato Institute
- Study No.: 00228 March 19, 2003
- Test method (virus): Cytopathic effect method (CPE)
- Test method (bacteria): Nutrient agar plate cultivation
- Tested model: Air purifier (BF-H201A)

Table 16.1 Elimination capacity of air purifier using TiO₂ photocatalysts (BF-H201A)

Tested bacteria	Elimination effects (%)
Influenzavirus A	99
<i>Escherichia coli</i>	99.95
MRSA (methicillin resistant <i>Staphylococcus aureus</i>)	99.94

Significantly, in the photocatalytic complete oxidation reaction, the bacteria was not only deactivated but also decomposed so that the anti-bacterial properties could be retained even with constant exposure to the bacterial shells. Table 1 shows the anti-bacterial properties of a wall-hanging type air purifier incorporating the TiO₂ photocatalyst (BF-H201A) in a demonstration of a one-pass operation. A “one-pass operation” allows air to pass through the air purifier from the air inlet port to the outlet port only once to evaluate the direct effectiveness of the purifier on the air (Research Center for Medical Environment, Kitasato Institute). Bacteria elimination of more than 99 % was observed even under such a one-pass operation, as shown in Table 1. These results clearly established that air purifiers employing the rectangular column-structure TiO₂ photocatalyst showed effective and high performance for bacteria elimination in air.

4 Conclusions

Investigations in the synthesis of highly active TiO₂ photocatalysts that can be directly anchored onto silica sheets were carried out in order to develop an effective and stable air purification system. The results obtained from the present study are as follows.

Highly active “rectangular column-structured TiO₂ crystals” which could be anchored onto silica sheets were developed. The rectangular column-structured TiO₂ crystals could be anchored perpendicularly onto a silica fiber substrate in a very dense state with stable chemical bonds. The TiO₂ crystals had a width of 100–500 nm and length of 1,000–5,000 nm, with anatase TiO₂ nanoparticles of 10–30 nm. Moreover, the rectangular columnar crystals were observed to have a hollow structure. Investigations on the complete oxidation reaction of acetaldehyde into CO₂ with these rectangular column-structured TiO₂ photocatalysts showed a high performance equivalent to or even higher than the most efficient standard P-25 powdered photocatalysts. Thus, effective and stable air purifying systems could be successfully developed with the incorporation of these TiO₂ photocatalyst sheets for the complete oxidation of organic compounds and bacteria in the gas phase.

Acknowledgments This work was supported by NEDO (New Energy and Industrial Technology Development Organization of Japan). We would like to express our gratitude for their kind support.

References

- Anpo M (ed) (2000) Photofunctional zeolites. Nova Sci, New York
- Anpo M (2004) Preparation, characterization, and reactivities of highly functional titanium oxide-based photocatalysts able to operate under UV-visible light irradiation: Approaches in realizing high efficiency in the use of visible light Bull Chem Soc Jpn 77:1427
- Anpo M, Dohshi S, Kitano M, Hu Y, Takeuchi M, Matsuoka M (2005) The Preparation and Characterization of Highly Efficient Titanium Oxide-Based Photofunctional Materials Annu Rev Mater Res 35:1
- Hwang JS, Chang JS, Park SE, Ikeue K, Anpo M (2005) Photoreduction of carbondioxide on surface functionalized nanoporous catalysts Top Catal 35:311
- Kudo T, Kudo Y, Ruike A, Hasegawa A, Kitano M, Anpo M (2007) The design of highly active rectangular column-structured titanium oxide photocatalysts and their application in purification systems Catal Today 122:14
- Kudo T, Kudo Y, Ruike A, Hasegawa A (2005) Design and development of highly efficient rectangular column structured titanium oxide photocatalysts anchored onto silica sheets Top Catal 35:225
- Kudo T, Nakamura Y, Ruike A (2003) Development of rectangular column structured titanium oxide photocatalysts anchored on silica sheets by a wet process Res Chem Intermed 29:631
- Yamashita H, Takeuchi M, Anpo M (2004) American Scientific Publishers, Los Angeles Visible-Light-Sensitive Photocatalysts In: Nalwa HS (ed) Encyclopedia of nanoscience and nanotechnology 10:639

Chapter 17

Photocatalytic Application of TiO₂ for Air Cleaning

Yong-Gun Shul, Hak-Soo Kim, Hyun-Jong Kim, and Myung-Keun Han

Abstract Photocatalytic process has been applied to the treatment of air pollutants. It is necessary to enhance the photocatalytic activity of TiO₂ and design of photocatalytic system, for the practical application. The practical aspects for the application of TiO₂ were discussed. Various species, such as transition metal ion, noble metal, metal oxide, and anion, could modify the surface of TiO₂ and improve the photocatalytic activity. Photoelectrocatalytic (PEC) system was very effective for the enhancement of photoactivity by applying a high voltage onto TiO₂ surface. It showed better photocatalytic activity for decomposition of various air pollutants and bacteria than TiO₂ photocatalysts. To apply the photocatalysts in a real environment, the stable immobilization of the catalyst on various substrates, such as steel plate, membrane, glass fiber, and so on, was very important. Based on these modified and/or immobilized TiO₂, photocatalysis has been widely used in air-cleaning systems.

1 Introduction

Photocatalytic oxidation of volatile organic compounds in water and air has received much attention as a potential technology for pollution abatement. A highly attractive advantage of the photocatalytic treatment is the decomposing of various kinds of organic compounds by using UV light as an energy source even under ambient temperature and pressure. A brief list of some of the many organic substrates that can be decomposed via photocatalytic reaction is given in Table 1 (Mills and Leहुnte 1997). The heterogeneous photocatalytic process used in pollutant degradation involves the adsorption of pollutants on the surface sites,

Y.-G. Shul (✉)

Department of Chemical Engineering, Yonsei University, Seoul, South Korea
e-mail: shulyg@yonsei.ac.kr

Table 1 Some examples of photocatalyst-assisted decomposition of organic substrates

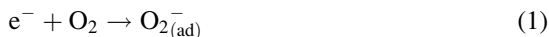
Class	Example
Alkanes	Methane, isobutane, pentane, heptane, cyclohexane, paraffin
Haloalkanes	Mono-, di-, tri-, and tetrachloromethane, trichloroethane, 1,1,1-trifluoro-2,2,2-trichloroethane
Aliphatic alcohols	Methanol, ethanol, isopropyl alcohol, glucose, sucrose
Aliphatic carboxylic acids	Formic, ethanoic, dimethylethanoic, propanoic, oxalic acids
Alkenes	Propene, cyclohexane
Haloalkenes	Perchloroethene, 1,2-dechloroethene, 1,1,2-trichloroethene
Aromatics	Benzene, naphthalene
Haloaromatics	Chlorobenzene, 1,2-dichlorobenzene, bromobenzene
Nitrohaloaromatics	3,4-Dichloronitrobenzene, trichloronitrobenzene
Phenols	Phenol, hydroquinone, catechol, 4-methylcatechol, resorcinol, o-, m-, p-cresol
Halophenols	2-, 3-, 4-Chlorophenol, pentachlorophenol, 4-fluorophenol, 3,4-difluorophenol
Aromatic carboxylic acids	Benzoic, 4-aminobenzoic, phthalic, salicylic, m- and p-hydroxybenzoic, chlorohydroxybenzoic acids
Polymers	Polyethylene, poly(vinyl chloride) (PVC)
Surfactants	Sodium dodecylsulphate(SDS), polyethylene glycol, sodium dodecyl benzene sulphonate, trimethyl phosphate, tetrabutylammonium phosphate
Herbicides	Methyl viologen, atrazine, simazine, promctron, propertryne, bentazon
Pesticides	DDT, parathion, lindane
Dyes	Methylene blue, rhodamine B, methyl orange, fluorescein

and the chemical reaction to convert the pollutant into carbon dioxide and water (Zou et al. 2006).

Although many semiconducting oxides have been investigated as potential photocatalysts, photooxidative TiO₂ gathers much attention due to a number of attractive characteristics: it is inexpensive, photochemically stable, and produces the highest oxidation rates of the many photoactive metal oxides investigated.

Compared to photocatalytic processes in solution, gas phase processes have various advantages. These are high diffusion rate of reagents and products, negligible photon absorption of air, high quantum efficiency (tenfold higher than those found for photodestruction of some organic substrates in aqueous solutions), and the usage of relatively low level UV light (Carp et al. 2004). The photocatalytic treatment of air pollutants offers the following distinctive advantages: (1) it is able to oxidize low-concentration and low flow rate waste stream at ambient temperature and pressures, (2) photocatalytic reactors may be integrated into new and existing heating, ventilation, and air conditioning systems due to their modular design, and room temperature operation, (3) it can be scaled to suit a wide variety of indoor air quality applications, and (4) it offers potential utilization of solar energy as a visible light source.

In the gas phase photocatalytic reaction, active oxygen species, such as O₂⁻, •OH, HO₂•, and O•, are produced from the reactions of positive hole (h⁺) and electrons (e⁻) with O₂ in air, H₂O, or OH⁻ group, and lattice oxygen of TiO₂ with the following processes (Hashimoto et al. 2005).



Of the oxygen species, OH is a well-known radical, which plays major roles in atmospheric chemistries in the gas phase. The active oxygen species can oxidize hazardous air pollutants (organics) to carbon dioxide, and SO₂ and NO_x to H₂SO₄ and HNO₃. In addition, TiO₂ photocatalysis is also considered to be effective for sterilization purposes as well. Bacteria, such as *Escherichia coli* (*E. coli*) and *Pseudomonas aeruginosa*, can completely disappear on TiO₂ under UV irradiation (Hashimoto et al. 2005).

However, the photocatalytic activity of TiO₂ should be improved and modified for the practical application to air cleaning system. Here, we describe the modification of the TiO₂ surface and design of photoelectrocatalytic (PEC) system for the enhancement of photocatalytic activity of TiO₂. Additionally, the immobilization of TiO₂ photocatalyst and its practical applications will be briefly introduced.

2 Modification of TiO₂ Surface

2.1 Transition Metal Doping (Modification with Transition Metal Ion)

Although TiO₂ is the most useful photocatalyst, the search for new materials in heterogeneous photocatalysis continues to be a matter of interest at the present. Many investigations have revealed that the deposition of metal ion on TiO₂ surface enhances the efficiency of photocatalytic redox processes (Choi et al. 1994; Lee et al. 2001). The transition metal ion doping species inhibit electron–hole recombination during illumination. The presence of metal ions determines the formation of a permanent space charge region whose electric force improves the efficiency of hole–electron separation and consequently the charge transfer. From a chemical point of view, moreover, it should be also observed that metal-ion-doped TiO₂ is equivalent to the introduction of defects, i.e., Ti³⁺ in the lattice. However, the reactivity of doped TiO₂ appears to be a complex function of the dopant

concentration, the energy level of the dopants within the TiO_2 lattice, their *d*-electronic configuration, the distribution of dopants, the electron-donor concentration, and the light intensity (Hoffmann et al. 1995). Also, the transition metal dopants play the roles of adsorption promoter and/or photocatalytic active site.

Figure 1 shows the reaction constants for the photocatalytic decomposition of acetaldehyde over Fe- and W-doped TiO_2 nanoparticles. The photocatalytic activity of iron- or tungsten-doped TiO_2 was higher than that of synthesized pure TiO_2 and commercial TiO_2 . The reaction constant was highly increased from 0.0201 to 0.0535 min^{-1} and 0.0785 min^{-1} for W- and Fe-doped TiO_2 , respectively. The presence of small amount of Fe or W ion in the TiO_2 nanoparticles could improve the photocatalytic activity. Fe and W ions could act as charge carrier trapping sites to suppress recombination and increase the lifetime of the separated electron and hole. Hoffmann et al. used laser flash photolysis measurements to show that the lifetime of the blue electron in the Fe-doped TiO_2 was increased to 50 ms, while the measured lifetime of the blue electron in undoped TiO_2 was $<200 \mu\text{s}$ (Choi et al. 1994). The relative increase in the concentration of the long-lived charge carriers resulted in a corresponding increase in photocatalytic activity.

The photocatalytic activity also depended on the calcinations temperature of Fe- or W-doped TiO_2 nanoparticles. The reaction rate was drastically increased after 300°C heat treatment. During the calcination, metal ion initially presented at the surface would diffuse into the lattice with increasing the crystallinity of TiO_2 (Litter and Navio 1996). This could promote the photocatalytic activity of metal-doped TiO_2 . However, in 500°C sintering, photoreactivity of Fe- or W-doped TiO_2 was slightly decreased. The bulk iron oxide and tungsten oxide which were formed on the surface of TiO_2 might lower the photocatalytic activity.

In the case of a high concentration of dopant, however, the photocatalytic activity was decreased below that of pure TiO_2 nanoparticle (Fig. 2). Some researchers have also reported similar results in which high concentration of metal ion or surface metal oxide could hinder the photocatalytic process of TiO_2 (Litter and Navio 1996; Anpo and Takeuchi 2003). The surface isolated metal ion species should be only

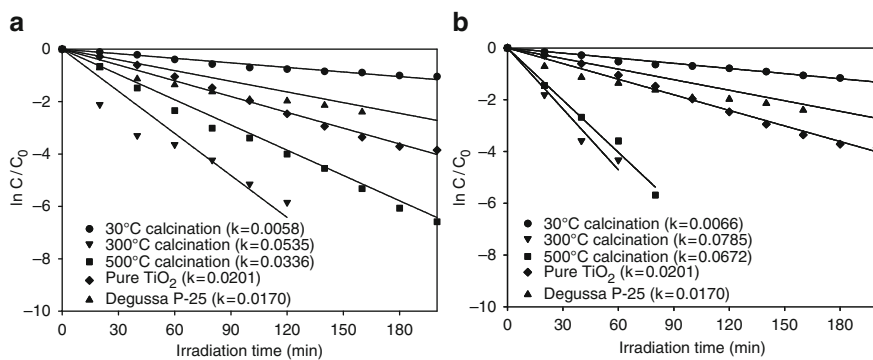


Fig. 1 Photocatalytic decomposition of acetaldehyde over 0.1 mol% (a) Fe- and (b) W- doped TiO_2 , pure TiO_2 , and commercial TiO_2 with various calcinations temperature (k is rate constant)

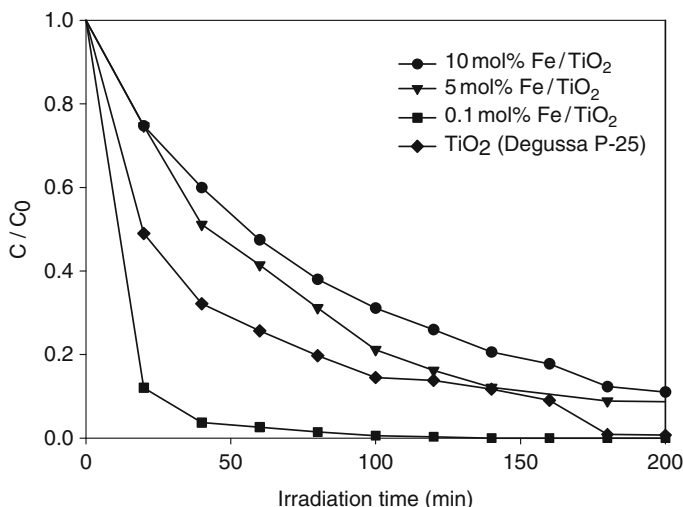


Fig. 2 Photocatalytic decomposition of acetaldehyde over Fe-doped TiO₂ with various concentration of Fe

active site for the photocatalytic reaction (Anpo and Takeuchi 2003). While a small amount of metal ion can form a well-dispersed monomeric site, a large amount can generate the bulk oxide species. The bulk metal oxide on the surface can absorb the light to prevent the activation of TiO₂ photocatalyst (Litter and Navio 1996). And, the high concentration of dopant can promote the formation of the charge carrier trapping site into the inside of the TiO₂ particle. If an electron is trapped in a deep trapping site, it will have a longer lifetime but it may also have a lower redox potential that could result in a decrease in activity (Linsebigler et al. 1995).

2.2 Deposition of Noble Metal (Modification with Noble Metal)

In photocatalysis, the addition of noble metals to TiO₂ can change the photocatalytic process. The noble metals of gold and platinum were usually introduced on TiO₂ surface to improve the photocatalytic activity (Linsebigler et al. 1995; Cho et al. 2002). Metal nanoparticles deposited on semiconductor surfaces play an important role in catalyzing interfacial charge transfer process (Linsebigler et al. 1995). Recent studies have shown that metal- or metal-ion-doped semiconductor composites exhibit shift in the Fermi level to more negative potentials (Wood et al. 2001; Jakob et al. 2003). Such a shift in the Fermi level improves the energetics of the composite system and enhances the efficiency of interfacial charge-transfer process.

It has been known that the Pt on the TiO₂ enhanced the photocatalytic reactivity. Figure 3(a) shows the photocatalytic decomposition of acetaldehyde over TiO₂ and Pt/TiO₂. The reaction constant of Pt/TiO₂, $11.39 \times 10^{-3} \text{ min}^{-1}$, was higher than that

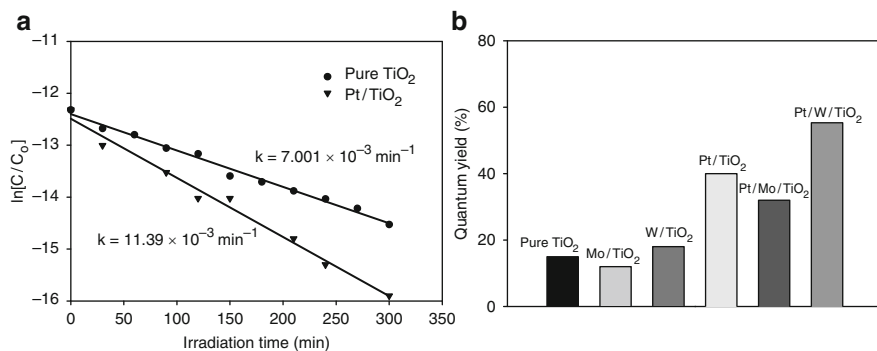
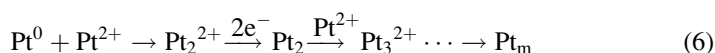


Fig. 3 The effect of Pt deposition on the photocatalytic degradation of acetaldehyde

of pure TiO_2 , $7.001 \times 10^{-3} \text{ min}^{-1}$. The role of Pt was to hinder the hole–electron charge pairs from recombination to improve the quantum yield of TiO_2 .

The photocatalytic activity of Pt/ TiO_2 strongly depends on the reduction method of Pt. While the Pt was generally reduced by H_2 -reduction method, it could be also successfully deposited on the TiO_2 surface by the photoreduction method. On the basis of EXAFS and XPS analysis (Yang et al. 1997), the particle growth mechanism of Pt was suggested as follows:



Pt is not completely reduced into a fully crystalline Pt phase even after 24 h and highly dispersed small Pt clusters are formed by photoreduction method. The interface between noble metal and TiO_2 was changed depending on the reduction condition. We have reported that the photoreduced Pt/ TiO_2 had a higher quantum yield than H_2 -reduced one (Yang et al. 1997). Furthermore, the deposition of Pt was also effective on the improvement of photocatalytic activity of above mentioned transition metal-doped TiO_2 . When the Pt was loaded on the Mo/ TiO_2 and W/ TiO_2 , the quantum yield of these were highly increased as shown in Fig. 3(b).

2.3 Silica-Supported TiO_2 (TiO_2 - SiO_2 ; Modification with Metal Oxide)

The combination of photoactive TiO_2 material with other metal oxide can be a strategy to improve the photocatalytic activity of TiO_2 . In most cases, mixed or supported TiO_2 showed higher photocatalytic activity than pure TiO_2 . Various oxide materials, such as SiO_2 , Al_2O_3 , zeolite, and mesoporous oxide, were examined. Among them, TiO_2 - SiO_2 has been widely used in industrial applications and most

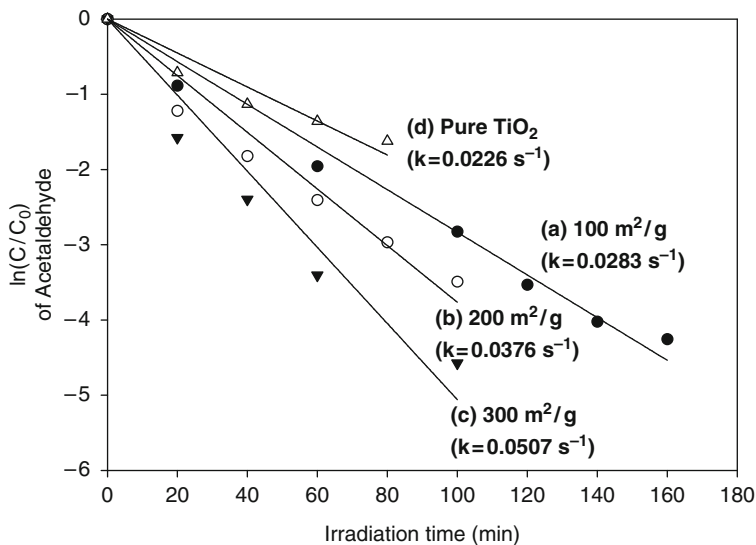


Fig. 4 Photocatalytic decomposition of acetaldehyde (500 ppm) over TiO₂-SiO₂ with various surface area

extensively studied. The relationship between surface area and photocatalytic activity of TiO₂-SiO₂ was shown in Fig. 4 (Shul et al. 2003). The content of TiO₂ was kept at 15 wt% in TiO₂-SiO₂ catalysts. Photocatalytic activity of TiO₂-SiO₂ photocatalysts was evaluated with the photocatalytic decomposition of acetaldehyde. The photocatalytic activity of TiO₂-SiO₂ was much higher than that of commercial TiO₂. Since the crystal size of titania was almost the same at 3.5 nm with anatase structure, the size effect of TiO₂ was negligible. As a result, the increased surface area of TiO₂-SiO₂ is supposed to be one possible reason for the improvement of the photocatalytic activity.

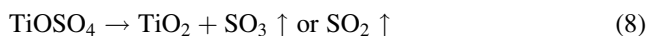
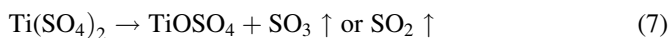
In addition, the enhanced photocatalytic activity of TiO₂-SiO₂ also can be attributed to the presence of an adsorbent (SiO₂), which could increase the concentration of adsorbed organic pollutants near the TiO₂ sites (Anderson and Bard 1995). The large adsorption sites of TiO₂-SiO₂ could have come from large amounts of hydroxyl groups on the surface of silica supports. It should be noteworthy that Ti-O-Si sites were generated near the TiO₂ phase on silica surface (Aronson et al. 1997; Lassaletta et al. 1995). The presence of adsorption sites on TiO₂-SiO₂ may help to adsorb the organics and increase the concentration of reactants near the TiO₂. In the case of TiO₂-Al₂O₃, however, the adsorbed decafluorobiphenyl on Al₂O₃ poorly moved from Al₂O₃ to TiO₂ and led to low photocatalytic activity (Dagan et al. 1995). Therefore, the mobility of reactants from adsorbent to photoactive site should also play an important role in photocatalysis.

TiO₂ particles with diameter less than 10 nm have shown enhanced photocatalytic activity. In the presence of silica substrate, the nanosized TiO₂ particles could be easily obtained because of the large surface area of the silica surface (Lassaletta et al.

1995). When the crystallite dimension of a semiconductor particle falls below a critical radius of approximately 10 nm, the charge carriers appear to behave quantum mechanically, as a simple particle in a box. As a result of this confinement, the energy gap between the valence and conduction bands (band-gap) is enlarged as the particle size of titanium oxide decreases. Thus, the oxidizing potential of the photon generated holes (h^+) and the reducing potential of the electrons (e^-) could increase with increasing band-gap. Fernandez et al. measured the band-gap energies of 3.3 and 4.1 eV for the pure TiO_2 (P-25) and TiO_2-SiO_2 , respectively (Lassaletta et al. 1995). The band-gap of TiO_2-SiO_2 was higher than that of pure TiO_2 by 800 mV. And the TiO_2-SiO_2 showed much higher photocatalytic activity than pure TiO_2 . It was reported that the quantum yield of the photocatalytic hydrogenation of propyne was increased from 0.0226 to 0.0718% as the particle size of TiO_2 was decreased from 110 to 39 Å (Anpo et al. 1987). However, the increased band-gap energy of TiO_2 on the silica surface is not simply determined by size of TiO_2 , because the silica could also modify the band-gap structure. The TiO_2-SiO_2 interface is formed by cross-linking Ti–O–Si bonds. The formation of Ti–O–Si bonds strongly modifies the electronic structure of the oxygen and titanium atoms at the interface of TiO_2-SiO_2 . And, this can also lead to modify the band-gap energy of TiO_2 (Gao and Wachs 1999). Therefore, band-gap structure in the TiO_2-SiO_2 should be attributed to a combination of quantum-size effect of TiO_2 and Ti–O–Si bonds formed on TiO_2-SiO_2 interface (Lassaletta et al. 1995). Due to these kinds of band-gap modifications, the TiO_2-SiO_2 photocatalyst may possess high photo-oxidation as well as photo-reduction capabilities by increased band-gap energy.

2.4 Sulfated TiO_2 (SO_4^{2-}/TiO_2 ; Modification with Anion)

When TiO_2 particles were prepared by various precursors, $Ti(SO_4)_2$ could produce very efficient TiO_2 powder as shown in Fig. 5. Generally, $Ti(SO_4)_2$ solution was thermally decomposed to TiO_2 by the following paths.



Some of retained sulfate ions interact with TiO_2 to generate the SO_4^{2-} sites on TiO_2 (Huang et al. 1998). The XPS spectra at Ti2p and S2p bands for TiO_2 prepared by $Ti(SO_4)_2$ are illustrated in Fig. 6. The binding energy for peak of S2p was 168.7 eV and those of Ti2p were 458.4 and 464.3 eV. These values reveal that Ti exists as Ti^{4+} and S does as SO_4^{2-} . However, Ti2p peaks are shifted to higher binding energy regions than pure TiO_2 powders by 0.8 eV. Since the electronegativity of sulfur is greater than that of Ti, this kind of binding energy shift is evidence for the formation of Ti–O–S bonds as SO_4^{2-}/TiO_2 on the TiO_2 surface. In other words, it can be concluded that the sulfate ion strongly interact with TiO_2 onto the surface.

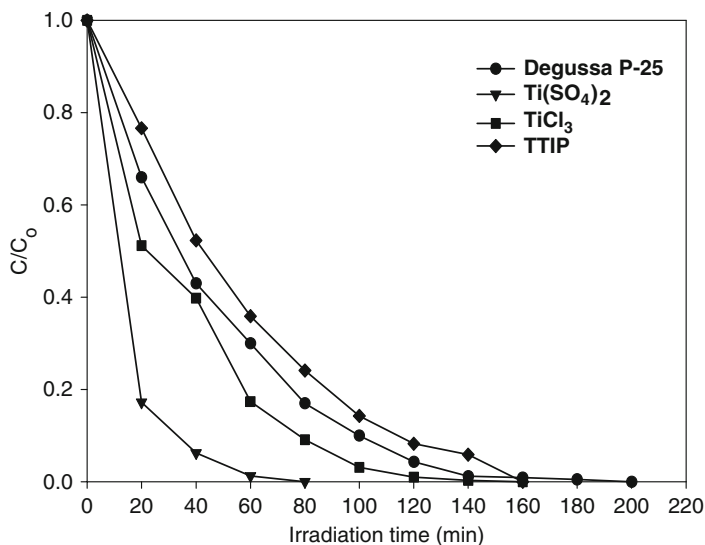


Fig. 5 Effect of Ti-precursors on the photocatalytic decomposition of acetaldehyde

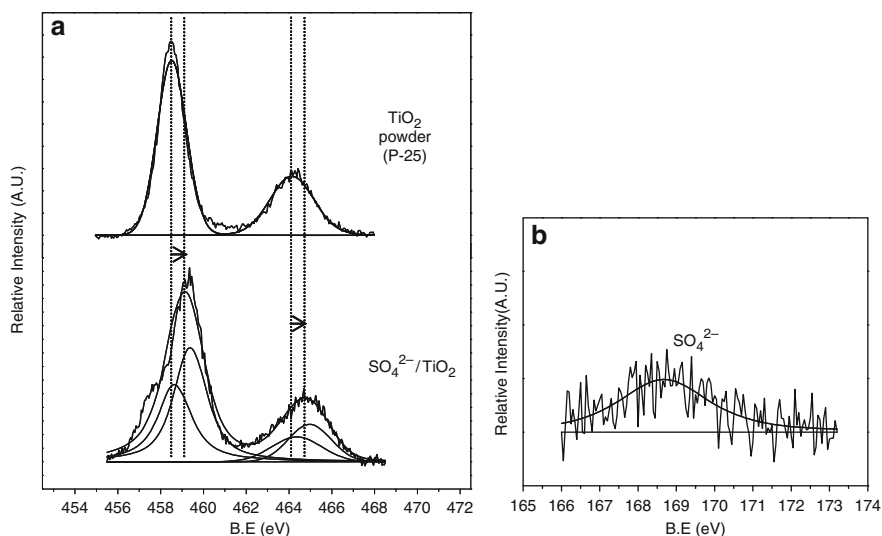


Fig. 6 XPS spectra of SO₄²⁻/TiO₂ at (a) Ti2p and (b) S2p bands

It has been reported that sulfated TiO₂ showed higher photocatalytic activity and selectivity than pure TiO₂ (Huang et al. 1998; Kim et al. 2003). Since the SO₄²⁻/TiO₂ has been well known as strong acidic catalyst, the sulfate ion might generate the bifunctional sites (acid sites and photoactive sites) on TiO₂ surface to promote the photocatalytic oxidation of acetaldehyde on TiO₂ (Shul et al. 2003).

The acidity of TiO₂ could effect on the photocatalytic reactions. It was also reported that the photocatalytic activity of TiO₂ could be improved by increasing or creating of surface acidity (Kozolv et al. 2000; Martra 2000). In the case of decomposition of acetaldehyde over TiO₂, acetaldehyde condensation reactions could be preceded with acetaldehyde on the Lewis acid sites of TiO₂ at 100°C (Idriss and Barteau 1996; Luo and Falconer 1999, 393). Since the acidity of catalyst may be correlated with the acetaldehyde conversion in catalytic reactions, acidic TiO₂ such as sulfated TiO₂ is expected to exhibit higher reaction in acetaldehyde decomposition than pure TiO₂ (Kim et al. 2005). The acid sites produced adsorption sites for the reactants. This fact suggests that the acid sites on TiO₂ could play the role of bifunctional sites having both acid sites and photoactive sites.

3 Photoelectrocatalytic System

The photocatalytic reaction is initiated from which the UV light excites electrons from the valence (VB) to the conduction band (CB) of the semiconductor catalyst, leaving holes behind at VB. The separated electron–hole charge pairs lead to the redox reactions with surface species. Also, in competition with the charge transfer to adsorbed species, recombination of the separated electron–hole pairs can occur in the volume of particle or on the surface with the release of heat (Linsebigler et al. 1995). Therefore, the retardation of electron–hole recombination is the promising way of improving the photocatalytic activity of TiO₂. Kamat and his coworkers suggested electrically assisted photocatalytic oxidation system to inhibit electron–hole recombination during illumination (Vinodgopal et al. 1993). The system successfully reduced the recombination rate of photogenerated electrons and holes by applying a positive potential (“bias”) across the photocatalyst particulate film as shown in Fig. 7a. Several researchers have reported that the effectiveness of supported photocatalysts can be improved by this system in aqueous phase (Vinodgopal et al. 1993; Candal et al. 2000). The electric force improves the efficiency of hole–electron separation and consequently the charge transfer.

Recently, we reported the application of PEC system for the fabrication of new type air cleaner (Hoffmann et al. 1995). The high-voltage electrical discharge was applied to the surface of TiO₂ in order to inhibit the recombination of photogenerated electrons and holes (Fig. 7b). For the confirmation of effectiveness of this system in gas phase, the photo-current was measured as shown in Fig. 8. Without any UV-irradiation and discharge, the initial current was approximately zero (Fig. 8a). When UV was irradiated on the surface of TiO₂ film, the photo-current (ΔC_1) was increased to 1.76×10^{-3} mA (Fig. 8b). When the electric discharge was applied to the system (without UV-irradiation), the initial current was 6.82×10^{-3} mA, as shown in Fig. 8c. On the irradiation of UV on the discharged TiO₂ film, the current difference (ΔC_2) between the electrically discharged and UV/discharged system was 2.17×10^{-3} mA (Fig. 8d). The electrically discharged system showed higher photo-current by 0.46×10^{-3} mA ($\Delta C_2 - \Delta C_1$). The increase of photo-current indicates that the

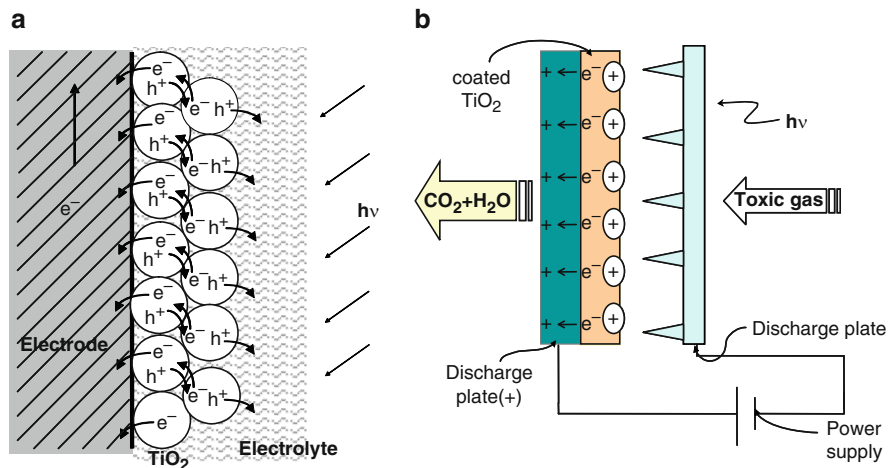


Fig. 7 (a) Electrically assisted photocatalytic oxidation system suggested by Kamat et al. and (b) photoelectrocatalytic (PEC) system suggested by Shul et al.

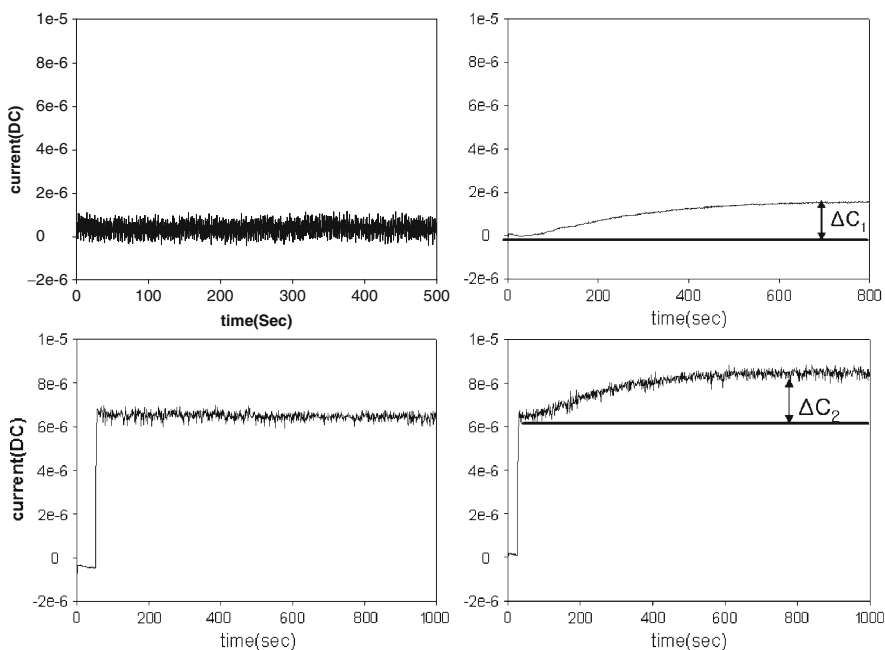


Fig. 8 Photo-current of (a, b) UV-only system and (c, d) photoelectrocatalytic (PEC) system

electrical discharge could drive away the photogenerated electrons from the TiO₂ film. In other words, the recombination of electro-hole pair should be retarded.

Figure 9 shows the PEC decomposition of benzene and acetaldehyde in the PEC system. As compared with conventional UV-TiO₂ system, the PEC system was

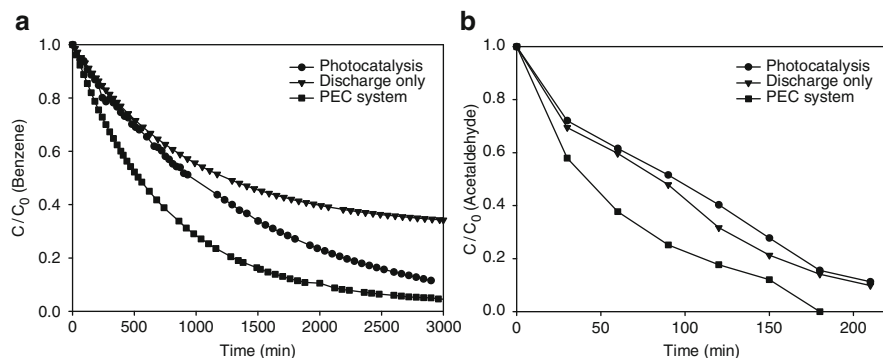


Fig. 9 Decomposition of (a) benzene and (b) acetaldehyde by the photocatalysis and PEC system

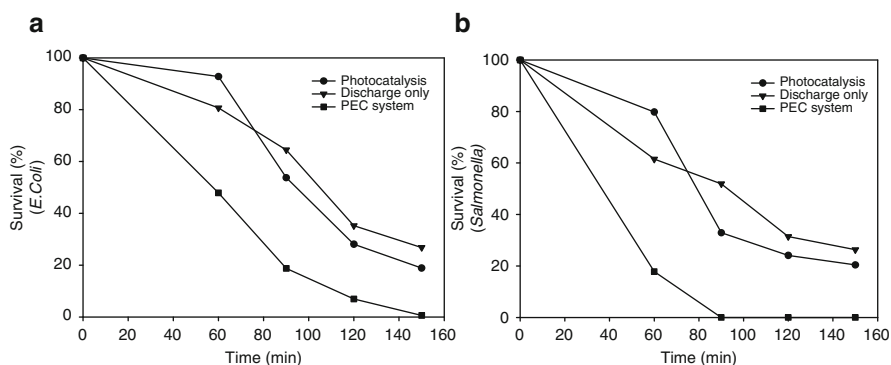


Fig. 10 Sterilization of (a) *E. coli* and (b) *Salmonella* by the photocatalysis and PEC system

more effective in eliminating gas phase pollutants. Also, the PEC system showed better sterilization activity than TiO_2 photocatalysis as shown in Fig. 10. Based on all these results, the PEC system could be applied to the practical treatment of air pollutants.

4 Photocatalytic Oxidation of CO Over $\text{Au}/\text{MnO}_x/\text{TiO}_2$ in PEC System

Carbon monoxide (CO) is one of the most important atmospheric pollutants because of its effects upon human health. Relatively low concentrations of CO can interfere in the O_2 transportation of the blood circulation system and high levels can be lethal. In addition, CO plays an important part in atmospheric chemistry due to its oxidation/reduction capacity. Although CO is produced in nature mainly by

CH₄ and other hydrocarbons oxidation, human activity contributes significantly to the CO concentration level (Briz et al. 2007).

The most intensively studied system is the case of Au supported on TiO₂. Neither Au nor TiO₂ alone is active for CO oxidation but their combination generates high catalytic activity. Gold dispersed as ultrafine particles and supported on TiO₂, in the conventional catalytic or combustion systems, exhibits an extraordinary high activity for low temperature catalytic oxidation of carbon monoxide. Also, Au/TiO₂ and Au/MnO_x/TiO₂ could effectively oxidize CO in the PEC system.

Figure 11 shows the oxidation of CO over various catalysts in the PEC system. The photocatalytic activity heavily depended on the selection of support in the following order: Au/MnO_x/TiO₂ > Au/TiO₂ > Au/MnO₂ > MnO_x/TiO₂. The most active catalyst was Au/MnO_x/TiO₂ of which the reaction constant was about five times higher than that of Au/TiO₂. In the case of MnO_x/TiO₂, the photocatalytic activity was very low, which means the gold was a crucial component for the oxidation of CO. When considering the activity of Au/TiO₂ and Au/MnO₂, the high activity of Au/MnO_x/TiO₂ was unexpected. The interactions among Au, MnO_x, and TiO₂ could have a synergetic effect on the photocatalytic decomposition of CO.

The high activity for CO oxidation of Au/MnO_x/TiO₂ could be explained by the state of Au on the MnO_x/TiO₂. We recently reported that the low loading of manganese could produce the active species such as metallic Au⁰ and perimeter interfacial Au^{δ+}, whereas high loading and subsequent formation of MnO₂ could increase the portion of inactive oxidic Au³⁺ species (Kim et al. 2006). They revealed that the catalytic active component was the metallic Au⁰ and perimeter interfacial Au^{δ+} species, which were dispersed on TiO₂ and Mn³⁺/TiO₂.

The enhanced catalytic activity of Au/MnO_x/TiO₂ was explained by the strong interaction among Au and MnO_x on TiO₂ as shown in Fig. 12. These metal–support

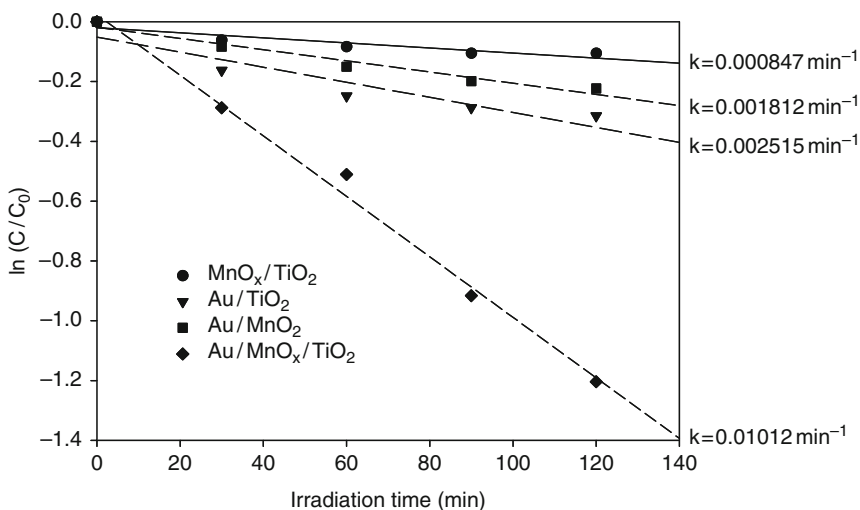


Fig. 11 Photoelectrocatalytic (PEC) oxidation of CO over various Au-doped catalysts

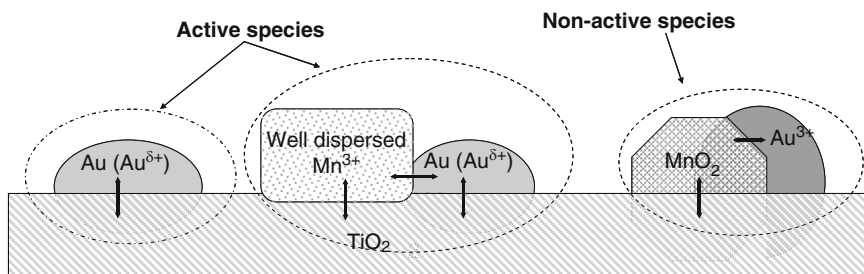


Fig. 12 Proposed model of Au/MnO_x/TiO₂

interactions should affect on the oxidation of CO. It is thought that lattice oxygen and surface OH groups on MnO_x/TiO₂ may be important to obtain high catalytic activity (Grisel et al. 2002). Introduction of MnO_x thus enables an extra route for the supply of active oxygen.

5 Immobilization of TiO₂ Particles

Thin film application: The design of supported TiO₂ on substrate, such as glass, plastic, steel plate, etc., would be of great significance for the practical application. Immobilization of TiO₂ strongly affected on the photocatalytic activity in TiO₂. Figure 13 shows that the activity of PEC system was greatly affected by the type of binders for the immobilization of TiO₂ powder on metal plate. Therefore, the feasibility of practical applications of photocatalysis depends on the stable immobilization of the catalyst powder on a support in such a way as to afford a reasonably high surface area without the loss of accessibility to the immobilized catalyst (Naskar et al. 1998).

Membrane application: The porous membrane coated with TiO₂ can play a role as photocatalytic membrane reactors to eliminate solid particles in waste stream. TiO₂ particles can be immobilized by the various chemical or physical methods, such as sol-gel coating, hydrothermal coating, binder coating, CVD, etc. Figure 14 shows the cross-section of TiO₂-immobilized tubular Al₂O₃ membranes in which TiO₂ was coated by three different methods as follows:

- TiO₂ sol was coated on the Al₂O₃ membrane by using the pressurized coating technique.
- Degussa P-25 was coated on the Al₂O₃ membrane by the suspension of TiO₂ powder in de-ionized water without binder and dried at 80°C.
- Degussa P-25 was coated on the Al₂O₃ membrane by the suspension of TiO₂ powder in silica sol, which was a binder for TiO₂ coating.

It was found that all methods provided thin layers of TiO₂ on the α-Al₂O₃ tube. Figure 14(a) shows the conversion ratio of acetaldehyde as a function of irradiation time under UV illumination. Method A showed the lowest photocatalytic

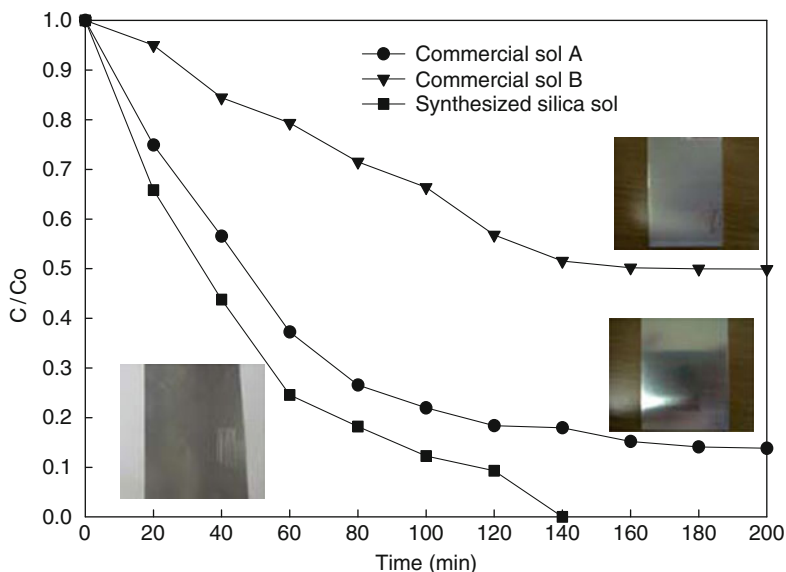


Fig. 13 Photoelectrocatalytic (PEC) decomposition of acetaldehyde with various coating sol for the immobilization of TiO₂

oxidation rate. When method B was used, the highest reaction rate was obtained. Method C showed little lower reactivity than method B, because of the SiO₂ binder for the adhesion of TiO₂ powder. The surface areas of immobilized photocatalysts were measured to confirm the effect of surface area of TiO₂. The samples prepared by method A, B, and C showed the area of 340.05, 319.55, and 366.60 m²/g including alumina substrate. As the surface area of TiO₂ layers decreased in the order method C > method B > method A, it was hard to relate with the activity order (method B > method C > method A). It might be due to the loss of effectiveness of immobilized photocatalyst. For examples, the most of TiO₂ particles is penetrated into the pore of the tube in method A, and it reduces the effectiveness of immobilized TiO₂ on surface of porous alumina.

Photocatalytic decomposition rate of acetaldehyde as a function of the layer thickness of TiO₂ from method B is presented in Fig. 14(b). As repeating the TiO₂ coating on Al₂O₃ membrane, the thickness increased up to 100 μm. However, the decomposition rate of acetaldehyde was not linearly increased with the thickness of TiO₂ layer. When the photocatalytic activity based on TiO₂ weight was calculated, the mass reactivity of TiO₂ showed high activity at 10 μm. The mass activity drastically decreased above 20 μm. The increase in thickness of TiO₂ layer was not effective to enhance the photocatalytic activity. It implies that the excess loading of TiO₂ does not help the photocatalytic reaction. Therefore, the effective thickness of TiO₂ layer thickness used for the decomposition of acetaldehyde seemed to measure up to 20 μm, the most effective thickness of TiO₂ being about 10 μm (Fig. 15).

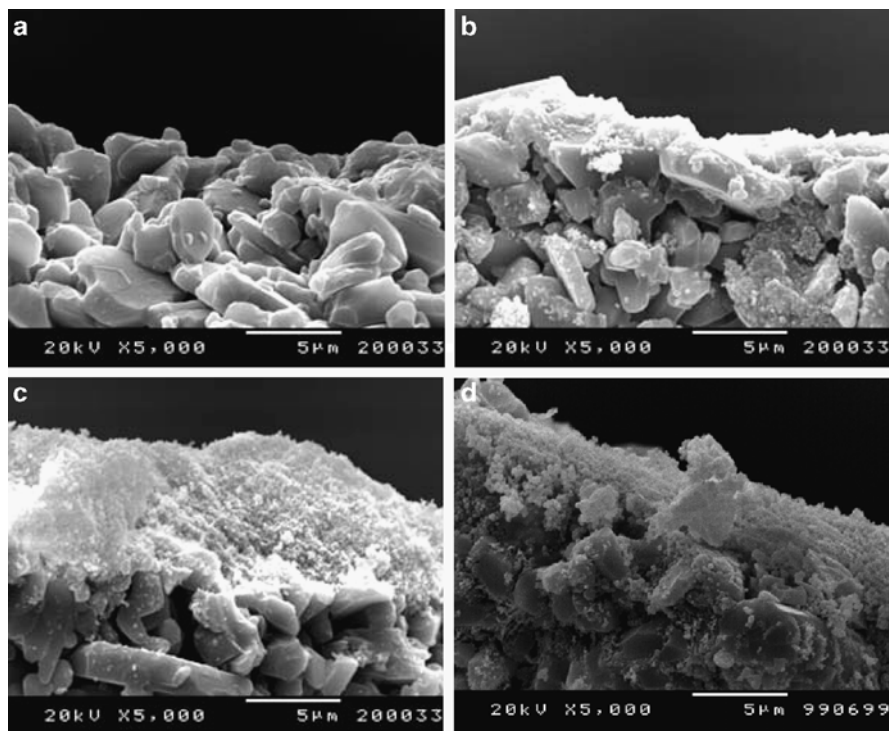


Fig. 14 Cross-sectional SEM images of immobilized TiO_2 on Al_2O_3 tube with various coating methods (**a**: Al_2O_3 substrate, **b**: method A, **c**: method B, **d**: method C)

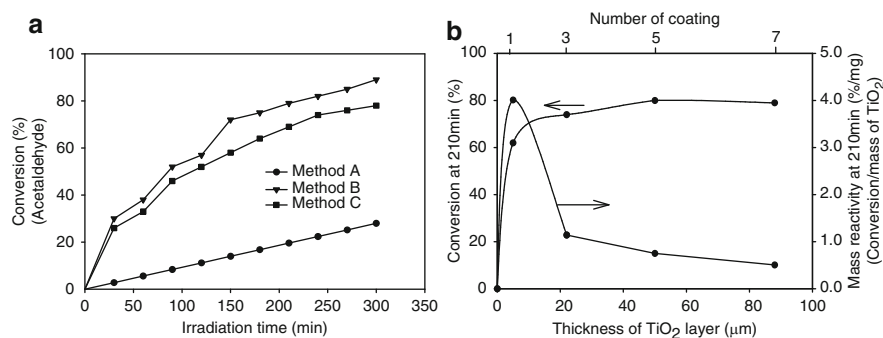


Fig. 15 Effect of coating method (**a**) and depth of TiO_2 layer (**b**) on photocatalytic decomposition of acetaldehyde

Fiber application: Among the various topological constructions of TiO_2 , fibrous materials are highly desirable for the practical use for catalysts. With this fiber, one can make a TiO_2 sheet based on paper-making process (Chu et al. 2002). According to the study of Sato et al., TiO_2 fibers formed by solvothermal reaction showed much

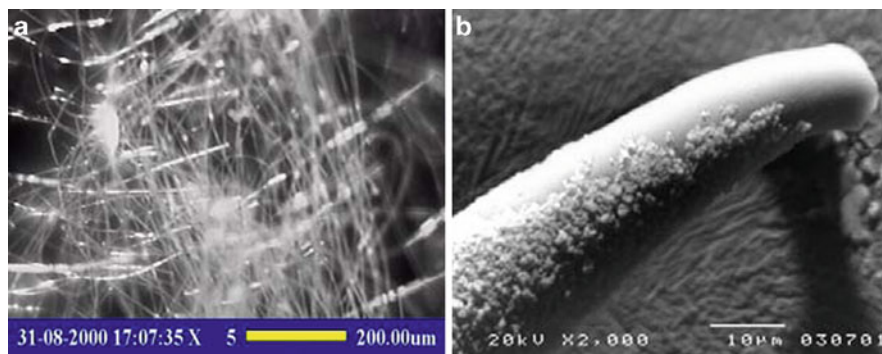


Fig. 16 (a) Optical micrograph of mesoporous silica fiber and (b) SEM image of TiO₂-loaded mesoporous silica fiber

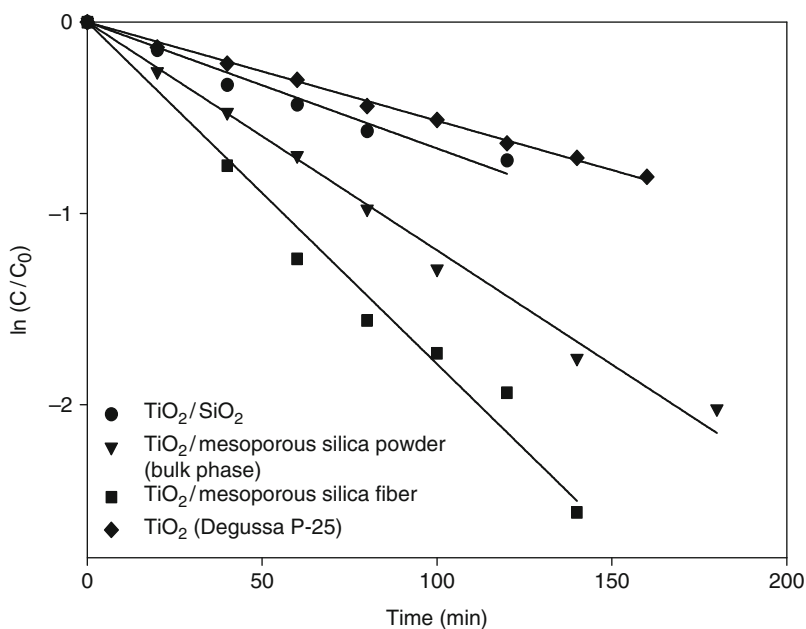


Fig. 17 Photocatalytic degradation of acetaldehyde over TiO₂-loaded silica fiber

higher hydrogen evolution activity than that of Degussa P-25 (Linsebigler et al. 1995). They are of great interest for possible applications to photovoltaic cells, catalysts, and semiconductor devices. However, the morphological control of the fiber structure of TiO₂ on a large scale is rather a difficult process.

We also synthesized the TiO₂ supported on mesoporous silica fibers (Kim et al. 2004). The silica fiber is generally optically transparent. Figure 16 shows the optical micrograph of mesoporous silica fiber and SEM image of TiO₂-loaded one. TiO₂

particles were successfully deposited on the surface of the mesoporous silica fiber. As the mesoporous silica fiber was immersed in $\text{Ti}(\text{SO}_4)_2$ solution and dried, TiO_2 particles could be dispersed both on the surface of fiber and inside of meso-pore. When TiO_2 was supported on porous solids, effective surface area of TiO_2 could be improved. While the surface area of the commercial $\text{TiO}_2(\text{P-25})$ was $55 \text{ m}^2/\text{g}$, the surface area of TiO_2 -loaded silica fiber was about $620 \text{ m}^2/\text{g}$. The enhanced surface area of mesoporous silica fiber could improve the photocatalytic activity of the supported TiO_2 . Photocatalytic activity of TiO_2 -supported silica fiber was evaluated with the photocatalytic decomposition of acetaldehyde (Fig. 17). The reaction constant of TiO_2 -supported silica fiber (0.0179 s^{-1}) was higher than those of $\text{TiO}_2\text{-SiO}_2$ (0.0066 s^{-1}) or pure TiO_2 (0.00526 s^{-1}). The optical transparency of mesoporous silica fiber as shown in Fig. 17 could be advantageous for the photocatalytic applications.

6 Air-Cleaning Systems Combined with Photocatalyst

There is an extremely wide range of applications for photocatalysis of TiO_2 . The initial commercialized products using the photocatalytic cleaning effect of TiO_2 was self-cleaning cover glass for tunnel light. A high pressure sodium lamp in tunnels emits UV light of about $3 \text{ mW}/\text{cm}^2$, at a position of its cover glass (Hashimoto et al. 2005). This UV is sufficient to keep the surface clean when the cover glass is coated with the TiO_2 photocatalyst. This cleaning based on the photocatalytic decomposition effect is now used in other various commercial products such as window blinds. This kind of photocatalytic effect can be also applicable to anti-bacterial ceramic tiles in an operating room. Furthermore, the photo-induced hydrophilicity of TiO_2 makes water droplets easier to remove by imparting water repellency to the surface of glass. The stains adsorbed on the TiO_2 surface can easily be washed by water, because water soaks between stains and the highly hydrophilic TiO_2 surface (Hashimoto et al. 2005). However, the typical indoor UV light intensity is almost three orders of magnitude weaker than the outdoor one. Hence, some more air-cleaning systems containing fans and filters are required for the improvement of indoor air quality.

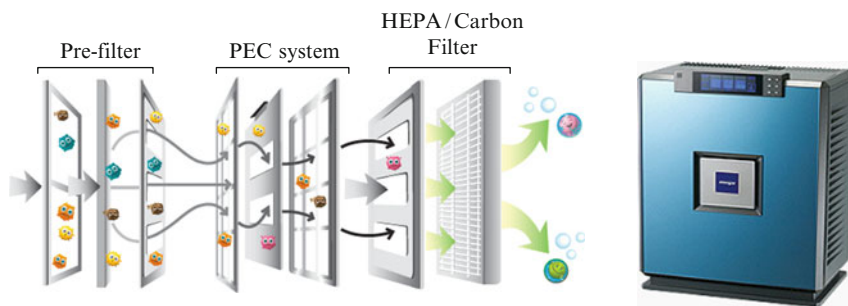


Fig. 18 Basic concept and external feature of commercial air cleaner based on PEC system

The PEC-based air cleaner was successfully commercialized in Korea. Figure 18 shows the basic concept and external features of commercial air cleaner. The PEC-based air-cleaning system was effective on the decomposition of various pollutants and microorganisms (Fig. 19). We also fabricated the small air cleaner using the PEC system (Fig. 20). LED array with UV-LED peak wavelength of about 380 nm was used as the source of UV light. Since it contains a small fan and filter with a PEC system, it can be applied to air cleaners for cars.

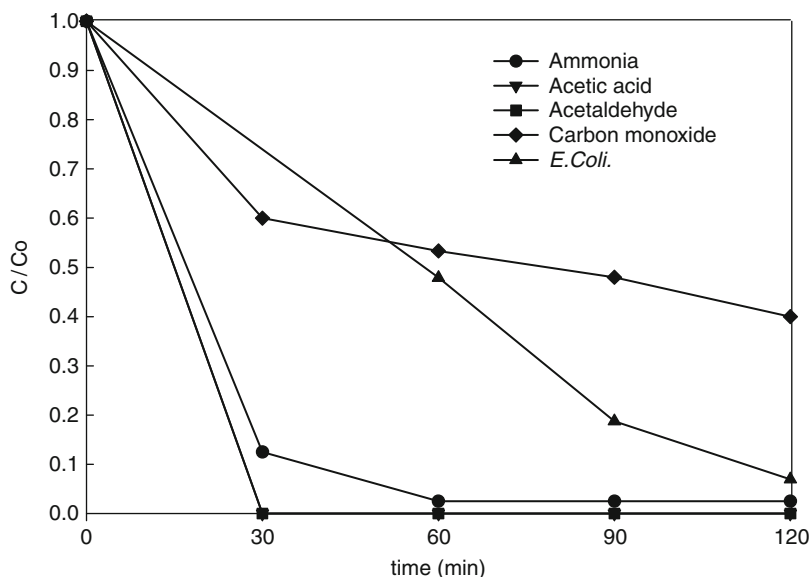


Fig. 19 Decomposition of various pollutants and microorganism by air cleaner based on the PEC system

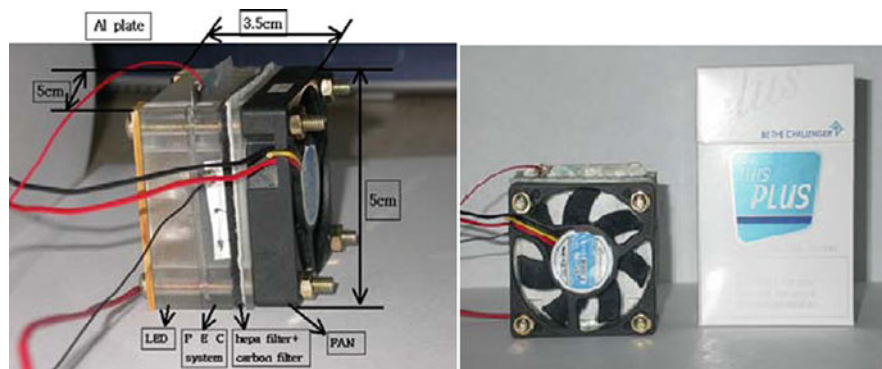


Fig. 20 Side and front view of small air cleaner based on the PEC system

7 Summary

Photocatalytic process has been used in the decomposition of noxious gases, odor-causing gases, and dirt, among others. The photocatalyst business is currently growing up, and many companies are proposing and developing materials, devices and systems for cleaning the polluted air. The physicochemical properties of TiO₂ should be engineered for the application of TiO₂ photocatalysts in air cleaning system. In this chapter, we have described surface modification of TiO₂, PEC system, and immobilization of photocatalysts to realize the air cleaning system. Besides these researches, various advanced investigations for the TiO₂ photocatalyst can be easily found in many countries. Therefore, we believe that these technologies including the ones we have mentioned earlier will further develop the TiO₂ photocatalysts and their application field.

References

- Anderson C, Bard AJ (1995) An improved photocatalyst of TiO₂/SiO₂ prepared by a sol-gel synthesis. *J Phys Chem* 99:9882–9885
- Anpo M, Shima T, Kodama S, Kubokawa Y (1987) Photocatalytic hydrogenation of propyne with water on small-particle titania: size quantization effects and reaction intermediates. *J Phys Chem* 91:4305–4310
- Anpo M, Takeuchi M (2003) The design and development of highly reactive titanium oxide photocatalysts operating under visible light irradiation. *J Catal* 216(2003):505
- Arabatzis IM, Stergiopoulos T, Andreeva D, Kitova S, Neophytides GS, Falaras P (2003) Characterization and photocatalytic activity of Au/TiO₂ thin films for azo-dye degradation. *J Catal* 220:127–135
- Aronson BJ, Blanford CF, Stein A (1997) Solution-phase grafting of titanium dioxide onto the pore surface of mesoporous silicates: synthesis and structural characterization. *Chem Mater* 9:2842–2851
- Briz S, de Castro AJ, Diez S, Lopez F, Schafer K (2007) Remote sensing by open-path FTIR spectroscopy. Comparison of different analysis techniques applied to ozone and carbon monoxide detection. *J Quant Spectrosc Radiat Transf* 103:314–330
- Candal RJ, Zeltner WA, Anderson MA (2000) Effects of pH and applied potential on photocurrent and oxidation rate of saline solutions of formic acid in a photoelectrocatalytic reactor. *Environ Sci Technol* 34:3443–3451
- Carp O, Huisman CL, Reller A (2004) Photoinduced reactivity of titanium dioxide. *Prog Solid State Chem* 32:33–177
- Cho SM, Joo H, Kim HJ, Shul YG (2002) The photodecomposition of acetaldehyde in gas phase using immobilized TiO₂ on porous alpha-Al₂O₃ tube. *J Adv Oxid Technol* 5:141–146
- Choi W, Termin A, Hoffmann MR (1994) The role of metal ion dopants in quantum-sized TiO₂: correlation between photoreactivity and charge carrier recombination dynamics. *J Phys Chem* 98:13669–13679
- Chu YH, Kim HJ, Song KY, Jung KT, Shul YG (2002) Preparation of mesoporous silica fiber matrix for VOC removal. *Catal Today* 74:249–256
- Dagan G, Sampath S, Lev O (1995) Preparation and utilization of organically modified silica-titania photocatalysts for decontamination of aquatic environments. *Chem Mater* 7:446–453

- Date M, Okumura M, Tsubota S, Haruta M (2004) Vital role of moisture in the catalytic activity of supported gold nanoparticles. *Angew Chem Int Ed* 43:2129–2132
- Dawson A, Kamat PV (2001) Semiconductor-metal nanocomposites. photoinduced fusion and photocatalysis of gold-capped TiO₂ (TiO₂/gold) nanoparticles. *J Phys Chem B* 105:960–966
- Dumitriu E, Hulea V, Fecheti I, Auroux A, Lacaze JF, Guimon C (2001) The aldol condensation of lower aldehydes over MFI zeolites with different acidic properties. *Microporous Mesoporous Mater* 43:341–359
- Fan L, Ichikuni N, Shimazu S, Uematsu T (2003) Preparation of Au/TiO₂ catalysts by suspension spray reaction method and their catalytic property for CO oxidation. *Appl Catal A Gen* 246:87–95
- Gao X, Wachs IE (1999) Titania–silica as catalysts: molecular structural characteristics and physico-chemical properties. *Catal Today* 51:233–254
- Grisel RJH, Weststrate CJ, Goossens A, Craje MWJ, van der Kraan AM, Nieuwenhuys BE (2002) Oxidation of CO over Au/MO_x/Al₂O₃ multi-component catalysts in a hydrogen-rich environment. *Catal Today* 72:123–132
- Hashimoto K, Irie H, Fujishima A (2005) (2005) TiO₂ photocatalysis: a historical overview and future prospects. *Jpn J Appl Phys* 44:8269–8285
- Hoffmann MR, Martin ST, Choi W, Bahnemann DW (1995) Environmental applications of semiconductor photocatalysis. *Chem Rev* 95:69–96
- Huang Y, Zhao B, Xie Y (1998) A novel way to prepare silica supported sulfated titania. *Appl Catal A Gen* 171:65–73
- Idriss H, Barteau MA (1996) Selectivity and mechanism shifts in the reactions of acetaldehyde on oxidized and reduced TiO₂(001) surfaces. *Catal Lett* 40:147–153
- Iizuka Y, Tode T, Takao T, Yatsu K, Takeuchi T, Tsubota S, Haruta M (1999) A kinetic and adsorption study of CO oxidation over unsupported fine gold powder and over gold supported on titanium dioxide. *J Catal* 187:50–58
- Jakob M, Levanon H, Kamat PV (2003) Charge distribution between UV-irradiated TiO₂ and gold nanoparticles: determination of shift in the fermi level. *Nano Lett* 3:353–358
- Kim HJ, Shul YG, Han H (2004) TiO₂ loaded mesoporous silica fiber for the photocatalytic application. *Stud Surf Sci Catal* 154:581
- Kim HJ, Nam KH, Shul YG (2003) Preparation of TiO₂ fiber and its photocatalytic properties. *Mater Sci Forum* 439:271–276
- Kim HJ, Shul YG, Han H (2005) Photocatalytic properties of silica-supported TiO₂. *Top Catal* 35:287
- Kim HJ, Han MK, Lee SM, Hwang DK, Shul YG (2006) *Top Catal* (submitted)
- Kozolv DV, Paukshtis EA, Savinov EN (2000) The comparative studies of titanium dioxide in gas-phase ethanol photocatalytic oxidation by the FTIR in situ method. *Appl Catal B Environ* 24:L7–L12
- Kraeutler B, Bard A (1978) Heterogeneous photocatalytic preparation of supported catalysts. Photodeposition of platinum on titanium dioxide powder and other substrates. *J Am Chem Soc* 100:4317
- Lassaletta G, Fernandez A, Espinos JP, Gonzalez-Eliphe AR (1995) Spectroscopic characterization of quantum-sized TiO₂ supported on silica: influence of size and TiO₂-SiO₂ interface composition. *J Phys Chem* 99:1484–1490
- Lee SS, Kim HJ, Jung KT, Kim HS, Shul YG (2001) Photocatalytic activity of metal ion doped titania. *Korean J Chem Eng* 18:914–918
- Linsebigler AL, Lu G, Yates JT (1995) Photocatalysis on TiO₂ surface: principles, mechanisms, and selected results. *Chem Rev* 95:735–758
- Litter MI, Navio JA (1996) Photocatalytic properties of iron-doped titania semiconductors. *J Photochem Photobiol A Chem* 98:171–181
- Luo S, Falconer JL (1999) Acetone and acetaldehyde oligomerization on TiO₂ surfaces. *J Catal* 185:393–407
- Martra G (2000) Lewis acid and base sites at the surface of microcrystalline TiO₂ anatase: relationships between surface morphology and chemical behavior. *Appl Catal A Gen* 200:275–285

- Mills A, Lehunte S (1997) An overview of semiconductor photocatalysis. *J Photochem Photobiol A Chem* 108:1–35
- Naskar S, Pillay SA, Chanda M (1998) Photocatalytic degradation of organic dyes in aqueous solution with TiO₂ nanoparticles immobilized on foamed polyethylene sheet. *J Photochem Photobiol A Chem* 113:257–264
- Ollis DF, Pelizzetti E, Serpone N (1991) Photocatalyzed destruction of water contaminants. *Environ Sci Technol* 25:1522–1529
- Shul YG, Kim HJ, Haam SJ, Han HS (2003) Photocatalytic characteristics of TiO₂ supported on SiO₂. *Res Chem Intermed* 29:849–859
- Vinodgopal K, Hotchandani S, Kamat PV (1993) Electrochemically assisted photocatalysis: titania particulate film electrodes for photocatalytic degradation of 4-chlorophenol. *J Phys Chem* 97:9040–9044
- Wood A, Giersig M, Mulvaney P (2001) Fermi level equilibration in quantum dot-metal nanojunctions. *J Phys Chem B* 105:8810–8815
- Yang JC, Kim YC, Shul YG, Lee CH, Lee TK (1997) Characterization of photoreduced Pt/TiO₂ and decomposition of dichloroacetic acid over photoreduced Pt/TiO₂ catalysts. *Appl Surf Sci* 121–122:525–529
- Yang JH, Henao JH, Raphulu MC, Wang Y, Caputo T, Groszek AJ, Kung M, Scurrell MS, Miller JT, Kung HH (2005) Activation of Au/TiO₂ catalyst for CO oxidation. *J Phys Chem B* 109:10319–10326
- Zou L, Luo Y, Hooper M, Hu E (2006) Removal of VOCs by photocatalysis process using adsorption enhanced TiO₂-SiO₂ catalyst. *Chem Eng Process* 45:959–964

Chapter 18

Photocatalytic Removal of Gas-Phase Elemental Mercury Using TiO₂

Tai Gyu “Teddy” Lee

Abstract A photochemical reaction by TiO₂ under UV irradiation has been proven to be a very promising technology for effective removal of air contaminants. However, because of UV’s high operating cost and harmfulness to humans, many researchers have been looking for alternative ways to activate the photocatalyst. For example, chemical doping enabled a modified TiO₂ to activate under visible light, however, so far, with a relatively low photoreactivity in most cases. Recently, various types of TiO₂ photochemical reactor systems with different light sources have been tested to oxidize/remove elemental mercury (Hg⁰) from a simulated combustion flue gas. Notably, the photochemical removal of Hg⁰ by pure TiO₂ under visible light (410–510 nm) was proven to be as highly effective as UV light. The results suggest that upon irradiation by visible light, TiO₂ may be used to selectively remove gas-phase Hg⁰ among other air contaminants (those that usually suffer from low photoreactivity even under the strongest UV light) from combustion flue gas.

1 Introduction

Mercury has been under the focus for sometime due to its high toxicity and a tendency to bio-accumulate. In the U.S., emissions from the stationary combustion sources account for approximately 80% of the total annual mercury emissions (Biswas 1999). On March 15, 2005, U.S. EPA has issued the Clean Air Mercury Rule to permanently cap and reduce mercury emissions from coal-fired power

T.G. “Teddy” Lee (✉)

Department of Chemical and Biomolecular Engineering, Yonsei University,
262 Seongsanno, Seodaemun-gu, 120-749 Seoul, Korea
e-mail: teddy.lee@yonsei.ac.kr

Table 1 Hg analysis of various types of vehicles and fuels (Won et al. 2007)

	Gasoline	Diesel	LPG
Original fuel Hg content (ng/L)	571.1 ± 4.5	185.7 ± 2.6	1,230.3 ± 23.5
Test at idling mode (ng/m ³)	1.5–9.1	1.6–3.5	10.2–18.6
Test at driving mode (ng/m ³)	3.8–16.8	2.8–8.5	20.0–26.9

plants. Furthermore, the U.S. government is actively engaged in researching and developing more economical ways to capture mercury.

Although not currently being regulated, considerable amount of mercury also comes from mobile sources. The Korea Ministry of Environment recently reported that the average blood Hg level of 4.55 µg/L was observed for people living inside 50 m vicinity of large traffic, whereas 3.84 µg/L was observed for people living more than 300 m away (Kim 2006). Table 1 shows the measured mercury contents of the fuel and automobile exhaust gas. Mercury was mostly in elemental form, and no detectable levels of particulate or oxidized mercury were measured.

Mercury exists in the flue gas as a vapor form due to its characteristic of high vapor pressure. Major chemical forms of mercury from combustion sources are oxidized mercury (Hg²⁺) and elemental mercury (Hg⁰). Hg²⁺ species, such as HgCl₂ and HgO, are easily removed by wet-type air pollution control devices (APCDs), such as flue gas desulfurization (FGD), due to its water-soluble property. On the other hand, Hg⁰ is difficult to control because of its insoluble property with water.

Using virgin or chemically-enhanced activated carbon (AC) as adsorbent is currently the most widely used technology for removing mercury from the stationary combustion sources, either injected or in a fixed-bed system. However, virgin AC usually suffers from slow adsorption rate, no selectivity over mercury, a high AC to mercury ratio, and consequently results in high operating costs. Chemical-impregnated ACs, in spite of the improved efficiency, also exhibit problems such as high operating costs and secondary contaminants from the impregnated chemicals (S-, I-, etc.).

Biswas and co-workers initiated and successfully demonstrated the idea of using TiO₂ under UV irradiation to remove gas-phase elemental mercury with considerably lower operating costs compared to AC (Wu et al. 1998; Lee et al. 2001).

In this chapter, several extended experiments and their results are reviewed on the selective removal of Hg⁰ by different types of TiO₂ reactor systems, under various irradiation sources, notably including visible light.

2 In Situ Generated TiO₂ by Gas-Phase Ti Precursor Injection

A novel methodology using in situ generated TiO₂ from gas-phase Ti precursor with UV has been proposed and tested for the capture of Hg⁰ in a combustion flue gas (Wu et al. 1998; Lee et al. 2001; Lee and Hyun 2006). The gas-phase Ti precursor enters the combustor and is readily oxidized to form sorbent particles.

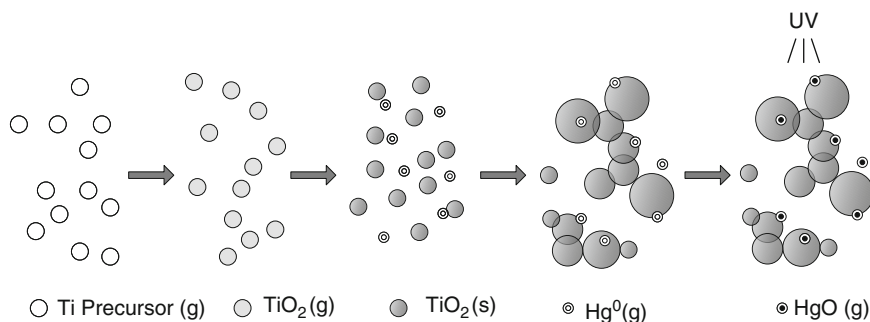
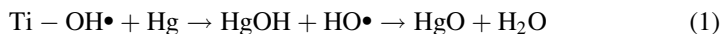


Fig. 1 A mechanistic pathway of the elemental mercury capture by in situ generated TiO₂ under UV irradiation (Wu et al. 1998)

These particles then are grown to be a highly agglomerated structure by coagulation and coalescence mechanisms, consisting of nano-sized (20–30 nm) particles. The structural characteristics of the in situ generated TiO₂ particles are critical to the effectiveness of the capture of Hg⁰. This proposed method can be very effective for the combustors with high difficulty of modification and also capable of suppressing the formation of submicrometer particles, resulting in lower emissions.

The mechanistic pathway of the elemental mercury capture process is illustrated in Fig. 1. This open-structured agglomerate with high surface area allows the effective irradiation by UV light and minimal mass transfer resistance for the Hg⁰. Thus, a low ratio of Ti to Hg⁰ is effective in obtaining high capture efficiencies.

A detailed description of the reaction between the in situ generated TiO₂ and Hg⁰ has been previously reported. The positive holes may result in OH radicals formation by adsorption of O₂ or H₂O, which then oxidize the mercury, thus creating a lower volatile form (HgO) that is retained on titania particle surface (Linsebigler et al. 1995; Wu et al. 1998; Lee et al. 2001; Lee and Hyun 2006):



A schematic diagram of the aerosol flow reactor system is shown in Fig. 2. The furnace aerosol reactor consisted of an alumina tube was used. Titanium (IV) isopropoxide, 97%, (Ti[OCH(CH₃)₂]₄, Aldrich) was used as a precursor for TiO₂. The photochemical reactor was made of borosilicate glass. The transmittance of the borosilicate glass was 94% at 360 nm, 72% at 320 nm, and 30% at 300 nm. The UV lamp (Spectronics, Type XX-40, 80 W) was 120 cm long, and the intensity at 365 nm was 1.85 mW/cm² at a distance of 25 cm. The total flow rate of air through the system was fixed at 1 lpm. The inlet Hg⁰ concentration was maintained at 5 µg/m³.

As previously reported (Wu et al. 1998; Lee et al. 2001; Lee and Hyun 2006), Hg⁰ was very effectively removed (>80%) up to the highest tested photochemical reaction temperature of 160°C, the typical temperature range (150–200°C) of the flue gas entering the electrostatic precipitator (ESP) in coal combustors, considering the utilization of the ESP corona as a potential source of UV irradiation.

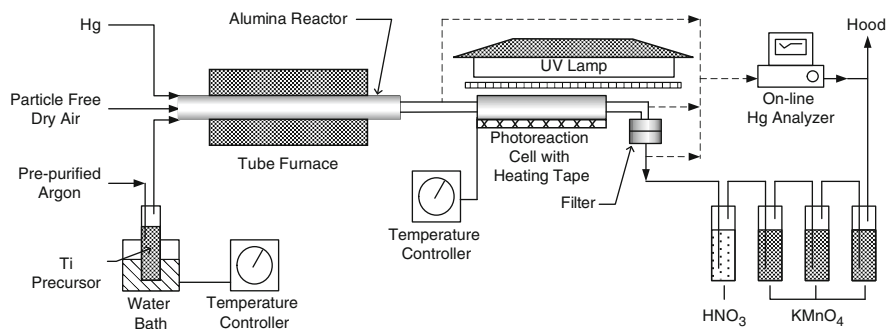


Fig. 2 A schematic diagram of the aerosol flow reactor system (Lee et al. 2002)

To verify the fact that mercury was actually adsorbed onto the TiO_2 surface and not simply discharged in different (non-elemental) forms, exhaust gas out of the photochemical reactor was sampled and then analyzed. No mercury was detected when the removal efficiency was almost 100% indicating no discharged in the oxidized form.

3 Bulk TiO_2 in a Rotating Glass-Type Reactor

A rotating glass-type reactor was specially designed to maintain the photocatalyst's consistency and even exposure to the light sources (Fig. 3).

A mixture of TiO_2 powder and glass beads was placed inside the reactor to maximize the contacting surface area mercury adsorbents and light exposure.

Dimensions of the borosilicate photochemical reaction cell were 10 cm in length and 2.5 cm in diameter. 0.3 g was used for all three types of TiO_2 . Hg^0 inlet concentration was $300\text{--}400\ \mu\text{g}/\text{m}^3$.

Three different commercially available TiO_2 were tested for their mercury-removal efficiency: Degussa P25, anatase (prepared from STS-01 titania sol, Ishihara, Japan), and rutile (53145-0601, Junsei, Japan). Average particle sizes (literature) of Degussa, anatase, and rutile TiO_2 were 30, 7, and 1.5 nm, respectively. Specific surface areas (BET) were measured to be $48.8 \pm 1.4\ \text{m}^2/\text{g}$ for Degussa P25, $375.3 \pm 0.7\ \text{m}^2/\text{g}$ for anatase, and $3.1 \pm 0.2\ \text{m}^2/\text{g}$ for rutile. Their Hg^0 -removal efficiencies were tested under various light sources; UV black light, UV sterilizing light, fluorescent light, and the blue light. Wavelengths of the light sources are shown in Fig. 4. Only after the analyzer reading had been stabilized, the light source was provided followed by the outlet Hg concentration measurement.

As shown in Fig. 5, higher than 99% Hg-removal efficiencies were observed for UV black light, UV sterilizing light, and fluorescent light. Under blue light, a slightly lower efficiency (still close to 85%) was observed. UV black light with

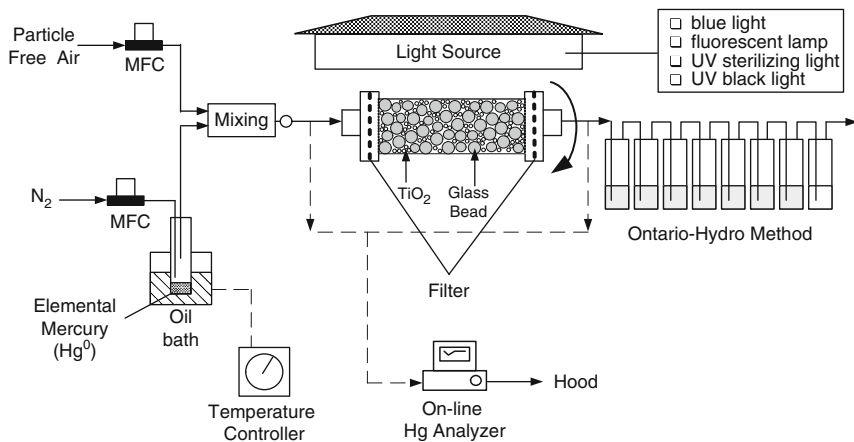


Fig. 3 A schematic diagram of the rotating-type reactor system

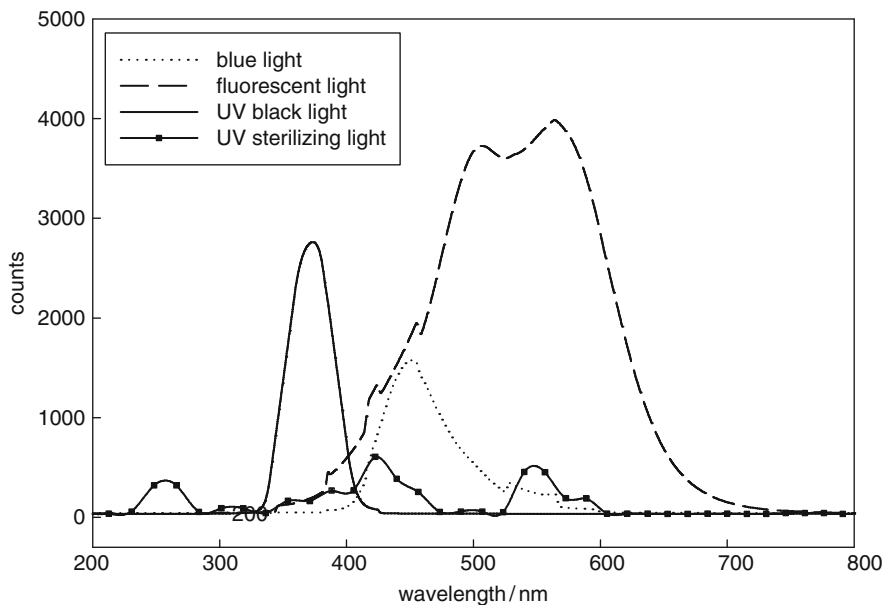


Fig. 4 Wavelengths of the light sources tested (Lee et al. 2004)

the light wavelength of 300–400 nm resulted in a relatively fast reaction than others. Under the conditions tested in this work, Hg⁰-removal efficiency did not seem to depend on the physical properties of selected TiO₂. Under blue light, only rutile form of TiO₂ showed a Hg-removal efficiency higher than 99%, which is due

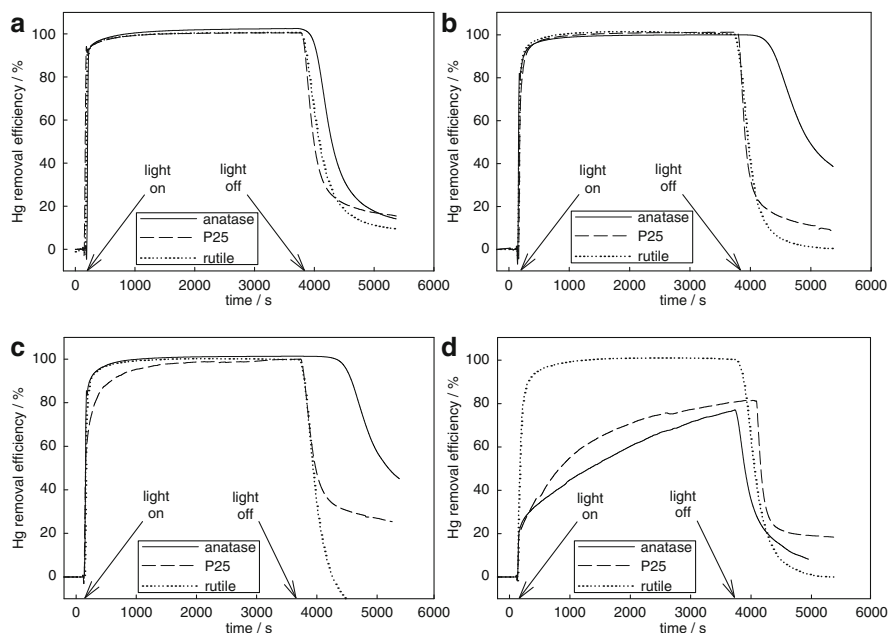


Fig. 5 Hg^0 -removal efficiency vs. reaction time: (a) UV black light, (b) UV sterilizing light, (c) fluorescent light, and (d) blue light (Lee et al. 2004)

Table 2 Comparison between TiO_2 and activated carbon (AC) (Lee et al. 2004)

	TiO_2	AC
Average time to reach 80% of the initial Hg conc.	≈ 570 h	≈ 40 h
Amount of Hg/kg of adsorbent	≈ 68.0 g	≈ 2.5 g
Average cost/kg of adsorbent ^a	$\approx \$30.0$	$\approx \$8.5$
Estimate cost/kg of Hg	$\approx \$440^b$	$\approx \$3,400$

^aLocal prices for the adsorbents may vary

^bElectricity cost is not included: 2×36 W for 570 h = ca. \$1.70

to the better correspondence of rutile TiO_2 to the light sources with longer wavelengths, such as blue light.

In this work, continuous mercury-removal efficiency higher than 99% was observed for the anatase TiO_2 for several minutes after the light was turned off. This was more evident for UV sterilizing and fluorescent light with significant portion of visible range wavelength; the photon (light) seemed to play its role before the succession of cyclic photochemical reaction steps making the catalytic turnover (Chanon and Schiavello 1997).

Breakthrough experiments were performed for TiO_2 (Degussa P25) with a low cost, easily maintainable fluorescent light (2×36 W) and AC ($1,133.6 \pm 11.2$ m²/g, Kuracoal-GW, Kuraray, Japan). As shown in Table 2, TiO_2 perform far better than AC in maintaining the high-efficiency Hg^0 removal.

4 Immobilized TiO_2 in a Thin Film Photochemical Reactor

Different types of TiO_2 (nanotitanosilicate fiber and Degussa P25) immobilized in a thin film reactor were tested for their photocatalytic ability to remove/oxidize gas-phase elemental mercury under various light sources. Figure 6 is a schematic diagram of the experimental setup. The TiO_2 -coated slide glass was placed in a container made with acrylic materials and the top was covered with light permeable quartz glass. Real-time measurements of Hg^0 concentration were carried out by on-line Hg analyzer (VM-3000, Mercury Instruments, Germany).

4.1 Nanotitanosilicate Fiber Generated by a Diffusion Flame Burner

A diffusion flame burner (Fig. 7) was designed to generate the nanotitanosilicate particles. The photocatalytic fibers are collected and grown on the surface of the slide glass ($75 \times 25 \text{ mm}$). It consists of a diffusion flame reactor with a precursor feed system consisting of a bubbler. Different ratio (wt%) of titanium tetraisopropoxide (TTIP) and tetraethyl orthosilicate (TEOS) mixtures (2:1, 4:1, 10:1, and 12:1) were introduced into the flame system by a carrier gas. Mass flow controllers were used to precisely control the flow rates of fuel (LPG), oxidants (O_2), sheath gas (N_2), and carrier gas. The mixture of precursors was dynamically stirred at room

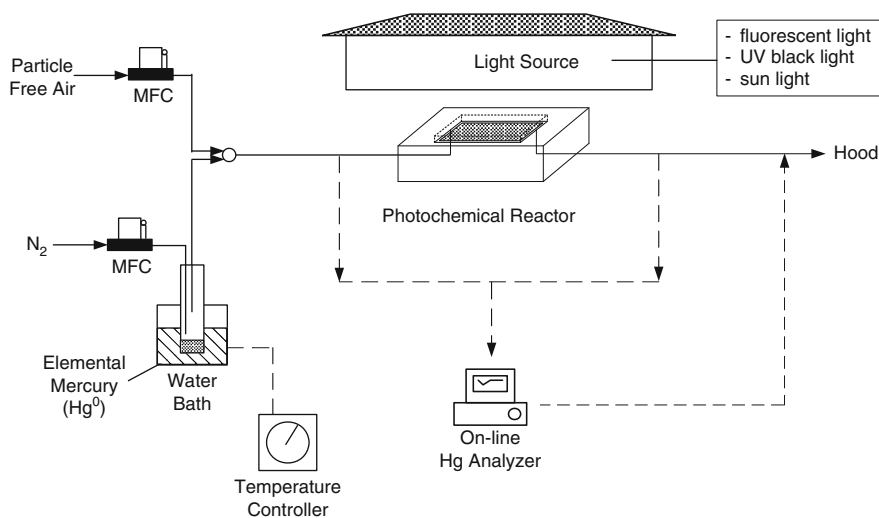


Fig. 6 A schematic diagram of the experimental setup (Jeon et al. 2008)

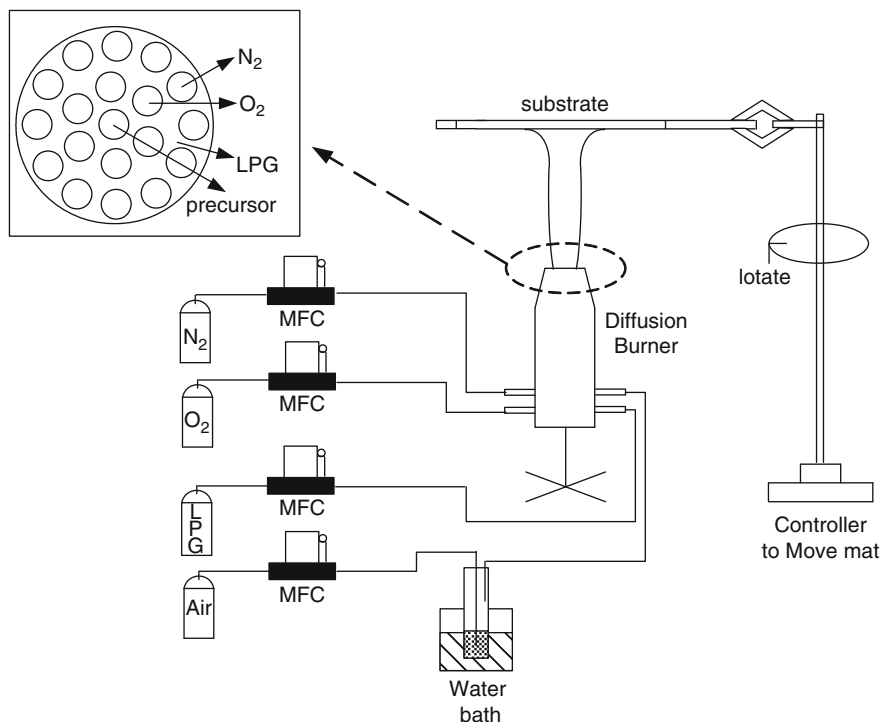


Fig. 7 A schematic diagram of the rotating flame burner (Jeon et al. 2008)

temperature for 20 min. The slide glass was continuously rotated horizontally passing through the middle of the flame (1,450–1,550°C) at 3 cm above the burner top.

The irradiation was provided only after the mercury concentration reading had been stabilized. Wavelength distributions of fluorescent light (2× FL40D, Osram Korea, Korea) and UV black light (2× TLD36w/08, Philips, Netherlands) were measured at 10 cm distance from the light source. As for sun light, measurement was carried out at the surface (Fig. 8).

Figure 9 shows the FE-SEM micrographs of the nanotitanosilicate samples prepared using three different carrier gases (air, N₂, and Ar). The diameter of the fiber was in the range of 50–100 nm, and the length was typically up to several tens of micrometers. A relatively rough and coarse surface was observed. The ratio of TTIP to TEOS was maintained at 12 to 1, and the amount of sample tested was 40 mg every time.

The photoreactivity for the three different carrier gases tested are shown in Table 3. First, under UV black light, the Hg⁰-removal efficiencies were relatively high for all three carrier gases. Unlike the case of air, the low Hg⁰-removal efficiencies of N₂- and Ar-derived nanotitanosilicate under the fluorescent and the

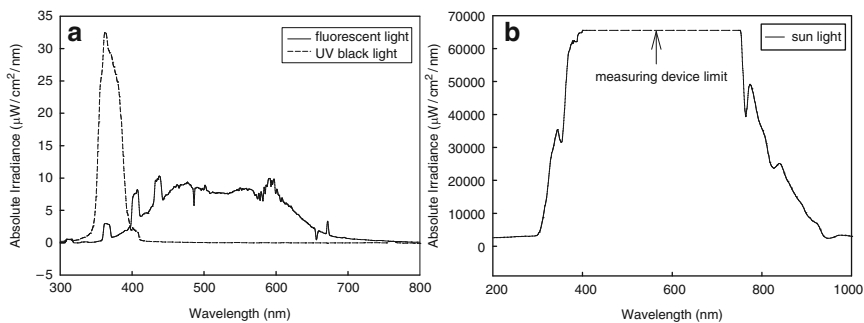


Fig. 8 Wavelength distributions of the light sources tested

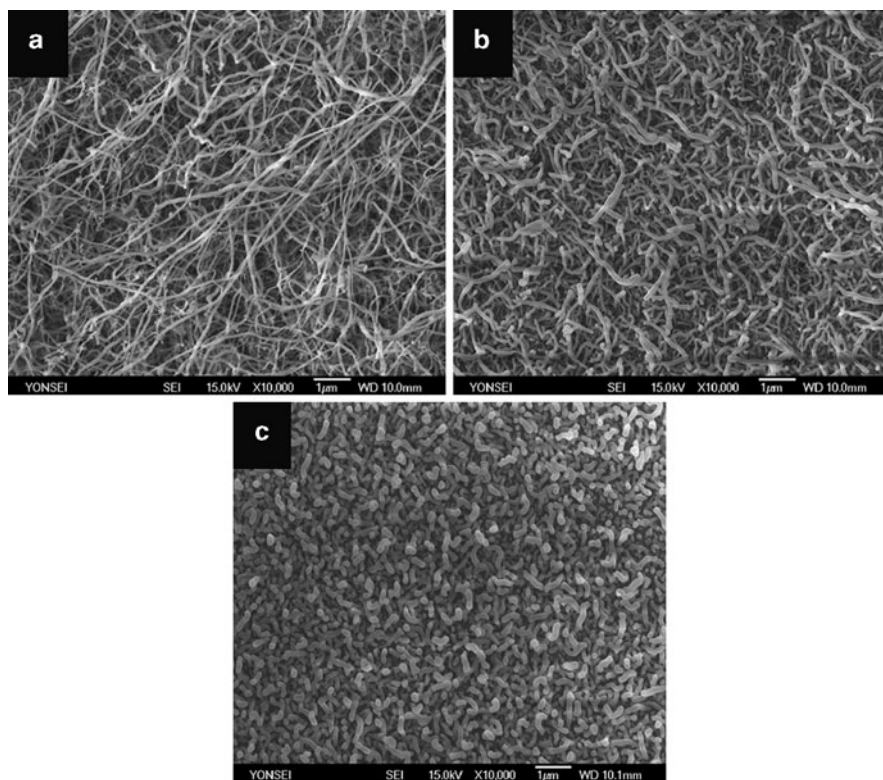


Fig. 9 SEM images of the fiber samples using (a) air, (b) N₂, and (c) Ar (Jeon et al. 2008)

sun light are due to the lack of rutile phase which corresponds better to the longer wavelengths which also explains the relatively high Hg⁰-removal efficiency of air-derived samples exhibiting both anatase and rutile phases under the fluorescent and

Table 3 Hg⁰ removal by the nanotitanosilicate (TTIP: TEOS = 12:1) (Jeon et al. 2008)

Carrier gas	Light sources	Hg ⁰ -removal efficiency (%)
Air	Fluorescent	88
	UV black	78
	Sun	51
N ₂	Fluorescent	9
	UV black	86
	Sun	17
Ar	Fluorescent	8
	UV black	85
	Sun	15

sun light. It should be noted that the efficiencies in Table 3 could be increased (as high as 100%) by increasing the amount of nanotitanosilicate. Experimental conditions were controlled to suppress the Hg⁰-removal effectiveness below 100% to compare between the tested samples.

4.2 Degussa P25

Degussa P25 was immobilized and tested for its ability to photo-oxidize gas-phase elemental mercury especially under the light with visible-range wavelength. A slide glass (5 × 5) was coated with 40 mg of TiO₂ (P25, Degussa, Germany) and then placed inside the photochemical reactor system previously described (Fig. 6).

The light sources with visible-range wavelengths were prepared by using a 125-cm long, 36-W fluorescent lamp (TLD 36w/08, Philips, Netherlands) with various cut-off filters (Filter Long 2'' SQ, Edmund Industrial Optics, U.S.) (Fig. 10). Figure 11 shows the wavelengths of the light sources tested.

A flow control system with installed Hg permeation tube (Mercury Calibrator, Tekran, U.S.) was used to provide an inlet gas with constant mercury concentration (400–430 µg/m³). Mercury concentration of the gas coming out of the photochemical reactor was continuously measured in real time before and after the photo-irradiation.

Table 4 shows the mercury-removal efficiency by the immobilized Degussa P25 under visible light generated using fluorescent light with cut-off filter. The efficiencies in Table 4 can be increased by simply increasing the amount of TiO₂ and the intensity of the visible light. This unusually high photoreactivity of undoped TiO₂ with Hg⁰ under the visible light still remains as a mystery and great interest to us, probably to many researchers in a field of photochemistry.

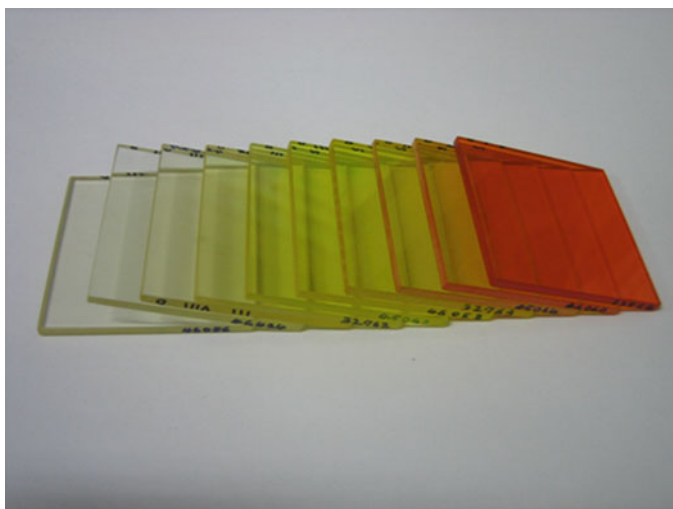


Fig. 10 A series of cut-off filters used to generate visible light from fluorescent light

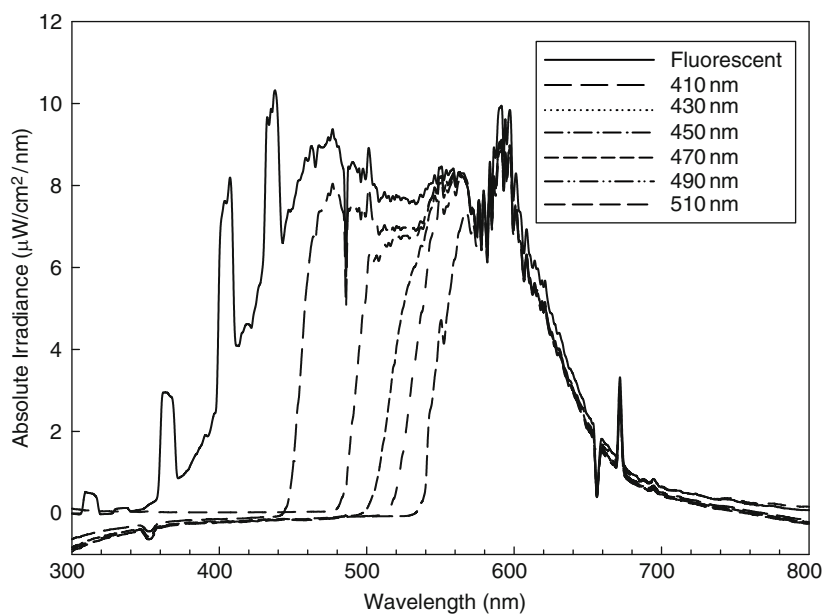


Fig. 11 Wavelengths of the light sources tested

Table 4 Hg⁰-removal efficiency of TiO₂ under visible light

Cut-off filter used (nm)	Hg ⁰ -removal efficiency (%)		
410	62	58	61
430	59	64	63
450	59	65	59
470	60	62	61
490	56	65	67
510	60	55	58

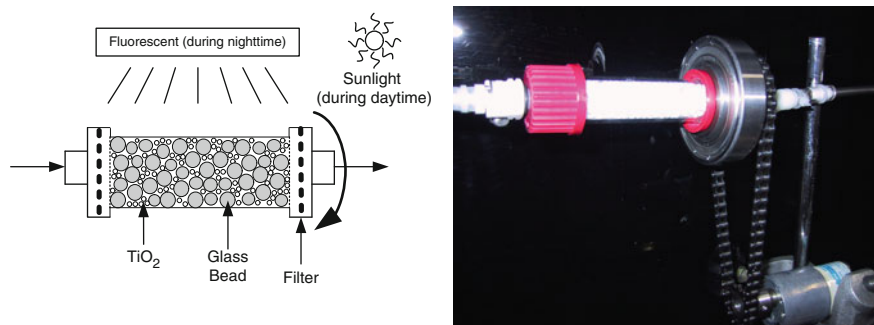


Fig. 12 The suggested rotating-type photochemical reactor system

5 Summary

A removal technology for the gas-phase elemental mercury using TiO₂ irradiated by various light sources was discussed. Unlike other air contaminants, photoreactivity of TiO₂ was high enough even under the visible light to oxidize the elemental mercury on the catalyst's surface. This is a very interesting result, suggesting the highly effective use of TiO₂ under visible light for the selective removal of gas-phase Hg⁰ among other air contaminants.

In terms of controlling the mercury emissions from stationary combustion sources, this technology can be a very attractive (efficient, economical, and selective under visible light) alternative to the conventional activated carbon systems. As for the practical use, we suggest the installation of the rotating glass-type photochemical reactor system (Fig. 12) charged with a mixture of TiO₂ powder and glass beads after the particle controlling devices (electrostatic precipitator and/or bag filter). During the daytime, free-of-charge sun light can be used as an irradiation source while a low-cost, easily maintainable fluorescent light may be enough at the nighttime or rainy days.

Acknowledgement The author would like to gratefully acknowledge Dr. Pratim Biswas who initiated the idea of using TiO₂ with UV in the gas-phase mercury removal for his inception, dedication, and guidance.

References

- Biswas P (1999) Mercury measurement and its control: what we know, have learned, and need to further investigate. *J Air Waste Manage Assoc* 49:1469–1473
- Chanon M, Schiavello M (1997) Introduction of photocatalysis. In: Chanon M (ed) *Homogeneous photocatalysis*. John Wiley, New York, p 5
- Jeon SH, Eom Y, Lee TG (2008) Photo-oxidation of the gas-phase elemental mercury by the nanotitanosilicate fibers. *Chemosphere* 71:969–974
- Lee TG, Hedrick E, Biswas P (2001) Comparison of mercury capture efficiencies of three different in situ generated sorbents. *AIChE J* 47:954–961
- Lee TG, Hedrick E, Biswas P (2002) Hg reactions in the presence of chlorine species: homogeneous gas phase and heterogeneous gas-solid phase. *J Air Waste Manage Assoc* 52:1316–1323
- Lee TG, Hyun JE (2006) Structural effect of the in situ generated titania on its ability to oxidize and capture the gas-phase elemental mercury. *Chemosphere* 62:26–33
- Lee YG, Park J-W, Kim J-H, Min BR, Jung J, Kim J, Lee TG (2004) Comparison of mercury removal efficiency from a simulated exhaust gas by several types of TiO₂ under various light sources. *Chem Lett* 33:36–37
- Linsebigler AL, Lu G, Yates JT (1995) Photocatalysis on TiO₂ surfaces: principles, mechanisms, and selected results. *Chem Rev* 95:735–758
- Kim SH (2006) Report on heavy metal concentration in human bloodstream. Korea Ministry of Environment, Republic of Korea
- Won JH, Park JY, Lee TG (2007) Mercury emissions from automobiles using gasoline, diesel, and LPG. *Atmos Environ* 41:7547–7552
- Wu CY, Lee TG, Tyree G, Arar E, Biswas P (1998) Capture of mercury in combustion systems by in situ generated titania particles with UV irradiation. *Environ Eng Sci* 15:137–148

Chapter 19

Photocatalytic Purification of Benzene in Air

Xinchen Wang and Xianzhi Fu

1 Introduction

Semiconductor photocatalysis for environmental purification has received a lot of attention in that (1) it involves the chemical destruction of pollutants rather than physical phase transfer, (2) clean and cheap oxygen from the air is used as an oxidizing agent, (3) the reaction can be conducted at low level of organic compounds under ambient condition, and (4) solar energy can be utilized to initiate photocatalytic reaction. Much of the photocatalysis research has been summarized in several reviews and books (Hoffmann et al. 1995; Kamat 1993; Fox and Dulay 1993; Hagfeldt and Grätzel 1995; Ollis and Al-Ekabi 1993; Blake 1994; Kaneko and Okura 2002), and a number of environmental products (e.g. air and water purification devices) based on the photocatalytic oxidation technique have been commercialized.

Principally, photochemical reactions occurring on the surface of semiconductor are initiated by electron and hole pairs generated by the illumination of semiconductor. The light-induced electron and hole are captured by trapping species absorbed on the semiconductor. Oxygen molecule is the trapping species of electrons when the process is employed for environmental remediation, whereas hydroxyl groups on the surface of semiconductor are commonly considered as the hole-trapping species. The capture of electron and hole pairs induces the formation of very reactive free radicals such as $O_2^{\cdot-}$, O_2^{\cdot} , HO_2^{\cdot} , OH^{\cdot} , and so on, initiating redox reactions that decompose organic compounds present on the surface of semiconductor (Hoffmann et al. 1995).

Many semiconductor materials, including metal oxides, sulfides, and nitrides (Kamat 1993; Hitoki et al. 2002; Sato et al. 2005), can act as photocatalysts.

X. Fu (✉)

Research Institute of Photocatalysis, State Key Laboratory Breeding Base of Photocatalysis, Fuzhou University, 350002 Fuzhou, China
e-mail: xzfu@fzu.edu.cn

Among these materials, titanium dioxide (TiO_2) is the most commonly used in photocatalytic environmental purification because of its high stability, non-toxicity, cheapness, as well as appropriate electronic band structure capable of oxidizing most organic compounds (Hoffmann et al. 1995; Kamat 1993; Fox and Dulay 1993). The application of TiO_2 photocatalysis for the remediation of contaminants in gas phase has been successful in treatment of a wide variety of volatile organic compounds (VOCs) such as alkenes and alkanes, aromatics, olefins, ketones, aldehydes, alcohols, aliphatic carboxylic acids, and so on (Fu et al. 1996). In many cases, complete oxidation of organic compounds has been reported.

Among the VOCs, benzene is an important pollutant emitted from various urban and industrial sources. It is known that benzene has severe health and environmental consequences due to its high toxicity and confirmed carcinogenicity (Alberic and Jardim 1997). Workers exposed to benzene fume, for example, run into an increased risk of leukemia and bone-marrow toxicity. A recent study has shown that even exposure to low levels (<1 ppm) of benzene can reduce blood cell counts in workers (Lan et al. 2004). The general public is also faced with the risks imposed by ubiquitous benzene as an air pollutant from cigarette smoke, gasoline vapors, and automobile emissions. It therefore comes as no surprise that benzene pollution of atmospheric environment has already become one of the main environmental problems facing humanity. In this respect, benzene together with its derivatives have been regarded as priority hazardous substances for which the development of efficient, cost-effective, and environmentally sustainable treatment methods is indispensable (1996).

This chapter examines the feature of photocatalytic reaction using TiO_2 for the degradation of benzene in dry air-stream and discusses the intrinsic limitation of TiO_2 for benzene removal. A highly efficient TiO_2 -based UV system for benzene photooxidation will then be developed. Finally, we will describe a visible light-driven system for the photooxidation of benzene and its derivatives in air under ambient condition.

2 Limitation of TiO_2 for Benzene Photooxidation

Photocatalytic treatment of volatile aromatic compounds over TiO_2 -based catalysts in gas phase has been investigated, and published research suggests that the catalysts are often deactivated, especially for the oxidation of benzene in dry air-stream. The deactivation is due to the deposition of less-reactive byproducts on the catalyst surface, making the photocatalytic purification of benzene very inefficient (Larson and Falconer 1997a; Einaga et al. 2002). We have also studied the feature of TiO_2 -based photocatalysts for benzene oxidation. The decomposition of benzene in gas-phase was studied with a single pass flow-type reactor operated at room temperature.

Figure 1 shows the time course of benzene photooxidation reaction over TiO_2 in dry air-stream at room temperature. Initially, the conversion of benzene is 13%, but

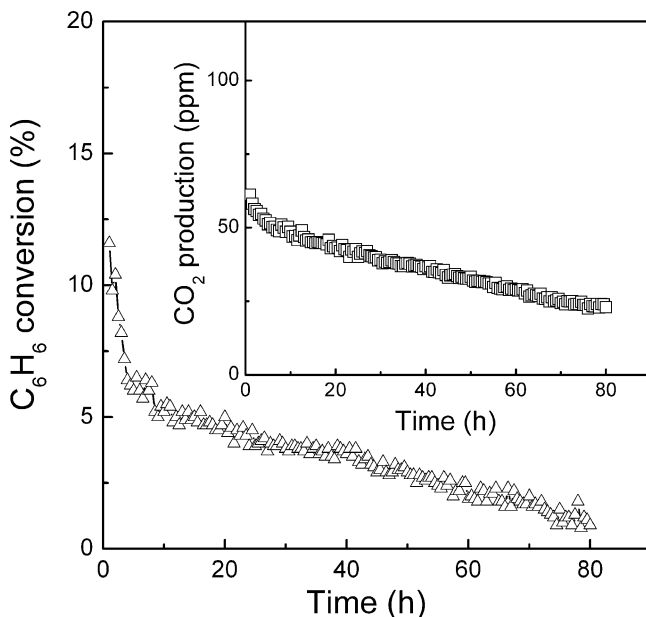


Fig. 1 Time course of photocatalytic oxidation of benzene over TiO_2 at room temperature. The reactor was a 11-cm long 2.4 mm diameter quartz tube surrounded by four 4-W UV lamps with a wavelength centered at 254 nm (Philips, TUV 4 W/G4 T5). Benzene (450 ppm) diluted in a zero air stream (21% O_2 , 79% N_2 , $\text{H}_2\text{O} < 5$ ppm, and total hydrocarbons < 1 ppm), flow rate (20 mL/min), and catalyst (0.3 g)

it gradually decreases to about zero with time on the stream. Only a small amount (20 ppm) of CO_2 is produced. The color of catalyst turns from white to black after the reaction (see Fig. 2). This is an indication that the deactivation is attributed to the blockage of photocatalytic active surface by stable reaction intermediates, probably polymeric products, on the TiO_2 . Indeed, IR analysis (Fig. 2) confirms such carbon deposits. A small band at $1,483\text{ cm}^{-1}$, assignable to aromatic ring stretching vibration (Bellamy 1975), reveals the formation of some aromatic species on the surface of the used TiO_2 (Wu et al. 2001). Two bands at $1,686$ and $1,711\text{ cm}^{-1}$ are assigned to $\text{C}=\text{O}$ stretchings (Einaga et al. 1999), suggesting that attack by the oxygen species upon the carbon deposits also occurred on the catalyst.

The carbon deposition on the surface of TiO_2 prevents the reactants in particular molecular oxygen from adsorbing onto the catalyst. The lack of O_2 is unfavorable for the oxidation of benzene because the complete oxidation of 1 M benzene stoichiometrically requires 7.5 M O_2 . Additionally, the absorbed O_2 can also serve as a trapping agent for electrons generated by UV illumination of TiO_2 (Fox and Dulay 1993). It is noted that the interfacial electron-transfer is a rate-determining step during the photocatalytic reaction (Hoffmann et al. 1995). Therefore, the lack of O_2 is detrimental to interfacial electron transfer and consequently accelerates the recombination of photogenerated electron-hole pairs, resulting in a low quantum yield.

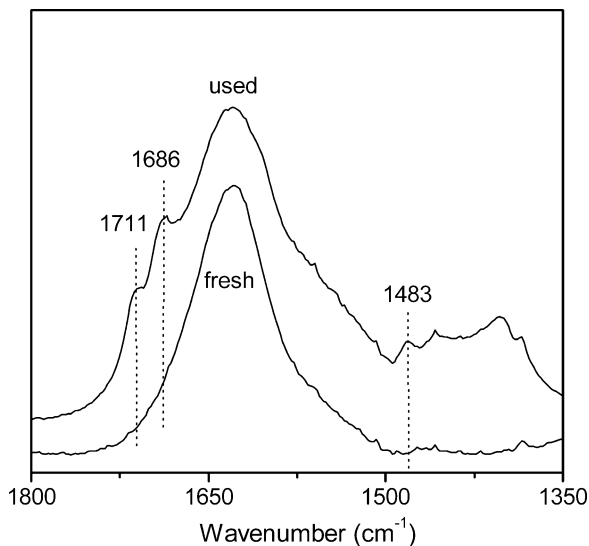


Fig. 2 IR spectra of the used TiO₂ sample after benzene photooxidation in dry air for 24 h, with fresh TiO₂ as a reference. The color of the fresh TiO₂ is white but it becomes black after the reaction (from Hou et al. 2006)

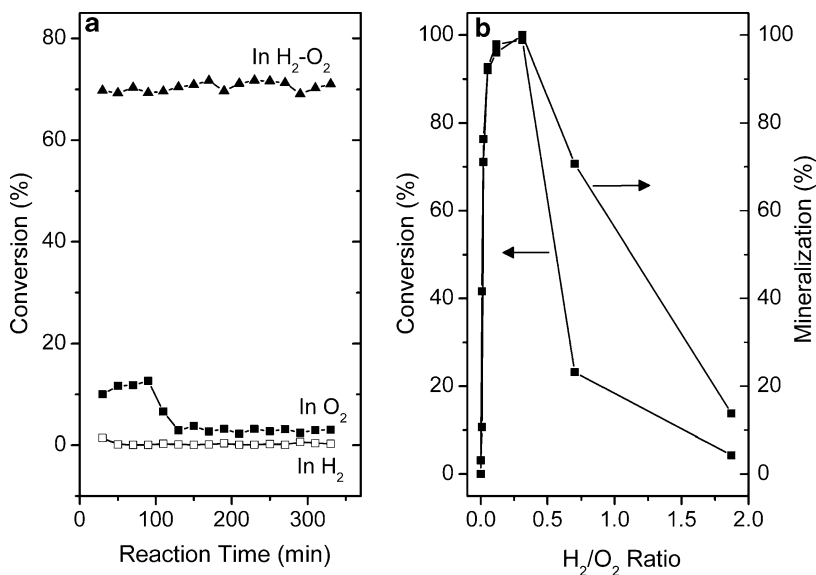


Fig. 3 (a) Effect of different reaction atmosphere on the conversion of benzene on 1 wt% Pt/TiO₂ photocatalyst at room temperature. (b) Effect of H₂/O₂ ratio on the photocatalytic performance of Pt/TiO₂ toward benzene photooxidation. Benzene (845 ppm) bubbled with oxygen and 7.8% hydrogen in nitrogen, total flow rate (50 mL/min), and catalyst (0.05 g) (from Fu XZ et al. *Chem. Commun.*, 2304 (2004))

The photocatalytic properties of Pt/TiO₂ for the oxidation of benzene in gas phase have also been examined. Although the Pt-loading improves the photocatalytic performance of TiO₂, the improvement is limited and the catalyst still suffers from deactivation as shown in Fig. 3.

In summary, TiO₂-based photocatalysts have limitations for purification of air polluted by benzene due to the low system efficiency caused by low quantum yield as well as deactivation of TiO₂. Our group has employed two approaches to overcome these limitations. One approach is to develop novel non-TiO₂-based materials as efficient photocatalysts, and it has been found recently that β-Ga₂O₃ and In(OH)₃ are photoactive for mineralizing benzene in air without the problem of catalyst deactivation (Hou et al. 2006). The other, which will be discussed here in detail, is the development of new TiO₂-based photocatalytic reaction system.

3 Development of Efficient UV System for Benzene Removal

3.1 Idea: Addition of H₂

In order for photocatalysis to be productive chemically, the recombination of electron-hole pair must be suppressed. This can be accomplished by effectively trapping the photogenerated electron, the photogenerated hole, or both (Fox and Dulay 1993). In this regard, a new strategy is developed herein to enhance greatly the performance of Pt/TiO₂ toward photocatalytic oxidation of benzene in dry air-stream under ambient condition. In this strategy, hydrogen gas is introduced into the O₂-rich photooxidation system to trigger a H₂-O₂ synergic effect in order to improve remarkably the system efficiency and overcome the deactivation of Pt/TiO₂. It is well known that both H₂ and O₂ can dissociatively adsorb on the surface of Pt particles to give O and H adatoms (Hayward and Trapnell 1964). These active surface O and H adatoms can serve as effective electron acceptors and electron donors, respectively, such that the recombination of photogenerated electron and hole can be significantly suppressed. Accordingly, a vast increase in the quantum efficiency of Pt/TiO₂ photocatalyst is achievable.

3.2 Enormous Increase in System Efficiency

The photocatalytic conversion of benzene over Pt/TiO₂ photocatalyst under different atmospheres was measured. In pure H₂ atmosphere (Fig. 3a), the conversion of benzene is about zero. Neither hydrogenation products (e.g. cyclohexane and cyclohexene) nor CO₂ is detected. This is expected because the photooxidation of benzene requires oxygen and the thermally catalytic hydrogenation of benzene typically occurs at higher temperature (Kazantsev et al. 1998). When the

experiment is conducted in pure O_2 atmosphere, the conversion is initially 16%, but it decreases drastically to 3% after reaction for 2 h. Meanwhile, no detectable CO_2 is observed. These indicate that only a small amount of benzene is partially oxidized. Surprisingly, when the feeding gas contains both H_2 and O_2 , the photocatalytic performance of Pt/TiO_2 enhances dramatically. The conversion of benzene increases up to 71%, accompanied by producing a large amount (2,853 ppm) of CO_2 corresponding to a benzene mineralization ratio of 78.3%. Both conversion and mineralization ratio can be maintained for more than 48 h. It should be noted that no enhancement in activity is observed when water vapor (~ 300 ppm) is added into the O_2 - Pt/TiO_2 system.

The dependence of conversion and mineralization on the H_2/O_2 ratio is shown in Fig. 3b. Result reveals that the photocatalytic activity of Pt/TiO_2 is dramatically improved even by adding trace H_2 , and the activity is sensitive to the H_2/O_2 ratio. When the ratio increases from 0 to 0.05, the conversion increases quickly from 3% to 93%. Increasing the ratio further from 0.05 to 0.31, the conversion increases slowly from 93% to 100%. It is noted that the complete mineralization of benzene to CO_2 and H_2O is achieved when the ratio is 0.31. However, if the H_2/O_2 ratio is further elevated to a value exceeding 0.31, a significant drop of both conversion and mineralization ratio occurs. These results reveal that an appropriate H_2/O_2 ratio is required for enhancing the efficiency of benzene photooxidation over Pt/TiO_2 . The optimum H_2/O_2 ratio is ca. 0.31, at which 100% benzene is decomposed completely and quickly to final products of CO_2 and H_2O . It is not surprising that too high H_2/O_2 ratio is disadvantageous to the complete degradation of benzene, because the oxidation of benzene stoichiometrically requires a large amount of O_2 . Moreover, the lack of O_2 is unfavorable for the separation of electron-hole pair.

Repetition tests of the Pt/TiO_2 for the photodegradation of benzene in dry air-stream were employed to examine the stability of the photocatalyst. The high photocatalytic activity of Pt/TiO_2 for the benzene oxidation is maintained well after testing for 22 h, by repeated use of the catalyst for four times (Fig. 4). In each run, the steady state of reaction is achieved after 200 min.

The new H_2 - O_2 - Pt/TiO_2 photoreaction system was extended to treat other toxic volatile organic compounds in air as shown in Fig. 5. The system is also efficient for the degradation of other VOCs under ambient conditions of room temperature and atmospheric pressure. The results show that when an alkyl (e.g. methyl or ethyl) is substituted onto the aromatic ring, the pollutants are easier to be decomposed as compared with benzene. The photocatalytic conversion of toluene and ethylbenzene on Pt/TiO_2 are 83% and 90% respectively, accompanied by a similar high mineralization of 86%. As the aromatic ring with alkyl (methyl or ethyl) has a higher electron cloud density on the conjugate ring, these reactant molecules are easily bound onto Pt particles and then attacked by active oxygen species. Contrarily, with a decrease in the electron cloud density of the cyclic six-ring-like cyclohexane, the conversion and mineralization are relatively lower (55% and 65%) than those of benzene. Photocatalytic oxidation of acetone was also conducted in this study because it has been detected as an intermediate of benzene photocatalytic degradation (Sitkiewitz and Heller 1996). Similar to the other VOCs

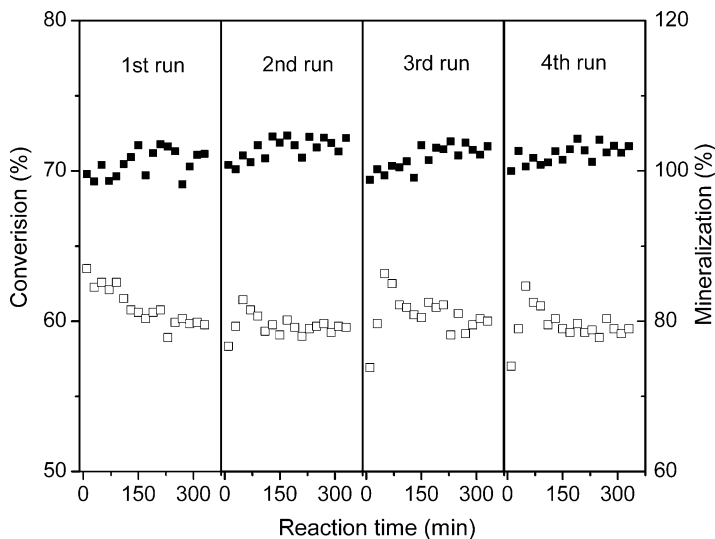


Fig. 4 Cycling runs for the photooxidation of benzene on Pt/TiO₂ in H₂-O₂ atmosphere (H₂/O₂ ratio: 0.02). Dark and white squares represent conversion and mineralization of benzene, respectively (from Fu XZ et al. *New J. Chem.*, 29, 1514 (2005))

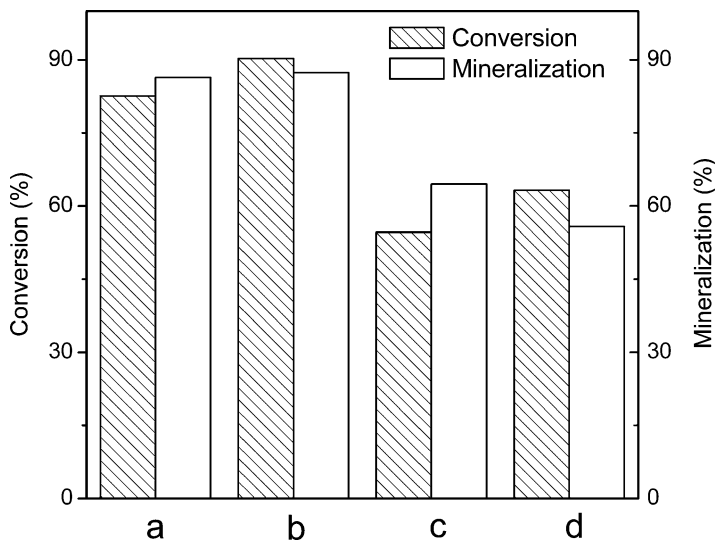


Fig. 5 Photooxidation of different pollutants on Pt/TiO₂ in H₂-O₂ atmosphere (H₂/O₂ ratio: 0.02) at room temperature: (a) toluene (852 ppm), (b) ethylbenzene (848 ppm), (c) cyclohexane (856 ppm), and (d) acetone (853 ppm). Total flow rate (50 mL/min) and catalyst (0.05 g) (from Fu XZ et al. *New J. Chem.*, 29, 1514 (2005))

considered, acetone could be photodegraded on Pt/TiO₂ in H₂-O₂ atmosphere. The conversion and mineralization are 63% and 56%, respectively. However, these values decrease correspondingly to 16% and 15% when the sample was tested in pure O₂ atmosphere. This indicates that acetone is easier to be photocatalytically decomposed on Pt/TiO₂ than other reactants in the absence of H₂.

3.3 Suppression of Carbon Deposition

As mentioned above, the poor performance of TiO₂-based photocatalysts for benzene oxidation is associated with the carbon deposition on the catalysts. Indeed, such an adverse carbon deposition can be suppressed significantly by the addition of hydrogen gas into the reaction system.

Figure 6 displays the IR spectra of Pt/TiO₂ before and after reaction in different atmosphere. In O₂, a small band at 1,487 cm⁻¹, assignable to aromatic ring stretching vibration (Bellamy 1975), suggests the deposition of certain aromatics on the catalyst. This band can be identified well by the corresponding difference IR spectra (Fig. 6, inset). No other characteristic bands of aromatic ring are observed in the range of 1,500–1,620 cm⁻¹ owing to the strong adsorption of H₂O and/or hydroxyl group in this region. The bands at ca. 1,206 cm⁻¹ and in the range of

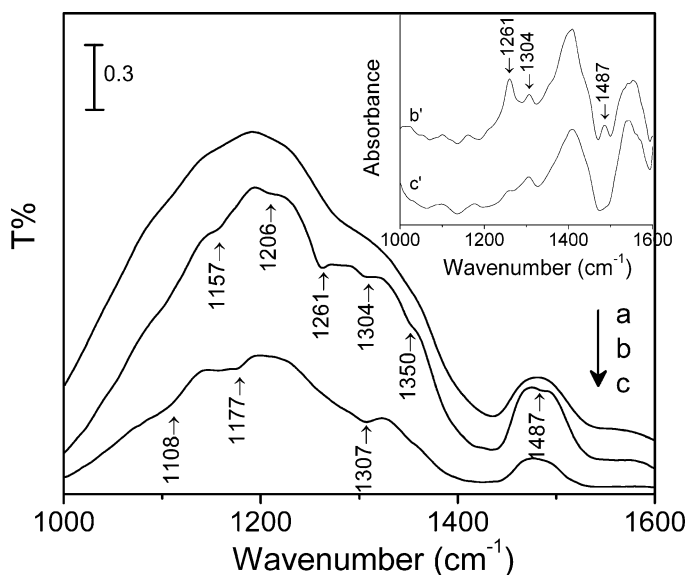
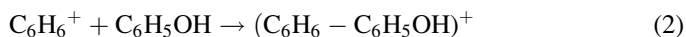
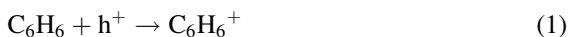


Fig. 6 IR spectra of Pt/TiO₂ in different atmosphere: (a) fresh Pt/TiO₂; (b) after benzene photooxidation in O₂ for 6 h; (c) after benzene photooxidation in H₂-O₂ (H₂/O₂ ratio: 0.02) for 6 h. The inset shows the difference IR spectra: b' = (b - a) and c' = (c - a) (from Fu XZ et al. *New J. Chem.*, 29, 1514 (2005))

1,260–1,410 cm^{-1} are assigned to the O–H deformation vibration of phenolic compounds (Bellamy 1975; Williams and Fleming 1987). Sasaki et al. have reported that the reaction of $\bullet\text{OH}$ radical with benzene in the presence of oxygen results in the production of phenol and benzoquinone (Kunai et al. 1986). Such a hydroxylation of benzene also occurs in our reaction system, and is caused by the $\bullet\text{OH}$ radicals generated from the oxidation of surface hydroxyl groups by a photogenerated hole (Anpo et al. 1985). Moreover, Barnes et al. have suggested that the appearance of characteristic band in the range of 1,170–1,140 cm^{-1} is related with the meta-substitution of aromatic ring (Bellamy 1975). In the O_2 atmosphere, since surface hydroxyl groups are consumed to produce phenol, the probability of benzene oxidation by the photogenerated hole increases (1) (Einaga et al. 1999). The resulting benzene cation radical, a strong electron acceptor (Komatsu and Lund 1972; Bedilo et al. 1998; Kurita et al. 1970), subsequently causes the meta-substitution of phenol (2). This additional reaction may thus lead to the formation of stable aromatic intermediates, deactivating the photocatalyst (Larson and Falconer 1997b).



Interestingly, in the H_2 – O_2 atmosphere, no aromatic products are detected after the reaction (Fig. 6c). The band at 1,307 cm^{-1} is due to in-plane O–H deformation vibration, whereas the band at 1,307 and 1,108 cm^{-1} is assigned to C–O stretch mode of alcohols or ethers (Williams and Fleming 1987). It appears that the cleavage of benzene rings takes place and some alcohols or ethers are produced as intermediates on the Pt/TiO₂. It deserves to be mentioned that strong anti-deactivation is obtained for the Pt/TiO₂ by adding trace H_2 into the O_2 -rich photooxidation system. This may be explained by the dissociative adsorption of H_2 on the surface of Pt particles to form H adatoms (Hayward and Trapnell 1964). Since the H adatom is a stronger hole acceptor compared with benzene, it can be easily oxidized by the photogenerated hole of TiO₂, thus inhibiting the formation of benzene cation radical and the subsequent aromatic intermediates. Moreover, owing to its small size and high mobility, the H adatoms may significantly perturb the metal surface structure inducing reconstruction/cleaning of the metal surface (Penner et al. 2003; Delmon 1933; Chen and White 1986), accounting for the long catalytic lifetime of Pt/TiO₂ in H_2 – O_2 atmosphere.

3.4 Acceleration of Electron–Hole Separation

The effect of adding of H_2 on the light-induced charge carriers was also investigated by surface photovoltage (SPV) spectroscopy. Figure 7 displays the SPV spectra of Pt/TiO₂ in both O_2 and H_2 – O_2 atmospheres. An increasing SPV response ranging

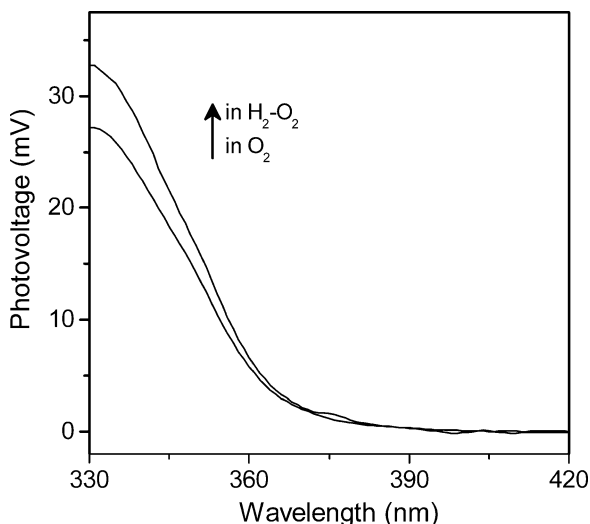


Fig. 7 Surface photovoltage (SPV) spectroscopy of Pt/TiO₂ in O₂ and H₂-O₂ atmosphere (H₂/O₂ ratio: 0.02) (from Fu XZ et al. *New J. Chem.*, 29, 1514 (2005))

from 370 nm to 330 nm is obtained by adding trace H₂ into the O₂-Pt/TiO₂ system. The result suggests that the separation efficiency of photogenerated electron-hole pair in the H₂-O₂-Pt/TiO₂ system is higher than that in the O₂-Pt/TiO₂ system. In principle, this can lead to the high quantum yield of Pt/TiO₂ photocatalyst for decomposing organic pollutants (Hoffmann et al. 1995).

3.5 Increase in the Formation of •OH Radicals

Hydroxyl radical plays an important role in heterogeneous photocatalysis. •OH radical is considered as principal reactive oxidant for the decomposition of organic compounds. Using DMPO (5,5-dimethyl-pyrroline-*n*-oxide) as a spin-trapping reagent, the formation of active radicals in H₂-O₂-Pt/TiO₂ photochemical system was tested by spin-trapping EPR technique (Fig. 8). Evidently, some active radicals are generated on the photoexcited Pt/TiO₂ in O₂ and H₂-O₂ atmosphere. When the system contains both H₂ and O₂, six strong peaks are clearly observed. The peaks are assignable to the DMPO-•CH₂OH adducts originated from the attack of •OH radicals on the methanol molecules [see (3)] (Zhao et al. 2002; Wu et al. 2000). The result demonstrates that a large amount of •OH radicals is produced, confirming the beneficial effect of H₂-O₂ in heterogeneous photocatalysis. However, for the system only containing pure oxygen, though some active radicals are also produced, they are too weak to be identified.

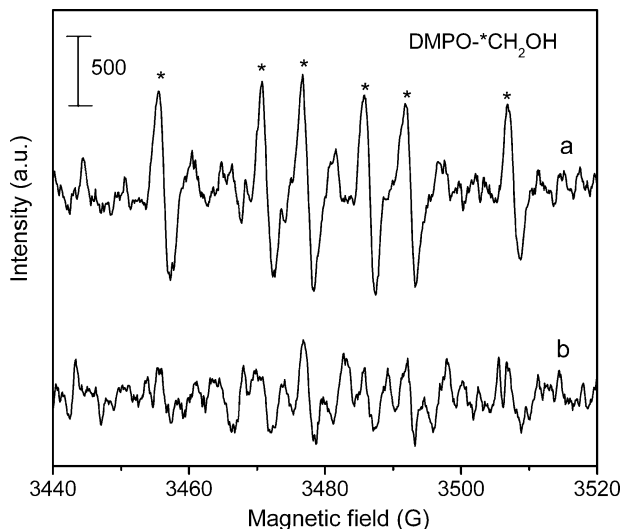
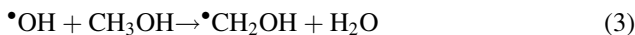


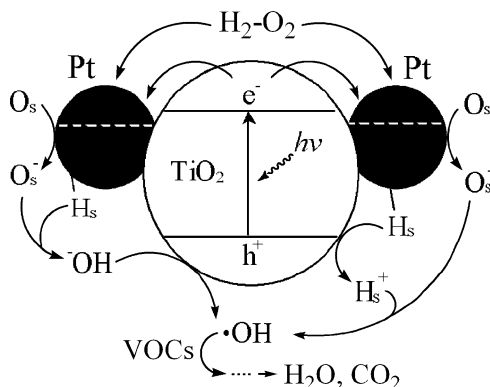
Fig. 8 Spin-trapping EPR spectra of methanolic dispersions containing Pt/TiO₂ and DMPO in the presence of (a) H₂-O₂ (H₂/O₂ ratio: ca. 1.0) and (b) O₂ (from Fu XZ et al. *New J. Chem.*, 29, 1514 (2005))



4 Photochemical Process in the System

Control experiments demonstrated that either pure TiO₂ or Pt (deposited on an insulator such as silica) alone was inert toward photodegradation of benzene. It is therefore believed that synergic combination of TiO₂, Pt, H₂, and O₂ accounts for the superior activity and durability of Pt/TiO₂. The photochemical process in the H₂-O₂-Pt/TiO₂ reaction system is proposed and elucidated in Fig. 9 and (4)–(9). The process may involve several steps: (a) O₂ and H₂ dissociatively adsorb on Pt particles to give surface O (O_s) and surface H (H_s) adatoms (Hayward and Trapnell 1964). (b) The resulting O_s adatom captures photogenerated electron from Pt particles, producing an O_s⁻ ion. (c) The H_s adatom migrates from Pt to the interface of Pt || TiO₂ (Benvenuti et al. 1999), and then serves as trapping agent for the hole, generating surface proton (H_s⁺) which further reacts with the O_s⁻ ion to give highly active •OH group. (d) The O_s⁻ ion could also react with the H_s adatom to produce OH⁻ that captures h⁺, leading to the formation of •OH radicals. These four processes are believed to generate a large amount of •OH groups, as proved by the spin-trapping EPR spectra. Since the oxidative degradation of organic compounds such as benzene is initiated by •OH (Ghigo and Tonachini 1999), a large

Fig. 9 Schematic illustration for the generation of $\bullet\text{OH}$ radical on Pt/TiO₂ photocatalyst at the presence of H₂ and O₂ (from Fu XZ et al. *Chem. Commun.*, 2304 (2004))



increase in the photocatalytic activity is possible. However, the excess H₂ would consume the produced hydroxyl radicals as shown in (10), resulting in the consequent decrease in the conversion (see Fig. 3b). Although (11) may also produce $\bullet\text{OH}$ radicals (Hayashi et al. 1998; Williams et al. 1992), we found that this non-photogenerated $\bullet\text{OH}$ has only slight effect on the overall catalytic performance, as revealed by the oxidation of benzene on Pt/TiO₂ in dark.



It is noted that the interfacial electron-transfer on the surface of semiconductor is a rate-determining step during the photocatalytic reactions (Hoffmann et al. 1995). Normally, the interfacial electron-transfer is accomplished by capturing the electron at surface-adsorbed O₂ on TiO₂ photocatalyst (Hoffmann et al. 1995). As the electron-affinity of O adatom (O/O⁻, 1.478 eV) is much higher than that of O₂ (O₂/O₂⁻, 0.43 eV) (Berry et al. 1965; Pack and Phelps 1966), the O adatom is a very stronger trapping agent for the electron (5) compared with O₂. Subsequent

capturing of the resulting O_s^- ion by H_s^+/H_s (7–8) could further favor the interfacial electron transfer on the surface of catalyst. An increase in the interfacial electron-transfer rate on the surface of photocatalyst is expected to result in higher quantum efficiencies for the photocatalytic reactions.

In the H_2-O_2-Pt/TiO_2 system, the mechanism for the photodegradation of benzene differs significantly from that in the O_2-Pt/TiO_2 system. In the latter, the surface hydroxyl groups are consumed to react with benzene to form some phenolic compounds without any regeneration. This may cause the deactivation of the Pt/ TiO_2 , as proved by the IR spectra. However, in the H_2-O_2-Pt/TiO_2 system, the H adatom on Pt/ TiO_2 is active for the photogeneration of $\bullet OH$ radical. The continuous formation of $\bullet OH$ radicals may thus contribute to the high photocatalytic activity and durability of Pt/ TiO_2 .

In summary, this study develops a very efficient photocatalytic system for decomposing benzene over Pt/ TiO_2 by adding trace H_2 into the O_2 -rich reaction system. The promotional effects of H_2 can be interpreted as (1) suppressing the deposition of persistent aromatic intermediates on the catalyst; (2) improving the separation efficiency of photogenerated electron-hole pair; and (3) promoting the formation of surface hydroxyl radicals.

5 Development of Sunlight System for Benzene Removal

The H_2-O_2-Pt/TiO_2 photoreaction system is highly efficient for the degradation of benzene under ambient conditions of room temperature and atmospheric pressure. Nevertheless, the system only works under UV irradiation because of the large band-gap energy of 3.2 eV for anatase TiO_2 . The UV region only accounts for ~4% of the total solar energy. Thus, the abundant visible light in the solar spectrum or artificial light sources cannot be utilized for photocatalytic air purification. The development of solar-driven photocatalytic reaction system for treating benzene is therefore desirable.

5.1 Idea: Sensitization of TiO_2 by $InVO_4$

Sensitization is a common approach to develop TiO_2 -based photocatalysts with response to visible light region. Excited by visible light, sensitizer adsorbed on TiO_2 injects charge carriers into the conduction band (CB) of TiO_2 , inducing a series of photochemical reactions on TiO_2 . Traditional photosensitizers are narrow band-gap semiconductors and organic dyes. Some of the photosensitization systems have achieved high quantum efficiency (Bach et al. 1998; Yu et al. 2003; Zou et al. 2001; Tang et al. 2004; Oshikiri et al. 2002; Oshikiri et al. 2003; Ye et al. 2002; Fu et al. 1997; Gregg and Sing 1997; Luo et al. 2003; Xiao et al. 2008; Kozlowski et al. 1983; Briggs and Seah 1990; Asahi et al. 2001; Liu et al. 2002; Chun et al.

2003; Tsuji et al. 2004; Hirakawa and Nosaka 2002; Wu et al. 1999; Wamer et al. 1997). However, the photosensitization system inevitably loses their light-responsive functions due to the poor stability of sensitizers, making the overall process impractical. The key challenge in sensitization-type photocatalysis is therefore finding sufficiently stable photosensitizer with appropriate electronic state.

Multimetallic oxides (e.g. InMO_4 [$M = \text{V}, \text{Nb}, \text{or Ta}$]) are stable inorganic solid state materials and have recently attracted a lot of attention as new photofunctional materials for hydrogen generation by splitting water under visible light irradiation (Zou et al. 2001; Tang et al. 2004; Oshikiri et al. 2002; Oshikiri et al. 2003). The electronic structure calculated from density functional theory (DFT) shows that the d-orbital of the transition metals in InMO_4 forms the bottom of the conduction band, whereas the top of the valence band consists of O2p and In5s orbitals (Ye et al. 2002). Generally, in a single-component metal oxide, the energy level of O2p orbital is located at about +3 eV vs. SHE. Thus, the band gap between the metal-d-level and O2p-level is too wide to absorb the visible light. In the case of InMO_4 , two kinds of polyhedrons (InO_6 and NbO_6 , TaO_6 or VO_4) coexist, and the valence band of InMO_4 is composed of both O2p and In5s orbits. As a result, the valence band energy of O2p-level in InMO_4 is about 1.0 eV more negative than the +3 eV (vs. SHE) of the O2p-level in a simple metal oxide like TiO_2 due to the hybridization of O2p and In5s orbits (Ye et al. 2002). This causes the narrowing of band gap energy in the InMO_4 , enabling them to respond to the visible light region.

This study explores the potential of multimetallic oxides like InVO_4 as a stable inorganic sensitizer to activate titania for the decomposition of benzene in air under visible light illumination. Since the electronic structure of InVO_4 matches with that of TiO_2 (see Fig. 10), an efficient surface charge separation between them is attainable (Ye et al. 2002).

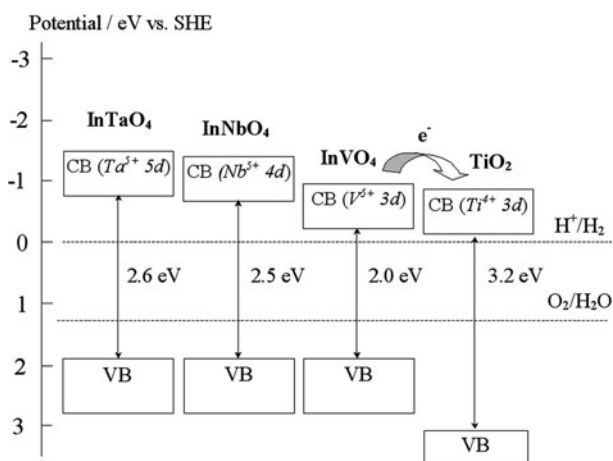


Fig. 10 Schematic illustration of band structure of InMO_4 and TiO_2 (modified from Ye et al. 2002)

5.2 Fabrication of $\text{InVO}_4/\text{TiO}_2$

The InVO_4 -modified TiO_2 was prepared by a sol–gel method. A solution containing InCl_3 and NaVO_3 with a molar ratio of 1:2 was adjusted to pH 8.0 by NaOH . The solution was placed in a Teflon-lined stainless steel autoclave and then hydrothermally treated at 150°C for 16 h. The resultant precipitate was washed with distilled water and then dispersed in a butyl ethanol solution. The mixture was distilled for 6 h to form a homogeneous InVO_4 sol solution. Titanium tetraisopropoxide was hydrolyzed under acidic conditions, and the resulting suspension was dialyzed to pH of ca. 4 and then forms a homogeneous sol (Fu et al. 1997). The InVO_4 and TiO_2 sols were mixed with 0.5 wt% InVO_4 in TiO_2 , stirred for 48 h, and then heated to remove solvents. The resultant xerogels were calcined at 450°C for 3 h, and then ground and sieved to obtain particulates with size of 0.21–0.25 mm.

5.3 Characterization of $\text{InVO}_4/\text{TiO}_2$

N_2 adsorption–desorption of the $\text{InVO}_4/\text{TiO}_2$ sample is found to be of type IV isotherms, typical of mesoporous solid (Gregg and Sing 1997). The pore size distribution plot shows a narrow pore size distribution with an average pore diameter of 10 nm (Fig. 11). The BET specific surface area and pore volume ($90 \text{ m}^2 \text{ g}^{-1}$, $0.28 \text{ cm}^3 \text{ g}^{-1}$) for the $\text{InVO}_4/\text{TiO}_2$ are larger than those of the pure TiO_2 ($62 \text{ m}^2 \text{ g}^{-1}$, $0.21 \text{ cm}^3 \text{ g}^{-1}$), which suggests that the addition of InVO_4 inhibits the sintering of sample during thermal treatment. The porous nature of $\text{InVO}_4/\text{TiO}_2$ was also

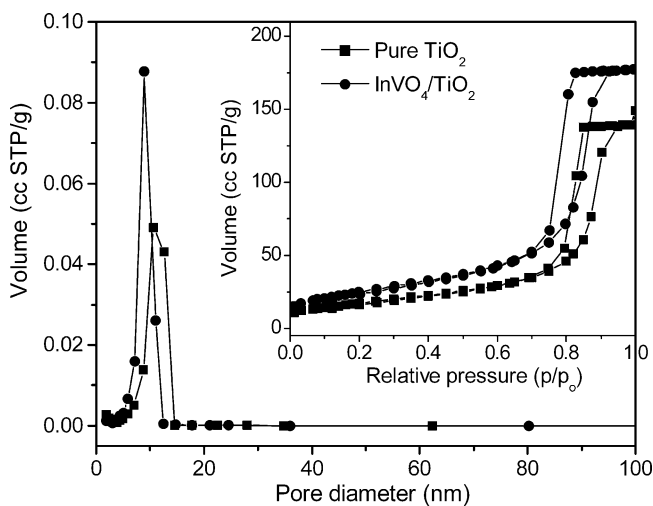


Fig. 11 Nitrogen-sorption isotherms and the pore size distribution plot for TiO_2 and $\text{InVO}_4/\text{TiO}_2$ (Xiao et al. 2008)

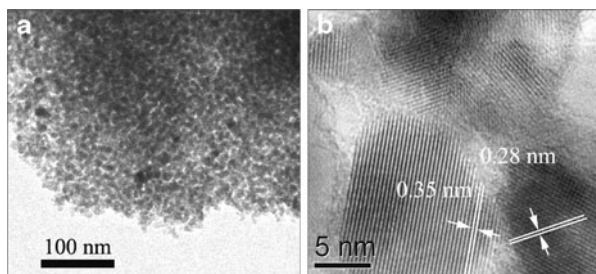


Fig. 12 (a) TEM image of $\text{InVO}_4/\text{TiO}_2$ catalyst and (b) HRTEM image of the sample (Xiao et al. 2008)

characterized by transmission electron microscopy (TEM) as shown in Fig. 12a, where a honey-comb structure with interconnected fine particulate morphology is clearly observed, indicating the inter-particle porosity (Luo et al. 2003).

The nanocrystalline nature of $\text{InVO}_4/\text{TiO}_2$ was examined by high-resolution TEM shown in Fig. 12b. The fringes appearing in the micrographs allow for the identification of the crystallographic spacing of TiO_2 and InVO_4 . The fringes of $d = 0.35$ nm and $d = 0.28$ nm observed in Fig. 12b match that of the (101) and (200) crystallographic planes of anatase TiO_2 and InVO_4 orthorhombic phase, respectively, indicating the existence of $\text{InVO}_4/\text{TiO}_2$ heterogeneous junctions. Interestingly, this kind of heterogeneous junction has hardly been observed for the $\text{InVO}_4/\text{TiO}_2$ sample without heat treatment and the $\text{InVO}_4\text{-TiO}_2$ sample by mechanically mixing. It seems that the strong interaction between the two materials is formed in the heating process, and this may account for the discrepant photocatalytic activity of the samples described below. In addition, the crystal size of the anatase TiO_2 estimated from the TEM image is ca. 11 nm, in agreement with the following XRD analysis.

The crystal phase of $\text{InVO}_4/\text{TiO}_2$ composite was examined by XRD, with pure InVO_4 and TiO_2 as comparisons. The InVO_4 is orthorhombic InVO_4 (ICSD010431) and the TiO_2 is bicrystalline structure mainly containing anatase (A) and rutile (R) (Fig. 13). For the $\text{InVO}_4/\text{TiO}_2$ with 0.5 wt% InVO_4 , no distinct peak corresponding to InVO_4 is observed. This is because the amount of InVO_4 is so small that it is beyond the detection of XRD, or InVO_4 exists in a highly dispersed form. When the amount of InVO_4 in TiO_2 exceeds 5 wt%, the peaks corresponding to orthorhombic InVO_4 appear, confirming the existence of InVO_4 in TiO_2 . The calculated results of the weight percentage of crystal phase (W) for the samples are shown in Table 1. A decrease in W_R value and an increase in W_A are detected for 0.5 wt% $\text{InVO}_4/\text{TiO}_2$ compared with TiO_2 , showing that adding small amount of InVO_4 intensively suppresses the phase transformation from anatase to rutile. Kozłowski et al. reported the opposite results relating to phase transformation of TiO_2 doped by V (Kozłowski et al. 1983). It might be concluded that the phase transformation of $\text{InVO}_4/\text{TiO}_2$ is not due to the V doping. Namely, the doping of V into TiO_2 lattice is unlikely in $\text{InVO}_4/\text{TiO}_2$ sample. Based on the XRD results, the crystal size (D) and the “ d ” space values between the crystal planes of the $\text{InVO}_4/\text{TiO}_2$ sample are also presented. No distinct changes in the crystal size and the “ d ” space values are

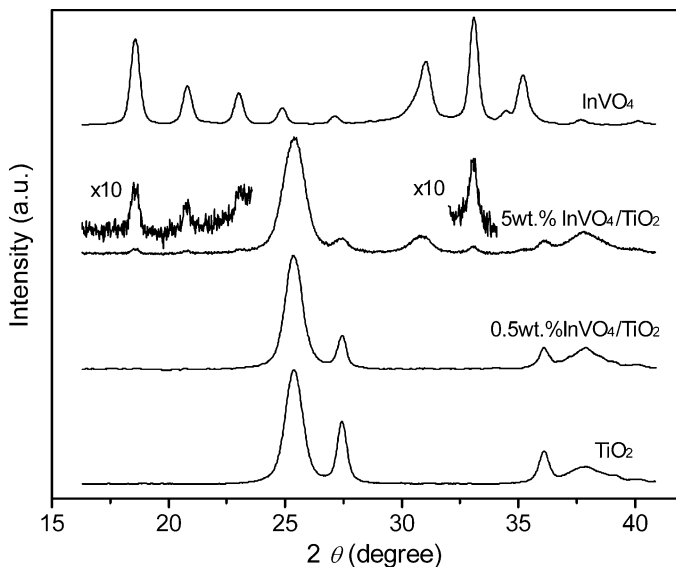


Fig. 13 XRD patterns of InVO_4 , TiO_2 , and $\text{InVO}_4/\text{TiO}_2$ (Xiao et al. 2008)

Table 1 The crystal size (D), the weight percentage of the crystal phase (W), and the distance between the crystal planes of TiO_2 modified by 0.5 wt% InVO_4 (Xiao et al. 2008)

Sample	D_{101} (nm)	W_A (%)	d_{101} (nm)	D_{110} (nm)	W_R (%)	d_{110} (nm)
TiO_2	10.8	62.8	0.3516	21.5	37.2	0.3248
$\text{InVO}_4/\text{TiO}_2$	10.7	74.5	0.3516	21.1	25.5	0.3248

Note: Anatase (101) peak at $2\theta = 25.4^\circ$ and rutile (110) peak at $2\theta = 27.4^\circ$ is used for the calculation of D , W , and d

observed for the anatase or rutile phase. This confirms that In or V does not incorporate into the lattice of TiO_2 .

The surface chemical composition and electronic states of the catalysts were determined by XPS analysis. The results also confirm the incorporation of InVO_4 with TiO_2 as shown in Fig. 14. Both In3d and V2p show their characteristic peaks of In^{3+} and V^{5+} (445.0 eV and 452.6 eV for In3d, 516.7 eV and 524.4 eV for V2p) (Briggs and Seah 1990). This suggests that no changes of the oxidation state of In and V occur at the surface during the thermal treatment of $\text{InVO}_4/\text{TiO}_2$ sample. Moreover, the value of Ti2p is fixed at 458.9 and 465.0 eV for TiO_2 and $\text{InVO}_4/\text{TiO}_2$. It means that the surface state of Ti on $\text{InVO}_4/\text{TiO}_2$ sample is not affected by the modification of In or V, implying that neither In nor V are doped into the lattice of TiO_2 .

Optical properties of the InVO_4 , TiO_2 , and $\text{InVO}_4/\text{TiO}_2$ samples were studied by UV/visible spectrum (Fig. 15). Compared to that (~ 400 nm) of pure TiO_2 , the absorption onset of $\text{InVO}_4/\text{TiO}_2$ is estimated at 540 nm. Apparently, the absorption of $\text{InVO}_4/\text{TiO}_2$ in the visible is due to the contribution of InVO_4 . The absorption

Fig. 14 X-ray photoelectron spectra (XPS) of $\text{InVO}_4/\text{TiO}_2$ (Xiao et al. 2008)

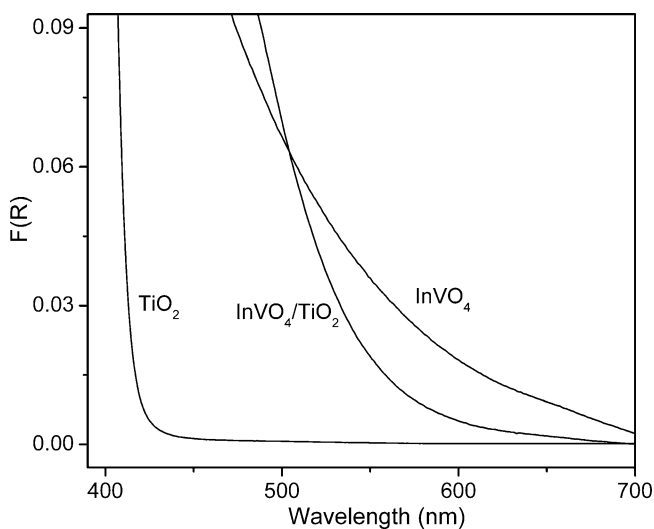
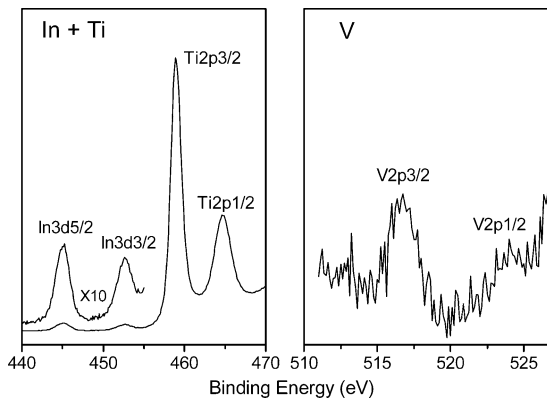


Fig. 15 Visible light absorption spectra of InVO_4 , TiO_2 , and $\text{InVO}_4/\text{TiO}_2$ (Xiao et al. 2008)

onset of InVO_4 is estimated at 590 nm corresponding to the band gap of 2.1 eV, in agreement with the literature (Ye et al. 2002). As a result of the modification of InVO_4 to TiO_2 , it seems that InVO_4 may photosensitize TiO_2 in visible light, permitting the photocatalyst to respond to a wide range of solar spectrum. This light-responsive range is much wider than that of $\text{TiO}_{2-x}\text{N}_x$ photocatalyst (<500 nm) reported by Asahi and coworkers (Asahi et al. 2001). However, it is known that the property of visible light absorption is not the exclusive factor responsible for the photocatalytic performance in visible light. The proper electronic band positions between InVO_4 and TiO_2 are also indispensable.

UPS together with UV/vis is a useful technique to determine band positions of semiconductors (Liu et al. 2002; Chun et al. 2003). UPS spectra of InVO_4 , TiO_2 and $\text{InVO}_4/\text{TiO}_2$ measured at sample biases of -5 V are shown in Fig. 16. According to

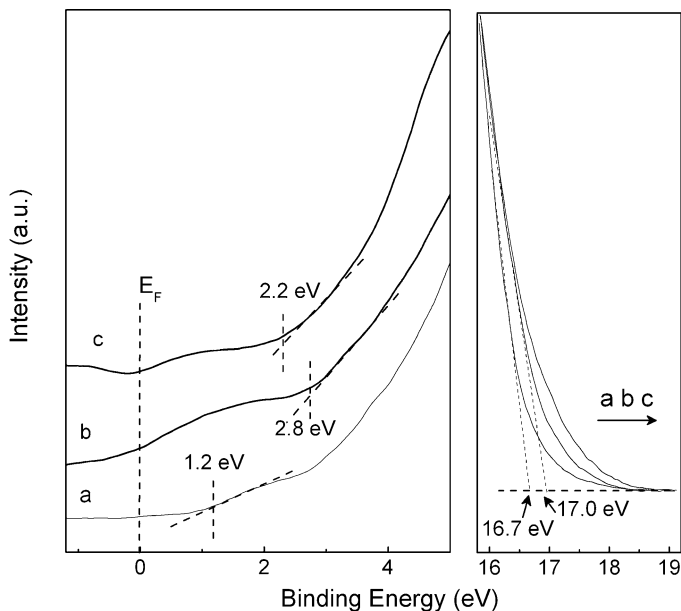


Fig. 16 Ultraviolet photoelectron spectra of InVO_4 (a), TiO_2 (b) and $\text{InVO}_4/\text{TiO}_2$ (c) (Xiao et al. 2008)

Table 2 Band energies of InVO_4 , TiO_2 , and $\text{InVO}_4/\text{TiO}_2$ by UV/vis and UPS (Xiao et al. 2008)

Sample	E_{BG} (eV)	E_{F} (eV)	E_{VB} (eV)	E_{CB} (eV)
InVO_4	2.1	-4.5	-5.7	-3.6
TiO_2	3.0	-4.2	-7.0	-4.0

the spectrum, the valence band maximum (E_{VB}) of InVO_4 is located at ca. -5.7 eV (vs. vacuum) determined by fitting a straight line into the leading edge. The secondary electron onset (SO) on the right side of the spectrum is 16.7 eV. The work function of InVO_4 is calculated to be 4.5 eV by subtracting the SO position of the He I UPS spectrum from the excitation energy (21.2 eV). The corresponding Fermi level (E_{F}) is located at -4.5 eV (vs. vacuum). Determined by the UV/vis, the value of band gap (E_{BG}) is 2.1 eV for InVO_4 . Therefore, the conduction band minimum (E_{CB}) of InVO_4 is located at ca. -3.6 eV (vs. vacuum). Similarly, the value of E_{BG} , E_{VB} , E_{F} , and E_{CB} determined by UV/vis and UPS are summarized in Table 2. The results reveal that the E_{CB} of TiO_2 is located at -4.0 eV (vs. vacuum), which is negative than that of InVO_4 as shown in Fig. 17. The difference of E_{CB} between InVO_4 and TiO_2 allows the transfer of electron from the CB of InVO_4 to that of TiO_2 , making the InVO_4 an efficient “electron pump” for the intrinsic visible light sensitization of TiO_2 . The injected electron in the TiO_2 can be captured by the surface adsorbed oxygen molecules presented on the catalysts, resulting in the formation of active oxygen species ($\text{O}_2^{\bullet-}$) that decompose VOCs.

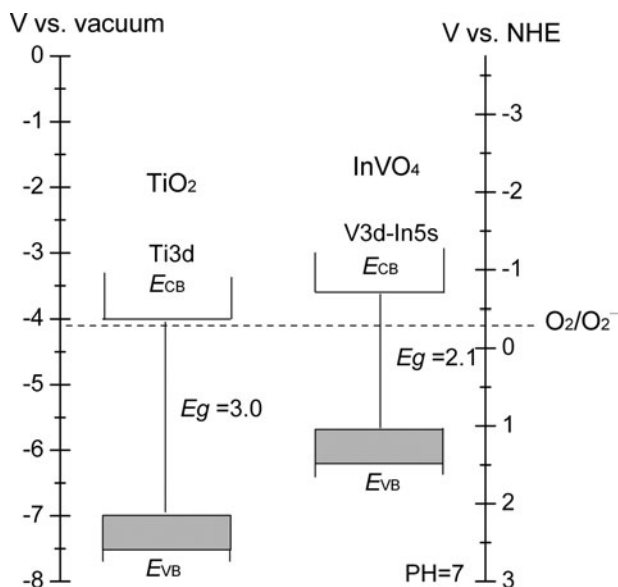


Fig. 17 Position of the E_{CB} and E_{VB} for TiO_2 and InVO_4 on the absolute vacuum energy scale and with respect to the normal hydrogen electrode (NHE). The relationship between the absolute vacuum energy (E_{abs}) and the normal electrode potential (E°) is expressed as follows: $E_{\text{abs}} = -E^\circ - 4.44$ (at 298 K). $E^\circ(\text{O}_2/\text{O}_2^{\bullet-})$ of -0.33 V is taken as a reference

5.4 Photocatalytic Performance of $\text{InVO}_4/\text{TiO}_2$

Activity test was carried out in a fixed-bed quartz reactor operated at a single-pass mode under ambient conditions. A 500 W Xe-arc lamp was equipped with IR- and UV-cutoff filter to give a visible light irradiation ($450 \text{ nm} \leq \lambda \leq 900 \text{ nm}$) with intensity of ca. 50 mW cm^{-2} on the reactor. Organic pollutants bubbled with oxygen in nitrogen were fed to 1.2 g of catalysts. The flow-rate of the stream was 50 mL/min.

Figure 18 displays the activity of $\text{InVO}_4/\text{TiO}_2$ for decomposing benzene in air under visible light irradiation. The conversion of benzene and the production of CO_2 are observed at steady state after 6 h of illumination, during which no byproducts are observed (Fig. 18a). The experiment is also carried out for 5 runs (with the time of every run 12 h) to examine the stability of the catalyst (Fig. 18b). In the first run, the photocatalytic conversion of benzene is 48.7%, and the amount of CO_2 produced from the reactions increases gradually up to 188 ppm. When the steady state is reached, the conversion is maintained at ca. 46.5% for the following four runs, and the production of CO_2 was ca. 180 ppm. Additionally, no benzene degradation and no CO_2 evolution in the control test (no photocatalyst) under visible light irradiation, confirmed that the decomposition of benzene occurred through photocatalysis and that the self-photolysis could be neglected.

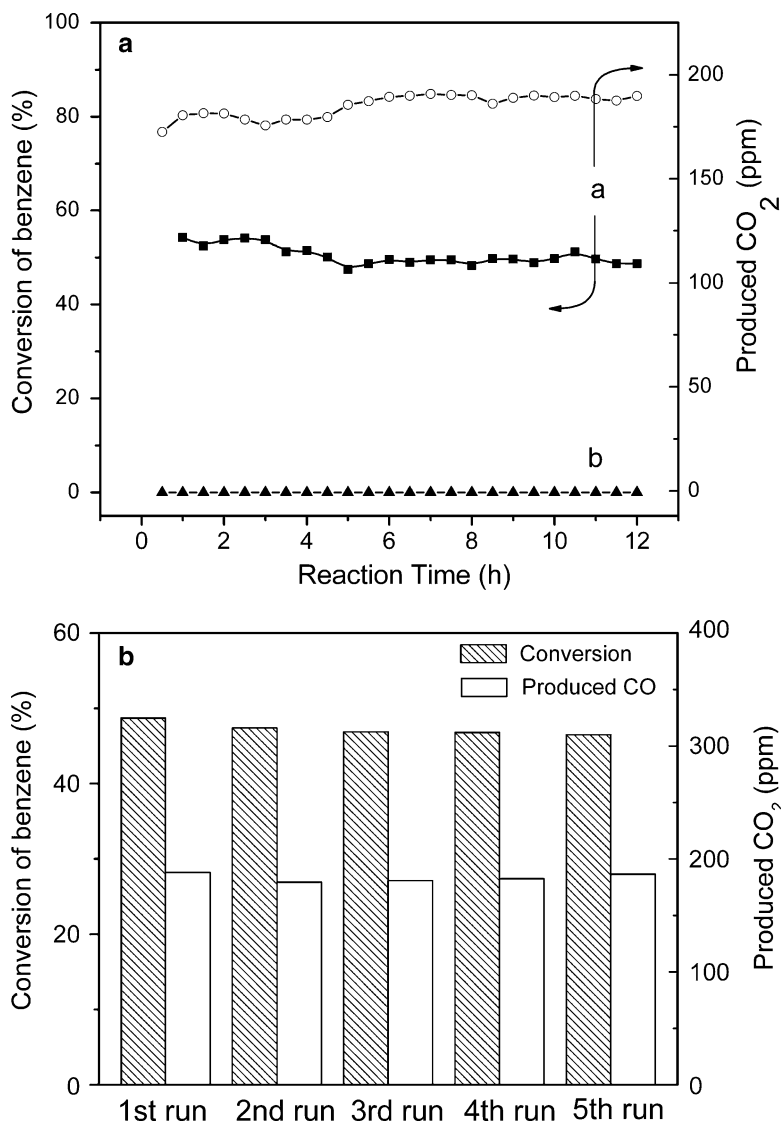


Fig. 18 (a) Photodegradation of benzene on InVO₄/TiO₂ (b) under visible light irradiation at room temperature. TiO_{2-x}N_x, InVO₄, TiO₂, and InVO₄/SiO₂ samples (b) are also taken for comparison. (b) Repetition tests of InVO₄/TiO₂ for the benzene photooxidation. Benzene (215 ppm), visible light (450 nm ≤ λ ≤ 900 nm), flow rate (50 mL/min), and catalyst (1.2 g) (Xiao et al. 2008)

To further understand the high photocatalytic performance of the InVO₄/TiO₂ catalyst, the nitrogen-doped TiO₂ visible light photocatalyst is chosen as a comparison. Noticeably, although a small amount of ethylene (17% of 620 ppm) can be photodegraded on TiO_{2-x}N_x irradiated by visible light, complete deactivation is

rapidly observed in the case of stubborn benzene degradation (Fig. 18a), resulting in the sample discoloration from yellowish to chocolate brown. It shows that some reaction intermediates are strongly adsorbed on the catalyst surface, deactivating the catalyst. On the contrary, deactivation and discoloration are not observed for $\text{InVO}_4/\text{TiO}_2$ even after the catalyst is evaluated for 60 h as shown in Fig. 18b. The high activity and good stability of the $\text{InVO}_4/\text{TiO}_2$ makes the material particularly attractive for VOCs degradation by utilization of solar energy.

As a comparison, measurements are also carried out to study the activity of pure TiO_2 , InVO_4 , and $\text{InVO}_4/\text{SiO}_2$ under visible light irradiation. No degradation of benzene is observed in these cases, indicating that no photocatalytic degradation of benzene takes place on TiO_2 or InVO_4 alone under our experimental conditions. Moreover, no photocatalytic activity under visible light irradiation can be found when testing the activity of $\text{In}_2\text{O}_3/\text{TiO}_2$, $\text{V}_2\text{O}_5/\text{TiO}_2$, and $(\text{In}_2\text{O}_3-\text{V}_2\text{O}_5)/\text{TiO}_2$ toward benzene decomposition. This suggests that it is the coexistence of InVO_4 and TiO_2 in the $\text{InVO}_4/\text{TiO}_2$ system that accounts for the visible light photocatalytic activity. In addition, no decomposition of benzene occurs by simply mixing the two powders of pure TiO_2 and InVO_4 together. Evidently, the result mentioned above suggests that interaction of InVO_4 with TiO_2 is required to activate TiO_2 for visible light photocatalysis and which contributes to the high activity and durability of the $\text{InVO}_4/\text{TiO}_2$. We also found that the $\text{InVO}_4/\text{TiO}_2$ must be sintered at temperatures between 300 and 500°C for the high photocatalytic performance under visible light irradiation. The optimum sintering temperature is 450°C. The results indicate that the strong interaction generated during the TiO_2 and InVO_4 crystallization enables the photoinduced electron to transfer from the CB of InVO_4 to that of TiO_2 .

The effect of InVO_4 concentration in TiO_2 on the visible light activity of $\text{InVO}_4/\text{TiO}_2$ was also investigated as shown in Fig. 19. In the absence of InVO_4 , the conversion is zero. The optimal concentration is 0.5 wt%. The activity of $\text{InVO}_4/\text{TiO}_2$ gradually decreases when the concentration of InVO_4 is increased from 0.5 to 10 wt%, at which the photocatalyst is virtually inactive for converting benzene. The same trend can be found when photocatalytic activity is measured for ethylene or other organic pollutants. It is known that an ideal sensitizer should be homogeneously attached to the semiconductor surface as nanoparticles (Tsuji et al. 2004). Such directly connected sensitizers are more effective in injecting electrons into the semiconductor as compared to those in the outer layers. When the concentration of InVO_4 is 0.5 wt%, InVO_4 is highly dispersed on the high surface area TiO_2 as small nanoparticles, as indicated by the absence of XRD signal in the sample. In the case of excessive InVO_4 , more and more TiO_2 will be shielded by the overgrowth InVO_4 . Since the pure InVO_4 is inactive toward benzene degradation, the shielding effect causes the reduction in the photosensitization efficiency of InVO_4 .

$\text{InVO}_4/\text{TiO}_2$ photocatalyst also exhibited good photocatalytic performance for the degradation of other VOCs under the visible light irradiation. As shown in Fig. 20, the conversion of the target reactants and the production of CO_2 are measured at steady state after reaction for 12 h. The photocatalytic conversion of cyclohexane, ethylbenzene, toluene, and acetone are 62%, 64%, 57%, and 31%,

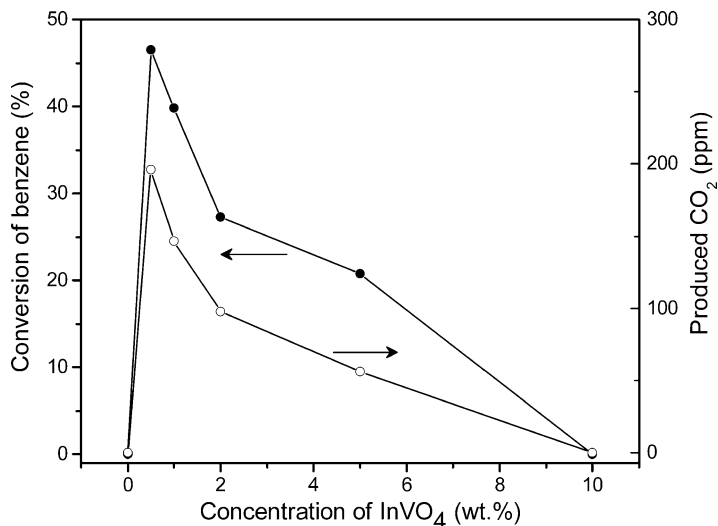


Fig. 19 Photocatalytic conversion of benzene on visible light driven InVO₄/TiO₂ as a function of InVO₄ concentration in the catalyst (Xiao et al. 2008)

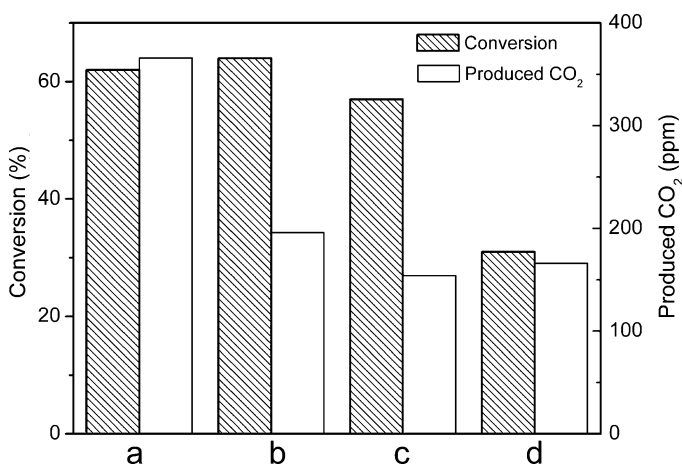


Fig. 20 Photooxidation of other VOCs on InVO₄/TiO₂ irradiated by visible light ($450 \text{ nm} \leq \lambda \leq 900 \text{ nm}$): (a) cyclohexane (250 ppm), (b) ethylbenzene (200 ppm), (c) toluene (200 ppm), and (d) acetone (500 ppm) (Xiao et al. 2008)

respectively. The corresponding CO₂ produced are 366, 196, 154, and 166 ppm, respectively. Similarly, no deactivation is detected on the InVO₄/TiO₂ photocatalyst. In addition, no obvious degradation of the target reactants can be detected on InVO₄ samples. The result demonstrates an effective photocatalysis for each of the target reactants on the InVO₄/TiO₂ photocatalyst. Hopefully, it makes the material attractive for the industrial utilization to decompose various VOCs by sunlight.

5.5 Photochemical Process in the System

In general, the photocatalytic reactions proceed mainly by the contributions of active oxygen species, such as $O_2^{\bullet-}$, $\bullet OH$, and H_2O_2 , among which $\bullet OH$ has been considered as key specie in the mineralization of many hazardous chemical compounds (Hoffmann et al. 1995; Ollis and Al-Ekabi 1993; Hirakawa and Nosaka 2002). In order to probe the reactive oxygen species generated during the visible light irradiation of $InVO_4/TiO_2$ system, EPR spin-trap technique (with DMPO) is used to monitor the intermediate radicals. It has been reported that the superoxide radical anion ($O_2^{\bullet-}$) remains stable in methanol medium and the hydroxyl radical ($\bullet OH$) can be detected in aqueous medium (Wu et al. 1999). Consequently, the EPR spectra of $DMPO-O_2^{\bullet-}$ and $DMPO-OH^{\bullet}$ adducts were investigated in irradiated methanol and aqueous dispersions, respectively.

Neither $DMPO-O_2^{\bullet-}$ nor $DMPO-OH^{\bullet}$ adducts are detected by EPR for the TiO_2 or $InVO_4$ system under visible light irradiation. Theoretically, $InVO_4$ should be active in the visible light, but the quantum efficiency might be too low to generate enough photoexcited radicals for the EPR detection. This accounts for the poor performance of $InVO_4$ toward VOCs photodegradation.

In the case of $InVO_4$ -sensitized TiO_2 , six characteristic peaks of the $DMPO-O_2^{\bullet-}$ adducts are observed as shown in Fig. 21. No such signals are detected in the dark or the blank test. As known above, CB potential of $InVO_4$ is ca. -0.84 (V vs. NHE), whereas the CB potential of TiO_2 is ca. -0.44 (V vs. NHE). These data point to an interfacial electron-transfer process between the $InVO_4$ and TiO_2 particles. The TiO_2 may act as an active center for hindering the recombination of photoinduced

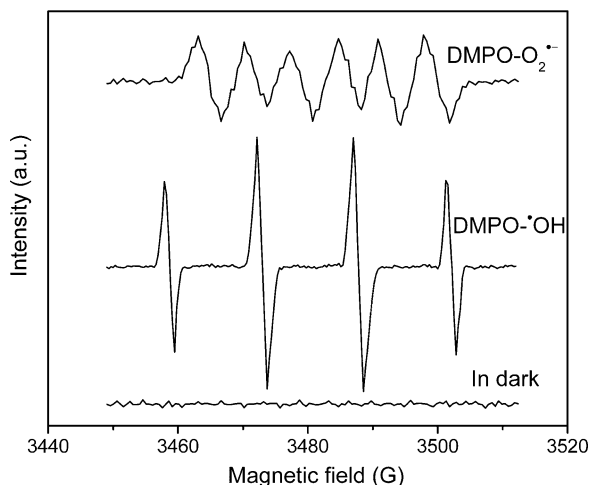
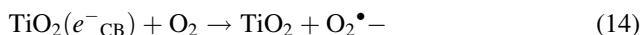
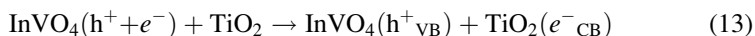
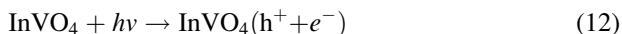
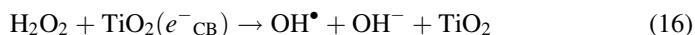
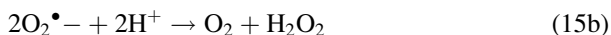
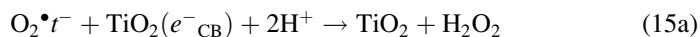


Fig. 21 EPR spectra of radical adducts with DMPO in $InVO_4/TiO_2$ dispersions: (a) $DMPO-O_2^{\bullet-}$ formed in irradiated methanol dispersions; (b) $DMPO-\bullet OH$ in irradiated aqueous dispersions; and (c) sample in methanol or aqueous dispersion before irradiation (Xiao et al. 2008)

electron–hole pairs and transfers electron to absorbed oxygen through its CB, subsequently resulting in a yield of $O_2^{\bullet-}$ radicals (12–14). We conclude that $O_2^{\bullet-}$ radicals are formed much more efficiently on $InVO_4/TiO_2$ than on the naked $InVO_4$ alone.



Moreover, the DMPO-•OH adducts with the characteristic 1:2:2:1 quartet pattern ($\alpha_N = \beta_H = 1.48$ mT) (Wamer et al. 1997) are also observed for $InVO_4/TiO_2$ in the ESR experiments. No such signals are detected in the dark or the blank test. Note that it is too weak for the hole (h_{VB}^+) of $InVO_4$ (+1.26 V vs. NHE) to oxidize hydroxyl to form •OH radical ($E_{OH^{\bullet}/OH^-} = +2.38$ V vs. NHE) (Tsuji et al. 2004) under visible light irradiation. It is proposed that the generation of •OH radical originates from $O_2^{\bullet-}$ radical as below (19.15–16). Certainly, the hole (h_{VB}^+) of $InVO_4$ can consume $O_2^{\bullet-}$ to form O_2 (17).



In summary, $InVO_4/TiO_2$ is a good visible light-driven photocatalyst for the purification of benzene in air. The light-induced electrons transfer from $InVO_4$ to TiO_2 , and then react with oxygen adsorbed on the TiO_2 , producing active $O_2^{\bullet-}$ and •OH radicals capable of decomposing organic compounds.

6 Conclusions

The gas–solid heterogeneous photocatalytic oxidation using TiO_2 is a promising approach for the purification of air polluted by VOCs. However, TiO_2 photocatalysis has its own limitations for the treatment of volatile aromatic compounds such as benzene due to the deactivation of the photocatalyst and cannot harvest visible light.

Adding trace H_2 gas into the $O_2-C_6H_6-Pt/TiO_2$ system can overcome the problem of deactivation, and the system efficiency can be increased by two orders of magnitude compared with that in the absence of H_2 . Nearly 100% of benzene in dry air-stream can be mineralized completely and quickly to CO_2 and H_2O at room

temperature. The main role of H_2 is the significant acceleration of electron–hole separation, the suppression of carbon deposition, and the increase in formation of active hydroxyl radicals.

Photosensitization of TiO_2 by stable $InVO_4$ extends the absorption of TiO_2 to the visible light region up to 540 nm, and induces the formation of reactive $O_2\cdot^-$ and $\cdot OH$ radicals in the resultant $InVO_4/TiO_2$ composite illuminated with visible light. The composite system is stable and effective toward the mineralization of benzene and its derivatives in air under ambient conditions of room temperature and atmospheric pressure without the problem of catalyst deactivation. Further increase in the quantum efficiency is still possible for this new visible light-driven photoreaction system by taking advantage of the H_2-O_2 and Pt synergic effects.

Acknowledgments The authors are supported by the NSF of China (Nos. 21033003 and 20603007), the 973 project (No. 2007CB613306), the NSF of Fujian Province of China (Nos. 2006 J0160 and 2008H0089), and the NCET of China (NCET-07-0192).

References

- Hoffmann MR, Martin ST, Choi W, Bahnemann DW (1995) *Chem Rev* 95:69
- Kamat PV (1993) *Chem Rev* 93:267
- Fox MA, Dulay MT (1993) *Chem Rev* 93:341
- Hagfeldt A, Grätzel M (1995) *Chem Rev* 95:49
- Ollis DF, Al-Ekabi H (eds) (1993) *Photocatalytic purification and treatment of water and air*, Elsevier, Amsterdam
- Blake DM (1994) Bibliography of work on the photocatalytic removal of hazardous compounds from water and air, National Renewable Energy Laboratory
- Kaneko M, Okura I (eds) (2002) *Photocatalysis science and technology*, Springer, Tokyo
- Hitoki G, Takata T, Kondo J, Hara M, Kobayashi H, Domen K (2002) *Chem Commun* 16:1698
- Sato J, Saito N, Yamada Y, Maeda K, Takata T, Kondo JN, Hara M, Kobayashi H, Domen K, Inoue Y (2005) *J Am Chem Soc* 127:4150
- Fu XZ, Zeltner WA, Anderson MA (1996) In: Kamat PV, Meisel D (eds) *Semiconductor nanoclusters-physical, chemical, and catalytic aspects*, vol 103, Elsevier, Amsterdam, p 445
- Alberic RM, Jardim WF (1997) *Appl Catal B: Environ* 14:55
- Lan Q, Zhang L, Li G, Vermeulen RV, Weinberg RS, Dosemeci M, Rappaport SM, Shen M, Alter BP, Wu Y, Kopp W, Waidyanatha S, Rabkin C, Guo W, Chanock S, Hayes RB, Linet M, Kim S, Yin S, Rothman N, Smith MT (2004) *Science* 306:1774
- (1996) Priority pollutants; code of federal regulations, Title 40, ch.1, part 423, appendix A, U. S. Government Printing Office, Washington, DC
- Larson SA, Falconer JL (1997a) *Catal Lett* 44:57
- Einaga H, Futamura S, Ibusuki T (2002) *Appl Catal B: Environ* 38:215
- Bellamy LJ (1975) *The infra-red spectra of complex molecules*. Chapman and Hall, London
- Wu W, Liao L, Lien C, Lin J (2001) *Phys Chem Chem Phys* 3:4456
- Einaga H, Futamura S, Ibusuki T (1999) *Phys Chem Chem Phys* 1:4903
- Hou YD, Wang XC, Wu L, Ding ZX, Fu XZ (2006) *Environ Sci Technol* 40:5799
- Hayward DO, Trapnell BMW (1964) *Chemisorption*. Butterworths, London
- Kazantsev RV, Gaidai NA, Nekrasov NV, Tenchev K, Petrov L, Lapidus AL (1998) *Kinet Catal* 39:363
- Sitkiewitz S, Heller A (1996) *New J Chem* 20:233

- Williams DH, Fleming I (1987) Spectroscopic methods in organic chemistry, McGraw-Hill Book Company (UK) Limited, London
- Kunai A, Hata S, Ito S, Sasaki K (1986) *J Am Chem Soc* 108:6012
- Anpo M, Shima T, Kubokawa Y (1985) *Chem Lett* 12:1799
- Komatsu T, Lund A (1972) *J Phys Chem* 76:1727
- Bedilo AF, Kim VI, Volodin AM (1998) *J Catal* 176:294
- Kurita Y, Sonoda T, Sato M (1970) *J Catal* 19:82
- Larson SA, Falconer JL (1997b) *Catal Lett* 44:57
- Penner S, Wang D, Su DS, Rupprechter G, Podloucky R, Schlögl S, Hayek K (2003) *Surf Sci* 532–535:276
- Delmon B (1933) In: Inui T, Fujimoto K, Uchijima T, Masai M (eds) *Studies in surface science and catalysis* 77, Elsevier: Kyoto, Japan
- Chen H, White JM (1986) *J Mol Catal* 35:355
- Zhao W, Chen C, Li X, Zhao J (2002) *J Phys Chem B* 106:5022
- Wu T, Liu G, Zhao J, Hidaka H, Serpone N (2000) *New J Chem* 24:93
- Benvenuti EV, Franken L, Moro CC, Davanzo CU (1999) *Langmuir* 15:8140
- Ghigo G, Tonachini G (1999) *J Am Chem Soc* 121:8366
- Hayashi T, Tanaka K, Haruta M (1998) *J Catal* 178:566
- Williams WR, Marks CM, Schmidt LD (1992) *J Phys Chem* 96:5922
- Berry RS, Mackie JC, Taylor RL, Lynch R (1965) *J Chem Phys* 43:3067
- Pack JL, Phelps AV (1966) *J Chem Phys* 44:1870
- Bach U, Lupo D, Comte P, Moser JE, Weissortel F, Salbeck J, Spreitzer H, Gratzel M (1998) *Nature* 395:583
- Yu JC, Wu L, Lin J, Li PS, Li Q (2003) *Chem Commun* 13:1552
- Zou ZG, Ye JH, Sayama K, Arakawa H (2001) *Nature* 414:645
- Tang JH, Zou ZG, Ye JH (2004) *Chem Mater* 16:1644
- Oshikiri M, Ye JH, Zou ZG, Kido G (2002) *J Chem Phys* 117:7313
- Oshikiri M, Boero M, Ye J, Aryasetiawan F, Kido G (2003) *Thin Solid Films* 445:168
- Ye JH, Zou ZG, Arakawa H, Oshikiri M, Shimoda M, Matsushita A, Shishido T (2002) *J Photochem Photobio A: Chem* 148:79
- Fu X, Walter A, Yang Q, Anderson MA (1997) *J Catal* 168:482
- Gregg SJ, Sing KSW (1997) Adsorption, surface area and porosity, Academic, London, pp 111–194
- Luo HM, Wang C, Yan YS (2003) *Chem Mater* 15:3841
- Xiao GC, Wang XC, Li DZ, Fu XZ (2008) *J Photochem Photobio A: Chem* 193:213
- Kozlowski R, Pettifer RF, Thomas JM (1983) *J Phys Chem* 87:5176
- Briggs D, Seah MP (1990) Practical surface analysis Auger and X-ray photoelectron spectroscopy. 2nd edn, vol I, Wiley, New York
- Asahi R, Morikawa T, Ohwaki T, Aoki K, Taga Y (2001) *Science* 293:269
- Liu G, Jaegermann W, He J, Sundström V, Sun L (2002) *J Phys Chem* 106:5814
- Chun W, Ishikawa A, Fujisawa H, Takata T, Kondo JN, Hara M, Kawai M, Matsumoto Y, Domen K (2003) *J Phys Chem* 107:1798
- Tsuji I, Kato H, Kudo A (2004) *Angew Chem Int Ed* 44:2
- Hirakawa T, Nosaka Y (2002) *Langmuir* 18:3247
- Wu T, Lin T, Zhao J, Hidaka H, Serpone N (1999) *Environ Sci Technol* 33:1379
- Wamer WG, Yin JJ, Wei RR (1997) *Free Rad Biol Med* 23:851

Chapter 20

The Effect of Addition of Pt on the Gas Phase Photocatalysis over TiO₂

Deniz Uner

Abstract It is now widely accepted that the presence of a metal, primarily Pt, improves the photocatalytic activity of TiO₂ both in the liquid and in the gaseous state reactions. The objective of this chapter is to provide a review on the postulated mechanisms of interaction of Pt and TiO₂ during photocatalytic reactions in the gas phase. The literature was reviewed to explore the following mechanisms: (1) Schottky effect for charge separation; (2) oxygen spillover from Pt to TiO₂; (3) reverse spillover of reactive intermediates from TiO₂ to Pt; (4) room temperature catalytic activity of Pt; (5) capture zone created by Pt; and (6) effect of Pt on the acidity of the OH groups. The intention is to provide an assessment for the complexity of the interaction between Pt and TiO₂, and enlist some existing unanswered questions for further research.

1 Introduction

Photocatalysis research nowadays is progressing in two main fronts: photooxidation of the pollutants and photocatalytic chemical conversions for value added products. The economical breakthrough of the photooxidation of the airborne pollutants has already been reached by marketable products such as self-cleaning window glasses, antibacterial surgical room tiles, self-cleaning paints, and wall tiles. All of these products are required to exhibit activity in the visible spectrum of the solar radiation. The primary objective is to use solar energy (or visible light) to activate the catalytic materials for hydrocarbon oxidation to carbon dioxide and water. The second frontier for the photocatalysis is to mimic nature and utilize solar energy for highly selective chemical conversions. The ultimate goal is to utilize

D. Uner

Chemical Engineering Department, Middle East Technical University, 06531 Ankara, Turkey
e-mail: uner@metu.edu.tr

solar energy for CO₂ fixation in order to produce commercially valuable chemical products. The ability to fine tune a photocatalyst better than a thermally activated catalyst makes the field of photocatalysis even more attractive. The reader is referred to several books and review articles published so far in the literature for detailed accounts of the photocatalytic reactions over TiO₂ (Anpo 1997, 2004; Channon 1997; Fox 1989; Fox and Dulay 1993; Kamat 1993; Linsebigler et al. 1995; Litter 1999; Schiavello 1997; Serpone and Pelizzetti 1989; Thompson and Yates 2006).

Irradiation of a photocatalyst by electromagnetic radiation of proper wavelength results in absorption of photons in the structure, exciting an electron from the valance band of the semiconductor to the conduction band. The electrons and holes generated as such can undergo several processes in the semiconductor. They can undergo intraband transitions, they can migrate to the surface and be trapped at the trap sites, or they can radiatively or non-radiatively recombine. The electrons trapped at the edge of the conduction band serve as the reduction centers, while the holes trapped at the valance band edges act as the oxidizing sites. The lifetimes of the charge carriers depend on how efficiently they are trapped. The trap sites for electrons are Ti⁴⁺ sites, while holes are trapped at the OH groups (Anpo et al. 1991). Electron and hole trapping proceed at different rates due to the differences in the mobilities of these charge carriers. Electron trapping can take place as fast as within 30 ps of generation, while hole trapping requires an average time of 250 ns. Their recombination process is second order at high concentration of charge carriers, while it is first order at low concentrations (Rothenberger et al. 1985).

It is widely accepted now that in the presence of Pt, photocatalytic reactions proceed more efficiently. The increase in the efficiency in the presence of a metal is mostly attributed to the band bending and the Schottky effect. In Fig. 1, the electronic excitation of a semiconductor photocatalyst is presented (Linsebigler et al. 1995). When the semiconductor photocatalyst is brought into contact with a metal (Fig. 1), the electrons populate on the metal if the Fermi level of the metal is lower than the conduction band edge of the semiconductor. This results in two major effects: (1) increased lifetimes of the charge carriers (electrons and holes) due to the

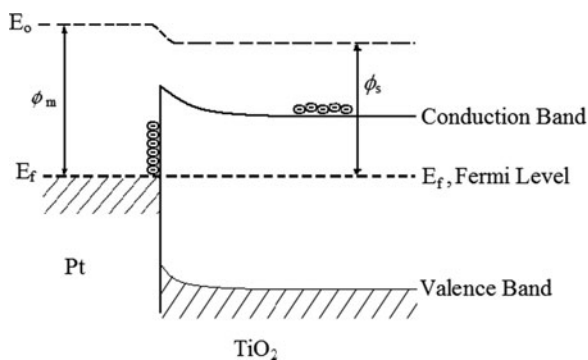


Fig. 1 Schematics of the photocatalytic excitation process in the presence of a metal

spatial separation and (2) decreased electron population within the semiconductor leading to the increased acidity of the OH groups (Jaffrezic-Renault et al. 1986). As a result of the charge separation, the lifetimes of the charge carriers' increase, which improves the reaction events taking place per photon absorbed, defined as the *quantum yield* of the reaction. The quantum yields of the reaction are higher if the charge carriers are used in reactions before recombination. Therefore, the quantum yields strongly depend on the availability of the charge carriers, but they also depend on how fast these charge carriers are consumed by the reactants or intermediates.

2 Gas Phase Photocatalysis over Pt/TiO₂

Pt forms islands over TiO₂ under the growth conditions in UHV systems (Steinruck et al. 1995). The size of the Pt particles formed on TiO₂ depends on the preparation conditions and loading. However, in most of the cases studied for photocatalysis, metal particles larger than 1 nm are observed. This size is large enough to stabilize a sufficient number of metal atoms to sustain an effective d-band. When Pt is incorporated in TiO₂ several effects can take place. The most widely accepted effect is the *charge separation due to the formation of a Schottky barrier* as described briefly above. The charge separation is an important constituent of the rate enhancement during photocatalysis. The formation of charge carriers is instantaneous. But the lifetimes of these charge carriers strongly depend on the bulk and surface electronic structure. For example, it has been reported in the literature that anatase traps holes ten times more efficiently than rutile (Riegel and Bolton 1995; Hurum et al. 2003). Electron-hole recombination process time constants are of the order of 10⁻⁷ s, but subsecond lifetimes are measured in the presence of Pt (Yamakata et al. 2001). It has now been unequivocally demonstrated that within 5 ps of formation, electrons populate around the Pt particles (Furube et al. 2001).

Besides the charge separation effect, Pt and other noble metals bring in their own catalytic activity to the whole catalytic process (Vorontsov et al. 2005). The early work of Haruta et al. (1989) has demonstrated room temperature activity of supported gold catalysts. Since then, the TiO₂-supported gold nanoparticles have been demonstrated to exhibit extraordinary activity at room temperatures or below (Valden et al. 1998; Chen and Goodman 2006). Therefore, it is important to note the fact that even at room temperature, Pt or other precious metals can contribute significantly to the catalytic processes taking place on the surface. These catalytic effects can be briefly listed as follows: (1) Pt adsorbs and dissociates oxygen more efficiently, in the dark, than TiO₂ (Courbon et al. 1984; Uner et al. 2003); (2) Pt is known to be more efficient in ring-opening reactions than titania; therefore, in the presence of Pt, the deactivation of the photocatalyst slows down tremendously (Fu et al. 1995; Mendez-Roman and Cardona-Martinez 1998; Fernandez-Garcia et al. 2007); (3) precious metals can participate the reaction after a "reverse spillover" process for oxidation (Bowker et al. 2002) or hydrogenation (Anpo et al. 1984); (4) in the presence of Pt, oxygen can spillover on TiO₂ to assist further

thermal and photooxidation reactions over TiO_2 (Falconer and Magrini-Bair 1998; Ozen and Uner 2001); (5) the charge separation in the presence of Pt depletes the TiO_2 from electrons, while the acidity of the OH groups acting as hole traps increases (Jaffrezic-Renault et al. 1986); (6) as a result of the relative magnitude of the surface free energies, Pt has a tendency to diffuse in the bulk of titania, or titania moieties can migrate to the surface of Pt which is sometimes called the Strong Metal Support Interaction (SMSI) effect (Diebold 2003).

Despite the numerous studies and excellent reviews, there is still much to understand about the surface reaction mechanisms of photocatalytic reactions. The role of electrons and holes as reaction initiators are imminently accepted. However, their role in the subsequent reaction steps is barely known. The simplest approach in the field is to treat photocatalytic surface reactions similar to the reactions in the dark after the initiation step. In such a case, the contribution from the thermal catalytic activity of the Pt gains more importance in driving the surface processes. It is clear that the photogeneration of electron–hole pairs is so fast that an adsorbed reactant has to be present on the surface to react (Fox 1989). Therefore, the rate of the adsorption step becomes as important to the quantum efficiencies as the rate of the electron hole recombination process. With this further questions arise: What is the rate determining process in a photocatalytic reaction? What are the rates of electron transfer and hole transfer processes? Are the electron transfer and hole transfer processes synchronized, or is one of them limiting the overall kinetics? In the next sections, we will try to answer some of these questions based on the published articles in the literature.

3 Charge Carrier Dynamics

Understanding the charge transfer processes is very important because electrochemical processes, electron transfer reactions, dye-sensitized solar cells, and photocatalysis are few of the fields based on the charge transfer processes. Current developments and existing unanswered questions “about charge transfer on the nanoscale” were collected in a recent review article (Adams et al. 2003). In this section, we will limit ourselves to the general characteristics of the charge transfer processes between a metal and a semiconductor during photocatalysis. In Fig. 2, possible optical transitions in a band gap are presented. The charge generation process upon illumination is instantaneous. Once the photon absorption takes place in the solid, the electrons from the valance band are transferred to the conduction band if the irradiating photon has sufficient energy to overcome the band gap. In TiO_2 , the general consensus is that Ti^{4+} acts as an electron trap and surface OH groups act as hole traps (Anpo et al. 1991). The electrons and holes trapped at the surface (or in the bulk) migrate in the structure, and some of them recombine radiatively or non-radiatively. In order to improve the quantum efficiencies, the principal objective is to utilize these charge carriers at a rate faster than they

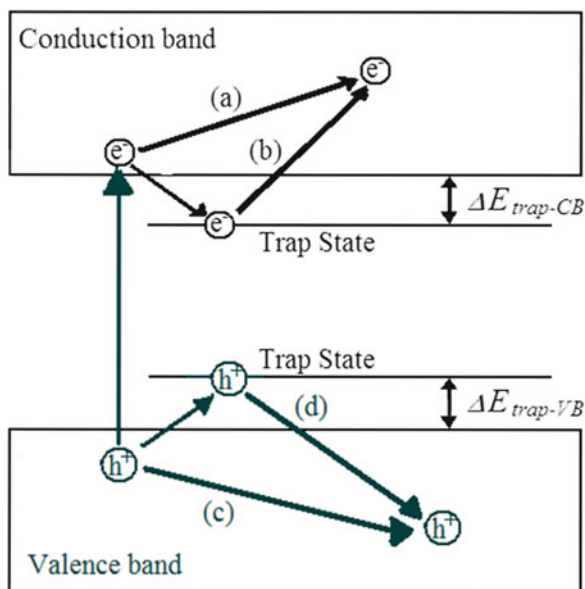


Fig. 2 Possible optical transitions in a band gap (Yamakata et al. 2001)

recombine. It is important to have a sufficient number of trap states on the surface to enable efficient charge separations.

The trap states on a platinized titania are Ti⁴⁺ sites, OH groups, and Pt particles. It is now very clearly understood that the presence of Pt assists charge separation: direct evidence is now presented that 5 ps within generation electrons are populated around Pt (Furube et al. 2001). The recombination processes are consequently delayed. Early work on charge carrier trapping and recombination dynamics (Rothenberger et al. 1985) report a rate constant for e⁻-h⁺ recombination of the order of 10⁷/s. The same authors also predicted that the rate of the recombination is 80 times faster than the rate of the hole trapping for particles of around 60 Å. The hole trapping in smaller particles is expected to be more efficient because the hole trapping takes place at the surface hydroxyl sites. As the particles get smaller, their surface area and the number of the hydroxyl groups on the surface increase, providing more sites for hole trapping. As mentioned above, the time required for electron trapping is shorter than 30 ps, while hole trapping requires an average of 250 ns (Rothenberger et al. 1985).

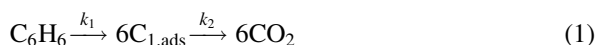
4 Effect of Pt on Photocatalytic Oxidation Kinetics

In this section, a broad kinetic analysis will be presented for the photocatalytic decomposition of benzene, and the effect of the metal addition on the kinetic parameters in the dark and under illumination will be analyzed. The data presented

in the literature on the photocatalytic oxidation of benzene also included the effect of temperature on the conversions in the dark (purely thermal reactions) and under illumination. The improvement in the performance of the photocatalyst in the presence of Pt was apparent in the light-off curves (Fu et al. 1995): the temperature required to obtain similar conversions decreased in the presence of Pt. This decrease, however, was more pronounced than the decrease in the temperature in the dark. In other words, the presence of Pt improved the kinetics beyond the catalytic effect of the metal itself.

Further effects of the presence of a metal were also reported. First, it was observed that in the presence of Pt, the deactivation due to the coke deposition slowed down during photocatalytic oxidation of VOCs (Fu et al. 1995; Ozbek and Uner 1999; Mendez-Roman and Cardona-Martinez 1998; Falconer et al. 2001). Second, the carbonation ratios (number of moles of CO₂ produced/number of moles of hydrocarbon reacted) increased with increasing space times. Furthermore, the catalyst activity decayed at a rate consistent with a single carbon containing species blocking a single surface adsorption site (Ozbek and Uner 1999; Fu et al. 1995).

In this part, we will develop a simplified reaction scheme to elucidate the role of the relative rates of the intermediate product formation on the overall reaction rates and deactivation for benzene photooxidation in a gas phase photocatalytic reactor. When developing the reaction model, we will assume that the thermal and material steady states have been established. The film mass transfer limitations were ignored in the reaction model because of the following reasons: (1) The temperatures used in the photoreaction were low enough so that the rate determining step could be the reaction itself; (2) a study by Alberici and Jardim (1997) established that in similar systems, the mass transfer limitations can be negligible even at Reynolds numbers as small as 20. Pore diffusion issues were not accounted for in the reaction model, because the photoreaction could only take place at the illuminated surface, and the rest of the catalyst bulk could only serve as a storage space for the reaction intermediates. It was further assumed that these approximations were valid for the thermal reaction studies as well. Finally, the experimental data were collected at very low concentration of one of the reactants, i.e., benzene; therefore, the contribution of the other reactant, i.e., oxygen, on the reaction kinetics could be neglected. With these assumptions, the reaction kinetics could be modeled around ideal reactors such as a CSTR or a plug flow reactor (PFR). First, it is postulated that the benzene photooxidation over TiO₂ surfaces can simply be represented as a series reaction:



In this reaction scheme, the effect of oxygen is not taken into account since both in the gas phase and probably on the surface it is present in large excess; thus the overall reaction scheme is little influenced by the changes in the oxygen concentration. C₁ in the reaction scheme represents a single carbon containing intermediate, producing CO₂. If one assumes a first order rate for each of the two reaction steps, one can calculate the benzene and CO₂ concentrations at the exit of the ideal PFR:

$$C_{C_6H_6} = C_{C_6H_{60}} e^{-k_1 \tau} \quad (2)$$

where τ is the space time or the residence time of the reactant flow; $C_{C_6H_6}$ is benzene concentration at the exit of the reactor; and $C_{C_6H_{60}}$ is the initial benzene concentration. The carbon dioxide concentration at the exit of the reactor can be calculated as six times the difference between the concentration difference of benzene between the inlet and the exit of the reactor:

$$C_{CO_2} = 6C_{C_6H_{60}} \left\{ 1 + \frac{k_1 e^{-k_2 \tau} - k_2 e^{-k_1 \tau}}{k_2 - k_1} \right\} \quad (3)$$

Thus, the carbonation ratio can also be calculated as the ratio of CO₂ formed to benzene consumed:

$$\frac{C_{CO_2}}{C_{C_6H_{60}} - C_{C_6H_6}} = 6 \left\{ \frac{1 + \frac{k_1 e^{-k_2 \tau} - k_2 e^{-k_1 \tau}}{k_2 - k_1}}{1 - e^{-k_1 \tau}} \right\} \quad (4)$$

This simple model is not at all rigorous in the detailed chemistry, but it offers significant insight into the surface phenomena. At this point, we will extend the level of approximation for mathematical simplicity and will assume that the intermediate species is in the gas phase. This assumption is not at all valid; however, it will allow us to proceed analytically in the developments. Thus the following expression is obtained for the intermediate concentrations as a function of rate constants and the space time:

$$C_{C_1} = 6C_{C_6H_{60}} k_1 \left\{ \frac{e^{-k_1 \tau} - e^{-k_2 \tau}}{k_2 - k_1} \right\} \quad (5)$$

In reality, the intermediate species will accumulate over the catalyst surface causing deactivation due to the site blocking. Of course, the deactivation process can be modeled as a first order process with an additional deactivation rate constant, k_d , but for the sake of simplicity of the present discussion that analysis is left out.

The model expressions derived here were justified based on the previous experimental work (Ozbek and Uner 1999). Equation (4) indicates that as the space time goes to zero, the carbonation ratio goes to infinity. In fact, this was observed experimentally in our previous work on photooxidation of benzene over TiO₂. At the lowest space times, experimentally measured carbonation ratios exceeded six, justifying the validity of the equations despite the simplicity of the analysis. These results imply that the relative magnitudes of k_1 and k_2 determine the carbonation ratio and the rates of deactivation. Thus, the alteration of these rate constants will alter the quantum yields of the photocatalytic reactions.

The derivations so far indicated two key points: (1) The benzene depletion rates can be represented as a first order reaction and (2) the carbonation ratios depended on the relative magnitudes of the benzene decomposition and CO₂ formation step rate constants.

To test the validity of the first order rates for the benzene decomposition step, the experimental data available in the literature were analyzed. A first order reaction rate model was to be applied to the light-off curves reported in literature with the hope to extract the reaction orders activation energies and Arrhenius constants of the reaction rate expression. In order to develop a workable model, several assumptions had to be made. Some of these assumptions were dictated by the experimentalists' choices, some of the assumptions were based on the previous publications.

The temperature-dependent conversion values were collected from the literature (Fu et al. 1995; Papaefthimiou et al. 1998). One of these studies (Fu et al. 1995) collected the thermal conversion data on benzene in a packed bed reactor in a study that was accompanied by a similar set of data collected under UV illuminated conditions. The other set of data allowed us compare the effect of the support such as TiO_2 or Al_2O_3 on the thermal reaction. Both sets of data were collected in packed bed reactors. When the external or internal mass transfer effects were neglected, the packed bed reactor could be modeled as a PFR. Since oxygen was in large excess, the reaction could be modeled as a pseudo-first or pseudo-second order in benzene concentration. Both cases were investigated, and little improvement in the quality of the fit by increasing the reaction order was observed. Without invoking any assumptions about the reaction mechanism, pseudo-first order reaction assumption was justified with the background that first order kinetics is generally valid in similar reaction systems (Ollis 2005; Emeline et al. 2005). The analytical solution of a first order reaction taking place in a PFR is given in (6):

$$-\ln(1-x) = \tau k_0 e^{-E_a/RT}, \quad (6)$$

where x is the fractional conversion of the reactant. By taking the natural logarithm of both sides of (6)

$$\ln\{-\ln(1-x)\} = \ln(\tau k_0) - E_a/RT, \quad (7)$$

one obtains an equation that should show a linear behavior of the $\ln\{-\ln(1-x)\}$ vs. $1/T$ plot. Such a plot was generated from the data of Fu et al. (1995) and is presented in Fig. 3.

As seen from Fig. 3, the fits were reasonably linear. Therefore, the slope could be used to obtain the activation energy and the intercept could be used to obtain τk_0 . This procedure was repeated for all the available thermal catalysis data and the results are presented in Fig. 4 and Table 1. In order to show the quality of the fit of the data with the model, the correlation coefficients (r^2) are also presented in Table 1. When examined, the results of activation energy calculations indicated that in the presence of Pt, the activation energy of the thermal oxidation of benzene reaction increased almost fourfold. The activation energies calculated from the data collected in two different laboratories on similar catalysts (0.1% Pt/ TiO_2 Fu et al. 1995, 0.3% Pt/ TiO_2 Papaefthimiou et al. 1998), however, were very close. The illumination with UV light alone reduced the activation energy of the reaction on TiO_2 surface by a factor of approximately 2. Similarly, the value of τk_0 decreased upon illumination.

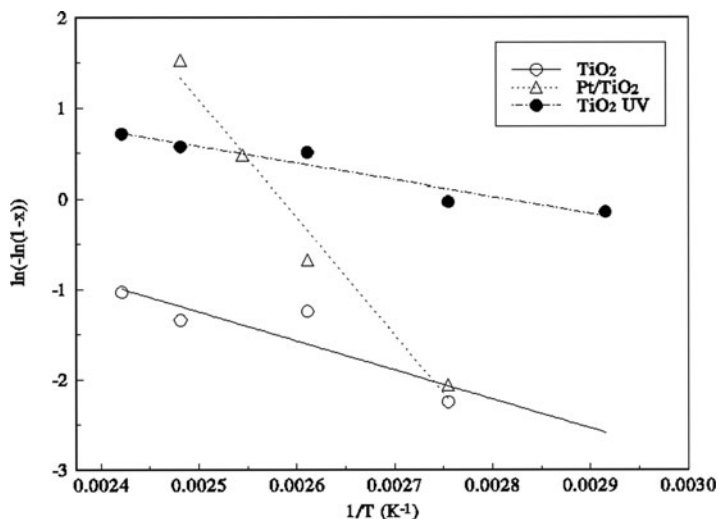


Fig. 3 The fit to the thermal and photocatalytic reaction of the benzene decomposition over TiO₂ and Pt/TiO₂. The empirical data are from Fu et al. (1995)

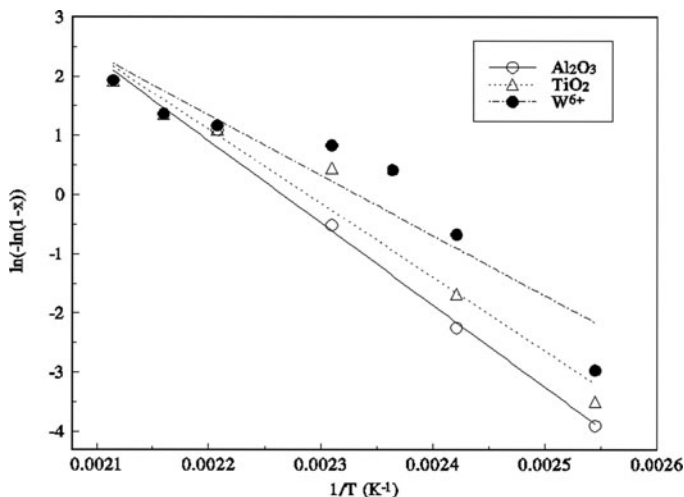


Fig. 4 The fit to the thermal catalytic reaction of the benzene decomposition over 0.3% Pt/TiO₂, 0.3% Pt/TiO₂(W⁶⁺) and 0.3% Pt/Al₂O₃. The empirical data are from (Papaefthimiou et al. 1998)

A similar analysis could not be performed on the photocatalytic reaction over 0.1% Pt/TiO₂ data because over the temperature range that the reaction was studied, the conversions were approximately 100% (Fu et al. 1995). So, one could conclude that the illumination decreased the apparent activation energy of the reaction; however, the Arrhenius pre exponentials remained nearly constant upon illumination. On the contrary, the presence of Pt increased both the activation energies of the thermal

Table 1 The extracted Arrhenius parameters, the correlation coefficients, and the sources of empirical information for thermal degradation of benzene to carbon dioxide and water

Catalyst	E_a (kJ/mol)	$\ln(\tau k_0)$	Space time, τ	r^2	Experimental data from reference
TiO ₂	26.8	6.8	1.8×10^9 g cat s/mol	0.83	Fu et al. (1995)
TiO ₂ illuminated	15.3	5.2	1.8×10^9 g cat s/mol	0.93	Fu et al. (1995)
0.1% Pt/TiO ₂	107.8	23.8	1.8×10^9 g cat s/mol	0.91	Fu et al. (1995)
0.3% Pt/TiO ₂	103.6	28.5	9.3×10^{-9} s	0.97	Papaefthimiou et al. (1998)
0.3% Pt/TiO ₂ (W ⁺⁶)	84.6	23.7	9.3×10^{-9} s	0.89	Papaefthimiou et al. (1998)
0.3% Pt/Al ₂ O ₃	115.3	31.4	9.3×10^{-9} s	0.99	Papaefthimiou et al. (1998)

reaction and the Arrhenius pre-exponentials simultaneously; thus the resulting effect was increased reaction rates and conversions.

The numbers presented in the above analysis have to be taken with caution because in packed bed geometries, not all of the catalyst is illuminated; therefore, a significant proportion of the reaction is still driven by only thermal effects. However, it is now established that the activation energy of the thermal reaction increases with the addition of Pt, while increased rates suggest that the steric effects and adsorbate mobilities play a significant role in the photocatalysis involving Pt/TiO₂. The analysis provided above gives some useful hints about how Pt is interacting with TiO₂ as a catalyst and how the catalytic process takes place.

It was observed that (Papaefthimiou et al. 1998) in the presence of Pt, the surface concentration of carbon layer decreased tremendously during ethanol oxidation over Al₂O₃. The presence of Pt inhibits deactivation as a result of carbon deposition both in benzene and ethanol oxidation over both TiO₂ and Al₂O₃ supports by facilitating the final oxidation step.

It is obvious that the later steps of carbon removal were facilitated in the presence of Pt. This effect is not related to the rate enhancement as a result of charge separation by forming a Schottky barrier. The charge separation influences the initiation steps of decomposition, while it is clear that the deactivation slows down as a result of the enhancement of the subsequent steps of the reaction.

The presence of Pt definitely assists oxygen adsorption, dissociation, and exchange over TiO₂ (Courbon et al. 1984). Adsorption heats of oxygen measured on pure and Pt containing TiO₂ revealed that in the presence of Pt, adsorption is dissociative and releases heat ~ 400 kJ/mol O₂. On the contrary, in the absence of Pt, oxygen adsorption is weak and non-dissociative (Uner et al. 2003; Uner and Uner 2005). Thus, the presence of Pt may facilitate oxygen dissociation and exchange between the gas phase and the surface; one of the initial steps of the photocatalytic oxidation processes. But it is also clear that Pt contributes significantly to the rates of the final oxidation steps, most probably CO oxidation.

Given that the effective activation energies of the reactions analyzed above increases along with an increase in Arrhenius pre-exponential factor in the presence

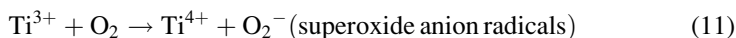
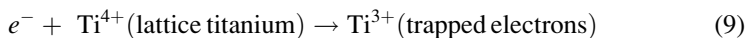
of Pt leads us to think that the adsorbate mobilities are higher in the Pt containing surfaces. It has already been proven that the adsorbates and the oxidizers possess very high mobility extending beyond the limits of the photoactive layers. In a cleverly designed experiment, Haick and Paz (2001) have demonstrated that the photocatalytic activity of TiO₂ stripes carried beyond their boundaries. The self-assembled monolayers of octadecyltrichlorosilane (OTS) retained over TiO₂-free silicon surface degraded almost at the same rate as their counterparts over TiO₂ surface. The authors argued that the oxidizer species could spill over to domains that are themselves not active to initiate degradation reactions. Once the reaction is initiated, the propagation steps can continue over the inactive surfaces. In another study, the same group reported that the domain size of the precious metal determines whether the presence of the metal is promoting or it is detrimental to the photocatalytic activity (Haick and Paz 2003). They deposited stripes of noble metals, Pt and Au, in different geometries such as alternating stripes of metal and TiO₂, stripes of metal over TiO₂, or an underlayer of metal onto which a TiO₂ overlayer is grown. They found out that the role of the metal was beyond the charge separation. They demonstrated that there is a complex mechanism of the degradation kinetics of the self-assembled monolayers of OTS. The mechanism they proposed required photocatalytic formation of oxidizer species, OH radicals, and the diffusion of these species to the metal layers to be reduced and back diffusion of the reduced species to the TiO₂ surface. The authors proposed that the size of the metallic domain influenced the rate of the back diffusion, and beyond an optimum size, the effect of the metal was detrimental.

The physical meanings of the rate constants in a photocatalytic reaction also contain complexities coming from activation by photons. The fact that a catalytic reaction is taking place on the surface embeds all of the fundamental principles of catalysis in a reaction mechanism. However, the reaction is initiated by a non-activated, temperature independent process of photon driven $e^- - h^+$ pair formation. Thus, a typical representation of the photocatalytic reaction has non-activated initiation steps combined with thermally driven subsequent reaction steps. The activation barriers of these subsequent steps should be low enough that once the reaction gets started, the thermal energy available in the system at low operational temperatures (~ 300 K) is sufficient to drive the reaction toward completion. Therefore, the effective activation energies measured experimentally belong to the compound effect of the subsequent bond formation and dissociation steps.

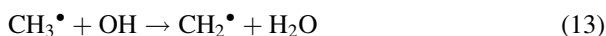
5 Surface Reaction Mechanisms over Pure and Pt/TiO₂

Any photocatalytic reaction involving water and oxygen initiates via the following steps (Anpo 2004):

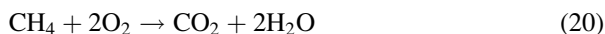




In this section, a purely speculative mechanism will be proposed for hydrocarbon oxidation below. In order to keep the analysis simple, methane molecule was selected to represent organic compounds. In this purely speculative mechanism, photogenerated OH[•] radicals are used to scavenge hydrogen atoms from methane molecule and form water, while the photogenerated O₂⁻ species are used to oxidize surface carbon.



The net reaction being



The mechanism postulated above for methane decomposition involves radical transfer to methane after the first proton abstraction step. After the initiation step, not OH[•] radicals, but surface OH groups are used for hydrogen abstraction in order to maintain the species balance and the charge neutrality. All of the carbon containing species are radicals, and, therefore, are expected to participate in the reaction rather fast, with the exception of CO. Therefore, it is acceptable to assume (17) as the rate limiting step, which was the case in the benzene oxidation model given in Sect. 4.

Over Pt containing TiO₂, O₂⁻ formation step will most probably take place on the metal instead of on the Ti⁺³ sites because it is clearly shown that the formation of Ti⁺³ species is inhibited in the presence of Pt (Anpo et al. 1984). There are two

subsequent processes that can take place: (1) The spillover of superoxide formed over the metal to TiO₂ or (2) reverse spillover of CO formed on TiO₂ to Pt to react with the O₂⁻ to form CO₂ (Bowker et al. 2002).

6 Adsorption and Exchange on Pt, TiO₂ and Pt/TiO₂

Early work on exchange of oxygen over pure and Pt containing TiO₂ revealed that the presence of Pt enhanced the oxygen exchange rates, however, excess Pt was detrimental to the process (Courbon et al. 1984). As can be seen from the reaction scheme given in Sect. 5, the initiation steps of electron and hole scavenging requires oxygen and OH groups continuously replenished by adsorbed water. In other words, the rate of adsorption of these reactants determines how well the charge carriers generated by photon absorption are utilized in the reaction network. As discussed above, the photogeneration takes place within a picosecond time frame, while the recombination and the decay of these charge carriers undergo several processes with time constants ranging from picoseconds to nanoseconds (Fox and Dulay 1993). The quantum efficiencies of the photocatalysts are, therefore, strongly influenced by how fast the charge carriers are used. It is well known that the charge carrier dynamics are strongly influenced by the presence of Pt. It is now unambiguously established that within 5 ps of formation, electrons are trapped around Pt, the trapping efficiency was strongly depended on the Pt loading (Furube et al. 2001). Furthermore, the presence of adsorbates influences the charge carrier recombination dynamics: adsorbed oxygen can act as an electron trap thus assisting charge separation (11), while adsorbed water act as a recombination center (Anpo et al. 1991).

The mechanisms of the photocatalytic reactions are broadly different from the corresponding dark equivalents because the initiation steps, as given in (8)–(11) require photon activation, and providing substantiate evidence for the intermediates of the subsequent steps as well as estimating kinetic constants for a detailed microkinetic analysis is very difficult. Instead, most of the researchers prefer to submit to relatively easy, however controversial, Langmuir–Hinshelwood (LH) analysis. The limitations of LH mechanism in a photocatalytic reaction are discussed broadly in the literature (Ollis 2005; Emeline et al. 2005). The major drawback stems from the lack of supporting information from the independent surface science work. However, its descriptive nature allows us infer new questions about the nature of the phenomena. Summarized briefly, LH kinetics represents a simple model involving fast adsorption of reactants such that the adsorption steps are equilibrated and kinetically limited to product formation steps. With these restrictions, a uni-molecular surface reaction undergoing according to the LH kinetics has the following rate expression:

$$-r_A = kKP_A/(1 + KP_A), \quad (21)$$

where k represents the rate constant of the kinetically significant step and K represents the equilibrium constant of the adsorption step. It is apparent from (21) that the kinetics is controlled by the adsorption equilibria depending on the values of the K and P_A . Under such conditions, and given that the adsorption and reaction processes are orders of magnitude slower than the charge carrier generation and recombination steps, the enhancement of the photocatalytic reaction rates significantly depends on the enhancement of the rates of the chemical processes starting from adsorption. K in a rate expression such as given in (21) can possess a variety of meanings whether the reaction model was derived by LH approximation by a pseudo-steady state approximation (Ollis 2005) or by involving different alternatives for the rate determining step such as photodesorption (Emeline et al. 2005). At any situation, the equilibrium surface coverage of the reactants can be represented by a Langmuir isotherm:

$$\theta_A = KP_A/(1 + KP_A) \quad (22)$$

The value of K depends fundamentally on two thermodynamic parameters: the heat of adsorption and the entropy change upon adsorption. The adsorption is more facile on the surfaces where higher heats are released, given that the entropy factors are not different. Given this, the heat of adsorption data, measured in the dark, of oxygen, water, and CO on various surfaces of Pt and TiO₂ are briefly compiled in Table 2. More comprehensive collection of literature data can be found in our previous publications. We reviewed the heats of adsorption data available in the literature for oxygen on Pt (Uner et al. 2003), oxygen on TiO₂ (Uner et al. 2003), and carbon monoxide on Pt (Uner and Uner 2005). Here, a brief summary is given to compare the adsorption kinetics data in terms of heat of adsorption or activation energies of desorption for oxygen, water and carbon monoxide over pure TiO₂ and Pt. The data refer to the measurements done in the absence of irradiation, therefore only represents the interaction of the adsorbate with the surface in the dark, which seems to be an inevitable component of every photocatalytic reaction. It is clearly seen from Table 2 that the heats of adsorption of photocatalytically important adsorbates measured in the dark are always higher on Pt than on TiO₂. From this, one can infer that the presence of Pt potentially enhances the kinetics of adsorption and/or desorption. This effect of Pt on the photocatalytic reactions is unfortunately not much explored, at least not as much as its role in assisting the charge separation.

On pure and Pt containing Degussa P-25, it was observed that presence of Pt can influence the adsorption amounts and kinetics of hydrogen and oxygen over TiO₂ (Uner et al. 2004). Indeed, improved oxygen adsorption amounts and adsorption kinetics were also observed in liquid phase photocatalysis in the presence of Pt (Kozlova and Vorontsov 2006). But this improvement in the adsorbed oxygen amounts was much greater than the Pt sites available, indicating that the presence of Pt improved the adsorption process by either spillover or by providing a capture zone. The effect of capture zone cannot be ruled out in the gas phase photocatalysis over Pt/TiO₂.

Table 2 Adsorption heats of oxygen, carbon monoxide, and water on Pt and TiO₂

Surface	Adsorbate	Adsorption mode	$E_{a,des}$ (kJ/mol)	ΔH_{ads} (kJ/ mol)	Ref
TiO ₂ (110)	H ₂ O	Molecular	71-90		Hugenschmidt et al. (1994)
TiO ₂ (110)	H ₂ O	Molecular		~90	Menetrey et al. (2003)
TiO ₂ (110)	H ₂ O	Dissociative		~120	Menetrey et al. (2003)
TiO ₂ (anatase)	CO	Molecular, σ - coordinated		60	Bolis et al. (1998)
Pd/TiO ₂ (110)	CO	Molecular	110		Bowker et al. (2002)
TiO ₂ (110)	CO	Molecular	38		Bowker et al. (2002)
1% Pt/ γ - Al ₂ O ₃	CO	Molecular		150	Uner and Uner (2005)
0.5% Pt/ TiO ₂	O ₂	Dissociative		320	Uner et al (2003)
1% Pt/TiO ₂	O ₂	Dissociative		380	Uner et al (2003)
1% Pt/ γ - Al ₂ O ₃	O ₂	Dissociative		400	Uner and Uner (2005)
TiO ₂ (110)	O ₂	Molecular	94		Gopel et al. (1983)
TiO ₂ (110)	O ₂	Molecular	108		Henderson et al. (1999)

The activation energy is coverage dependent, where is the fractional surface coverage of H₂O

The terms *capture zone*, *collection zone*, and *porthole effect* all describe similar phenomena. The capture zone effect is different from spillover in the sense that in spillover adsorption takes place in one segment of the surface and the adsorbed species migrate to the next to be stored or reacted there. On the contrary, adsorption by capture zone effect requires the impingement of the molecules both on the metal and the support. If the molecules striking on the support can be trapped long enough and if they possess enough mobility, they could eventually reach the metal particles to react there (Rumpf et al. 1988; Libuda and Freund 2005). Rumpf et al. (1988) indeed observed the turnover frequencies of CO₂ formation higher than that could be accounted for the sticking coefficients of CO on the Pd surface only over Pd/Al₂O₃. They developed a mathematical model to describe the capture zone, or collection zone around the metal particles. The kinetics of reaction is proportional to the ratio of the areas of the collection zone to the area of the particle; therefore, as the particle size decreased, the turnover frequencies increased.

CO adsorbs on Pd/TiO₂ surfaces by a precursor mechanism, with sticking coefficients independent of coverage (Bowker et al. 2002). Similar behavior is expected for Pt/TiO₂ systems. Global measurements were done in our laboratory to understand the effect of Pt on oxygen and carbon monoxide adsorption amounts over titania (Ozen 2001). The results are presented in Table 3 for oxygen and

Table 3 Oxygen adsorption on TiO₂ (Ozen 2001)

Pt wt %	μ mol Pt/g cat	μ mol O ₂ /g cat at 150 Torr	μ mol O ₂ /g cat. at 600 Torr
0	0	2.0	82.1
0.1	5.1	3.4	94.9
0.5	25.6	74.1	354.3
1.0	51.2	68.8	333.8

Table 4 Carbon monoxide adsorption on TiO₂ (Ozen 2001)

Pt wt %	μ mol Pt/g cat.	μ mol CO/g cat. at 150 Torr	μ mol CO/g cat. at 600 Torr
0	0	19.6	91.6
0.5	25.6	23.2	126.7
1.0	51.2	26.7	136.5

Table 4 for carbon monoxide adsorption over pure and platinumized titania. The amounts adsorbed at two different pressures, 150 and 600 Torr, were given for both CO and O₂. The adsorption isotherm of O₂ was represented by two Langmuir type curves, one of which showed saturation at around 150 Torr. It should also be noted that 150 Torr is very close to the partial pressure of oxygen in air at atmospheric pressure (160 Torr). 600 Torr was the upper limit of the adsorption apparatus for pressure measurements. Oxygen adsorption data at 150 Torr indicated little improvement upon doping titania with 0.1 wt% Pt, significant improvement when Pt loading was increased to 0.5%, further increase in Pt amounts did not increase the oxygen adsorption amounts. Similar conclusions could be inferred for CO adsorption as well. Our interpretation of the data without any further support from surface analysis studies is as follows: at the lowest loadings, Pt can be atomically dispersed on the surface, possesses enough mobility to penetrate subsurface layers of TiO₂, thus not changing the oxygen adsorption capacity of the surface much. As the Pt loading was increased to 0.5%, large stable crystallites were formed on the surface, which were capable of oxygen adsorption and dissociation. Further increase in the metal loading decreased the metal dispersions, and the metal support interface.

For oxygen adsorption data, the maximum observed in the saturation coverages at both 150 Torr and 600 Torr at 0.5% Pt loading is strongly correlated with the decrease in the metal dispersions measured on the same catalysts (Uner et al. 2003). This huge increase in oxygen adsorption amounts in the presence of Pt clearly indicated the catalytic role of the Pt in the overall photocatalytic reaction network. It should also be noted that the increase in the adsorption amounts was much higher than the new sites generated upon introduction of Pt in the system, even in the extreme situation of mono-dispersed Pt. In contrast to oxygen adsorption amounts, CO amounts increased in the presence of Pt, but only slightly (Table 4).

7 Photocatalytic CO Oxidation in the Presence of Pt

The key findings from the models presented in Sects. 4 and 5 can be listed as (1) the oxidation of the hydrocarbons was limited by the oxidation kinetics of a surface intermediate containing a single carbon species and (2) the catalyst deactivation was taking place by carbon deposition, which followed a carbon deposition rate at a carbon:site stoichiometry of 1:1. In the presence of Pt, primarily three processes take place that slow down the deactivation: (1) Pt enhances the ring-opening reactions for the oxidation of cyclic aromatic compounds (Mendez-Roman and Cardona-Martinez 1998; Fernandez-Garcia et al. 2007); (2) Larger molecules are cracked over TiO₂ and smaller molecules migrate onto Pt for further oxidation (Papaefthimiou et al. 1999). (3) The kinetics of the final oxidation step was enhanced in the presence of Pt (Vorontsov and Dubovitskaya 2004; Papaefthimiou et al. 1999). One can postulate a hydrocarbon oxidation mechanism, such that carbon-carbon bond breaking and carbon-hydrogen bond breaking are required before carbon-oxygen bond making. In such a situation, deactivation by coke deposition is justifiable. Carbon species striped off most of the hydrogen atoms cannot migrate over the surface due to the strong carbon to surface bonds required to compensate for the loss of carbon-hydrogen and carbon-carbon bonds. However, if the carbon containing species is oxidized to CO, reverse spillover of CO from TiO₂ to Pt surface is possible (Bowker et al. 2002).

CO oxidation over pure and Pt containing catalysts was studied by various groups (Vorontsov et al. 1997; Einaga et al. 2003; Hwang et al. 2003; Ozen 2001). All of these studies revealed that the CO oxidation reaction in the dark and under illumination took place over Pt sites. The dependency of the reaction rate on the incident light intensity was measured and compared for pure and platinumized TiO₂: over pure TiO₂ the reaction rate dependency on the light intensity went with a power of 0.5, while in the presence of Pt that value increased to 0.7. Furthermore, oxidation of CO proceeded with oxygen species generated from gas phase oxygen, but not from the OH on the surface and the presence of water vapor was detrimental for the photocatalytic CO oxidation over both TiO₂ and Pt (Einaga et al. 2003). The active species for CO oxidation was reported to be gas phase oxygen. Other oxidizers such as H₂O and N₂O were not active (Hwang et al. 2003). The CO oxidation studies clearly indicate the role of Pt beyond simply modifying the photocatalysts for the charge separation. Apparently, the CO oxidation is taking place over Pt sites, while photocatalytic component of the reaction is taking place via TiO₂ surface. However, the implications of CO oxidation reaction to hydrocarbon oxidation reactions should be treated with caution. During hydrocarbon photo-oxidation, carbon oxidation to carbon dioxide takes place which was accompanied by oxygen reduction to water. Therefore, electron-hole pairs generated upon illumination are simultaneously utilized by different species. On the contrary, during CO oxidation, reduced (oxygen) and oxidized (CO) species are required to form bonds, thus, spatial proximity is also required. Finally, it is worthwhile to note that in the presence of CO excessive wetting of Pt on TiO₂ surfaces was observed

(Steinruck et al. 1995). When CO and Pt were co-deposited, Pt particles were spread on the surface of TiO₂, apparently the presence of CO influencing the interfacial energies between Pt and TiO₂.

In this section, a very brief summary was given about the effect of Pt on the CO photooxidation kinetics. The primary conclusion is that the thermal component of a photocatalytic reaction cannot be ruled out, especially in the presence of a noble metal on the surface. Carefully controlled and detailed low temperature studies are required to quench the thermal component of the photocatalytic reactions completely, especially in the presence of noble metals in order to reveal the pure photocatalytic reaction components and the mechanisms.

8 Photocatalytic CO₂ Reduction on Pt/TiO₂

The majority of the photocatalytic CO₂ reduction work published so far comes from Anpo group. The research in Anpo's group is oriented toward introducing visible light activity to TiO₂. In a recent publication, they reviewed how visible light activity can be introduced to TiO₂ (Anpo and Takeuchi 2003). In this section, a recent work from our group will be presented about how Pt addition influenced the CO₂ reduction ability of TiO₂ thin and thick films (Ozcan et al. 2006). Thin and thick films of TiO₂ were prepared over glass beads. Pt was incorporated in the films either by adding the precursor in the sol [Pt(in)] or on the films by wet impregnation [Pt(on)]. The UV activity for CO₂ reduction reaction of these catalysts proceeded in the following order TiO₂ < Pt(in)TiO₂ < Pt(on)TiO₂. The activity enhancement of Pt(in) catalysts was probably due to the segregated Pt atoms or clusters to the surface of TiO₂ films during calcination. The films themselves did not exhibit any activity under visible light irradiation; however, when doped with organic sensitizers, visible light activity was observed. Interestingly, when the organic sensitizers were introduced in the system, pure TiO₂ was performing better than Pt(in)TiO₂. Apparently, Pt in the TiO₂ structure acted as recombination centers and annihilated the charge carriers transferred to the semiconductor by the organic sensitizers. On the other hand sensitizer molecules on Pt(on)TiO₂ exhibited the best performance. We interpreted this situation as electrons transferred to TiO₂ more efficiently in the presence of Pt. Our data supported the idea that the electrons were generated by the sensitizers, sensitizers were adsorbed on Pt, and electrons had to be transported through Pt ballistically, with their own momentum, (Nienhaus 2002; McFarland and Tang 2003) to TiO₂ for further chemistry.

9 The Acidity, Pt, and Gas Phase Photocatalysis

Schwab effect of the first kind is described as the situation when the catalytic activity of a semiconductor is affected by its contact with a metal (Boudart and Djega-Mariadassou 1984). This is an identical situation of Schottky effect.

However, during thermal catalytic reactions, transport of electrons play a minor role in comparison to the rest of chemistry going on around the surface. A catalyst exhibiting Schwab effect should have altered OH group acidities depending on the direction of the charge transport. The acidity of the reaction medium was proven to improve the photocatalytic activity of pure and Pt containing TiO₂ Kozlova and Vorontsov (2006); Kozlov et al. (2003). The surface of TiO₂ dominated by Ti⁴⁺ cations possess Lewis acidity as correlated by the relative bond strengths of the adsorbing Lewis bases: ammonia, diethyl amine, and dimethyl amine (Farfan-Arribas and Madix 2003). In the presence of Pt, the surface acidity of TiO₂ can change significantly. The point of zero charge, pH at which the surface is neutral, decreased as the Pt amounts on the surface increased. This effect was attributed to the depletion of the semiconductor from electrons as a result of charge separation due to the Schottky barrier. The net effect of electron depletion from the semiconductor was reflected in the increase in the OH group Brønsted acidities (Jaffrezic-Renault et al. 1986).

Modification of TiO₂ by other oxides is also known to alter the acidic character and therefore the reactivity of the surface. For example, SiO₂, TiO₂, and SiO₂-TiO₂ cofumed mixed oxide were investigated by IR of adsorbed pyridine. The native oxides possessed Lewis acidity, while the mixed oxide possessed Brønsted acidity as indicated by the IR bands. The mixed oxide catalyst is more active and also the deactivation is slower, indicating the role of Brønsted acidity in the photocatalytic decomposition of toluene. The Brønsted acid sites may have assisted in the ring opening reactions. Furthermore, toluene adsorption capacity of the mixed oxide also increased due to the change in the nature of the acidity (Mendez-Roman and Cardona-Martinez 1998). Incorporation of W⁺⁶ also influences the acidic nature of TiO₂. W⁺⁶ centers provide both Brønsted and Lewis acid centers on the catalyst. These improved acidic character of the surface influence adsorption and reaction of molecules with polarized functional groups with affinities for the acidic surfaces. The loading of WO₃ was important because too high loading can start to serve as the recombination centers of charge carriers, decreasing catalytic activity (Keller et al. 2003).

10 Optimum Pt Loading, Optimum Particle Size

The Pt or metal loading seems to improve the photocatalytic reactions in the gas or in the liquid phase only to a certain extent. Further loading is reported to be detrimental in the gas phase mineralization of butyl acetate centers (Keller et al. 2003); in photoelectrochemical reduction of methyl orange (Li and Li 2002); and in gas phase photooxidation of ethanol and acetone (Vorontsov and Dubovitskaya 2004) to name a few examples. Oxygen isotope exchange also exhibited a maximum in Pt loading (Courbon et al. 1984). These and other effects were explained by several postulates as follows: (1) the metal domain size beyond an optimum inhibits the back diffusion of hydroxyl peroxy radicals (Haick and Paz 2003) and (2) as the

metal loading increases, the metals start to act as recombination centers (Keller et al. 2003; Vorontsov and Dubovitskaya 2004).

Here the author will postulate two speculative theories, both of which needs to be verified by careful studies. The first theory is based on the capture zone effect. The TOF of the reaction involving collection zone increases with the ratio of the area of the collection zone to the area of the particle (Rumpf et al. 1988). As the loading increases if the particle size remains constant, the collection zones overlap and the rates increase. However, if the loading increases and the metal particle size also increases, the effectively utilized surface area decreases and the TOFs decrease.

The second and more speculative theory is based on the ballistic transport of electrons in the metals. This phenomenon is receiving much attention in the literature recently (Nienhaus 2002). McFarland and Tang (2003) have published the performance of a new photovoltaic device, their design was based on the ballistic transport, of electrons through the metal layer between a dye sensitizer and TiO_2 instead of a redox pair used in dye sensitized solar cells. In addition to this, Park and Somorjai (2006a, b) published a series of articles on how they designed Schottky diodes involving a metal supported on TiO_2 to generate currents from the chemical energy released during an exothermic reaction. On this system, they generated hot electrons which can be ballistically transported to the semiconductor and generated chemocurrents. In both systems, the ballistic transport can take place on the condition that the excess kinetic energies of the generated electrons are larger than the Schottky barrier and the metal size is smaller than the mean free path of the electron.

11 Conclusions

In this chapter, the author tried to establish that the metal incorporation in TiO_2 can initiate several surface processes. The most important and widely acknowledged process is the formation of a Schottky barrier for charge separation. But the following processes cannot be ruled out as dominant mechanisms.

1. Enhanced kinetics of oxygen adsorption and dissociation over Pt, followed by oxygen spillover to the support for further chemistry;
2. Improved kinetics of ring opening reactions at the Pt sites for the carbonation of cyclic or aromatic compounds;
3. Reverse spillover of CO formed over TiO_2 to Pt sites for further oxidation;
4. Increased acidity of the OH groups on TiO_2 as a result of the charge separation induced by the presence of Pt;
5. Altered semiconductor electronic structure of TiO_2 due to the migration of Pt atoms to the bulk of the semiconductor, or due to the decoration of the metal by semiconductor moieties, also known as SMSI effect.

The present challenge in front of catalysis research is to elucidate the relative contributions of each of these effects in order to be able to design improved photocatalysts for more sophisticated reaction systems.

Acknowledgments The financial support for this work was provided by Turkish Scientific and Technological Research Council (TUBITAK) under research grants no MISAG 96 and CAYDAG 106Y075. Esen Ozbay is acknowledged for the reproduction of Fig. 1 and Fig. 2.

References

- Adams DM, Brus L, Chidsey CED, Creager S, Creutz C, Kagan CR, Kamat PV, Lieberman XM, Lindsay OS, Marcus RA, Metzger RM, Michel-Beyerle ME, Miller JR, Newton MD, Rolison DR, Sankey O, Schanze KS, Yardley J, Zhu X (2003) Charge transfer on the nanoscale: current status. *J Phys Chem B* 107:6668–6697
- Alberici RM, Jardim WF (1997) Photocatalytic destruction of VOCs in the gas phase using titanium dioxide. *Appl Catal B* 14:55–68
- Anpo M (1997) *Surface photochemistry*. Wiley, Chichester
- Anpo M (2004) Preparation, characterization, and reactivities of highly functional titanium-oxide based photocatalysts able to operate under UV-visible light irradiation: approaches in realizing high efficiency in the use of visible light. *Bull Chem Soc Jpn* 77:1427–1442
- Anpo M, Takeuchi M (2003) The design and development of highly reactive titanium oxide photocatalysts operating under visible light irradiation. *J Catal* 216:505–516
- Anpo M, Aikawa N, Kubokawa Y (1984) Photocatalytic hydrogenation of alkynes and alkenes with water over TiO₂. Pt-loading effect on the primary processes. *J Phys Chem* 88:3998–4000
- Anpo M, Chiba K, Tomonari M, Coluccia S, Che M, Fox MA (1991) Photocatalysis on native and platinum loaded TiO₂ and ZnO catalysts: origin of different reactivities on wet and dry metal oxides. *Bull Chem Soc Jpn* 64:543–551
- Blount, M.C. and Falconer, J.L. (2001) Characterization of adsorbed species on TiO₂ after photocatalytic oxidation of toluene. *J. Catal.* 200:21–33
- Bolis V, Cerrato G, Magnacca G, Morterra C (1998) Surface acidity of metal oxides. Combined microcalorimetric and IR-spectroscopic studies of variously dehydrated systems. *Thermochim Acta* 312:63–77
- Boudart M, Djega-Mariadassou G (1984) *Kinetics of heterogeneous catalytic reactions*. Princeton University Press, Princeton, NJ
- Bowker M, Stone P, Bennett R, Perkins N (2002) CO adsorption on a Pd/TiO₂(110) model catalyst. *Surf Sci* 497:155–165
- Channon M (1997) *Homogeneous photocatalysis*. Wiley, Chichester
- Chen M, Goodman DW (2006) Catalytically active gold: from nanoparticles to ultrathin films. *Acc Chem Res* 39:739–746
- Courbon H, Herrmann J-M, Pichat P (1984) Effect of platinum deposits on oxygen adsorption and oxygen isotope exchange over variously pretreated, ultraviolet-illuminated powder TiO₂. *J Phys Chem* 88:5210–5214
- Diebold U (2003) The surface science of titanium dioxide. *Surf Sci Rep* 48:53–229
- Einaga H, Harada M, Futamura S, Ibusuki T (2003) Generation of active sites for CO photooxidation on TiO₂ by platinum deposition. *J Phys Chem B* 107:9290–9297
- Emeline AV, Ryabchuk VK, Serpone N (2005) Dogmas and misconceptions in heterogeneous photocatalysis. Some enlightened reflections. *J Phys Chem B* 109:18515–18521
- Falconer JL, Magrini-Bair KA (1998) Photocatalytic and thermal catalytic oxidation of acetaldehyde on Pt/TiO₂. *J Catal* 179:171–178

- Farfan-Arribas E, Madix RJ (2003) Characterization of the acid-base properties of the TiO₂(110) surface by adsorption of amines. *J Phys Chem B* 107:3225–3233
- Fernandez-Garcia M, Fuerte A, Hernandez-Alonso MD, Soria J, Martinez-Arias A (2007) Platinization of sunlight active Ti-W mixed oxide photocatalysts. *J Catal* 245:84–90
- Fox MA (1989) Mechanistic photocatalysis in organic synthesis. In: Serpone N, Pelizzetti E (eds) *Photocatalysis: fundamentals and applications*. Wiley, New York, pp 421–456
- Fox MA, Dulay MT (1993) Heterogeneous photocatalysis. *Chem Rev* 93:341–357
- Fu XZ, Zeltner WA, Anderson MA (1995) The gas-phase photocatalytic mineralization of benzene on porous titania-based catalysts. *Appl Catal B* 6:209–224
- Furube A, Asahi T, Masuhara H, Yamashita H, Anpo M (2001) Direct observation of a picosecond charge separation process in photoexcited platinum-loaded TiO₂ particles by femtosecond diffuse reflectance spectroscopy. *Chem Phys Lett* 336:424–430
- Gopel W, Rucker G, Feierabend R (1983) Intrinsic defects of TiO₂(110): interaction with chemisorbed O₂, H₂, CO, and CO₂. *Phys Rev B* 28:3427–3438
- Haick H, Paz Y (2001) Remote photocatalytic activity as probed by measuring the degradation of self assembled monolayers anchored near microdomains of titanium dioxide. *J Phys Chem B* 105:3045–3051
- Haick H, Paz Y (2003) Long range effects of noble metals on the photocatalytic properties of titanium dioxide. *J Phys Chem B* 107:2319–2326
- Haruta M, Yamada N, Kobayashi T, Iijima S (1989) Gold catalysts prepared by coprecipitation for low temperature oxidation of hydrogen and of carbon monoxide. *J Catal* 115:301–309
- Henderson MA, Epling WS, Perkins CL, Peden CHF, Diebold U (1999) Interaction of molecular oxygen with the vacuum-annealed TiO₂(110) surface: molecular and dissociative channels. *J Phys Chem* 103:5328–5337
- Hugenschmidt MB, Gamble L, Campbell CT (1994) The interaction of H₂O with a TiO₂(110) surface. *Surf Sci* 302:329–340
- Hurum DC, Agrios AG, Gray KA, Rajh T, Thurnauer MC (2003) Explaining the enhanced photocatalytic activity of Degussa P25 mixed phase TiO₂ using EPR. *J Phys Chem B* 107:4545–4549
- Hwang S, Lee MC, Choi W (2003) Highly enhanced photocatalytic oxidation of Co on titania deposited with Pt particles: kinetics and mechanism. *Appl Catal B* 46:49–63
- Jaffrezic-Renault N, Pichat P, Foissy A, Mercier R (1986) Effect of deposited Pt particles on the surface charge of TiO₂ aqueous suspensions by potentiometry, electrophoresis, and labeled ion adsorption. *J Phys Chem* 90:2733–2738
- Kamat PV (1993) Photochemistry on nonreactive and reactive (semiconductor) surfaces. *Chem Rev* 93:267–300
- Keller V, Bernhardt P, Garin F (2003) Photocatalytic oxidation of butyl acetate in vapor phase on TiO₂, Pt/TiO₂ and WO₃/TiO₂ catalysts. *J Catal* 215:129–138
- Kozlov D, Bavykin D, Savinov E (2003) Effect of the acidity of TiO₂ surface on its photocatalytic activity in acetone gas-phase oxidation. *Catal Lett* 86:169–172
- Kozlova EA, Vorontsov AV (2006) Noble metal and sulfuric acid modified TiO₂ photocatalysts: mineralization of organophosphorous compounds. *Appl Catal B* 63:114–123
- Li FB, Li XZ (2002) Surface characterization and photocatalytic reactivity of innovative Ti/TiO₂ and Ti/Pt–TiO₂ mesh photoelectrodes. *J Appl Electrochem* 32:203–210
- Libuda J, Freund H-J (2005) Molecular beam experiments on model catalysts. *Surf Sci Rep* 57:157–298
- Linsebigler AL, Lu G, Yates JT Jr (1995) Photocatalysis on TiO₂ surfaces: principles, mechanisms, and selected results. *Chem Rev* 95:735–758
- Litter MI (1999) Heterogeneous photocatalysis. Transition metal ions in photocatalytic systems. *Appl Catal B* 23:89–114
- McFarland EW, Tang J (2003) A photovoltaic device structure based on internal electron emission. *Nature* 421:616–618
- Mendez-Roman R, Cardona-Martinez N (1998) Relationship between the formation of surface species and catalyst deactivation during the gas phase photocatalytic oxidation of toluene. *Catal Today* 40:353–365

- Menetrey M, Markovits A, Minot C (2003) Reactivity of a reduced metal oxide surface: hydrogen, water and carbon monoxide adsorption on oxygen defective rutile TiO₂(110). *Surf Sci* 524:49–62
- Nienhaus H (2002) Electronic excitations by chemical reactions on metal surfaces. *Surf Sci Rep* 45:1–78
- Ollis DF (2005) Kinetics of liquid phase photocatalyzed reactions: an illuminating approach. *J Phys Chem B* 109:2439–2444
- Ozbek S, Uner DO (1999) The deactivation behavior of the TiO₂ used as photocatalyst for benzene oxidation. *Stud Surf Sci Catal* 126:411–414
- Ozcan O, Yukruk F, Akkaya EU, Uner D (2006) Dye sensitized artificial photosynthesis in the gas phase over thin and thick TiO₂ films under UV and visible light irradiation. *Appl Catal B* 71:291–297
- Ozen I (2001) Thermal and photocatalytic oxidation of carbon monoxide over titanium dioxide-effects of platinum deposition, MS Thesis, Middle East Technical University, Ankara
- Ozen I, Uner D (2001) Heterogeneous photo and thermal catalytic oxidation of CO: effects of metal deposition. *Stud Surf Sci Catal* 133:445–452
- Papaefthimiou P, Ioannides T, Verykios XE (1998) Performance of doped Pt/TiO₂ (W6⁺) catalysts for combustion of volatile organic compounds (VOCs). *Appl Catal B* 15:75–92
- Papaefthimiou P, Ioannides T. and Verykios X.E. (1999) VOC removal: investigation of ethylacetate oxidation over supported Pt catalysts *Catal. Today* 54: 81–92
- Park JY, Somorjai GA (2006a) Energy conversion from catalytic reaction to hot electron current with metal-semiconductor Schottky nanodiodes. *J Vac Sci Technol B* 24:1967–1971
- Park JY, Somorjai GA (2006b) The catalytic nanodiode: detecting continuous electron flow at oxide-metal interfaces generated by a gas-phase exothermic reaction. *Chemphyschem* 7:1409–1413
- Riegel G, Bolton JR (1995) Photocatalytic efficiency variability in TiO₂ particles. *J Phys Chem* 99:4215–4224
- Rothenberger G, Moser J, Gratzel M, Serpone N, Sharma DK (1985) Charge carrier trapping and recombination dynamics in small semiconductor particles. *J Am Chem Soc* 107:8054–8059
- Rumpf F, Poppa H, Boudart M (1988) Oxidation of carbon monoxide on palladium: role of the alumina support. *Langmuir* 4:722–728
- Schiavello M (1997) *Heterogeneous photocatalysis*. Wiley, Chichester
- Serpone N, Pelizzetti E (1989) *Photocatalysis: fundamentals and applications*. Wiley, New York
- Steinruck H-P, Pesty F, Zhang L, Madey TE (1995) Ultrathin films of Pt on TiO₂ (110): growth and chemisorption induced surfactant effects. *Phys Rev B Condens Matter* 51:2427–2439
- Thompson TL, Yates JT (2006) Surface science studies of the photoactivation of TiO₂: new photochemical processes. *Chem Rev* 106:4428–4453
- Uner M, Uner D (2005) Adsorption calorimetry in supported catalyst characterization: adsorption structure sensitivity on Pt/γ-Al₂O₃. *Thermochim Acta* 434:107–112
- Uner D, Tapan NA, Ozen I, Uner M (2003) Oxygen adsorption over Pt/TiO₂ catalysts. *Appl Catal A Gen* 251(2):225–234
- Valden M, Lai X, Goodman DW (1998) Onset of catalytic activity of gold clusters on titania with the appearance of nonmetallic properties. *Science* 281:1647–1650
- Vorontsov AV, Dubovitskaya VP (2004) Selectivity of photocatalytic oxidation of gaseous ethanol over pure and modified TiO₂. *J Catal* 221:102–109
- Vorontsov AV, Savinov EN, Barannik GB, Troitsky VN, Parmon VN (1997) Quantitative studies on the heterogeneous gas-phase photooxidation of CO and simple VOCs by air over TiO₂. *Catal Today* 39:207–218
- Vorontsov AV, Kozlov DV, Smirniotis PG, Parmon VN (2005) TiO₂ photocatalytic oxidation: II. Gas-phase processes. *Kinet Catal* 46(3):422–436
- Yamakata A, Ishibashi T, Onishi H (2001) Time-resolved infrared absorption spectroscopy of photogenerated electrons in platinumized TiO₂ particles. *Chem Phys Lett* 333:271–277

Chapter 21

Photoreactions of Organic Compounds with TiO₂ Single Crystal Surfaces

Hicham Idriss

Abstract In this work the photoreactions of two organic molecules: acetic acid and ethanol, over rutile TiO₂(110), TiO₂(011) and the (011) reconstructed surface of TiO₂(001) single crystals are presented. Comparison with the corresponding dark reaction is also given. The steady state reaction at 320 K of acetic acid over the {011}-faceted surface of TiO₂(001) under UV irradiation indicated the formation of methane, ethane and CO₂. These are the expected products of the so-called “Photo-Kolbe” reaction of acetic acid. While the formation of methane was not sensitive to the addition of molecular oxygen and could be carried out in UHV conditions catalytically that of ethane required the continual addition of gas phase molecular oxygen for its photo-catalytic production to occur. The quantum yield of the reaction was computed equal to 0.05, while the depletion layer width and barrier height were found equal to 18 nm and 0.18 eV, respectively. The photoreaction of ethanol conducted over the rutile TiO₂(110) surface indicated that, oxidation of ethoxides to acetate species occurs under molecular oxygen within the investigated pressure range (10⁻⁶–10⁻⁹ torr). In the absence of molecular oxygen (base pressure 2 × 10⁻¹⁰ torr) or in presence of molecular hydrogen with a pressure up to 10⁻⁶ torr negligible photo-reaction occurred. Fitting the observed decay of ethoxides upon irradiation with a Langmuir-type analysis, as a function of gas phase molecular oxygen, the binding constant of the later was found equal to ca. 2 × 10⁷ torr⁻¹. This value, together with the initial surface coverage of ethoxide of 0.5 with respect to surface Ti atoms, may indicate that the number of adsorbed molecular oxygen needed for maximum reaction rate is similar to that of the free surface Ti atoms.

H. Idriss (✉)

Department of Chemistry, University of Aberdeen, Aberdeen, UK

e-mail: h.idriss@abdn.ac.uk

1 Introduction

Photoreactions on TiO₂ single crystal surfaces have received increasing interest in recent years mainly due to the high potential of TiO₂ in light harvesting devices. Many reviews have been devoted to photochemical processes over TiO₂ powder (Ryabchuk 2004; Ni et al. 2007; Carp et al. 2004) and one on TiO₂ single crystal (Linsebigler et al. 1995) in which detailed information related to the motivation and basic concepts of the processes involved are given. Although the state of research surely deserves a review now, this chapter is not intended as a review article but as a focus on some specific results related to the reactions of two organic compounds on TiO₂ single crystal surfaces. The chapter does not include detailed structural, electronic and spectroscopic analysis of TiO₂ surfaces as many other relevant reviews and research articles have presented these in comprehensive ways (Diebold 2003; Henderson 2002; Zapol and Curtiss 2007; Lindsay et al. 2005, among others). In the last decade several organic compounds were studied, within the framework of photoreaction over model TiO₂ surfaces and these include ethanol (CH₃CH₂OH) (Jayaweera et al. 2007), acetic acid (CH₃COOH) (Wilson and Idriss 2003; Idriss et al. 2002), trimethylacetic acid (CH₃)₃CCOOH (White et al. 2003; Henderson et al. 2006; Lyubinetsky et al. 2007), 2-chloro-ethyl ethyl sulfide (ClCH₂CH₂SCH₂CH₃) (Thompson et al. 2004) and acetone (CH₃COCH₃) (Henderson 2005a, b). This chapter's focus is on two molecules: acetic acid and ethanol. Acetic acid is an ideal prototype of carboxylic acids and ethanol is, in addition of being the alcohol analogue of the acetic acid, a promising energy carrier for many applications because it is regarded as a bio-renewable compound. The surface of rutile TiO₂(110) single crystal is shown in Fig. 1 with a brief explanation as it has been presented in many details elsewhere. The other surface, the (011), is shown in Fig. 2. The surface does reconstruct to a 2 × 1 (Di Valentin et al. 2005; Beck et al. 2004; Dulub et al. 2006; Beck et al. 2004; Bech et al. 2005). Initial structure determination images indicated the presence of a titanyl group (Ti=O), or terminal oxygen. This structure was based on STM (Di Valentin et al. 2005; Beck et al. 2004), DFT computation (Dulub et al. 2006) and ESDIAD (Diebold 2006) results. More recently the structure was revisited by Torrelles et al. 2008 and Gong et al. A more convincing was obtained not invoking Ti=O bonds; this model is presented in Figure 2.

A brief description of the photo-excitation process of TiO₂ too follows. Unlike metals, which have a continuum of electronic states, semiconductors contain a “void” energy region called the band gap (E_{bg}) extending from the top of the valence band (VB) to the bottom of the conduction band (CB). The preliminary process for heterogeneous catalysis of inorganic and organic molecules by semiconductors is the creation of electron-hole pairs. In order to remove an electron from the VB, radiation with a suitable energy must be used such that $h\nu$ has energy greater than or equal to the band gap, where h is Planck's constant (6.626×10^{-34} J s) and ν is the frequency of light (s^{-1}). Following this, the fate of the electron and hole may pursue several pathways. Of interest to us are those at the surface or which have migrated to the surface so that they may combine with an

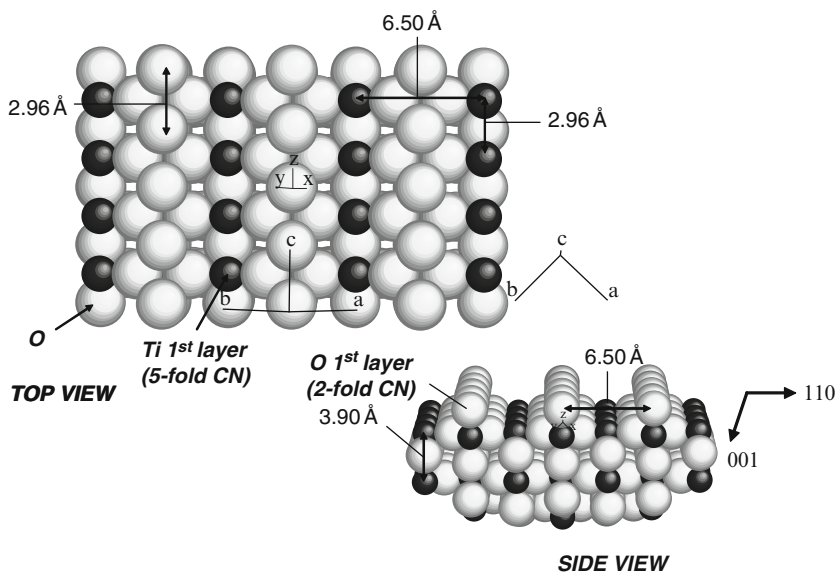


Fig. 1 Schematic representation of the surface of rutile TiO₂(110)-(1 × 1). Dark balls: Ti⁴⁺, light balls O²⁻, the surface consists of alternating rows of Ti_{5c} and O_{2c} along the [001] direction

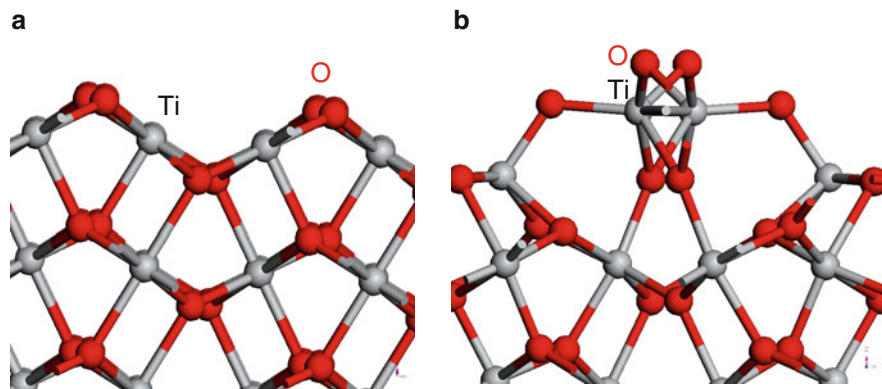


Fig. 2 Fig. 2 TiO₂(011) surface. (a) The 1 × 1 terminated TiO₂(011) surface represents alternating layers of two- and threefold coordinated O atoms, with fivefold coordinated Ti atoms sandwiched between. Ti atoms undergo lateral relaxation due to unbalanced surface oxygen coordination. (b) The 2 × 1 reconstructed surface of the TiO₂(011) features fivefold Ti atoms and twofold O atoms.

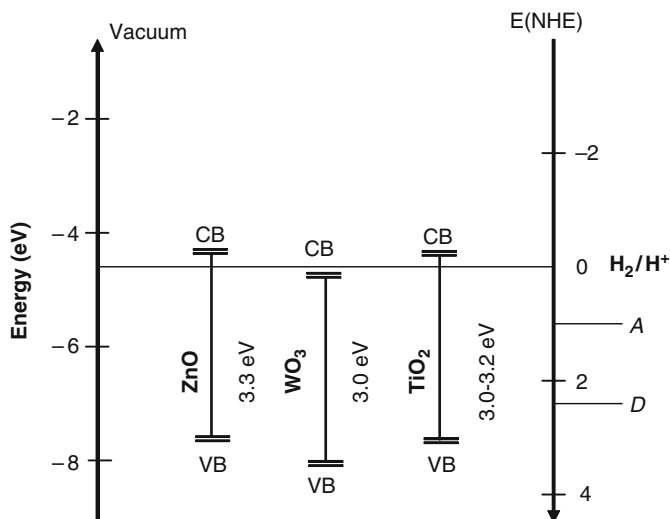


Fig. 3 A schematic of the band gap of three metal oxides with a very similar band gap: ZnO, WO₃ and TiO₂. *VB* valence band, *CB* conduction band, *A* electron acceptor molecular level, *D* electron donor molecular level. *NHE* normalized hydrogen electrode with respect to the H⁺/H₂ pair

electron acceptor such as O₂ and an electron donor such as ROH, where R is an alkyl chain, for an example. Because of energy transfer restrictions the electron acceptor energy level needs to be lower than the conduction band level and the electron donor energy level needs to be higher than the energy level of the valence band. This process is schematically presented in Fig. 3.

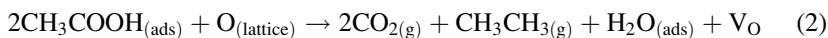
In the figure three metal oxides are represented: TiO₂, ZnO and WO₃. The three have very similar band gap energy yet they differ considerably in their photocatalytic activity. ZnO has a high photo-luminescence yield (thus the electron-hole recombination process is very efficient, with high yield; if Y represents the yield of photoreaction it is then proportional to the ratio of the rate constant of electron (or charge) transfer (k_{ET}) over that of the recombination process k_R): $Y \propto \frac{k_{ET}}{k_R}$ and is thus not a highly active photo-catalyst. The CB band level of WO₃ is below that of TiO₂ or ZnO as well as the H⁺/H₂ levels. This for example makes the polycrystalline WO₃ not active for water splitting to H₂ and O₂. Chemical stability is also another factor for a successful semiconductor. In the case of ZnO, for example, the decomposition/desorption of organic molecules may take Zn cations with them (such as the decomposition of carboxylate species (Idriss and Barteau 1992; Vohs and Barteau 1989; Barteau 1996; Halevi and Vohs 2006)) and this would affect the surface atomic order. This is not the case for TiO₂. In general, our present knowledge of the surfaces and surface reactions of TiO₂ single crystals is far higher than that of ZnO and WO₃ and probably any other metal oxide.

Considerable effort is presently devoted to doping of TiO₂ with anions such as nitrogen anions in order to decrease its band gap by creating electronic states below the conduction band and thus allowing the doped material to absorb energy in the

visible light, while keeping the conduction band electronic states and levels unchanged (Bever et al. 2006; Diwald et al. 2004). This work is at present in its initial stage and only sporadic surface reactions have been studied.

2 Acetic Acid on TiO₂(011) Single Crystal

Our first example involves the reaction of acetic acid over the (011) surface of reconstructed TiO₂(001) rutile single crystal. Several detailed studies have been conducted concerning the photoreactions of acetic acid over TiO₂ powders. The products and intermediates observed have been investigated using several techniques including infra-red (IR) (Liao et al. 2001), mass spectroscopy (Muggli and Falconer 1999a, b), electron spin resonance (Nosaka et al. 1996), and photo-electrochemical studies (Kraeutler and Bard 1978 among others). The main reaction has been termed Photo-Kolbe with the products being ethane, methane, and carbon dioxide. The two reaction pathways identified are as follows:



where (ads) stands for adsorbate, (g) for gas and V_O for surface oxygen vacancy.

The reactions of carboxylic acids were studied under UV light by several authors (Ollis et al. 1984; Muggli and Falconer 1999ab). Reaction [1] is proposed to occur via a methyl radical ($\cdot\text{CH}_3$) which after recombination with a hydrogen radical ($\cdot\text{H}$) produces methane and CO₂, while reaction [2] is proposed to occur via a recombination of two ($\cdot\text{CH}_3$) molecules forming ethane, CO₂, and H₂O. These species have been thoroughly investigated, with perhaps the most compelling evidence coming from a study involving mono-deuterated acetic acid (CH₃COOD) (Muggli et al. 1999). The authors found no incorporation of deuterium into ethane but D₂O and CH₃D did form in high yield, indicating the simple reaction scheme is indeed correct. Perhaps the most important difference is that reaction [2] requires lattice oxygen: addition of oxygen into the gas phase increased the production of ethane (Muggli et al. 1999).

Acetic acid when adsorbed on rutile TiO₂(011) and (110) single crystals is dissociated into acetate species (CH₃COO⁻), bound to titanium atoms, and the proton forming (-OH) with the twofold surface oxygen atoms in the case of the (110) surface and most likely the onefold oxygen atom in the case of the 2 × 1 (011) surface. Over TiO₂(110) single crystal the carboxylate is bound in a bidentate configuration, with a saturation coverage of 0.5 or close (Idriss et al. 2002; Cocks et al. 1997a; Guo et al. 1997; Guo and Williams 1999; Hayden et al. 1999; Sayago et al. 2004; Fukui and Iwasawa 2000). These species have been well studied via X-ray photoelectron spectroscopy (XPS) (Idriss and Barteau 2000; Kim and Barteau 1990a, b), ultra-violet photoelectron spectroscopy (UPS) (Kim et al. 1998), temperature programmed

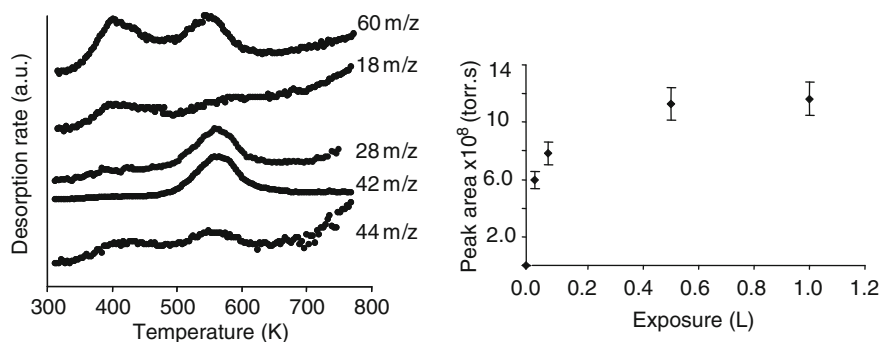


Fig. 4 TPD (*left*) and computed total desorption of products (*right*) of acetic acid on the {011}-faceted surface of TiO₂(001) single crystal. The exposure of acetic acid was not corrected to gauge sensitivity. Although the data at 0.5 and 1 L are marginally affected by the pumping speed those at 0.05 and 0.1 L might

desorption (TPD) (Henderson 1997), electron stimulated desorption ion angular distributions (ESDIAD) (Cocks et al. 1997b), and scanning tunneling microscopy (STM) (Morikawa et al. 2004). Although less work has been devoted to the reaction of acetic acid over the (011) surface in the dark/dark surface, it appears based on DFT computation and XPS (McGill and Idriss 2006; quah et al. 2010) that the most stable adsorption configuration is that of a bidentate. This theoretical result is in line with TPD results of acetic acid where the acetate desorption peak saturates at about 0.5 L exposure, Fig. 4.

The dark reaction of acetic acid is best presented first as a reference guide (Wilson and Idriss 2002, 2003). On the {011}-faceted surface acetic acid (m/z 60) was mainly dehydrated to ketene (m/z 42) and water (at 570 K). Some decomposition to CO, CO₂ at 610 K also occurred Fig. 4. More information regarding the dehydration reaction of acetic acid to ketene may be found in (Barteanu 1996; Titheridge et al. 2003).

2.1 Steady State Reactions of Acetic Acid Under UV Irradiation

In the absence of UV no other products but acetic acid were observed at the reaction temperature (320 K). Steady state with UV illumination was conducted at several acetic acid pressures (as monitored by its 60 m/z signal) between 5×10^{-10} and 6×10^{-7} torr at ca. 320 K. Figure 5 shows a representative data conducted on the {011}-faceted TiO₂(001) single crystal surface with acetic acid pressure equal to 2.5×10^{-9} torr in the presence of background oxygen molecules (non-calibrated background of molecular oxygen signal estimated less than 5×10^{-10} torr). Three products, carbon dioxide, methane and ethane are clearly seen as a jump in the line spectra from the initial baseline value. Both CO₂ (m/z 44) and methane (m/z 16)

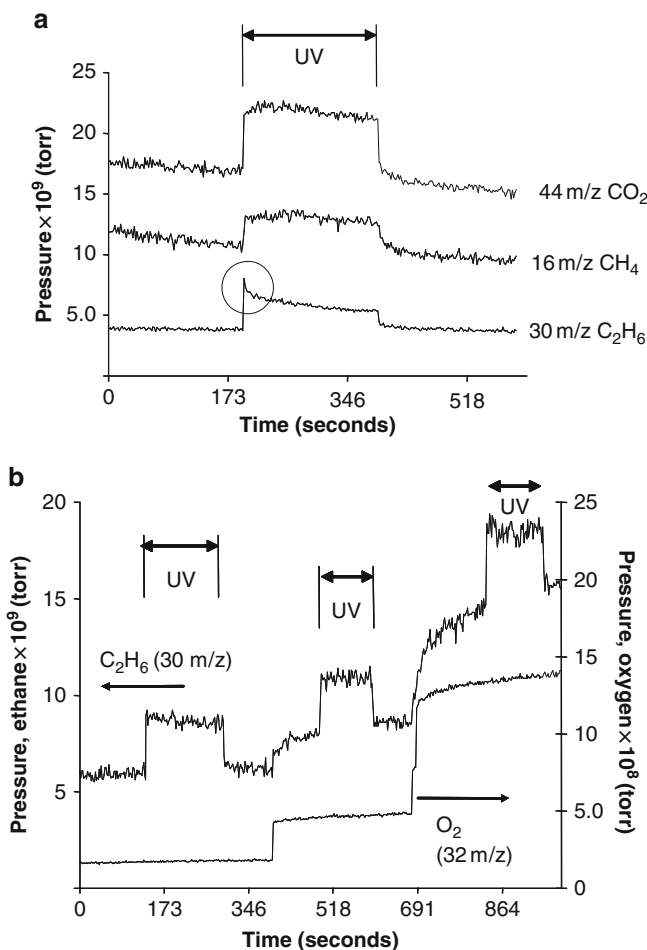


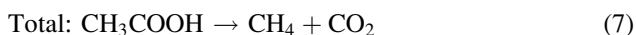
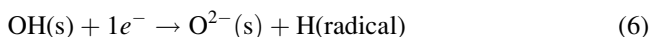
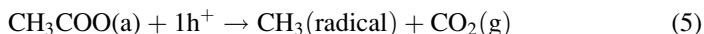
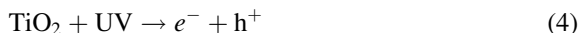
Fig. 5 (a) Steady-state acetic acid pressure 2.5×10^{-9} torr on the {011}-faceted TiO₂(001) surface. (b) Effect of O₂ pressure on the formation of ethane from acetic acid under UV

reach a steady state of formation as the UV shutter is opened, while in contrast ethane (m/z 30) formation reaches a high value initially and drops to a steady value after a short time (<20 s).

The catalytic formation of ethane is associated with the consumption of lattice oxygen, reaction [2] that appears to be regenerated by gas phase O₂, since in the absence of gas phase oxygen ethane formation decreases with time Fig. 5. A CH₃ radical that is formed by the decomposition of acetate may either combine with a H radical to give methane or with another CH₃ radical to give ethane.

Since the formation of methane does not necessarily require the presence of oxygen then acetates, surface hydroxyls and the electron-hole pairs are the key components.

Upon UV irradiation and electron transfer, from the O2p to the Ti3d orbitals, acetate species may react with a hole by regenerating an electron and forming CO₂ and one methyl radical. The methyl radical may then react with a hydrogen atom of a surface hydroxyl making CH₄ and the remaining oxygen radical would take an electron from the newly regenerated Ti³⁺ on which it is bonded to become O²⁻.



The first part for the formation of ethane proceeds in a similar manner, except that hydrogen atoms formed during the dissociative adsorption would be eliminated as water, by abstracting one oxygen atom per one water molecule from the surface. O₂ molecules from the gas phase are dissociatively adsorbed on the surface to oxygen atoms; the exact process for the dissociative adsorption is not well known but is thought to occur preferentially on oxygen point defect sites as well as on steps. These oxygen atoms would diffuse to surface oxygen vacancies to regenerate them. In this process each oxygen atom takes back two electrons from the two Ti atom to which it is bonded as in the case of the (110) or the 2 × 1 (011) surface. It is clear that in presence of gas phase oxygen that methane and ethane formation routes compete with each other. This competition explains the decrease in methane yield with increasing oxygen pressure as seen in Fig. 6.

A physical description of the reaction may be given as follows. In electron or charge-transfer processes, between a semiconductor and an adsorbate, photo-generation of electrons and holes determines the extent of reaction. As indicated above, in competition with this process, electron-hole recombination takes place. The photo-catalytic activity has been shown to depend on several parameters such as surface structure (Brinkely and Engel 2000), particles size (Reztova et al. 1999; Furube et al. 1999), defects (Henderson et al. 1999), doping (Karakitsu and Verykios 1993; Hengelin 1989) and the formation of n-p compounds (Wang et al. 2005). There are basically three requirements for a high catalytic activity:

1. that the photo-generated charge carriers exist near the surface,
2. that they have a long lifetime and
3. that the rate of charge transfer is large.

The rate of electron-hole pair recombination affects the lifetime of the charge carriers and thus directly affects the catalytic activity. Decreasing the band bending increases the rate of recombination because there is less driving force for electron-hole separation (and vice versa). It is worth indicating that for an *n*-type semiconductor the minority carriers, which are the holes, preferentially migrate to the surface because

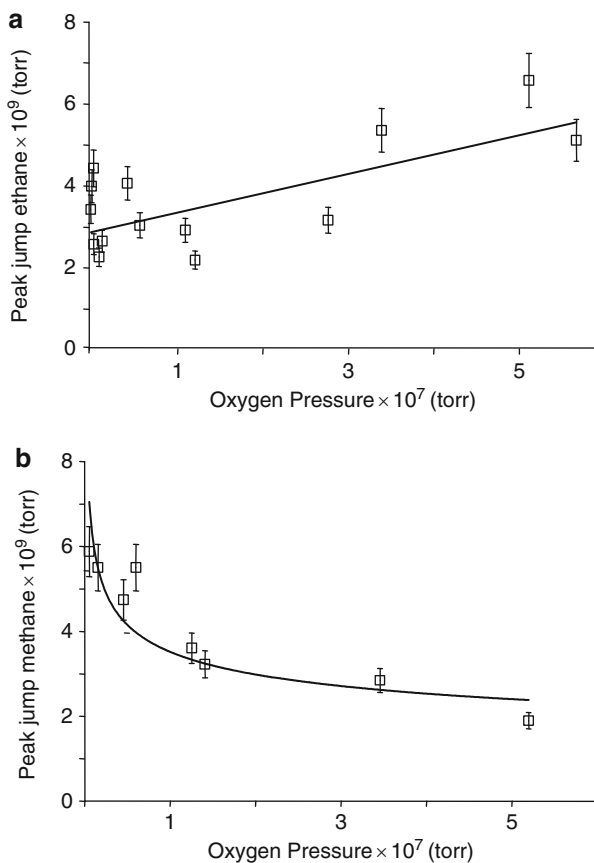


Fig. 6 (a) Ethane (m/z 30), and (b) methane, photo-productions, as a function of oxygen pressure, constant acetic acid pressure (5×10^{-9} torr) over the {011}-faceted TiO₂(001) single crystal surface

of the direction of the electric field (Grätzel 1988). Thus, an observed photo-reaction rate might be explained by knowledge developed from “light induced charge separation theories” and in particular the effect of depletion-layer on the photo-reaction of a semiconductor.

We first start with a qualitative description as outlined by the dissociative adsorption equation:



where Ti and O represent surface atoms.

Adsorption of an acetic acid molecule on a Ti–O center results in the formation of an acetate and a surface hydroxyl. Upon illumination of TiO₂ (n-type semiconductor) and creation of the charge carriers, h^+ and e^- , migration of h^+ to the surface occurs due to field provoked by the depletion layer and this leads to a hydroxyl radical formation.

Simultaneously, reactions of an electron with an acceptor center (such as with an adsorbed O_2) will lead to O_{-2} (Howe and Grätzel 1985; Mönch 1995).

The quantum yield, η , of a photoreaction is related to the depletion layer, W . In the case of TiO_2 it is a layer depleted of the majority carriers (electrons) and the distance between the Fermi level and the conduction-band minimum will be increased. In other words, the band will be bent upward. Absorption of photons will generate electron-hole pairs in the depletion layer and their generation rate is in general, constant through the layer (provided its width is sufficiently small compared to the penetration depth of light). Equation (9) relates the quantum yield to the width of the depletion layer, W (Grätzel):

$$\eta = \frac{L + W}{1/\alpha + L} \quad (9)$$

with α the extinction coefficient that may be taken as to $2.6 \times 10^4 \text{ cm}^{-1}$ at 320 nm, (Grätzel) and L , the minority carrier diffusion length.

The calculation of L is a little tedious but can be done using some approximation; more details are given by Wilson et al. (2003) Using the above equation one finds W close to 18 nm. Knowing W it is possible to calculate the height of the depletion layer:

$$e|V| = \frac{e^2}{2\epsilon\epsilon_0} n_i W^2 \quad (10)$$

where the dielectric constant ϵ along the (001) direction for TiO_2 (the bulk structure of the {011}-faceted surface) is equal to 170 (Handbook of Physics and Chemistry 1995). The number of charge carriers, n_i , has been computed by several workers and values between 10^{23} and 10^{25} per m^3 were reported. With $n_i = 10^{25} \text{ m}^{-3} \text{ W}^{-1}$ is found equal to 0.18 V for the (011) faceted $TiO_2(001)$ rutile single crystal.

It is instructive to estimate the maximum quantum yield, η , expected with the above-quoted numbers. Assuming that a barrier height of 1.0 eV is reached (it is about 0.5 eV for a typical semiconductor (Mönch)) η of ca. 0.25 caused by a depletion layer of 50 nm can be obtained. This is probably the highest level expected for this reaction over the rutile $TiO_2(011)/(001)$ surface/bulk material.

Results of acetic acid photoreaction over $TiO_2(001)$ single crystal surfaces (Wilson and Idriss 2002, Wilson and Idriss 2003), together with those on polycrystalline surfaces (Muggli and Falconer 1999 a and b; Ollis et al. 1984), indicate that O_2 is required for the Photo-Kolbe reaction to occur in a catalytic way. As indicated in (21.2) O_2 is needed to regenerate the surface oxygen vacancies formed due to water formation (as a side reaction). However there is more into O_2 molecules than a regeneration of surface oxygen vacancies.

As shown in Fig. 7, O_2 may combine with electrons transferred to the conduction band and form O_2^- . More recent results on $TiO_2(110)$ single crystal indicate that this pathway might actually contribute in the photoreaction in addition to (or instead of) the traditionally accepted route of OH radicals (White et al. 2003; Henderson 2005a, b; Henderson et al. 2006). XPS C1s study has shown that O_2 molecules in the gas phase are required for the removal of acetate species on $TiO_2(110)$ single

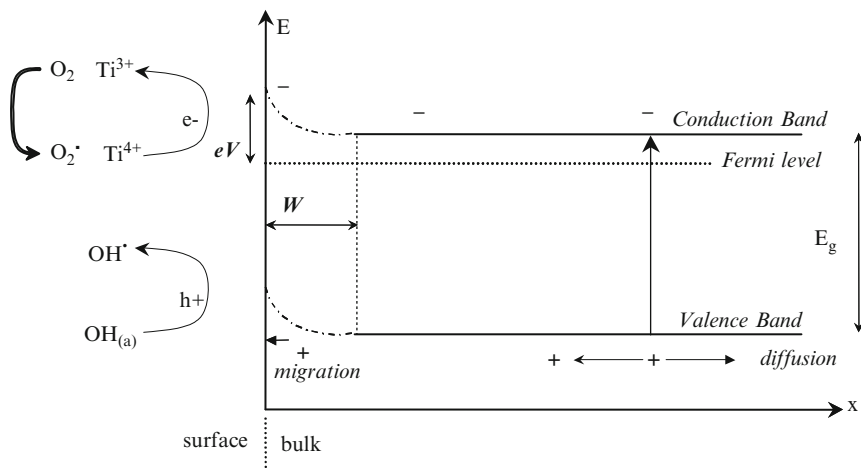


Fig. 7 A schematic representation of the space charge region of *n*-TiO₂. E_g , band gap; W , depletion width; eV , barrier height; x is distance into the material from the surface and E is the energy scale. Also shown the reaction of OH_s with holes formed at the VB and Ti_s (and adsorbed O_2 molecules) with electrons at the CB

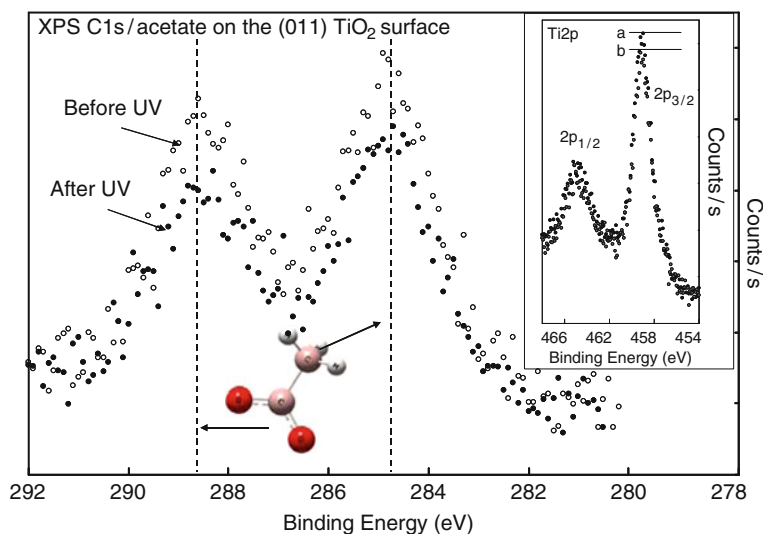


Fig. 8 XPS C1s of acetic acid over TiO₂(011) surface before and after UV excitation in presence of 1×10^{-6} torr of O_2 (37 min). The coverage is estimated from the attenuation of the Ti2p peak (inset: a = before adsorption, b after saturation coverage at 300 K) as 0.48 (Quah et al. 2010) using the inelastic mean free path (IMFP) $\lambda = 1.2$ nm for $\approx 1,000$ eV kinetic energy of the photoelectron (the IMFP is taken from Fuentes et al. 2002)

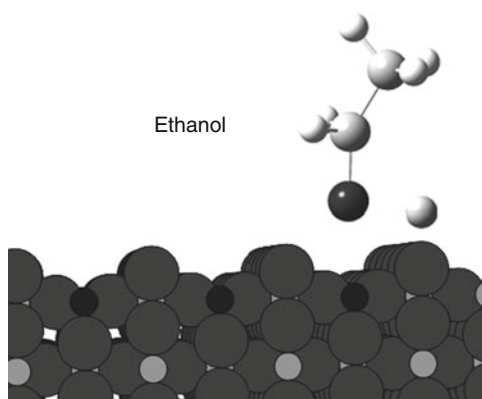
crystal (Idriss et al. 2002) and a more recent work on the TiO₂(011) single crystal does also indicate that adsorbed acetate needs gas phase O_2 to leave the surface Fig. 8.

3 Ethanol Photo-Reactions on TiO₂(110) Single Crystal

The second example involves ethanol reactions over the TiO₂(110) single crystal surface. In many respects ethanol adsorption is close to that of acetic acid on TiO₂ surfaces. Ethanol is dissociatively adsorbed at 300 K, where ethoxide species are on surface Ti atoms and the hydrogen atoms are situated over bridging surface oxygen atoms, forming thus a hydroxyl species. The saturation coverage at 300 K of ethanol is computed equal to 0.5 with respect to the fivefold-coordinated surface Ti atoms (Jayaweera et al. 2007). STM studies of few alcohols were conducted recently and the presence of both the alkoxides and surface hydroxyls were successfully imaged (Zhang et al. 2007).

As shown in Fig. 9 ethanol may adsorb via its molecular O2p with the empty d-orbitals of Ti⁴⁺ cations leading to subsequent O–H bond dissociation upon interaction with bridging surface oxygen atoms. The surface coverage of 0.5 is not necessarily because ethoxide species, formed upon dissociative adsorption of ethanol molecules, are bonded through their oxygen atoms to two surface Ti atoms, such as the case of carboxylic acids (Cocks et al. 1997a, b; Guo et al. 1997; Hayden et al. 1999; Sayago et al. 2004; Fukui et al. 2000 among others). An ethanol molecule is most likely adsorbed onto one Ti atom but the relatively bulky –CH₂CH₃ chain of two adjacent ethoxide species might cause repulsive interaction, which effectively leaves every other Ti site empty. An estimate of the size of an ethoxide species (using the DFT-B3LYP; 6-31G(d,p) method) gives a diameter close to 5 Å which may need a 2 × 1 unit cell to be accommodated. IR studies of ethanol and methanol over CeO₂ powder surfaces have suggested the presence of di- and tri-coordinated alkoxide species previously (Lamotte et al. 1988; Yee et al. 2000; Sheng et al. 2002), this is most likely occurring on defected (high Miller indices steps or point defects) sites and may not occur on the flat TiO₂(110) surface along the [001] direction. At 300 K, adsorption of ethanol produces two, not well resolved C(1s) peaks at 286.8 and 285.5 eV that can be attributed to the –CH₂O– and –CH₃ carbons, respectively (Fig. 10 at 300 K). The intensity of the two peaks appears with approximately 1:1 ratio and a peak separation of about 1.3 eV, which is close to the C 1s spectra of gas

Fig. 9 A side view of the (110) surface of the rutile TiO₂. Small circles Ti atoms, large circles O atoms. A representation of an adsorbed ethoxide species on top of a Ti_{5c} (5c for fivefold coordinated) is also seen. The H resulting from the dissociative adsorption is on top of the twofold coordinated surface O atoms (bridging O atoms). The atomic scale between ethanol and TiO₂ is not drawn to scale



phase ethanol (Siegbahn et al. 1969) and previously reported work of ethanol on other TiO₂ surfaces (Farfan-Arribas and Madix 2002; Kim and Barteau 1990b).

Figure 10 also shows the effect of annealing to increment temperatures on the population of surface species, after surface saturation with ethanol at 300 K. Heating to higher temperatures resulted in decreasing the surface population due to further reactions. The considerable reduction in surface population is mostly a consequence of the re-combinative desorption of ethanol.



(a) for adsorbed and (br) for bridging.

This is consistent, in general, with desorption of alcohols and carboxylic acids from the surfaces of numerous oxides including TiO₂ surfaces (Diebold 2003; Idriss et al. 2002). The decrease in peak intensity is not occurring at the same rate for both functional groups (-CH₃ and -CH₂O-). The inset in Fig. 10 shows that the peak areas changes with increment temperatures, in arbitrary units. The dissymmetry of the disappearance increases with increasing the annealing temperature. Concomitant with ethanol desorption water desorption occurs:



where V_O = surface oxygen vacancy and (a) for adsorbed.

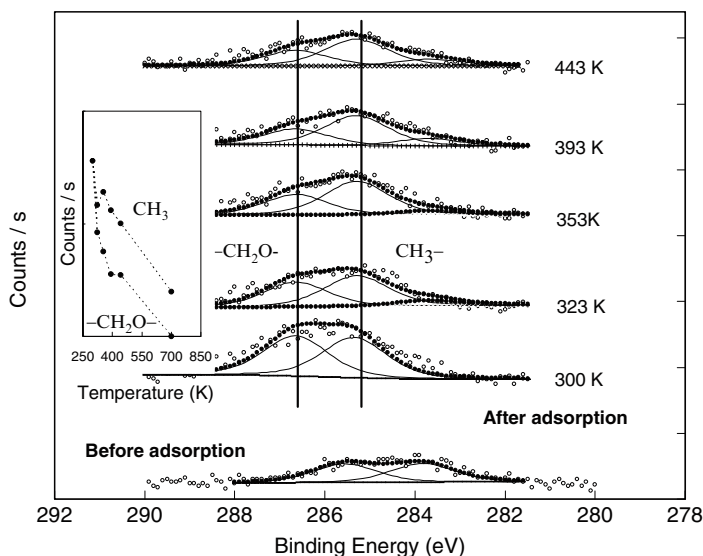


Fig. 10 Effect of temperature on surface ethoxide signal adsorbed (at 300 K) on TiO₂(110) single crystal as monitored by the XPS C(1s) lines. The inset shows the computed peak areas of both XPS C(1s) at 285.5 and 286.8 eV attributed to the -CH₃ and -CH₂O- group as a function of temperature

The removal of a fraction of surface oxygen (most likely the bridging surface oxygen atoms) will create sites for a preferential interaction with the oxygen atoms of surface ethoxides in the process of breaking a fraction of the C–O bond species to re-generate the removed bridging oxygen atoms. This may result in a further screening of ethoxide surface species and the apparent enhancement of the C1s electron signal from the $-\text{CH}_3$ group when compared to that of $-\text{CH}_2\text{O}-$ group.

Figure 11 presents an ethanol-dosed TiO_2 surface at 300 K that has been subjected to UV illumination at 10^{-6} torr of molecular oxygen. Upon UV irradiation two main changes are observed. (i) A slight decrease of the peak areas of both functional groups with increasing irradiation time and (ii) a clear formation of a peak at about 290 eV that is attributed to a RCOO(a) species. Photo-excitation results in the transfer of electrons from the valence band (occupied states containing contribution from $\text{O}2\text{p}$) to the conduction band (empty states containing contribution from $\text{Ti}3\text{d}$ level). The decrease of the ethoxide C1s peaks is most likely due to their reaction with O_2^- and/or O^\bullet , these are formed from captors of the excited electron according to:

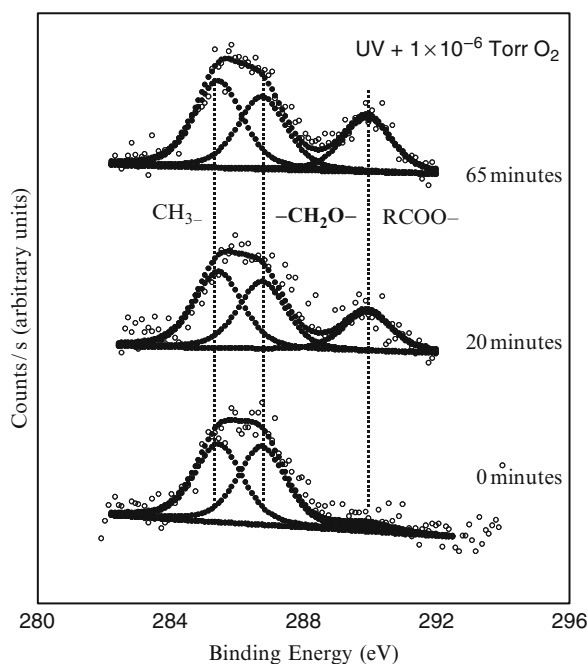
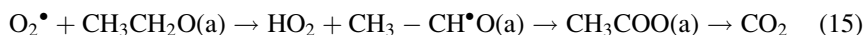


Fig. 11 XPS C(1s) of ethanol adsorbed on $\text{TiO}_2(110)$ at 300 K at saturation; before and after different UV illumination at different time intervals, in the presence of oxygen pressure = 1×10^{-6} torr

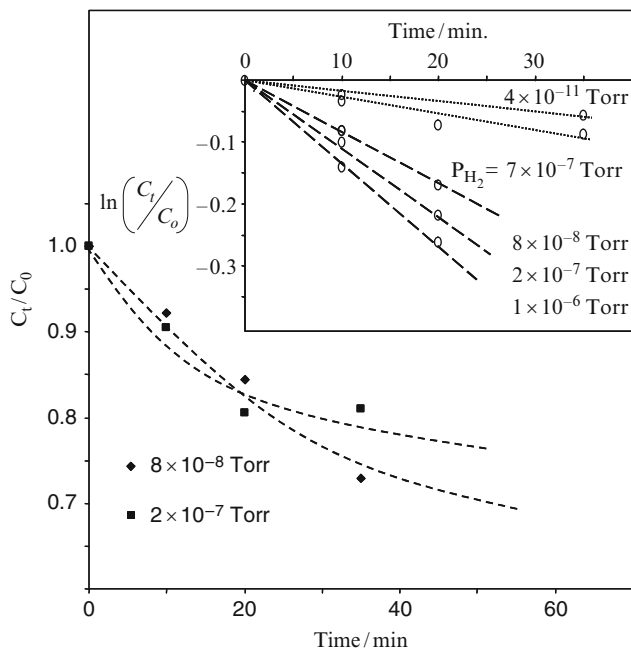


Fig. 12 Computed peak areas of XPS C(1s) as a function of UV illumination time under different oxygen pressures. Inset: Initial linear drop of the computed peak areas under four different pressures. Included in the figure an additional run under H₂ (7×10^{-7} torr) for comparison with the one in “near” absence of O₂

The two successive arrows indicate multiple reaction steps of non identified intermediates.

In Fig. 12 changes in ethoxides concentration expressed as C_t/C_o , where C_t is the areas of the two C1s peaks of the ethoxide species at time t and C_o is their peak areas before irradiation, are plotted as a function of time.

Assuming a simple exponential decay of the reactant, ethoxide species, with time:

$$C_t = C_o \exp(-kt) \text{ or } C_t = C_o \exp(-FQt) \quad (16)$$

$$\text{Or } Q = \frac{1}{Ft} \ln \frac{C_o}{C_t} \quad (17)$$

where k is a pseudo first order rate constant in min^{-1} and t time in minutes, F is the UV flux and Q is the cross section in cm^{-2} . Q is found equal to ca. $2 \times 10^{-18} \text{ cm}^{-2}$ at a pressure of 1×10^{-6} torr of O₂.

In Fig. 13 a plot of the changes in surface coverage as a function of gas phase oxygen pressure is presented. The weak dependency, approaching zero order, of the

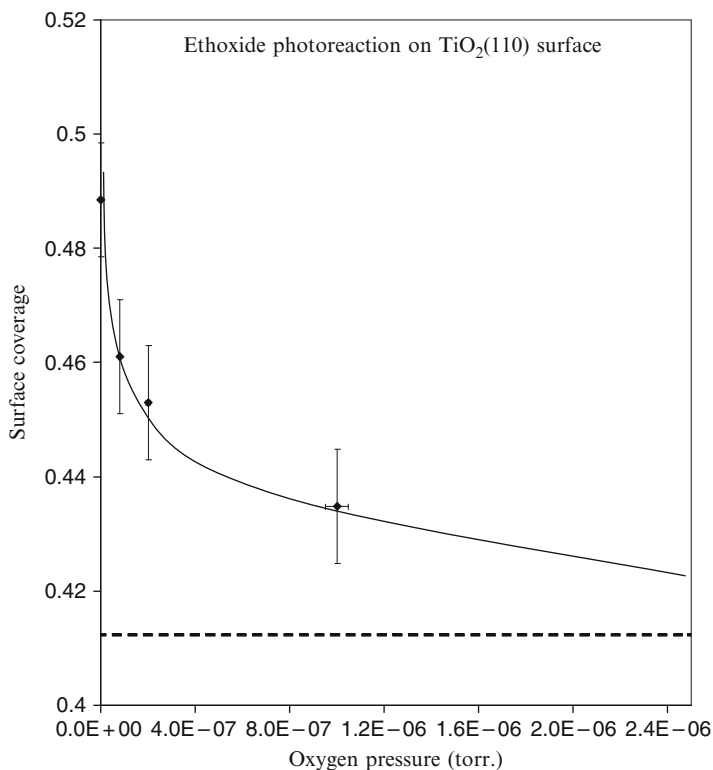
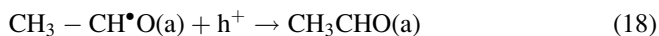


Fig. 13 Decrease in surface coverage of ethoxide species after 10 min irradiation with UV at different O₂ pressure

rate of ethoxide reactions on molecular oxygen at high pressures is clear. It is worth indicating that this rate is not that of ethanol photo-catalytic oxidation to CO₂, but is only that of the decrease of ethoxide species in an initially saturated surface. Some of these ethoxides give acetate species as seen in Fig. 11. The reaction intermediates have been studied on powder TiO₂ and are found to involve the dehydrogenation product CH₃CHO (Reztova et al. 1999) formed by the removal of the electron from the radical of (15):



Acetaldehyde then further react in a complex set of reactions, not well understood to give the final product CO₂. During this oxidation acetate species may be formed. The peak at 290 eV is thus attributed to acetate species (CH₃CHO + 2O(s) → CH₃COO(a) + OH). The decay of acetate species on this (110) surface, formed

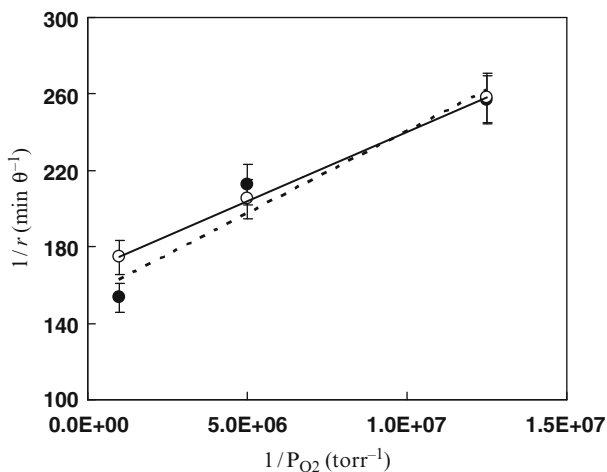


Fig. 14 A plot of $1/r$ versus $1/P_{O_2}$ for the photo-decomposition of ethanol, the rate is obtained from the decrease of the C1s XPS peaks attributed to ethoxide species after 10 min of irradiation time (*dashed lines*) and after 20 min (*solid lines*)

Table 1 TPD peak temperature and computed desorption energy for acetic acid over the {011}-faceted TiO₂(001) and TiO₂(011) surfaces

Acetic acid	Mode	Peak temperature	Desorption/adsorption energy, kJ mol ⁻¹	References
TPD (prefactor, $\nu = 10^{13} \text{ s}^{-1}$) {011}-faceted TiO ₂ (001)		400 K	105	Wilson and Idriss (2003)
TPD (prefactor, $\nu = 10^{13} \text{ s}^{-1}$) {011}-faceted TiO ₂ (001)		570 K	150	Wilson and Idriss (2003)
DFT/GGA-PW91 ($\theta = 0.5$) TiO ₂ (011)	Monodentate		100	McGill and Idriss (2008)
DFT/GGA-PW91 ($\theta = 0.5$) TiO ₂ (011)	Bidentate		160	McGill and Idriss (2008)

from dissociatively adsorbed acetic acid at 300 K, has been previously computed (11) and was found of the same order of magnitude to that of ethanol reported in this work. It is unclear why acetate formed by the oxidation of ethanol appears less reactive than those formed from acetic acid dissociation. One explanation might be

due to the involvement of surface oxygen in the formation of acetate species from ethanol. It is unclear if these acetate species are spectators that will end by blocking most reactive sites or that if they are removed from the surface, in particular, if water molecules are present. Much work needs to be done in this direction to answer further the many questions left.

The question related to the adsorption site of molecular oxygen on the surface of the semiconductor is an important one and deserves further thought and experiments. Some information might be extracted from the ethanol study. Since the initial surface is $\frac{1}{2}$ covered with ethanol at all O_2 pressures considered in the work and the rate increases with increasing pressure, it is clear that reversible O_2 adsorption (i.e. following Langmuir-type adsorption isotherm) is responsible for the increase in the reaction rate. Numerous work in surface science on $TiO_2(110)$ single crystal surfaces has studied the irreversible mode of adsorption of O_2 . It was found that the adsorption of O_2 occurs exclusively on surface oxygen defects (Henderson et al. 1999; Wu et al. 2003). While this is valid at low temperatures at room temperatures O_2 molecules has a negligible sticking coefficient number. Although at the pressure range of 10^{-7} – 10^{-8} torr there is enough molecular oxygen to irreversibly adsorb on, surface defects, it is most likely that reversible molecular adsorption of oxygen is responsible for the observed decay of ethoxides.

It is possible to plot the rate of reaction using the Langmuir-Hinshelwood kinetics

$$r = \frac{kKP_{O_2}}{1 + KP_{O_2}} \quad \text{or} \quad \frac{1}{r} = \frac{1}{k} + \frac{1}{kKP_{O_2}} \quad (19)$$

where r is the rate, K is the binding constant of oxygen, assuming that the rate is independent of the concentration of ethanol at surface saturation.

Figure 14 presents the reciprocal rate as a function of the reciprocal O_2 pressure. The linearity is reasonable for the rate computed after 10 or 20 min. The binding constant K for O_2 , found using (21.19), was equal to $2.4 \times 10^7 \text{ torr}^{-1}$ for the data after 20 min or equal to $1.7 \times 10^7 \text{ torr}^{-1}$ for the data after 10 min. Since $\frac{1}{2}$ of Ti atoms are already filled with ethanol, θ_{O_2} is reasonably taken as the number of free Ti atoms, the other $\frac{1}{2}$ or 2.6×10^{14} Ti atoms per cm^2 . At 300 K and with an approximate chamber of a volume = 0.4 m^3 and assuming that each free Ti atom reversibly adsorbs one oxygen molecule the pressure required to fully saturate them is 2.6×10^{-6} torr. Within experimental errors this is in line with the pressure dependence of the decay of ethoxides on O_2 pressure, Fig. 13.

4 Conclusions

The photoreactions of two organic molecules: acetic acid and ethanol, over rutile $TiO_2(110)$, $TiO_2(011)$ and the (011) reconstructed surface of $TiO_2(001)$ single crystals are presented and discussed in this chapter. The objective was not to test for structure

sensitive reactions under UV between the crystal surfaces as such, since the present knowledge does not allow for conclusions in this regard. Simpler conclusions can however be drawn from this work. Molecular oxygen is needed for an appreciable yield for ethanol and acetic photodecomposition. In particular, gas phase oxygen molecules are needed to photo-oxidise ethoxide species to acetates at room temperature and to make ethane from acetic acid in steady state conditions. It is unclear where molecular oxygen is adsorbed on the surfaces of TiO₂ single crystal. From the kinetics of the reaction it appears that the number of molecular oxygen needed is similar to that of free Ti sites in the case of ethanol photodecomposition.

References

- Bartean MA (1996) Organic reactions at well-defined oxide surfaces. *Chem. Rev.* 96, 1413–1430; and references therein
- Beck TJ, Klust A, Batzill M, Diebold U, Di Valentin C, Selloni A (2004) Surface structure of TiO₂(011)-(2 × 1). *Phys Rev Lett* 93:036104-1–036104-4
- Beck TJ, Klust A, Batzill M, Diebold U, Di Valentin C, Tilocca A, Selloni A (2005) Mixed dissociated/molecular monolayer of water on the TiO₂(011)-(2 × 1) surface. *Surf Sci* 591: L267–L272
- Belver C, Bellod R, Stewart SJ, Requejo FG, Fernández-García M (2006) Nitrogen-containing TiO₂ photocatalysts. Part 2. Photocatalytic behavior under sunlight excitation. *Appl Catal B: Environ* 65:309–314
- Brinkley D, Engel T (2000) Evidence for structure sensitivity in the thermally activated and photocatalytic dehydrogenation of 2-Propanol on TiO₂. *J Phys Chem B* 104:9836–9841
- Carp O, Huisman CL, Reller A (2004) Photoinduced reactivity of titanium dioxide. *Prog Solid Stat Chem* 32:33–177
- Cocks ID, Guo Q, Patel R, Williams EM, Roman E, de Segovia JL (1997a) The structure of TiO₂(110) (1 × 1) and (1 × 2) surfaces with acetic acid adsorption: a PES study. *Surf Sci* 377–379:135–139
- Cocks ID, Guo Q, Williams EM (1997b) ESDIAD studies of the structure of TiO₂(110) (1 × 1) and (1 × 2) surfaces and interfaces in conjunction with LEED and STM. *Surf Sci* 390:119–125
- Di Valentin C, Tilocca A, Selloni A, Beck TJ, Klust A, Batzill M, Losovyj Y, Diebold U (2005) Adsorption of water on reconstructed Rutile TiO₂(011)-(2 × 1): Ti=O double bonds and surface reactivity. *J Am Chem Soc* 127:9895–9903
- Diebold U (2003) The surface science of titanium dioxide. *Surf Sci Rep* 48:53–229
- Diebold U (2006) SS1-FriM American Vacuum Society 53rd Annual Meeting, San Francisco, CA
- Diwald O, Thompson TL, Zubkov T, Goralski EG, Walck SD, Yates JT Jr (2004) Photochemical activity of nitrogen-doped rutile TiO₂(110) in visible light. *J Phys Chem B* 108:6004–6008
- Dulub O, Di Valentin C, Selloni A, Diebold U (2006) Structure, defects, and impurities at the rutile TiO₂(011)-(2 × 1) surface: A scanning tunneling microscopy study. *Surf Sci* 600:4407–4417
- Farfan-Arribas E, Madix RJ (2002) Role of defects in the adsorption of aliphatic alcohols on the TiO₂(110) surface. *J Phys Chem B* 2002(106):10680–10692
- Fuentes GG, Elizalde E, Yubero F, Sanz JM (2002) Electron inelastic mean free path for Ti, TiC, TiN and TiO₂ as determined by quantitative reflection electron energy-loss spectroscopy. *Surf Interface Anal* 33:230–237
- Fukui K-I, Iwasawa Y (2000) Fluctuation of acetate ions in the (2 × 1)-acetate overlayer on TiO₂(110)-(1 × 1) observed by noncontact atomic force microscopy. *Surf Sci* 464:L719–L726

- Furube A, Asahi T, Masuhara H, Yamashita H, Anpo M (1999) Charge carrier dynamics of standard TiO₂ catalysts revealed by femtosecond diffuse reflectance spectroscopy. *J Phys Chem B* 103:3120–3127
- Gong X-Q, Khorshidi N, Stierle A, Vonk V, Ellinger C, Dosch H, Cheng H, Selloni A, He Y, Dulub O, Diebold U (2009) The 2 × 1 reconstruction of the rutile TiO₂(011) surface: A combined density functional theory, X-ray diffraction, and scanning tunneling microscopy study. *Surf. Sci.* 66: 138–144
- Grätzel M (1988) Heterogeneous photochemical electron transfer. Editor in Chief David R. Lide CRC Press, Boca Raton, FL
- Guo Q, Williams EM (1999) The effect of adsorbate–adsorbate interaction on the structure of chemisorbed overlayers on TiO₂(110). *Surf Sci* 433–435:322–326
- Guo Q, Cocks I, Williams EM (1997) The orientation of acetate on a TiO₂(110) surface. *J Chem Phys* 106:2924–2931
- Halevi B, Vohs JM (2006) TPD study of the reaction of CH₃CH₂SH and (CH₃CH₂)₂S₂ on ZnO (0001) and ZnO. *Catal Lett* 111:1–4
- (1995) Handbook of physics and chemistry, 78th ed. CRC Press, Boca Raton, FL
- Hayden BE, King A, Newton MA (1999) Fourier transform reflection–absorption IR spectroscopy study of formate adsorption on TiO₂(110). *J Phys Chem B* 103:203–208
- Henderson MA (1997) Complexity in the decomposition of formic acid on the TiO₂(110) surface. *J Phys Chem B* 101:221–229
- Henderson MA (2002) The interaction of water with solid surfaces, fundamental aspects revisited. *Surf Sci Rep* 46:1–308
- Henderson MA (2005a) Acetone and water on TiO₂(110): competition for sites. *Langmuir* 21, 3443–3450 and references therein
- Henderson MA (2005b) Photooxidation of acetone on TiO₂(110): conversion to acetate via methyl radical ejection. *J Phys Chem B* 109:12062–12070
- Henderson MA, Epling WS, Perkins CL, Peden CHF, Diebold U (1999) Interaction of molecular oxygen with the vacuum-annealed TiO₂(110) surface: molecular and dissociative channels. *J Phys Chem* 103:5328–5337
- Henderson MA, White JM, Uetsukab H, Onishi H (2006) Selectivity changes during organic photooxidation on TiO₂: role of O₂ pressure and organic coverage. *J Catal* 238:153–164
- Hengelin A (1989) Small-particle research: physicochemical properties of extremely small colloidal metal and semiconductor particles. *Chem. Rev.* 89, 1861–1873; and references therein
- Howe RF, Grätzel M (1985) EPR observation of trapped electrons in colloidal titanium dioxide. *J Phys Chem* 89:4495–4499
- Idriss H, Barteau MA (1992) Photoluminescence from zinc oxide powder: a probe of reaction mechanisms and surface modification. *J Phys Chem* 96:3382–3388
- Idriss H, Barteau MA (2000) Active sites on oxides: from single crystals to catalysts. *Adv Catal* 45:261–331
- Idriss H, Légaré P, Maire G (2002) Dark and photoreactions of acetates on TiO₂(110) single crystal surface. *Surf Sci* 515:413–420
- Jayaweera PM, Quah EL, Idriss H (2007) Photoreaction of ethanol on TiO₂(110) single crystal surface. *J. Phys. Chem. C* 111, 1764–1769
- Karakitsu KE, Verykios XE (1993) Effects of altrivalent cation doping of titania on its performance as a photocatalyst for water cleavage. *J Phys Chem* 97:1184–1189
- Kim KS, Barteau MA (1990a) Structure and composition requirements for deoxygenation, dehydration, and ketonization reactions of carboxylic acids on TiO₂(001) single-crystal surfaces. *J Catal* 125:353–375
- Kim KS, Barteau MA (1990b) Reactions of aliphatic alcohols on the {011}-faceted TiO₂(001) surface. *J Mol Catal* 63:103–117
- Kim SH, Stair PC, Weitz E (1998) Photochemistry in CH₃I adlayers on TiO₂(110) studied with postirradiation thermal desorption. *Langmuir* 14:4156–4161
- Kraeutler B, Bard AJ (1978) Heterogeneous photocatalytic synthesis of methane from acetic acid – new Kolbe reaction pathway. *J. Am. Chem. Soc.* 100:2239–2240

- Lamotte J, Morávek V, Bensitel M, Lavalley JC (1988) FT-IR study of the structure and reactivity of methoxy species on ThO₂ and CeO₂. *React Kinet Catal* 36:113–118
- Liao L-F, Lien C-F, Lin J-L (2001) FTIR study of adsorption and photoreactions of acetic acid on TiO₂. *Phys Chem Chem Phys* 3:3831–3837
- Lindsay R, Wander A, Ernst A, Montanari B, Thornton G, Harrison NM (2005) Revisiting the surface structure of TiO₂(110): a quantitative low energy electron diffraction study. *Phys Rev Lett* 94:246102-1–246102-4
- Linsebigler AL, Lu G, Yates JT Jr (1995) Photocatalysis on TiO₂ surfaces: principles, mechanisms, and selected results. *Chem. Rev.* 95, 735–758; and references therein
- Lyubinetzky IZ, Yu Q, Henderson MA (2007) Direct observation of adsorption evolution and bonding configuration of TMAA on TiO₂(110). *J Phys Chem C* 111:4342–4346
- McGill PR, Idriss H (2008) DFT study of carboxylic acids modes of adsorption on rutile TiO₂(011) surfaces. *Surf. Sci.* 602: 3688–3695
- Mönch W (1995) Semiconductor surfaces and interfaces. Ertl G (ed) Springer series in surface sciences, Heidelberg, Berlin
- Morikawa Y, Takahashi I, Aizawa M, Namai Y, Sasaki T, Iwasawa Y (2004) First-principles theoretical study and scanning tunneling microscopic Observation of dehydration process of formic acid on a TiO₂(110) surface. *J Phys Chem B* 108:14446–14451
- Muggli DS, Falconer JL (1999a) Parallel pathways for photocatalytic decomposition of acetic acid on TiO₂. *J Catal* 187:230–237
- Muggli DS, Falconer JL (1999b) Role of lattice oxygen in photocatalytic oxidation on TiO₂. *J Catal* 191:318–325
- Ni M, Leung MK, Leung DY, Sumathy K (2007) A review and recent developments in photocatalytic water-splitting using TiO₂ for hydrogen production. *Renewable Sust Energy* 11:401–425
- Nosaka Y, Koenuma K, Ushida K, Kira A (1996) Reaction mechanism of the decomposition of acetic acid on illuminated TiO₂ powder studied by means of in situ electron spin resonance measurements. *Langmuir* 12:736–738
- Ollis DF, Hsiao C-Y, Budiman L, Lee C-L (1984) Heterogeneous photoassisted catalysis: conversions of perchloroethylene, dichloroethane, chloroacetic acids, and chlorobenzenes. *J Catal* 88:89–96
- Quah EL, Wilson JN, Idriss H (2010) Photoreaction of the Rutile TiO₂(011) Single-Crystal Surface: Reaction with Acetic Acid. *Langmuir* 26(9):6411–6417
- Reztova T, Chang C-H, Koresh J, Idriss H (1999) Dark and photoreactions of ethanol and acetaldehyde over TiO₂/carbon molecular sieve fiber. *J Catal* 185:223–235
- Ryabchuk V (2004) Photophysical processes related to photoadsorption and photocatalysis on wide band gap solids: a review. *Int J Photoenergy* 6:95–113
- Sayago DI, Polcik M, Lindsay R, Toomes RL, Hoeft JT, Kittel M, Woodruff DP (2004) Structure determination of formic acid reaction products on TiO₂(110). *J Phys Chem B* 108:14316–14323
- Sheng PY, Yee A, Bowmaker GA, Idriss H (2002) H₂ production from ethanol over Rh-Pt/CeO₂ catalysts. The role of Rh for the efficient dissociation of the carbon–carbon bond. *J Catal* 208:393–403
- Siegbahn K, Nordling C, Johansson G, Hedman J, Heden PF, Hamrin K, Gelius U, Bergmark T, Werne LO, Baer Y (1969) ESCA applied to free molecules. North Holland, Amsterdam
- Thompson TL, Panayotov DA, Yates JT Jr, Martyanov I, Klabunde K (2004) Photodecomposition of adsorbed 2-chloroethyl ethyl sulfide on TiO₂: involvement of lattice oxygen. *J Phys Chem B* 108:17857–17865
- Titheridge DJ, Wilson JN, Idriss H (2003) Reaction pathways of carboxylic acids over TiO₂ single crystal surfaces: diketene formation from bromo-acetic acid. *Res Chem Inter* 29:553–574
- Torrelles X, Cabailh G, Lindsay R, Bikondoa O, Roy J, Zegenhagen J, Teobaldi G, Hofer WA, Thornton G. (2008) Geometric Structure of TiO₂ (011) 2 x 1. *Phys. Rev. Lett.* 101:185501-1 185501-4
- Vohs JM, Barteau MA (1989) Formation of stable alkyl and carboxylate intermediates in the reactions of aldehydes on the zinc oxide (0001) surface. *Langmuir* 5:965–972

- Wang X-T, Zhong S-H, Xiao XF (2005) Photo-catalysis of ethane and carbon dioxide to produce hydrocarbon oxygenates over ZnO-TiO₂/SiO₂ catalyst. *J Mol Catal A: Chem* 229:87–93
- White JM, Szanyi J, Henderson MA (2003) The photon-driven hydrophilicity of titania: a model study using TiO₂(110) and adsorbed trimethyl acetate. *J Phys Chem B* 107:9029–9033
- Wilson JN, Idriss H (2002) Structure-sensitivity and photo-catalytic reactions of semiconductors. Effect of the last layer atomic arrangement. *J Am Chem Soc* 124:11284–11285
- Wilson JN, Idriss H (2003) Effect of surface reconstruction of TiO₂(001) single crystal on the photoreaction of acetic acid. *J Catal* 214:46–52
- Wu W, Selloni A, Lazzeri M, Nayak SK (2003) Oxygen vacancy mediated adsorption and reactions of molecular oxygen on the TiO₂(110) surface. *Phys Rev B* 68, 241402-1: 241402-4 (and references therein)
- Yee A, Morrison SJ, Idriss H (2000) The reactions of ethanol over M/CeO₂ catalysts, M = Rh, Pd, or Pt. Evidence of carbon-carbon bond dissociation at low temperatures. *Catal Today* 63:327–335
- Zapol P, Curtiss LA (2007) Organic molecule adsorption on TiO₂ nanoparticles: a review of computational studies of surface interactions. *J Comp Theort Nanosci* 4:222–230
- Zhang Z, Bondarchuk O, Kay BD, White JM, Dohnálek Z (2007) Direct visualization of 2-butanol adsorption and dissociation on TiO₂(110). *J Phys Chem C* 111:3021–3027

Part V
Photo-Induced Superhydrophilicity
for Materials with Self-Cleaning
Properties

Chapter 22

Investigations of the Photoinduced Superhydrophilicity of the TiO₂ Photocatalyst Surface by Near-Infrared Spectroscopy

Masato Takeuchi, Gianmario Martra, Salvatore Coluccia,
and Masakazu Anpo

Abstract When H₂O molecules desorb from the TiO₂ surfaces during UV light irradiation, the vibrational spectroscopies, FT-IR and NIR, revealed that the H-bond interaction between H₂O molecules decreased. This observation clearly suggests that the photo-induced high wettability of TiO₂ surface is closely related to the decrease in the surface tension of H₂O clusters to form H₂O thin layers. The partial elimination of the hydrocarbons from the TiO₂ surfaces by photocatalytic oxidation was seen to be another major factor, providing free spaces on the surface where the H₂O clusters could spill over and spread out to form the thin H₂O layers. The superhydrophilic properties of the TiO₂ photocatalyst surfaces by a lessening in the amount of H₂O adsorbed on the surfaces can be expressed as hydrophobic compared with the initial state before UV light irradiation. Moreover, the temperature changes of the TiO₂ powder samples during UV light irradiation were found to show a good correspondence with the changes in the contact angle of H₂O droplets on the TiO₂ thin film surfaces. Especially, the time scale for hydrophilic conversion on the TiO₂ surfaces under UV light irradiation was in good agreement with the decrease in the amount of H₂O molecules adsorbed on the surfaces but not the amount of the hydrocarbons eliminated by the photocatalytic oxidation reactions, showing that the adsorption and desorption of H₂O molecules are generally sensitive to the temperature changes of solid surfaces.

1 Introduction

Since the discovery of the photoinduced superhydrophilicity of TiO₂ thin films in 1997 (Wang et al. 1997), TiO₂ thin film photocatalysts have attracted much attention as photofunctional materials for self-cleaning, anti-fogging, and anti-bacterial

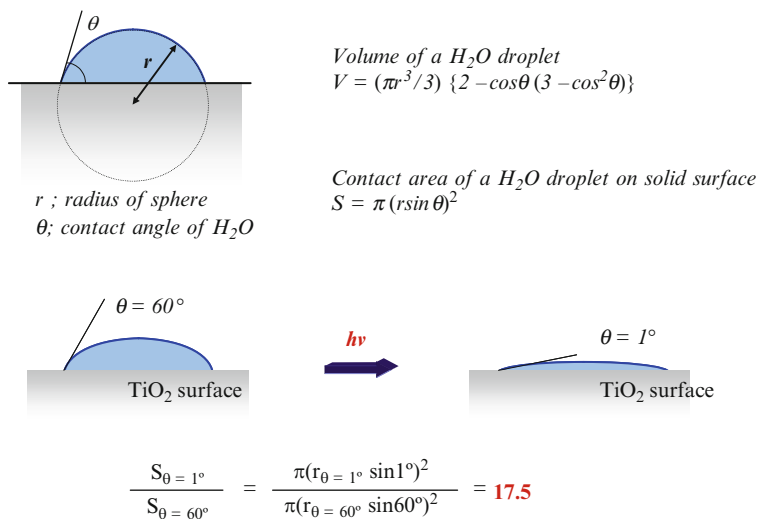
M. Takeuchi (✉)
Osaka Prefecture University, Osaka, Japan
e-mail: masato-t@chem.osakafu-u.ac.jp

applications (Fujishima et al. 1999; Fujishima et al. 2000). This phenomenon has been reported to be achieved by increasing the amount of hydroxyl groups of TiO₂ surfaces by the dissociative adsorption of H₂O molecules during UV light irradiation (Wang et al. 1998; Sakai et al. 1998; Wang et al. 1999). Hashimoto et al. have also mentioned that the photocatalytic oxidation of organic compounds on TiO₂ film surfaces is not related to this phenomenon due to the differing performances in the photocatalytic degradation of methylene blue and the surface wettability of TiO₂ and SrTiO₃ films (Miyachi et al. 2000). In recent years, the origin of the photoinduced hydrophilic properties of TiO₂ surfaces has been proposed as a meta-stable surface with increased tensile stress by the dissociative adsorption of H₂O molecules (Shibata et al. 2003). The adsorption states of H₂O molecules on TiO₂ single crystals under high vacuum condition have also been investigated by scanning tunneling microscopic observations (Brookes et al. 2001; Mezheny et al. 2003). However, the mechanism of this UV light driven phenomenon has yet to be clarified by experimental results. As shown in Scheme 1, the volume (V) and contact area (S) of a H₂O droplet on a solid surfaces (θ : contact angle, r : radius of H₂O droplet as a sphere) can be calculated as:

$$V = (\pi r^3 / 3) \{2 - \cos \theta (3 - \cos^2 \theta)\}$$

$$S = \pi (r \sin \theta)^2$$

When a H₂O droplet showing a contact angle of 60° reaches a contact angle of 1° by UV light irradiation, the contact area (S) between the solid surface and the H₂O droplet can be mathematically calculated to increase up to 17.5 times. Although this



Scheme 1 Relationships between the contact angle (θ), volume (V), and contact area (S) of an H₂O droplet on a solid surface

phenomenon is explained by the two-dimensional capillary effect (Wang et al. 1998), the density of the hydroxyl groups on the TiO_2 surfaces should increase at least several times during UV light irradiation to explain this big difference. However, direct experimental results showing that the hydroxyl groups on the TiO_2 surfaces increase under UV light irradiation have yet to be clearly reported since the discovery of this phenomenon. Furthermore, as shown in Fig. 1, the contact angles of the H_2O droplets on the TiO_2 thin film gradually increased under dark conditions after UV light irradiation was discontinued. On the contrary, when the film was outgassed at room temperature (r.t.) for 5 min, the high-wettable surface achieved by UV light irradiation was found to disappear immediately. These results could not be explained by the newly formed hydroxyl groups on the TiO_2 surfaces by UV light irradiation since such hydroxyl groups on oxide surfaces cannot be removed by outgassing at r.t. White et al. have concluded by TPD analyses of TiO_2 single crystals under ultrahigh vacuum conditions that the dissociation of H_2O to form OH groups is not required for the wetting phenomena since neither dissociation of H_2O nor oxygen vacancies control hydrophilicity (White et al. 2003). However, the results shown in Fig. 1 clearly indicate that analyses under high vacuum conditions may not clarify the origin of the photoinduced superhydrophilicity on TiO_2 surfaces. Analysis of the chemical states of hydroxyl groups and adsorption states of H_2O molecules on TiO_2 surfaces should, thus, be investigated in ambient conditions.

In this chapter, the detailed adsorption states of H_2O molecules on TiO_2 surfaces during UV light illumination under ambient conditions were investigated by near-infrared (NIR) absorption spectroscopy. The mechanism and driving force for the photoinduced hydrophilic conversion have been discussed with regard to the hydrogen bond structures of the H_2O molecules adsorbed on the TiO_2 surfaces.

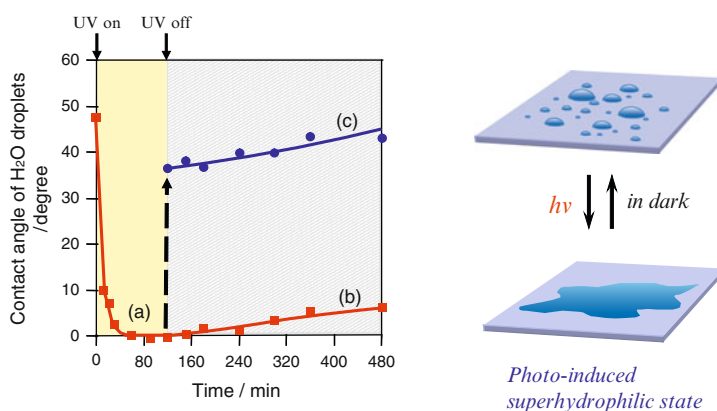


Fig. 1 Time profiles of the contact angles of H_2O droplets on TiO_2 thin film surfaces: (a) under UV light irradiation (ca. 1.0 mW/cm^2); (b) when the samples are stored in the dark; and (c) after the samples in (a) were evacuated at 298 K and stored under dark conditions

2 The Hydrogen-Bonded Structure of H₂O Molecules Adsorbed on TiO₂ Surfaces Under Ambient Conditions

2.1 Near-Infrared Spectra of H₂O Molecules Adsorbed on TiO₂ Surfaces

FT-IR measurement is one of the most powerful methods to investigate the adsorption states of H₂O molecules on solid surfaces (Munuera and Stone 1971; Primet et al. 1971; Morterra 1988; Burneau et al. 1990). However, since middle-infrared beams (MIR: 4,000–400 cm⁻¹; 2,500–25,000 nm) are sensitive to H₂O, it is difficult to investigate the adsorption states of H₂O on solid surfaces under aerated conditions. On the contrary, the small molar absorption coefficient of the overtone or combination bands due to H₂O molecules observed in near-infrared (NIR: 12,500–4,000 cm⁻¹; 800–2,500 nm) regions makes it possible to measure the absorption spectra of H₂O adsorbed on solid surfaces in air. The NIR absorption spectra of liquid water, ice, and water vapor have widely been investigated in order to clarify the structures of the complex hydrogen-bonded H₂O molecules (Buijs and Choppin 1963; McCabe et al. 1970; Fornes and Chaussidon 1978; Chalmers and Griffiths 2002; Ozaki and Kawata 1996). The diffuse reflectance NIR (DR-NIR) absorption spectra of H₂O adsorbed on TiO₂ surfaces are shown in Fig. 2a. Small absorption bands could be observed at around 1,940 and 1,450 nm. The absorption at 1,940 nm can be assigned to the combination ($\delta + \nu_{\text{asym}}$) band (Fornes and Chaussidon 1978; Chalmers and Griffiths 2002; Ozaki and Kawata 1996) and the small absorption at 1,450 nm assigned to the combination ($\nu_{\text{sym}} + \nu_{\text{asym}}$) band (McCabe et al. 1970; Chalmers and Griffiths 2002; Ozaki and Kawata 1996) (ν_{sym} : symmetric stretching, δ : bending, ν_{asym} : asymmetric stretching of the H₂O molecule). A sharp absorption peak at 1,380 nm assigned to the overtone (2 ν) band of the silanol groups of the quartz cell (Chalmers and Griffiths 2002) did not change even after evacuation at 1,073 K, indicating that the silanol

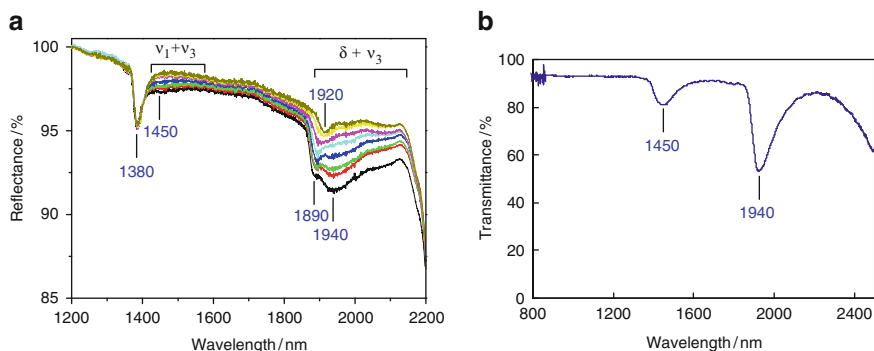


Fig. 2 Near-infrared absorption spectra of: (a) H₂O adsorbed on TiO₂ surfaces outgassed at r.t. (from bottom to top) in air, 60, 12.8, 5.1, 0.18, 0.02, 0.001 Torr; and (b) liquid H₂O (optical path length: ca. 80 μ m)

Table 1 List of the combination bands due to the different states of H₂O molecules observed in the near-infrared (NIR) region

Ice		Liquid near freezing point		Liquid near boiling point		Vapor		Assignments
(nm)	(cm ⁻¹)	nm	(cm ⁻¹)	nm	(cm ⁻¹)	nm	(cm ⁻¹)	
1,025	(9,760)	979	(10,210)	967	(10,340)	942	(10,613)	2ν ₁ + ν ₃
1,250	(7,990)	1,200	(8,310)	1,160	(8,640)	1,135	(8,807)	ν ₁ + ν ₂ + ν ₃
1,492	(6,700)	1,453	(6,880)	1,425	(7,020)	1,380	(7,252)	ν ₁ + ν ₃
1,780	(5,620)	1,780	(5,620)	1,786	(5,600)	–	–	ν ₂ + ν ₃ + ν _L
1,988	(5,030)	1,938	(5,160)	1,916	(5,220)	1,875	(5,332)	ν ₂ + ν ₃

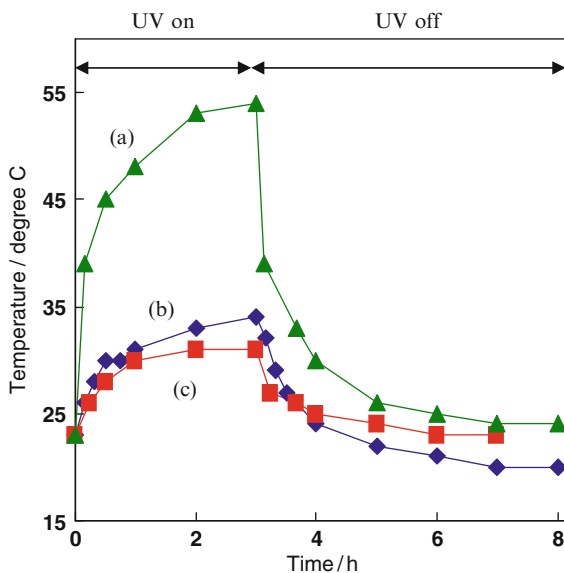
ν₁: symmetric stretching (3,657 cm⁻¹); ν₂: bending (1,595 cm⁻¹); ν₃: asymmetric stretching (3,756 cm⁻¹); ν_L: hindered rotation (600 cm⁻¹)

groups of the quartz cell do not affect the NIR absorption spectra of these powder samples. Most of the combination band at around 1,940 nm was found to disappear and a small band at 1,920 nm remained after evacuation at r.t. Moreover, this small band at 1,920 nm disappeared completely after evacuation at 473 K. These results clearly show that these combination bands due to H₂O molecules observed in the NIR regions are attributed to the physisorbed H₂O molecules rather than the hydroxyl groups of the TiO₂ surfaces. Detailed explanations of the absorption bands will be discussed from the standpoint of the hydrogen bonds in the H₂O clusters. The NIR absorption spectrum of liquid H₂O in a FT-IR cell equipped with CaF₂ windows (optical pass length: ca. 80 μm) is shown in Fig. 2b as reference. Liquid H₂O showed similar absorption bands at 1,940 and 1,450 nm to the H₂O molecules adsorbed on the TiO₂ surfaces. The assignments of the combination bands of the H₂O molecules are extracted from Refs. (Buijs and Choppin 1963; McCabe et al. 1970; Fornes and Chaussidon 1978; Chalmers and Griffiths 2002; Ozaki and Kawata 1996) and summarized in Table 1. From these results, the small absorption bands observed in the NIR spectra of the TiO₂ samples could be assigned to the H₂O molecules. Since the absorption bands at 1,940 and 1,890 nm (as a shoulder) are similar to liquid and gas phase H₂O molecules, respectively, the former band can be assigned to the “hydrogen-bonded H₂O” and the latter to the “less hydrogen-bonded H₂O” or “hydrogen bond-free H₂O.”

2.2 The Effect of UV Light Irradiation on the Structure of the H₂O Clusters Adsorbed on TiO₂ Surfaces

When solid surfaces are irradiated with light, the surface temperature increases by the heating effect of the light source, meaning that the entropy of the solid surfaces will always increase during light irradiation. The temperature changes of the TiO₂ samples during UV light irradiation under different conditions are shown in Fig. 3. When an H₂O filter to block infrared beams from an Hg lamp was not used, the

Fig. 3 Temperature changes during UV light irradiation for 3 h under various irradiation conditions and storage in the dark for 5 h: (a) without any filters; (b) with a 10-mm-thick H₂O filter in a Pyrex glass tray; and (c) with both a 10-mm-thick H₂O filter and H₂O cooling bath



temperature of the TiO₂ sample was found to increase up to ca. 328 K by the heating effect of the light source (initial temperature: ca. 298 K). When an H₂O filter (thickness: ca. 10 mm) in a Pyrex glass tray was used to block infrared beams from the light source, the temperature of the TiO₂ sample increased up to ca. 308 K. Even when an H₂O bath was also used with the H₂O filter in order to cool the powder sample, the temperature of the sample increased up to ca. 303 K. Immediately after the Hg lamp was turned off, the powder sample quickly cooled and gradually recovered its initial temperature. From these thermodynamic considerations, adsorption of H₂O on surfaces with increased entropy cannot be increased by light irradiation. In fact, Munuera et al. (Munuera et al. 1979) and Bahnemann et al. (Mendive et al. 2006) have reported that H₂O desorbs from TiO₂ surfaces during UV light irradiation.

Combination ($\delta + \nu_{\text{asym}}$) absorption bands due to the H₂O molecules adsorbed on the TiO₂ samples during UV light irradiation are shown in Fig. 4. Since UV light was irradiated from a medium pressure Hg lamp (Polymer 401, Helios Italquartz SRL) without any cutoff filters to control the wavelength of the irradiated light and H₂O filters to block the infrared light, the temperature of the TiO₂ samples increased up to ca. 323 K. The H₂O molecules adsorbed on TiO₂, in particular the hydrogen-bonded H₂O at around 1,940 nm, were found to decrease during UV light irradiation. The adsorption of H₂O was then found to recover gradually when the TiO₂ sample was placed under dark conditions. After UV light irradiation, when the TiO₂ sample was placed in the cold, e.g., on a stone table in a dark room, the adsorption of H₂O on the TiO₂ surface was confirmed to recover very quickly. These results clearly indicate that the H₂O molecules on TiO₂ surfaces desorb

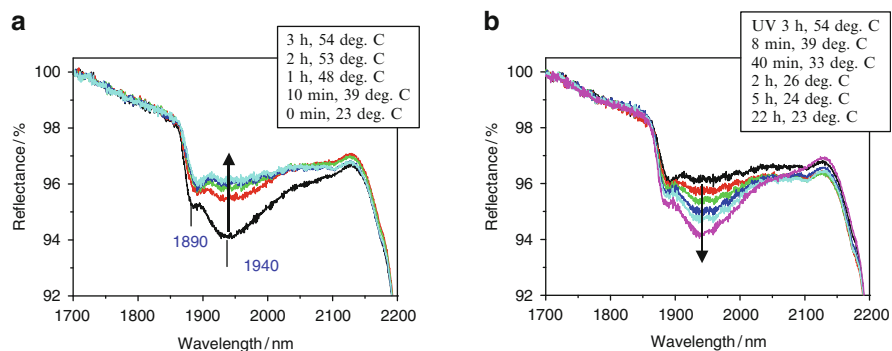


Fig. 4 Near-infrared absorption spectra of H₂O adsorbed on TiO₂ surfaces: (a) under UV light irradiation of 0, 10, 60, 120, and 180 min (from *bottom* to *top*); (b) after the samples in (a) were stored in the dark for 0, 8, 40, 120, 300, and 1,320 min (from *top* to *bottom*)

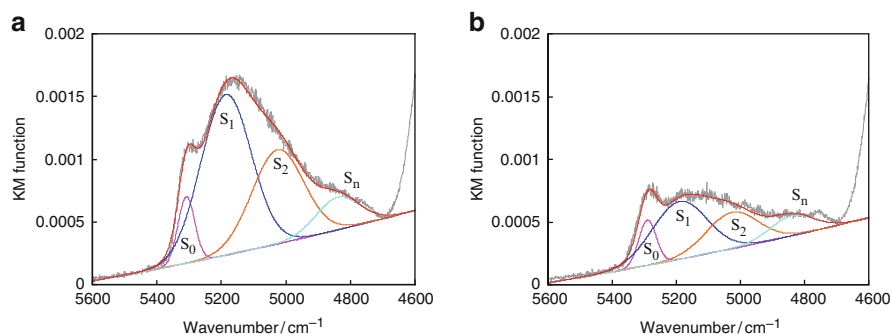


Fig. 5 Deconvoluted spectra of combination ($\delta + \nu_{\text{asym}}$) bands of the H₂O molecules adsorbed on TiO₂ surfaces: (a) before UV light irradiation and (b) after UV light irradiation for 3 h

during UV light irradiation and adsorb again on the TiO₂ surfaces after UV light irradiation is discontinued, depending on the temperature changes of the samples.

The NIR absorption spectra of the H₂O molecules adsorbed on the TiO₂ surface before and after UV light irradiation for 3 h were deconvoluted, as shown in Fig. 5. The NIR spectra could be deconvoluted into four components. When intermolecular hydrogen bonds are involved, two kinds of hydrogen bonds, such as a hydrogen-bond donor and a hydrogen-bond acceptor, can be considered (Takeuchi et al. 2005a). When one H₂O molecule interacts with the other by a hydrogen bond, as illustrated in Scheme 2, molecule (A) works as a hydrogen-bond acceptor and molecule (B) works as a hydrogen-bond donor. The O atom of molecule (A) strongly attracts not only the H atom of molecule (A) but also the H atom of the neighboring molecule (B) due to its high electronegativity. The polarization of the H₂O molecule arises from the former interaction while the latter works as the driving force for intermolecular hydrogen bonds. In this case, the OH bond of molecule (B) is strongly affected but the OH bond of molecule (A) is less affected.

Scheme 2 Interaction between two H₂O molecules by hydrogen bonds:
 (a) hydrogen-bond acceptor;
 (b) hydrogen-bond donor

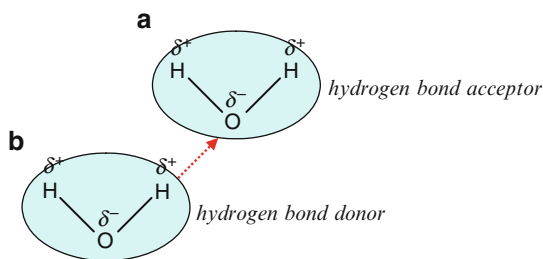


Table 2 Different chemical states of H₂O molecules depending on the number of hydrogen bonds on the TiO₂ surfaces before and after UV light irradiation

	Wavenumber/cm ⁻¹ (wavelength/nm)	
	Before UV light irradiation	After UV light irradiation for 3 h
<i>S</i> ₀	5,309 cm ⁻¹ (1,884 nm) 6.3%	5,290 cm ⁻¹ (1,890 nm) 11.3%
<i>S</i> ₁	5,186 cm ⁻¹ (1,928 nm) 50.3%	5,190 cm ⁻¹ (1,927 nm) 45.4%
<i>S</i> ₂	5,028 cm ⁻¹ (1,989 nm) 32.4%	5,026 cm ⁻¹ (1,990 nm) 28.8%
<i>S</i> _{<i>n</i>}	4,840 cm ⁻¹ (2,076 nm) 11.0%	4,839 cm ⁻¹ (2,067 nm) 14.5%

*S*₀: H₂O without active H-bonds; *S*₁: H₂O with 1 active H-bond; *S*₂: H₂O with 2 active H-bonds; *S*_{*n*}: H₂O with 2 active H-bonds and 1 (or 2) passive H-bond(s) (polymeric-chained H₂O molecules)

This means that the hydrogen bond donor may show a large shift in the chemical states of the H₂O molecule as compared to a hydrogen bond acceptor. From these considerations, the hydrogen bond donors/acceptors are expressed as “active hydrogen bonds” and “passive hydrogen bonds.” One H₂O molecule can possess four hydrogen bonds (two active and two passive) at the maximum, but the active hydrogen bond is much more important than the passive one. However, it is actually difficult to distinguish the two types of hydrogen bonds among the H₂O molecules.

The wavenumbers, wavelengths, and relative peak areas of the four components are summarized in Table 2. As mentioned above, since the H₂O vapor shows an intense peak at 1,875 nm, component *S*₀ can be associated with the hydrogen bond-free H₂O molecules. On the contrary, since liquid H₂O and ice show broad absorption at 1,938 and 1,988 nm, respectively, three components (*S*₁, *S*₂, and *S*_{*n*}) can be assigned to the hydrogen bonded H₂O molecules depending on the number of active hydrogen bonds. It is significant that component *S*₀ increased from 6.3% to 11.3% by UV light irradiation of the TiO₂. This clearly means that the distribution of the hydrogen bonds in the H₂O molecules adsorbed on the TiO₂ surfaces decreased during UV light irradiation.

Figure 6 shows the structure models of the H₂O clusters on the TiO₂ surface before and after UV light irradiation (Takeuchi et al. 2005b). When the TiO₂ surfaces are irradiated with UV light, the distribution of the hydrogen bonds in

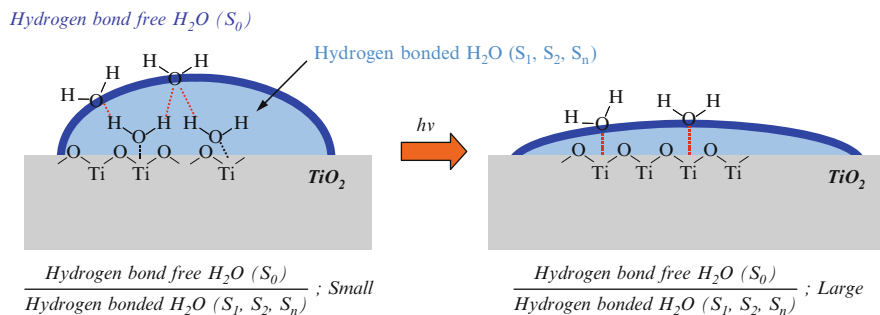


Fig. 6 Schematic diagrams of the shapes of the H₂O clusters on the TiO₂ surfaces before and after UV light irradiation

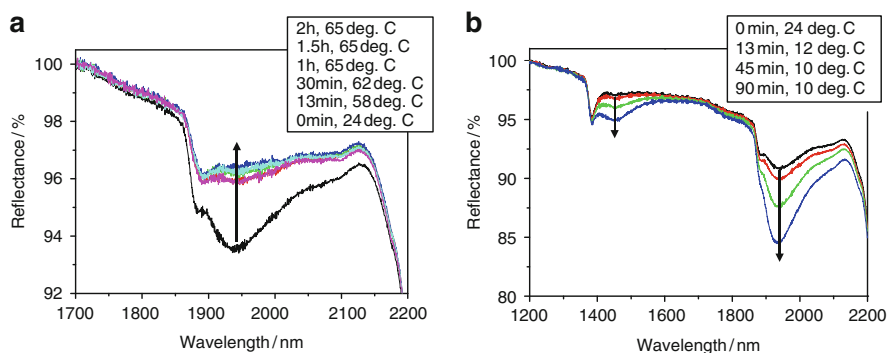


Fig. 7 Near-infrared absorption spectra of H₂O adsorbed on TiO₂ surfaces: (a) TiO₂ samples heated by an electric hot plate for 0, 13, 30, 60, 90, and 120 min (from *bottom* to *top*) and (b) TiO₂ samples cooled by ice water for 0, 13, 45, and 90 min (from *top* to *bottom*)

the H₂O molecules decreases, resulting in a lessening of the surface tension of the H₂O clusters. These changes in the surface tension resulting from a decrease in the amount of adsorbed H₂O molecules can be associated with the driving force behind the spreading out of the H₂O clusters thermodynamically on the TiO₂ surfaces.

The NIR absorption spectra of H₂O adsorbed on the TiO₂ surfaces after heating by an electric hot plate and after cooling by ice water are shown in Fig. 7. When the TiO₂ sample was heated up to 338 K, the H₂O molecules on the surfaces were desorbed (vaporization), resulting in a decrease in the distribution of the hydrogen bonds. On the contrary, when the TiO₂ powder was cooled to around 283 K, the adsorption of H₂O on the surface increased (condensation), resulting in an increase in the distribution of the hydrogen bonds. These results clearly indicate that the adsorption and desorption of H₂O molecules on oxide surfaces are completely dependent on the temperature changes.

3 Surface Wettability of TiO₂ Thin Films

3.1 The Effect of Heating or UV Light Irradiation on the Surface Wettability of TiO₂ Thin Film Photocatalysts

The heating effect on the surface wettability of the TiO₂ thin films was investigated in detail. Figure 8 shows the changes in the contact angles of the H₂O droplets on the TiO₂ thin films when the samples were heated on a hot plate at ca. 323 K in the dark or were irradiated with UV light (ca. 1.0 mW/cm²) with and without an H₂O filter to block the heating effect from the Hg lamp. The TiO₂ thin films showed an H₂O contact angle of 0° by UV light irradiation within 30 min despite the use of an H₂O filter. On the contrary, when the film was heated at 323 K under dark conditions, the H₂O contact angles were found to decrease to ca. 30° and then level off. The surface of the TiO₂ thin film did not show a superhydrophilic state (contact angle of less than 5° for the H₂O droplets); however, the surface wettability was improved by heating at 323 K without UV light irradiation. The surface wettability against H₂O could be improved by the heating effect because the adsorption of hydrocarbons were inhibited (Garbassi et al. 1994). Since the hydrocarbons adsorbed on the TiO₂ surfaces could hardly be decomposed by heating at around 323 K, hydrophilic conversion by the heating effect may be associated with the desorption of the H₂O molecules from the TiO₂ surfaces.

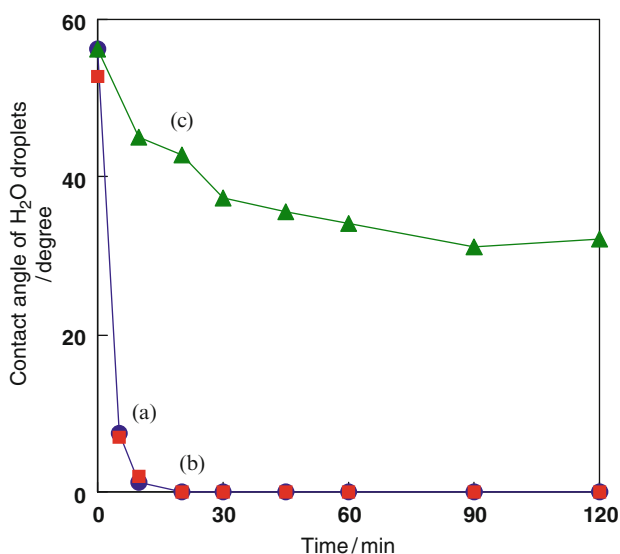


Fig. 8 Effect of heating on the changes in the contact angles of H₂O droplets on TiO₂ thin films under UV light irradiation using a 100-W high pressure Hg lamp (ca. 1.0 mW/cm²): (a) with a 10-mm-thick H₂O filter; (b) without an H₂O filter; and (c) with heating at around 323 K in the dark

The phenomenon of windows fogging up in the winter season is not caused by the hydrophobicity of the window surfaces. When H_2O vapor in air is condensed on the window surfaces and cooled by low outdoor temperatures, the window glass fogs up. It is known that windows insulated to keep out the outdoor cold or heated by an internal heater can effectively avoid surface condensation of H_2O droplets. These natural phenomena show us that the window-fogging is caused by an increase in the amount of H_2O adsorption due to temperature changes.

However, the superhydrophilic states of the TiO_2 surfaces could be obtained only by UV light irradiation, as shown in Fig. 8. In order to elucidate the role of UV light on the photoinduced superhydrophilicity of TiO_2 surfaces, changes in the surface wettability on the films under UV light irradiation under different atmospheric conditions were investigated. As shown in Fig. 9, when the TiO_2 thin films were irradiated with UV light using a 24-W conventional fluorescent valve (ca. $25\text{--}30\ \mu\text{W}/\text{cm}^2$) under O_2 (purity $>99.9\%$) or a synthesized air ($\text{O}_2/\text{N}_2 = 1/4$) flow, the films were found to show high wettability. However, when these TiO_2 thin films were irradiated under a flow of N_2 (purity $>99.9\%$), the contact angles of the H_2O droplets did not change at all. Moreover, when the O_2 flow was switched to N_2 flow, the hydrophilic conversion of the TiO_2 surface was found to stop and level off. These results clearly indicate that the coexistence of O_2 is necessary for the photoinduced hydrophilic conversion of the TiO_2 surfaces.

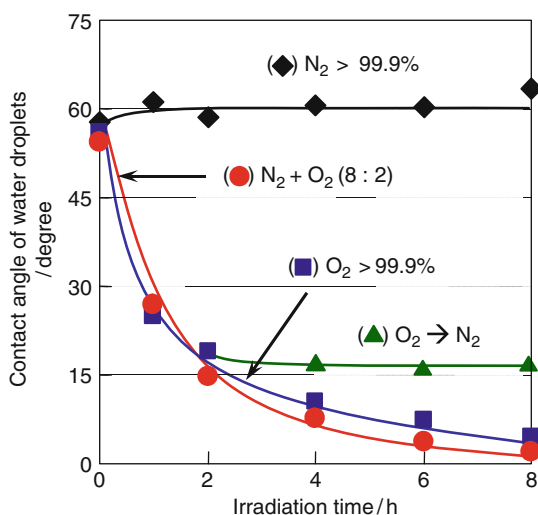


Fig. 9 Effect of the coexistence gases under UV light irradiation by using a 24-W conventional fluorescent valve (ca. $25\text{--}30\ \mu\text{W}/\text{cm}^2$) on changes in the contact angles of H_2O droplets on TiO_2 thin films: (a) in synthetic air ($\text{N}_2/\text{O}_2 = 4/1$); (b) in O_2 (purity $>99.9\%$); (c) in N_2 (purity $>99.9\%$); and (d) when O_2 flow was switched to N_2

3.2 Photocatalytic Oxidation of Hydrocarbons Adsorbed on TiO₂ Surfaces for the Hydrophilic Conversion of TiO₂ Thin Films

To clarify the role of O₂, the photocatalytic decomposition of acetaldehyde with sufficient amounts of O₂ or N₂ on TiO₂ thin films under UV light irradiation (ca. 1.0 mW/cm²) was investigated. When the TiO₂ thin film was irradiated with UV light in O₂ atmosphere, the acetaldehyde was decomposed into CO₂ and H₂O in an efficient photocatalytic reaction, as shown in Fig. 10. On the contrary, when the TiO₂ thin film was irradiated in N₂ atmosphere, the acetaldehyde was hardly decomposed and small amounts of CO were formed as a partial oxidative product. Moreover, when these TiO₂ thin films were irradiated in O₂ or N₂ atmosphere under UV light irradiation (ca. 25–30 μW/cm²), the amount of hydrocarbons adsorbed on the TiO₂ films could be estimated by the C1s XPS spectra. As can be seen in Fig. 11, the intensity of the C1s peak decreased only when the TiO₂ films were irradiated with UV light in O₂ atmosphere. These results obtained by XPS analyses correspond well to those for the photocatalytic decomposition of acetaldehyde in O₂ or N₂ atmosphere, clearly indicating that hydrocarbons adsorbed on the TiO₂ surfaces are efficiently decomposed only when the TiO₂ surfaces are irradiated with UV light in O₂ atmosphere.

The relationship between the surface wettability of the TiO₂ thin films treated by various methods and the relative amounts of the hydrocarbons determined from the C1s XPS peak intensities is summarized in Table 3. The TiO₂ thin films after calcination at 723 K in air for 1 h showed a contact angle of 0° for the H₂O droplets (high wettable state) while more than half the amount of hydrocarbons was found to be removed. The TiO₂ thin films rinsed in 2 M NaOH solution at 323 K for 1 min showed a contact angle of 11° and a removal of about 30% of the hydrocarbons.

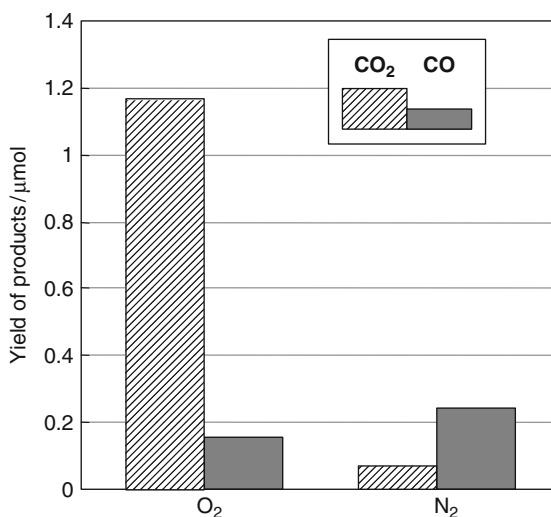


Fig. 10 Photocatalytic degradation of acetaldehyde in the presence of O₂ or N₂ on the TiO₂ thin films prepared on quartz substrates under UV light irradiation using a 100-W high pressure Hg lamp (ca. 1.0 mW/cm²) for 3 h

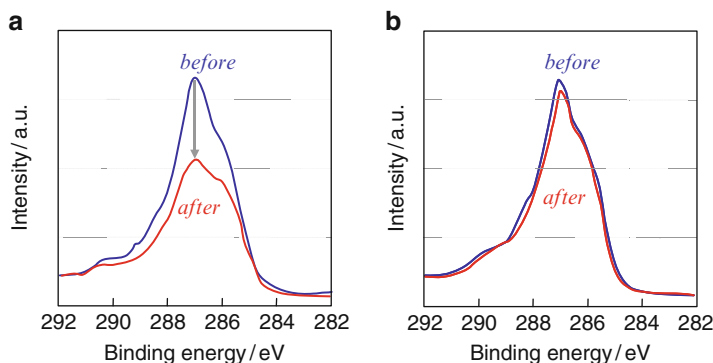


Fig. 11 C 1s XPS spectra of TiO₂ thin films under UV light irradiation using a 24-W conventional fluorescent valve (ca. 25–30 $\mu\text{W}/\text{cm}^2$) for 8 h in the presence of (a) O₂ and (b) N₂ gases

Table 3 Relationship between the contact angles of H₂O droplets on the TiO₂ thin films and the relative amounts of hydrocarbons as determined by the intensity of the C1s XPS spectra after various pretreatments

Pretreatments	Contact angle of H ₂ O (deg.)	Relative intensity of C1s peak at 286.4 eV ^a
(1) Before treatment	49.3	100
(2) Washed by distilled H ₂ O for 1 min	20.1	98.5
(3) Rinsed in NaOH (2 M, 323 K) soln. for 1 min	11.2	71.2
(4) Calcination at 723 K for 1 h	0	40.1
(5) UV light irradiation for 3 h (1 mW/cm ²)	0	64.7

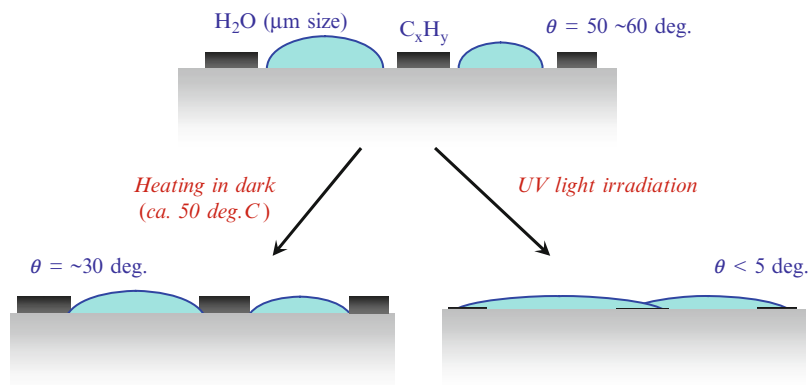
^aThe influence of hydrocarbons from XPS apparatus was not subtracted

Moreover, the hydrocarbons were hardly removed by washing in distilled H₂O, although these TiO₂ thin films showed a contact angle of 20° for the H₂O droplets. These results clearly suggest that the surface wettability of the TiO₂ films can be improved by the removal of the hydrocarbons by different treatments to UV light irradiation. It has been reported that the surface wettability of nonalkaline silica glass can be improved by vacuum UV light (172 nm) irradiation in O₃ atmosphere, since the hydrocarbons adsorbed on glass surfaces could be decomposed (Iso et al. 1999; Vig and Lebus 1976). Iso et al. have also reported that an improvement in surface wettability can be obtained by vacuum UV light irradiation under synthesized air (N₂/O₂ = 4/1) atmosphere, while on the other hand, the contact angles of H₂O on silica glass did not change by vacuum UV light irradiation in N₂ atmosphere (Iso et al. 1999). SiO₂ surfaces generally do not show any photocatalytic reactivity for the degradation of hydrocarbons in air; however, hydrocarbons adsorbed on silica surfaces have been reported to be decomposed by vacuum UV light (172 nm) irradiation in O₃ or O₂ atmosphere, leading to an improvement of the surface wettability.

3.3 Mechanism for the Photoinduced Hydrophilic Conversion of TiO₂ Photocatalyst Surfaces Under UV Light Irradiation

From these investigations, the mechanism behind the photoinduced wettability changes of TiO₂ surfaces could be proposed, as shown in Scheme 3. When the TiO₂ thin films are heated at ca. 323 K under dark conditions, the H₂O molecules desorb from the TiO₂ surfaces; however, the hydrocarbons are not removed, leading to a decrease in the contact angles of H₂O until 30° and then leveling off. On the contrary, when the TiO₂ surfaces are irradiated with UV light, the H₂O molecules desorb from the surfaces by the effect of heating from the light source and, at the same time, the hydrocarbons adsorbed on the TiO₂ surfaces are partially decomposed by photocatalytic degradation. The partial removal of hydrocarbons from the TiO₂ surfaces and the decrease in the distribution of the hydrogen-bond in the H₂O clusters adsorbed on the TiO₂ surfaces lead to an efficient diffusion of the H₂O molecules onto the free spaces of the TiO₂ surfaces, resulting in the formation of a widely spread out H₂O multilayer. The TiO₂ surfaces on which the H₂O and hydrocarbons are reduced exhibited high surface wettability against H₂O.

From the viewpoint of surface science, the hydrophilicity or hydrophobicity of solid surfaces indicates the strong or weak interaction of the H₂O molecules with the solid surfaces, respectively. These surface properties are essentially investigated and discussed using such surface scientific techniques as FT-IR, adsorption isotherm, and adsorption heat measurements. However, solid surfaces that show high wettability against H₂O are recognized to be hydrophilic but, as shown in Fig. 12, the surface wettability is not considered to be in good proportion to the hydrophilic or hydrophobic properties determined by the amount of H₂O adsorbed on the solid surface. When large amounts of H₂O molecules adsorb on hydrophilic TiO₂ surfaces, such H₂O molecules interact with each other by hydrogen bonds and form bulky H₂O clusters due to the high surface tension of the H₂O molecules.



Scheme 3 Proposed mechanism for the improvement of the surface wettability of TiO₂ photocatalyst surfaces under UV light irradiation

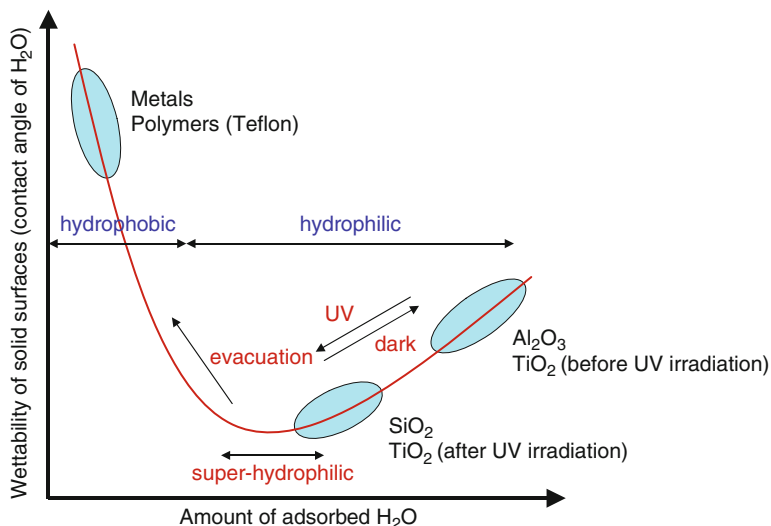


Fig. 12 Relationship between the surface wettability against H_2O and the amount of H_2O adsorbed on solid surfaces

Furthermore, since the Ti^{4+} sites of such hydrophilic TiO_2 surfaces can also work as strong adsorption sites for hydrocarbon molecules, the TiO_2 surfaces simultaneously show oleophilic properties. The surfaces generally show a high contact angle for H_2O droplets of around 60° at the initial stage before UV light irradiation. However, when the TiO_2 surfaces are irradiated with UV light, the hydrocarbons on the surfaces are decomposed as a photocatalytic reaction and the H_2O adsorbed is vaporized by the heating effect of the light source, resulting in H_2O clusters with small surface tension that can spread out thermodynamically.

In conclusion, the wettability of TiO_2 surfaces cannot be defined only by the surface hydrophilic or hydrophobic properties. The amount of hydrocarbons adsorbed on the surfaces that can be controlled by the photocatalytic reaction is the other important factor determining the wettability of the TiO_2 surfaces.

References

- Wang R, Hashimoto K, Fujishima A, Chikuni M, Kojima E, Kitamura A, Shimohigoshi M, Watanabe T (1997) Light-induced amphiphilic surfaces. *Nature* 388:431
- Fujishima A, Hashimoto K, Watanabe T (1999) TiO_2 photocatalysis fundamentals and applications, BKC, Inc.
- Fujishima A, Rao TN, Tryk DA (2000) Titanium dioxide photocatalysis *J. Photochem. Photobiol., C: Photochem. Rev.*, 1:1; and references therein
- Wang R, Hashimoto K, Fujishima A, Chikuni M, Kojima E, Kitamura A, Shimohigoshi M, Watanabe T (1998) Photogeneration of Highly Amphiphilic TiO_2 Surfaces. *Adv Mater* 10:135

- Sakai N, Wang R, Fujishima A, Watanabe T, Hashimoto K (1998) Effect of Ultrasonic Treatment on Highly Hydrophilic TiO₂ Surfaces. *Langmuir* 14:5918
- Wang R, Sakai N, Fujishima A, Watanabe T, Hashimoto K (1999) Studies of Surface Wettability Conversion on TiO₂ Single-Crystal Surfaces. *J Phys Chem B* 103:2188
- Miyauchi M, Nakajima A, Fujishima A, Hashimoto K, Watanabe T (2000) Photoinduced Surface Reactions on TiO₂ and SrTiO₃ Films: Photocatalytic Oxidation and Photoinduced Hydrophilicity. *Chem Mater* 12:3
- Shibata T, Irie H, Hashimoto K (2003) Enhancement of Photoinduced Highly Hydrophilic Conversion on TiO₂ Thin Films by Introducing Tensile Stress. *J Phys Chem B* 107:10696
- Brookes IM, Muryn CA, Thornton G (2001) Imaging Water Dissociation on TiO₂(110). *Phys Rev Lett* 87 Art. No. 266103
- Mezhenny S, Maksymovych P, Thompson TL, Diwald O, Stahl D, Walck SD, Yates JT Jr (2003) STM studies of defect production on the TiO₂(110)-(1×1) and TiO₂(110)-(1×2) surfaces induced by UV irradiation. *Chem Phys Lett* 369:152
- White JM, Szanyi J, Henderson M (2003) The Photon-Driven Hydrophilicity of Titania: A Model Study Using TiO₂(110) and Adsorbed Trimethyl Acetate. *J Phys Chem B* 107:9029
- Munuera G, Stone FS (1971) Adsorption of water and organic vapours on hydroxylated rutile. *Discuss Faraday Soc* 52:205
- Primet M, Pichat P, Mathieu M-V (1971) Infrared study of the surface of titanium dioxides. I. Hydroxyl groups. *J Phys Chem* 75:1216
- Morterra C (1988) An infrared spectroscopic study of anatase properties. Part 6. Surface hydration and strong Lewis acidity of pure and sulphate-doped preparations. *J Chem Soc Faraday Trans 1*, 84:1617
- Burneau A, Barres O, Gallas JP, Lavalley JC (1990) Comparative study of the surface hydroxyl groups of fumed and precipitated silicas. 2. Characterization by infrared spectroscopy of the interactions with water. *Langmuir* 6:1364
- Buijs K, Choppin GR (1963) Near-Infrared Studies of the Structure of Water. II. Ionic Solutions. *J Chem Phys* 39:2035
- McCabe WC, Subramanian S, Fisher HF (1970) Near-infrared spectroscopic investigation of the effect of temperature on the structure of water. *J Phys Chem* 74:4360
- Fornes V, Chaussidon J (1978) An interpretation of the evolution with temperature of the v₂+v₃ combination band in water. *J Chem Phys* 68:4667
- Chalmers JM, Griffiths PR (2002) *Handbook of vibrational spectroscopy*, vol. 3, Wiley, New York
- Ozaki Y, Kawata S (1996) *Near infrared spectroscopy (Kin-Sekigai-Bunko)*. Japan Scientific Societies Press, Tokyo
- Munuera G, Rives-Arnau V, Saugedo A (1979) Photo-adsorption and photo-desorption of oxygen on highly hydroxylated TiO₂ surfaces. Part 1. Role of hydroxyl groups in photo-adsorption. *J Chem Soc Faraday Trans 1*, 75:736
- Mendive CB, Bredow T, Blesa MA, Bahnemann DW (2006) ATR-FTIR measurements and quantum chemical calculations concerning the adsorption and photoreaction of oxalic acid on TiO₂. *Phys Chem Chem Phys* 8:3232
- Takeuchi M, Martra G, Coluccia S, Anpo M (2005a) Investigations of the Structure of H₂O Clusters Adsorbed on TiO₂ Surfaces by Near-Infrared Absorption Spectroscopy. *J Phys Chem B* 109:7387
- Takeuchi M, Sakamoto K, Martra G, Coluccia S, Anpo M (2005b) Mechanism of Photoinduced Superhydrophilicity on the TiO₂ Photocatalyst Surface. *J Phys Chem B* 109:15422
- Garbassi F, Morra M, Occhiello E (1994) *Polymer surfaces from physics to technology*. Willey, New York
- Iso S, Igarashi T, Matsuo H (1999) Study on UV/O₃ cleaning by Xe₂ excimer lamp. *J Illum Eng Inst Jpn* 83:273
- Vig JR, Lebus JW (1976) UV/ozone cleaning of surfaces. *IEEE Trans Parts, Hybrids, Packag* 12:365

Part VI
Photocatalytic Water-splitting for the
Evolution of H₂ from H₂O

Chapter 23

Photocatalytic Hydrogen Production from Water on Visible Light-Responsive TiO₂ Thin Films Under Solar Light Irradiation

Masaaki Kitano, Masato Takeuchi, Masaya Matsuoka, Michio Ueshima, and Masakazu Anpo

Abstract The recent progress in the photocatalytic decomposition of water by visible light-responsive TiO₂ (Vis-TiO₂) thin film photocatalysts is reviewed here. Special attention is focused on the separate evolution of H₂ and O₂ from water using Vis-TiO₂ thin films prepared by a radio-frequency magnetron sputtering method. These Vis-TiO₂ thin films were found to act as efficient photocatalysts for the decomposition of water with the separate evolution of H₂ and O₂ from H₂O under visible or solar light irradiation.

1 Introduction

In recent years, an increase in world population and industrial development have led to accelerated energy consumption and the unabated release of toxic agents into the air and water, causing such adverse effects as pollution-related diseases and global warming. It is, therefore, of great importance to achieve sustainable development without environmental destruction. In line with these objectives, the application of pollution-free photocatalysis in many chemical processes has recently attracted a great deal of attention (Anpo 2004). The high activity and stability as well as availability of TiO₂ photocatalysts are especially interesting for such practical applications as the purification of toxic compounds in polluted water and air, the photocatalytic decomposition of water, and the development of anti-fogging films and photovoltaic cells (Fujishima et al. 2000).

In the pioneering work of Fujishima and Honda (1972), UV light irradiation of a TiO₂ photoelectrode in aqueous solution led to the production of H₂ and O₂ on a Pt electrode and TiO₂ photoelectrode, respectively, onto which a small electric voltage

M. Kitano (✉)

Industry-University Cooperation Organization, Osaka Prefecture University, Osaka, Japan
e-mail: kitano@chem.osakafu-u.ac.jp

was applied. However, due to a large band gap of 3.20 eV, only a small UV fraction of the 2–3% of solar light that reaches the Earth can be utilized. Sensitization of the TiO₂ to react to a much larger visible region is, therefore, of great importance (Anpo and Takeuchi 2003). Several investigations have been carried out to develop visible light-responsive TiO₂ (Vis-TiO₂) photocatalysts by adding small amounts of such components as cations or metal oxides (Choi et al. 1994). In recent years, the physical doping of transition metal ions such as V, Cr, Fe, Co, and Ni into TiO₂ by an advanced ion-implantation technique has been shown to enable TiO₂ photocatalysts to work under visible light (Anpo 1997). Another promising approach involves the anion doping of TiO₂ films and nanostructures. Efforts have also been made to narrow the band gap by doping with carbon (Irie et al. 2003), nitrogen (Asahi et al. 2001), and sulfur (Umebayashi et al. 2002). Such procedures shift the valence band to a less positive potential, thereby decreasing the band gap. Recently, the splitting of water has been achieved by using other photocatalytic materials under visible light (Zou et al. 2001; Sayama et al. 2001; Maeda et al. 2006). However, powdered photocatalytic systems yield a mixture of H₂ and O₂ since the redox sites to produce H₂ and O₂ are in close proximity. To obtain pure H₂ gas that can be easily and safely utilized as fuel on a large, global scale, the separate evolution of H₂ and O₂ from water using thin film photocatalysts operating under solar energy is strongly desired (Anpo et al. 2005).

In this chapter, a radio-frequency magnetron sputtering (RF-MS) method has been applied to synthesize such Vis-TiO₂ thin films and their efficiency for the photocatalytic splitting of water was investigated.

2 Photocatalytic Decomposition of Water into H₂ and O₂ Using Visible Light-Responsive TiO₂ Thin Films

2.1 Effect of the Sputtering Parameters on the Photocatalytic Activity of TiO₂ Thin Films for the Water-Splitting Reaction

The development of Vis-TiO₂ photocatalysts has been investigated by the substitutional doping of metals or nonmetals with the aim of extending the absorption edge into visible light regions and to improve the photocatalytic reactivity. However, most of these modified TiO₂ photocatalysts are in powder form and, thus, have limitations for practical or industrial applications. The development of stable and easily applicable TiO₂ thin films which can operate not only under UV but also under visible light is, therefore, of great importance (Anpo 2004). With this objective in mind, an RF-MS deposition method was applied to prepare Vis-TiO₂ thin film photocatalysts (Takeuchi et al. 2001). The system is equipped with a substrate (quartz or Ti foil) center positioned in parallel just above the source material, that is, the calcined TiO₂ plate. The target-to-substrate distance (D_{T-S}) was fixed at a value between the range of 70 and 90 mm. The calcined TiO₂ plate is sputtered by

Ar plasma by inducing an RF power of 300 W in Ar atmosphere, and the TiO_2 thin film is prepared on the quartz or Ti metal foil substrate mounted on the heater. The substrate temperature (T_S) was held at a fixed degree between the range of 473 and 873 K. Pt deposition was also performed by the RF-MS method at T_S of 298 K. Figure 1a, b, d shows the UV-vis transmission spectra of the TiO_2 thin films prepared on the quartz substrates under various substrate temperatures. The D_{T-S} was kept constant at 80 mm. The thickness for all the films was fixed at around 1.2 μm . The TiO_2 thin films prepared at T_S of 473 K with D_{T-S} of 80 mm (denoted as UV- TiO_2 -(473,80)) show no absorption in wavelengths longer than 380 nm, while the films prepared at 673 K (Vis- TiO_2 -(673,80)) and at 873 K (Vis- TiO_2 -(873,80)) are yellow-colored and exhibit considerable absorption in wavelengths region longer than 380 nm, enabling the absorption of visible light. Among these three types of TiO_2 thin films, Vis- TiO_2 -(873,80) exhibited an adsorption edge at the longest wavelength regions of around 600 nm. Control of the substrate temperature during the simple one-step TiO_2 deposition process was, thus, found to be one of the major contributing factors in controlling the efficiency of visible light absorption (Kitano et al. 2005). Furthermore, the absorption spectra of Vis- TiO_2 -(873) shifted toward longer wavelength regions with a decrease in D_{T-S} from 90 to 70 mm (Fig. 1c-e). These TiO_2 thin films are referred to as Vis- TiO_2 -(873, D_{T-S}).

It is known that sputtered atoms from the target material experience many collisions with the sputtering gas molecules before they reach the substrate. The amount of sputtered atoms that reach the substrate and their kinetic energy may, thus, increase with a decrease in D_{T-S} . Under conditions of short D_{T-S} , the TiO_2 thin film is easily reduced by bombardment with the large amount of high energy sputtered atoms in the deposition process. Figure 2 shows the SIMS depth profiles of UV- TiO_2 and Vis- TiO_2 -(873, D_{T-S}), revealing that the concentrations of the

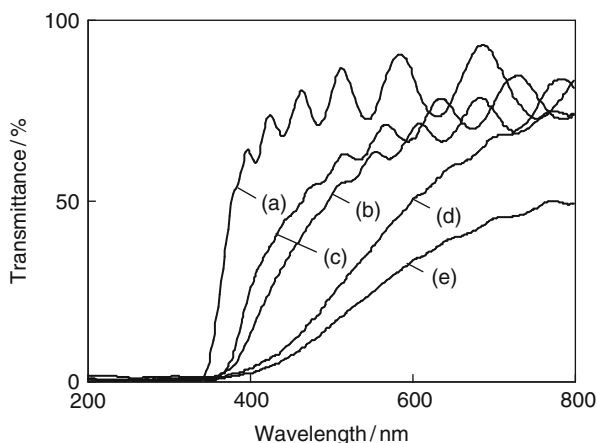
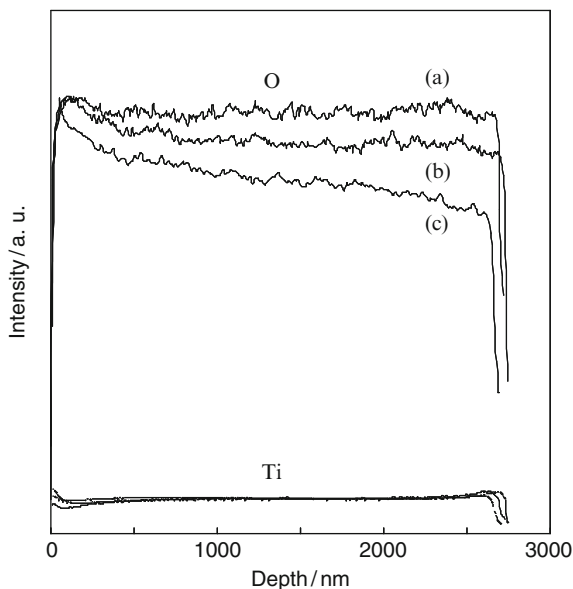


Fig. 1 UV-vis transmission spectra of TiO_2 thin films prepared on a quartz substrate under various substrate temperatures (T_S) and the target-to-substrate distance (D_{T-S}). T_S (K): (a) 473, (b) 673, and (c-e) 873; D_{T-S} (mm): (c) 90, (a, b, d) 80, and (e) 70

Fig. 2 Depth distribution profiles of O and Ti for (a) UV-TiO₂-(473,80), (b) Vis-TiO₂-(873,80), and (c) Vis-TiO₂-(873,70) thin films, as determined by SIMS measurements



O²⁻ ions for Vis-TiO₂-(873,80) and Vis-TiO₂-(873,70) gradually decrease from the top surface (O/Ti ratio of 2.00 ± 0.01) to the inside bulk, although no significant changes were observed for UV-TiO₂ which is composed of stoichiometric TiO₂ (2.00 ± 0.01). The O/Ti values of the inside bulk for Vis-TiO₂-(873,80) and Vis-TiO₂-(873,70) were found to be 1.93 and 1.70, respectively. These results clearly indicate that the higher the kinetic energy of the sputtered atoms, the lower the O/Ti ratio of the TiO₂ thin films, accompanied by a large shift in their absorption band toward visible light regions. Such a unique anisotropic structure was seen to play an important role in the modification of the electronic properties, thus enabling the absorption of visible light (Matsuoka et al. 2005).

The photocatalytic activity of Pt-loaded TiO₂ thin films was investigated under UV and visible light irradiation. The apparent quantum efficiencies for the photocatalytic evolution of H₂ or O₂ from water involving sacrificial reagents are summarized in Table 1. Both the UV-TiO₂ and Vis-TiO₂ thin film photocatalysts loaded with Pt were found to be effective in decomposing water into H₂ and O₂ under UV light. On the other hand, the photocatalytic evolution of H₂ and O₂ from water, including sacrificial reagents such as CH₃OH or AgNO₃, proceeded only with Pt-loaded Vis-TiO₂ under visible light irradiation. The electronic band gap of Vis-TiO₂ can be considered significantly smaller than that of UV-TiO₂ (i.e., 3.2 eV). However, the conduction band edge (E_{CB}) and valence band edge (E_{VB}) may be so located as to facilitate the decomposition of H₂O into H₂ and O₂. Moreover, it was found that the quantum yields for H₂ and O₂ evolution under visible light irradiation on Pt-loaded Vis-TiO₂-(873, D_{T-S}) remarkably increased with a decrease in D_{T-S} from 90 to 80 nm (Table 1). This enhanced photocatalytic activity can be ascribed to the large shift of the absorption edge of Vis-TiO₂-(873,80) toward visible light

Table 1 Quantum yields for H₂ and O₂ evolution from aqueous solutions of methanol and silver nitrate on TiO₂ thin films under UV and visible light irradiation

Photocatalyst	Quantum yield (%)			
	$\lambda = 360$ nm		$\lambda = 420$ nm	
	H ₂ ^a	O ₂ ^b	H ₂ ^a	O ₂ ^b
UV-TiO ₂ -(473,80)	26.2	12.6	0.00	0.00
Vis-TiO ₂ -(673,80)	27.2	38.0	0.13	0.85
Vis-TiO ₂ -(873,70)	5.2	8.2	0.05	0.18
Vis-TiO ₂ -(873,80)	34.2	60.0	1.25	2.43
Vis-TiO ₂ -(873,90)	26.5	32.8	0.10	0.58

^aFrom 50 vol% aqueous methanol solutions^bFrom 0.05 M aqueous silver nitrate solution

regions as compared to Vis-TiO₂-(873,90). A further decrease in the D_{T-S} led to a dramatic decrease in the quantum yields for H₂ and O₂ evolution under both UV and visible light irradiation despite the strong visible light absorption of Vis-TiO₂-(873,70). The typical absorption band of Vis-TiO₂-(873,70) in the range of 600–800 nm can be ascribed to the Ti³⁺ centers (Torimoto et al. 1996) formed by the strong attack of the high-energy sputtered atoms or Ar plasma around the TiO₂ target. In fact, an ESR signal due to the Ti³⁺ centers ($g_{\perp} = 1.975$ and $g_{\parallel} = 1.940$) (Hurum et al. 2003) was observed for Vis-TiO₂-(873,70).

Thus, formed Ti³⁺ may act as the recombination centers of the photo-formed electrons and holes, leading to a decrease in the photocatalytic activity of Pt-Vis-TiO₂-(873,70). These results show that a slight decrease in the O/Ti ratio of the TiO₂ thin films plays an important role in the preparation of visible light-responsive catalysts.

The photoelectrochemical properties of the Vis-TiO₂ films prepared on a Ti foil substrate (Vis-TiO₂/Ti) under visible light were also investigated in 0.05 M NaOH aqueous solution. An anodic photocurrent was observed even under visible light irradiation up to 520 nm, with a band gap energy determined to be about 2.5 eV. To assess the flat band potential, the current–voltage characteristics of UV-TiO₂-(473,80)/Ti and Vis-TiO₂-(873,80)/Ti were also investigated. The zero current potential of UV-TiO₂-(473,80)/Ti (−0.91 V vs. SCE at pH 12.3) was more negative than that of Vis-TiO₂-(873,80)/Ti (−0.82 V vs. SCE at pH 12.3). This potential is equivalent to the flat band potential (E_{FB}) in polycrystalline semiconductors from which E_{CB} can be evaluated. The E_{CB} of UV-TiO₂-(473,80)/Ti and Vis-TiO₂-(873,80)/Ti is estimated to be approximately −1.11 and −1.02 V versus SCE at pH 12.3, respectively, since, in general, the energy difference between E_{CB} and E_{FB} has been assumed to be 0.2 eV for oxide semiconductors. Taking these results into consideration, the band structures of these thin films are summarized in Fig. 3.

To investigate the long-term stability of Vis-TiO₂-(873,80)/Ti, the relationship between the anodic photocurrent and irradiation time was measured under visible light irradiation. The anodic photocurrent was observed to be constant during approximately 20 h consecutive measurement under visible light longer than 450 nm,

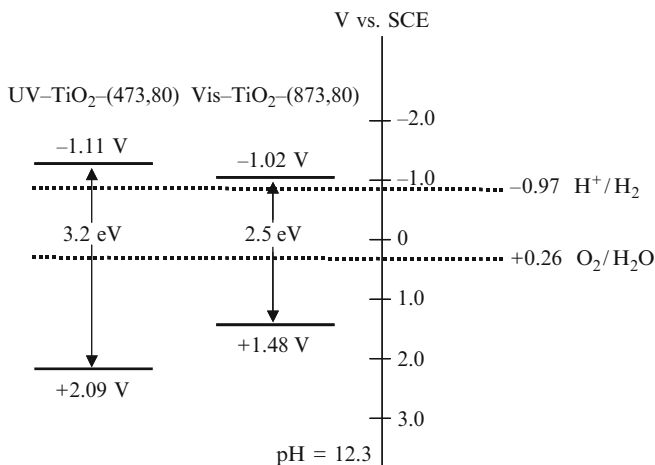


Fig. 3 Apparent conduction band (E_{CB}) and valence band (E_{VB}) energy levels of the TiO_2 thin films as determined from photoelectrochemical experiments in 0.05 M NaOH (pH 12.3)

indicating that Vis- TiO_2 -(873,80)/Ti exhibits long-term stability. Moreover, repetitive use of the Vis- TiO_2 -(873,80)/Ti thin films was possible for the photocatalytic reaction while the photocatalytic activity remained stable even after a year. In fact, no noticeable differences were seen in the UV-vis spectra and XRD patterns of Vis- TiO_2 -(873,80) before and after photoelectrochemical measurements.

The separate evolution of H_2 and O_2 from water was investigated with a TiO_2 thin film device prepared by an RF-MS method (Kitano et al. 2007).

The TiO_2 thin film device (Vis- TiO_2 -(873,80)/Ti/Pt) consists of Ti foil of 50 μm thickness and a Vis- TiO_2 -(873,80) thin film deposited on one side and, on the other side, with Pt. The prepared TiO_2 thin film device was mounted on an H-type glass container, as shown in Fig. 4, separating the two aqueous solutions. The TiO_2 side of the thin film device was immersed in 1.0 M NaOH aqueous solution and the Pt side was immersed in 0.5 M H_2SO_4 aqueous solution in order to add a small chemical bias between the two aqueous solutions. As shown in Fig. 5, H_2 and O_2 could be separately produced on this Vis- TiO_2 -(873,80)/Ti/Pt thin film device under visible light ($\lambda \geq 420$ and 450 nm), while no reaction proceeded on a similar UV- TiO_2 -(473,80)/Ti/Pt thin film device. However, in the initial stage, the ratio of H_2/O_2 shows a deviation from the stoichiometric value of 2 (up to 4 h). A small amount of organic compounds involved in the aqueous solution are considered to be decomposed during the initial stage. After 4 h, the stoichiometric decomposition of water could be observed. In fact, the rates of H_2 evolution were 0.18 $\mu\text{mol h}^{-1}$ ($\lambda \geq 420$ nm) and 0.088 $\mu\text{mol h}^{-1}$ ($\lambda \geq 450$ nm) while the O_2 evolution rates were 0.090 $\mu\text{mol h}^{-1}$ ($\lambda \geq 420$ nm) and 0.043 $\mu\text{mol h}^{-1}$ ($\lambda \geq 450$ nm), respectively, showing a good stoichiometry of 2:1 for $\text{H}_2:\text{O}_2$. Moreover, the separate evolution of H_2 and O_2 from water was investigated under solar light irradiation with the Vis- TiO_2 -(873,80)/Ti/Pt thin film device. Light irradiation was carried out with a

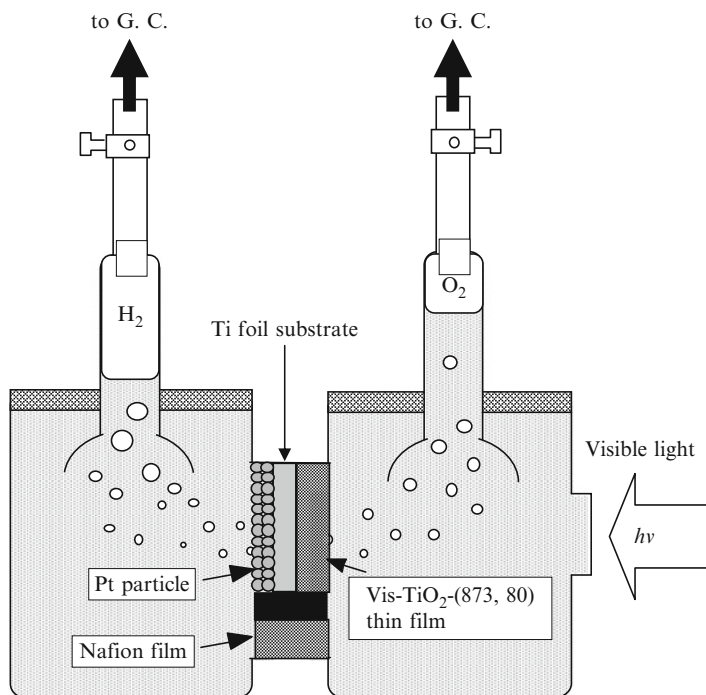


Fig. 4 H-type glass container for the separate evolution of H_2 and O_2 using a TiO_2 thin film device ($\text{Vis-TiO}_2\text{-(873,80)/Ti/Pt}$). TiO_2 side: 1.0 M NaOH aq. and Pt side: 0.5 M H_2SO_4 aq.

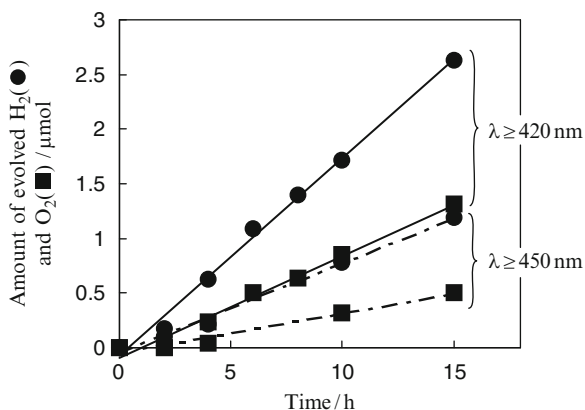


Fig. 5 Time profile of the photocatalytic decomposition of H_2O with the separate evolution of H_2 and O_2 under visible light on a $\text{Vis-TiO}_2\text{-(873,80)/Ti/Pt}$ thin film device in an H-type glass container of two aqueous phases having different pH values. TiO_2 side: 1.0 M NaOH aq. and Pt side: 0.5 M H_2SO_4 aq.

sunlight-gathering system that could remove the UV rays in sunlight. Sunlight irradiation of this device successfully led to the stoichiometrical evolution of H₂ and O₂ from the Pt and Vis-TiO₂ sides, respectively (Kitano et al. 2007). It was, thus, confirmed that Vis-TiO₂-(873,80)/Ti/Pt thin film photocatalysts are an effective photofunctional material for applications in systems for clean and safe H₂ production from water using the most abundant energy source, solar light.

2.2 Effect of Chemical Etching by HF Solution on the Photocatalytic Activity of Visible Light-Responsive TiO₂ Thin Films for the Water-Splitting Reaction

The effect of chemical etching on the photocatalytic activity of the Vis-TiO₂-(873,80) thin film photocatalyst was also investigated in order to improve the photocatalytic activity. Chemical etching was carried out by immersing the thin films in a 0.045 vol% HF solution for 1 h. The obtained HF-treated Vis-TiO₂-(873,80)/Ti thin films were then referred to as HF-Vis-TiO₂/Ti. After chemical etching, the samples were rinsed in deionized water to cleanse the surface and then dried at 373 K for 1 h. The photoelectrochemical properties of the Vis-TiO₂/Ti thin films before and after chemical etching by HF solution were investigated in order to clarify its effect on the reactivity. Figure 6 shows the cyclic voltammogram of the Vis-TiO₂/Ti and HF-Vis-TiO₂/Ti electrodes under chopped UV or visible light irradiation. Dark currents were negligible under scanning potentials from -0.4 to +1.5 V versus SCE, while the anodic photocurrent increased with an increase in the anodic bias. The observed photocurrent represents the anodic oxidation of water to oxygen by the photogenerated holes at each electrode under UV or visible light irradiation. Figure 6 shows that the HF-Vis-TiO₂/Ti electrode exhibits a much higher photocurrent than Vis-TiO₂/Ti under both UV and visible light. Moreover, the apparent quantum efficiencies, that is, the incident photon-to-current conversion efficiency (IPCE), of these electrodes are defined as the number of electrons collected per incident photon and determined by measuring the photocurrent (I_{ph}) of the electrodes at each excitation wavelength using the following equation (Kikuchi et al. 2006):

$$\text{IPCE}(\%) = \frac{1,240 \times I_{\text{ph}}(\text{A cm}^{-2})}{\lambda(\text{nm}) \times I_{\text{inc}}(\text{W cm}^{-2})} \times 100,$$

where I_{inc} is the incident light intensity (W cm^{-2}) and λ is the excitation wavelength (nm). The IPCE values at 1.0 V are summarized in Table 2 and it can be seen that HF treatment is effective for an improvement of the photoelectrochemical performance of the Vis-TiO₂/Ti films.

Figure 7 shows the SEM images of the surface morphology of Vis-TiO₂/Ti before and after HF treatment. It appears that the surface roughness increases and the interspaces between the columnar TiO₂ crystallites are extended by HF treatment. In fact, the surface area of the Vis-TiO₂/Ti thin film increased with an increase in the treatment time. The effect of HF treatment on the surface areas of the Vis-TiO₂/Ti

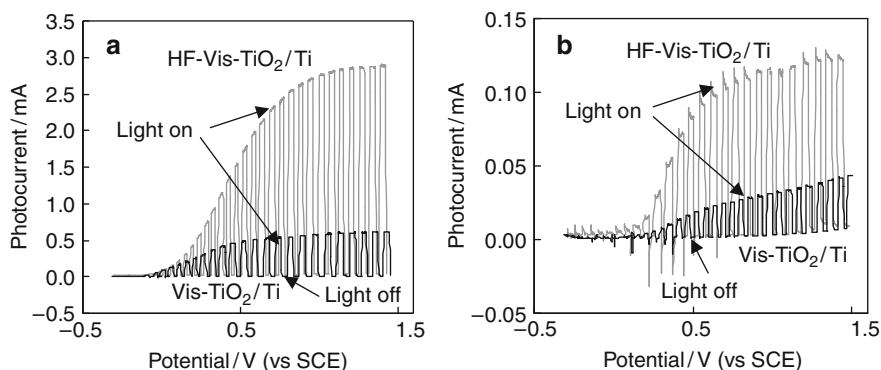
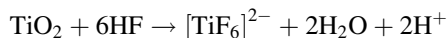


Fig. 6 Cyclic voltammogram of Vis-TiO₂/Ti and HF-Vis-TiO₂/Ti electrode under chopped (a) UV and (b) visible light irradiation ($\lambda \geq 420$ nm). Electrolyte: 0.1 M HClO₄ aq.

Table 2 IPCE of UV-TiO₂/Ti, Vis-TiO₂/Ti, and HF-Vis-TiO₂/Ti measured in 0.1 M HClO₄ aqueous solution at +1.0 V versus SCE

Electrode	IPCE (%)	
	$\lambda = 360$ nm	$\lambda = 420$ nm
UV-TiO ₂	18	0
Vis-TiO ₂	40	5.6
HF-Vis-TiO ₂	66	9.4

thin films was investigated by BET surface measurements using krypton as the adsorbate. The surface areas of Vis-TiO₂/Ti and HF-Vis-TiO₂/Ti (5×20 mm²) were 379 and 559 cm², respectively, indicating that the surface of Vis-TiO₂/Ti can be effectively etched by immersion into the HF solution. The surface of the Vis-TiO₂/Ti thin film was considered to be dissolved in HF solution through the following reaction (Cai et al. 2005):



These results indicate that HF-Vis-TiO₂/Ti has shorter diffusion lengths for the photoformed holes to reach the solid–liquid interfaces than untreated Vis-TiO₂/Ti. AC-impedance measurements of Vis-TiO₂/Ti and HF-Vis-TiO₂/Ti were performed to determine their donor density (N_d) which can be obtained from the Mott–Schottky equation:

$$1/C^2 = (2/e\epsilon\epsilon_0 N_d)(V - V_{fb} - kT/e),$$

where C is the space charge capacitance, ϵ is the dielectric constant of the semiconductor (the value $\epsilon = 120$ was used for the polycrystalline n -TiO₂), ϵ_0 is the permittivity of the vacuum, V is the electrode potential, V_{fb} is the flat band potential, k is the Boltzmann constant, e is the electronic charge, and T is the absolute

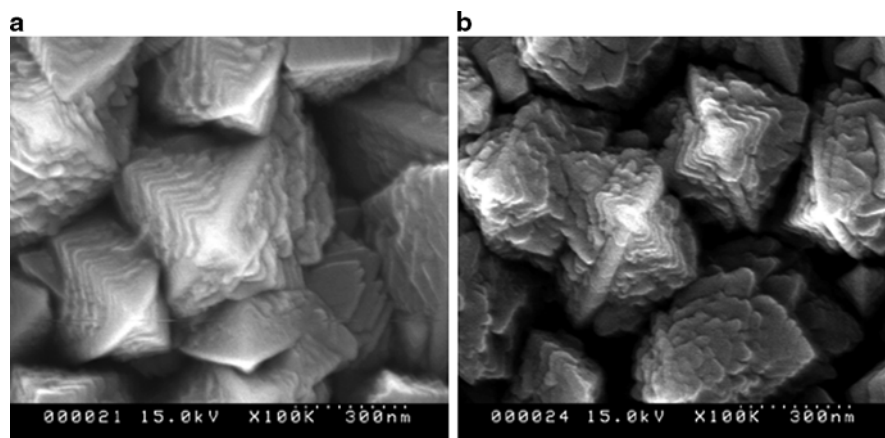


Fig. 7 SEM images of (a) Vis-TiO₂/Ti and (b) HF-Vis-TiO₂/Ti thin films

temperature. The donor densities of Vis-TiO₂/Ti and HF-Vis-TiO₂/Ti at an AC frequency of 1,000 Hz were calculated to be 2.63×10^{20} and $4.65 \times 10^{20} \text{ cm}^{-3}$, respectively. Donor density is an important parameter for the semiconductivity and higher donor densities can lower the bulk resistance and enhance the photocurrent (Zhao et al. 1998). It was, thus, considered that the photogenerated electrons of HF-Vis-TiO₂/Ti could reach the TiO₂/substrate interface more easily as compared to Vis-TiO₂/Ti due to its higher conductivity. From these characterization studies, it was concluded that the high surface area and conductivity play an important role in improving the photoelectrochemical performance of HF-Vis-TiO₂/Ti.

Field experiments were conducted outdoors under natural sunlight on a clear sunny day in August. Figure 8 shows the H-type glass container with a sunlight-gathering system which was able to remove most of the UV rays in sunlight. Figure 9 shows the separate evolution of H₂ and O₂ from water under sunlight using the HF-Vis-TiO₂/Ti/Pt photocatalyst. Here, H₂ and O₂ are shown to evolve in stoichiometric ratio under sunlight irradiation while the H₂ evolution ratio was $18 \mu\text{mol h}^{-1} \text{ cm}^{-2}$ in the early initial stage (up to 2.5 h), while no gas evolution was observed under dark conditions even under the same experimental conditions. The solar energy conversion efficiency (η) in the presence of an external applied potential was estimated by the following equation (Khan et al. 2002):

$$\eta(\%) = 100 \times j \times (1.23 - E_{\text{app}}) / I_0,$$

where j is the current density (mA cm^{-2}) estimated from the H₂ evolution rate, E_{app} is the applied chemical bias (0.826 V), and I_0 is the intensity of the incident light (125 mW cm^{-2}). The efficiency of solar energy conversion was calculated to be approximately 0.3% which could be improved under natural sunlight since light irradiation is carried out with a sunlight-gathering system that removes the UV rays found in sunlight. In fact, the maximum efficiency of solar energy conversion was

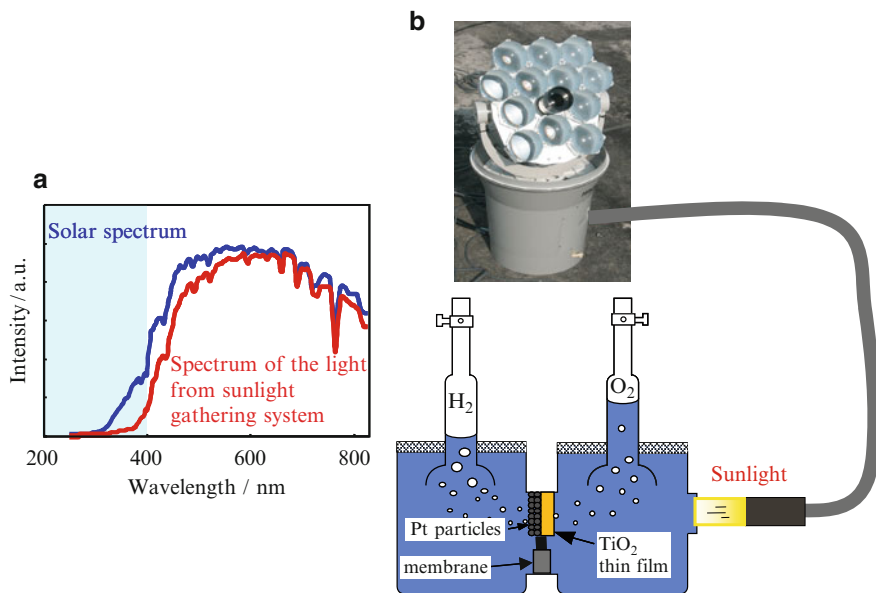
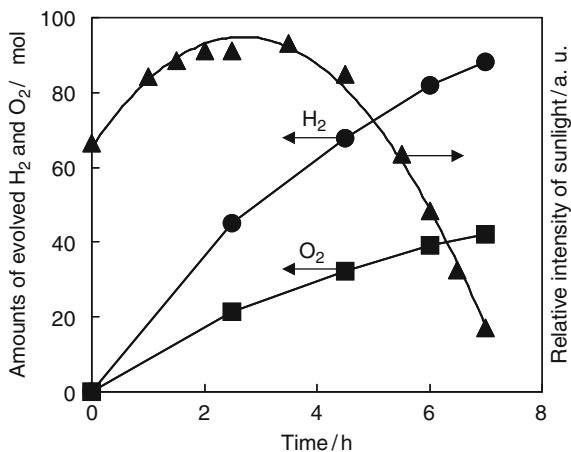


Fig. 8 (a) The spectra of sunlight and the light from the sunlight-gathering system. (b) H-type glass container with a sunlight-gathering system

Fig. 9 Separate evolution of H₂ and O₂ on the HF-Vis-TiO₂/Ti/Pt thin film photocatalyst irradiated by light beams from a sunlight-gathering system using the H-type glass container shown in Fig. 8



found to be 0.85% at a bias voltage of 0.5 V when the efficiency was investigated with a conventional electrochemical setup (HZ3000, Hokuto Denko) under natural sunlight. It was, thus, demonstrated that the surface etching of the TiO₂ thin films by HF treatment is, in fact, an effective method in improving the photocatalytic reactivity as well as photoelectrochemical performance.

3 Effect of Nitrogen Substitution on the Photocatalytic Activity of TiO₂ Thin Films for the Water-Splitting Reaction

Much work has recently been carried out in the development of Vis-TiO₂ by the doping of various anions, such as N, S, or C, as a substitute for oxygen in the TiO₂ lattice (Asahi et al. 2001; Umebayashi et al. 2002; Irie et al. 2003). For these anion-doped TiO₂ photocatalysts, the mixing of the p-states of the doped anion (N, S, C) with the O 2p-states was reported to shift the valence band edge upwards to narrow the band gap energy of TiO₂. However, most of these nitrogen-doped TiO₂ exhibited visible light absorption as a shoulder in the wavelength range of 400–600 nm (Asahi et al. 2001), indicating that the isolated N 2p-orbitals are formed above the O 2p-orbitals. This is due to the limited concentration of nitrogen that could be doped into the TiO₂ lattice at a very low range of <2%. However, we have successfully prepared high nitrogen-substituted TiO₂ (N-TiO₂) thin films by an RF-MS method in an N₂/Ar gas mixture (Kitano et al. 2006). The N-TiO₂ thin films were prepared by an RF-MS method using a calcined TiO₂ plate as the source material and Ar gas and N₂ gas as the sputtering gases. The concentration of N₂ in the sputtering gas [N₂/(N₂ + Ar)] was varied from 2 to 40%. A TiO₂ thin film was also prepared by the RF-MS method in an O₂/Ar gas mixture (O₂/Ar = 4%), that is, TiO₂(O₂/Ar). Figure 10 shows the UV-vis absorption spectra of the N-TiO₂ and TiO₂(O₂/Ar) thin films prepared on a quartz substrate with a film thickness of 1.2 μm. The TiO₂(O₂/Ar) thin films prepared under an O₂/Ar gas mixture were colorless and transparent to visible light, thus enabling the absorption of only UV light of wavelengths shorter than 390 nm.

On the other hand, N-TiO₂ thin films with low concentrations of substituted nitrogen (<2%) exhibited visible light absorption as a shoulder in the wavelength range of 400–500 nm, indicating that the isolated N 2p-orbitals are formed above the O 2p-orbitals. Furthermore, the absorption band of N-TiO₂ with high concentrations of substituted nitrogen of more than 2% shifted smoothly toward visible light regions, as shown in Fig. 10b–e. The steep absorption edges in the visible light region are evidence of the narrowing of the band gap energy. The band gap energy of the N-TiO₂ thin films was estimated to be around 2.58–2.25 eV from the onset of the absorption edges, which is much smaller than for TiO₂(O₂/Ar) (3.2 eV). The narrowing of the band gap is considered to be due to the mixing of the N 2p-states with the O 2p-states on the top valence band (Asahi et al. 2001).

The effect of the concentration of the substituted nitrogen on the photocatalytic activity of the N-TiO₂ thin films was evaluated by measuring the anodic photocurrent under UV and visible light irradiation. The photoelectrochemical properties of N-TiO₂ prepared on an ITO electrode were examined using an aqueous solution of 0.25 M K₂SO₄ (pH 6.7). It was found that the anodic photocurrent increased with an increase in the concentration of the substituted nitrogen, reaching a maximum with the 6% nitrogen-substituted TiO₂ thin film which exhibited the highest activity in photocurrent conversion under UV and visible light irradiation. Figure 11 shows the photocurrent observed for the N-TiO₂/ITO electrode with substituted nitrogen

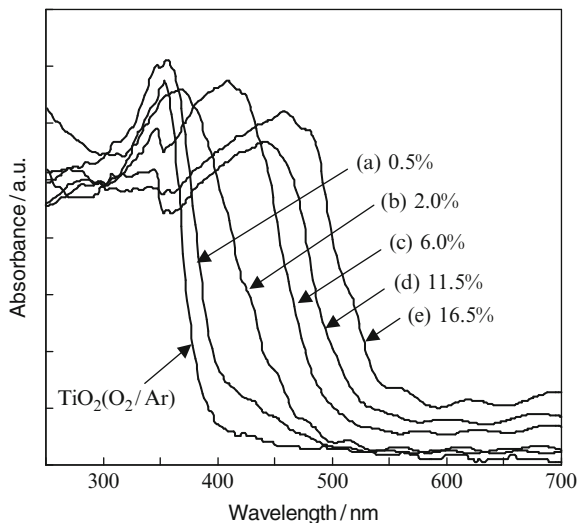


Fig. 10 UV-vis absorption spectra of TiO₂(O₂/Ar) and N-TiO₂ thin films substituted with various concentrations of nitrogen by an RF-MS method in an N₂/Ar gas mixture

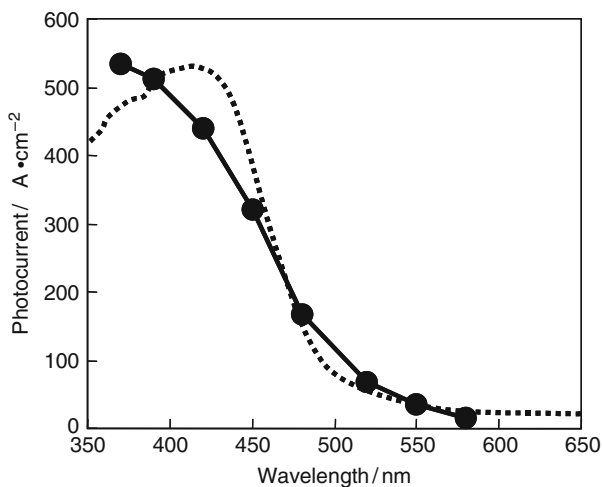


Fig. 11 Relative photocurrent, as a function of the cutoff wavelength of the incident light, for the N-TiO₂/ITO electrode measured in 0.25 M K₂SO₄ aqueous solution at +1.0 V versus SCE. Broken line shows the UV-vis absorption spectrum of N-TiO₂/ITO

of 6.0% as a function of the incident light wavelength which was controlled by cutoff filters. These measurements were carried out with a bias of +1.0 V versus SCE and dark currents were negligible under these conditions. The photoelectrochemical onset of N-TiO₂ was located at approximately 550 nm and showed a good parallel relationship between the photoresponse and absorption spectrum.

These results clearly show that the observed photocurrent originated from a band gap transition. The quantum yield, or absorbed photon-to-current conversion efficiency (APCE), defined as the number of electrons collected per absorbed photons, was determined by measuring the photocurrent of the N-TiO₂/ITO electrode at each excitation wavelength using the following equation (Kitano et al. 2006):

$$\text{APCE}(\%) = \frac{\text{number of reacted electrons}}{\text{number of absorbed photons}} \times 100.$$

The APCE at 1.0 V (vs. SCE) reached 25.2 and 22.4% under UV ($\lambda = 360$ nm) and visible light irradiation ($\lambda = 420$ nm), respectively. Moreover, the photoelectrochemical decomposition of water was carried out under biased conditions. As shown in Fig. 12, H₂ and O₂ evolved in a stoichiometric ratio under visible light ($\lambda \geq 450$ nm), while no gas evolution was observed in the dark under the same experimental conditions. The total amount of evolved H₂ was estimated to be 13 μmol from the photocurrent (35 μA) observed for 20 h. The calculated value was in rough agreement with the experimental value. These results indicate that the observed photocurrent is attributed to the photo-oxidation of water into O₂ and not to the photo-oxidation of the N-TiO₂ thin film itself. It was, thus, demonstrated that the RF-MS method was effective in the preparation of high nitrogen-substituted TiO₂ thin film photocatalysts for the production of H₂ in the photoelectrochemical splitting of water under sunlight irradiation.

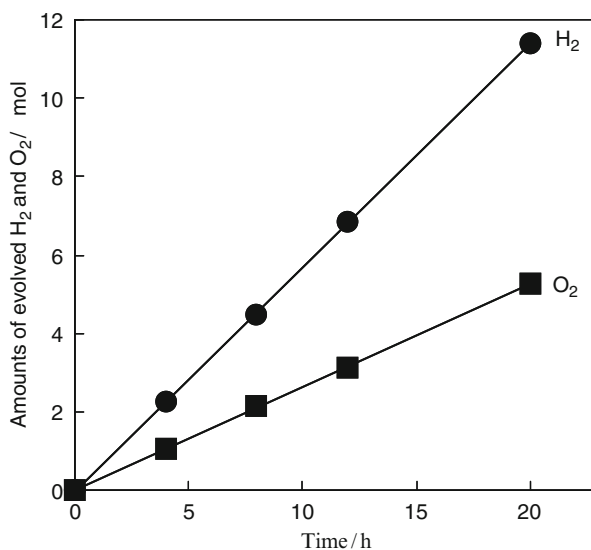


Fig. 12 Reaction time profiles of the photoelectrochemical decomposition of water on N-TiO₂/Ti and the Pt electrode under visible light irradiation ($\lambda \geq 450$ nm). The applied bias was 1.5 V versus the Pt counter electrode

4 Summary

Vis-TiO₂ thin films were successfully developed by an RF-MS deposition method using a TiO₂ plate as the source material and pure Ar gas as the sputtering gas. Vis-TiO₂ thin films treated with HF solution (HF-Vis-TiO₂) were found to exhibit a remarkable enhancement in their photoelectrochemical performance not only under UV but also under visible light irradiation as compared to untreated Vis-TiO₂. The stoichiometrical and separate evolution of H₂ and O₂ could also be successfully achieved using the HF-Vis-TiO₂/Ti/Pt thin film photocatalyst, and a solar energy conversion efficiency of 0.85% at a bias voltage of 0.5 V was also observed. Moreover, nitrogen-substituted TiO₂ (N-TiO₂) thin film photocatalysts could also be prepared by an RF-MS method using a N₂/Ar sputtering gas mixture. The N-TiO₂ thin film photocatalysts prepared on conducting glass electrodes showed anodic photocurrents attributed to the photo-oxidation of water under visible light, its extent depending on the wavelengths up to 550 nm. N-TiO₂ thin film photocatalysts were also found to be effective in initiating significant reactions such as the production of H₂ in the photoelectrochemical splitting of water under sunlight irradiation.

Acknowledgments This work was supported by a “Grant-in-Aid for the Creation of Innovations through Business–Academic–Public Sector Cooperation” (No. 13308) from the Ministry of Education, Culture, Sports, Science, and Technology of Japan. The authors would like to express sincere thanks for their kind support.

References

- Anpo M (1997) Photocatalysis on titanium oxide catalysts: Approaches in achieving highly efficient reactions and realizing the use of visible light. *Catal Surv Jpn* 1:169–179
- Anpo M (2004) Preparation, characterization, and reactivities of highly functional titanium oxide-based photocatalysts able to operate under UV–Visible light irradiation: Approaches in realizing high efficiency in the use of visible light. *Bull Chem Soc Jpn* 77:1427–1442
- Anpo M, Takeuchi M (2003) The design and development of highly reactive titanium oxide photocatalysts operating under visible light irradiation. *J Catal* 216:505–516
- Anpo M, Dohshi S, Kitano M, Hu Y, Takeuchi M, Matsuoka M (2005) The preparation and characterization of highly efficient titanium oxide-based photofunctional materials. *Annu Rev Mater Res* 35:1–27
- Asahi R, Morikawa T, Ohwaki T, Aoki K, Taga Y (2001) Visible-light photocatalysis in nitrogen-doped titanium oxides. *Science* 293:269–271
- Cai QY, Paulose M, Varghese OK, Grimes CA (2005) The effect of electrolyte composition on the fabrication of self-organized titanium oxide nanotube arrays by anodic oxidation. *J Mater Res* 20:230–236
- Choi WY, Termin A, Hoffman MR (1994) The role of metal ion dopants in quantum-sized TiO₂: Correlation between photoreactivity and charge carrier recombination dynamics. *J Phys Chem* 98:13669–13679
- Fujishima A, Honda K (1972) Electrochemical photolysis of water at a semiconductor electrode. *Nature* 238:37–38

- Fujishima A, Rao TN, Tryk DA (2000) Titanium dioxide photocatalysis. *J Photochem Photobiol C: Photochem Rev* 1:1–21
- Hurum DC, Agrios AG, Gray KA, Rajh T, Thurnauer MC (2003) Explaining the enhanced photocatalytic activity of Degussa P25 mixed-phase TiO₂ using EPR. *J Phys Chem B* 107:4545–4549
- Irie H, Watanabe Y, Hashimoto K (2003) Carbon-doped anatase TiO₂ powders as a visible-light sensitive photocatalyst. *Chem Lett* 32:772–773
- Khan SUM, Al-Shahry M, Ingler WB Jr (2002) Efficient photochemical water splitting by a chemically modified *n*-TiO₂. *Science* 297:2243–2245
- Kikuchi H, Kitano M, Takeuchi M, Matsuoka M, Anpo M, Kamat PV (2006) Extending the photoresponse of TiO₂ to the visible light region: Photoelectrochemical behavior of TiO₂ thin films prepared by the radio frequency magnetron sputtering deposition method. *J Phys Chem B* 110:5537–5541
- Kitano M, Takeuchi M, Matsuoka M, Thomas JM, Anpo M (2005) Preparation of visible light-responsive TiO₂ thin film photocatalysts by an RF magnetron sputtering deposition method and their photocatalytic reactivity. *Chem Lett* 34:616–617
- Kitano M, Funatsu K, Matsuoka M, Ueshima M, Anpo M (2006) Preparation of nitrogen-substituted TiO₂ thin film photocatalysts by the radio frequency magnetron sputtering deposition method and their photocatalytic reactivity under visible light irradiation. *J Phys Chem B* 110:25266–25272
- Kitano M, Takeuchi M, Matsuoka M, Thomas JM, Anpo M (2007) Photocatalytic water splitting using Pt-loaded visible light-responsive TiO₂ thin film photocatalysts. *Catal Today* 120:133–138
- Maeda K, Teramura K, Lu D, Takata T, Saito N, Inoue Y, Domen K (2006) Photocatalyst releasing hydrogen from water: Enhancing catalytic performance holds promise for hydrogen production by water splitting in sunlight. *Nature* 440:295
- Matsuoka M, Kitano M, Takeuchi M, Anpo M, Thomas JM (2005) Photocatalytic water splitting on visible light-responsive TiO₂ thin films prepared by a RF magnetron sputtering deposition method. *Top Catal* 35:305–310
- Sayama K, Mukasa K, Abe R, Abe Y, Arakawa H (2001) Stoichiometric water splitting into H₂ and O₂ using a mixture of two different photocatalysts and an IO₃⁻/I⁻ shuttle redox mediator under visible light irradiation. *Chem Commun* 2416–2417
- Takeuchi M, Anpo M, Hirao T, Itoh N, Iwamoto N (2001) Preparation of TiO₂ thin film photocatalysts working under visible light irradiation by applying a RF magnetron sputtering deposition method. *Surf Sci Jpn* 22:561–565
- Torimoto T, Fox RJ, Fox MA (1996) Photoelectrochemical doping of TiO₂ particles and the effect of charge carrier density on the photocatalytic activity of microporous semiconductor electrode films. *J Electrochem Soc* 143:3712–3717
- Umabayashi T, Ymaki T, Itoh H, Asai K (2002) Band gap narrowing of titanium dioxide by sulfur doping. *Appl Phys Lett* 81:454–456
- Zhao GL, Utsumi S, Kozuka H, Yoko T (1998) Photoelectrochemical properties of sol-gel-derived anatase and rutile TiO₂ films. *J Mater Sci* 33:3655–3659
- Zou Z, Ye J, Sayama K, Arakawa H (2001) Direct splitting of water under visible light irradiation with an oxide semiconductor photocatalyst. *Nature* 414:625–627

Chapter 24

Construction of Solid-State Thin Film Solar Cell by Applying Visible Light-Responsive TiO₂ Thin Film Materials

Masaya Matsuoka, Masayuki Minakata, Afshin Ebrahimi,
Masakazu Anpo, Hung-chang Chen, and Wen-ting Lin

Abstract A radio frequency magnetron sputtering (RF-MS) deposition method was employed to prepare visible light-responsive TiO₂ thin films (Vis-TiO₂) which can absorb visible light above 400 nm and be applied as a working electrode for sandwich-type two-electrode dye-sensitized solar cells (DSSCs). The effects of Cu₂O and CuI deposition on the photovoltaic cell performance of these Vis-TiO₂/ITO-glass electrodes were also investigated. The Cu₂O/Vis-TiO₂/ITO-glass electrode exhibited higher photovoltaic cell performance than that without Cu₂O deposition, showing that electron injection from the photoexcited Cu₂O into the conduction band of the Vis-TiO₂ thin film plays an important role in increasing the photovoltaic cell performance. Furthermore, it was found that the deposition of CuI as well as the UV-TiO₂ thin film was also effective in enhancing the photovoltaic cell performance of the Vis-TiO₂/ITO-glass electrode. To construct solar cells using solid electrolytes, the gelation of a NaI/I₂ redox electrolyte was investigated using poly(acrylic acid) partial potassium salt. Finally, it was demonstrated that a DSSC system applying Vis-TiO₂/N719/CuI/Au is a promising candidate in the development of unique all solid-type DSSC systems.

1 Introduction

In recent years, dye-sensitized solar cells (DSSCs) have attracted much attention as new types of solar cells (SCs) due to their low production cost and high solar-to-electric energy conversion efficiency. Grätzel et al. have reported on the

M. Anpo (✉)
Department of Applied Chemistry, Graduate School of Engineering,
Osaka Prefecture University, 1-1 Gakuen-cho, Naka-ku, Sakai, Osaka 599-8531, Japan
e-mail: anpo@chem.osakafu-u.ac.jp

fabrication of DSSCs using a porous TiO_2 working electrode sensitized with a ruthenium complex which shows solar-to-electric energy conversion efficiency of up to 7–11% (O'Regan and Grätzel 1991; Grätzel 2004). It has also been reported that the performance of DSSCs greatly depends on the morphologies as well as the electronic structures of the semiconducting materials used for the working electrode (Islam et al. 2001; Pavasupree et al. 2006; Sirimanne and Tributsch 2007; Siripala et al. 2003).

Recently, we have reported on a radio frequency magnetron sputtering (RF-MS) deposition method which enables the precise control of the morphologies as well as the electronic structures of TiO_2 thin films deposited on various substrates. For example, visible light-responsive TiO_2 thin films (Vis- TiO_2) consisting of well-defined columnar TiO_2 crystallites and prepared by the RF-MS deposition method under a high substrate temperature (873 K) were observed to absorb visible light of wavelengths up to 600 nm (Anpo and Takeuchi 2003; Anpo, et al. 2005; Matsuoka et al. 2007; Kitano et al. 2007). In the present chapter, sandwich-type two-electrode DSSCs were fabricated using a Vis- TiO_2 electrode sensitized by a N3 dye, and their photovoltaic performances were investigated. Special attention is focused on the relationship between the photovoltaic performance of the DSSCs and their morphologies as well as the electronic structures of the TiO_2 thin film electrodes. Furthermore, this chapter deals with the construction of unique photovoltaic cells composed of TiO_2 - Cu_2O or TiO_2 - CuI composite thin films ($\text{Cu}_2\text{O}/\text{Vis-TiO}_2/\text{ITO-glass}$ or $\text{CuI}/\text{Vis-TiO}_2/\text{ITO-glass}$), for the development of unique solid-state photovoltaic cells. A DSSC system constructed with a Vis- TiO_2 thin film photocatalyst, a N719 dye, CuI thin layer and a gold electrode ($\text{Vis-TiO}_2/\text{N719}/\text{CuI}/\text{Au}$) was prepared as a promising candidate in the development of unique all solid-state photovoltaic cell systems.

1.1 Investigations on the Photovoltaic Cell Performance of SCs and DSSCs Constructed with Vis- TiO_2 Thin Film Electrodes

Visible light-responsive TiO_2 thin film (Vis- TiO_2) was prepared by an RF-MS method using a calcined TiO_2 plate (High Purity Chemicals Lab., Corp., Grade: 99.99%) as the source material and Ar (99.995%) as the sputtering gas. Conducting ITO-glass of $8 \times 40 \text{ mm}^2$ (ITO) was used for the substrate and the deposition area was adjusted to $8 \times 17 \text{ mm}^2$. The system was equipped with a substrate center positioned in parallel just above the source material, with a target-to-substrate distance fixed at 75 mm. Prior to the introduction of the sputtering gas, the chamber was evacuated to lower than $1.03 \times 10^{-3} \text{ Pa}$ and the sputtering gas was then introduced at a pressure of 2.0 Pa. Pre-sputtering with Ar gas was carried out for 20 min before each deposition in order to remove any contamination on the surface of the substrates. The Vis- TiO_2 thin films were then prepared on the substrates by inducing an RF power of 300 W with the

substrate temperature held at 873 K. The deposition time was adjusted from 100 to 1,000 min. After deposition, yellow-colored and transparent TiO_2 thin films were obtained. Hereafter, the prepared TiO_2 thin films will be denoted as Vis- TiO_2/ITO . A Cu_2O thin film was deposited on Vis- TiO_2/ITO by anodic electrodeposition from an aqueous solution of copper acetate (0.02 M) and sodium acetate (0.1 M) at 333 K under an applied potential of -0.2 V vs. SCE. This electrode will be denoted as $\text{Cu}_2\text{O}/\text{Vis-TiO}_2/\text{ITO}$. A CuI thin film was deposited on the Vis- TiO_2/ITO -glass by an impregnation method from an acetonitrile solution of copper iodide followed by calcination in N_2 atmosphere at 473 K for 2 h. This electrode will be denoted as $\text{CuI}/\text{Vis-TiO}_2/\text{ITO}$.

In the case of constructing the Vis- $\text{TiO}_2/\text{N719}/\text{CuI}/\text{Au}$ system, Vis- TiO_2 was sensitized with a N719 dye, while an Au electrode was deposited from an Au nano-colloid solution for 24 h, and CuI was deposited from a saturated $\text{CuI}/\text{CH}_3\text{CN}$ solution. Optical transmittance measurements were carried out with a UV-Vis spectrophotometer (Shimadzu, UV-2200A). An HZ 3,000 automatic polarization system (Hokuto Denko) was employed for the electrochemical measurements. The cyclic voltammogram of the various electrodes were obtained in a conventional three-electrode electrochemical cell, where the TiO_2 electrode, Pt electrode, and saturated calomel electrode (SCE) were set as the working, counter, and reference electrodes, respectively. The working electrode was irradiated by a 500-W Xe arc lamp in 0.25 M K_2SO_4 solution (pH = 6) which was mechanically stirred and degassed by purging with 99.99% pure Ar gas during the experiments. The working electrode area was about 1.0 cm^2 and the electrode was irradiated on the front side (light incident on the electrolyte/electrode interface).

The photocurrent-voltage curves of the solar cells (SC_{Vis} and SC_{UV}) fabricated using bare Vis- TiO_2/ITO or UV- TiO_2/ITO without sensitization with N3 dyes are shown in Fig. 1. The short circuit photocurrent density (J_{sc}), open circuit voltage (V_{oc}), fill factor (ff), and solar-to-electric energy conversion efficiency (η) were determined by the photocurrent-voltage curves. The SC_{Vis} was observed to exhibit higher photovoltaic performance ($J_{\text{sc}} = 0.65 \text{ mA}/\text{cm}^2$, $V_{\text{oc}} = 0.61 \text{ V}$, $ff = 0.38$, $\eta = 0.15\%$) than SC_{UV} ($J_{\text{sc}} = 0.17 \text{ mA}/\text{cm}^2$, $V_{\text{oc}} = 0.49 \text{ V}$, $ff = 0.38$, $\eta = 0.03\%$), as shown in Fig. 1. The high photovoltaic performance of SC_{Vis} can be ascribed to efficient visible light absorption of the Vis- TiO_2 electrode as well as the facile diffusion of the electrolyte into the deep inside bulk of the electrode through the large interspaces among the columnar TiO_2 crystallites (Anpo and Takeuchi 2003; Anpo, et al. 2005; Matsuoka et al. 2007; Kitano et al. 2007). The thus prepared SC_{Vis} can generate enough electrical power to work a small music box under sunlight irradiation, as shown in Fig. 2. The photocurrent-voltage curves of the DSSCs (DSSC_{Vis} and DSSC_{UV}) fabricated using Vis- TiO_2/ITO or UV- TiO_2/ITO sensitized with the N3 dye are also shown in Fig. 1.

DSSC_{Vis} exhibits higher photovoltaic performance ($J_{\text{sc}} = 3.50 \text{ mA}/\text{cm}^2$, $V_{\text{oc}} = 0.81 \text{ V}$, $ff = 0.53$, $\eta = 1.48\%$) than DSSC_{UV} ($J_{\text{sc}} = 0.78 \text{ mA}/\text{cm}^2$, $V_{\text{oc}} = 0.74 \text{ V}$, $ff = 0.43$, $\eta = 0.25\%$). The high photovoltaic performance of DSSC_{Vis} can be explained by the following factors: one is related to the unique morphology of the Vis- TiO_2 electrode which enables the facile diffusion of the electrolyte into the

Fig. 1 Photocurrent-voltage curve of SCs (a, b) or DSSCs (c, d) prepared from TiO₂ thin films. (a) UV-TiO₂, (b) Vis-TiO₂, (c) UV-TiO₂ with a N3 dye and (d) Vis-TiO₂ with a N3 dye (sputtering time: 100 min, AM-1.5 100 mW/cm², electrolyte: 0.5 M LiI + 0.05 M I₂ + 0.5 M TBP in ACN)

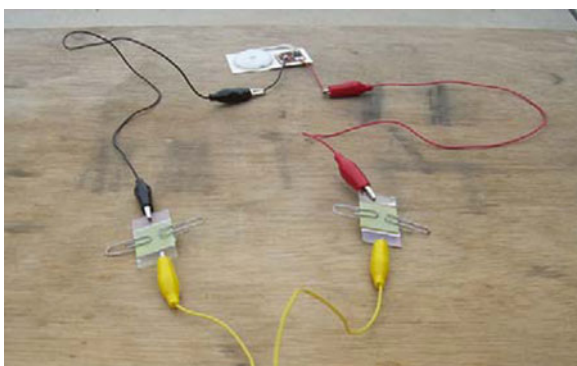
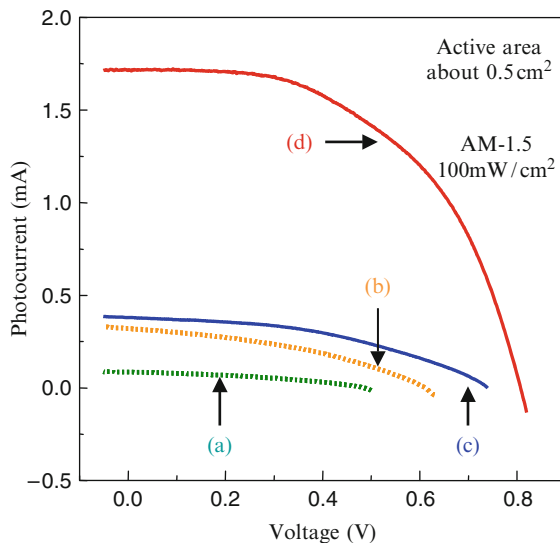


Fig. 2 Demonstration of Vis-TiO₂ solar cells connected to a music box

deep inside bulk of the Vis-TiO₂ electrode, as in the case of SC_{Vis}. The other factor is related to the difference in the energy levels of the conduction band edge (E_{CB}) of Vis-TiO₂ and UV-TiO₂. The E_{CB} of Vis-TiO₂ (-1.02 V) shifts more positively than that of UV-TiO₂ (-1.11 V), as shown in Fig. 3. (Kitano et al. 2007; Matsumoto 1996). The higher photovoltaic performance of DSSC_{Vis} can be ascribed to the lower energy level of the E_{CB} of Vis-TiO₂ than that of UV-TiO₂, thus realizing efficient electron injections from the photo-excited N3 dyes into the conduction band (CB) of Vis-TiO₂ as compared to UV-TiO₂, as shown in Fig. 3.

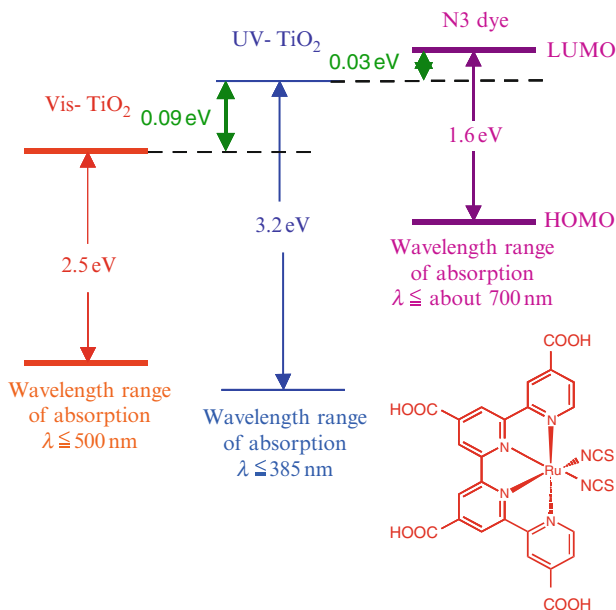


Fig. 3 Comparison of the estimated positions of the N3 dye frontier orbitals with the band edges of UV-TiO₂ and Vis-TiO₂

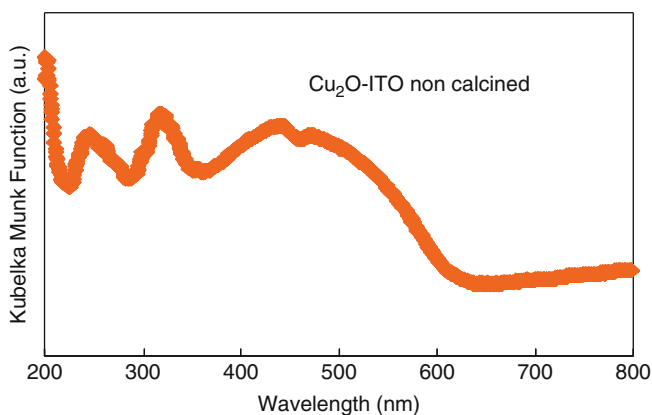


Fig. 4 UV-Vis diffuse reflectance absorption spectrum of the Cu₂O/ITO electrode

1.2 Investigations on the Photovoltaic Cell Performance of Cu₂O/Vis-TiO₂/ITO and CuI/Vis-TiO₂/ITO Electrodes

The UV-Vis diffuse reflectance absorption spectrum of the Cu₂O/ITO electrode is shown in Fig. 4. A typical visible absorption band due to Cu₂O, a typical p-type semiconducting material, can be observed below 600 nm, suggesting the successful

formation of the Cu_2O film on the conducting ITO-glass substrate. It can clearly be seen that the $\text{Cu}_2\text{O}/\text{Vis-TiO}_2/\text{ITO}$ electrode prepared by the electrodeposition method is also able to absorb visible light at wavelengths below 550 nm, as shown in Fig. 5. The time dependence for the photocurrent of the $\text{Cu}_2\text{O}/\text{Vis-TiO}_2/\text{ITO}$ electrode prepared at different anodic electrodeposition times is shown in Fig. 6.

The photocurrent of $\text{Cu}_2\text{O}/\text{Vis-TiO}_2/\text{ITO}$ prepared with an electrodeposition time of 30 s gradually decreased with an increase in the irradiation time. However, $\text{Cu}_2\text{O}/\text{Vis-TiO}_2/\text{ITO}$ prepared with an electrodeposition time of 10 s showed high and stable photocurrent even under prolonged light irradiation. The photoelectrochemical performances of the $\text{Cu}_2\text{O}/\text{Vis-TiO}_2/\text{ITO}$ -glass electrodes were investigated by photocurrent measurements. The $\text{Cu}_2\text{O}/\text{Vis-TiO}_2/\text{ITO}$ electrode showed lower photocurrent than that of Vis-TiO_2 , as shown in Fig. 7. However, $\text{Cu}_2\text{O}/\text{Vis-TiO}_2/\text{ITO}$ calcined in N_2 at 443 K shows higher photocurrent than that of Vis-TiO_2 ,

Fig. 5 UV-Vis diffuse reflectance absorption spectrum of the $\text{Cu}_2\text{O}/\text{Vis-TiO}_2/\text{ITO}$ electrode

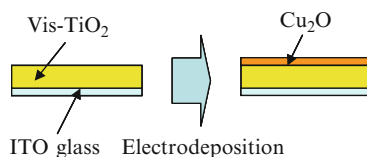
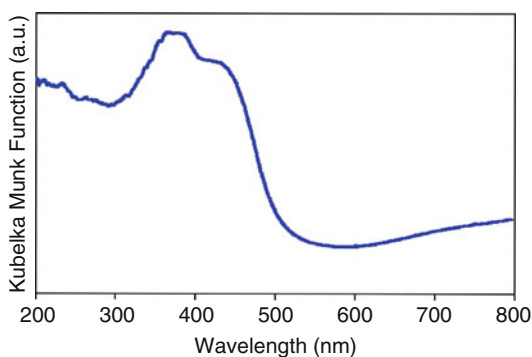
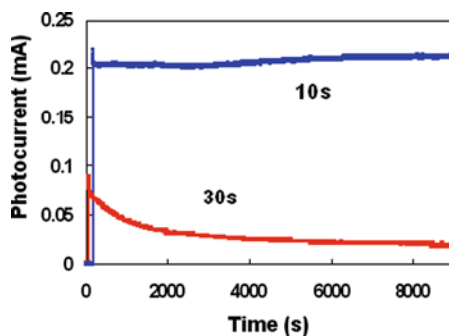


Fig. 6 Photocurrent time dependence of the $\text{Cu}_2\text{O}/\text{Vis-TiO}_2/\text{ITO}$ -glass electrode prepared at different anodic electrodeposition times



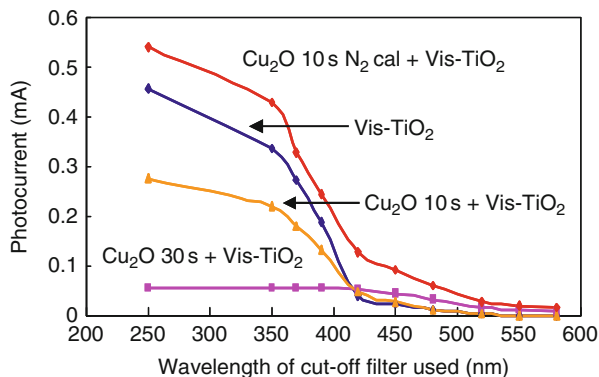


Fig. 7 Effect of irradiated light wavelengths on the photocurrent of various $\text{Cu}_2\text{O}/\text{Vis-TiO}_2/\text{ITO}$ electrodes

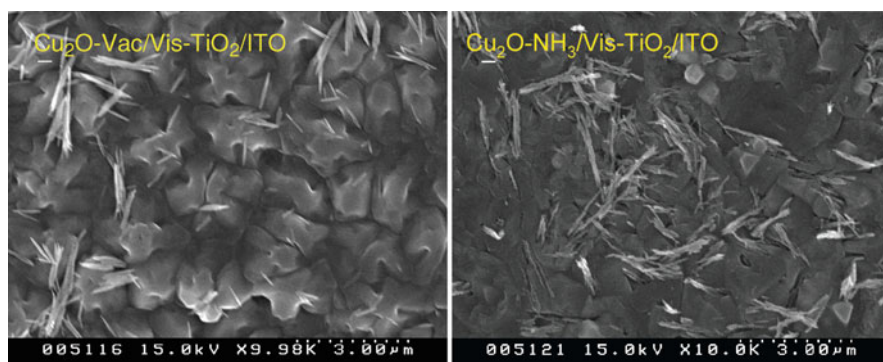


Fig. 8 SEM images of $\text{Cu}_2\text{O}/\text{Vis-TiO}_2/\text{ITO}$ electrodes calcined in vacuum and NH_3 . Electrodeposition time: 10 min, calcination temperature: 473 K, calcination time: 2 h

especially under visible light irradiation of wavelengths longer than 450 nm. These results clearly suggest that the photoelectrochemical performance as well as absorption efficiency toward visible light for the $\text{Vis-TiO}_2/\text{ITO}$ electrode were dramatically improved by the deposition of the Cu_2O film by a simple electrodeposition method. Furthermore, it was found that the electrodeposition time greatly affected the photoelectrochemical performance of the $\text{Cu}_2\text{O}/\text{Vis-TiO}_2/\text{ITO}$ electrodes, i.e., the electrode prepared by an electrodeposition time of 10 s showed much higher photoelectrochemical performance than that prepared at 30 s.

The SEM images of $\text{Cu}_2\text{O}/\text{Vis-TiO}_2/\text{ITO}$ calcined in vacuum and NH_3 gas are shown in Fig. 8. It can be seen that the surface roughness of the Cu_2O layer on $\text{Cu}_2\text{O-NH}_3/\text{Vis-TiO}_2/\text{ITO}$ is significantly less than that of $\text{Cu}_2\text{O-Vac}/\text{Vis-TiO}_2/\text{ITO}$. BET surface area measurements of the $\text{Cu}_2\text{O}/\text{Vis-TiO}_2/\text{ITO}$ electrodes were also performed. The surface areas of $\text{Cu}_2\text{O-NH}_3/\text{Vis-TiO}_2/\text{ITO}$ are slightly larger than that of $\text{Cu}_2\text{O-Vac}/\text{Vis-TiO}_2/\text{ITO}$, as shown in Table 1.

Table 1 The surface areas of the $\text{Cu}_2\text{O}/\text{Vis-TiO}_2/\text{ITO}$ electrodes calcined in vacuum and NH_3

	Surface area (cm^2)
Vac	53.21
NH_3	55.42

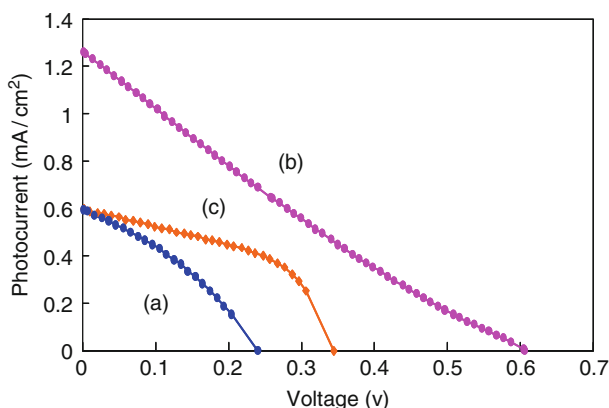


Fig. 9 I-V curves of SCs constructed with: (a) $\text{Cu}_2\text{O-Vac}/\text{Vis-TiO}_2/\text{ITO}$; (b) $\text{Cu}_2\text{O-NH}_3/\text{Vis-TiO}_2/\text{ITO}$; and (c) $\text{Vis-TiO}_2/\text{ITO}$ electrodes. Electrodeposition time: 10 min, Calcination temperature: 473 K, Calcination time: 2 h, Sputtering time: 300 min (Vis-TiO_2), Light source: solar simulator $100 \text{ mW}/\text{cm}^2$, Electrolyte: $0.5 \text{ M NaI}/0.025 \text{ M I}_2 \text{ aq}$

The I - V curves of SCs constructed with various working electrodes are depicted in Fig. 9. The sputtering times were fixed at 300 min for all of the electrodes. The cell performance of the SC constructed with $\text{Cu}_2\text{O-Vac}/\text{Vis-TiO}_2/\text{ITO}$ can be seen to be lower than that constructed with $\text{Vis-TiO}_2/\text{ITO}$. However, a dramatic increase in the cell performance can be observed for the SC constructed with $\text{Cu}_2\text{O-NH}_3/\text{Vis-TiO}_2/\text{ITO}$. The cell performances of SCs constructed with $\text{Vis-TiO}_2/\text{ITO}$ (device A), $\text{Cu}_2\text{O-Vac}/\text{Vis-TiO}_2/\text{ITO}$ (device B), and $\text{Cu}_2\text{O-NH}_3/\text{Vis-TiO}_2/\text{ITO}$ (device C) are shown in Table 2. The short-circuit photocurrent density (J_{sc}), open-circuit photovoltage (V_{oc}), and fill factor (ff) of device A under AM-1.5 full sunlight were 0.6 mA cm^{-2} , 0.35 mV , and 0.48 , respectively, yielding an overall conversion efficiency (η) of 0.1% . The corresponding parameters (J_{sc} , V_{oc} , ff , and η) for device B were 0.59 mA cm^{-2} , 0.24 mV , 0.38 , and 0.055% , respectively, showing lower efficiency than device A. However, device C exhibited higher performance than device A, showing that the calcination treatment of the $\text{Cu}_2\text{O}/\text{Vis-TiO}_2/\text{ITO}$ electrode in NH_3 was quite effective in enhancing the cell performance of the SCs, where the Cu_2O thin layer acts as an effective inorganic sensitizer to improve visible light absorption.

We have also investigated the photoelectrochemical performance of SCs constructed with a $\text{CuI}/\text{Vis-TiO}_2/\text{ITO}$ electrode. The current voltage responses of the thin film electrodes under visible light irradiation ($\lambda > 420 \text{ nm}$, $100 \text{ mW}/\text{cm}^2$, irradiation area: 0.9 cm^2) from a 500 W Xe lamp are shown in Fig. 10. The

Table 2 Cell performances of SCs constructed with: (A) Vis-TiO₂/ITO; (B) Cu₂O-Vac/Vis-TiO₂/ITO; and (C) Cu₂O-NH₃/Vis-TiO₂/ITO electrodes

	J _{sc}	V _{oc}	ff	η
(A)	0.6	0.35	0.48	0.1
(B)	0.59	0.24	0.38	0.055
(C)	1.3	0.61	0.22	0.17

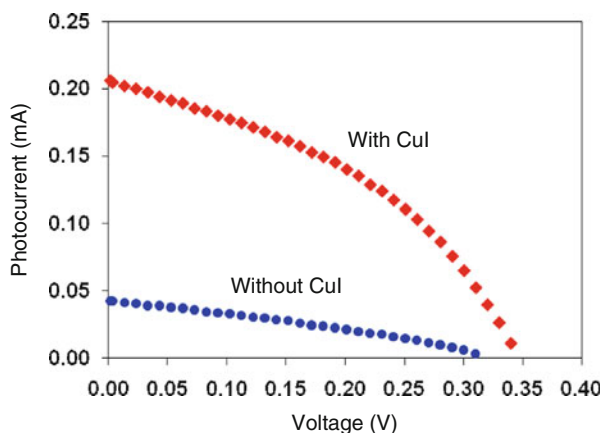


Fig. 10 Photovoltaic cell performance of SCs constructed with Vis-TiO₂/ITO-glass and CuI/Vis-TiO₂/ITO-glass electrodes

Vis-TiO₂/ITO-glass electrode showed a large short circuit photocurrent of 50 $\mu\text{A}/\text{cm}^2$ and an open circuit photovoltage of 300 mV. The photovoltaic cell performance of the Vis-TiO₂/ITO-glass electrode remarkably increased after CuI deposition ($J_{sc} = 210 \mu\text{A}/\text{cm}^2$, $V_{oc} = 340 \text{ mV}$). These results indicate that electron injection from the photoexcited CuI into the conduction band of the Vis-TiO₂ thin film plays an important role in increasing the photovoltaic cell performance of the Vis-TiO₂/ITO-glass electrode.

1.3 Investigations on the Photovoltaic Cell Performance of SCs Constructed with Double-Layered TiO₂ Thin Film Electrodes

The I-V curves of SCs constructed with Vis-TiO₂/ITO (device X) and Vis-TiO₂/UV-TiO₂/ITO (device Y) are shown in Fig. 11. The cell performances of devices X and Y are also listed in Table 3. The J_{sc} , V_{oc} , and ff of device X under AM-1.5 full sunlight were 0.6 mA cm^{-2} , 0.35 mV, and 0.48, respectively, yielding an overall conversion efficiency (η) of 0.1%. The corresponding parameters (J_{sc} , V_{oc} , ff, and η) of device Y were 0.65 mA cm^{-2} , 0.38 mV, 0.47, and 0.12%, respectively, showing higher solar cell performance than device X. The thin UV-TiO₂ film deposited

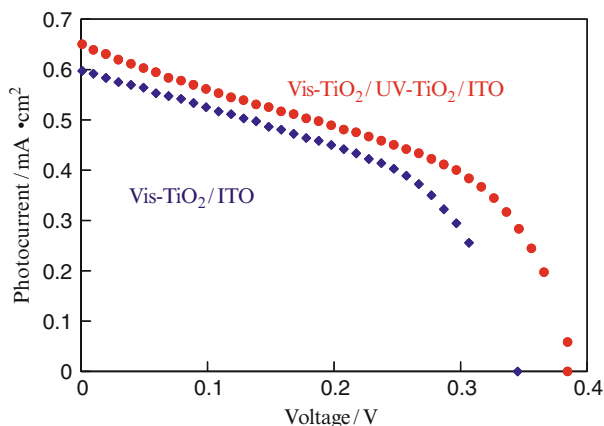


Fig. 11 I-V curves of SCs constructed with Vis-TiO₂/ITO and Vis-TiO₂/UV-TiO₂/ITO. Sputtering time: 10 min (UV-TiO₂), 300 min (Vis-TiO₂) light source: solar simulator 100 mW/cm² electrolyte: 0.5 M NaI/0.025 M I₂ aq

Table 3 Cell performances of SCs constructed with Vis-TiO₂/ITO and Vis-TiO₂/UV-TiO₂/ITO

	Voc (V)	Jsc (mA/cm ²)	ff	η (%)
Vis-TiO ₂	0.35	0.6	0.48	0.1
Vis-UV-TiO ₂	0.38	0.65	0.47	0.12

between the ITO substrate and Vis-TiO₂ film was considered to act as a barrier layer, preventing the back electron transfer from the ITO substrate to the electrolyte.

The I-V curves of SCs constructed with Vis-TiO₂/ITO (device X) and UV-TiO₂/Vis-TiO₂/ITO (device Z) are shown in Fig. 12. Jsc, Voc, and ff of device Z under AM-1.5 full sunlight were 0.81 mA cm⁻², 0.38 mV, and 0.53, respectively, yielding an overall conversion efficiency (η) of 0.16%, showing higher solar cell performance than device X. The thin UV-TiO₂ film was considered to act as a scattering barrier layer which improved the light absorption efficiency of the Vis-TiO₂ film on the ITO substrate.

1.4 Development of DSSC Using UV-TiO₂/Vis-TiO₂/ITO and Investigations on its Photovoltaic Cell Performance

The UV-TiO₂/Vis-TiO₂/ITO electrode was sensitized with a N719 dye and used as the working electrode for the DSSC. The I-V curves of DSSCs constructed with the Vis-TiO₂/ITO (device α) and UV-TiO₂/Vis-TiO₂/ITO (device β) electrodes are

shown in Fig. 13. The cell performances of device α and β are depicted in Table 4. The J_{sc} , V_{oc} , and ff of device α under AM-1.5 full sunlight were 5.9 mA cm^{-2} , 0.69 mV , and 0.4 , respectively, yielding an overall conversion efficiency (η) of 1.6% . The corresponding parameters (J_{sc} , V_{oc} , ff , and η) of device β are 7.5 mA cm^{-2} , 0.66 mV , 0.36 , and 1.8% , respectively, showing higher solar cell performance than

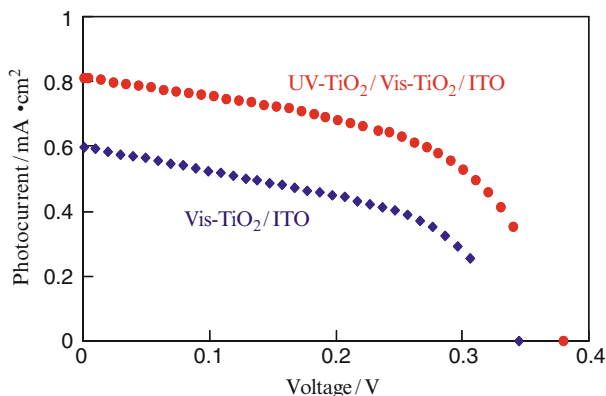


Fig. 12 I-V curves of SCs constructed with Vis-TiO₂/ITO and UV-TiO₂/Vis-TiO₂/ITO. Sputtering time: 10 min (UV-TiO₂), 300 min (Vis-TiO₂) light source: solar simulator 100 mW/cm^2 , electrolyte: $0.5 \text{ M NaI}/0.025 \text{ M I}_2 \text{ aq}$

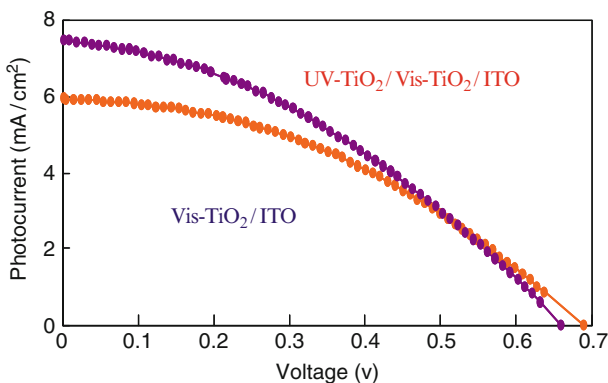


Fig. 13 I-V curves of DSSCs constructed with Vis-TiO₂/ITO and UV/Vis-TiO₂/ITO electrodes. Sputtering time: 10 min (UV-TiO₂), 300 min (Vis-TiO₂) light source: solar simulator 100 mW/cm^2 electrolyte: $0.5 \text{ M LiI}/0.05 \text{ M I}_2/0.5 \text{ M TBP}$ in acetonitrile

Table 4 The cell performances of DSSCs constructed with Vis-TiO₂/ITO and UV/Vis-TiO₂/ITO sensitized with the N719 dye

With dye	J_{sc} (mA)	V_{oc} (V)	ff	η (%)
Vis	5.9	0.69	0.4	1.6
UV/Vis	7.5	0.66	0.36	1.8

device α . It was concluded that the thin UV-TiO₂ film deposited on the Vis-TiO₂ film also acts as the scattering barrier layer which improved the light absorption efficiency of Vis-TiO₂-ITO sensitized with the N719 dye.

1.5 Preparation of Solar Cells (SCs) Using Polymer Hydro-Gel Electrolytes and Investigations on the Photovoltaic Cell Performance of UV-TiO₂/ITO-PEN and Vis-TiO₂/ITO-Glass Electrodes

To construct a solar cell using a solid electrolyte, gelation of a NaI/I₂ redox electrolyte was investigated using poly(acrylic acid) partial potassium salt. The addition of 10% poly(acrylic acid) partial potassium salt into the NaI/I₂ redox electrolyte led to the stable formation of a brown redox electrolyte gel, as shown in Fig. 14. The thus prepared NaI/I₂ redox electrolyte gel was used for the solid electrolyte of the photovoltaic cell. The performance of a photovoltaic cell constructed by the UV-TiO₂/ITO-PEN electrode, Pt counter electrode and NaI/I₂ redox electrolyte gel is also shown in Fig. 14. It was found that the photovoltaic cell performance was remarkably enhanced with the use of a NaI/I₂ redox gel as the electrolyte under full arc irradiation from the Xe lamp, showing it can be considered an effective candidate in the development of stable solid-state SCs using electrolytes with low fluidity. The performance of a photovoltaic cell constructed with the Vis-TiO₂/ITO-glass electrode, Pt counter electrode, and NaI/I₂ redox electrolyte gel is also shown in Fig. 15. It was found that the photovoltaic cell performance of the Vis-TiO₂/ITO-glass electrode can also be remarkably enhanced by using the NaI/I₂ redox electrolyte gel as the electrolyte.

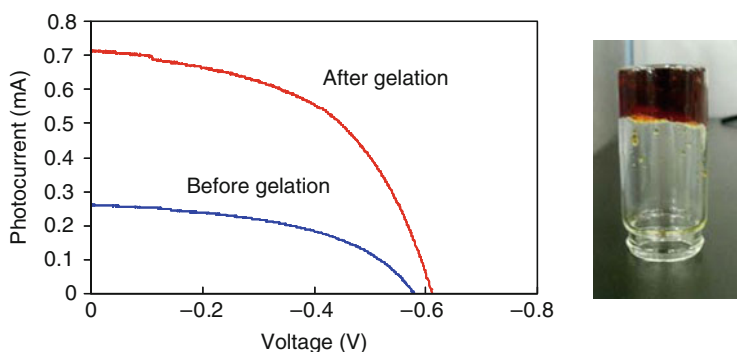


Fig. 14 Performance of a photovoltaic cell constructed with the UV-TiO₂/ITO-PEN electrode, Pt counter electrode and NaI/I₂ redox electrolyte gel

1.6 Development of an all Solid-State DSSC (Vis-TiO₂/N719/CuI/Au) System and Investigations into its Photovoltaic Cell Performance

Finally, to construct an all solid-state DSSC, we have developed an effective Vis-TiO₂/N719/CuI/Au system. Here, Vis-TiO₂ was sensitized with the N719 dye while an Au electrode was deposited from an Au nano colloid solution for 24 h and CuI was deposited from a saturated CuI/CH₃CN solution. An electron was injected into the conduction band of TiO₂ from the photo-excited N719 dye, and at the same time, an electron was supplied into the N719 dye from the Au electrode through the CuI layer. The photovoltaic performance of this all solid-state DSSC (Vis-TiO₂/N719/CuI/Au) system measured under light intensity of AM-1.5 (100 mW/cm²) and irradiation area of 0.71 cm² is shown in Fig. 16. It was clearly observed that the

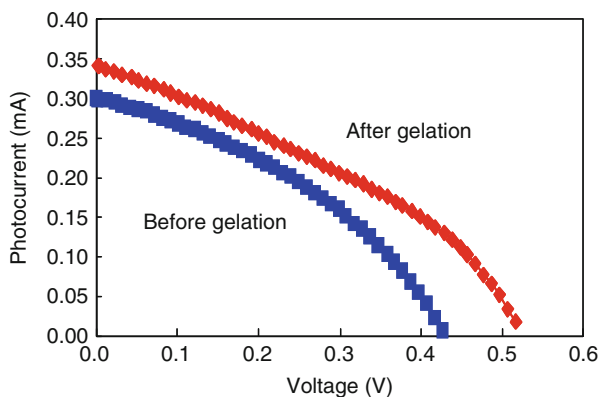


Fig. 15 Performance of a photovoltaic cell constructed with the Vis-TiO₂/ITO-glass electrode, Pt counter electrode and NaI/I₂ redox electrolyte gel

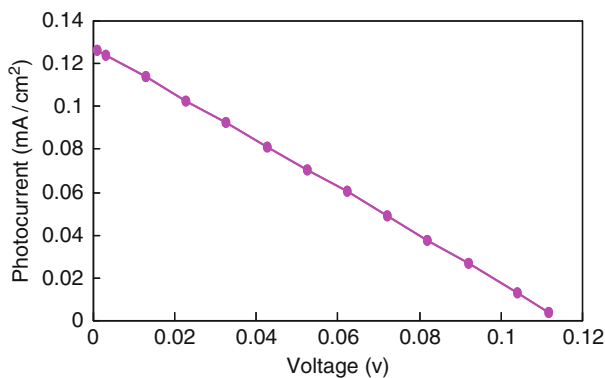


Fig. 16 Photovoltaic performance of an all solid-state DSSC (Vis-TiO₂/N719/CuI/Au) system. Light intensity: AM-1.5 (100 mW/cm²), irradiation area: 0.71 cm²

Vis-TiO₂/N719/CuI/Au system can, in fact, act as an all solid-state DSSC, showing this approach to construct DSSCs using stacked layers of dye-sensitized TiO₂ and CuI to be a promising and effective method.

2 Summary

Unique visible light-responsive TiO₂ thin films (Vis-TiO₂) which can absorb visible light of wavelengths up to 600 nm and consist of well-defined columnar TiO₂ crystallites were prepared by a RF-MS deposition method under a high substrate temperature (873 K). Sandwich-type two-electrode DSSCs were fabricated using a Vis-TiO₂ electrode sensitized by a N3 dye and their photovoltaic performances were investigated. The effects of Cu₂O and CuI deposition on the photovoltaic cell performance of Vis-TiO₂/ITO-glass electrodes were then investigated. The Cu₂O/Vis-TiO₂/ITO-glass electrode exhibited higher photovoltaic cell performance than that without Cu₂O deposition, showing that electron injection from the photoexcited Cu₂O into the conduction band of the Vis-TiO₂ thin film plays an important role in increasing the photovoltaic cell performance. These results demonstrate the possibility of constructing high performance solid-state SCs by utilizing the p-n junction formed between a p-type Cu₂O and n-type Vis-TiO₂. Furthermore, it was found that the deposition of CuI as well as of a UV-TiO₂ thin film was also effective in enhancing the photovoltaic cell performance of the Vis-TiO₂/ITO-glass electrode. In order to construct SCs using solid electrolytes, the gelation of a NaI/I₂ redox electrolyte was investigated by using poly(acrylic acid) partial potassium salt. It was found that the photovoltaic cell performance of the UV-TiO₂/ITO-PEN and Vis-TiO₂/ITO-glass electrodes were remarkably enhanced by using a NaI/I₂ redox electrolyte gel as the electrolyte under full arc irradiation from a Xe lamp, showing that it is a useful agent to construct stable solid SCs using electrolytes with low fluidity. Finally, a successful demonstration of a DSSC system constructed with a Vis-TiO₂ thin film photocatalyst, the N719 dye, CuI thin layer, and a gold electrode, i.e., Vis-TiO₂/N719/CuI/Au, could be realized as a promising candidate in the development of all unique solid-type DSSC systems.

References

- Anpo M, Takeuchi M (2003) The design and development of highly reactive titanium oxide photocatalysts operating under visible light irradiation. *J Catal* 216:505–516
- Anpo M, Dohshi S, Kitano M, Hu Y, Takeuchi M, Matsuoka M (2005) The preparation and characterization of highly efficient titanium oxide-based photofunctional materials. *Ann Rev Mater Res* 35:1–27
- Grätzel M (2004) Conversion of sunlight to electric power by nanocrystalline dye-sensitized solar cells. *J Photochem Photobiol A Chem* 164:3–14

- Islam A, Sugihara H, Singh LP, Hara K, Katoh R, Nagawa Y, Yanagida M, Takahashi Y, Murata S, Arakawa H (2001) Synthesis and photophysical properties of ruthenium(II) charge transfer sensitizers containing 4, 4'-dicarboxy-2, 2'-biquinoline and 5, 8-dicarboxy-6, 7-dihydro-dibenzo [1, 10]-phenanthroline. *Inorg Chim Acta* 322:7–16
- Kitano M, Takeuchi M, Matsuoka M, Thomas JM, Anpo M (2007) Photocatalytic water splitting using pt-loaded visible light-responsive TiO₂ thin film photocatalysts. *Catal Today* 120:133–138
- Matsumoto Y (1996) Energy positions of oxide semiconductors and photocatalysis with iron complex oxides. *J Solid State Chem* 126:227–234
- Matsuoka M, Kitano M, Takeuchi M, Tsujimaru K, Anpo M, Thomas JM (2007) Photocatalysis for new energy production – recent advances in photocatalytic water splitting reactions for hydrogen production. *Catal Today* 122:51–61
- O'Regan B, Grätzel M (1991) A low-cost, low-cost, high efficiency solar-cell based on dye-sensitized colloidal TiO₂ films. *Nature* 353:737–740
- Pavasupree S, Ngamsinlapasathian S, Nakajima M, Suzuki Y, Yoshikawa S (2006) Synthesis, characterization, photocatalytic activity and dye-sensitized solar cell performance of nanorods/nanoparticles TiO₂ with mesoporous structure *J. Photochem Photobiol A Chem* 184:163–169
- Sirimanne PM, Tributsch H (2007) Generation of inhomogeneous photocurrent in solid-state TiO₂ vertical bar dye vertical bar CuI cells and effect of ligands attached to surfactant on morphology of CuI films. *Solar Energ* 81:535–539
- Siripala W, Ivanovskaya A, Jaramillo TF, Baek SH, McFarland EW (2003) A Cu₂O/TiO₂ heterojunction thin film cathode for photoelectrocatalysis. *Energ Mater Solar Cells* 77:229–237

Part VII
Photocatalytic Organic Syntheses

Chapter 25

Photocatalytic Transformations of Sulfur-Based Organic Compounds*

Alexander V. Vorontsov and Panagiotis G. Smirniotis

Abstract Organic sulfur compounds play significant roles in the life of modern humankind. There are many instances of the need to destroy or convert sulfur compounds into useful products. Photocatalytic reactions are capable of removing and transforming these compounds. High reactivity of sulfur compounds allows utilization of a variety of photocatalysts – heterogeneous like TiO_2 or other species, homogeneous, heterogeneous, or heterogenized. The transformations are mediated by electron transfer with generation of sulfur radical cations, energy transfer, or hydrogen atom transfer. Further reactions majorly comprise S-oxidation, α -C–H deprotonation, C–S bond cleavage, and polymerization. Reactions with photogenerated OH^\cdot radicals are also possible.

Introduction

Organic sulfur compounds include various substances containing one or several sulfur atoms in -2 , -1 , 0 , $+2$, $+4$, and $+6$ oxidation state. Compounds with S-oxidation states -2 and -1 are called *reduced sulfur compounds*. Atoms surrounding sulfur in these substances possess electron affinity lower or close to that of elemental sulfur and sulfur atoms carry a small negative charge. Common examples of reduced organic sulfur compounds comprise:

* It is a revised and enriched version of the article published in the journal Russian Chemical Reviews, Vorontsov AV (2008) Photocatalytic transformations of organic sulfur compounds and H_2S . Russ Chem Rev 77(10):909–926. doi:10.1070/RC2008v077n10ABEH003805.

A.V. Vorontsov (✉)

Boreskov Institute of Catalysis, Novosibirsk State University, Novosibirsk 630090, Russia
e-mail: voronts@catalysis.ru

RSH	Thiols (called also mercaptans), R = alkyl, aryl
RSR	Sulfides
RSSR	Disulfides
RS _n R	Polysulfides
(RO) ₃ P=S	Phosphorothioates (monothiophosphate)
(RO) ₂ SP=S	Phosphorothioates (dithiophosphate)
(R ₂ N) ₂ C=S	Thioureas
R ₂ N-C(S)-OR	Thiocarbamates
R ₂ N-C(S)-SR	Dithiocarbamates
Aromatic sulfur compounds (sulfur inside an aromatic ring)	

Sulfur compounds with positive charge on sulfur atom can be called *oxidized sulfur compounds*. They can be obtained by oxidation or oxygenation of reduced sulfur compounds. The following list gives typical oxidized sulfur organic compounds.

RS(O)R	Sulfoxides
RS(O) ₂ R	Sulfones
RSOH	Sulfenic acids (unstable)
RSO ₂ H	Sulfinic acids
RSO ₃ H	Sulfonic acids

There are compounds containing two or more sulfur atoms in both negative and positive oxidation state which can be called mixed oxidation state sulfur compounds.

RS(O)SR	Thiosulfates
RS(O) ₂ SR	Thiosulfonates

Organic sulfur compounds play a bifacial role in the life of modern humankind. Development of modern effective pesticides has played a very important role in rising productivity of agriculture. Many reduced sulfur compounds are used in organic synthesis, as biocorrosion inhibitors, as rubber vulcanization additives, as flammable gas additive, and as radioprotective agents. On another hand, reduced sulfur compounds often pose problems and necessity of their removal and destruction. A common example is undesirable malodorous sulfur-containing products of biodegradation. Toxic sulfurous pesticides contaminate waters in many agriculturally active regions. Some of reduced sulfur compounds represent the deadly toxic chemical warfare agents. Finally, removal of sulfur compounds below ppm level is a challenge for fuel industry.

According to the chemical weapon convention, production of chemical warfare agents is prohibited, and the existing stockpiles are to be irreversibly destroyed. The most terrible classes of chemical agents are nerve agents that disable transmission of signals by nerves and blister agents that cause persistent damage of skin and other exposed organs. Formulas of major chemical agents are shown in Fig. 1. VX, which is phosphorothioate, is considered as the deadliest warfare agent. Its toxicity

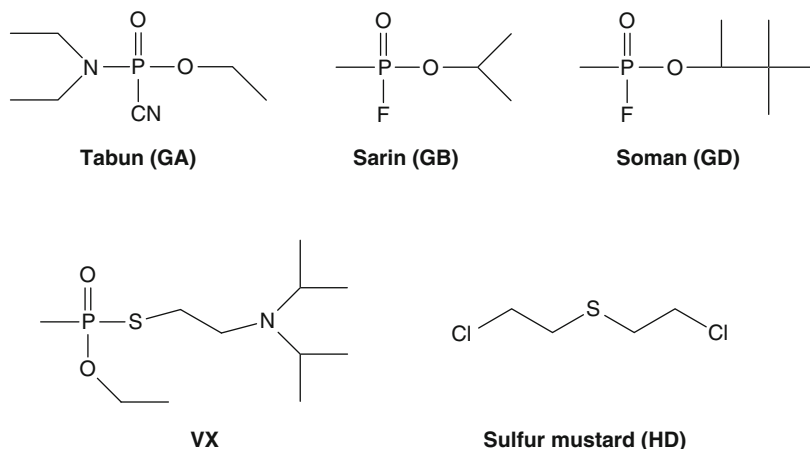


Fig. 1 Major chemical warfare agents. VX and HD are reduced sulfur organic compounds

is associated with the presence of the P–S bond. Sulfur mustard, or yperite, also designated as HD, is a blister agent. It is a sulfide and the only chemical agent that is considered to be effective if used in modern combat. Unlike VX and other chemical agents, thickened compositions containing HD are quite persistent under ambient conditions. Thus, contaminated areas remain dangerous for a long time causing troops to wear protective clothing that decreases combat performance. The decontamination with the use of photocatalysis is possible and the prospects were considered (Seto 2009; Hirakawa et al. 2009).

While large quantities of sulfur compounds are impossible to destroy using photocatalytic methods due to immense number of photons needed, these methods can be very competitive for treatment of solutions or air streams with low content of sulfur compounds.

Sulfur compounds represent a very interesting object from the point of view of fundamental mechanistic research. It is usually taken for granted that photocatalytic oxidation of organic and inorganic compounds over TiO₂ is initiated by reactions with hydroxyl radicals. This holds for the cases when oxidation of water molecule by photogenerated holes is faster than direct oxidation of substrate molecule. However, for a number of substrates with low redox potential, direct oxidation by photogenerated holes is possible. For example, for organic sulfides, the redox potential was reported to be as low as $E^0 = +1.7$ V vs. SHE (standard hydrogen electrode; Glass 1999). It is much lower if one compares it to the potential for water oxidation into hydroxyl radical $E^0 = +2.59$ – 2.74 V vs. SHE (Buxton et al. 1988). Thus, reduced sulfur compounds give a unique opportunity to trace reactions initiated by the direct oxidation by photogenerated holes. Transformations of sulfur compounds are fascinatingly diverse and regular at the same time. In this chapter, we challenge to uncover photocatalytic reactions of sulfur compounds and their inherent laws.

Properties of Organic Sulfur Compounds

Organic sulfur compounds can be divided into the three major groups according to the chemical character of radicals attached to sulfur atom. These groups have common types of photocatalytic chemical transformations. Compounds can also contain halogen atoms.

1. Aliphatic sulfur compounds contain aliphatic or alicyclic carbon fragment attached to sulfur atom. Sulfides or disulfides can contain sulfur atom included into a carbon cycle.
2. Aromatic sulfur compounds contain aromatic radicals attached to sulfur atoms, for example, diphenylsulfide $C_6H_5SC_6H_5$, or sulfur atom is included into the aromatic ring like in thiophene.
3. Heteroatomic sulfur compounds comprise diverse molecules that contain phosphorus and possibly nitrogen in close proximity to the sulfur atom.

This division is simplistic and serves for the sake of brevity since the last group of compounds can be subdivided into various classes of organic compounds.

A set of *aliphatic sulfur compounds* tested in photocatalytic reactions is listed in Table 1. Here we consider basic physical and chemical properties of aliphatic sulfur compounds. Sulfur atom electronegativity $\chi_S = 2.58$ excellently matches the electronegativity of carbon atom $\chi_C = 2.55$. This fact results in unpolar character of reduced organic sulfur compounds. Aliphatic reduced sulfur compounds usually have melting point much below $0^\circ C$. Ethylmercaptane CH_3CH_2SH possesses the lowest melting point of $-144^\circ C$. Other thiols melt at higher temperature, e.g., $-123^\circ C$ for CH_3SH . Aliphatic sulfides RSR and disulfides $RSSR$ have melting point around $-100^\circ C$. The boiling point of aliphatic sulfur compounds is usually above room temperature. The exceptions are hydrogen sulfide ($-60^\circ C$) and methylmercaptan ($+6^\circ C$). Ethylmercaptane and dimethylsulfide have boiling point at about $+36^\circ C$. Heavier sulfides and all disulfides boil around $+100^\circ C$ or higher.

Thiols or mercaptans (RSH) possess strong unpleasant odor. The odor perception threshold of thiols is thought to be as low as several nanograms per cubic meter of air. Due to this property, thiols are used as odorants for fuel gases. Thiols form weak hydrogen bonds $S-H \cdots S$ in concentrated solutions and in pure liquid or solid state. This hydrogen bond is, however, too weak compared, for example, to water, to significantly increase the boiling or melting point. Thiols are weak acids. In water at $25^\circ C$ $pK_a = 10-11$. Adiabatic ionization potential for thiols is relatively low: e.g., 9.44 eV for CH_3SH . Larger molecules of thiols have lower ionization potentials, e.g., 9.31 eV for CH_3CH_2SH . Standard oxidation potential for thiols in neutral pH is around -1.3 V vs. SHE (Wardman 1989). The most prominent chemical property of thiols is the ability to be easily oxidized into disulfides according to the following reaction:

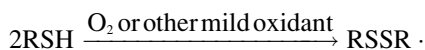
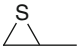

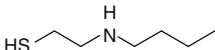


Table 1 Aliphatic organic sulfur substrates studied

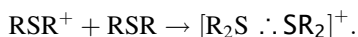
Substrate	System	References
H ₂ S	Air, TiO ₂	Canela et al. (1998)
CH ₃ SH	Air, Ag-TiO ₂	Kato et al. (2005)
CH ₃ CH ₂ SH	Air, TiO ₂	Kachina et al. (2006)
CH ₃ SCH ₃	Air, TiO ₂	Peral and Ollis (1997)
	Air, TiO ₂	Demeestere et al. (2005a)
	Air, S-TiO ₂	Demeestere et al. (2005b)
	Air, DCA/SiO ₂	Latour et al. (2005)
	CH ₃ CN, W ₁₀ O ₃₂ ⁴⁻	Chambers and Hill (1990)
	Air, S-TiO ₂	Jo and Shin (2010)
ClCH ₂ SCH ₂ Cl	CH ₃ CN, W ₁₀ O ₃₂ ⁴⁻	Chambers and Hill (1990)
CH ₃ SSCH ₃	Air, TiO ₂	Canela et al. (1999)
CH ₃ CH ₂ SCH ₂ CH ₃	Air, TiO ₂	Vorontsov et al. (2001)
	Air, TiO ₂	Vorontsov et al. (2003a)
	Air, TiO ₂	Kozlov et al. (2003)
	TiO ₂ /SiO ₂	Panayotov et al. (2003)
CH ₃ SCH ₂ CH ₂ Cl	CH ₃ CN, TiO ₂	Fox et al. (1990)
	Air, TiO ₂	Martyanov and Klabunde (2003)
CH ₃ CH ₂ SCH ₂ CH ₂ Cl	CH ₃ CN, TiO ₂	Fox et al. (1990)
	Air, TiO ₂	Vorontsov et al. (2003b)
	TiO ₂ /SiO ₂	Thompson et al. (2004)
	TiO ₂ /SiO ₂	Panayotov et al. (2003)
	TiO ₂ /SiO ₂	Panayotov et al. (2004)
ClCH ₂ CH ₂ SCH ₂ CH ₂ Cl	Air, M-TiO ₂ -SiO ₂	Neatu et al. (2009)
	CH ₂ Cl ₂ , Au/TiO ₂	Neatu et al. (2010)
<i>n</i> -(C ₄ H ₉) ₂ S	CH ₃ CN, DCA/SiO ₂	Soggiu et al. (1999)
	CH ₃ CN, TiO ₂	Davidson and Pratt (1983)
	CH ₃ CN, DCA/SiO ₂	Lacombe et al. (2002)
<i>n</i> -(C ₄ H ₉) ₂ S ₂	CH ₃ CN, DCA/SiO ₂	Lacombe et al. (2002)
<i>t</i> -(C ₄ H ₉) ₂ S	CH ₃ CN, TiO ₂	Davidson and Pratt (1983)
<i>n</i> -(C ₆ H ₁₃) ₂ S	CH ₃ CN, TiO ₂	Davidson and Pratt (1983)
	Air, TiO ₂	Canela et al. (1999)
	Air, TiO ₂	Canela et al. (1999)
	H ₂ O, TiO ₂	Vorontsov et al. (2002b)

DCA = 9,10-dicyanoanthracene (photosensitizer)

This reaction is fastest in basic media because the thiolate anions RS^- are very easy to oxidize (e.g., $E^0 = -0.75$ V vs. SHE for mercaptoethanol, Wardman 1989) into RS^\cdot radicals called thiyl radicals compared to thiols (e.g., $E^0 = -1.3$ V vs. SHE for mercaptoethanol, Wardman 1989). The thiyl radicals dimerize into $RSSR$ at a diffusion-limited rate. The relatively low energy of S–H bond (~ 360 kJ/mol) makes hydrogen abstraction from thiols a fast reaction. Thus, thiols are good radical scavengers and used as radioprotective agents.

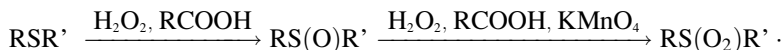
Organic aliphatic sulfides RSR' , or thioethers, are colorless liquids that are nonsoluble in water and soluble in the majority of organic solvents. Pure sulfides are thought to be odorless, but sulfurous impurities often cause strong unpleasant smell of commercially available sulfides. Adiabatic ionization potential of aliphatic sulfides is quite low: it decreases from 8.7 eV for CH_3SCH_3 and 8.42 eV for $C_2H_5SC_2H_5$ to 8.20 eV for diisopropylsulfide and methyl vinylsulfide (NIST database). Oxidation potential was determined by pulse radiolysis method for CH_3SCH_3 as $E^0 = -1.66$ V and for $t-(C_4H_9)_2S$ as $E^0 = -1.63$ V vs. SHE (Glass 1999). Electrochemical oxidation can be also used to generate aliphatic sulfides, but oxidation potentials cannot be determined due to irreversible character of oxidation. A variety of chemical oxidants are thought to produce sulfide radical cations as intermediates during oxidation.

A very interesting property of aliphatic sulfide radical cations is the ability to form two-center three-electron bond (2c, 3e) with electron rich centers as illustrated by the following equation.

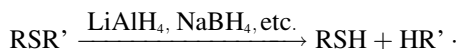


Enthalpy of this reaction was measured experimentally and calculated theoretically to be near 110 kJ/mol.

Aliphatic sulfides undergo chemical reactions at sulfur atom and at carbon fragment. Sulfur atom can be oxidized into sulfoxides and further into sulfone by a variety of oxidizing agents according to the next equation.

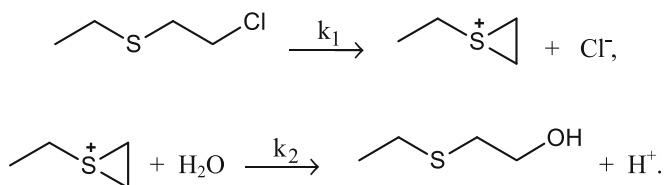


Reduction of sulfides can be performed with the help of strong reducing agents, and it results in formation of a thiol and a hydrocarbon.



Reactions at carbon fragment of aliphatic sulfides are similar to those of alkanes. If one of hydrogens in this fragment is substituted by a halogen atom, sulfides demonstrate very interesting reactions of nucleophilic substitution. These reactions consist of two steps. In the first, rate-determining step, sulfur displaces chlorine atom via intramolecular reaction. The cyclic ethylenesulfonium ion intermediate

reacts with hydroxyl ions or water to produce alcohol. The scheme below shows these reactions for 2-chloroethyl ethylsulfide.



Aromatic sulfur compounds that have been studied in photocatalytic reactions are listed in Table 2. The physical properties of reduced sulfur compounds with benzene rings are greatly affected by these rings. They usually have high melting and boiling points. For example, benzyl phenylsulfide melts at +42°C and boils at +197°C. Diphenylsulfide melts at a lower temperature of −26°C, but boils at a higher temperature of +296°C.

Thiophene refers to heterocyclic aromatic reduced sulfur compounds. It probably has the lowest boiling point (+84°C) among all aromatic sulfur compounds. Fusing benzene rings with thiophene to form benzothiophene and dibenzothiophene strongly increases the boiling point to 221 and 333°C, respectively.

Adiabatic (vertical) ionization potentials are relatively low for aromatic sulfides that contain phenyl fragments attached to sulfur atom. For example, for diphenyl sulfide, it is 7.9 eV. Ionization of heterocyclic aromatic compounds results in loss of aromaticity. This causes high values of ionization potentials, e.g., 8.9 eV for thiophene. Redox properties of aromatic sulfides have been studied well because they form relatively stable radical cations and the voltammetric waves are reversible. Despite the big difference in ionization potentials of aromatic and aliphatic sulfides, oxidation potentials for aromatic sulfides are only slightly lower (e.g., for diphenylsulfide −1.53 V vs. SHE) than that for aliphatic sulfides.

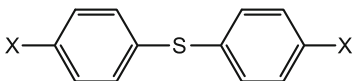
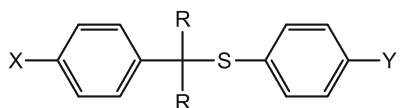
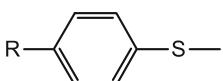
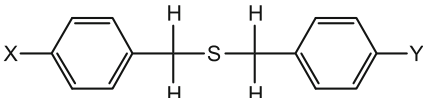
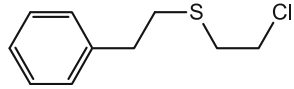
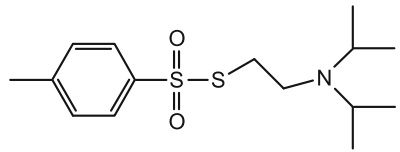
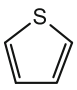
Chemical properties of aromatic thiols and sulfides are similar to those of aliphatic compounds. Heterocyclic aromatic sulfur compounds demonstrate lower reactivity of sulfur due to aromaticity. However, sulfur in, for example, thiophene still can be oxidized into sulfoxide and sulfone.

Oxidized aromatic organic sulfur compounds are represented by sulfonic acids RSO_3H . These are compounds with a low volatility and strong acidic properties. $\text{p}K_{\text{a}}$ values for aromatic sulfonic acids are around 2 in DMSO and 0–1 in water. They are soluble in water.

Compounds with mixed oxidation state of sulfur atoms are represented in Table 2 by diisopropylaminoethyl 4-methylbenzene thiosulfonate. Thiosulfonates are generally soluble in water and hydrolyze gradually into thiols and sulfinic acids.

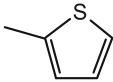
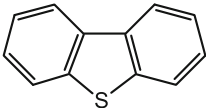
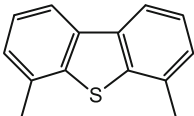
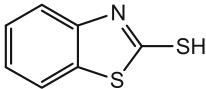
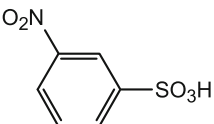
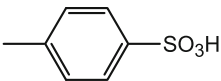
A separate group of reduced organic sulfur compounds is formed by *heteroatomic organic sulfur compounds* that contain nitrogen and phosphorus as heteroatoms. Due to the possible practical applications for water purification, these compounds are represented in photocatalytic studies mainly by pesticides. Selected heteroatomic organic sulfur compounds that comprise their major classes studied in photocatalytic reactions are shown in Table 3.

Table 2 Aromatic organic sulfur substrates studied

Substrate	System	References
 Phenylsulfides	CH ₃ CN, DCA/ SiO ₂ CH ₃ CN, TiO ₂ CH ₃ CN, TiO ₂ CH ₃ CN, TiO ₂	Soggiu et al. (1999) Fox and Abdel-Wahab (1990) Baciocchi et al. (1997b) Davidson and Pratt (1983)
 Aryl benzylsulfides	CH ₃ CN, DCA CH ₃ CN, TiO ₂ CH ₃ CN/H ₂ O, TiO ₂	Baciocchi et al. (1997a) Baciocchi et al. (1997b) Adam et al. (1998) Vosooghian and Habibi (2007)
 Methyl phenylsulfides	CH ₃ CN or CH ₃ OH, TiO ₂ CH ₃ CN/H ₂ O, TiO ₂	Somasundaram and Srinivasan (1998) Tachikawa et al. (2003) Tachikawa et al. (2006) Vosooghian and Habibi (2007)
 Benzylsulfides	CH ₃ CN, TiO ₂ CH ₃ CN/H ₂ O, TiO ₂	Fox and Abdel-Wahab (1990) Vosooghian and Habibi (2007)
 2-Phenethyl-2-chloroethylsulfide	Water, TiO ₂ Air, TiO ₂	Vorontsov et al. (2002a)
 Diisopropylaminoethyl 4-methylbenzene thiosulfonate	CH ₃ CN, TiO ₂	Vorontsov et al. (2005)
 Thiophene	Air, TiO ₂ CH ₂ Cl ₂ + H ₂ O, TiO ₂	Canela et al. (1999) Sokmen et al. (2001)

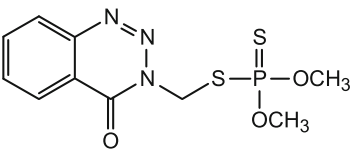
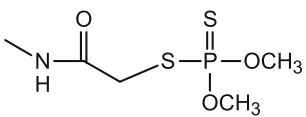
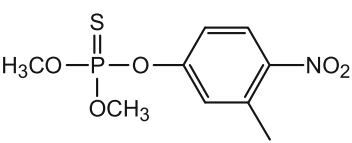
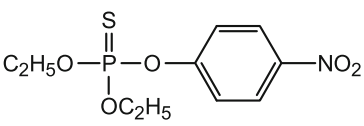
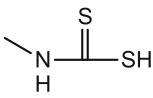
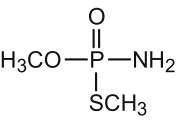
(continued)

Table 2 (continued)

Substrate	System	References
		
2-Methylthiophene		
	CH ₃ CN, TiO ₂	Abdel-Wahab and Gaber (1998)
	CH ₃ CN, TiO ₂	Matsuzawa et al. (2002)
	C ₇ H ₈ , POM	Mei et al. (2003)
	C ₁₄ H ₃₀ , TiO ₂	Robertson and Bandosz (2006)
Dibenzothiophene		
	CH ₃ CN, TiO ₂	Matsuzawa et al. (2002)
Dimethyl dibenzothiophene		
	H ₂ O, TiO ₂	Habibi et al. (2001)
	H ₂ O, La-TiO ₂	Li et al. (2004)
2-Mercaptobenzothiazole		
	H ₂ O, TiO ₂	Rachel et al. (2002)
<i>m</i> -Nitrosulfonic acid		
	H ₂ O, TiO ₂	Haarstrick et al. (1996)
<i>p</i> -Toluenesulfonic acid		

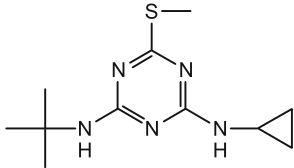
Pesticides comprise several types of chemicals for elimination of harmful or undesirable microorganisms, plants, or animals. Among them are insecticides that remove insects mostly by damaging their nervous system. Many insecticides inhibit acetylcholinesterase enzyme that is needed for removal of acetylcholine released during nerve impulse transmission. Sulfur-containing insecticides are represented by the following chemical classes:

Table 3 Selected heteroatomic organic sulfur compounds studied

Substrate	System	References
	H ₂ O, TiO ₂	Dominguez et al. (1998)
Azynthos-methyl		
	H ₂ O, TiO ₂	Dominguez et al. (1998) Oller et al. (2005)
Dimethoate		
	H ₂ O, TiO ₂ H ₂ O, TiO ₂ , PW ₁₂ O ₄₀ ³⁻	Kerzhentsev et al. (1996) Topalov et al. (2003) Kormali et al. (2004)
Fenitrothion		
	H ₂ O, TiO ₂	Doong and Chang (1998)
Parathion		
	H ₂ O, TiO ₂	Vidal and Luengo (2001)
Vapam		
	H ₂ O, TiO ₂	Malato et al. (2000)
Methamidophos		
	H ₂ O, TiO ₂	Konstantinou et al. (2001)

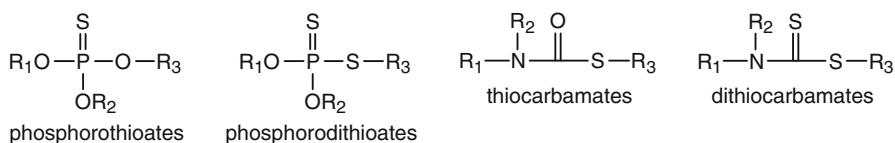
(continued)

Table 3 (continued)

Substrate	System	References
		
Irgarol VX (see Fig. 1)	CH ₂ Cl ₂ , Au/TiO ₂	Neatu et al. (2010)

- Organophosphorous compounds (phosphorothioates and phosphorodithioates)
- Thiocarbamates (monothiocarbamates and dithiocarbamates)

Phosphorothioates possess P=S bond, phosphorodithioates have S–P=S group. Thiocarbamates and dithiocarbamates include analogous fragments with carbonyl group instead of phosphorous atom.



Organophosphorous insecticides are very toxic for humans. Lethal dose of parathion is estimated as LD₅₀ 6–50 mg/kg. Carbamates can be even more toxic. The most toxic insecticide ever used is probably aldicarb (LD₅₀ 0.9 mg/kg).

Among listed in Table 3 is irgarol, which is a sulfur-containing *herbicide*. It inhibits photosynthesis and, due to low toxicity to animals and poor solubility in water, is used for algae growth control over surfaces submerged in water. In contrast to insecticides, herbicides usually do not contain P–S bonds, but have sulfide groups RSR– attached to triazine ring. For example, irgarol and prometryne have CH₃S– group. Thiocarbamates are also applied as herbicides. Molinate and Eptam have CH₃CH₂S– group, thiocarbamil has PhCH₂S– attached to carbamate group.

Pesticides are usually crystalline solids or thick liquids at room temperature with boiling point above 200°C. Major pesticides have low solubility in water and good solubility in organic solvents.

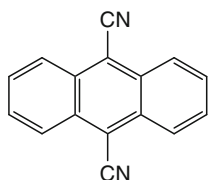
Products of Photocatalytic Transformations

Composition and distribution of products of photocatalytic reactions of organic sulfur compounds depend on the type of organic compound, on the presence or absence of

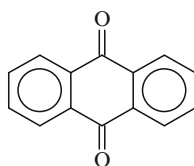
oxygen (aerobic and anaerobic reactions), and on phase of organic compound (gas phase and liquid phase reactions). Liquid phase reactions are affected by the type of solvent (protic–aprotic, polar–nonpolar). The effects of these factors are considered separately for aliphatic, aromatic, and heteroatomic organic sulfur compounds.

Aliphatic Organic Sulfur Compounds

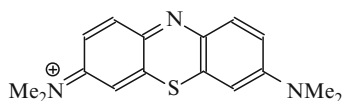
Aerobic photocatalytic transformations of aliphatic organic sulfur compounds proceed with oxidation of sulfur atom, cleavage of C–S bond, and oxidation at carbon atoms. The distribution of products depends on type of solvent, photocatalyst, and phase of reaction. Homogeneous photocatalysts include decatungstate $W_{10}O_{32}^{4-}$ in its amine salts, organic sensitizers like dicyanoanthracene, anthraquinone, and methylene blue. These photocatalysts can be employed in heterogenized form like grafted on silica. The mostly used heterogeneous photocatalyst is TiO_2 with some works employing CdS.



9,10-Dicyanoanthracene
DCA



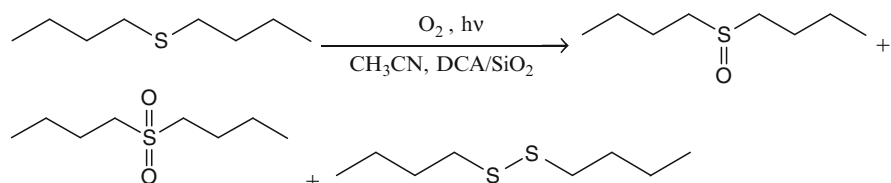
Anthraquinone
ANT



Methylene Blue
MB

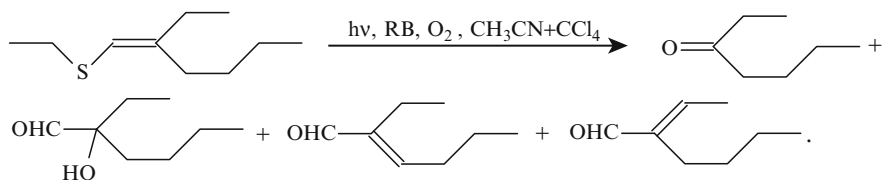
Acetonitrile is often used as a *nonaqueous solvent* for photocatalytic reactions because of its high stability towards oxidation. Aliphatic *sulfides* are most often subjects of experimentation. Sulfones and sulfoxides were reported as the sole reaction products for photocatalytic oxidation in oxygenated acetonitrile of aliphatic compounds 2-chloroethyl ethyl sulfide on TiO_2 (Fox et al. 1990), dimethyl sulfide, dibutyl sulfide, and 2-chloroethyl ethylsulfide on $W_{10}O_{32}^{4-}$ (Chambers and Hill 1990). However, attempts to identify other more volatile products like ethylene, chloroethylene, acetaldehyde, etc. were not undertaken in these works.

Transformations of di-*n*-butylsulfide were studied over pure and silica grafted photosensitizers (DCA, benzophenone, *N*-methylquinolinium) in oxygenated acetonitrile solution. The major product of dibutylsulfide reaction is dibutylsulfoxide. Smaller quantities of dibutylsulfone and dibutyldisulfide are also generated as the equation below shows. Formation of disulfide corresponds to cleavage of C–S bond of original sulfide molecule (Soggiu et al. 1999; Lacombe et al. 2002; Baciocchi et al. 2003).



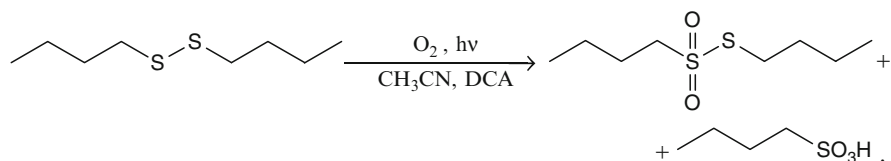
Chemical warfare agent HD, which is bis(2-chloroethyl)sulfide, undergoes photocatalytic destruction in CH_2Cl_2 solution over activated carbon loaded TiO_2 and nitrogen-doped TiO_2 under irradiation with Hg or Ne lamps (Cojocar et al. 2009). Formation of intermediate products, bis(2-chloroethyl)disulfide, bis(2-chloroethyl) sulfone, and bis(2-chloroethyl) sulfoxide, was suggested before the final inorganic products are produced. Activated carbon additions to TiO_2 were beneficial for faster destruction. Chloroethylene, CO_2 , and SO_2 were detected as the HD degradation gaseous products over TiO_2/SiO_2 , $Fe/TiO_2/SiO_2$, $V/TiO_2/SiO_2$, and $Mn/TiO_2/SiO_2$, the reaction rate increases in this sequence of photocatalysts (Neatu et al. 2009). The products show that sulfur oxidation, C–S bond cleavage, and hydrogen atom transfer are operative in HD photocatalytic transformation.

Reactions of oxidation at carbon atoms of sulfides were observed for ethyl 2-ethylhexene-1 sulfide transformations in $CH_3CN + CCl_4$ solution with Rose Bengal and DCA photocatalysts as the next equation illustrates (Ando et al. 1979).

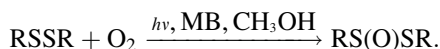


The reaction is not mediated by singlet oxygen because singlet oxygen scavenger β -carotene does not change the products significantly.

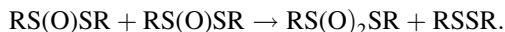
Photocatalytic reaction of dibutyl *disulfide* over grafted DCA demonstrates predominant formation of dibutylthiosulfonate with concomitant formation of butanesulfonic acid according to the following equation (Lacombe et al. 2002).



Photocatalytic oxidation of various disulfides in methanol solution of methylene blue resulted in formation of thiosulfonates (Murray and Jindal 1972).



Dimethyl thiosulfinate and diethyl thiosulfinate are unstable and disproportionate into the corresponding thiosulfonate and disulfide as the next equation shows.



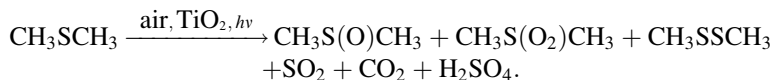
Other thiosulfonates – di-*tert*-butyl, diphenyl, diisopropyl – were stable and were not oxidized further. Thus, thiosulfonates can be obtained selectively with MB. The reaction was suggested to proceed with participation of singlet oxygen.

Gas phase photocatalytic transformations possess specific features that influence product formation. Compounds with low volatility do not have chances to be removed from the photocatalyst surface other than be converted into more volatile products. On the other hand, reduced organic sulfur compounds upon progressive oxidation are converted into oxidized sulfur products and finally into H_2SO_4 . In the row of consecutive oxidation products of sulfur moiety, only SO_2 has chance of escaping from the photocatalyst surface. Other products accumulate over the photocatalyst surface. Strongly adsorbed products limit the availability of reaction sites of photocatalyst surface for further reaction. Thus, photocatalyst deactivation develops after certain quantity of reduced sulfur compound is converted. Despite deactivation, gas phase photocatalysis is more attractive for practical realization because quantum efficiency of gas phase reactions is often one order of magnitude higher than that in liquid phase.

The simplest reduced sulfur compound is H_2S . It is converted over TiO_2 photocatalyst into sulfuric acid that stays on the catalyst surface (Canela et al. 1998).

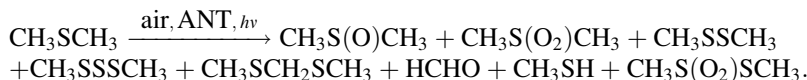
In photocatalytic transformations of ethanethiol, the following gas phase products were identified: SO_2 , CH_3COOH , CO , and CO_2 . Surface products were not analyzed (Kachina et al. 2006).

Dimethylsulfide is the next compound in the row of molecule complexity that was studied in detail. Products of degradation were distributed between gas phase and surface of TiO_2 catalyst according to their volatility. CO_2 , SO_2 , and dimethyl disulfide were detected in gas phase, whereas dimethyl sulfoxide, dimethyl sulfone, methanesulfonic acid, and H_2SO_4 were identified in isopropanol extracts from used photocatalyst (Demeestere et al. 2005a, b).



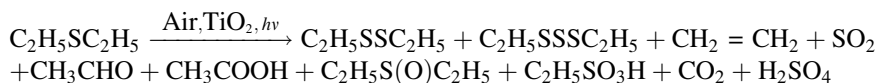
Product corresponding to C–S bond cleavage (dimethyldisulfide) was detected in quantity similar to quantity of dimethyl sulfoxide and dimethyl sulfone. Thus, sulfur oxidation and molecule cleavage have the same importance in this reaction.

If silica grafted organic sensitizer (ANT, or DCA) is utilized as photocatalyst for dimethyl sulfide oxidation, only products of incomplete oxidation are detected in gas phase and catalyst surface according to the following scheme (Latour et al. 2005).



Major products were dimethyl sulfoxide, dimethyl sulfone, and dimethyl disulfide. The same major products as for initial stages of TiO₂ photocatalysis possibly indicate the same initial reaction mechanism.

Photocatalytic reaction of airborne diethyl sulfide vapor over TiO₂ has been studied relatively thoroughly. Distribution of products of diethyl sulfide oxidation depends on conditions of reaction, humidity, light intensity, contact time, catalyst mass, as well as on time of reaction due to developing of catalyst deactivation. Major gaseous intermediate products are diethyl disulfide, ethylene, acetaldehyde, acetic acid, SO₂. Major surface intermediate products are diethyl trisulfide, diethyl sulfoxide, and ethylsulfonic acid (Vorontsov et al. 2001, 2003a, b).



Generally, the product composition resembles that of dimethyl sulfide reaction. The difference lies in the formation of ethylene from diethyl sulfide possibly via hydrogen transfer reaction. This route is impossible for dimethyl sulfide that does not contain long enough alkyl group for alkene formation.

The gas phase photocatalytic transformation of the last reduced organic sulfur compound considered here is 2-chloroethyl ethylsulfide (CEES). This molecule is quite similar to chemical agent mustard gas (HD). The presence of chlorine atom introduces hydrolysis reaction into the transformation scheme. Hydrolysis results in hydroxyethyl ethylsulfide. However, intact CEES also takes part in reactions to produce diverse products. Since CEES possesses two nonequivalent alkyl radicals attached to sulfur atom, the C–S bond cleavage reactions produce products from both radicals. Thus, ethylene and chloroethylene, acetaldehyde and chloroacetaldehyde, and SO₂ are present in gas phase products. Diethyl disulfide, chloroethyl ethylsulfide, bis(2-chloroethyl)disulfide, and chloroethyl ethylsulfoxide are the major surface extracted products. Figure 2 illustrates major intermediate transformation products of CEES over TiO₂ (Vorontsov et al. 2003a, b; Martyanov and Klabunde 2003).

The products corresponding to hydrolysis of C–Cl bond of the products in Fig. 2 were also detected (Han et al. 2008). It was found that sulfated TiO₂ possesses higher stability in CEES destruction than pristine TiO₂.

Anaerobic reactions proceed without participation of oxygen. Such photocatalytic reaction of dimethyl sulfide on decatungstate photocatalyst gives 1,2-bis(methylthio)ethane with >90% yield (Chambers and Hill 1990).

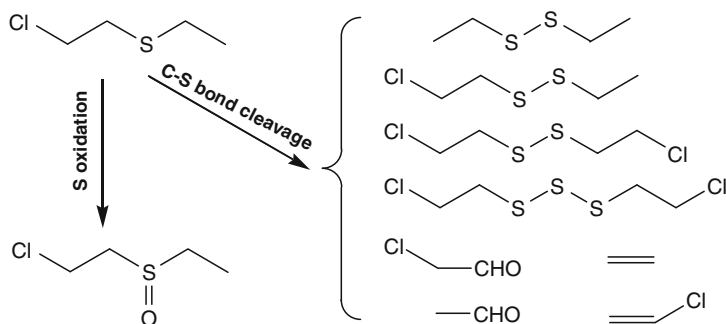
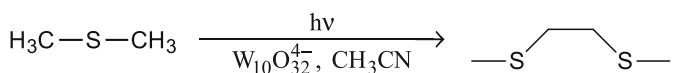


Fig. 2 Major CEES photocatalytic transformations intermediate products



This product arises as a result of recombination of two radicals $\text{CH}_3\text{SCH}_2\cdot$ that were formed by hydrogen atom transfer to excited photocatalyst, WO. It is interesting that the dimer formation was not observed in aerobic conditions which favor the formation of sulfoxide and sulfone (Chambers and Hill 1990).

Aromatic Organic Sulfur Compounds

Specifics of aromatic compounds consist in high stability of radical cations and radical intermediates due to delocalization, and this favors the formation of the corresponding products. Aromatic organic sulfur compounds were studied almost exclusively in dissolved state because of the low volatility of these compounds. The products formed in photocatalytic transformations depend markedly on sulfur substrate structure, photocatalyst, presence or absence of oxygen, and media of reaction. First, we consider *aerobic* conditions of photocatalytic reactions. These conditions favor oxidation and complete mineralization.

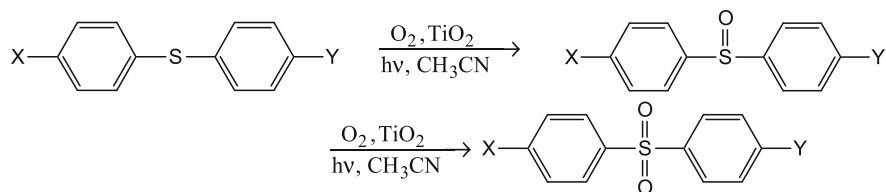
In aqueous media partial and deep oxidation products can be formed, whereas in organic solvents complete oxidation is never observed. Strongly oxidizing photocatalysts such as wide band-gap oxide semiconductors (TiO_2 , ZnO) and polyoxometalates can drive up to complete oxidation into inorganic products. Organic molecular photocatalysts (sensitizers, dyes) usually give only partial oxidation products. Composition of products observed inevitably depends on the irradiation time since photocatalytic oxidation products tend to be oxidized up to the final products.

First we consider *nonaqueous solvents* that mostly favor the formation of partial oxidation products.

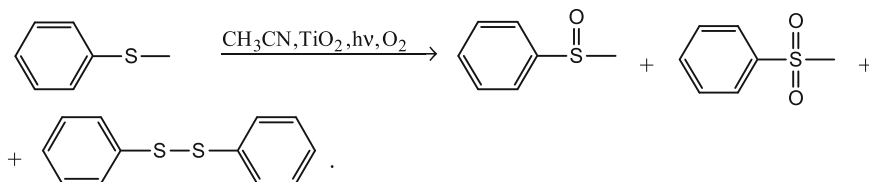
Aromatic *sulfides* undergo photocatalytic transformations whose products are associated with oxidation of sulfur atom, breakage of C-S bond, and radical

reactions at the carbon atoms. As it will be shown below, the structure of the sulfide affects the principal route of transformation and products.

Phenyl sulfides oxidation basically proceeds at sulfur atom if the carbons belong to aromatic rings only. Diphenyl sulfide produces almost exclusively diphenyl sulfoxide and sulfone over $W_{10}O_{32}^{4-}$ photocatalyst in CH_3CN (Chambers and Hill 1990). Same reaction products are observed for phenylsulfides with TiO_2 photocatalyst (Fox and Abdel-Wahab 1990).

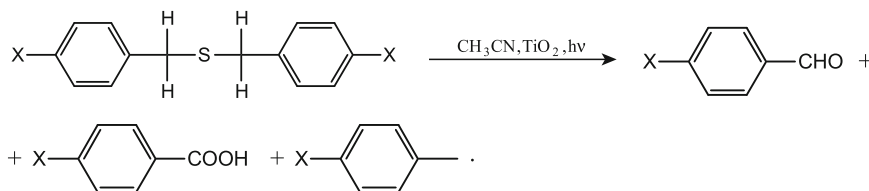


Methyl phenylsulfides react in a way very similar to diphenyl sulfides without organic substituents. Again sulfoxide and sulfone are the major products for this case as exemplified for methyl phenylsulfide below (Somasundaram and Srinivasan 1998; Vossooghian and Habibi 2007).

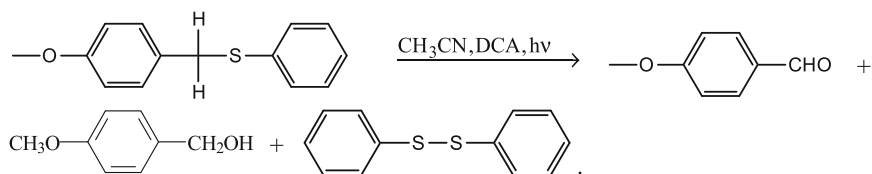


The same products were observed over $W_{10}O_{32}^{4-}$ photocatalyst in CH_3CN media (Chambers and Hill 1990). Sulfoxide and sulfone are also reported as the product of tetrahydrothiophene oxidation over $W_{10}O_{32}^{4-}$ photocatalyst in CH_3CN (Chambers and Hill 1990).

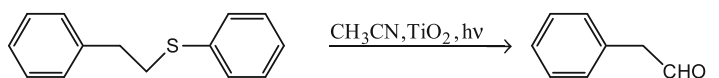
Introduction of CH_2 group adjacent to the sulfur atom in aromatic sulfides dramatically changes products distribution. Benzyl sulfides mostly undergo rupture of sulfur-carbon bond in oxygenated acetonitrile suspension of UV-irradiated TiO_2 according to the following equation (Fox and Abdel-Wahab 1990).



Unsymmetrical aromatic sulfides having phenyl and alkylphenyl groups attached to sulfur atom also mostly follow C-S bond cleavage. Sulfur atom in products is mainly connected to the phenyl ring (Baciocchi et al. 1997b).



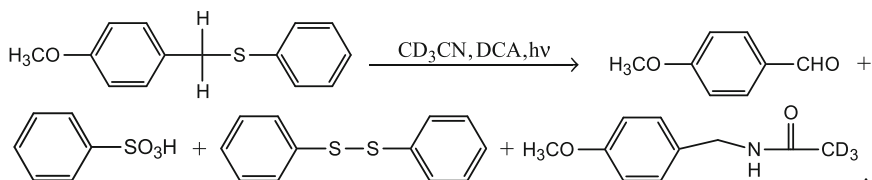
The oxidation of the corresponding sulfoxide (4-methoxybenzyl phenylsulfoxide) also resulted in the cleavage of the C–S bond connected to the alkyl group. Introduction of more lengthy alkyl group in alkylphenyl phenylsulfide does not change the major direction of photocatalytic transformation. Rupture of C–S bond with the alkyl group in phenethyl phenyl sulfide is the predominant reaction as the following equation shows:



Substantial amounts of phenethyl phenyl sulfoxide are also formed in this reaction.

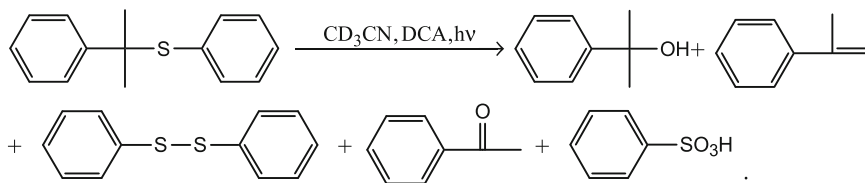
Organic sensitizer molecules in dissolved or heterogenized state are called molecular photocatalysts. Similarly to titanium dioxide, they interact with substrate and, upon light quanta absorption, induce chemical transformations. Molecular photocatalysts in an excited state are capable of performing energy transfer or electron transfer reactions. Among the energy transfer reactions is the formation of singlet oxygen (1O_2). 9,10-Dicyanoanthracene (DCA) homogeneous photocatalyst was employed for oxidation of several organic sulfur-containing substrates. Aromatic compounds undergo reactions with formation of products very similar to those obtained over titanium dioxide photocatalyst.

Accordingly, benzyl phenylsulfides in deuterated acetonitrile form corresponding benzaldehydes. However, significant amount of benzylacetamide is generated. This product was not detected over TiO_2 photocatalyst. The presence of deuterium clearly shows that acetamide is produced from reaction with solvent (Baciacchi et al. 1997a).



In the case of quaternary benzylic carbon atom, fragmentation of C–S bond is also the major reaction pathway. 2-Phenyl-2-propanol is regarded as the major product of this fragmentation, methylstyrene and acetophenone being formed in

slightly smaller quantities. Interestingly, products of reaction with solvent, acetonitrile, were not formed in this reaction (Baciocchi et al. 1997a).

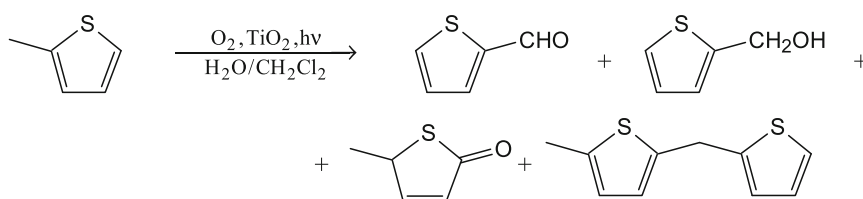


To sum up, reactions in acetonitrile solutions result in three types of products. The first type corresponds to oxidation of sulfur atoms into the corresponding sulfoxides and sulfones. The second type corresponds to cleavage of C–S bond with formation of alcohol and aldehyde groups from the carbon atom. The third type corresponds to oxidation at carbon atoms not associated directly with sulfur atom. These major product types preserve for other reaction media.

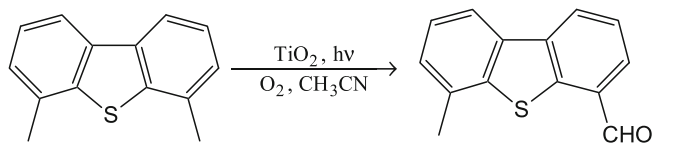
The sulfur atom oxidation is the predominant pathway of photocatalytic oxidation if the *sulfur atom is inserted in a cycle of aromatic compounds*. So, dibenzothiophene underwent oxidation of the sulfur atom to form sulfoxide and sulfone as the main products. Analogous products were observed from thioxanthone and thioxanthene, analogs of dibenzothiophene that contain two sulfur atoms inside the central carbon cycle (Abdel-Wahab and Gaber 1998). These sulfur atoms underwent consecutive oxidation into sulfoxide and sulfone groups.

Sulfur organic compounds with *side alkyl groups attached to aromatic ring* have the additional pathway of alkyl group reactions. Such reactions can include oxidation or other processes characteristic for radicals centered at the side alkyl group.

Methylthiophene transformations were studied in suspension of TiO₂ in water with dichloromethane (1:1) since methylthiophene is insoluble in pure water. Main products corresponded to radical transformations of the side methyl group and included thiophene aldehyde, hydroxymethylthiophene, methylthiophenone, and dimers and trimers of methylthiophene as the equation below shows (Sokmen et al. 2001).

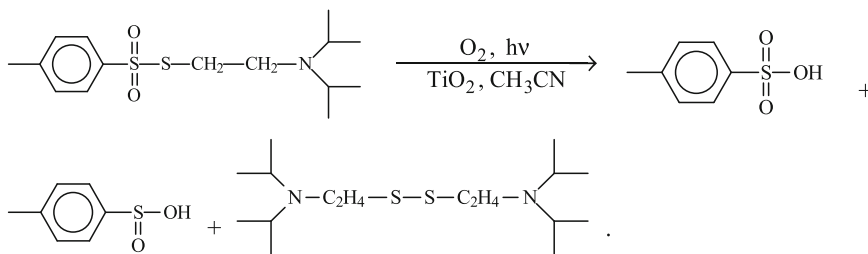


4,6-Dimethyldibenzothiophene underwent oxidation of one of the two methyl groups to form the corresponding aldehyde (Matsuzawa et al. 2002).



This contrasts with oxidation of dibenzothiophene which results in oxidation of sulfur atom.

Thiosulfonates are organic sulfur compounds with mixed sulfur oxidation state, +3 and -1 . Aerobic photocatalytic oxidation of an organic thiosulfonate, 2-diisopropylaminoethyl-4-methylbenzenethiosulfonate (DAMT), over TiO_2 in acetonitrile resulted majorly in cleavage of S–S bond and oxidation of sulfur atom (Vorontsov et al. 2005).

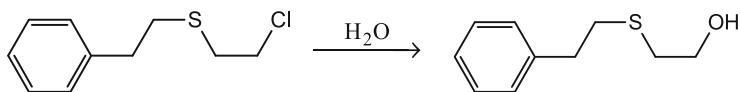


These products are formed as a result of interaction with TiO_2 surface since the DAMT radical cation decomposes into different products without the surface. Minor degradation pathways included cleavage of the sulfide C–S bond with formation of diisopropylvinylamine and diisopropylethylamine and cleavage of C–N bond with formation of diisopropylamine (Vorontsov et al. 2005).

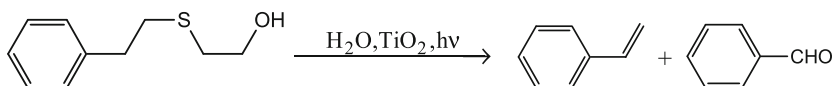
Aqueous systems. Photocatalytic reactions of organic sulfur compounds in aqueous or mixed organic–aqueous solutions usually lead to a greater variety of products than reactions in pure acetonitrile.

Aromatic *thiols* undergo deep photocatalytic oxidation in aqueous TiO_2 system. Interestingly, disulfide intermediate was not detected in many cases for oxidation of thiols. This can be explained by its fast transformation into deeper oxidation products. 2-Mercaptobenzothiazole was converted over Nd^{3+} doped TiO_2 photocatalyst into benzothiazole, hydroxybenzothiazole, benzothiazolesulfonic acid, and anilinesulfonic acid as intermediate products and inorganic acids and NH_4^+ as the final products (Li et al. 2006b).

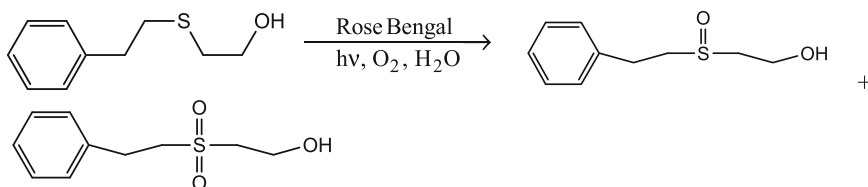
Pure aqueous solutions are suitable for carrying out photocatalytic transformations of sulfur compounds with significant solubility in water. Such compounds should possess highly polar groups. Alternatively, such groups can be generated in situ during or prior to the photocatalytic reaction. This possibility was realized in degradation of 2-phenethyl-2-chloroethyl *sulfide* which reactively dissolves in water according to the following equation.



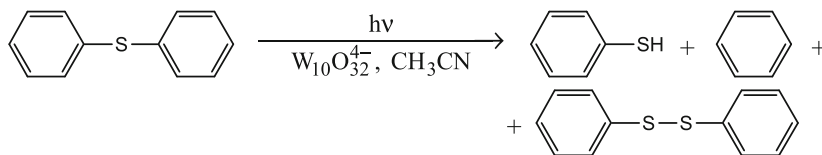
Photocatalytic transformations of 2-phenethyl-2-hydroxyethylsulfide, which is water-soluble, result in predominant formation of C–S bond cleavage products. Styrene was the major product; benzaldehyde and 2-phenethylsulfinic acid formed in significant quantities. Other numerous products are present in much smaller quantities. Sulfoxide and sulfone products were not detected (Vorontsov et al. 2002a).



2-Phenethyl-2-hydroxyethylsulfide photocatalytic oxidation with Rose Bengal dye in aqueous solution and on the surface of nylon textile results in formation of the corresponding sulfoxide and sulfone (Brewer et al. 2010). These products are in agreement with singlet oxygen-mediated oxidation, typical for dye sensitizers.

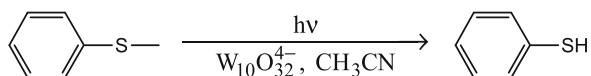


Anaerobic photocatalytic transformations of *sulfides* proceed via C–S bond cleavage and hydrogen atom transfer. Diphenyl sulfide is transformed into thiophenol and diphenyl disulfide with 60% total yield as well as benzene with 95% yield (Chambers and Hill 1990).



Analogous anaerobic reaction of thioanisol produces thiophenol (Chambers and Hill 1990). Decatungstate photocatalyst is reduced during this reaction to $\text{W}_{10}\text{O}_{32}^{5-}$ and $\text{W}_{10}\text{O}_{32}^{6-}$ since the reoxidation via hydrogen production is a

much slower reaction under these conditions.



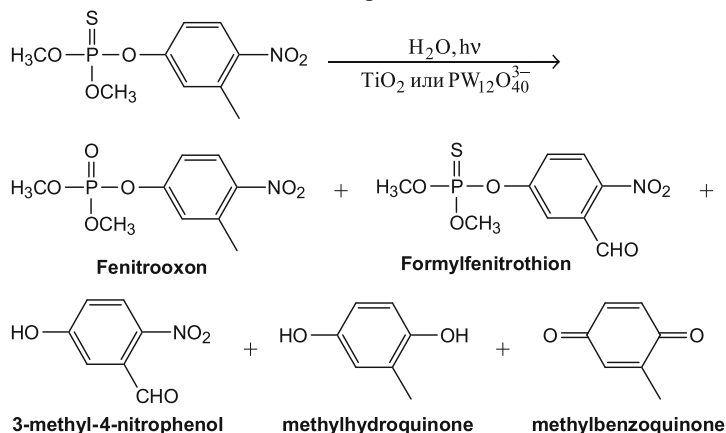
Gas phase. Photocatalytic oxidation of vapors of 2-phenethyl-2-chloroethylsulfide by oxygen of air over TiO_2 proceeds with much higher rate compared to liquid phase. The major intermediate product of oxidation is styrene which did not appear in the gas phase, but resided over the photocatalyst surface. The final oxidation products were CO_2 , H_2O and sulfuric acid, the latter resided on the photocatalyst surface.

Heteroatomic Organic Sulfur Compounds

Purification of water from pesticides represents very important environmental task in view of their very high toxicity and widespread agricultural application. Thus, an extensive list of publications can be provided to illustrate water purification from pesticides. Due to the presence of heteroatoms of phosphorus and nitrogen, these compounds possess unique chemical structures and distinct routes of photocatalytic transformations.

Phosphorothioates undergo photocatalytic reactions leading to oxidative replacement of sulfur with oxygen, cleavage of bonds, and oxidation of organic fragments. Further extended oxidation can lead to complete mineralization into carbon dioxide, water, and inorganic acids.

Fenitrothion is a *monothiophosphate*. Its oxidation followed similar degradation pathways for photocatalysts TiO_2 and $\text{PW}_{12}\text{O}_{40}^{3-}$ (Kormali et al. 2004). Formation of the large fragments shown in the scheme below was augmented by formic and acetic acids (Kerzhentsev et al. 1996; Topalov et al. 2003).

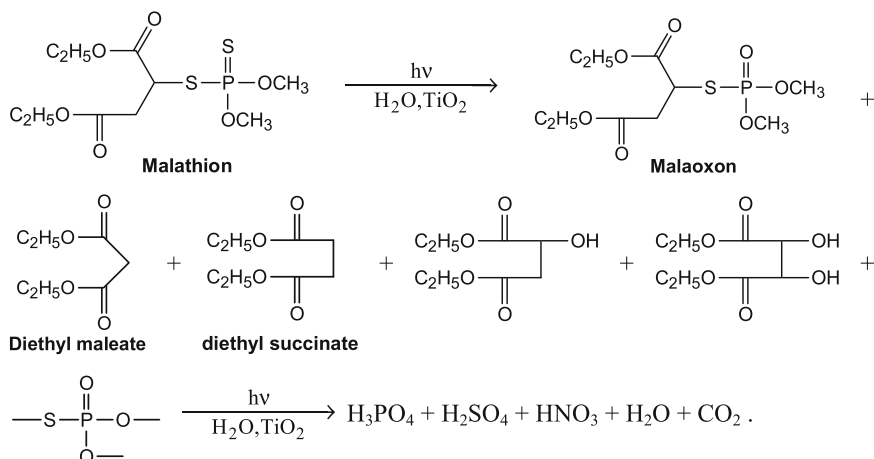


Oxidative replacement of sulfur in P=S group, cleavage of P-O bond, and oxidation of aromatic methyl group were the starting routes of fenitrothion

degradation. The final oxidation products were H_3PO_4 , HNO_3 , HNO_2 , CO_2 , and H_2O (Kormali et al. 2004). Analogous products were detected for dichlofenthion (monothiophosphate) oxidation over TiO_2 (Konstantinou et al. 2001).

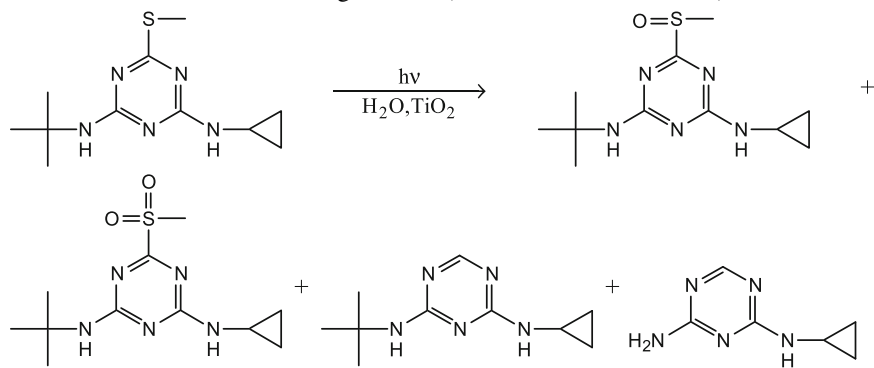
Photocatalytic destruction of fenitrothion with Fe^{III} oxalate system $[\text{Fe}(\text{C}_2\text{O}_4)_3]^{3-}$ results in two products, fenitrooxon and 3-methyl-4-nitrophenol. The oxidation did not lead to complete mineralization of fenitrothion; only a small decrease in total organic carbon was detected (Katsumata et al. 2010).

Malathion is a *dithiophosphate*. Its photocatalytic destruction with TiO_2 produced a variety of products reflecting the oxidation and substitution of sulfur in $\text{P}=\text{S}$ group, cleavage of $\text{P}-\text{S}$ and $\text{C}-\text{S}$ bonds, and oxidation at carbon atoms (Kralj et al. 2007).



The diethyl succinate fragment is formed by $\text{C}-\text{S}$ bond cleavage with hydrogen transfer. It is further hydroxylated. Further deep oxidation steps lead to formation of mineral acids and CO_2 .

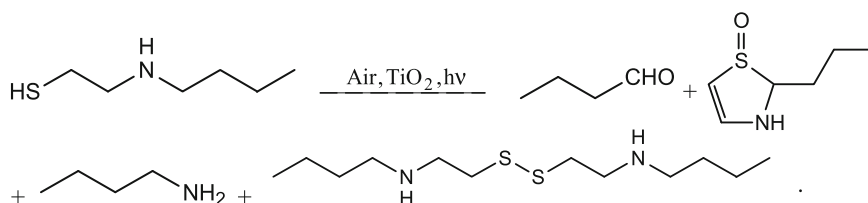
Irgarol is an *s*-triazine herbicide. Its photocatalytic destruction in aerated suspension of TiO_2 followed the initial pathways of sulfur oxidation, cleavage of carbon-sulfur and carbon-nitrogen bond (Konstantinou et al. 2001).



Further oxidation leads to cleavage of C–N and C–S bonds and oxidation of the triazine ring.

As shown above, sulfides follow the route of sulfur atom oxidation to sulfoxide and sulfone. Further transformations of sulfone follow the routes that were considered in detail in the previous two subsections. Additional routes of oxidation are associated with the presence of specific fragments like triazine ring and its substituents.

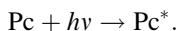
The presence of heteroatoms other than sulfur in reduced organic sulfur compounds can drastically complicate the product composition. Photocatalytic oxidation of 2-(butylamino)ethanethiol in aqueous suspension of TiO_2 generated more than 30 intermediate products (Vorontsov et al. 2002b). The final products of oxidation were carbon dioxide, sulfuric acid, and ammonia. Major intermediate products are showed in the next reaction scheme.



Dimerization of the thiol occurred at the start of reaction. Further transformations resulted in formation of various linear and cyclic products, 2-propyldihydrothiazole-S-oxide being considered as the main cyclic product formed. Formation of cyclic products should be attributed to the presence of nitrogen atom in the starting molecule, because cyclization was never observed for other sulfides.

Mechanisms of Photocatalytic Transformations

Photocatalytic reactions are started since absorption of quantum of light by photocatalyst entity.

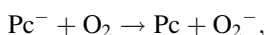
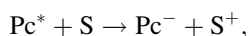


The energy of excitation of photocatalyst is then spent in series of reaction steps leading from reagents to products. The reaction with participation of excited photocatalyst is called *primary photocatalytic reaction*. The reaction proceeding with participation of products of the primary photocatalytic reactions is called *secondary photocatalytic reaction*. The sequence of steps comprising primary and secondary photocatalytic reactions is called *mechanism of photocatalytic reaction*.

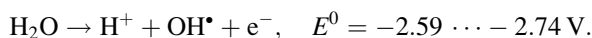
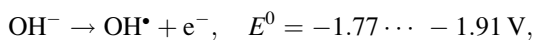
There are a limited number of possible *primary photocatalytic reactions*. The following primary reactions are possible with participation of organic sulfur compounds:

- Photoinduced electron transfer (PET)
- Energy transfer (EnT)
- Hydrogen atom transfer (HAT)

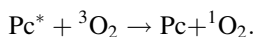
PET is very often considered as the sole primary photocatalytic reaction for various types of photocatalysts and photocatalytic reactions. It can indeed give the major input for reactions proceeding in water or other highly polar solvents like acetonitrile. These solvents strongly stabilize charged species forming in the electron transfer process:



where Pc^* is excited photocatalyst, S is organic sulfur compound. Water can directly participate in PET with formation of hydroxyl radicals that initiate oxidation. In aqueous systems, one electron oxidation of water can proceed according to the following equations (Buxton et al. 1988).



Energy transfer is an important primary photochemical and photocatalytic reaction. It is often considered as a physical process leading to transfer of excitation from one species to another. However, it has been proved for many examples that energy transfer proceeds through formation of the complex of the energy donor and energy acceptor with chemical binding. Thus, it can be considered as a chemical process. Energy transfer results in production of very active singlet oxygen $^1\text{O}_2$ from normal triplet oxygen $^3\text{O}_2$ for many organic sensitizers as the following reaction illustrates.



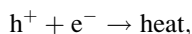
Singlet oxygen drives oxidation of many compounds including sulfur organic compounds. It seems that energy transfer is also an important step in heterogeneous photocatalysis including TiO_2 photocatalysis. Singlet oxygen is produced on TiO_2 with quantum yield as high as 0.38 and lifetime 2–2.5 μs (Daimon et al. 2007). This energy transfer is possible even upon irradiation of TiO_2 with $\lambda = 532 \text{ nm}$ as a result of two-photon excitation which was proved by the quadratic dependence of $^1\text{O}_2$ production rate on irradiance (Li et al. 2009). Direct energy transfer from

photocatalyst to substrate should be also possible for organic compounds with proper electronic spectrum.

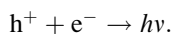
Hydrogen atom transfer proceeds from organic sulfur compounds to photocatalysts with significant radical character of excited state such as ketones and polyoxometallates. Labile hydrogen atoms are transferred preferably.

Secondary photocatalytic reactions proceed starting from products of primary reactions.

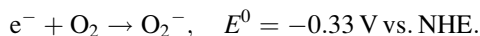
For heterogeneous semiconductor photocatalysts, which are represented in majority of cases by TiO₂ or modified TiO₂, band-gap excitation results in transfer of electron from valance band to conduction band. The electron and hole are formed as a result of excitation. These photogenerated species take part in electron transfer reactions at the semiconductor surface, or they can recombine with heat generation:



or with light emission in a process called luminescence:



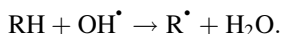
For most often used photocatalyst, TiO₂ in anatase modification, the conduction band potential is -0.12 V vs. NHE at pH = 0. In oxygenated solutions or gas phase, photogenerated electrons can react with oxygen to produce radical anions:



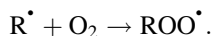
Since the production of O₂^{·-} in homogeneous phase is energetically unfavorable, these radicals probably stay adsorbed at the TiO₂ surface.

Valence band holes can oxidize solvent, which for water leads to hydroxyl radicals production. The hydroxyl radicals are responsible for initiation of oxidation reactions. Sometimes, sacrificial electron acceptors are added into the photocatalytic system in order to avoid participation of electrons in reactions of organic moieties. These electron acceptors capture photogenerated electrons. In particular, silver sulfate was used to avoid reactions of substrate degradation products with electrons or oxygen radical anions (Baciocchi et al. 1997b).

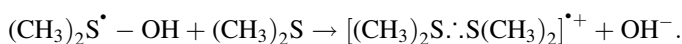
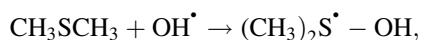
Hydroxyl radicals OH[·] are strong oxidants and hydrogen abstraction reagent. Majority of organic compounds undergo hydrogen abstraction as a result of reaction with hydroxyl radical:



This is also the case for organic sulfides in gas phase (Hynes et al. 1986). It was established that hydrogen abstraction from secondary carbon atoms prevails over that from primary carbon atoms. The product of hydrogen abstraction is then subject to reaction with O₂ to form peroxy radicals:



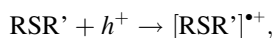
Peroxy radicals undergo various uni- and bimolecular reactions described in detail in the volume edited by Alfassi (1997). These reactions lead to oxygenated products with hydroxyl, carbonyl, and carboxyl functionalities. In reactions of reduced organic sulfur compounds, the products sometimes completely correspond to hydroxyl radical attack with subsequent peroxy radicals chemistry. For example, photocatalytic destruction of pesticides is often considered as started by OH radicals. However, destruction of many molecules is better described as initiated by electron transfer to holes. Alternatively, organic sulfur compounds in solutions can be oxidized by hydroxyl radicals into radical cations as exemplified for dimethyl sulfide below.



Oxidation by hydroxyl radical is also possible without participation of another sulfide molecule.

Alternatively, holes can oxidize sulfur organic compounds directly. Photogenerated holes for most used photocatalyst, anatase TiO_2 , have reduction potential of approximately +3 V vs. NHE. Such a high potential makes possible a variety of oxidation reactions. This electron transfer can be more favorable thermodynamically since organic sulfur compounds oxidation potentials -1.0 to -1.9 V vs. SHE (Glass 1999) are generally lower than oxidation potential of water (-2.59 to -2.74 V).

Thus, direct reaction with photogenerated holes,

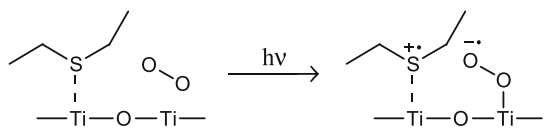


is more energetically favorable than production of hydroxyl radicals.

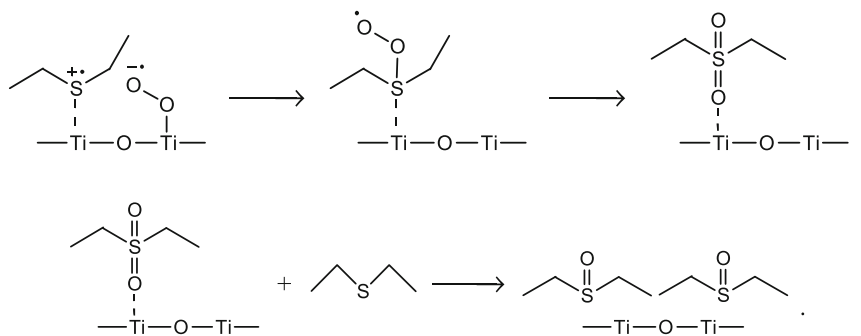
While alkylsulfide radical cations are short-living intermediates that are difficult to observe, arylsulfide radical cations were detected by ESR and by time-resolved diffuse reflectance spectroscopy (Tachikawa et al. 2003). Quantity of radical cation produced correlated with the quantity of substrate over TiO_2 surface, as one could expect from the Langmuir–Hinshelwood reaction model. It should be mentioned that the charge of the radical cation can be considered as delocalized for adsorbed radical cations.

For the case of the direct oxidation, photocatalytic degradation of sulfides on TiO_2 photocatalyst can be described by the following mechanism.

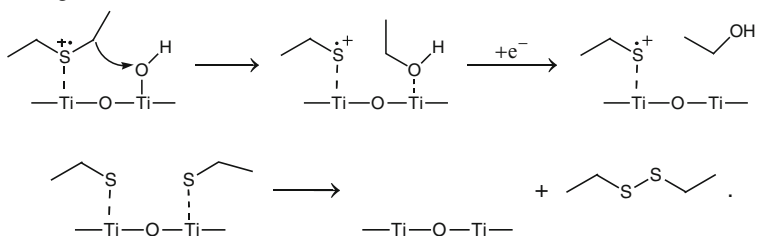
1. Excitation of TiO_2 , electron transfer from sulfide and to oxygen:



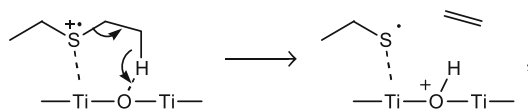
2. Formation of sulfoxide and sulfone:



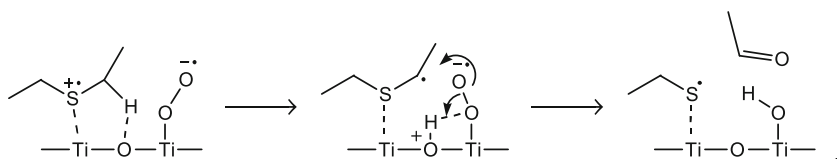
3. Cleavage of C-S bond with formation of disulfide and alcohol:



4. Cleavage of C-S bond with formation of alkene (and disulfide as shown above):



5. Cleavage of C-S bond with formation of aldehyde (and disulfide as shown above):

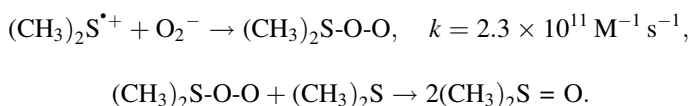


Concomitant to this mechanism, hydroxyl radical-initiated oxidation is possible as well.

In the case of molecular photocatalysis, photocatalyst molecules in an excited state usually have electron in lowest unoccupied molecular orbital (LUMO), whereas one electron in highest occupied molecular orbital (HOMO) is missing. Primary photocatalytic reactions of the excited molecular photocatalyst include electron transfer that results in formation of radical cation of sulfur compound and reduced photocatalyst. In the case of molecular photocatalysts with high oxidation potential like polyoxometallates, hydroxyl radicals can also form and initiate the oxidation.

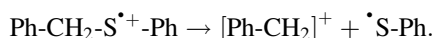
The radical cations of organic sulfur compounds in liquid phase undergo a variety of further chemical transformations summarized as follows.

(A) *Sulfur atom oxidation*. Sulfur radical cations readily react with O_2^- , e.g.,

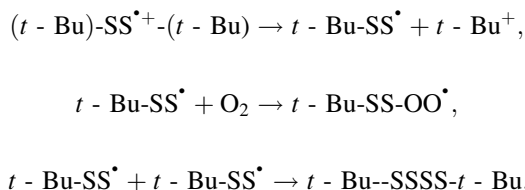


Direct reaction of sulfur radical cations with oxygen is relatively slow ($k < 10^6 \text{ M}^{-1} \text{ s}^{-1}$), though other mechanisms of interaction with molecular oxygen are possible as well.

(B) *C-S bond cleavage*. This reaction is well established for arylalkylsulfide radical cations, e.g.,

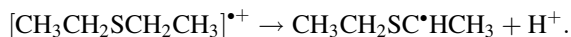


It is also observed for alkylsulfides and alkyldisulfides:



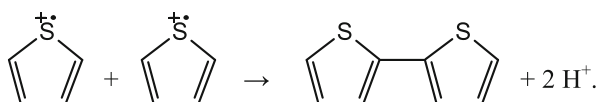
In the later case, tetrasulfide product RSSSSR is formed. Formation of polysulfides is usual for photocatalytic transformations. Thus, C-S bond cleavage is one of the major photocatalytic transformation routes.

(C) *α -Carbon atom (α -C-H) deprotonation*. Sulfur radical cations were found to be strong acids. For example, pK_A of $(CH_3)_2S^+$ is estimated as 0 and pK_A of $\text{PhCH}_2\text{S}^+\text{Ph}$ as -3. Accordingly, the yield of products of deprotonation for aromatic sulfides is higher than for aliphatic sulfides.

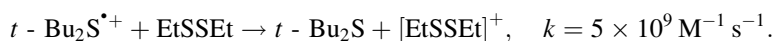


The product of deprotonation is equal to the product of direct reaction with hydroxyl radical–hydrogen atom abstraction. The carbon-centered radical can further react with oxygen and follow the peroxy radical chemistry. TiO₂ surface was found to accelerate the deprotonation reactions compared to homogeneous photocatalysts.

- (D) C–C bond cleavage is possible if stable enough products are formed. This reaction called α -cleavage is usual in mass spectrometry (Mc Lafferty and Turecek 1993).
- (E) *Dimerization or polymerization*. This reaction is observed for thiophene radical cations. Suggested products of dimerization of 1-methylthiophene are shown in the Sect. 3.2. Thiophene radical cations can react according to dimerization and deprotonation mechanism.



- (F) *Reduction*. Radical cations of sulfides possess significant potential for oxidation of, for example, disulfides or thiols:



Different reduced organic sulfur compounds undergo different steps of radical cation transformations. The basic steps of the transformation can be traced from the products of reaction, which were outlined in Sect. 3. Thus, formation of sulfoxides and sulfones testifies to S-oxidation, polysulfides and aldehydes signify C–S bond cleavage, and oxidation at carbon adjacent to sulfur means α -C–H deprotonation or OH• radical attack. It should be noted that only initial few steps of photocatalytic oxidation can be traced for sure from detected products because the pathways of photocatalytic oxidation form a complex network that usually does not allow dependable determination of predominant route for formation of secondary or tertiary or further products.

The excited molecular photocatalyst can transfer excitation energy to another species. Singlet oxygen ¹O₂ is formed from usual triplet oxygen upon energy transfer. ¹O₂ can drive partial oxidation reactions of organic sulfur compounds. Finally, excited molecular photocatalyst with significant radical character can initiate hydrogen atom transfer from the sulfur organic compounds to the photocatalyst. Radical is formed which can further undergo various transformations – dimerization, oxidation, etc.

Rates of Degradation

Photocatalytic reactions differ principally from other types of catalytic reactions in that they involve quanta of light as a reagent. There are two major quantitative characteristics of photocatalytic reaction: rate of reaction and quantum efficiency.

While the first characteristic is defined as quantity of transformations per time unit, the latter is defined by the next formula.

$$\varphi = \frac{W}{F} 100\%,$$

where W is rate of reaction (mol/s), F is light flux entering the photocatalyst surface (mol photons/s, Einstein/s). Photocatalytic reactions usually involve more than one quantum of light to proceed from reagents to stable products. To take into account the minimum number of photons needed for the reaction, m , overall quantum efficiency is introduced:

$$\varphi_o = m \frac{W}{F} 100\%.$$

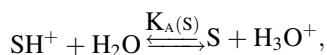
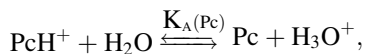
Quantum efficiency is introduced for several reasons among which are to provide estimate how efficiently light is used and to allow comparison of reactions carried out under different conditions of irradiation.

Liquid Phase Reactions

Liquid phase photocatalytic transformations of reduced organic sulfur substrates can proceed at a steady rate for a long time because catalyst deactivation usually does not occur in the liquid phase. This makes studies of kinetics in liquid phase a relatively easy task. Liquid phase reactions are carried out in batch (static) reactors. Alternatively, recirculation reactors can be used. Under high recirculation rates, such reactors are equivalent to well-stirred batch reactors.

Influence of Solution pH

Concentration of H^+ exerts strong influence on the rate of photocatalytic reactions in solutions. This effect is primarily associated with a change of adsorption equilibrium. Charges of photocatalyst molecules or particles and charges of oxidizable substrate species are directly connected with solution acidity according to acid–base equilibriums:



where $K_A(\text{Pc})$ is constant of acidity of photocatalyst Pc, $K_A(\text{S})$ is constant of acidity of substrate. At pH of solution equal to $\text{p}K_A$, half of species are in protonated state. Close approach of substrate and photocatalyst is considered as a necessary step of photocatalytic reaction.

Species with the same sign of electrical charge repel from each other. Thus, for example, in strongly acidic media both photocatalyst and substrate are protonated and positively charged. Their interaction is weak compared to neutral media, and the rate of a photocatalytic reaction is small.

For the same given photocatalyst, the influence of solution pH will depend on the nature of the substrate. For example, photocatalytic oxidation of methyl phenylsulfide is fastest at pH 8–9. The reaction rate decreases at higher and lower pH values. However, photocatalytic degradation of methyl benzimidazolylsulfide, propyl benzimidazolylsulfide, and 3-propenyl benzimidazolylsulfide has a maximum rate at pH around 6 (Habibi and Vosooghian 2005). Photocatalytic oxidation usually produced a variety of intermediate products, among which are various acids. Thus, usually solution pH decreases during photocatalytic oxidation. The initial pH is constant for only few first minutes of reaction. Therefore, the actual pH that affects the process can be strongly different from the initial pH that is reported. Another complexity of pH effect is due to the different $\text{p}K_A$ of intermediate products of photocatalytic oxidation. Acids can have lower $\text{p}K_A$ than the starting substrate and optimum pH for degradation of products can be lower than optimum pH for oxidation of the starting substrate. As an example of a substrate with complex dependence of oxidation rate on pH, we consider 2-(butylamino)ethanethiol (BAET).

Photocatalytic degradation of BAET was studied in aqueous suspension of TiO_2 Degussa P25, which is considered as the most active commercially available photocatalyst for liquid phase. Degradation was not detected if the starting solution is acidified and $\text{pH} < 9$. This is obviously associated with protonation of the secondary amino group of BAET as well as protonation of the TiO_2 surface. The natural pH of 250 mg/l BAET solution is about 9, and the maximum mineralization rate was measured at this pH. Very interesting kinetics of degradation were observed at pH 11. Total organic carbon content was constant for the first 100 min of reaction indicating that no mineralization took place during this period. Thereafter, mineralization started at a high rate so that at 250 min of reaction the same conversion of TOC was obtained as that at pH 9. While BAET molecules can undergo photocatalytic reactions at pH 11, since this molecule should be neutral, acidic products of BAET oxidation such as sulfinic and sulfonic as well as carbonic acids are negatively charged. They do not undergo further reactions until quantities of acids formed are enough to neutralize basic pH (Vorontsov et al. 2004).

Substrate Concentration Effect

Rates of liquid phase photocatalytic reactions usually increase with the increase of substrate concentration. Numerous compounds are usually present in solution

during photocatalytic oxidation because of formation of intermediate and final products. The rate of the initial compound degradation can be approximated by the following equation:

$$W = \frac{kK_S C_S}{1 + K_S C_S + \sum K_i C_i},$$

where S refers to initial substrate, and *i* refers to various species arising during degradation, *K* and *C* are the corresponding adsorption constants and concentrations. Usually values of *K_i* and *C_i* are unknown that complicates description of degradation kinetics at high conversions. At the start of reaction, only substrate S is present. Therefore, the initial rate of degradation is well described by the above equation with all products concentrations *C_i* = 0. The rate of degradation rises with the increase of substrate concentration and levels off at substrate concentration corresponding to about monolayer coverage.

Accordingly, for high initial concentration of substrate, the starting part of kinetic curve is usually linear. Later, it gains nearly exponential shape corresponding to first order. For low initial substrate concentration, the whole kinetic plot is well fitted by the first order kinetics.

Effect of Solvent

Photocatalytic reactions are in fact charge transfer reactions. In the case of TiO₂, photogenerated electrons and holes react with species situated near the TiO₂ surface with production of the corresponding reduced and oxidized product species. Reduced sulfur compounds usually have standard redox potential of cation formation lower than that of hydroxyl radical formation from water. Thus, radical cations are produced as intermediate species and they were detected experimentally for several types of sulfur organic substrates.

Solvent polarity influences energy of radical cation solvation approximately according to the following Born equation

$$\Delta G_{\text{solv}} = \frac{e^2}{2r} \left(\frac{1}{\varepsilon} - 1 \right),$$

where *r* is cation radical radius, *ε* is solvent dielectric constant, *e* is electron charge (in CGS system). Thus, in solvents with high dielectric constant, formation of cation radical is more favorable.

Correlation of rate of photocatalytic oxidation with solvent dielectric constant was observed experimentally for reactions of methyl phenylsulfide and methyl benzimidazolylsulfide over TiO₂ photocatalyst (Habibi et al. 2005). The highest rate of degradation was observed in water (*ε* = 80), and it decreased dramatically in

the following row: acetonitrile ($\epsilon = 38$), methanol ($\epsilon = 33$), ethanol ($\epsilon = 24$), carbon tetrachloride ($\epsilon = 2.2$). This is in agreement with necessity for stabilization of sulfide radical cation by solvent media.

Effect of Hydrogen Peroxide

Hydrogen peroxide is capable to react directly with organic sulfides in solutions. Dibenzothiophene conversion reached value of 54% in 8 h for 3% H_2O_2 solution in acetonitrile with initial dibenzothiophene concentration 0.5 mM. The photocatalytic oxidation of dibenzothiophene is accelerated by a factor of two if hydrogen peroxide is added. The acceleration, however, is less than the rate of direct oxidation by H_2O_2 (Matsuzawa et al. 2002). Therefore, additions of hydrogen peroxide are not efficient for photocatalytic oxidation of organic sulfur compounds in liquid phase.

Gas Phase Reactions

Gas phase reactions of sulfur compounds at ambient conditions inevitably lead to catalyst deactivation. However, kinetic features of oxidation process can be traced during the time before deactivation. The effect of reaction conditions on deactivation and reactivation behavior is reported in the next subchapter.

Substrate Concentration Effect

Influence of the concentration of compound to be oxidized is traditionally described by the single site Langmuir–Hinshelwood model.

$$W = \frac{kKC}{1 + KC},$$

where W is rate of reaction, k is reaction rate constant, K is substrate adsorption constant, C is concentration of substrate. Usually good fit of experimental data to equation 22 is obtained, especially if relatively narrow substrate concentration range is used. Linear form of the Langmuir–Hinshelwood equation can be used for checking on its validity.

At low concentrations of gas phase substrate, the rate of degradation often demonstrates first order with respect to substrate concentration. This is in agreement with Langmuir–Hinshelwood equation for the case of surface coverage much below monolayer, i.e., $KC \ll 1$.

Air Humidity Effect

The influence of air humidity is rarely reported for photocatalytic oxidation of gaseous reduced organic sulfur compounds.

Photocatalytic oxidation of methylmercaptan CH_3SH was reported to have maximum rate at a relative air humidity of 43% (Li et al. 2006a, b). At lower and higher humidity levels, the CH_3SH conversion observed was lower. Methylmercaptan is a weak acid ($\text{p}K_{\text{A}} = 10.3$). Moderate amounts of adsorbed water can be expected to dissolve this substrate and increase thereby its availability for surface photocatalytic reactions. Another aspect of water effect can be associated with surface dissolution of reaction products. Sulfinic, sulfonic, and sulfuric acids can be displaced from surface sites into polylayers of adsorbed water freeing thereby sites for photocatalytic reaction.

Temperature Effect

Rise of temperature usually results in an increase of oxidation rate. In photocatalytic oxidation of ethanethiol, temperature increase from 100 to 180°C resulted in the rise of reaction rate constant from 0.4 to 5.0 $\text{mmol m}^{-3} \text{s}^{-1}$, while adsorption constant of single site Langmuir–Hinshelwood model used decreased from 371 to 24 $\text{m}^3 \text{mol}^{-1}$. The opposite effect of the rate constant and adsorption constant allowed only a small growth of ethanethiol conversion rate with rise of temperature. The obtained apparent activation energy is equal to 42 kJ mol^{-1} , whereas entropy of adsorption is estimated as $-70 \text{ J mol}^{-1} \text{ K}^{-1}$ and enthalpy of adsorption is equal to -45 kJ mol^{-1} (Kachina et al. 2006).

Catalyst Deactivation and Reactivation

Liquid Phase Reactions

In very many instances deactivation of photocatalyst is not observed for liquid phase photocatalytic reactions. Products of reaction can be efficiently removed from photocatalyst surface to solution. A decrease in activity for the first run was reported for oxidation of dodecylbenzenesulfonic acid and activity stayed constant for further runs (Dominguez et al. 1998).

Photocatalytic reactions of some organic substrates indeed can result in catalyst deactivation. Products of such reactions are not soluble in solvent used. One example is destruction of pesticide vapam® in aqueous TiO_2 slurry (Table 25.3). Deposition of sulfur was observed by XPS analysis of photocatalyst after destruction. Changes in surface of photocatalyst are considered to be responsible for gradual decrease of catalytic activity in five consecutive runs of vapam® destruction (Vidal and Luengo 2001).

Gas Phase Reactions

Photocatalyst deactivation is commonly observed in degradation of gas phase sulfur compounds over solid photocatalysts. The final product of sulfur atoms oxidation over band-gap-irradiated TiO₂ was determined to be sulfuric acid. Being nonvolatile under ambient conditions, this product accumulates over the photocatalyst surface and blocks active sites. Accumulation of intermediate products of oxidation should also be considered as contribution to catalyst deactivation.

The onset of catalyst deactivation is characterized by a decrease of the CO₂ generation rate. Intermediate products of oxidation appear in a larger concentration in the gas phase. Complete catalyst deactivation is signified by complete loss of conversion. Catalyst deactivation was experimentally observed for diethyl sulfide, dimethyl sulfide, 2-chloroethyl ethylsulfide, and other compounds.

Deactivation of TiO₂ surface during diethyl sulfide (DES) photocatalytic oxidation was studied in relatively good detail from parametric and mechanistic points of view.

The available catalyst surface area was found to be the determining factor for the quantity of diethyl sulfide converted before catalyst deactivation. A growth of the TiO₂ catalyst surface area in a row 50, 75, 120, and 340 m²/g steadily resulted in an increase of the quantity of DES consumed, with the catalyst mass being constant. Alternatively, increase of the mass of TiO₂ catalyst in a reactor from 180 to 330 mg resulted in increase of DES quantity converted before deactivation from 5 to 6.5 μmol/m².

Water vapor content can exert significant and opposite influence on DES and dimethyl sulfide photocatalytic oxidation. Generally, water displaces other species from the photocatalyst surface sites. In the case of heavy load of the photocatalyst surface with organic material, water can help to drive oxidation by freeing some sites for adsorption of oxygen. Multilayers of water can dissolve such excessive material. If quantities of adsorbed molecules to be destroyed are low, water molecules decelerate oxidation by excessive removing of adsorbed species. These tendencies are observed for DES oxidation. Before catalyst deactivation develops, water vapor content rising from 1,900 to 22,000 ppm produces pronounced negative effect on catalyst stability. After catalyst deactivation starts, complete mineralization into inorganic products actually ceases. In this case, a water vapor content increase results in an increase of DES conversion. Very dry air always has a negative effect on oxidation rates because water is important for efficient separation of photogenerated charges in TiO₂.

Concentration of DES in a reactor feed also influences conversion reached before catalyst deactivates. Quantity of DES converted before deactivation develops rises from 6.5 to 13.7 μmol/m² when feed concentration decreased from 350 to 87 ppm. This interesting phenomenon is attributable to a more balanced course of reaction at low DES concentrations. Complete oxidation product, sulfuric acid, has more time to diffuse to nonirradiated parts of photocatalyst. Partial oxidation products are formed in smaller quantities at a lower DES concentration leaving more surface sites available for sulfuric acid. At a high DES concentration, the process of complete oxidation is retarded; partial oxidation prevails.

This behavior is easy to observe in a static (batch) gas phase reactor. There is an induction period before carbon dioxide starts evolving at a higher rate in DES oxidation. After DES concentration falls to a low value, an active CO₂ generation begins. Catalyst deactivated to a higher degree shows a longer induction period. In fact, DES and diethyl disulfide possess lower ionization potential (8.4 eV) than any other intermediate products of DES oxidation. Photogenerated holes in TiO₂ therefore will predominantly react with DES and DEDES, rather than with any other substance over TiO₂ surface. According to this theory, oxidation of other partial oxidation products can proceed only after DES and DEDES are oxidized.

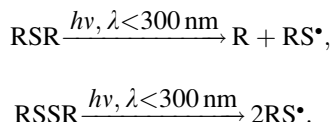
Deactivated photocatalysts can usually be regenerated by some reactivation procedure. Several types of reactivation methods have been tested.

- (A) Prolonged UV irradiation of deactivated photocatalyst in humidified air. This procedure delivers only partial reactivation: conversion of DES was only 1.6 $\mu\text{mol}/\text{m}^2$ as compared to conversion of 5 $\mu\text{mol}/\text{m}^2$ before deactivation.
- (B) UV irradiation of deactivated photocatalyst in humidified air until CO₂ evolution stops, followed by washing with water. This method results in almost complete reactivation: conversion of DES was 4 $\mu\text{mol}/\text{m}^2$ over reactivated photocatalyst. A disadvantage of this procedure is the long time required for irradiation. On the positive end, the wash water contains only sulfuric acid.
- (C) Washing with water. This is a fast reactivation procedure which delivers almost complete reactivation: conversion of DES was 3.9 $\mu\text{mol}/\text{m}^2$ over reactivated photocatalyst. However, wash water contains significant amounts of partial oxidation products along with sulfuric acid. Such water requires additional oxidation treatment before disposal.
- (D) Heat treatment. Heating deactivated photocatalyst at 124°C resulted in recovery of only 1/3 activity of the initial catalyst. This is equivalent to result of procedure (A). Indeed, such heat treatment would remove some volatile partial oxidation products leaving H₂SO₄ and sulfonic acids intact.

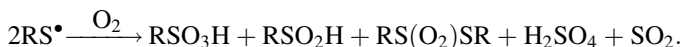
Thus, among the different reactivation procedures, washing with water produced the best results. However, some portion of initial activity could not be recovered. This can be associated with the fact that concentrated sulfuric acid is known to dissolve titanium dioxide. It is believed that H₂SO₄ etches TiO₂ surface in sulfides oxidation as well. Infrared spectroscopy showed that bidentate sulfate species are present in TiO₂ after reactivation by thorough wash with water. This indicates irreversible changes of TiO₂ surface develop during deactivation.

Role of Photochemical Reactions

Organic sulfur compounds are known to undergo photochemical degradation and oxidation even in the absence of any photosensitizer or photocatalyst. Absorption of a quantum of ultraviolet light by *sulfides and disulfides* is considered to produce cleavage of a C–S or S–S bond (Robert-Banchereau et al. 1997).



Thiyl radicals RS^\bullet formed react with oxygen molecules to produce thiylperoxyl radicals RSO_2^\bullet that give rise to a wide variety of photolytic products. The main sulfur-containing products detected in various solvents for photolysis of sulfides and disulfides are represented in the next reaction (Robert-Banchereau et al. 1997).



It is notable that products of purely photochemical reactions of sulfides and disulfides generally resemble products of their photocatalytic reactions. This implies the resemblance of their mechanisms.

Photocatalytic reactions are often carried out with mercury lamps as the light source. Low pressure mercury lamps emit mainly at 254 nm, whereas medium pressure mercury lamps emit at 254, 365 and many other bands. Photocatalysis over TiO_2 requires wavelengths shorter than 400 nm; direct photolysis of sulfur compounds can proceed under irradiation of 254 nm band of mercury lamps. For medium pressure mercury lamps, the band 365 nm has the highest intensity among other UV bands. Therefore, with equal quantum efficiencies for photocatalysis and photolysis, the rate of photocatalytic reaction should be higher under irradiation of a medium pressure Hg lamp. In fact, this is not always the case.

In particular, it was found that 2-phenethyl-2-chloroethylsulfide (PECES) undergoes photolysis as well as photocatalytic destruction under irradiation of medium pressure mercury lamp in aqueous TiO_2 suspension. PECES takes part in hydrolysis with dissolution. Both PECES and the product of its hydrolysis, 2-phenethyl-2-hydroxyethylsulfide, are transformed into inorganic compounds under irradiation. Simultaneous photolysis and photocatalysis under the full light of the Hg lamp lead to complete destruction in 250 min. If harsh ultraviolet light with $\lambda < 300$ nm is removed by pyrex filter, complete degradation finishes in more than 600 min. Direct photolysis at these wavelengths did not proceed. Thus, direct photolysis of PECES is much more efficient for its mineralization than photocatalysis (Vorontsov et al. 2002a).

Direct photolysis was suggested as a possible decontamination technique. Irradiation of sulfur mustard vapors or droplets resulted in their chemical transformations. Vapor phase photolysis produced nonvolatile products that deposited onto reactor walls. Major identified products included bis(2-chloroethyl)disulfide and bis(2-chloroethyl)sulfoxide. Besides, a kind of polymer containing $-\text{SCH}_2\text{CH}_2\text{Cl}$ and $-\text{OCH}_2\text{CH}_2\text{Cl}$ groups is suggested as one of the main products (Zuo et al. 2005a). High toxicity of sulfur mustard is caused by the presence of $\text{SCH}_2\text{CH}_2\text{Cl}$ moiety which readily alkylates skin proteins causing severe blisters. Since photolysis does not remove these groups efficiently, it cannot be considered as an

effective decontamination method. Formation of disulfide as one of the main products suggests that sulfur-carbon bond cleavage is again the major primary photochemical process.

Destruction of gaseous sulfur organic compounds in air under the light of germicidal mercury lamp can possibly proceed also due to reactions with ozone molecules which are generated under irradiation from oxygen molecules of air. Methylmercaptane (CH_3SH) was observed to be effectively removed from air during irradiation of 254 nm, whereas no degradation was detected for irradiation of 365 nm (Li et al. 2006a, b). CH_3SH has two absorption bands at 230 and 205 nm, both situated far from main lamp emission band. Thus, the input of both direct photolysis and reactions with O_3 cannot be excluded.

Heteroatomic organic sulfur compounds are also subject to direct photolysis. Photolysis of phosphorothioates was reported to proceed slower than photocatalytic degradation and with formation of different set of intermediate products (Kormali et al. 2004). Direct photolysis of insecticides fenitrothion and methyl-parathion (monothiophosphates) produced the corresponding oxons and nitrophenols with quantum yield 0.3% (Weber et al. 2009). These products are similar to products of photocatalytic oxidation.

A chemical warfare agent, VX, was subjected to photolysis study in liquid state. VX has absorption bands in the region of wavelengths around 230 nm. Germicidal lamp irradiation gave rise to a variety of products that resided in liquid phase or moved into gas phase (Zuo et al. 2005b). The major detected products comprise diisopropylaminoethylthiol, thioethylethylmethylphosphonate, and other compounds containing P-S bond. The composition of products implies that several types of chemical bonds are cleaved in primary photochemical reactions, namely P-S, S-C, and C-N. Isomerization reactions also proceed with participation of initial VX as well as products of its photochemical transformations.

The data considered in this chapter show that direct photolysis should always be kept in mind when dealing with photocatalytic transformations of organic sulfur compounds.

Conclusions

Reduced organic sulfur compounds undergo diverse steps of photocatalytic oxidation that can be well described by applying chemistry of sulfur radical cations, singlet oxygen, and radicals. However, the presence of the photocatalyst can significantly change the pathways of transformations. Complete mineralization to innocuous products and inorganic precipitates can be achieved by selecting the appropriate operating conditions.

Acknowledgments We acknowledge the NATO Science for Peace Programme support via projects 974209 and 981461 and ISTC funding via project 3305.

References

- Abdel-Wahab AA, Gaber AEM (1998) TiO₂-photocatalytic oxidation of selected heterocyclic sulfur compounds. *J Photochem Photobiol A* 114:213–218
- Adam W, Arguello JE, Penenory AB (1998) Photochemical electron-transfer reactions between sulfides and tetranitromethane. Oxidation vs fragmentation of the sulfide radical-cation intermediate. *J Org Chem* 63:3905–3910
- Alfassi ZB (ed) (1997) Peroxyl radicals. Wiley, New York
- Ando W, Nagashima T, Saito K, Kohmoto S (1979) Dye- and dicyanoanthracene-photosensitized oxygenations of sulphur compounds. Product selectivity. *J Chem Soc Chem Commun* 154–156
- Baciocchi E, Crescenzi C, Lanzalunga O (1997a) Photoinduced electron transfer reactions of benzyl phenyl sulfides promoted by 9, 10-dicyanoanthracene. *Tetrahedron* 53:4469–4478
- Baciocchi E, Giacco TD, Ferrero MI, Rol C, Sebastiani GV (1997b) Oxidation of aromatic sulfides photosensitized by TiO₂ in CH₃CN in the presence of Ag₂SO₄. The role of TiO₂ in the chemistry of sulfide radical cations. *J Org Chem* 62:4015–4017
- Baciocchi E, Giacco TD, Elisei F, Gerini MF, Guerra M, Lapi A, Liberali P (2003) Electron transfer and singlet oxygen mechanisms in the photooxygenation of dibutyl sulfide and thioanisole in MeCN sensitized by *N*-methylquinolinium tetrafluoroborate and 9, 10-dicyanoanthracene. The probable involvement of a thiadioxirane intermediate in electron transfer photooxygenations. *J Am Chem Soc* 125:16444–16454
- Borio O, Gawlik BM, Bellobono IR, Muntau H (1998) Photooxidation of prometryn and prometon in aqueous solution by hydrogen peroxide on photocatalytic membranes immobilising titanium dioxide. *Chemosphere* 37:975–989
- Brewer SA, Perdomo Artilles C, Taylor JA, Dennis M (2010) Photosensitive dyes and self-detoxifying textiles: degradation products and dye durability. *Appl Surf Sci* 256:1908–1912
- Buxton GV, Greenstock CL, Helman WP, Ross AB (1988) Critical review of rate constants for reactions of hydrated electrons, hydrogen atoms and hydroxyl radicals (OH/O⁻) in aqueous solution. *J Phys Chem Ref Data* 17:513–817
- Canela MR, Alberici RM, Jardim WF (1998) Gas-phase destruction of H₂S using TiO₂/UV–VIS. *J Photochem Photobiol A* 112:73–80
- Canela MC, Alberici RM, Sofia RCR, Eberlin MN, Jardim WF (1999) Destruction of malodorous compounds using heterogeneous photocatalysis. *Environ Sci Technol* 33:2788–2792
- Chambers RC, Hill CL (1990) Redox catalysis involving substrate photooxidation with catalyst regeneration by substrate reduction. Simultaneous oxidative C–H bond cleavage and reductive C–S bond cleavage in thioethers catalyzed by W₁₀O₃₂⁴⁻. *J Am Chem Soc* 112:8427–8433
- Cojocar B, Neatu S, Parvulescu VI, Somoghi V, Petrea N, Epure G, Alvaro M, Garcia H (2009) Synergism of activated carbon and undoped and nitrogen-doped TiO₂ in the photocatalytic degradation of the chemical warfare agents soman, VX, and yperite. *ChemSusChem* 2:427–436
- Davidson RS, Pratt JE (1983) The titanium dioxide sensitized photo-oxidation of sulphides. *Tetrahedron Lett* 52:5903–5906
- Demeestere K, Dewulf J, Witte BD, Langenhove HV (2005a) Titanium dioxide mediated heterogeneous photocatalytic degradation of gaseous dimethyl sulfide: Parameter study and reaction pathways. *Appl Catal B* 60:93–106
- Demeestere K, Dewulf J, Ohno T, Salgado PH, Langenhove HV (2005b) Visible light mediated photocatalytic degradation of gaseous trichloroethylene and dimethyl sulfide on modified titanium dioxide. *Appl Catal B* 61:140–149
- Dominguez C, Garcia J, Pedraz MA, Torres AA, Galan MA (1998) Photocatalytic oxidation of organic pollutants in water. *Catal Today* 40:85–101
- Doong R, Chang W (1998) Photodegradation of parathion in aqueous titanium dioxide and zero valent iron solutions in the presence of hydrogen peroxide. *J Photochem Photobiol A Chem* 116:221–228

- Fox MA, Abdel-Wahab AA (1990) Selectivity of the TiO₂-mediated photocatalytic oxidation of thioethers. *Tetrahedron Lett* 31:4533–4536
- Fox MA, Kim Y-S, Abdel-Wahab AA (1990) Photocatalytic decontamination of sulfur-containing alkyl halides on irradiated semiconductor suspensions. *Catal Lett* 5:369–376
- Glass RS (1999) Sulfur radical cations. *Top Curr Chem* 205:1–87
- Haarstrick A, Kut OM, Heinzle E (1996) TiO₂-assisted degradation of environmentally relevant organic compounds in wastewater using a novel fluidized bed photoreactor. *Environ Sci Technol* 30:817–824
- Habibi MH, Vosoughian H (2005) Photocatalytic degradation of some organic sulfides as environmental pollutants using titanium dioxide suspension. *J Photochem Photobiol A Chem* 174:45–52
- Habibi MH, Tangestaninejad S, Yadollahi B (2001) Photocatalytic mineralization of mercaptans as environmental pollutants in aquatic system using TiO₂ suspension. *Appl Catal B Environ* 33:57–63
- Han ST, Zhang GY, Xi HL, Xu DN, Fu XZ, Wang XX (2008) Sulfated TiO₂ decontaminate 2-CEES and DMMP in vapor phase. *Catal Lett* 122:106–110
- Hirakawa T, Mera N, Sano T, Negishi N, Takeuchi K (2009) Decontamination of chemical warfare agents by photocatalysis. *Yakugaku Zasshi* 129:71–92
- Hynes AJ, Wine PH, Semmes DH (1986) Kinetics and mechanism of OH reactions with organic sulfides. *J Phys Chem* 90:4148–4156
- Jo WK, Shin MH (2010) Applicability of a continuous-flow system inner-coated with S-doped titania for the photocatalysis of dimethyl sulfide at low concentrations. *J Environ Manage* 91:2059–2065
- Kachina A, Preis S, Kallas J (2006) Catalytic TiO₂ oxidation of ethanethiol for environmentally benign air pollution control of sulfur compounds. *Environ Chem Lett* 4:107–110
- Kato S, Hirano Y, Iwata M, Sano T, Takeuchi K, Matsuzawa S (2005) Photocatalytic degradation of gaseous sulfur compounds by silver-deposited titanium dioxide. *Appl Catal B* 57:109–115
- Katsumata H, Okada T, Kaneco S, Suzuki T, Ohta K (2010) Degradation of fenitrothion by ultrasound/ferrioxalate/UV system. *Ultrason Sonochem* 17:200–206
- Kerzhentsev M, Guillard C, Herrmann JM, Pichat P (1996) Photocatalytic pollutant removal in water at room temperature: case study of the total degradation of the insecticide fenitrothion (phosphorothioic acid O, *O*-dimethyl-*O*-(3-methyl-4-nitrophenyl) ester). *Catal Today* 27:215–220
- Konstantinou IK, Sakellarides TM, Sakkas VA, Albanis TA (2001) Photocatalytic degradation of selected *s*-triazine herbicides and organophosphorus insecticides over aqueous TiO₂ suspensions. *Environ Sci Technol* 35:398–405
- Kormali P, Dimoticali D, Tsipi D, Hiskia A, Papaconstantinou E (2004) Photolytic and photocatalytic decomposition of fenitrothion by PW₁₂O₄₀³⁻ and TiO₂: a comparative study. *Appl Catal B Environ* 48:175–183
- Kozlov DV, Vorontsov AV, Smirniotis PG, Savinov EN (2003) Gas-phase photocatalytic oxidation of diethyl sulfide over TiO₂: kinetic investigations and catalyst deactivation. *Appl Catal B* 42:77–87
- Kralj MB, Cernigoj U, Franko M, Trebse P (2007) Comparison of photocatalysis and photolysis of malathion, isomalathion, malaaxon, and commercial malathion – products and toxicity studies. *Water Res* 41:4504–4514
- Lacombe S, Cardy H, Simon M, Khoukh A, Soumillion JP, Ayadim M (2002) Oxidation of sulfides and disulfides under electron transfer or singlet oxygen photosensitization using soluble or grafted sensitizers. *Photochem Photobiol Sci* 1:347–354
- Latour V, Pigot T, Mocho P, Blanc S, Lacombe S (2005) Supported photosensitizers as new efficient materials for gas-phase photo-oxidation. *Catal Today* 101:359–367
- Li FB, Li XZ, Hou MF (2004) Photocatalytic degradation of 2-mercaptobenzothiazole in aqueous La³⁺-TiO₂ suspension for odor control. *Appl Catal B Environ* 48:185–194

- Li XZ, Hou MF, Li FB, Chua H (2006a) Photocatalytic oxidation of methyl mercaptan in foul gas for odor control. *Ind Eng Chem Res* 45:487–494
- Li FB, Li XZ, Ng KH (2006b) Photocatalytic degradation of an odorous pollutant: 2-mercapto-benzothiazole in aqueous suspension using Nd^{3+} - TiO_2 catalysts. *Ind Eng Chem Res* 45:1–7
- Li W, Gandra N, Courtney SN, Gao R (2009) Singlet oxygen production upon two-photon excitation of TiO_2 in chloroform. *Chemphyschem* 10:1789–1793
- Malato S, Blanco J, Richter C, Maldonado MI (2000) Optimization of pre-industrial solar photocatalytic mineralization of commercial pesticides. *Appl Catal B Environ* 25:31–38
- Martyanov IN, Klabunde KJ (2003) Photocatalytic oxidation of gaseous 2-chloroethyl ethyl sulfide over TiO_2 . *Environ Sci Technol* 37:3448–3453
- Matsuzawa S, Tanaka J, Sato S, Ibusuki T (2002) Photocatalytic oxidation of dibenzothiophenes in acetonitrile using TiO_2 : effect of hydrogen peroxide and ultrasound irradiation. *J Photochem Photobiol A* 149:183–189
- Mattsson A, Lejon C, Stengl V, Bakardjieva S, Oplustil F, Andersson PO, Osterlund L (2009) Photodegradation of DMMP and CEES on zirconium doped titania nanoparticles. *Appl Catal B Environ* 92:401–410
- Mc Lafferty FW, Turecek F (1993) Interpretation of mass spectra. University Science Book, Sausalito, CA
- Mei H, Mei BW, Yen TF (2003) A new method for obtaining ultra-low sulfur diesel fuel via ultrasound assisted oxidative desulfurization. *Fuel* 82:405–414
- Murray RW, Jindal SL (1972) Photosensitized oxidation of dialkyl disulfides. *J Org Chem* 37:3516–3520
- Neatu S, Parvulescu VI, Epure G, Petrea N, Somoghi V, Ricchiardi G, Bordiga S, Zecchina A (2009) M/ TiO_2 / SiO_2 (M=Fe, Mn, and V) catalysts in photo-decomposition of sulfur mustard. *Appl Catal B Environ* 91:546–553
- Neatu S, Cojocaru B, Parvulescu VI, Somoghi V, Alvaro M, Garcia H (2010) Visible-light C-heteroatom bond cleavage and detoxification of chemical warfare agents using titania-supported gold nanoparticles as photocatalyst. *J Mater Chem* 20:4050–4054
- Oller I, Gernjak W, Maldonado MI, Fernandez-Ibanez P, Blanco J, Sanchez-Perez JA, Malato S (2005) Degradation of the insecticide dimethoate by solar photocatalysis at pilot plant scale. *Environ Chem Lett* 3:118–121
- Panayotov DA, Paul DK, Yates JT (2003) Photocatalytic oxidation of 2-chloroethyl ethyl sulfide on TiO_2 - SiO_2 powders. *J Phys Chem B* 107:10571–10575
- Panayotov D, Kondratyuk P, Yates JT (2004) Photooxidation of a mustard gas simulant over TiO_2 - SiO_2 mixed-oxide photocatalyst: site poisoning by oxidation products and reactivation. *Langmuir* 20:3674–3678
- Peral J, Ollis DF (1997) TiO_2 photocatalyst deactivation by gas-phase oxidation of heteroatom organics. *J Mol Catal A Chem* 115:347–354
- Rachel A, Sarakha M, Subrahmanyam M, Boule P (2002) Comparison of several titanium dioxides for the photocatalytic degradation of benzenesulfonic acids. *Appl Catal B Environ* 37:293–300
- Robert-Banchereau E, Lacombe SA, Ollivier J (1997) Unsensitized photooxidation of sulfur compounds with molecular oxygen in solution. *Tetrahedron* 53:2087–2102
- Robertson J, Bandosz TJ (2006) Photooxidation of dibenzothiophene on TiO_2 /hectorite thin films layered catalyst. *J Colloid Interface Sci* 299:125–135
- Seto Y (2009) Decontamination of chemical and biological warfare agents. *Yakugaku Zasshi* 129:53–69
- Soggiu N, Cardy H, Jivan JLH, Leray I, Soumillion JP, Lacombe S (1999) Organic sulfides photooxidation using sensitizers covalently grafted on silica: towards a more efficient and selective solar photochemistry. *J Photochem Photobiol A* 124:1–8
- Sokmen M, Allen DW, Hewson AT, Clench MR (2001) Photocatalytic oxidative degradation of 2-methylthiophene in suspensions of TiO_2 : identification of intermediates and degradation pathways. *J Photochem Photobiol A* 141:63–67

- Somasundaram N, Srinivasan C (1998) Oxidation of aryl methyl sulfides and sulfoxides on irradiated TiO₂. *J Photochem Photobiol A* 115:169–173
- Tachikawa T, Tojo S, Fujitsuka M, Majima T (2003) One-electron oxidation of aromatic sulfides adsorbed on the surface of TiO₂ particles studied by time-resolved diffuse reflectance spectroscopy. *Chem Phys Lett* 382:618–625
- Tachikawa T, Tojo S, Fujitsuka M, Majima T (2006) One-electron oxidation pathways during β -cyclodextrin-modified TiO₂ photocatalytic reactions. *Chem Eur J* 12:7585–7594
- Thompson TL, Panayotov DA, Yates JT, Martyanov I, Klabunde K (2004) Photodecomposition of adsorbed 2-chloroethyl ethyl sulfide on TiO₂: involvement of lattice oxygen. *J Phys Chem B* 108:17857–17865
- Topalov A, Molnar-Gabor D, Abramovic B, Korom S, Pericin D (2003) Photocatalytic removal of the insecticide fenitrothion from water sensitized with TiO₂. *J Photochem Photobiol A Chem* 160:195–201
- Vidal A, Luengo MAM (2001) Inactivation of titanium dioxide by sulphur: photocatalytic degradation of Vapam®. *Appl Catal B Environ* 32:1–9
- Vorontsov AV, Savinov EN, Davydov L, Smirniotis PG (2001) Photocatalytic destruction of gaseous diethyl sulfide over TiO₂. *Appl Catal B* 32:11–24
- Vorontsov AV, Panchenko AA, Savinov EN, Lion C, Smirniotis PG (2002a) Photocatalytic degradation of 2-phenethyl-2-chloroethyl sulfide in liquid and gas phases. *Environ Sci Technol* 36:5261–5269
- Vorontsov AV, Davydov L, Reddy EP, Lion C, Savinov EN, Smirniotis PG (2002b) Routes of photocatalytic destruction of chemical warfare agents simulants. *New J Chem* 26:732–744
- Vorontsov AV, Savinov EN, Lion C, Smirniotis PG (2003a) TiO₂ reactivation in photocatalytic destruction of gaseous diethyl sulfide in a coil reactor. *Appl Catal B* 44:25–40
- Vorontsov AV, Lion C, Savinov EN, Smirniotis PG (2003b) Pathways of photocatalytic gas phase destruction of HD stimulant 2-chloroethyl ethyl sulfide. *J Catal* 220:414–423
- Vorontsov AV, Chen Y-C, Smirniotis PG (2004) Photocatalytic oxidation of VX simulant 2-(butylamino)ethanethiol. *J Hazard Mater B* 113:89–95
- Vorontsov AV, Charvy C, Lion C (2005) Photocatalytic destruction of a thiosulfonate. *Top Catal* 35:245–253
- Vosooghian H, Habibi MH (2007) Photooxidation of some organic sulfides under UV light irradiation using titanium dioxide photocatalyst. *Int J Hydrogen Energy* 89759
- Wardman P (1989) Reduction potentials of one-electron couples involving free radicals in aqueous solution. *J Phys Chem Ref Data* 18:1637–1755
- Weber J, Kurkova R, Klanova J, Klan P, Halsall CJ (2009) Photolytic degradation of methylparathion and fenitrothion in ice and water: implications for cold environments. *Environ Pollut* 157:3308–3313
- Zuo GM, Cheng ZX, Li GW, Wang LY, Miao T (2005a) Photoassisted reaction of sulfur mustard under UV light irradiation. *Environ Sci Technol* 39:8742–8746
- Zuo GM, Cheng ZX, Li GW, Wang LY, Chen H (2005b) Photoassisted reaction of chemical warfare agent VX droplets under UV light irradiation. *J Phys Chem A* 109:6912–6918

Chapter 26

TiO₂-Based Photocatalysis for Organic Synthesis

Vincenzo Augugliaro, Tullio Caronna, Agatino Di Paola, Giuseppe Marci, Mario Pagliaro, Giovanni Palmisano, and Leonardo Palmisano

Abstract A major aim of the contemporary chemistry is to replace old environmentally hazardous processes with new, energy efficient routes allowing to reduce or totally avoid the use and production of harmful chemicals and to maximise the quantity of raw material that ends up in the final product. This chapter gives an account of TiO₂-based selective photocatalysis as a green synthetic tool for the production of organics. Some case studies of the most common transformations carried out by means of photocatalytic reactions are illustrated in a midway perspective between photochemistry and organic chemistry.

1 Introduction

Heterogeneous photocatalysis by using semiconductor materials is an unconventional technology that has been mainly applied to degrade organic and inorganic pollutants both in vapor and liquid phases (Schiavello 1988; Hoffmann et al. 1995; Linsebigler et al. 1995; Fujishima et al. 2000; Herrmann 1995).

Its main advantages consist not only in the mild conditions under which the process is carried out (typically room temperature and pressure), but also in the possibility to abate refractory, very toxic and non-biodegradable molecules. Many semiconductors have been tested as photocatalysts, but it is generally accepted that TiO₂, due to its low cost and high activity and stability under irradiation, is the most reliable material.

Applications of heterogeneous photocatalysis as a synthetic route have also been tested, but they are less common because the photocatalytic reactions have always

L. Palmisano (✉)

“Schiavello-Grillone” Photocatalysis Group, Dipartimento di Ingegneria Chimica dei Processi e dei Materiali, Università degli Studi di Palermo, Viale delle Scienze, 90128 Palermo, Italy
e-mail: palmisano@dicpm.unipa.it

been considered as highly unselective processes, especially when they take place in water. Nevertheless, many selective reactions were carried out by employing not only titanium dioxide, but also other semiconductors and silica (Fox 1983; Yoshida et al. 1999; Kisch 2001; Palmisano et al. 2007b). Moreover, several irradiated organic species are able to promote electron exchange processes catalyzing different organic syntheses with considerable selectivities (Maldotti et al. 2002).

Yet, the stringent environmental limitations for chemical processes are driving the researchers to find new green syntheses performed in solvent-free reactors or in green solvents, as water or supercritical CO₂, and to avoid the use of heavy metals as catalysts, since they have a high environmental impact. Synthetic organic chemistry is also evolving along this route, and it has recently been discovered that in many cases both water-soluble and water-insoluble molecules can react faster in water compared to traditional organic solvent (Li and Chen 2006; Narayan et al. 2005; Jacobson et al. 1999; Das et al. 2004; Rafelt and Clark 2000).

2 Photocatalysts

Semiconductor photocatalysts have been mainly used in powdered form. Yet, their heterogenization over a solid support is desirable since preventing a separation step after that the reaction took place is of primary significance in industrial applications. TiO₂ exists in three different crystalline modifications (anatase, rutile and brookite). Anatase is widely considered the most active phase, rutile is thermodynamically the most stable phase, whereas brookite has been rarely employed because is rather difficult to be prepared.

Both commercial and home-prepared TiO₂ samples have been used for photocatalytic syntheses. Commercial Degussa P25 is by far the most used material.

The yield and selectivity of the organic products can be strongly influenced by the crystal polymorph form and size of the TiO₂ particles. Degussa P25 is for instance a mixture of ca. 80% anatase and 20% rutile with an average particle size of 30 nm and a specific surface area of ca. 50 m² g⁻¹. Recently, poorly crystalline TiO₂ catalysts revealed more selective for partial oxidation reactions (Palmisano et al. 2007c) than commercial crystalline samples, due probably to their lowest oxidizing power.

Home-made TiO₂ has usually been prepared by sol-gel techniques using Ti alkoxides or TiCl₄ solutions. The TiO₂ surface was modified by impregnation with aqueous salt solutions or by metallization with noble metals, such as Ag, Pd, Ru or Pt. TiO₂ was anchored onto Vycor glass by reaction between surface OH groups of Vycor and TiCl₄ (Anpo and Chiba 1992). Highly dispersed TiO₂ catalysts were prepared within zeolite cavities (Yamashita et al. 1998). TiO₂ pillars incorporated between silicate layers of nanometre size (Yoneyama et al. 1989) exhibited shape selectivity because of the hydrophobic nature of pillared clay (Shimizu et al. 2002).

Supported TiO₂ was prepared via different methods: dip or spin coating, evaporation techniques and flame aerosol processes. TiO₂ thin films have been applied, for instance, in the synthesis of alcohols and ketones from hydrocarbons (Sahle-Demessie et al. 1999). Self-standing transparent silica thin films containing TiO₂ were synthesized for the photocatalytic reduction of CO₂ (Ikeue et al. 2002; Shioya et al. 2003).

3 Oxidations

Industrial processes for oxidation reactions are generally conducted at high temperature and pressure, using heavy metals (e.g., Cr and Mn salts or V₂O₅) or moisture-sensitive oxidants (Li and Chen 2006; Narayan et al. 2005; Jacobson et al. 1999; Das et al. 2004; Rafelt and Clark 2000). In our times, the use of clean primary oxidants, harmless catalysts and solar light as a free green photons source is strongly recommended by the scientific community and the international public opinion.

Photooxidation is, by far, the most frequent reaction class that involves organic substrates. When water is used as the solvent, the complete mineralization of the organic compound usually prevails due to the presence of highly oxidizing hydroxyl radicals. Instead, in non-aqueous solutions, it is usual to obtain rather high chemical yields of oxidation products, although sometimes with very low quantum yields/efficiencies. Most of the photooxidations have concerned aliphatic and aromatic alkanes and alkenes derivatives, and particular attention has been devoted to the selective oxidation of alcohols to carbonyls.

3.1 *Hydrocarbons Oxidation*

The conversion of relatively inexpensive substrates, such as alkanes, into highly desirable products, as alcohols, ketones, aldehydes and carboxylic acids is of great significance to the chemical industry. Photocatalysis was reported to be an alternative technology to produce the above mentioned products since it usually does not employ highly polluting transition metal complexes as the most part of industrial processes do.

Earliest studies (Mozzanega et al. 1977; Fujihira et al. 1981; Fox et al. 1990) showed that toluene derivatives can be oxidized to aldehydes in the gas phase, while hydroxylation or coupling reactions occur in aqueous TiO₂ suspensions (see Fig. 1).

Toluene was oxidized by using liquid organic oxygenated dispersions of pure or Fe-doped TiO₂ (Navio et al. 1996). The main products were benzyl alcohol, benzaldehyde and benzoic acid, together with some coupling products and traces of cresols. It is worth nothing that the same compounds were detected during toluene degradation carried out in water solution (Marcì et al. 2003).

The photooxidation of toluene has been carried out also in gas-solid regime by using as catalyst polycrystalline anatase TiO₂ (Augugliaro et al. 1999). The reacting gaseous mixture was toluene, air and water in various molar ratios. The main

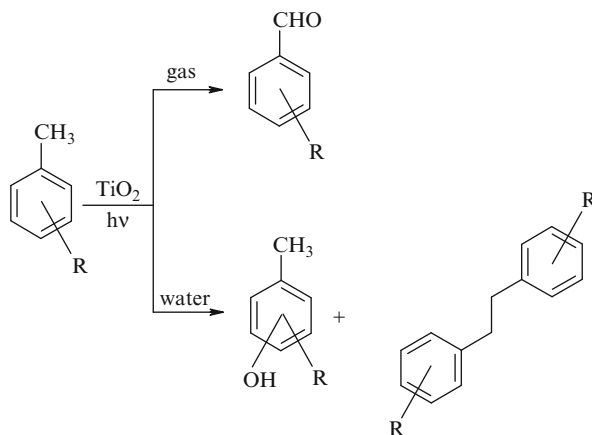
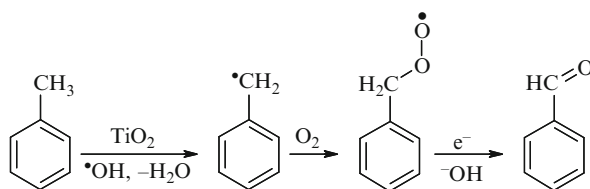


Fig. 1 Products of photocatalytic oxidation from toluene derivatives

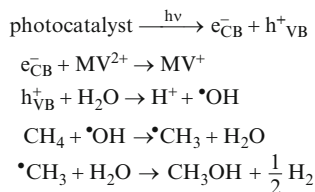


Scheme 1 Formation of benzaldehyde by oxidation of toluene

oxidation product was benzaldehyde but benzene, benzyl alcohol and traces of benzoic acid, phenol and unidentified but compounds were also detected. The molar conversion to benzaldehyde with respect to the initial amount of toluene was ca. 20% in the best experimental conditions. The presence of oxygen was essential for the occurrence of the photoreaction while water played an important role in order to maintain the catalyst activity. A hypothesized reaction mechanism for the production of benzaldehyde is shown in Scheme 1.

Hydrocarbons, such as toluene, cyclohexane, methylcyclohexane and ethylbenzene, have been successfully oxidized with good yields to alcohols, aldehydes and ketones in TiO₂ Degussa P25 aqueous suspensions (Gonzalez et al. 1999).

The photocatalytic oxidation of cyclohexane on TiO₂ was investigated in neat cyclohexane and in various solvents (Almquist and Biswas 2001). The reaction rate and selectivity for the formation of cyclohexanol and cyclohexanone depended on the relative strengths of adsorption of cyclohexane, solvent and products on the catalyst. The product-formation rate significantly increased by employing a solvent that was not competitive with cyclohexane for the active reaction sites. Dichloromethane was the best solvent with regard to the formation of cyclohexanol and cyclohexanone, whereas 2-propanol, chloroform and benzene were the most unfavourable.

Scheme 2 Photocatalyzed conversion of methane

TiO₂ film reactors were used for the partial oxidation of cyclohexane in gas phase (Sahle-Demessie et al. 1999). The films were prepared by three different methods (dip coating using titanium isopropoxide or commercially available titanium dioxide particles, sol-gel process and flame aerosol process) and irradiated with UV-light. The best results in terms of activity for the formation of cyclohexanol and cyclohexanone were obtained with the films produced by flame aerosol, with a selectivity toward the two products of 98%. The best selectivity (99.2%) was achieved with films prepared by the sol-gel method, but the activity was very low.

A particular attention deserves the partial oxidation of an abundant natural gas as methane that could be used as a feedstock for the production of chemicals. Methane was photocatalytically converted to methanol and hydrogen at 367K and atmospheric pressure (Noceti et al. 1997), but in this case the used catalyst was WO₃ doped with copper, lanthanum or platinum species. The sintered catalyst was suspended in water containing methyl viologen as electron transfer reagent. The suggested reaction pathway is shown in Scheme 2.

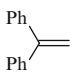
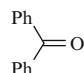
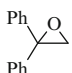
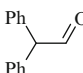
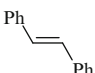
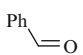
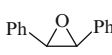
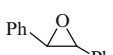
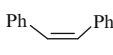
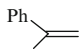
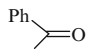
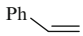
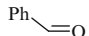
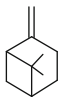
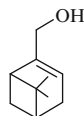
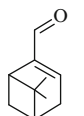
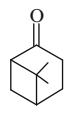
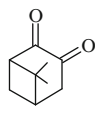
3.2 Olefins Oxidative Cleavage

The epoxidation of alkenes is a relevant industrial reaction (Shi 2004; Lane and Burgess 2003; Zuwei et al. 2001; de Bruin et al. 2004) since the epoxide functional groups are present in many starting materials for industrial syntheses. Epoxides are most frequently obtained from alkenes and peracids but several photocatalytic selective oxidations catalyzed by TiO₂ have been studied.

Acetonitrile-based solvents were used for the oxidative cleavage of arylated alkenes in the presence of different semiconductors irradiated with UV-light (Fox and Chen 1981). Table 1 reports the results obtained in the presence of TiO₂.

Titanium-coated crystalline SiO₂ is known to catalyze propene epoxidation by using hydrogen peroxide (Lane and Burgess 2003). Preventing the use of the latter compound (H₂O₂) is a major requirement in epoxidation because of economic and safety reasons. Photocatalytic epoxidation of propene by molecular oxygen was carried out by using TiO₂-dispersed SiO₂ catalysts, prepared via impregnation or sol-gel methods (Yoshida et al. 1999). The reaction was performed in gas phase at room temperature and acetaldehyde, acetone, ethene, butene, propanal, acrolein, CO and CO₂ were the by-products. The most selective photocatalysts were prepared by the

Table 1 Photocatalytic oxidation of alkenes on TiO₂ in air-saturated CH₃CN

Alkene	Conversion (%)	Products (chemical yields %)			
	85	 (84)	 (14)	 (2)	
	85	 (33)	 (11)	 (42)	 (14)
	50	 (100)			
	43	 (17)			
	29	 (12)	 (12)	 (24)	 (24)

Reprinted from Fox and Chen (1981), copyright with permission from American Chemical Society

sol-gel technique. A selectivity of 57.5% toward the formation of propene oxide with a conversion of 9.2% was reached. Comparable conversions were obtained with the catalyst prepared via impregnation, but the selectivity was only 40.8% in this case.

Similar catalysts were used (Li and Kutsal 2002) for the gas phase styrene epoxidation by O₂ over TiO₂ nanoparticles, highly dispersed in a SiO₂ matrix (prepared via a sol-gel method) under mild conditions. The principal products were styrene oxide, benzaldehyde and CO₂. The performance of the home-prepared catalysts for styrene oxidation was compared with that of TiO₂ Degussa P25. The commercial catalyst showed high selectivity for the photocatalytic mineralization (98.5% for CO₂ and 1.5% for benzaldehyde) with a conversion of 95%. Conversely, the best TiO₂/SiO₂ sample gave selectivities of 62.2%, 23.1% and 14.7% for styrene oxide, benzaldehyde and CO₂, respectively, with a conversion of 18.1%. The influence of water vapor was also investigated and the addition of 5 ml of H₂O to the above mentioned system decreased the styrene oxide selectivity from 62.2 to 15.6%. This decrease is attributable to the expected generation of high active and low selective hydroxyl radicals, capable of deeper oxidation and of complete mineralization of styrene.

A recent research (Shiraishi et al. 2005a) concerns the acetonitrile-assisted highly selective epoxidation of various alkenes on Ti-containing silica with a hexagonal MCM-41 structure, using molecular oxygen. The authors claim that

the relatively poor selectivity (ca. 60%) reached in previous studies depended on alkenes and O₂⁻ radicals that promoted the formation of side products, such as alcohols and ketones. Photocatalytic epoxidation of various cyclic and linear olefins on the novel catalyst in liquid phase proceeded with excellent selectivity (>98%), whereas the use of the same catalyst in gas phase or with bulk TiO₂ in liquid phase showed much lower selectivity. The presented epoxide selectivities are the highest values among those obtained in the photocatalytic systems reported so far. Remarkably, they obtained unprecedented stereoretentivities (selectivity >99%) in the oxidation of *cis*- and *trans*-2-hexene.

3.3 Alcohols Oxidation

Finding new processes for the oxidation of alcohols to carbonyl compounds has been a main topic of industrial chemistry, since traditional processes made use of toxic transition metal salts, generating high amounts of wastes (ten Brinks et al. 2000; Enache et al. 2006). Recently, some atom efficient catalytic systems mostly based on Ru and Pd-Au have been developed (Pagliaro et al. 2005).

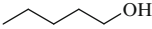
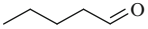
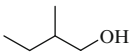
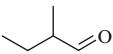
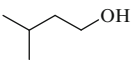
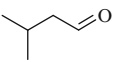
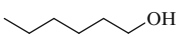
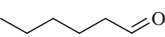
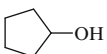
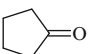
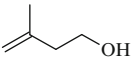
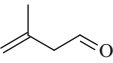
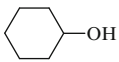
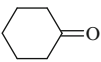
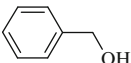
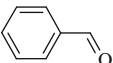
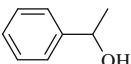
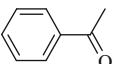
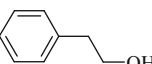
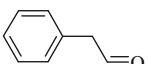
Gas phase oxidation of various alcohols by means of TiO₂-coated pads was performed with good results (Pillai and Sahle-Demessie 2002). The reaction occurred in air in the presence or absence of vapor. Water had a good influence for regenerating hydroxyl groups on the catalyst surface but was not essential, since this regeneration could be carried out by the alcohol itself. Products, conversions and selectivities for the various alcohols studied are reported in Table 2.

The oxidation of selected aryl alcohols by using irradiated TiO₂ in O₂-saturated acetonitrile, yielded aldehydes or ketones and traces of acids as products (Mohamed et al. 2002). Benzyl alcohol, 1-phenylethanol, benzhydrol, hydrobenzoin, 4,4'-dimethoxyhydrobenzoin, 4,4'-dichlorohydrobenzoin and 4-chloro-benzhydrol have been oxidized with conversions higher than 90% and high yields in the desired products.

The oxidation of 2-propanol by semiconductor-zeolite composites was investigated by employing TiO₂ or CdS and Y zeolite (Green and Rudham 1993). TiO₂-based composites were prepared via tetraethyl titanate impregnation followed by hydrolysis and calcination. The catalysts were suspended in pure 2-propanol saturated with O₂ or mixtures of N₂ and O₂. Only propanone was obtained without other products arising from further oxidations.

Remarkably, to the best of our knowledge, no attempts of performing selective photocatalytic oxidation of alcohols to aldehydes in water are reported. A recent work (Palmisano et al. 2007c) concerned the selective oxidation of 4-methoxybenzyl alcohol to the corresponding aldehyde that is an intermediate in many different industrial processes. The synthesis was carried out in organic-free water suspensions of home-prepared TiO₂, at room temperature. 4-methoxybenzaldehyde (or *p*-anisaldehyde) is a compound used in sweet blossom and in flavor compositions for confectioneries and beverages. The nanostructured catalyst synthesized by boiling

Table 2 Products, conversions and selectivities obtained in gas phase photocatalytic oxidation of alcohols

Alcohol	Product	Conversion (%)	Selectivity (%)
		18	>95
		20	>95
		24	>95
		26	>95
		37	>95
		14	>95
		21	>95
		35	>95
		97	7 (83 styrene)
		53	26 (48 benzaldehyde, 10 acetophenone)

Reprinted from Pillai and Sahle-Demessie (2002), copyright with permission from Elsevier

aqueous solutions of TiCl_4 , in mild conditions, showed a much higher yield (41.5% mol) than that obtained with commercial samples (see Table 3). The only by-products present were traces of 4-methoxybenzoic acid (only for long-lasting runs) and opening products, CO_2 being the other main oxidation product.

Table 3 Photocatalytic oxidation of 4-methoxybenzyl alcohol to 4-methoxyaldehyde

Catalyst ^a	Boiling time (h)	SSA (m ² g ⁻¹) ^b	Irradiation time (h) ^c	Selectivity (mol%) ^c
TiO ₂ Merck	–	10	5.2	12.0
TiO ₂ Degussa P25	–	50	0.9	8.7
TiO ₂ HP	0.5	235	7.7	41.5
TiO ₂ HP	2.0	226	4.7	36.7
TiO ₂ HP	4.0	220	3.9	35.6
TiO ₂ HP	6.0	206	2.8	31.1
TiO ₂ HP	8.0	108	3.2	32.5

^a“HP” stands for home prepared

^bBET-specific surface areas

^cThese values refer to a conversion of ca. 65% mol

From Palmisano et al. (2007c)

Increasing the boiling time resulted in higher crystallinity and activity of the catalyst, which afforded progressively lower yields in aldehyde. The selectivity values obtained with the commercial catalysts drastically decreased with irradiation time and decreasing the catalyst amount of these samples did not result in significant enhancement of the selectivity for the aldehyde formation. Conversely, the poorly crystalline home prepared samples gave rise to yields of ca. 35% even when the conversion was ca. 80% and no catalyst deactivation was observed.

3.4 Hydroxylation of Aromatics

The hydroxylation of aromatics is of particular interest to the chemical industry. Among the photocatalytic reactions affording aromatics oxidation, the conversion of benzene to phenol is perhaps the most interesting reaction since phenol is precursor of resins and preservative for pharmaceutical aid. The dihydroxybenzenes, such as catechol and hydroquinone, are also high value chemicals and are widely used as photography chemicals, antioxidants and polymerization inhibitors.

Due to the high positive energy of the photogenerated holes, most organic compounds undergo complete oxidation when TiO₂ is used as photocatalyst. To obtain a selective photooxidation, the high oxidation power of TiO₂ must be controlled by changing the structure of the active species. TiO₂-pillared clays were fairly effective for the photocatalytic degradation of benzene (Shimizu et al. 2002). The samples showed a higher selectivity than Degussa P25 for the partial oxidation products because of their pore structure. The distribution among the different oxidation products depended on the type of clay host.

Benzene was converted to phenol in aqueous TiO₂ Degussa P25 suspensions containing acetonitrile as cosolvent (Park and Choi 2005). After 4 h, phenol selectivity was 86% corresponding only to 2.6% conversion of benzene. The addition of Fe³⁺, H₂O₂ or Fe³⁺ and H₂O₂ highly enhanced the phenol conversion yield and selectivity. Surface modifications of TiO₂ significantly influenced the

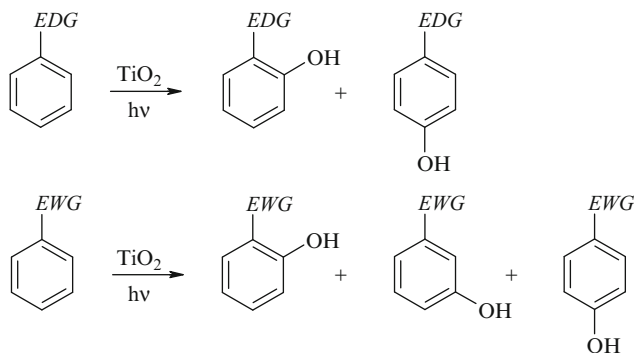


Fig. 2 Main hydroxylated products obtained during the photocatalytic oxidation of aromatic compounds containing either an electron donor group (EDG) or an electron withdrawing group (EWG)

conversion of benzene. Pt deposition markedly increased the phenol yield and selectivity. Surface fluorination enhanced the phenol production and total hydroxylation, but the selectivity was reduced. The addition of $\text{HNa}_2\text{PW}_{12}\text{O}_{40}$ as homogeneous photocatalyst increased the phenol yield from 2.6 to 11%.

Samples of mesoporous TiO_2 prepared with different methods showed a very high selectivity (>80%) in benzene hydroxylation to phenol, even if the conversion was in the range 10–40% (Shiraishi et al. 2005b). Authors explained these findings by considering that the hydroxylation reaction takes place on the catalyst surface and consequently only the adsorbed molecules can react. The conversion was very low because the catalyst surface was essentially internal to the pores, but the selectivity was very high. Indeed benzene strongly adsorbed onto the catalyst differently from phenol.

Recently, evidence was found that the aromatic compounds photoadsorbed on the catalyst surface undergo two competing reaction pathways: (a) hydroxylation of the aromatic ring or (b) multi-step oxidation reactions to complete mineralization. In the first case, the OH radical attack follows the selectivity rules known for homogeneous electrophilic aromatic substitution when the oxidized compound contains an electron donor group (Palmisano et al. 2006; 2007a). Hence, the only *ortho*- and *para*-isomers are obtained (see Fig. 2). In the presence of an electron withdrawing group, all three hydroxylated isomers are formed. This is a general behavior, confirmed by all the oxidation intermediates found in literature. The explanation put forward to explain these findings considers that the attack is reversible forming intermediates with different capacity to be oxidized to the final products.

4 Reductions

Chemical reductions are crucial reactions in organic chemistry and are usually conducted by using harmful or environmentally unsafe species, such as iron

ammonium chloride, sulfides, hydrogen, borohydrides, carbon monoxide and in general activated metals. Safer routes are the electrochemical and photocatalytic processes.

Photocatalytic reductions occur by the transfer of conduction band or trapped electrons to electron acceptors. The reduction efficiency is related to the reduction potential of the species present at the surface of the semiconductor. Due to the position of the TiO₂ conduction band, oxygen strongly competes for the electrons so that the reduction of an organic compound is hindered.

The photoreduction of organic electron acceptors, such as nitroaromatics can be carried out in the absence of oxygen, and in the presence of sacrificial electron donors whose role is to scavenge valence band holes, thereby reducing the undesired recombination of photoexcited electron-hole pairs.

4.1 *N-Containing Aromatics Reduction*

The photoreduction of nitrobenzene and its derivatives by irradiated TiO₂ is particularly attractive since anilines are important chemical intermediates for the synthesis of valuable dyestuffs and various drugs, such as, for example, 4-acetamidophenol (paracetamol).

A wide variety of aromatic nitrocompounds were reduced to amines with very high yields by the irradiation of suspensions of TiO₂ Degussa P25 in ethanol (Mahdavi et al. 1993). A hydroxylamine intermediate was detected during the photo-induced reduction of *p*-nitroacetophenone. The proposed reduction mechanism is illustrated in Fig. 3. The electrons photogenerated reduce the nitrocompound, whereas the holes oxidize ethanol to acetaldehyde with the formation also of hydrogen. The hydrogen produced during the above-mentioned process can also cause the reduction of the nitro-group.

Nitrobenzene, 3- and 4-nitrotoluene and nitrobenzotrile were reduced in degassed TiO₂ slurries (Ferry and Glaze 1998). The obtained products were aniline-derivatives and traces of nitroso-intermediates. Methanol or 2-propanol played the role of electron donors in the reaction system. Identical rates and selectivities were achieved in the presence of either solvents revealing the minor relevance of the chemical nature of the alcohol. High yields in anilines were obtained in the case

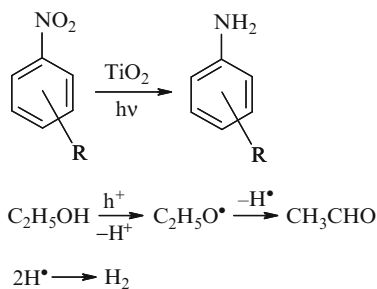
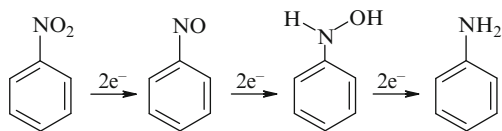
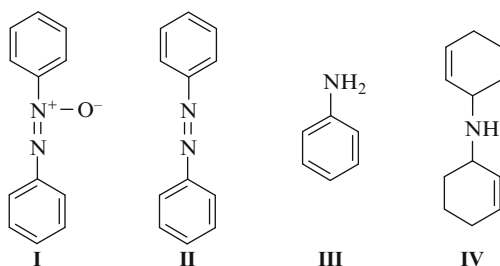


Fig. 3 Mechanism of the photocatalytic reduction of nitrocompounds in the presence of an alcohol

Scheme 3 Photocatalytic reduction of nitrobenzene over TiO₂**Fig. 4** Products of nitrobenzene photoreduction in the presence of cyclohexene

of nitrobenzene and nitrotoluenes, whereas low selectivities were found in the conversion of nitrobenzonitriles. Hydroxylamine intermediates were inferred but not detected directly. The sequential hypothesized reduction of the nitrogroup is illustrated in Scheme 3.

Nitrobenzene reduction in the presence of cyclohexene allowed to obtain interesting functionalizations of the nitro-organic (Maldotti et al. 2000). Deaerated nitrobenzene/cyclohexene mixtures (3:1 v/v) were irradiated by UV-light at room temperature and pressure in the presence of various semiconductors (TiO₂, WO₃ and CdS) and in homogeneous conditions. Figure 4 represents the four identified products that amounted to about 90% of the reduced substrate. *I* and *IV* were the most abundant products in homogeneous conditions, whereas *II* was prevalently formed in the presence of TiO₂, with a selectivity of 47%.

No reactivity was found without cyclohexene or irradiation, and bicyclohexene, cyclohex-2-en-1-one and cyclohex-2-en-1-ol were detected as cyclohexene oxidation products. The presence of a semiconductor inhibited the formation of *IV*, probably because the high surface coverage by intermediates drastically reduced the chance of reaction between a reduction product of nitrobenzene, as C₆H₅NH•, and an oxidation product of cyclohexene, as C₆H₉•, that would lead to *IV*.

4-Nitrophenol was selectively reduced to 4-aminophenol in different alcohols (methanol, ethanol, 1-propanol, 2-propanol, 1-butanol and 2-butanol) in the presence of Degussa P25 TiO₂ suspensions irradiated by UV-light (Brezová et al. 1997). The influence of solvent properties, such as viscosity, relative permittivity, refractive index and polarity/polarisability, on the reaction rate was carefully analysed. Viscosity and polarity/polarisability parameter, i.e., the ability of the solvent to stabilise a charge or dipole by means of its dielectric effect were found to play an important role in the photoreduction. In particular, an increase in the polarity/polarisability parameter corresponded to a better stabilization of the produced charged intermediate species and hence to a higher reaction rate.

The reduction of *p*-chloronitrobenzene in UV-irradiated TiO₂ slurries was studied in the absence of oxygen and in the presence of sacrificial electron donors (Zhang et al. 2006). The effect of the electron donor (methanol, ethanol, 2-propanol and formic acid) was studied and the best yield in *p*-chloroaniline (almost 99%) was reached with a 2-propanol/formic acid ratio equal to nine on volume base. Different TiO₂ samples were tested and Degussa P25 was found to be the best catalyst both for conversion and yield.

4.2 CO₂ Reduction to Useful Organics

The continuously increasing concentration of CO₂ in the atmosphere has induced the researchers to find new solutions to convert the high amounts of the exceeding CO₂ to useful chemicals. Many environmental problems, such as the raise in temperature caused by the green house effect, derive from the high CO₂ concentrations. Preventing this event with the development of alternative clean fuel sources is a major goal of the current chemistry. Photocatalytic reduction of CO₂ by using photoactive species is a possible solution for this problem even if CO₂ is, thermodynamically, a very stable molecule, and it is very difficult to be reduced. The possibility of producing formaldehyde, methanol and methane is of particular interest because of the large use of chemicals, such as formaldehyde and methanol, and fuels like methanol and methane.

Both liquid and gaseous systems (Anpo and Chiba 1992; Ikeue et al. 2002) were extensively used with different catalysts. In one of the first reports on this topic (Inoue et al. 1979), formic acid, formaldehyde, methanol and methane were produced upon illumination of aqueous suspensions of semiconductor powders as TiO₂ and SrTiO₃. The efficiency of CO₂ reduction was very low when H₂O was used as reductant, and this is the major drawback of this process.

HCOOH, HCHO and CH₃OH were obtained in alkaline aqueous suspensions of TiO₂ doped with Nb, Cr or RuO₂ (Halmann et al. 1984). HCOOH was found to be the main product in all the runs, while methanol was always formed in very modest amounts. Doping with RuO₂ increased the CH₃OH yield. The low efficiency of the formation of reduced compounds has been attributed to the existence of a highly efficient reverse reaction in which a reduced intermediate species as the radical-anion CO₂⁻ is oxidized by a photogenerated OH radical. An interesting remark is the enhancement of the products in the presence of sulfide ions that could be responsible for an enhanced electron-hole separation.

Addition of copper(II) into the TiO₂ matrix improves the efficiency and selectivity for the CH₃OH formation (Yamashita et al. 1994). The authors suggested that Cu⁺ could play a significant role in the formation of CH₃OH as also found in the photoelectrochemical production of methanol from aqueous solutions of CO₂ (Frese 1991). Photocatalysts with various copper species (Cu⁰, Cu^I and Cu^{II}) were prepared by an impregnation method on commercial TiO₂ Degussa P25 (Slamet et al. 2005). In all cases, CH₃OH was the main product and the highest

yield was achieved with a 3% CuO/TiO₂ catalyst. CH₃OH was favourably produced on copper loaded TiO₂ synthesized via an improved modified sol-gel process (Tseng et al. 2004). Cu(I) acts as an electron trap and avoids the recombination of electrons and holes increasing the photoefficiency of the process.

Selective reduction to CH₃OH was recently performed by using a 355 nm UV laser and TiO₂, NiO and ZnO as catalysts (Yahaya et al. 2004). A very low CH₃OH yield was achieved with TiO₂. Other side products obtained also in small concentrations were CH₃COOH in the liquid phase and CH₄ and CO in the gas phase.

The presence of a hole scavenger is effective to enhance the photoreduction of CO₂. CH₄ was the main reaction product when CO₂ was reduced in aqueous 2-propanol solutions, in which TiO₂ Degussa P25 was suspended (Kaneko et al. 1998; Dey et al. 2004). Acetone was also observed because of oxidation of 2-propanol. No CH₃OH was detected. The proposed reaction mechanism (Kaneko et al. 1998) is illustrated in Scheme 4.

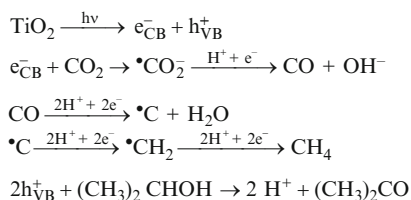
The photocatalytic reduction of CO₂ in the presence of H₂O in gas phase is particularly attractive and has been investigated on various TiO₂ catalysts. CH₄, CH₃OH and CO can be obtained, but the efficiency and the selectivity of the photoreaction depends on the kind of TiO₂, the ratio CO₂/H₂O and the reaction temperature.

UV irradiation of four standard powdered TiO₂ catalysts at 275K (Yamashita et al. 1994) gave CH₄ and trace amounts of C₂H₄ and C₂H₆. The different CH₄ yields were attributed to the differences in the band gap and/or the concentration of the surface OH groups.

Cu/TiO₂ catalysts with a Cu loading of 0.3–1.0 wt% (Yamashita et al. 1994; Anpo et al. 1995) were less effective for the photocatalytic production of CH₄ but more efficient for the formation of CH₃OH. As revealed by the XPS spectra, the main Cu species in the catalyst was Cu⁺. The addition of excess Cu (>3 wt%) to TiO₂ prevented the formation of CH₃OH. The activity decreased after long reaction times due to the presence of graphitic carbon species on the surface of the catalysts.

CH₄ and CH₃OH were obtained in the presence of TiO₂(100) single-crystal rutile (Anpo et al. 1995), whereas only CH₃OH was detected with TiO₂(110). This finding was attributed to the different surface geometry of the two catalysts. The surface with a higher [Ti]/[O] surface ratio, i.e., TiO₂(100), has larger spaces for the direct contact with CO₂ and H₂O molecules so that the reduction of CO₂ to CH₄ results more facile.

UV irradiation of highly dispersed anchored TiO₂ catalysts (Anpo et al. 1995) led to the evolution of CH₄, CH₃OH and CO. The total yields of products were



Scheme 4 CO₂ reduction in the presence of TiO₂ and 2-propanol

larger at 323K than at 275K, indicating that the photocatalytic reaction proceeds more efficiently at higher temperatures. The efficiency increased with an increase in the H₂O/CO₂ ratio but an excess amount of H₂O suppressed the reaction.

In the presence of titanium oxides highly dispersed within zeolites and mesoporous molecular sieves (Yamashita et al. 1998) or Ti-containing porous (Ikeue et al. 2002) and mesoporous (Shioya et al. 2003) silica thin films, the reduction of CO₂ with H₂O led to the formation of CH₄, CH₃OH as well as CO and O₂ as minor products. These catalysts revealed a high selectivity to produce CH₄.

A fixed-bed gas-solid photocatalytic reactor provided with commercial TiO₂ pellets, irradiated by UV-light, was used for the reduction of CO₂ to CH₄ (Tan et al. 2006). The yield of CH₄ was higher than that obtained from processes using thin films or anchored TiO₂ catalysts and comparable to that of the powders. CO and H₂ were also detected. The photocatalytic process with the pellet forms has the advantage to be free from filtration to recover the catalysts from the gaseous product mixture.

5 Other Reactions

In this section, some of the copious developed photocatalytic syntheses, not easily attributable to the oxidations or reductions sections, are reported. Semiconductors such as TiO₂ have found wide applications in different processes (Maldotti et al. 1990; Park et al. 1995, 2001; Ohtani et al. 1990; Pace et al. 2000).

Remarkably, organic solvents or mixtures of organics and water were generally applied, although a few syntheses were performed in water or ethanol. Among the organic solvents, CH₃CN has been by far the most used, and it has been for instance applied in the preparation of perfluorinated aromatic compounds catalyzed by TiO₂ coupled with AgF (Wang and Mallouk 1990). The reported method, safer than the analogous earlier ones, yielded only one product with selectivities of 57%. Even polymerizations in acetonitrile at TiO₂/Pt surfaces were formerly studied for the case of γ -methyl methacrylate (Kraeutler et al. 1979). Amino acids (such as glycine, alanine, serine, aspartic acid and glutamic acid) can be produced in aqueous ammoniacal suspensions of platinumized TiO₂ powders saturated with methane (Dunn et al. 1981). Near ultraviolet light was the irradiation source and methanol, ethanol and methylamine were found as minor products of this photocatalytic endothermic process.

Dihydropyrazine and 2-methylpiperazine photocatalytic syntheses were performed by means of UV-irradiated semiconductor/zeolite systems (Subba Rao et al. 2000; Subba Rao and Subrahmanyam 2002). The reagents were ethylenediamine and propylene glycol or only *N*-(β -hydroxypropyl) ethylenediamine. TiO₂, ZnO or CdS were used as the semiconductors in acetonitrile solutions with bubbling oxygen. The maximum yield in dihydropyrazine (Fig. 5, I) was 20.4% with 2 wt% TiO₂ supported on H β (a zeolite with a ratio SiO₂/Al₂O₃ = 20), whereas

Fig. 5 Reaction products in semiconductor/zeolite photocatalyzed syntheses

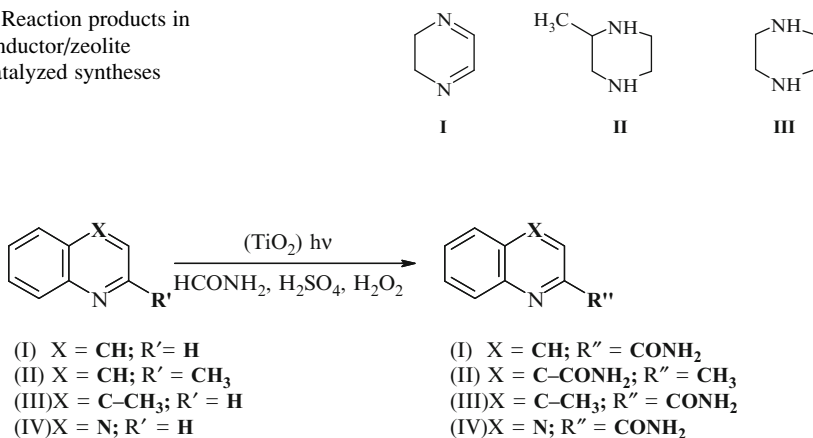


Fig. 6 Sunlight-induced functionalisation of heterocyclic bases

2-methylpiperazine (Fig. 5, II) was obtained with a yield of 31.9% with 5 wt% TiO₂ supported on H β . In the last case, piperazine (Fig. 5, III) was also formed with a yield of 14.8%. The irradiation times were 15 and 12 h in the two syntheses.

Heterocyclic bases were functionalized (Caronna et al. 2003) by reaction with amides under sunlight illumination (Fig. 6). The reactions were carried out in the presence of H₂SO₄ and H₂O₂ which does not absorb solar light. The presence of TiO₂ was found to be beneficial or necessary to obtain the products, whereas no transformation took place in the dark. The decomposition of H₂O₂ via electron transfer from the excited TiO₂ forming an OH⁻ ion and an •OH radical was hypothesised. The hydroxyl radical abstracts the hydrogen from the amide generating an amide radical which attacks the heterocyclic base.

Similar results were obtained bubbling O₂ instead of using hydrogen peroxide (Caronna et al. 2007a).

The reaction of some heterocyclic bases (quinoline, quinaldine and lepidine) with ethers (tetrahydropyran, dioxane, dioxolane, diethylether and trioxane) in the presence of TiO₂ was also studied to extend the applicability of the above described syntheses (Caronna et al. 2005) and interesting reactivities were found. In particular, the derivatives obtained by using trioxane as radical source with various bases open the route to the simple production of valuable heterocyclic aldehydes, due to the high yield acidic hydrolysis of the obtained compounds. The hypothesized reaction mechanism shown in Fig. 7 involves the formation of an α -oxyalkyl radical, which subsequently attacks the base. The radical could be generated either by hydrogen abstraction from the carbon atom α to the oxygen or by means of an electron transfer from the oxygen followed by deprotonation from the carbon α to the oxygen radical cation. The reaction yields reached values up to 75% when TiO₂ was used as catalyst.

Interestingly, when aldehydes were used as radical source in the presence of salfied heteroaromatic bases, a mixture of acylated and alkylated bases were

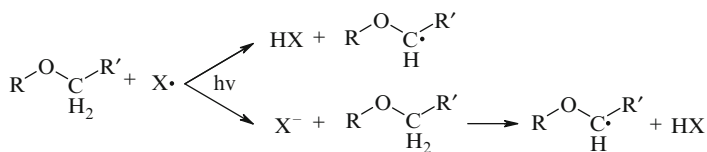


Fig. 7 Hypothesized mechanism of formation of the α -oxyalkyl radical in the presence of irradiated TiO₂

obtained (the alkyl radical coming from the loss of CO from the acyl radical). The ratio between the two products was dependent from the aldehyde and from the base used in this reaction. These ratios were different from those obtained using Fe⁺² and H₂O₂ to create the acyl radical. The authors explained the results in terms of reversibility of the intermediates and direct participation of TiO₂ in their oxidation (Caronna et al. 2007b).

The selective cyclization of amino acids in deaerated aqueous suspensions was studied in the presence of TiO₂ or CdS particles (Ohtani et al. 1995a, b; 2003). This reaction is formally a deamination not involving a redox process. In Fig. 8, the formation of pipercolinic acid by cyclization of lysine is described.

The reaction is hypothesized to proceed via combination of oxidation and reduction and the formed product (pipercolinic acid) retained its (S)-configuration only when the reaction was promoted by TiO₂, whereas an almost racemic compound was formed by using CdS particles. The highest selectivity reached with a hydrothermal crystallized TiO₂ was 77% with a conversion of 92%. This shows, once more, as photocatalytic selectivity can be tuned by varying the catalyst properties or the experimental conditions. It should be stressed that the significance of these syntheses comes from the aqueous media used as solvents and from the optical activity of pipercolinic acid (only in its (S)-configuration), which is a crucial intermediate in the preparation of biologically active heterocyclic species (used for example as anesthetics).

A possible green route was published for the photocatalytic formation of aromatic carbamate through the formation of isocyanates as intermediates. As shown in Fig. 9, the corresponding carbamate was prepared through ethanol-assisted carbonylation of *p*-nitrotoluene at room temperature and pressure, in N₂-saturated TiO₂ Degussa P25 suspensions, irradiated by light with $\lambda > 380$ nm (Maldotti et al. 2005). The process reached a selectivity of ca. 85% with a conversion of ca. 26%. The secondary product was *p*-toluidine. This reaction allowed to avoid the use of a poisonous and corrosive gas as phosgene, used for the industrial preparations of aromatic isocyanates that are currently obtained by the reduction and phosgenation of nitroarenes.

Phenanthrene acetonitrile solutions were irradiated ($\lambda > 340$ nm) in the presence of TiO₂ Degussa P25, with 8% water and oxygen as oxidant (Higashida et al. 2006). The formation of a coumarin compound at room conditions was reported by the authors. This kind of compounds retains appeal since they are intermediates for a variety of chemicals, including pharmaceuticals and fluorescent dyestuffs. The

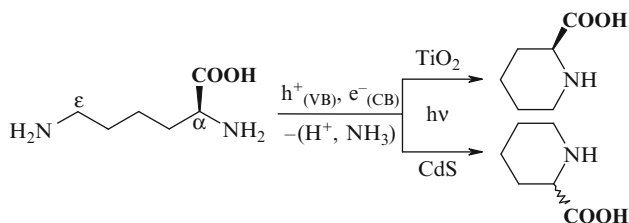


Fig. 8 Photocatalytic cyclization of lysine to pipercolinic acid

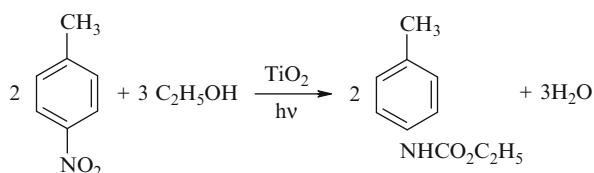


Fig. 9 Photocatalytic carbonylation of p-nitrotoluene

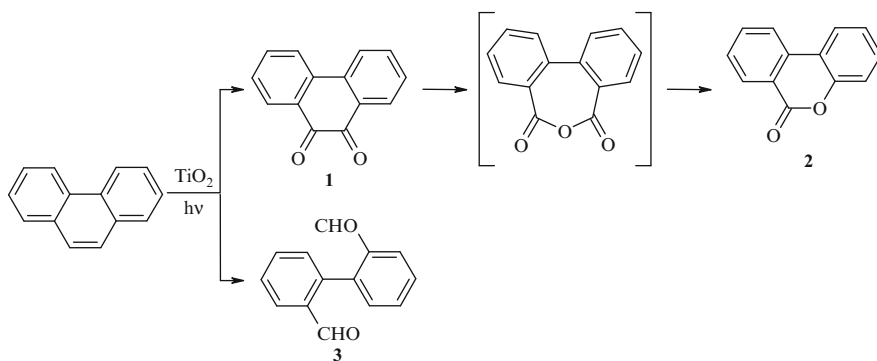


Fig. 10 Photocatalytic oxidation of phenanthrene to a coumarin compound

reaction mechanism is illustrated in Fig. 10, and the main product (2) was obtained with a yield of 45% after 100 h of irradiation.

The authors stressed the fact that the sum of initial formation rate of 1, 2 and 3 was almost equal to the phenanthrene decrease, thus attesting that the reaction pathways are two, at least in the first step of the reaction. The authors found no reactivity in the absence of either light or oxygen and estimated an apparent quantum efficiency around 17% by using light of ca. 365 nm. Finally, the production of 2 in this one-pot reaction results attractive because the conventional syntheses of such species from commercial compounds require many steps.

6 Conclusion

This chapter shows that photocatalysis can be applied as a green synthetic route in organic chemistry. A selection of results concerning selective photocatalytic reactions clearly shows that semiconductors are proficient catalysts and can be applied in different processes with appreciable results. Guidelines in seeking new synthetic routes in photocatalysis should follow the “green chemistry” principles (see “The Twelve Principles of Green Chemistry” in Anastas and Warner 1998). In particular, the implementation of systems making use of renewable feedstock as sunlight and biomass-based raw materials, environmentally friendly solvents and catalysts avoiding the presence of heavy metals is highly requested in chemistry nowadays along with the maximization of the raw materials amount ending up into the final product (atom-efficient processes). Photocatalysis will play a major role in this evolution.

Acknowledgments This work is dedicated with deep affection to University of Palermo’s Professor Mario Schiavello, who retired in 2006. The financial support from MIUR (Rome) and from the Quality College del Cnr is gratefully acknowledged.

References

- Almquist CB, Biswas P (2001) The photo-oxidation of cyclohexane on titanium dioxide: an investigation of competitive adsorption and its effects on product formation and selectivity. *Appl Catal A Gen* 214:259–271
- Anastas PT, Warner JC (1998) *Green chemistry: theory and practice*. New York, Oxford University Press
- Anpo M, Chiba K (1992) Photocatalytic reduction of CO₂ on anchored titanium oxide catalysts. *J Mol Catal* 74:207–212
- Anpo M, Yamashita H, Ichihashi Y, Ehara S (1995) Photocatalytic reduction of CO₂ with H₂O on various titanium oxide catalysts. *J Electroanal Chem* 396:21–26
- Augugliaro V, Coluccia S, Loddo V, Marchese L, Martra G, Palmisano L, Schiavello M (1999) Photocatalytic oxidation of gaseous toluene on anatase TiO₂ catalyst: mechanistic aspects and FT-IR investigation. *Appl Catal B Environ* 20:15–27
- Brezová V, Blažková A, Šurina I, Havlínová B (1997) Solvent effect on the photocatalytic reduction of 4-nitrophenol in titanium dioxide suspensions. *J Photochem Photobiol A Chem* 107:233–237
- Caronna T, Gambarotti C, Palmisano L, Punta C, Recupero F (2003) Sunlight induced functionalisation of some heterocyclic bases in the presence of polycrystalline TiO₂. *Chem Commun* 2350–2351
- Caronna T, Gambarotti C, Palmisano L, Punta C, Recupero F (2005) Sunlight-induced reactions of some heterocyclic bases with ethers in the presence of TiO₂. A green route for the synthesis of heterocyclic aldehydes. *J Photochem Photobiol A Chem* 171:237–242
- Caronna T, Gambarotti C, Mele A, Pierini M, Punta C, Recupero F (2007a) A green approach to the amidation of heterocyclic bases: the use of sunlight and air. *Res Chem Intermed* 33:311–317
- Caronna T, Gambarotti C, Palmisano L, Punta C, Pierini M, Recupero F (2007b) Sunlight induced functionalisation reactions of heteroaromatic bases with aldehydes in the presence of TiO₂: a hypothesis on the mechanism. *J Photochem Photobiol A Chem* 189:322–328

- Das B, Banerjee J, Mahender G, Majhi A (2004) Organic reactions in water: an efficient zinc-mediated stereoselective synthesis of (E)- and (Z)-trisubstituted alkenes using unactivated alkyl halides. *Org Lett* 6:3349–3352
- de Bruin B, Budzelaar PHM, Gal AW (2004) Functional models for rhodium-mediated olefin-oxygenation catalysis. *Angew Chem Int Ed* 43:4142–4157
- Dey GR, Belapurkar AD, Kishore K (2004) Photo-catalytic reduction of carbon dioxide to methane using TiO₂ as suspension in water. *J Photochem Photobiol A Chem* 163:503–508
- Dunn WW, Aikawa Y, Bard AJ (1981) Heterogeneous photosynthetic production of amino acids at Pt/TiO₂ suspensions by near ultraviolet light. *J Am Chem Soc* 103:6893–6897
- Enache DI, Edwards JK, Landon P, Solsona-Espriu B, Carley AF, Herzing AA, Watanabe M, Kiely CJ, Knight DW, Hutchings GJ (2006) Solvent-free oxidation of primary alcohols to aldehydes using Au-Pd/TiO₂ catalysts. *Science* 311:362–365
- Ferry JL, Glaze WH (1998) Photocatalytic reduction of nitro organics over illuminated titanium dioxide: role of the TiO₂ surface. *Langmuir* 14:3551–3555
- Fox MA (1983) Organic heterogeneous photocatalysis: chemical conversions sensitized by irradiated semiconductors. *Acc Chem Res* 16:314–321
- Fox MA, Chen C (1981) Mechanistic features of the semiconductor photocatalyzed olefin-to-carbonyl oxidative cleavage. *J Am Chem Soc* 103:6757–6759
- Fox MA, Kim Y-S, Abdel-Wahab AA, Dulay M (1990) Photocatalytic decontamination of sulfur-containing alkyl halides on irradiated semiconductor suspensions. *Catal Lett* 5:369–376
- Frese KW (1991) Electrochemical reduction of CO₂ at intentionally oxidized copper electrodes. *J Electrochem Soc* 138:3338–3344
- Fujihira M, Satoh Y, Osa T (1981) Heterogeneous photocatalytic oxidation of aromatic compounds on TiO₂. *Nature* 293:206–207
- Fujishima A, Rao TN, Tryk DA (2000) Titanium dioxide photocatalysis. *J Photochem Photobiol C* 1:1–21
- Gonzalez MA, Howell SG, Sikdar SK (1999) Photocatalytic selective oxidation of hydrocarbons in the aqueous phase. *J Catal* 183:159–162
- Green KJ, Rudham R (1993) Photocatalytic oxidation of propan-2-ol by semiconductor-zeolite composites. *J Chem Soc/Faraday Trans* 89:1867–1870
- Halmann M, Katzir V, Borgarello E, Kiwi J (1984) Photoassisted carbon dioxide reduction on aqueous suspensions of titanium dioxide. *Sol Energy Mater* 10:85–91
- Herrmann JM (1995) Heterogeneous photocatalysis: an emerging discipline involving multiphase systems. *Catal Today* 24:157–164
- Higashida S, Harada A, Kawakatsu R, Fujiwara N, Matsumura M (2006) Synthesis of a coumarin compound from phenanthrene by a TiO₂-photocatalyzed reaction. *Chem Commun* 2804–2806
- Hoffmann MR, Martin ST, Choi W, Bahnemann DW (1995) Environmental applications of semiconductor photocatalysis. *Chem Rev* 95:69–96
- Ikeue K, Nozaki S, Ogawa M, Anpo M (2002) Characterization of self-standing Ti-containing porous silica thin films and their reactivity for the photocatalytic reduction of CO₂ with H₂O. *Catal Today* 74:241–248
- Inoue T, Fujishima A, Konishi S, Honda K (1979) Photoelectrocatalytic reduction of carbon dioxide in aqueous suspensions of semiconductor powders. *Nature* 277:637
- Jacobson GB, Lee CT Jr, da Rocha SRP, Johnston KP (1999) Organic synthesis in water/carbon dioxide emulsions. *J Org Chem* 64:1207–1210
- Kaneko S, Shimizu Y, Ohta K, Mizuno T (1998) Photocatalytic reduction of high pressure carbon dioxide using TiO₂ powders with a positive hole scavenger. *J Photochem Photobiol A Chem* 115:223–226
- Kisch H (2001) Semiconductor photocatalysis for organic syntheses. *Adv Photochem* 62:93–143
- Kraeutler B, Reiche H, Bard AJ, Hocker RG (1979) Initiation of free radical polymerization by heterogeneous photocatalysis at semiconductor powders. *J Polym Sci/Polym Lett Ed* 17:535–538

- Lane BS, Burgess K (2003) Metal-catalyzed epoxidations of alkenes with hydrogen peroxide. *Chem Rev* 103:2457–2474
- Li C, Chen L (2006) Organic chemistry in water. *Chem Soc Rev* 35:68–82
- Li X, Kotal CJ (2002) Photocatalytic selective epoxidation of styrene by molecular oxygen over highly dispersed titanium dioxide species on silica. *J Mat Sci Lett* 21:1525–1527
- Linsebigler AL, Lu G, Yates JT Jr (1995) Photocatalysis on TiO₂ surfaces: principles, mechanisms, and selected results. *Chem Rev* 95:735–758
- Mahdavi F, Bruton TC, Li Y (1993) Photoinduced reduction of nitro compounds on semiconductor particles. *J Org Chem* 58:744–746
- Maldotti A, Amadelli R, Bartocci C, Carassiti V (1990) Photo-oxidative cyanation of aromatics on semiconductor powder suspensions I: oxidation processes involving radical species. *J Photochem Photobiol A Chem* 53:263–271
- Maldotti A, Andreotti L, Molinari A, Tollari S, Penoni A, Cenini S (2000) Photochemical and photocatalytic reduction of nitrobenzene in the presence of cyclohexene. *J Photochem Photobiol A Chem* 133:129–133
- Maldotti A, Molinari A, Amadelli R (2002) Photocatalysis with organized systems for the oxofunctionalization of hydrocarbons by O₂. *Chem Rev* 102:3811–3836
- Maldotti A, Amadelli R, Samiolo L, Molinari A, Penoni A, Tollari S, Cenini S (2005) Photocatalytic formation of a carbamate through ethanol-assisted carbonylation of p-nitrotoluene. *Chem Commun* 1749–1751
- Marcì G, Addamo M, Augugliaro V, Coluccia S, García-López E, Lodo V, Martra G, Palmisano L, Schiavello M (2003) Photocatalytic oxidation of toluene on irradiated TiO₂: comparison of degradation performance in humidified air, in water and in water containing a zwitterionic surfactant. *J Photochem Photobiol A Chem* 160:105–114
- Mohamed OS, Gaber AEM, Abdel-Wahab AA (2002) Photocatalytic oxidation of selected aryl alcohols in acetonitrile. *J Photochem Photobiol A Chem* 148:205–210
- Mozzanega MN, Herrmann JM, Pichat P (1977) Oxydation d'alkyltoluenes en alkylbenzaldehydes au contact de TiO₂ irradié sous UV. *Tetrahedron Lett* 18:2965–2966
- Narayan S, Muldoon J, Finn MG, Fokin VV, Kolb HC, Barry Sharpless K (2005) “On Water”: unique reactivity of organic compounds in aqueous suspension. *Angew Chem Int Ed* 44:3275–3279
- Navio JA, García Gomez M, Pradera Adrian MA, Fuentes Mota JJ (1996) Partial or complete heterogeneous photocatalytic oxidation of neat toluene and 4-picoline in liquid organic oxygenated dispersions containing pure or iron-doped titania photocatalysts. *J Mol Catal A Chem* 104:329–339
- Noceti RP, Taylor CE, D'Este JR (1997) Photocatalytic conversion of methane. *Catal Today* 33:199–204
- Ohtani B, Tsuru S, Nishimoto S-I, Kagiya T, Izawa K (1990) Photocatalytic one-step syntheses of cyclic imino acids by aqueous semiconductor suspensions. *J Org Chem* 55:5551–5553
- Ohtani B, Iwai K, Kominami H, Matsuura T, Kera Y, Nishimoto S (1995a) Titanium(IV) oxide photocatalyst of ultra-high activity for selective N-cyclization of an amino acid in aqueous suspensions. *Chem Phys Lett* 242:315–319
- Ohtani B, Kawaguchi J, Kozawa M, Nakaoka Y, Nosaka Y, Nishimoto S (1995b) Effect of platinum loading on the photocatalytic activity of cadmium(II) sulfide particles suspended in aqueous amino acid solutions. *J Photochem Photobiol A Chem* 90:75–80
- Ohtani B, Pal B, Ikeda S (2003) Photocatalytic organic syntheses: selective cyclization of amino acids in aqueous suspensions. *Catal Surv Asia* 7:165–176
- Pace A, Buscemi S, Vivona N, Caronna T (2000) Sensitized photoreduction of nitrosoazoles on titanium dioxide. *Heterocycles* 53:183–190
- Pagliaro M, Campestrini S, Ciriminna R (2005) Ru-based oxidation catalysis. *Chem Soc Rev* 34:837–845

- Palmisano G, Addamo M, Augugliaro V, Caronna T, García-López E, Loddo V, Palmisano L (2006) Influence of the substituent on selective photocatalytic oxidation of aromatic compounds in aqueous TiO₂ suspensions. *Chem Commun* 1012–1014
- Palmisano G, Addamo M, Augugliaro V, Caronna T, Di Paola A, García-López E, Loddo V, Marci G, Palmisano L, Schiavello M (2007a) Selectivity of hydroxyl radical in the partial oxidation of aromatic compounds in heterogeneous photocatalysis. *Catal Today* 122:118–127
- Palmisano G, Augugliaro V, Pagliaro M, Palmisano L (2007b) Photocatalysis: a promising route for 21st century organic chemistry. *Chem Commun* 3425–3437
- Palmisano G, Yurdakal S, Augugliaro V, Loddo V, Palmisano L (2007c) Photocatalytic selective oxidation of 4-methoxybenzyl alcohol to aldehyde in aqueous suspension of home-prepared TiO₂ catalyst. *Adv Synth Catal* 349:964–970
- Park H, Choi W (2005) Photocatalytic conversion of benzene to phenol using modified TiO₂ and polyoxometalates. *Catal Today* 101:291–297
- Park KH, Joo HS, Ahn KI, Jun K (1995) One step synthesis of 4-ethoxy-1, 2, 3, 4-tetrahydroquinoline from nitroarene and ethanol: a TiO₂ mediated photocatalytic reaction. *Tetrahedron Lett* 36:5943–5946
- Park JW, Hong MJ, Park KK (2001) Photochemical reduction of 1, 2-diketones in the presence of TiO₂. *Bull Korean Chem Soc* 22:1213–1216
- Pillai UR, Sahle-Demessie E (2002) Selective oxidation of alcohols in gas phase using light-activated titanium dioxide. *J Catal* 211:434–444
- Rafelt JS, Clark JH (2000) Recent advances in the partial oxidation of organic molecules using heterogeneous catalysis. *Catal Today* 57:33–44
- Sahle-Demessie E, Gonzalez M, Wang Z, Biswas P (1999) Synthesizing alcohols and ketones by photoinduced catalytic partial oxidation of hydrocarbons in TiO₂ film reactors prepared by three different methods. *Ind Eng Chem Res* 38:3276–3284
- Schiavello M (ed) (1988) *Photocatalysis and Environment. Trends and Applications*. Kluwer, Dordrecht
- Shi Y (2004) Organocatalytic asymmetric epoxidation of olefins by chiral ketones. *Acc Chem Res* 37:488–496
- Shimizu K-I, Kaneko T, Fujishima T, Kodama T, Yoshida H, Kitayama Y (2002) Selective oxidation of liquid hydrocarbons over photoirradiated TiO₂ pillared clays. *Appl Catal A* 225:185–191
- Shioya Y, Ikeue K, Ogawa M, Anpo M (2003) Synthesis of transparent Ti-containing mesoporous silica thin film materials and their unique photocatalytic activity for the reduction of CO₂ with H₂O. *Appl Catal A Gen* 254:251–259
- Shiraishi Y, Morishita M, Hirai T (2005a) Acetonitrile-assisted highly selective photocatalytic epoxidation of olefins on Ti-containing silica with molecular oxygen. *Chem Commun* 5977–5979
- Shiraishi Y, Saito N, Hirai T (2005b) Adsorption-driven photocatalytic activity of mesoporous titanium dioxide. *J Am Chem Soc* 127:12820–12822
- Slamet, Nasution HW, Purnama E, Kosela S, Gunlazuardi J (2005) Photocatalytic reduction of CO₂ on copper-doped Titania catalysts prepared by improved-impregnation method. *Catal Commun* 6:313–319
- Subba Rao KV, Subrahmanyam M (2002) Synthesis of 2-methylpiperazine by photocatalytic reaction in a non-aqueous suspension of semiconductor-zeolite composite catalysts. *Photochem Photobiol Sci* 1:597–599
- Subba Rao KV, Srinivas B, Prasad AR, Subrahmanyam M (2000) A novel one step photocatalytic synthesis of dihydropyrazine from ethylenediamine and propylene glycol. *Chem Commun* 1533–1534
- Tan SS, Zou L, Hu E (2006) Photocatalytic reduction of carbon dioxide into gaseous hydrocarbon using TiO₂ pellets. *Catal Today* 115:269–273
- ten Brinks GJ, Arends IWCE, Sheldon RA (2000) Green, catalytic oxidation of alcohols in water. *Science* 287:1636–1639

- Tseng I-H, Wu JCS, Chou H-Y (2004) Effects of sol-gel procedures on the photocatalysis of Cu/TiO₂ in CO₂ photoreduction. *J Catal* 221:432–440
- Wang CM, Mallouk TE (1990) New photochemical method for selective fluorination of organic molecules. *J Am Chem Soc* 112:2016–2018
- Yahaya AH, Gondal MA, Hameed A (2004) Selective laser enhanced photocatalytic conversion of CO₂ into methanol. *Chem Phys Lett* 400:206–212
- Yamashita H, Nishiguchi H, Kamada N, Anpo M, Teraoka Y, Hatano H, Ehara SK, Palmisano L, Sclafani A, Schiavello M, Fox MA (1994) Photocatalytic reduction of CO₂ with H₂O on TiO₂ and Cu/TiO₂ catalysts. *Res Chem Intermed* 20:815–823
- Yamashita H, Fujii Y, Ichihashi Y, Zhang SG, Ikeue K, Park DR, Koyano K, Tatsumi T, Anpo M (1998) Selective formation of CH₃OH in the photocatalytic reduction of CO₂ with H₂O on titanium oxides highly dispersed within zeolites and mesoporous molecular sieves. *Catal Today* 45:221–227
- Yoneyama H, Haga S, Yamanaka S (1989) Photocatalytic activities of microcrystalline titania incorporated in sheet silicates of clay. *J Phys Chem* 93:4833–4837
- Yoshida H, Murata C, Hattori T (1999) Photocatalytic epoxidation of propene by molecular oxygen over highly dispersed titanium oxide species on silica. *Chem Commun* 1551–1552
- Zhang T, You L, Zhang Y (2006) Photocatalytic reduction of p-chloronitrobenzene on illuminated nano-titanium dioxide particles. *Dyes Pigm* 68:95–100
- Zuwei X, Ning Z, Yu S, Kunlan L (2001) Reaction-controlled phase-transfer catalysis for propylene epoxidation to propylene oxide. *Science* 292:1139–1141

Chapter 27

Photocatalytic Organic Syntheses

Hisao Yoshida

Abstract TiO₂ and related photocatalysts can promote productive reactions for organic syntheses, e.g., selective partial oxidation of hydrocarbons by molecular oxygen or water, hydrogenation with water, decarboxylation, C–C bond formation, C–N bond formation, isomerization, and so on. Various kinds of TiO₂ photocatalysts were employed for each reaction, such as anatase and rutile TiO₂, mesoporous TiO₂, platinum-loaded TiO₂, and highly dispersed titanium oxide species on supports. In this chapter, representative photocatalytic systems for organic syntheses are reviewed briefly.

1 Introduction

To realize a sustainable society, current insufficient chemical processes that consume excess energy, require harmful chemicals, and emit byproducts or pollutants should be reconstructed into environmentally harmonious processes. Thus, the development of new environmentally harmonious catalytic reactions that can proceed at room temperature and are totally clean, safe, and efficient with minimum energy consumption, with minimum emission without byproducts, is desired.

Photocatalysis has received much attention for the organic syntheses because of its following excellent potentials. (1) They can proceed under mild condition without hazardous chemicals, which provides us a safety process. (2) The energy of the excitation light is large enough to excite molecules and can compensate an increase in Gibbs free energy of the reaction system, which can promote an up-hill type reaction ($\Delta G > 0$) for synthesis even at room temperature. (3) Some kinds of photocatalysts, typically TiO₂ photocatalysts, exhibit strong oxidative property in

H. Yoshida (✉)
Department of Applied Chemistry, Graduate School of Engineering,
Nagoya University, Nagoya, Japan
e-mail: yoshidah@apchem.nagoya-u.ac.jp

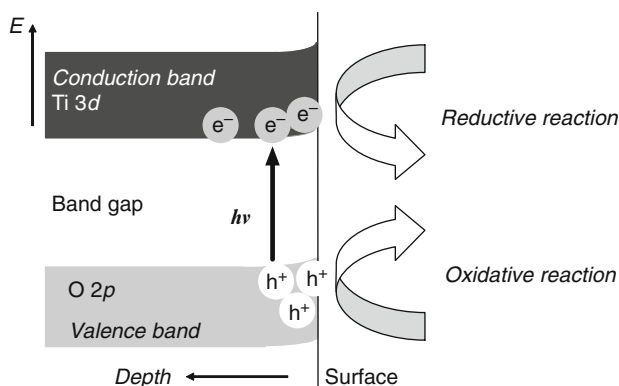


Fig. 1 Photoexcitation to form electrons and holes on TiO₂ photocatalyst, leading to reductive and oxidative elementary reactions

the presence of oxygen and water molecules, and reductive potential for hydrogen evolution from water when platinum is loaded. (4) Many kinds of photocatalysis have unique mechanisms different from those in usual catalytic reactions, which can provide new simple reaction systems. (5) In some cases, photocatalysis can break the thermodynamic equilibrium. These features should allow us to obtain innovative reaction systems in the near future.

In a photocatalytic system, photoenergy produces both excited electrons and holes simultaneously, which could promote reductive and oxidative elementary reactions, respectively (Fig. 1). The type of the total photocatalytic reaction would be categorized by the objective compound; for example, the reaction where the objective compound is oxidized is usually categorized as an oxidative reaction, although the other molecule should be reduced instead. Besides oxidative and reductive reactions, there are many kinds of other photocatalytic reactions, such as isomerization, cyclization, coupling, and so on. However, the elementary reactions for these should be described as oxidation, reduction, and energy transfer.

There are many reports for productive photocatalytic reactions on titanium oxide-based photocatalysts such as TiO₂, platinum-loaded TiO₂, highly dispersed titanium oxide on silica, and so on (Fox and Dulay 1993; Pichat 1994; Kisch 1994; Maldotti et al. 2002; Ohtani et al. 2003; Yoshida 2003; Palmisano et al. 2007; Yuliati and Yoshida 2008; Shiraiishi and Hirai 2008). In this chapter, representative photocatalytic reactions for organic syntheses such as partial oxidations and other reactions are briefly reviewed.

2 Oxidative Photocatalytic Synthesis

TiO₂ photocatalysts have been intensively studied and in recent years widely applied to environmental purification, including self-cleaning surfaces, due to their high photocatalytic activities for complete oxidation of organic compounds. Continuous photoirradiation on TiO₂ should produce many electrons and holes on the surface

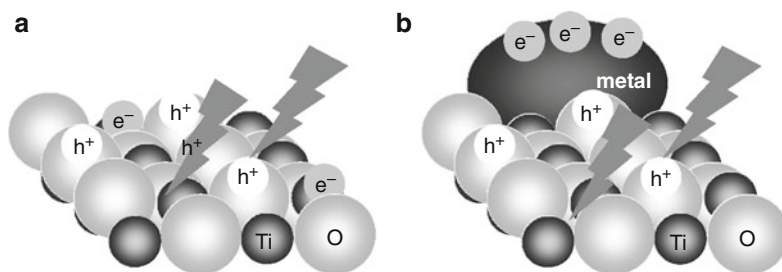
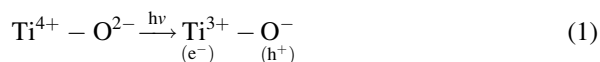


Fig. 2 Illustrations of photoexcitation state of TiO₂ surface (a) and metal-loaded TiO₂ surface (b)

titanium and oxygen atoms (Fig. 2a), although these electrons and holes have only a short lifetime. When suitable metal particles such as platinum nanoparticles exist on the surface (Fig. 2b), the electrons tend to be localized on the metal particles, which promotes separation between electrons and holes. This provides longer lifetime of the excited state and enhances the photocatalytic activity. It is suggested that when the reaction starts, these multiple active holes on the surface would strongly promote complete oxidation of substrate with the participation of oxygen and/or water molecules. Therefore, in order to realize the oxidative organic syntheses on TiO₂, we must control the oxidation activity. Some strategies have been employed, including the design of the photocatalysts and the design of the reaction condition, for example, using highly dispersed titanium oxide as a single site on support, or using other mild oxidants rather than molecular oxygen.

In the former case, the photoexcitation on highly dispersed and isolated titanium oxide species on support such as silica has been explained as follows. Upon photoirradiation, these species can be excited through charge transfer processes as shown in (1) (Anpo et al. 1985; Anpo and Che 2000).



When the support is an insulator, the excitation state is localized at the isolated titanium oxide species; in other words, an exciton is localized and isolated. In this case, the photoexcitation could be described on a molecular orbital level; the schematic drawing of photoexcitation mechanism is shown in Fig. 3a. An electron in the ground state of the Ti–O bond is excited by photoirradiation to an unoccupied singlet orbital, followed by further transition to the triplet state via intersystem crossing if available. This final excitation state would have a long lifetime since further transition to ground state is inhibited. Figure 3b shows an illustration of photoexcited highly dispersed titanium oxide species on silica, where the photoactive sites are proposed to be tetrahedral TiO₄ species. This localized excitation state on the single site should be more favorable for selective reactions, such as partial oxidation, with unique selectivity. This would be the most characteristic property of these kinds of photocatalysts.

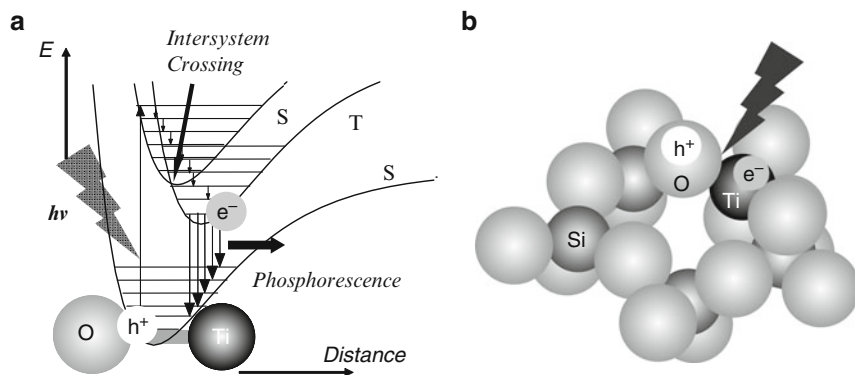


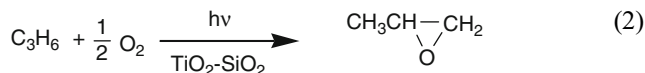
Fig. 3 (a) Photoexcitation in single-site photocatalyst and (b) an illustration of localized photoexcitation state of active sites

For the latter case, the reaction condition should be controlled to give a desired active oxygen species for the reaction, typically with a limitation of molecular oxygen and water, which provides selective and unique oxidative reactions. For example, TiO_2 or Pt/TiO_2 photocatalysts in the presence of oxygen in aqueous solution oxidize many kinds of organic compounds to CO_2 and H_2O by generating some kinds of active oxygen radical species such as hydroxyl radical ($\cdot\text{OH}$), superoxide anion radical ($\text{O}_2^{\cdot-}$), hydroperoxide radical (HO_2^{\cdot}), singlet oxygen ($^1\text{O}_2$), and hydrogen peroxide (H_2O_2) on the surface. On the contrary, in the absence of oxygen, the objective compounds are oxidized by limited kinds of oxidants such as the surface hydroxyl radical ($\cdot\text{OH}$).

Selective oxidation of hydrocarbons has been reviewed elsewhere (Pichat 1994; Maldotti et al. 2002) and only representative examples are shown in this section.

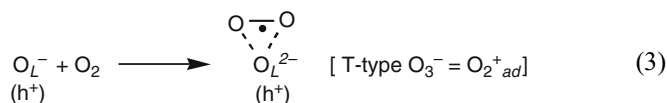
2.1 Photoepoxidation of Alkenes by Molecular Oxygen

The epoxidation of propene to propene oxide (PO) is an important catalytic process in the chemical industry. However, the direct propene epoxidation by molecular oxygen, which is an ideal oxidant from the economic and environmental viewpoints, is difficult due to the high reactivity of the allylic C–H bonds which leads to side reactions. Photocatalytic systems have been proposed as one of the potential approaches for partial oxidation of hydrocarbons by molecular oxygen. Silica and silica-based photocatalysts have been reported to be active in photoepoxidation of propene by molecular oxygen (Tanaka et al. 1993; Yoshida et al. 1997; Yoshida et al. 1999; Yoshida et al. 2000b; Murata et al. 2001; Murata et al. 2002; Murata et al. 2003; Yoshida et al. 2003a; Amano et al. 2004). Among them, highly dispersed titanium oxide on silica exhibits high selectivity with high activity such as 60% (2) (Yoshida et al. 1999; Murata et al. 2002; Murata et al. 2003).



In the diffuse reflectance UV-visible spectrum, the Ti species in the sol-gel-prepared $\text{TiO}_2\text{-SiO}_2$ sample of low Ti content (less than 0.34 mol%) shows a narrow adsorption band only in the region of wavelength less than 250 nm (Fig. 4), suggesting that the major species are atomically dispersed tetrahedral TiO_4 species at a single site. The sample (e.g., 0.08 mol% Ti) shows the highest PO selectivity such as 60% at 4.4% conversion after 2-h irradiation in a closed system, indicating that the isolated TiO_4 species are responsible for the PO formation with high selectivity. On the contrary, aggregated titanium oxide species on the samples of larger Ti content are active mainly for the side reactions to form aldehyde compounds (Murata et al. 2003).

From the ESR and stoichiometric reactivity tests of radical species, the following reaction mechanism is proposed (Murata et al. 2003). On the isolated tetrahedral Ti species, a $[\text{Ti}^{3+}\text{-O}_L^-]$ radical pair is formed through electron transition from lattice oxygen (O_L^{2-}) to titanium (Ti^{4+}) by UV excitation (1). The Ti^{3+} moiety, the excited electron on Ti, reacts with O_2 to form O_2^- , which is stable even at room temperature. However, the O_2^- radical cannot activate propene. The O_L^- moiety, a hole center on lattice oxygen, reacts with O_2 to form T-type O_3^- (3) as confirmed by ESR spectra shown in Fig. 5.



Note that these photoformed T-type O_3^- species are electrophilic since they originate from a hole (h^+) and O_2 . It was confirmed that the hole moved to the

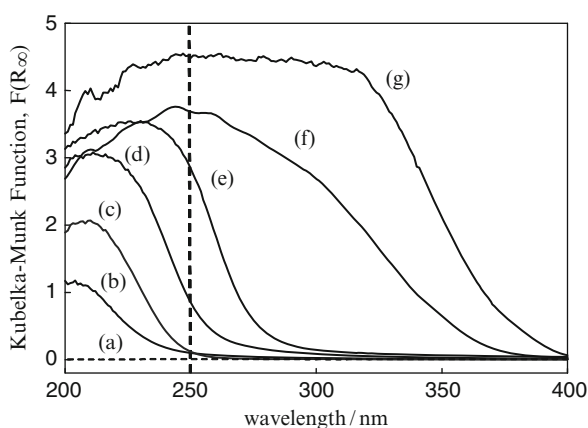


Fig. 4 DR-UV spectra of SiO_2 (a), $\text{TiO}_2\text{-SiO}_2$ samples with Ti contents of 0.08 (b), 0.34 (c), 1.0 (d), 4.1 (e), 8.3 mol% (f), and bulk TiO_2 (mixture of anatase and rutile) (g)

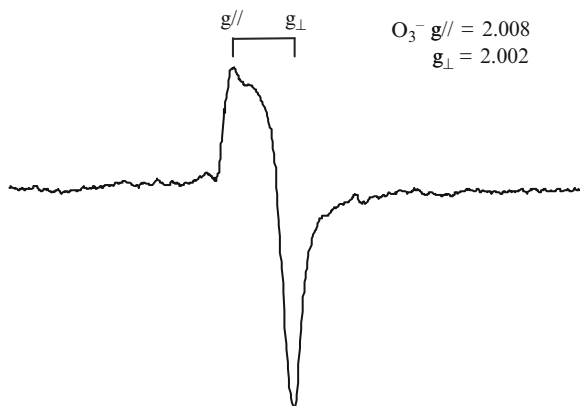


Fig. 5 ESR spectra of photoformed T-type O_3^- species on the TiO_2 - SiO_2 sample with 0.34 mol% Ti in the presence of O_2 (1.0 Torr). This spectrum was obtained from the spectrum recorded after photoirradiation at 77 K by subtracting the spectrum of O_2^- species recorded after successive warming to room temperature

adsorbed O_2 moiety from the O_L^- (Murata et al. 2005). Thus, this O_3^- radical can be expressed as adsorbed O_2^+ species on the lattice oxygen. This electrophilic O_2^+ radical species reacts with the double bond of propene to yield PO as shown in Fig. 6. In this reaction, the localization of the hole on the O_2^+ species seems to be important. The lower selectivity of the aggregated titanium oxide species would be attributed to the lower stability of the O_3^- and high activity for the consecutive reaction of PO. Since aggregated titanium oxide species would form band structure to some extent, it is considered that the excitation state could not be localized on a certain bond of the active species. The sol-gel method is more suitable for formation of the highly dispersed TiO_4 species than the conventional impregnation method (Yoshida et al. 1999; Murata et al. 2002).

The photocatalytic epoxidation of propene was also examined in a flow type reactor as a step toward the practical use (Amano et al. 2006). Table 1 shows the results of propene epoxidation of propene using some kinds of photocatalysts. It is noted that $\text{TiO}_2/\text{SiO}_2$ photocatalyst exhibits higher PO selectivity such as 50% at high conversion level than other silica-based photocatalysts such as $\text{Nb}_2\text{O}_5/\text{SiO}_2$ (Tanaka et al. 1993), MgO/SiO_2 (Yoshida et al. 1997), $\text{CrO}_3/\text{SiO}_2$ (Murata et al. 2001), ZnO/SiO_2 (Yoshida et al. 2003), $\text{V}_2\text{O}_5/\text{SiO}_2$ (Amano et al. 2004). On the contrary, TiO_2 semiconductor photocatalyst cannot promote the selective epoxidation of propene but shows a high conversion for complete oxidation.

Alkene epoxidation by molecular oxygen over $\text{TiO}_2/\text{SiO}_2$ photocatalyst has been applied to larger molecules in liquid phase. Ti-containing mesoporous silica with hexagonal structure prepared by a conventional surfactant-templating method shows photocatalytic activity for epoxidation of cyclohexene in a gas-solid heterogeneous reaction system, although the selectivity is low, such as 11% at 9% conversion (Shiraishi et al. 2005a). However, in a liquid-solid heterogeneous reaction system with acetonitrile (MeCN), the selectivity for epoxidation of

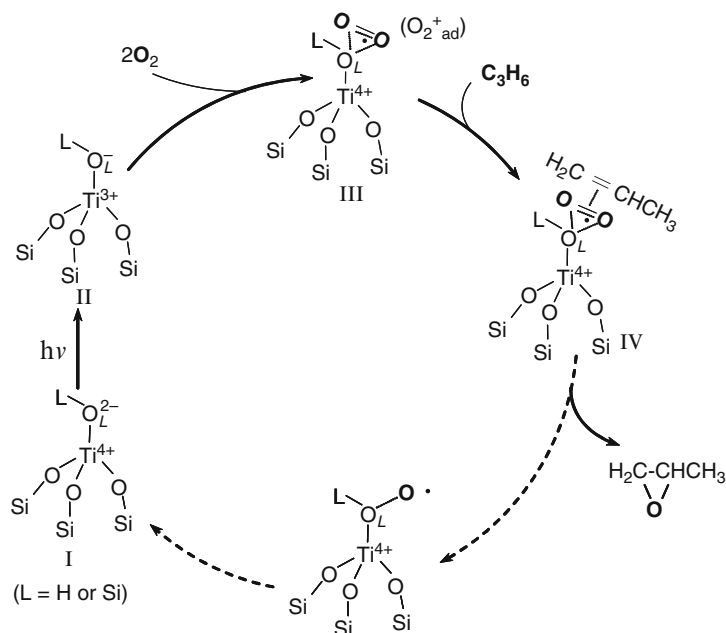


Fig. 6 Proposed mechanism for the formation of PO over the TiO₄ species on silica

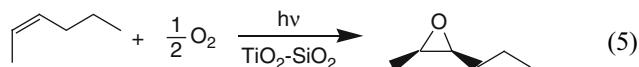
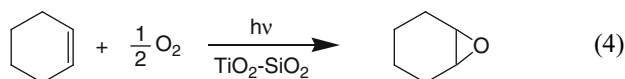
Table 1 Results of photooxidation of propene by O₂ at 303 K^a

Photocatalyst ^b	Conversion (μmol/h)	PO yield (μmol/h)	PO selectivity (%)
TiO ₂ (0.1)/SiO ₂	36	18	50
V ₂ O ₅ (0.15)/SiO ₂	69	26	37
Nb ₂ O ₅ (0.1)/SiO ₂	31	12	40
CrO ₃ (0.1)/SiO ₂	3	1	42
ZnO(0.1)/SiO ₂	3	2	62
MgO(0.1)/SiO ₂	2	1	74
SiO ₂	2	1	73
TiO ₂ (JRC-TiO-4)	67	0	0

^a Catalyst 0.3 g, Total flow rate 100 ml/min, propene 20%, O₂ 10%, irradiation, 240 < λ < 440 nm.

^b The values in parentheses are contents of metal, M/(M + Si) mol%

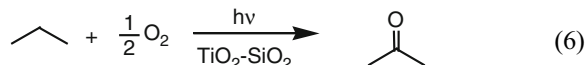
cyclohexene was enhanced to 71% at a similar conversion level (4). Photocatalytic epoxidation of various cyclic and linear olefins in the liquid–solid system with MeCN also proceeds with excellent selectivity (more than 98%). In these systems, the configuration around C=C moiety of olefins retained in the resulting epoxide, for example, *cis*- and *trans*-2-hexene are converted to *cis*- and *trans*-2,3-epoxyhexane, respectively, with more than 99% selectivity (5).



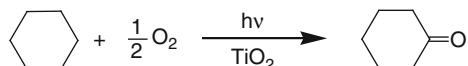
In organic solvents, TiO_2 photocatalyst of both anatase and rutile types can also promote the selective epoxidation of linear olefins such as 1-hexene, 1-decene, and 1-hexadecene by molecular oxygen (Ohno et al. 1998). Among them, the highest epoxidation selectivity (79%) was obtained in the case of 1-hexene. In these reactions, it is proposed that the direct oxidation of the olefins by hole on TiO_2 occurred first to form a cation radical of olefins, followed by the reaction with activated oxygen by an excited electron.

2.2 Photooxidation of Alkanes by Molecular Oxygen

Photooxidation of propane by using molecular oxygen has been investigated on some kinds of highly dispersed metal oxide photocatalysts on silica support such as alkali-ion-modified $\text{V}_2\text{O}_5/\text{SiO}_2$ (Amano and Tanaka 2006) and $\text{TiO}_2/\text{SiO}_2$ (Yoshida et al. 1996; Yoshida et al. 1997; Tanaka et al. 2002). For selective oxidation of propane by molecular oxygen on $\text{TiO}_2/\text{SiO}_2$ samples, acetone and CO_x (CO or CO_2) are obtained as major products and ethanal, propanal, propene, and ethene are detected as minor products. Acetone was obtained as the main product on the $\text{TiO}_2/\text{SiO}_2$ sample having moderate aggregation of TiO_6 clusters, with the highest selectivity of 95% (Yoshida 1997; Tanaka et al. 2002) (6).



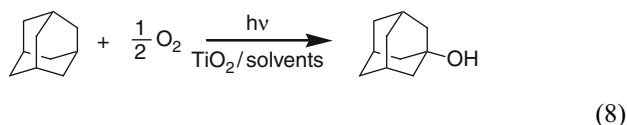
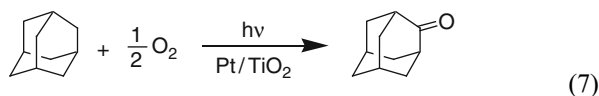
Photooxidations of liquid alkanes by molecular oxygen on TiO_2 photocatalyst also have been investigated (Giannotti et al. 1983; Pichat 1994), where the major products are the corresponding ketones. For example, for photooxidation of cyclohexane, the main product was cyclohexanone, while cyclohexanol and CO_2 are observed as the minor products (Mu et al. 1989) (7). When platinum-loaded TiO_2 is used, the selectivity for cyclohexanol increased, although it is still a minor product.



In the liquid–solid system using TiO_2 photocatalyst, the solvent effect on products selectivity and reaction rate can be observed; for example, in the case of

cyclohexane photooxidation in neat cyclohexane, cyclohexanone is obtained selectively; on the contrary, the presence of CH_2Cl_2 promotes also the formation of cyclohexanol (Boarini et al. 1998).

As for the photooxidation of adamantane using Pt/TiO_2 , 2-adamantanone is selectively yielded (Giannotti et al. 1983) (8). However, in a mixed organic solvent of CH_3CN and $\text{C}_3\text{H}_7\text{CN}$, 1-adamantanol is obtained as the major product by using TiO_2 photocatalyst (Ohno et al. 2003) (9).



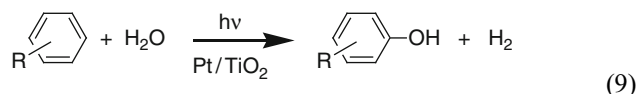
2.3 Photooxidation of Aromatic Compounds by Oxygen or Water

Phenols are also important industrial chemicals due to their wide usage. In current processes, phenols are produced through multistep processes using molecular oxygen, such as so-called cumene process, cymene process, and so on. However, these processes involve consumption of propene and production of acetone, and these multistep processes with a low overall yield typically less than 5% should require high energy consumption. Formation of byproducts is also a problem; especially in the case of alkylphenols production, the selectivity should be limited due to the undesirable oxidation of side chains. Thus, development of novel and simple processes is desired in the view point of “green chemistry.”

Several investigations of photooxidation of benzene and toluene have been carried out by using TiO_2 and Pt/TiO_2 photocatalyst with water and molecular oxygen in the early 1980s (Izumi et al. 1980; Fujihira et al. 1981a, b; Fujihira et al. 1982; Shimamura et al. 1983; Teratani et al. 1984; Takagi et al. 1985). In these cases, the presence of molecular oxygen seems necessary to accelerate the photocatalytic oxidation of benzene and toluene. However, it is suggested that the photoexcited electrons on TiO_2 could reduce oxygen species, which promotes the oxidation of the side chain of toluene, while the photoformed holes oxidize water and toluene, producing cresol (Shimamura et al. 1983). In the experiments in acetonitrile solvent, it was revealed that the presence of water increased the formation of cresol.

Recently, selective aromatic-ring hydroxylations of benzene and alkylbenzenes to produce the corresponding phenols were successfully carried out over platinum-loaded TiO_2 photocatalyst by using water molecule as an oxidant in the absence of oxygen (Yoshida et al. 2008). Although some side reactions such as coupling, side-chain oxidation, and hydrogenation of phenols were also observed, the amounts of

these byproducts could be reduced by the selection of irradiation light wavelength around 400 nm and optimization of Pt-loading amount around 1.0 wt%. The former would limit the direct hole oxidation of alkylbenzene, and reduce the coupling reactions, while the latter would be important for the inhibition of coupling reactions and formation of H₂. When the selectivity for the aromatic-ring hydroxylation is high, the stoichiometric formation of hydrogen to that of phenols can be experimentally confirmed, indicating that water molecule would function as an oxidant to produce phenols and hydrogen as shown in (10).



For example, the hydroxylation selectivity was 97% for toluene and more than 99% for *tert*-butyl benzene after photoirradiation for 3 h. It is proposed that the photo-formed hole on the TiO₂ surface would react with water molecule and produce an electrophilic active oxygen species on the surface, and these would selectively attack the aromatic ring to form phenols. The phenols are hardly converted further, resulting in the high selectivity.

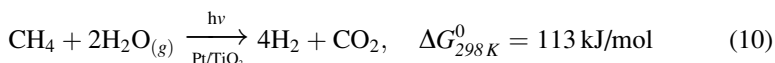
Mesoporous TiO₂ without addition of a noble metal was recently found to promote the hydroxylation of benzene to form around 80% phenol selectively. (Shiraishi et al. 2005b). It was claimed that the high selectivity over the additive-free TiO₂ was obtained due to the adsorption property of mesoporous TiO₂; this TiO₂ adsorbed benzene but scarcely adsorbed phenol.

2.4 Photooxidation of Methane by Water to Yield Hydrogen

Hydrogen is an environmentally benign fuel, which is suitable for the sustainable society, and its production from renewable resources and natural energy is desired. Methane is not only used as a fuel and a chemical resource, but it also attracts much attention as a hydrogen resource due to its highest H/C value among hydrocarbons, and actually several systems for steam reforming of methane including water–gas shift reaction have been established for hydrogen production. Although methane is converted to CO₂ in the steam reforming of methane, CO₂ could become the biomass through photosynthesis and the biomass could be again converted to methane by the aid of biotechnology or biomass technology. Thus, if biomethane is employed, methane is essentially recognized as one of the renewable resources. However, it is known that the steam reforming system involves endothermic reaction and requires high temperature, which consumes a large energy.

The photocatalytic reactions to produce hydrogen can proceed between water and many kinds of reductants such as alcohols (Kawai and Sakata 1980a, b; Sakata and Kawai 1981), CO (Sato and White 1980a, b,) and ethane (Sato and White

1980a, b); some kinds of carbon-related materials such as active carbon (Sato and White 1980b; Kawai and Sakata 1979), coal, tar sand (Hashimoto et al. 1984); and also some kinds of biomass such as sugar, starch, and cellulose (Kawai and Sakata 1980a, b). Compared with them, methane, as the most stable hydrocarbon, gives a largely positive Gibbs free energy change for this kind of reaction. Recently, Pt/TiO₂ photocatalyst was found to produce hydrogen from methane and water in a mild condition upon photoirradiation, which can be described as *photocatalytic steam reforming of methane* (PSRM) (Yoshida et al. 2008):

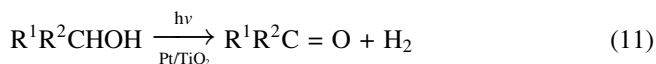


In a flow-type photocatalytic reactor, H₂ and CO₂ were obtained as main products on Pt(0.1 wt%)/TiO₂, with only a trace amount of C₂H₆ and CO as byproducts. The molar ratio of H₂ to CO₂ in the outlet gas was about 4, suggesting that the main reaction would be PSRM as shown in (11).

The surface intermediates with estimated average composition of (CH₂O)_n were formed during the reaction, and they can react further with water to produce H₂ and CO₂ under photoirradiation. The accumulation of the surface intermediates is one of the important factors determining the photocatalytic reaction rate; too much accumulation of surface intermediates decreases the formation rate of the products, while moderate amount of them makes the surface more hydrophobic and increases the adsorption of methane, so that the reaction rate is considerably enhanced.

2.5 Photooxidation of Alcohols by Water

In the absence of oxygen, Pt/TiO₂ photocatalyst converts alcohols such as methanol, ethanol, and 2-propanol to the corresponding dehydrogenation products such as formaldehyde, acetaldehyde, and acetone, respectively, with the formation of equimolar H₂ (12), while *t*-butyl alcohol is converted into 2,5-dimethyl-2,5-hexanediol with the formation of H₂ through intermolecular dimerization in this system since *t*-butyl alcohol has no α -hydrogen (Ohtani et al. 2003). In these oxidative reactions, alcohols are oxidized by photoformed holes, while photoexcited electrons reduce water (or H⁺) to form H₂.



3 Other Photocatalytic Synthesis Reactions

Although the studies on oxidation are the most major in the field of photocatalytic syntheses, other reactions also have been widely studied so far, such as reduction, C–C bond formation, C–N bond formation, isomerization, and so on. In this section, several representative photocatalytic reactions are shown.

3.1 *Photocatalytic Hydrogenation of Alkynes and Alkenes with Water*

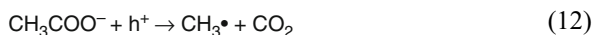
Photocatalytic reactions of alkynes and alkenes with adsorbed water have been investigated over TiO_2 (Boonstra and Mutsaers 1975). The main reaction is hydrogenation, accompanied by double and triple bond fission (hydrogenolysis). The formation of the oxidation products such as CO and CO_2 is also confirmed (Anpo et al. 1984a). Unloaded TiO_2 predominantly gives the hydrogenolysis products, while Pt-loaded TiO_2 significantly enhances hydrogenation reaction without the bond fission (Anpo et al. 1984a, b). For example, propyne is converted to methane and ethane rather than propene over TiO_2 photocatalyst, while the formation of propene is much enhanced over Pt/ TiO_2 . In addition, Pt/ TiO_2 shows the material balance between the yields of the reduction and oxidation products. ESR study revealed that the photoformed electron located on Ti^{3+} could not be easily observed on Pt/ TiO_2 , meaning that the photoformed electron can be easily transferred from TiO_2 to Pt particles. The electron on Pt would promote the reduction of H^+ to form H radical, promoting the hydrogenation of unsaturated hydrocarbons without bond fission. On the contrary, the photoformed hole located on TiO_2 would oxidize OH^- rather than hydrocarbons, promoting oxidation reaction.

The quantum size effect is obviously confirmed in this reaction system (Anpo et al. 1987). For both rutile and anatase TiO_2 photocatalysts, the quantum yields for the photohydrogenolysis increase when the particle size of TiO_2 decreases. In particular, for the samples of particle size less than 10 nm, a significant increase in the yields is observed for both types of TiO_2 photocatalysts. When the particle size of the TiO_2 decreases, the blue shift of the absorption band edge in UV spectra becomes significant, although the BET surface area increases monotonously. The quantum yields for the photohydrogenation over Pt/ TiO_2 photocatalyst are also much affected by the small particle size. The increase in the quantum yields of both photocatalytic reactions with decreasing particle diameter of TiO_2 is closely associated with the size quantization effect, resulting in a large modification of the energy level in the photoexcited state of TiO_2 particles. The high efficiency of the low Ti content samples among the samples of the highly dispersed titanium oxide anchored on porous Vycor glass (Anpo et al. 1985) and TiO_2 – SiO_2 mixed oxide prepared by coprecipitation method (Anpo et al. 1986a, b) might be related to this size effect.

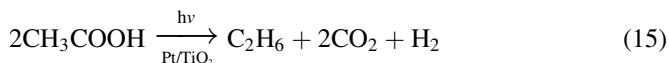
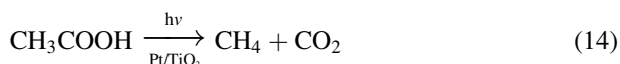
In these photoreaction systems with TiO₂, the bond fission of the unsaturated bond occurs on TiO₂ surface with the trapped electron and hole pairs. The close association of photoformed electron and hole pairs is suggested to be important for the bond fission. When this reaction is examined on highly dispersed titanium oxide anchored on porous Vycor glass (Anpo et al. 1985) and TiO₂-SiO₂ mixed oxide prepared by coprecipitation method (Anpo et al. 1986a, b), the samples of low Ti content show an efficient photocatalytic activity, supporting that the electron-hole pair on the surface promotes this reaction.

3.2 Photocatalytic Decarboxylation of Carboxylic Acid

Kolbe reaction of acetic acid yields ethane and carbon dioxide from acetic acid/acetate electrolysis. Similarly, photoassisted oxidation of acetate ion produces ethane in acetonitrile solution at TiO₂ electrodes in both the single-crystal and chemical vapor-deposited polycrystalline forms, which is described as photo-Kolbe reaction (Kraeutler and Bard 1977) (13 and 14).



On the contrary, Pt-loaded TiO₂ photocatalyst promotes decarboxylation of acetic acid to yield methane and carbon dioxide, with minor products of ethane and hydrogen in aqueous media in the absence of oxygen (Kraeutler and Bard 1978a) (15 and 16).



Although the evolution of carbon dioxide in this photocatalytic reaction is common with the usual Kolbe product mentioned above, product distribution is different from each other; i.e., the photocatalytic reaction over Pt-loaded TiO₂ shows evolution of methane. However, the fraction of ethane increases with increasing gas evolution rate (Kraeutler and Bard 1978b), suggesting that in both cases, methyl radical should be formed commonly as one of the active intermediates and ethane should be formed by the coupling of two methyl radicals. In these reactions, the Gibbs free energy of the reaction system decreases.

This photo-Kolbe reaction can be applied to other saturated carboxylic acids such as propionic acid, *n*-butyric acid, *n*-valeric acid, pivalic acid, or adamantane-1-carboxylic acid to yield corresponding alkane and carbon

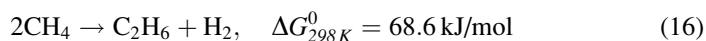
dioxide (Kraeutler and Bard 1978b). Adipic acid, a six-carbon saturated aliphatic dicarboxylic acid, is also decomposed by Pt/TiO₂ photocatalyst to yield valeric acid, *n*-butane, and carbon dioxide where the photo-Kolbe reaction occurs (Izumi et al. 1981).

Detailed studies revealed the mechanism of photo-Kolbe reaction to be complex even in the case of acetic acid due to many side reactions (Yoneyama et al. 1983; Sakata et al. 1984; Kaise et al. 1993).

3.3 Photocatalytic Direct Methane Coupling

Photocatalysts can promote dimerization of cyclic enol or allyl ethers and cyclic olefins (Kisch 1994). The substances are photocatalytically activated to form dehydrogenated radicals, which form products through C–C bond formation. Recently, direct methane coupling as one of the most difficult dimerizations has also been investigated.

Methane utilization is one of the important issues that has been investigated for many decades. One of the attractive studies is on direct conversion of methane to higher hydrocarbons and hydrogen,



which was found to proceed photocatalytically at room temperature (Kato et al. 1998; Yoshida et al. 2000a; Yoshida et al. 2002). This reaction is an up-hill type reaction where photoenergy compensates an increase in Gibbs free energy of the reaction system. Several silica-based photocatalysts have been reported to exhibit activities for the photoreaction, such as silica–alumina (Kato et al. 1998; Yoshida et al. 2000a, b; Yoshida et al. 2002), silica-supported zirconia (Yoshida et al. 2003b), silica-supported magnesia (Yuliati et al. 2005a), H⁺-exchanged zeolites (Kato et al. 2002), mesoporous silica materials (Yuliati et al. 2006a), and ceria-based photocatalysts (Yuliati et al. 2005b), as well as titania-loaded photocatalysts such as silica–alumina–titania (Yoshida et al. 2003c), silica-supported ceria–titania (Yuliati et al. 2006b, c), and silica–titania prepared by sol–gel method (Yuliati et al. 2006b, c). The highly dispersed metal oxide species has been suggested to play an important role in the photocatalytic non-oxidative direct methane coupling (Yoshida 2003; Yoshida 2005). Photoluminescence study revealed that atomically isolated metal–oxygen bond, e.g., Mg–O, Al–O, and Zr–O, on silica matrix exhibits a characteristic phosphorescence spectrum with fine structure due to vibrational energy levels of ground state for a certain metal–oxygen bond, and these photo-active sites are suggested as photocatalytic active sites.

On the contrary, TiO₂ photocatalyst cannot function as photocatalysts for this reaction. Although ethane is obtained, production of hydrogen as product is not observed (Yoshida et al. 2003a, b, c). This would be due to the fact that TiO₂ can be easily reduced under photoirradiation in the presence of reductive gases such as

methane (reactant), and ethane and hydrogen (products). Among these highly dispersed metal oxide photocatalysts mentioned above, the titanium-related catalysts exhibited high performance for this photocatalytic direct methane coupling. It is suggested that the high dispersion on silica matrix should be important to make the photocatalytic active sites stable under such a reductive atmosphere.

In order to increase the photocatalytic activity of these highly dispersed photocatalysts, some ideas have been examined to increase the number of photocatalytic active sites and to develop the activity of the active sites using additives. On TiO₂-SiO₂ system, the well-controlled sol-gel process was examined to form the large number of the active sites (Yuliati et al. 2006a, b, c). On the contrary, as a new concept to obtain a large number of the active sites as a single site, doubly loaded photocatalysts were demonstrated by using Ti and Ce species, both of which have been found to be photocatalytically active for this reaction (Yuliati et al. 2006a, b, c). The photocatalysts were prepared by a simple two-step impregnation method, where the Ti species was dispersed on silica in advance, followed by loading the Ce species.

On the silica-alumina-titania photocatalysts prepared by sol-gel method, synergy effect of TiO₄ and AlO₄ tetrahedral species on silica matrix is clearly demonstrated as these species pairs exhibit a unique photoabsorption band at 220–300 nm, centered at 245 nm, in the UV spectrum and the wavelength region is actually responsible for the photocatalytic activity (Yoshida et al. 2003a, b, c).

It should be noted that the ethane yield on these photocatalysts was much higher than the one calculated from the thermodynamic equilibrium constant (Yuliati, and Yoshida 2008). This means that the photocatalyst selectively promotes the forward reaction, methane activation (probably to form methyl radical), than the reverse reaction, activation of ethane and/or hydrogen. This would be one of the advantages of the photocatalytic systems as mentioned above.

3.4 Photocatalytic Production of Amino Acids

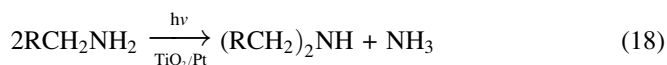
Photoirradiation of aqueous 2 M NH₄Cl or NH₃ (ca. 28%) deaerated solution under slow, continuous bubbling of methane in the presence of Pt/TiO₂ photocatalyst for more than 60 h produced a mixture of amino acid, although the total yield of amino acid was less than 0.5 μmol (Reiche and Bard 1979). The products are the mixture of amino acids such as glycine, alanine, serine, aspartic acid, and glutamic acid. For example, the reaction can be described as follows:



This is an up-hill type reaction with a large increase in Gibbs free energy ($\Delta G_{298\text{K}} = 204$ kJ/mol), which is characteristic of photocatalysis. This result is very interesting in considering the initial stage of chemical evolution and prebiological synthesis of organic compounds from simple components. This reaction also provides some possibilities for the development of new chemical synthesis methods.

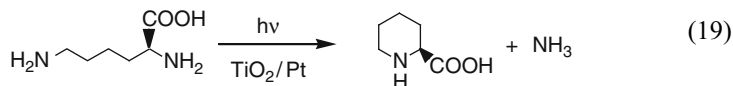
3.5 Photocatalytic Deaminocondensation

In an aqueous solution, in the absence of oxygen, Pt/TiO₂ photocatalyst can convert primary amines having branched hydrocarbon chain, such as iso-propylamine, to ketones through deamination, with the equimolar formation of H₂ (Ohtani et al. 2003). In these cases, the amines would be oxidized by photoformed holes directly or indirectly, and water would be reduced by photoformed electron. However, a primary amine having a straight chain, e.g. propylamine, is converted into its corresponding secondary amine, e.g., dipropylamine, with the formation of NH₃ in the presence of TiO₂/Pt (TiO₂ ground with 5 wt% platinum black) (Nishimoto et al. 1983). In this case, the amount of H₂ evolution observed was very small. Thus, this reaction is described as intermolecular deaminodimerization (18).



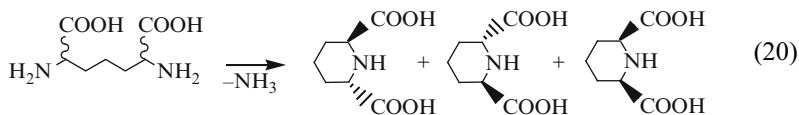
For this reaction, the amines must possess at least one methylene group neighboring the amino group. When the substrate has two terminal amino groups, intramolecular deaminocondensation (deaminocyclization) occurs to yield a cyclic secondary amine, e.g., 1,4-diaminobutane (tetramethylenediamine) is converted into pyrrolidine (tetramethyleneimine) with high yield (67% for 20 h) and high selectivity (93%, molar ratio of product secondary amine to NH₃) (Nishimoto et al. 1983).

Photocatalytic one-step syntheses of cyclic imino acids can be promoted by aqueous TiO₂/Pt suspension (Ohtani et al. 1990). For example, pipercolinic acid (PCA) is obtained from L-lysine with the formation of NH₃.



In this reaction process, racemic products should be obtained when the α -amino group is activated and the original configuration is lost, while optically active L-product should be obtained when ϵ -amino group is activated and the original configuration of α -carbon is retained. It is noted that TiO₂/Pt photocatalyst prefers L-rich product and CdS/Pt photocatalyst gives racemic products (Ohtani et al. 1990).

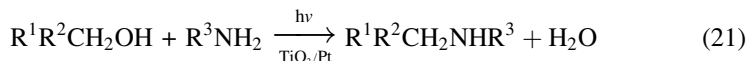
As for the deaminocyclization of 2,6-diaminopimelic acid to yield piperidine-2,6-dicarboxylic acid (PDC), TiO₂/Pt gives *cis*-PDC and racemic PCA (decarboxylated byproducts). On the contrary, bare CdS gives *trans*- and *cis*-PDC without appreciable formation of PCA. Platinum addition accelerates *cis*-PDC formation preferably (Ohtani et al. 1995; Ohtani et al. 2003).



The *cis/trans* selectivity, which is affected by the addition of platinum, is explained by the proposed mechanism for the reduction of a cyclic Schiff base (CSB) intermediate (Ohtani et al. 2003). Assuming that the CSB would adsorb at nitrogen leading to a carboxylic group to upside of the surface, the *trans*-form might be produced if the semiconductor surface reduces the adsorbed CSB by excited electron, followed by hydrogen addition from the solution phase (Fig. 7a). On the contrary, the *cis*-form might be produced if two activated hydrogen atoms on platinum surface are added to CSB (Fig. 7b). In the case of TiO₂/Pt, since reduction by H atoms would predominantly occur on platinum surface where excited electrons are localized, *cis*-PDC would be produced mainly.

3.6 Photocatalytic N-Alkylation of Amines or Ammonia

Photocatalytic syntheses of secondary and tertiary amines from amines and alcohols can be carried out by TiO₂/Pt suspension (Ohtani et al. 1986a, b). By selecting the amines and alcohols, various symmetrical and unsymmetrical amines are synthesized upon photoirradiation through N-alkylation of amines, e.g., N-ethyl and N-isopropyl derivatives are produced in ethanol and 2-propanol, respectively. Tertiary alcohol such as 2-methyl-2 propanol cannot give appreciable amount of N-alkylated products.



Byproducts are small amounts of H₂ and dehydrogenated products of the alcohols, aldehydes, or ketones. It is proposed that this photocatalytic N-alkylation of amines with alcohols starts with photocatalytic dehydrogenation of alcohols as shown in (12) mentioned above. Then, between the formed carbonyl compound and the amine, dehydration should occur, followed by thermal hydrogenation of the intermediates on platinum; the reaction scheme for primary amine is described as follows (23). Secondary amines are produced by the reaction between the primary amine and the carbonyl compound.

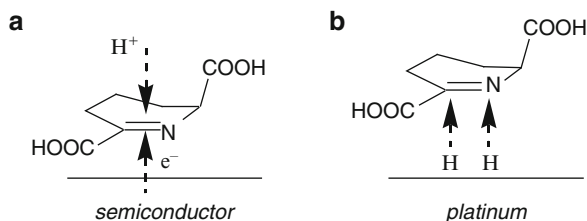
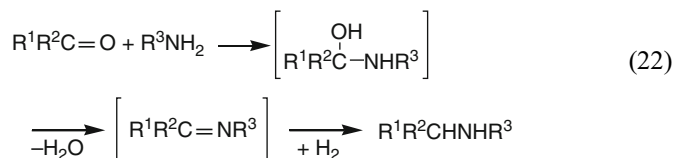
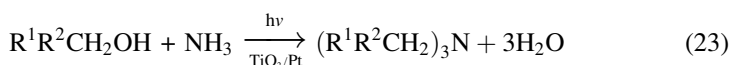


Fig. 7 Possible mechanism of *trans*- and *cis*-piperidine-2,6-dicarboxylic acid (PDC) formation on the photocatalyst surface. (a) *trans*-PDC formation typically on the semiconductor, (b) *cis*-PDC formation typically on platinum



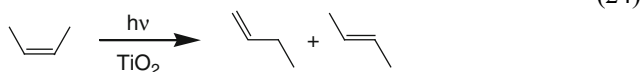
Among the primary amines used in this study, benzylamine was N-alkylated most readily and aniline most slowly (Ohtani et al. 1986a, b), suggesting that the methylene group neighbor to amine should be important. This implies the other possibility for the reaction mechanism, where an amino group is activated to become an imino group by releasing hydrogen at α -carbon (Nishimoto et al. 1983).

In a similar way, ammonia in alcohols is also N-alkylated to produce tertiary amines by photoirradiated TiO_2/Pt (Ohtani et al. 1986a, b).



3.7 Photocatalytic Isomerization of Alkenes

Isomerization of alkenes has been investigated on metal oxides such as porous silica-glass (Morikawa et al. 1977) and on metal sulfides such as CdS (Al-Ekabi and Mayo 1984). In these systems, mainly the *cis-trans* isomerization, i.e., geometrical isomerization, proceeds photocatalytically. On the contrary, over TiO_2 and ZnO, double bond shift isomerization and geometrical isomerization of butenes are enhanced under UV irradiation (Kodama et al. 1982).



On TiO_2 , reactivity of 2-butenes is much higher than that of 1-butene, which is completely different from that predicted from thermodynamic equilibrium. ESR and products analysis revealed that the photo-formed O_L^- species (hole center on the surface lattice oxygen) or $[\text{Ti}^{3+}-\text{O}_L^-]$ pairs on TiO_2 would have an interaction with butene to open the C=C bond to form the radical intermediate species in the photocatalytic isomerization, while the surface OH^- species as well as the O_L^- participates in the hydrogen shift, i.e., the double bond shift isomerization (Anpo et al. 1986b).

Photocatalytic isomerization reactions proceed with higher efficiency than other photocatalytic reactions, for example, the reactions including H_2 evolution. This is probably due to the small change of the potential energy from the initial state (reactant) to the final state (product).

4 Conclusion

As mentioned above, the characteristic of photocatalysis enables a wide variety of unique reactions since the oxidative and reductive reactions simultaneously occur on separate sites (e.g., on platinum and TiO₂ surface) or the pair sites (e.g., Ti³⁺–O[–]) of the surface. Moreover, it is realized that we can design the photocatalytic reaction systems by selecting the photocatalysts and reaction conditions; e.g., the type of the photocatalyst (bare TiO₂, platinum-loaded TiO₂, mesoporous TiO₂, supported TiO₂, etc.), the phase (gas–solid or liquid–solid system), the atmosphere (the presence or absence of molecular oxygen and water, etc.), the solvent (water or organic), the wavelength of irradiation light, and so on.

In this chapter, only representative reactions of light molecules by the photocatalytic systems employing TiO₂ and related photocatalysts are shown. Many valuable photocatalytic reactions are not mentioned here, such as organic syntheses for fine chemicals, and there are also many types of photocatalysts besides TiO₂ and the related photocatalysts, such as semiconductors, polyoxoanions, metal complexes, zeolites, highly dispersed supported metal oxides, and so on (Fox and Dulay 1993; Pichat 1994; Kisch 1994; Maldotti et al. 2002; Ohtani et al. 2003; Yoshida 2003; Palmisano et al. 2007; Yuliati and Yoshida 2008; Shiraishi and Hirai 2008).

It is expected that these photocatalytic systems will be applicable for practical uses in the near future in order to realize the environmentally harmonious chemical processes. Furthermore, the study of the unique photocatalytic reaction mechanism would be of benefit not only for the development of photocatalytic systems but also for the development of general catalytic reaction systems for green chemical processes.

References

- Al-Ekabi H, Mayo PD (1984) Surface photochemistry: photocatalysed olefin cis–trans equilibrium mediated by CdS. *J Chem Soc Chem Commun* 1231–1232
- Amano F, Tanaka T, Funabiki T (2004) Steady-state photocatalytic epoxidation of propene by O₂ over V₂O₅/SiO₂ photocatalysts. *Langmuir* 20:4236–4240
- Amano F, Yamaguchi T, Tanaka T (2006) Photocatalytic oxidation of propylene with molecular oxygen over highly dispersed titanium, vanadium, and chromium oxides on silica. *J Phys Chem* 110:281–288
- Amano F, Tanaka T (2006) Propylene oxide synthesis and selective oxidation over supported metal oxide photocatalysts with molecular oxygen. *Chem Lett* 35:468–473
- Anpo M, Aikawa N, Kodama S, Yutaka Kubokawa Y (1984a) Photocatalytic hydrogenation of alkynes and alkenes with water over titanium dioxide. Hydrogenation accompanied by bond fission. *J Phys Chem* 88:2569–2572
- Anpo M, Aikawa N, Kubokawa Y (1984b) Photocatalytic hydrogenation of alkynes and alkenes with water over titanium dioxide. Platinum loading effect on the primary processes. *J Phys Chem* 88:3998–4000

- Anpo M, Aikawa N, Kubokawa Y, Che M, Louis C, Giamello E (1985) Photoluminescence and photocatalytic activity of highly dispersed titanium oxide anchored onto porous Vycor glass. *J Phys Chem* 89:5017–5021
- Anpo M, Nakaya H, Kodama S, Kubokawa Y, Domen K, Onishi T (1986a) Photocatalysis over binary metal oxides. Enhancement of the photocatalytic activity of titanium dioxide in titanium-silicon oxides. *J Phys Chem* 90:1633–1636
- Anpo M, Yabuta M, Kodama S, Kubokawa Y (1986b) Photocatalytic isomerization of butenes over TiO₂. Photo-formed active species and characteristics of reaction. *Bull Chem Soc Jpn* 59:259–264
- Anpo M, Shima T, Kodama S, Kubokawa Y (1987) Photocatalytic hydrogenation of propyne with water on small-particle titania: size quantization effects and reaction intermediates. *J Phys Chem* 91:4305–4310
- Anpo M, Che M (2000) Application of photoluminescence techniques to the characterization of solid surface in relation to adsorption, catalysis, and photocatalysis. *Adv Catal* 44:119–257
- Boarini P, Carassiti V, Maldotti A, Amadelli R (1998) Photocatalytic oxygenation of cyclohexane on titanium dioxide suspensions: effect of the solvent and of oxygen. *Langmuir* 14:2080–2085
- Boonstra AH, Mutsaers CAHA (1975) Photohydrogenation of ethyne and ethene on the surface of titanium dioxide. *J Phys Chem* 79:2025–2072
- Fox MA, Dulay MT (1993) Heterogeneous photocatalysis. *Chem Rev* 93:341–357
- Fujihira M, Satoh Y, Osa T (1981a) Heterogeneous photocatalytic oxidation of aromatic compounds on TiO₂. *Nature* 293:206–208
- Fujihira M, Satoh Y, Osa T (1981b) Heterogeneous photocatalytic oxidation of aromatic compounds on semiconductor materials: the photo-Fenton type reaction. *Chem Lett* 10:1053–1056
- Fujihira M, Satoh Y, Osa T (1982) Heterogeneous photocatalytic reactions on semiconductor materials. III. Effect of pH and Cu²⁺ ions on the photo-Fenton type reaction. *Bull Chem Soc Jpn* 55:666–671
- Giannotti C, Le Greneur S, Watts O (1983) Photo-oxidation of alkanes by metal oxide semiconductors. *Tetrahedron Lett* 24:5071–5072
- Hashimoto K, Kawai T, Sakata T (1984) Photocatalytic reactions of hydrocarbons and fossil fuels with water. Hydrogen production and oxidation. *J Phys Chem* 88:4083–4088
- Izumi I, Dunn WW, Wilbourn KO, Fan FF, Bard AJ (1980) Heterogeneous photocatalytic oxidation of hydrocarbons on platinized titanium dioxide powders. *J Phys Chem* 84:3207–3210
- Izumi I, Fan FF, Bard AJ (1981) Heterogeneous photocatalytic decomposition of benzoic acid and adipic acid on platinized titanium dioxide powder. The photo-Kolbe decarboxylative route to the breakdown of the benzene ring and to the production of butane. *J Phys Chem* 85:218–223
- Kaise M, Kondoh H, Nishihara C, Nozoye H, Shindo H, Nimura S, Kikuchi O (1993) Photocatalytic reactions of acetic acid on platinum-loaded TiO₂: ESR evidence of radical intermediates in the photo-Kolbe reaction. *J Chem Soc Chem Commun* 395–396
- Kato Y, Yoshida H, Hattori T (1998) Photoinduced non-oxidative coupling of methane over silica-alumina and alumina around room temperature. *Chem Commun* 2389–2390
- Kato Y, Yoshida H, Hattori T (2002) Photo-induced non-oxidative coupling of methane over H-zeolite around room temperature. *Micropor Mesopor Mater* 51:223–231
- Kawai T, Sakata T (19269) Hydrogen evolution from water using solid carbon and light energy. *Nature* 282:283–284
- Kawai T, Sakata T (1980) Photocatalytic hydrogen production from liquid methanol and water. *J Chem Soc Chem Commun* 694–695
- Kawai T, Sakata T (1980b) Conversion of carbohydrate into hydrogen fuel by a photocatalytic process. *Nature* 286:474–476
- Kisch H (1994) Preparative photoreactions catalyzed by semiconductor powders. *J Prakt Chem* 336:635–648
- Kodama S, Yabuta M, Kubokawa Y (1982) Photocatalytic isomerization of butenes over TiO₂ and ZnO. *Chem Lett* 11:1671–1674

- Kraeutler B, Bard AJ (1977) Photoelectrosynthesis of ethane from acetate ion at an n-type titanium dioxide electrode. The photo-Kolbe reaction. *J Am Chem Soc* 99:7729–7731
- Kraeutler B, Bard AJ (1978a) Heterogeneous photocatalytic synthesis of methane from acetic acid – new Kolbe reaction pathway. *J Am Chem Soc* 100:2239–2240
- Kraeutler B, Bard AJ (1978b) Heterogeneous photocatalytic decomposition of saturated carboxylic acids on titanium dioxide powder. Decarboxylative route to alkanes. *J Am Chem Soc* 100:5985–5992
- Maldotti A, Molinari A, Amadelli R (2002) Photocatalysis with organized systems for the oxofunctionalization of hydrocarbons by O₂. *Chem Rev* 102:3811–3836
- Morikawa A, Hattori M, Yagi K, Otsuka K (1977) Photocatalytic isomerization of butene-2 on porous silica glass. *Z Phys Chem* 104:309–320
- Mu W, Herrmann J-M, Pichat P (1989) Room temperature photocatalytic oxidation of liquid cyclohexane into cyclohexanone over neat and modified TiO₂. *Catal Lett* 3:73–84
- Murata C, Yoshida H, Hattori T (2001) Visible-light-induced epoxidation of propene by molecular oxygen over chromia-silica catalysts. *Chem Commun* 2412–2413
- Murata C, Yoshida H, Hattori T (2002) Titania-silica catalysts prepared by sol–gel method for photoepoxidation of propene with molecular oxygen. *Stud Surf Sci Catal* 143:845–853
- Murata C, Yoshida H, Kumagai J, Hattori T (2003) Active sites and active oxygen species for photocatalytic epoxidation of propene by molecular oxygen over TiO₂–SiO₂ binary oxides. *J Phys Chem B* 107:4364–4373
- Murata C, Hattori T, Yoshida H (2005) Electrophilic property of O₃[–] photoformed on isolated Ti species in silica promoting alkene epoxidation. *J Catal* 231:292–299
- Nishimoto S, Ohtani B, Yoshikawa T, Kagiya T (1983) Photocatalytic conversion of primary amines to secondary amines and cyclization of polymethylene- α , ω -diamines by an aqueous suspension of TiO₂/Pt. *J Am Chem Soc* 105:7180–7182
- Ohno T, Nakabeya K, Matsumura M (1998) Epoxidation of olefins on photoirradiated titanium dioxide powder using molecular oxygen as an oxidant. *J Catal* 176:76–81
- Ohno T, Mitsui T, Matsumura M (2003) TiO₂-photocatalyzed oxidation of adamantane in solutions containing oxygen or hydrogen peroxide. *J Photochem Photobio A* 160:3–9
- Ohtani B, Osaki H, Nishimoto S, Kagiya T (1986a) A novel photocatalytic process of amine N-alkylation by platinumized semiconductor particles suspended in alcohols. *J Am Chem Soc* 108:308–310
- Ohtani B, Osaki H, Nishimoto S, Kagiya T (1986b) A redox combined photocatalysis: New method of N-alkylation of ammonia by TiO₂/Pt suspended in alcohols. *Tetrahedron Lett* 27:2019–2022
- Ohtani B, Tsuru S, Nishimoto S, Kagiya T, Izawa K (1990) Photocatalytic one-step syntheses of cyclic imino acids by aqueous semiconductor suspensions. *J Org Chem* 55:5551–5553
- Ohtani B, Kusakabe S, Okada K, Tsuru S, Izawa K, Amino Y, Nishimoto S (1995) Stereoselective synthesis of piperidine-2, 6-dicarboxylic acids by photocatalytic reaction of aqueous cadmium (II) sulfide dispersion. *Tetrahedron Lett* 36:3189–3192
- Ohtani B, Pal B, Ikeda S (2003) Photocatalytic organic syntheses: selective cyclization of amino acids in aqueous suspensions. *Catal Surv Asia* 7:165–176
- Palmisano G, Augugliaro V, Pagliaro M, Palmisano L (2007) Photocatalysis: a promising route for 21st century organic chemistry. *Chem Commun* 3425–3437
- Pichat P (1994) Partial or complete heterogeneous photocatalytic oxidation of organic compounds in liquid organic or aqueous phases. *Catal Today* 19:313–333
- Reiche H, Bard AJ (1979) Heterogeneous photosynthetic production of amino acid from methane-ammonia-water at Pt/TiO₂. Implications in chemical evolution. *J Am Chem Soc* 101:3127–3128
- Sakata T, Kawai T (1981) Heterogeneous photocatalytic production of hydrogen and methane from ethanol and water. *Chem Phys Lett* 80:341–344
- Sakata T, Kawai T, Hashimoto K (1984) Heterogeneous photocatalytic reactions of organic acids and water. New reaction paths besides the photo-Kolbe reaction. *J Phys Chem* 88:2344–2350

- Sato S, White JM (1980a) Photoassisted water-gas shift reaction over platinumized titanium dioxide catalysts. *J Am Chem Soc* 102:7206–7210
- Sato S, White JM (1980b) Reactions of water with carbon and ethylene over illuminated Pt/TiO₂. *Chem Phys Lett* 70:131–134
- Shiraishi Y, Morishita M, Hirai T (2005) Acetonitrile-assisted highly selective photocatalytic epoxidation of olefins on Ti-containing silica with molecular oxygen. *Chem Commun* 5977–5979
- Shiraishi Y, Saito N, Hirai T (2005b) Adsorption-driven photocatalytic activity of mesoporous titanium dioxide. *J Am Chem Soc* 127:12820–12822
- Shiraishi Y, Hirai T (2008) Selective organic transformation on titanium oxide-based photocatalysts. *J Photochem Photobiol C* 9:157–170
- Shimamura Y, Misawa H, Oguchi T, Kanno T, Sakuragi H, Tokumaru K (1983) Titanium dioxide photocatalyzed oxidation of aromatic hydrocarbons: the role of water and oxygen to induce aromatic hydroxylation. *Chem Lett* 12:1691–1694
- Takagi K, Fujioka T, Sawaki Y, Iwamura H (1985) An ¹⁸O-tracer study on the TiO₂-sensitized photooxidation of aromatic compounds. *Chem Lett* 14:913–916
- Tanaka T, Nojima H, Yoshida H, Nakagawa H, Funabiki T, Yoshida S (1993) Preparation of highly dispersed niobium oxide on silica by equilibrium adsorption method. *Catal Today* 16:297–307
- Tanaka T, Teramura K, Yamamoto T, Takenaka S, Yoshida S, Funabiki T (2002) TiO₂/SiO₂ photocatalysts at low levels of loading: preparation, structure and photocatalysis. *J Photochem Photobiol A: Chem* 148:277–281
- Teratani S, Takagi Y, Takahashi M, Noda H, Ikuo A, Tanaka K (1984) Photocatalyzed hydroxylation of benzene in the presence of semiconductors. *Nihon Kagakukaishi* 283–291
- Yoneyama H, Takao Y, Tamura H, Bard AJ (1983) Factors influencing product distribution in photocatalytic decomposition of aqueous acetic acid on platinumized titania. *J Phys Chem* 87:1417–1422
- Yoshida H, Tanaka T, Yamamoto M, Yoshida T, Funabiki T, Yoshida S (1992) Epoxidation of propene by gaseous oxygen over silica and Mg-loaded silica under photoirradiation. *J Catal* 171:351–357
- Yoshida H, Murata C, Hattori T (1999) Photocatalytic epoxidation of propene by molecular oxygen over highly dispersed titanium oxide species on silica. *Chem Commun* 1551–1552
- Yoshida H, Kato Y, Hattori T (2000a) Photoinduced non-oxidative methane coupling over silica-alumina. *Stud Surf Sci Catal* 130:659–664
- Yoshida H, Murata C, Hattori T (2000b) Screening study of silica-supported catalysts for photoepoxidation of propene by molecular oxygen. *J Catal* 194:364–372
- Yoshida H, Matsushita N, Kato Y, Hattori T (2002) Active sites in sol-gel prepared silica-alumina for photoinduced non-oxidative methane coupling. *Phys Chem Chem Phys* 4:2459–2465
- Yoshida H, Shimizu T, Murata C, Hattori T (2003a) Highly dispersed zinc oxide species on silica as active sites for photoepoxidation of propene by molecular oxygen. *J Catal* 220:226–232
- Yoshida H, Chaskar MG, Kato Y, Hattori T (2003b) Active sites on silica-supported zirconium oxide for photoinduced direct methane conversion and photoluminescence. *J Photochem Photobiol A* 160:47–53
- Yoshida H, Matsushita N, Kato Y, Hattori T (2003c) Synergistic active sites on SiO₂-Al₂O₃-TiO₂ photocatalysts for direct methane coupling. *J Phys Chem B* 107:8355–8362
- Yoshida H (2003) Silica-based quantum photocatalysts for selective reactions. *Curr Opin Solid Mater Sci* 7:435–442
- Yoshida H (2005) Active sites of silica-based quantum photocatalysts for non-oxidative reactions. *Catal Surv Asia* 9:1–9
- Yoshida H, Yuzawa H, Aoki M, Otake K, Itoh H and Hattori T (2008) Photocatalytic hydroxylation of aromatic ring by using water as an oxidant. *Chem Commun* 4634–4636

- Yoshida H, Hirao K, Nishimoto J, Shimura K, Kato S, Itoh H, Hattori T (2008) Hydrogen production from methane and water on platinum loaded titanium oxide photocatalysts. *J Phys Chem C* 112:5542–5551.
- Yoshida S, Takenaka S, Tanaka T, Hirano H, Hayashi H (1996) Highly dispersed titanium oxide on silica: preparation, characterization by XAFS, and photocatalysis. *Stud Surf Sci Catal* 40:871–880
- Yoshida S, Takenaka S, Tanaka T, Funabiki T (1997) Ultrahighly dispersed titanium oxide on silica: Effect of precursors on the structure and photocatalysis. *J Phys IV France* 7, C2-859-861
- Yuliati L, Hattori T, Yoshida H (2005a) Highly dispersed magnesium oxide species on silica as photoactive sites for photoinduced direct methane coupling and photoluminescence. *Phys Chem Chem Phys* 7:195–201
- Yuliati L, Hamajima T, Hattori T, Yoshida H (2005) Highly dispersed Ce(III) species on silica and alumina as new photocatalysts for non-oxidative direct methane coupling. *Chem Commun* 4824–4826
- Yuliati L, Tsubota M, Satsuma A, Itoh H, Yoshida H (2006a) Photoactive sites on pure silica materials for non-oxidative direct methane coupling. *J Catal* 238:214–220
- Yuliati L, Itoh H, Yoshida H (2006b) Modification of highly dispersed cerium oxides on silica with highly dispersed titanium oxides as a new photocatalyst design for nonoxidative direct methane coupling. *Chem Lett* 35:932–933
- Yuliati L, Itoh H, Yoshida H (2006c) Preparation of isolated highly dispersed titanium oxides on silica by sol–gel method for photocatalytically non-oxidative direct methane coupling. *Stud Surf Sci Catal* 162:961–968
- Yuliati L, Yoshida H (2008) Photocatalytic conversion of methane. *Chem Soc Rev* 37:1592–1602

Part VIII
Renewable Energy from the Photocatalytic
Reduction

Chapter 28

Renewable Energy from the Photocatalytic Reduction of CO₂ with H₂O

Jeffrey C.S. Wu

Abstract Sun is the Earth's ultimate and inexhaustible energy source. With the advantage of generating renewable energy, one of the best routes to remedy CO₂ is to transform it to hydrocarbons using photoreduction. CO₂ was photocatalytically reduced to produce methanol in an aqueous batch reactor and a steady-state optical–fiber reactor under UV irradiation. Titania and Cu-loaded titania were synthesized using titanium (IV) butoxide by sol-gel method. The catalyst was dip-coated on optical fiber. The optical–fiber photoreactor, comprised of nearly 120 photocatalyst-coated fibers, was designed and assembled to transmit and spread light uniformly inside the reactor. The coating film consisted of very fine spherical particles with diameters of near 14 nm. The XRD spectra indicated the anatase phase for all TiO₂ and Cu/TiO₂ catalysts. XPS analysis revealed primary Cu₂O species on the TiO₂ supports. The most active Cu species on TiO₂ surface were Cu₂O clusters and they played an important role for the formation of methanol. The methanol yield rates increased with UV irradiative intensity. Maximum methanol rate was 0.45 μmol/g cat h using 1.2 wt% Cu/TiO₂ catalyst at 129 kPa of CO₂, 2.6 kPa of H₂O, and 5,000 s mean residence time under 16 W/cm² UV irradiation. Higher than 2 wt% Cu loading gave a lower rate of methanol yield rate because of the masking effect of Cu₂O clusters on the TiO₂ surface. A Langmuir–Hinshelwood model was established by correlating experimental data to describe the kinetic behavior. An optimum pressure ratio of H₂O/CO₂ was found in the photoreduction of CO₂ for maximum methanol yield rate.

J.C.S. Wu (✉)

Department of Chemical Engineering, National Taiwan University, Taipei, Taiwan
e-mail: cswu@ntu.edu.tw

1 Introduction

Greenhouse gases such as CO_2 , CH_4 , and CFCs are the primary causes of global warming. The atmospheric concentration of CO_2 has steadily increased owing to human activity and this accelerates the greenhouse effect. The Kyoto Protocol of the United Nations Framework Convention on Climate Change mandated a return of CO_2 emission levels to those of 1990. On the other hand, upgrading CO_2 to reusable hydrocarbons is one of the best routes to overcome the energy shortage.

Figure 1 depicts the energy cycle using carbon as a carrier. Not only all live use solar energy presently, but also the fossil fuel is the storage of solar energy via photosynthesis in the past. In nature, CO_2 is removed from the environment by photosynthesis. The energy obtained from sunlight is ultimately used to convert CO_2 into glucose – a sugar molecule that stores the energy obtained from the Sun in its chemical bonds. All energy forms except geothermal or nuclear – such as fossil fuel, biomaterial, hydropower, and wind – are various kinds of transformation from Sun either in the past or in the present. Thus, solar energy is the Earth's ultimate energy supply. One of promising routes is that artificial photosynthesis may be implemented via the photoreduction of CO_2 to produce hydrocarbons. That is, solar energy is directly transformed and stored as chemical energy. Consequently, the photoreduction of CO_2 to chemicals, such as methanol, is particularly interesting, and achieving a high efficiency for this reaction is highly desired. Moreover, methanol is the most promising photoreduced product of carbon dioxide because it can be transformed into other useful chemicals using conventional chemical technologies. Methanol also can be easily transported, stored, and used as gasoline additives for automobiles.

The energy grade of CO_2 is low from a thermodynamic perspective, accounting for why any transformation to hydrocarbon requires energy infusion. The energy source should be provided without producing more CO_2 . Plants use solar energy to

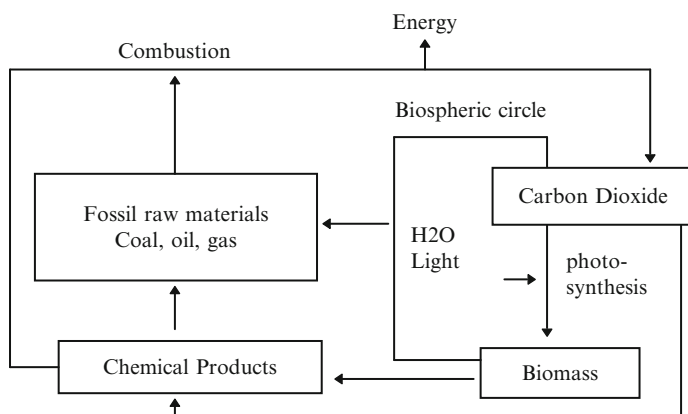
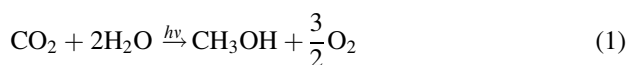


Fig. 1 Energy cycle used carbon as energy carrier

perform photosynthesis, but the efficiency of energy transformation is low at the cost of supporting their lives. Even under the optimal artificial conditions, energy efficiency can only reach about 10% in macroalga under full sunlight (Laws and Berning 1991).

Many researchers have shown that CO₂ can be reduced in water vapor or solvent by photocatalysts such as TiO₂ (Anpo et al. 1995; Guan et al. 2003; Pathak et al. 2004; Wu et al. 2005; Yamashita et al. 1998) and ZnS (Kuwabata et al. 1994). However, the efficiency of photoconversion is still very low. Equation (1) gives an example of overall photoreduction transforming CO₂ to methanol. Based on thermodynamics, transforming 1 mole of CO₂ into methanol requires 228 kJ (ΔH) at 298 K. Furthermore, the Gibbs free energy of (1) is 698.7 kJ (ΔG) at 298 K, indicating that the equilibrium is highly unfavorable to the product, methanol, and oxygen.



The efficient photoreduction of CO₂ with H₂O is one of the most challenging tasks in photocatalysis. As well known, titania is a photoexcited catalyst. The bandgap of anatase form TiO₂ is 3.2 eV, making it a perfect candidate for UV illumination. Titania-supported copper plays a crucial role for promoting the reduction of CO₂ in methanol formation (Hirano et al. 1992). One of our objectives aims to improve the photoreduction efficiency by using supported transition-metal titania catalysts in a novel photoreactor.

Practical applications of TiO₂ photocatalyst for the remediation of vapor-phase CO₂ streams often require immobilizing the photocatalyst in a packed-bed photoreactor. However, traditional packed-bed reactor with light irradiation either from side or from center always projects shadow on the other side of catalyst particle. Thus, maximum 50% of photocatalyst surface cannot be activated in a photo-driven reaction. The transmission and uniform distribution of light energy are important in designing a photoreactor which differs completely from a traditional reactor. A variety of heterogeneous supports have been explored, including glass surface (Al-Ekabi and Serpone 1988; Yatmaz et al. 2001), quartz rods (Lin and Valsaraj 2003; Danion et al. 2004), and monoliths (Sánchez et al. 1999; Hossain and Raupp 1999). However, most reactors are suffered a low ratio of catalyst surface to reactor volume.

A bundle of optical fibers can provide a very high exposure surface in a photoreactor. TiO₂-coated fiber-optical cable reactors have demonstrated some

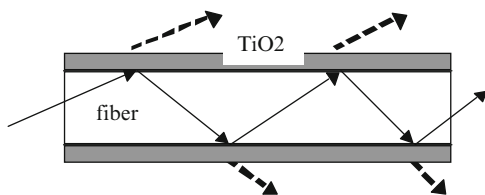


Fig. 2 Light transmission and spread of TiO₂-coated optical fiber

inherent advantages over packed-bed reactors in photoreactions (Hofstadler et al. 1994; Peill and Hoffmann 1995). Figure 2 shows that light is transmitted into an optical fiber. The light is split into two beams when hitting the internal surface fiber, due to the difference of refraction index between the TiO_2 coating and the silica core. Part of the light is reflected and transmitted along the fiber, while the rest penetrates and excites the titania layer at the interface. The light gradually spreads and diminishes to the end of the fiber. The electron-hole (e^- and h^+) pairs are generated on TiO_2 catalyst, then conduct the following photo-driven reactions. Therefore, an optical fiber is that it can deliver light uniformly to the catalyst surface, increasing the efficiency of photon conversion in a photoreactor.

This chapter reports the development of a photoreactor system in order to carry out the photoreduction of CO_2 , that is, artificial photosynthesis. In regard to the light source, artificial light can be used currently. However, light energy can be collected from the Sun using a focus reflection dish in the future.

2 Theoretical Light Transmission in an Optical Fiber

Beam propagation method (BPM) is used to calculate the transmission loss on an optical fiber (Chu et al. 2006). Figure 3 shows the power loss in a 5-mm long TiO_2 -coated optical fiber. The transmission loss only slightly increases with increasing TiO_2 thickness from 50 to 350 nm. The power loss is due to the photoenergy absorbed by TiO_2 film, which decays exponentially along the optical fiber. Based on this result, it is estimated that the remaining power decrease to 1% in a 11.4-cm long optical fiber. The length of optical fiber should be designed longer than 11.4 cm, so that all photoenergy would be absorbed by the surface TiO_2 film in a photoreactor.

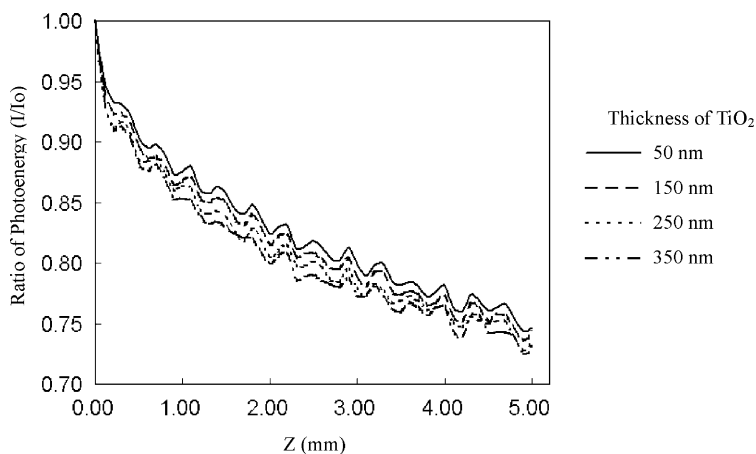


Fig. 3 The remaining photoenergy in an optical fiber along the transmission length (Z), light wavelength 365 nm

3 Experimental

3.1 Preparation of Powder Catalyst

Catalysts were prepared via the sol-gel route illustrated in Fig. 4. The precursor was titanium (IV) butoxide (Ti(OC₄H₉)₄, 97% in *n*-butanol) purchased from Aldrich (USA). The hydrolysis process was performed in a glove box maintained at a relative humidity under 25% by purging with tank nitrogen. To avoid rapid precipitation during polycondensation and the formation of unstable colloidal sols, the hydrolyzing water was homogeneously released by the esterification of butanol and acetic acid (Wu and Yeh 2001). The basic aim was to provide the appropriate stoichiometric quantity of water to hydrolyze titanium butoxide during hydrolysis. A typical batch contained 0.02 mole titanium butoxide, 0.08 mole anhydrous butanol (min. 99.8%), and 0.08 mole glacial acetic acid (min. 99.7%). The clear solution was stirred for 8 h at which time the pH value became stabilized. The final pH value of the solution approached 3.56. The transparent sol was dried from room temperature to 150°C in an oven, then transferred to a furnace and calcined at 500°C to burn off hydrocarbons. The sample was crushed into a powder in a mortar. The JRC-2 and P25 titania powders were obtained from Fuji Titan (Japan) and

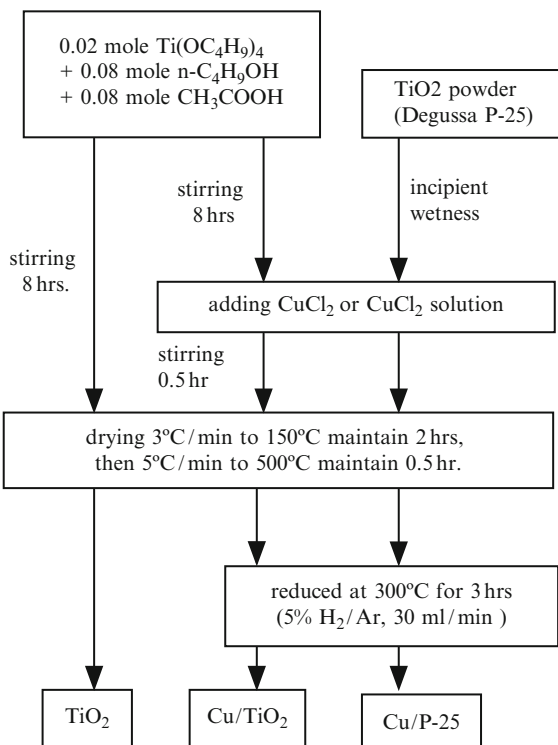


Fig. 4 Synthesis procedure of the powder photocatalysts

Degussa (Germany), respectively, for comparison. Copper-loaded titania (Cu/TiO_2) was impregnated by adding CuCl_2 during the sol-gel process and incipient wetness method, respectively, following calcination similar to that of TiO_2 .

3.2 Preparation of TiO_2 -Coated Optical Fiber

The TiO_2 solutions were prepared for coating on optical fibers using a thermal hydrolysis method. The procedure and condition are shown in Fig. 5. Titanium (IV) butoxide and polyethylene glycol (PEG, molecular weight of 20,000, Merck, Darmstadt, Germany) were added to a 0.1 M nitric acid solution. The volume ratio of titanium butoxide to HNO_3 was 1:6, and the weight of PEG was 50% of TiO_2 . An appropriate amount of metal precursor, such as CuCl_2 , was added to obtain the desired metal loading of TiO_2 . The mixed solution was heated to 80°C for 8 h. PEG was added to prevent cracking during the drying and calcination of the film. Furthermore, PEG increased the viscosity of the solution and dispersed TiO_2 particles uniformly in the solution. The appearance of pure TiO_2 solution was transparently milky.

Optical fibers were obtained from the E-Tone Technology Company of Taiwan. The polymeric shield on the optical fiber was burned off in a furnace at 400°C . The remaining quartz fiber had a diameter of $112\ \mu\text{m}$. Each quartz fiber was cleaned by a 5 M NaOH solution in an ultrasonic cleaner, then rinsed in deionized water and dried before applying dip-coating procedure. The bare fiber was immersed into the solution vertically, then pulled up at various rates by a step motor. The rates of pulling-up ranged from 5 to 50 mm/min. The TiO_2 film was dried in air at 150°C by

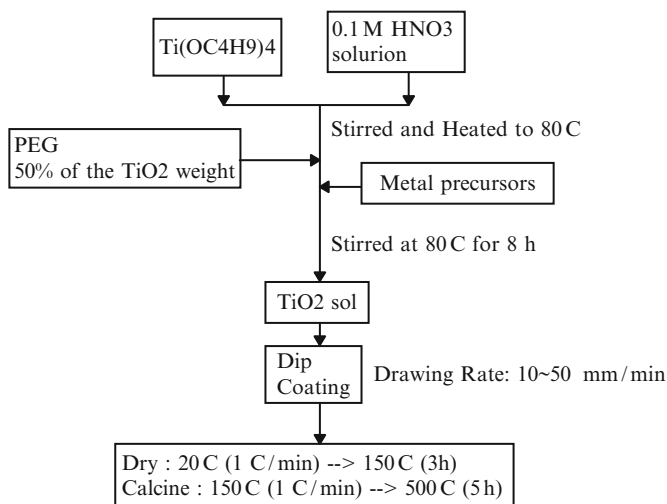


Fig. 5 Procedure of sol for dip coating

a rate of 1°C/min from the ambient temperature, and maintained at 150°C for 3 h. Then, it was calcined at 500°C for another 5 h. The TiO₂ film on support was durable and passed the “Cross-Cut Tape Test,” according to the methods ISO 2409 and ASTM D3359 (Lo and Wu 2005).

3.3 Characterization of Catalysts

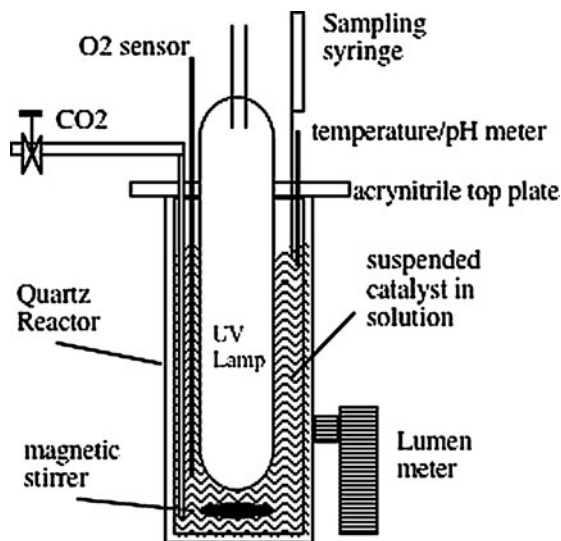
The crystalline phase was identified by an X-ray diffractometer, MAC Science M03XHF, scanning from 20° to 80°. The specific surface area of catalysts was measured by N₂ adsorption in a Micromeritics ASAP 2000. A diffusive reflective UV–Vis spectrophotometer (Varian Cary 100) was employed to measure the UV–Vis absorption at wavelengths from 200 to 800 nm. The particle size distribution in aqueous solution was obtained using a Coulter LS230 particle size analyzer. Transmission electron microscopy (TEM) and scanning electron microscopy (SEM) with energy-dispersive X-ray spectrometer (SEM-EDS, Philips XL30, EDAX DX4) were used to observe the morphology of catalysts and estimate the elemental ratio. The chemical status of the catalyst surface was analyzed by X-ray photoelectron spectroscopy (XPS). The XPS was conducted on a spectrometer of VG Microtech MT500 with an Mg-K_α radiation as the excitation source ($h\nu = 1,253.6$ eV). All binding energies were referenced to oxygen (1 s) at 530.7 eV (Bhattacharya et al. 1997) and carbon (1 s) at 285.6 eV.

3.4 Catalytic Photoreduction of CO₂ in Aqueous Solution

Figure 6 schematically illustrates a batch photoreactor. The system was illuminated by an 8-W xenon lamp with a peak light intensity at 254 nm in the center of the quartz reactor. The entire system was shielded by a metal case during the reaction to prevent interference from outside light. Catalyst powder (0.15–0.6 g) was suspended in 300 ml of 0.2 N NaOH aqueous solutions for typical batches. Supercritical-fluid grade CO₂ was purchased from Air Products (USA) to avoid any hydrocarbon contamination. It was certified maximum hydrocarbons less than 20 ppb. CO₂ was bubbled through the reactor for at least 30 min to purge air and to saturate the solution. The reactor was tightly closed during the reaction, and the CO₂ pressure was maintained in the range of 101.3–135.6 kPa. A magnetic stirrer agitated the catalyst-suspended solution at the bottom to prevent sedimentation of the catalyst. The steady-state temperature of the solution rose to almost 50°C during illumination.

The release of O₂ during the reaction would account for direct evidence of CO₂ photoreduction (1). An oxygen sensor (Mettler Toledo InPro[®] 6000 series) was placed in the reactor to monitor the concentration of dissolved O₂ during the photoreduction. The sensor was calibrated using the dual-point mode before measuring O₂

Fig. 6 Photoreactor in aqueous solution



concentration. The O_2 sensor was inserted into oxygen-free gel until the “ready” sign was on, to fix the zero point. Then, the sensor was put into O_2 -saturated solution until “ready” and the value were attuned to a verified concentration (8.2 ppm, $25^\circ C$). A needle-type probe was inserted in the reactor to extract samples. The liquid sample (<0.5 ml) was collected in a vial wrapped in aluminum foil to reduce interference from the indoor fluorescent light before analysis. After the catalyst’s sedimentation, 1–10 μl liquid sample was withdrawn and analyzed in a GC/FID equipped with a 3-m long Porapak Q column. Analysis results indicated that methanol was the dominant hydrocarbon. Formic acid, formaldehyde, and ethanol were detected from some catalytic reactions, in amounts much less than that of methanol.

Blank reactions were conducted to ensure that hydrocarbon production was due to the photoreduction of CO_2 , and to eliminate surrounding interference. One blank was UV illuminated without the catalyst, and another was in the dark with the catalyst and CO_2 under the same experimental conditions. An additional blank test was UV illuminated with the catalyst filling N_2 rather than CO_2 . No hydrocarbon was detected in the above three blank tests.

3.5 Catalytic Photoreduction of CO_2 in Vapor Phase

An optical-fiber photoreactor (OFPR) was designed and assembled to transmit light from one side of the OFPR module to the fiber-supported TiO_2 film, as shown in Fig. 7. About 120 fibers with 16 cm long were inserted into the OFPR, which had a diameter of 3.2 cm and was 16 cm long (Fig. 7a). The circular side plates of OFPR were sealed using O-rings and the system passed the leakage test (Fig. 7b).

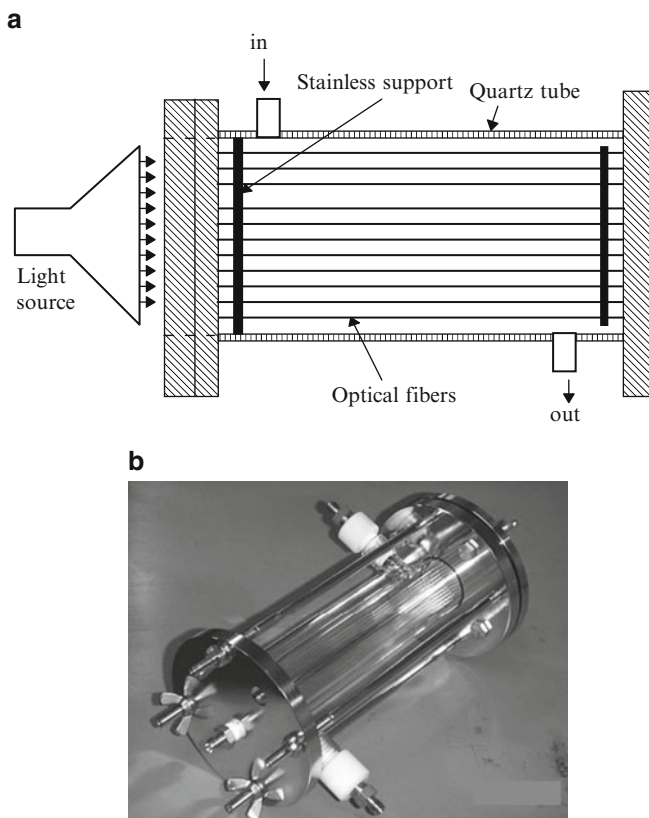


Fig. 7 (a) Schematics of optical-fiber photoreactor. (b) Picture of optical-fiber photoreactor

Figure 8 schematically illustrates the OFPR system. The OFPR was irradiated through the quartz window of one side using a Hg lamp with a peak light intensity at 365 nm. The light intensity entering the quartz window could be adjusted from 1 to 16 W/cm². The whole OFPR was wrapped using aluminum foil to avoid the interference of indoor lamps during the reaction. Supercritical-fluid grade CO₂ was bubbled through a pure water saturator to carry moisture. The reactor was tightly closed and maintained at 75°C by heating tape during the reaction. The reactor was purged for 1 h using helium before switching to CO₂. The flow rate of CO₂ was ~3 ml/min and this was equivalent to a residence time of 5,000 s based on the reactor volume. The pressure of CO₂ was in the range of 105–140 kPa and the water pressure could be adjusted by the temperature of saturator. All reaction data were taken at steady state which could be attained in about 1 h after turning on the UV light.

Reaction products were analyzed via a gas sampling loop of 2.5 ml on-line by the same GC above. Analysis results indicated that methanol was the dominant

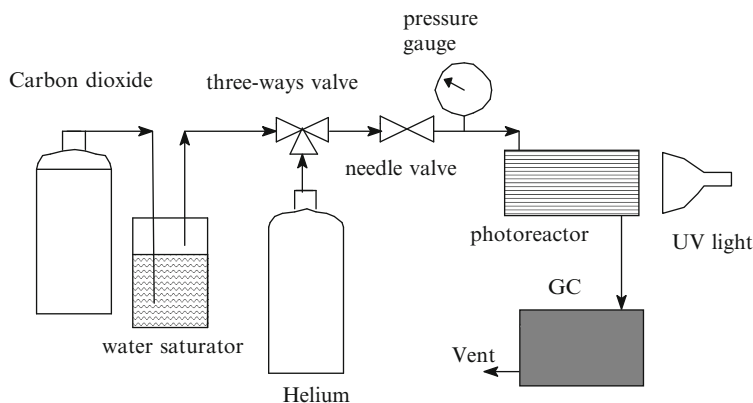


Fig. 8 Photoreaction system

hydrocarbon. Blank reactions were also carried out to ensure that hydrocarbon production was solely from the photoreduction of CO_2 .

4 Results and Discussion

4.1 Characteristics of Powder Catalysts

The XRD spectra in Fig. 9 verified the anatase phase of JRC-2, P25, TiO_2 , and Cu/TiO_2 . A previous investigation has indicated that anatase TiO_2 is the most active phase for photocatalytic reaction (Linsebigler et al. 1995). Two small Cu diffraction peaks appeared near $2\theta = 43.3^\circ$ and 52° on 6.7 wt% Cu/TiO_2 . No Cu peak was observed on 2.0 wt% Cu/TiO_2 , perhaps due to the slight Cu loading or the extremely small Cu clusters. The grain sizes of all sol-gel-derived TiO_2 were nearly 20 nm, as calculated from the Scherrer equation. The particle sizes were consistent with the TEM observation displayed in Fig. 10. As shown in Fig. 10a, the particles of sol-gel-derived TiO_2 were uniform and the diameter was between 10 and 25 nm. Figure 10b reveals that copper clusters were well dispersed on the surface of TiO_2 . Copper clusters were expected to be present on the surface of the TiO_2 particle because the CuCl_2 was added after hydrolysis of titanium butoxide during the preparation (Fig. 4). Zhang et al. (1998) suggested that pure TiO_2 grain sizes with a diameter ranging from 11 to 21 nm were of a size that maximized photocatalytic efficiency. When the particle size was less than 5–10 nm, the surface recombination of electron–hole pairs becomes significant, resulting in low photocatalytic efficiency. Figure 11 shows the actual particle size distributions of catalysts in an aqueous suspension. For TiO_2 and 2 wt% Cu/TiO_2 , the median particle sizes were near 70 and 50 nm, respectively. P25 exhibited two modes of particle size distribution, near 45 and 75 nm.

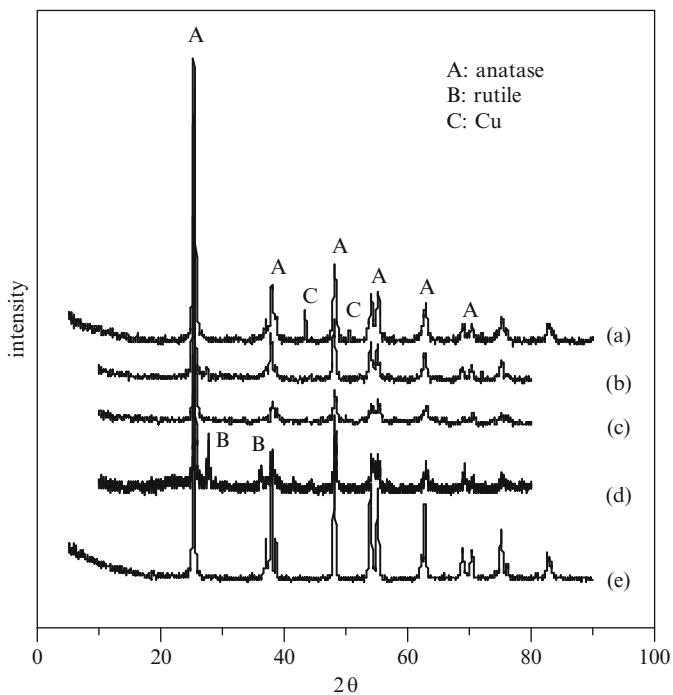


Fig. 9 XRD spectra of TiO₂ and Cu/TiO₂: (a) 6.7 wt% Cu/TiO₂, (b) 2.0 wt% Cu/TiO₂, (c) TiO₂, (d) P25, and (e) JRC-2

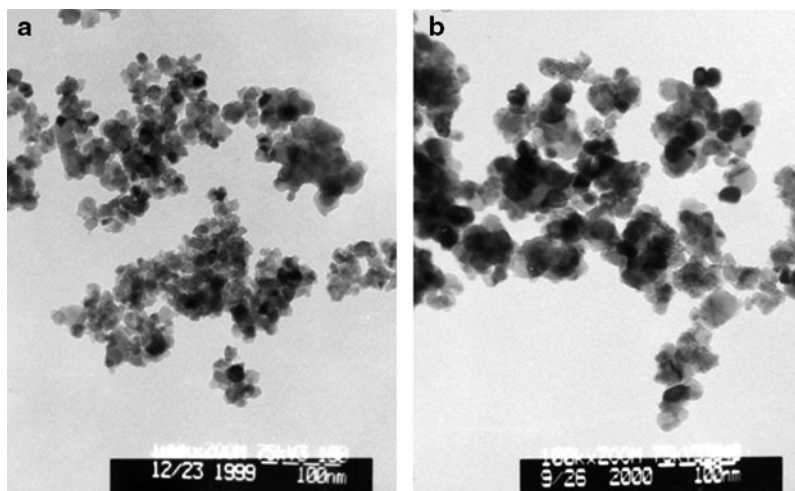


Fig. 10 TEM photographs: (a) TiO₂ and (b) 3.3 wt% Cu/TiO₂

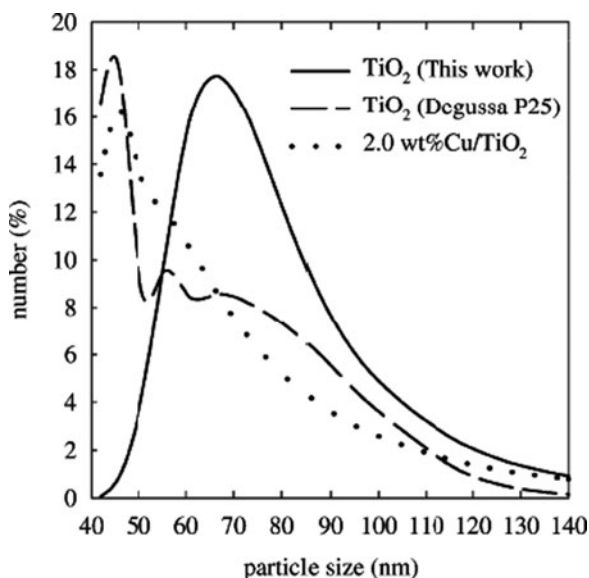


Fig. 11 The particle size distributions of P25, TiO₂, and Cu/TiO₂

Table 1 The properties of catalysts and methanol yields

Catalyst	Surface area (m ² /g)	Crystalline size ^a (nm)	Bandgap ^b (eV)	6-h methanol yield (μmol/g cat)
TiO ₂ (this work)	63	18	2.95	4.7
Degussa P25	50 ^c	21	3.47	38.2
JRC-2	16 ^c	42	3.27	3.4
0.6% Cu/TiO ₂	34	–	–	60.0
1.0% Cu/TiO ₂	40	20	2.99	37.7
2.0% Cu/TiO ₂	28	20	2.99	72.9
3.3% Cu/TiO ₂	26	20	2.92	118.5
6.0% Cu/TiO ₂	–	–	2.86	89.7
6.7% Cu/TiO ₂	28	17	3.05	20.0

^aEstimated from FWHM of XRD by Scherrer equation

^bEstimated from UV–Vis spectra

^cFrom manufacturer

Table 1 summarizes the properties of the catalysts. The bandgap can be estimated by extrapolating the rising portion of the UV spectrum to the abscissa at zero absorption (Sanchez and Lopez 1995). The bandgaps of JRC-2 and P25 are 3.27 and 3.47 eV, respectively, while those of sol-gel TiO₂ and Cu/TiO₂ are nearby 3.00 eV. Notably, the bandgap is governed by the crystalline structure and the defects in the TiO₂ network. A related investigation suggested that small bandgaps were caused by the stoichiometric deficiency of Ti/O from the sol-gel processes (Sanchez and Lopez 1995). The specific surface area of sol-gel-derived catalysts

Table 2 The element molar ratio of catalysts calculated from XPS and EDS analysis

Catalyst (wt% Cu/TiO ₂)	Cu/Ti		
	Bulk	EDS	XPS
0.6	0.007	0.013	–
1.0	0.012	–	0.063
2.0	0.02	0.035	0.119
3.3	0.04	0.053	0.138
6.7	0.09	0.091	0.165

EDS energy-dispersive X-ray spectroscopy, XPS X-ray photoelectron spectroscopy

ranged from 25 to 63 m²/g. The specific surface area of sol-gel TiO₂ was larger than that of commercial JRC-2 or P25.

Table 2 lists the elemental ratio of Cu/Ti estimated from XPS and EDS. The bulk ratio of Cu/Ti was the molar ratio of Cu and Ti in the sol-gel preparation (Fig. 4). The discrepancy between the Cu/Ti ratio obtained by EDS and XPS indicated that most Cu was on the surface of the TiO₂ support. The source of these two kinds of probes, X-ray (XPS) and electron (EDS), with different incident energies, 50 eV and 15 keV, indicates that elements were detected with different depths, ~10 nm and ~1 μm, from the surface (Vickerman 1997). Accordingly, the quantitative results of XPS show the outmost surface of catalyst, while those of EDS give the deep structural layers and represent near-bulk property.

Figure 12 displays the Ti (2p) XPS spectra of TiO₂, P25, JRC-2, and 2 wt% Cu/TiO₂. The binding energies of Ti 2p_{3/2} and 2p_{1/2} of 2 wt% Cu/TiO₂ are the same as those of pure titania at 459.4 and 465.3 eV, respectively, indicating the integrity of the TiO₂ structure, which was not modified by copper impregnation. Figure 13 shows the results of Cu (2p) XPS spectra on Cu/TiO₂ with three different Cu loadings. According to the positions of binding energies (2p_{3/2}, 932.8 eV; 2p_{1/2}, 952.8 eV) and the shape of the peaks, the copper on the surface of TiO₂ might exist in multiple-oxidation states, but Cu(I) would be the primary species (Tseng et al. 2004).

4.2 Characteristics of Catalyst Coated on Optical Fibers

Figure 14a, b, c, and d shows the SEM micrographs of bare optical fiber, the cross section of TiO₂ film, the cross section of Cu/TiO₂ film, and top view of TiO₂ film on top of the fibers, respectively. The bare fiber was smooth after removing polymeric shield, as shown in Fig. 14a. The thickness of TiO₂ and 1.2 wt% Cu/TiO₂ films was 129 and 53 nm on the surface of optical fiber, respectively, as shown in Fig. 14b, c. Figure 14d shows that the TiO₂ film consisted of very fine spherical particles with diameters of ~14 nm. The film was transparent, colorless, and uniformly flat without cracks. The films of TiO₂ and other Cu-loaded TiO₂ on fibers also had the same thickness. Figure 15 shows the elemental analysis of the bare optical fiber by EDS. Only silicon and oxygen were observed, indicating that

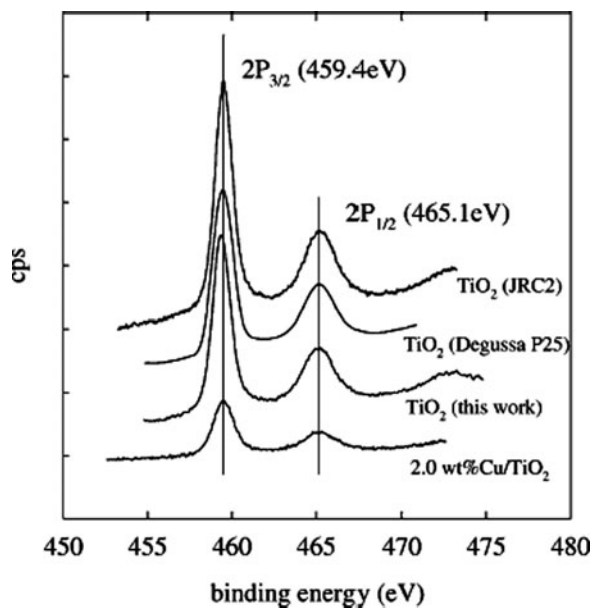


Fig. 12 XPS spectra of Ti 2p of catalysts

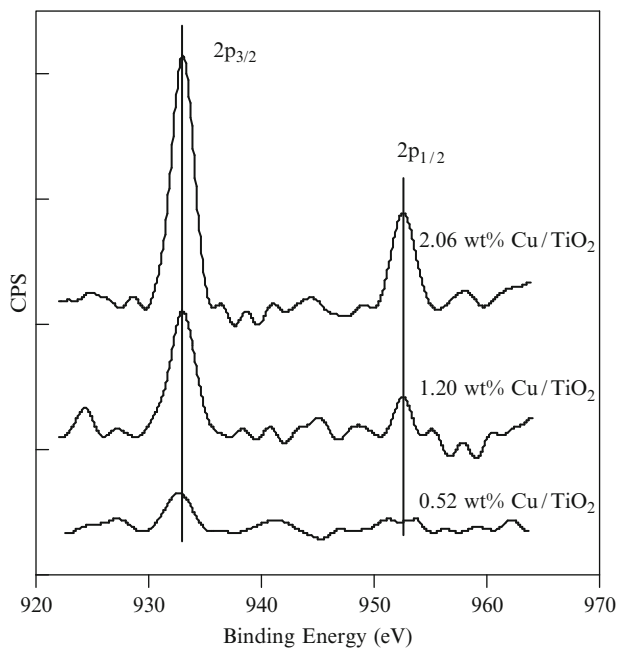


Fig. 13 XPS spectra of Cu 2p on Cu/ TiO_2 catalysts

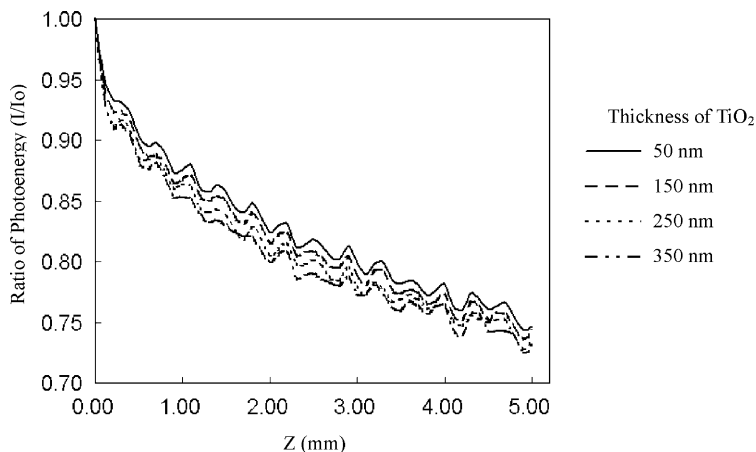


Fig. 14 SEM micrographs: (a) an optical fiber, (b) the cross section of TiO₂ film on an optical fiber, (c) the cross section of 1.2 wt% Cu/TiO₂ film on an optical fiber, and (d) the top view of TiO₂ film on an optical fiber

the surface of optical fiber is pure silica after burning off polymeric shield at 400°C in air.

The XRD spectra in Fig. 16 show the diffraction pattern of various Cu/TiO₂ and pure TiO₂ films. Thermal treatment at 500°C for 5 h resulted in well-crystallized anatase-type TiO₂. No copper diffraction peak was observed in the XRD spectra, indicating that copper was finely dispersed on TiO₂. The TiO₂ films absorbed light below a wavelength of 380 nm in the UV–Vis spectra (not shown), indicating its bandgap near 3.3 eV.

4.3 Photoreduction of CO₂ in Aqueous Solution

Figure 17 shows the dependence of methanol formation on UV illumination time. Various yields of methanol were obtained in a period depending on the catalysts.

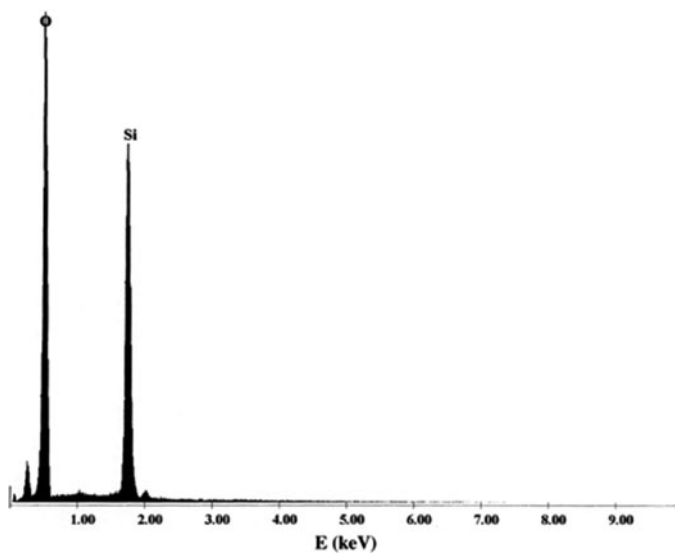


Fig. 15 EDS elemental analysis of bare optical fiber

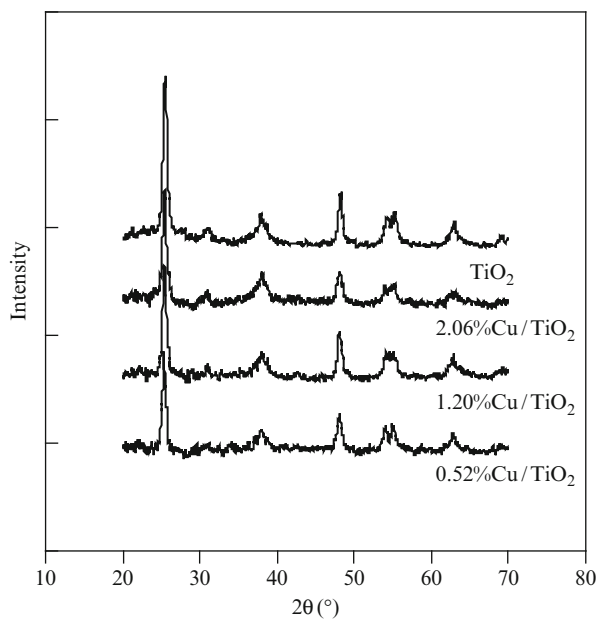


Fig. 16 XRD spectra of TiO_2 and Cu/ TiO_2 catalyst films on optical fiber

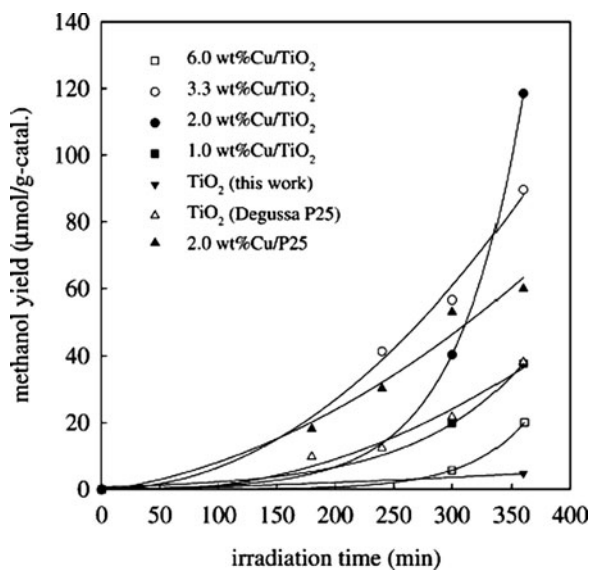


Fig. 17 Time dependence on the methanol yields of various catalysts (UV = 254 nm)

In all cases, methanol was generated after nearly 180 min. The formation of methanol was found much more effective on supported Cu titania catalyst (Yamashita et al. 1994). Methane, formic acid, and other hydrocarbons might have been generated, but in quantities too low to be detected. The results showed that the sol-gel-derived Cu/TiO₂ outperformed P25, JRC-2, and 2 wt% Cu/P25. Table 1 also lists the methanol yields of various catalysts under 6-h irradiation. The presence of copper plays an important role, while specific surface area is obviously not a main factor in photocatalytic reactions (Anpo et al. 1987).

Contact between TiO₂ and metal generally involves a redistribution of electric charge. In the presence of copper clusters, electrons are enriched owing to the alignment of Fermi levels of the metal and the semiconductor, that is, the Schottky barrier (Linsebigler et al. 1995). Copper then serves as an electron trapper and prohibits the recombination of hole and electron. In addition, the rapid transfer of excited electrons to the copper cluster enhances the separation of holes and electrons (Hirano et al. 1992), significantly promoting the efficiency of photon conversion. The formation of methanol was more efficient than that of other hydrocarbons in the presence of supported Cu⁺ on TiO₂ from the CO₂ and H₂O system (Yamashita et al. 1994).

Oxygen is expected as a product of the CO₂ reduction (1). Figure 18 shows that the time dependency of oxygen generation approximately matches that of the methanol yield. Free O₂ was suggested as being adsorbed on the surface of TiO₂ in the presence of water (Yamashita et al. 1994). Consequently, the oxygen sensor detected only little dissolved oxygen in these experiments. The O₂ concentration also plateaued after 16–20 h of reaction, revealing possible O₂ consumption by methanol reoxidation.

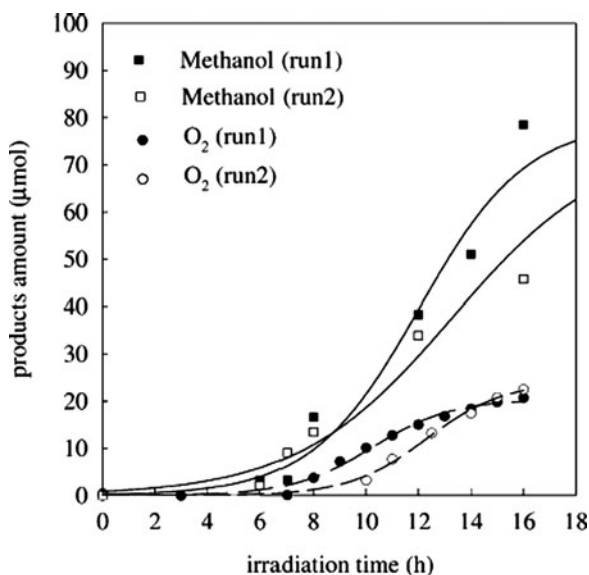


Fig. 18 The dissolved O₂ of two 2.0 wt% Cu/TiO₂ catalysts during reaction

NaOH solution was crucial in the photoreduction of CO₂ in aqueous solution (Kaneco et al. 1998). The methanol yield substantially increased with the addition of NaOH in our experiments, perhaps due to the following two reasons. First, the high concentration of OH⁻ ions in aqueous solution could act as strong hole scavengers and form OH radicals, thereby reducing the recombination of hole–electron pairs. The longer decay time of surface electrons would certainly facilitate the reduction of CO₂. Second, caustic NaOH solution dissolves more CO₂ than does pure water. The initial pH value of 0.2 N NaOH solution was approximately 13.3, and decreased to nearly 7.3 after bubbling CO₂ in the reactor. Notably, photoreduction may have been accelerated by the high concentration of HCO₃⁻.

4.4 Photoreduction of CO₂ in Optical–Fiber Reactor

Figure 19 shows the methanol yield rates versus light intensity under the partial pressures of CO₂ and H₂O at 129 and 2.6 kPa, respectively, in the steady-state OFPR at 75°C. The yield rate increased with light intensity in the range of 1–16 W/cm². Pure TiO₂ gave very little methanol yield rate, while Cu/TiO₂ significantly improved the yield rate. The maximum yield rate of methanol was 0.45 μmol/g cat h using 1.2 wt% Cu/TiO₂ catalyst under a light intensity of 16 W/cm². Since the primary status of copper was Cu(I) (as shown in Fig. 13), Cu₂O was suggested to be the active center for methanol formation in CO₂ photoreduction (Tseng et al. 2002, 2004). Increasing Cu loading resulted in increasing

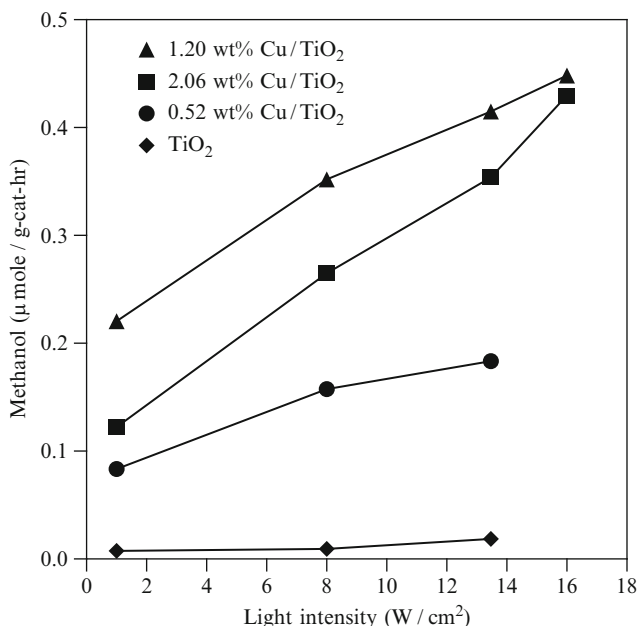


Fig. 19 The methanol yield in optical-fiber photoreactor, reaction temperature 75°C, CO₂ pressure 129 kPa, and H₂O pressure 2.6 kPa (UV = 365 nm)

photoactivity, as expected. Cu₂O could also serve as an electron trap to reduce the recombination rate of electron-hole pairs during photoexcitation of photocatalyst. Surface hydroxyls (OH) of TiO₂ could also promote the adsorption of the reactant, CO₂, so that the photoreaction was enhanced (Tseng et al. 2002). Thus, the overall photoactivity of CO₂ reduction significantly increased. However, excess Cu₂O clusters on the surface also masked the surface of TiO₂, resulting in less light exposure of catalyst. Consequently, the photoexcitation of electron and hole pair was declined because less photoenergy was absorbed. So, there would be an optimum Cu loading on Cu/TiO₂ catalysts for maximum methanol yield rate. An Cu loading of 1.2 wt% was found to give the highest yield rates of methanol under our experimental conditions.

The influences of CO₂ and water pressure were also investigated. Figure 20 shows the methanol yield rates versus different CO₂ pressures under fixed light intensity (13.5 W/cm²) and water pressure (2.6 kPa) at 75°C. The methanol yield rates increased with CO₂ pressure, reaching a maximum of 0.415 μmol/g cat h at 129 kPa, then decreased with further increasing of CO₂ pressure on 1.20 wt% Cu/TiO₂. The other two catalysts showed similar trends with lower methanol yield rates. Figure 21 shows the methanol yield rates versus various pressure ratios of H₂O/CO₂ under fixed light intensity, 13.5 W/cm². The methanol yield rates also increased with H₂O/CO₂ ratios, then decreased with higher ratios. Such phenomena implied a competitive adsorption of reactants, that is, CO₂ and H₂O, on the active sites during photoreduction. Thus, there existed optimum pressures of CO₂ and H₂O in the photoreduction.

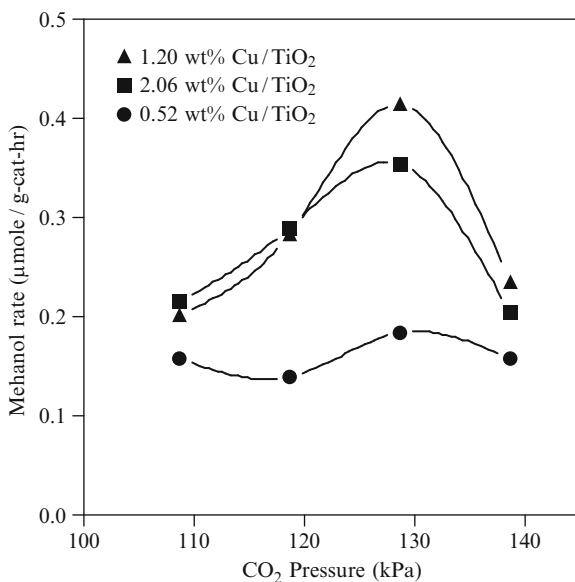


Fig. 20 The methanol yield in optical-fiber photoreactor, reaction temperature 75°C, light intensity 13.5 W/cm², and H₂O pressure 2.6 kPa

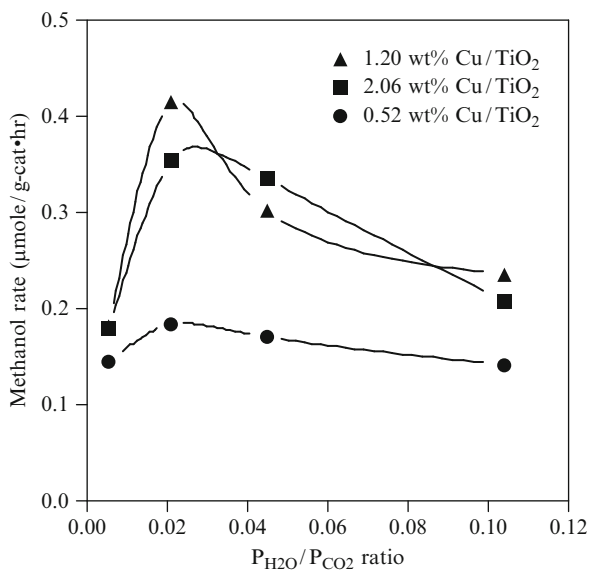


Fig. 21 The methanol yield in optical-fiber photoreactor, reaction temperature 75°C, and light intensity 13.5 W/cm²

As shown in (2), a Langmuir–Hinshelwood model was employed to correlate the experimental data of CO₂, water, light intensity, and methanol yield rate. Both reactants, CO₂ and H₂O, were assumed to be adsorbed on the same active sites of the catalyst surface. The reaction was considered to be irreversible because the partial pressures of products – methanol and oxygen – were very low. Multiple-variable nonlinear regression was applied the data of 1.20 wt% Cu/TiO₂. The best fitted rate constant, k , and adsorption equilibrium constants, H₂O (K_1) and CO₂ (K_2), are listed in Table 3. The value of water adsorption equilibrium constant, K_1 , was 0.517 kPa⁻¹ that was nearly three orders of magnitude higher than that of CO₂, K_2 , 0.0001 kPa⁻¹. The value of K_2 was near zero, indicating that the adsorption of CO₂ was very weak, while water was strongly adsorbed on the catalyst surface:

$$\text{Rate} = \frac{kP_{\text{H}_2\text{O}}^2 P_{\text{CO}_2} I^a}{(1 + K_1 P_{\text{H}_2\text{O}} + K_2 P_{\text{CO}_2})^3}, \quad (2)$$

where k is the methanol rate constant (μmol/g cat kPa³ h), I the light intensity (W/cm²), a the power of light intensity (–), K_1 the adsorption equilibrium constant of H₂O (kPa⁻¹), and K_2 the adsorption equilibrium constant of CO₂ (kPa⁻¹).

It is well known that the surface of TiO₂ becomes superhydrophilic when irradiated by UV light. Therefore, water molecules would cover most of the surface of TiO₂ catalyst during photoreduction. Our CO₂ photoreduction was carried out at very low water pressure ranging from 0.72 to 12 kPa. At high H₂O/CO₂ ratio, CO₂ would need to compete with H₂O on the active sites in order to react with adsorbed H₂O. Thus, reducing H₂O pressure (or raising CO₂ pressure) increases the reaction rate. However, when H₂O pressure is much lower than that of CO₂, for example, H₂O/CO₂ < 0.02, less water coverage could decrease the reaction rate. Therefore, there exists an optimum CO₂ pressure at a given H₂O pressure, or an optimum H₂O/CO₂ ratio as shown in Figs. 20 and 21, respectively.

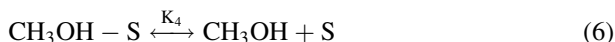
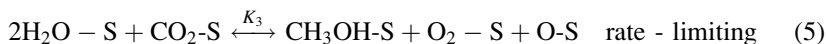
Apparent elementary steps of the CO₂ photoreduction are derived in (3)–(8) according to the results of Langmuir–Hinshelwood model (2). The rate-limiting step was assigned to be the formation of methanol (5). The detailed mechanism of the methanol formation could not be revealed from our present study. The adsorption of CO₂ and H₂O and the desorption of methanol and oxygen were not bottlenecks of the photoreduction of CO₂ under our experimental conditions.



Table 3 Adsorption equilibrium and rate constants^a of Langmuir–Hinshelwood model

Parameters	Value	Error with 95% confidence
k (μmol/g cat kPa ³ h)	2.481×10^{-3}	$\pm 1.149 \times 10^{-3}$
a	0.20	± 0.16
K_1 (kPa ⁻¹)	0.517	± 0.112
K_2 (kPa ⁻¹)	0.0001	± 0.0022

^aEstimated by correlation of experimental data on 1.20 wt% Cu/TiO₂ catalyst



As the effect of light intensity, the power of light intensity was estimated to be ~ 0.2 in the methanol rate equation (2) within $1\text{--}16 \text{ W/cm}^2$ UV irradiation. In general, photoactivity would be directly proportional to the light intensity. However, if more light flux was supplied than the demand of photoreaction, the power of light intensity in the rate equation would gradually shift from 1 to less than 0.5 (Kim and Hong 2002). The light flux of our experiment was probably oversupplied. In such a case, the light flux should be decreased in order to increase quantum efficiency. On the other hand, larger reactor volume or higher CO_2 flow rate can be used under the same light flux.

The activity of a photocatalytic reaction is usually difficult to compare between research reports. Our photoactivity is presented by product yield or yield rate, that is, $\mu\text{mol}/(\text{g cat})$ or $\mu\text{mol}/(\text{g cat h})$. One should note that the yield rate of photo-products can be changed substantially under different experimental conditions such as UV wavelength, UV intensity, additives of reaction media, and reactor configuration. Other variables – such as CO_2 pressure, moisture, and residence time – are also important factors in photoreducing CO_2 .

5 Conclusion

The catalytic reduction of CO_2 has great advantages over green plants of not having to support a living system. Ideally, the transformation of photo-to-chemical energy by a nonliving catalyst should be more efficient than that by a life-supporting one. This research has demonstrated a photo-efficient reactor for converting solar energy to chemical energy. Methanol was favorably produced on Cu/TiO_2 catalysts under UV irradiation. The Cu-loaded titania is a highly efficient photocatalyst for CO_2 reduction since copper is an effective electron trapper, able to reduce the recombination of electron–hole pairs. The photoreduction of CO_2 with H_2O vapor was successfully demonstrated in a photoreactor with Cu/TiO_2 -coated optical fibers. So far, the maximum methanol yield rate was $0.46 \mu\text{mol}/\text{g cat h}$ under 365-nm UV irradiation. Compared with a packed-bed reactor, optical fibers provide a uniform

light distribution in a photoreactor, which spreads light energy more efficiently than a traditional reactor. Thus, light energy can be spread more efficiently. In addition, a higher processing capacity is possible because the catalyst can disperse on a large external area of optical fibers in a given reactor volume. Furthermore, an optical–fiber photoreactor is a promising reactor that can be used in gas or aqueous phases in other photoreactions in the future.

Acknowledgments Financial supports of National Science Council under grant NSC95-EPA-Z-002-007 and of Ministry of Economic Affairs, Taiwan, under grant 95-EC-17-A-09-S1-019 are gratefully acknowledged.

References

- Al-Ekabi H, Serpone N (1988) Kinetics studies in heterogeneous photocatalysis. I. Photocatalytic degradation of chlorinated phenols in aerated aqueous solutions over titania supported on a glass matrix. *J Phys Chem* 92:5726–5731
- Anpo M, Shima T, Kodama S, Kubokawa Y (1987) Photocatalytic hydrogenation of CH₃CCH with H₂O on small-particle TiO₂: size quantization effects and reaction intermediates. *J Phys Chem* 91:4305–4310
- Anpo M, Yamashita H, Ichihashi Y, Ehara S (1995) Photocatalytic reduction of CO₂ with H₂O on various titanium oxide catalysts. *J Electroanal Chem* 396:21–26
- Bhattacharya AK, Pyke DR, Reynolds R, Walker GS, Werrett CR (1997) The use of Ols charge referencing for the X-ray photoelectron spectroscopy of Al/Si, Al/Ti and Al/Zr mixed oxides. *J Mater Sci Lett* 16(1):1–3
- Chu T, Huang H, Tsai D (2006) Optical effect of fibers with TiO₂ nano film for photocatalyst reactor. In: Annual meeting of physics, Taipei, Taiwan, 17 January 2006
- Danion A, Disdier J, Guillard C, Abdelmalek F, Jaffrezic-Renault N (2004) Characterization and study of a single-TiO₂-coated optical fiber reactor. *Appl Catal B Environ* 52:213–223
- Guan G, Kida T, Harada T, Isayama M, Yoshida A (2003) Photoreduction of carbon dioxide with water over K₂Ti₆O₁₃ photocatalyst combined with Cu/ZnO catalyst under concentrated sunlight. *Appl Catal A Gen* 249:11–18
- Hirano K, Inoue K, Yatsu T (1992) Photocatalysed reduction of CO₂ in aqueous TiO₂ suspension mixed with copper powder. *J Photochem Photobiol A Chem* 64:255–258
- Hofstadler K, Bauer R, Novallc S, Heisler G (1994) New reactor design for photocatalytic wastewater treatment with TiO₂ immobilized on fused-silica glass fibers: photomineralization of 4-chlorophenol. *Environ Sci Technol* 28:670–674
- Hossain MM, Raupp GB (1999) Polychromatic radiation field model for a honeycomb monolith photocatalytic reactor. *Chem Eng Sci* 54:3027–3034
- Kaneco S, Shimizu Y, Ohta K, Mizuno T (1998) Photocatalytic reduction of high pressure carbon dioxide using TiO₂ powders with a positive hole scavenger. *J Photochem Photobiol A Chem* 115:223–226
- Kim SB, Hong SC (2002) Kinetic study for photocatalytic degradation of volatile organic compounds in air using thin film TiO₂ photocatalyst. *Appl Catal B Environ* 35:305–315
- Kuwabata S, Nishida K, Tsuda R, Inoue H, Yoneyama H (1994) Photochemical reduction of carbon dioxide to methanol using ZnS microcrystallite as a photocatalyst in the presence of methanol dehydrogenase. *J Electrochem Soc* 141(6):1498–1503
- Laws EA, Berning JL (1991) Photosynthetic efficiency optimization studies with the macroalga *Gracilaria tikvahiae*: implications for CO₂ emission control from power plants. *Bioresour Technol* 37:25–33

- Lin HF, Valsaraj KT (2003) A titania thin film annular photocatalytic reactor for the degradation of polycyclic aromatic hydrocarbons in dilute water streams. *J Hazard Mater* 99:203–219
- Linsebigler AL, Lu G, Yates JT Jr (1995) Photocatalysis on TiO₂ surface: principles, mechanisms, and selected results. *Chem Rev* 95:735–758
- Lo CF, Wu JCS (2005) Preparation and characterization of TiO₂-coated optical-fiber for photo reactor. *J Chin Inst Chem Eng* 36(2):119–125
- Pathak P, Meziani MJ, Li Y, Cureton LT, Sun Y-P (2004) Improving photoreduction of CO₂ with homogeneously dispersed nanoscale TiO₂ catalysts. *Chem Commun* 10:1234–1235
- Peill NJ, Hoffmann MR (1995) Development and optimization of a TiO₂-coated fiber-optic cable reactor: photocatalytic degradation of 4-chlorophenol. *Environ Sci Technol* 29:2974–2981
- Sanchez E, Lopez T (1995) Effect of the preparation method on the band gap of titania and platinum–titania sol-gel materials. *Mater Lett* 25:271–273
- Sánchez B, Cardona AI, Romero M, Avila P, Bahamonde A (1999) Influence of temperature on gas-phase photo-assisted mineralization of TCE using tubular and monolithic catalysts. *Catal Today* 54:369–377
- Tseng I-H, Chang W-C, Wu JCS (2002) Photoreduction of CO₂ using sol-gel-derived titania and titania-supported copper catalysts. *Appl Catal B Environ* 37:37–48
- Tseng I-H, Wu JCS, Chou H-Y (2004) Effects of sol-gel procedures on the photocatalysis of Cu/TiO₂ in CO₂ photoreduction. *J Catal* 221:432–440
- Vickerman JC (1997) Surface analysis – the principal techniques. Wiley, New York
- Wu JCS, Yeh C-Y (2001) Sol-gel derived photosensitive TiO₂ and Cu/TiO₂ using homogeneous hydrolysis technique. *J Mater Res* 16:615–620
- Wu JCS, Lin H-M, Lai C-L (2005) Photo reduction of CO₂ to methanol using optical–fiber photo reactor. *Appl Catal A Gen* 296:194–200
- Yamashita H, Nishiguchi H, Kamada N, Anpo M (1994) Photocatalytic reduction of CO₂ with H₂O on TiO₂ and Cu/TiO₂ catalysts. *Res Chem Interme* 20(8):825–833
- Yamashita H, Fujii Y, Ichihashi Y, Zhang SG, Ikeue K, Park DR, Koyano K, Tatsumi T, Anpo M (1998) Selective formation of CH₃OH in the photocatalytic reduction of CO₂ with H₂O on titanium oxides highly dispersed within zeolites and mesoporous molecular sieves. *Catal Today* 45:221–227
- Yatmaz HC, Wallis C, Howarth CR (2001) The spinning disc reactor – studies on a novel TiO₂. *Chemosphere* 42:397–403
- Zhang Z, Wang C-C, Zakaria R, Ying JY (1998) Role of particle size in nanocrystalline TiO₂-based photocatalysts. *J Phys Chem B* 102:10871–10878

Part IX
Photofunctionalization

Chapter 29

Photofunctionalization of TiO₂ for Optimal Bone-titanium Integration: A Novel Phenomenon of Super Osseointegration

Takahiro Ogawa

Abstract Osteoporotic fractures, degenerative changes in joints, and edentulous jaws are quite common clinical problems. Owing to its bone bonding property, the so-called osseointegration or bone-titanium integration, titanium implants are used as a reconstructive anchor in such diseases and disorders, despite unsolved concerns of medical and societal concerns and cost issues. Here, we present ultraviolet (UV) light-treated titanium surfaces with markedly increased bone-forming and bonding capacity. The UV-treated surface offers an osteoblast-affinity environment, as demonstrated by enhanced attachment, spread, proliferation, and functional differentiation of bone-forming cells (osteoblasts). New bone formation spreads extensively onto the UV-treated titanium implants with virtually no intervention by soft tissue, maximizing the bone-implant contact up to nearly 100% compared with 55% of untreated titanium. The UV treatment accelerates the establishment of implant biomechanical fixation by fourfold. These cell-affinity properties strongly correlated with UV-catalytic removal of hydrocarbons from the TiO₂ surface. The data suggest that this photofunctionalization converts bioinert titanium to bioactive titanium, enabling more rapid and complete establishment of bone-titanium integration. We propose to define the unique biological phenomenon specifically induced around this novel titanium surface as “super osseointegration” and expect it to have immediate and broad applications in dental and orthopedic fields because it is simple, highly effective, and inexpensive.

T. Ogawa (✉)

Laboratory for Bone and Implant Sciences (LBIS), Division of Advanced Prosthodontics, Weintraub Center for Reconstructive Biotechnology, Biomaterials and Hospital Dentistry, UCLA School of Dentistry, Los Angeles, CA, USA
e-mail: togawa@dentistry.ucla.edu

1 Introduction

Osteoporotic bone fractures and degenerative changes in joints are common severe health problems. Annual expenditures attributable to osteoporotic fractures alone are estimated to be \$13.8 billion in the USA (Ray et al. 1997). More than 500,000 procedures are performed annually in the USA for hip and knee reconstruction. Although titanium implants are essential as anchors for these procedures (Fig. 1a), implant failure due to incomplete bone-titanium bonding and delayed detachment at the interface is a critical problem that compromises prognosis and predictability of the treatment. Therefore, rapid and firm establishment of bone-to-titanium implant bonding has been a persistent challenge (LeGeros and Craig 1993; Puleo and Nanci 1999; Pilliar 2005).

Compared to conventional removable denture prostheses, restorative treatment of missing teeth using dental titanium implants (Fig. 1b) improves chewing function (Geertman et al. 1996; Carlsson and Lindquist 1994; Pera et al. 1998; van Kampen et al. 2004), nutritional status (Nowjack-Raymer and Sheiham 2003), speech (Heydecke et al. 2004), and the quality of life (Melas et al. 2001). However, the application of implant therapy in dentistry is limited because of various risk factors, including insufficient quality and quantity of the host bone (van Steenberghe et al. 2002), systemic conditions (Ozawa et al. 2002; Nevins et al. 1998) and age (Zhang et al. 2004; Takeshita et al. 1997). The protracted healing time (4–6 months) required for titanium implants to integrate with the bone also limits their application. In the USA, 10% of adults and one-third of adults aged >65 years are fully edentulous (Nowjack-Raymer and Sheiham 2003; Doundoulakis et al. 2003). Despite its increasing need in an aging society, dental implant therapy has been employed in only 2% of potential patients (Annual industry report 2003).

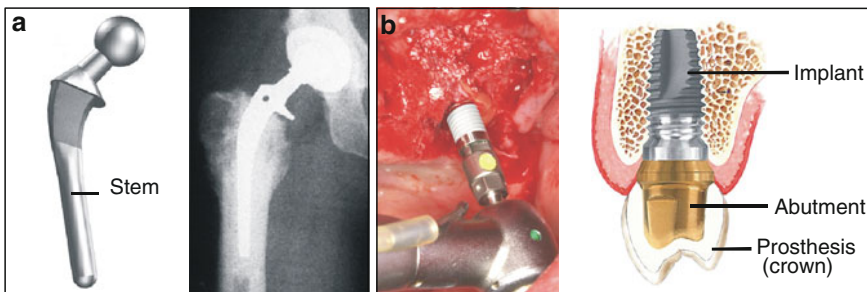


Fig. 1 Orthopedic (a) and dental (b) implants, made of commercially pure titanium or titanium alloy. (a) A femoral stem implant used to total hip replacement including hip joint (*left image*). The stem part of the titanium device is placed into the femur of the recipient. An X-ray image after the implant in place (*right image*). (b) A dental implant being in place surgically into the upper jaw bone of a patient (*left image*). A schematic diagram of the components of a prosthetic tooth restored using an implant (*right image*). After the implant bonds to host bone, parts of abutment and crown are fabricated. The key to successful implant therapy, regardless of orthopedic or dental use, is sturdy biomechanical and biological bonding between the titanium implant and host bone, which is termed “bone-titanium integration” or “osseointegration”

Dental and orthopedic implants are artificial fixtures placed surgically into bone anchors to reconstruct or as substitutes for missing and diseased bone, joints, and teeth. Because titanium is a light, strong, corrosion-resistant metal with great biocompatibility, most currently used implants are made of commercially pure titanium or titanium alloy, such as Ti6Al4V alloy (titanium containing 6% aluminum and 4% vanadium). Successful implant anchorage depends on the quantity of bone directly deposited onto the titanium surface without soft/connective tissue intervention. This is termed “bone-titanium integration” or “osseointegration.” Current dental and orthopedic titanium implants have been developed based on this concept and are called “osseointegrated implants.” However, the total implant area successfully covered with bone (bone-titanium contact percentage) remains to be $45 \pm 16\%$ (Weinlaender et al. 1992), which is far below the ideal 100%. The reason why bone tissue does not form entirely around the implant, as well as the mechanism underlying the phenomenon of osseointegration, is unknown.

In this chapter, we show that the UV light-treated titanium induces unique bone formation around its surface and remarkably accelerates and enhances the process of bone-titanium implant integration biologically and biomechanically. This effect has been demonstrated in multiple surface topography types of titanium and is described in detail elsewhere (Aita et al. 2009). We also discuss the biological breakthrough and therapeutic significance of this UV-mediated titanium surface modification. We expect that UV-treated titanium should have an immediate, extensive clinical application in the orthopedic and dental fields, ranging from screws and plates for bone and spine repair to root- and stem-form implants for replacing teeth and diseased bone and joints.

2 Enhanced Attachment and Spread of Bone-Forming Cells (Osteoblasts) on UV-Treated Titanium

The process of bone formation involves (1) attachment of bone-forming cells (osteoblasts) to areas where bone tissue needs to be generated or regenerated, (2) settlement (spread) of osteoblasts to initiate the subsequent steps of biological function, (3) growth (proliferation) of osteoblasts to expand their population, (4) maturation (differentiation) of osteoblasts to produce necessary proteins for bone formation, and (5) calcification (mineralization) around the secreted proteins. To investigate the biological effects of UV-treatment of titanium, we, first, examined the attachment and spread of osteoblasts to UV-treated titanium surfaces *in vitro* (in a controlled environment of a biological model) and then determined whether UV-treatment was able to create an osteoblast-affinity environment. Disks (20 mm in diameter) made of commercially pure titanium were prepared for experimental purposes and treated with sulfuric acid. This acid-etching process has been widely used in manufacturing dental implants to create microlevel roughness, whose Ra is approximately 550 μm (Fig. 2a). The titanium disks were treated with UV light for 48 h using a bactericidal lamp (intensity; ca. 0.1 mW/cm² [$\lambda = 360 \pm 20$ nm] and 2 mW/cm² [$\lambda = 250 \pm 20$ nm]).

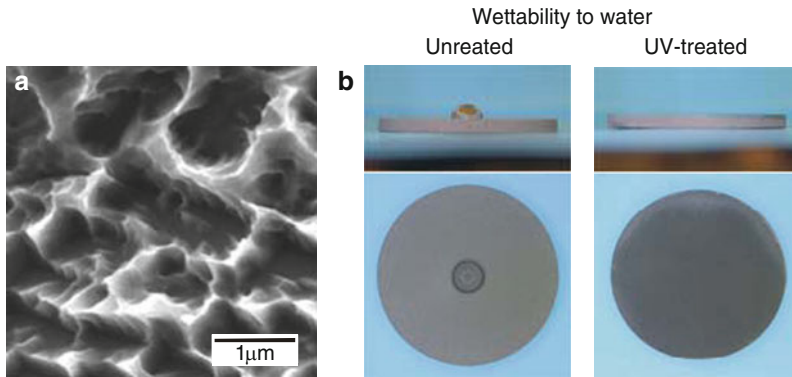


Fig. 2 (a) Scanning electron micrograph of the acid-etched titanium disk used in this study, depicting sharp peaks and valleys with micronscale compartmental structures. (b) Wettability to 10 μL H_2O of the acid-etched titanium disk (20 mm in diameter) before and after the UV light treatment at an intensity of ca. 0.1 mW/cm^2 ($\lambda = 360 \pm 20$ nm) and 2 mW/cm^2 ($\lambda = 250 \pm 20$ nm) for 48 h, depicting a conversion from hydrophobic to superhydrophilic surfaces

During the process, the contact angle of an H_2O droplet, which was 88.4° , decreased to 0° , indicating the conversion of hydrophobic surfaces to superhydrophilic surfaces (Fig. 2b).

Osteoblastic cells derived from rat bone marrow were seeded on the titanium disks with or without UV pretreatment for 48 h. After 3 h of incubation, the number of cells attached to the UV-treated surface was approximately four times greater than those attached to the untreated control surface (Fig. 3a). We examined the UV dose-dependency to confirm UV-promoted osteoblast attachment. The rate of cell attachment continued to increase significantly with an increase in the UV treatment time up to 48 h ($p < 0.01$, ANOVA; Fig. 3b). Osteoblasts that were incubated for 3 h on titanium disks were dual-stained for nuclear and cytoskeleton visualization to examine their spreading behavior. Confocal microscopic images revealed that cells were clearly larger and the cellular processes stretched to a greater extent on UV-treated surfaces than on untreated control surfaces (Fig. 3c). Cytoskeletal development was remarkably advanced on the UV-treated surface. Morphometric evaluations for the area, and the perimeter of the cells showed greater values of these parameters for UV-treated titanium surfaces (histograms in Fig. 3c), suggesting that this unique titanium surfaces facilitated the settlement of osteoblasts following the enhanced attachment.

3 Enhanced Proliferation, Maturation and Mineralization of Osteoblasts on UV-Treated Titanium Surfaces

Osteoblast proliferation was evaluated by BrdU incorporation into the DNA during mitosis. BrdU incorporation per cell at day 2 of culture was higher in osteoblasts cultured on the UV-treated surface (Fig. 4a). We next examined the rate of osteoblast

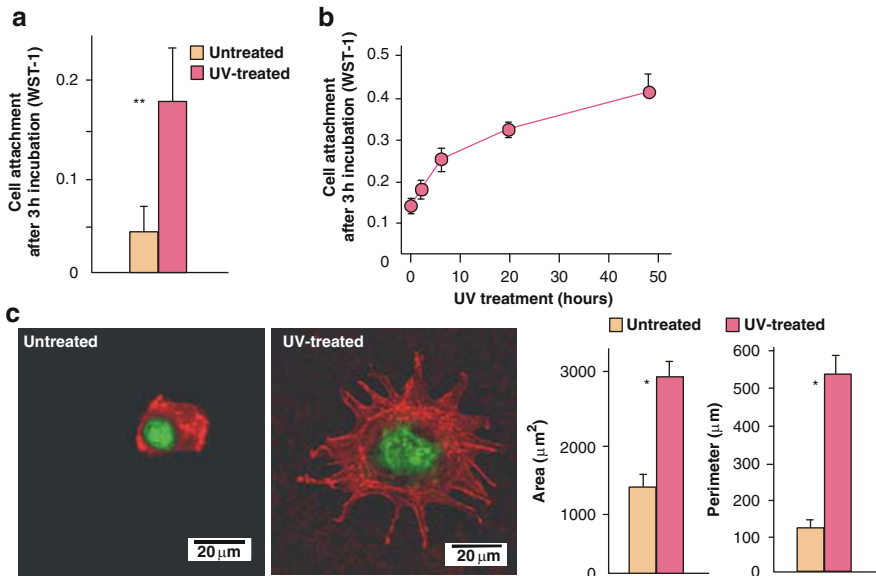


Fig. 3 Ultraviolet (UV) light-induced bone-forming cell (osteoblast)-affinity titanium surfaces. (a) Relative number of osteoblasts attached to titanium surfaces with and without UV pretreatment after 3 h incubation, evaluated by WST-1 colorimetry. Osteoblasts were derived from the rat bone marrow. (b) The rate of osteoblast attachment to titanium surfaces plotted against the hours of UV pretreatment. Data are shown as the mean \pm SD ($n = 3$) and are statistically significant between UV-treated and untreated control surfaces $**p < .01$, respectively. (c) Initial osteoblast spread and cytoskeletal arrangement on titanium surfaces. Confocal microscopic images of osteoblasts with dual staining of DAPI for nuclei (blue) and rhodamine phalloidin for actin filaments (red) (left panels). Cell morphometric evaluations were performed using the images (histograms). Data are shown as the mean \pm SD ($n = 9$), and are statistically significant between UV light-treated and untreated control surfaces $*p < 0.05$

differentiation. Alkaline phosphatase (ALP) activity is an indicator for the activity level of bone-forming cells and an early-stage marker of their functional differentiation. At day 10, the area covered by ALP-positive cells on the UV-treated surfaces was two times that on the control surfaces (Fig. 4b). Moreover, there was a greater amount of calcium deposited on the UV-treated surface, indicating that the mineralization was also enhanced on titanium surfaces treated with UV (Fig. 4c).

4 UV Treatment Accelerates and Enhances the Fixation of Implants In Vivo

Establishing in vivo (within the living body) implant fixation is the most pertinent variable that reflects the clinical capacity of implants as load-bearing devices. In vivo stability of titanium implants with or without the UV treatment was

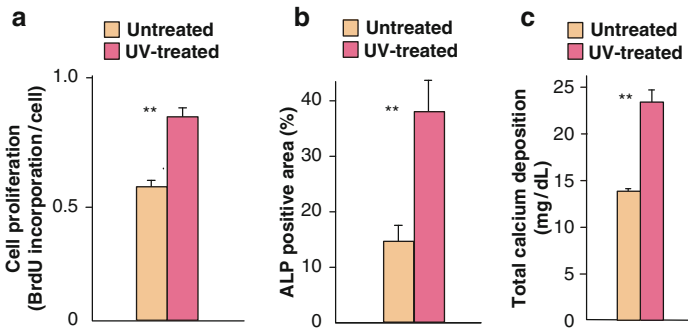


Fig. 4 Enhanced function of bone-forming cell (osteoblasts) on UV-treated titanium surfaces in vitro. (a) Cell proliferative activity of rat bone marrow-derived osteoblasts, evaluated by BrdU incorporation per cell at day 2 of culture. (b) UV-enhanced alkaline phosphatase (ALP) activity, an early-stage maker of osteoblasts. The ALP-positive area as a percentage of culture area was measured with a digital image analyzer. (c) Mineralizing capability (late-stage marker) of osteoblasts, evaluated by total calcium deposition using o-cresolphthalein-based colorimetric method. Data are shown as the mean \pm SD ($n = 3$) and are statistically significant between UV light-treated and untreated control surfaces $**p < 0.01$

examined using the established biomechanical implant push-in test in the rat model (Ogawa et al. 2000) (Fig. 5a). Cylindrical implants (2 mm in length and 1 mm in diameter) were placed into rat femur, and the femurs were extracted and embedded into resin at weeks 2 and 4 postimplantation. The position of the implant was confirmed using microCT images not to be involved in the growth plate or the lateral and bottom cortical bony support. The implants, while being pushed in vertically, gave a mechanically predictable load-displacement curve, and the force at the point of breakage (maximum force on the load-displacement curves) was measured as the push-in value. The push-in value at the early healing stage of week 2 soared 3.1 times for the surface with UV light treatment (Fig. 5b). At the late stage of healing (week 4), the push-in value was 60% higher for the UV-treated implants than the untreated implants.

5 Maximized Bone-Titanium Integration by UV Treatment

UV treatment may accelerate and enhance the fixation of titanium implants titanium implants by increasing bone volume around the implants, bone-to-implant contact, or a combination of both. To address these issues, we performed histological and histomorphometric analyses of bone tissue around the implants. Cylindrical implants with or without UV treatment were placed into the rat femur, and the nondecalcified cross-sections perpendicular to the long axis of the implant were processed for Goldner's trichrome histology. Histological images around

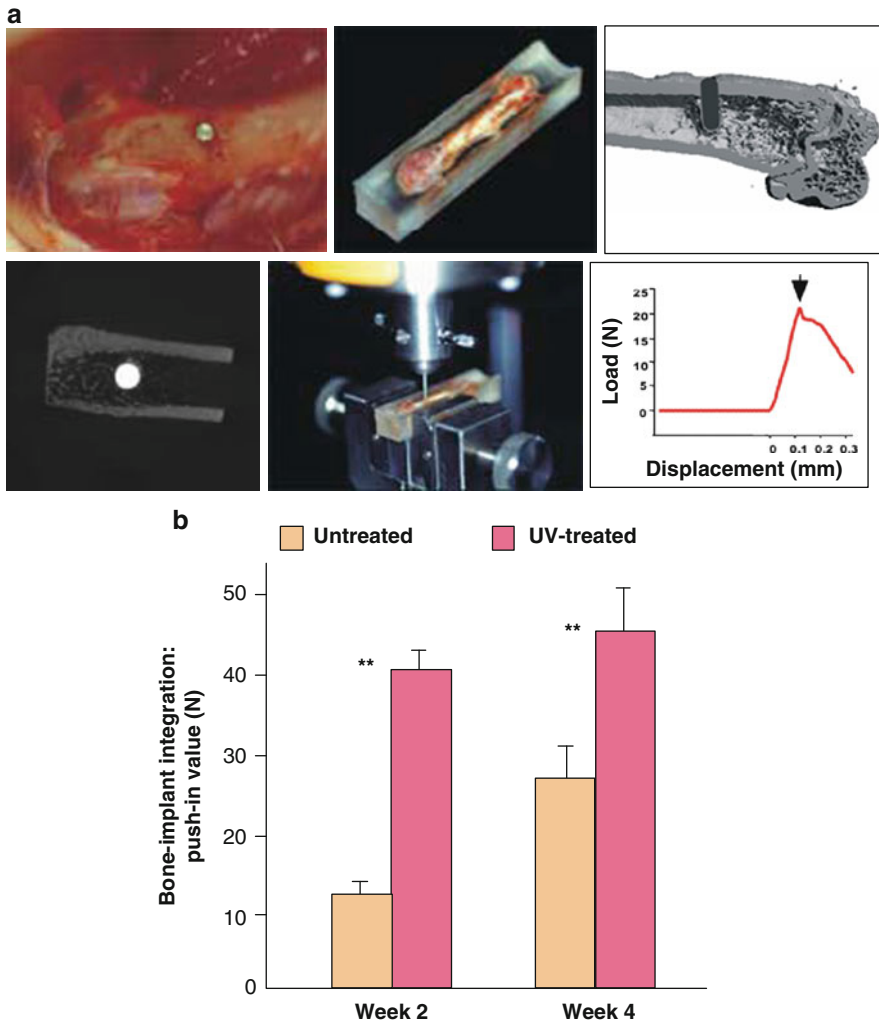


Fig. 5 UV light-enhanced bone-titanium integration evaluated by biomechanical push-in test in vivo. **(a)** The experimental procedure. Titanium implants with or without the UV light treatment were placed into the rat femur. The femur specimen with an implant was harvested and embedded into the methacrylate block. MicroCT was used to confirm the implants were free from cortical bone support from the lateral and bottom sides of the implant. Biomechanical stability of the implants was then evaluated at 2 and 4 weeks postimplantation by measuring the breakage strength against push-in load (arrow). **(b)** Push-in value of the acid-etched implants with and without UV treatment. Data are shown as the mean \pm SD ($n = 5$). Statistically significant between the untreated control and UV light-treated surfaces, ** $p < 0.01$

the adjacent area to the implant surface revealed clear differences in the pattern of bone formation between the untreated control and UV-treated implants, as bone generation occurred more extensively around the UV-treated implant (arrow

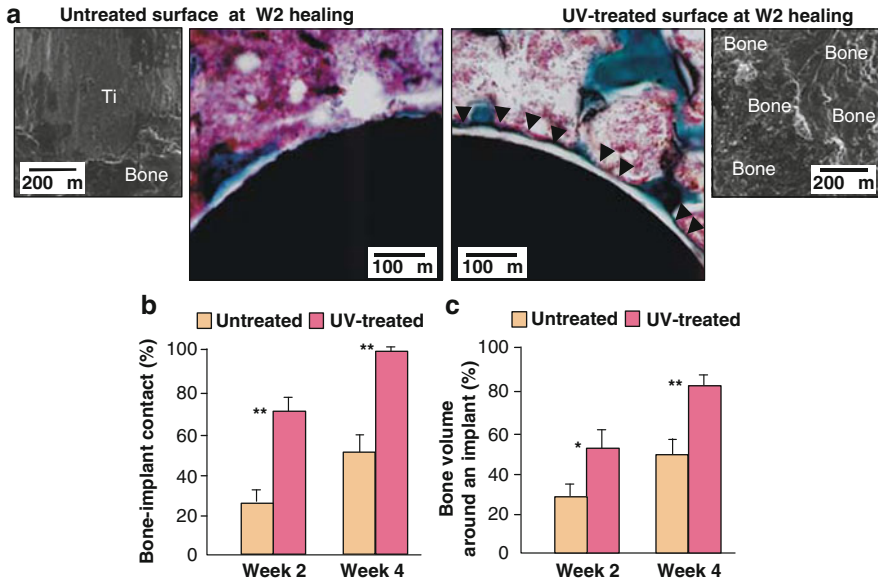


Fig. 6 Promoted peri-implant bone generation around UV-treated titanium implants in vivo. (a) Representative histological images of the titanium implants with Goldner’s trichrome stain (color images), along with SEM images of implant surfaces retrieved at week 2 of healing (*black* and *white* images). Histological images were created by cross-sectioning the implant perpendicular to its longitudinal axis, while the SEM images were taken at the implant-bone interface after retrieving the implant. Note that week 2 UV-treated implant is associated with vigorous bone formation that prevents soft tissue from intervening between the bone and implants, leading to direct and extensive bone deposition onto the implant surface (*arrow heads*). In contrast, the bone around the untreated control appears to be fragmentary. Average histomorphometric values of bone-implant contact (b) and bone volume (c) are shown ($n = 4$). Results are statistically significant between the UV light-treated and untreated control surfaces, $**p < 0.01$, $*p < 0.05$, respectively

heads in Fig. 6a color images). There was superior continuity of bone tissue along the UV-treated implant due to the well-spread generation of bone fragments, compared with that around the untreated implants. Scanning electron micrograms showed almost complete coverage of bone on the UV-treated surface (black and white images in Fig. 6), confirming the histological findings. In contrast, the surface of the untreated implants was largely exposed without new bone formation.

Bone histomorphometry revealed that the percentage of bone-implant contact for the UV-treated implants was consistently greater than for the untreated control implants (2.8 times at week 2 and 2.0 times at week 4) (Fig. 6b). Of note, the bone-implant contact percentage was 98.2% for the UV-treated surface. Further, the bone volume was consistently greater for the UV-treated implants than for the control implants (Fig. 6c).

6 Inverse Correlation Between Carbon Element on Titanium and its Osteoblast Attractiveness

Chemical analysis of the acid-etched titanium surface was performed to identify factors responsible for the enhanced bioactivity. XPS spectra revealed that the C1s peak decreased with an increase in the UV treatment time, whereas Ti2p and O1s peaks increased (Fig. 7a). Particularly, a shoulder peak at about 288 eV ascribed to oxygen-containing hydrocarbons strongly adsorbed on TiO₂ surfaces disappeared (data not shown). The percentage of atomic carbon continued to decrease from >50% to <20% after up to 48 h of the UV treatment. We attempted to determine the role of surface hydrocarbon in determining the bioactivity of titanium surfaces using the titanium surfaces UV-treated for different time periods. A least mean square approximation revealed that the rate of osteoblast attachment increased exponentially with progressive removal of carbon (Fig. 7b). Interestingly, the contact angle of H₂O did not correlate with the rate of osteoblast attachment (Fig. 7c).

7 Proposed Mechanism Underlying the UV-Enhanced Bone Cell Affinity

The mechanism linking the removal of hydrocarbon and the enhanced attractiveness of proteins and cells needs further investigation. Osteoblastic cells and most proteins are negatively charged. When oxygen-containing hydrocarbons covering TiO₂ surfaces (Uetsuka et al. 2004; Henderson et al. 2006) are removed by the UV

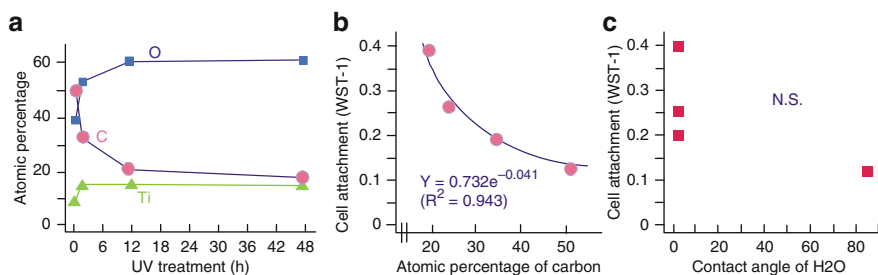


Fig. 7 UV-light-induced changes in surface chemistry of titanium in association with their biological effects. **(a)** Atomic percentage of the acid-etched titanium surface in change with different time periods of the UV treatment, evaluated by electron spectroscopy for chemical analysis (ESCA) using an X-ray photoelectron spectroscopy (XPS). **(b)** Osteoblast attachment rate after 3 h incubation plotted against the atomic percentage of carbon on the acid-etched titanium surface, showing their significant inverted exponential correlation. **(c)** Osteoblast attachment rate (I) plotted against the H₂O contact angle on the acid-etched titanium surface, showing no significant correlation between them

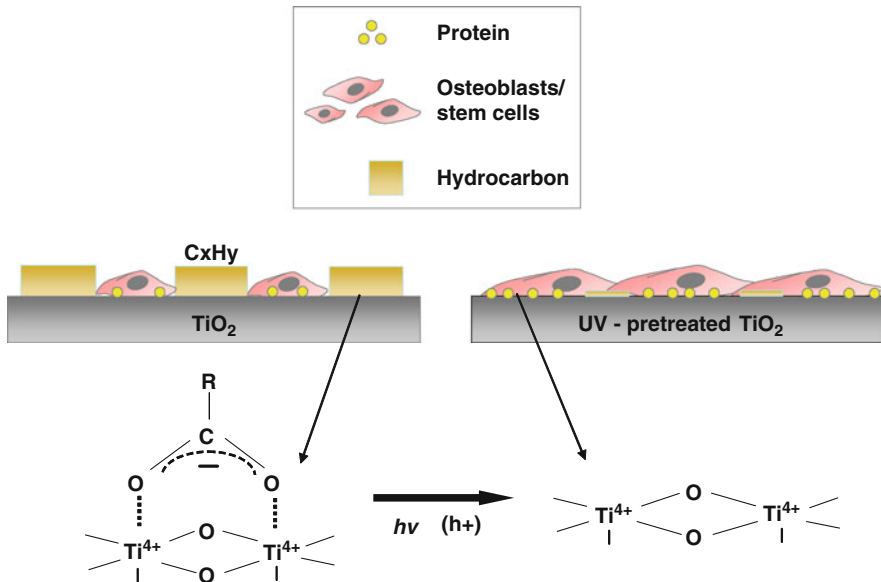


Fig. 8 Schematic description of a proposed photofunctionalization of TiO₂ illustrating the photo-generation of bioaffinity TiO₂ surface that accelerates and enhances protein adsorption, and attachment and spread of osteoblasts, leading to bone-titanium integration of the nearly 100%. These initial biological processes are distinguished from the process that has been understood for osseointegration. Taken together with the near perfect bone-titanium contact percentage that overwhelms the reported numbers in the literature, this unique biological phenomenon induced around UV-treated titanium is proposed to be defined as “superosseointegration”

light treatment, Ti⁴⁺ sites are exposed, which may promote the interaction between the proteins and cells, and such cationic sites. Although detail analyses of surface energy, electric charge, and other properties are required to identify the underlying mechanism, the generation of a bioaffinity TiO₂ surface associated with the photodecomposition of hydrocarbons is schematically proposed in Fig. 8.

8 Biocompatibility and Effectiveness of UV-Treated Titanium in Human Cells

Although titanium is an established biocompatible material, the UV treatment may possibly cause physicochemical and other unknown changes on titanium surfaces that have adverse biological effects. From this viewpoint, the behavior and reaction of human cells on the UV-treated titanium surface were examined. Human mesenchymal stem cells were cultured on the acid-etched titanium surfaces with and without the UV treatment. The live/dead stain images revealed no difference in the percentage of live cells between the two cultures after 24 h of incubation (Fig. 9a),

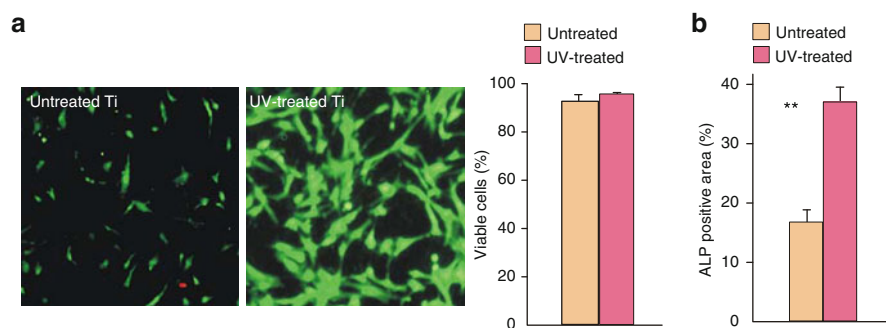


Fig. 9 Biological effectiveness and safety of UV-treated titanium in human cells. **(a)** Viability of human mesenchymal stem cells 24 h after seeding onto the untreated and UV-treated Ti surfaces. Results of live/dead assay evaluated by dual stain of calcein AM (live; *green*) and ethidium homodimer-1 (dead; *red*). **(b)** ALP activity in human osteoblastic cells cultured on Ti surfaces with and without UV pretreatment. The cells were cultured on the osteogenic induction medium. The ALP-positive area is shown as a percentage of culture area. Data are shown as mean \pm SD ($n = 3$). $**p < 0.01$, statistically significant difference between untreated and UV light-treated titanium

denying the possible cytotoxic effect of UV-treated surface. There was substantially higher (over twofold) ALP activity in the human osteogenic cells on the UV-treated surface than on the untreated surface (Fig. 9b), confirming a similar efficacy of the UV treatment on human cells to that on rat cells.

9 Biological Breakthrough by UV-Mediated Photofunctionalization of Titanium: From Bioinert to Bioactive

One problem that must be resolved to generate more bone faster is the biological dilemma of an inverted correlation between proliferation and differentiation rates in osteoblasts (Stein and Lian 1993; Siddhanti and Quarles 1994; Alborzi et al. 1996; Owen et al. 1990). This applies to the bone formation around titanium implants. For instance, microroughened titanium surfaces have advantages over machined, smooth surfaces in that they not only increase tissue-titanium mechanical interlocking, but also promote osteoblastic differentiation (Ogawa et al. 2002), resulting in faster bone formation (Ogawa and Nishimura 2003). However, there is less bone mass around the roughened surface (Ogawa et al. 2002), in accordance with the diminished osteoblastic proliferation (Takeuchi et al. 2005; Bachle and Kohal 2004). This paper has reported that osteoblastic differentiation, as represented by ALP activity and calcium deposition, remained elevated during enhanced cell proliferation, indicating that UV-treated surfaces enable an increase in osteoblastic proliferation without sacrificing differentiation.

The mechanisms underlying bone-titanium integration have been poorly understood (Brunski et al. 2000; Sykaras et al. 2000). For instance, the coverage of bone (bone-Ti contact percentage) remains $45 \pm 16\%$ (Weinlaender et al. 1992), which is far below the ideal 100%, and a vast majority of implants fail due to bone and implant interfacial failure (Espehaug et al. 2002). An explanation as to why the bone tissue does not grow entirely around the implant remains elusive. The critical inferiority of the untreated surface demonstrated in this study may provide a potential clue to help explain the low reported bone-titanium contact percentage. Nevertheless, UV-treated surfaces drastically enhanced the bone-titanium contact to near the maximum level of 98.2%. Titanium has been used as a bioinert implantable material due to its great anticorrosion property. As comprehensively demonstrated in this chapter and our recent studies (Aita et al. 2009), UV-treated titanium surfaces attract bone-forming cells and necessary proteins, related to the UV-catalyzed changes in surface physicochemistry, converting titanium surface from bioinert to bioactive. We postulate that the biological process of bone generation induced around this bioactive surface is distinctive and that the level of bone-titanium integration (osseointegration), which is achieved by this novel titanium surface, is far beyond the level of osseointegration that has been recognized since 1960s. Therefore, we propose to define the biological phenomenon uniquely induced around the UV-treated titanium as “super osseointegration.”

10 Therapeutic Significance

Titanium implants have become an essential treatment modality in bone and teeth reconstructive surgeries in dental and orthopedic fields. However, there has been a pressing clinical demand to reduce patient morbidity, improve outcome predictability, avoid complications, and expand treatment indications. To meet these demands, considerable efforts have been made toward the development of new titanium surface modification technologies for obtaining improved osteoconductivity.

Topographical modification of titanium surfaces has been achieved successfully and the so-called rough surfaces have demonstrated the ability to improve the biological potential of titanium in terms of osteoblast attachment, differentiation, protein production, and gene expression *in vitro* and *in vivo* (Ogawa et al. 2000; Ogawa and Nishimura 2003; Takeuchi et al. 2005; Butz et al. 2006; Ogawa and Nishimura 2006; Masuda et al. 1998; Cooper 2000; Butz et al. 2005). However, it seems difficult to produce compelling data that shows significant advantages of the new modification over the existing surfaces. Even with aggressive implementation of nanotechnology in the field, it seems challenging to further enhance the level of bioactivity to a biologically significant level over the established affinity between osteoblasts and microscale topography (Goransson et al. 2009; Meirelles et al. 2008a; Meirelles et al. 2008b). Technologically, controlling the size and shape of titanium at the nanoscale, as well as a large-scale surface modification applicable to implant products, needs further breakthrough (Ogawa et al. 2008). Additionally, the

cost-effectiveness of such a modification process has to be considered. Moreover, devices and parameters capable of characterizing and quantifying nanoscale surface topography and roughness are yet to be established, thus creating another difficulty in evaluating the nanotopography-osteogenic cell interactions.

Surface chemistry has been another target in modification of Ti surfaces. A number of methods, subtractive and additive procedures, including the use of different acidic and alkaline liquids to treat titanium surfaces for different processing time and temperatures and the use of chemical deposition techniques under modified electrical environments, have been introduced. Such methods produce varying titanium surface chemistries, particularly in terms of the Ti/O ratio, thickness of the oxidized layer, crystallization properties, and surface impurities (Saruwatari et al. 2005; Tsukimura et al. 2008; Variola et al. 2008), resulting in different osteogenic cell responses (Tsukimura et al. 2008; Variola et al. 2008). Most of these chemical modifications concomitantly alter the surface topography (Saruwatari et al. 2005), making it difficult to understand the pure contribution of surface chemistry to the alteration of titanium bioactivity (Variola et al. 2008; Att et al. 2007).

Based on our recent studies, the UV treatment presented here is assumed to be universal as long as the material contains titanium (Aita et al. 2009), and even for other implantable materials (Att et al. 2009). The major benefit of this treatment is threefold stronger anchorage of the implants at the early healing stage, which corresponds to 4-time acceleration in the establishment of bone-titanium integration (Ogawa et al. 2000). We expect that this novel technology will have immediate and extensive applications in dental, facial, and orthopedic implant therapies because of its simplicity, high efficacy, and low cost.

Acknowledgements This work was supported by JIADS, JAMSEA, and Implant-Perio Study Group. The author would like to express special appreciation to Drs. Masato Takeuchi and Masakazu Anpo (Osaka Prefecture University) for their dedicated support and help with the data collection, analysis, and interpretation of titanium surface characterization.

References

- Aita H, Hori N, Takeuchi M, Suzuki T, Yamada M, Anpo M, Ogawa T (2009) The effect of ultraviolet functionalization of titanium on integration with bone. *Biomaterials* 30:1015
- Alborzi A, Mac K, Glackin CA, Murray SS, Zernik JH (1996) Endochondral and intramembranous fetal bone development: osteoblastic cell proliferation, and expression of alkaline phosphatase, m-twist, and histone H4. *J Craniofac Genet Dev Biol* 16:94
- Annual industry report (2003) US markets for dental implants: executive summary. *Implant Dent* 12:108
- Att W, Tsukimura N, Suzuki T, Ogawa T (2007) Effect of supramicron roughness characteristics produced by 1- and 2-step acid etching on the osseointegration capability of titanium. *Int J Oral Maxillofac Implants* 22:719
- Att W, Takeuchi M, Suzuki T, Kubo K, Anpo M, Ogawa T (2009) Enhanced osteoblast function on ultraviolet light-treated zirconia. *Biomaterials* 30(7):1273–1280

- Bachle M, Kohal RJ (2004) A systematic review of the influence of different titanium surfaces on proliferation, differentiation and protein synthesis of osteoblast-like MG63 cells. *Clin Oral Implants Res* 15:683
- Brunski JB, Puleo DA, Nanci A (2000) Biomaterials and biomechanics of oral and maxillofacial implants: current status and future developments. *Int J Oral Maxillofac Implants* 15:15
- Butz F, Aita H, Takeuchi K, Ogawa T (2005) Enhanced mineralized tissue adhesion to titanium over polystyrene assessed by the nano-scratch test. *J Biomed Mater Res A* 74:164
- Butz F, Aita H, Wang CJ, Ogawa T (2006) Harder and stiffer bone osseointegrated to roughened titanium. *J Dent Res* 85:560
- Carlsson GE, Lindquist LW (1994) Ten-year longitudinal study of masticatory function in edentulous patients treated with fixed complete dentures on osseointegrated implants. *Int J Prosthodont* 7:448
- Cooper LF (2000) A role for surface topography in creating and maintaining bone at titanium endosseous implants. *J Prosthet Dent* 84:522
- Doundoulakis JH, Eckert SE, Lindquist CC, Jeffcoat MK (2003) The implant-supported overdenture as an alternative to the complete mandibular denture. *J Am Dent Assoc* 134:1455
- Espehaug B, Furnes O, Havelin LI, Engesaeter LB, Vollset SE (2002) The type of cement and failure of total hip replacements. *J Bone Joint Surg Br* 84:832
- Geertman ME, Boerrieger EM, Van't Hof MA, Van Waas MA, van Oort RP, Boering G, Kalk W (1996) Two-center clinical trial of implant-retained mandibular overdentures versus complete dentures-chewing ability. *Community Dent Oral Epidemiol* 24:79
- Goransson A, Arvidsson A, Currie F, Franke-Stenport V, Kjellin P, Mustafa K, Sul YT, Wennerberg A (2009) An in vitro comparison of possibly bioactive titanium implant surfaces. *J Biomed Mater Res A* 88(4):1037–1047
- Henderson MA, White JM, Uetsuka H, Onishi H (2006) Selectivity changes during organic photooxidation on TiO₂: Role of O-2 pressure and organic coverage. *J Catal* 238:153
- Heydecke G, McFarland DH, Feine JS, Lund JP (2004) Speech with maxillary implant prostheses: ratings of articulation. *J Dent Res* 83:236
- LeGeros RZ, Craig RG (1993) Strategies to affect bone remodeling: osteointegration. *J Bone Miner Res* 8(Suppl 2):S583
- Masuda T, Yliheikkilä PK, Felton DA, Cooper LF (1998) Generalizations regarding the process and phenomenon of osseointegration. Part I. In vivo studies. *Int J Oral Maxillofac Implants* 13:17
- Meirelles L, Melin L, Peltola T, Kjellin P, Kangasniemi I, Currie F, Andersson M, Albrektsson T, Wennerberg A (2008a) Effect of Hydroxyapatite and Titania Nanostructures on Early In Vivo Bone Response. *Clin Implant Dent Relat Res* 10(4):245–254
- Meirelles L, Albrektsson T, Kjellin P, Arvidsson A, Franke-Stenport V, Andersson M, Currie F, Wennerberg A (2008b) Bone reaction to nano hydroxyapatite modified titanium implants placed in a gap-healing model. *J Biomed Mater Res A* 87(3):624–631
- Melas F, Marcenes W, Wright PS (2001) Oral health impact on daily performance in patients with implant-stabilized overdentures and patients with conventional complete dentures. *Int J Oral Maxillofac Implants* 16:700
- Nevins ML, Karimbux NY, Weber HP, Giannobile WV, Fiorellini JP (1998) Wound healing around endosseous implants in experimental diabetes. *Int J Oral Maxillofac Implants* 13:620
- Nowjack-Raymer RE, Sheiham A (2003) Association of edentulism and diet and nutrition in US adults. *J Dent Res* 82:123
- Ogawa T, Nishimura I (2003) Different bone integration profiles of turned and acid-etched implants associated with modulated expression of extracellular matrix genes. *Int J Oral Maxillofac Implants* 18:200
- Ogawa T, Nishimura I (2006) Genes differentially expressed in titanium implant healing. *J Dent Res* 85:566
- Ogawa T, Ozawa S, Shih JH, Ryu KH, Sukotjo C, Yang JM, Nishimura I (2000) Biomechanical evaluation of osseous implants having different surface topographies in rats. *J Dent Res* 79:1857
- Ogawa T, Sukotjo C, Nishimura I (2002) Modulated bone matrix-related gene expression is associated with differences in interfacial strength of different implant surface roughness. *J Prosthodont* 11:241

- Ogawa T, Saruwatari L, Takeuchi K, Aita H, Ohno N (2008) Ti nano-nodular structuring for bone integration and regeneration. *J Dent Res* 87:751
- Owen TA, Aronow M, Shalhoub V, Barone LM, Wilming L, Tassinari MS, Kennedy MB, Pockwinse S, Lian JB, Stein GS (1990) Progressive development of the rat osteoblast phenotype in vitro: reciprocal relationships in expression of genes associated with osteoblast proliferation and differentiation during formation of the bone extracellular matrix. *J Cell Physiol* 143:420
- Ozawa S, Ogawa T, Iida K, Sukotjo C, Hasegawa H, Nishimura RD, Nishimura I (2002) Ovariectomy hinders the early stage of bone-implant integration: histomorphometric, biomechanical, and molecular analyses. *Bone* 30:137
- Pera P, Bassi F, Schierano G, Appendino P, Preti G (1998) Implant anchored complete mandibular denture: evaluation of masticatory efficiency, oral function and degree of satisfaction. *J Oral Rehabil* 25:462
- Pilliar RM (2005) Cementless implant fixation—toward improved reliability. *Orthop Clin North Am* 36:113
- Puleo DA, Nanci A (1999) Understanding and controlling the bone-implant interface. *Biomaterials* 20:2311
- Ray NF, Chan JK, Thamer M, Melton LJ 3rd (1997) Medical expenditures for the treatment of osteoporotic fractures in the United States in 1995: report from the National Osteoporosis Foundation. *J Bone Miner Res* 12:24
- Saruwatari L, Aita H, Butz F, Nakamura HK, Ouyang J, Yang Y, Chiou WA, Ogawa T (2005) Osteoblasts generate harder, stiffer, and more delamination-resistant mineralized tissue on titanium than on polystyrene, associated with distinct tissue micro- and ultrastructure. *J Bone Miner Res* 20:2002
- Siddhanti SR, Quarles LD (1994) Molecular to pharmacologic control of osteoblast proliferation and differentiation. *J Cell Biochem* 55:310
- Stein GS, Lian JB (1993) Molecular mechanisms mediating proliferation/differentiation interrelationships during progressive development of the osteoblast phenotype. *Endocr Rev* 14:424
- Sykaras N, Iacopino AM, Marker VA, Triplett RG, Woody RD (2000) Implant materials, designs, and surface topographies: their effect on osseointegration. A literature review. *Int J Oral Maxillofac Implants* 15:675
- Takehita F, Murai K, Ayukawa Y, Suetsugu T (1997) Effects of aging on titanium implants inserted into the tibiae of female rats using light microscopy, SEM, and image processing. *J Biomed Mater Res* 34:1
- Takeuchi K, Saruwatari L, Nakamura HK, Yang JM, Ogawa T (2005) Enhanced intrinsic biomechanical properties of osteoblastic mineralized tissue on roughened titanium surface. *J Biomed Mater Res A* 72A:296
- Tsukimura N, Kojima N, Kubo K, Att W, Takeuchi K, Kameyama Y, Maeda H, Ogawa T (2008) The effect of superficial chemistry of titanium on osteoblastic function. *J Biomed Mater Res A* 84:108
- Uetsuka H, Onishi H, Henderson MA, White JM (2004) Photoinduced redox reaction coupled with limited electron mobility at metal oxide surface. *J Phys Chem B* 108:10621
- van Kampen FM, van der Bilt A, Cune MS, Fontijn-Tekamp FA, Bosman F (2004) Masticatory function with implant-supported overdentures. *J Dent Res* 83:708
- van Steenberghe D, Jacobs R, Desnyder M, Maffei G, Quirynen M (2002) The relative impact of local and endogenous patient-related factors on implant failure up to the abutment stage. *Clin Oral Implants Res* 13:617
- Variola F, Yi JH, Richert L, Wuest JD, Rosei F, Nanci A (2008) Tailoring the surface properties of Ti6Al4V by controlled chemical oxidation. *Biomaterials* 29:1285
- Weinlaender M, Kenney EB, Lekovic V, Beumer J 3rd, Moy PK, Lewis S (1992) Histomorphometry of bone apposition around three types of endosseous dental implants. *Int J Oral Maxillofac Implants* 7:491
- Zhang H, Lewis CG, Aronow MS, Gronowicz GA (2004) The effects of patient age on human osteoblasts' response to Ti-6Al-4V implants in vitro. *J Orthop Res* 22:30

Part X
Conclusions and Emerging Applications

Chapter 30

Emerging Applications of TiO₂ -Based Composites

Prashant V. Kamat and M. Anpo

During the last few decades efforts have been made to design semiconductor and metal nanostructures for a variety of applications. Of particular interest are TiO₂ nanostructures that provide the basis for photocatalysis and dye-sensitized solar cells. The popularity of TiO₂ can also be seen in everyday applications. The commercial use of TiO₂ in paints and toothpaste has popularized TiO₂ in household products. The US Food and Drug Administration (FDA) lists titanium dioxide (73.575) as a color additive for food and exempts it from certification. The FDA sets the limit of 1% by weight in food products (GSFA CI-Pigment White 6; CI (1975) No. 77891). Food products such as powdered donuts, white chocolate, and dairy products make use of TiO₂ as a food additive to enhance the color and/or anti-caking activity.

Aside from its use as a brightening agent in commercial products, TiO₂ is a large bandgap semiconductor. Its response to ultraviolet light and/or electric field makes it attractive for designing next-generation devices. TiO₂ nanostructures have already shown promise in developing next-generation solar cells. Furthermore, the utilization of these nanoparticles in many commercially available photocatalytic devices has opened up new ways to design green oxidation technologies for environmental remediation. In this chapter, we will highlight several important applications of TiO₂ and the underlying principles. Most of the discussions have been extracted from previously published review articles (Kamat and Meisel 2002; Kamat 2007, 2008).

M. Anpo (✉)

Department of Applied Chemistry, Osaka Prefecture University, College of Engineering,
Gakuen-cho 1-1, Sakai, Osaka 599-8531, Japan
e-mail: anpo@chem.osakafu-u.ac.jp

1 Photocatalysis

Technological advances in the area of photocatalysis have already led to product development for a variety of day-to-day uses. Commercial products such as self-cleaning glasses and disinfectant tiles and filters for air purification demonstrate the early successes of nanosystems for environmental applications (Fujishima et al. 1999). Earlier reviews (Kamat 1993; Hoffmann et al. 1995; Serpone 1997) focused on the principles and mechanisms of photocatalytic reactions in advanced oxidation processes (AOP).

The participation of a semiconductor nanoparticle in a photocatalytic process can be either direct or indirect as illustrated in Fig. 1a, b, respectively.

Charge separation in semiconductor particles occurs when they are subjected to bandgap excitation. The photogenerated electrons and holes are capable of oxidizing or reducing the adsorbed substrates (Fig. 1a). Alternatively, the semiconductor nanoclusters also promote a photocatalytic reaction by acting as mediators for the charge transfer between two adsorbed molecules (Fig. 1b). This process, which is commonly referred to as photosensitization, is extensively used in photoelectrochemistry and imaging science. In the first case, the bandgap excitation of a semiconductor particle is followed by the charge transfer at the semiconductor/electrolyte interface. In the second case, however, the semiconductor nanoparticle quenches the excited state by accepting an electron and then transferring the charge to another substrate or generating photocurrent. The contaminant dye itself can act as a sensitizer and undergo oxidative degradation (Fig. 1b). Such an approach was found to be useful in discoloration of the textile dye on TiO_2 nanoparticles (Vinodgopal et al. 1996; Nasr et al. 1996). The energies of the semiconductor's conduction and valence bands and the redox potential of the adsorbed molecule control the reaction course of the photochemical reaction.

The TiO_2 photocatalyst has been the popular choice in much of the published photocatalysis work. Its large bandgap energy (3.2eV) necessitates UV-excitation to induce charge separation within the particle. In a 1955 pioneering article,

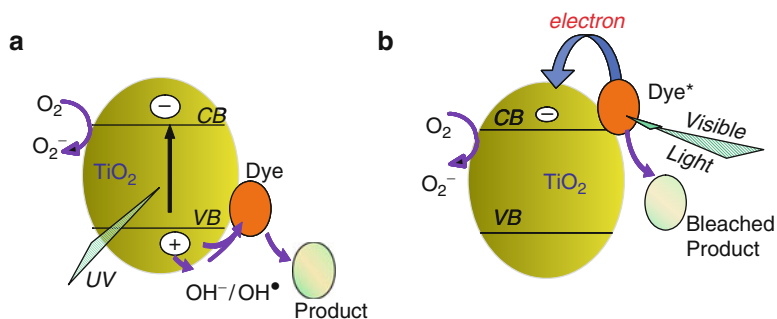


Fig. 1 Photoinduced charge transfer processes in semiconductor nanoclusters. (a) Under bandgap excitation and (b) sensitized charge injection by exciting adsorbed dye molecules. *CB* and *VB* refer to conduction and valence bands of the semiconductor, respectively

Markham pointed out the photocatalytic properties of zinc oxide, titanium oxide, and antimony trioxide under UV irradiation (Markham-Sr 1955). In aqueous solutions, the holes are scavenged by surface hydroxide groups to generate •OH radicals, which then induce the oxidation of organics (Kraeutler et al. 1978; Anpo et al. 1985; Howe and Graetzel 1985; Micic et al. 1993a, b). The •OH radical-mediated oxidation has been successfully employed in the mineralization of many chemical contaminants. Interestingly, electron scavenging becomes the rate-limiting factor in such oxidation processes (Gerischer and Heller 1991, 1992; Wang et al. 1992; Peterson et al. 1991; Vinodgopal et al. 1993; Kesselman et al. 1993, 1994). Alternative methods have also been suggested, for example, by applying an electrochemical bias to the TiO₂ particulate film electrode, to promote charge separation (Vinodgopal et al. 1993). On the contrary, both reductive and oxidative steps can be beneficially used to degrade aromatic compounds such as trinitrophenol (Schmelling et al. 1996).

Several research groups have attempted to extend the photoresponse into the visible by doping TiO₂ with transition metal ions. In many instances, this doping procedure directly influences the intrinsic properties of the semiconductor and extends its photoresponse into the visible (Martin et al. 1994a; Anpo et al. 1998; Di Paola et al. 2002). Nitrogen doped into substitutional sites of TiO₂ has shown bandgap narrowing as well as photocatalytic activity in the visible (Asahi et al. 2001). Films and powders of TiO_{2-x}N_x have shown an improvement over TiO₂ under visible light (up to 500nm) irradiation.

1.1 Combining Photocatalysis with Other Advanced Oxidation Processes

Combining photocatalysis with another AOP such as sonolysis can be an effective approach to improve the mass transfer of reactants and products to and from the catalytic surface in photocatalytic reactions (Johnston and Hocking 1993; Stevenson et al. 1997; Serpone et al. 1994; Szweczyk 1997; Pernas et al. 1998). While hydroxyl radicals play a role in TiO₂ photocatalysis, direct hole induced oxidation on the catalyst surface opens up an alternative route in the degradation mechanism (Stafford et al. 1996). The TiO₂ photocatalysis process is most useful in its ability to degrade polar compounds rapidly. When highly polar compounds are formed during the oxidation of organic contaminants, complete breakdown to CO₂ and H₂O (mineralization) is quickly realized. While many organic compounds are readily broken down, not all compounds are readily transformed by this heterogeneous oxidation system.

The merits of combining sonolysis and photocatalysis were evaluated by investigating the degradation of an azo dye, naphthol blue black (NBB) (Stock et al. 2000), and a herbicide, 2,4-dichlorophenoxyacetic acid (2,4-D) (Peller et al. 2003). Whereas sonolysis was effective in the initial degradation of 2,4-D, photocatalysis

was more efficient in decreasing the total organic carbon (TOC). Moreover, the combined approach also minimized the production of chemical intermediates such as chlorinated phenols (Peller et al. 2003). The combination approach overcomes the deficiencies of the individual techniques and makes the overall remediation process more effective. The added benefit of sonication on photocatalysis may be due to several reasons. For example, during combined sonolysis and photocatalysis experiments, the photocatalyst is expected to be well dispersed and its surface constantly refreshed. In addition, mass transport of reactants and products to and from the catalyst surface is improved as the slurry is constantly agitated.

1.2 Semiconductor–Metal Nanocomposites

By designing semiconductor–metal composite nanoparticles, it is possible to improve the catalytic properties of photocatalysts (Fig. 2). Contact of the metal with the semiconductor indirectly influences the energetics and interfacial charge transfer processes in a favorable way. The deposition of a noble metal on semiconductor nanoparticles is an essential factor for maximizing the efficiency of photocatalytic reactions (Bard 1982). A common assumption is that the noble metal (e.g., Pt) acts as a sink for photoinduced charge carriers and promotes interfacial charge transfer processes. Such TiO_2/Pt -based composites have become the basis for the photocatalytic splitting of water to produce hydrogen.

Metal islands or nanoparticles deposited on a semiconductor surface undergo Fermi level equilibration following the charging with photogenerated electrons. The effect of Fermi level equilibration is predominantly seen when the metal deposits consist of small islands or small particles. Unlike bulk metals, the nanoparticles do not often exhibit ohmic contact with the semiconductor surface. During extended UV photolysis, electron capture by metal islands of Ag, Au, and Cu becomes inhibited as their Fermi levels shift closer to the conduction band of the semiconductor. Pt, on the contrary, acts as an electron sink and fails to achieve

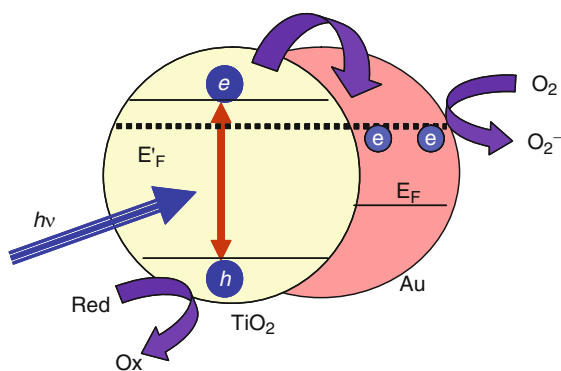
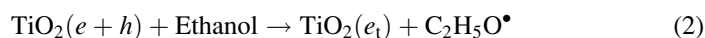
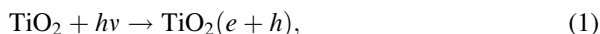


Fig. 2 Charge transfer and Fermi-level equilibration in a metal–semiconductor nanocomposite. E'_F and E_F refer to Fermi levels before and after equilibration

Fermi-level equilibration. Based on photoelectrochemical studies, a Fermi-level shift of about ~150mV was observed for the TiO₂/Au composite film (Chandrasekharan and Kamat 2000; Subramanian et al. 2003). Metal nanoparticles deposited on TiO₂ films thus prove beneficial for improving the photoelectrochemical and photocatalytic performance. Semiconductor–metal composites are expected to have a significant role in the design of photocatalytic systems for solar hydrogen production (Park and Bard 2005; Mor et al. 2006).

2 Electron Trapping and Storage

Semiconductor nanoparticles exhibit an interesting property of storing electrons and holes at trap sites. This redox property opens the way to modulate electron charging of these particles using photoexcitation and electrochemical bias. After TiO₂ nanoparticles are subjected to bandgap excitation ($\lambda < 350$ nm), they undergo charge separation (reactions (1) and (2)). Whereas a majority of these charge carriers recombine, a fraction of these charge carriers get trapped at the surface vacancies. The photogenerated holes (h) are scavenged by ethanol, leaving the conduction band electrons (e) trapped in the particle. The trapping of electrons (e_t) at the Ti⁴⁺



centers has been extensively investigated using transient absorption spectroscopy (Maruthamuthu et al. 1995; Kamat et al. 1994), microwave conductivity (Warman et al. 1991; Fessenden and Kamat 1995; Martin et al. 1994b), and EPR techniques (Howe and Graetzel 1985; Graetzel and Howe 1990; Rajh et al. 1996). The spectra in Fig. 3 show the absorption changes associated with UV irradiation of TiO₂ colloids. Based on an extinction coefficient of $760\text{M}^{-1}\text{cm}^{-1}$, we estimated that about 3,770 electrons are stored per particle of 12nm average diameter. This is consistent with the value estimated using the density of electronic states, n_C , available in the conduction band of TiO₂ (Rothenberger et al. 1985).

2.1 Photochromic and Electrochromic Effects

The presence of alkali metal ions is crucial for the stabilization of excess charge trapped within the nanoparticles. Intercalation of metal ions within the nanoparticle can become a limiting factor as the rate of transport of these ions decreases with

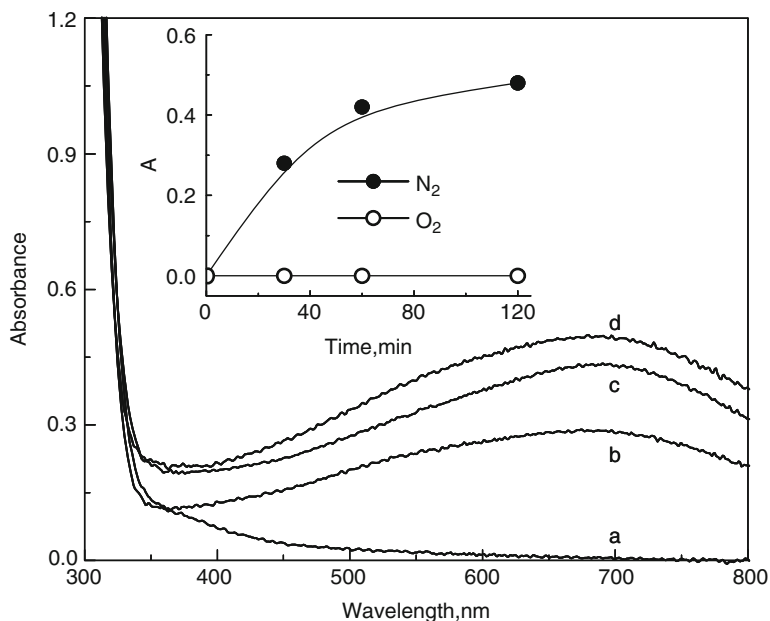
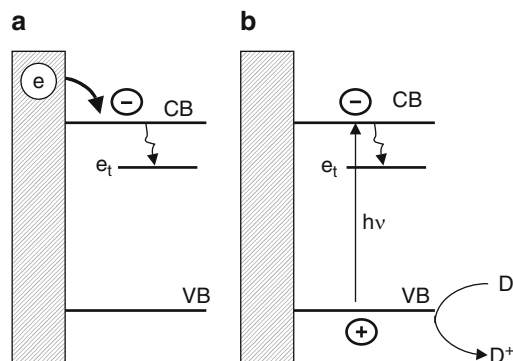


Fig. 3 Absorbance spectra of 5.5 mM deaerated TiO₂ suspension in 1:1 (v/v) ethanol–toluene recorded following different periods of UV illumination ($\lambda > 300\text{nm}$): (a) 0, (b) 30, (c) 60, and (d) 120min. Inset shows the effect of O₂ and N₂ on the absorbance change at 675nm during UV irradiation (from Subramanian et al. (2004), reprinted with permission from the American Chemical Society)

increasing metal oxide film thickness. This in turn controls the rate of coloration and recovery of the photochromic and electrochromic effects. Limited efforts have also been made to employ mixed TiO₂/WO₃ (Hashimoto and Matsuoka 1991), WO₃/V₂O₅ (Ozer and Lampert 1999), and WO₃/MoO₃ (Papaefthimiou et al. 1999) systems for enhancing the efficiency of electrochromic effects. The beneficial aspect of these nanostructured semiconductor films in electrochromic devices is yet to be explored in a systematic way.

The absorption of nanostructured TiO₂ films can be tuned by applying different applied negative potentials. With increasing negative potentials, one observes an increase in absorption in the red-IR, thus giving the film a blue color. Switching the electrode to positive bias reverses the coloration effects. The onset potential at which the electrochromic effect is observed corresponds to the flat band potential of the corresponding semiconductor and is dependent on the pH of the medium. With increasing pH, the onset of electrochromic effect shifts to more negative potentials (O'Regan et al. 1991a, b). By monitoring optical absorbance, Fitzmaurice and his coworkers (O'Regan et al. 1991a, b; Redmond et al. 1993; Redmond and Fitzmaurice 1993; Butler et al. 1993) determined the flat band potentials of nanostructured films of TiO₂ and the extinction coefficient of the trapped electrons.

Fig. 4 (a) Electrochemically induced and (b) photoinduced charge separation and electron trapping processes leading to color changes in metal oxide semiconductor nanocrystallites. *CB* and *VB* refer to conduction and valence bands of the semiconductor, e_t refers to surface traps, and D refers to hole scavenger



As confirmed by spectroelectrochemical studies of TiO₂ particulate films (O'Regan et al. 1991a, b), the inherent semiconductor properties, such as trapping of electrons at the defect sites, are responsible for the coloration effects (Fig. 4). Electrochemical and photoelectrochemical approaches have supported this mechanism for coloration in TiO₂ and WO₃ colloids (Bedja et al. 1993) and nanostructured films (Hotchandani et al. 1994). The net color change was found to be spectrally similar whether one employed direct bandgap excitation of WO₃ nanoparticles or subjected them to a negative electrochemical bias.

2.2 Electron Storage with Ag Core–TiO₂ Shell Nanostructures

By capping a noble metal with a semiconductor shell one, a new series of photocatalysts can be designed. For example, Ag@TiO₂ clusters are able to store electrons under UV irradiation and discharge them on demand in the dark (Hirakawa and Kamat 2004, 2005). When such metal core–semiconductor shell composite particles were subjected to UV irradiation, a blue shift in the plasmon absorption band from 470 to 420nm was observed (Fig. 5).

The 50-nm shift in the plasmon absorption reflects increased electron density in the Ag core during photoirradiation. Since TiO₂ undergoes charge separation under UV irradiation, the photogenerated electrons are transferred quickly to Ag nanocore as the two systems undergo charge equilibration. Metal particles such as silver and gold have favorable Fermi levels ($E_F \sim 0.4V$) and are good electron acceptors, facilitating quick electron transfer from excited TiO₂. The transfer of electrons from the excited semiconductor to the metal is an important aspect that dictates the overall energetics of the composite and hence the efficiency of photocatalytic reduction process (Subramanian et al. 2003, 2004; Shanghavi and Kamat 1997; Wood et al. 2001).

Figure 6 shows the reproducibility of plasmon absorption peak response to the UV irradiation and air exposure in the dark. The plasmon absorption band shifts

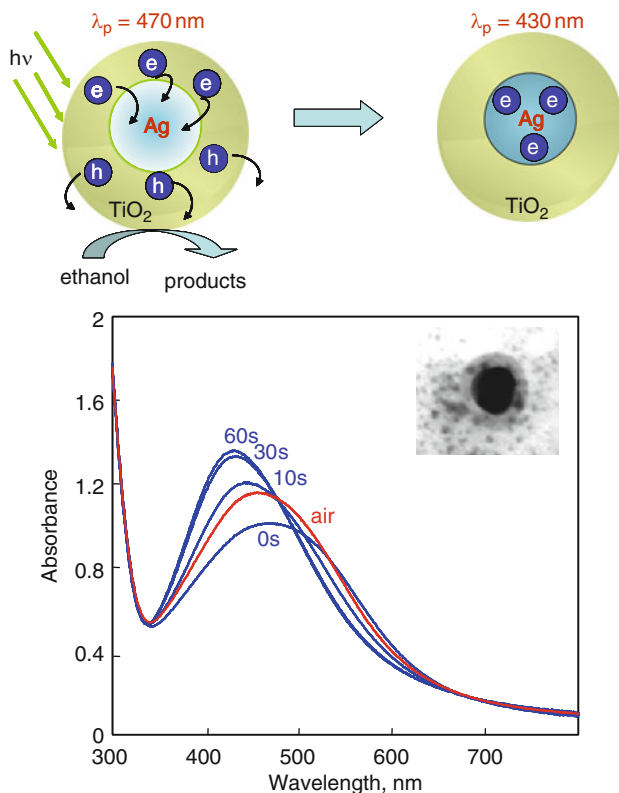
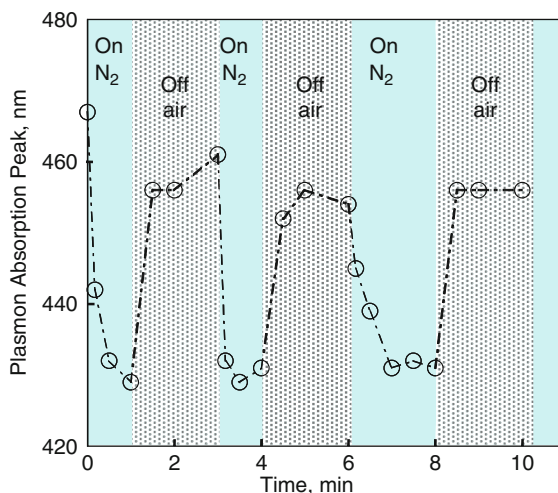


Fig. 5 Photoinduced charge separation and storage in Ag core–TiO₂ shell nanocomposite particles (see inset for TEM image). A shift in the plasmon absorption can be seen upon excitation with UV light (from Hirakawa and Kamat (2004), reprinted with permission from the American Chemical Society)

from 470 to 420 nm during 1-min UV irradiation of deaerated Ag@TiO₂ suspension. The plasmon absorption regains the original spectral features when the stored electrons are discharged in dark by exposing to air. It is possible to repeat the photoinduced charging and dark discharge cycles repeatedly and reproduce the plasmon absorption response to stored electrons (Fig. 6).

Estimating the stored electrons by titration with thionine dye showed that one can store more than 50 electrons in the silver core and discharge them on demand (Hirakawa and Kamat 2004, 2005). In other words, stored electrons can be utilized to carry out catalytic reduction in the dark. The formation of C₆₀^{•-} with characteristic absorption in the IR region (1,075 nm) can be used to obtain quantitative information on the electron transfer yield. These metal core–semiconductor shell composite clusters are photocatalytically active and are useful to promote light-induced electron transfer reactions. Exploring the catalytic activity of such composite structures could pave the way for designing novel light-harvesting systems.

Fig. 6 Response of plasmon absorbance peak to electron storage following UV irradiation of deaerated Ag@TiO₂ colloidal suspension in ethanol and dark discharge in air (from Hirakawa and Kamat (2004) and Hirakawa and Kamat (2005), reprinted with permission from the American Chemical Society)



3 TiO₂ as Sensors

A variety of oxide-based sensors for environmental applications have been developed in recent years, including SnO₂-based semiconductor systems that have been used as conductometric gas sensors (Sberveglieri 1995; Barsan et al. 1999), CO gas sensors (Al-Homoudi et al. 2007), and a TiO₂ electrode used for determining the chemical oxygen demand (COD) of water (Kim et al. 2001). The use of TiO₂ systems in sensors has been drawing increasing attention. Organized arrays of TiO₂ nanotubes have been integrated into a thin-cell photoelectrocatalytic reactor for the rapid determination of COD in wastewater samples. Carbon nanotube (CNT) template-based porous TiO₂ films have been used to immobilize glucose oxidase (GOD) and employed in the fabrication of a biosensor (Bao et al. 2008). The fabricated GOD sensor showed good stability and high electrochemical activity, and opened up its use as an enzymatic sensor.

LiCl-doped TiO₂ electrospun nanofibers have been shown to be effective as humidity nanosensors (Li et al. 2008). The as-prepared humidity sensor exhibited excellent sensing characteristics, including ultrafast response (≤ 3 s) and recovery (≤ 7 s) times for measuring relative humidity (RH) over a wide range (11–95%) in room temperature (25°C) air with the impedance changing from 10^7 to 10^4 Ω . TiO₂-based nanosensors have potential for use in devices, with good reproducibility, linearity, and stability.

4 TiO₂-Based Photoelectrochemical Solar Cells

Various strategies have been developed to construct photoelectrochemical solar cells using TiO₂ nanostructure architectures. Some of these strategies include (1) dye-sensitized solar cells (DSSC), (2) semiconductor nanocrystal quantum dot-sensitized solar cells (QDSSC), and (3) carbon nanostructure-based solar cells.

4.1 Dye-Sensitized Solar Cells (DSSC)

The high porosity of mesoscopic semiconductor films enables the incorporation of sensitizing dyes in high concentrations. The nanostructured TiO₂ films modified with a ruthenium complex exhibit photoconversion efficiencies of 11%, which is comparable to that of amorphous silicon-based photovoltaic cells (Nazeeruddin et al. 1993; Cahen et al. 2000; Graetzel 1997, 2001; Sauvé et al. 2000a). By optimizing the design of light-harvesting molecules (sensitizers), it should be possible to suppress the interfacial charge recombination and improve the cross section for light absorption.

When an electrode is illuminated with visible light, the sensitizer molecules absorb the light and inject electrons into the semiconductor particles. (Representative systems, for example, include SnO₂ (Bedja et al. 1994), ZnO (Bedja et al. 1997), or TiO₂ (Fessenden and Kamat 1995; Kamat 1989; Vinodgopal et al. 1995; Martini et al. 1997; Nasr et al. 1998a; Khazraji et al. 1999).) The injected electrons are then collected at the conducting glass surface to generate anodic photocurrent. The redox couple (e.g., I₃⁻/I⁻) present in the electrolyte quickly regenerates the sensitizer (Nasr et al. 1998b). The quenching of the excited sensitizer by the redox couple can easily be suppressed with the use of C₆₀ clusters. C₆₀ clusters act as a relay to shuttle electrons across the interface (Kamat et al. 2004). The charge injection between the excited sensitizer and the semiconductor film can be readily modulated by applying external bias (Kamat et al. 1996; Tachibana et al. 2001; Sauvé et al. 2000b). Ru(II) trisbipyridyl-complex modified TiO₂ nanostructured films exhibit incident photon to charge carrier generation efficiency (IPCE) of nearly 90% under optimized light-harvesting conditions (Nazeeruddin et al. 1993). The photoresponse of these nanostructured semiconductor films can be tuned by choosing an appropriate sensitizer.

Recently, interest has been shown in developing ordered arrays of TiO₂ nanotubes either by electrochemical etching of Ti foil in a fluoride medium or by depositing TiO₂ rods on a conducting surface (Mor et al. 2006; Imai et al. 1999; Tian et al. 2003; Wu and Yu 2004; Ruan et al. 2005; Paulose et al. 2006; Adachi et al. 2003). Using this strategy, nanotube- (Macak et al. 2005) and nanowire-based (Law et al. 2005) dye-sensitized solar cells have also been reported. Over the last decade, a number of research groups have worked on fine tuning the performance of the electrode structure, TiO₂ surface, sensitizing molecules, regenerative redox couples, and electrolyte medium. Despite this large body of work, the maximum attainable efficiency has remained in the range of 10–11%. A detailed discussion on various aspects of dye-sensitized solar cells can be found in other chapters of this book and review articles (Galoppini 2004; Gratzel 2005; Bisquert et al. 2004; Meyer 2005).

4.2 Quantum Dot-Sensitized Solar Cells (QDSSC)

By coupling a short bandgap semiconductor such as CdSe with TiO₂, it is possible to maximize the charge separation efficiency through charge rectification. Suitable matching of the conduction and valence bands of the two semiconductors allows accumulation of electrons and holes in two separate particles, thereby allowing sufficient time to capture one of the charge carriers at the electrode surface. For example, chemically or electrochemically deposited or self-assembled CdS and CdSe nanocrystallites have been shown to inject electrons into wider gap materials such as TiO₂ (Gerischer and Luebke 1986; Sasha and Gary 1994; Yochelis and Hodes 2004; Niitsoo et al. 2006; Hao et al. 1999; Fang et al. 1997; Wijayantha et al. 2004; Robel et al. 2006; Mora-Sero et al. 2007; Lee et al. 2007; Prabakar et al. 2006; Lopez-Luke et al. 2008; Si et al. 2008). This process is often referred to as type II mechanism, which is analogous to dye sensitization of semiconductor films, the dye being replaced by a short bandgap semiconductor (Fig. 7). Semiconductor quantum dots (QDs) such as CdSe, InAs, PbS, and PbSe with their tunable band edge offer new opportunities for harvesting light energy in the visible region of the solar spectrum (Nozik 2002; Wang 2000; Plass et al. 2002; Yu et al. 2006).

The photoelectrochemical response of the CdSe QDs deposited on an optically transparent electrode (OTE/TiO₂/CdSe films) to monochromatic light irradiation can be analyzed in terms of IPCE, also referred to as external quantum efficiency. IPCE is determined from short circuit photocurrents (J_{sc}) monitored at different excitation wavelengths (λ) using the expression:

$$IPCE\% = \frac{1,240 \times J_{\text{short circuit}}(A/cm^2)}{\lambda(nm) \times I_{\text{incident}}(W/cm^2)} \times 100\%,$$

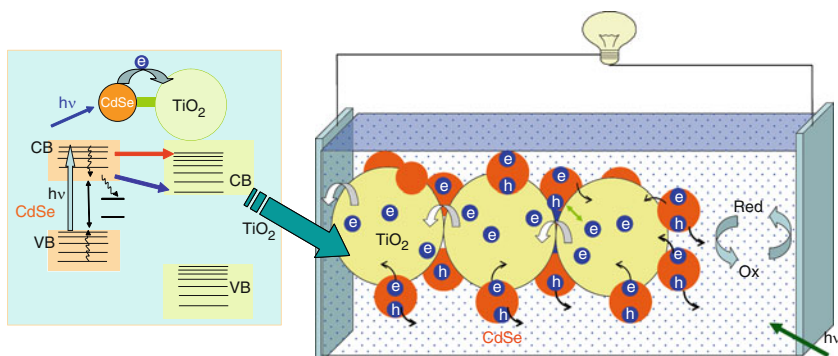


Fig. 7 Principle of operation of quantum dot-sensitized solar cell (QDSSC). Charge injection from excited CdSe quantum dots (QDs) into TiO₂ nanoparticles is followed by collection of charges at the electrode surface. The redox electrolyte (e.g., sulfide/polysulfide) scavenges the holes and thus ensures regeneration of the CdSe

where I_{incident} is the incident power of the monochromatic light. The IPCE action spectra for OTE/TiO₂(NP)/CdSe and Ti/TiO₂(NT)/CdSe electrodes are presented in Fig. 8. (NP and NT represent nanoparticle and nanotube films, respectively.) The photocurrent action spectra obtained with 3.7, 3.0, 2.6, and 2.3 nm CdSe particles exhibit current peaks at 580, 540, 520, and 505 nm, which closely match their absorption features. These observations confirm that the photocurrent generation at OTE/TiO₂(NP)/CdSe and Ti/TiO₂(NT)/CdSe electrodes originates from the individual CdSe QDs and that their size quantization property is responsible for tuning the performance of QD solar cells (Kongkanand et al. 2008). Similar observation of band-edge tuning has been reported for CdSe QDs (Lee et al. 2008a) and bismuth sulfide QDs (Peter et al. 2003) adsorbed onto TiO₂ particles.

Comparison of IPCE at the excitonic peaks shows an interesting dependence on the particle size. The higher IPCE values obtained with 2.3- and 2.6-nm CdSe QDs indicated that the smaller size particles are more energetic in their excited state and are capable of injecting electrons into TiO₂ at a faster rate. Arguments have been made in the literature for injection of hot electrons from the quantized semiconductor particles (Ross and Nozik 1982; Rosenwaks et al. 1994). Careful analysis of the ultrafast kinetic measurements needs to be pursued in order to establish the contribution of hot electron injection in such systems.

It is also interesting to note that the maximum IPCE values obtained with CdSe QDs linked to TiO₂ particles and tubes are different. The maximum IPCE values in the visible region (Fig. 8) range from 25 to 35% for OTE/TiO₂(NP)/CdSe electrodes, while they vary from 35 to 45% for OTE/Ti/TiO₂(NT)/CdSe electrodes. These IPCE values are relatively higher than those reported in the literature for the sensitization of

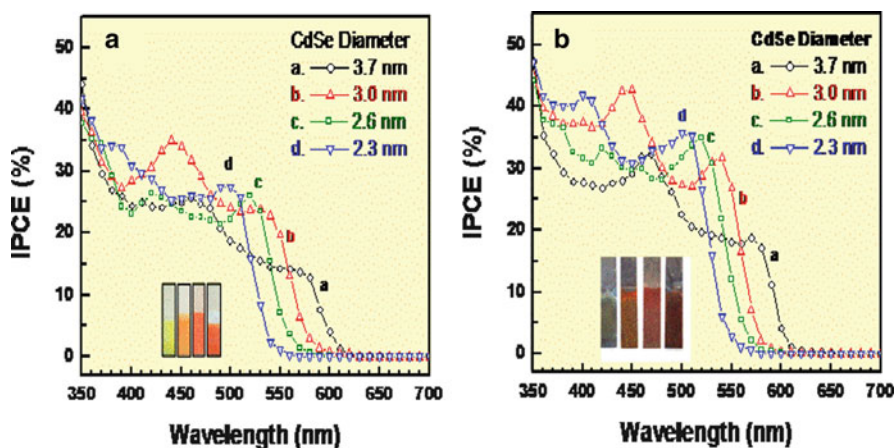


Fig. 8 Photocurrent action spectra recorded in terms of incident photon to charge carrier generation efficiency (IPCE) of (a) OTE/TiO₂(NP)/CdSe and (b) Ti/TiO₂(NT)/CdSe electrodes (electrodes are shown in the inset). The individual IPCE responses correspond to (a) 3.7-, (b) 3.0-, (c) 2.6-, and (d) 2.3-nm diameter CdSe QDs anchored on nanostructured TiO₂ films. 0.1M Na₂S solution was used as redox electrolyte (from Kongkanand et al. (2008), reprinted with permission from the American Chemical Society)

TiO₂ films (IPCE = 25%) (Shen et al. 2004) and ZnO nanorods (IPCE = 18%) (Leschkies et al. 2007) with CdSe QDs. Higher power conversion efficiency has also been reported by Toyoda and coworkers using TiO₂ inverse opal structures (Diguna et al. 2007) and coating with ZnS (Shen et al. 2008). Other studies have also observed enhancement in photocurrent response using TiO₂ nanotubes (Si et al. 2008; Lee et al. 2008b; Shen et al. 2006), nanowires (Lee et al. 2008b), and nanobelts (Chong et al. 2007). High external quantum efficiencies (>70%) in ferro-/ferricyanide solutions have been obtained for ZnO/CdSe core-shell nanowire arrays annealed at 400°C (Tena-Zaera et al. 2007). Structural transition in nanocrystalline CdSe nanowire shell, from cubic zinc blende to hexagonal wurtzite, seems to play an important role in enhancing photocurrent generation. These results demonstrate the necessity of optimizing nanostructure assemblies in an orderly fashion.

Since smaller size semiconductor QDs exhibit higher photoconversion efficiency but absorb fewer lower energy photons than larger size particles, we can anchor the quantized particles on a nanotube array to maximize the capture of the incident light while collecting and transmitting electrons through the TiO₂ tube network (Fig. 9). The excess energy of electrons of small size particles is lost once they are transferred to a TiO₂ scaffold. Such a rainbow cell configuration, however, allows the faster electron injection rate of small size particles to be effectively coupled with the greater absorption range of large particles.

The photoelectrochemical behavior of the CdSe QD-based solar cell demonstrates the feasibility of employing semiconductor nanocrystals for harvesting light energy. Injection of both hot and thermalized electrons from excited CdSe QDs into TiO₂ nanoparticles is the primary step in the photocurrent generation. Charge

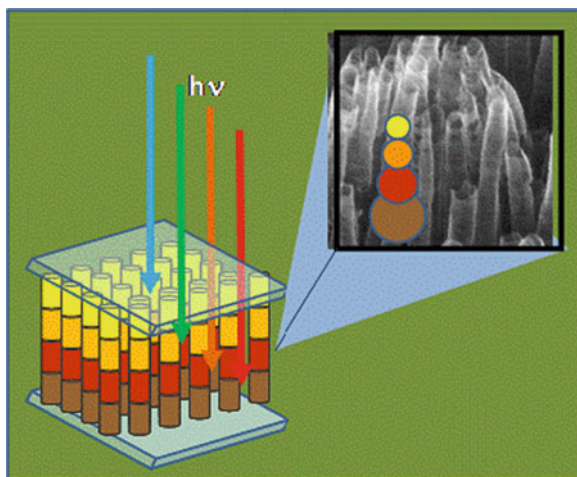


Fig. 9 Artistic impression of a rainbow solar cell assembled with different size CdSe QDs on TiO₂ nanotube array (from Kongkanand et al. (2008), reprinted with permission from the American Chemical Society)

recombination and scattering at the CdSe/TiO₂ heterointerface and grain boundaries within the TiO₂ network limit the photoconversion efficiency of these solar cells.

4.3 Carbon Nanotubes/TiO₂ Composites-Based Solar Cells

Unique electrical and electronic properties, wide electrochemical stability window, and high surface area have prompted many researchers to employ carbon nanostructures such as single wall carbon nanotube (SWCNT) assemblies for energy conversion devices (Hammel et al. 2004; Wang et al. 2003; Rajesh et al. 2003). Efforts to synthesize semiconductor–CNT composite films have shown significant progress in recent years (Baughman et al. 2002; Sheeney-Haj-Khia et al. 2005; Huang and Gao 2004; Banerjee and Wong 2003, 2004; Chaudhary et al. 2004; Haremza et al. 2002; Ravindran et al. 2003; Shan and Gao 2006). The use of a nanotube support to anchor semiconductor particles provides a convenient way to capture photogenerated charge and transport them to the electrode surface.

Of particular interest is the semiconductor–CNT composite that is capable of generating photocurrent from visible light with unusually high efficiency (Sheeney-Haj-Khia et al. 2005; Robel et al. 2005). Excited state interaction between TiO₂ (Kongkanand et al. 2007; Jung et al. 2002; Kongkanand and Kamat 2007; Yu et al. 2007), ZnO (Vietmeyer et al. 2007), and CdS (Sheeney-Haj-Khia et al. 2005; Robel et al. 2005; Lee et al. 2008c) and CNs has been investigated in detail by monitoring the luminescence quenching or by Fermi-level equilibration. The role of SWCNT in enhancing the photoelectrochemical performance of TiO₂ film was probed by varying the ratio of TiO₂/SWCNT in the composite film. A commercially available TiO₂ (Degussa P-25) suspension in water was drop-cast onto a carbon fiber electrode (CFE) with and without SWCNT. Figure 10 compares the photocurrent observed with CFE/TiO₂ and CFE/SWCNT/TiO₂ electrodes at different loading of TiO₂ particles. In the case of CFE/TiO₂ film, we observed an increase in photocurrent with increased TiO₂ loading (at loadings below 2mg/cm²) as more of the excited TiO₂ particles undergo charge separation and participate in the photocurrent generation. At higher TiO₂ loadings, we observed saturation in the photocurrent, showing the limitations of light absorption within the TiO₂ film. It is interesting to note that the photocurrent observed at these TiO₂ loadings is significantly greater than the photocurrent observed without the SWCNT support. The usefulness of SWCNT support architecture in improving the photocurrent generation in TiO₂-based photoelectrochemical solar cells is discussed elsewhere (Kongkanand et al. 2007; Brown et al. 2008). Two-dimensional carbon nanostructures such as graphene sheets offer new ways to disperse semiconductor and metal nanoparticles (Williams et al. 2008; Muszynski et al. 2008). Utilization of such nanocomposites in energy conversion devices has yet to be tested for the effectiveness of graphene as a support carbon nanomat.

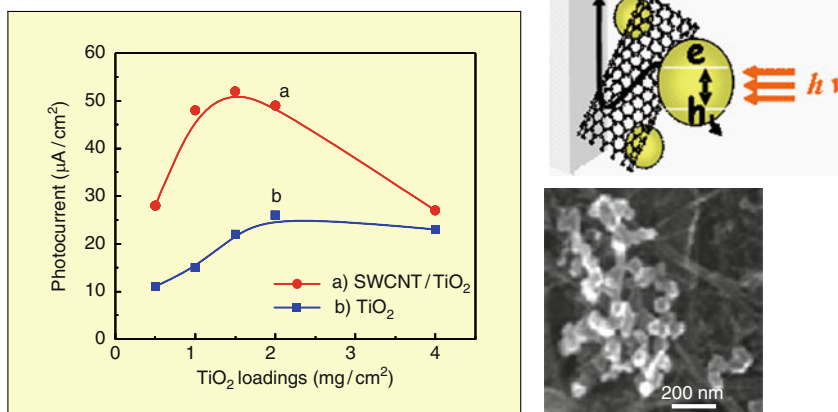


Fig. 10 Left: Photocurrent response as a function of the amount of TiO₂ deposited on carbon fiber electrode (CFE): (a) In the presence and (b) absence of SWCNT scaffold. SWCNT concentration was maintained constant at 0.2mg/cm², while TiO₂ loading was varied. Right: Scheme showing the electron transport through SWCNT and SEM image of the SWCNT–TiO₂ composite (from Kongkanand et al. (2007), reprinted with permission from the American Chemical Society)

5 Photocatalyst-Based Hybrid Methanol Fuel Cells

For more than two decades, the electrode assembly employed in the operation of a direct methanol fuel cell (DMFC) has relied on Pt-Ru catalyst anchored on a carbon support (Carrette et al. 2000; Wasmus and Kuver 1999; Maynard and Meyers 2002; Eikerling et al. 2004). A proton exchange membrane (PEM) separates the C/Pt-Ru anode and C/Pt cathode, and allows ion transport between the two cell compartments. In a recent study (Drew et al. 2005), we showed that TiO₂ photocatalyst particles can be incorporated in the anode along with the Pt-Ru catalyst and carried out methanol oxidation both electrocatalytically and photocatalytically in a synergistic way. We made use of the photocatalytic properties of TiO₂ to boost the traditionally attained current from the oxidation of methanol at the Pt-Ru catalyst system. Figure 11 illustrates the principle of methanol oxidation at the hybrid electrode and the response of the hybrid fuel cell to UV excitation. An increase in the current during UV excitation represents the contribution from the photocatalytic oxidation at the TiO₂ surface. The power characteristics of the hybrid cell also showed an overall improvement in the deliverable power when exposed to UV light.

Although the use of photocatalyst is likely to have limited applications, such simple approaches can greatly minimize the use of precious metals while delivering higher output. The presence of oxides can also minimize the poisoning effect. One possible application of such photocatalyst-based hybrid cells might be in outdoor fixtures where single stack fuel cells can be spread out to capture sunlight. The rising clean energy demand will compel us to find hybrid devices that can be tailored to specific applications.

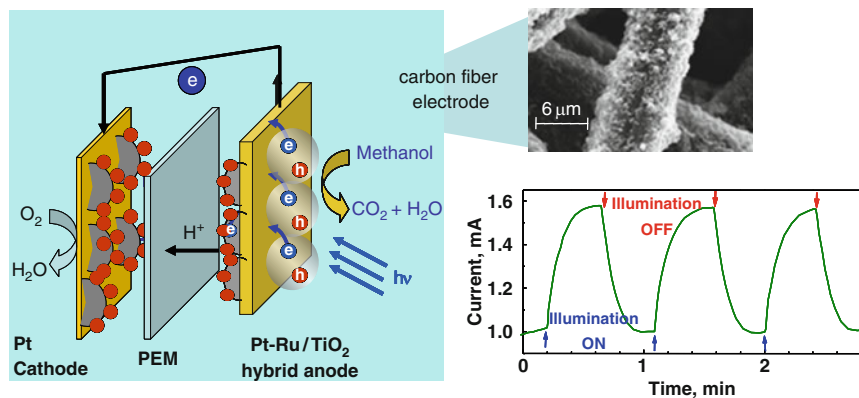


Fig. 11 Schematic diagram illustrating the operation of a hybrid cell incorporating the principle of electrocatalysis and photocatalysis (*left*). The boost in the current is seen when the cell is illuminated with UV light (*right*). A magnified view of the CFE showing the deposition of Pt-Ru and TiO₂ particles is also shown (from Drew et al. (2005), reprinted with permission from the American Chemical Society)

6 Concluding Remarks

TiO₂ will continue to play a major role in many future applications. Just a few applications, which provide ways to capture the semiconducting properties in photocatalysis and energy conversion devices, have been discussed here. The use of TiO₂ as a photocatalyst is still hindered by the fact that it responds only to UV excitation. Continued efforts to extend the response to the visible range have met with only limited success. Semiconductor–metal nanocomposites that improve the selectivity and efficiency of the photocatalytic process are expected to draw the attention of future research.

Acknowledgments This work is supported by the US Department of Energy (DOE), Office of Science, Basic Energy Sciences. This is contribution NDRL No. 4781 from the Notre Dame Radiation Laboratory.

References

- Adachi M, Murata Y, Okada I, Yoshikawa S (2003) Formation of titania nanotubes and applications for dye-sensitized solar cells. *J Electrochem Soc* 150:G488–G493
- Al-Homoudi IA, Thakur JS, Naik R, Auner GW, Newaz G (2007) Anatase TiO₂ films based CO gas sensor: film thickness, substrate and temperature effects. *Appl Surf Sci* 253:8607–8614
- Anpo M, Shima T, Kubokawa Y (1985) ESR and photoluminescence evidence for the photocatalytic formation of OH[•] radicals on small TiO₂ particles. *Chem Lett* 1799–1802

- Anpo M, Ichihashi Y, Takeuchi M, Yamashita H (1998) Design of unique TiO₂ photocatalysts by an advanced metal ion-implantation method and photocatalytic reactions under visible light irradiation. *Res Chem Intermed* 24:143–149
- Asahi R, Morikawa T, Ohwaki T, Aoki K, Taga Y (2001) Visible-light photocatalysis in nitrogen-doped titanium oxides. *Science* 293:269–271
- Banerjee S, Wong SS (2003) In situ quantum dot growth on multiwalled carbon nanotubes. *J Am Chem Soc* 125:10342–10350
- Banerjee S, Wong SS (2004) Formation of CdSe nanocrystals onto oxidized, ozonized single-walled carbon nanotube surfaces. *Chem Commun* 1866–1867
- Bao SJ, Li CM, Zang JF, Cui XQ, Qiao Y, Guo J (2008) New nanostructured TiO₂ for direct electrochemistry and glucose sensor applications. *Adv Funct Mater* 18:591–599
- Bard AJ (1982) Design of semiconductor photoelectrochemical systems for solar energy conversion. *J Phys Chem* 86:172–177
- Barsan N, Schweizer-Berberich M, Gopel W (1999) Fundamental and practical aspects in the design of nanoscaled SnO₂ gas sensors: a status report. *Fresenius J Anal Chem* 365:287–304
- Baughman RH, Zakhidov AA, de Heer WA (2002) Carbon nanotubes – the route toward applications. *Science* 297:787–792
- Bedja I, Hotchandani S, Kamat PV (1993) Photoelectrochemistry of quantized WO₃ colloids. Electron storage, electrochromic, and photoelectrochromic effects. *J Phys Chem* 97:11064–11070
- Bedja I, Hotchandani S, Kamat PV (1994) Preparation and characterization of thin SnO₂ nanocrystalline semiconductor films and their sensitization with bis(2, 2'-bipyridine)(2, 2'-bipyridine-4-4'-dicarboxylic acid)ruthenium complex. *J Phys Chem* 98:4133–4140
- Bedja I, Kamat PV, Hua X, Lappin AG, Hotchandani S (1997) Photosensitization of nanocrystalline ZnO films by Bis(2, 2'-bipyridine)(2, 2'-bipyridine-4, 4'-dicarboxylic acid)ruthenium(II). *Langmuir* 13:2398–2403
- Bisquert J, Cahen D, Hodes G, Rühle S, Zaban A (2004) Physical chemical principles of photovoltaic conversion with nanoparticulate, mesoporous dye-sensitized solar cells. *J Phys Chem B* 108:8106–8118
- Brown PR, Takechi K, Kamat PV (2008) Single-walled carbon nanotube scaffolds for dye-sensitized solar cells. *J Phys Chem C* 112:4776–4782
- Butler L, Redmond G, Fitzmaurice D (1993) Preparation and spectroscopic characterization of highly confined nanocrystallites of GaAs in decane. *J Phys Chem* 97:10750–10755
- Cahen D, Hodes G, Graetzel M, Guillemoles JF, Riess I (2000) Nature of photovoltaic action in dye-sensitized solar cells. *J Phys Chem* 104:2053–2059
- Carrette L, Friedrich KA, Stimming U (2000) Fuel cells: principles, types, fuels, and applications. *Chem Phys Chem* 1:162–193
- Chandrasekharan N, Kamat PV (2000) Improving the photoelectrochemical performance of nanostructured TiO₂ films by adsorption of gold nanoparticles. *J Phys Chem B* 104:10851–10857
- Chaudhary S, Kim JH, Singh KV, Ozkan M (2004) Fluorescence microscopy visualization of single-walled carbon nanotubes using semiconductor nanocrystals. *Nano Lett* 4:2415–2419
- Chong SV, Suresh N, Xia J, Al-Salim N, Idriss H (2007) TiO₂ nanobelts/CdSSe quantum dots nanocomposite. *J Phys Chem C* 111:10389–10393
- Di Paola A, Marci G, Palmisano L, Schiavello M, Uosaki K, Ikeda S, Ohtani B (2002) Preparation of polycrystalline TiO₂ photocatalysts impregnated with various transition metal ions: characterization and photocatalytic activity for degradation of 4-nitrophenol. *J Phys Chem B* 106:637–645
- Diguna LJ, Shen Q, Kobayashi J, Toyoda T (2007) High efficiency of CdSe quantum-dot-sensitized TiO₂ inverse opal solar cells. *Appl Phys Lett* 91:023116
- Drew K, Girishkumar G, Vinodgopal K, Kamat PV (2005) Boosting the fuel cell performance with a semiconductor photocatalyst. TiO₂/Pt-Ru hybrid catalyst for methanol oxidation. *J Phys Chem B* 109:11851–11857

- Eikerling M, Iaselevich AS, Komyshev AA (2004) How good are the electrodes we use in PEFC? *Fuel Cells* 4:131–140
- Fang J, Wu J, Lu X, Shen Y, Lu Z (1997) Sensitization of nanocrystalline TiO₂ electrode with quantum sized CdSe and ZnTCPc molecules. *Chem Phys Lett* 270:145
- Fessenden RW, Kamat PV (1995) Rate constants for charge injection from excited sensitizer into SnO₂, ZnO, and TiO₂ semiconductor nanocrystallites. *J Phys Chem* 99:12902–12906
- Fujishima A, Hashimoto K, Watanabe T (1999) TiO₂ photocatalysis. Fundamentals and applications. Bkc, Inc., Tokyo, p 176
- Galoppini E (2004) Linkers for anchoring sensitizers to semiconductor nanoparticles. *Coord Chem Rev* 248:1283–1297
- Gerischer H, Heller A (1991) The role of oxygen in photooxidation of organic molecules on semiconductor particles. *J Phys Chem* 95:5261–5267
- Gerischer H, Heller A (1992) Photocatalytic oxidation of organic molecules at TiO₂ particles by sunlight in aerated water. *J Electrochem Soc* 139:113–118
- Gerischer H, Luebke M (1986) A particle size effect in the sensitization of TiO₂ electrodes by a CdS deposit. *J Electroanal Chem* 204:225–227
- Graetzel M (1997) Nanocrystalline electronic junctions. In: Kamat PV, Meisel D (eds) *Semiconductor nanoclusters – physical, chemical and catalytic aspects*. Amsterdam, Elsevier Science, pp 353–375
- Graetzel M (2001) Photoelectrochemical cells. *Nature* 414:338
- Graetzel M, Howe RF (1990) Electron paramagnetic resonance studies of doped TiO₂ colloids. *J Phys Chem* 94:2566–2572
- Graetzel M (2005) Solar energy conversion by dye-sensitized photovoltaic cells. *Inorg Chem* 44:6841–6851
- Hammel E, Tang X, Trampert M, Schmitt T, Mauthner K, Eder A, Potschke P (2004) Carbon nanofibers for composite applications. *Carbon* 42:1153–1158
- Hao E, Yang B, Zhang J, Zhang X, Sun J, Shen J (1999) Assembly of alternating TiO₂/CdS nanoparticle composite films. *J Mater Chem* 8:1327–1328
- Haremsza JM, Hahn MA, Krauss TD (2002) Attachment of single CdSe nanocrystals to individual single-walled carbon nanotubes. *Nano Lett* 2:1253–1258
- Hashimoto S, Matsuoka H (1991) *J Electrochem Soc* 138:2403
- Hirakawa T, Kamat PV (2004) Electron storage and surface plasmon modulation in Ag@TiO₂ clusters. *Langmuir* 20:5645–5647
- Hirakawa T, Kamat PV (2005) Charge separation and catalytic activity of Ag@TiO₂ core-shell composite clusters under UV-irradiation. *J Am Chem Soc* 127:3928–3934
- Hoffmann MR, Martin ST, Choi W, Bahnemann DW (1995) Environmental applications of semiconductor photocatalysis. *Chem Rev* 95:69–96
- Hotchandani S, Bedja I, Fessenden RW, Kamat PV (1994) Electrochromic and photoelectrochromic behavior of thin WO₃ films prepared from quantum size colloidal particles. *Langmuir* 10:17–22
- Howe RF, Graetzel M (1985) EPR observation of trapped electrons in colloidal TiO₂. *J Phys Chem* 89:4495–4499
- Huang Q, Gao L (2004) Synthesis and characterization of CdS/multiwalled carbon nanotube heterojunctions. *Nanotechnology* 15:1855–1860
- Imai H, Takei Y, Shimizu K, Matsuda M, Hirashima H (1999) Direct preparation of anatase TiO₂ nanotubes in porous alumina membranes. *J Mater Chem* 9:2971–2972
- Johnston AJ, Hocking P (1993) Ultrasonically accelerated photocatalytic waste water treatment. In: *Emerging technologies in hazardous waste management III*. ACS symposium series. Washington, DC, p 106–118
- Jung KH, Hong JS, Vittal R, Kim KJ (2002) Enhanced photocurrent of dye-sensitized solar cells by modification of TiO₂ with carbon nanotubes. *Chem Lett* 864–865

- Kamat PV (1989) Photoelectrochemistry in particulate systems. 9. Photosensitized reduction in a colloidal TiO₂ system using anthracene-9-carboxylic acid as the sensitizer. *J Phys Chem* 93:859–864
- Kamat PV (1993) Photochemistry on nonreactive and reactive (semiconductor) surfaces. *Chem Rev* 93:267–300
- Kamat PV (2007) Meeting the clean energy demand: nanostructure architectures for solar energy conversion. *J Phys Chem C* 111:2834–2860
- Kamat PV (2008) Quantum dot solar cells. Semiconductor nanocrystals as light harvesters. *J Phys Chem C* 112:18737–18753. doi: 10.1021/jp806791s
- Kamat PV, Meisel D (2002) Nanoparticles in advanced oxidation processes. *Curr Opin Colloid Interface Sci* 7:282–287
- Kamat PV, Bedja I, Hotchandani S (1994) Photoinduced charge transfer between carbon and semiconductor clusters. One-electron reduction of C₆₀ in colloidal TiO₂ semiconductor suspensions. *J Phys Chem* 98:9137–9142
- Kamat PV, Bedja I, Hotchandani S, Patterson LK (1996) Photosensitization of nanocrystalline semiconductor films. Modulation of electron transfer between excited ruthenium complex and SnO₂ nanocrystallites with an externally applied bias. *J Phys Chem* 100:4900–4908
- Kamat PV, Haria M, Hotchandani S (2004) C₆₀ cluster as an electron shuttle in a Ru(II)-polypyridyl sensitizer based photochemical solar cell. *J Phys Chem B* 108:5166–5170
- Kesselman JM, Kumar A, Lewis NS (1993) Fundamental photoelectrochemistry of TiO₂ and SrTiO₃ applied to environmental problems. In: Ollis DF, Al-Ekabi H (eds) *Photocatalytic purification and treatment of water and air*. Amsterdam, Elsevier Science Publishers, pp 19–37
- Kesselman JM, Shreve GA, Hoffmann MR, Lewis NS (1994) Flux-matching condition at TiO₂ photoelectrodes: Is interfacial electron transfer to O₂ rate-limiting in the TiO₂-catalyzed degradation of organics? *J Phys Chem* 98:13385–13395
- Khazraji AC, Hotchandani S, Das S, Kamat PV (1999) Controlling dye (merocyanine-540) aggregation on nanostructured TiO₂ films. An organized assembly approach for enhancing the efficiency of photosensitization. *J Phys Chem B* 103:4693–4700
- Kim YC, Sasaki S, Yano K, Ikebukuro K, Hashimoto K, Karube I (2001) Photocatalytic sensor for the determination of chemical oxygen demand using flow injection analysis. *Anal Chim Acta* 432:59–66
- Kongkanand A, Kamat PV (2007) Electron storage in single wall carbon nanotubes. Fermi level equilibration in semiconductor – SWCNT suspensions. *ACS Nano* 1:13–21
- Kongkanand A, Domínguez RM, Kamat PV (2007) Single wall carbon nanotube scaffolds for photoelectrochemical solar cells. Capture and transport of photogenerated electrons. *Nano Lett* 7:676–680
- Kongkanand A, Tvrdy K, Takechi K, Kuno MK, Kamat PV (2008) Quantum dot solar cells. Tuning photoresponse through size and shape control of CdSe-TiO₂ architecture. *J Am Chem Soc* 130:4007–4015
- Kraeutler B, Jaeger CD, Bard AJ (1978) Direct observation of radical intermediates in the radical formation by electron spin resonance. *J Am Chem Soc* 100:4903–4905
- Law M, Greene LE, Johnson JC, Saykally R, Yang P (2005) Nanowire dye-sensitized solar cells. *Nature Mater* 4:455–459
- Lee JC, Sung YM, Kim TG, Choi HJ (2007) TiO₂-CdSe nanowire arrays showing visible-range light absorption. *App Phys Lett* 91, Art. 113104
- Lee HJ, Yum J-H, Leventis HC, Zakeeruddin SM, Haque SA, Chen P, Seok SI, Gratzel M, Nazeeruddin MK (2008a) CdSe quantum dot-sensitized solar cells exceeding efficiency 1% at full-sun intensity. *J Phys Chem C* 112:11600–11608
- Lee JC, Kim TG, Choi HJ, Sung YM (2008b) Enhanced photochemical response of TiO₂/CdSe heterostructured nanowires. *Crystal Growth Des* 8:750
- Lee W, Lee J, Lee S, Yi W, Han SH, Cho BW (2008c) Enhanced charge collection and reduced recombination of CdS/TiO₂ quantum-dots sensitized solar cells in the presence of single-walled carbon nanotubes. *Appl Phys Lett* 92, Art 153510

- Leschkies KS, Divakar R, Basu J, Enache-Pommer E, Boercker JE, Carter CB, Kortshagen UR, Norris DJ, Aydil ES (2007) Photosensitization of ZnO nanowires with CdSe quantum dots for photovoltaic devices. *Nano Lett* 7:1793–1798
- Li ZY, Zhang HN, Zheng W, Wang W, Huang HM, Wang C, MacDiarmid AG, Wei Y (2008) Highly sensitive and stable humidity nanosensors based on LiCl doped TiO₂ electrospun nanofibers. *J Am Chem Soc* 130:5036–5037
- Lopez-Luke T, Wolcott A, Xu LP, Chen SW, Wcn ZH, Li JH, De La Rosa E, Zhang JZ (2008) Nitrogen-doped and CdSe quantum-dot-sensitized nanocrystalline TiO₂ films for solar energy conversion applications. *J Phys Chem C* 112:1282–1292
- Macak JM, Tsuchiya H, Ghicov A, Schmuki P (2005) Dye-sensitized anodic TiO₂ nanotubes. *Electrochem Commun* 7:1133–1137
- Markham-Sr MC (1955) Photocatalytic properties of oxides. *J Chem Ed* 32:540
- Martin SC, Morrison CL, Hoffmann MR (1994a) Photochemical mechanism of size-quantized vanadium-doped TiO₂ particles. *J Phys Chem* 98:13695–13704
- Martin ST, Herrmann H, Choi W, Hoffmann MR (1994b) Time resolved microwave conductivity. Part 1. TiO₂ photoreactivity and size quantization. *Faraday Trans* 90:3315–3322
- Martini I, Hodak J, Hartland G, Kamat PV (1997) Ultrafast study of interfacial electron transfer between 9-anthracene-carboxylate and TiO₂ semiconductor particles. *J Chem Phys* 107:8064–8072
- Maruthamuthu P, Sharma DK, Serpone N (1995) Subnanosecond relaxation dynamics of 2, 2'-azinobis(3-ethylbenzothiazoline-6-sulfonate) and chlorpromazine. Assessment of photosensitization of a wide band gap metal oxide semiconductor TiO₂. *J Phys Chem* 99:3636–3642
- Maynard HL, Meyers JP (2002) Miniature fuel cells for portable power: design considerations and challenges. *J Vac Sci Technol B* 20:1287–1297
- Meyer GJ (2005) Molecular approaches to solar energy conversion with coordination compounds anchored to semiconductor surfaces. *Inorg Chem* 44:6852–6864
- Micic OI, Zhang Y, Cromack KR, Trifunac AD, Thurnauer MC (1993a) Photoinduced hole transfer from TiO₂ to methanol molecules in aqueous solution studied by electron paramagnetic resonance. *J Phys Chem* 97:13284–13288
- Micic OI, Zhang Y, Cromack KR, Trifunac AD, Thurnauer MC (1993b) Trapped holes on TiO₂ colloids studied by electron paramagnetic resonance. *J Phys Chem* 97:7277–7283
- Mor GK, Varghese OK, Paulose M, Shankar K, Grimes CA (2006) A review on highly ordered, vertically oriented TiO₂ nanotube arrays: fabrication, material properties, and solar energy applications. *Solar Energy Mater Solar Cells* 90:2011–2075
- Mora-Sero I, Bisquert J, Dittrich T, Belaidi A, Susha AS, Rogach AL (2007) Photosensitization of TiO₂ layers with CdSe quantum dots: correlation between light absorption and photoinjection. *J Phys Chem C* 111:14889–14892
- Muszynski R, Seger B, Kamat P (2008) Decorating graphene sheets with gold nanoparticles. *J Phys Chem C* 112:5263–5266
- Nasr C, Vinodgopal K, Hotchandani S, Chattopadhyaya A, Kamat PV (1996) Environmental photochemistry on semiconductor surfaces. Visible light induced degradation of a textile diazo dye, naphthol blue black on TiO₂ particles. *J Phys Chem* 100:8436–8442
- Nasr C, Hotchandani S, Kamat PV (1998a) Photoelectrochemistry of composite semiconductor thin films. II. Photosensitization of SnO₂/TiO₂ coupled system with a ruthenium polypyridyl complex. *J Phys Chem B* 102:10047–10056
- Nasr C, Hotchandani S, Kamat PV (1998b) Role of iodide in photoelectrochemical solar cells. Electron transfer between iodide ions and ruthenium polypyridyl complex anchored on nanocrystalline SiO₂ and SnO₂ films. *J Phys Chem B* 102:4944–4951
- Nazeeruddin MK, Kay A, Rodicio I, Humphry BR, Mueller E, Liska P, Vlachopoulos N, Graetzel M (1993) Conversion of light to electricity by cis-X₂bis(2, 2'-bipyridyl)-4, 4'-dicarboxylate ruthenium(II) charge-transfer sensitizers (X = Cl-, Br-, I-, CN-, and SCN-) on nanocrystalline TiO₂ electrodes. *J Am Chem Soc* 115:6382–6390

- Niitsoo O, Sarkar SK, Pejoux C, Ruhle S, Cahen D, Hodes G (2006) Chemical bath deposited CdS/CdSe-sensitized porous TiO₂ solar cells. *J Photochem Photobiol A Chem* 181:306–313
- Nozik AJ (2002) Quantum dot solar cells. *Physica E Low Dimens Syst Nanostruct* 14:115–120
- O'Regan B, Graetzel M, Fitzmaurice D (1991a) Optical electrochemistry. 2. Real-time spectroscopy of conduction band electrons in a metal oxide semiconductor electrode. *J Phys Chem* 95:10525–10528
- O'Regan B, Graetzel M, Fitzmaurice D (1991b) Optical electrochemistry I: steady-state spectroscopy of conduction band electrons in a metal oxide semiconductor electrode. *Chem Phys Lett* 183:89–93
- Ozer N, Lampert CM (1999) Electrochromic performance of sol-gel deposited WO₃-V₂O₅ films. *Thin Solid Films* 349:205–211
- Papaefthimiou S, Leftheriotis G, Yianoulis P (1999) Study of electrochromic cells incorporating WO₃, MoO₃, WO₃-MoO₃ and V₂O₅ coatings. *Thin Solid Films* 344:183–186
- Park JH, Bard AJ (2005) Unassisted water splitting from bipolar Pt/dye-sensitized TiO₂ photoelectrode arrays. *Electrochem Solid State Lett* 8:G371–G375
- Paulose M, Shankar K, Varghese OK, Mor GK, Grimes CA (2006) Application of highly-ordered TiO₂ nanotube-arrays in heterojunction dye-sensitized solar cells. *J Phys D Appl Phys* 39:2498–2503
- Peller J, Wiest O, Kamat PV (2003) Synergy of combining sonolysis and photocatalysis in the degradation and mineralization of chlorinated aromatic compounds. *Environ Sci Technol* 37:1926–1932
- Pernas E, O'Shea K, Saires J (1998) The influence of mineralization products on the coagulation of TiO₂ photocatalyst. In: ACSN meeting (ed) Prepr Ext Abstr. ACS National Meeting. American Chemical Society, Environ. Chem. Div. p 18–21
- Peter LM, Wijayantha KGU, Riley DJ, Waggett JP (2003) Band-edge tuning in self-assembled layers of Bi₂S₃ nanoparticles used to photosensitize nanocrystalline TiO₂. *J Phys Chem B* 107:8378–8381
- Peterson MW, Turner JA, Nozik AJ (1991) Mechanistic studies of the photocatalytic behavior of TiO₂. Particles in a photoelectrochemical slurry cell and the relevance to photodetoxification reactions. *J Phys Chem* 95:221–225
- Plass R, Pelet S, Krueger J, Gratzel M, Bach U (2002) Quantum dot sensitization of organic-inorganic hybrid solar cells. *J Phys Chem B* 106:7578–7580
- Prabakar K, Takahashi T, Nakashima T, Kubota Y, Fujishima A (2006) Optimization and deposition of CdS thin films as applicable to TiO₂/CdS composite catalysis. *J Vac Sci Technol A* 24:1613–1617
- Rajesh B, Thampi KR, Bonard JM, Mathieu HJ, Xanthopoulos N, Viswanathan B (2003) Conducting polymeric nanotubules as high performance methanol oxidation catalyst support. *Chem Commun* 2022–2023
- Rajh T, Ostafin AE, Micic OI, Tiede DM, Thurnauer MC (1996) Surface modification of small particle TiO₂ colloids with cysteine for enhanced photochemical reduction. An EPR study. *J Phys Chem* 100:4538–4545
- Ravindran S, Chaudhary S, Colburn B, Ozkan M, Ozkan CS (2003) Covalent coupling of quantum dots to multiwalled carbon nanotubes for electronic device applications. *Nano Lett* 3:447–453
- Redmond G, Fitzmaurice D (1993) Spectroscopic determination of flatband potentials for polycrystalline TiO₂ electrodes in nonaqueous solvents. *J Phys Chem* 97:1426–1430
- Redmond G, Fitzmaurice D, Graetzel M (1993) Effect of surface chelation on the energy of an intraband surface state of a nanocrystalline TiO₂ film. *J Phys Chem* 97:6951–6954
- Robel I, Bunker B, Kamat PV (2005) SWCNT-CdS nanocomposite as light harvesting assembly. Photoinduced charge transfer interactions. *Adv Mater* 17:2458–2463
- Robel I, Subramanian V, Kuno M, Kamat PV (2006) Quantum dot solar cells. Harvesting light energy with CdSe nanocrystals molecularly linked to mesoscopic TiO₂ films. *J Am Chem Soc* 128:2385–2393

- Rosenwaks Y, Thacker BR, Nozik AJ, Ellingson RJ, Burr KC, Tang CL (1994) Ultrafast photoinduced electron transfer across semiconductor-liquid interfaces in the presence of electric fields. *J Phys Chem* 98:2739–2741
- Ross RT, Nozik AJ (1982) Efficiency of hot-carrier solar energy converters. *J Appl Phys* 53:3813–3818
- Rothenberger G, Moser J, Graetzel M, Serpone N, Sharma DK (1985) Charge carrier trapping and recombination dynamics in small semiconductor particles. *J Am Chem Soc* 107:8054–8059
- Ruan C, Paulose M, Varghese OK, Mor GK, Grimes CA (2005) Fabrication of highly ordered TiO₂ nanotube arrays using an organic electrolyte. *J Phys Chem B* 109:15754–15759
- Sasha G, Gary H (1994) Quantum size effects in the study of chemical solution deposition mechanisms of semiconductor films. *J Phys Chem* 98:5338
- Sauvé G, Cass ME, Doig SJ, Lauer mann I, Pomykal K, Lewis NS (2000a) High quantum yield sensitization of nanocrystalline titanium dioxide photoelectrodes with cis-dicyanobis (4, 4'-dicarboxy-2, 2'-bipyridine)osmium(II) or Tris(4, 4'-dicarboxy-2, 2'-bipyridine)osmium (II) complexes. *J Phys Chem B* 104:3488–3491
- Sauvé G, Cass ME, Coia G, Doig SJ, Lauer mann I, Pomykal KE, Lewis NS (2000b) Dye sensitization of nanocrystalline titanium dioxide with osmium and ruthenium polypyridyl complexes. *J Phys Chem* 104:6821–6836
- Sberveglieri G (1995) Recent developments in semiconducting thin-film gas sensors. *Sensors Actuators B Chem* 23:103–109
- Schmelling D, Gray KA, Kamat PV (1996) Role of reduction in the photocatalytic degradation of trinitrotoluene. *Environ Sci Technol* 30:2547–2555
- Serpone N (1997) Relative photonic efficiencies and quantum yields in heterogeneous photocatalysis. *J Photochem Photobiol A Chem* 104:1–12
- Serpone N, Trezian R, Hidaka H, Pelizzetti E (1994) Ultrasonic induced dehalogenation and oxidation of 2-, 3-, and 4-chlorophenol in air-equilibrated aqueous media. Similarities with irradiated semiconductor particulates. *J Phys Chem* 98:2634–2640
- Shan Y, Gao L (2006) In situ coating carbon nanotubes with wurtzite ZnS nanocrystals. *J Am Ceram Soc* 89:759–762
- Shanghavi B, Kamat PV (1997) Interparticle electron transfer in metal/semiconductor composites. Picosecond dynamics of CdS capped gold nanoclusters. *J Phys Chem B* 101:7675–7679
- Sheeney-Haj-Khia L, Basnar B, Willner I (2005) Efficient generation of photocurrents by using CdS/Carbon nanotube assemblies on electrodes. *Angew Chem Int Edit* 44:78–83
- Shen Q, Arae D, Toyoda T (2004) Photosensitization of nanostructured TiO₂ with CdSe quantum dots: effects of microstructure and electron transport in TiO₂ substrates. *J Photochem Photobiol A Chem* 164:75–80
- Shen Q, Katayama K, Sawada T, Yamaguchi M, Toyoda T (2006) Optical absorption, photoelectrochemical, and ultrafast carrier dynamic investigations of TiO₂ electrodes composed of nanotubes and nanowires sensitized with CdSe quantum dots. *Jpn J Appl Phys* 45:5569–5574
- Shen Q, Kobayashi J, Diguna LJ, Toyoda T (2008) Effect of ZnS coating on the photovoltaic properties of CdSe quantum dot-sensitized solar cells. *J App Phys* 103
- Si HY, Sun ZH, Zhang HL (2008) Photoelectrochemical response from CdSe-sensitized anodic oxidation TiO₂ nanotubes. *Colloids Surf A Physicochem Eng Asp* 313:604–607
- Stafford U, Gray KA, Kamat PV (1996) Photocatalytic oxidation of 4-chlorophenol on TiO₂: a comparison with γ -radiolysis. In: Roth J, Bowers A (eds) *Chemical oxidation: technologies for the 90's*. Lancaster, Technomic Publishing Co., pp 193–204
- Stevenson M, Bullock K, Lin W-Y, Rajeshwar K (1997) Sonolytic enhancement of the bacterial activity of irradiated titanium dioxide suspensions in water. *Res Chem Intermed* 23:311–324
- Stock NL, Peller J, Vinodgopal K, Kamat PV (2000) Combinative sonolysis and photocatalysis for textile dye degradation. *Environ Sci Technol* 34:1747–1750

- Subramanian V, Wolf EE, Kamat PV (2003) Green emission to probe photoinduced charging events in ZnO-Au nanoparticles. Charge distribution and fermi-level equilibration. *J Phys Chem B* 107:7479–7485
- Subramanian V, Wolf EE, Kamat PV (2004) Catalysis with TiO₂/Au nanocomposites. Effect of metal particle size on the fermi level equilibration. *J Am Chem Soc* 126:4943–4950
- Szewczyk DA (1997) The degradation of 2-chlorophenol by sonolysis and photocatalysis on TiO₂ in aqueous solution. In: Book of abstracts, 213th American Chemical Society National Meeting. American Chemical Society, San Francisco
- Tachibana Y, Haque SA, Mercer IP, Moser JE, Klug DR, Durrant JR (2001) Modulation of the rate of electron injection in dye-sensitized nanocrystalline TiO₂ films by externally applied bias. *J Phys Chem B* 105:7424–7431
- Tena-Zaera R, Katty A, Bastide S, Levy-Clement C (2007) Annealing effects on the physical properties of electrodeposited ZnO/CdSe core-shell nanowire arrays. *Chem Mater* 19:1626–1632
- Tian ZRR, Voigt JA, Liu J, McKenzie B, Xu HF (2003) Large oriented arrays and continuous films of TiO₂-based nanotubes. *J Am Chem Soc* 125:12384–12385
- Vietmeyer F, Seger B, Kamat PV (2007) Anchoring ZnO particles on functionalized single wall carbon nanotubes. Excited state interactions and charge collection. *Adv Mater* 19:2935–2940
- Vinodgopal K, Hotchandani S, Kamat PV (1993) Electrochemically assisted photocatalysis. TiO₂ particulate film electrodes for photocatalytic degradation of 4-chlorophenol. *J Phys Chem* 97:9040–9044
- Vinodgopal K, Hua X, Dahlgren RL, Lappin AG, Patterson LK, Kamat PV (1995) Photochemistry of Ru(bpy)₂(dcbpy)²⁺ on Al₂O₃ and TiO₂ surfaces. An insight into the mechanism of photosensitization. *J Phys Chem* 99:10883–10889
- Vinodgopal K, Wynkoop D, Kamat PV (1996) Environmental photochemistry on semiconductor surfaces: a photosensitization approach for the degradation of a textile azo dye, acid orange 7. *Environ Sci Technol* 30:1660–1666
- Wang ZL (2000) Transmission electron microscopy of shape-controlled nanocrystals and their assemblies. *J Phys Chem* 104:1153–1175
- Wang CM, Heller A, Gerischer H (1992) Palladium catalysis of O₂ reduction by electrons accumulated on TiO₂ particles during photoassisted oxidation of organic compounds. *J Am Chem Soc* 114:5230–5234
- Wang J, Deo RP, Poulin P, Mangey M (2003) Carbon nanotube fiber microelectrodes. *J Am Chem Soc* 125:14706–14707
- Warman JM, de Haas MP, Pichat P, Serpone N (1991) Effect of isopropyl alcohol on the surface localization and recombination of conduction-band electrons in Degussa P25 TiO₂. A pulse-radiolysis time-resolved microwave conductivity study. *J Phys Chem* 95:8858–8861
- Wasmus S, Kuver A (1999) Methanol oxidation and direct methanol fuel cells: a selective review. *J Electroanal Chem* 461:14–31
- Wijayantha KGU, Peter LM, Otley LC (2004) Fabrication of CdS quantum dot sensitized solar cells via a pressing route. *Solar Energy Mater Solar Cells* 83:363–369
- Williams G, Seger B, Kamat PV (2008) TiO₂-graphene nanocomposites. UV-assisted photocatalytic reduction of graphene oxide. *ACS Nano* 2:1487–1491
- Wood A, Giersig M, Mulvaney P (2001) Fermi level equilibration in quantum dot-metal nanojunctions. *J Phys Chem B* 105:8810–8815
- Wu JJ, Yu CC (2004) Aligned TiO₂ nanorods and nanowalls. *J Phys Chem B* 108:3377–3379
- Yochelis S, Hodes G (2004) Nanocrystalline CdSe formation by direct reaction between Cd ions and selenosulfate solution. *Chem Mater* 16:2740–2744
- Yu P, Zhu K, Norman AG, Ferrere S, Frank AJ, Nozik AJ (2006) Nanocrystalline TiO₂ solar cells sensitized with InAs quantum dots. *J Phys Chem B* 110:25451–25454
- Yu H, Quan X, Chen S, Zhao H (2007) TiO₂-multiwalled carbon nanotube heterojunction arrays and their charge separation capability. *J Phys Chem C* 111:12987–12991

Index

A

- Absorbed photon-to-current conversion efficiency (APCE), 558
- Acetic acid decomposition, 213–214
- Acetic acid, TiO₂
 - electron/charge-transfer processes, 510
 - ethane and methane formation, 509–510
 - space charge region, 512–513
 - steady-state acetic acid pressure, 508, 509
 - temperature programmed desorption (TPD) results, 508
 - XPS C(1s), 512, 513
- Acid orange 7, 381–382
- Acid orange 52. *See* Methyl orange
- Adamantane photocatalytic oxidation, 256–257
- Adsorbed Fe³⁺ ions. *See* S-/N-doped TiO₂ powder
- Adsorption and exchange, Pt/TiO₂
 - oxygen and carbon monoxide, 492, 493
 - photocatalytic reaction mechanisms, 491–492
 - thermodynamic parameters, 492
- Advanced oxidation processes (AOP), 369–370, 719–720
- Ag core-TiO₂ shell nanostructures
 - photoinduced charge separation and storage, 723–724
 - plasmon absorbance peak, 724–725
- Agrochemical pesticides and herbicides
 - acute toxicity, 323
 - analytical procedures
 - NH₄⁺ and NO₃⁻ ion formation, 326–327
 - temporal spectral changes, 326
 - total organic carbon (TOC) loss, 326
 - Asulam, 324
 - base-catalyzed elimination process, 323
 - Diphenamid, 323–324
 - food safety, 322
 - FTIR spectral patterns
 - CH₃SO₃H intermediate product, 336
 - Oxamyl characteristic bands, 334
 - hydrophobic contaminant, 322
 - materials, 325
 - molecular orbital calculation
 - Asulam, 336, 340
 - Diphenamid, 336, 339
 - Methomyl, 336, 338
 - OH radical abstraction, 338
 - Oxamyl, 336, 337
 - N and S functions, conversion, 329–334
 - oxamyl and methomyl structure, 322, 323
 - photomineralization, 326
 - temporal CO₂ evolution yield, 328
 - TOC, normalized temporal decrease, 328, 329
 - rate-determining factors, 322
 - wastewater treatment, 321
- Air-cleaning system. *See* Photocatalytic oxidation
- Air purifying systems
 - elimination capacity, 412
 - formaldehyde decomposition, 410, 411
 - GC/MS peaks, 411
 - sick house syndrome, 409, 410
- Alcohol oxidation, 629–631
- Aliphatic organic sulfur compounds, 590–594
- Amino acids production, 661
- Anatase-TiO₂ morphological characteristics, 279
- Anatase-type nanocrystalline TiO₂ powders
 - characterization of, 115–118
 - THyCA-TiO₂ photocatalytic activity, 118–119
- Anatase vs. rutile phase, 278
- Anion-doped titanium dioxide
 - carbon-doped titanium dioxide (*see* Carbon doped titanium dioxide)

- Anion-doped titanium dioxide (*cont.*)
 combined sol-gel/hydrothermal treatment, 56
 fluorine-doped titanium dioxide, 61–62
 N,F-and N,S-codoped titanium dioxide, 74–81
 nitrogen-doped titanium dioxide (*see* Nitrogen-doped titanium dioxide)
 sulfur-doped titanium dioxide, 60–61
 visible-light-activity, 56–57
- Area vs. weight ratios, anatase-rutile phase (WA/WR), 160, 161
- Aromatic organic sulfur compounds, 594–600
- Aromatics hydroxylation, 631–632
- Asulam
 carbamate-type herbicide, 324
 molecular orbital calculation, 336, 340
 structure, 324
- B**
- Band gap energy, 506
- Benzene, photocatalytic purification
 efficient UV system development
 carbon deposition, suppression of, 458–459
 electron-hole separation, 459–460
 •OH radicals formation, 460–461
 photochemical process, 461–463
 system efficiency, increase, 455–458
 limitation, TiO₂, 452–455
 semiconductor photocatalysis, 451
 sunlight system development, TiO₂/InVO₄
 characterization, 465–470
 fabrication, 465
 photocatalytic performance, 470–473
 photochemical process, 461–463
 sensitization, 463–464
- Binary oxide formation
 Bi₁₂TiO₂₀
 band structure and density of state, 248, 249
 organic contaminants decomposition, 247, 248
 UV-vis/diffuse reflectance spectra, 248
 CASTEP program package, 248, 249
- Bone cell affinity, 707–708
- Bone-forming cells. *See* Osteoblasts
- Brookite-type nanocrystalline TiO₂ powders
 characterization of, 119–121
 photocatalytic activity, 121–122
- Broyden–Fletcher–Goldfarb–Shannon algorithm, 327
- Bulk TiO₂, gas-phase elemental mercury, 440–442
- C**
- Calcination effects
 acetic acid decomposition, 213–214
 OH LIF intensity
 chemical surface structure, 208
 delay time dependence, 207
 Q₁(6) transition, 207
 ST-01 and P25 TiO₂ powders, 208
 surface OH groups
 adsorbed water molecules, 1H NMR spectrum, 210
 time profiles, chemical shift, 210, 211
 trapped holes
 g values, paramagnetic species, 209
 photoinduced ESR spectra, 209, 210
- Carbon doped titanium dioxide
 aging time effect, 58, 59
 C atoms content, 60
 hydrothermal method usage, 59
 photochemical water splitting, 57
 photoelectrode thermal treatment, 57
 surface states, 57
 thin dense and mesoporous films,
 optical absorption spectra, 58
 VLA photoactivity, 59
- Carbon monoxide (CO)
 oxidation, 495–496
 PEC system, 426–428
- Carbon nanotubes, 730–731
- CASTEP program package, 248, 249
- Catalyst deactivation and reactivation
 gas phase reaction, 614–615
 liquid phase reaction, 613
- Catalytic photoreduction, CO₂ in
 aqueous solution, 679–680, 687–690
 optical–fiber reactor, 690–694
 vapor phase, 680–682
- Charge transfer process, 482–483
- Chemical etching, effect of
 cyclic voltammogram, 553
 incident photon-to-current conversion efficiency (IPCE), 552–553
 SEM images, 554
 sunlight-gathering system, 554, 555
- Chlorophenols
 hydroxyl radicals, 365
 nitrogen-doped TiO₂, 366, 367

- rate constants, 364, 365
 - visible light-assisted photomineralization, 367
 - Chlortoluron degradation, 376
 - Conductor-like screening model orbital (COSMO) procedure, 327
 - Contact angles, H₂O droplets, 144, 145
 - COSMO. *See* Conductor-like screening model orbital procedure
 - Crystalline phase and morphology control
 - microemulsion-mediated hydrothermal method
 - anatase formation mechanism, 10, 11
 - SO₄²⁻-anatase content vs. mole percentage, 9
 - steric effect, 11
 - ultrasound irradiation
 - cationic surfactant
 - cetyltrimethylammonium (CTAB), 13
 - HCl concentration, 11
 - protonation, 13
 - Ti(OC₄H₉)₄ hydrolysis, 11
 - Cu₂O/Vis-TiO₂/ITO and CuI/Vis-TiO₂/ITO electrodes, 563–567
- D**
- Deaminocondensation, 662–663
 - Decarboxylation, carboxylic acid, 659–660
 - Degussa P25, 446–448
 - Development and sensitization, TiO₂
 - band calculation, 257
 - chemical states, doped atoms, 258–259
 - Fe ions, oxidation states, 256
 - hydroxylated adamantane compound
 - synthesis, 265–268
 - incident light wavelength dependence, 272
 - materials and instruments, 254–255
 - photocatalytic oxidation
 - adamantane, 256–257
 - 2-methylpyridine, 257, 268–269
 - 2-propanol, 256, 269–272
 - 2-propanol decomposition rate, 272
 - S-doped
 - electronic structure, 259
 - Fe compounds dispersibility, 264–265
 - first-principles band calculation, 257
 - 2-propanol photodecomposition, anatase phase, 265, 266
 - XRD spectra, adsorbed Fe³⁺, 264, 265
 - S-/N-doped TiO₂ powder
 - absorption spectra, 260–262
 - ESR spectra, 261–264
 - physical properties, 257, 258
 - preparation of, 255
 - reduction and air oxidation, 256
 - Diffusion flame burner. *See* Nanotitanosilicate fiber
 - Diphenamid
 - herbicides, 323
 - molecular orbital calculations, 336, 339
 - structure, 324
 - Direct methane coupling, 660–661
 - Diuron degradation, 375–377
 - Doped TiO₂ sample
 - band gap energy calculations
 - Coulomb repulsion, 87
 - C-*vs.* N-doped rutile, 92
 - DFT band structure, N-, 85, 86
 - electronic band structural change, 89
 - experimental *vs.* calculated values, 90, 91
 - FIREBALL simulation technique, 90
 - fudge factor, 82
 - intrinsic absorption edge, 93
 - Perdew–Burke–Ernzerhof (PBE) exchange correlation, 85
 - photoinduced electron transfer, 88
 - pure *vs.*, N-doped band structure, 84, 85
 - scissors operator, 82
 - S-doping levels, DFT analysis, 83
 - supercell types, 82
 - WIEN97 code, 82
 - band gap narrowing
 - absorption spectra, TiO_{2-x}N_x
 - photoinduced color centers, 102, 103
 - photobleaching kinetics, 103, 104
 - photocoloration, TiO₂/polymer compositions, 101, 102
 - surface photoinduced redox processes, 101
 - optical properties
 - AB1 absorption band, 97
 - absorption spectrum, nitrogen-doped rutile crystal, 95, 96
 - difference DRS spectra, 93, 94
 - F-type centers, 98–100
 - Kroger–Vink notation, 98
 - numerical analysis, 94
 - phase composition, 96
 - Doping, TiO₂
 - with electronegative elements, nitrogen chemical potential, 294
 - DRIFT spectra, 292, 293
 - light-to-chemistry conversion, 296
 - localized electronic states, 292, 293
 - morphological/surface variables, 292

- physico-chemical basis, 296
 - point/extended defects, 291
 - structural and photo-chemical characterization, 291
 - synthesis, 291
 - Taq3 reference result, 292
 - Ti⁵(IV) species, 295
 - XANES and EXAFS spectroscopy, 294–296
 - with metal cations
 - high concentration, 281–285
 - inclusion, 281
 - intermediate band-based two-photon processes, 281
 - low concentration, 285–290
 - physical and electronic characteristics
 - atomic displacements, 280
 - dopant concentration, 280
 - electron-hole trapping, 279
 - electron-phonon coupling, 280
 - Double-layered TiO₂ thin film electrodes, 567–568
 - Dye-sensitized solar cells (DSSC), 726
- E**
- Effective molecular width (EMW), 227
 - Electron–hole
 - recombination, 386
 - separation, 459–460
 - Electron–phonon coupling, 280
 - Electron trapping and storage
 - Ag core–TiO₂ shell nanostructures, 723–725
 - photochromic and electrochromic effects, 721–723
 - EMW. *See* Effective molecular width
 - Epoxidation, alkenes
 - ESR and stoichiometric reactivity tests, 651, 652
 - PO formation mechanism, 653
 - Ethanol photo-reactions, TiO₂
 - Langmuir–Hinshelwood kinetics, 519
 - photo-decomposition, 519, 520
 - surface coverage, ethoxide species, 517, 518
 - temperature effect, 515
 - XPS C(1s), 516, 517
 - Ethyl orange, 384
- F**
- FIREBALL simulation technique, 90
 - FLAPW. *See* Full-potential linearized augmented plane wave
- Fluorine doped titanium dioxide, 61–62
 - Franck–Condon principle, 75
 - FTIR spectral patterns
 - CH₃SO₃H intermediate product, 336
 - Oxamyl characteristic bands, 334
 - Full-potential linearized augmented plane wave (FLAPW), 241, 242
- G**
- Gas-phase elemental mercury, photocatalytic removal
 - bulk TiO₂, 440–442
 - immobilized TiO₂
 - Degussa P25, 446–448
 - nanotitanosilicate fiber, 443–446
 - in situ generated TiO₂, 438–440
 - Gas phase reaction
 - catalyst deactivation and reactivation, 614–615
 - degradation, rates of
 - air humidity influence, 613
 - substrate concentration effect, 612
 - temperature effect, 613
 - Gas-phase Ti precursor injection. *See* In situ generated TiO₂, gas-phase elemental mercury
 - Gibbs free energy, 225
- H**
- Highest occupied molecular orbital (HOMO), 218
 - Highly active TiO₂ photocatalysts
 - characterizations, 404–405
 - microstructure, 406–408
 - photocatalytic reactivity
 - evaluation of, 405
 - reaction time profiles, 408, 409
 - rectangular column-structured
 - applications for, 409–412
 - preparation of, 404–405
 - High photocatalytic activity. *See* Titanium oxide-based powders
 - HOMO. *See* Highest occupied molecular orbital
 - HyCOM–TiO₂ films absorption spectra, 128
 - Hydrocarbons oxidation, 625–627
 - Hydrogenation, alkynes and alkenes, 658–659
 - Hydrogen bonded structure, H₂O molecules
 - NIR spectra, 530–531
 - UV light irradiation, effect components, 533

- deconvoluted spectra, 533
- H₂O clusters, structure models, 534, 535
- H₂O filter, 531–533
- hydrogen-bond acceptor and donor, 533, 534
- NIR absorption spectra, 533, 535
- Hydrogen production, photocatalysis
 - chemical etching, effect of
 - cyclic voltammogram, 553
 - incident photon-to-current conversion efficiency (IPCE), 552–553
 - SEM images, 554
 - sunlight-gathering system, 554, 555
- nitrogen substitution, effect of
 - quantum yield/APCE, 558
 - relative photocurrent, 557
 - UV–vis absorption spectra, 556, 557
- sputtering parameters, effect of
 - conduction band (E_{CB}) and valence band (E_{VB}) energy levels, 549, 550
 - depth distribution profiles, 547, 548
 - quantum yields, H₂ and O₂ evolution, 548, 549
 - time profile, 550, 551
 - UV–vis transmission spectra, 547
- Hydroxylated adamantane compound
 - synthesis, 265–268
- I**
- ICB. *See* Ionized cluster beam deposition
- Immobilized TiO₂, gas-phase elemental mercury
 - Degussa P25, 446–448
 - nanotitanosilicate fiber
 - Hg⁰ removal, 446
 - rotating flame burner, 443, 444
 - SEM images, 444, 445
 - wavelength distributions, 444, 445
- Incident photon-to-current conversion efficiency (IPCE), 552–553
- In situ* generated TiO₂, gas-phase elemental mercury, 438–440
- In vivo* implant fixation, super osseointegration, 703–704
- Ion engineering method. *See* Ionized cluster beam (ICB) deposition
- Ionized cluster beam (ICB) deposition
 - dry coating process, 134
 - reactivity enhancement
 - acetaldehyde, photocatalytic oxidation, 147, 148
 - binding energy, 146
 - loaded vs. unloaded film, 145, 146
 - Pt LIII-edge XANES spectra, 147, 148
 - Pt loading, 145
 - thin film preparation
 - highly transparent TiO₂, 137–139
 - TiO₂/SiO₂ and TiO₂/B₂O₃ binary oxide, 139–145
 - well-defined TiO₂, 135–137
- Isomerization, alkenes, 664
- Isoproturon degradation, 376
- L**
- Langmuir–Hinshelwood (LH) kinetics, 491, 519
- Langmuirian adsorption parameters, 127
- Lanthana (La₂O₃) loading
 - characteristic bands, 173
 - defect sites, 177
 - monolayer dispersion capacity, 177
 - particle size, 175
 - TiO₂-900 vs. La₂O₃/TiO₂, 175
- Laser-induced fluorescence (LIF)
 - spectroscopy, TiO₂
 - heterogeneous catalysis, 187
 - higher sensitivity, 186
 - in situ* laser induced luminescence spectroscopy setup, 186–187
 - molecule spectroscopic technique, 186
 - solid semiconductors, surface process, 187
- LDA. *See* Local density approximation
- LH kinetics. *See* Langmuir–Hinshelwood (LH) kinetics
- LIF. *See* Laser-induced fluorescence
- Ligand-to-metal charge transfer transition (LMCT), 221
- Liquid phase reaction
 - catalyst deactivation and reactivation, 613
 - degradation rates
 - hydrogen peroxide effect, 612
 - solution pH, influence, 609–610
 - solvent effect, 611–612
 - substrate concentration effect, 610–611
- LMCT. *See* Ligand-to-metal charge transfer transition
- Local density approximation (LDA), 241, 242
- Lowest unoccupied molecular orbital, 218
- LUMO. *See* Lowest unoccupied molecular orbital

M

- m*-dinitrobenzene (*m*-DNB) degradation, 386, 387
- Metal cation doping, TiO₂
- high concentration
 - asymmetric coordination, XANES spectra, 283, 284
 - microemulsion-based preparation method, 281–282
 - quantum mechanical calculations, 283
 - toluene gas phase oxidation, photocatalytic activity, 282
 - W L_r-edge XANES spectra, 282, 283
 - inclusion, 281
 - intermediate band-based two-photon processes, 281
 - low concentration
 - anatase-rutile transformation, 288
 - charge carrier lifetimes, 285
 - EPR spectra, iron-doped systems, 287
 - toluene mineralization, photocatalytic activity, 289
 - vanadium dopant, 288–289
- Metal doping method
- charge generation, amorphous photocatalyst, 238
 - dopant ions energy levels, 239, 240
 - hybrid titania (Pt(IV)/AMM-Ti), diffuse reflectance spectra, 237
 - interfacial charge transfer, 237
 - ion beam technologies, 240
 - microemulsion, 238
 - photoreactivities, 236–237
 - toluene mineralization, 238
 - transition metal ions, 236
- Methomyl
- acaricide, 322
 - highly water soluble, 323
 - hydrolysis half-lives, 325
 - molecular orbital calculation, 336, 338
 - structure, 323
- Methyl orange, 382–384
- 2-Methylpyridine photocatalytic oxidation, 257, 268–269
- Molecular shave transformation, 228
- Multifunctional photocatalysts, preparation. *See* Titania (TiO₂)
- N**
- N*-alkylation, amines/ammonia, 663–664
- N and S functions, conversion, 329–334
- Nanotitanosilicate fiber

- Hg⁰ removal, 446
 - rotating flame burner, 443, 444
 - SEM images, 444, 445
 - wavelength distributions, 444, 445
- N*-containing aromatics reduction, 633–635
- Near-infrared (NIR) spectra, 530–531
- NIR spectra. *See* Near-infrared (NIR) spectra
- Nitroaromatic compounds
 - contamination by, 384–385
 - electron–hole recombination, 386
 - explosives, 385
 - m*-dinitrobenzene (*m*-DNB), photocatalytic degradation, 386, 387
- Nitrogen-doped titanium dioxide (TiO₂), 366, 367
 - annealing, 63
 - Ar⁺-ion sputtering, 66
 - band gap energies, 69
 - belt-like rutile particles, 71, 72
 - β-substituted N, 67
 - calcination, 62–63
 - crystallized anatase TiO_{2-x}N_x films, 65
 - DC magnetron sputtering, 64
 - DRS spectra, 68
 - electrochemical potentials, 64
 - ethylene glycol degradation, 72
 - high-energy ball milling, P-25 TiO₂, 65
 - hydrolysis, 65
 - hyponitrite and nitrite ions, 65
 - isopropanol degradation, 63
 - molecularly chemisorbed dinitrogen, 63
 - nanocomposite, 71
 - nanocrystalline porous thin films, 64
 - nanoparticles, 68
 - nanotube fabrication, 70
- N,F-codoped titanium dioxide (NFT)
 - absorption features, 72, 74, 75
 - energy states, 77
 - NTO, FTO and NFTO comparison, 77–78
 - photoactivity, 76–77
 - PL spectra, 74–76
 - sol-gel/solvo-thermal method, 78
 - XPS spectra, 79, 80
- nitridation, 65
- N,S-codoped titanium dioxide
 - photoactivity, 81
 - XPS spectra, 79–80
- photoactivity and preparation condition, 69
- photocatalytic activity and quantum
 - efficiencies, NO_x degradation, 71, 73
- reverse micelle microemulsion method, 70
- self-organized nano-tubes, 70

- substrate adsorption, photoassisted processes, 72, 74
 - surficial organotitanium complexes, 68
 - synthesis method, 62
 - TiO_{2-x}N_x testing, 70
 - UV-visible absorption spectra, 71, 74
 - visible-light responses, 66
 - XPS spectra, 65–67
 - XRD spectra, 68
 - Nitrogen substitution, effect of
 - quantum yield/APCE, 558
 - relative photocurrent, 557
 - UV-vis absorption spectra, 556, 557
 - Nonmetal doping method
 - density of states (DOSs) calculation
 - full-potential linearized augmented plane wave (FLAPW), 241, 242
 - local density approximation (LDA), 241, 242
 - DMPO-OH^{SSS} adduct, ESR signals, 243, 244
 - F-doped TiO₂
 - flower morphology, FESEM and TEM, 245, 246
 - UV-vis adsorption spectra, 243, 244
 - XPS spectra, 245, 246
 - HF, hydrolysis reaction product, 245
 - requirements or conditions, 241
 - UV-vis spectra, N-doped TiO₂, 242
- O**
- OH radicals
 - formation mechanism
 - peroxy species, 212, 213
 - reaction scheme, 212, 213
 - surface structure, irradiation, 212
 - surface-trapped hole, 212
 - laser induced fluorescence (LIF) method
 - delay time dependence, 207
 - excitation spectra, 207
 - experimental set-up detection, 206–207
 - Olefins oxidative cleavage, 627–629
 - Organic sulfur compound, products of
 - aliphatic, 590–594
 - aromatic, 594–600
 - heteroatomic, 600–602
 - properties, 582–589
 - Organic synthesis, TiO₂-based photocatalysis
 - carbonylation, 639, 640
 - cyclization, 639, 640
 - heterogeneous photocatalysis, 623–624
 - oxidations
 - alcohols oxidation, 629–631
 - aromatics hydroxylation, 631–632
 - hydrocarbons oxidation, 625–627
 - olefins oxidative cleavage, 627–629
 - α-oxyalkyl radical formation, 638, 639
 - photocatalysts, 624–625
 - reductions
 - CO₂, 635–637
 - N-containing aromatics, 633–635
 - semiconductor/zeolite photocatalyzed syntheses, 638
 - sunlight-induced functionalisation, 638
 - Orthopedic and dental implants, 700, 701
 - Osteoblasts
 - attachment and spread, 701–702
 - carbon element, inverse correlation, 707
 - proliferation, maturation and mineralization, 702–703
 - Oxamyl
 - highly water-soluble, 323
 - molecular orbital calculations, 336, 337
 - nitrogen-and sulfur-bearing pesticide, 322
 - oral acute toxicity, 325
 - structure, 323
 - temporal variations, FTIR spectral patterns, 334, 336
 - Oxidation, acetaldehyde with O₂, 307–310
 - Oximecarbamates class, 323
 - α-Oxyalkyl radical formation, 638, 639
- P**
- Parametric method 3 (PM3), 327
 - Perdew–Burke–Ernzerhof (PBE) exchange correlation, 85
 - Pesticides,
 - advanced oxidation processes (AOPs), 369–370
 - phenylureas
 - chlortoluron degradation, 376
 - Diuron degradation, 375–377
 - general structure, 373, 375
 - isoproturon degradation, 376
 - transformation pathway, 376–378
 - s-triazines, 371–373
 - Phase composition, semiquantitative analysis, 159–160
 - Phenol compounds
 - chlorophenols
 - hydroxyl radicals, 365
 - nitrogen-doped TiO₂, 366, 367
 - rate constants, 364, 365

- visible light-assisted photomineralization, 367
 - nitrophenols, 367–369
 - photocatalytic ozonation, 362
- Phenylureas
 - chlortoluron degradation, 376
 - Diuron degradation, 375–377
 - general structure, 373, 375
 - isoproturon degradation, 376
 - transformation pathway, 376–378
- Phonons, 280
- Photocatalysis. *See* Surface chemistry, TiO₂
- Photocatalysis, hydrogen production
 - chemical etching, effect of
 - cyclic voltammogram, 553
 - incident photon-to-current conversion efficiency (IPCE), 552–553
 - SEM images, 554
 - sunlight-gathering system, 554, 555
 - nitrogen substitution, effect of
 - quantum yield/APCE, 558
 - relative photocurrent, 557
 - UV–vis absorption spectra, 556, 557
 - sputtering parameters, effect of
 - conduction band (E_{CB}) and valence band (E_{VB}) energy levels, 549, 550
 - depth distribution profiles, 547, 548
 - quantum yields, H₂ and O₂ evolution, 548, 549
 - time profile, 550, 551
 - UV–vis transmission spectra, 547
- Photocatalyst-assisted decomposition, 415, 416
- Photocatalyst-based hybrid methanol fuel cells, 731–732
- Photocatalytic organic syntheses
 - amino acids production, 661
 - deaminocondensation, 662–663
 - decarboxylation, carboxylic acid, 659–660
 - direct methane coupling, 660–661
 - epoxidation, alkenes
 - ESR and stoichiometric reactivity tests, 651, 652
 - PO formation mechanism, 653
 - hydrogenation, alkynes and alkenes, 658–659
 - isomerization, alkenes, 664
 - N*-alkylation, amines/ammonia, 663–664
 - photoexcitation state, 649, 650
 - photooxidation of
 - alcohols, 657
 - alkanes, 654–655
 - aromatic compounds, 655–656
 - methane, 656–657
 - reductive and oxidative elementary reactions, 648
- Photocatalytic oxidation
 - adamantane, 256–257
 - advantages, 416
 - air-cleaning system, 432–433
 - carbon monoxide (CO), 426–428
 - 2-methylpyridine, 257, 268–269
 - photocatalyst-assisted decomposition, 415, 416
 - photoelectrocatalytic (PEC) system
 - decomposition of, 425, 426
 - photo-current of, 424, 425
 - sterilization of, 426
 - 2-propanol, 256, 269–272
 - TiO₂ immobilization, 428–432
 - TiO₂ surface, modification
 - noble metal deposition, 419–420
 - silica-supported TiO₂, 420–422
 - sulfated TiO₂, 422–424
 - transition metal doping, 417–419
- Photocatalytic ozonation, 362
- Photocatalytic performance. *See* Surface phase structures
- Photocatalytic purification, benzene. *See* Benzene, photocatalytic purification
- Photocatalytic reactivity
 - evaluation of, 405
 - reaction time profiles, 408, 409
- Photocatalytic reactivity, NO decomposition
 - UV light irradiation
 - preparation temperature effect, 307, 308
 - reaction time profiles, 307
 - visible light irradiation
 - preparation temperature effect, 308–310
 - reaction time profiles, 308, 309
- Photocatalytic removal, gas-phase elemental mercury. *See* Gas-phase elemental mercury, photocatalytic removal
- Photocatalytic transformations, sulfur-based organic compounds
 - catalyst deactivation and reactivation
 - gas phase reaction, 614–615
 - liquid phase reaction, 613
 - chemical warfare agents, 580, 581
 - degradation, rates of
 - gas phase reaction, 612–613
 - liquid phase reaction, 609–612
 - mechanism of
 - chemical transformations, 607–608
 - direct oxidation, 605–606
 - energy transfer, 603
 - hydrogen abstraction, 604

- hydrogen atom transfer, 604
- molecular photocatalysis, 607
- PET, 603
- primary and secondary reaction, 602
- radical cations, 605
- organic sulfur compound, products of
 - aliphatic, 590–594
 - aromatic, 594–600
 - heteroatomic, 600–602
 - properties, 582–589
- pesticides, 580
- photochemical reactions, role of, 615–617
- S-oxidation states, 579
- Photoelectrocatalytic (PEC) system
 - carbon monoxide (CO), 426–428
 - decomposition of, 425, 426
 - photo-current of, 424, 425
 - sterilization of, 426
- Photoelectrochemical solar cells
 - carbon nanotubes, 730–731
 - dye-sensitized solar cells (DSSC), 726
 - quantum dot sensitized solar cells (QDSSC), 727–730
- Photo-excitation process, TiO₂, 3–4
- Photoinduced charge transfer processes, 718
- Photoinduced superhydrophilicity, TiO₂
 - contact angle/volume/contact area relationship, 528
 - hydrogen bonded structure, H₂O molecules
 - NIR spectra, 530–531
 - UV light irradiation, effect, 531–535
 - surface wettability
 - hydrophilic conversion, mechanism, 540–541
 - photocatalytic oxidation, hydrocarbons, 538–539
 - UV light irradiation, effect, 536–539
 - time profiles, contact angles, 529
 - two-dimensional capillary effect, 529
- Photoluminescence spectroscopic studies, TiO₂ photocatalyst
 - characteristics
 - features, 188
 - indirect wide gap semiconductor, 188
 - luminescence centers, 191
 - oxygen vacancies, 190, 191
 - phase transformation, 188–189
 - photoluminescence vs. UV-Raman spectra, 189
 - surface stoichiometry and states, 189
 - crystal structure, 186
 - laser-induced fluorescence (LIF) heterogeneous catalysis, 187
 - higher sensitivity, 186
 - in situ laser induced luminescence spectroscopy setup, 186–187
 - molecule spectroscopic technique, 186
 - solid semiconductors, surface process, 187
- molecule adsorption, influence
 - C1–C3 alcohols, adsorbates, 193
 - ionization potential, 192, 193
 - photoluminescence quenching, 192, 193
 - radiative deactivation, charge-transfer excited state, 191
 - water on TiO₂ surface, 194
- non-destructive method, 185
- photocatalytic reaction
 - additive ionization potential effect, 197, 198
 - hydrogenolysis reaction yield, 197
 - trichloroethylene (TCE) decomposition, photoactivity, 198, 199
- platinum loading
 - photocatalytic activity, TiO₂ vs. Pt/TiO₂, 195, 196
 - photoinduced-carriers recombination, 196
 - solid surface characterization, 185
- Photomineralization, 326, 349
- temporal CO₂ evolution yield, 328
- TOC, normalized temporal decrease, 328, 329
- Photooxidation, organic syntheses
 - alcohols, 657
 - alkanes, 654–655
 - aromatic compounds, 655–656
 - methane, 656–657
- Photostimulated adsorption spectra, H₂ and O₂, 38–40
- Photovoltaic cell performance, SCs and DSSCs
 - Cu₂O/Vis-TiO₂/ITO and CuI/Vis-TiO₂/ITO electrodes, 563–567
 - double-layered TiO₂ thin film electrodes, 567–568
 - UV-TiO₂/ITO-PEN and Vis-TiO₂/ITO-glass electrodes, 570
 - UV-TiO₂/Vis-TiO/ITO, 568–570
 - Vis-TiO₂/N719/CuI/Au system, 571–572
 - Vis-TiO₂ thin film electrodes, 560–563
- Plug flow reactor (PFR), 484
- PM3. *See* Parametric method 3
- Point charge and electron density calculations, 327
- molecular orbital calculation
 - Asulam, 336, 340

- Diphenamid, 336, 339
- Methomyl, 336, 338
- Oxamyl, 336, 337
- OH radical abstraction, 338
- Polymer hydro-gel electrolytes, 570
- Polymeric materials, purification and treatment
 - application field, 361
 - application, polymer science
 - photocatalyst-polymer composite, 390–391
 - pigment, photocatalyst, 390
 - polymeric substrate, functional coating, 391–396
 - nitroaromatic compounds, 384–387
 - contamination by, 384–385
 - electron-hole recombination, 386
 - explosives, 385
 - m*-dinitrobenzene (*m*-DNB),
 - photocatalytic degradation, 386, 387
 - nitrogen-containing inorganic compounds, 387–389
 - operational parameters, 351–354
 - pesticides
 - advanced oxidation processes (AOPs), 369–370
 - phenylureas, 373–379
 - s*-triazines, 371–373
 - phenol compounds
 - chlorophenols, 364–367
 - nitrophenols, 367–369
 - photocatalytic ozonation, 362
 - photocatalytic wastewater process, 348
 - photomineralization, 349
 - pyrimidine and derivatives
 - metal ion effects, 359–360
 - oxidation mechanism, 355–357
 - pH effect, 358–359
 - TiO₂ property effect, 360–361
 - synthetic dyes
 - acid orange 7, 381–382
 - chemical structures, 379–380
 - ethyl orange, 384
 - methyl orange, 382–384
- Porous Vycor glass, 191, 197
- Preparation and characteristics, VLA TiO₂
 - carbon doped specimens
 - aging time effect, 58, 59
 - C atoms content, 60
 - hydrothermal method usage, 59
 - photochemical water splitting, 57
 - photoelectrode thermal treatment, 57
 - surface states, 57
 - thin dense and mesoporous films,
 - optical absorption spectra, 58
 - VLA photoactivity, 59
 - density of states (DOS) calculations, 57
 - fluorine doped specimens, 61–62
 - N,F codoped specimens
 - centrifugation, 79
 - Franck-Condon principle, 75
 - lattice ion polarizability, 75
 - NFT powder preparation, 75
 - origin unidentified energy state (OUES), 75
 - PL spectrum, NFT-900 sample, 75, 76
 - surface characteristics, 76
 - valence and conduction band energy state, 75, 77
 - XPS spectra, 78
 - nitrogen doped specimens
 - annealing, 63
 - Ar⁺-ion sputtering, 66
 - band edge electrochemical potentials, 64
 - band gap energies, 69
 - belt-like rutile particles, 71, 72
 - β-substituted N, 67
 - calcination, 62–63
 - crystallized anatase TiO_{2-x}N_x films, 65
 - DC magnetron sputtering, 64
 - DRS spectra, 68
 - electrochemical potentials, 64
 - ethylene glycol degradation, 72
 - high-energy ball milling, P-25 TiO₂, 65
 - hydrolysis, 65
 - hyponitrite and nitrite ions, 65
 - isopropanol degradation, 63
 - molecularly chemisorbed dinitrogen, 63
 - nanocomposite, 71
 - nanocrystalline porous thin films, 64
 - nanoparticles, 68
 - nanotube fabrication, 70
 - N,S codoped specimens
 - high-resolution XPS spectra, 79, 80
 - nanocrystalline mesoporous,
 - preparation, 79
 - red shift, 81
 - sulfur doped specimens, 60–61
 - VLA requirements, 56–57
- 2-Propanol photocatalytic oxidation, 256
- N-doped, 269
- S-doped
 - crystal structure change, 272
 - Fe³⁺ ion adsorption, NaBH₄ treatment, 269, 271

- Propene oxide (PO) formation. *See*
Epoxidation, alkenes
- Pt/TiO₂, gas phase photocatalysis
acidity, Pt, and gas phase, 496–497
adsorption and exchange
oxygen and carbon monoxide, 492, 493
photocatalytic reactions, mechanisms,
491–492
thermodynamic parameters, 492
advanced oxidation processes (AOP),
719–720
charge transfer processes, 482–483
CO oxidation, 495–496
CO₂ reduction, 496
optimum metal loading and particle size,
497–498
oxidation kinetics, effect of
benzene depletion rates and carbonation
ratios, 485
extracted Arrhenius parameters, 486,
488
film mass transfer limitations, 484
plug flow reactor (PFR), 484
thermal and photocatalytic reaction, 487
photoinduced charge transfer processes,
718
semiconductor-metal nanocomposites,
720–721
surface reaction mechanisms, 489–491
- Q**
Quantum dot sensitized solar cells (QDSSC),
727–730
- R**
Radio-frequency-magnetron sputtering (RF-
MS) deposition method, 42, 560
Rectangular column-structured TiO₂
photocatalysts
air purifying systems
elimination capacity, 412
formaldehyde decomposition, 410, 411
GC/MS peaks, 411
sick house syndrome, 409, 410
internal structure, 407, 408
preparation of, 404–405
SEM images, 406
TEM image, 407
Renewable energy
catalytic photoreduction, CO₂ in
aqueous solution, 679–680, 687–690
optical-fiber reactor, 690–694
vapor phase, 680–682
characterization of
catalysts, 679
optical fibers, 685–687
powder catalysts, 682–685
energy cycle, 674
preparation of
powder catalyst, 677–678
TiO₂-coated optical fiber, 678–679
theoretical light transmission, 676
TiO₂-coated optical fiber, light
transmission, 675, 676
RF-MS. *See* Radio-frequency-magnetron
sputtering deposition method
RF-MS deposition method. *See* Visible
light-responsive photocatalysts,
TiO₂ thin film
Rotating glass-type reactor. *See* Bulk TiO₂,
gas-phase elemental mercury
- S**
Scherrer's equation, 16, 305, 306
SDA. *See* Structure directing agents
S-doped TiO₂
electronic structure, 259
Fe compounds dispersibility, 264–265
first-principles band calculation, 257
2-propanol photodecomposition, anatase
phase, 265, 266
XRD spectra, adsorbed Fe³⁺, 264, 265
Second generation photocatalysts. *See*
Visible-light-active photocatalysts,
TiO₂
Semiconductor-metal nanocomposites,
720–721
Semiconductor photocatalysts, 624–625
Semiconductor/zeolite photocatalyzed
syntheses, 638
Sensors, 725
Silica-supported TiO₂, 420–422
Single-site TiO₂ photocatalysts
design and development, visible-light
responsive
time profiles, NO decomposition,
229, 230
transition metal ion implantation, 229
V-Ti-HMS, diffuse reflectance
UV-vis absorption spectra,
229, 230
excitation and charge separation, 218
excited states and reactivity

- ligand-to-metal charge transfer transition (LMCT), 221
- photoluminescence quenching, (ex-Ti-oxide/Y-zeolite), 222
- radiative decay process, 221
- HOMO, 218
- LUMO, 218
- Nitric oxide (NO) photocatalytic decomposition
 - coordination number vs. selectivity, 223
 - N₂ formation, efficiency and selectivity, 223
 - reaction mechanism, 223, 224
- organic compounds, size-screening oxidation
 - effective molecular width (EMW), 227
 - molecular shave transformation, 228
 - titanosilicate molecular sieves (TS-1 and TS-2), 226–227
- particle size reduction, 218
- photocatalytic reduction, CO₂ with H₂O
 - CH₄ and CH₃OH yields, 225, 228
 - Gibbs free energy, 225
 - H₂O adsorption isotherms, 225, 226
 - hydrophilic–hydrophobic property, zeolite cavities, 225
- preparation of
 - hydrothermal synthesis, 219
 - ion-exchange method, 219
 - XANES and FT-EXAFS, 220–221
- size quantization effect, 218, 229
- S-/N-doped TiO₂ powder
 - absorption spectra, 260–262
 - ESR spectra, 261–264
 - physical properties, 257, 258
 - preparation of, 255
 - reduction and air oxidation, 256
- Solid-state DSSC, 571–572
- Solid-state thin film solar cell
 - photovoltaic cell performance, SCs and DSSCs
 - Cu₂O/Vis-TiO₂/ITO and CuI/Vis-TiO₂/ITO electrodes, 563–567
 - double-layered TiO₂ thin film electrodes, 567–568
 - UV-TiO₂/ITO-PEN and vis-TiO₂ /ITO-glass electrodes, 570
 - UV-TiO₂ /Vis-TiO /ITO, 568–570
 - Vis-TiO₂ /N719/CuI/Au system, 571–572
 - Vis-TiO₂ thin film electrodes, 560–563
- RF-MS deposition method, 560
- Solvothermal method. *See* Titanium oxide-based powders
- Sputtering parameters, effect of
 - conduction band (E_{CB}) and valence band (E_{VB}) energy levels, 549, 550
 - depth distribution profiles, 547, 548
 - quantum yields, H₂ and O₂ evolution, 548, 549
 - time profile, 550, 551
 - UV–vis transmission spectra, 547
- s-triazines, 371–373
- Structure directing agents (SDA), 219, 220
- Sulfated TiO₂, 422–424
- Sulfur-based organic compounds. *See* Photocatalytic transformations, sulfur-based organic compounds
- Sulfur doped titanium oxide, 60–61
- Super osseointegration
 - carbon element, inverse correlation, 707
 - orthopedic and dental implants, 700, 701
 - photofunctionalization, bioinert to bioactive, 709–710
 - therapeutic significance, 710–711
- UV treated titanium
 - biocompatibility and effectiveness, 708–709
 - bone cell affinity, 707–708
 - bone-titanium integration, 704–706
 - in vivo* implant fixation, 703–704
 - osteoblasts, 701–703
- Surface band bending, 191, 193
- Surface chemistry, TiO₂
 - calcination effects
 - acetic acid decomposition, 213–214
 - OH LIF intensity, 208
 - surface OH groups, 210–211
 - trapped holes, ESR spectroscopy, 208–210
 - OH radicals
 - formation mechanism, 211–213
 - laser induced fluorescence (LIF) method, 206–208
- Surface phase significance, photocatalysis. *See* Titania phase transformation
- Surface phase structures
 - bulk rutile and surface anatase content, 177, 178
 - surface-phase junction, 179
 - TiO₂(A)/TiO₂(R), SEM, 179, 180
 - wet impregnation method, 179
- Surface wettability, TiO₂ thin films
 - binary oxide films, 144–145

- hydrophilic conversion, mechanism, 540–541
- photocatalytic oxidation, hydrocarbons, 538–539
- UV light irradiation, effect, 536–539
- Synthetic dyes
 - acid orange 7, 381–382
 - chemical structures, 379–380
 - ethyl orange, 384
 - methyl orange, 382–384
- T**
- TD. *See* Thermal decomposition method
- Temperature-programmed desorption (TPD) spectra
 - CO₂, 42–43
 - features, 44
 - O₂, 43
- Thermal decomposition (TD) method, 122
- Thin film photochemical reactor. *See* Immobilized TiO₂, gas-phase elemental mercury
- Thin film preparation
 - highly transparent TiO₂
 - clear interference fringes, 137
 - film thickness, 137, 138
 - photocatalytic reactivity vs. BET surface area and wavelengths, 139
 - preedge peaks, XANES spectra, 137
 - UV-vis absorption (transmittance) spectra, 137, 138
 - TiO₂/SiO₂ and TiO₂/B₂O₃ binary oxide
 - photocatalytic reactivity, 142–144
 - structure and optical property, 139–142
 - surface wettability, 144–145
 - well-defined TiO₂
 - accelerated ion-solid surface interactions, 135–136
 - ICB deposition method, schematic diagram, 136–137
- Thin films, TiO₂
 - photocatalytic activity, 129–130
 - preparation of, 128–129
- TiO₂ based composites, applications
 - electron trapping and storage
 - Ag core-TiO₂ shell nanostructures, 723–725
 - photochromic and electrochromic effects, 721–723
 - photocatalysis
 - advanced oxidation processes (AOP), 719–720
 - photoinduced charge transfer processes, 718
 - semiconductor-metal nanocomposites, 720–721
 - photocatalyst-based hybrid methanol fuel cells, 731–732
 - photoelectrochemical solar cells
 - carbon nanotubes, 730–731
 - dye-sensitized solar cells (DSSC), 726
 - quantum dot sensitized solar cells (QDSSC), 727–730
 - sensors, 725
- TiO₂-coated optical fiber
 - catalytic photoreduction, CO₂ in, 690–694
 - characterization of, 685–687
 - light transmission, 675, 676
 - preparation of, 678–679
- TiO₂/InVO₄, sunlight system development
 - characterization
 - nitrogen-sorption isotherms and pore size distribution plot, 465
 - TEM image, 466
 - ultraviolet photoelectron spectra, 468, 469
 - visible light absorption spectra, 468
 - X-ray photoelectron spectra (XPS), 467, 468
 - XRD patterns, 466, 467
 - fabrication, 465
 - photocatalytic performance, 470–473
 - photochemical process, 461–463
 - sensitization, 463–464
- TiO₆ octahedral chains, 278
- TiO₂ property effect, 360–361
- TiO₂-silica gel (SiO₂) composites, 122–127
 - comparison with, 127
 - photocatalytic nitrogen oxides (NO_x) removal
 - activated carbon and hydroxyapatite effects, 126
 - fixed-bed continuous flow reactor, 125
 - Langmuirian adsorption parameters, 127
 - time course, NO_x concentration, 125, 126
 - water adsorption, 126
 - physical properties, 122
 - SEM photograph, 123, 124
 - specific surface areas (S_{BET}), 124
 - titanium(IV) tert-butoxide solvothermal decomposition, 122
 - XRD patterns, 123

- TiO₂ single crystal surfaces, photoreactions
 acetic acid
 electron/charge-transfer processes, 510
 ethane and methane formation, 509–510
 space charge region, 512–513
 steady-state acetic acid pressure,
 508, 509
 temperature programmed desorption
 (TPD) results, 508
 XPS C(1s), 512, 513
 band gap energy, 506
 ethanol photo-reactions
 Langmuir–Hinshelwood kinetics, 519
 photo-decomposition, 519, 520
 surface coverage, ethoxide species,
 517, 518
 temperature effect, 515
 XPS C(1s), 516, 517
- TiO₂/SiO₂ and TiO₂/B₂O₃ binary oxide films
 photocatalytic reactivity, 142–144
 structure and optical property
 absorption edges and transparency, 139
 coordination number and bond length,
 141, 142
 K-edge XANES spectra, 141
 UV-vis absorption (transmittance)
 spectra, 139, 140
 surface wettability, 144–145
- Titania (TiO₂)
 Au/Fe³⁺ on
 crystalline sizes, 30
 first-order kinetics model, 30
 photocatalytic degradation data, 30
 preparation procedure, 29
 synergistic effects, 31
 XRD patterns, 29
 bathochromic shift, light absorption, 7
 gold-deposited
 4f region, XPS spectra, 27, 28
 MO photodegradation rate, 28
 particle size and distribution, 25
 TEM observations, 27
 noble metal (Ag) deposited
 decomposed methyl orange percentage,
 25, 26
 deposition precipitation (DP)
 method, 25
 3d high-resolution XPS spectrum,
 25, 26
 reaction mechanism, 25
 nonmetal (N)-doped, preparation of
 dichlorophenol, probe organic pollutant
 molecule, 19
 fitting XPS spectra, N 1s region, 19, 20
 2p_{3/2} core levels, 19
 rhodamine B and 2,4-dichlorophenol
 decomposition rate, 21–22
 preparation of
 microemulsion-mediated hydrothermal
 method, 8–11
 ultrasound irradiation, 11–13
 synthesis, mesoporous
 anatase framework, 14
 average pore diameter, 16
 crystallization, 14
 hysteresis loop, 16
 nanocrystalline particle assembly,
 14–18
 photocatalytic activity testing, 17, 18
 Scherrer equation, 16
 thermal stability, 16
 Ti-10-U, TEM image, 14, 15
 type IV gas adsorption isotherm, 16, 17
 undoped vs. La³⁺ doped titania, 17
 wide-angle XRD patterns, 14
 transitional metal-doped, hydrothermal
 treatment
 interfacial charge transfer reaction, 24
 photodecolorized amounts of XRG,
 Fe-doped, 23
 UV-vis DRS, Cr³⁺ doped, 23, 24
- Titania phase transformation
 anatase and rutile spectral characteristics
 Raman spectra, 158, 159
 UV-vis diffuse reflectance spectra,
 157, 158
 anatase vs. rutile phase, 154
 elevated calcination temperatures
 agglomerated particles, 171–172
 microstructure, 170
 nucleation modes, 161
 phase transformation scheme, 171, 172
 rutile particle growth, TEM, 161, 163
 rutile phase weight percentage, 165–166
 visible Raman spectra, anatase-rutile
 mechanical mixture, 160, 161
- La₂O₃ loading
 characteristic bands, 173
 defect sites, 177
 monolayer dispersion capacity, 177
 particle size, 175
 TiO₂-900 vs. La₂O₃/TiO₂, TEM
 micrographs, 175
 semiquantitative analysis, phase
 composition, 159–160
 surface phase structures

- bulk rutile and surface anatase
 - content, 177, 178
 - surface-phase junction, 179
 - TiO₂(A)/TiO₂(R), SEM, 179, 180
 - wet impregnation method, 179
 - UV Raman spectroscopy
 - fluorescence interference, 156
 - light scattering process, 155
 - limitations, 155, 156
 - scattering intensity, 156
 - zirconia phase evolution, 156, 157
 - Titanium oxide (TiO₂)
 - acetic acid
 - electron/charge-transfer processes, 510
 - ethane and methane formation, 509–510
 - space charge region, 512–513
 - steady-state acetic acid pressure, 508, 509
 - temperature programmed desorption (TPD) results, 508
 - XPS C(1s), 512, 513
 - ethanol photo-reactions
 - Langmuir-Hinshelwood kinetics, 519
 - photo-decomposition, 519, 520
 - surface coverage, ethoxide species, 517, 518
 - temperature effect, 515
 - XPS C(1s), 516, 517
 - immobilization, 428–432
 - surface modification
 - noble metal deposition, 419–420
 - silica-supported TiO₂, 420–422
 - sulfated TiO₂, 422–424
 - transition metal doping, 417–419
 - Titanium oxide-based powders
 - high activity photocatalyst design, 115
 - hydrothermal reactions, 114
 - nanocrystalline
 - anatase-type, 115–118
 - brookite-type, 119–122
 - semiconductor photocatalysts, 114
 - solvothermal method, 114
 - thin films
 - photocatalytic activity, 129–130
 - preparation of, 128–129
 - TiO₂-silica gel (SiO₂) composites
 - comparison with, 127
 - photocatalytic nitrogen oxides (NO_x) removal, 124–127
 - physical properties, 122
 - SEM photograph, 123, 124
 - specific surface areas(S_{BET}), 124
 - titanium(IV) ter-butoxide solvothermal decomposition, 122
 - XRD patterns, 123
 - Titanosilicate molecular sieves (TS-1 and TS-2)
 - MFI and MEL structure, 227
 - pore dimensions, 227
 - Total organic carbon (TOC)
 - normalized temporal decrease, 328, 329
 - pesticides, 369
 - photo-assisted mineralization, 326
 - sulfur-based organic compounds, 593
 - Transition metal doping, 417–419
 - Transition metal-ion doped titanium dioxides
 - Au-doped TiO₂, 54
 - cerium(III)-doped TiO₂, 56
 - Cr ion-doped TiO₂, 50–52
 - DRS spectra, 52
 - RF-MS deposition, 50
 - UV-vis absorption spectra, 50–51
 - UV-vis transmittance spectra, 52
 - XAFS spectra, 51
 - Fe ion-doped TiO₂
 - flame spray pyrolysis, 53
 - UV-visible DRS spectra, 53–54
 - zinc-ferrite doped titania, 54, 55
 - platinum-loaded TiO₂, 55
 - Two-dimensional capillary effect, 529
- U**
- Undoped (pristine) TiO₂
 - photoactivity
 - AB1 and AB2 absorption bands, 45
 - adsorbed organic impurity removal, 41–42
 - carbonaceous species type, 41
 - color centers, 41–42
 - flame reactor method, 38
 - O₂ and CO₂ TPD spectra, 42–44
 - photostimulated adsorption of H₂ and O₂, quantum yields, 38–40
 - pyrolysis, 41
 - radio-frequency-magnetron sputtering (RF-MS) deposition method, 42
 - preparation and characteristics
 - band structure, 47–48
 - energy release, residual oxidation, 46–47
 - hydrolysis and calcination, 45–46
 - sol-gel synthesis, 48, 49
 - Ti(i-PrO)₄, 45
 - Ti(n-BuO)₄, 48–49

- upconversion luminescence agent, 50
 - XPS spectra, 48–49
 - UV light irradiation effect
 - hydrogen bonded structure, H₂O molecules components, 533
 - deconvoluted spectra, 533
 - H₂O clusters, structure models, 534, 535
 - H₂O filter, 531–533
 - hydrogen-bond acceptor and donor, 533, 534
 - NIR absorption spectra, 533, 535
 - surface wettability, TiO₂ thin films
 - hydrophilic conversion, mechanism, 540–541
 - photocatalytic oxidation, hydrocarbons, 538–539
 - UV Raman spectroscopy
 - fluorescence interference, 156
 - light scattering process, 155
 - limitations, 155, 156
 - scattering intensity, 156
 - zirconia phase evolution, 156, 157
 - UV system development
 - carbon deposition, suppression of, 458–459
 - electron-hole separation, 459–460
 - OH radicals formation, 460–461
 - photochemical process, 461–463
 - system efficiency, increase, 455–458
 - UV-TiO₂/ITO-PEN and Vis-TiO₂/ITO-glass electrodes, 570
 - UV-TiO₂/Vis-TiO/ITO, 568–570
 - UV treated titanium
 - biocompatibility and effectiveness, 708–709
 - bone cell affinity, 707–708
 - bone-titanium integration, 704–706
 - in vivo* implant fixation, 703–704
 - osteoblasts, 703–704
- V**
- Visible-light-active photocatalysts, TiO₂
 - anion-doped TiO₂, 38
 - band gap energy calculations, 47–59
 - band gap narrowing, 66–69
 - catalytic efficacy, 37
 - flatband potentials (V_{fb}), 37
 - heterogeneous photocatalysis, 36–37
 - optical properties, 59–66
 - photoactivated semiconductor particles, 37
 - photo-induced surface redox, 37–38
 - preparation and characteristics
 - anion doped specimens, 56–81
 - transition metal-ion doped specimens, 50–56
 - undoped specimens, 45–50
 - pristine first generation material, 37
 - semiconductor particulate systems, 36
 - sensitizers, 36
 - solar energy conversion, 36–37
 - undoped (pristine) TiO₂ photoactivity
 - AB1 and AB2 absorption bands, 45
 - adsorbed organic impurity removal, 41–42
 - carbonaceous species type, 41
 - color centers, 41–42
 - diffuse reflectance spectra, 6–7
 - flame reactor method, 38
 - intrinsic defects formation, 7–8
 - O₂ and CO₂ TPD spectra, 42–44
 - photostimulated adsorption of H₂ and O₂, quantum yields, 38–40
 - pyrolysis, 41
 - radio-frequency-magnetron sputtering (RF-MS) deposition method, 42
 - Visible light-assisted photomineralization, 367
 - Visible light responsive photocatalysts, TiO₂
 - anatase-TiO₂ morphological characteristics, 279
 - anatase vs. rutile phase, 278
 - chemical methods
 - binary oxide formation, 247–249
 - electronic structure control, 235–236
 - metal-doping, 236–240
 - nonmetal doping, 241–247
 - photocatalytic mechanism, dye-sensitized, 235, 236
 - crystallographic phases, 278
 - doping
 - with electronegative elements, 290–296
 - with metal cations, 281–290
 - physical and electronic characteristics, 279–280
 - drawback, 278
 - features, 278
 - sensitizers, 278
 - solid semiconductors, 277
 - TiO₆ octahedral chains, 278
 - Visible light-responsive photocatalysts, TiO₂ thin film
 - absorption mechanism
 - surface morphology and roughness, 310
 - Ti/O ratios, depth profiles, 311–312
 - physical and optical properties, 304–306
 - particle size estimation, 305, 306

- UV-vis absorption (transmittance) spectra, 304, 305
 - XRD patterns, 305, 306
 - preparation of
 - ion production, sputtered, 304
 - RF-MS deposition method, 303–304
 - sputtering target, 304
 - various PVD methods, 303
 - preparation on polycarbonate substrates
 - bandgap excitation, 313
 - contact angle, 314
 - photo-induced superhydrophilicity, UV light intensity effect, 312
 - sputtering gas pressures, 312, 313
 - surface wettability, 314
 - UV light
 - preparation temperature effect, 307, 308
 - reaction time profiles, 307
 - visible light
 - preparation temperature effect, 308–310
 - reaction time profiles, 308, 309
 - Visible light-responsive TiO₂ (Vis-TiO₂) thin film. *See* Hydrogen production, photocatalysis
 - Vis-TiO₂/N719/CuI/Au system, 571–572
 - Vis-TiO₂ thin film electrodes, 560–563
- W**
- Water decomposition, photocatalysis. *See* Hydrogen production, photocatalysis
- Water-splitting reaction**
- chemical etching, effect of
 - cyclic voltammogram, 553
 - incident photon-to-current conversion efficiency (IPCE), 552–553
 - SEM images, 554
 - sunlight-gathering system, 554, 555
 - nitrogen substitution, effect of
 - quantum yield/APCE, 558
 - relative photocurrent, 557
 - UV–vis absorption spectra, 556, 557
 - sputtering parameters, effect of
 - conduction band (E_{CB}) and valence band (E_{VB}) energy levels, 549, 550
 - depth distribution profiles, 547, 548
 - quantum yields, H₂ and O₂ evolution, 548, 549
 - time profile, 550, 551
 - UV–vis transmission spectra, 547
- Window MOPAC program, 327
- X**
- X-ray photoelectron spectra (XPS) C(1s), 467, 468
 - acetic acid, TiO₂, 512, 513
 - ethanol photo-reactions, TiO₂, 516, 517
- Z**
- Zeolite cavities, 225